INTEGRATING PALEOCLIMATE, STRATIGRAPHY, SEDIMENTOLOGY & PALEONTOLOGY IN HUMAN EVOLUTION AND DISPERSAL STUDIES - FROM EARLY HOMININS TO THE HOLOCENE

EDITED BY: Verena E. Foerster, Christian Zeeden and Annett Junginger
PUBLISHED IN: Frontiers in Earth Science

frontiers Research Topics

frontiers

ISSN 1664-8714
ISBN 978-2-88976-209-5
DOI 10.3389/978-2-88976-209-5

About Frontiers

Frontiers is more than just an open-access publisher of scholarly articles: it is a pioneering approach to the world of academia, radically improving the way scholarly research is managed. The grand vision of Frontiers is a world where all people have an equal opportunity to seek, share and generate knowledge. Frontiers provides immediate and permanent online open access to all its publications, but this alone is not enough to realize our grand goals.

Frontiers Journal Series

The Frontiers Journal Series is a multi-tier and interdisciplinary set of open-access, online journals, promising a paradigm shift from the current review, selection and dissemination processes in academic publishing. All Frontiers journals are driven by researchers for researchers; therefore, they constitute a service to the scholarly community. At the same time, the Frontiers Journal Series operates on a revolutionary invention, the tiered publishing system, initially addressing specific communities of scholars, and gradually climbing up to broader public understanding, thus serving the interests of the lay society, too.

Dedication to Quality

Each Frontiers article is a landmark of the highest quality, thanks to genuinely collaborative interactions between authors and review editors, who include some of the world's best academicians. Research must be certified by peers before entering a stream of knowledge that may eventually reach the public - and shape society; therefore, Frontiers only applies the most rigorous and unbiased reviews.
Frontiers revolutionizes research publishing by freely delivering the most outstanding research, evaluated with no bias from both the academic and social point of view. By applying the most advanced information technologies, Frontiers is catapulting scholarly publishing into a new generation.

What are Frontiers Research Topics?

Frontiers Research Topics are very popular trademarks of the Frontiers Journals Series: they are collections of at least ten articles, all centered on a particular subject. With their unique mix of varied contributions from Original Research to Review Articles, Frontiers Research Topics unify the most influential researchers, the latest key findings and historical advances in a hot research area! Find out more on how to host your own Frontiers Research Topic or contribute to one as an author by contacting the Frontiers Editorial Office: frontiersin.org/about/contact

INTEGRATING PALEOCLIMATE, STRATIGRAPHY, SEDIMENTOLOGY & PALEONTOLOGY IN HUMAN EVOLUTION AND DISPERSAL STUDIES - FROM EARLY HOMININS TO THE HOLOCENE

Topic Editors:
Verena E. Foerster, University of Cologne, Germany
Christian Zeeden, Leibniz Institute for Applied Geophysics (LIAG), Germany
Annett Junginger, University of Tübingen, Germany

Citation: Foerster, V. E., Zeeden, C., Junginger, A., eds. (2022). Integrating Paleoclimate, Stratigraphy, Sedimentology & Paleontology in Human Evolution and Dispersal Studies - from Early Hominins to the Holocene. Lausanne: Frontiers Media SA. doi: 10.3389/978-2-88976-209-5

Table of Contents

frontiers | Frontiers in Earth Science

EDITORIAL
published: 29 April 2022
doi: 10.3389/feart.2022.892664

Editorial: Integrating Paleoclimate, Stratigraphy, Sedimentology, and Paleontology in Human Evolution and Dispersal Studies—from Early Hominins to the Holocene

Verena Foerster[1]*, *Christian Zeeden*[2] *and Annett Junginger*[3,4]

[1]Institute of Geography Education, University of Cologne, Cologne, Germany, [2]Leibniz Institute for Applied Geophysics (LIAG), Hannover, Germany, [3]Department of Geoscience, Eberhard Karls University Tübingen, Tübingen, Germany, [4]Senckenberg Centre for Human Evolution and Palaeoenvironment, Tübingen, Germany

Keywords: paleoclimate, paleoecology, paleontology, human evolution, dispersal of *Homo sapiens*

Editorial on the Research Topic

Integrating Paleoclimate, Stratigraphy, Sedimentology, and Paleontology in Human Evolution and Dispersal Studies—from Early Hominins to the Holocene

In the last decade, both timeframe and regional understanding of human evolution and dispersal has been under profound revision due to a number of new fossil and artifact finds, new advances in dating techniques, fast growing genetic data availability, and comprehensive new insights into paleoenvironmental dynamics (Hublin et al., 2017; Stringer and Galway-Witham, 2017; Hershkovitz et al., 2018; Bergström et al., 2021). Long-established hypotheses on how climate change and human origins are interrelated have been challenged by those advances and force the community to spatio-temporally rethink human-climate concepts in a broader context (Scerri et al., 2018; Galway-Witham et al., 2019; Mounier and Lahr, 2019; Bergström et al., 2021). In order to evaluate the impact that different timescales and magnitudes of climatic shifts might have had on the living conditions of prehistoric humans, we need reliable and continuous reconstructions of paleoenvironmental conditions and fluctuations from the vicinity of paleoanthropological and archaeological sites (Cohen et al., 2016; Campisano et al., 2017; Litt et al., 2021; Cohen et al., 2022).

As a contribution towards a better understanding of these human-climate interactions across time and space, the main objective of this research topic (RT) was to showcase interdisciplinary work in (geo)archaeology, paleoecology, paleoclimate, stratigraphy, and paleoenvironmental reconstructions. New methods for dealing with challenging archive conditions and dating issues are constantly discussed in the community. Integrating those results across disciplines may contribute to providing an improved framework of external threshold conditions that may have been important in limiting but also facilitating population dynamics.

Twenty-one papers were published after peer reviews, comprising seventeen Original Research articles, one Brief Research Report, one Method paper and two Reviews. The contributions presented within the first part of this RT cover sites across Africa, as the region of modern human origins, the Nile Valley and the Levante, representing one of the major trajectories in human dispersal studies as well as paleoenvironmental research. A second focus of this issue is Eurasian climate dynamics during the last glacial cycle as relevant boundary conditions for early modern human occupation (or the lack thereof).

Edited and reviewed by:
Steven L. Forman,
Baylor University, United States

***Correspondence:**
Verena Foerster
V.Foerster@uni-koeln.de

Specialty section:
This article was submitted to Quaternary Science, Geomorphology and Paleoenvironment, a section of the journal Frontiers in Earth Science

Received: *09 March 2022*
Accepted: *06 April 2022*
Published: *29 April 2022*

Citation:
Foerster V, Zeeden C and Junginger A (2022) Editorial: Integrating Paleoclimate, Stratigraphy, Sedimentology, and Paleontology in Human Evolution and Dispersal Studies—from Early Hominins to the Holocene. Front. Earth Sci. 10:892664. doi: 10.3389/feart.2022.892664

HUMAN-CLIMATE INTERACTIONS ACROSS TIME AND SPACE: AFRICA

The first group of contributions focusses on human-climate interactions in Africa, highlighting studies from several key regions associated with milestones in human evolution across time.

Reporting from the Middle and Later Stone Age site of the Umhlatuzana rockshelter, South Africa, Reidsma et al. present a grid-based, multi-proxy geoarchaeological study that illustrates the relationship between environmental change and occupation intensity.

Highlighting a cluster of research activities from eastern Africa, Yost et al. present a phytolith and microcharcoal based record from the Turkana Basin WTK13 drill core in Kenya. A millennial-scale resolution from one of the proven habitats of *Homo ergaster/erectus* revealed cyclic (21-ka) changes in precipitation, fire activity and grass community composition between 1.87 and 1.38 Ma. Phytoliths indicate that Nariokotome Boy walked across a landscape that was seasonally wet, densely vegetated, and dominated by short stature grasses, sedges, and other herbaceous plants. Those tectonic landscapes are characterized by highly variable soil properties creating potentially attractive habitats for animals and humans. The study by Kübler et al. reveals strong correlations between the geotectonic setting and long-term soil nutrient status in the southern Kenya Rift. Importantly, known hominin sites in the region are located either along corridors of long-term Calcium availability or at short-term nutrient hotspots potentially related to active CO_2 degassing along active fault zones. Results imply a strategic advantage of nutrient-rich regions for hominin subsistence strategies, such as provision of predictable constraints on the distribution and mobility of grazing animals in complex tectonic settings.

Presenting first results from an advanced hyperspectral bidirectional analysis on discrete samples from the 620-ka Chew Bahir record in southern Ethiopia, Arnold et al. contribute to an advanced and refined proxy understanding by applying an innovative and minimally invasive method. Specific absorption bands have been found to be diagnostic for the occurrence of clay minerals, analcime and calcite, with analcime pointing at arid to hyper arid intervals. The hyper spectral based findings enable the authors to test proxy formation and weathering models on the one hand and allow for new capacities for climate-relevant studies in the future on the other hand. With the application of cross-species hybridization capture to lacustrine sediment samples from the Chew Bahir record, Krueger et al. were able to determine biological taxa from sedimentary ancient DNA (sedaDNA) traces. The frontier in sedaDNA research could be extended by this contribution as recovering sedaDNA fragments from especially tropical archives had proven to be challenging due to typically highly degraded DNA. In this contribution, different taxonomic groups as far back as ~150 ka BP, give direct insights into changes in the specific biodiversity during major eastern African climate shifts at Chew Bahir.

As an alternative age-model approach and to significantly increase the accuracy of tuned age models, Duesing et al. test a new wavelet-based multiband agemodeling technique (MUBAWA) on a synthetic data set and the Chew Bahir composite core. Unlike in traditional tuning approaches, the authors use here the application of an adaptive bandpass filter that is able to address the problem of continuous sedimentation rate changes, which naturally occur during lacustrine sedimentation. Based on modern surface samples within the Chew Bahir Basin, Gebregiorgis et al., provide information on modern sedimentation processes and authigenic mineral formation in the basin and catchment. This is an important pre-requisite for the understanding of chemical proxy formation through time and therewith ultimately contributes to an improved paleoclimate proxy interpretation. Using whole-rock and authigenic clay geochemistry and geochemical modeling to understand the hydrogeochemical processes in the paleo-lake and saline brines, the authors find modern analogues to Late Quaternary sediments that were deposited during known past humid or arid intervals.

The timing and nature of the insolation controlled but spatially complex African Humid Period (AHP) (~15–5 ka) (e.g., Shanahan et al., 2015) has been an intensely debated topic and several contributions can report new data on this crucial time interval.

Fischer et al. have addressed the void of the unknown pace and magnitude of past moisture fluctuations in southern Ethiopia during the last 20,000 years by applying a new lake balance modeling approach. They combine a Hydro-balance model with a Surface Energy Balance Algorithm (SEBAL) for the last orbital driven dry-wet-dry cycle of the AHP. Therewith Fischer et al. contribute new information on the nature, pace and magnitude of pronounced hydroclimatic shifts and can moreover provide a first regional order-of-magnitude range for hydroclimatic changes on much longer time scales. A geoarchaeological study by Hensel et al. at Sodicho Rockshelter in the southwestern Ethiopian Highlands dates back to ~27 ka BP and provides evidence from sedimentological and geochemical analyses for high altitude settlements by hunter-gatherers during the Late Pleistocene and Holocene, including the arid Last Glacial Maximum (~21 ± 2 ka). The occupation phases were interrupted due to past environmental changes including the AHP and Holocene volcanic activities. The results partially reduce a chronostratigraphic gap corresponding to MIS2, which is common in the Horn of Africa. Jaeschke et al. provide new insights into the 12,500-years moisture history of the Ethiopian Highlands, preserved in Lake Dendi sediments. A combination of plant-wax δD and δ13C values alongside with palynological data showcases the sensitive vegetational response of the high mountain area to shifting monsoonal regimes of moisture influx and therewith contributes new insights into the much debated termination of the AHP.

Much further to the N-West, a set of mid- to late Holocene isotope-based reconstructions on bivalve shells and fish otoliths from Banc d'Arguin, a paleo-estuary in the coastal zone of Mauritania, also addresses the AHP. Based on δ18O records

and Sr isotope ratios, the contribution by Höpker et al. present evidence for a rather gradual aridification pattern at the end of the AHP.

DISPERSAL OUT-OF-AFRICA AND BEYOND

The timeframe of the worldwide expansion of modern humans as the latest major dispersal event out-of-Africa is generally agreed to have occurred after ~50–60 ka BP as genetic data suggests (e.g., Galway-Witham et al., 2019; Bergström et al., 2021). The expansion along the Nile Valley and into the Levante represents one of the major dispersal routes of modern humans but also earlier human and hominin migration waves (Schultz and Maslin, 2013; Stringer and Galway-Witham, 2017; Litt et al., 2021). The integration of paleoenvironmental records, findings from paleoanthropological archaeological sites and a robust chronology play an important role to an enhanced understanding of human-climate interactions in human dispersal studies (Litt et al., 2021).

Integrating a variety of studies from geology, paleoenvironmental, anthropological, genetic, and archaeological research results, Leplongeon gives an interdisciplinary overview about the role that the Nile valley could have played as an environmental refuge area and/or a natural pathway and corridor facilitating dispersal post "Out-of-Africa" at the end of the Pleistocene between 28,000 and 15,000 years ago. Recent genetic data highlighted complex population dynamics in northern Africa, including "back-into-Africa" dispersals, but the role of the main Nile Valley in these population dynamics remains unclear. Excavations at the site MAR-1 (S-Greece) revealed evidence of hominin presence ~444 ka ago (~MIS12) and Bludau et al. present a first multi-proxy paleoenvironmental reconstruction from this new paleoanthropological key site. The results suggest the site to be a protected region surrounded by high mountains and under the constant influence of water, thus representing potentially ideal refugium conditions for hominins.

A suite of contributions discusses the paleoenvironmental context of early humans, and their possible habitats in Eurasia. This includes several studies on loess-paleosol sequences as well as several contributions which have both a methodological, provenance and a paleoenvironmental focus. Most contributions from Eurasia study loess-paleosol sequences in the Danube catchment, but two papers also explore the Rhine valley in Germany, and the north-western part of the Indian subcontinent.

While for Asia a suite of high-resolution multi-proxy datasets exist from loess, such studies are yet missing or sparse in Europe. Laag et al., provide a multi-proxy ~430 ka dataset from a loess-paleosol sequence in the Middle Danube Basin. Their study combines rock magnetism and colorimetry in a novel way, and demonstrates the added value of combing color and rock magnetic information. Advanced rock-magnetic experiments enabled to identify and characterize preserved (crypto-) tephra layers which provide great potential for gaining absolute age control in loess deposits when traditional radiometric dating methods reach their dating limits. Pötter et al. provide an impressive amount of both grain size and geochemical data from the Lower Danube Basin. Regarding the provenance, the authors find a close relation to loess in the Middle Danube Basin, as well as a transitional (not sharp) north/south separation of the Lower Danube loess.

Fitzsimmons et al. argue for a more holistic integration of paleoenvironmental and archaeological datasets, even in cases where archaeological evidence may be not be particularly rich or diagnostic. Authors make their point using two Paleolithic open-air "off-sites" from Romania, where a combination of sedimentological and pedological description and luminescence dating facilitates the placement of the archaeological finds in the wider paleoenvironmental and archaeological context.

Loess palaeosol sequences provide important evidence about the climate when anatomically modern humans colonized Europe. However, one of the main obstacles for the interpretation of climatic and environmental information preserved in these sedimentary archives is the uncertainty of the age-depth relationship. In order to create a robust age model with reduced uncertainty, Scheidt et al. performed a comparative study of different dating methods on a loess-palaeosol sequence near Lake Balta Alba in Romania and conclude that ages should be obtained using at least two independent, complementary dating methods. Nett et al. investigated the sedimentological and archaeological context and content of the archaeological Site Crveka-At in the Middle Danube Basin. The complex and challenging-to-interpret grain size distributions imply archaeological site formation in contrasting depositional environments typical for fluvial channels, lakeshores, and alluvial fan or delta settings. The study confirms that the Crvenka-At locality is an Aurignacian site with multiple-occupations, dated to 36.4 ± 2.8 ka. Staying in the Danube, Zeeden and Hambach provide data of magnetic susceptibility properties and especially the Anisotropy of the magnetic susceptibility from the famous archaeological site Willendorf (Austria). They investigate the site formation of the Willendorf archaeological site using mainly the anisotropy of the magnetic susceptibility.

The inorganic and organic carbon stable isotope signatures of the Remagen-Schwalbenberg Loess-Paleosol-Sequence in the Rhine valley are investigated by Vinnepand et al. Assessing both carbon pools facilitates insights into the carbonate metabolism and hence, sedimentary and pedogenic processes throughout the Upper Pleistocene at the site. The organic carbon stable isotope signature is regarded as a mixed signal influenced by sediment moisture regimes, decomposition, and stabilization that may be decoded in future contributions.

Finally, Dar and Zeeden review the current state of paleoenvironmental research and information derived from loess in Kashmir. While multiple studies have been carried out on the loess-paleosol sequences, high-resolution physical property data were yet sparse or missing. Yet, an integral picture of the Kashmir loess-pleosol sequences is missing,

while the potential of understanding Indian Monsoon dynamics better is enhanced.

This Research Topic summarizes recognizable progress that has been achieved in broadening methodological perspectives, connecting focus areas and thinking outside the box highlighting the integration of interdisciplinary research in human evolution and dispersal studies.

AUTHOR CONTRIBUTIONS

All three authors equally contributed to this Research Topic and wrote the Editorial, with VF and AJ focussing on the research activities in Africa and CZ highlighting the contributions in Eurasia and Europe. All authors have approved the Editorial for publication.

REFERENCES

Bergström, A., Stringer, C., Hajdinjak, M., Scerri, E. M. L., and Skoglund, P. (2021). Origins of Modern Human Ancestry. *Nature* 590, 229–237. doi:10.1038/s41586-021-03244-5

Campisano, C. J., Cohen, A. S., Arrowsmith, J. R., Asrat, A., Behrensmeyer, A. K., Brown, E. T., et al. (2017). The Hominin Sites and Paleolakes Drilling Project: High-Resolution Paleoclimate Records from the East African Rift System and Their Implications for Understanding the Environmental Context of Hominin Evolution. *PaleoAnthropology*, 1–43. doi:10.1130/abs/2017am-295426

Cohen, A., Campisano, C., Arrowsmith, R., Asrat, A., Behrensmeyer, A. K., Deino, A., et al. (2016). The Hominin Sites and Paleolakes Drilling Project: Inferring the Environmental Context of Human Evolution from Eastern African Rift lake Deposits. *Sci. Dril.* 21, 1–16. doi:10.5194/sd-21-1-2016

Cohen, A. S., Campisano, C. J., Arrowsmith, J. R., Asrat, A., Beck, C. C., Behrensmeyer, A. K., et al. (2022). Reconstructing the Environmental Context of Human Origins in Eastern Africa through Scientific Drilling. *Annu. Rev. Earth Planet. Sci.* 50, 451–476. doi:10.1146/annurev-earth-031920-081947

Galway-Witham, J., Cole, J., and Stringer, C. (2019). Aspects of Human Physical and Behavioural Evolution during the Last 1 Million Years. *J. Quat. Sci.* 34 (6), 355–378. doi:10.1002/jqs.3137

Hershkovitz, I., Weber, G. W., Quam, R., Duval, M., Grün, R., Kinsley, L., et al. (2018). The Earliest Modern Humans outside Africa. *Science* 359 (6374), 456–459. doi:10.1126/science.aap8369

Hublin, J.-J., Ben-Ncer, A., Bailey, S. E., Freidline, S. E., Neubauer, S., Skinner, M. M., et al. (2017). New Fossils from Jebel Irhoud, Morocco and the Pan-African Origin of *Homo sapiens*. *Nature* 546 (7657), 289–292. doi:10.1038/nature22336

Litt, T., Richter, J., and Schäbitz, F. (2021). *The Journey of Modern Humans from Africa to Europe. Culture-Environmental Interaction and Mobility*. Stuttgart: Schweizerbart Science Publishers.

Mounier, A., and Lahr, M. M. (2019). Deciphering African Late Middle Pleistocene Hominin Diversity and the Origin of Our Species. *Nat. Commun.* 10 (1), 3406–3413. doi:10.1038/s41467-019-11213-w

Scerri, E. M. L., Thomas, M. G., Manica, A., Gunz, P., Stock, J. T., Stringer, C., et al. (2018). Did Our Species Evolve in Subdivided Populations across Africa, and Why Does it Matter? *Trends Ecology Evolution* 33 (8), 582–594. doi:10.1016/j.tree.2018.05.005

Shanahan, T. M., McKay, N. P., Hughen, K. A., Overpeck, J. T., Otto-Bliesner, B., Heil, C. W., et al. (2015). The Time-Transgressive Termination of the African Humid Period. *Nat. Geosci* 8 (2), 140–144. doi:10.1038/ngeo2329

Shultz, S., and Maslin, M. (2013). Early Human Speciation, Brain Expansion and Dispersal Influenced by African Climate Pulses. *PLoS One* 8 (10), e76750. doi:10.1371/journal.pone.0076750

Stringer, C., and Galway-Witham, J. (2017). On the Origin of Our Species. *Nature* 546 (7657), 212–214. doi:10.1038/546212a

Conflict of Interest: The authors declare that the research was conducted in the absence of any commercial or financial relationships that could be construed as a potential conflict of interest.

frontiers in Earth Science

ORIGINAL RESEARCH
published: 29 November 2019
doi: 10.3389/feart.2019.00314

Pronounced Northwest African Monsoon Discharge During the Mid- to Late Holocene

Sebastian N. Höpker[1,2,3], Henry C. Wu[1]*, Peter Müller[1,4], Jean-Paul Barusseau[5], Robert Vernet[6], Friedrich Lucassen[7], Simone A. Kasemann[7] and Hildegard Westphal[1,2]*

[1] Leibniz Centre for Tropical Marine Research (ZMT) GmbH, Bremen, Germany, [2] Faculty of Geosciences, University of Bremen, Bremen, Germany, [3] Environmental Research Institute, School of Science, Faculty of Science and Engineering, University of Waikato, Hamilton, New Zealand, [4] BDG Berufsverband Deutscher Geowissenschaftler e.V., Bonn, Germany, [5] UMR 5110 Centre de Formation et de Recherche sur les Environnements Méditerranéens, University of Perpignan Via Domitia, Perpignan, France, [6] Institut Mauritanien de Recherches Scientifiques, Nouakchott, Mauritania, [7] Faculty of Geosciences and MARUM – Center for Marine Environmental Sciences, University of Bremen, Bremen, Germany

OPEN ACCESS

Edited by:
Michaël Hermoso, Université du Littoral Côte d'Opale, France

Reviewed by:
Anne-Marie Lezine, UMR 7159 Laboratoire d'Océanographie et du Climat Expérimentations et Approches Numériques (LOCEAN), France
Andrea Zerboni, University of Milan, Italy

***Correspondence:**
Sebastian N. Höpker
seb.hoepker@gmail.com
Henry C. Wu
henry.wu@leibniz-zmt.de

Specialty section:
This article was submitted to Quaternary Science, Geomorphology and Paleoenvironment, a section of the journal Frontiers in Earth Science

Received: *16 July 2019*
Accepted: *11 November 2019*
Published: *29 November 2019*

Citation:
Höpker SN, Wu HC, Müller P, Barusseau J-P, Vernet R, Lucassen F, Kasemann SA and Westphal H (2019) Pronounced Northwest African Monsoon Discharge During the Mid- to Late Holocene. Front. Earth Sci. 7:314. doi: 10.3389/feart.2019.00314

The mid- to late Holocene aridification pattern of NW Africa remains a matter of controversial debate. While many marine climate reconstructions indicate a relatively abrupt aridification at ~5.5 ka BP, terrestrial palaeoclimate records rather show a spatially and temporally heterogeneous transition towards the modern arid state. To bridge conflicting evidence, we analysed high-resolution (sub-seasonal) ontogenetic oxygen isotope ($\delta^{18}O$) records and bulk $^{87}Sr/^{86}Sr$ ratios of bivalve shells and fish otoliths of estuarine-associated species. Samples were excavated from archaeological deposits formed during the mid- to late Holocene in a large palaeo-estuary east of the Banc d'Arguin, Mauritania. The mid-Holocene (~5.2 ka BP) $\delta^{18}O$ records indicated unrealistically high water temperatures when assuming a modern value for $\delta^{18}O_{Seawater}$, suggesting a substantial input of isotopically lighter water to the study area. Respective salinity estimates consistently indicated persistent monsoonal discharge. Moreover, $^{87}Sr/^{86}Sr$ ratios of bivalve shells deviated considerably from the rather stable global seawater composition, further supporting the presence of significant terrestrial runoff between 5.0 and 5.3 ka BP. Altogether, our results support doubts regarding an abrupt termination of the African Humid Period (AHP) in the coastal areas of NW Africa, and show that fully marine conditions were established along the Banc d'Arguin by ~3.0 ka BP.

Keywords: African Humid Period, Mauritania, sclerochronology, bivalves, fish otoliths, archaeology, oxygen isotopes, $^{87}Sr/^{86}Sr$

INTRODUCTION

Previous studies consistently show that large parts of the present-day Sahara and Sahel region were dominated by dense savannah and shrub vegetation between ~15 and ~5 ka BP, the so-called African Humid Period (AHP) (Ritchie et al., 1985; deMenocal et al., 2000; Kuhlmann et al., 2004; Holz et al., 2007; Kröpelin et al., 2008; Roberts, 2014). During this period and several preceding humid episodes throughout the late Quaternary, increased Northern Hemisphere summer insolation induced a northward migration of the Intertropical Convergence Zone (ITCZ)

and the associated rain belt, and a significant intensification of the African monsoon. Across northern Africa, remnants of large palaeo-lakes and extensive fluvial networks illustrate the substantially altered hydroclimate during these periodic wet phases, which allowed for widespread human occupation of landscapes that are nowadays marked by (hyper)arid conditions with sparse or no vegetation (Kuper and Kröpelin, 2006). Enhanced monsoonal precipitation supplied a major drainage system covering much of modern Mauritania and the Arguin Basin during the AHP, with densely distributed archaeological shell midden deposits depicting numerous mid- to late Holocene settlements throughout the palaeo-estuary (Skonieczny et al., 2015) (**Figure 1**).

The exact timing and nature of the termination of the AHP and the transition to the modern arid state, however, remain a matter of considerable debate (Kröpelin et al., 2008; Claussen et al., 2013; Pausata et al., 2016). Many open marine dust records indicate an abrupt aridification around 5.5 ka BP, potentially triggered by bio-geophysical feedback mechanisms amplifying the gradually declining insolation during the mid- to late Holocene (deMenocal et al., 2000; Kuhlmann et al., 2004; McGee et al., 2013) (**Figures 2A,B**). Similarly, sedimentary leaf wax records from the Gulf of Guinea have recently been used to argue for a rapid termination of the AHP (Collins et al., 2017). The records ultimately linked the aridification to extratropical temperature changes and a non-linear response that resulted in the alteration of atmospheric circulation patterns. However, reconstructions of humidity and recent novel quantitative estimations of palaeo-precipitation using sediment cores retrieved off the coast of NW Africa depict a more gradual decrease in rainfall towards modern conditions (Tjallingii et al., 2008; Tierney et al., 2017) (**Figures 2C,D**). This is further supported by highly resolved dust records in a sediment core from the Mauritanian continental shelf (Hanebuth and Henrich, 2009). Various terrestrial and archaeological deposits from coastal settlements in turn suggest a spatially as well as temporally heterogeneous change in hydroclimate during the mid- to late Holocene (**Figure 2F**). These records provide evidence of a more gradual transition to the present-day arid state (Vernet and Tous, 2004; Vernet, 2007; Kröpelin et al., 2008; Armitage et al., 2015; Bloszies et al., 2015; Shanahan et al., 2015). Examples include several terrestrial and continental records from pollen-based reconstructions of hydroclimate and dendrochronology from the central Sahara that indicate spells of drought and regional progressive desertification (Cremaschi and Zerboni, 2009; Lézine, 2009; Lézine et al., 2011), which is further supported by palaeo-lake deposits, such as Lake Yoa in Chad (Lézine et al., 2011). Sea surface temperatures of the eastern tropical Atlantic remained relatively constant and were similar to modern values throughout the Holocene (Zhao et al., 1995; Kim et al., 2007) (**Figure 2E**), possibly punctuated by variable coastal upwelling intensities in response to changes in the trade wind regimes (Talbot, 1981; Romero et al., 2008; Hély et al., 2014).

Considering the conflicting evidence from different proxy records, climate model simulations increasingly fail to reproduce the suggested abruptness of the mid-Holocene climate transition (Liu et al., 2007; Rachmayani et al., 2015; Shanahan et al., 2015; Pausata et al., 2016), and strongly underestimate reconstructed precipitation rates over NW Africa (Tierney et al., 2017). A number of studies have further noted that interpretations of different proxy systems, even within the same archive, may inherently lead to contrasting conclusions given the varying nature of the respective environmental controls (Castañeda et al., 2016). In consequence, we are still lacking a holistic understanding of the temporal and spatial aridification pattern of NW Africa during the Holocene, and subsequently of the underlying mechanisms governing the intensity and spatial extent of the West African Monsoon. This in turn prohibits reliable predictions regarding the response of the West African climate to future global changes.

In this study, we use oxygen isotope ($\delta^{18}O$) records of modern and archaeological bivalve shells (*Senilia senilis*) and catfish otoliths (*Carlarius* spp.) from the Banc d'Arguin, Mauritania, to complement conflicting evidence from marine and terrestrial proxy archives, and provide further information on the timing of the Holocene termination of monsoonal precipitation. Sub-seasonally resolved $\delta^{18}O$ records of both *S. senilis* shells and catfish otoliths have previously been shown to reliably trace environmental conditions, allowing for water temperature estimates with absolute uncertainties of $\leq 1.5°C$ (Surge and Walker, 2005; Lavaud et al., 2013; Müller et al., 2015). Variable growth patterns throughout the organisms' lifetimes, however, hamper a straightforward conversion of ontogenetic data from incrementally banded skeletal structures into time series of environmental parameters, such as temperature or salinity (Goodwin et al., 2003). In the absence of a standardised method, a vast range of approaches has been used to align biological proxy records with instrumental data. However, many methods are not readily traceable and consequently lack reproducibility to assess their reliability. To this effect, we used a linear interpolation technique developed by Müller et al. (2015), where the proxy records are mathematically aligned with environmental data via carefully determined temporal reference points. This method has been shown to allow for a flexible and transparent establishment of temporal frameworks for sclerochronological records that also accommodates for growth variations (Müller et al., 2015).

Given the association of the studied taxa with estuarine environments, their ontogenetic $\delta^{18}O$ signatures are predicted to be influenced by freshwater discharge with strong negative excursions in ambient $\delta^{18}O_{Water}$ values reflecting the drainage of isotopically lighter monsoon precipitation (Surge and Walker, 2005; Azzoug et al., 2012a,b). Therefore, ontogenetic $\delta^{18}O$ records are expected to show combined signals of seasonal water temperature and freshwater discharge during times of increased riverine input into the coastal zone of the Banc d'Arguin. Considering observations of relatively constant water temperatures in coastal NW Africa throughout the Holocene (Zhao et al., 1995; Kim et al., 2007), a disentangling of these combined signals is possible with the resulting $\delta^{18}O$-based salinity reconstructions expected to depict brackish conditions. Moreover, $\delta^{18}O$ records of specimen subject to monsoonal activity are expected to show generally more pronounced seasonal signals.

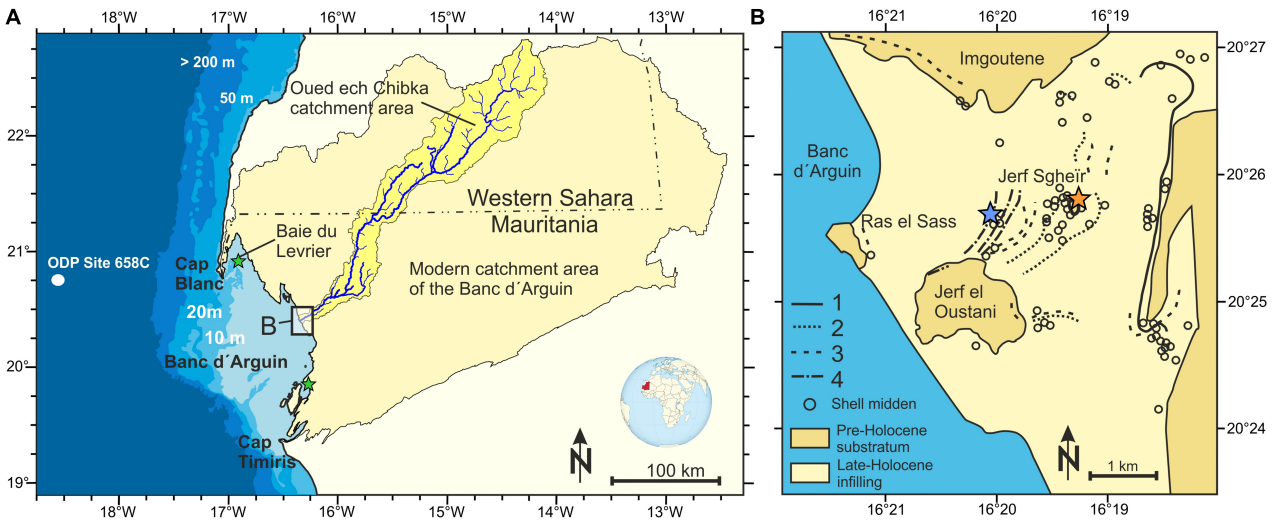

FIGURE 1 | Research area at Banc d'Arguin, Mauritania, NW Africa. **(A)** NW African coastline bathymetry with the shallow Banc d'Arguin, and the modern catchment area draining into the Banc d'Arguin. Approximate sample locations of modern catfish otoliths (Baie du Lévrier) and bivalve shells (near Iwik, southern part of the Banc d'Arguin; see Lavaud et al., 2013 for details) are indicated by green stars. **(B)** Close-up of the study site in the hinterland of Ras el Sass in the mouth of a large palaeo-estuary (Skonieczny et al., 2015). The location of shell midden alignments and beach ridges show the human occupation pattern following the coastal progradation throughout the mid- to late Holocene: 1: > 5000 years BP according to archaeological evidence; 2: Jerf Sgheïr shell midden of this study (5320–5020 years BP); 3: Tintan group (4600–4000 years BP); 4: Last Neolithic groups (3300 years BP). Archaeological ages adapted from Barusseau et al. (2007). Approximate locations of mid-Holocene and late Holocene samples are indicated by orange and blue markers, respectively. The map and inlet map were created using the SRTM 1 Arc-Second (USGS, 2004) dataset (available at https://earthexplorer.usgs.gov/). The catchment area in **A** was calculated using the SCALGO Live Global online platform (www.scalgo.com/live) based on World HydroSHEDS (Lehner et al., 2008, available at http://www.hydrosheds.org/). Maps were modified manually.

When using geochemical proxies from archaeological midden constituents, however, a potential alteration of the sample material due to pre-depositional cooking treatments needs to be considered. For instance, heating has been shown to potentially induce mineralogical phase changes (e.g. Andrus and Crowe, 2002; Milano and Nehrke, 2018) and/or microstructural alterations (e.g. Maritan et al., 2007; Cremaschi et al., 2015). Moreover, the original $\delta^{18}O$ signatures of skeletal aragonite can evidently be altered when subjected to prehistoric cooking methods, which may lead to considerable errors in palaeoenvironmental reconstructions (Andrus and Crowe, 2002; Milano et al., 2016; Müller et al., 2017). In this study, we use carbonate clumped isotope thermometry to evaluate the preservation state and reliability of proxy interpretations of samples used in this study. This method has recently been demonstrated as a valuable tool to detect and quantify such potential bias based on the temperature-dependent re-equilibration of clumped isotopes in aragonite (Müller et al., 2017).

To further support the ontogenetic $\delta^{18}O$ records, we present bulk strontium isotope ratios ($^{87}Sr/^{86}Sr$) from the two skeletal materials as an additional indicator for freshwater influx. $^{87}Sr/^{86}Sr$ signatures in biogenic carbonates effectively reflect the Sr isotopic composition of the ambient water during the incorporation of strontium into the carbonate structure due to the lack of any significant mass fractionation (Palmer and Edmond, 1989). Given the long residence time of Sr in the ocean, $^{87}Sr/^{86}Sr$ values of seawater are globally highly consistent [ca. 0.70918 ± 0.00001; two standard deviations (SD)] (Faure and Mensing, 2005) and have remained essentially constant over the past ~40 ka (Mokadem et al., 2015). Sr isotope signatures of riverine water are in turn primarily governed by the respective catchment geology, and are typically considerably different to those observed in seawater. While there is no modern freshwater influx available as reference along the Mauritanian coast, measurements of hinterland dust sources and sediments derived from granitic bedrock located in the palaeo-drainage area to the Banc d'Arguin consistently indicate more radiogenic $^{87}Sr/^{86}Sr$ values than those of seawater of up to 0.74 (e.g. Scheuvens et al., 2013; Zhao et al., 2018). Since Sr concentrations of seawater (ca. 7.74 ppm) are typically one to two magnitudes higher than those observed in average river water (Faure and Mensing, 2005), a pronounced deviation from the marine end-member in bulk otolith or bivalve samples is expected to reflect an influx of substantial volumes of riverine discharge to the organisms' habitat over their lifetime.

MATERIALS AND METHODS

Sample Material and Background

Modern sea catfish (*Carlarius parkii* and *Carlarius heudelotii*) otoliths were extracted from individuals caught by local fishermen in the central Baie du Lévrier in November 2011 (Müller et al., 2015) and in March 2012 (this study). Modern

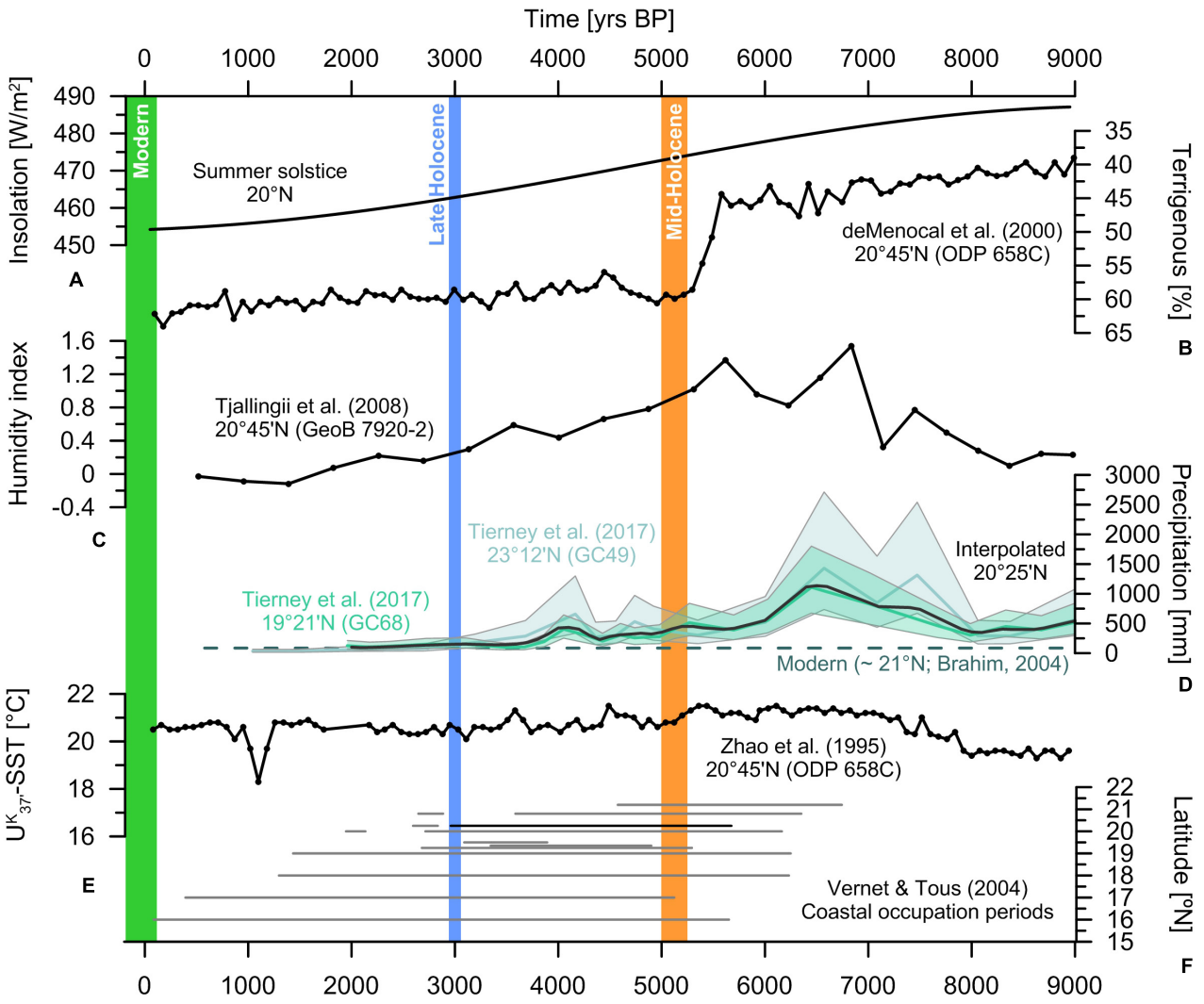

FIGURE 2 | Palaeoclimate records of NW Africa. **(A)** Summer (solstice) insolation at 20°N (Laskar et al., 2004). **(B)** Terrestrial dust export at ODP site 658C (deMenocal et al., 2000). **(C)** Continental humidity index based on grain-size measurements of GeoB 7920-2 (Tjallingii et al., 2008). **(D)** δD-based precipitation reconstruction (Tierney et al., 2017) with a temporal and spatial interpolation at 20°25°N and the modern annual precipitation at ~21°N (Brahim, 2004). **(E)** Holocene alkenone water temperature record from ODP site 658C (Zhao et al., 1995). **(F)** Periods of coastal occupation along the West African coast (Vernet and Tous, 2004). The Ras el Sass area is marked in black. Time periods covered by sample material discussed in this study are shown as green, blue, and orange columns for the modern (2010–2012 AD), late Holocene (ca. 3.0 ka BP), and mid-Holocene (ca. 5.3–5.0 ka BP), respectively.

bivalves (*S. senilis*) were originally assessed in Lavaud et al. (2013) and used for additional analyses herein.

The archaeological samples were excavated from a succession of shell midden deposits in the vicinity of the palaeo-island Jerf Sgheïr in the Ras el Sass area, Mauritania, NW Africa (**Figure 1** and **Supplementary Figure S1**, see Barusseau et al., 2007 for details on archaeological deposits in this region). The mid-Holocene otoliths and bivalve shells were previously discussed in Müller et al. (2017) regarding potential alterations due to pre-depositional cooking treatments, and are further analysed in this study. In addition, data from two late Holocene *Carlarius* spp. otoliths from the same study site that were prepared for analyses following the procedure described in Müller et al. (2017) are presented. An overview of samples used in this study can be found in **Table 1**. All otoliths and bivalve shells were ultrasonically cleaned in deionised water, and carefully dried at 30 °C for 48 h. The outermost layers of bivalve shells and otoliths were manually removed using a Dremel® tool to exclude potential surficial contamination.

Mineralogical Analysis and Radiocarbon Dating

The mineralogy of the two late Holocene otoliths was assessed using a Philips X'Pert Pro diffractometer equipped with a Cu-tube (kα 1.541, 45 kV, 40.0 mA) at the University of Bremen, Germany. A continuous scan from 3–85° 2θ with a step size of 0.016° 2θ was carried out, and data were processed using the Philips

TABLE 1 | Mauritanian bivalve shells and fish otoliths used in this study.

Material	Sample ID	Organism	Location	First published
Fish otolith	RAH1	*Carlarius heudelotii*	Baie du Lévrier	Müller et al. (2015)
Fish otolith	RAP1	*Carlarius parkii*	Baie du Lévrier	This study
Bivalve shell	#3009	*Senilia senilis*	Iwik	Lavaud et al. (2013)
	#3122			
	#3211			
Fish otolith	OTO-B5 OTO-B6	*Carlarius* spp.	Jerf Sgheïr 20°25'37"N 16°19'34"W	This study
Fish otolith	OTO-B3	*Carlarius* spp.	Jerf Sgheïr 20°25'37"N 16°19'34"W	Müller et al. (2017)
	OTO-B4			
	OTO-B8			
	OTO-B9			
Bivalve shell	JS-SS-1	*Senilia senilis*	Jerf Sgheïr 20°25'37"N 16°19'34"W	Müller et al. (2017)
	JS-SS-2			
	JS-SS-3			
	JS-SS-4			
	JS-SS-5			
	JS-SS-6			
	JS-SS-10			

software X'Pert HighScore™. Aragonite and calcite abundances were determined based on the relative peak areas of aragonite (1,1,1; peak at $2\theta = 26.1°$) and low-Mg calcite (1,0,1; peak at $2\theta = 29.6°$) against calibrated standard material.

Radiocarbon dating of the two otoliths was carried out at the Poznań Radiocarbon Laboratory, Poznań, Poland, following standard procedures for accelerator mass spectrometry. Conventional radiocarbon ages were calibrated with OxCal 4.3 (Bronk Ramsey, 1995) using the Marine13 calibration curve (Reimer et al., 2013), and assuming a local reservoir age of $\Delta R = -300$ years (Müller et al., 2017). This value of ΔR presents an estimated average for the mid- to late Holocene based on various paired radiocarbon dates from terrestrial and marine materials (Saliège, unpublished). Mineralogical data and radiocarbon ages of samples used in this study are compiled in **Table 2**.

Ontogenetic $\delta^{18}O$ Analyses of Modern and Holocene Samples

The preparation of otolith and bivalve shell thick and thin sections, and ontogenetic sub-sampling for $\delta^{18}O$ analysis were completed at the Leibniz Centre for Tropical Marine Research (ZMT), Bremen, Germany, as described in detail in Müller et al. (2015). Otolith thick sections were drilled using a Merchantec® Micromill equipped with a 150 μm diameter drill bit from the edge of the otolith towards the core with a spacing between samples of ca. 100 μm, yielding between 47 and 57 discrete sub-samples. Thick sections of bivalve shells were used to sample along the outer shell layer from the hinge towards the ventral margin with average spacing of ca. 500 μm, which resulted in 35–61 discrete sub-samples per shell.

The $\delta^{18}O$ values of individual otolith and shell sub-samples (~50 μg) were determined using a Finnigan MAT 251 gas isotope ratio mass spectrometer (IRMS) connected to a Kiel III device at the MARUM – Center for Marine Environmental Sciences, University of Bremen, Germany, and a Thermo Finnigan MAT 253 IRMS connected to a Kiel IV device at the Leibniz Centre for Tropical Marine Research (ZMT), Bremen, Germany. Repeated standard measurements (NBS 19 and in-house working standards) revealed an external precision (1SD) for all measurements of better than ±0.07‰ for all $\delta^{18}O$ analyses.

Temporal Alignment of Ontogenetic $\delta^{18}O$ Records

In order to produce sub-seasonally resolved reconstructions of Holocene water temperatures and salinities, the ontogenetic otolith and bivalve $\delta^{18}O$ records (**Supplementary Figures S2**, **S3**) were converted into time series using the linear interpolation approach of Müller et al. (2015), and SST records for the Banc d'Arguin (see **Supplementary Figures S4**, **S5** and the **Supplementary Material** for details on the temporal alignment and interpolation approach). The linear interpolation model for the temporal alignment assumed a sinusoidal growth oscillation and winter growth cessations. The potential absolute uncertainty of linear interpolation models was estimated to be ca. 1.15°C based on mean absolute errors (MAEs) between $\delta^{18}O$-based reconstructed water temperatures from modern bivalves and observed SSTs in the Banc d'Arguin (a detailed description of the error estimation can be found in the **Supplementary Material**).

Ontogenetic $\delta^{18}O$ Records-Based Temperature and Salinity Reconstructions

Modern and Holocene water temperatures were reconstructed using the equation of Thorrold et al. (1997) for the fish otoliths, and the equation of Grossman and Ku (1986) for the bivalve shells assuming a constant $\delta^{18}O_{Seawater}$ composition of +0.68‰ (Müller et al., 2015) and +1.57‰ VSMOW (Lavaud et al., 2013), respectively. These newly established ontogenetic $\delta^{18}O$ datasets were combined with previously published $\delta^{18}O$ records of a modern catfish otolith (*C. heudelotii* from Müller et al., 2015), three modern bivalve shells (*S. senilis* from Lavaud et al., 2013) and three mid-Holocene bivalve shells (*S. senilis* from Müller et al., 2017).

For subsequent reconstructions of modern and Holocene (palaeo-) salinities, we assumed that the mid- to late Holocene water temperatures were similar to the modern values, which has been shown in several previous studies for the eastern tropical Atlantic (Zhao et al., 1995; Kim et al., 2007). Ontogenetic $\delta^{18}O_{Water}$ values were calculated based on the measured

TABLE 2 | Clumped isotope, mineralogy and radiocarbon data of the modern and Holocene specimens.

Sample	Species	Δ_{47} (‰, ARF)	SE (±) (‰, ARF)	Aragonite (wgt %)	Calcite (wgt %)	^{14}C age (years BP)	Uncertainty (± years)	ΔR (years)	Cal. years BP from	Cal. years BP to	Median	Uncertainty + (years)	Uncertainty – (years)
RAP-1	*C. parkii*	–	–	100	0	Modern	–	–	–	–	–	–	–
RAH-1	*C. heudelotii*	–	–	98	2	Modern	–	–	–	–	–	–	–
Late Holocene otoliths													
OTO-B5	*Carlarius* spp.	0.668	0.013	100	0	3170	40	–300	3100	2830	2960	140	130
OTO-B6	*Carlarius* spp.	0.691	0.014	–	–	3250	30	–300	3180	2950	3070	110	110
Mid-Holocene otoliths													
OTO-B3	*Carlarius* spp.	0.716	0.013	100	0	4920	30	–300	5330	5070	5260	70	190
OTO-B4	*Carlarius* spp.	0.714	0.011	95	5	4970	30	–300	5430	5250	5320	110	70
OTO-B8	*Carlarius* spp.	0.704	0.014	100	0	4920	35	–300	5390	5260	5260	130	200
OTO-B9	*Carlarius* spp.	0.667	0.016	100	0	4970	35	–300	5440	5320	5320	120	80
Mid-Holocene bivalves													
JS-SS-1	*S. senilis*	0.666	0.014	100	0	4830	35	–300	5270	4990	5130	140	140
JS-SS-2	*S. senilis*	0.601	0.014	100	0	4770	35	–300	5210	4880	5020	190	140
JS-SS-3	*S. senilis*	0.667	0.013	100	0	4845	35	–300	5280	4020	5150	130	130
JS-SS-4	*S. senilis*	0.631	0.012	100	0	–	–	–	–	–	–	–	–
JS-SS-5	*S. senilis*	0.661	0.013	100	0	–	–	–	–	–	–	–	–
JS-SS-6	*S. senilis*	0.716	0.013	100	0	–	–	–	–	–	–	–	–
JS-SS-10	*S. senilis*	0.622	0.017	100	0	–	–	–	–	–	–	–	–

Clumped isotope analyses were performed at the Stable Isotope Laboratory (SIL) at the Rosenstiel School of Marine and Atmospheric Science (RSMAS) of the University of Miami, FL, United States, following the protocol previously described in detail in Müller et al. (2017). Mineralogical analyses were performed at the University of Bremen, Germany. Radiocarbon dating was done at the Poznań Radiocarbon Laboratory, Poland. Radiocarbon ages were calibrated using OxCal 4.3 (Bronk Ramsey, 1995) with the Marine13 calibration curve (Reimer et al., 2013) and a local ΔR value of -300 years (Müller et al., 2017).

ontogenetic $\delta^{18}O_{Carbonate}$ values and corresponding interpolated SSTs after the temporal alignment of individual $\delta^{18}O$ records with the averaged SST time series. For the fish otoliths, we used the equation of Thorrold et al. (1997):

$$10^3 \ln \alpha = 18.56 \cdot \left(10^3 \cdot T^{-1}[K]\right) - 32.54$$

with

$$\alpha = \frac{\delta_{Aragonite} + 10^3}{\delta_{Water} + 10^3}$$

The conversion from the VPDB into the VSMOW scale was done using the equation of Gonfiantini et al. (1995) defined as:

$$\delta^{18}O\ [VSMOW] = 1.03091 * \delta^{18}O\ [VPDB] + 30.91$$

For the calculation of $\delta^{18}O_{Water}$ values from the bivalve shell $\delta^{18}O$ records, we used the equation of Grossman and Ku (1986) in the same form as used by Lavaud et al. (2013):

$$T\ [^{\circ}C] = 21.8 - 4.69 \cdot \left(\delta^{18}O_{Aragonite\ [VPDB]} - (\delta^{18}O_{Seawater\ [VSMOW]} - 0.27)\right)$$

For the modern fish otoliths and bivalve shells, the resulting $\delta^{18}O_{Seawater}$ time series were transformed into salinity time series using a linear mixing model based on modern marine and freshwater end-members. For the approximation of the modern and Holocene marine end-members, we used the local $\delta^{18}O_{Water}$-salinity model of Lavaud et al. (2013) following the equation:

$$\delta^{18}O_{Seawater}\ [VSMOW] = 0.2692 * Salinity - 9.1949$$

and the average SODA sea surface salinity (Carton and Giese, 2008) with a spatial coverage of 1° by 1° (20–21°N, 16–17°W) of the Banc d'Arguin averaged over a 10-year period (1999–2009) resulting in a marine end-member with a salinity of 36.69 and a $\delta^{18}O_{Seawater}$ value of 0.68‰ VSMOW. For the modern freshwater end-member, we used a modelled $\delta^{18}O_{Precpitation}$ value representative of the Mauritanian hinterland (salinity = 0, $\delta^{18}O_{Precpitation}$ = -3.35‰ VSMOW) obtained using the OIPC (Bowen and Revenaugh, 2003; Bowen, 2015; IAEA/WMO, 2015) (Ver. 2.2., available at wateriso.utah.edu/waterisotopes).

For the late Holocene, we used the same marine end-member, and the freshwater end-member (i.e. $\delta^{18}O_{Precpitation}$) has been approximated based on spatially and temporally interpolated δD data from Tierney et al. (2017) and the equation of Craig (1961):

$$\delta D\ [VSMOW = 8 \cdot \delta^{18}O\ [VSMOW] + 10$$

We used the δD records of sediment cores GC49 (23.206°N) and GC68 (19.363°N) by Tierney et al. (2017) and associated age models to interpolate the δD values at 20.417°N (Jerf Sghеïr shell midden successions) in 100 year intervals. This calculation resulted in a late Holocene $\delta^{18}O_{Precpitation}$ value of −3.45‰ VSMOW, which is similar to the modern value. For the mid-Holocene, the same approach resulted in a freshwater end-member with a $\delta^{18}O_{Precpitation}$ value of −4.25‰ VSMOW.

The combined absolute uncertainty of the $\delta^{18}O_{Carbonate}$-based salinity reconstructions was approximated by combining the average MAE resulting from the temporal alignment of the modern *S. senilis* shells with averaged OI-SST data (±1.15°C, translating into a salinity error of ±2.21 practical salinity units; S_p) with the uncertainty of mid- to late Holocene water temperature reconstructions (±1°C, translating into a salinity error of 1.92 S_p). This error estimation resulted in a total absolute uncertainty of the salinity reconstruction of ±4.13 S_p.

Sr-Isotope ($^{87}Sr/^{86}Sr$) Analysis

Strontium isotope ratios of bulk bivalve and otolith samples (i.e. material representing the entire lifespan of each individual) were determined by using a Thermo Scientific Triton Plus thermal ionisation mass spectrometer (TIMS) in the Isotope Geochemistry Laboratory at MARUM, Bremen, Germany. Approximately 2 mg of homogenised carbonate powder were dissolved in 2 M HNO_3, dried and re-dissolved in 500 µl of 2 M HNO_3 in preparation for the chemical separation of Sr from unwanted matrix elements. Following a setup and procedure adapted from Deniel and Pin (2001), Sr was extracted using miniature columns loaded with ca. 70 µl of Sr-spec ion exchange resin (Eichrom Technologies, LLC, United States). The collected Sr was loaded on single Re filaments with Ta-oxide emitter, and analysed by TIMS using a multidynamic acquisition routine. All $^{87}Sr/^{86}Sr$ ratios were normalised to a $^{86}Sr/^{88}Sr$ ratio of 0.11940 to correct for instrumental mass fractionation. The long-term external instrumental reproducibility with respect to NIST 987 standard material is 0.710249 ± 0.000014 (2SD, n = 263).

Clumped Isotope Analysis

The powdered bulk skeletal samples were analysed for clumped isotopes to assess for potential alterations due to pre-depositional cooking treatments (Andrus and Crowe, 2002; Müller et al., 2017). The mid-Holocene samples were previously presented and detailed in Müller et al. (2017) (**Table 2**). Clumped isotope analysis of the late Holocene otolith samples followed established methodology presented in Müller et al. (2017) and was completed at the Stable Isotope Laboratory of the Rosenstiel School of Marine and Atmospheric Science (RSMAS), University of Miami, Miami, FL, United States. Data reduction, normalisation for Δ_{47} and temperature calculations were carried out as previously described in Affek and Eiler (2006) and Huntington et al. (2009). The external instrumental precision (presented as average standard errors of individual measurements) was determined by repeated measurements of a Carrara marble (mean Δ_{47} = 0.4001 ± 0.0294‰; n = 191). Translation into the absolute reference frame (ARF) with 1000, 50 and 25°C water equilibrated gasses was completed with the method of Dennis et al. (2011).

RESULTS

To assess mid- to late Holocene changes in monsoonal discharge in NW Africa, we analysed modern and archaeological catfish otoliths and bivalve shells from the Banc d'Arguin, Mauritania (see **Table 1** for an overview of samples).

The preservation state of all fossil carbonate samples was assessed via X-ray diffraction (XRD) and thin section microscopy, both of which indicate near pristine conditions comparable to those of modern equivalents. XRD measurements suggest very good preservation of the initial primarily aragonitic mineralogy and calcite fractions ranging from the undetectable to less than 2%, with the exception of OTO-B4 (indicating ca. 5% calcite, **Table 2**). Microstructure analysis by scanning electron microscope (SEM) of samples used confirms the structural integrity and does not show any evidence for internal cementation or re-mineralisation (see **Supplementary Figure S6** for exemplary images). Given their archaeological origin, we assessed the Holocene samples for any potential alteration related to prehistoric cooking practices using clumped isotope thermometry. Both late Holocene otolith Δ_{47} values range from 0.668 to 0.691‰, consistent in magnitude with the mid-Holocene otoliths (0.667–0.714‰) reported in Müller et al. (2017), placing them within the limits of potential minor alterations (**Figure 3** and **Table 2**). In line with recent experimental evidence indicating that radiocarbon is not sensitive to heating induced in cooking practices (Lindauer et al., 2018), we accept our ^{14}C ages to be reliable.

The ontogenetic $\delta^{18}O$ records of all carbonate samples show a pronounced seasonality with clear sinusoidal patterns (**Supplementary Figures S2**, **S3**). Similar to the *C. heudelotii* otolith $\delta^{18}O$ record from Müller et al. (2015), the $\delta^{18}O$ record of the modern *C. parkii* otolith RAP-1 varies between −0.45 and +1.47‰ VPDB with an average $\delta^{18}O_{Carbonate}$ composition of +0.17‰ VPDB (**Figure 4A** and **Supplementary Figures S2**, **S4**). Assuming a constant $\delta^{18}O_{Seawater}$ of +0.68‰ VSMOW, these values translate into water temperatures ranging from 18.0 to 27.1°C with an average value of 24.1°C (**Figure 4B** and **Supplementary Figures S2**, **S4**).

Ontogenetic $\delta^{18}O$ records of the late Holocene *Carlarius* spp. otoliths exhibit a similar range between −0.59 and +2.03‰ VPDB with average values of +0.80 and +0.35‰ VPDB, translating into water temperatures ranging from 15.5 to 27.8°C with average values of 21.1 and 23.3°C (**Figure 4B** and **Supplementary Figures S2**, **S4**).

Mid-Holocene otoliths also show pronounced seasonal cycles within their ontogenetic $\delta^{18}O$ records (**Supplementary Figure S2**). However, their $\delta^{18}O_{Carbonate}$ values are considerably lower than their modern and late Holocene equivalents, varying between −2.61 and +1.18‰ VPDB with average values from −0.94 to −0.14‰ VPDB. These $\delta^{18}O_{Carbonate}$ values translate into reconstructed water temperatures ranging from 19.4 to 37.9°C and average values between 25.6 and 29.5°C (**Figure 4B**). The average seasonal minimum and maximum water temperature based on the mid-Holocene otolith samples was found to be 21.4 and 34.7°C.

The $\delta^{18}O$ records of mid-Holocene *S. senilis* shells show minimal and maximal values of −3.33 and +1.68‰ VPDB (**Supplementary Figure S3**). Assuming a constant $\delta^{18}O_{Seawater}$ value of +1.57‰ VSMOW, these values suggest ambient water temperatures between 20.0 and 43.5°C (**Figure 4B**).

To assess temporal differences in the seasonality amongst samples, we further established the mean seasonal amplitude of each ontogenetic $\delta^{18}O$ record. For consistency and robustness, we computed the averages of all clearly distinguishable local maxima and all local minima as observed in the raw ontogenetic $\delta^{18}O$ records of each sample (see **Supplementary Figures S2**, **S3**). The seasonal amplitude was estimated as the difference between mean maxima and minima, accordingly, while the range of all ontogenetic $\delta^{18}O$ values was considered in addition (**Figure 5**, c.f. Bougeois et al., 2014). For modern bivalve shells, the mean seasonal amplitude was found to be ca. 2.0‰, slightly higher than observed in modern catfish otoliths (ca. 1.4‰). In comparison, the late Holocene otolith OTO-B5 exhibits a distinctly higher amplitude, whereas OTO-B6 is consistent with the modern average. In contrast, all mid-Holocene otoliths show amplitudes higher than their modern equivalents. Mid-Holocene bivalve shells show variable seasonal amplitudes compared to the modern average, with many sample records exhibiting a large internal variability. The ranges of most of their ontogenetic records are noticeably higher than those of their modern equivalents. Similarly, mid-Holocene otoliths show ranges consistently greater than those in modern specimen, whereas late Holocene otoliths are coherent with modern samples.

To further constrain the potential influence of isotopically lighter freshwater runoff, we used the ontogenetic $\delta^{18}O$ records to reconstruct salinity under the assumption that water temperatures were similar during the mid-Holocene as observed today. We aligned all ontogenetic $\delta^{18}O$ records to averaged modern water temperature time series (**Supplementary Figures S4**, **S5**) and approximated $\delta^{18}O_{Water}$ values. Salinities were subsequently estimated using different $\delta^{18}O_{Water}$-salinity models (**Figure 6**). We used modelled modern $\delta^{18}O_{Precipitation}$ obtained using the Online Isotopes in Precipitation Calculator (Bowen and Revenaugh, 2003; Bowen, 2015; IAEA/WMO, 2015) (OIPC, Ver. 2.2, available at wateriso.utah.edu/waterisotopes) and sediment core-based δD-data from Tierney et al. (2017) for the approximation of Holocene $\delta^{18}O_{Precipitation}$ (**Figure 6**). Using this approach, the modern average reconstructed salinities are in very good agreement with the measured values ∼36 S_p for the fish otoliths (Müller et al., 2015) and ∼40 S_p for the *S. senilis* shells (Lavaud et al., 2013) (**Figures 4C**, **6**). The late Holocene otoliths also show purely marine conditions with salinities varying around the modern value of ∼36 S_p. In contrast, mid-Holocene salinity reconstructions indicate consistently brackish to marine conditions within the coastal zones with average salinities ranges of 25.7–31.8 S_p and 27.5–34.1 S_p for the catfish otoliths and the bivalve shells, respectively (**Figure 4C**).

$^{87}Sr/^{86}Sr$ ratios of all mid-Holocene bivalve samples are considerably higher than the marine end-member of 0.70918 (**Figure 4D**) with averages ranging from ca. 0.70928 to 0.70934. The $^{87}Sr/^{86}Sr$ ratios are highly consistent amongst different bivalve samples. In otoliths, the mid-Holocene $^{87}Sr/^{86}Sr$ ratios range from ca. 0.70921 to 0.70924, whereas those of late Holocene specimens are coherent with seawater (**Figure 4D**). The modern catfish otoliths, in contrast, exhibit considerable deviations from the seawater end-member as well as among samples, with relatively radiogenic $^{87}Sr/^{86}Sr$ ratios of up to ca. 0.70929, similar to those observed in mid-Holocene bivalve shells.

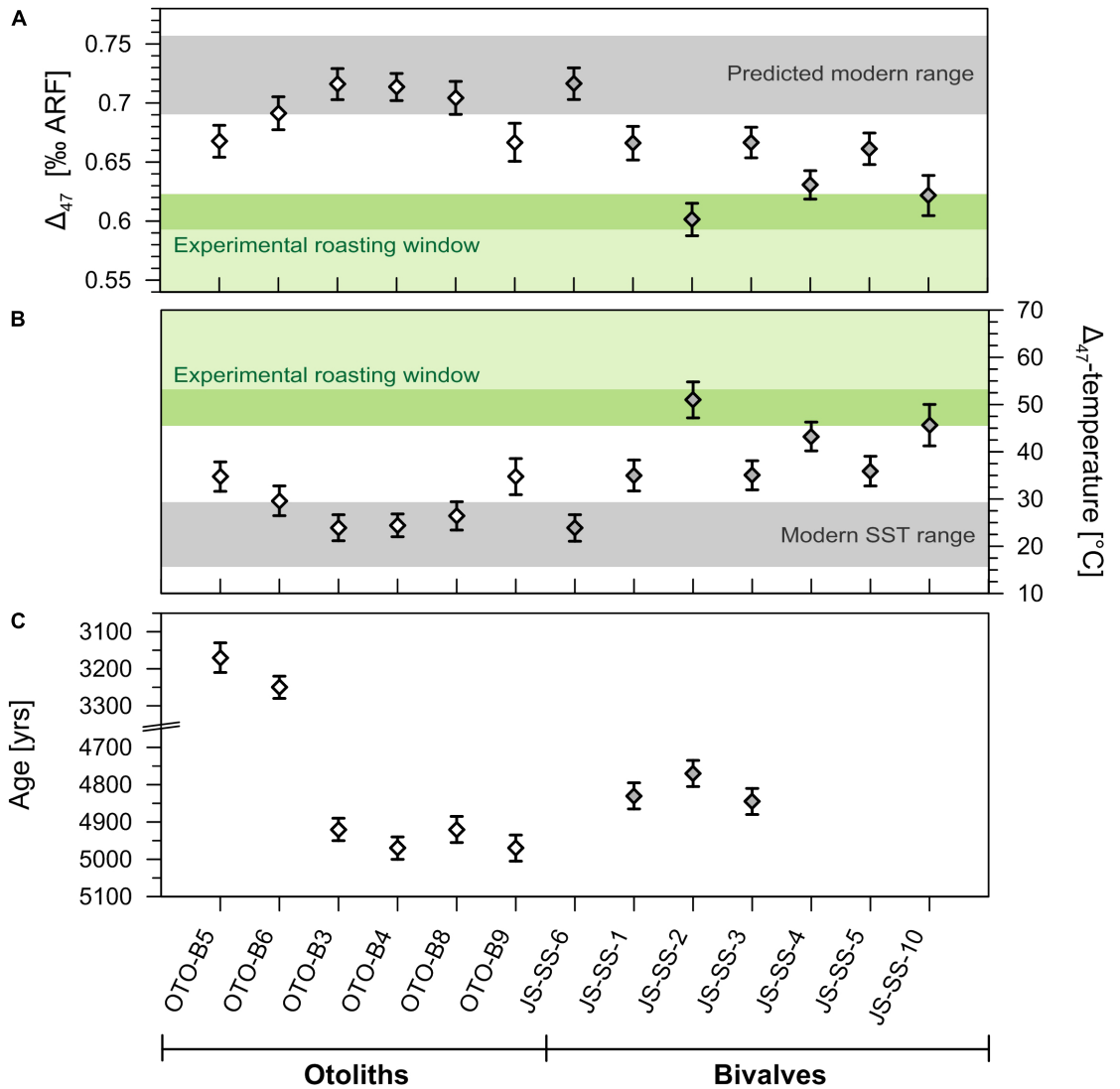

FIGURE 3 | Clumped isotope geochemistry and radiocarbon ages of Holocene specimens. **(A)** Clumped isotope data of the Holocene otoliths and bivalve shells. Mid-Holocene samples have previously been discussed in Müller et al. (2017). **(B)** Δ_{47}-based water temperatures estimated using the equation of Dennis et al. (2011). Error bars represent average standard errors (SE) of the individual Δ_{47}-measurements. The shaded grey areas represent predicted Δ_{47}-values in **A** based on the seasonal SST range from Lavaud et al. (2013) shown in **B**. Shaded green areas represent the experimental Δ_{47}-/temperature windows for prehistoric cooking (roasting at ca. 174°C) from Müller et al. (2017) for ca. 6 h (light green) and a more realistic cooking duration of > 30 min (dark green). Only very few mid-Holocene shells exhibit Δ_{47} values that suggest a potential alteration due to prehistoric cooking practices (roasting), whereas fish otoliths show little indication of significant pre-depositional heating. **(C)** Radiocarbon ages were calibrated using OxCal 4.3 (Bronk Ramsey, 1995) with the Marine13 calibration curve (Reimer et al., 2013) and a local ΔR value of −300 years (Müller et al., 2017).

DISCUSSION

The key findings of our study are based on the oxygen and strontium isotope records of archaeological bivalve shells and catfish otoliths from the Banc d'Arguin, Mauritania, which collectively provide strong evidence of significant freshwater discharge to the region between ca. 5.3 and 5.0 ka BP. Importantly, our data thereby contradict existing datasets derived from marine sediment cores off the Mauritanian coast, which indicate an abrupt cease of pronounced precipitation across NW Africa by about 5.5 ka BP (deMenocal et al., 2000).

As a modern reference for our reconstructions of water temperature and salinity, we established new ontogenetic $\delta^{18}O$ records of a *C. parkii* otolith, RAP-1, which are consistent in their seasonal cyclicity and magnitude with the *C. heudelotii* otolith $\delta^{18}O$ record from Müller et al. (2015). Both otolith $\delta^{18}O$ signatures yield water temperature estimates that are in good agreement with the modern seasonal water temperature amplitude on the Banc d'Arguin (**Figure 2E**). Despite possible discrepancies between reconstructed and recorded SSTs, ontogenetic $\delta^{18}O$ records of both catfish species occurring on the Banc d'Arguin (*C. heudelotii* and *C. parkii*),

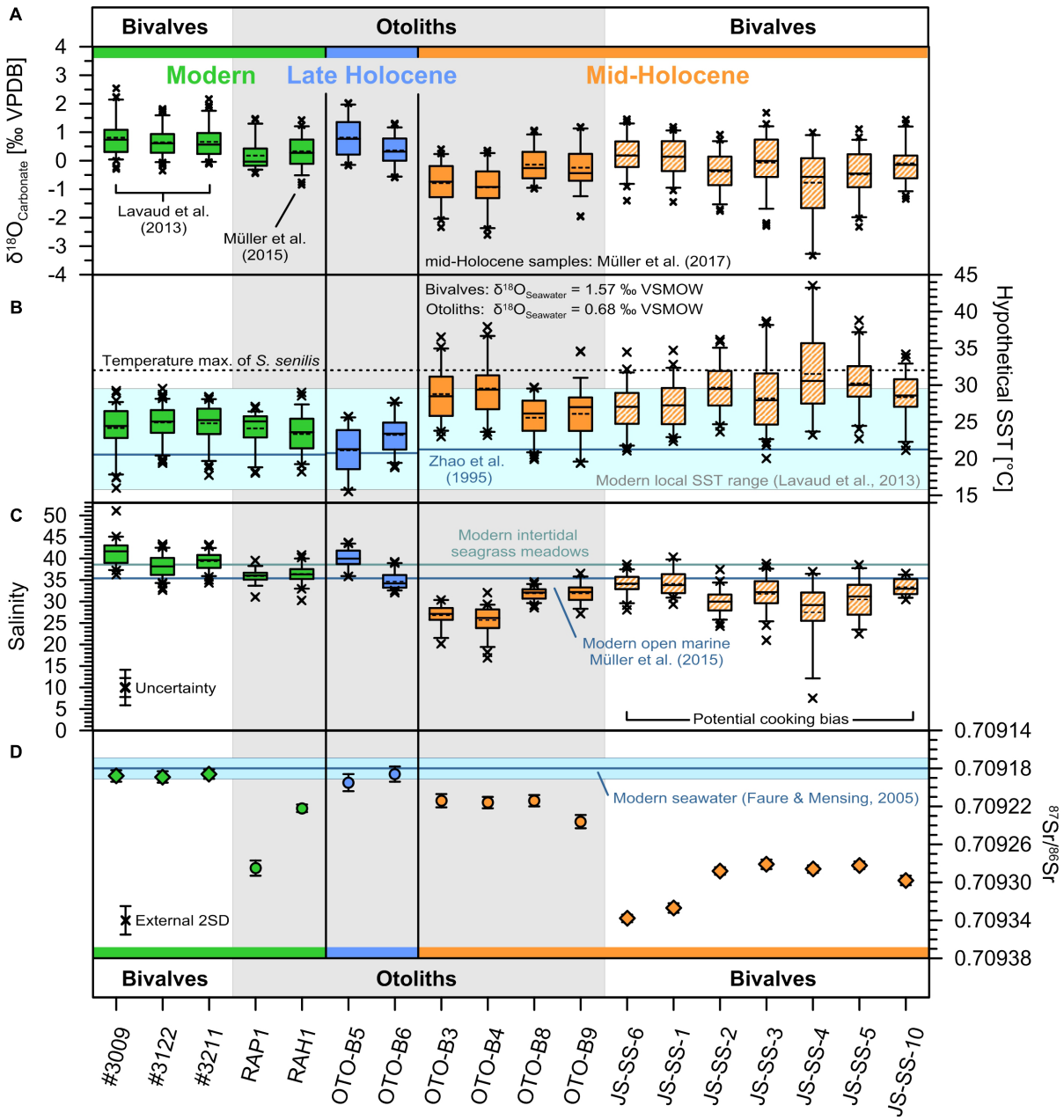

FIGURE 4 | Isotope records and proxy reconstructions of Mauritanian bivalve shells and otoliths. **(A)** Boxplot of measured bivalve shell and otolith $\delta^{18}O$ data (grey demarcation) from previously published modern *S. senilis* for Banc d'Arguin, Mauritania (Lavaud et al., 2013), and the modern *C. heudelotii* otolith record from the Banc d'Arguin (Müller et al., 2015). Modern (2010–2012 AD) samples are shown in green, late Holocene (ca. 3.0 ka BP) otolith samples in blue, and mid-Holocene (ca. 5.3–5.0 ka BP) samples in orange. Striated boxes of the mid-Holocene bivalves $\delta^{18}O$ data indicate potential minor alteration due to the exposure to prehistoric cooking methods prior to deposition (Müller et al., 2017). The box and whiskers represent the interquartile range and 5th/95th percentiles, respectively. The analytical uncertainty of the $\delta^{18}O$ analysis is smaller than the symbol size (±0.07‰ VPDB). Data points outside the whiskers represent statistical outliers. Solid and dotted horizontal lines inside the box show the median and average reconstructed water temperature values, respectively. **(B)** Boxplot of the hypothetical $\delta^{18}O$-derived SST assuming constant modern $\delta^{18}O_{Seawater}$ values with the modern seasonal water temperature range of the inner Banc d'Arguin from Lavaud et al. (2013) and the upper water temperature limit for *S. senilis* from Azzoug et al. (2012b) and the references therein for comparison. **(C)** Boxplot showing the reconstructed salinities using modern water temperature data and the different $\delta^{18}O_{Seawater}$-salinity relationships (**Figure 6**). The combined uncertainty includes the water temperature uncertainty of ±1°C (inner error bars) and the potential misalignment accounting for on average 1.15°C (outer error bars). Horizontal lines represent the average modern salinity of the open Banc d'Arguin of 36.7 S_p (Müller et al., 2015) and the intertidal areas in the eastern Banc d'Arguin of 40 S_p (Lavaud et al., 2013). **(D)** Bulk $^{87}Sr/^{86}Sr$ records of modern and Holocene carbonate samples. Note that the *y*-axis is inverted to facilitate comparisons between $^{87}Sr/^{86}Sr$ records and $\delta^{18}O$-based salinity reconstructions. Sample error bars for $^{87}Sr/^{86}Sr$ indicate two standard errors (SE) of the mean. The external instrumental uncertainty is given as 2SD (n = 263). The modern seawater composition of 0.70918 and corresponding 2SD (±0.00001) (Faure and Mensing, 2005) are indicated by the horizontal line and shading, respectively.

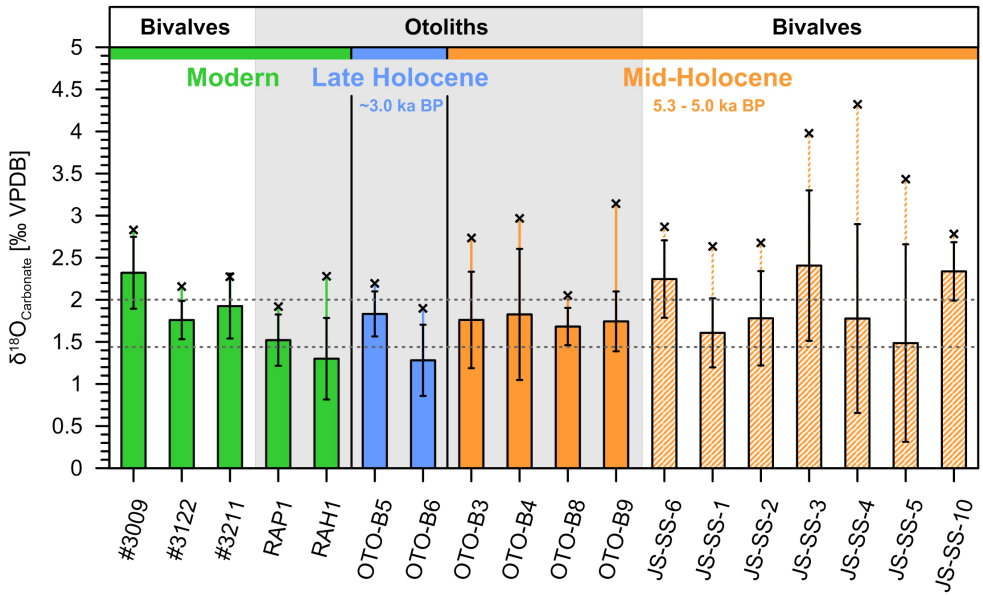

FIGURE 5 | Carbonate $\delta^{18}O$ seasonal amplitudes and ranges. Bars present the mean seasonal amplitude computed as the difference between the averages of all clearly distinguishable local minima and maxima in the raw ontogenetic $\delta^{18}O$ records of each sample (see **Supplementary Figures S2**, **S3**). Error bars indicate the propagated standard deviation (1SD). The horizontal dashed lines mark the modern mean values for bivalves (ca. 2.0‰) and otoliths (ca. 1.4‰). Black cross symbols above bars present the absolute range of values in a given record.

whose otoliths can hardly be distinguished in archaeological deposits, provide reliable records of environmental conditions experienced during the lifetime of the organism.

The late Holocene *Carlarius* spp. otoliths also show clear seasonal cycles within their ontogenetic $\delta^{18}O$ records (**Supplementary Figure S2**), with measured $\delta^{18}O$ values translating into water temperatures ranging from 15.5 to 27.8°C with average values of 21.1 and 23.3°C (**Figure 4B** and **Supplementary Figures S2**, **S4**). These hypothetical $\delta^{18}O$-based water temperatures are only slightly lower than those observed today. However, considering the uncertainty of modern otolith temperature reconstructions of $\leq \pm 1.16$°C (Müller et al., 2015), the late Holocene otolith $\delta^{18}O$-based water temperature reconstructions are in good agreement with alkenone-based SST estimates of the same period. The latter also indicate similar conditions in the mid-Holocene and present day (**Figure 2E**; Zhao et al., 1995; Kim et al., 2007). Therefore, the late Holocene *Carlarius* spp. otolith data do not show any evidence for isotopically lighter freshwater discharge, which in turn confirms previous studies that showed fully established arid conditions in most parts of NW Africa by ~3.0 ka BP (deMenocal et al., 2000; Kröpelin et al., 2008).

In contrast, mid-Holocene *S. senilis* shells exhibit $\delta^{18}O$ signatures that suggest ambient water temperatures between 20.0 and 43.5°C when assuming a constant $\delta^{18}O_{Seawater}$ value of +1.57‰ VSMOW (**Figure 4B**). However, alkenone-based temperatures during this period only ranged between 27.0 and 31.5°C (**Figure 2E**). Thus, the mid-Holocene *S. senilis* shells substantially overestimate modern seasonal water temperature minima and maxima by +6.1 and +7.7°C, respectively. Similarly, mid-Holocene otoliths show $\delta^{18}O_{Carbonate}$ values considerably lower than the modern and late Holocene specimens. In consequence, reconstructed water temperatures indicate average seasonal minimum and maximum water temperatures of ca. 21.4 and 34.7°C, which is +5.5 and +5.2°C warmer than observed today during the cold and warm season, respectively.

The clumped isotope analyses suggest that some of the *S. senilis* shells examined in this study may have been exposed to heat (prehistoric cooking) prior to deposition (Müller et al., 2017). This may have caused an alteration of their original $\delta^{18}O$ shell records towards lower isotopic values (i.e. higher reconstructed SSTs), mimicking the effect of elevated water temperatures or potential freshwater runoff (**Figure 3**). However, there is a robust agreement between potentially cooked (roasted) bivalve shells and the essentially pristine fish otoliths, suggesting that the initial $\delta^{18}O$ shell values remained effectively unchanged during any pre-depositional treatments. Importantly, even if assuming a pre-depositional alteration by heating, experimentally determined effects of different cooking practices on carbonate $\delta^{18}O$ values strongly suggest that the magnitude of modern water temperature overestimations by the ontogenetic $\delta^{18}O$ shell records are considerably larger than any expected cooking bias ($\leq$ 0.90‰ VPDB) (Müller et al., 2017). Based on the experimental findings, we are confident that any possible contributions of prehistoric cooking to the observed depletions in $\delta^{18}O$ shell values are limited and not decisive for our interpretations. Therefore, we conclude that the *S. senilis* $\delta^{18}O$ records still provide reliable palaeoenvironmental data from the mid-Holocene. Clumped isotopes of mid- and late Holocene fish otoliths are in turn largely coherent, and do not indicate

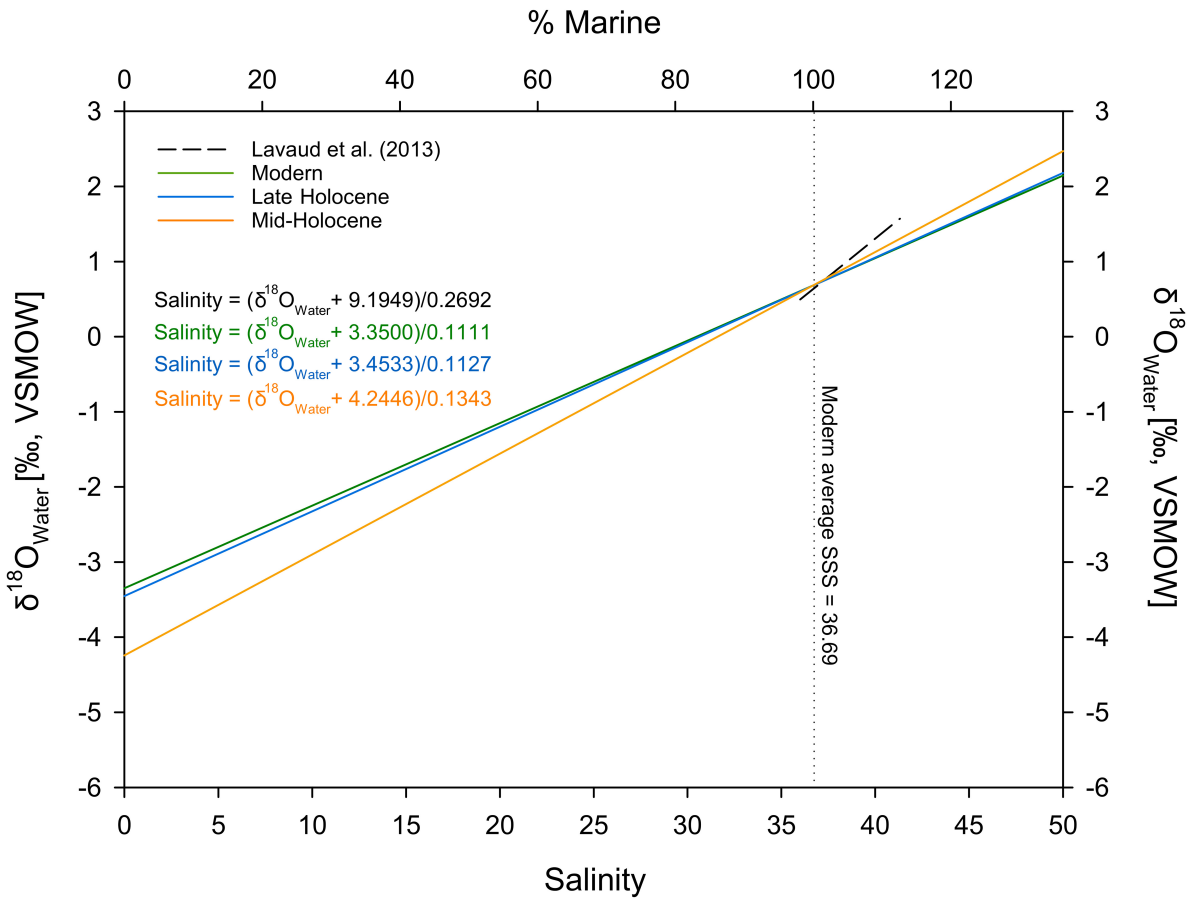

FIGURE 6 | $\delta^{18}O_{Seawater}$–salinity models used for the estimation of mid- to late Holocene sea surface salinities (SSS). The modern average SSS was used as the marine end-member and corresponding $\delta^{18}O_{Seawater}$ values were calculated using the modern $\delta^{18}O_{Seawater}$–salinity relationship of Lavaud et al. (2013). The intercept with the axis of ordinate shows the $\delta^{18}O$ values of the freshwater end-members derived using the OIPC (Bowen and Revenaugh, 2003; Bowen, 2015; IAEA/WMO, 2015) (Ver. 2.2., available at wateriso.utah.edu/waterisotopes) and δD-based approximations using the data of Tierney et al. (2017) for the modern and Holocene time intervals, respectively.

any significant effects of pre-depositional heating at higher temperatures by roasting or burning (> 170°C) that could introduce larger errors to $\delta^{18}O$-based water temperature and salinity reconstructions.

The consistently high mid-Holocene water temperature estimates found in several otoliths and bivalve shells are in strong opposition to different climate models (ca. +0.4 to +1.5°C) (Kim et al., 2007; Kutzbach and Liu, 1997) as well as marine palaeoclimate records from NW Africa for this time, which consistently indicate similar SSTs during the mid- to late Holocene as observed today (e.g. Zhao et al., 1995; Elderfield and Ganssen, 2000; Kim et al., 2007). Likewise, the foraminifera $\delta^{18}O$ record of the eastern tropical Atlantic was found to be rather stable during this period, indicating no major change in $\delta^{18}O_{Seawater}$ values during the mid- to late Holocene (Kim et al., 2007). However, it must be noted that a number of studies have suggested variable intensities of coastal upwelling off Mauritania during the Holocene, and some variability in water temperatures in response cannot be excluded. Pollen records from West Africa presented in Hély et al. (2014) indicate prolonged dry seasons and possibly associated intensified trade winds during the mid-Holocene that could have promoted upwelling along the Mauritanian coast (Talbot, 1981). However, along the inshore Banc d'Arguin corresponding to the location of the palaeo-estuary, satellite derived SST and nutrient data depict a notably limited influence of upwelling today (Carlier et al., 2015). A low input of upwelled water to the essentially sheltered inner Banc d'Arguin was further supported by N isotopic signatures in fish and their potential food sources, suggesting very limited supply of upwelled nutrients to inshore species (Carlier et al., 2015). Considering these observations, temperature variability is likely of lesser importance to the overall $\delta^{18}O$ composition of these waters in near-shore habitats, particularly for bivalves living within the palaeo-estuary.

Importantly, neither the relatively small variation in SST nor potential changes in $\delta^{18}O_{Seawater}$ values explain the high water temperatures found consistently among various skeletal components. Only shell gathering in intertidal pool environments with SSTs > 35°C by the Neolithic communities may have led to the strong overestimation of reasonable

water temperatures. However, the considerably lower maximal temperature tolerance of *S. senilis* of ∼32°C (Azzoug et al., 2012b), as well as the agreement of modern *S. senilis* shells with water temperature data from such intertidal environments (Lavaud et al., 2013), strongly suggest that this overestimation is most likely related to isotopically lighter freshwater discharge during the mid-Holocene.

Temporal differences are also reflected in the seasonality of raw ontogenetic $\delta^{18}O$ of samples from the different time periods, described here in terms of seasonal range and seasonal amplitude (**Figure 5**). Taking into account the distinct ecologies of studied taxa, mid-Holocene bivalve shells and catfish otoliths both have considerably higher ranges in their $\delta^{18}O$ records than their modern equivalents, whereas late Holocene otoliths are in turn consistent in this regard with modern specimens. Estimated mean seasonal amplitudes, however, are altogether less coherent with the assumption of a generally enhanced seasonal signal during the mid-Holocene. While mid-Holocene otolith samples show seasonal amplitudes consistently higher than the modern otolith average in line with pronounced seasonal discharge, mid-Holocene bivalve shell records vary considerably and generally depict a larger inter-annual variability than modern examples. However, discrepancies in the seasonal signatures of individual bivalves can be expected, given that the individual geographic location within the estuarine system plays a critical role in their exposure to discharge considering the (palaeo-)hydrology of the Banc d'Arguin (Barusseau et al., 2007). The large ranges of mid-Holocene shell records, on the other hand, support the presence of significant influx of isotopically lighter freshwater, although the latter may have not been strictly seasonally confined. Late Holocene otolith seasonal signals are consistent with modern records, which is in good agreement with the proposed lack of seasonal precipitation by ca. 3.0 ka BP.

In order to further constrain the potential influence of isotopically lighter freshwater runoff, and disentangle the origin of $\delta^{18}O_{Carbonate}$ values, we reconstructed ontogenetic salinity records under the assumption of comparable water temperatures during the mid-Holocene to those observed today. Based on different $\delta^{18}O_{Water}$-salinity models (**Figure 6**), the modern average reconstructed salinities are highly consistent with the measured values of ∼36 S_p for the otoliths (Müller et al., 2015) and ∼40 S_p for *S. senilis* shells (Lavaud et al., 2013) (**Figure 4C**). Similarly, essentially pure marine conditions are indicated by the late Holocene otoliths with salinities comparable to the modern value of ∼36 S_p. In the case of the mid-Holocene carbonate samples, however, the salinity reconstructions suggest consistently brackish to marine conditions within the coastal zones with average values between 25.7 and 31.8 S_p, and 27.5 and 34.1 S_p for the catfish otoliths and the bivalve shells, respectively. Regardless of the uncertainty of absolute salinity estimates (± ca. 4.1 S_p) due to unknown absolute water temperatures during the Holocene and potential temporal misalignments, the results thereby indicate lower salinities/$\delta^{18}O_{Seawater}$ at ∼5.2 ka BP that suggest considerable freshwater runoff even after the supposed aridification event at ∼5.5 ka BP.

Nonetheless, we note that the intra-shell salinity variations for the mid-Holocene shells range from relatively constant marine conditions (e.g. JS-SS-6, 1 and 10) to highly variable salinities, i.e. reflecting marine to brackish conditions (e.g. JS-SS-3, 4 and 5; **Figure 4C**). The fish otoliths, on the other hand, show remarkable differences with OTO-B3 and B4 indicating predominantly brackish conditions, whereas OTO-B8 and B9 suggest primarily near-marine salinities. While the salinity variations among the bivalve shells might be related to their spatial distribution within the estuarine mouth (i.e. high versus low salinity zones), the strong variation among the otoliths may suggest variable inter-annual discharge rates as a consequence of climate instability at ∼5.2 ka BP. However, the absence of clear freshwater-signals in individual samples does not necessarily exclude the persistence of monsoonal precipitation, but may be linked to the use of different gathering grounds by the respective coastal population across the estuary, and/or the ability of fish to move within the coastal zone. Moreover, it is important to note that the possibility of changes in the evaporative budget may present an additional control on observed oxygen isotopic signatures, and that Holocene salinity reconstructions may potentially be sensitive to non-intuitive variations in freshwater isotopic end-members linked to atmospheric processes (Leduc et al., 2013).

To complement ontogenetic $\delta^{18}O$ measurements, we further analysed bulk carbonate samples for Sr isotopes as a proxy for riverine Sr contributions into the coastal area of the Banc d'Arguin. In contrast to the $\delta^{18}O$ records, carbonate $^{87}Sr/^{86}Sr$ signatures are not sensitive to water temperature, and are little affected by kinetic fractionation. Thus, they present a means to further constrain the origin of observed $\delta^{18}O$ signals. The $^{87}Sr/^{86}Sr$ ratios of all mid-Holocene bivalve samples are considerably higher than the marine end-member of 0.70918 (**Figure 4D**), suggesting the presence of riverine discharge during the mid-Holocene. Despite a lack of modern reference values of terrestrial runoff along the Mauritanian coast, the consistently elevated ratios of bivalve shells are in good agreement with those of Sr sources expected to be drained during the AHP. Bedrock and derived soil or dust across NW Africa exhibit generally more radiogenic $^{87}Sr/^{86}Sr$ signatures relative to seawater (Scheuvens et al., 2013), and respective weathering products transported by runoff can be assumed to show similar isotopic ratios. Indeed, recent evidence suggests that the mobilisation of weathering products may have been significantly amplified by increasing human activity and associated land-use for grazing during the mid- to late Holocene (Wright, 2017; Zerboni and Nicoll, 2019). Regardless, the $^{87}Sr/^{86}Sr$ ratios are highly consistent amongst different bivalve samples, suggesting similar degrees of exposure to a non-marine Sr source during their lifetime (**Figure 4D**).

Similarly, otoliths from the mid-Holocene also depict a coherent, although not as pronounced deviation from the seawater composition. This offset relative to bivalve shells from this period may be linked to differences between the taxa and their respective mobility. For example, *Carlarius* spp. are exposed to purely marine conditions during their reproductive stage, but may also move between preferred habitats throughout their lifetime regardless of maturity, whereas bivalves are sessile. In contrast, the late Holocene otoliths show $^{87}Sr/^{86}Sr$ ratios

indistinguishable from those of seawater. This is in good agreement with $\delta^{18}O$-based salinity reconstructions that suggest a lack of significant freshwater influx by this time. Arid conditions are well reflected in modern bivalve shells, whose $^{87}Sr/^{86}Sr$ signatures consistently depict marine values. $^{87}Sr/^{86}Sr$ signatures of modern catfish otoliths exhibit unexpected deviations from the seawater end-member, as well as inconsistencies among samples. Considering that there is virtually no freshwater discharge to the Banc d'Arguin today, the origin of the modern otolith $^{87}Sr/^{86}Sr$ signatures is unclear. One potential source of non-marine strontium may be provided by anthropogenic inputs (e.g. sewage). These inputs can locally alter the natural Sr isotopic composition of water (Böhlke and Horan, 2000) and the catfish may have been exposed when dwelling close to townships along the shallow eastern Baie du Lévrier. The ingestion of radiogenic sediments due to the bottom feeding of catfish may further contribute to the observed Sr isotopic signatures, although the dietary contribution of Sr to otoliths is likely inconsequential (Walther and Thorrold, 2006), and comparable $^{87}Sr/^{86}Sr$ anomalies are absent in late Holocene specimens. We considered the possibility of diagenetic alterations to the observed $^{87}Sr/^{86}Sr$ signatures (see for example Marcano et al., 2015), and the influence of contamination by detrital matter to be minimal based on initial treatments and investigations. Despite the inconsistencies in $^{87}Sr/^{86}Sr$ in modern catfish otoliths, we consider the Holocene records to be reliable and reflective of the presence and absence of terrestrial runoff to the Banc d'Arguin in the mid- and late Holocene, respectively. This is further supported by their generally good agreement with the $\delta^{18}O$ proxy records, the environmental controls of which are distinctly different and independent from those governing $^{87}Sr/^{86}Sr$ signatures in water. $^{87}Sr/^{86}Sr$ values of dissolved Sr, which is incorporated into otoliths and bivalve shells without considerable isotopic fractionation, are not affected by water temperature or evaporation (Doebbert et al., 2014). While observed $\delta^{18}O$ records may to some extent be influenced by variations in water temperature and/or local evaporative regimes, the consistently elevated $^{87}Sr/^{86}Sr$ signatures of mid-Holocene samples can be expected to be unaffected by such changes. Our Sr isotope data thus support the assumption that $\delta^{18}O$ records can be interpreted primarily in terms of local salinity variations in response to terrestrial discharge of freshwater, rather than changes in water temperature or the evaporation budget.

Altogether, our bivalve shell and otolith records thereby depict mid-Holocene freshwater runoff that is likely indicative of persistent, but possibly ceasing monsoonal activity across large parts of NW Africa between ca. 5.0 and 5.3 ka BP. Furthermore, our records confirm the establishment of the modern arid state by ∼3.0 ka BP, corresponding largely to continental records and archaeological evidence for this region (Cremaschi et al., 2006; Kröpelin et al., 2008).

CONCLUSION

By providing strong evidence for isotopically lighter monsoon discharge at ∼5.2 ka BP at ∼20.5°N, our data support the hypothesis of a prolonged transitional termination of the AHP with a likely gradual aridification of the coastal zones along the Banc d'Arguin during the mid-Holocene, and the establishment of arid conditions by ∼3.0 ka BP. The $^{87}Sr/^{86}Sr$ analyses largely agree with $\delta^{18}O$-based salinity estimations, and provide additional indications for significant precipitation across the NW African hinterland after the suggested abrupt aridification event around 5.5 ka BP. Our data are consistent with the precipitation reconstructions of Tierney et al. (2017), which also indicate the persistence of considerable rainfall until ∼3–4 ka BP. Moreover, our record is coherent with the local occupation history in the Ras el Sass area that was abandoned at ∼3 ka BP, most likely as a consequence of decreasing surface freshwater availability (Vernet and Tous, 2004). On a broader scale, our data support the concept of a temporally and spatially heterogeneous aridification of NW Africa throughout the mid- to late Holocene as indicated by various continental records and archaeological sequences (Kröpelin et al., 2008; Lézine et al., 2011). The abrupt increase of dust export at ∼5.5 ka BP may, however, indicate the onset of a general aridification trend across NW Africa, but the likely integration over a large dust source area may have masked regional deviations from this overall climatic shift. Nevertheless, our data show that arid conditions were established at ∼20.5°N by ∼3.0 ka BP. Finally, the vast successions of shell middens along the Banc d'Arguin allow for the establishment of highly resolved records of Holocene climate variability and thereby provide a valuable means to further constrain the nature and timing of the AHP termination.

DATA AVAILABILITY STATEMENT

The datasets analysed for this study can be found at PANGAEA®, Data Publisher for Earth & Environmental Science, https://doi.pangaea.de/10.1594/PANGAEA.889705.

AUTHOR CONTRIBUTIONS

PM and HW designed the research. PM and SH completed the sampling and sample analysis. PM, SH, and HCW completed the data analysis and interpretations, and served as primary authors. FL, SK, and SH carried out the Sr-isotope analysis. J-PB and RV recovered the shell samples and were responsible for local logistics, archaeological expertise, and permitting in Mauritania. All authors discussed the results and wrote the manuscript.

FUNDING

Funding for this study was provided by the Leibniz Centre for Tropical Marine Research (ZMT), Bremen, Germany. Sr analyses were additionally financed through the project "New Regional Formations," kindly supported by the VolkswagenStiftung, Hanover, Germany, and its funding line "Key Issues for Research and Society."

ACKNOWLEDGMENTS

We thank the following people for their assistance and support: Romain Lavaud and Julien Thébault for providing the modern bivalve samples; Philippe Tous for providing modern otolith samples; Peter K. Swart, Philip T. Staudigel, and Sean. T. Murray (RSMAS, University of Miami) for clumped isotope analysis assistance; Sebastian Flotow (ZMT) for sample preparation; Henning Kuhnert (University of Bremen) and Dorothee Dasbach (ZMT) for oxygen isotope analysis; Christoph Vogt (University of Bremen) for help with XRD analysis; SCALGOlive (www.scalgo.com) for providing the modern catchment area data; Janna Just for informative comments and suggestions; Matthias López-Correa and André Klicpera for helpful discussions; and the reviewers for constructive criticisms and helpful suggestions to improve this manuscript.

SUPPLEMENTARY MATERIAL

The Supplementary Material for this article can be found online at: https://www.frontiersin.org/articles/10.3389/feart.2019.00314/full#supplementary-material

REFERENCES

Affek, H. P., and Eiler, J. M. (2006). Abundance of mass 47 CO_2 in urban air, car exhaust, and human breath. *Geochim. Cosmochim. Acta* 70, 1–12. doi: 10.1016/j.gca.2005.08.021

Andrus, C. F. T., and Crowe, D. E. (2002). Alteration of otolith aragonite: effects of prehistoric cooking methods on otolith chemistry. *J. Archaeol. Sci.* 29, 291–299. doi: 10.1006/jasc.2001.0694

Armitage, S. J., Bristow, C. S., and Drake, N. A. (2015). West African monsoon dynamics inferred from abrupt fluctuations of Lake Mega-Chad. *Proc. Natl. Acad. Sci. U.S.A.* 112, 8543–8548. doi: 10.1073/pnas.1417655112

Azzoug, M., Carré, M., Chase, B. M., Deme, A., Lazar, A., Lazareth, C. E., et al. (2012a). Positive precipitation-evaporation budget from AD 460 to 1090 in the Saloum Delta (Senegal) indicated by mollusk oxygen isotopes. *Glob. Planet. Change* 9, 54–62. doi: 10.1016/j.gloplacha.2012.08.003

Azzoug, M., Carré, M., and Schauer, A. J. (2012b). Reconstructing the duration of the West African monsoon season from growth patterns and isotopic signals of shells of *Anadara senilis* (Saloum Delta, Senegal). *Palaeogeogr. Palaeoclimatol. Palaeoecol.* 346–347, 145–152. doi: 10.1016/j.palaeo.2012.06.001

Barusseau, J.-P., Vernet, R., Saliège, J.-F., and Descamps, C. (2007). Late Holocene sedimentary forcing and human settlements in the Jerf el Oustani - Ras el Sass = Occupation humaine et forçages sédimentaires à l'Holocène final dans la région de Jerf el Oustani - Ras el Sass (Banc d'Arguin, Mauritanie). *Géomorphol. Reli. Process. Environ.* 7, 17–28. doi: 10.4000/geomorphologie.634

Bloszies, C., Forman, S. L., and Wright, D. K. (2015). Water level history for Lake Turkana, Kenya in the past 15,000 years and a variable transition from the African Humid Period to Holocene aridity. *Glob. Planet. Change* 132, 64–76. doi: 10.1016/j.gloplacha.2015.06.006

Böhlke, J. K., and Horan, M. (2000). Strontium isotope geochemistry of groundwaters and streams affected by agriculture, Locust Grove, MD. *Appl. Geochem.* 15, 599–609. doi: 10.1016/S0883-2927(99)00075-X

Bougeois, L., de Rafélis, M., Reichart, G. J., de Nooijer, L. J., Nicollin, F., and Dupont-Nivet, G. (2014). A high resolution study of trace elements and stable isotopes in oyster shells to estimate Central Asian Middle Eocene seasonality. *Chem. Geol.* 363, 200–212. doi: 10.1016/j.chemgeo.2013.10.037

Bowen, G. J. (2015). *The Online Isotopes in Precipitation Calculator, version 2.2*. Available at: wateriso.utah.edu/waterisotopes (accessed December, 2008).

Bowen, G. J., and Revenaugh, J. (2003). Interpolating the isotopic composition of modern meteoric precipitation. *Water Resour. Res.* 39:1299. doi: 10.1029/2003WR002086

Brahim, K. (2004). *Ecologie et Biologie de L'émissole Lisse Mustelus Mustelus (Linné, 1758) Sur Les Côtes de Mauritanie*. Brest: Thèse Université de Bretagne Occidentale.

Bronk Ramsey, C. (1995). Radiocarbon calibration and analysis of stratigraphy: the OxCal program. *Radiocarbon* 37, 425–430. doi: 10.1017/S0033822200030903

Carlier, A., Chauvaud, L., van der Geest, M., Le Loc'h, F., Le Duff, M., Vernet, M., et al. (2015). Trophic connectivity between offshore upwelling and the inshore food web of Banc d'Arguin (Mauritania): new insights from isotopic analysis. *Estuar. Coast. Shelf Sci.* 165, 149–158. doi: 10.1016/j.ecss.2015.05.001

Carton, J. A., and Giese, B. S. (2008). A reanalysis of ocean climate using simple ocean data assimilation (SODA). *Mon. Weather Rev.* 136, 2999–3017. doi: 10.1175/2007MWR1978.1

Castañeda, I. S., Schouten, S., Pätzold, J., Lucassen, F., Kasemann, S., Kuhlmann, H., et al. (2016). Hydroclimate variability in the Nile River Basin during the past 28,000 years. *Earth Planet. Sci. Lett.* 438, 47–56. doi: 10.1016/j.epsl.2015.12.014

Claussen, M., Bathiany, S., Brovkin, V., and Kleinen, T. (2013). Simulated climate-vegetation interaction in semi-arid regions affected by plant diversity. *Nat. Geosci.* 6, 954–958. doi: 10.1038/ngeo1962

Collins, J. A., Prange, M., Caley, T., Gimeno, L., Beckmann, B., Mulitza, S., et al. (2017). Rapid termination of the African Humid Period triggered by northern high-latitude cooling. *Nat. Commun.* 8:1372. doi: 10.1038/s41467-017-01454-y

Craig, H. (1961). Isotopic variations in meteoric waters. *Science* 133, 1702–1703. doi: 10.1126/science.133.3465.1702

Cremaschi, M., Pelfini, M., and Santilli, M. (2006). Cupressus dupreziana: a dendroclimatic record for the middle-late Holocene in the central Sahara. *Holocene* 16, 293–303. doi: 10.1191/0959683606hl926rr

Cremaschi, M., and Zerboni, A. (2009). Early to middle Holocene landscape exploitation in a drying environment: two case studies compared from the central Sahara (SW Fezzan, Libya). *Comptes Rendus Geosci.* 341, 689–702. doi: 10.1016/j.crte.2009.05.001

Cremaschi, M., Zerboni, A., Charpentier, V., Crassard, R., Isola, I., Regattieri, E., et al. (2015). Early-Middle Holocene environmental changes and pre-Neolithic human occupations as recorded in the cavities of Jebel Qara (Dhofar, southern Sultanate of Oman). *Quat. Int.* 382, 264–276. doi: 10.1016/j.quaint.2014.12.058

deMenocal, P. B., Ortiz, J., Guilderson, T., Adkins, J., Sarnthein, M., Baker, L., et al. (2000). Abrupt onset and termination of the African Humid Period: rapid climate responses to gradual insolation forcing. *Quat. Sci.* 19, 347–361. doi: 10.1016/s0277-3791(99)00081-5

Deniel, C., and Pin, C. (2001). Single-stage method for the simultaneous isolation of lead and strontium from silicate samples for isotopic measurements. *Anal. Chim. Acta* 426, 95–103. doi: 10.1016/S0003-2670(00)01185-1185

Dennis, K. J., Affek, H. P., Passey, B. H., Schrag, D. P., and Eiler, J. M. (2011). Defining an absolute reference frame for "clumped" isotope studies of CO_2. *Geochim. Cosmochim. Acta* 75, 7117–7131. doi: 10.1016/j.gca.2011.09.025

Doebbert, A. C., Johnson, C. M., Carroll, A. R., Beard, B. L., Pietras, J. T., Rhodes Carson, M., et al. (2014). Controls on Sr isotopic evolution in lacustrine systems: Eocene green river formation. *Wyo. Chem. Geol.* 380, 172–189. doi: 10.1016/j.chemgeo.2014.04.008

Elderfield, H., and Ganssen, G. (2000). Past temperature and $\delta^{18}O$ of surface ocean waters inferred from foraminiferal Mg/Ca ratios. *Nature* 405, 442–445. doi: 10.1038/35013033

Faure, G., and Mensing, T. M. (2005). *Isotopes : Principles and Applications*, 3rd Edn. Hoboken, NJ: wiley.

Gonfiantini, R., Stichler, W., and Rozanski, K. (1995). "Standards and intercomparison materials distributed by the International Atomic Energy Agency for stable isotope measurements," in *Proceedings of the Consultants Meeting on Reference and Intercomparison Materials for Stable Isotopes of Light Elements*, (Vienna: IAEA), 13–29.

Goodwin, D. H., Schöne, B. R., and Dettman, D. L. (2003). Resolution and fidelity of oxygen isotopes as paleotemperature proxies in bivalve mollusk shells:

models and observations. *Palaios* 18, 110–125. doi: 10.1669/0883-1351(2003)18<110:rafooi>2.0.co;2

Grossman, E. L., and Ku, T.-L. (1986). Oxygen and carbon isotope fractionation in biogenic aragonite: temperature effects. *Chem. Geol. Isot. Geosci. Sect.* 59, 59–74. doi: 10.1016/0168-9622(86)90057-90056

Hanebuth, T. J. J., and Henrich, R. (2009). Recurrent decadal-scale dust events over Holocene western Africa and their control on canyon turbidite activity (Mauritania). *Quat. Sci. Rev.* 28, 261–270. doi: 10.1016/j.quascirev.2008.09.024

Hély, C., Lézine, A. M., Ballouche, A., Cour, P., Duzer, D., Guinet, P., et al. (2014). Holocene changes in African vegetation: tradeoff between climate and water availability. *Clim. Past* 10, 681–686. doi: 10.5194/cp-10-681-2014

Holz, C., Stuut, J. B. W., Henrich, R., and Meggers, H. (2007). Variability in terrigenous sedimentation processes off northwest Africa and its relation to climate changes: inferences from grain-size distributions of a Holocene marine sediment record. *Sediment. Geol.* 202, 499–508. doi: 10.1016/j.sedgeo.2007.03.015

Huntington, K. W., Eiler, J. M., Affek, H. P., Guo, W., Bonifacie, M., Yeung, L. Y., et al. (2009). Methods and limitations of 'clumped' CO_2 isotope ($\Delta 47$) analysis by gas-source isotope ratio mass spectrometry. *J. Mass Spectrom.* 44, 1318–1329. doi: 10.1002/jms.1614

IAEA/WMO, (2015). *Global Network of Isotopes in Precipitation*. Vienna: IAEA.

Kim, J.-H., Meggers, H., Rimbu, N., Lohmann, G., Freudenthal, T., Müller, P. J., et al. (2007). Impacts of the North Atlantic gyre circulation on Holocene climate off northwest Africa. *Geology* 35, 387–390. doi: 10.1130/G23251A.1

Kröpelin, S., Verschuren, D., Lézine, A. M., Eggermont, H., Cocquyt, C., Francus, P., et al. (2008). Climate-driven ecosystem succession in the Sahara: the past 6000 years. *Science* 320, 765–768. doi: 10.1126/science.1154913

Kuhlmann, H., Meggers, H., Freudenthal, T., and Wefer, G. (2004). The transition of the monsoonal and the N Atlantic climate system off NW Africa during the Holocene. *Geophys. Res. Lett.* 31:L22204. doi: 10.1029/2004GL021267

Kuper, R., and Kröpelin, S. (2006). Climate-controlled Holocene occupation in the Sahara: motor of Africa's evolution. *Science* 313, 803–807. doi: 10.1126/science.1130989

Kutzbach, J. E., and Liu, Z. (1997). Response of the African monsoon to orbital forcing and ocean feedbacks in the middle Holocene. *Science* 278, 440–443. doi: 10.1126/science.278.5337.440

Laskar, J., Robutel, P., Joutel, F., Gastineau, M., Correia, A. C. M., and Levrard, B. (2004). A long-term numerical solution for the insolation quantities of the Earth. *Astron. Astrophys.* 428, 261–285. doi: 10.1051/0004-6361, 20041335

Lavaud, R., Thébault, J., Lorrain, A., van der Geest, M., and Chauvaud, L. (2013). *Senilia senilis* (Linnaeus, 1758), a biogenic archive of environmental conditions on the Banc d'Arguin (Mauritania). *J. Sea Res.* 76, 61–72. doi: 10.1016/j.seares.2012.11.003

Leduc, G., Sachs, J. P., Kawka, O. E., and Schneider, R. R. (2013). Holocene changes in eastern equatorial Atlantic salinity as estimated by water isotopologues. *Earth Planet. Sci. Lett.* 362, 151–162. doi: 10.1016/j.epsl.2012.12.003

Lehner, B., Verdin, K., and Jarvis, A. (2008). New global hydrography derived from spaceborne elevation data. *Eos Trans. Am. Geophys. Union* 89, 93–94. doi: 10.1029/2008EO100001

Lézine, A. M. (2009). Timing of vegetation changes at the end of the Holocene humid period in desert areas at the northern edge of the Atlantic and Indian monsoon systems. *Comptes Rendus Geosci.* 341, 750–759. doi: 10.1016/j.crte.2009.01.001

Lézine, A. M., Zheng, W., Braconnot, P., and Krinner, G. (2011). Late Holocene plant and climate evolution at Lake Yoa, northern Chad: pollen data and climate simulations. *Clim. Past* 7, 1351–1362. doi: 10.5194/cp-7-1351-2011

Lindauer, S., Milano, S., Steinhof, A., and Hinderer, M. (2018). Heating mollusc shells – A radiocarbon and microstructure perspective from archaeological shells recovered from Kalba, Sharjah Emirate, UAE. *J. Archaeol. Sci. Rep.* 21, 528–537. doi: 10.1016/j.jasrep.2018.08.041

Liu, Z., Wang, Y., Gallimore, R., Gasse, F., Johnson, T., deMenocal, P., et al. (2007). Simulating the transient evolution and abrupt change of Northern Africa atmosphere-ocean-terrestrial ecosystem in the Holocene. *Quat. Sci. Rev.* 26, 1818–1837. doi: 10.1016/j.quascirev.2007.03.002

Marcano, M. C., Frank, T. D., Mukasa, S. B., Lohmann, K. C., and Taviani, M. (2015). Diagenetic incorporation of Sr into aragonitic bivalve shells: implications for chronostratigraphic and palaeoenvironmental interpretations. *Depos. Rec.* 1, 38–52. doi: 10.1007/BF01530197

Maritan, L., Mazzoli, C., and Freestone, I. (2007). Modelling changes in mollusc shell internal microstructure during firing: implications for temperature estimation in shell-bearing pottery. *Archaeometry* 49, 529–541. doi: 10.1111/j.1475-4754.2007.00318.x

McGee, D., deMenocal, P. B., Winckler, G., Stuut, J.-B. W., and Bradtmiller, L. I. (2013). The magnitude, timing and abruptness of changes in North African dust deposition over the last 20,000 yr. *Earth Planet. Sci. Lett.* 37, 163–176. doi: 10.1016/j.epsl.2013.03.054

Milano, S., and Nehrke, G. (2018). Microstructures in relation to temperature-induced aragonite-to-calcite transformation in the marine gastropod *Phorcus turbinatus*. *PLoS One* 13:e0204577. doi: 10.1371/journal.pone.0204577

Milano, S., Prendergast, A. L., and Schöne, B. R. (2016). Effects of cooking on mollusk shell structure and chemistry: implications for archeology and paleoenvironmental reconstruction. *J. Archaeol. Sci. Rep.* 7, 14–26. doi: 10.1016/j.jasrep.2016.03.045

Mokadem, F., Parkinson, I. J., Hathorne, E. C., Anand, P., Allen, J. T., and Burton, K. W. (2015). High-precision radiogenic strontium isotope measurements of the modern and glacial ocean: limits on glacial-interglacial variations in continental weathering. *Earth Planet. Sci. Lett.* 415, 111–120. doi: 10.1016/j.epsl.2015.01.036

Müller, P., Staudigel, P. T., Murray, S. T., Vernet, R., Barusseau, J.-P., Westphal, H., et al. (2017). Prehistoric cooking versus accurate palaeotemperature records in shell midden constituents. *Sci. Rep.* 7:3555. doi: 10.1038/s41598-017-03715-3718

Müller, P., Taylor, M. H., Klicpera, A., Wu, H. C., Michel, J., and Westphal, H. (2015). Food for thought: mathematical approaches for the conversion of high-resolution sclerochronological oxygen isotope records into sub-annually resolved time series. *Palaeogeogr. Palaeoclimatol. Palaeoecol.* 440, 763–776. doi: 10.1016/j.palaeo.2015.09.032

Palmer, M. R., and Edmond, J. M. (1989). The strontium isotope budget of the modern ocean. *Earth Planet. Sci. Lett.* 92, 11–26. doi: 10.1016/0012-821X(89)90017-90014

Pausata, F. S. R., Messori, G., and Zhang, Q. (2016). Impacts of dust reduction on the northward expansion of the African monsoon during the Green Sahara period. *Earth Planet. Sci. Lett.* 434, 298–307. doi: 10.1016/j.epsl.2015.11.049

Rachmayani, R., Prange, M., and Schulz, M. (2015). North African vegetation-precipitation feedback in early and mid-Holocene climate simulations with CCSM3-DGVM. *Clim. Past* 11, 175–185. doi: 10.5194/cp-11-175-2015

Reimer, P. J., Bard, E., Bayliss, A., Beck, J. W., Blackwell, P. G., Ramsey, C. B., et al. (2013). IntCal13 and marine13 radiocarbon age calibration curves 0-50,000 years cal BP. *Radiocarbon* 55, 1869–1887. doi: 10.2458/azu-js-rc.55.16947

Ritchie, J. C., Eyles, C. H., and Haynes, C. V. (1985). Sediment and pollen evidence for an early to mid-Holocene humid period in the eastern Sahara. *Nature* 314, 352–355. doi: 10.1038/314352a0

Roberts, N. (2014). *The Holocene – An Environmental History*. 3rd Edn. Blackwell: Wiley.

Romero, O. E., Kim, J.-H., and Donner, B. (2008). Submillennial-to-millennial variability of diatom production off Mauritania, NW Africa, during the last glacial cycle. *Paleoceanography* 23:A3218. doi: 10.1029/2008PA001601

Scheuvens, D., Schütz, L., Kandler, K., Ebert, M., and Weinbruch, S. (2013). Bulk composition of northern African dust and its source sediments - A compilation. *Earth Sci. Rev.* 116, 170–194. doi: 10.1016/j.earscirev.2012.08.005

Shanahan, T. M., McKay, N. P., Hughen, K. A., Overpeck, J. T., Otto-Bliesner, B., Heil, C. W., et al. (2015). The time-transgressive termination of the African Humid Period. *Nat. Geosci.* 8, 140–144. doi: 10.1038/ngeo2329

Skonieczny, C., Paillou, P., Bory, A., Bayon, G., Biscara, L., Crosta, X., et al. (2015). African humid periods triggered the reactivation of a large river system in Western Sahara. *Nat. Commun.* 6, 6–11. doi: 10.1038/ncomms9751

Surge, D., and Walker, K. J. (2005). Oxygen isotope composition of modern and archaeological otoliths from the estuarine hardhead catfish (*Ariopsis felis*) and their potential to record low-latitude climate change. *Palaeogeogr. Palaeoclimatol. Palaeoecol.* 228, 179–191. doi: 10.1016/j.palaeo.2005.03.051

Talbot, M. R. (1981). Holocene changes in tropical wind intensity and rainfall: evidence from southeast Ghana. *Quat. Res.* 16, 201–220. doi: 10.1016/0033-5894(81)90045-90044

Thorrold, S. R., Campana, S. E., Jones, C. M., and Swart, P. K. (1997). Factors determining $\delta^{13}C$ and $\delta^{18}O$ fractionation in aragonitic otoliths of marine fish.

Geochim. Cosmochim. Acta 61, 2909–2919. doi: 10.1016/S0016-7037(97)00141-145

Tierney, J. E., Pausata, F. S. R., and deMenocal, P. B. (2017). Rainfall regimes of the Green Sahara. *Sci. Adv.* 3:e1601503. doi: 10.1126/sciadv.1601503

Tjallingii, R., Claussen, M., Stuut, J.-B. W., Fohlmeister, J., Jahn, A., Bickert, T., et al. (2008). Coherent high- and low-latitude control of the northwest African hydrological balance. *Nat. Geosci.* 1, 670–676. doi: 10.1038/ngeo289

USGS, (2004). *Shuttle Radar Topography Mission, 1 Arc Second scene SRTM_u03_n008e004, Unfilled Unfinished 2.0. Global Land Cover Facility*. College Park, MD: University of Maryland.

Vernet, R. (2007). *Le golfe d'Arguin de la Préhistoire à L'histoire Littoral et Plaines Intérieures*. Nouakchott: Parc National du Banc d'Arguin.

Vernet, R., and Tous, P. (2004). Les amas coquilliers de Mauritanie occidentale et leur contexte paléoenvironnemental (VIIe-IIe millénaires BP). *Préhistoire Anthropol. Méditerranéennes* 13, 55–69.

Walther, B., and Thorrold, S. (2006). Water, not food, contributes the majority of strontium and barium deposited in the otoliths of a marine fish. *Mar. Ecol. Prog. Ser.* 311, 125–130. doi: 10.3354/meps311125

Wright, D. K. (2017). Humans as agents in the termination of the African Humid Period. *Front. Earth Sci.* 5:1–14. doi: 10.3389/feart.2017.00004

Zerboni, A., and Nicoll, K. (2019). Enhanced zoogeomorphological processes in North Africa in the human-impacted landscapes of the Anthropocene. *Geomorphology* 331, 22–35. doi: 10.1016/j.geomorph.2018.10.011

Zhao, M., Beveridge, N. A. S., Shackleton, N. J., Sarnthein, M., and Eglinton, G. (1995). Molecular stratigraphy of cores off northwest Africa: sea surface temperature history over the last 80 Ka. *Paleoceanography* 10, 661–675. doi: 10.1029/94PA03354

Zhao, W., Balsam, W., Williams, E., Long, X., and Ji, J. (2018). Sr-Nd-Hf isotopic fingerprinting of transatlantic dust derived from North Africa. *Earth Planet. Sci. Lett.* 486, 23–31. doi: 10.1016/j.epsl.2018.01.004

Conflict of Interest: The authors declare that the research was conducted in the absence of any commercial or financial relationships that could be construed as a potential conflict of interest.

frontiers in Earth Science

REVIEW
published: 22 April 2020
doi: 10.3389/feart.2020.00113

Loess-Palaeosol Sequences in the Kashmir Valley, NW Himalayas: A Review

Reyaz A. Dar[1] and Christian Zeeden[2]*

[1] Department of Earth Sciences, University of Kashmir, Srinagar, India, [2] LIAG - Leibniz Institute for Applied Geophysics, Hanover, Germany

Loess deposits and intercalated palaeosols are widespread in the Quaternary record, and these have been extensively used to gain insights into continental paleoclimatic and paleo-environmental conditions and changes. Especially over Eurasia, loess geoarchives play an important role for our understanding of past changes. Loess covers almost 500 km^2 of the Kashmir Valley in north-western India, it occurs dominantly in plateau positions, but also on terraces and sometimes forms slope deposits with thicknesses ranging from several to more than 20 m. For the time being, however, the timing of the initiation of the loess accumulation, the provenance, the grain size composition and also the paleo-environment have not been studied systematically and yet only little quantitative data is available. Yet it is clear that deposition rates are at least comparable to European loess, and that the presence of multiple palaeosols intercalated in the loess can provide valuable information on the history of the region. The limited available data hinders regional and continental correlation, and tapping its value as archive of past environmental changes in this sensitive region with influence from Westerlies and the Indian Monsoon. However, several characteristic palaeosol patterns can be traced throughout the Kashmir valley, which provide stratigraphic information. Several studies investigate physical and chemical properties of the loess-paleosol sequences and conclude to its aeolian origin and recording of past climates. The intensity of soil formation phases is traced through various proxies in low resolution and yet without conclusive age control. Here we review the exiting literature, available data, and interpretations from loess-palaeosol sequences in the Kashmir Valley. These are placed in the context of our own observations and loess from the Indian subcontinent.

Keywords: Kashmir, loess, paleoclimate, Pir-Panjal Range, Karewa, quaternary

OPEN ACCESS

Edited by:
Davide Tiranti,
Agenzia Regionale per la Protezione Ambientale (ARPA), Italy

Reviewed by:
Mingrui Qiang,
South China Normal University, China
Tobias Sprafke,
University of Bern, Switzerland

****Correspondence:***
Reyaz A. Dar
reyazdar@kashmiruniversity.ac.in;
reyazsopore@gmail.com

Specialty section:
This article was submitted to Quaternary Science, Geomorphology and Paleoenvironment, a section of the journal Frontiers in Earth Science

Received: *13 December 2019*
Accepted: *26 March 2020*
Published: *22 April 2020*

Citation:
Dar RA and Zeeden C (2020) Loess-Palaeosol Sequences in the Kashmir Valley, NW Himalayas: A Review. Front. Earth Sci. 8:113. doi: 10.3389/feart.2020.00113

INTRODUCTION

Loess-Palaeosol Sequences

Since the middle of the 19th century, the term loess has become common in Earth Sciences and many researchers have tried to define it (Sprafke and Obreht, 2016 and references therein). Among them, Pye (1995) has given a simple definition of loess as "terrestrial clastic sediment, composed predominantly of silt-size particles, formed essentially by the accumulation of wind-blown dust." Loess mainly consists of quartz, micas, feldspars, clay minerals, and varying amounts of calcium carbonate.

The processes of particle formation, transport, deposition, and post-depositional modification to the formation of sometimes thick loess deposits are argued to be closely linked to glacial geomorphic processes and changes in regional and global climate (e.g., Muhs, 2009, 2018; Újvári et al., 2016). Both glacial and non-glacial sources (mainly rivers and deserts) have been envisaged as the source regions for loess (e.g., Smalley, 1972; Wright, 2001; Sun et al., 2002; Smalley et al., 2009). Since loess is deposited directly from the atmosphere, it forms one of the few geological archives that can record atmospheric circulation (e.g., Porter, 2001; Muhs and Bettis, 2003; Smalley et al., 2011; Muhs et al., 2013; Obreht et al., 2015, 2017; Zeeden et al., 2015), and can be used for assessing the role of dust in climate change (e.g., Harrison et al., 2001).

The accumulation of loess requires both aeolian material and a trap for deposition; it has been argued that at least a sparse vegetation cover or topographic barriers are necessary for the trapping of aeolian dust (see e.g., Tsoar and Pye, 1987; Mason et al., 1999; Iriondo and Kröhling, 2007). In Kashmir, the topography has probably always been diverse enough for trapping of material. Also it may be assumed that the area was covered by sparse vegetation (C_3 and C_4types) over the last glacial/interglacial cycles (Krishnamurthy et al., 1986; Dar et al., 2015b). Here we assume a similar substrate for pedogenesis throughout the Kashmir valley and through time. Although this is not a known, nothing indicates a spatial or temporal difference.

Loess deposits have been reported from around the globe, and Quaternary loess deposits in China are the thickest, preserving records of the entire Quaternary and reaching further back in time (e.g., Ding et al., 2002a; Vandenberghe et al., 2004; Sun et al., 2006; Hao and Guo, 2007). In the Indian subcontinent, loess deposits are reported in a paleoenvironmental context from the Kashmir Valley, Potwar Plateau, Peshawar Basin (e.g., Kusumgar et al., 1980; Bronger et al., 1987b; Pant et al., 2005). Holocene loess deposits are reported from the several valleys in the western to central southern Himalaya and the Central Himalaya (Williams and Clarke, 1984; Basavaiah and Khadkikar, 2004; Pant et al., 2005), and recently aeolian silt-size deposits are reported from the Indo-Gangetic Plain (Liu et al., 2017) and Deccan Plateau (Liu et al., 2019). Studies on Quaternary climate change have fostered the interest in loess research because of sometimes high accumulation rates allowing for temporally highly resolved studies on the paleoenvironments. Further, the relatively well-developed chronological framework in Asia and the widespread occurrence over Eurasia (e.g., Chlachula et al., 1997; Ding et al., 2002b; Hao et al., 2012; Yang and Ding, 2014; Zeeden et al., 2016, 2018b; Veres et al., 2018; Vlaminck et al., 2018; Wang et al., 2018) make loess-paleosol sequences the most widely distributed geoarchives for studying past climate dynamics. Loess intercalated with palaeosols is a valuable source for studying paleoclimate dynamics because soil properties and features depend on the environmental conditions at the time of formation (e.g., Dodonov et al., 2006; Buggle et al., 2011). The presence of palaeosols within the loess deposits indicates relative landscape stability. It is well established that loess deposits are common in the mid-latitude Quaternary geological record covering ∼10% of the Earth's surface (Pécsi, 1990; Muhs and Bettis, 2003; Muhs, 2013), and loess has a special preservation potential for archeology (Händel et al., 2009).

Aeolian loess deposits occur as sediments overlying the widespread fluvial and lacustrine sediments in the intermontane Kashmir Valley. The dust parent material is assumed to be dominantly formed by glacial erosion and/or erosion by other geomorphic processes within the valley and its surrounding mountain ranges. Whether further transport from outside the valley plays a major role is subjects of ongoing debates. In either case, the loess deposits of Kashmir provide a unique opportunity to investigate paleoclimate change and monsoon variations in the NW Himalayas in the context of uplift of the Himalayas and central Asian high mountains.

Geological Setting of Kashmir and the Loess-Palaeosol Sequences

The oval shaped Kashmir Valley is located at an average altitude of 1800 m above sea level and lies between 33°20′ and 34°41′ N latitude and 73°55′ and 75°37′E longitude (**Figures 1**, **2**) in the western Himalayas. It is located between the Greater Himalaya in the northeast and the Pir-Panjal Ranges in the southwest. Formation of the valley and its sedimentary filling deposits are attributed to the rise of the Pir-Panjal Range, associated with the Himalayan orogeny, which impounded the ancient drainage into the lake known as Karewa Lake (e.g., Bhatt, 1976; Singh, 1982; Kotlia, 1985a,b; Bronger et al., 1987b; Singh Kotlia and Dayal Mathur, 1992; Basavaiah et al., 2010; Dar et al., 2013, 2015b). The Karewa Lake sediments, known in geological literature as Karewa Group, range in age from lower Pliocene to middle Pleistocene (Bhatt, 1976; Singh, 1982; Basavaiah et al., 2010). The sediments of the Karewa Group are underlying the loess, and are divided into different formations based on their stratigraphy and lithology. The sediments of the Hirpur Formation (Lower Karewa) comprise a thick succession of conglomerate beds, gray clays and medium to coarse grained sand beds. It can be further sub-divided into the Dubjan, Rembiara, and Methawoin Members. With the continuous uplift of the Pir-Panjal Range and the onset of Pleistocene glacial aridity, the Nagum Formation (Upper Karewa) deposits were exposed after draining and desiccation of the lake, and were subsequently overlain by aeolian loess (Burbank and Johnson, 1982; Agrawal et al., 1989; Babeesh et al., 2017). The sediments of the Nagum Formation are again divided into Shopian, Pampore and Krungus Members. The Dilpur Formation represents loess (like) deposits, occurring as overlying the paleo-landscape in the form of terrace-, slope- and plateau-deposits with thickest sequences preserved in plateau and terrace settings. Loess deposits show variable thickness along and across the Kashmir Valley with thickness ranging from > 20 m in the south-western side to several m in the north-eastern side of the valley (Bronger et al., 1987a and also own observations). While loess in higher positions of the south-western flank is mostly of plateau-type and shows a laterally continuous character, toward the basin more reworking and channeling can be observed in several gravel- and clay pits west of Srinagar. In some slope positions, loess-paleosol sequences are covering the previous morphology. The

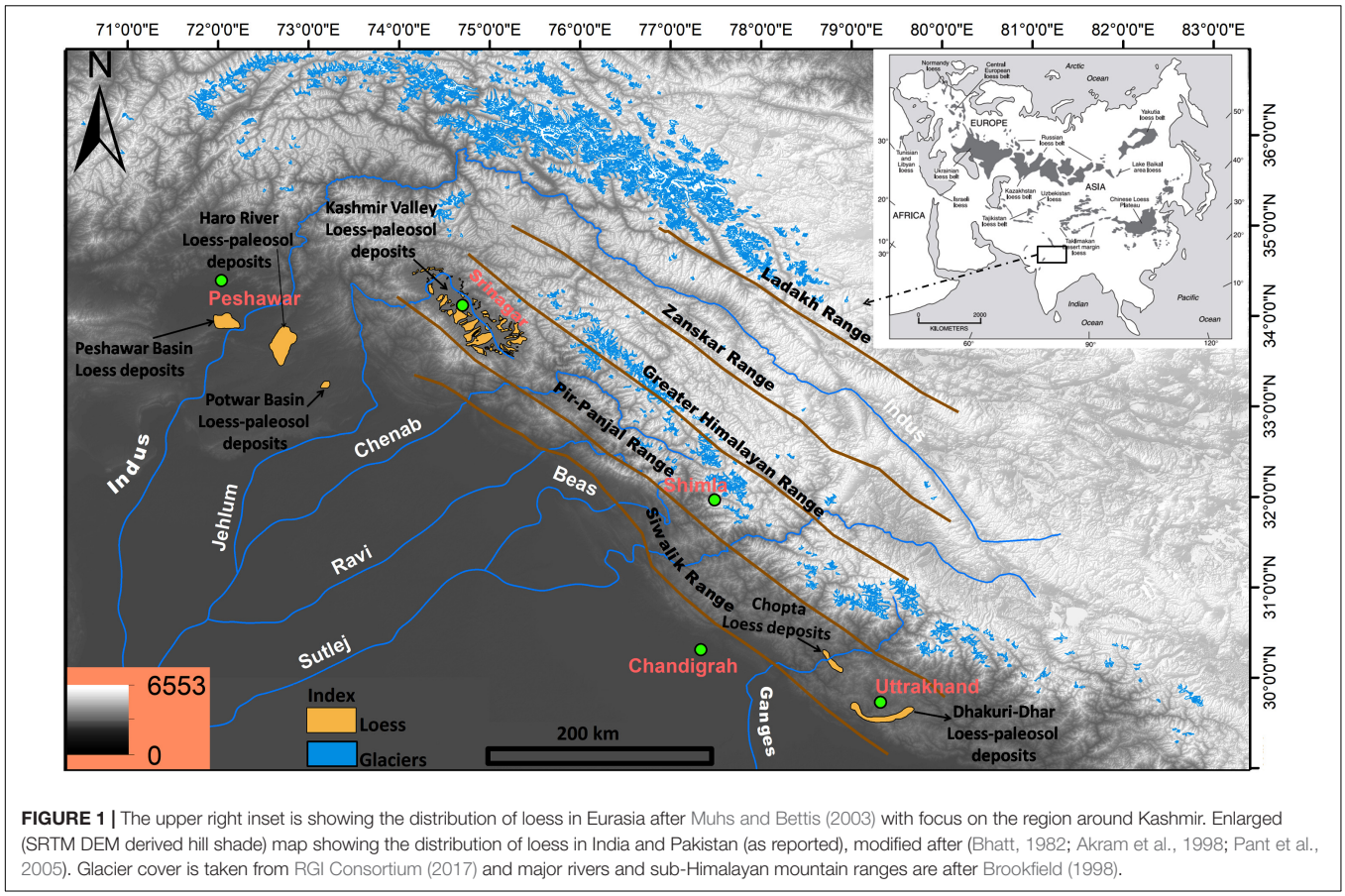

FIGURE 1 | The upper right inset is showing the distribution of loess in Eurasia after Muhs and Bettis (2003) with focus on the region around Kashmir. Enlarged (SRTM DEM derived hill shade) map showing the distribution of loess in India and Pakistan (as reported), modified after (Bhatt, 1982; Akram et al., 1998; Pant et al., 2005). Glacier cover is taken from RGI Consortium (2017) and major rivers and sub-Himalayan mountain ranges are after Brookfield (1998).

main areas of loess deposition are on the south-western side of the Kashmir valley, this is linked to the drying of the lacustrine environment which gave space to terrestrial conditions and thus loess accumulation space earlier on this side, where the Pir-Panjal Range is uplifting. Also the gentle morphology contributes to the higher preservation potential. Several outcrops allow assessment of the spatial homogeneity of the deposits over 10s–100s of meters. Especially toward the Pir-Panjal flank, the loess is often homogenous over such distances (and possibly wider). In contrast, toward the Valley the loess tends to become incised in some instances, so that care must be taken when sampling for palaeo-studies. Loess deposits of the Kashmir Valley provide one of the most valuable paleoenvironmental archives in the Quaternary of the Indian subcontinent but are yet little studied.

Climate and Its Evolution

Currently the rainfall pattern in the Kashmir valley (~710 mm/year) is dominated by western disturbances (WDs), and also has contributions from SW monsoons (Dar et al., 2015b). Variations in precipitation and temperature within the valley are mainly the result of altitude and aspect. Meteorological data shows that the annual temperature in the Kashmir Valley varies from -10 to 35°C (Zaz et al., 2019).

The onset of the monsoon climate system in Asia is by some authors attributed to the uplift of the Tibetan Plateau (TP) which started ~14 Ma ago (Edwards et al., 1996), although this is subject of ongoing debate. The formation of tectonic basins along the Himalayan and Kunlun mountain ranges is accompanied by deposition of thick gravel beds (500–1000 m in thickness), especially in lacustrine and fluvio-lacustrine sediments during the Late Miocene-Pliocene-Early Pleistocene also reflect the intensive tectonic movements around the Qinghai-Xizang TP (An et al., 1999). The uplift resulted in the formation of a well-established latitudinal gradient of increasing aridity toward the central parts of the TP and Himalayas (e.g., Wünnemann et al., 2008, 2010). The uplift of the TP accelerated during the Plio-Pleistocene epoch, accompanied by global atmospheric reorganizations, global cooling and loess sedimentation, which was probably also triggered by enhanced wind activity associated with the connection between the great east Asian trough and the Siberian anticyclone (Zhao and Morgan, 1985). This phenomenon has also been responsible for changes in precipitation and intensification of monsoon climate within the Indian region (Ganjoo and Shaker, 2007). However, the uplift of the Pir-Panjal Range on the southwestern side of the Kashmir Valley has locally played a major role in determining the climatic conditions. The Pir-Panjal Range attained a height of 1400–5000 m over the last 4 Ma due to tectonic uplift (Burbank and Johnson, 1982; Agrawal, 1985) and has acted as a barrier for southwestern monsoon winds and precipitation, thus changing the climatic conditions of the valley from tropical to more arid (Basavaiah et al., 2010). The Tibetan Plateau uplift (and coeval global CO_2 drawdown)

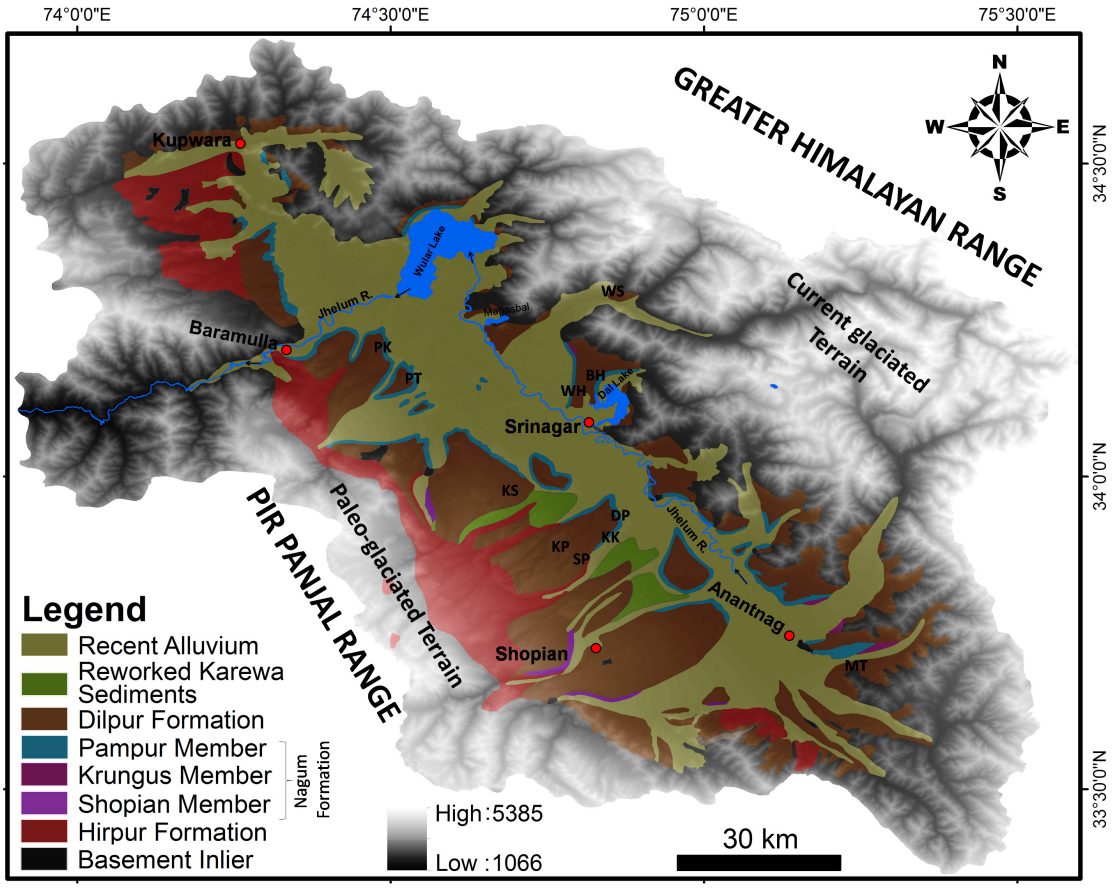

FIGURE 2 | Spatial distribution of various sediments of the Karewa Group in the Kashmir Valley after Bhatt (1982). Abbreviations MT, SP, KS, PT, PK, DP, KP, KK, BH, WH, and WS indicate the localities Mattan, Shankerpora, Khan Sahib, Pattan, Putkhah, Dilpur, Karapur, KhanchiKol, Burzahom, Wanihama, and Wuyil Sind, respectively. The Dilpur Formation represents loess and loess like sediments. The altitude is derived from SRTM (DEM; Farr et al., 2007).

has most probably contributed to the cooling processes and the onset of strong Quaternary glaciations. Quantifying the timing and extent of glaciation and the ensuing aridity of the Kashmir Himalayas and in the broader Himalaya is a prerequisite for linking Himalayan climatic fluctuations to global climate changes. Loess-palaeosol sequences, being sensitive to changes in configuration and intensification of atmospheric circulation, can provide valuable information on the local environmental change (e.g., An et al., 1999; Obreht et al., 2016).

Loess and lake sediments form the substrate for the most fertile soils in most of the Kashmir Valley and its enormous agricultural potential. The alluvial soils, derived mostly from the erosion of loess capped landscapes, cover most of the valley floor and the river flood plains. As per the United States Department of Agriculture [USDA] (1999) soil taxonomy classification, soils developed on loess in the valley are of thick organic rich mollisol and alfisol type soils, sometimes partly eroded at the top. The valley flanks comprise inceptisols as forest soils, and the upper reaches of the Pir-Panjal range are grass-covered entisols under pastures (Mahapatra et al., 2000). Various high-quality crops are grown on loess and loess-derived soils. In the higher reaches mixed broad-leaved and coniferous forest vegetation including Pinus excels, *Populus* sp., *Ulmus* spp., and Cedrus deodara etc. are prevalent. Entisols are used as pastures.

STRATIGRAPHY AND CHRONOLOGY

Available Data

Accurate chronological data is essential to understand and establish the timing of events documented within geoarchives in general and also loess deposits (e.g., Singhvi et al., 1987; Zeeden et al., 2018a,b). A number of techniques, including relative and radiometric dating techniques, have been used to understand the chronology of loess-palaeosol sequences. However, in the Kashmir Valley the initiation of loess deposition has remained a matter of debate and direct chronologies have been established so far only for the upper part of the loess-palaeosol formations (**Table 1**). The Loess-palaeosol sequences of the Dilipur Formation are clearly occurring in the Brunhes normal chron and are for sure younger 781 ka (Ogg, 2012).

Rendell and Townsend (1988) provide a minimum age from luminescence dating of ∼143 ka for the loess in Kashmir. Singhvi et al. (1987) date the uppermost thick Bt horizon, occurring below

TABLE 1 | Stratigraphic data and ideas as in literature, ordered by year.

Aim of study/data	Outcome/interpretation	References
Magnetostratigraphy, Luminescence dating	Loess of Brunhes Chron age, younger 780 ka	Agrawal et al., 1979
^{14}C dating	The last deglaciation started at ca. 18 ka	Kusumgar et al., 1980
Magnetostratigraphy	Lake deposits in Kashmir are spanning ∼4 Ma	Burbank and Johnson, 1982
^{14}C dating	Loess in Kashmir is younger 100 ka and has sedimentation rate of∼26 m/100 ka	Kusumgar et al., 1986
Pedostratigraphy	Loess in Kashmir comprises 4 glacial/interglacial cycles, and is older ∼350 ka	Bronger et al., 1987a
Luminescence dating	The topmost well developed soil is related to the last interglacial	Singhvi et al., 1987
Identification of glacials and interglacials	Loess in Kashmir is younger 200 ka	Agrawal et al., 1988
Luminescence dating	Loess in Kashmir is dated to ∼100 ka at ∼10 m, ages are probably too young	Rendell and Townsend, 1988
Identification of glacials and interglacials, ^{14}C dating	Loess in Kashmir spans the last ∼200 ka	Agrawal et al., 1989
Rock magnetism and correlation to marine d^{18}O data	Loess is older 200 ka	Gupta et al., 1991
OSL dating	Manasbal section is dated to MIS 3-2	Babeesh et al., 2017
^{14}C dating	Kashmir loess encompasses 1–2 glacial/interglacial cycles	Meenakshi et al., 2018

a triplet of "humus rich soil horizons" to the last interglacial (∼100–120 ka). The three humic horizons above this thick Bt horizon are dated to ∼80–50 ka. Babeesh et al. (2017) use optically stimulated luminescence to date the upper 8.7 m of the Manasbal section to the last 40 ka.

Agrawal et al. (1988) proposed the loess-palaeosol sequences to date back to ca. 200 ka, based on field observations and previous literature. Based on extrapolating sedimentation rates of a part of loess-palaeosols from the last glacial cycle, the reinterpretation of TL dates by Rendell et al. (1989) and correlation of loess to the marine oxygen isotope stratigraphy, Gupta et al. (1991) suggested that the base of the loess sequence is approximately 225 ka. Their correlation approach, however, is inconsistent with luminescence data by Singhvi et al. (1987), and an underestimation of the ages is probable.

Bronger et al. (1987a) states that at least four well developed soils are preserved in loess-palaeosol sequences in the Kashmir valley. Based on convincing dates of the uppermost one representing the MIS5e, Singhvi et al. (1987) suggest a time span of >300 ka based on thermoluminescence (TL) dating is a minimum age.

Lithostratigraphy and Pedostratigraphy

It is evident that thicker and older loess-palaeosol sequences are present at the Pir-Panjal flank than at the Himalayan flank and in the center of the Kashmir valley (e.g., Bronger et al., 1987a; Singhvi et al., 1987; Agrawal et al., 1988, and also own observations). Below the recent soil complex, which includes a humic topsoil and a thick Bt horizon, four gray-black soils are present in a (more or less pedogenetically altered) upper loess package. While previous studies were unsure whether three or four gray/blackish soils are present in this package, the recent literature and our own observations (at Wanihama near Burzahom, the Khan Sahib area and Shankerpora) strongly suggest four differently expressed gray/blackish soils in this loess package (**Figure 3**) above the first dark brown palaeosol (K-S1; **Figure 3**). Three gray/black soil horizons at the base of the upper loess package (K-L1) are present. Of these the uppermost one is weakest expressed, and the lower two ones are separated by an ochrish pedogenetically overprinted loessy material. This triplet represents an excellent marker package which is consistently observed in the Kashmir valley. The K-L1 is present in most places and confined at the base by a thick and dark brown Bt horizon (K-S1), which may (or may not) be genetically connected to the humic horizon above (Bronger et al., 1987a; Singhvi et al., 1987; Agrawal et al., 1988; also own observations).

The loess-palaeosol sequences below the K-S1 are not exposed in many places, making an equally consistent and reliable stratigraphic description challenging. Further, stacking of palaeosols into pedocomplexes and little separating loess is complicating a description and interpretation (Bronger et al., 1987a), our observations support this. However, the following older and second loess complex (K-L2) contains a (weak) grayish double-soil present at least in Shankerpora and the Khan Sahib area (Dar et al., 2015c; own observations; see **Figures 3**, **4C,D**), and is followed by another brown soil. Below this interval we refer to the describing literature (i.a. Bronger et al., 1987a; Gupta et al., 1991; Dar et al., 2015b; Chandra et al., 2016; Ahmad and Chandra, 2018). Literature and own observations suggest at least two further well-developed soils and loess package between these (Bronger et al., 1987a; Dar et al., 2015a).

The loess generally overlies fluvial or lacustrine sediments (**Figures 4B,C,F**). We observe the lowermost loess being overlain by non-aeolian sediments in the transition from fluvial/lacustrine to aeolian sedimentation. The transition of fluvial/lacustrine and aeolian sedimentation is not always sharp, but may start with (pedogenetically overprinted) loess, then go back to a limnic environment and then become fully aeolian. This is the result of changing water levels of water bodies and may be expected form a sedimentological and sequence stratigraphic point of view.

Chronostratigraphic Information

Magnetostratigraphy places the loess of the Kashmir Valley in the Brunhes normal polarity chron, younger 780 ka (Basavaiah et al., 2010 and references therein). Due to lacustrine sediments above

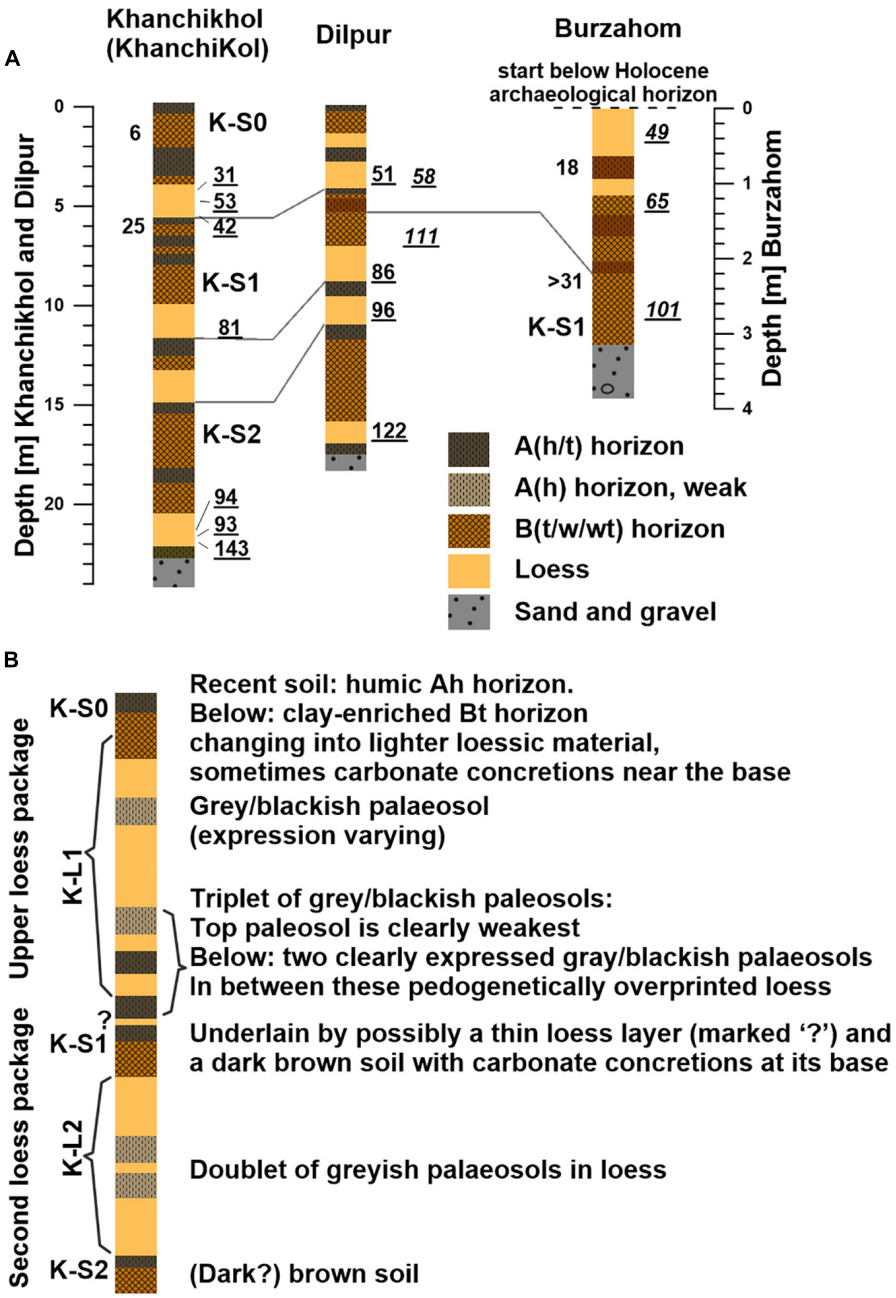

FIGURE 3 | (A) Comparison of selected loess-paleosol sections which have been dated. Ages are rounded and given in ka. Stratigraphic positions are indicated as good as possible, correlation to stratigraphic unit is correct but the exact positioning is only indicative here. Logs are summarized and simplified from Kusumgar et al. (1986), Bronger et al. (1987a), and Singhvi et al. (1987). Thermoluminescence ages are plotted right of section logs, here after Rendell and Townsend (1988; bold and underlined), and from Singhvi et al. (1987; bold, underlined and italic). ^{14}C ages from Kusumgar et al. (1986) are included left of the stratigraphic columns. Note that other dates are available but cannot be placed in the stratigraphies unambiguously. Correlations are after Bronger et al. (1987a) and Singhvi et al. (1987) and Gupta et al. (1991). Note that ^{14}C ages are systematically younger than thermoluminescence ages. Please see the here introduced nomenclature for loess and palaeosol sequences as K-S0 to K-S2 and K-L1 to K-L2. At the Himalayan Flank only the K-S1 is present, while older loess is described from the Valley toward the Pir-Panjal flank. **(B)** Generalized stratigraphy of the upper/younger Kashmir loess–palaeosol sequences across the Kashmir Valley. At some localities, loess below these two packages is outcropping, but we can at this point not describe a general pattern. Below the here generalized stratigraphy, the stratigraphy is less clear to us. Several (2 at least, possibly more) well expressed paleosols follow. These are not always separated by loessy material. We name the Soils K-S0 (recent soil) to K-S2 (second thick brows soil) and the upper two loess units K-L1 and K-L2. These are descriptive terms here and are no indication of time or glacial/interglacial cycles due to a lack of reliable chronology. Please note the maker triplet of soils in **(B)**, which sometimes represents the upper part of an amalgamated K-S1 pedocomplex, and sometimes is separated by loess layers, see also **Figures 4D,E**.

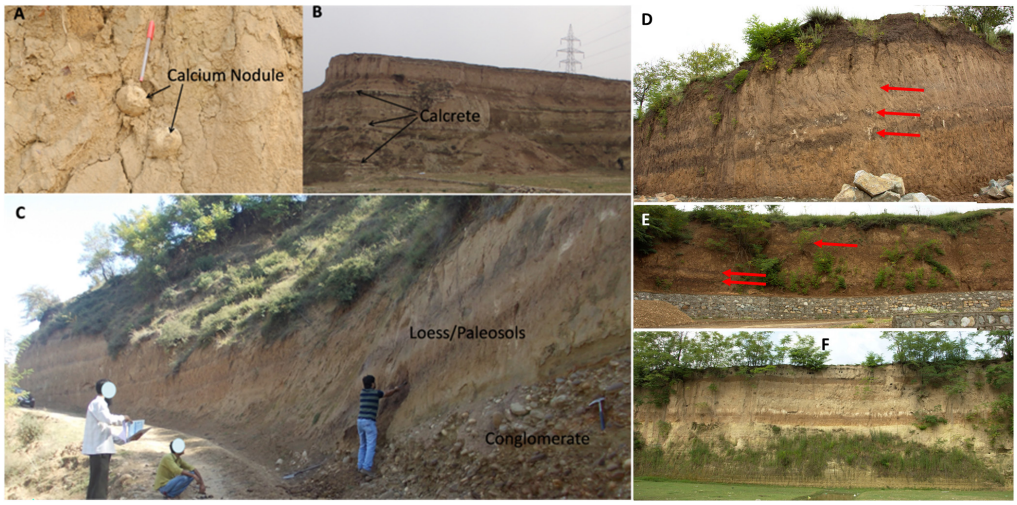

FIGURE 4 | Field photographs showing **(A)** calcium carbonate nodules in the 5th well developed palaeosol at the Shankerpora village section **(C)**, **(B)** three calcrete layers in lacustrine sediments near the town of Pampore underlying loess, reflecting dry and arid climatic conditions. These calcrete layers in Central Kashmir are chronologically and stratigraphically equivalent to the loess in the south-western Kashmir Valley (see Dar et al., 2015a for further explanation), **(C)** loess palaeosol sequence section near Shankerpora Village directly overlying the conglomerate bed of the Shopian Member of the Karewa Group. **(D, E)** Are images of the marker triplet, which is exposed in a road cut near Khan Sahib, in a plateau position **(D)**, and a slope position **(E)**. **(F)** Shows the loess overlying lacustrine deposits at Wanihama. The lower vegetated part of the wall shows clear layering of lacustrine carbonates.

the Matuyama-Brunhes boundary, one may expect a considerably younger age. Generally, luminescence dating and ^{14}C dating suggest inconsistent ages for the Kashmir loess-palaeosol deposits with ^{14}C dates suggesting younger ages. ^{14}C dating is generally accomplished using microscopic organic matter extracted from palaeosols, and not on macro remains. Luminescence dates from the 1980s may also be difficult when compared to recent data.

Here we introduce a palaeosol numbering K-S1, K-S2, and K-S2 The gray/blackish and humus-rich soils in the K-L1 show no strong Bt horizons and are interpreted to represent short and/or weak soil formation phases. The thick Bt K-S1 has been suggested to represent MIS 5e by Singhvi et al. (1987). ^{14}C dates are in contrast to this suggestion and imply much younger ages for the K-S1, and imply higher sedimentation rates of ∼26 m for the last 100 ka (Kusumgar et al., 1986). The ^{14}C-dating of the marker triplet (see **Figure 3**) of grayish soils preserved across the Kashmir Valley yielded ages of ∼9, 15, and 20 BP (Meenakshi et al., 2018) from the Shankerpora section. However, the marker triplet clearly lies below the topmost blackish palaeosol dated to ∼22,500 ka BP (Krishnamurthy et al., 1982) and 14–21 ka PB (Agrawal et al., 1989). Meenakshi et al. (2018) also calibrated the age of the local LGM to 18.6–22.3 ka. This apparent inconsistency still suggests a rather high sedimentation rate, but does not give confidence in the ^{14}C dates.

Two studies (Bronger et al., 1987a; Gupta et al., 1991) attempt a comparison of the Kashmir loess-palaeosol sequences with global climate evolution, and conclude that the loess-palaeosol sequences of the Kashmir valley span at least several glacial/interglacial cycles. While Bronger et al. (1987a) suggests at least 4 glacial-interglacial cycles and a minimum duration of 350 ka, Gupta et al. (1991) suggest an age of >200 ka based on (tentative and possibly questionable) correlation to marine $d^{18}O$ data.

Stratigraphic Summary

Although it may be argued that an adequate chronological database is available for Kashmir loess, the inconsistency between the chronologies makes it challenging to interpret the soil forming episodes in the context of global climatic events and evolution. The difference between the luminescence and ^{14}C ages may be due to the high inorganic carbonate content of up to >20%, and the visible carbonate movement in the profiles. This may alter the carbonate isotopic composition in samples and explain the inconsistencies between ^{14}C dating studies. Also processes of loess deposition and soil formation may play a role, as the former gives the age of the initiation of loess accumulation and the latter the age of soil formation. Therefore, differences between these chronologies may be expected, but not in the reported magnitude and inconsistency. There is a clear need for the establishment of a reliable chronology of the loess-palaeosol sequences for placing these reliable in a regional and global context. There is a clear need for the establishment of a reliable chronology of the loess-palaeosol sequences for placing these reliable in a regional and global context.

PALEOENVIRONMENTAL PROXY DATA AND INFERENCES

Paleoenvironmental proxy data are so far available in a limited quantity from the loess deposits of Kashmir (**Table 2**). Although the semi-quantitative early studies (e.g., Agrawal et al., 1979, 1988; Bronger et al., 1987a; Singhvi et al., 1987) are very valuable,

no quantitative and reproducible high-resolution studies of any proxy data have been carried out. The following sections provide an overview of the existing paleoenvironmental proxy studies in Kashmir loess.

Rock Magnetic Properties

Yet, two studies report on the magnetic susceptibility and its frequency dependency from loess in Kashmir. Kusumgar et al. (1986) dates the ∼25 m long Khanchikhol-I and Burzahom sections by ^{14}C, and also provide data for the magnetic susceptibility (χ, reported in a range from 10 to 50 without dimensions) and the frequency dependent magnetic susceptibility (χ_{fd}, in a range from 2 to 12%). Also Gupta et al. (1991) report χ ranging from $2*10^{-6}$ and $2*10^{-7}$ SI units and χ_{fd} of 2–12% for several loess sections, and use the rock magnetic data and the soil stratigraphy for correlation between these profiles. They also suggest that the χ_{fd} is increased in soils relative to palaeosols in a similar fashion as in eastern Asia, although by now it is clear that there are clear differences within Asian records (e.g., Ding et al., 1999). It is relevant to notice that there seems to be a higher magnetic susceptibility in soils for most of the upper ∼10 m of profiles. Below, this relationship seems less clear and especially B-horizons show partly lowest magnetic susceptibilities. This is similar to loess from Pakistan, where no clear magnetic enhancement could be detected (Akram et al., 1998).

A study including the temperature dependent magnetic susceptibility and also isothermal remanent magnetization is available from the Central Himalaya (Pant et al., 2005). Their study suggests the presence of magnetite and maghemite in palaeosols, and a dominance of magnetite and hematite in loess with a minor maghemite contribution. If this is representative also for Kashmir loess is to be tested in the future.

Grain Size Data

The available literature reveals that the grain size of Kashmir loess is dominated by silt-size particles in the range from 6 to 20 μ, making up 30–40% of the total sample and the clay content ranging commonly from 25 to 35% (Bronger et al., 1987a). The grain size has mostly been used to discriminate the source of dust and quantify the degree of weathering (Bronger et al., 1987a; Babeesh et al., 2017), while no study has been published so far which has used grain size as proxy for paleoenvironments. Bronger et al. (1987a) suggest that some of the loess may be reworked local lake sediments, but also argue that the fine grain size (compared to European loess) suggests a distant source beyond the Kashmir Valley itself.

Geochemistry of Kashmir Loess

Geochemical studies did not differentiate systematically between loess and soils, and several observations cannot be related to stratigraphic information in detail. Studying the geochemistry of loess sediment is a powerful tool to understand its origins, transportation, and post-depositional modification. More importantly, geochemical studies may provide insights into Quaternary climate change (e.g., Schaetzl et al., 2018; Han et al., 2019). A fair amount of geochemical data has been generated on the loess-palaeosol sequences of the Kashmir Valley (Lodha et al., 1987, 1988; Ahmad and Chandra, 2013). Lodha et al. (1987, 1988) carried out an XRF study of loess-palaeosol sediments, and they suggested that K, Rb, Fe, Ti, Zn, Cu, and Mn are generally elevated in palaeosols, whereas Ca and Sr have relatively high concentrations in loess layers. They suggested that such concentration of elements in palaeosols is related to the pedogenic modification of the parent loess. Subsequently, Lodha et al. (1987) found that the concentration of iron and titanium are higher in loess profiles along the Pir-Panjal flank than on the Himalaya margin of the Kashmir Valley. The Pir-Panjal is dominated by basic rocks, mostly Panjal traps, compared to the Greater Himalayan flank of the Kashmir Valley which is dominated by carbonates (Dar et al., 2014).

Recently, Ahmad and Chandra (2013) analyzed the loess-palaeosol sediments for major, trace and REE elements to determine their chemical composition, provenance and intensity of paleo-weathering. Based on weathering indices such as the Chemical Index of Alteration (CIA), Chemical Index of Weathering (CIW), and Plagioclase Index of Alteration (PIA) values (71.87, 83.83, and 80.57 respectively) and the A-CN-K diagram of the loess-palaeosol sequences, they suggested that these sediments have experienced a weak to moderate degree of chemical weathering. They further suggested that these sediments reflect a similar composition and alteration history across the Kashmir valley. Their Chondrite normalized REE-patterns are characterized by moderate enrichment of LREEs, a relatively flat HREE pattern (Gd_{CN}/Yb_{CN} = 1.93–2.31), a lack of a prominent negative Eu anomaly (Eu/Eu^* = 0.73–1.01, average = 0.81) and variable amounts of total REE (ΣREE = 156–226 ppm). The lack

TABLE 2 | Summary of physical- and chemical studies on Kashmir loess.

Type of data	Outcome/interpretation	References
Rock magnetism: magnetic susceptibility and frequency dependent magnetic susceptibility	Loess is related to global climate evolution, different interpretations by authors	Kusumgar et al., 1986; Gupta et al., 1991
Element geochemistry	Provenance is stable, weathering intensity varies	Lodha et al., 1987, 1988; Ahmad and Chandra, 2013; Chandra and Ahmad, 2013; Chandra et al., 2016; Babeesh et al., 2017
Isotope geochemistry	Pleistocene climate- and precipitation changes	Krishnamurthy et al., 1982, 1986; Dar et al., 2015b
XRD clay mineralogy	Clay is mainly Smectite, illite, chlorite, and kaolinite occur	Chandra et al., 2016; Meenakshi et al., 2018
Grainsize	Varying depositional processes	Babeesh et al., 2017
Micromorphology	Intensity of soil formation, relation to paleoclimate	Bronger et al., 1987a; Chandra and Ahmad, 2013; Dar et al., 2015a,b; Chandra et al., 2016

of a negative Eu anomaly reflects partial weathering of plagioclase feldspar, which also reflects its paucity in the source area.

Clay Mineralogy

On the basis of an XRD study (Chandra et al., 2016) concluded that the palaeosols' clay mineral composition is dominated by smectite, illite and chlorite-kaolinite with contributions of chlorite. It should be noted that smectite is commonly found in arid to semi-arid climatic regions. Under intense weathering conditions it can alter halloysite and kaolinite (Cai et al., 2008). Its presence in soils represents poorly drained environments and a climate characterized by strong seasonal precipitation (Bellotto et al., 1995).

Stable Isotopic Studies on Kashmir Loess

Paleoenvironmental studies using the stable C and O isotopic compositions of organic matter, calcium nodules (see **Figure 4A**), and other material preserved in the loess-palaeosols have been carried out on material from the Kashmir Valley. The work by Krishnamurthy et al. (1982, 1986) and Dar et al. (2015b) studies the paleovegetation and paleoenvironmental setting using stable oxygen and carbon isotopic signatures (**Table 3**). The nodules of 1–3 cm size were handpicked from the Bk horizons of the paleosol profiles from three loess-paleosol sections (Shankerpora, Khan Sahib and Putkhah), and have been analyzed for C and O isotopic signatures (Dar et al., 2015b). The overall $\delta^{13}C$ values of the pedogenic carbonates from three loess-palaeosol sections Shankerpora (SK), Khan Sahib (KS) and Putkhah (PK) range from -4.96 to -8.28‰. The reported $\delta^{13}C$ values suggest that the C_4 fraction of the local flora has gradually increased in the valley during the formation of most of the palaeosols analyzed in the study with the exception of palaeosols SK-7 (-7.64‰) and KS-2 (-8.28‰; see Dar et al., 2015b) and palaeosol-1 (18 ± 2 ky) at Burzahom (Krishnamurthy et al., 1982), which reflect less arid climate and the presence of more C_3 type plants.

The $\delta^{18}O$ values of the pedogenic carbonates suggest that cooler and possibly drier than present conditions prevailed at the time of nodule formation (Dar et al., 2015b). The observed relationship between $\delta^{13}C$ and $\delta^{18}O$ is consistent with carbonate precipitation at times of enhanced westerly precipitation influence.

Micromorphological Studies of Kashmir Loess

The imprint of pedological features related to different environmental conditions is strongly influenced by climate. Palaeosols often preserve records of the paleoenvironment in their pedogenic features (e.g., Kemp and Zárate, 2000; Kemp, 2001; Scarciglia et al., 2003; Srivastava et al., 2010). In this framework, understanding of the local pedogenetic response to climate change can be improved by micromorphological analysis. In the Kashmir Valley few studies have reported the micromorphological investigations of loess-palaeosol sequences. Initially these deposits were misinterpreted as loessic loam, loamy silt and brown silty clay (de Terra and Patterson, 1940). However, Pant et al. (1978) were the first to perform a Scanning Electron Microscopic (SEM) study of the quartz sand grains of these deposits and suggested their eolian origin. Thereafter, several studies have been carried out to deduce Quaternary climate changes in the Kashmir Valley using thin section micromorphology of paleosols (Bronger et al., 1987a; Gardner, 1989; Dar et al., 2015a; Chandra et al., 2016). On the basis of micromorphological studies, Bronger et al. (1987a) suggested that warm and mostly humid climatic conditions prevailed during the formation of the top three palaeosols across the Kashmir Valley. Similarly, Gardner (1989) proposed that the palaeosols represent similar climatic conditions except for the two palaeosols formed in the later part of the last glacial period. The most common micromorphological features reported from Kashmir loess-palaeosols are channel/void- and ped-microstructures, massive microstructures, clay coatings, concentrations of calcite in the form of coatings and nodules, iron staining, iron manganese oxides, pedotubules, and disseminated organic matter (Dar et al., 2015a). A study also reported the co-existence of pedogenic $CaCO_3$ and clay coatings, suggesting decalcification followed by clay illuviation (**Figure 5**). This is interpreted as reflecting progressive drier climatic episodes following the partially moist climate associated with Quaternary climate changes, as has been found elsewhere (Badía et al., 2009). Khormali et al. (2003) suggested that clay gets translocated in moist climatic conditions and is covered by carbonate as the climate gets drier. Besides, the ped microstructures formed by shrinking-swelling reveal seasonal wetting and drying conditions (Dar et al., 2015a).

Paleopedology in the Context of Chronology

Loess-palaeosol sequences in Kashmir have traditionally been used for studying stratigraphic and relative paleoenvironmental variations expressed by the intensity of soil formation. The paleosoils intercalated in loess can be seen throughout the Kashmir valley with some regional variations (Bronger et al., 1987a; Agrawal et al., 1988). Changes in the paleoclimatic conditions during pedogenesis are reflected by lithological features such as the amount of organic matter, different clay minerals and their content, color, presence/absence of calcium carbonate and the depth of carbonate leaching in the loess palaeosol sequences. The palaeosols generally show elevated organic matter contents compared to the loess, and weak to moderately developed illuvial clay pedofeatures, suggesting subtle to substantial climatic changes that influence the relative rates of material supply, pedogenesis and weathering (Dar et al., 2015a). According to Dar et al. (2015a), the palaeosols formed under stable landscape conditions when loess deposition was episodic, or accumulation decreased to the point where pedogenesis could outpace the eolian input.

A semi-quantitative pedological assessment helps understanding past environments and their variability. For example, three humus rich "Aht" horizons representing three warm and humid climatic conditions (between 80 and 50 kyr) were recognized (Bronger et al., 1987a). They also suggested

TABLE 3 | Pedological and isotopic characteristics of the top three palaeosols preserved across the Kashmir valley, and reference to key papers.

Site/Location	Material	Depth (m)	$\delta^{13}C$ (‰ VPDB)	$\delta^{18}O$ (‰ VPDB)	Horizon	Color	Age in years	References
Khan Sahib (KH)	KH-S1	1.90	−4.96	−6.55	Aht	10YR6/4	NA	^Agrawal et al., 1989; Dar et al., 2015a,b
					Btk	7.5YR5/3		
	KH-S2	3.60	−6.22	−6.47	Aht	10YR6/4	17,740 ± 630^	
					Btk	10YR5/4		
	KH-S3	5.50	−4.88	−6.78	Aht	7.5YR5/3	21,840 ± 1150^	
					Btk	7.5YR8/2		
Putkhah (PK)	PK-S1	1.50	−5.50	−7.3	Ah	10YR7/3	NA	^Agrawal et al., 1989; Dar et al., 2015a,b
					Bt	10YR6/3		
	PK-S2	3.00	−5.27	−7.93	Aht	10YR6/3	18,550 ± 600^	
					Bt	10YR47/3		
	PK-S3	4.25	−6.31	−5.75	Aht	10YR5/3	25,800 ± 1110^	
					Btk	10YR5/4		
Burzahom (BZ)	BZ- S1	1.29	−25.3# OM	−7 ± 0.3# (Avg.)	Bwk	10YR7	42,452–45,877* 18,890 ± 830 750#	#Krishnamurthy et al., 1982; Chandra and Ahmad, 2013; Meenakshi et al., 2018
		1.79				10YR 6/3	45,877–47,726*	
	BZ- S2	2.06	−16.2# OM	−7 ± 0.3# (Avg.)	Ahk	10YR 6/3	47,726–49,438*	
		2.31			Bt	10YR7/3	49,438–53,205*	
	BZ- S3	2.86	−21.9# OM	−7 ± 0.3# (Avg.)	Aht	10YR 6/3	53,205–55,945*	
		3.26			Bt	10YR 5/4	55,945–62,657*	
Shankerpora (SP)	SP-S1	1.00	–	–	Aht	10YR4/2	8648–9016*	Dar et al., 2015b; Meenakshi et al., 2018
		1.63			Bwt	10YR5/4	9833–10,229*	
	SP-S2	2.65	–	–	Ah	10YR5/2	18,468–18,868*	
		3.15			Bw	10YR6/4	22,001–22,511*	
	SP-S3	3.88	–	–	Aht	10YR5/6	28,189–28,972*	
		4.1			Bwt	10YR4/4	33,565–34,357*	

The asterisks "^" "#," and "" respectively indicate the source of chronological and isotopic data from Krishnamurthy et al. (1982), Agrawal et al. (1989), and Meenakshi et al. (2018).*

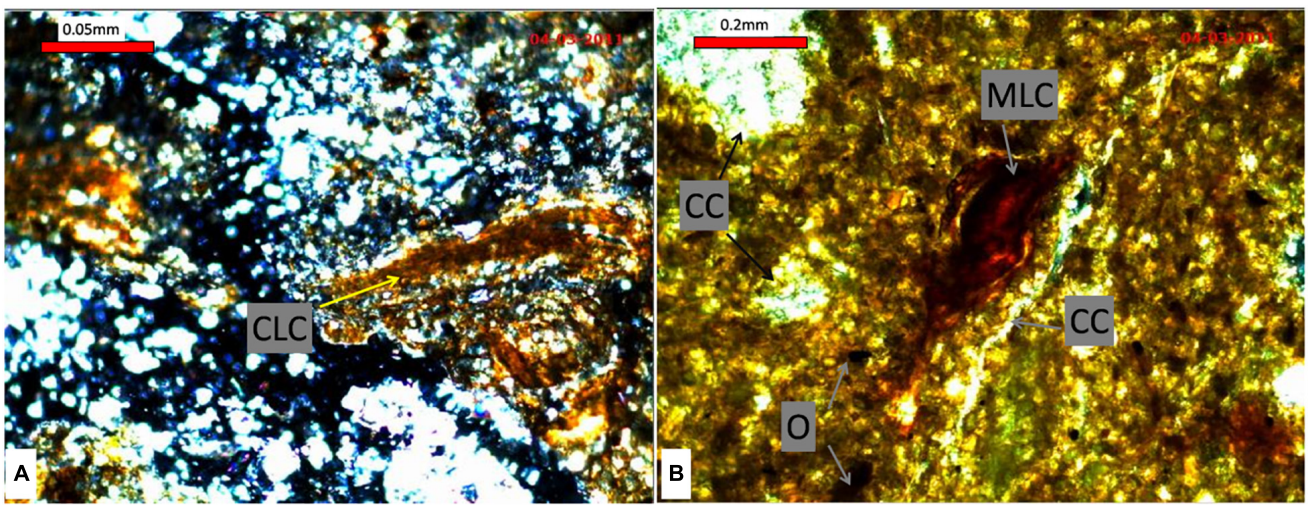

FIGURE 5 | Photomicrographs of the Khan Sahib section showing **(A)** clay coating (CLC) in a root cavity, quartz grains in a partly altered loess layer KS- L1 and **(B)** showing micro laminated clay coating (MLC), opaque minerals (O) channel and void filled with calcium carbonate (CC) in paleosol profile Btk (KS-S4) at the Khan Sahib (Dar et al., 2015a).

that during the middle Pleistocene at least four Bwt, or thick Bt horizons developed in loess reflecting four interglacial periods, with climates similar to the present-day. Based on the available ^{14}C dates of the Khanchi Kol-I section, Kusumgar et al. (1986) proposed that the palaeosols dated to ca. 5000, ca 18,000 and > 31,000 BP all represent major climatic oscillations indicating interglacial conditions, also around the LGM. Recently, optically stimulated luminescence (OSL) dating of loess like palaeosols in the Manasbal section (total section thickness 10.6 m) yielded ages of 41.7 ± 8.0 ka (at a depth of 8.7 m), and 14.6 ± 3.8 ka (at a depth of 2.9 m), coinciding with the age of marine isotope stages (MIS) 3 and late MIS2, respectively (Babeesh et al., 2017). The palaeosol formed during the MIS3 shows well-developed Ah/Btk characteristics, reflecting rather wet climatic conditions. A gradual increase in arid and drier climatic conditions is revealed by the $CaCO_3$ content and C/N ratio of the palaeosols at a depth of 6.50 m (Babeesh et al., 2017). They also suggested that Bwk horizons at a depth of 2.90 m represent the late MIS2 post-LGM period.

Paleopedology contributed most to the understanding of past environments in Kashmir. Despite the progress made by above mentioned studies on the paleoenvironmental signature using a pedological approach, more systematic high-resolution quantitative work is needed in this direction. In particular, the relation to a reliable chronostratigraphy can lead to a better understanding of the climate evolution and its global context.

Paleovegetation

Reconstructions of the paleovegetation from Kashmir have recently received increasing attention. Krishnamurthy et al. (1982, 1986) and Dar et al. (2015b) analyzed vegetation from loess. Previous studies are focusing on pollen-based vegetation reconstructions from the lacustrine sediments predating or associated with the loess accumulation phase (Agrawal et al., 1989 and the references therein). Stable isotopic signatures of pedogenic carbonates and organic fractions demonstrate that C_4 plants dominated the vegetation during the time of loess deposition. The $\delta^{13}C$ values suggest that the sampled palaeosols formed under hotter and drier interglacial or interstadial conditions than present and/or the last interglacial period (Krishnamurthy et al., 1986). Although the presence of wetter periods cannot be ruled out, that would require higher resolution isotopic analysis as this is not reflected by the analyzed pedogenic carbonate nodules and organic matter from the palaeosols (Krishnamurthy et al., 1982, 1986; Dar et al., 2015b). The dominance of C_4 vegetation may also be considered as a result of the strengthening of WDs as the seasonal variations of drying and wetting associated with these winds allow C_4 vegetation to survive better than C_3 plants (Dar et al., 2015b). However, the palaeosol dated 18 ± 2ka (e.g., at the Burzahom section; see **Figure 2** for location) indicates the presence C_3 type of vegetation (Krishnamurthy et al., 1982, 1986). Interestingly, the $\delta^{13}C$ values reveal that monsoon systems may have been of less intensity since the start of loess deposition. The monsoon winds may also have operated less efficiently even in the peninsular India during the last interglacial periods, thus resulting in less precipitation and hotter and drier conditions in Kashmir (Krishnamurthy et al., 1986).

On the basis of $^{13}C/^{12}C$ and C/N ratios of Karewa lake sediments, three major periods of reduced water levels with enhanced contribution from terrestrial vegetation are revealed, probably associated with the onset of Quaternary glaciation which amplified aridity that led to loess deposition (Krishnamurthy et al., 1986). The paleopedology has not yet been used to assess paleo-vegetation and its development.

Summarizing, reconstructing the paleovegetation is difficult for the Late Quaternary, as loess is not commonly preserving pollen, and the Lake Karewa dried to give place to terrestrial environments. Isotope data are probably the best way forward, although interpretations have to be taken with care (Obreht et al., 2019). Agrawal et al. (1989) reconstructed a general cooling and drying trend over the last several million years from Lake Karewa sediments, but details of the timing and patterns of this change are yet to be determined.

Paleo-Precipitation and -Temperature Reconstructions

Paleosols can be used for proving quantitative information of precipitation and temperature in the past (e.g., Kraus, 1999). However, quantitative paleo-precipitation and paleo-temperature estimates for the Kashmir Valley are yet missing. So far, the mean annual precipitation (MAP) and mean annual temperature (MAT) were investigated by Ahmad (2012) from three loess-palaeosol sequences at Karapur, Dilpurand and Burzahom. The MAP and MAT values were derived from the weathering indices (CIA values) of the loess palaeosol sequences. The concept being that high precipitation and warm temperatures enhance the extent of chemical weathering, whereas low precipitation and/or cold temperature weakens the intensity of chemical weathering (White and Blum, 1995; Sheldon et al., 2002). The availability of water and warmth enhances the depletion of alkali- and alkaline earth elements at the cost of refractory elements such as aluminum (Sheldon et al., 2002). Therefore, changes in weathering intensity with stratigraphy reflects the variation in past temperature and precipitation. The derived MAP value of the Kashmir loess and palaeosols ranges from ∼59 to 564 mm with an average of 419 mm. The reconstructed MAT values range from ∼10.55 to 12.57°C with an average of 11.73°C. On the basis of the MAP and MAT values, Ahmad (2012) advocated that the climatic conditions in the valley mostly fluctuated between cold arid to warm semi-arid during the Late Quaternary – a clear contradiction to the intense soils described by e.g., Bronger et al. (1987a). Generally it is suggested that the climate of the Kashmir Valley varied between cold-arid and warm semi-arid during the Late Quaternary (Ahmad and Chandra, 2018). The climatic variability has mainly been investigated for the Holocene (Singh, 1963; Dodia, 1983; Agrawal, 1992; Spate, 2019), and quantification of the climatic signatures preserved within soils is yet best addressed by pedology. Due to a lack in reliable chronology, millennial-scale (and or centennial-scale) climatic oscillations, which can represent very valuable for

correlation (e.g., Shi et al., 2003; Zeeden et al., 2018c), are not yet reported from Kashmir. Summarizing, the timing and intensity of paleoclimatic changes in Kashmir over the late Quaternary is yet rather incomplete.

Provenance of Kashmir Loess

The provenance of the dust for Kashmir loess is poorly established and remains a matter of ongoing debate. In their pioneering work, de Terra and Patterson (1940) suggested the source dust for loess beyond the Pir-Panjal Range. Subsequently, (Lodha et al., 1985, 1987) worked on the major and trace element concentrations of these sediments using EDXRF. Based on iron and titanium concentrations in loess-palaeosol profiles along the Pir-Panjal flank and Greater Himalayan flank, they suggested that the source material of Kashmir loess is local. Similarly, Gupta et al. (1991) suggest that the source of loess is local, based on thickness and magnetic susceptibility variations among the analyzed loess layers. Dilli and Pant (1994) stated that loess was derived from the region, where both acidic and basic rocks and their metamorphic equivalents predominate. Further, the relatively high content of coarse and medium silt size particles suggests that the source of the silt is predominantly local (Gardner, 1989). The possible source of dust could be the mountain ranges delimiting the Kashmir Valley, as these are dotted with extensive glacial landforms reflecting the existence of extensive valley glaciers during the later Quaternary period (Dar et al., 2017). Therefore, it may be argued that these glaciers might have produced large quantities of glacial outwash and fine sediments through glacial grinding. However, recent geochemical studies of the loess-palaeosol sequences puts forward that these sediments are derived from mixed sources of mafic and felsic rocks suggesting larger provenance regions with variable geological settings (Ahmad and Chandra, 2013; Babeesh et al., 2017; Bhat et al., 2019). This suggests that a major contribution from outside the Kashmir valley exists. Candidate regions are the Peshwar Basin in Pakistan, from where large amounts of loess have been reported. A fine component brought form the Thar desert is also possible.

KASHMIR LOESS IN A REGIONAL CONTEXT

Loess in the Indian Subcontinent and Kashmir

From India loess data is sparse, and although the distribution can be expected to be widespread (Smalley et al., 2009), loess has hardly been reported from India for unclear reasons. Smalley et al. (2016) state (for both India and Pakistan) "the conditions appear to be perfect for the formation of large deposits." Juyal et al. (2000) report aeolian sandy silt with ∼60% silt and ∼40% fine sand from the last glacial cycle in the Mahi Basin, western India. (Liu et al., 2017) report rather coarse loess from southwest of Delhi, and suggest a more widespread occurrence in the Indo-Gangetic plain in the triangle of Delhi, Jaipur and Agra. Our observations confirm the presence of silty aeolian material as described by Liu et al. (2017) near Delhi airport. Further, Liu et al. (2019) suggest an aeolian origin of lateritic soils in the Deccan Plateau. These studies from India south of the Himalayas show a similar Rare Earth Element (REE) geochemistry as loess from China and also Kashmir, but a silt grain size dissimilar from the Kashmir loess (Ahmad and Chandra, 2013). However, because loess in India and China can be expected to have different sources, the similarity of REEs in loess in India and Kashmir cannot be taken as indication for a common source. Also for some Himalayan and Tibetan valleys loess is reported (Dill et al., 2003; Sun et al., 2007; Jones and Pal, 2009).

The topic of loess, and other Late Quaternary paleoclimate archives, has not been investigated more in Pakistan than in India during the last decades, and Muhs (2018) states that the extent of loess in Pakistan is only vaguely known. Several loess areas are reported from the Peshwar Basin, specifically the area around Nowshera west of the confluence of the Kabul and Indus Rivers (Din and Yoshida, 1997), the Haro River Loess-Palaeosol deposits (Din and Yoshida, 1997), the area of Islamabad (Calkins et al., 1975; Warwick and Wardlaw, 2007).

The most valuable literature containing hard data are Din and Yoshida (1997) and Akram et al. (1998), who report on grain size properties and further rock magnetic properties from a ∼17 m loess-palaeosol profile from the Haro loess area in Pakistan. No systematic magnetic enhancement is observed (Akram et al., 1998; their **Figure 7**) which led Akram et al. (1998) to the statement "The loess-palaeosol sequence in Attock basin, Pakistan does not show "Chinese Loess Plateau type" correlation between magnetic susceptibility and loess/palaeosol facies." The fact that the magnetic susceptibility is enhanced in the topmost soils and meters, but follows no clear patterns in older soils and deeper parts of profiles seems a similarity between the loess in Pakistan and Kashmir. To our knowledge no study on loess in Pakistan relates physical sediment properties to age, preventing any robust conclusions on the timing of past environmental change. The grain size may be similar or coarser for loess from the Attock Basin in Pakistan than for Kashmir loess. Most data from the Attock Basin have a median grain size of ∼30 μm (Din and Yoshida, 1997). Especially because the Peshwar Basin in northern Pakistan is located in a similar geographic situation as the Kashmir Valley in India, extensive loess areas spanning at least the last glacial cycle may be expected. Bibi et al. (2019) report on loess from the Peshwar Basin for the last glacial maximum with a maximum thickness of ∼5 m. They also found loess intercalated with lacustrine sediments. Also in Kashmir non-aeolian sediments occur on top of loess in some positions (own observation in the Khan Sahib area).

We agree that a much more widespread occurrence of both typical and fine loess and also rather coarse "desert loess" is expected in the Indian subcontinent. Yet, descriptions are missing, but we are optimistic that more research will be conducted in this direction in the future. This is also because of a general scarcity of well understood paleoenvironmental reconstructions from the Indian subcontinent beyond the Holocene.

An Eurasian Context

While numerous studies report on loess from the Eurasian loess belt, in the last decades a shift toward establishing quantitative records for comparison between areas and sections is apparent. This facilitates comparison of terrestrial loess archives over Eurasia and with marine proxy data (e.g., Hovan et al., 1989; Zhou et al., 1995; Vlaminck et al., 2016; Lauer et al., 2017; Zeeden et al., 2018b; Perić et al., 2019), also for loess in Kashmir (Gupta et al., 1991). For loess in Kashmir and the whole Indian subcontinent, yet only rather little quantitative data are available in low resolution compared to studies from Europe (e.g., Antoine et al., 2009; Obreht et al., 2017), Central Asia (e.g., Ding et al., 2002b; Cheng et al., 2012; Wang et al., 2018; Jia et al., 2019) and East Asia (e.g., Ding et al., 2005; Hao and Guo, 2005; Yang and Ding, 2014). The topic of loess in India has been discussed during the last decades without much actual data, and Smalley et al. (2009) highlight this knowledge gap by stating "Loess in India has been neglected". Especially because the loess in Kashmir has potential to show the interaction of Westerlies with the Indian Monsoon system this is surprising and probably also caused by political difficulties in the last decades.

The patterns found in the Kashmir loess-palaeosol sequences are considerably different from other places in Eurasia. Because ^{14}C dates are mostly inconsistent between studies and with luminescence ages, the age of loess is interpreted differently by several authors (e.g., Bronger et al., 1987a; Singhvi et al., 1987; Agrawal et al., 1989). The correlation to the marine oxygen isotope record by Gupta et al. (1991) needs to be taken with caution in our opinion, and reliable work on the chronology of the Kashmir loess is necessary.

OUTLOOK

With the emergence of various methods allowing for reconstructing the paleoenvironment reproducibly from loess-palaeosol sequences, a growing number of quantitative studies on loess have been published worldwide. Our review reveals that only few studies, aimed at addressing the composition, timing and extent of past climatic variations, have been carried out on the Kashmir loess-palaeosol sequences so far. Since these are important archives for answering questions related on Kashmir and the wider Himalayas including the interaction of westerlies and the Indian Monsoon system, a wealth of information can be expected in these geoarchives when investigated in detail.

Paramount to the understanding of the loess is a better knowledge of its origin. The palaeosols are well developed and stratigraphically distinctive in the Kashmir Valley and have yet been used for local correlations, mainly due to their nature different from many other northern hemisphere geoarchives. Although some initiatives have been taken in this direction, the lack of well-established chronologies prevented this from being informative. The timing and extent of aeolian loess deposition in the Kashmir Himalayas, and in the broader Himalaya, is a prerequisite for understanding Himalayan climate fluctuations in the context of Eurasian and global climate change. Identifying the principal dust source is to be accomplished, and both grain size and geochemical data may help solve this question. Only the application and consistent interpretation of multiple proxies will allow a robust interpretation regarding the Quaternary evolution of the area, as shown e.g., by Hošek et al. (2015), Krauß et al. (2016), and Obreht et al. (2016). An integrated approach involving the use of rock magnetic studies, stable carbon and oxygen isotopes, phytoliths, grain size analysis and mollusk-based paleoclimatic studies may improve our understanding of the Quaternary climatic conditions of the region. We suggest obtaining chronometric dates, and obtain climate proxy data in high resolution from several sections for a reliable understanding of the deposits. In addition, geochemical data needs to be collected from possible sources to understand the dust source(s).

SUMMARY

Loess in Kashmir comprises several 10s of meters, and probably represents the last several 100 thousand years in some places. While most research focused on the last glacial cycle due to better dating possibilities, the onset of loess deposition is controversial and seems to begin much later than in most of Asia and Europe and in the Brunhes Chron.

This review gives a detailed account of past studies and available data from loess-palaeosol sequences in the Kashmir valley (NW Himalayas), and we point out caveats in research to be filled. Yet, both proxy data and dating of Kashmir loess is very limited. While pedological investigations have been carried out throughout the valley, almost no quantitative climate proxy data is available. Although the loess-palaeosol sequences show clear alterations, their relationships with hemispheric and global climate evolution is yet based on limited data and is therefore unsolved at least on an orbital time scale. The inconsistency between the published chronologies (luminescence and ^{14}C) makes it difficult to interpret the driving mechanisms of soil forming episodes.

We highlight the need for high-resolution multi-proxy studies as from other loess areas, and a reliable understanding of the chronology.

AUTHOR CONTRIBUTIONS

RD and CZ wrote this review manuscript.

ACKNOWLEDGMENTS

We thank Gábor Újvári and two reviewers for constructive and insightful comments that greatly improved the manuscript. Funding by the DFG (grant ZE 1145/2-1, project number 432194908) is highly appreciated and made this work possible.

REFERENCES

Agrawal, D. P. (1985). "Cenozoic climatic changes in Kashmir: the multidisciplinary data," in *Climate and Geology of Kashmir and Central Asia: The Last 4 Million Years*, eds D. P. Agrawal, S. Kusumgar, and R. V. Krishnamurthy (New Delhi: Today and Tomorrow's), 1–12.

Agrawal, D. P. (1992). *Man and Environment in India Through Ages: An Interdisciplinary Study of the Indian Quaternary with Focus on North-West*. New Delhi: Books & Books.

Agrawal, D. P., Dodia, R., Kotlia, B. S., Razdan, H., and Sahni, A. (1989). The Plio-Pleistocene geologic and climatic record of the Kashmir valley, India: a review and new data. *Palaeogeogr. Palaeoclimatol. Palaeoecol.* 73, 267–286. doi: 10.1016/0031-0182(89)90008-4

Agrawal, D. P., Juyal, N., Sharma, P., Gardner, R., and Rendell, H. (1988). Palaeogeography of the loess deposits of Kashmir. *Proceedings of the Indian National Science Academy* 54, 383–389.

Agrawal, D. P., Krishnamurthy, R. V., Kusumgar, S., Nautiyal, V., Athavale, R. N., and Radhakrishnamurthy, C. (1979). Chronostratigraphy of loessic and lacustrine sediments in the Kashmir Valley, India. *Acta Geol. Acad. Sci. Hung.* 22, 185–196.

Ahmad, I. (2012). *Geochemical Study of Loess-PaleosolQuaternary Sediments of Karewa Basin with Reference to paleoclimate of Kashmir valley*. Ph.D. thesis, University of Kashmir, Srinagar.

Ahmad, I., and Chandra, R. (2013). Geochemistry of loess-paleosol sediments of Kashmir Valley, India: provenance and weathering. *J. Asian Earth Sci.* 66, 73–89. doi: 10.1016/j.jseaes.2012.12.029

Ahmad, I., and Chandra, R. (2018). Paleoenvironmental reconstructions of the late quaternary Loess-Paleosol sediments of Kashmir Valley. *J. Appl. Geochem.* 20, 59–90.

Akram, H., Yoshida, M., and Ahmad, M. N. (1998). Rock magnetic properties of the late Pleistocene Loess-Paleosol deposits in Haro River area, Attock basin, Pakistan: is magnetic susceptibility a proxy measure of paleoclimate? *Earth Planet Space* 50, 129–139. doi: 10.1186/BF03352094

An, Z., Wang, S., Wu, X., Chen, M., Sun, D., Liu, X., et al. (1999). Eolian evidence from the Chinese Loess Plateau: the onset of the Late Cenozoic Great Glaciation in the Northern Hemisphere and Qinghai-Xizang Plateau uplift forcing. *Sci. China Ser. D Earth Sci.* 42, 258–271. doi: 10.1007/BF02878963

Antoine, P., Rousseau, D.-D., Fuchs, M., Hatté, C., Gauthier, C., Marković, S. B., et al. (2009). High-resolution record of the last climatic cycle in the southern Carpathian Basin (Surduk, Vojvodina, Serbia). *Quat. Int.* 198, 19–36. doi: 10.1016/j.quaint.2008.12.008

Babeesh, C., Achyuthan, H., Jaiswal, M. K., and Lone, A. (2017). Late Quaternary loess-like paleosols and pedocomplexes, geochemistry, provenance and source area weathering, Manasbal, Kashmir Valley, India. *Geomorphology* 284, 191–205. doi: 10.1016/j.geomorph.2017.01.004

Badía, D., Martí, C., Palacio, E., Sancho, C., and Poch, R. M. (2009). Soil evolution over the Quaternary period in a semiarid climate (Segre river terraces, northeast Spain). *CATENA* 77, 165–174. doi: 10.1016/j.catena.2008.12.012

Basavaiah, N., Appel, E., Lakshmi, B. V., Deenadayalan, K., Satyanarayana, K. V. V., Misra, S., et al. (2010). Revised magnetostratigraphy and characteristics of the fluviolacustrine sedimentation of the Kashmir basin, India, during Pliocene-Pleistocene. *J. Geophys. Res. Solid Earth* 115:B08105. doi: 10.1029/2009JB006858

Basavaiah, N., and Khadkikar, A. S. (2004). Environmental magnetism and its application towards palaeomonsoon reconstruction. *J. Ind. Geophys. Uni.* 8, 1–14.

Bellotto, M., Gualtieri, A., Artioli, G., and Clark, S. M. (1995). Kinetic study of the kaolinite-mullite reaction sequence Part I: Kaolinite dehydroxylation. *Phys. Chem. Miner.* 22, 207–217. doi: 10.1007/BF00202253

Bhat, N. A., Singh, B. P., Bhat, A. A., Nath, S., and Guha, D. B. (2019). Application of Geochemical Mapping in Unraveling Paleoweathering and Provenance of Karewa Deposits of South Kashmir, NW Himalaya, India. *J. Geol. Soc. India* 93, 68–74. doi: 10.1007/s12594-019-1124-x

Bhatt, D. K. (1976). Stratigraphical status of the Karewa group of Kashmir, India. *Himalayan Geol.* 6, 197–208.

Bhatt, D. K. (1982). A review of the stratigraphy of the Karewa Group (Pliocene/Quaternary), Kashmir. *Man Environ.* 6, 46–55.

Bibi, M., Wagreich, M., Iqbal, S., Gier, S., and Jan, I. U. (2019). Sedimentation and glaciations during the Pleistocene: palaeoclimate reconstruction in the Peshawar Basin, Pakistan. *Geol. J.* 55, 671–693. doi: 10.1002/gj.3445

Bronger, A., Pant, R. K., and Singhvi, A. K. (1987a). Pleistocene climatic changes and landscape evolution in the Kashmir Basin, India: paleopedologic and chronostratigraphic studies. *Quat. Res.* 27, 167–181. doi: 10.1016/0033-5894(87)90075-5

Bronger, A., Pant, R., and Singhvi, A. (1987b). "Micromorphology, mineralogy, genesis and dating of loess-paleosol sequences and their application to Pleistocene chronostratigraphy and paleoclimate: a comparison between Southeast Central Europe and the Kashmir Valley," in *Aspects of Loess Research*, ed. T. Liu (Beijing: China Ocean Press), 121–129.

Brookfield, M. E. (1998). The evolution of the great river systems of southern Asia during the Cenozoic India–Asia collision: rivers draining southwards. *Geomorphology* 22, 285–312. doi: 10.1016/s0169-555x(97)00082-2

Buggle, B., Glaser, B., Hambach, U., Gerasimenko, N., and Markoviæ, S. (2011). An evaluation of geochemical weathering indices in loess–paleosol studies. *Quat. Int.* 240, 12–21. doi: 10.1016/j.quaint.2010.07.019

Burbank, D. W., and Johnson, G. D. (1982). Intermontane-basin development in the past 4 Myr in the north-west Himalaya. *Nature* 298, 432–436. doi: 10.1038/298432a0

Cai, G., Guo, F., Liu, X., Sui, S., Li, C., and Zhao, L. (2008). Geochemistry of Neogene sedimentary rocks from the Jiyang basin, North China Block: the roles of grain size and clay minerals. *Geochem. J.* 42, 381–402. doi: 10.2343/geochemj.42.381

Calkins, J. A., Offield, T. W., Abdullah, S. K., and Ali, S. T. (1975). *Geology of the Southern Himalaya in Hazara, Pakistan, and Adjacent Areas*. Washington, DC: United States Department of the Interior.

Chandra, R., and Ahmad, I. (2013). Pedostratigraphy, pedological and geochemistry of Kashmir loess: implications for chemical weathering history and paleoclimatic reconstruction. *Eur. Sci. J.* 3, 467–478.

Chandra, R., Ahmad, I., and Quarshi, A. (2016). Pedological and geochemical characterization of loess-paleosol sediments of Karewa basin: implications for paleoclimatic reconstruction of Kashmir valley. *J. Geol. Soc. India* 4, 38–54.

Cheng, H., Zhang, P. Z., Spötl, C., Edwards, R. L., Cai, Y. J., Zhang, D. Z., et al. (2012). The climatic cyclicity in semiarid-arid central Asia over the past 500,000 years. *Geophys. Res. Lett.* 39:L01705. doi: 10.1029/2011GL050202

Chlachula, J., Rutter, N. W., and Evans, M. E. (1997). A late Quaternary loess – paleosol record at Kurtak, southern Siberia. *Can. J. Earth Sci.* 34, 679–686. doi: 10.1139/e17-054

Dar, R. A., Chandra, R., and Romshoo, S. A. (2013). Morphotectonic and lithostratigraphic analysis of intermontane Karewa Basin of Kashmir Himalayas, India. *J. Mt. Sci.* 10, 1–15. doi: 10.1007/s11629-013-2494-y

Dar, R. A., Chandra, R., Romshoo, S. A., and Kowser, N. (2015a). Micromorphological investigations of the Late Quaternary loess–paleosol sequences of the Kashmir Valley, India. *J. Asian Earth Sci.* 111, 328–338. doi: 10.1016/j.jseaes.2015.07.004

Dar, R. A., Chandra, R., Romshoo, S. A., Lone, M. A., and Ahmad, S. M. (2015b). Isotopic and micromorphological studies of Late Quaternary loess–paleosol sequences of the Karewa Group: inferences for palaeoclimate of Kashmir Valley. *Quat. Int.* 371, 122–134. doi: 10.1016/j.quaint.2014.10.060

Dar, R. A., Chandra, R., Romshoo, S. A., Lone, M. A., and Ahmad, S. M. (2015c). Reply to the comment by Shah on "Isotopic and micromorphological studies of Late Quaternary loess-paleosol sequences of the Karewa Group: inferences for palaeoclimate of Kashmir Valley.". *Quat. Int.* 374, 200–202. doi: 10.1016/j.quaint.2015.03.029

Dar, R. A., Jaan, O., Murtaza, K. O., and Romshoo, S. A. (2017). Glacial-geomorphic study of the Thajwas glacier valley, Kashmir Himalayas, India. *Quat. Int.* 444, 157–171. doi: 10.1016/j.quaint.2017.05.021

Dar, R. A., Romshoo, S. A., Chandra, R., and Ahmad, I. (2014). Tectono-geomorphic study of the Karewa Basin of Kashmir Valley. *J. Asian Earth Sci.* 92, 143–156. doi: 10.1016/j.jseaes.2014.06.018

de Terra, H., and Patterson, T. T. (1940). Studies on the Ice Age in India and Associated Human Cultures. *J. Geol.* 48, 110–111. doi: 10.1086/624867

Dill, H. G., Khadka, D. R., Khanal, R., Dohrmann, R., Melcher, F., and Busch, K. (2003). Infilling of the Younger Kathmandu–Banepa intermontane lake basin during the Late Quaternary (Lesser Himalaya, Nepal): a sedimentological study. *J. Quat. Sci.* 18, 41–60. doi: 10.1002/jqs.726

Dilli, K., and Pant, R. K. (1994). Clay-minerals as indicators of the provenance and Paleoclimatic record of the Kashmir-loess. *J. Geol. Soc. India* 44, 563–574.

Din, N., and Yoshida, M. (1997). Particle-Size Distribution of Late Pleistocene Loess-Paleosol Deposits in Attock Basin, Pakistan. *Quat. Res.* 36, 43–53. doi: 10.4116/jaqua.36.43

Ding, Z., Sun, J., Rutter, N. W., Rokosh, D., and Liu, T. (1999). Changes in sand content of loess deposits along a north–south transect of the Chinese Loess Plateau and the implications for desert variations. *Quat. Res.* 52, 56–62. doi: 10.1006/qres.1999.2045

Ding, Z. L., Derbyshire, E., Yang, S. L., Sun, J. M., and Liu, T. S. (2005). Stepwise expansion of desert environment across northern China in the past 3.5 Ma and implications for monsoon evolution. *Earth Planet. Sci. Lett.* 237, 45–55. doi: 10.1016/j.epsl.2005.06.036

Ding, Z. L., Derbyshire, E., Yang, S. L., Yu, Z. W., Xiong, S. F., and Liu, T. S. (2002a). Stacked 2.6-Ma grain size record from the Chinese loess based on five sections and correlation with the deep-sea δ18O record. *Paleoceanography* 17, 1–21. doi: 10.1029/2001PA000725

Ding, Z. L., Ranov, V., Yang, S. L., Finaev, A., Han, J. M., and Wang, G. A. (2002b). The loess record in southern Tajikistan and correlation with Chinese loess. *Earth Planet. Sci. Lett.* 200, 387–400. doi: 10.1016/s0012-821x(02)00637-4

Dodia, R. (1983). *Palynological Investigations on the Kashmir Valley India*, Ph.D. thesis, Gujarat University, Ahmedabad:.

Dodonov, A. E., Sadchikova, T. A., Sedov, S. N., Simakova, A. N., and Zhou, L. P. (2006). Multidisciplinary approach for paleoenvironmental reconstruction in loess-paleosol studies of the Darai Kalon section, Southern Tajikistan. *Quat. Int.* 152–153, 48–58. doi: 10.1016/j.quaint.2005.12.001

Edwards, M. A., Kidd, W. S. F., Li, J., Yue, Y., and Clark, M. (1996). Multi-stage development of the southern Tibet detachment system near Khula Kangri. New data from Gonto La. *Tectonophysics* 260, 1–19. doi: 10.1016/0040-1951(96)00073-X

Farr, T. G., Rosen, P. A., Caro, E., Crippen, R., Duren, R., Hensley, S., et al. (2007). The Shuttle Radar Topography Mission. *Rev. Geophys.* 45:RG2004. doi: 10.1029/2005RG000183

Ganjoo, R. K., and Shaker, S. (2007). Middle Miocene pedological record of monsoonal climate from NW Himalaya (Jammu & Kashmir State), India. *J. Asian Earth Sci.* 29, 704–714. doi: 10.1016/j.jseaes.2006.04.011

Gardner, R. (1989). Late Quaternary loess and paleosols, Kashimir valley, India. *Z. Geomorph. NF Suppl. Bd.* 76, 225–245.

Gupta, S. K., Sharma, P., Juyal, N., and Agrawal, D. P. (1991). Loess—palaeosol sequence in Kashmir: correlation of mineral magnetic stratigraphy with the marine palaeoclimatic record. *J. Quat. Sci.* 6, 3–12. doi: 10.1002/jqs.3390060103

Han, L., Hao, Q., Qiao, Y., Wang, L., Peng, S., Li, N., et al. (2019). Geochemical evidence for provenance diversity of loess in southern China and its implications for glacial aridification of the northern subtropical region. *Quat. Sci. Rev.* 212, 149–163. doi: 10.1016/j.quascirev.2019.04.002

Händel, M., Simon, U., Einwögerer, T., and Neugebauer-Maresch, C. (2009). Loess deposits and the conservation of the archaeological record—The Krems-Wachtberg example. *Quat. Int.* 198, 46–50. doi: 10.1016/j.quaint.2008.07.005

Hao, Q., and Guo, Z. (2005). Spatial variations of magnetic susceptibility of Chinese loess for the last 600 kyr: implications for monsoon evolution. *J. Geophys. Res. Solid Earth* 110:B12101.

Hao, Q., and Guo, Z. (2007). Magnetostratigraphy of an early-middle Miocene loess-soil sequence in the western Loess Plateau of China. *Geophys. Res. Lett.* 34:L18305.

Hao, Q., Wang, L., Oldfield, F., Peng, S., Qin, L., Song, Y., et al. (2012). Delayed build-up of Arctic ice sheets during 400,000-year minima in insolation variability. *Nature* 490, 393–396. doi: 10.1038/nature11493

Harrison, S. P., Kohfeld, K. E., Roelandt, C., and Claquin, T. (2001). The role of dust in climate changes today, at the last glacial maximum and in the future. *Earth Sci. Rev.* 54, 43–80. doi: 10.1016/s0012-8252(01)00041-1

Hošek, J., Hambach, U., Lisá, L., Grygar, T. M., Horáček, I., Meszner, S., et al. (2015). An integrated rock-magnetic and geochemical approach to loess/paleosol sequences from Bohemia and Moravia (Czech Republic): implications for the Upper Pleistocene paleoenvironment in central Europe. *Palaeogeogr. Palaeoclimatol. Palaeoecol.* 418, 344–358. doi: 10.1016/j.palaeo.2014.11.024

Hovan, S. A., Rea, D. K., Pisias, N. G., and Shackleton, N. J. (1989). A direct link between the China loess and marine δ18O records: aeolian flux to the north Pacific. *Nature* 340, 296–298. doi: 10.1038/340296a0

Iriondo, M. H., and Kröhling, D. M. (2007). Non-classical types of loess. *Sediment. Geol.* 202, 352–368. doi: 10.1016/j.sedgeo.2007.03.012

Jia, J., Wang, B., Lu, C., Wang, Y., Zhu, L., and Xia, D. (2019). New insights into the magnetic characteristics of high mountain loess in Central Asia and its paleoclimatic implications. *Quat. Int.* 502, 71–77. doi: 10.1016/j.quaint.2019.01.031

Jones, S. C., and Pal, J. N. (2009). The Palaeolithic of the Middle Son valley, north-central India: changes in hominin lithic technology and behaviour during the Upper Pleistocene. *J. Anthropol. Archaeol.* 28, 323–341. doi: 10.1016/j.jaa.2009.05.003

Juyal, N., Raj, R., Maurya, D. M., Chamyal, L. S., and Singhvi, A. K. (2000). Chronology of Late Pleistocene environmental changes in the lower Mahi basin, western India. *J. Quat. Sci.* 15, 501–508. doi: 10.1002/1099-1417(200007)15:5<501::aid-jqs528>3.0.co;2-j

Kemp, R. A. (2001). Pedogenic modification of loess: significance for palaeoclimatic reconstructions. *Earth Sci. Rev.* 54, 145–156. doi: 10.1016/s0012-8252(01)00045-9

Kemp, R. A., and Zárate, M. A. (2000). Pliocene pedosedimentary cycles in the southern Pampas, Argentina. *Sedimentology* 47, 3–14. doi: 10.1046/j.1365-3091.2000.00274.x

Khormali, F., Abtahi, A., Mahmoodi, S., and Stoops, G. (2003). Argillic horizon development in calcareous soils of arid and semiarid regions of southern Iran. *CATENA* 53, 273–301. doi: 10.1016/s0341-8162(03)00040-7

Kotlia, B. S. (1985a). Vertebrate fossils and palaeoenvironment of the Karewa Intermontane Basin, Kashmir, northwestern India. *Curr. Sci.* 54, 1275–1277.

Kotlia, B. S. (1985b). *Vertebrate Palaeontology and Palaeoecology of the Karewa Group Kashmir a Biostratigraphical Study*. Ph.D. thesis, Panjab University, Chandigarh.

Kraus, M. J. (1999). Paleosols in clastic sedimentary rocks: their geologic applications. *Earth Sci. Rev.* 47, 41–70. doi: 10.1016/S0012-8252(99)00026-4

Krauß, L., Zens, J., Zeeden, C., Schulte, P., Eckmeier, E., and Lehmkuhl, F. (2016). A Multi-Proxy Analysis of two Loess-Paleosol Sequences in the Northern Harz Foreland, Germany. *Palaeogeogr. Palaeoclimatol. Palaeoecol.* 461, 401–417. doi: 10.1016/j.palaeo.2016.09.001

Krishnamurthy, R. V., Bhattacharya, S. K., and Kusumgar, S. (1986). Palaeoclimatic changes deduced from 13 C/ 12 C and C/N ratios of Karewa lake sediments, India. *Nature* 323, 150–152. doi: 10.1038/323150a0

Krishnamurthy, R. V., DeNiro, M. J., and Pant, R. K. (1982). Isotope evidence for Pleistocene climatic changes in Kashmir, India. *Nature* 298, 640–641. doi: 10.1038/298640a0

Kusumgar, S., Agrawal, D. P., Juyal, N., and Sharma, P. (1986). Palaeosols within Loess: dating Palaeoclimatic Events in Kashmir. *Radiocarbon* 28, 561–565. doi: 10.1017/S0033822200007724

Kusumgar, S., Agrawal, D. P., and Krishnamurthy, R. V. (1980). Studies on the loess deposits of the Kashmir valley and 14C dating. *Radiocarbon* 22, 757–762. doi: 10.1017/S0033822200010122

Lauer, T., Vlaminck, S., Frechen, M., Rolf, C., Kehl, M., Sharifi, J., et al. (2017). The Agh Band loess-palaeosol sequence – A terrestrial archive for climatic shifts during the last and penultimate glacial–interglacial cycles in a semiarid region in northern Iran. *Quat. Int.* 429, 13–30. doi: 10.1016/j.quaint.2016.01.062

Liu, X., Ma, M., Wu, H., and Zhou, Z. (2017). Identification of aeolian loess deposits on the Indo-Gangetic Plain (India) and their significance. *Sci. China Earth Sci.* 60, 428–437. doi: 10.1007/s11430-016-5167-1

Liu, X., Mao, X., Yuan, Y., and Ma, M. (2019). Aeolian accumulation: an alternative origin of laterite on the Deccan Plateau, India. *Palaeogeogr. Palaeoclimatol. Palaeoecol.* 518, 34–44. doi: 10.1016/j.palaeo.2019.01.003

Lodha, G., Sawhney, K., Razdan, H., Agrawal, D., and Juyal, N. (1988). Characterization of loess-palaeosol sequences in Kashmir (India) valley using multi-element concentration data. *Proc. Indian Natl. Sci. Acad. Part A Phys. Sci.* 54, 365–377.

Lodha, G. S., Sawhney, K. J. S., Razdan, H., Agrawal, D. P., and Juyal, N. (1987). Geochemical studies on Kashmir loess profiles. *Proc. Indian Acad. Sci.* 96, 135–145. doi: 10.1007/BF02839265

Lodha, G. S., Sawhney, K. J. S., Razdan, H., and Lal, M. (1985). Trace elements in the Kanchi Nala,(Kashmir) loess deposits. *Clim. Geol. Kashmir Cent. Asia Last* 4, 147–150.

Mahapatra, S. K., Walia, C. S., Sidhu, G. S., Rana, K. P. C., and Tarsem, L. (2000). Characterization and classification of the soils of different physiographic units

in the subhumid eco-system of Kashmir region. *J. Indian Soc. Soil Sci.* 48, 572–577.

Mason, J. A., Nater, E. A., Zanner, C. W., and Bell, J. C. (1999). A new model of topographic effects on the distribution of loess. *Geomorphology* 28, 223–236. doi: 10.1016/s0169-555x(98)00112-3

Meenakshi, P., Shrivastava, J. P., Chandra, R., Chopra, S., Roonwal, G. S., et al. (2018). High resolution 14C AMS ages (50 ka) of organic matter associated with the loess-palaeosol Holocene-Late Pleistocene (8–130 ka) sediments of Dilpur Formation, Karewa Group, Kashmir, India. *Quat. Geochronol.* 47, 170–179. doi: 10.1016/j.quageo.2018.06.004

Muhs, D. R. (2009). "Eolian sediments and processes," in *Encyclopedia of Paleoclimatology and Ancient Environments*, ed. V. Gornitz (Dordrecht: Springer), 312–319. doi: 10.1007/978-1-4020-4411-3_81

Muhs, D. R. (2013). "Loess and its Geomorphic, Stratigraphic, and Paleoclimatic Significance in the Quaternary," in *Treatise on Geomorphology*, ed. J. F. Shroder (San Diego, CA: Academic Press), 149–183. doi: 10.1016/b978-0-12-374739-6.00302-x

Muhs, D. R. (2018). The geochemistry of loess Asian and North American deposits compared. *J. Asian Earth Sci.* 155, 81–115. doi: 10.1016/j.jseaes.2017.10.032

Muhs, D. R., and Bettis, E. A. (2003). "Quaternary loess-Paleosol sequences as examples of climate-driven sedimentary extremes," in *Special Paper 370: Extreme Depositional Environments: Mega end Members in Geologic Time*, eds M. A. Chan and A. W. Archer (Boulder, CO: Geological Society of America), 53–74. doi: 10.1130/0-8137-2370-1.53

Muhs, D. R., Budahn, J. R., McGeehin, J. P., Bettis, E. A., Skipp, G., Paces, J. B., et al. (2013). Loess origin, transport, and deposition over the past 10,000 years, Wrangell-St. Elias National Park, Alaska. *Aeolian Res.* 11, 85–99. doi: 10.1016/j.aeolia.2013.06.001

Obreht, I., Hambach, U., Veres, D., Zeeden, C., Bösken, J., Stevens, T., et al. (2017). Shift of large-scale atmospheric systems over Europe during late MIS 3 and implications for Modern Human dispersal. *Sci. Rep.* 7:5848. doi: 10.1038/s41598-017-06285-x

Obreht, I., Zeeden, C., Hambach, U., Veres, D., Marković, S. B., Bösken, J., et al. (2016). Tracing the influence of Mediterranean climate on Southeastern Europe during the past 350,000 years. *Sci. Rep.* 6:36334. doi: 10.1038/srep36334

Obreht, I., Zeeden, C., Hambach, U., Veres, D., Marković, S. B., and Lehmkuhl, F. (2019). A critical reevaluation of palaeoclimate proxy records from loess in the Carpathian Basin. *Earth Sci. Rev.* 190, 498–520. doi: 10.1016/j.earscirev.2019.01.020

Obreht, I., Zeeden, C., Schulte, P., Hambach, U., Eckmeier, E., Timar-Gabor, A., et al. (2015). Aeolian dynamics at the Orlovat loess–paleosol sequence, northern Serbia, based on detailed textural and geochemical evidence. *Aeolian Res.* 18, 69–81. doi: 10.1016/j.aeolia.2015.06.004

Ogg, J. G. (2012). "Chapter 5 - Geomagnetic Polarity Time Scale," in *The Geologic Time Scale*, eds F. M. Gradstein, J. G. Ogg, M. D. Schmitz, and G. M. Ogg (Boston, MA: Elsevier), 85–113. doi: 10.1016/b978-0-444-59425-9.00005-6

Pant, R. K., Agrawal, D. P., and Krishnamurthy, R. V. (1978). "Scanning electron microscope and other studies on the Karewa beds of Kashmir," in *Scanning Electron Microscopy in the Study of Sediments,* ed. W. B. Whalley (Norwich: Geol Proc), 275–282.

Pant, R. K., Basavaiah, N., Juyal, N., Saini, N. K., Yadava, M. G., Appel, E., et al. (2005). A 20-ka climate record from Central Himalayan loess deposits. *J. Quat. Sci.* 20, 485–492. doi: 10.1002/jqs.938

Pécsi, M. (1990). Loess is not just the accumulation of dust. *Quat. Int.* 7-8, 1–21. doi: 10.1016/1040-6182(90)90034-2

Perić, Z., Lagerbäck Adolphi, E., Stevens, T., Újvári, G., Zeeden, C., Buylaert, J.-P., et al. (2019). Quartz OSL dating of late quaternary Chinese and Serbian loess: a cross Eurasian comparison of dust mass accumulation rates. *Quat. Int.* 502, 30–44. doi: 10.1016/j.quaint.2018.01.010

Porter, S. C. (2001). Chinese loess record of monsoon climate during the last glacial–interglacial cycle. *Earth Sci. Rev.* 54, 115–128. doi: 10.1016/s0012-8252(01)00043-5

Pye, K. (1995). The nature, origin and accumulation of loess. *Quat. Sci. Rev.* 14, 653–667. doi: 10.1016/0277-3791(95)00047-X

Rendell, H. M., Gardner, R. A. M., Agrawal, D. P., and Juyal, N. (1989). Chronology and stratigraphy of Kashmir Loess. *Z. Geomorphol. Suppl.* 76, 213–223.

Rendell, H. M., and Townsend, P. D. (1988). Thermoluminescence dating of a 10 m loess profile in Pakistan. *Quat. Sci. Rev.* 7, 251–255. doi: 10.1016/0277-3791(88)90012-1

RGI Consortium (2017). *Randolph Glacier Inventory – A Dataset of Global Glacier Outlines: Version 6.0. Technical Report, Global Land Ice Measurements from Space*. Boulder, CO: Digital Media. doi: 10.7265/N5-RGI-60

Scarciglia, F., Terribile, F., and Colombo, C. (2003). Micromorphological evidence of paleoenvironmental changes in Northern Cilento (South Italy) during the Late Quaternary. *Catena* 54, 515–536. doi: 10.1016/s0341-8162(03)00124-3

Schaetzl, R. J., Bettis, E. A., Crouvi, O., Fitzsimmons, K. E., Grimley, D. A., Hambach, U., et al. (2018). Approaches and challenges to the study of loess—Introduction to the LoessFest Special Issue. *Quat. Res.* 89, 563–618. doi: 10.1017/qua.2018.15

Sheldon, N. D., Retallack, G. J., and Tanaka, S. (2002). Geochemical Climofunctions from North American Soils and Application to Paleosols across the Eocene-Oligocene Boundary in Oregon. *J. Geol.* 110, 687–696. doi: 10.1086/342865

Shi, C., Zhu, R., Glass, B. P., Liu, Q., Zeman, A., and Suchy, V. (2003). Climate variations since the last interglacial recorded in Czech loess. *Geophys. Res. Lett.* 30:1562. doi: 10.1029/2003GL017251

Singh, G. (1963). A preliminary survey of the post-glacial vegetational history of the Kashmir valley. *Palaeobotanist* 12, 73–108.

Singh, I. B. (1982). Sedimentation pattern in the Karewa Basin, Kashmir Valley, India, and its geological significance. *J. Palaeontol. Soc. India* 27, 71–110.

Singh Kotlia, B., and Dayal Mathur, P. (1992). Morphologic, sinumetric and enamel investigations of the pliocene arvicolids (Rodentia) from the Karewas of Kashmir, India. *Geobios* 25, 781–796. doi: 10.1016/S0016-6995(92)80060-Q

Singhvi, A. K., Bronger, A., Pant, R. K., and Sauer, W. (1987). Thermoluminescence dating and its implications for the chronostratigraphy of loess-paleosol sequences in the Kashmir Valley (India). *Chem. Geol.* 65, 45–56.

Smalley, I., Marković, S. B., and Svirčev, Z. (2011). Loess is [almost totally formed by] the accumulation of dust. *Quat. Int.* 240, 4–11. doi: 10.1016/j.quaint.2010.07.011

Smalley, I., McLaren, S., O'Hara-Dhand, K., and Bentley, S. P. (2016). Loess and bee-eaters III: birds and ground in the Punjab and the Indus region. *Quat. Int.* 399, 234–239.

Smalley, I., O'Hara-Dhand, K., Wint, J., Machalett, B., Jary, Z., and Jefferson, I. (2009). Rivers and loess: The significance of long river transportation in the complex event-sequence approach to loess deposit formation. *Quat. Int.* 198, 7–18. doi: 10.1016/j.quaint.2008.06.009

Smalley, I. J. (1972). The interaction of great rivers and large deposits of primary loess. *Trans. N. Y. Acad. Sci.* 34, 534–542.

Spate, M. (2019). "Reconsidering Archaeological and Environmental Proxies for Long Term Human-Environment Interactions in the Valley of Kashmir," in *Socio-Environmental Dynamics along the Historical Silk Road*, eds L. E. Yang, H.-R. Bork, X. Fang, and S. Mischke (Cham: Springer), 123–149. doi: 10.1007/978-3-030-00728-7_6

Sprafke, T., and Obreht, I. (2016). Loess: rock, sediment or soil – What is missing for its definition? *Quat. Int.* 399, 198–207. doi: 10.1016/j.quaint.2015.03.033

Srivastava, P., Rajak, M. K., Sinha, R., Pal, D. K., and Bhattacharyya, T. (2010). A high-resolution micromorphological record of the Late Quaternary paleosols from Ganga–Yamuna interfluve: stratigraphic and paleoclimatic implications. *Quat. Int.* 227, 127–142. doi: 10.1016/j.quaint.2010.02.019

Sun, D., Bloemendal, J., Rea, D. K., Vandenberghe, J., Jiang, F., An, Z., et al. (2002). Grain-size distribution function of polymodal sediments in hydraulic and aeolian environments, and numerical partitioning of the sedimentary components. *Sediment. Geol.* 152, 263–277.

Sun, J., Li, S.-H., Muhs, D. R., and Li, B. (2007). Loess sedimentation in Tibet: provenance, processes, and link with Quaternary glaciations. *Quat. Sci. Rev.* 26, 2265–2280. doi: 10.1016/j.quascirev.2007.05.003

Sun, Y., Clemens, S. C., An, Z., and Yu, Z. (2006). Astronomical timescale and palaeoclimatic implication of stacked 3.6-Myr monsoon records from the Chinese Loess Plateau. *Quat. Sci. Rev.*25, 33–48. doi: 10.1016/j.quascirev.2005.07.005

Tsoar, H., and Pye, K. (1987). Dust transport and the question of desert loess formation. *Sedimentology* 34, 139–153. doi: 10.1111/j.1365-3091.1987.tb00566.x

Újvári, G., Kok, J. F., Varga, G., and Kovács, J. (2016). The physics of wind-blown loess: implications for grain size proxy interpretations in Quaternary paleoclimate studies. *Earth Sci. Rev.* 154, 247–278. doi: 10.1016/j.earscirev.2016.01.006

United States Department of Agriculture [USDA] (1999). *Soil Taxonomy: A Basic System of Soil Classification for Making and Interpreting Soil Surveys*, 2nd Edn. Washington, DC: USDA.

Vandenberghe, J., Lu, H., Sun, D., van Huissteden, (Ko), J. and Konert, M. (2004). The late Miocene and Pliocene climate in East Asia as recorded by grain size and magnetic susceptibility of the Red Clay deposits (Chinese Loess Plateau). *Palaeogeogr. Palaeoclimatol. Palaeoecol.* 204, 239–255.

Veres, D., Tecsa, V., Gerasimenko, N., Zeeden, C., Hambach, U., and Timar-Gabor, A. (2018). Short-term soil formation events in last glacial east European loess, evidence from multi-method luminescence dating. *Quat. Sci. Rev.*200, 34–51. doi: 10.1016/j.quascirev.2018.09.037

Vlaminck, S., Kehl, M., Lauer, T., Shahriari, A., Sharifi, J., Eckmeier, E., et al. (2016). Loess-soil sequence at Toshan (Northern Iran): insights into late Pleistocene climate change. *Quat. Int.* 399, 122–135. doi: 10.1016/j.quaint.2015.04.028

Vlaminck, S., Kehl, M., Rolf, C., Franz, S. O., Lauer, T., Lehndorff, E., et al. (2018). Late Pleistocene dust dynamics and pedogenesis in Southern Eurasia – Detailed insights from the loess profile Toshan (NE Iran). *Quat. Sci. Rev.*180, 75–95. doi: 10.1016/j.quascirev.2017.11.010

Wang, Y., Jia, J., Liu, H., Lu, C., Xia, D., and Lu, H. (2018). The magnetic susceptibility recorded millennial-scale variability in central Asia during last glacial and interglacial. *Geophys. J. Int.* 215, 1781–1788. doi: 10.1093/gji/ggy378

Warwick, P. D., and Wardlaw, B. R. (2007). *Regional Studies of the Potwar Plateau Area, Northern Pakistan*. Available online at: http://pubs.er.usgs.gov/publication/b2078 (accessed July 27, 2019).

White, A. F., and Blum, A. E. (1995). Effects of climate on chemical_ weathering in watersheds. *Geochim. Cosmochim. Acta* 59, 1729–1747. doi: 10.1016/0016-7037(95)00078-E

Williams, M. A. J., and Clarke, M. F. (1984). Late Quaternary environments in north-central India. *Nature* 308, 633–635. doi: 10.1038/308633a0

Wright, J. S. (2001). "Desert" loess versus "glacial" loess: quartz silt formation, source areas and sediment pathways in the formation of loess deposits. *Geomorphology* 36, 231–256. doi: 10.1016/S0169-555X(00)00060-X

Wünnemann, B., Demske, D., Tarasov, P., Kotlia, B. S., Reinhardt, C., Bloemendal, J., et al. (2010). Hydrological evolution during the last 15kyr in the Tso Kar lake basin (Ladakh, India), derived from geomorphological, sedimentological and palynological records. *Quat. Sci. Rev.*29, 1138–1155. doi: 10.1016/j.quascirev.2010.02.017

Wünnemann, B., Reinhardt, C., Kotlia, B. S., and Riedel, F. (2008). Observations on the relationship between lake formation, permafrost activity and lithalsa development during the last 20 000 years in the Tso Kar basin, Ladakh, India. *Permafr. Periglac. Process*. 19, 341–358. doi: 10.1002/ppp.631

Yang, S., and Ding, Z. (2014). A 249 kyr stack of eight loess grain size records from northern China documenting millennial-scale climate variability. *Geochem. Geophys. Geosyst.* 15, 798–814. doi: 10.1002/2013GC005113

Zaz, S. N., Romshoo, S. A., Krishnamoorthy, R. T., and Viswanadhapalli, Y. (2019). Analyses of temperature and precipitation in the Indian Jammu and Kashmir region for the 1980–2016 period: implications for remote influence and extreme events. *Atmos. Chem. Phys.* 19, 15–37.

Zeeden, C., Dietze, M., and Kreutzer, S. (2018a). Discriminating luminescence age uncertainty composition for a robust Bayesian modelling. *Quat. Geochronol.* 43, 30–39. doi: 10.1016/j.quageo.2017.10.001

Zeeden, C., Hambach, U., and Händel, M. (2015). Loess magnetic fabric of the Krems-Wachtberg archaeological site. *Quat. Int.* 372, 188–194. doi: 10.1016/j.quaint.2014.11.001

Zeeden, C., Hambach, U., Obreht, I., Hao, Q., Abels, H. A., Veres, D., et al. (2018b). Patterns and timing of loess-paleosol transitions in Eurasia: constraints for paleoclimate studies. *Glob. Planet. Change* 162, 1–7. doi: 10.1016/j.gloplacha.2017.12.021

Zeeden, C., Kels, H., Hambach, U., Schulte, P., Protze, J., Eckmeier, E., et al. (2016). Three climatic cycles recorded in a loess-palaeosol sequence at Semlac (Romania) – Implications for dust accumulation in south-eastern Europe. *Quat. Sci. Rev.*154, 130–142. doi: 10.1016/j.quascirev.2016.11.002

Zeeden, C., Hambach, U., Veres, D., Fitzsimmons, K., Obreht, I., Bösken, J., et al. (2018c). Millennial scale climate oscillations recorded in the Lower Danube loess over the last glacial period. *Palaeogeogr. Palaeoclimatol. Palaeoecol.* 509, 164–181. doi: 10.1016/j.palaeo.2016.12.029

Zhao, W.-L., and Morgan, W. J. (1985). Uplift of Tibetan Plateau. *Tectonics* 4, 359–369. doi: 10.1029/TC004i004p00359

Zhou, L. P., Dodonov, A. E., and Shackleton, N. J. (1995). Thermoluminescence dating of the orkutsay loess section in Tashkent region, Uzbekistan, Central Asia. *Quat. Sci. Rev.*14, 721–730.

Conflict of Interest: The authors declare that the research was conducted in the absence of any commercial or financial relationships that could be construed as a potential conflict of interest.

frontiers in Earth Science

ORIGINAL RESEARCH
published: 30 June 2020
doi: 10.3389/feart.2020.00197

Determining the Pace and Magnitude of Lake Level Changes in Southern Ethiopia Over the Last 20,000 Years Using Lake Balance Modeling and SEBAL

Markus L. Fischer[1,2], Monika Markowska[1,3], Felix Bachofer[4], Verena E. Foerster[5], Asfawossen Asrat[6], Christoph Zielhofer[7], Martin H. Trauth[8] and Annett Junginger[1,2]*

[1] Department of Geosciences, Eberhard Karls University Tübingen, Tübingen, Germany, [2] Senckenberg Centre for Human Evolution and Paleoenvironment (S-HEP), Tübingen, Germany, [3] Department of Climate Geochemistry, Max Planck Institute for Chemistry, Mainz, Germany, [4] Earth Observation Centre, German Aerospace Center (DLR), Wessling, Germany, [5] Institute of Geography Education, University of Cologne, Cologne, Germany, [6] School of Earth Sciences, Addis Ababa University, Addis Ababa, Ethiopia, [7] Institute of Geography, University of Leipzig, Leipzig, Germany, [8] Institute of Geosciences, University of Potsdam, Potsdam, Germany

OPEN ACCESS

Edited by:
David K. Wright, University of Oslo, Norway

Reviewed by:
Nick Andrew Drake, King's College London, United Kingdom
Seifu Admassu Tilahun, Bahir Dar University, Ethiopia
Sylvia G. Dee, Rice University, United States

***Correspondence:**
Markus L. Fischer
markus_fischer@posteo.de

Specialty section:
This article was submitted to Quaternary Science, Geomorphology and Paleoenvironment, a section of the journal Frontiers in Earth Science

Received: *12 March 2020*
Accepted: *18 May 2020*
Published: *30 June 2020*

Citation:
Fischer ML, Markowska M, Bachofer F, Foerster VE, Asrat A, Zielhofer C, Trauth MH and Junginger A (2020) Determining the Pace and Magnitude of Lake Level Changes in Southern Ethiopia Over the Last 20,000 Years Using Lake Balance Modeling and SEBAL. Front. Earth Sci. 8:197. doi: 10.3389/feart.2020.00197

The Ethiopian rift is known for its diverse landscape, ranging from arid and semi-arid savannahs to high and humid mountainous regions. Lacustrine sediments and paleo-shorelines indicate water availability fluctuated dramatically from deep fresh water lakes, to shallow highly alkaline lakes, to completely desiccated lakes. To investigate the role lakes have played through time as readily available water sources to humans, an enhanced knowledge of the pace, character and magnitude of these changes is essential. Hydro-balance models are used to calculate paleo-precipitation rates and the potential pace of lake level changes. However, previous models did not consider changes in hydrological connectivity during humid periods in the rift system, which may have led to an overestimation of paleo-precipitation rates. Here we present a comprehensive hydro-balance modeling approach that simulates multiple rift lakes from the southern Ethiopian Rift (lakes Abaya, Chamo, and paleo-lake Chew Bahir) simultaneously, considering their temporal hydrological connectivity during high stands of the African Humid Period (AHP, ~15–5 ka). We further used the Surface Energy Balance Algorithm for Land (SEBAL) to calculate the evaporation of paleo-lake Chew Bahir's catchment. We also considered the possibility of an additional rainy season during the AHP as previously suggested by numerous studies. The results suggest that an increase in precipitation of 20–30% throughout the southern Ethiopian Rift is necessary to fill paleo-lake Chew Bahir to its overflow level. Furthermore, it was demonstrated that paleo-lake Chew Bahir was highly dependent on the water supply from the upper lakes Abaya and Chamo and dries out within ~40 years if the hydrological connection is cut off and the precipitation amount decreases to present day conditions. Several of such rapid lake level fluctuations, from a freshwater to a saline lake, might have occurred during the termination of the AHP, when humid conditions were less stable. Fast changes in fresh water availability requires high adaptability for humans living in the area and might have exerted severe environmental stress on humans in a sub-generational timescale.

Keywords: African humid period, precipitation changes, abrupt and gradual changes, Chew Bahir, Lake Abaya, Lake Chamo, human-environment interaction

INTRODUCTION

Eastern African precipitation is characterized by large interannual to centennial variability (Lamb et al., 1998; Nicholson, 2000; Junginger et al., 2014; Liu et al., 2017), controlling water resource availability in the region. This is accentuated by the uneven spatial distribution of precipitation, from the lowlands (<500 m) to the high plateaus (>4,000 m), due to the extreme topography of the East African Rift System (EARS) (Nicholson, 2017). In recent decades a decline in precipitation has led to an increase in the intensity and frequency of drought periods (Funk et al., 2008; Viste, 2012; Rowell et al., 2015).

Water availability has always played a fundamental role in eastern Africa, and fluctuations in eastern Africa's hydroclimate in the past have had a dramatic impact on human societies. Changes in orbital insolation during the late Pleistocene to Middle Holocene caused an "African Humid Period" (AHP; ∼15–5 ka BP; deMenocal et al., 2000; Barker et al., 2004), when increased precipitation triggered changes in vegetation (Lamb et al., 2004), dust dynamics (Zielhofer et al., 2017), lake expansion and increased river flow (Barker et al., 2004; Costa et al., 2014; Revel et al., 2014; Bloszies et al., 2015). In the wider region, these environmental changes during the AHP have been associated with multiple migration dynamics, such as the reoccupation of the Sahara ∼10.5 ka BP (Kuper and Kröpelin, 2006; Drake et al., 2013; Larrasoaña et al., 2013; Manning and Timpson, 2014), cultural innovation (Lario et al., 1997) and overlapped with a demographic transition to the Neolithic age (Manning and Timpson, 2014; Honegger and Williams, 2015). An increase in arid conditions has been documented during the termination of the AHP ∼5 ka BP in eastern Africa (e.g., deMenocal et al., 2000; Barker et al., 2004; Foerster et al., 2012; Junginger et al., 2014; Bloszies et al., 2015). This aridification trend coincides with societal adaptations, such as the introduction of pastoralism to eastern Africa, and the emergence of highly organized and complex state-level societies (demenocal, 1995; Brooks, 2006; Kuper and Kröpelin, 2006; Garcin et al., 2012; Foerster et al., 2015). Environmental changes likely provide both opportunities and constraints, due to variability in water resources and food availability, necessitating adaptation. To better understand potential links between cultural changes and climate variability, paleoclimate records can be used in conjunction with archaeological records to reconstruct major influences on modern civilizations.

In eastern Africa, however, there are still spatial and chronological gaps in paleoclimate records, which are largely non-quantitative and often regionally specific. Discrepancies particularly occur between records from marine archives, and lacustrine sites and also whether lacustrine sites are located within or outside the EARS. Existing records covering the AHP, report conflicting accounts of past climate variability in the region, with some studies suggesting a rapid onset and termination of the AHP (deMenocal et al., 2000; Tierney et al., 2013; Collins et al., 2017), while others indicate a rapid onset but more gradual termination and climate evolution in response to insolation forcing (Renssen et al., 2006; Asrat et al., 2007; Foerster et al., 2012; Junginger et al., 2014; Trauth et al., 2018). While lakes with a constant groundwater/geothermal supply were mostly stable (e.g., Lake Tilo on the Ethiopian Plateau, Telford and Lamb, 1999), river-fed EARS lakes, such as Chew Bahir or Ziway-Shala in Ethiopia (Gillespie et al., 1983; Foerster et al., 2012) or Lakes Elementeita-Nakuru (Richardson and Dussinger, 1986), paleo-Lake Suguta in Kenya (Junginger et al., 2014) or Lake Manyara (Bachofer et al., 2015) demonstrated greater variability in lake levels in response to short-term precipitation-evaporation changes (**Figure 1**).

The first steps toward quantifying precipitation rates during the AHP and lake responses to a changing precipitation-evaporation budget were conducted for several basins in the EARS by applying Lake Balance Modeling (LBM) (**Figure 1**; Hastenrath and Kutzbach, 1983; Bergner et al., 2003; Dühnforth et al., 2006; Kniess, 2006; Borchardt and Trauth, 2012; Junginger and Trauth, 2013). LBM uses field observations, such as ^{14}C dated shorelines and overflow sills high above modern lakes (indicative of higher moisture availability), to calculate paleo-lake volumes, levels and paleo-precipitation rates. Such attempts of quantifying environmental parameters using field observations (e.g., shorelines) or proxy data (e.g., leaf waxes, stable isotopes, dust, pollen) through modeling approaches are defined as so-called Proxy System Modeling (PSM), as presented by Evans et al. (2013) or Dee et al. (2018).

For the AHP, the reconstruction of environmental parameters, such as paleo-temperatures, is based for example on GDGT and Tex_{86} proxies from lake sediments (e.g., Verschuren, 2004; Berke et al., 2012a; Damsté et al., 2012; Loomis et al., 2012, 2014, 2015). Precipitation reconstructions are usually created using pollen (e.g., Lamb et al., 2004; Vincens et al., 2005; Umer et al., 2007; Rucina et al., 2009; Marchant et al., 2018), stalagmites (e.g., Baker et al., 2010), leaf waxes (e.g., Berke et al., 2012b; Costa et al., 2014), and the aforementioned LBMs. Due to the lack of the aforementioned proxy data in our study region, Chew Bahir in southern Ethiopia, an LBM is chosen to calculate paleo-precipitation rate changes.

Previously developed LBMs for the EARS, however, only looked at individual basins and therefore did not consider the hydrological connection via surface overflow of many rift basins (**Figure 1**). Consequently, the hydrological inflow budget of these interconnected lakes may have been underestimated, affecting the calculated paleo-precipitation estimates from the LBMs. Another aspect that was not considered in previous LBMs is change in seasonality. For the AHP it is hypothesized that an additional rainy season developed due to a shift of the Congo Air Boundary (CAB) during the northern hemisphere summer months, therefore tremendously impacting seasonality, environment and associated feedback mechanisms (e.g., Junginger and Trauth, 2013; Costa et al., 2014; Bloszies et al., 2015; Beck et al., 2019).

Here we present a comprehensive hydro-balance modeling approach that simulates firstly multiple rift lakes from the southern Ethiopian Rift (**Figure 1**; Abaya, Chamo, Chew Bahir). For this purpose, we developed a LBM for the region, which is a further development of the former models (e.g., Blodgett et al., 1997; Lenters and Cook, 1999). We have applied a combined

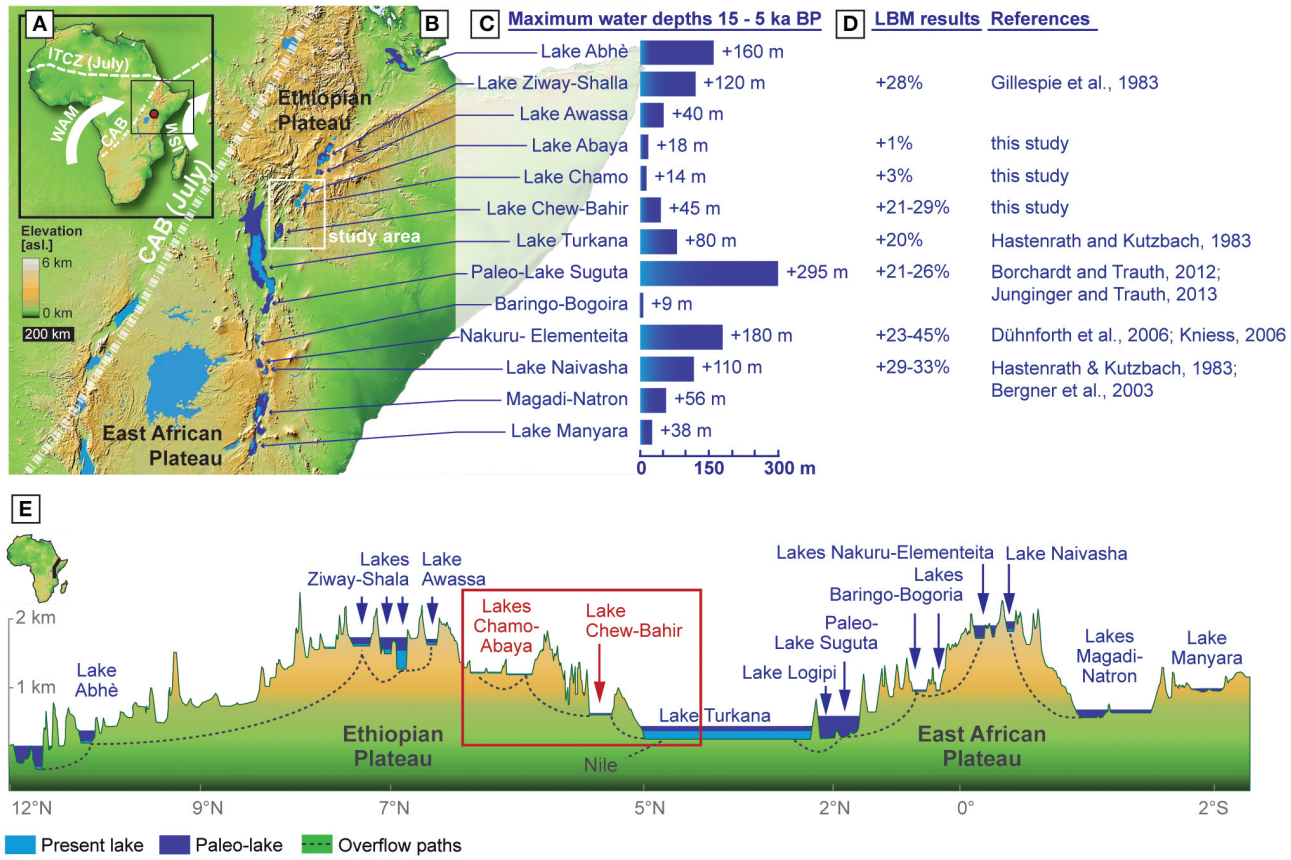

FIGURE 1 | Overview of the study area, lake levels and lake-balance modeling results from previous an current studies: **(A)** Elevation map of Africa and the positions of major air boundaries and convergence zones during the NH summer. Indian Summer Monsoon (ISM), West African Monsoon (WAM), the Inter Tropical Convergence Zone (ITCZ), and Congo Air Boundary (CAB). **(B)** Elevation map of eastern Africa with the study area, major lakes, study area (white box) and the CAB position in July. **(C,D)** Known paleo-lake depths within the EARS during the African Humid Period (AHP) and published paleo-precipitation rates estimates using different lake-balance approaches and associated references. **(E)** Transect of the EARS from north-east to south, with modern and paleo level lake extents (light and dark blue, respectively), the study area (red box), and major drainage direction (dotted line). North-South transect of the eastern branch of the EARS, with modern and paleo-lake extents (light and dark blue, respectively), the study area (red box), and major drainage direction (dotted line). The figure was modified after Junginger and Trauth (2013).

catchment approach including surface and subsurface flows. Two approaches were used to estimate the evapotranspiration; a bulk transfer equation and the Surface Energy Balance Algorithm for Land (SEBAL). The paleo-precipitation required during the AHP to fill lakes to their previous high-stands will be calculated under different scenarios including the incorporation of an additional rainy season as previously suggested by multiple studies (e.g., Junginger et al., 2014; Bloszies et al., 2015; Beck et al., 2019) and the theoretical feedback due to vegetation changes. We furthermore provide lake regression and transgression times under abrupt and gradual changes, in order to demonstrate the sensitivity of the investigated lake systems to changes in precipitation. Based on the outcome of the model, we compare lake response times to abrupt and gradual precipitation changes to aridity proxy data of an 11 m-long sediment core from the margin of paleo-lake Chew Bahir, which was published by Foerster et al. (2015) to reconstruct the paleo-lake level evolution of Chew Bahir during the past 20 ka.

REGIONAL SETTING

The Investigated Catchments

There are three adjoining North-South trending, endorheic basins at the southern end of the Main Ethiopian Rift (MER) which are part of the greater (4,000 km) EARS. These are the basins of Lake Abaya, Lake Chamo, and paleo-lake Chew Bahir, from north to south, respectively (**Figure 1**). Lake Abaya (6.4°N, 37.95°E, 7 m deep, and lake surface area of 1,081 km^2) is the northern-most and highest elevated (1,176 m a.s.l.) basin with a catchment size of 16,203 km^2 (**Figure 2**). The major rivers draining into Lake Abaya include the Gelana, Bilate, Gidabo, Hare, Baso, and Amesa Rivers (Tiruneh, 2005). Lake Chamo (5.8°N,37.6°E, ∼1,109 m a.s.l., 14 m deep, 310 km^2 lake surface area) to the south is separated from Lake Abaya by the Quaternary Tosa Sucha Volcano (Ebinger et al., 1993; **Figure 2J**). The Kulfo River to the west is the main tributary, while Sile and Wezeka rivers are smaller tributaries into Lake Chamo (Tiruneh, 2005). The Kulfo River is also connected to Lake

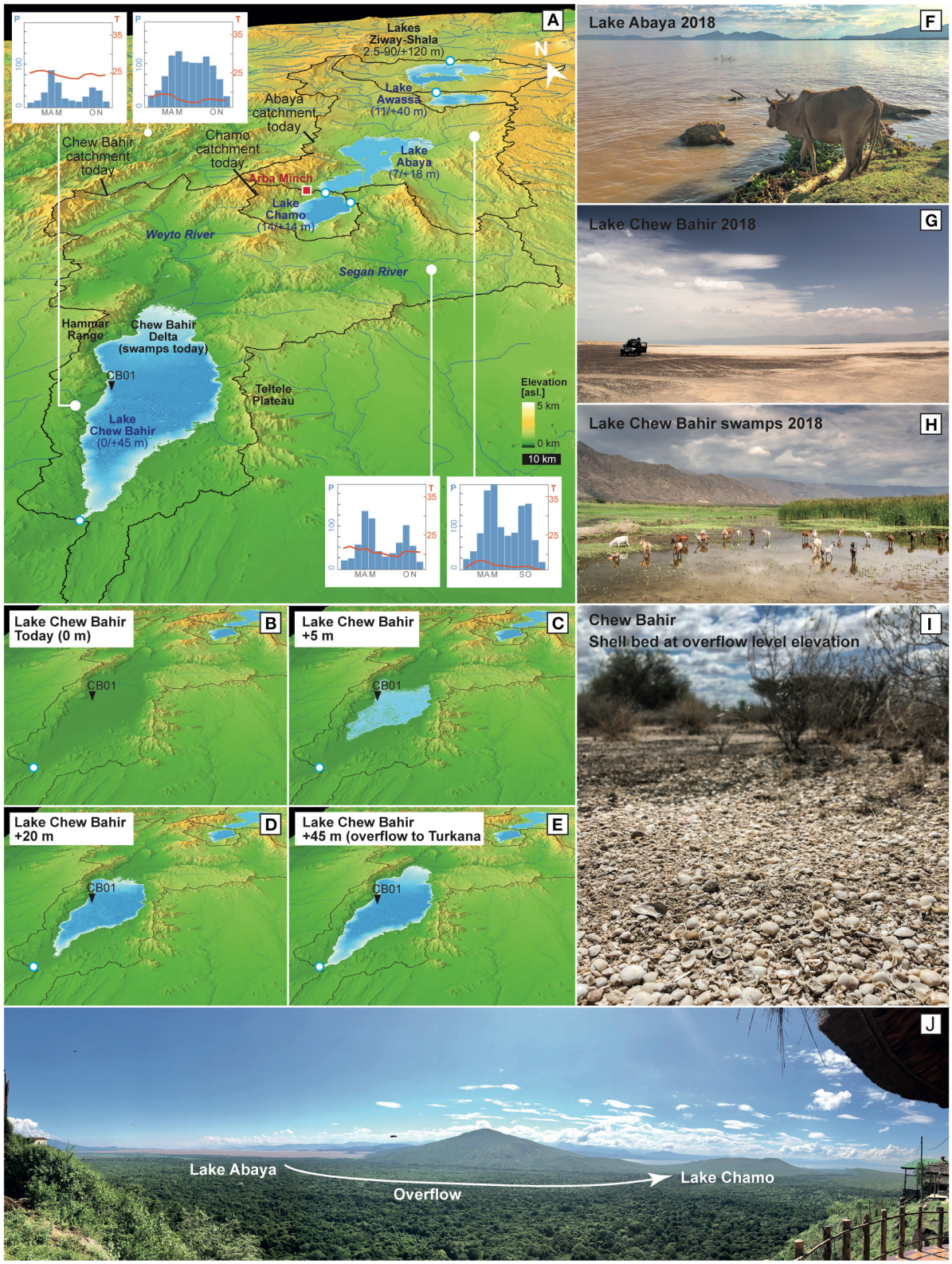

FIGURE 2 | Geographical features of the studied lake basins: **(A)** Modern catchment boundaries, monthly temperature means in °C and precipitation in mm/month (IRI, last accessed 11/2019), overflow sill locations (white-blue circles), and paleo-lake dimensions with modern/paleo-depths in numbers. **(B–E)** Modeling outputs of paleo-lake Chew Bahir's dimension during different lake filling steps from modern to +5, +20, and +45 m when reaching the overflow level. **(F–J)** Pictures from study sites by A. Junginger.

Abaya during wet periods when lake levels are higher (Tiruneh, 2005). The catchment area of Lake Chamo is ∼1,793 km^2. Both lakes, Chamo and Abaya are bounded by the Gamo-Gidole horst to the west and the Amaro horst to the east reaching elevations over 3,000 m a.s.l. and consisting mainly of Cenozoic rift volcanics unconformably overlaying Precambrian basement rocks (Davidson, 1983; Ebinger et al., 1993). Paleo-lake Chew Bahir (4.1–6.3°N, 36.5–38.1°E, ∼498 m a.s.l, **Figures 1**, **2**) to the south is most of the year a 210 km^2 saline mudflat and the lowest in elevation of the herein investigated basins. The Chew Bahir surface comprises deltaic ephemeral swamps at its northerly and north easterly reaches, where the perennial Weyto and Segan rivers drain the north-western and north-eastern sides of the catchment, respectively (**Figure 2**). The catchment (20,650 km^2) is bound by the MER rift shoulders, in the east by the Teltele Plateau (up to 1,600 m a.s.l.) and in the west by the Hammar Range (up to 1,300 m a.s.l.). The elevation of the rift shoulders decreases in a southerly direction. The northern side of the catchment is bound by uplifted Proterozoic metamorphic rocks and Cenozoic rift volcanics (Davidson, 1983; **Figures 1**, **2**), hydrologically separating it from the Chamo and Abaya catchments. To the south, Cenozoic rift volcanics from the foothills of the Hammar Range prevent a direct hydrological link with the Turkana basin, today. The dry southern-most part of the catchment borders Kenya.

Overflow Regime

Several paleo-shorelines, wave cut notches and sediment characteristics in the Ethiopian Rift and plateau regions, such as Lake Abhé (Gasse and Street, 1978), Lake Ziway-Shala-Abiyata (Gillespie et al., 1983; Chalié and Gasse, 2002), Lake Dendi (Wagner et al., 2018), or Lake Ashenge (Marshall et al., 2009) show evidence of deep lakes during the AHP. During those high stands, these lakes were overflowing into rivers that connected to other lake basins. Awulachew (2006) reported that lakes Abaya and Chamo were previously connected via surface streams. Here, Lake Abaya connected via an old channel through the Kulfo river with Lake Chamo (**Figure 2**). Awulachew (2006) and Kassa (2015) report of evidence that during high stands, Lake Chamo overflowed into the river Metenafesha and into the Sermale stream, both being tributaries of the Segan river, which in turn feeds paleo-lake Chew Bahir. During a field campaign in November 2018, paleo-shoreline deposits (shell beds) at Chew Bahir could be identified at the same elevation as the overflow sill (**Figure 2**). As calculated in section Digital Elevation Model Analysis, Lake Abaya's overflow sill to the Chamo catchment is at 1,194 m a.s.l. (6°0′40.38″N, 37°34′50.45″E) 18 m above its present lake level. Lake Chamo reaches its overflow sill to the Chew Bahir catchment at 1,123 m a.s.l. (5°51′49.66″N, 37°38′31.78″E), which is 14 m above its modern lake surface. The Chew Bahir basin has an overflow sill at 543 m a.s.l. (4°13′30.58″N, 36°39′35.19″E) to Lake Turkana, 45 m above the basin floor.

Vegetation

Modern vegetation in the Chew Bahir catchment is typically sparse and follows an east-west gradient (Friis et al., 2010). The eastern part of the Chew Bahir basin is classified as Acacia-Commiphora woodland and bushland, whereas the western part is described as Combretum-Terminalia woodland and wooded grassland (Friis et al., 2010). The higher elevated parts of the study area, such as close to Arba Minch (**Figure 2**), comprise evergreen Afro-Montane forest and grassland complex, which transitions to moist evergreen Afro-Montane forest in the north. The vegetation in the even higher mountainous areas are dominated by Afro-alpine vegetation with an Ericaceous Belt (Friis et al., 2010).

Climate

Seasonal rainfall in Chew Bahir is associated with the annual passage of a tropical rain belt (often referred to as the Inter Tropical Convergence Zone, ITCZ), which is predominantly fueled by the Indian Ocean (**Figure 1**, Levin et al., 2009; Nicholson, 2017). Generally, the tropical rain belt migrates between 10° North and South of the equator, resulting in a bimodal precipitation pattern close to the equator and an unimodal pattern at its limits (Nicholson, 1996). Consequently, the lower elevations of the Chew Bahir catchment precipitation is bimodal, with the "Belg" rains from March to May (long rains) and the "short rains" in October–November (**Figure 2**). The highlands northwest of Chew Bahir, including the Abaya and Chamo catchments, experience an unimodal rainfall pattern with only one longer wet season from March to November (Segele and Lamb, 2005; Williams and Funk, 2011). This wet season is, fueled by two different sources, with the "Belg" rains lasting from March to May and the "Kiremt" rains from June to September. The Kiremt rains are hypothesized to originate from the Atlantic Ocean-derived southwestern humid Congo air stream (Nicholson, 1996; Camberlin, 1997; Lamb et al., 2000). The eastern limit of this air stream is marked by the Congo Air Boundary, which separates the humid air masses from the west from dry air masses in the east (Nicholson, 1996). Annual to decadal fluctuations in the intensity and strength of precipitation are possibly related to a direct response to sea-surface temperature variations in the Indian and Atlantic Oceans (Nicholson, 2017). Compared to other areas at similar latitudes in Africa, Ethiopia receives considerably more rainfall due to its position in the MER and the resulting orographic effects (Nicholson, 2017).

MATERIALS AND METHODS

We developed a LBM to quantify the present day and paleo-water balances of paleo-lake Chew Bahir, Lake Chamo and Lake Abaya. The model was coded in R and is available at GitHub (https://github.com/MLFischer/Lake-Balance-Model, 03/2019). In summary, a Digital Elevation Model (DEM) was used to delineate the catchment boundaries, lake bathometry, lake volumes and overflow sills (section Digital Elevation Model Analysis). The annual modern water balances were calculated for Lakes Abaya, Chamo and paleo-lake Chew Bahir (section Lake Balance of Lakes Abaya, Chamo, and Paleo-Lake Chew Bahir). Evaporation was estimated for the paleo-lake Chew Bahir catchment using SEBAL [section Surface Energy Balance

Algorithm for Land (SEBAL)]. After parametrizing the model based on present-day conditions, we modeled the most recent lake high-stands of Lake Chamo, Abaya and paleo-lake Chew Bahir during the AHP (section Paleo-Lake Modeling). In section Calculation of Amplifier Lake Characteristics, we calculated the Hypsometric Integral (HI) and Aridity Index (AI) for the paleo-lake Chew Bahir, Lake Abaya and Chamo catchments which are used to define the Amplifier Lake characteristic of lake basins in the EARS following Olaka et al. (2010). In section Lake Level Reconstruction of Paleo-Lake Chew Bahir, we apply the modeled lake responses of paleo-lake Chew Bahir to various changes is precipitation and thus lake-level scenarios to changes in a K-proxy record from a drill-core taken from the paleo-lake Chew Bahir basin (Foerster et al., 2012, 2015; Trauth et al., 2018) and reconstruct the paleo-lake level of the past 20 ka.

Digital Elevation Model Analysis

The catchment boundary delineation was based on the DEM resulting from the Shuttle Radar Topography Mission (SRTM C-band; http://www2.jpl.nasa.gov/srtm/). The flow directions, flow accumulations, catchment boundaries and hydro-junctions (maximum possible lake extent) were calculated with the workflow for deranged terrains from the ArcHydro toolbox of ArcGIS 10.3 (Merwade, 2012). The DEM of each catchment was processed using the *freq* function in the R raster-package to produce an elevation frequency table, which then is used to compute the basin hypsometry and paleo-lake bathymetry (R Core Team, 2019).

Lake Balance Model

Three processing steps were applied for calculating the modern day annual water balance as later summarized in Equation (3). The parameters used in this model are climate parameter based on interpolated global gridded climate data (New et al., 2002), remote sensing data (Friedl et al., 2010; Platnick et al., 2015) and evaporation parametrization approaches (Schmugge and André, 1991). The input parameters are annual averages and they are summarized in **Table 1**.

The first was to calculate surface temperatures by a radiation-based surface energy flux (Equation 1). The energy balance was calculated using Newton's method to determine the surface temperature. The energy fluxes were assumed to be in an equilibrium state and include: the incoming short-wave radiation (R_{sw}), the incoming long-wave radiation (R_{ld}) with the surface emissivity (ε), the long-wave radiation (R_{lu}) emitted by the Earth's surface, the sensible heat flux (H) and the latent heat flux ($L \cdot ET_a$), with L being the latent heat of vaporization, and ET_a the rate of actual evaporation (Blodgett et al., 1997; Lenters and Cook, 1999).

$$\mathrm{R_{sw}} - \mathrm{R_{lu}} + \epsilon\,\mathrm{R_{ld}} - \mathrm{H} - \mathrm{L} \cdot \mathrm{ET_a} = 0 \tag{1}$$

In the second step (Equation 2), ET_a was calculated using the bulk transfer formula described by Brutsaert (1982), with the surface-drag coefficient (C_D), the wind speed (U), the soil moisture availability (f), the gas constant for dry air (R), the surface (T_s) and air (T_a) temperatures, the relative humidity (rh), and the saturation vapor pressure ($es(T_s)$) as a function of surface and air temperature.

$$\mathrm{ET_a} = \frac{0.622 \cdot \mathrm{C_D} \cdot \mathrm{U} \cdot \mathrm{f}}{RT_a}\left[\mathrm{es}\,(\mathrm{T_s}) - \mathrm{rh} \cdot \mathrm{es}\,(\mathrm{T_a})\right] \tag{2}$$

The resulting ET_a on land and water was calculated with Equations (1) and (2) from the environmental parameters summarized in **Table 1**. A sensitivity analysis of ET_a for paleo-lake Chew Bahir to major environmental parameters, such as air temperature (T_a), cloud cover, relative humidity (rh), and wind speed (U) was performed.

The third step involved calculating the annual lake water balance of lakes Abaya, Chamo and paleo-lake Chew Bahir using ET_a on land (E_l) and water (E_w), the precipitation amount from the Tropical Rainfall Measuring Mission (TRMM, Bookhagen, in review) (P_{bas}) and the basin-wide subsurface outflow/inflow (S_{bas}) following Equation (3). A positive and negative water balance suggest an increase and decrease in lake water volume,

TABLE 1 | Summary of input parameters for the LBM of Chew Bahir, Chamo, and Abaya.

Parameter	Symbol (Unit)	Chew Bahir		Chamo		Abaya		Confidence	References
		Lake	Land	Lake	Land	Lake	Land		
Cloud free shortwave radiation	R_sw (W/m²)	415		415		415		±3	Berger and Loutre, 1991
Shortwave cloud parameters	a, b	0.39, 0.38		0.39, 0.38		0.39, 0.38		–	Bookhagen et al., 2001
Longwave cloud parameters	a_2, b_2	0.22, 2.0		0.22, 2.0		0.22, 2.0		–	Bookhagen et al., 2001
Air pressure	p (kPa)	95.67	88.5	88.7	85.13	87.9	81.7	–	Barometric elevation formula
Cloud coverage	cc	0.44	0.61	0.37	0.55	0.31	0.54	±0.05	Platnick et al., 2015
Relative humidity	rh	0.55	0.57	0.57	0.57	0.57	0.58	±0.05	New et al., 2002
Windspeed	ws (m s^{-1})	2.56	2.13	1.71	1.72	1.46	1.42	±0.3	New et al., 2002
Air temperature	t_a (°C)	26.35	22.75	21.95	20.15	21.55	18.35	±0.5	New et al., 2002
Surface drag coefficient	cds	7.3×10^{-4}	5.9×10^{-3}	7.3×10^{-4}	6.6×10^{-3}	7.3×10^{-4}	7.6×10^{-3}	$\pm 0.2 \times 10^{-3}$	Schmugge and André, 1991
Surface albedo	albedo	0.06	0.14	0.06	0.126	0.06	0.136	±0.02	Friedl et al., 2010
Surface emissivity	emis	0.98	0.96	0.98	0.96	0.98	0.96	±0.02	Friedl et al., 2010
Moisture availability	f	1.00	0.137	1.00	0.198	1.00	0.25	±0.05	Schmugge and André, 1991

respectively. The modern-day conditions of Lake Abaya, Lake Chamo and paleo-lake Chew Bahir were assumed to be in equilibrium, where $\Delta V = 0$ as suggested in previous studies, such as Bookhagen et al. (2001), Bergner et al. (2003), and Junginger and Trauth (2013). The water surplus was assumed to be groundwater recharge in contrast to previous LBM studies, which used a fixed precipitation to groundwater ratio (Blodgett et al., 1997), a fix value (Bergner et al., 2003) or that the groundwater recharge rate is zero (e.g., Bookhagen et al., 2001; Dühnforth et al., 2006; Junginger and Trauth, 2013).

$$\Delta V_{lake} = P_{bas} - \left[E_w \alpha_w + E_l (1 - \alpha_w)\right] - S_{bas} = 0 \quad (3)$$

The SEBAL Method

Southern Ethiopia is a data-sparse region, with few continuously monitored weather stations, making quantification of the evaporation difficult on a catchment scale. Hence, we used a second approach called Surface Energy Balance Algorithm for Land (SEBAL; Bastiaanssen et al., 1998a,b). SEBAL calculates the Earth's surface instantaneous energy flux (Equation 4) at the moment of satellite overpass, to determine the latent heat flux as the residual (Bastiaanssen et al., 1998a,b).

In order to populate the SEBAL input parameters, satellite remote sensing data products of the Moderate-Resolution Imaging Spectroradiometer (MODIS) were identified and resampled to an uniform spatial resolution of 500 m (**Table 2**). To quantify monthly evaporation (Zhang et al., 2011; Borchardt and Trauth, 2012), the available MODIS datasets for an average reference year (2010 CE, Kiptala et al., 2013) were processed. The selection criterion applied was a clear sky coverage of higher than 90 percent. The Land Cover MCD12Q1 was further utilized to estimate the surface roughness length and the surface drag coefficient, following Wieringa (1992).

To calculate ET_a based on the surface energy fluxes we employed the net radiation (R_n) equation (Equation 4). ET_a was calculated using the soil heat flux G, which accounts for the amount of radiant energy released or absorbed at the soil surface per unit time, the sensible heat flux H and the latent heat flux λE, which resolves as residual of Equation (4):

$$R_n = G + H + \lambda E \quad (4)$$

R_n was estimated following the clear sky approach described in Allen et al. (2007) as a function of the day of the year, longitude, latitude, altitude, α, ε and atmospheric emissivity.

G was calculated with Equation (5) as a function of R_n, α and the Normalized Difference Vegetation Index (NDVI), which is a standardized proxy for vegetation density and greenness (Bastiaanssen, 2000).

$$\frac{G}{R_n} = \frac{T_s}{\alpha}\left(0.0038\alpha + 0.0074\alpha^2\right)\left(a - 0.98 \cdot NDVI^4\right) \quad (5)$$

H was determined using Equation (6), with the specific heat of air at a constant pressure (C_p), density of moist air (p), the vertical temperature gradient (dT), and the aerodynamic heat transfer resistance (r_{ah}) (Bastiaanssen et al., 1998a).

$$H = \frac{pC_p dT}{r_{ah}} \quad (6)$$

To solve Equation (6) we applied an approach by Zhang et al. (2011) that utilizes the wind field data by New et al. (2002). The frictional velocity and the aerodynamic resistance to heat transport were calculated for each pixel according to the wind-field and the logarithmic wind-profile. Both variables converge through an iterative atmospheric stability correction depending on the Monin-Obukov-Length (Bastiaanssen et al., 1998a,b). The resulting calculated dT leads to H (Bastiaanssen et al., 1998a,b). The evaporation fraction (Δ) was calculated to solve for daily evaporation (ET_{24}) from the instantaneous heat fluxes (Bastiaanssen, 2000; Bastiaanssen et al., 2005) with Equation (7).

$$\Delta = \frac{\lambda E}{R_n - G} = \frac{\lambda E}{\lambda E + H} \quad (7)$$

ET_{24} is a function of daily net radiation (R_{n24}) and Δ (Bastiaanssen, 2000). R_{n24} was calculated following De Bruin and Stricker (2000) through the integrated sinusoidal daily illumination and the extra-terrestrial solar radiation.

$$ET_{24} = \frac{86300 \cdot 10^3}{\lambda p_w} \Delta R_{n24} \quad (8)$$

The daily evaporation (ET_{24}) was averaged each month to calculate the monthly evaporation. Missing data for months with only cloudy days were interpolated from the adjacent months. To calculate ET_a, we applied a slight modification of the water balance by Thornthwaite and Mather (1955). We defined the modeled monthly evaporation as ET_p. Following that, we calculated the catchment average ET_p per month and compared them to the precipitation average from the TRMM dataset (Bookhagen, in review). Two assumptions have been

TABLE 2 | Moderate-Resolution Imaging Spectroradiometer (MODIS) products and bands used for SEBAL calculation.

Product	Band	Temporal granularity	Pixel size (m)	Data references
MOD11A1	Land Surface Temperature Daily	Daily	1,000	Wan et al., 2015
	Emissivity Band 31			
	Emissivity Band 32			
	Day View Time			
	Clear Day Coverage			
MOD09GA	Surface Reflectance Band 1–7	Daily	500	Vermote and Wolfe, 2015
	Solar Azimuth			
	Solar Zenith			
MOD13Q1	NDVI	16 day	250	Didan, 2015
MCD12Q1	Land Cover Type 2 (UMD)	Yearly	500	Friedl et al., 2010

considered when calculating the monthly water balance: (1) The total monthly ET_a is smaller than the total monthly precipitation (P) and the available soil water (SW) in the catchment. (2) 50% of the monthly water surplus, if occurring, is stored in the soil for the next month (SW) and 50% of the water surplus results in groundwater recharge (GW). In months where $ET_p < P$, we set $ET_a = ET_p$. However, in months where $ET_p > P$ the monthly ET_a was calculated by multiplying ET_p by the ratio of available water and ET_p (Thornthwaite and Mather, 1955; Borchardt and Trauth, 2012). The ET_a spatial distribution of humid months does not need to be corrected, as it remains the ET_p distribution. During dry months ET_a was further modified using the normalized Topographic Wetness Index (TWI; Kirkby and Beven, 1979) as shown in Equation (9). This spatial correction factor using the TWI reflects the orographic influence on the soil water distribution.

$$ET_a(x,y) = ET_p(x,y) \cdot [TWI_{norm}(x,y) + (\frac{\sum availableWater}{\sum potentialEvaporation} - TWI\_norm)] \quad (9)$$

In a last step, we compared the SEBAL and the bulk transfer LBM derived ET_a estimates on land, as well as the subsurface recharge rates for the Chew Bahir catchment to assess the two different approaches. Lake evaporation estimates for Chamo and Abaya were compared to measured pan evaporation data over the years 1985–2005 from the Arba Minch weather station (6°2′N, 37°33′E), which is located between lakes Abaya and Chamo (Belete, 2009).

Paleo-Lake Modeling Method

Model Calculation

In order to assess the sensitivity of lake levels to changes in precipitation and the impact of hydrological connectivity between basins, we combined the LBM's of Lake Abaya, Lake Chamo and paleo-lake Chew Bahir. The annual water balance of each catchment (Equation 3) and the consequent lake volumes were calculated to derive the potential change of lake surface areas. Annual changes in the total lake surface area were considered at the end of each annually modeled time-step and the ratio of land and water were adjusted to reflect the new surface evaporation fluxes for each modeled year. Furthermore, at each annual time step the overflow threshold was considered and an additional drainage function was activated if the lake water level exceeded the height of the overflow sill that was calculated in the DEM analysis (section Digital Elevation Model Analysis). For example, if the surface water level for Lake Abaya equals the overflow threshold, the water surplus is accounted for as inflow into the Chamo catchment and added to the water balance. The TRMM derived precipitation rates were multiplied by the total area of each catchment to calculate the volume of the total water influx. The computed ET_a over water was multiplied by the lake area to derive the evaporated water volume above each lake and the ET_a over land was multiplied by the remaining catchment areas to calculate the total ET_a.

Modeling Increased Precipitation Scenarios

We modeled various changes in precipitation over the Abaya, Chamo, and Chew Bahir catchments to estimate the increase in precipitation that was required for paleo-lake Chew Bahir to reach its overflow sill, the point where paleo-lake Chew Bahir drained into Lake Turkana during lake high-stands in the AHP (Foerster et al., 2012). Covering both decadal and centennial transitions of paleo-lake Chew Bahir (Trauth et al., 2018), we ran 500-years simulations of the LBM. The precipitation is increasing by 0.1% in each simulation, providing a total of 300 simulations with modeled precipitation increases from 0 to 30% of present day. This allowed us to calculate both the transition times for paleo-lake Chew Bahir; to go from "no lake" conditions to a "flooded basin" and the amount of increased precipitation that would be required. In the simulations, the exchange rates between the basins were calculated and the amount of the water volume influx from Lake Abaya to Lake Chamo and Lake Chamo to paleo-lake Chew Bahir were quantified as a proportion of its total water budget. Due to a lack of paleo-vegetation information and its impact on the actual evaporation and resulting precipitation in the study region for the AHP, we used the estimates of a 7–15% increased precipitation during the AHP in the Kenyan Rift published by Bergner et al. (2003). Those estimates are presented as vegetation threshold within our results and are based on the same parametrization approach as our LBM and are coming from a comparable landscape composition.

Modeling Seasonality Changes in Precipitation

Previous studies have suggested a change in the seasonality of precipitation during the AHP, due to a shift in the Congo Air Boundary, resulting in additional precipitation during July to September in equatorial regions in eastern Africa (e.g., Junginger, 2011; Junginger and Trauth, 2013; Costa et al., 2014; Junginger et al., 2014; Bloszies et al., 2015; Beck et al., 2019). This would have resulted in a change of the evaporative potential on land, compared to present day, due to an increased potential moisture source over what were previously dry months ($ET_p > P$). We calculate the difference between ETa and ET_p using SEBAL from July to September and add this evaporation amount to Chew Bahir's catchment actual evaporation rate on land. We omit the catchment of the lakes Abaya and Chamo from this procedure as they don't have this modern day lack ($ET_p < P$) of evaporable water for these months.

Transition Times for Onset and Termination of AHP

The timing of precipitation change was also modeled using different scenarios to estimate the temporal reaction of paleo-lake Chew Bahir's volume to abrupt and gradual precipitation changes during the onset and termination of the AHP. The first scenario (S1) was an abrupt transition, simulated by an instantaneous increase in precipitation to the threshold (TS) amount required to force paleo-lake Chew Bahir to the overflow sill. However, this only represents the minimum precipitation required to fill Paleo-lake Chew Bahir to the overflow level, therefore we additionally considered two scenarios, in which the threshold could have been exceeded (S2: TS+5%, S3:

TS+10%). We simulated a gradual increase in precipitation from modern day conditions to TS over 50, 100, 250, and 500 years. The termination of the AHP was also simulated, where the abrupt scenario saw an immediate transition from increased precipitation rates (TS) to modern day precipitation. The gradual offset was simulated by decreasing the precipitation amount linearly from TS to the modern day amount within 50, 100, 250, and 500 years.

Amplifier Lake Characteristics

In order to compare the basins of Lake Abaya, Lake Chamo and paleo-lake Chew Bahir with other lakes within the EARS, we calculated the hypsometric integral (*HI*; Pike and Wilson, 1971) following Equation (10).

$$HI = \frac{mean\ elevation - minimum\ elevation}{maximum\ elevation - minimum\ elevation} \quad (10)$$

We calculated the *AI* of each, individual catchment as the quotient precipitation (mm a^{-1}) and potential evaporation (mm a^{-1}, Thornthwaite, 1948) within each catchment. The term amplifier lake characterizes lakes in the EARS that react very sensitively to even moderate climate changes (Street-Perrott, 1985; Olaka et al., 2010; Trauth et al., 2010). We compared the HI and AI of paleo-lake Chew Bahir, lakes Abaya, and Chamo with other lake basins and classified amplifier lakes in the EARS based on Olaka et al. (2010).

Chew Bahir Lake Level Reconstruction

To translate changes indicated by climate proxies in the Chew Bahir drill core sediments into actual lake level changes, we used the established aridity proxy potassium (K) (Foerster et al., 2012, 2015, 2018; Trauth et al., 2018). High K concentrations in the sedimentary record have been documented to be strongly controlled by the hydrochemistry of the paleo-lake and porewaters. Such changes in salinity and alkalinity are typically caused by a drier climate and associated lake water evaporation (Foerster et al., 2018). For our study, we are using the most complete and high resolution record from Chew Bahir for the last 20 ka BP, a composite of pilot core CB-01 and CB-03, as discussed in Foerster et al. (2015). In our study, we compare the timing of K-changes with modeled response times of paleo-lake Chew Bahir's lake level, and interpret whether long-term and short-term fluctuations can be explained by abrupt or gradual changes in precipitation based on their duration and also K content.

RESULTS

DEM Analysis Overflow Regime

As summarized in **Table 3**, an additional 25.2 km^3 of water would be required to initiate drainage at the overflow sill from Lake Abaya toward Lake Chamo, resulting in an increased lake surface area of 3.6%. To initiate overflow from Lake Chamo toward Chew Bahir, only an additional 5.2 km^3 is required, which would increase the lake area by 5%. Paleo-lake Chew Bahir would require 83.2 km^3 for the lake level to reach the overflow sill and initiate drainage into Lake Turkana. In this scenario, paleo-lake Chew Bahir would cover 12% of the total catchment area.

TABLE 3 | Summary of major output parameters.

Parameter	Unit	Chew Bahir	Chamo	Abaya
DIGITAL ELEVATION MODEL ANALYSIS				
Catchment size	km^2	20,650	1,793	16,203
Modern day lake level	m a.s.l.	498	1,109	1,176
Maximum lake level	m a.s.l.	543	1,123	1,194
Modern day lake area	km^2	0	310	1,081
Maximum lake area	km^2	2,486	394	1,557
Additional lake volume	km^3	83	5	25
Modern day lake area ratio, α_w	%	0	17	6
Maximum lake area ratio, α_w	%	12	22	9.6
Hypsometric Integral		0.23	0.15	0.25
Aridity Index		0.83	1.33	1.72
LAKE BALANCE MODEL				
Precipitation modern, P_{bas} (rate, volume)	(mm a^{-1}, km^3)	917, 18.9	1,211, 2.2	1,407, 22.8
Precipitation paleo 20–30% increased, P_{bas} (rate)	(mm a^{-1})	1,100–1,192	1,453–1,574	1,688–1,829
Groundwater, S_{bas} (rate, volume)	(mm a^{-1}, km^3)	24, 0.5	80, 0.1	260, 4.2
Evaporation on land, E_l (rate, volume)	(mm a^{-1}, km^3)	892, 18.4	1,060, 1.6	1,123, 17
Evaporation on water, E_w (rate, volume)	(mm a^{-1}, km^3)	1,908, 0	1,550, 0.5	1,513, 1.6

Lake Balance Model Results

Sensitivity tests of the major environmental parameters in the LBM including temperature, cloud cover, humidity and wind speed were calculated for the paleo-lake Chew Bahir catchment (**Figure 3**). For example, a modeled mean temperature rise of 1°C with an error below 1°C (New et al., 2002) would result in an increase of 4.7% (42 mm a^{-1}) in ET_a for the average land evaporation in the paleo-lake Chew Bahir catchment (**Figure 3A**). Cloud cover measurements from MODIS typically have an error below 5% (Platnick et al., 2015). An increase in average cloud cover by 5% would decrease ET_a by ∼4% (367 mm a^{-1}, **Figure 3B**). The dataset of the relative humidity shows errors up to ±15% (New et al., 2002). Hence, an increase in the average relative humidity of 15% would decrease ET_a on land by 8.7% (78 mm a^{-1}, **Figure 3C**). The windspeed dataset has the highest errors and according to New et al. (2002) the maximum deviation for specific measures sites in eastern Africa ranges between 40 and 60%. For example, an increase in wind speed of 1 m s^{-1} (corresponding to a 45% deviation) would enhance ET_a by 19.5% (174 mm a^{-1}, **Figure 3C**).

SEBAL Results

Using 43 days with a clear sky of the reference year, the calculated mean R_n was 459 W m^{-2} (σ = 54 W m^{-2}), the average G was 75 W m^{-2} (σ = 8.6 W m^{-2}), and H was 130 W m^{-2} (σ

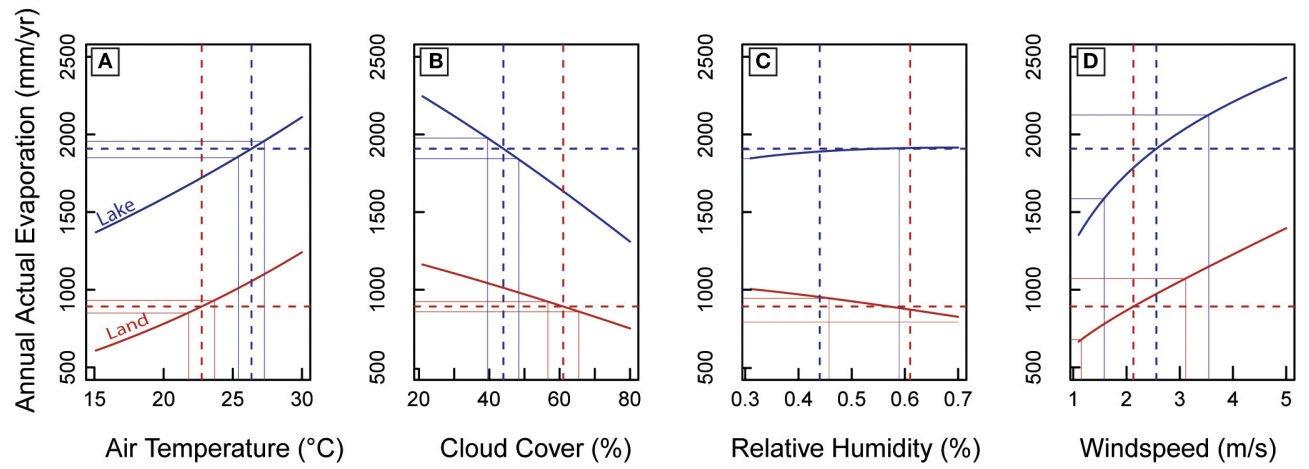

FIGURE 3 | The effects of environmental parameters on lake and land evaporation for the Chew Bahir basin: **(A)** air temperature, **(B)** cloud cover, **(C)** relative humidity, and **(D)** windspeed. Dashed lines indicate used input parameter and resulting annual actual evaporation of the LBM. Solid thin lines indicate maximum/minimum errors with resulting maxima/minima of the annual actual evaporation.

= 27.3 W m^{-2}). Those fluxes result in Δ of 0.64 (σ = 0.074) and λE of 0.38 mm h^{-1} (σ = 0.07). RN_{24} was 137 W m^{-2} (σ = 7.07 W m^{-2}), resulting in ET_{24} of 3.18 mm d^{-1} (σ = 0.33 mm d^{-1}).

The annual water balance shows a bimodal precipitation (916 mm a^{-1}) and ET_a (847 mm a^{-1}) and an unimodal ET_p (see **Figure 4B**). The spatial distribution (see **Figure 4A**) of ET_a ranges from 52 to 1,360 mm a^{-1}. The southern part of the catchment has the lowest values, whereas the northern and elevated rift shoulders, with streams and adjacent wetlands, has the highest ET_a due to greater water availability.

Evaporation Estimate Comparison

Using the SEBAL approach, ET_a was 847 mm a^{-1} for the paleo-lake Chew Bahir catchment, compared to 892 mm a^{-1} using the bulk transfer method, which is a relative difference of 5% (45 mm a^{-1}). This leads to a shift in the closed water balance of the paleo-lake Chew Bahir catchment and a difference in the estimated catchment-wide groundwater recharge rates between 69 mm a^{-1} (SEBAL) and 24 mm a^{-1} (LBM). We calculated annual lake evaporation for Lake Abaya of 1,513 mm and for Lake Chamo of 1,550 mm a^{-1} using the bulk transfer Lake Balance Model. At the Arba Minch metrological station (6°2'N, 37°33'E), class A pan evaporation was measured from 1985 to 2005 AD, with an average of 2,191 mm a^{-1}. This results, with a correction factor of 0.85, in a 20-years average annual lake evaporation of 1,862 mm a^{-1} as calculated by Belete (2009). These values differ from our model results by 16.7 to 18.7%, which could be related to a high uncertainty of the individually determined correction factor for pan evaporation data.

Combined Lake Balance Model and Paleo-Water Balances Results

Modeling Increased Precipitation Scenarios

The transition of paleo-lake Chew Bahir from "no lake" to "overflow conditions" at a lake surface level of 543 m a.s.l., 45 m above basin floor, was simulated over a period of 500 years. The transition occurs at a minimum precipitation increase at a TS of 6.5% compared to modern day 12-years TRMM average and occurs within 302 years (**Figure 5A**). The transition time required to go from "no lake" to "overflow conditions" decreases with increasing precipitation to, for example, 39 years (TS+5% = 11.5%) and 21 years (TS+10% = 16.5%), as indicated by stars in **Figure 5A**.

The water flux from one basin to the next basin increases linearly as soon as the overflow threshold of each basin is reached (**Figure 5B**). For example, the water flux from Lake Chamo to paleo-lake Chew Bahir increases starting from zero when precipitation is enhanced by 1.1%, and rises up to 3.9 km^3 a^{-1} when precipitation is 16.5% higher than today.

The calculated inflow ratio for paleo-lake Chew Bahir describes the ratio between the annual water derived by precipitation within the catchment and the inflow from Lake Chamo (**Figure 5C**). The inflow ratio quantifies the high importance of the extended catchment of Lake Abaya and Lake Chamo for the water balance of paleo-lake Chew Bahir. The inflow ratio of Chew Bahir increases starting from 0 to 1.1% enhanced precipitation and reaches 6.3% when precipitation enhances to the threshold precipitation (TS = 6.5%) for overflow conditions.

Seasonality Changes Results

The difference in annual evaporation on land of 167.6 mm for the paleo-lake Chew Bahir catchment that we assessed needs to be considered to compensate for the additional rainy months from June to September according to the SEBAL processing. This difference in annual evaporation on land results in an increased threshold to achieve the transition from "no lake" to "overflow conditions." When considering a third rainy season to have been active during the AHP, the threshold precipitation to fill paleo-lake Chew Bahir up to its overflow level would have increased

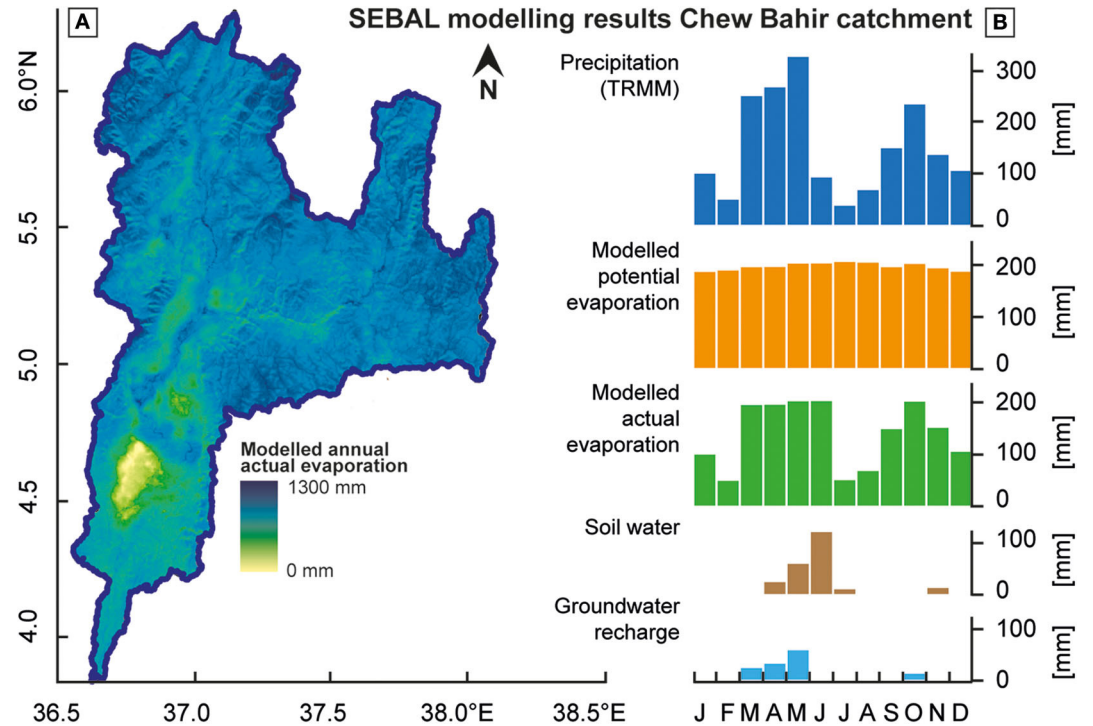

FIGURE 4 | SEBAL results for paleo-lake Chew Bahir catchment: **(A)** Map of actual evaporation distribution throughout the catchment. **(B)** Monthly precipitation and monthly water balance of the Chew Bahir catchment.

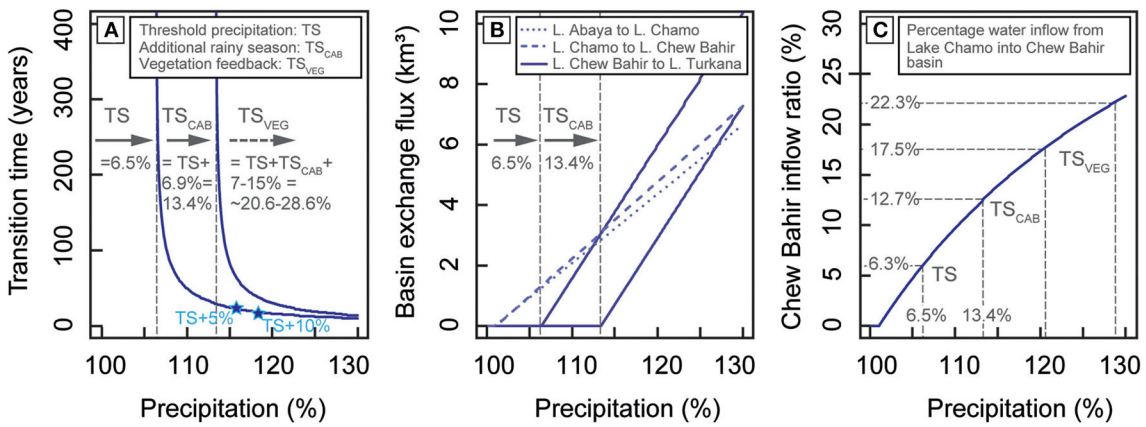

FIGURE 5 | The effects of precipitation increase on the investigated lake basins: **(A)** Transition times of paleo-lake Chew Bahir from "no lake" to "overflowing lake" into Lake Turkana under minimum threshold (TS) conditions where seasonality has not changed; under the consideration of an additional rainy season caused by a shift of the location of the Congo Air Boundary (TS_{CAB}); and the incorporation of theoretically vegetation feedback (TS_{VEG}) with values taken from Bergner et al. (2003), since no local paleo-data are available. The graph shows the increasing pace of lake level rise with increasing precipitation. **(B)** Water mass exchange between the three investigated basins for the scenarios, TS and TS_{CAB}. **(C)** Precipitation and overflowing Lake Chamo-Abaya as relative water sources of paleo-lake Chew Bahir showing the importance of an enlarged catchment of Chew Bahir during overflow times of all lakes. Whereas, under TS conditions Chew Bahir inflow ratio is at 6.3%, the inflow doubles up to 12.7% when considering an additional rainy season.

by 6.9% (TS_{CAB} = TS+6.9% = 13.4%) compared to the modern day precipitation amount (**Figures 5A,C**). The consideration of a changing vegetation on the evaporation and the resulting necessity of an increased precipitation is 7–15%, as suggested by Bergner et al. (2003). This leads to a combined threshold TS_{VEG} of 20.6 to 28.6% (TS_{VEG} = TS+TS_{CAB}+ 7–15% = 20.6–28.6%; 20–30% rounded) compared to the modern day annual precipitation (**Figures 5A,C**).

AHP Transition Times Results

For abrupt "lake fill" scenarios (**Figure 6A**), the lake filling curve using the minimum precipitation amount of 13.4% (TS_{CAB}) required to fill paleo-lake Chew Bahir up its overflow sill, leads to a slow, around 300 years, asymptotic reaction of the lake surface level over time as soon as paleo-lake Chew Bahir derives a constant water flux from Lake Chamo. Whereas, an increase of the precipitation amount for example by 5% (TS_{CAB}+5%) or 10% (TS_{CAB}+10%) above the threshold (TS_{CAB}) leads to a fast transition of paleo-lake Chew Bahir from "no lake" to "overflow conditions" within 30 and 22 years, respectively. Lake Abaya and Lake Chamo, however, are showing for all simulated precipitation signals decadal to sub-decadal transition times.

For gradual "lake fill" scenarios (**Figure 6B**) within 50, 100, 250, and 500 years from the modern day precipitation amount to the threshold, the same asymptotic lake surface level reaction pattern in time is identified, but it is delayed through the gradual precipitation signal. This gradual delay factor leads to corresponding centennial transition (>350 years) times. Lake Abaya and Lake Chamo show for all simulated gradual "lake fill" scenarios filling times between 40–160 and 50–180 years, respectively.

We simulated abrupt "lake drain" scenarios (**Figure 6C**) starting with lakes at their specific overflow sill: Lake Abaya at +18 m, Lake Chamo at +14 m, and paleo-lake Chew Bahir at +45 m above the modern day lake surface levels. For this scenario paleo-lake Chew Bahir would have been dried out within 45 years, whereas Lake Chamo and Lake Abaya would need more than 100 years to reach their new equilibrium state.

The simulation of gradual "lake drain" scenarios within 50, 100, 250, or 500 years to modern day conditions leads to delayed transition times of paleo-lake Chew Bahir from 70 up to 370 years before drying up (**Figure 6D**). Under gradual precipitation decrease Lake Abaya dries up between 170 and >500 years, and Lake Chamo takes the longest with 370 to >500 years.

Amplifier Lake Characteristic Results

Following the main principles for amplifier lake characterization (HI 0.23–0.3; Olaka et al., 2010; **Figure 7**), Chew Bahir (HI: 0.23, AI: 0.83) and Abaya (HI: 0.25, AI: 1.72) can be characterized as amplifier lakes. Chew Bahir is with an AI < 1 characterized as a

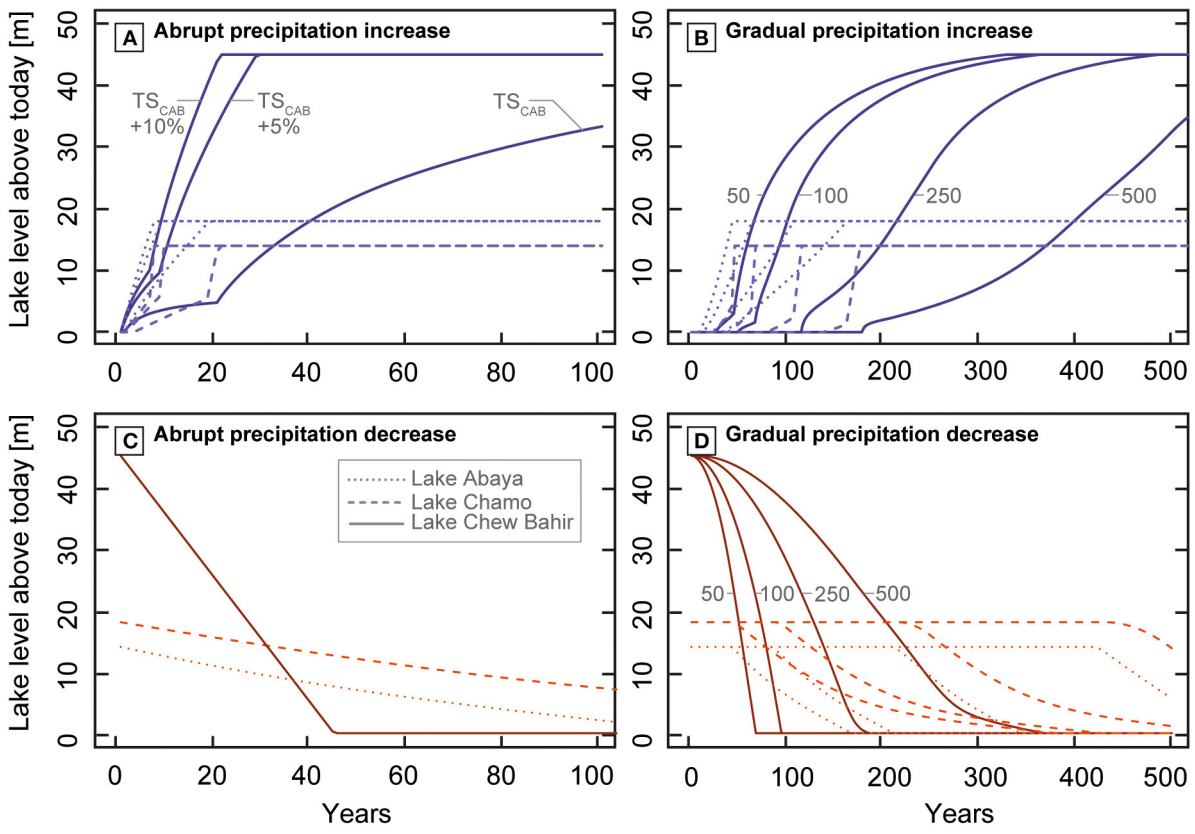

FIGURE 6 | Modeled pace of lake transitions under abrupt and gradual precipitation changes: **(A)** Abrupt increase in precipitation from modern values to TS_{CAB} values (13.4%) as a minimum possible amount of rainfall to fill up the investigated lake basins. TS_{CAB} +5% and TS_{CAB} +10% are provided as examples for even higher precipitation that was provided during the AHP, for example. **(B)** Lake fill scenario under gradual increase in precipitation from modern values to TS_{CAB} values over 50, 100, 250, and 500 years. **(C)** Abrupt decrease in precipitation from TS_{CAB} to modern values. **(D)** Lake regression scenario under gradual decrease in precipitation from TS_{CAB} to modern values over 50, 100, 250, and 500 years.

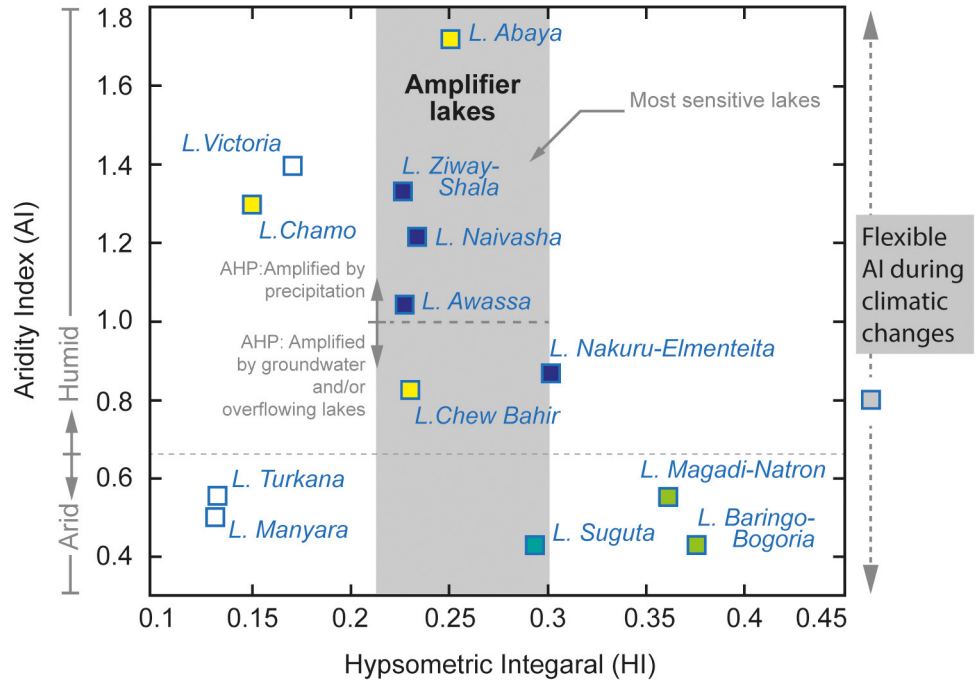

FIGURE 7 | The characterization of amplifier lakes: Hypsometric integral (HI) and Aridity Index (AI) of major lake basins within the EARS as published by Olaka et al. (2010) including new calculated values of paleo-lake Chew Bahir, Lake Abaya, and Lake Chamo (in yellow) from this study. Amplification of precipitation changes occurs in lakes with HI of 0.23–0.3 according to Olaka et al. (2010). We postulate that AI has changed in the course of climatic changes and thus amplification influences, such as groundwater and precipitation.

lake with slightly higher potential evaporation than precipitation, whereas Abaya is the wettest of all investigated basins with AI>1 (**Figure 7**). Lake Chamo (HI: 0.15, AI: 1.33) cannot be considered as an amplifier lake.

DISCUSSION

Advantages and Limitation of the LBM

Paleo-Precipitation Estimates

The results from the hydro-balance modeling show that a surplus in precipitation of 20–30% compared to present day values is required to fill the presently dry paleo-lake Chew Bahir to its overflow sill at 545 m a.s.l. and a depth of ∼45 m, resulting in a ∼2,500 km^2 large freshwater lake. These final estimates are the result of three different assumptions: (1) TS of +6.5% accounts for the minimum precipitation required to fill paleo-lake Chew Bahir to its overflow level (classical hydro-balance approach), (2) TS_{CAB} equals the sum of TS+6.9% to include extra precipitation outside the current rainy season from the theoretical shift of the CAB over the rift region during the AHP as suggested by previous studies (e.g., Junginger, 2011; Costa et al., 2014; Junginger et al., 2014; Bloszies et al., 2015; Beck et al., 2019), and (3) TS_{VEG} equals the sum TS+TS_{CAB} +7–15% precipitation to include the impact of vegetation feedback (**Figure 5**). Vegetation feedback, which increases transpiration and thus precipitation was approximated in our model, based on biosphere-feedback modeling results (7–15%; Bergner et al., 2003) from the nearby Lake Naivasha basin in the central Kenya rift, due to a lack of direct paleo-vegetation data. Numerous studies from eastern Africa strongly suggest a pronounced vegetation change between the AHP and today (e.g., Lamb et al., 2004; Vincens et al., 2005; Umer et al., 2007; Rucina et al., 2009; Marchant et al., 2018) and that vegetation feedback played an important role in precipitation (e.g., Claussen et al., 2017). However, local and regional information during the AHP (e.g., pollen, non-pollen palynomorphs, charcoal or phytoliths from sediments) are currently lacking and would help refine estimates of paleo-precipitation changes due to vegetation feedback, allowing for improved estimations of past hydrological budgets in southern Ethiopia.

Our modeling results of precipitation increase (20–30%) for paleo-lake Chew Bahir are of the same order of magnitude as results for similar studies within the EARS during the AHP (**Figure 1**), such as Ziway–Shala (+28%, Gillespie et al., 1983), Lake Turkana (+20%, Hastenrath and Kutzbach, 1983), Suguta Valley (+26%, Junginger and Trauth, 2013), Lake Nakuru–Elmenteita (+23–45%%, Dühnforth et al., 2006; Kniess, 2006), and Lake Naivasha (+29–33%, Hastenrath and Kutzbach, 1983; Bergner et al., 2003). However, almost all results stem from different modeling approaches. None of the previous models have considered hydrological connectivity or the impact on evaporation (ET_a) due to a third rainy season. The latter would have had especially affected the catchments of Lake Turkana, Lake Nakuru-Elementeita, Lake Naivasha and paleo-Lake Suguta, as they most likely experienced a precipitation increase due to the

change in the position of the CAB during the AHP (Junginger et al., 2014). We therefore propose that lake catchments and LBM results in the EARS under the potential influence of the CAB during the AHP would require additional increased precipitation.

Another important aspect in hydrological modeling of eastern African rift lakes is the inclusion of basin surface connectivity in major humid periods (**Figure 1**). Paleo-lake Chew Bahir received 15–25% of its additional water during the AHP from overflowing lakes Abaya and Chamo via the Segan River. Such hydrological connectivity during the AHP almost doubled the catchment size of Chew Bahir from 20,650 to 38,647 km^2 (**Figure 2**). However, hydrological basin connectivity was likely intermittent, only occurring during strong humid phases (**Figure 8**). Intermittent connectivity during high-stands could have been caused by short-term abrupt changes in the position of the CAB and associated temporal cut offs from the surplus of water. Such intermittent surficial hydrological connectivity is likely relevant for all EARS lakes in the mid and lower altitudes, such as lakes Abhé, Turkana, Suguta, Baringo-Bogoria, Magadi, and Manyara (**Figure 1E**).

The water balance has varied due to increased precipitation and changes in other environmental parameters (e.g., as mentioned in **Table 1**) which influence the inflows and outflows into the basin. It is difficult to quantify these parameters (e.g., cloud cover, wind speed, and relative humidity) during the AHP. Proxy record reconstructions over the AHP however, can provide some insights. The GDGT based temperature reconstruction for eastern Africa by Loomis et al. (2012) reveals a colder climate at the beginning of the AHP at around 15 ka BP and a climate which was up to 3°C between 12 and 5 ka BP. Based on our sensitivity analysis for environmental parameters (section Lake Balance Model), an increase of around three Kelvin could increase the actual evaporation by up to 14%. A decrease in temperature of three Kelvin could lower the evaporation by the same amount. In terms of the resulting precipitation estimates, the early AHP with a slightly colder climate would need a slightly lower precipitation amount to reach a positive water budget, whereas the late phase of the AHP would need a slight higher precipitation amount to reach a positive water budget.

In summary, our study reveals the same magnitude of precipitation increase (+20–30% of modern day) in eastern Africa for the AHP as most other studies, but separates this threshold into parts. Those parts would need to be added (precipitation during modern day dry months) or subtracted (paleo hydrological connectivity) for other lake basins within the EARS, but can only be quantified in a site specific manner.

Evaporation Estimates Discussion

We compensated the lack of ground measured climate data by using remote sensing MODIS products, modeled climate data and calculated the actual evaporation additionally through SEBAL. This algorithm as proposed by Bastiaanssen et al. (1998a,b) has been applied in numerous variations depending on the data, landscapes and research designs. Studies showed inaccuracy of SEBAL at a field-scale and suggested to use METRIC or SEBS instead (e.g., Losgedaragh and Rahimzadegan, 2018). Mkhwanazi et al. (2015) implemented advective conditions within the SEBAL for crop evaporation studies on a field-scale, because the algorithm underestimate actual evaporation with a mean bias Error of 17.1%. SEBAL for catchment-scale studies instead showed an accuracy above 95% (Bastiaanssen et al., 2005). A 3 years SEBAL application in Tanzania and Kenya with a comparable research design as our application achieved a difference between the SEBAL results and the water balance of the catchment of 12%. For a SEBAL application in the Suguta Valley the SEBAL ET_a is 5% lower than the bulk transfer calculated ET_a of the LBM (Borchardt and Trauth, 2012; Junginger and Trauth, 2013).

The evaporation estimates of the SEBAL, the bulk-transfer formula and the pan-evaporation measurement have been compared and vary between 5 and 18.7%. This means the input water fluxes for the LBM could vary at the same magnitude. But those fluxes are not independent, instead the modern day water budget for each year is in balance. An increase in ET_aon land would necessarily imply, ET_a on water or the groundwater recharge rate is overestimated. The same yields for the sensitivity analysis of the bulk-transfer derived ET_a. The variation of the evaporation rate depending on the environmental parameters shows possible inter-annual variability and possible micro-climate caused differences within the catchment. This spatial variety is mapped by SEBAL. However, besides the sensitivity, spatial variety and inter-annual variability, the accuracy of each multi-annual average water flux rate is due to the multi-method verification and the closed water balance of each catchment with an definite error below 20%. The different subdivisions of precipitation within each catchment between ET_a on water and land affects the paleo-precipitation threshold in approximately one-tenth of the maximum deviation between ET_a on water and land. This leads to a robust error of the threshold of 2% and an overall paleo-precipitation threshold for paleo-lake Chew Bahir of plus 20–30% precipitation in a multi-annual average compared to the modern day conditions.

Subsurface Flows Discussion

Endorheic basins, and their subsequent lakes, can be classified into three groups; (1) flow-through lakes, (2) discharge lakes, and (3) recharge lakes (e.g., Olaka, 2011 and references therein). Flow-through lakes are balanced ($S_{bas} = 0$). Discharge lakes are positively affected by groundwater flowing into the lake ($S_{bas} > 0$) and recharge lakes lake water seeps into the groundwater ($S_{bas} < 0$). During the AHP, when the overall moisture availability in the atmosphere was much higher and lake levels rose, changes in the groundwater levels may have changed the classification and status of the basin. Changes in groundwater inflows and outflows, would have subsequent impacts on the overall lake water balance. For example, groundwater discharge into lake basins could reduce their sensitivity to reduced precipitation input in short-term dry periods and potentially delay lake desiccation in protracted dry phases. This is a possible mechanism to explain why extremely arid catchments, such as paleo-Lake Suguta or Lake Nakuru-Elementeita, developed and maintained paleo-lakes which were 10–300 m deeper than today (Olaka et al.,

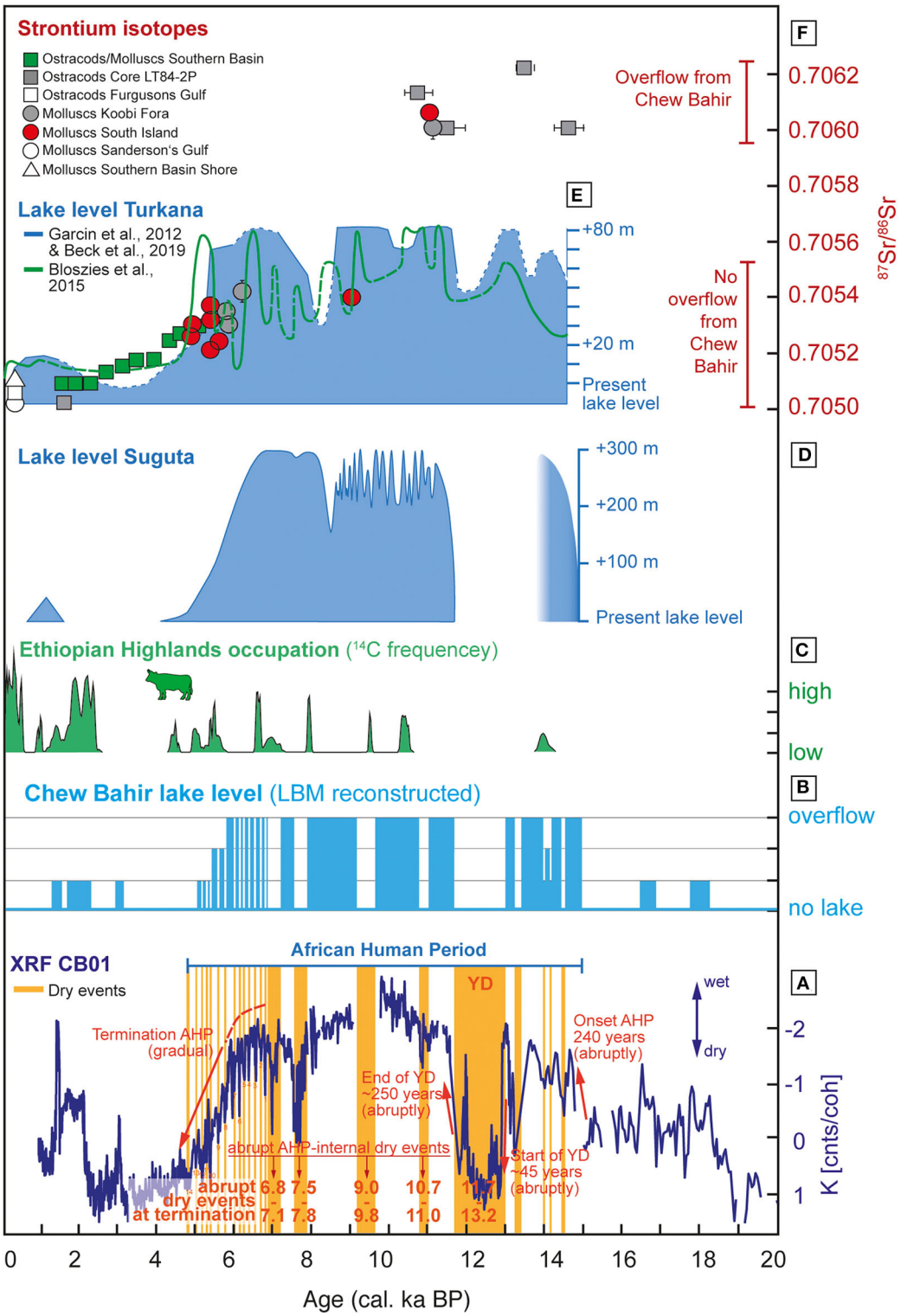

FIGURE 8 | Chew Bahir LBM-based paleo-lake level reconstruction and comparison to adjacent lakes: **(A)** CB01 K proxy-record by Foerster et al. (2015) with dry events discussed in the text and transition modes. **(B)** Reconstructed lake level curve of Chew Bahir based on the lake-balance model (LBM) applied to changes in the K concentration of CB01. **(C)** Human occupation history of the Ethiopian highlands implies enhanced activities when lakes in the lower elevated rift basins, such as paleo-lake Chew Bahir became to saline or even dried up. The Ethiopian highlands may thus have been a refuge area during unfavorable times as Foerster et al. (2015) suggested. Cow indicates cultural transition from fishing/hunting/gathering to herding in the Ethiopian Highlands. **(D)** Lake level reconstruction of Suguta Valley (Junginger et al., 2014) as the mirror basin of Chew Bahir. **(E)** Lake level reconstruction of Lake Turkana by Garcin et al. (2012) and Beck et al. (2019) (blue, shaded curve), and by Bloszies et al. (2015) (green). **(F)** Strontium isotopes measured on aquatic fossils from lake Turkana sediments (van der Lubbe et al., 2017).

2010). For example, Olaka (2011) estimated response times of 2–2.7 ka for groundwater to drain a 41 km^3 large aquifer underneath the Eburro volcano complex located between Lake Naivasha and Lake Nakuru in the central Kenya Rift (**Figure 1**). Unfortunately, the southern MER lack this kind of information, despite preliminary evidence of significant groundwater aquifers in the central part of the Ethiopian rift (Kebede and Travi, 2012).

In terms of the groundwater recharge rate and the subsequent effect on the paleo-precipitation threshold for the African Humid Period, we parameterised the groundwater recharge rate as the surplus of the water balance budget, which is in contrast to previous LBM studies (see section Lake Balance of Lakes Abaya, Chamo, and Paleo-Lake Chew Bahir). Based on Chernet (1993) recharge rates between 50 and 150 mm a^{-1} are typical, which would be ∼5–15% of the annual precipitation within the Chew Bahir catchment. We calculated a groundwater recharge rate of 24 mm a^{-1} using the LBM and 69 mm a^{-1} using SEBAL. These comparisons show the possible errors of our modeling results due to this uncertainty, which are a quantity smaller than the annual fluxes in precipitation and evaporation (Dühnforth et al., 2006).

Lake Response Times Discussion

Amplifier Lake Characteristics

Olaka et al. (2010) postulated that amplifier lakes, where AI < 1 ($ET_p > P$), likely received greater groundwater or surface inputs during the AHP, in order to maintain expansive lake systems in semiarid to arid regions in the EARS. In contrast, lakes with AI > 1 ($ET_p < P$), which are prevalent on the high plateaus of the rift margins and Ethiopian Domes (**Figure 1**), are and were during the AHP amplified through precipitation. However, these calculations are based on present day conditions and may be irrelevant in a paleo context where P and ET_p would have been vastly different, and consequently the AI. We expect in a paleo context, that the position of the AI for the respective paleo lakes would likely shift vertically along the y-axes of **Figure 7** over time periods of 10–10,000 years. Based on our LBM, for example, the rate of groundwater feeding paleo-lake Chew Bahir today remains smaller than the rate of groundwater discharge within the catchment and is furthermore a magnitude smaller than the water mass exchange rates due to precipitation, evaporation and surface basin connectivity. However, the groundwater system could act as a millennial-scale buffer, which is recharged during major humid periods may slow the transition to lake desiccation in drier periods (e.g., Garcin et al., 2009; Olaka, 2011).

Although Lake Chamo is not characterized as an amplifier lake, it can receive additional surface inflows from Lake Abaya, due to the very shallow overflow between the two lakes (**Figures 1**, **2**). Due to the extremely shallow overflow sill of Lake Abaya toward Lake Chamo and toward paleo-lake Chew Bahir, we hypothesize that even sub-decadal precipitation shifts may have triggered overflow to the paleo-lake Chew Bahir basin, and thus would have caused abrupt changes in the water budget of paleo-lake Chew Bahir. It is therefore highly likely that paleo-lake Chew Bahir was able to change during the AHP from a fresh-water lake to a desert within only a couple of decades. Such sensitivity to even moderate climate changes makes the paleo-lake Chew Bahir basin responsive to even sub-decadal climate fluctuations in contrast to, for example the Suguta Valley, which has a greater buffering capacity to short-term variability in precipitation, due to its larger size and depth of the paleo-lake (paleo-lake depth of 295 m), and higher overflow sill (**Figures 1**, **8**).

We understand paleo-lake Chew Bahir as a double amplifier lake, pronouncing the unique and high sensitivity of the landscape and lakes water-level reaction to precipitation signals. This is due to (1) the classification of its catchment as an amplifier lake (**Figure 1**) and (2) the importance of the catchment of lakes Chamo and Abaya for the paleo water balance of paleo-lake Chew Bahir. This expansion of paleo-lake Chew Bahirs catchment in case of over-spilling lakes Abaya and Chamo into the Chew Bahir basin amplifies the lakes reaction to precipitation changes and causes rapid filling if there is a significant water drain, or rapid draining if this hydrological connectivity gets cut off.

Pace and Magnitude of Lake Level Changes

In a previous study by Trauth et al. (2018) a change point analysis was applied to the aridity proxy K-record by Foerster et al. (2012, 2015) to investigate the timing and duration of climatic changes. Our study now is able to add the character and magnitude of lake level changes and thus allows to infer direct implications to biosphere impacts.

Trauth et al. (2018) stated that the most dramatic changes occurred during the onset of the AHP and the interruption by the Younger Dryas (YD), a global cold event, known as a pronounced dry episode in eastern Africa (e.g., Barker et al., 2004). The onset of the AHP in the Chew Bahir basin, so Trauth et al. (2018), occurred within ∼240 years (15.7–15.46 ka BP). Within such period of time, paleo-lake Chew Bahir would have been able to reach the overflow sill toward Lake Turkana (**Figures 1**, **8**). The extreme arid interval in Chew Bahir between 13.2 and 11.73 ka BP, largely coinciding with the YD chronozone, shows abrupt changes in the K- record. Those were presumably expressed in an abrupt lake level drop (within 45 years) and lake level rise (within 250 years) in Chew Bahir. After the return to full humid conditions, the AHP main phase was interrupted by four dry spells at 11–10.7, 9.8–9.0, 7.8–7.5 and 7.1–6.8 ka BP. Those dry events are also reflected in records from lakes Turkana and paleo-lake Suguta (**Figure 8**), Mount Kilimanjaro (Thompson et al., 2002), Arabia (Fleitmann et al., 2003), as well as marine records off the NE coast of Africa (e.g., Gupta et al., 2003). Most of these dry episodes have lasted around 300 years. We expect, from a modeling perspective, these dry spells to have been long enough to desiccate paleo-lake Chew Bahir completely.

Trauth et al. (2018) highlights fourteen 20–80 years lasting dry events within the K-proxy record during the overall gradual termination of the AHP. According to our LBM, decadal dry events of 40 years or longer were able to dry up the Chew Bahir basin completely. Dry periods of 40 years or shorter still caused a considerable reduction in lake level though not a complete desiccation (**Figure 8**). Over the entire length of the AHP termination, Chew Bahir appears to have been under severe desiccation pressure. Such rainfall variability was also recorded in stalagmites in the near-by south-eastern rift shoulders of

Ethiopia during times of a progressively drier climate (Baker et al., 2010). However, short-term precipitation changes may have filled lakes Abaya and Chamo up to their shallow overflow sills and provided Chew Bahir every now and then with enough water to delay the drying up process. The short-term flickers at the end of the AHP suggest, that paleo-lake Chew Bahir had not enough time between those flickers to have reached the overflow sill again. This assumption is supported by the finding of van der Lubbe et al. (2017), who used strontium isotopes as a water provenance proxy over the AHP and found no indication of a contribution of Chew Bahir water after 6 ka into Lake Turkana (**Figure 8F**).

The recent dry period after the termination of the AHP, which has left the Chew Bahir basin dry for most of the time, is interrupted by brief excursions to wetter conditions at 3, 2.2, and 1.3 ka BP (**Figure 8A**). Such a lowering of K concentration in the sediments of paleo-lake Chew Bahir points toward a lake transgression and thus a positive water budget during this time. Based on the results of our LBM, we conclude that even though the duration of these events would have allowed a rise of Chew Bahir's paleolake level, it is unlikely that the lake has reached maximum lake depths during these short-term humid episodes. This conclusion is supported by two arguments: (1) We expect a different climatic forcing mechanism than during the AHP, where a precession minimum caused enhanced humidity and the shift of rain belts over the study region (e.g., Costa et al., 2014; Junginger et al., 2014; Bloszies et al., 2015; Beck et al., 2019). For the past ∼5 ka, for example, short-term changes in sea surface temperatures and associated circulation systems could account for these short-term increases in precipitation (e.g., Nicholson, 2017; Bayon et al., 2019). (2) The second argument against maximum water levels in Chew Bahir is that K concentrations do not reach AHP minima. A clear signal whether our assumption, that lake Chew Bahir has not reached its overflow level, is true may only be proved by poxies that could reflect paelo-water provenance, such as strontium isotopes in aquatic fossils, as van der Lubbe et al. (2017) have shown. In summary, paleo-lake Chew Bahir was a large paleo-lake during the AHP that dried up abruptly at least 19 times within decades resulting in a desert-like rift floor similar to today. Such rapid environmental changes must have had a tremendous impact on the biosphere including humans.

Implications for Human Adaptations

A first attempt of comparing an available archaeological record from hypothesized refuge areas in the region with inferred phases of climatic stress from the Chew Bahir K-proxy record was made by Foerster et al. (2015, 2016) for the last 20 ka. The study used scarce but available radiocarbon frequencies of documented archaeological sites in the lush mountainous regions of SW Ethiopia as a possible indicator for changes in settlement activities in the highlands during dry periods in the lowlands, which are indicated by high K content in the drill core sediments of Chew Bahir (note inverse scale, **Figure 8**). Even though age model uncertainties, the indefinite incompleteness and natural biases in the archaeological record naturally constrain the possibility to directly correlate climatic and archaeological data sets (see Foerster et al., 2015, 2016) and references therein), the patterns found in the comparative study are a valuable starting point to indirectly infer shifts in human settlement activity, bearing the role of external factors in mind. The results tentatively suggest that both, long and short-term climatic change could have affected settlement patterns and cultural innovation differently, though the factor of human decision-making within environmental boundaries played an important but further incalculable role (Foerster et al., 2015).

On the one hand, short-term episodes of pronounced aridity in the lower elevated lake basins, such as Chew Bahir could have been a push-factor for a refugium-directed vertical movement of groups with highly mobile hunter-gatherers (**Figure 8C**). A now further specified variable is the climatic component in this comparison as shown in our study. The Southern Ethiopian Rift has responded sensitively to even shorter dry spells, so that living conditions would have deteriorated quickly when the rift floor became too dry. One of the reasons why hunter-gatherers might have returned to the South Ethiopian Rift region after such dry spells, could have been their dietary style at that time, that was mainly devoted to fishing (e.g., Owen et al., 1982; Hildebrand et al., 2018). The long-term transitions, on the other hand, driven by changes in orbital controlled insolation, could have fueled cultural adaptation and significant changes in the social organization within groups. Only after the gradual end of the AHP with the near-desiccation of almost all lakes in the Kenyan and Ethiopian rift over a longer period (>1,000 years), a cultural transition from hunter-gathering to pastoralism occurred (e.g., Marshall and Hildebrand, 2002; Garcin et al., 2012; Lesur et al., 2014). The change from fishing to herding seems to have been a dynamic process, since the introduction of cattle was catalyzed by the immigration of herders that were escaping the progressively drying Sahara region, where pastoralism had been introduced much earlier (e.g., Kuper and Kröpelin, 2006; Hildebrand and Grillo, 2012). The dried up lake beds and former lake margins could have provided new land and grazing grounds for this new life style, which also made people independent from fishing (e.g., Garcin et al., 2012).

Trauth et al. (2010) introduced the theoretical concept of allopatric speciation through precession forced long-term (>10,000 years) population separation and remixing within the EARS due to appearing and disappearing rift lakes. Based on our study results, the Chew Bahir, Abaya, and Chamo basins can be excluded from this concept, due to their extreme sensitive amplifier lake characteristics. We expect, from a modeling perspective, that these lakes reacted on much shorter time scales (<100 a), suggesting that intensive adaption was required from humans living at the lakes margins (cultural buffering; Galway-Witham et al., 2019). One of those adaptive strategies could have been short-term migration, either vertically to the nearby more humid higher elevated grounds (Foerster et al., 2015; Ossendorf et al., 2019) or longitudinally and latitudinally to lake or river refugia that were not affected by the dry spells. Both would have contributed to a periodic cultural and genetic exchange, which is thought to be one of the key drivers in cultural innovation and, on longer time scales, evolution (Lahr and Foley, 1998;

Scerri et al., 2018; Galway-Witham et al., 2019), with innovations being generally favored by the exchange of cultural information (Ackermann et al., 2016).

CONCLUSION

We developed a comprehensive Lake Balance Model (LBM) for the southern Ethiopian rift with focus on paleo-lake Chew Bahir and its catchment as a first contribution to better understand the potential response of paleo-lake Chew Bahir to precipitation changes. We conclude that the following paleo-precipitation estimates would have been necessary to fill paleo-lake Chew Bahir until its overflow level: (1) the classic LBM approach resulted in a 6.5% (TS) precipitation increase, (2) the addition of a third rainy season in the region from July to September would cause a 6.9% (TS_{CAB}) increase, leading to a total of $TS+TS_{CAB} = 13.4\%$. (3) The inclusion of vegetation feedback of +7–15%, resulted in an additional precipitation, which sums up to a robust estimate of ∼20–30% increased precipitation compared to the modern day amount for the paleo-lake Chew Bahir during the African Humid Period. We furthermore determined the amplifier lake characteristics of Lakes Abaya (HI = 0.25, AI = 1.72), Chamo (HI = 0.15, AI = 1.33) and Chew Bahir (HI = 0.23, AI = 0.83). We found that the sensitivity of lake levels is greatly increased during periods of high humidity due to overflowing lakes along the EARS axis and enhanced surface flow. Such additional water resources should be taken into account in the analysis of the paleo-hydrology of other lakes in the EARS when abrupt or gradual changes in the proxies are observed. Accordingly, we implemented all additional factors in our new LBM and were able to calculate lake level response times to abrupt and gradual precipitation changes and characterize lake level changes from K-proxy changes in a drill core from Chew Bahir. Based on our LBM results, we can now support the proposed abruptness of the onset of the AHP in southern Ethiopia by Trauth et al. (2018), similar to the beginning and end of the millennial-scale dry episode during the Younger Dryas. The results of our LBM furthermore support the gradual termination of the AHP, with the model indicating that the reported 20–80 years lasting dry events that are punctuating the termination could have been able to dry up the paleo-lake completely, when caused by abrupt precipitation changes.

DATA AVAILABILITY STATEMENT

The hydro-balance model coded in R is available at GitHub (https://github.com/MLFischer/Lake-Balance-Model, 03/2019).

AUTHOR CONTRIBUTIONS

This study was designed and financed by AJ and MF. MF developed and performed the final LBM. MM, FB, VF, MT, and AJ contributed the data and analysis tools. All authors contributed to the article and approved the submitted version.

FUNDING

The research has been funded by the Ministry of Culture and Science (MWK) of Baden Württemberg, Germany, the Stiftung der deutschen Wirtschaft and the Open Access Publishing Fund of the University of Tübingen.

ACKNOWLEDGMENTS

This study was conducted as part of the project Wet Feet or Walking on Sunshine of AJ funded by the Ministry of Culture and Science (MWK) of Baden Württemberg, Germany and by Stiftung der deutschen Wirtschaft financing the doctoral project of MF. We thank the three reviewers for their helpful comments, which improved the quality of this manuscript. We also acknowledge support by the Open Access Publishing Fund of the University of Tübingen. We thank Bodo Bookhagen from the University of Potsdam for his advises in using MODIS data. We were also grateful for valuable insights from long-term field experience in southern Ethiopia given by Frank Schäbitz from the University of Cologne and Henry Lamb from the University of Aberystwyth. Walter Düsing (University of Potsdam) and Fabian Sittaro (University of Leipzig): thank you for your inspiring discussions about paleo-data analysis, hydro-balance models, vegetation models, and life.

REFERENCES

Ackermann, R. R., Mackay, A., and Arnold, M. L. (2016). The hybrid origin of "modern" humans. *Evol. Biol.* 43, 1–11. doi: 10.1007/s11692-015-9348-1

Allen, R. G., Tasumi, M., Morse, A., Trezza, R., Wright, J. L., Bastiaanssen, W., et al. (2007). Satellite-based energy balance for mapping evapotranspiration with internalized calibration (METRIC)—applications. *J. Irrig. Drainage Eng.* 133, 395–406. doi: 10.1061/(ASCE)0733-9437(2007)133:4(395)

Asrat, A., Baker, A., Mohammed, M. U., Leng, M. J., Calsteren, P. V., and Smith, C. (2007). A high-resolution multi-proxy stalagmite record from Mechara, Southeastern Ethiopia: palaeohydrological implications for speleothem palaeoclimate reconstruction. *J. Quat. Sci.* 22, 53–63. doi: 10.1002/jqs.1013

Awulachew, S. B. (2006). Investigation of physical and bathymetric characteristics of Lakes Abaya and chamo, Ethiopia, and their management implications. *Lakes Reserv. Res. Manag.* 11, 133–140. doi: 10.1111/j.1440-1770.2006.00300.x

Bachofer, F., Quénéhervé, G., Maerker, M., and Hochschild, V. (2015). Comparison of SVM and boosted regression trees for the delineation of lacustrine sediments using multispectral ASTER data and topographic indices in the Lake Manyara basin. *Photogrammetrie-Fernerkundung-Geoinformation* 2015, 81–94. doi: 10.1127/pfg/2015/0251

Baker, A., Asrat, A., Fairchild, I. J., Leng, M. J., Thomas, L., Widmann, M., et al. (2010). Decadal-scale rainfall variability in Ethiopia recorded in an annually laminated, holocene-age, stalagmite. *Holocene* 20, 827–836. doi: 10.1177/0959683610365934

Barker, P. A., Talbot, M. R., Street-Perrott, F. A., Marret, F., Scourse, J., Odada, E. O. (2004). "Late Quaternary climatic variability in intertropical Africa," in *Past Climate Variability through Europe and Africa, Developments in Paleoenvironmental Research*, vol. 6. eds R. W. Battarbee, F. Gasse, C. E. Stickley (Dordrecht: Springer), 117–138. doi: 10.1007/978-1-4020-2121-3_7

Bastiaanssen, W. G. (2000). SEBAL-based sensible and latent heat fluxes in the irrigated Gediz Basin, Turkey. *J. Hydrol.* 229, 87–100. doi: 10.1016/S0022-1694(99)00202-4

Bastiaanssen, W. G., Menenti, M., Feddes, R. A., and Holtslag, A. A. M. (1998a). A remote sensing surface energy balance algorithm for land (SEBAL). 1. Formulation. *J. Hydrol.* 212, 198–212. doi: 10.1016/S0022-1694(98)00253-4

Bastiaanssen, W. G., Pelgrum, H., Wang, J., Ma, Y., Moreno, J. F., Roerink, G. J., et al. (1998b). A remote sensing surface energy balance algorithm for land (SEBAL).: Part 2: validation. *J. Hydrol.* 212, 213–229. doi: 10.1016/S0022-1694(98)00254-6

Bastiaanssen, W. G. M., Noordman, E. J. M., Pelgrum, H., Davids, G., Thoreson, B. P., and Allen, R. G. (2005). SEBAL model with remotely sensed data to improve water-resources management under actual field conditions. *J. Irrig. Drainage Eng.* 131, 85–93. doi: 10.1061/(ASCE)0733-9437(2005)131:1(85)

Bayon, G., Schefuß, E., Dupont, L., Borges, A. V., Dennielou, B., Lambert, T., et al. (2019). The roles of climate and human land-use in the late Holocene rainforest crisis of Central Africa. *Earth Planet. Sci. Lett.* 505, 30–41. doi: 10.1016/j.epsl.2018.10.016

Beck, C. C., Feibel, C. S., Wright, J. D., and Mortlock, R. A. (2019). Onset of the African humid period by 13.9 kyr BP at kabua gorge, turkana Basin, Kenya. *Holocene* 29, 1011–1019. doi: 10.1177/0959683619831415

Belete, A. (2009). *Climate change impact on lake abaya water level* (M.Sc. thesis), Addis Ababa University, Ethiopia. Available online at: http://etd.aau.edu.~et/dspace/bitstream/123456789/2635/1/177302481896682308384642126172115638 06

Berger, A., and Loutre, M. F. (1991). Insolation values for the climate of the last 10 million years. *Quat. Sci. Rev.* 10, 297–317. doi: 10.1016/0277-3791(91)90033-Q

Bergner, A. G., Trauth, M. H., and Bookhagen, B. (2003). Paleoprecipitation estimates for the Lake Naivasha basin (Kenya) during the last 175 ky using a lake-balance model. *Global Planet Change.* 36, 117–136. doi: 10.1016/S0921-8181(02)00178-9

Berke, M. A., Johnson, T. C., Werne, J. P., Grice, K., Schouten, S., and Damsté, J. S. S. (2012b). Molecular records of climate variability and vegetation response since the late pleistocene in the lake victoria basin, East Africa. *Quat. Sci. Rev.* 55, 59–74. doi: 10.1016/j.quascirev.2012.08.014

Berke, M. A., Johnson, T. C., Werne, J. P., Schouten, S., and Damsté, J. S. S. (2012a). A mid-Holocene thermal maximum at the end of the African Humid Period. *Earth Planet. Sci. Lett.* 351–352, 95–104. doi: 10.1016/j.epsl.2012.07.008

Blodgett, T. A., Isacks, B. L., and Lenters, J. D. (1997). Constraints on the origin of paleolake expansions in the central andes. *Earth Interact.* 1, 1–28.doi: 10.1175/1087-3562(1997)001<0001:COTOOP>2.3.CO;2

Bloszies, C., Forman, S. L., and Wright, D. K. (2015). Water level history for lake turkana, Kenya in the past 15,000 years and a variable transition from the African humid period to holocene aridity. *Glob. Planet. Change* 132, 64–76. doi: 10.1016/j.gloplacha.2015.06.006

Bookhagen, B. (in review). *High resolution spatiotemporal distribution of rainfall seasonality and extreme events based on a 12-year TRMM time series, in review. [Data set]* Available online at: http://www.geog.ucsb.edu/~bodo/TRMM/ (accessed Agust 1, 2018).

Bookhagen, B., Haselton, K., and Trauth, M. H. (2001). Hydrological modelling of a pleistocene landslide-dammed lake in the santa maria basin, NW Argentina. *Palaeogeogr. Palaeoclimatol. Palaeoecol.* 169, 113–127. doi: 10.1016/S0031-0182(01)00221-8

Borchardt, S., and Trauth, M. H. (2012). Remotely-sensed evapotranspiration estimates for an improved hydrological modeling of the early holocene mega-lake suguta, northern Kenya Rift. *Palaeogeogr. Palaeoclimatol. Palaeoecol.* 361, 14–20. doi: 10.1016/j.palaeo.2012.07.009

Brooks, N. (2006). Cultural responses to aridity in the middle holocene and increased social complexity. *Quat. Int.* 151, 29–49. doi: 10.1016/j.quaint.2006.01.013

Brutsaert, W. (1982). *Evaporation Into the Atmosphere: Theory, History, and Applications*. Dordrecht: Reidel.

Camberlin, P. (1997). Rainfall anomalies in the source region of the Nile and their connection with the Indian summer monsoon. *J. Clim.* 10, 1380–1392. doi: 10.1175/1520-0442(1997)010<1380:RAITSR>2.0.CO;2

Chalié, F., and Gasse, F. (2002). Late glacial–holocene diatom record of water chemistry and lake level change from the tropical east african rift lake abiyata (Ethiopia). *Palaeogeogr. Palaeoclimatol. Palaeoecol.* 187, 259–283. doi: 10.1016/S0031-0182(02)00480-7

Chernet, T. (1993). *Hydrogeology of Ethiopia and Water Resources Development*. Addis Ababa: EIGS.

Claussen, M., Dallmeyer, A., and Bader, J. (2017). "Theory and modeling of the African humid period and the green Sahara," in *Oxford Research Encyclopedia of Climate Science*. doi: 10.1093/acrefore/9780190228620.013.532

Collins, J. A., Prange, M., Caley, T., Gimeno, L., Beckmann, B., Mulitza, S., et al. (2017). Rapid termination of the african humid period triggered by northern high-latitude cooling. *Nat. Commun.* 8:1372. doi: 10.1038/s41467-017-01454-y

Costa, K., Russell, J., Konecky, B., and Lamb, H. (2014). Isotopic reconstruction of the african humid period and congo air boundary migration at lake tana, Ethiopia. *Quat. Sci. Rev.* 83, 58–67. doi: 10.1016/j.quascirev.2013.10.031

Damsté, J. S. S., Ossebaar, J., Schouten, S., and Verschuren, D. (2012). Distribution of tetraether lipids in the 25-ka sedimentary record of Lake Challa: extracting reliable TEX86 and MBT/CBT palaeotemperatures from an equatorial African lake. *Quat. Sci. Rev.* 50, 43–54. doi: 10.1016/j.quascirev.2012.07.001

Davidson, A. (1983). The Omo river project, reconnaissance geology and geochemistry of parts of Ilubabor, kefa, gemu gofa and sidamo, Ethiopia. *Ethiop. Inst. Geol. Surv. Bull.* 2, 1–89.

De Bruin, H. A. R., and Stricker, J. N. M. (2000). Evaporation of grass under non-restricted soil moisture conditions. *Hydrol. Sci. J.* 45, 391–406. doi: 10.1080/02626660009492337

Dee, S. G., Russell, J. M., Morrill, C., Chen, Z., and Neary, A. (2018). PRYSM v2.0: a proxy system model for lacustrine archives. *Paleoceanogr. Paleoclimatol.* 33, 1250–1269. doi: 10.1029/2018PA003413

deMenocal, P., Ortiz, J., Guilderson, T., Adkins, J., Sarnthein, M., Baker, L., et al. (2000). Abrupt onset and termination of the African Humid Period: rapid climate responses to gradual insolation forcing. *Quat. Sci. Rev.* 19, 347–361. doi: 10.1016/S0277-3791(99)00081-5

demenocal, P. B. (1995). Plio-pleistocene African climate. *Science* 270, 53–59. doi: 10.1126/science.270.5233.53

Didan, K. (2015). *MOD13Q1 MODIS/Terra Vegetation Indices 16-Day L3 Global 250m SIN Grid V006 [Data set].* NASA EOSDIS Land Processes DAAC. Available online at: https://doi.org/10.5067/MODIS/MOD13Q1.006 (accessed August 1, 2018).

Drake, N. A., Breeze, P., and Parker, A. (2013). Palaeoclimate in the saharan and arabian deserts during the middle palaeolithic and the potential for hominin dispersals. *Quat. Int.* 300, 48–61. doi: 10.1016/j.quaint.2012.12.018

Dühnforth, M., Bergner, A. G., and Trauth, M. H. (2006). Early holocene water budget of the nakuru-elmenteita basin, central Kenya Rift. *J. Paleolimnol.* 36, 281–294. doi: 10.1007/s10933-006-9003-z

Ebinger, C. J., Yemane, T., Woldegabriel, G., Aronson, J. L., and Walter, R. C. (1993). Late eocene–recent volcanism and faulting in the southern main Ethiopian rift. *J. Geol. Soc.* 150, 99–108. doi: 10.1144/gsjgs.150.1.0099

Evans, M. N., Tolwinski-Ward, S. E., Thompson, D. M., and Anchukaitis, K. J. (2013). Applications of proxy system modeling in high resolution paleoclimatology. *Quat. Sci. Rev.* 76, 16–28. doi: 10.1016/j.quascirev.2013.05.024

Fleitmann, D., Burns, S. J., Mudelsee, M., Neff, U., Kramers, J., Mangini, A., et al. (2003). Holocene forcing of the Indian monsoon recorded in a stalagmite from southern Oman. *science* 300, 1737–1739. doi: 10.1126/science.1083130

Foerster, V., Deocampo, D. M., Asrat, A., Günter, C., Junginger, A., Krämer, K. H., et al. (2018). Towards an understanding of climate proxy formation in the chew bahir basin, southern Ethiopian Rift. *Palaeogeogr. Palaeoclimatol. Palaeoecol.* 501, 111–123. doi: 10.1016/j.palaeo.2018.04.009

Foerster, V., Junginger, A., Langkamp, O., Gebru, T., Asrat, A., Umer, M., et al. (2012). Climatic change recorded in the sediments of the chew bahir basin, southern Ethiopia, during the last 45,000 years. *Quat. Int.* 274, 25–37. doi: 10.1016/j.quaint.2012.06.028

Foerster, V., Vogelsang, R., Junginger, A., Asrat, A., Lamb, H. F., Schaebitz, F., et al. (2015). Environmental change and human occupation of southern Ethiopia and northern Kenya during the last 20,000 years. *Quat. Sci. Rev.* 129, 333–340. doi: 10.1016/j.quascirev.2015.10.026

Foerster, V., Vogelsang, R., Junginger, A., Asrat, A., Lamb, H. F., Schaebitz, F., et al. (2016). Reply to the comment on "Environmental change and human occupation of southern Ethiopia and northern Kenya during the last 20,000 years. Quaternary Science Reviews 129: 333-340". *Quat. Sci. Revi.* 141, 130–133. doi: 10.1016/j.quascirev.2016.04.003

Friedl, M. A., Sulla-Menashe, D., Tan, B., Schneider, A., Ramankutty, N., Sibley, A., et al. (2010). MODIS Collection 5 global land cover: algorithm refinements and characterization of new datasets. *Remote Sens. Environ.* 114, 168–182. doi: 10.1016/j.rse.2009.08.016

Friis, I., Demissew, S., and Breugel, P. V. (2010). Atlas of the potential vegetation of Ethiopia. *Biol. Skrif.* 58, 1–307. doi: 10.1093/aob/mcq242

Funk, C., Dettinger, M. D., Michaelsen, J. C., Verdin, J. P., Brown, M. E., Barlow, M., et al. (2008). Warming of the Indian ocean threatens eastern and southern african food security but could be mitigated by agricultural development. *Proc. Natl. Acad. Sci. U.S.A.* 105, 11081–11086. doi: 10.1073/pnas.0708196105

Galway-Witham, J., Cole, J., and Stringer, C. (2019). Aspects of human physical and behavioural evolution during the last 1 million years. *J. Quat. Sci.* 34, 355–378. doi: 10.1002/jqs.3137

Garcin, Y., Junginger, A., Melnick, D., Olago, D. O., Strecker, M. R., and Trauth, M. H. (2009). Late pleistocene–holocene rise and collapse of lake suguta, northern Kenya Rift. *Quat. Sci. Rev.* 28, 911–925. doi: 10.1016/j.quascirev.2008.12.006

Garcin, Y., Melnick, D., Strecker, M. R., Olago, D., and Tiercelin, J. J. (2012). East African mid-holocene wet–dry transition recorded in palaeo-shorelines of lake turkana, northern Kenya Rift. *Earth Planet. Sci. Lett.* 331, 322–334. doi: 10.1016/j.epsl.2012.03.016

Gasse, E., and Street, F. A. (1978). Late Quaternary lake-level fluctuations and environments of the northern Rift Valley and Afar region (Ethiopia and Djibouti). *Palaeogeogr. Palaeoclimatol. Palaeoecol.* 24, 279–325. doi: 10.1016/0031-0182(78)90011-1

Gillespie, R., Street-Perrott, F. A., and Switsur, R. (1983). Post-glacial arid episodes in Ethiopia have implications for climate prediction. *Nature* 306:680. doi: 10.1038/306680a0

Gupta, A. K., Anderson, D. M., and Overpeck, J. T. (2003). Abrupt changes in the Asian southwest monsoon during the Holocene and their links to the North Atlantic Ocean. *Nature* 421:354. doi: 10.1038/nature01340

Hastenrath, S., and Kutzbach, J. E. (1983). Paleoclimatic estimates from water and energy budgets of East African lakes. *Quat. Res.* 19, 141–153. doi: 10.1016/0033-5894(83)90001-7

Hildebrand, E. A., and Grillo, K. M. (2012). Early herders and monumental sites in eastern Africa: dating and interpretation. *Antiquity* 86, 338–352. doi: 10.1017/S0003598X00062803

Hildebrand, E. A., Grillo, K. M., Sawchuk, E. A., Pfeiffer, S. K., Conyers, L. B., Goldstein, S. T., et al. (2018). A monumental cemetery built by eastern Africa's first herders near Lake Turkana, Kenya. *Proc. Natl. Acad. Sci. U.S.A.* 115, 8942–8947. doi: 10.1073/pnas.1721975115

Honegger, M., and Williams, M. (2015). Human occupations and environmental changes in the Nile valley during the holocene: the case of kerma in upper nubia (northern Sudan). *Quat. Sci. Rev.* 130, 141–154. doi: 10.1016/j.quascirev.2015.06.031

Junginger, A. (2011). *East African climate variability on different time scales: the Suguta Valley in the African-Asian Monsoon Domain* (Doctoral dissertation), University of Potsdam, Germany.

Junginger, A., Roller, S., Olaka, L. A., and Trauth, M. H. (2014). The effects of solar irradiation changes on the migration of the congo air boundary and water levels of paleo-lake suguta, northern Kenya Rift, during the African humid period (15–5 ka BP). *Palaeogeogr. Palaeoclimatol. Palaeoecol.* 396, 1–16. doi: 10.1016/j.palaeo.2013.12.007

Junginger, A., and Trauth, M. H. (2013). Hydrological constraints of paleo-lake suguta in the northern kenya rift during the African humid period (15–5 ka BP). *Glob. Planet. Change* 111, 174–188. doi: 10.1016/j.gloplacha.2013.09.005

Kassa, T. G. (2015). *Holocene Environmental History of Lake Chamo, South Ethiopia* (Doctoral dissertation), University of Cologne, Germany.

Kebede, S., and Travi, Y. (2012). Origin of the δ18O and δ2H composition of meteoric waters in Ethiopia. *Quat. Int.* 257, 4–12. doi: 10.1016/j.quaint.2011.09.032

Kiptala, J. K., Mohamed, Y., Mul, M. L., and Van der Zaag, P. (2013). Mapping evapotranspiration trends using MODIS and SEBAL model in a data scarce and heterogeneous landscape in Eastern Africa. *Water Resour. Res.* 49, 8495–8510. doi: 10.1002/2013WR014240

Kirkby, M. J., and Beven, K. J. (1979). A physically based, variable contributing area model of basin hydrology. *Hydrol. Sci. J.* 24, 43–69. doi: 10.1080/02626667909491834

Kniess, U. (2006). *Hydrologische Modellierung im Zentralen Kenya-Rift* (Unpublished Diploma thesis), University of Potsdam, Germany.

Kuper, R., and Kröpelin, S. (2006). Climate-controlled Holocene occupation in the Sahara: motor of Africa's evolution. *Science* 313, 803–807. doi: 10.1126/science.1130989

Lahr, M., and Foley, R. A. (1998). Towards a theory of modern human origins: geography, demography, and diversity in recent human evolution. *Am. J. Phys. Anthropol.* 107, 137–176. doi: 10.1002/(SICI)1096-8644(1998)107:27+<137::AID-AJPA6>3.0.CO;2-Q

Lamb, A. L., Leng, M. J., Lamb, H. F., and Mohammed, M. U. (2000). A 9000-year oxygen and carbon isotope record of hydrological change in a small Ethiopian crater lake. *Holocene* 10, 167–177. doi: 10.1191/095968300677444611

Lamb, A. L., Leng, M. J., Mohammed, M. U., and Lamb, H. F. (2004). Holocene climate and vegetation change in the main ethiopian rift valley, inferred from the composition (C/N and δ13C) of lacustrine organic matter. *Quat. Sci. Rev.* 23, 881–891. doi: 10.1016/j.quascirev.2003.06.010

Lamb, P. J., Bell, M. A., and Finch, J. D. (1998). "Varibility of Sahelian disturbance lines and rainfall during 1951-87," in *Water Resources Variability in Africa during XXth Century*, eds E. Servat et al. (IAHS), 19–26.

Lario, J., Sanchez-Moral, S., Fernandez, V., Jimeno, A., and Menendez, M. (1997). Palaeoenvironmental evolution of the blue Nile (Central Sudan) during the early and mid-holocene (Mesolithic-Neolithic transition). *Quat. Sci. Rev.* 16, 583–588. doi: 10.1016/S0277-3791(96)00053-4

Larrasoaña, J. C., Roberts, A. P., and Rohling, E. J. (2013). Dynamics of green Sahara periods and their role in hominin evolution. *PLoS ONE* 8:e76514. doi: 10.1371/journal.pone.0076514

Lenters, J. D., and Cook, K. H. (1999). Summertime precipitation variability over South America: Role of the large-scale circulation. *Monthly Weather Rev.* 127, 409–431. doi: 10.1175/1520-0493(1999)127<0409:SPVOSA>2.0.CO;2

Lesur, J., Hildebrand, E. A., Abawa, G., and Gutherz, X. (2014). The advent of herding in the horn of africa: new data from Ethiopia, Djibouti and Somaliland. *Quat. Int.* 343, 148–158. doi: 10.1016/j.quaint.2013.11.024

Levin, N. E., Zipser, E. J., and Cerling, T. E. (2009). Isotopic composition of waters from Ethiopia and Kenya: insights into moisture sources for eastern Africa. *J. Geophys. Res. Atmospheres.* 114:D23. doi: 10.1029/2009JD012166

Liu, C., Ikeda, K., Rasmussen, R., Barlage, M., Newman, A. J., Prein, A. F., et al. (2017). Continental-scale convection-permitting modeling of the current and future climate of North America. *Clim. Dynam.* 49, 71–95. doi: 10.1007/s00382-016-3327-9

Loomis, S. E., Russell, J. M., Eggermont, H., Verschuren, D., and Damsté, J. S. S. (2014). Effects of temperature, pH and nutrient concentration on branched GDGT distributions in East African lakes: Implications for paleoenvironmental reconstruction. *Org. Geochem.* 66, 25–37. doi: 10.1016/j.orggeochem.2013.10.012

Loomis, S. E., Russell, J. M., Ladd, B., Street-Perrott, F. A., and Damsté, J. S. S. (2012). Calibration and application of the branched GDGT temperature proxy on East African lake sediments. *Earth Planet. Sci. Lett.* 357, 277–288. doi: 10.1016/j.epsl.2012.09.031

Loomis, S. E., Russell, J. M., and Lamb, H. F. (2015). Northeast African temperature variability since the Late Pleistocene. *Palaeogeogr. Palaeoclimatol. Palaeoecol.* 423, 80–90. doi: 10.1016/j.palaeo.2015.02.005

Losgedaragh, S. Z., and Rahimzadegan, M. (2018). Evaluation of SEBS, SEBAL, and METRIC models in estimation of the evaporation from the freshwater lakes (Case study: Amirkabir dam, Iran). *J. Hydrol.* 561, 523–531. doi: 10.1016/j.jhydrol.2018.04.025

Manning, K., and Timpson, A. (2014). The demographic response to Holocene climate change in the Sahara. *Quat. Sci. Rev.* 101, 28–35. doi: 10.1016/j.quascirev.2014.07.003

Marchant, R., Richer, S., Boles, O., Capitani, C., Courtney-Mustaphi, C. J., Lane, P., et al. (2018). Drivers and trajectories of land cover change in East Africa: Human and environmental interactions from 6000 years ago to present. *Earth Sci. Rev.* 178, 322–378. doi: 10.1016/j.earscirev.2017.12.010

Marshall, F., and Hildebrand, E. (2002). Cattle before crops: the beginnings of food production in Africa. *J. World Prehistory* 16, 99–143. doi: 10.1023/A:1019954903395

Marshall, M. H., Lamb, H. F., Davies, S. J., Leng, M. J., Kubsa, Z., Umer, M., et al. (2009). Climatic change in northern Ethiopia during the past 17,000 years: a diatom and stable isotope record from Lake Ashenge. *Palaeogeogr. Palaeoclimatol. Palaeoecol.* 279, 114–127. doi: 10.1016/j.palaeo.2009.05.003

Merwade, V. (2012). *Watershed and Stream Network DelineationUsing Arc Hydro Tools.* Available online at: https://web.ics.purdue.edu/~vmerwade/education/terrain_processing.pdf (accessed August 2018).

Mkhwanazi, M., Chavez, J. L., and Andales, A. A. (2015). SEBAL-A: A remote sensing ET algorithm that accounts for advection with limited data. Part I: Development and validation. *Remote Sens.* 7, 15046–15067. doi: 10.3390/rs71115046

New, M., Lister, D., Hulme, M., and Makin, I. (2002). A high-resolution data set of surface climate over global land areas. *Clim. Res.* 21, 1–25. doi: 10.3354/cr021001

Nicholson, S. E. (1996). A review of climate dynamics and climate variability in Eastern Africa. *Limnol. Climatol. Paleoclimatol.* 25–56. doi: 10.1201/9780203748978-2

Nicholson, S. E. (2000). The nature of rainfall variability over Africa on time scales of decades to millenia. *Glob. Planet. Change* 26, 137–158. doi: 10.1016/S0921-8181(00)00040-0

Nicholson, S. E. (2017). Climate and climatic variability of rainfall over eastern Africa. *Rev. Geophys.* 55, 590–635. doi: 10.1002/2016RG000544

Olaka, L. A. (2011). *Hydrology across scales: sensitivity of East African lakes to climate changes* (Doctoral dissertation), Universität Potsdam, Germany.

Olaka, L. A., Odada, E. O., Trauth, M. H., and Olago, D. O. (2010). The sensitivity of East African rift lakes to climate fluctuations. *J. Paleolimnol.* 44, 629–644. doi: 10.1007/s10933-010-9442-4

Ossendorf, G., Groos, A. R., Bromm, T., Tekelemariam, M. G., Glaser, B., Lesur, J., et al. (2019). Middle stone age foragers resided in high elevations of the glaciated bale mountains, Ethiopia. *Science* 365, 583–587. doi: 10.1126/science.aaw8942

Owen, R. B., Barthelme, J. W., Renaut, R. W., and Vincens, A. (1982). Palaeolimnology and archaeology of holocene deposits north-east of lake turkana, Kenya. *Nature* 298:523. doi: 10.1038/298523a0

Pike, R. J., and Wilson, S. E. (1971). Elevation-relief ratio, hypsometric integral, and geomorphic area-altitude analysis. *Geol. Soc. Am. Bull.* 82, 1079–1084. doi: 10.1130/0016-7606(1971)821079:ERHIAG2.0.CO;2

Platnick, S., Ackerman, S. A., King, M. D., Meyer, K., Menzel, W. P., Holz, R. E., et al. (2015). *MODIS atmosphere L2 cloud product (06_L2), NASA MODIS Adaptive Processing System*. Goddard Space Flight Center. doi: 10.5067/MODIS/MYD06_L2.006

R Core Team (2019). *R: A Language and Environment for Statistical Computing*. Vienna: R Foundation for Statistical Computing. Available online at: http://www.R-project.org/

Renssen, H., Brovkin, V., Fichefet, T., and Goosse, H. (2006). Simulation of the holocene climate evolution in northern Africa: the termination of the African humid period. *Quat. Int.* 150, 95–102. doi: 10.1016/j.quaint.2005.01.001

Revel, M., Colin, C., Bernasconi, S., Combourieu-Nebout, N., Ducassou, E., Grousset, F. E., et al. (2014). 21,000 Years of Ethiopian African monsoon variability recorded in sediments of the western nile deep-sea fan. *Reg. Environ. Change* 14, 1685–1696. doi: 10.1007/s10113-014-0588-x

Richardson, J. L., and Dussinger, R. A. (1986). Paleolimnology of mid-elevation lakes in the Kenya Rift Valley. *Hydrobiologia* 143, 167–174. doi: 10.1007/BF00026659

Rowell, D. P., Booth, B. B., Nicholson, S. E., and Good, P. (2015). Reconciling past and future rainfall trends over East Africa. *J. Clim.* 28, 9768–9788. doi: 10.1175/JCLI-D-15-0140.1

Rucina, S. M., Muiruri, V. M., Kinyanjui, R. N., McGuiness, K., and Marchant, R. (2009). Late quaternary vegetation and fire dynamics on mount Kenya. *Palaeogeogr. Palaeoclimatol. Palaeoecol.* 283, 1–14. doi: 10.1016/j.palaeo.2009.08.008

Scerri, E. M., Thomas, M. G., Manica, A., Gunz, P., Stock, J. T., Stringer, C., et al. (2018). Did our species evolve in subdivided populations across Africa, and why does it matter? *Trends Ecol. Evol.* 33, 582–594. doi: 10.1016/j.tree.2018.05.005

Segele, Z. T., and Lamb, P. J. (2005). Characterization and variability of Kiremt rainy season over Ethiopia. *Meteorol. Atmospher. Phys.* 89, 153–180. doi: 10.1007/s00703-005-0127-x

Street-Perrott, F. A., Harrison, S. P. (1985). "Lake levels and climate reconstruction," in *Paleoclimate Analysis and Modeling*, ed A. D. Hecht (New York, NY: John Wiley), 291–340.

Telford, R. J., and Lamb, H. F. (1999). Groundwater-mediated response to Holocene climatic change recorded by the diatom stratigraphy of an Ethiopian crater lake. *Quat. Res.* 52, 63–75. doi: 10.1006/qres.1999.2034

Thompson, L. G., Mosley-Thompson, E., Davis, M. E., Henderson, K. A., Brecher, H. H., Zagorodnov, V. S., et al. (2002). Kilimanjaro ice core records: evidence of holocene climate change in tropical Africa. *Science* 298, 589–593. doi: 10.1126/science.1073198

Thornthwaite, C. W. (1948). An approach toward a rational classification of climate. *Geogr. Rev.* 38, 55–94. doi: 10.2307/210739

Thornthwaite, C. W., and Mather, J. R. (1955). *The Water Balance*. Centerton: Drexel Institute of Technology, Laboratory of Climatology.

Tierney, J. E., Smerdon, J. E., Anchukaitis, K. J., and Seager, R. (2013). Multidecadal variability in East African hydroclimate controlled by the Indian Ocean. *Nature* 493:389. doi: 10.1038/nature11785

Tiruneh, A. T. (2005). *Water quality monitoring in lake abaya and lake chamo region* (Doctoral dissertation), University of Siegen, Germany.

Trauth, M. H., Foerster, V., Junginger, A., Asrat, A., Lamb, H. F., and Schaebitz, F. (2018). Abrupt or gradual? Change point analysis of the late pleistocene–holocene climate record from chew bahir, southern Ethiopia. *Quat. Res.* 90, 321–330. doi: 10.1017/qua.2018.30

Trauth, M. H., Maslin, M. A., Deino, A. L., Junginger, A., Lesoloyia, M., Odada, E. O., et al. (2010). Human evolution in a variable environment: the amplifier lakes of Eastern Africa. *Quat. Sci. Rev.* 29, 2981–2988. doi: 10.1016/j.quascirev.2010.07.007

Umer, M., Lamb, H. F., Bonnefille, R., Lézine, A. M., Tiercelin, J. J., Gibert, E., et al. (2007). Late pleistocene and holocene vegetation history of the Bale mountains, Ethiopia. *Quat. Sci. Rev.* 26, 2229–2246. doi: 10.1016/j.quascirev.2007.05.004

van der Lubbe, H. J. L., Krause-Nehring, J., Junginger, A., Garcin, Y., Joordens, J. C. A., Davies, G. R., et al. (2017). Gradual or abrupt? Changes in water source of Lake Turkana (Kenya) during the African Humid Period inferred from Sr isotope ratios. *Quat. Sci. Rev.* 174, 1–12. doi: 10.1016/j.quascirev.2017.08.010

Vermote, E., and Wolfe, R. (2015). "MOD09GA MODIS/terra surface reflectance daily L2G global 1kmand 500m SIN grid V006 [Data set]," in *NASA EOSDIS Land Processes DAAC*. Available online at: https://doi.org/10.5067/MODIS/MOD09GA.006 (accessed January 8, 2020).

Verschuren, D. (2004). "Decadal and century-scale climate variability in tropical Africa during the past 2000 years," in *Past Climate Variability through Europe and Africa. Developments in Paleoenvironmental Research*, vol 6, eds R. W. Battarbee, F. Gasse, C. E. Stickley (Dordrecht: Springer), 139–158. doi: 10.1007/978-1-4020-2121-3_8

Vincens, A., Buchet, G., Williamson, D., and Taieb, M. (2005). A 23,000 yr pollen record from Lake Rukwa (8 S, SW Tanzania): new data on vegetation dynamics and climate in Central Eastern Africa. *Rev. Palaeobot. Palynol.* 137, 147–162. doi: 10.1016/j.revpalbo.2005.06.001

Viste, E. M. (2012). *Moisture transport and precipitation in Ethiopia* (Doctoral dissertation), University of Bergen, Norway.

Wagner, B., Wennrich, V., Viehberg, F., Junginger, A., Kolvenbach, A., Rethemeyer, J., et al. (2018). Holocene rainfall runoff in the central Ethiopian highlands and evolution of the River Nile drainage system as revealed from a sediment record from Lake Dendi. *Glob. Planet. Change* 163, 29–43. doi: 10.1016/j.gloplacha.2018.02.003

Wan, Z., Hook, S., and Hulley, G. (2015). "MOD11A1 MODIS/Terra land surface temperature/emissivity daily L3 global 1km SIN grid V006 [Data set]," in *NASA EOSDIS Land Processes DAAC*. Available online at: https://doi.org/10.5067/MODIS/MOD11A1.006 (accessed January 8, 2020).

Wieringa, J. (1992). Updating the Davenport roughness classification. *J. Wind Eng. Indus. Aerodyn.* 41, 357–368. doi: 10.1016/0167-6105(92)90434-C

Williams, A. P., and Funk, C. (2011). A westward extension of the warm pool leads to a westward extension of the walker circulation, drying eastern Africa. *Clim. Dyn.* 37, 2417–2435. doi: 10.1007/s00382-010-0984-y

Zhang, X. C., Wu, J. W., Wu, H. Y., and Li, Y. (2011). Simplified SEBAL method for estimating vast areal evapotranspiration with MODIS data. *Water Sci. Eng.*4, 24–35. doi: 10.3882/j.issn.1674-2370.2011.01.003

Zielhofer, C., von Suchodoletz, H., Fletcher, W. J., Schneider, B., Dietze, E., Schlegel, M., et al. (2017). Millennial-scale fluctuations in Saharan dust supply across the decline of the African humid period. *Quat. Sci. Rev.* 171, 119–135. doi: 10.1016/j.quascirev.2017.07.010

Conflict of Interest: The authors declare that the research was conducted in the absence of any commercial or financial relationships that could be construed as a potential conflict of interest.

frontiers in Earth Science

ORIGINAL RESEARCH
published: 10 July 2020
doi: 10.3389/feart.2020.00276

Combining Inorganic and Organic Carbon Stable Isotope Signatures in the Schwalbenberg Loess-Palaeosol-Sequence Near Remagen (Middle Rhine Valley, Germany)

Mathias Vinnepand[1], Peter Fischer[1], Kathryn Fitzsimmons[2], Barry Thornton[3], Sabine Fiedler[1] and Andreas Vött[1]*

[1] Institute of Geography, Johannes Gutenberg University Mainz, Mainz, Germany, [2] Research Group for Terrestrial Palaeoclimates, Max Planck Institute for Chemistry, Mainz, Germany, [3] Environmental and Biochemical Sciences Group, The James Hutton Institute, Aberdeen, United Kingdom

OPEN ACCESS

Edited by:
Annett Junginger, University of Tübingen, Germany

Reviewed by:
Andrea Zerboni, University of Milan, Italy
Igor Obreht, RWTH Aachen University, Germany

****Correspondence:***
Mathias Vinnepand
mavinnep@uni-mainz.de

Specialty section:
This article was submitted to Quaternary Science, Geomorphology and Paleoenvironment, a section of the journal Frontiers in Earth Science

Received: *31 March 2020*
Accepted: *17 June 2020*
Published: *10 July 2020*

Citation:
Vinnepand M, Fischer P, Fitzsimmons K, Thornton B, Fiedler S and Vött A (2020) Combining Inorganic and Organic Carbon Stable Isotope Signatures in the Schwalbenberg Loess-Palaeosol-Sequence Near Remagen (Middle Rhine Valley, Germany). Front. Earth Sci. 8:276. doi: 10.3389/feart.2020.00276

Western Central European Loess-Palaeosol-Sequences (LPS) provide valuable terrestrial records of palaeoenvironmental conditions, which formed in response to variability in the North Atlantic climate systems. Over the last full glacial cycle (∼130 ka), climate oscillations within these systems are best documented in deep sea- and ice cores; the responses of terrestrial systems are not yet fully understood. A better understanding of metabolism governing input and output variables of organic- and inorganic C pools is, however, crucial for investigating landscape-atmospheric feedback processes and in particularly, for understanding the formation of calcareous LPS as environmental archives. Here we quantify the contributions of primary carbonates (PC) and secondary carbonates (SC) to the overall inorganic carbon pool down a LPS at the Schwalbenberg site, based on the natural abundance ratio of stable carbon isotopes ($\delta^{13}C$) and contents of the organic- and inorganic C pools. This facilitates detailed insights into the carbonate metabolism and hence, loessification and percolation processes. PC accumulate predominantly in cold phases during periods of reduced biological activity and become leached during wetter and warmer periods contemporary with higher rates of SC re-precipitation and total organic carbon (TOC) increases due to enhanced biomass production. We find that mineral dust input is most significant during stadials, as well as toward the end of warmer interstadials, characterised by gradual cooling back to stadial conditions. Pedogenesis in the Schwalbenberg LPS kept pace with surface accumulation of mineral dust. This indicates that palaeosols are of accretionary nature, which gives raise to the idea of incorporation of former topsoils in preserved subsoil horizons. Our study decodes fundamental aspects of the link between atmospheric dust circulation and terrestrial records in western Central Europe. In addition, interdependencies between factors governing the regional moisture budged and LPS can be reconstructed in a more holistic way than before.

Keywords: Loess-Palaeosol-Sequences, stable isotopes, environmental change, OIS 3, Schwalbenberg LPS

INTRODUCTION

Terrestrial carbon pools respond to changes in climate by trapping or releasing carbon to the atmosphere (Adams and Post, 1999; von Lützow and Kögel-Knabner, 2009). Consequently, total organic carbon (TOC) and total inorganic carbon (TIC) records derived from terrestrial archives can be used for correlations with ice core data along with independent age control (Adams and Post, 1999; Hatté et al., 1999). These correlations, however, pre-require detailed understanding of formation processes of investigated archives against the background of climate and environmental changes affecting terrestrial carbon pools. In context of calcareous western European Loess-Palaeosol-Sequences (LPS), we may quantify processes involved in loess formation under cold (periglacial) climate conditions and those allowing for pedogenesis under warmer interstadial or interglacial conditions. In general, loess is defined as aeolian deposits of predominantly silt-sized mineral dust (Pécsi, 1990), which undergoes syn- and post-depositional modification to produce a characteristic "loess-like-structure"; this process is often referred to as "loessification" (Sprafke and Obreht, 2016). Many processes involved are likely to be pedogenic in nature (Kemp, 2001). In this context, the role of leaching of primary carbonates (PC) and re-precipitation of hydrogenous carbonate ions as secondary carbonates (SC) is under debate (Pécsi, 1990; Sprafke and Obreht, 2016). The quantification of PC and SC, based on the natural abundance ratio of stable carbon isotopes in TIC ($\delta^{13}C_{(TIC)}$), provides a promising tool to gain insight into the role of carbonate metabolism during loess formation and to relate this processes to the palaeoenvironmental conditions prevailing during LPS formation. In particular, this can inform us about past water percolation in loess and palaeosols (cf. Zamanian et al., 2016). Under semi-arid to arid periglacial settings, water supply is a limiting factor for plant growth (Hatté et al., 2001). The first reaction of plants to drought stress is stomatal closure in order to minimise water loss during respiration (Pirasteh-Anosheh et al., 2016), leading to reduced discrimination against heavier ^{13}C isotopes in plants using the C3 photosynthesis pathway (Farquhar et al., 1982; O'Leary, 1988). Consequently, water availability to plants can be estimated if the original isotopic composition of plants is preserved in organic matter (OM) (Hatté et al., 2001), particularly in environments with limited decomposition rates, carbon turnover and root mixing. Based on this, palaeo-precipitation has been inferred from TOC in loess (Hatté et al., 2001). However, since $\delta^{13}C_{(TIC)}$ and $\delta^{13}C_{(TOC)}$ in loess sections are sensitive to water availability being multi-causal, addressing both C pools is most promising to enable more detailed insights into palaeoenvironmental processes. Moreover, differentiation of PC and SC is crucial to set up non-biased weathering indices (Buggle et al., 2011) and to understand the role of PC enriched in mineral dust during LPS formation (Kemp, 2001). In this study, we combine TIC and TOC isotope geochemistry to produce a detailed reconstruction of past dust dynamics, pedogenic processes and surface water availability of plants in light of palaeoclimate and palaeoenvironmental changes. We compare $\delta^{13}C_{(TIC)}$ and $\delta^{13}C_{(TOC)}$ to investigate processes possibly affecting both signals for core REM 3A drilled at the Schwalbenberg site. The 26 m long core reflects palaeoenvironmental conditions during the Last Glacial Cycle (LGC) (∼130 ka) in high resolution. We aim to get detailed insights into the carbonate metabolism of the LPS to estimate the degree of loessification and PC input.

REGIONAL SETTINGS

The Schwalbenberg site is located south of Remagen in the Middle Rhine valley close to the confluence of the rivers Rhine and Ahr (cf. **Figure 1**). During the LGC, thick LPS were formed by accumulation of mineral dust, loessification and pedogenesis above fluvial deposits, so far correlated to the Lower Middle Terrace of the Rhine River (Boenigk and Frechen, 2006; Schirmer, 2012). This fluvial terrace is dedicated to the penultimate glaciation and exhibits an elevation of 79 m a.s.l. (∼ 26 m above the current channel) (Boenigk and Frechen, 2006). At the Schwalbenberg itself, several valleys incised into the plateau-like loess cover. These structures are directed toward the River Rhine and follow a course almost parallel to the River Ahr. A steep slope on the south-eastern fringe of the Schwalbenberg marks the transition from the Lower Middle Terrace to the Weichselian Lower Terraces and the Holocene flood plain. The Schwalbenberg LPS has been the subject of investigations since Bibus (1980) first described the stratigraphy of an outcrop on the southern margin of the hill. At this locality a unique number of brownish palaeosols are visible within the loess sediments. Since soils reflecting interstadial climate conditions as known from Greenland ice cores for the late OIS 3 are largely missing in Central European LPS (cp. Schirmer, 2016) the question arose, whether the soils formed autochthonous or if they were the result of reworking mechanisms (Bibus, 1980). Based on litho- and pedological evidence, complemented by sedimentological, geochemical and micro-morphological proxy-data, Schirmer (2012) and Schirmer et al. (2012) addressed the eight interstadial soils as autochthonous formations being part of an LPS which mirror-pictures the OIS 3 climate succession in terms of frequency and intensity (**Figure 1**). However, chronological control is still lacking. This OIS 3 sequence was subsequently described as the "Ahrgau Subformation" (Schirmer, 2013) comprising eight interstadial soils embedded with loess, reworked loess and Gelic Gleysols. Apart from the analyses mentioned above, a sediment core (REM 1A) has been investigated by Klasen et al. (2015) trying to develop a luminescence chronology approximately 200 m distant to the outcrop (**Figure 1**). Results suggest differences in LPS formation and/or preservation throughout OIS 2 and OIS 4, whereas the sections covering OIS 3 show comparable composition and thickness further upslope. In addition, Klasen et al. (2015) and Profe et al. (2016) conducted geochemical analyses by means of x-ray fluorescence measurements. While Klasen et al. (2015) assumed changing source areas to cause differences in luminescence behaviour, Profe et al. (2016) reconstructed weathering indices and a conceptual model including multiple sediment recycling and sorting effects. In

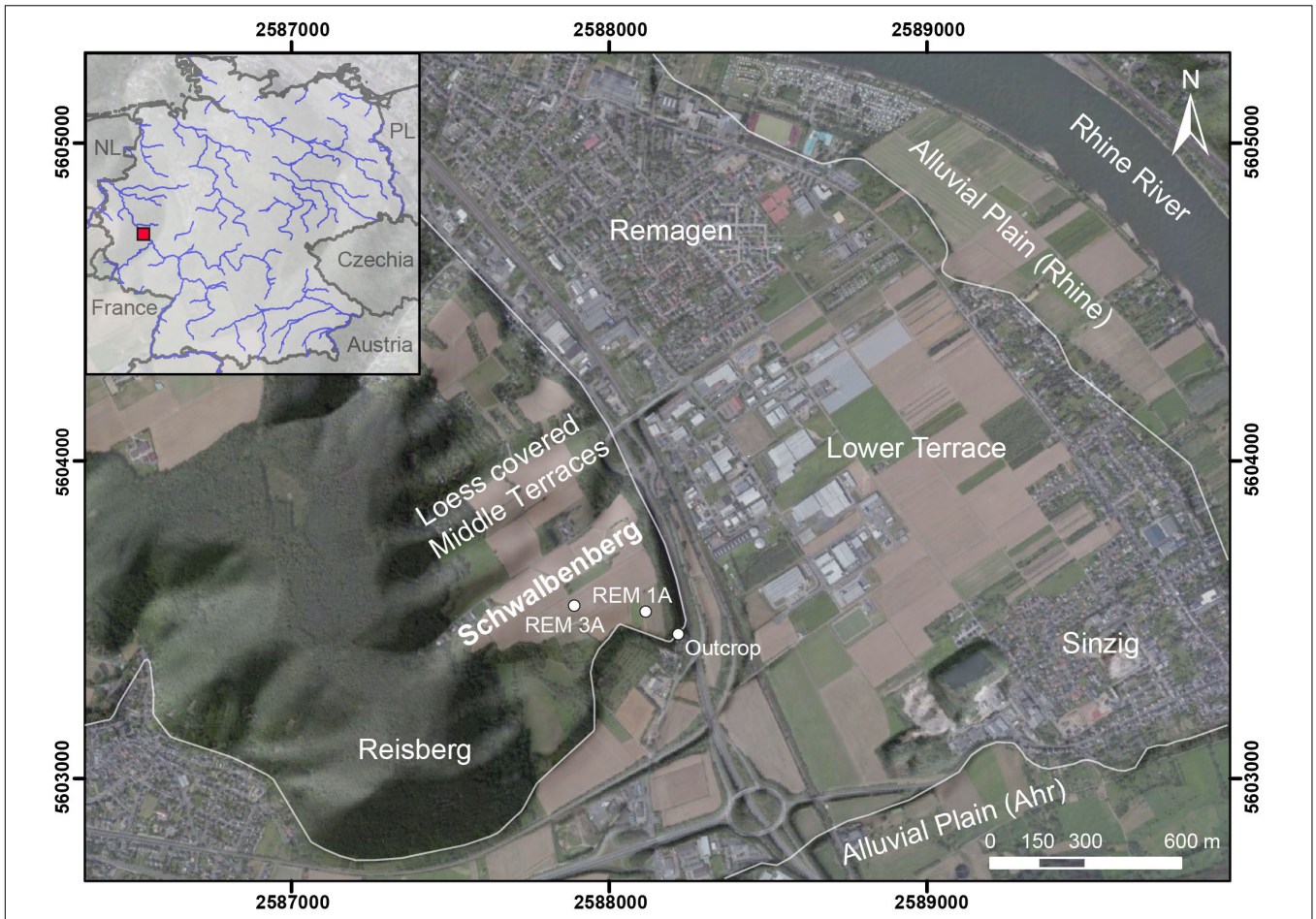

FIGURE 1 | Overview of the Schwalbenberg site in the Lower Middle Rhine Valley, Germany. The plateau-like loess relief developed on top of the Lower Middle Terrace dedicated to the penultimate glaciation (e.g., Boenigk and Frechen, 2006). Schirmer and co-workers (e.g., Schirmer, 2012; Schirmer et al., 2012) formerly investigated a 13 m thick LPS outcrop (white dot). Later on, geochemical investigations (XRF) were performed on samples derived from this outcrop by Profe et al. (2016). Sediment core (REM 1A) was obtained in mid-slope position by Klasen et al. (2015) trying to develop a luminescence chronology. The 26 m thick sediment core under investigation (REM 3A) is located in interfluve position of the Schwalbenberg.

context to this contribution, it is important to notice that Profe et al. (2016) addressed the problems of secondary calcification dynamics when applying certain element ratios. However, stable C isotope investigations have not been performed so far, which will shed new light on the formation of the Schwalbenberg LPS.

THEORETICAL BACKGROUND

During photosynthesis, plants discriminate against the heavier ^{13}C due to its lower reactivity compared to ^{12}C (Melander and Saunders, 1979). The degree of discrimination differs distinctly amongst photosynthesis pathways (O'Leary, 1981). This explains why $\delta^{13}C_{(TOC)}$ in soils and sediments is largely determined by the photosynthesis pathway under which C is sequestered in plant material (O'Leary, 1988). For the investigated Schwalbenberg LPS, the $\delta^{13}C_{(TOC)}$ are in the range of predominant C3 vegetation. Plants of this photosynthesis pathway type use the Calvin Cycle exclusively (mean −27‰ $\delta^{13}C_{VPDB}$) and dominate all forest plant communities and most plants of temperate zones (Boutton, 1996). The absence of C3/C4 vegetation shifts facilitates detailed reconstruction of carbonate metabolism without interferences. Moreover, ecological factors causing smaller isotopic fractionations like physiological water stress of plants can be addressed (Farquhar et al., 1982).

Inorganic Carbon in Loess-Palaeosol-Sequences

Three major inorganic carbon pools contribute to the overall TIC content in LPS: biogenic carbonates are formed in animals and plants as part of their skeletons or segregations (Zamanian et al., 2016; Prud'homme et al., 2018). Geogenic carbonates (PC) originate from physically weathered carbonaceous rocks within the source area of mineral dust, having $\delta^{13}C$ values close to 0‰ (West et al., 1988), and pedogenic (SC) having $\delta^{13}C$ values 14.4‰

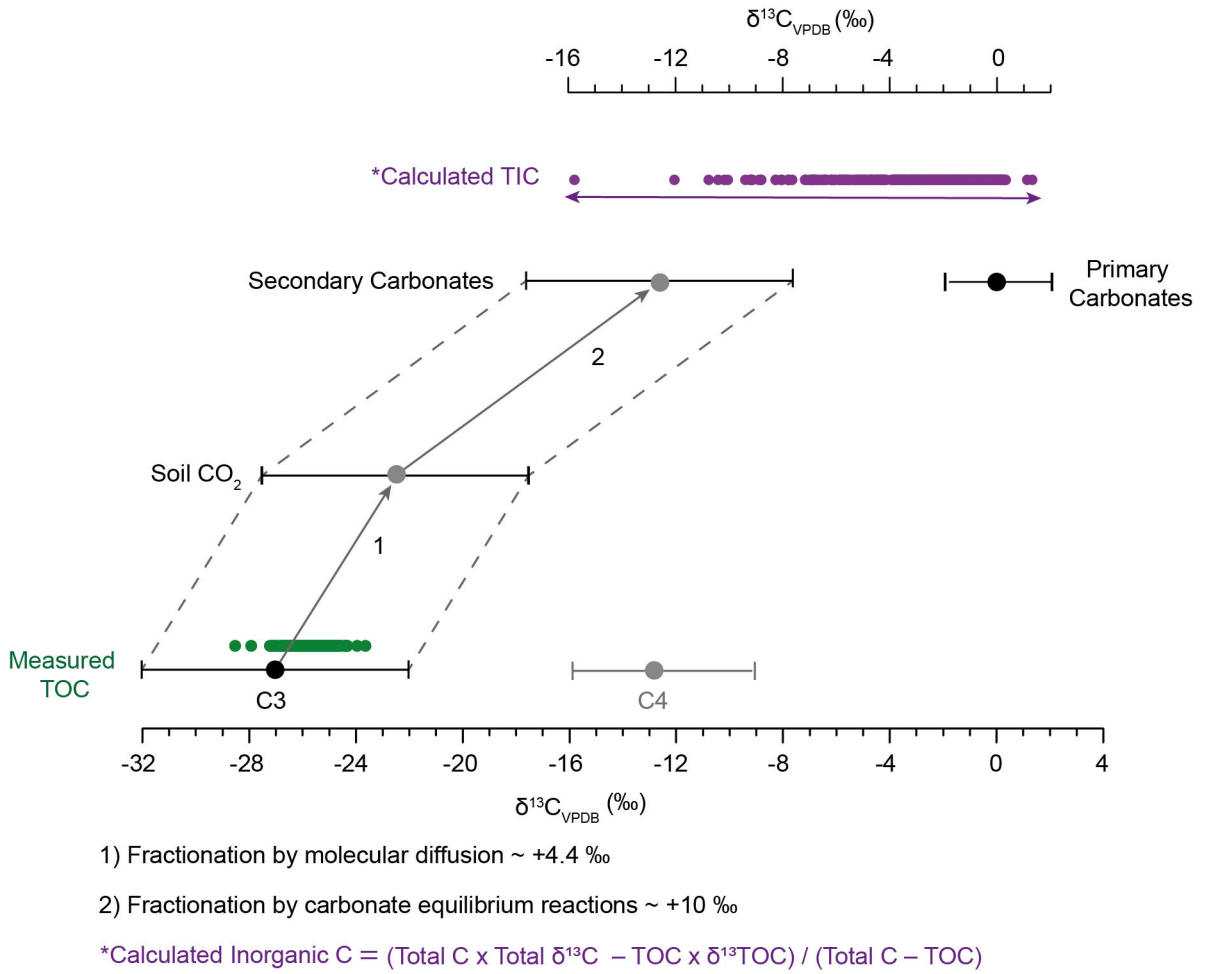

FIGURE 2 | Model of stable C isotope fractionation in calcareous terrestrial systems (redrawn from Nordt et al., 1998). Green dots represent measured $\delta^{13}C_{(TOC)}$ composition of core REM 3A. Purple dots indicate calculated δ^{13} of total inorganic C (Total C – TOC). The range of values confirms the presence of primary and secondary carbonates, which can be differentiated and quantified by end-member modelling (Salomons and Mook, 1976).

more positive than the associated OM (**Figure 2**). PC are subject to dissolution depending on contemporary climate parameters (in particular precipitation), water percolation dynamics and sediment properties (pH of the soil solution, amount of dissolved inorganic carbon through soil atmospheric CO_2 pressure pCO_2). The resulting ions are transported with soil water and precipitate as SC when the soil solution is supersaturated, in particular close to roots, in response to increasing evapotranspiration or decreasing pCO_2. Moreover, physical barriers for water percolation (e.g., related to significant decreases in particle size), may lead to accumulation of SC. Strongly decreasing pCO_2 toward the surface additionally governs the spatial distribution of SC and restricts the upward migration of ions, despite percolation of water being multidirectional (Zamanian et al., 2016). During SC precipitation, the stable carbon isotopic composition of soil CO_2 and diffusional effects determine the overall $\delta^{13}C$ values of the SC (**Figure 2**; Cerling et al., 1991). In this context, root and rhizomicrobial respiration contribute most of CO_2 in soils. Consequently, decomposition of soil organic matter (SOM) affects δ^{13} of SC only to a minor extent (Kuzyakov, 2006). Atmospheric CO_2 diffusion into soils caused by frost dynamics may shift the $\delta^{13}C$ of SC in the upper 50 cm of soils toward more positive values (Cerling, 1984). However, this is negligible in case of vegetation cover (Zamanian et al., 2016).

$\delta^{13}C$ of Total Organic Carbon ($\delta^{13}C_{(TOC)}$) in Loess

Organic carbon input to soils is mainly derived from leaf litter, root litter and exudates; faunal contribution is low (Wardle, 1992). In contrast to environments, allowing for soil formation, the TOC pool in loess is formed in relatively arid environments characterised by sparse vegetation cover, low carbon turnover rates and high mineral dust accumulation. Such environments largely restrict biases of the original isotope signal due to microbial degradation or selective preservation of recalcitrant substances and rhizosphere

disturbance (Hatté and Schwartz, 2003). The $\delta^{13}C_{(TOC)}$ in loess therefore predominantly reflects the original isotopic signal of the former vegetation ($\delta^{13}C$ of plants ($\delta^{13}C_{(PL)}$).

The following presumptions are commonly applied, when interpreting $\delta^{13}C_{(PL)}$ of C3 plants: variation in atmospheric $\delta^{13}CO_2$ has a direct impact on $\delta^{13}C_{(PL)}$, since atmospheric CO_2 forms the substrate for photosynthesis (Farquhar et al., 1989). The effect of varying atmospheric CO_2 concentration on $\delta^{13}C_{(PL)}$, has been investigated by several authors, who found a linear response of $\delta^{13}C_{(PL)}$ ($-0.02‰$ ppm^{-1} CO_2) (e.g., Feng and Epstein, 1995). However, this relationship remains under debate (Hare et al., 2018). Environmental stress may cause different degrees of isotope fractionation between plant species, as well as intra-species variation in fractionation due to genetic predisposition or differences in nutrient supply. Organs of individual plants may exhibit different $\delta^{13}C$ values (O'Leary, 1981). In light of open landscapes under which TOC in loess has been formed, we presume few plant species (mostly grasses and mosses) to be dominant (cf. Hatté and Schwartz, 2003). This would reduce the effect in variation of isotope fractionation among plant species in the resulting $\delta^{13}C_{(PL)}$ pool. Following this premise, the C pool can be regarded as a single entity in which components show somewhat similar linear responses to environmental stress (cf. Hatté and Schwartz, 2003). Temperature-related effects on $\delta^{13}C_{(PL)}$ values are difficult to assess. Several studies indicate some limited influence of temperature; others found no influence (O'Leary, 1981). On this basis we consider temperature effects to be negligible (O'Leary, 1981; Farquhar et al., 1982). Light variation potentially effect $\delta^{13}C_{(PL)}$ but only in case of large variation, such as doubling the insolation (Yakir and Israeli, 1995). There is no evidence for solar insolation shifts being this large during the LGC (Berger and Loutre, 1991). However, differences in light intensity may reach critical degrees in dense forest ecosystems. Along with variations between $\delta^{13}CO_2$ at soil surfaces (being in particularly influenced by soil atmospheric $\delta^{13}CO_2$) and $\delta^{13}CO_2$ at the canopy level (mostly reflecting atmospheric $\delta^{13}CO_2$) (Kohn, 2010). The greatest effect on C3 $\delta^{13}C_{(PL)}$ can be explained by physiological response to water availability and thereby drought stress (Kohn, 2010) in the absence of canopy effect and under relatively constant atmospheric $\delta^{13}CO_2$. Typically, the first reaction of plants to drought is stomatal closure (Pirasteh-Anosheh et al., 2016), leading to limitation of CO_2 diffusion into plants capable of increasing $\delta^{13}C_{(PL)}$ by up to $4‰$ (Farquhar et al., 1982; Stevenson et al., 2005; Kohn, 2010). In cases where precipitation exceeds ∼1500 mm yr^{-1} (Kohn, 2010), C3 plants do not show a significant reaction in their ^{13}C discrimination intensity, since there is no need for stomata closure in response to drought stress (Kohn, 2010; Thornton et al., 2015).

TOC/N$_{(total)}$

The ratio of organic carbon and total nitrogen (TOC/$N_{(total)}$) in leaves varies between plant species and is highest in evergreen (∼50) and deciduous trees (∼20). C3 herbages yield the lowest TOC/$N_{(total)}$ values (∼16.5) (Zheng and Shangguan, 2007). Decomposition of OM implies the ingestion of TOC and its partial degassing as CO_2, but also stabilisation processes. In contrast, N is incorporated in amino acids of microorganisms. Hence, smaller TOC/$N_{(total)}$ ratio indicate enhanced decomposition in case the original elemental composition does not dominate the TOC/$N_{(total)}$ ratio, due to large variation of TOC/$N_{(total)}$ in plant species (Zech et al., 2007).

TOC/PC

A ratio which combines TOC and PC may provide a useful proxy for palaeoenvironmental conditions, since both agents respond to variability in temperature, precipitation, vegetation cover, and land surface stability. Enhanced mineral dust input associated with cold conditions and reduced vegetation cover leads to the enrichment of PC and may dilutes a weak TOC signal. Climate conditions conducive to soil formation often support vegetation cover – which increases TOC input to the soil through decomposition – coeval with decreased PC input. Enhanced precipitation and especially CO_2 input by plants and microbes to the soil leads to stronger leaching of PC; this latter factor exceeds the effects of temperature for the solubility of carbonates (Zamanian et al., 2016). Assuming that the loess parent material yields $\delta^{13}C_{(TIC)}$ values of $0‰$ potentially produces a linear bias in the calculation of PC and SC. This value has been reported for limestone (West et al., 1988) and calcareous sediments and is also supported by measured stable carbon isotopic composition of "pure" loess sections throughout the REM 3A core. Here we test the TOC/PC ratio as proxy governed by the response of geomorphological and pedogenic processes to climate oscillations.

MATERIALS AND METHODS

Drilling of sediment cores was performed using a Nordmeyer RS 0/2.3 drill rig in upslope position in order to gain a preferably complete LPS. We executed vibracoring using 1 m long closed steel augers equipped with plastic liners. After drilling, cores were opened in the laboratory, photo-documented and described based on sedimentological and pedological characteristics (Ad-hoc-Ag Boden, 2005), soil classification followed the IUSS Working Group WRB (2015). However, palaeosols can hardly be classified in an accurate manner according to available nomenclature codes as these are designed for modern soils exposed to atmospheric alterations (Nettleton et al., 1998, 2000). Consequently, these nomenclatures do not account for post-burial processes including possible destruction of key soil attributes (James et al., 1998; Zerboni et al., 2011). In light of this limitation, we apply palaeosol classification similar to the WRB classification of modern soils. One half of the core was sampled in 2.5 cm intervals. Every second sample was carefully sieved (≤2 mm), dried (50°C) and homogenised by ball milling (5 min, 450 rounds/min) for further analysis.

EA-IRMS

We determined the bulk C ($C_{(total)}$), TOC and the natural abundance ratio of stable C isotopes by performing single

sample analysis. Two international reference materials (USGS40 and USGS41) were run in duplicate with every batch of 15 samples allowing a two point normalisation procedure to be performed for $\delta^{13}C$ with the same frequency. A quality control (QC) material (top soil) was measured with each batch of 15 samples; any two consecutive 2σ failures or a single 3σ failure of this QC material triggered repeated analysis of the sample batches at either side of it. Additionally, we performed tests to establish the lower limit of the amount of carbon necessary to give stable $\delta^{13}C$ and %C values. Any sample containing less than the established lower limits was re-analysed using more material. $C_{(total)}$ and $\delta^{13}C_{(total)}$ were measured by running 5 mg sample aliquots in tin cups. Since the nitrogen content can be significantly altered by HCl pre-treatment of samples (Brodie et al., 2011), we only used N data determined from untreated sample material. TOC and $\delta^{13}C_{(TOC)}$ were determined on 8 mg of sample aliquots after removal of carbonates by treatment with 0.5 M HCl in silver cups (in-cup acidification) (Midwood and Boutton, 1998). After each acidification step, the sample aliquots were dried (50°C for several hrs). This was repeated until no fizzing of CO_2 was visible anymore under a binocular microscope. The C and $\delta^{13}C$ of $C_{(total)}$ and TOC allow for calculation of TIC and its stable C isotopic composition ($\delta^{13}C_{(TIC)}$). All analyses were performed using a Flash EA 1112 Series Elemental Analyser connected through a Conflo III to a DeltaPlus V isotope ratio mass spectrometer (all Thermo Finnigan, Bremen, Germany). The $\delta^{13}C$ isotope ratios were normalised to the VPDB scale using International Atomic Energy Agency reference materials USGS40 and USGS41 (both L-glutamic acid). The C and N contents of the samples were calculated from the area output of the mass spectrometer calibrated against a topsoil standard, which was analysed with every batch of 15 samples. Long-term precision for a QC standard (top soil) (n = 116) was total carbon 3.77% (1σ = 0.12), $\delta^{13}C$ −27.79‰ (1σ = 0.14), and nitrogen 0.27% (1σ = 0.02%). The 1σ values of N, C and its stable isotope composition reflect the error margins. Values below this threshold have not been plotted in the figures. In normal operation, the CO_2 peak derived from the carbon content of the sediment sample was diluted with helium before it entered the mass spectrometer, but for samples of small carbon content (≤400 μg C) samples remained undiluted. After each run of the acidified sample aliquots, the measured TOC was checked for large shifts in its isotopic composition indicative for the presence of remaining carbonates (Boutton, 1996). This allows for crosschecking both, the reliability of the TOC content values and the $\delta^{13}C_{(TOC)}$ composition.

Calculation of Inorganic C and Its $\delta^{13}C$ Based on EA-IRMS Results

$\delta^{13}C_{(TIC)}$ was calculated using a mass balance equation

$$\delta^{13}C_{(TIC)} = ((C_{(total)} \times \delta^{13}C_{(total)}) - (TOC \times \delta^{13}C_{(TOC)}))/ (C_{(total)} - TOC) \quad (1)$$

Relative secondary carbonate (SC) proportion was calculated according to Salomons and Mook (1976):

$$SC = ((\delta^{13}C_{(TIC)} - \text{parent material } \delta^{13}C_{(TIC)}{}^{*}) / (\delta^{13}C_{(TOC)} + 14.4‰{}^{**})) \times 100 \quad (2)$$

* parent material $\delta^{13}C_{(TIC)}$ was assumed to be 0‰ based on observed $\delta^{13}C_{(TIC)}$ values in relatively unweathered loess sections and on literature data (West et al., 1988).

** 14.4‰ coefficient for fractionation due to molecular diffusion and carbonate equilibrium reactions (Nordt et al., 1998).

$$PC = 100 - SC \quad (3)$$

PC and SC contents were subsequently related to the TIC content of the respective samples to derive the weight % of both carbonate types.

Gasbench-IRMS

In order to validate calculated TIC content and its isotopic composition, we selected and re-measured 30 samples along a prominent soil complex (12–13 m in REM 3A) clearly traceable in Ca values of the downslope section, to ensure that our measure encompasses a wide range between low and high amounts of TIC. 400–500 μg of sample material was dissolved (2 h reaction time) with concentrated phosphoric acid in He-flushed borosilicate exetainers at 72°C (Gasbench II device). Subsequently the resulting CO_2 was measured using a continuous-flow IRMS (Thermo Finnigan MAT 253). Isotope data and concentration of TIC were calibrated against the NSB-19 calibrated IVA Carrara marble. Internal precision was 1σ = 0.02‰. Calculated TIC values are highly correlated with measured TIC (r^2 = 0.94, $p > 0.0001$). The same is true for its stable C isotopic composition (r^2 = 0.92, $p > 0.0001$). We checked, if calculated TIC contents (see "Calculation of Inorganic C and Its $\delta^{13}C$ Based on EA-IRMS Results") matched directly measured TIC values derived from the same samples (see "EA-IRMS") after applying the loss-of-ignition method at 550°C for 3.5 h. No relationship between these data can be observed casting doubts on both- TOC and TIC contents derived by the loss-of-ignition method applied to calcareous sediments.

RESULTS

Litho- and Pedostratigraphy of Core REM 3A

Cores REM 3A and REM 3B were drilled in upslope position of the Schwalbenberg close to Remagen (Middle Rhine valley, Germany; 50.562243° N, 7.239667° E). We performed drilling of REM 3B to a depth of 30 m below surface (b.s.) some 50 cm distant from REM 3A to extend the 26 m long record down to the underlying fluvial sediments. However, the sequence below 26 m b.s. is decalcified. Therefore, here we restrict the core description to core REM 3A (cf. **Figure 3**). Units (B-G) refer to significant shifts in lithology (note that unit A, consisting of fluvial deposits below the LPS, as well as the lowermost part of unit B are not part

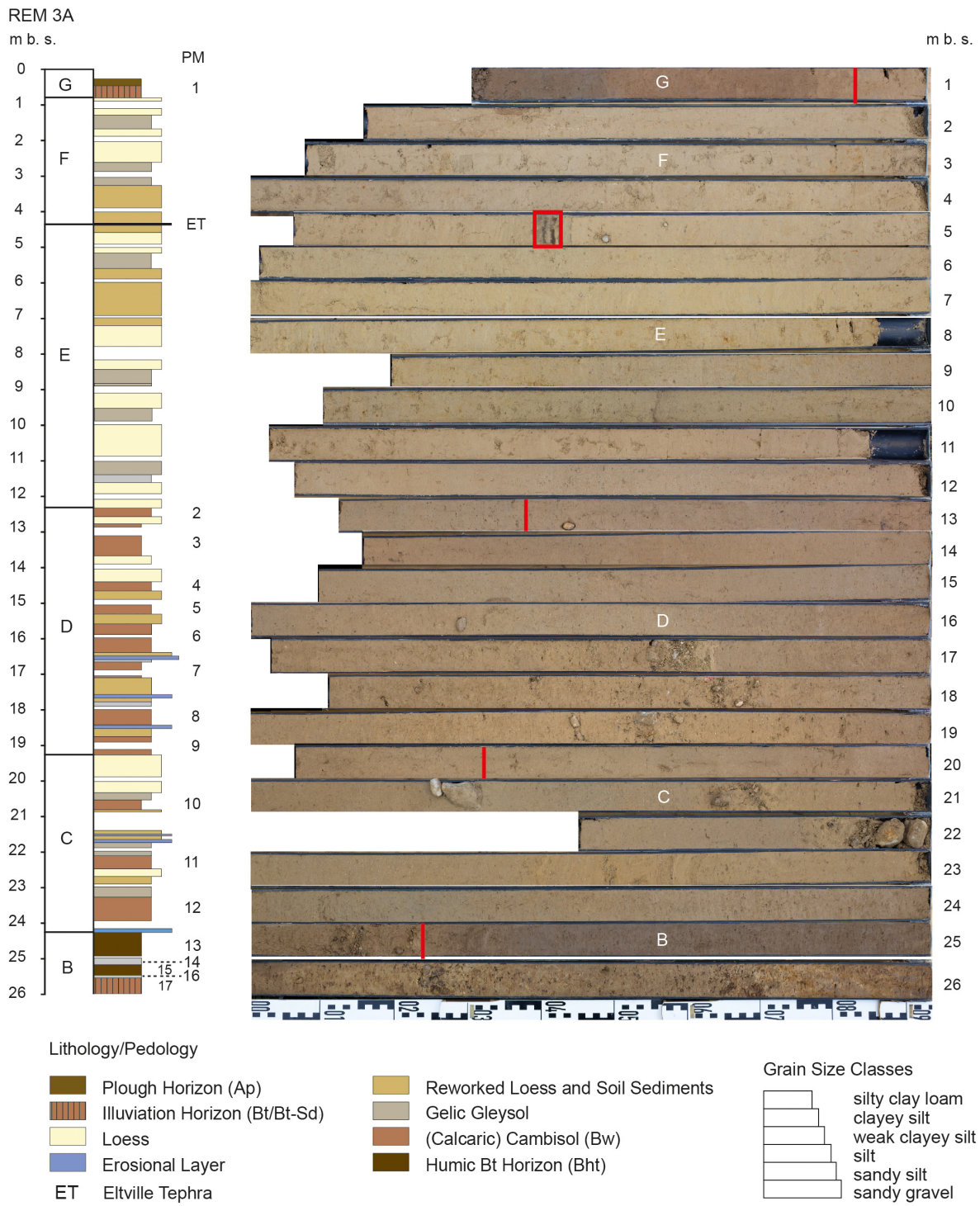

FIGURE 3 | Litho- and pedostratigraphy and photo of core REM 3A. Units B–G (indicated by red bars and white text in the photo) are described in the text (note that unit A as well as the lowermost part of unit B are not part of the core REM 3A, but REM 3B). The underlying Lower Middle Terrace of the penultimate glaciation (Boenigk and Frechen, 2006) constrains the LPS formation to the Last Glacial Cycle (terrace sediments where detected in core REM 3B, not depicted here). Soil horizons apart from Gelic Gleysols are defined as pedogenic members numbered from bottom to top (PM 1–17). Soil classification followed the IUSS Working Group WRB (2015). However, Sew and Sd horizons are based on German classification. Estimated age of the Eltville-Tephra according to Zens et al. (2017) and Förster et al. (2020).

of the core REM 3A, but REM 3B). Soil horizons apart from Gelic Gleysols are defined as pedogenic members (in the following PM) numbered from top to bottom. The lowermost unit B of the core exhibits a clayey, decalcified horizon of a truncated Stagnic Luvisol (PM 17) at its base (Sew and Sd horizons are based on German classification). It is characterised by pronounced clay cutanes followed by a leached greyish horizon (PM 16). On top of this, a weakly humic, greyish clayey horizon (PM 15) is developed. After another bleached horizon (PM 14) a dark brown, humus-enriched horizon occurs (PM 13), indicating reworking processes toward the top by intercalated layers of silt and coarse sand and a distinct erosional unconformity reflected by a gravel layer at a depth of 24.25 m b.s.. A Calcaric Cambisol (PM 12) followed by a Gelic Gleysol introduce unit C, which is characterised by reworked loess and first almost unaltered loesses (predominantly in its uppermost part). Additionally, intercalated pebbles and sand layers prove reworking processes. PM 11 contains a Calcaric Cambisol and is followed by a Gelic Gleysol characterised by carbonate pseudomycelia and an auger-filling carbonate concretion (20.27–20.32 m b.s.) indicating intensive secondary carbonate dynamics. Based on macroscopic core description the following unit D, which is characterised by a total of eight Bw horizons of Calcaric Cambisols, can be subdivided in two different parts. The lower part reaches from 18.82 up to 16.4 m b.s. and contains distinct gravel layers and reworked loess. The soil horizons (PM 9, 8, 7) show increasing intensity of pedogenic features from bottom to top. In the upper part, no more coarse-grained layers were observed. Bw horizons of Calcaric Cambisols are separated by reworked loess (PM 6, 5, 4) and loess (PM 3, 2). The thickest loess layer occurs between PM 4 and 3. Unit E is characterised by dominating yellow and grey hue values and increasing carbonate contents. Between 12.36 and 7.27 m b.s. loess sediments with intercalated Gelic Gleysols occur. This section is covered by laminated reworked loess followed by a Gelic Gleysol and another loess layer. Between 4.44 and 4.38 m b.s. the Eltville-Tephra occurs in small layers. This volcanic material is an important stratigraphic marker horizon in Western Central Europe. Klasen et al. (2015) dated the sediments below and above the tephra layer based on luminescence dating to 23.0 ± 2.3 and 21.3 ± 2.1 ka, respectively. Within the given errors, ages are in agreement with the age for the Eltville-Tephra provided by Zens et al. (2017) of 24 ka, which was recently approved by Förster et al. (2020). A comparison of the geochemical composition of the tephra from Schwalbenberg with tephra layers observed in the Auel and Dehner maar cores assumed to reflect the Eltville tephra indicate the material to be identical (personal communication Frank Sirocko). A Gelic Gleysol between 2.67 and 3.31 m marks the end of the laminated loess sections and is followed by homogeneous loess and the uppermost Gelic Gleysol. The loess on its top is characterised by numerous carbonate concretions. Unit G comprises the Holocene soil, which is represented by a truncated Luvisol.

Inorganic C and Its Stable Isotopic Composition

The decalcification line at 24.32 m marks the transition to the uppermost part of unit B which is characterised by low TIC values (**Figure 4**). Moreover, $\delta^{13}C_{(TIC)}$ curve shows a prominent trend toward more positive values. Unit C is characterised by $\delta^{13}C_{(TIC)}$ (**Figure 4**) being most negative within the lower parts of the Calcaric Cambisol (PM 12) and significantly increasing toward the following Gelic Gleysol. Unit C shows distinct maximum TIC values in the Gelic Gleysols on top of PM 11 and PM 10, respectively. High TIC values additionally occur in the reworked loess between 22.7 and 23.00 m b.s.. These maxima are accompanied by high $\delta^{13}C_{(TIC)}$ values. Minima are bound to lowest parts of Calcaric Cambisol horizons (PM 11, 10). Notably, TIC and $\delta^{13}C_{(TIC)}$ curves show decreasing values in the loess layer toward unit D. Regarding the TIC curve, in unit D all Calcaric Cambisols show lower values at their base and increasing values toward the overlying layers, only in PM 8 and PM 3 distinct minima occur. This pattern is also well reflected by $\delta^{13}C_{(TIC)}$. Reworked loess layers are associated with maximum values of $\delta^{13}C_{(TIC)}$. In contrast, unit C is characterised by less pronounced shifts in both records. Notably, minimum values of TIC occur in reworked loess layers below and above the Eltville-Tephra layer. Especially the thick laminated reworked loess between 7.27 and 5.64 m b.s. in unit E shows most positive values of $\delta^{13}C_{(TIC)}$. A second maximum is observed in a loess layer between 10 and 11 m b.s.. The uppermost part of unit F is characterised by slightly increasing TIC values and more positive $\delta^{13}C_{(TIC)}$ values.

Calculated Primary and Secondary Carbonates and Stable Isotope Signature of Total Organic Carbon ($\delta^{13}C_{(TOC)}$)

Based on an end-member-modelling approach (see "Calculation of Inorganic C and Its $\delta^{13}C$ Based on EA-IRMS Results"), we calculated the PC and SC contents using the isotopic composition of inorganic $\delta^{13}C$ (**Figures 4**, **5**). This facilitates more detailed insights into the carbonate metabolism, which is largely dependent on factors such as water availability and percolation. We also plotted the $\delta^{13}C$ curve of TOC reflecting physiological response of plants within the loess sections (Hatté et al., 1999). Focussing the palaeosols in units C and D, SC were generally enriched toward the base while PC increased in the opposite direction toward the top of the soil horizons and reached their maxima slightly above. Only within PM 8 and 2, SC showed minimum values at the base and increased values upward, the same trend was observed for PC. Distinct minima of SC and maxima of PC occurred between individual Calcaric Cambisols. In the lower part of unit E, SC are again enriched at the base of Gelic Gleysols and show absolute minima in loess and reworked loess. In unit F, SC slightly decreased from the reworked loess above the Eltville-Tephra layer toward the following Gelic Gleysol, while no clear trend was visible for the uppermost part of the unit. The same is true for PC, which increased toward the Gelic Gleysol and remained on comparably high values above. Regarding the $\delta^{13}C_{(TOC)}$ curve, a clear trend toward more positive values was observed from unit B toward the base of unit C and from the base of unit D up to the middle of unit E (7.2 m b.s.) indicating an overall decrease of water availability. Interestingly, unit C and the upper part of units E and F (above 7.2 m b.s.) are characterised by

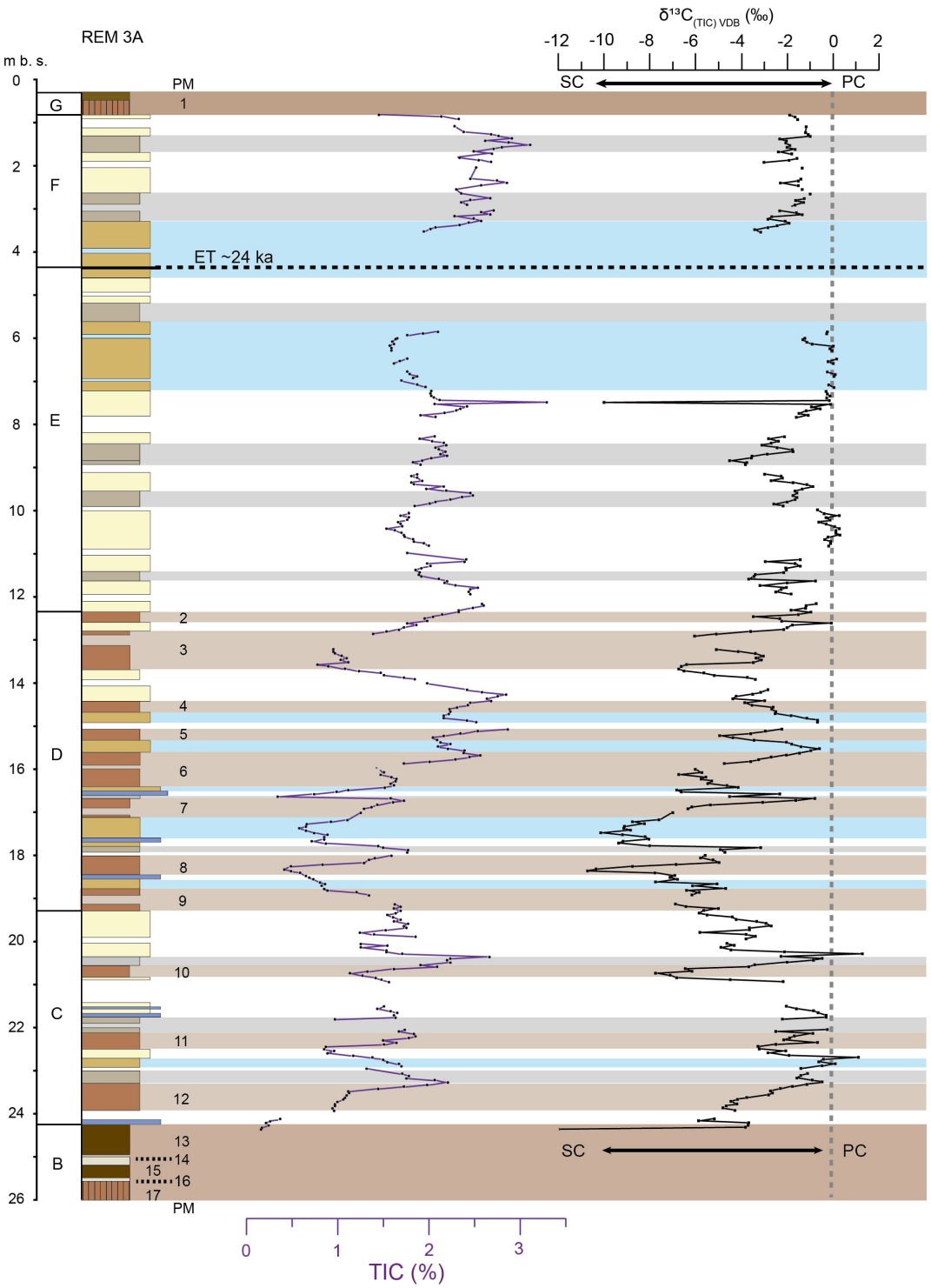

FIGURE 4 | Total inorganic C [TIC; (left, purple)] and its calculated stable C isotope composition [$\delta^{13}C_{(TIC)VPDB}$; (right, black)] where more depleted $\delta^{13}C$ values point toward enhanced SC concentration and values close to 0 indicate dominance of PC. Absolute minima in both curves are connected to pedogenic members (PM, see **Figure 3**) and occur locally in reworked loess layers (blue bars) indicating additional depletion processes. Gelic Gleysols are indicated by grey bars, Calcaric Cambisols by light brown bars and soil horizons associated with interglacial and early glacial conditions are represented by dark brown bars. Note that the lowermost part of unit (B) and the entire Holocene topsoil (A) are decalcified. Thus, no values are depicted. Estimated age of the Eltville-Tephra according to Zens et al. (2017) and Förster et al. (2020). Litho- and pedostratigraphic legend according to **Figure 3**.

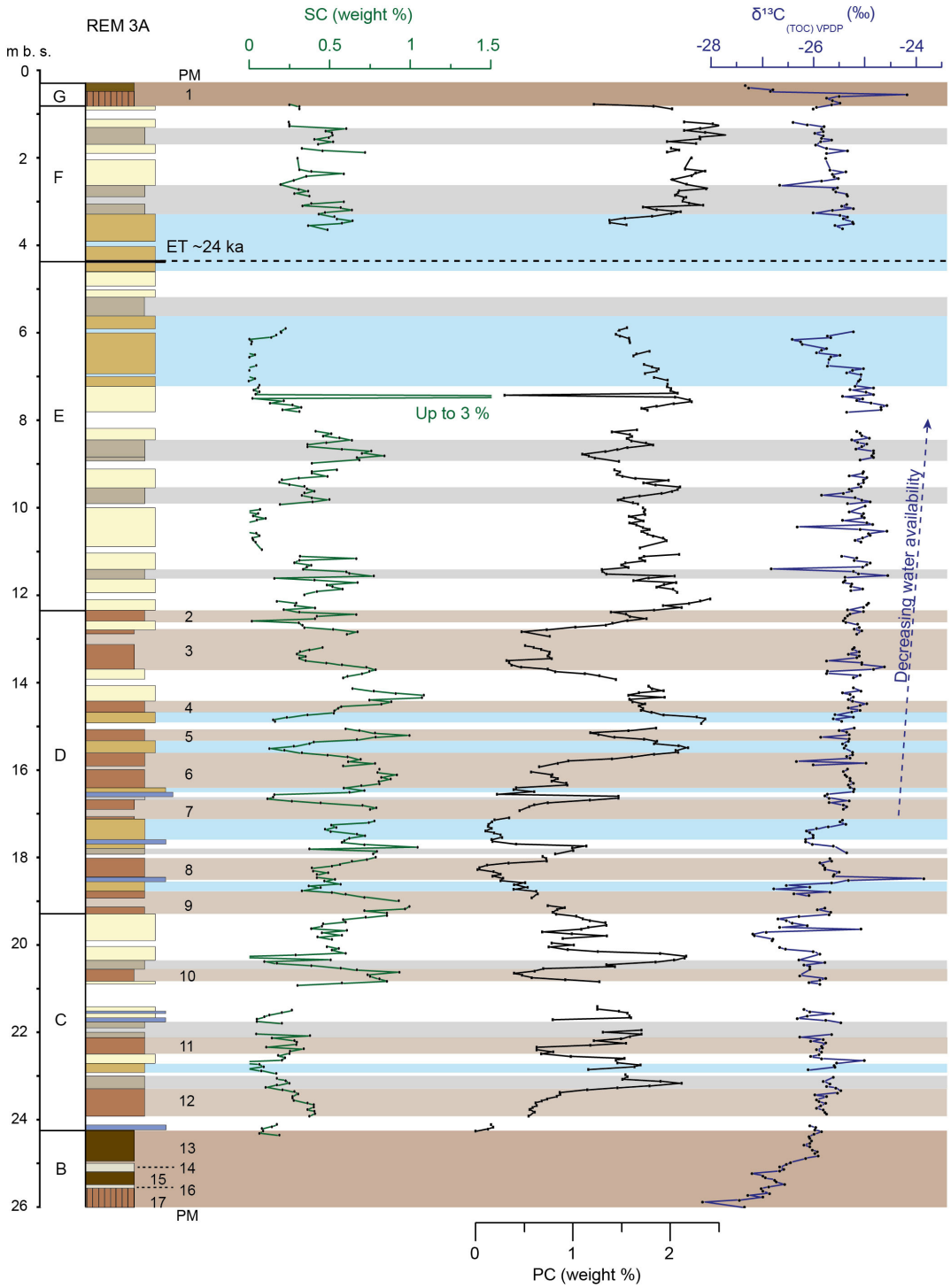

FIGURE 5 | Calculated primary and secondary carbonate contents (in weight % of TIC, see **Figure 4**) and $\delta^{13}C_{(TOC)VPDB}$. The latter reflects water availability of plants within loess and reworked loess layers, whereas in soils decomposition has to be considered (see **Figure 6**). Gelic Gleysols are indicated by grey bars, Calcaric Cambisols by light brown bars and soil horizons associated with interglacial and early glacial conditions are represented by dark brown bars. Note that the lowermost part of unit (B) and the entire Holocene topsoil (A) are decalcified. Thus, no values are depicted. Estimated age of the Eltville-Tephra according to Zens et al. (2017) and Förster et al. (2020). Litho- and pedostratigraphic legend according to **Figure 3**.

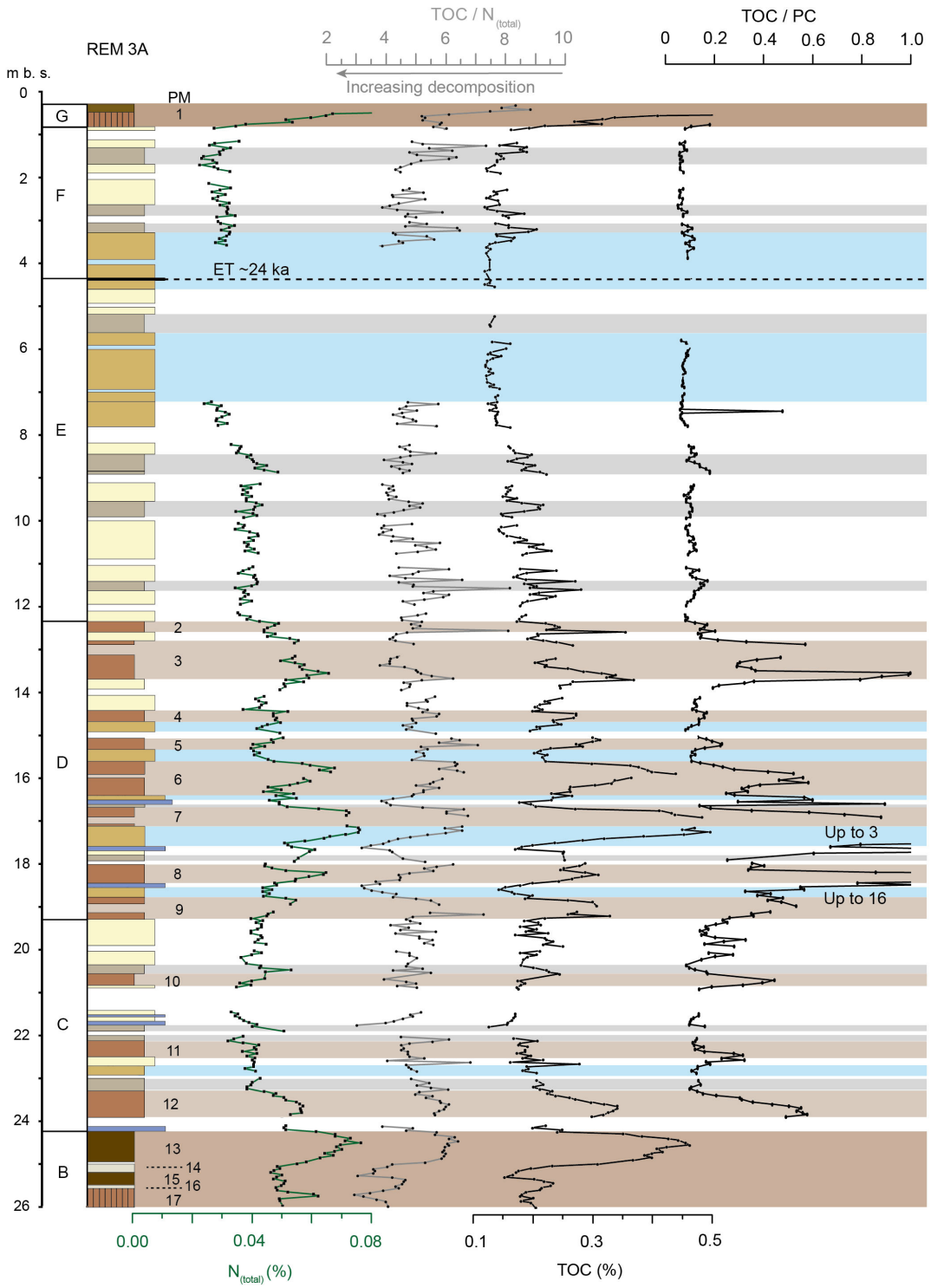

FIGURE 6 | Nitrogen ($N_{(Total)}$), total organic carbon (TOC), and their ratio (TOC/ $N_{(Total)}$) as well as the ratio of organic carbon and primary carbonates (TOC/PC) interpreted as ecological Proxies reflecting climate variability and decomposition. Values below error ranges are not depicted. Error ranges: Total *N* = 0.017%, TOC = 0.122%. Gelic Gleysols are indicated by grey bars, Calcaric Cambisols by light brown bars and soil horizons associated with interglacial and early glacial conditions are represented by dark brown bars. Note that the lowermost part of unit (B) and the entire Holocene topsoil (A) are decalcified. Thus, no values are depicted. Estimated age of the Eltville-Tephra according to Zens et al. (2017) and Förster et al. (2020). Litho- and pedostratigraphic legend according to **Figure 3**.

relatively constant values with a slight tendency toward more negative values.

Decomposition, Bioactivity and Mineral Dust Dynamics

The total nitrogen ($N_{(total)}$) and TOC contents are very low ranging between values of 0.02–0.08% and 0.05–0.5%, respectively (**Figure 6**). However, the $N_{(Total)}$, $TOC/N_{(total)}$ and TOC curves are characterised by higher values within Calcaric Cambisols compared to loess and reworked loess sections (**Figure 6**). In addition, Gelic Gleysols are characterised by enhanced TOC and $TOC/N_{(Total)}$. Distinct minima in both, $TOC/N_{(Total)}$ and TOC are related to coarse grained layers. The lowermost unit B exhibits slightly enhanced $N_{(Total)}$ values at the uppermost part of the clay enriched horizon (PM 17) of the Stagnic Luvisol. PM 16, 15, and 14 show low $N_{(Total)}$ concentration, while the humic illuviation horizon (PM 13) exhibits the highest values for $N_{(Total)}$ of the entire section. TOC values and the TOC/ $N_{(Total)}$ ratio show a slight maximum within PM 15 and a distinct maximum peak within PM 13. Apart from the Calcaric Cambisol of PM 12 characterised by maximum values in all curves, unit C is generally characterised by significantly lower values than unit B. In its lowermost part, TOC and $N_{(Total)}$ distinguish loess and reworked sediments from palaeosols. PM 11 is well reflected by the TOC/PC ratio. In contrast, the uppermost Calcaric Cambisol of unit C (PM 10) is characterised by increasing $N_{(Total)}$ and TOC values toward the top (and in the covering Gelic Gleysol). In contrast, highest TOC/PC values are located within the lowermost part in this Calcaric Cambisol (likewise for PM 11). Unit D shows a prominent saw-tooth pattern in $N_{(Total)}$ and TOC lasting from PM 7 to 4 and from 3 to 2. However, the TOC/ $N_{(Total)}$ ratio remains at a comparably high level for PMs 9 to 5. TOC/ $N_{(Total)}$ values in PMs 4, 3, and 2 are in the range of values observed in loess in the uppermost part of unit D. In contrast to all other proxies the TOC/PC ratio exhibits its highest values in PM 8. The lowermost part of this Cambisol is entirely free of PC (see also **Figure 6**). In contrast, PM 7 exhibits slightly higher, but still low PC values. PM 6 shows lowest $TOC/N_{(Total)}$ values at its bottom. In contrast, highest TOC/ $N_{(Total)}$, TOC and TOC/PC values are located at its upper part, the very top is characterised by strongly decreasing TOC and TOC/PC and TOC/ $N_{(Total)}$ being on a level as before. PM 5 exhibits most similar curve patterns for all proxies, but PM 4 is characterised by only slightly changing $N_{(Total)}$ values, whereas TOC/ $N_{(Total)}$ and TOC curve patterns are similar to those of PM 5 (but the values are lower). PM 3 exhibits maxima at its base and top and a minimum peak in-between. PM 2 is separated by a loess layer from the underlying PM 3. Strongly decreasing TOC/PC values show that the loess layer as well as PM 2 are characterised by strongly enhanced PC input. Interestingly, almost all Gelic Gleysols above the last Calcaric Cambisol of unit D are characterised by increased TOC values, whereas TOC/PC and $N_{(Total)}$ values remain low. This is, however, not true for a Gelic Gleysol from 8.50 to 9 m, which is traceable in all presented proxies.

DISCUSSION

In the following discussion we focus on presented proxy data against the background of sedimentary and pedogenic processes involved in the formation of the Schwalbenberg LPS as depicted in sediment core REM 3A. As a reliable age model is not yet available for the new core and within the Schwalbenberg II section (e.g., Schirmer, 2012; Profe et al., 2016) and only for the Sinzig Soils S2 and S3 (cp. **Figure 7**) reliable age estimates exist (App et al., 1995; Schirmer, 2012), we will briefly discuss the proxy data in context to records of global climate and environmental change of the LGC. However, we focus on the methodological approach yielding new insights into LPS formation.

Mineral Dust, Loessification and Water Dynamics

If precipitation affects calcareous mineral dust after deposition, the water would dissolve PC, which re-precipitate as SC quickly due to the surrounding alkaline environment with low bioactivity (Zamanian et al., 2016). This implies that every rainfall or melting of snow potentially leads to formation of thin SC structures capable to contributing to cementation of the sediment. In loess research much attention has been drawn on processes contributing to the "loess-like-structure" and hence cementation (Sprafke and Obreht, 2016). If relatively high quantities in SC are required to generate the loess-like structure, one would expect $\delta^{13}C_{(TIC)}$ values to be more negative similar to those observed within the "pure" loess sections in the investigated archive. In this context, one could argue that mixing of atmospheric and soil CO_2 leads to more positive values (Quade et al., 1989). We consider the role of CO_2 mixing of minor influence since we expect at least limited respiration by soil organisms and roots during phases of dust accumulation. Further potential masking of the isotopic signal could be related to input of SC received from other sites by Aeolian transport as well as differences in isotopic composition of carbonates in the source region. In this context, the heavy mineral assemblage of sediments in the study region points to the catchment area of the River Rhine as major source area (Janus, 1988). In general, the Rhine catchment mostly contains Mesozoic limestone of southern Germany and the alpine area as well as some Tertiary limestone (Brunnacker, 1983). The carbonates in theses sedimentary rocks exhibit $\delta^{13}C$ values ranging from −3 up to 2‰ $\delta^{13}C_{PDB}$ (Baertschi, 1957; Keith and Weber, 1964). Fluvial transport of PC appears to have little effect on the original isotopic composition of the carbonates. This has been shown by carbon isotope values in PC derived from overbank deposits of the Lower Terrace of the river Rhine between Koblenz and Bonn (in the vicinity of our study site) being in the range of PC in the catchment area of the river Rhine (Manze et al., 1974). More positive $\delta^{13}C_{(TIC)}$ values in the lower part of unit E (12.36–7.27 m b.s.) and in the uppermost part of unit F (3.31–0.74 m b.s.) compared to the loess layers in unit C (especially between 20.30 and 19.32 m b.s.) could be interpreted in terms of high accumulation rates under dryer climate conditions, which would

allow for rapid coverage of formerly deposited material and thus, for its protection from atmospheric processes accompanied with less SC formation. Such a scenario is also supported by relatively more positive $\delta^{13}C_{(TOC)}$ values. Overall, there is evidence for increasing aridification from OIS 3 toward OIS 2 at Nussloch in Central Europe, reflected by $\delta^{13}C$ of earthworm calcites (Prud'homme et al., 2018), $\delta^{13}C$ of TOC (Hatté et al., 1999), and grain size trends (Antoine et al., 2001). Moreover, a trend toward more positive $\delta^{13}C_{(TOC)}$ values can be observed at Achenheim (Hatté et al., 1999), but also within a transect toward SE-Europe up to the southern limit of the European loess belt in Serbia (Obreht et al., 2014). For the Belotinac section (Serbia), this trend is accompanied by increasing grain sizes (Obreht et al., 2014). Erosional unconformities, however, between PM 11 and 10, PM 9 and 8, and PM 7 and 6 are characterised by low PC and SC values indicating input of pre-weathered material. In contrast, erosional unconformities located between PM 13 and 12, and PM 8 and 7 are characterised by depleted PC but high SC values pointing toward re-precipitation of SC in response to differences in grain size. The highest overall SC concentrations are located within Calcaric Cambisols, indicating environmental conditions which allowed for PC leaching and subsequent re-precipitation. Regarding PC and SC contents in context to $\delta^{13}C_{(TOC)}$, an interpretation of $\delta^{13}C_{(TOC)}$ as proxy for palaeo-precipitation (Hatté et al., 1999, 2001) is not straightforward. This becomes obvious especially in the laminated loess layer between 7.27 and 5.64 m b.s., which is characterised by lowest SC values in the entire record. The $\delta^{13}C_{(TOC)}$ indicates moister conditions may be due to increased precipitation but could also be explained by thawing of the permafrost. At Nussloch, laminated sediments close to the Eltville-Tephra have been described to be typical for niveo-aeolian loess (Antoine et al., 2001). Niveo-aeolian loess consists of alternating snow and loess layers where the snow melts during summer periods (Pye and Tsoar, 2009). In case the permafrost-table is high, this leads to enhanced water-saturation in the active layer and allows for grain-size sorting related to fluvio-aeolian conditions (Vandenberghe, 2013). However, this may also happen without snow being embedded into the loess as melting of the uppermost centimetres of the active layer can release considerable amounts of water (Reyes and Lougheed, 2015). Therefore, water availability for plants may increase independent from precipitation, and water logging becomes progressively more significant with increasing stands of the permafrost table in response to reduced mean temperatures (cf. Fischer et al., 2017). Moreover, an increasing permafrost table would change the soil moisture flows leading to depletion of SC at the water divide and accumulation in downslope positions (Wang and Anderson, 2000). Consequently, this scenario can explain enhanced water availability indicated by $\delta^{13}C_{(TOC)}$ in loess contemporary with $\delta^{13}C_{(TIC)}$ values being close to zero during coldest phases of the LGC (**Figure 5**).

Our results indicate that "loessification" did not necessarily require enhanced quantities of SC at the Schwalbenberg site. In addition, curve patterns of both $\delta^{13}C_{(TIC)}$ and $\delta^{13}C_{(TOC)}$ indicate phases characterised by high accumulation rates under dryer climate conditions, showing that combining the isotope signatures offers considerable potential toward an understanding of past climate conditions.

Decalcification and Formation of Palaeosols

The calculated PC and SC contents in context to TIC (**Figures 5**, **7**) are interpreted to reflect carbonate metabolism along the core and thus give evidence for leaching and re-precipitation intensity within the palaeosols. TOC (**Figure 6**) is reflecting biomass production and its incorporation into the sediments and soils and increases with the duration of environmental conditions allowing for soil formation. In this context, the TOC/PC ratio (**Figure 6**) shows intensity of soil formation, when PC values decrease and TOC increase and allows tracing of dust input reflecting the accretionary character of the palaeosols within the Schwalbenberg LPS. Starting from the lowermost part of unit C, PM 12 is a well-developed soil indicated by high TOC/PC and SC values. All other Calcaric Cambisols in this unit are less pronounced in the TOC/PC but show strong influence of SC metabolism. The focus is drawn on unit D. Intensity of soil development is increasing from PM 9 over PM 8, culminating in PM 7. In the following, TOC/PC indicate decreasing development intensity over PM 6–4, while PM 3 is strongly developed again. Overall, the curve progression and its striking agreement with litho- and pedostratigraphic findings indicate a direct relation to climate oscillations during the LGC. Schirmer (2012) has already addressed the direct impact of climate oscillations on the formation of the 13 m thick Schwalbenberg II section, which is the *locus typicus* for the so called "Ahrgau-Subformation" (Schirmer, 2013). It is characterised by eight palaeosols identified as *in situ* formations reflecting climate oscillations of OIS 3 as recorded in Greenland ice cores in great detail. Based on our TIC and PC and calcium contents adapted from Profe et al. (2016), we can reliably correlate PM 5–2 of sediment core REM 3A to the upper part of the Schwalbenberg II section (Remagen Soils R4 and R5, Sinzig Soils S1–S3, **Figure 7**). As shown in **Figure 7**, PM 5 can be correlated to R4. Micro-morphological investigations of R4 indicate very low carbonate contents (Schirmer et al., 2012). However, R4 is characterised by increasing Ca-values toward its top, which is also observed in TIC and PC values of PM 5. The offset between PC and TIC in PM 5 indicate intensive SC accumulation. PM 4 correlates with R5. From a micro-morphological perspective, R5 is the most intensively developed soil of the Upper Remagen Soils (R3–R5) at the Schwalbenberg II section (Schirmer et al., 2012). TOC and maxima in the dissolved iron index identify R3 as most intense soil, which is so far not correlated to REM 3A. The lowermost part of PM 3 correlated to S1, is characterised by most depleted PC concentrations but intensive secondary carbonate precipitation (**Figures 6**, **7**). In contrast to PM 3 and the correlated S1 and S2 soils, PM 2 and S3 are developed in overall increasing alkaline environments as suggested by TIC, PC, and Ca, respectively. A high PC content is also confirmed for S3 by micro-morphological investigations (Schirmer et al., 2012). Our results show that PM 8 and the

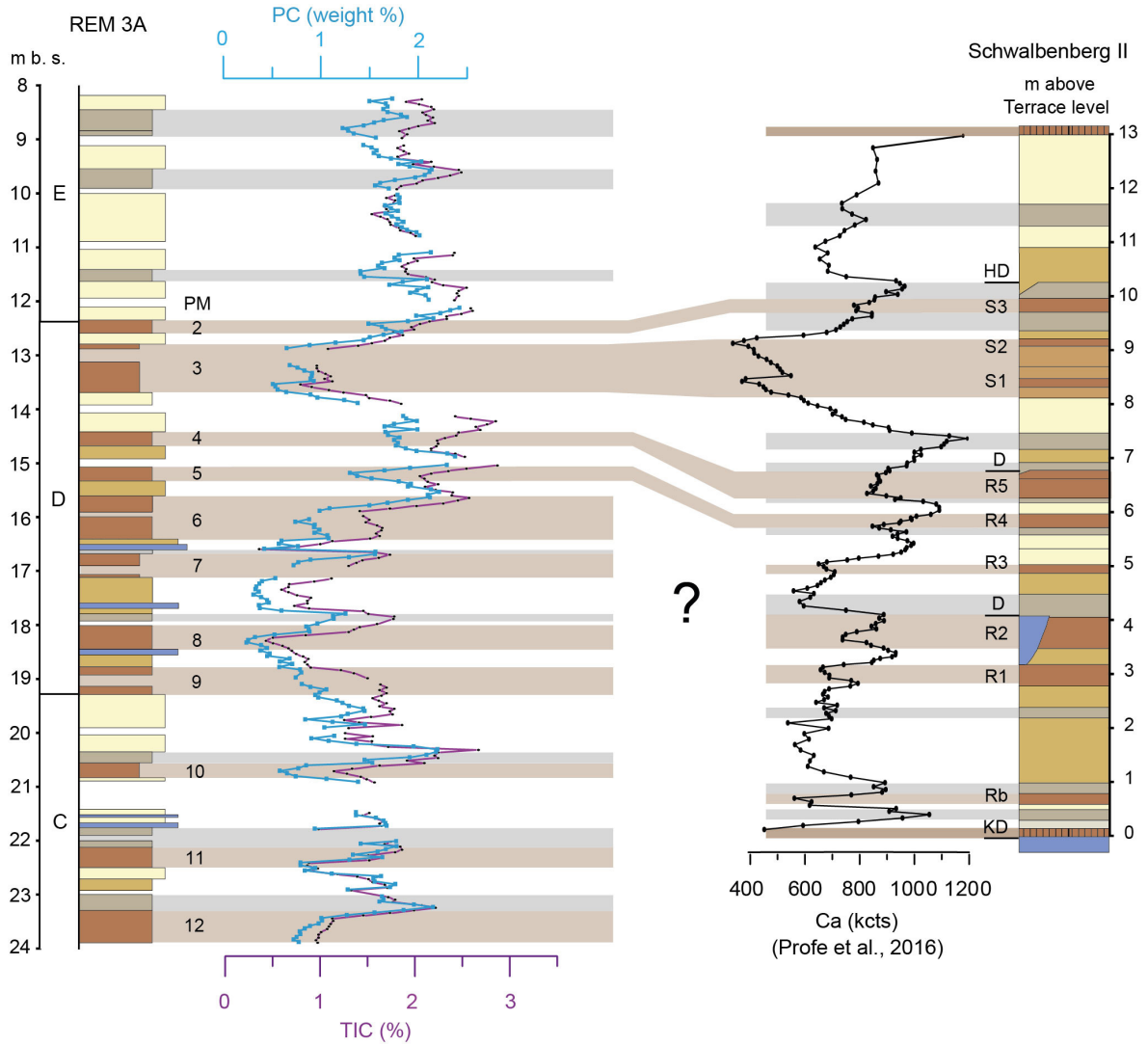

FIGURE 7 | Comparison of the TIC and Ca records and stratigraphy of the REM 3A and Schwalbenberg II section (re-drawn from Schirmer, 2012). Correlation for the uppermost parts of unit D and the Ahrgau Formation (starting above R1 up to the Hesbaye Discordance (HD)) reflecting late OIS 3 shows striking agreement amongst both LPS. However, R1 and R2 of the lower Remagen Soils and R3 of the upper Remagen Soils cannot be undoubtedly correlated to either PM (pedogenic member) 7,8,9. KD, Keldach Discordance; Rb, Reisberg Soil; D, Discordances; R1–R5, Remagen Soils; S1–S3, Sinzig Soils. Litho- and pedostratigraphic legend and pedogenic member (PM) according to **Figure 3**. Gelic Gleysols are indicated by grey bars, Calcaric Cambisols by light brown bars and soil horizons associated with interglacial and early glacial conditions are represented by dark brown bars.

lowermost part of PM 3 experienced most intensive leaching of PC amongst all Calcaric Cambisols present in REM 3A. Pronounced weathering is confirmed for the uppermost part of R1, R2, and R3 as well as for S1 and S2 by LOG (Rb/K) (Profe et al., 2016). This supports our PC results suggesting intensive leaching of most sections within the lowermost part of unit D (up to 15.50 m), which should contain the lower Remagen Soils R1 and R2 as well as R3. However, PC abundance in palaeosols appear to be inconsistent with classic concepts of soil formation, which would require complete decalcification prior to subsequent pH-dependent processes like brunification. In contrast, remarkably high PC contents are also reported for initial soil horizons toward the end of MIS 3 at the Krems-Wachtberg site (Lower Austria), where soil formation is assumed to have taken place within an alkaline environment (Meyer-Heintze et al., 2017). Based on our data, the presence of PC in a soil matrix points to an accretionary nature of most observed palaeosols in the Schwalbenberg LPS. This has also been addressed by Schirmer (2012), showing that the location of peaks in all proxies (in particularly TOC and clay content) indicates syn-pedogenetic sedimentation, at least in Remagen Soil 3 (R3). Moreover, the dissolved iron index indicates decreasing weathering toward the top of R2 and R4 (Schirmer et al., 2012).

Overall, the TOC/PC ratio proofs to be a very sensitive measure for intensity of pedogenesis at Schwalbenberg.

Correlation of Calcaric Cambisols across the slope based on PC, SC, and Ca is most promising for the Sinzig soils (S1–S3) and the upper Remagen Soils (R4–R5) (PM equivalents 5-2), but remains challenging for PM below. We relate this to differences in secondary carbonate formation and accumulation.

Decomposition

All data indicating decomposition show no general down-core trend toward enhanced degradation of TOC (**Figure 6**). This shows that long-term stabilisation constrained further decomposition of TOC (von Lützow et al., 2006; Zech et al., 2007). This is favoured by occlusion of OM into- and adsorption onto aggregates and minerals (von Lützow et al., 2006), as well as spatial inaccessibility of OM to biota (Moinet et al., 2018). TOC, $N_{(Total)}$ content and $TOC/N_{(Total)}$ show similar patterns indicating that control mechanisms of net primary production (NPP) and decomposition are largely climate dependent (Davidson and Janssens, 2006). Overall, palaeosols show distinct differences in trends of $TOC/ N_{(Total)}$. The case that $TOC/ N_{(Total)}$ values are lowest at the bottom of a soil, is the one to be expected. This is the case for PM 14, 13, 8, 6 reflecting well-developed Calcaric Cambisols most likely associated with long and warm periods of soil formation. In contrast, reverse conditions indicate erosional- and subsequent accumulation phases.

Toward a Conceptual Model of LPS Genesis

Ice core data suggest decreasing atmospheric temperature and increasing mineral dust content of the Northern Hemisphere toward the end of Greenland interstadials (GI) during OIS 3 (Ruth et al., 2003; Rasmussen et al., 2014; Rousseau et al., 2017). Since the Schwalbenberg LPS proves to be very sensitive to North Atlantic atmospheric oscillations, we hypothesise that the TOC/PC ratio is sensitive to display these atmospheric patterns. Warmer and moister interstadial periods favour pedogenesis, which starts from a stable land surface and is directed downward (Kemp, 2001). The first soil forming processes in calcareous loess involve decalcification and thus, leaching of PC. However, PC contents in REM 3A suggest an increasing input of mineral dust toward the top of palaeosols. If dust accumulation had ceased, observed clear separation of most palaeosols by calcareous loess in the Schwalbenberg LPS appears not to be plausible. We emphasise that mineral dust accumulation did not cease during formation of most interstadial soils. This implies that soils reflect the balance between mineral dust input keeping pace with soil formation. For our conceptual model, we presume the following conditions: climate warming coincides with increase of bioactivity, precipitation and decreasing mineral dust input. In turn, dust input increases as temperature and precipitation decrease. Enhanced precipitation and bioactivity during interstadials lead to increased leaching of PC and vice versa. TOC is a function of NPP and decomposition, both being largely dependent on prevailing climate. Starting from these premises the observed lowermost gradients of the TOC/PC ratio are a function of intensity and duration of pedogenesis. Climate deterioration toward the end of interstadials cause dilution of the overall TOC signal due to accumulation of PC, reflected in higher ratio values in the upper parts of palaeosols. An accretionary nature of palaeosols may also explain the absence of topsoil horizons (A-horizon) in many LPS. This common feature is often attributed to erosion due to large environmental changes at the end of interstadials/interglacials (Bronger et al., 1998). The absence of A horizons could be also explained by transformation of former A-horizons into B horizons by intercalation of illuvial components (clay and carbonates) (McDonald and Busacca, 1992; Kemp and Zárate, 2000). Such a scenario would be supported by gradually cooling and dust input toward the end of interstadials as indicated by the TOC/PC ratio. However, erosion prior to overprinting and transformation cannot be excluded. Starting from the premise that pedogenesis did not lead to complete decalcification and that the PC content of provided mineral dust did not change in order of magnitude over time, we can reconstruct pedogenetic scenarios and estimate intensity and duration of interstadials which formed the soils. Such reconstructions would require reliable age models for the Schwalbenberg LPS, which are not yet available. Only for the upper Sinzig Soils chronostratigraphic data, allowing for a correlation to certain GIs, are available. Against this background we only apply our conceptual model to the upper part of unit D. This can be extended to the entire sequence as reliable age constraints become available, contributing to a better understanding of the formation of the Schwalbenberg LPS. Sinzig Soil S2 yields an radiocarbon age of 33.350 ± 380 calBP (KIA22208, Schirmer, 2012), and Sinzig Soil S3 an age of 32.660 ± 350 calBP (KIA22209, Schirmer, 2012); App et al. (1995) give two radiocarbon ages for the archaeological find layer which corresponds to Sinzig Soil S3 yielding consistent ages of 32.480 ± 410 calBP (Pta-2722) and 32.670 ± 500 calBP (Pta-2721) [given ages were re-calibrated using the CalPal software version 2019.8 and the CalPal-2007_{HULU} (Weninger and Jöris, 2008) calibration curve]. Based on this and lithostratigraphical evidence, Schirmer (2012) correlated Sinzig Soil S2 to GI 7 and Sinzig Soil S3 to GI 6. However, S2 (correlated to the upper part of PM 3 in REM 3A) has been recently discussed to have formed during GI 6 and S3 (correlated to PM 2 in REM 3A) during GI 5 (Profe et al., 2016). GI 5 and GI 6 are characterised by rather short and less pronounced warm phases compared to previous GI 7 and in particularly GI 8 (Kindler et al., 2014; Rasmussen et al., 2014). These short and less pronounced warm phases have been discussed to be on the margin of conditions allowing for Cambisol formation (Profe et al., 2016). At the Nussloch site (∼170 km SE of Remagen), the last brown soil (Lohne Soil) has been correlated as soil complex to GI 8 and 7 and the first Gelic Gleysol (or tundra gley) is correlated to GI 6 (Moine et al., 2017).

Our results show that the lowermost part of PM 3, correlated to Sinzig Soil S1 (**Figure 7**) experienced intensive carbonate leaching and TOC accumulation (**Figures 5**, **6**). Macroscopic features indicate that this part of PM 3 is one of the most intensive palaeosols in unit D. This suggests that the lowermost part of PM 3 was formed during GI 8 rather than GI 7. The new TOC/PC ratio shows a pronounced maximum (values up to 1) in the lower part of PM 3 (**Figure 6**). In contrast, TOC/PC values decrease in

the lowermost part of PM 3. This progression is predominately governed by increasing PC toward the loess below PM 3, indicating downward leaching of carbonates in an environment with limited dust input. The strong increase of PC coinciding with a minimum in TOC/PC values at the centre of PM 3 indicate stadial conditions at the end of the GI in which Sinzig Soil S1 formed. The abruptness of PC increase may point toward conditions inhibiting strong dust input and/or preservation of PC during formation of the lowermost palaeosol. In contrast, the lower, but still relatively high TOC/PC level in the centre of PM 3 indicate loess accumulation during stadial conditions and subsequent overprinting by the overlying palaeosol (Sinzig Soil S2, upper part of PM 3). TOC/PC ratio clearly indicates that this upper part of PM 3 overprinted the underlying loess pointing to intensive pedogenesis. In this context, it is important to note that the uppermost maximum in TOC/PC is still higher than in many other Calcaric Cambisols in the core. Interestingly, the TOC/PC ratio shows a diminution toward the top of PM 2, indicating increases dust input toward the end of the GI. Overall, our results suggest that the lowermost part of PM 3 (correlated to Sinzig Soil S1) is most likely to reflect a long and warm interstadial, such as GI 8, whereas the uppermost part of PM 3 (correlated to Sinzig Soil S2) likely formed during GI 7. In this context, pollen data from maar lake archives from the Eifel area (Sirocko et al., 2016) indicate a distinct opening of the landscape in the transition from GI 8 to GI 7 characterised by a change from boreal forest (landscape evolution zone 7) to steppe conditions (landscape evolution zone 6). Our results support the idea that Sinzig Soil S3 (PM 2) reflects the last brown Calcaric Cambisol within a trend toward colder climate conditions at the margin of climates allowing for Cambisol formation (cf. Profe et al., 2016). Similar TOC/PC values within PM 2 and the first Gelic Gleysol above may render this embryonic soil as a candidate to reflect GI 5 being comparatively long and intense as GI 6 (cf. discussion Profe et al., 2016). In contrast to Nussloch at Schwalbenberg local conditions obviously allowed for later formation of one further brown soil. However, Schirmer (2012) discussed erosion of a Calcaric Cambisol in this part of the LPS. In this context, he argued that lithological properties of the Gelic Gleysol above S3 shows characteristics of the Ahrgau loess (Schirmer, 2012). We emphasis the role of factors maybe inhibiting formation of Calcaric Cambisols, but allow for Gelic Gleysols to develop. These may encompass increasing cold-arid conditions toward begin of OIS 2. Increasing aridity is indicated by progressively more positive $\delta^{13}C_{(TOC)}$ values in loess-sections at the Schwalbenberg and Nussloch sites (Hatté et al., 1999). Interestingly, our data suggest coincidentally increasing PC. Both factors are likely to directly respond to reduced temperatures (cf. Ruth et al., 2003).

Based on secure correlation of all Sinzig Soils [defined at the down-slope Schwalbenberg II section (Schirmer, 2012)] to PMs occurring at the water divide of the Schwalbenberg, no diminution of the interstadial solcomplex (OIS 3) toward upslope position can be observed, as suggested by Schirmer (2012). This is supported by geochemical investigations of the REM 1A core in mid-slope position (Klasen et al., 2015). In contrast, thickness of units reflecting the Interpleniglacial or OIS 3 appears to be consistent across the slope.

CONCLUSION AND FUTURE PERSPECTIVES

Combined investigations of TOC and TIC, as well as their stable isotope composition facilitates more detailed insights into reactions of the sedimentary and pedogenic processes to prevailing climate than addressing only one of the C pools. Hydraulic conditions governing water availability for plants can be discussed in terms of precipitation, sediment properties and permafrost dynamics in a more holistic way. In this context, we showed that enhanced water availability for plants indicated by $\delta^{13}C_{(TOC)}$ is not necessarily a function of increased precipitation but can also be caused by increased sediment moisture due to permafrost dynamics. Direct responses of terrestrial C pools to North Atlantic atmospheric and climate oscillations are likely to be reflected by the TOC/PC ratio, which is shown by a correlation of the new sediment core REM 3A to the Schwalbenberg II section. Moreover, the TOC/PC proves the accretionary nature of interstadial soils within the Schwalbenberg LPS. Beyond climatic features, we showed that cementation of mineral dust did not require high quantities of SC in the Schwalbenberg LPS, indicating that other cementation agents may play a significant role. Despite these advances, reconstructing decomposition environments and water availability for plants during time of soil formations remains difficult to assess. The main reason for this is the fact that the original isotopic signal of plants mark the starting point for further isotope fractionation during decomposition. Consequently, the resulting isotopic depth profiles can be regarded as a mixed signal including effects of water dynamics during plants lifespan, decomposition and stabilisation. Therefore, additional, investigation of compound specific $\delta^{13}C$ on recalcitrant substances like lignin is promising for isolating the effects of palaeo-precipitation and decomposition-induced changes of the isotope composition of TOC soils.

DATA AVAILABILITY STATEMENT

All datasets presented in this study are included in the article/**Supplementary Material**.

AUTHOR CONTRIBUTIONS

MV, PF, and AV wrote main parts of the manuscript. PF, AV, and KF designed the TerraClime project. BT and MV performed geochemical measurements and calculations. MV and SF conducted gasbench measurements. All authors contributed to discussion and edited the manuscript.

FUNDING

This manuscript contributes to the TerraClime Project funded by the German Research Foundation (DFG) (VO 938/25-1; FI 1941/5-1; FI 1918/4-1). BT received funding from the Rural and

Environmental Science and Analytical Services Division (RESAS) of the Scottish Government.

ACKNOWLEDGMENTS

We would like to thank Frank Sirocko for the information concerning the geochemical analysis of volcanic ash derived from the REM3 core. Moreover, constructive and valuable comments of two reviewers helped to significantly improve the manuscript.

SUPPLEMENTARY MATERIAL

The Supplementary Material for this article can be found online at: https://www.frontiersin.org/articles/10.3389/feart.2020.00276/full#supplementary-material

REFERENCES

Adams, J., and Post, W. M. (1999). A preliminary estimate of changing calcrete carbon storage on land since the Last Glacial Maximum. *Glob. Planet. Change* 20, 243–256. doi: 10.1016/s0921-8181(99)00015-6

Ad-hoc-Ag Boden (2005). Sponagel, H., Ad-hoc-Arbeitsgruppe Boden der Staatlichen Geologischen Dienste und der Bundesanstalt für Geowissenschaften und Rohstoffe, Bundesanstalt für Geowissenschaften und Rohstoffe eds Bodenkundliche Kartieranleitung: mit 103 Tabellen und 31 Listen. 5., verbesserte und erweiterte Auflage. Stuttgart: E. Schweizerbart'sche Verlagsbuchhandlung (Nägele und Obermiller).

Antoine, P., Rousseau, D. D., Zöller, L., Lang, A., Munaut, A. V., Hatté, C., et al. (2001). High-resolution record of the last Interglacial–glacial cycle in the Nussloch loess–palaeosol sequences, Upper Rhine Area, Germany. *Quat. Int.* 76–77, 211–229. doi: 10.1016/S1040-6182(00)00104-X

App, V., Auffermann, B., Hahn, J., Pasda, C., and Stephan, E. (1995). "Die altsteinzeitliche fundstelle auf dem schwalbenberg bei remagen," in *Berichte zur Archäologie an Mittelrhein und Mosel*, Vol. 4, ed. W. Wegner (Koblenz: Gesellschaft für Archäologie an Mittelrhein und Mosel), 11–27.

Baertschi, P. (1957). Messung und deutung relativer Häufigkeitsvariationen von 018 und C13 in Karbonatgesteinen und Mineralien. *Schweiz. Mineral. Petrogr. Mitt.* 87, 75–152.

Berger, A., and Loutre, M. F. (1991). Insolation values for the climate of the last 10 million years. *Quat. Sci. Rev.* 10, 297–317. doi: 10.1016/0277-3791(91)90033-Q

Bibus, E. (1980). *Zur Relief-, Boden- und Sedimententwicklung am Unteren Mittelrhein*. Frankfurt: Frankfurter Geowissenschaftliche.

Boenigk, W., and Frechen, M. (2006). The Pliocene and quaternary fluvial archives of the Rhine system. *Quat. Sci. Rev.* 25, 550–574. doi: 10.1016/j.quascirev.2005.01.018

Boutton, T. W. (1996). "Stable carbon isotope ratios of soil organic matter and their use as indicators of vegetation and climate change," in *Mass Spectrometry of Soils*, eds T. W. Boutton and S. Y. Yamasaki (New York, NY: Marcel Dekker), 47–82.

Brodie, C. R., Leng, M. J., Casford, J. S. L., Kendrick, C. P., Lloyd, J. M., Yongqiang, Z., et al. (2011). Evidence for bias in C and N concentrations and δ13C composition of terrestrial and aquatic organic materials due to pre-analysis acid preparation methods. *Chem. Geol.* 282, 67–83. doi: 10.1016/j.chemgeo.2011.01.007

Bronger, A., Winter, R., and Heinkele, T. (1998). Pleistocene climatic history of East and Central Asia based on paleopedological indicators in loess–paleosol sequences. *Catena* 34, 1–17. doi: 10.1016/s0341-8162(98)00078-2

Brunnacker, K. (1983). Isotopendaten im lößkalk der europäischen periglazialzone. *Mitt. Österrereichischen Geol. Ges.* 76, 205–211.

Buggle, B., Glaser, B., Hambach, U., Gerasimenko, N., and Markoviæ, S. (2011). An evaluation of geochemical weathering indices in loess–paleosol studies. *Quat. Int.* 240, 12–21. doi: 10.1016/j.quaint.2010.07.019

Cerling, T. E. (1984). The stable isotopic composition of modern soil carbonate and its relationship to climate. *Earth Planet. Sci. Lett.* 71, 229–240. doi: 10.1016/0012-821X(84)90089-X

Cerling, T. E., Solomon, D. K., Quade, J., and Bowman, J. R. (1991). On the isotopic composition of carbon in soil carbon dioxide. *Geochim. Cosmochim. Acta* 55, 3403–3405. doi: 10.1016/0016-7037(91)90498-T

Davidson, E. A., and Janssens, I. A. (2006). Temperature sensitivity of soil carbon decomposition and feedbacks to climate change. *Nature* 440, 165–173. doi: 10.1038/nature04514

Farquhar, G. D., Ehleringer, J. R., and Hubick, K. T. (1989). Carbon isotope discrimination and photosynthesis. *Annu. Rev. Plant Physiol. Plant Mol. Biol.* 40, 503–537. doi: 10.1146/annurev.pp.40.060189.002443

Farquhar, G. D., O'Leary, M., and Berry, J. (1982). On the relationship between carbon isotope discrimination and the intercellular carbon dioxide concentration in leaves. *Funct. Plant Biol.* 9, 121–137. doi: 10.1071/PP9820121

Feng, X., and Epstein, S. (1995). Carbon isotopes of trees from arid environments and implications for reconstructing atmospheric CO2 concentration. *Geochim. Cosmochim. Acta* 59, 2599–2608. doi: 10.1016/0016-7037(95)00152-2

Fischer, P., Hambach, U., Klasen, N., Schulte, P., Zeeden, C., Steininger, F., et al. (2017). Landscape instability at the end of MIS 3 in western Central Europe: evidence from a multi proxy study on a loess-palaeosol-sequence from the eastern lower Rhine embayment, Germany. *Quat. Int.* 502, 119–136. doi: 10.1016/j.quaint.2017.09.008

Förster, M. W., Zemlitskaya, A., Otter, L. M., Buhre, S., and Sirocko, F. (2020). Late Pleistocene Eifel eruptions: insights from clinopyroxene and glass geochemistry of Tephra layers from Eifel Laminated Sediment Archive sediment cores. *J. Quat. Sci.* 35, 186–198. doi: 10.1002/jqs.3134

Hare, V. J., Loftus, E., Jeffrey, A., and Ramsey, C. B. (2018). Atmospheric CO2 effect on stable carbon isotope composition of terrestrial fossil archives. *Nat. Commun.* 9:252. doi: 10.1038/s41467-017-02691-x

Hatté, C., Antoine, P., Fontugne, M., Lang, A., Rousseau, D. D., and Zöller, L. (2001). δ 13 C of loess organic matter as a potential proxy for paleoprecipitation. *Quat. Res.* 55, 33–38. doi: 10.1006/qres.2000.2191

Hatté, C., Fontugne, M., Rousseau, D. D., Antoine, P., Zöller, L., Tisnérat-Laborde, N., et al. (1999). δ13C variation of loess organic matter as a record of the vegetation response to climate changes during the Weichselian. *Geology* 26, 583–586.

Hatté, C., and Schwartz, D. (2003). Reconstruction of paleoclimates by isotopic analysis: what can the fossil isotopic record tell us about the plant life of past environments? *Phytochem. Rev.* 2, 163–177. doi: 10.1023/B:PHYT.0000004260.40656.c0

IUSS Working Group WRB (2015). *World Reference Base for Soil Resources 2014, Update 2015 International Soil Classification System for Naming Soils and Creating Legends for Soil Maps*. Rome: IUSS.

James, W. C., Mack, G. H., and Monger, H. C. (1998). Paleosol classification. *Quat. Int.* 51, 8–9. doi: 10.1016/s1040-6182(98)90186-0

Janus, U. (1988). *Löss der Südlichen Niederrheinischen Bucht*. Doctoral dissertation, Kölner Geographische Arbeiten, Köln.

Keith, M. L., and Weber, J. N. (1964). Carbon and oxygen isotopic composition of selected limestones and fossils. *Geochim. Cosmochim. Acta* 28, 1787–1816. doi: 10.1016/0016-7037(64)90022-5

Kemp, R. A. (2001). Pedogenic modification of loess: significance for palaeoclimatic reconstructions. *Earth Sci. Rev.* 54, 145–156. doi: 10.1016/s0012-8252(01)00045-9

Kemp, R. A., and Zárate, M. (2000). Pliocene pedosedimentary cycles in the southern Pampas, Argentina. *Sedimentology* 47, 3–14. doi: 10.1046/j.1365-3091.2000.00274.x

Kindler, P., Guillevic, M., Baumgartner, M., Schwander, J., Landais, A., and Leuenberger, M. (2014). Temperature reconstruction from 10 to 120 kyr b2k from the NGRIP ice core. *Clim. Past* 10, 887–902. doi: 10.5194/cp-10-887-2014

Klasen, N., Fischer, P., Lehmkuhl, F., and Hilgers, A. (2015). Luminescence dating of loess deposits from the Remagen-Schwalbenberg site, Western Germany. *Geochronometria* 42, 67–77.

Kohn, M. J. (2010). Carbon isotope compositions of terrestrial C3 plants as indicators of (paleo)ecology and (paleo)climate. *Proc. Natl. Acad. Sci. U.S.A.* 107, 19691–19695. doi: 10.1073/pnas.1004933107

Kuzyakov, Y. (2006). Sources of CO2 efflux from soil and review of partitioning methods. *Soil Biol. Biochem.* 38, 425–448. doi: 10.1016/j.soilbio.2005.08.020

Manze, U., Vogel, J., Streit, R., and Brunnacker, K. (1974). Isotopenuntersuchungen zum kalkumsatz im Löß. *Geol. Rundsch.* 63, 885–896.

McDonald, E. V., and Busacca, A. J. (1992). Late quaternary stratigraphy of loess in the channeled scabland and Palouse regions of Washington state. *Quat. Res.* 38, 141–156. doi: 10.1016/0033-5894(92)90052-K

Melander, L., and Saunders, W. H. (1979). *Reaction Rates of Isotopic Molecules*. New York, NY: Wiley.

Meyer-Heintze, S., Sprafke, T., Schulte, P., Terhorst, B., Lomax, J., Fuchs, M., et al. (2017). The MIS 3/2 transition in a new loess profile at Krems-Wachtberg East – A multi-methodological approach. *Quat. Int.* 464, 370–385. doi: 10.1016/j.quaint.2017.11.048

Midwood, A. J., and Boutton, T. W. (1998). Soil carbonate decomposition by acid has little effect on δ13C of organic matter. *Soil Biol. Biochem.* 30, 1301–1307. doi: 10.1016/s0038-0717(98)00030-3

Moine, O., Antoine, P., Hatté, C., Landais, A., Mathieu, J., Prud'homme, C., et al. (2017). The impact of last glacial climate variability in west-European loess revealed by radiocarbon dating of fossil earthworm granules. *Proc. Natl. Acad. Sci. U.S.A.* 24, 6209–6214. doi: 10.1073/pnas.1614751114

Moinet, G. Y. K., Hunt, J. E., Kirschbaum, M. U. F., Morcom, C. P., Midwood, A. J., and Millard, P. (2018). The temperature sensitivity of soil organic matter decomposition is constrained by microbial access to substrates. *Soil Biol. Biochem.* 116, 333–339. doi: 10.1016/j.soilbio.2017.10.031

Nettleton, W. D., Brasher, B. R., Benham, E. C., and Ahrenst, R. J. (1998). A classification system for buried palaeosols. *Quat. Int.* 51, 175–183. doi: 10.1016/s1040-6182(97)00043-8

Nettleton, W. D., Olson, C. G., and Wysocki, D. A. (2000). Paleosol classification: problems and solutions. *Catena* 41, 61–92. doi: 10.1016/s0341-8162(00)00109-0

Nordt, L. C., Hallmark, C. T., Wilding, L. P., and Boutton, T. W. (1998). Quantifying pedogenic carbonate accumulations using stable carbon isotopes. *Geoderma* 82, 115–136. doi: 10.1016/s0016-7061(97)00099-2

Obreht, I., Buggle, B., Catto, N., Markovic, S., Bösel, S., Vandenberghe, D., et al. (2014). The late Pleistocene Belotinac section (southern Serbia) at the southern limit of the European loess belt: environmental and climate reconstruction using grain size and stable C and N isotopes. *Quat. Int.* 334–335, 10–19. doi: 10.1016/j.quaint.2013.05.037

O'Leary, M. H. (1981). Carbon isotope fractionation in plants. *Phytochemistry* 20, 553–567. doi: 10.1016/0031-9422(81)85134-5

O'Leary, M. H. (1988). Carbon isotopes in photosynthesis. *Bioscience* 38, 328–336. doi: 10.2307/131073

Pécsi, M. (1990). Loess is not just the accumulation of dust. *Quat. Int.* 7–8, 1–21. doi: 10.1016/1040-6182(90)90034-2

Pirasteh-Anosheh, H., Saed-Moucheshi, A., Pakniyat, H., and Pessarakli, M. (2016). "Stomatal responses to drought stress," in *Water Stress and Crop Plants: A Sustainable Approach*, ed. P. Ahmad (Hoboken, NJ: Wiley), 24–35.

Profe, J., Zolitschka, B., Schirmer, W., Frechen, M., and Ohlendorf, C. (2016). Geochemistry unravels MIS 3/2 paleoenvironmental dynamics at the loess–paleosol sequence Schwalbenberg II, Germany. *Palaeogeogr. Palaeoclimatol. Palaeoecol.* 459, 537–551. doi: 10.1016/j.palaeo.2016.07.022

Prud'homme, C., Lécuyer, C., Antoine, P., Hatté, C., Moine, O., Fourel, F., et al. (2018). δ 13 C signal of earthworm calcite granules: a new proxy for palaeoprecipitation reconstructions during the last glacial in Western Europe. *Quat. Sci. Rev.* 179, 158–166. doi: 10.1016/j.quascirev.2017.11.017

Pye, K., and Tsoar, H. (2009). *Aeolian Sand and Sand Dunes*. Berlin: Springer.

Quade, J., Cerling, T. E., and Bowman, J. R. (1989). Systematic variations in carbon and oxygen isotopic composition of pedogenic carbonate along elevation transects in the southern Great Basin, United States. *Geol. Soc. Am. Bull.* 101, 464–475. doi: 10.1130/0016-7606(1989)101<0464:svitca>2.3.co;2

Rasmussen, S. O., Bigler, M., Blockley, S. P., Blunier, T., Buchardt, S. L., Clausen, H. B., et al. (2014). A stratigraphic framework for abrupt climatic changes during the last glacial period based on three synchronized Greenland ice-core records: refining and extending the INTIMATE event stratigraphy. *Quat. Sci. Rev.* 106, 14–28. doi: 10.1016/j.quascirev.2014.09.007

Reyes, F. R., and Lougheed, V. L. (2015). Rapid nutrient release from permafrost thaw in arctic aquatic ecosystems. *Arct. Antarct. Alp. Res.* 47, 35–48. doi: 10.1657/AAAR0013-099

Rousseau, D. D., Boers, N., Sima, A., Svensson, A., Bigler, M., Lagroix, F., et al. (2017). (MIS3 & 2) millennial oscillations in Greenland dust and Eurasian Aeolian records – A paleosol perspective. *Quat. Sci. Rev.* 169, 99–113. doi: 10.1016/j.quascirev.2017.05.020

Ruth, U., Wagenbach, D., Steffensen, J. P., and Bigler, M. (2003). Continuous record of microparticle concentration and size distribution in the central Greenland NGRIP ice core during the last glacial period. *J. Geophys. Res.* 108, 1–12. doi: 10.1029/2002JD002376

Salomons, W., and Mook, W. G. (1976). Isotope geochemistry of carbonate dissolution and reprecipitation in soils. *Soil Sci.* 122, 15–24. doi: 10.1097/00010694-197607000-00003

Schirmer, W. (2012). Rhine loess at schwalbenberg II - MIS 4 and 3. *Eiszeitalter Ggw.* 61, 32–47. doi: 10.3285/eg.61.1.03

Schirmer, W. (2013). *Ahrgau-Subformation. Lithostratigraphisches Lexikon*. Hannover: BGR.

Schirmer, W. (2016). Late Pleistocene loess of the lower Rhine. *Quat. Int.* 411, 44–61. doi: 10.1016/j.quaint.2016.01.034

Schirmer, W., Ikinger, A., and Nehring, F. (2012). Die terrestrischen Böden im Profil schwalbenberg/Mittelrhein. *Mainzer Geowissensch. Mitt.* 40, 53–78.

Sirocko, F., Knapp, H., Dreher, F., Förster, M. W., Albert, J., Brunck, H., et al. (2016). Reconstruction of landscape evolution zones (LEZ) from laminated Eifel maar sediments of the last 60,000 years. *Glob. Planet. Change* 142, 108–135. doi: 10.1016/j.gloplacha.2016.03.005

Sprafke, T., and Obreht, I. (2016). Loess: rock, sediment or soil – What is missing for its definition? *Quat. Int.* 399, 198–207. doi: 10.1016/j.quaint.2015.03.033

Stevenson, B. A., Kelly, E. F., McDonald, E. V., and Busacca, A. J. (2005). The stable carbon isotope composition of soil organic carbon and pedogenic carbonates along a bioclimatic gradient in the Palouse region, Washington State, USA. *Geoderma* 124, 37–47. doi: 10.1016/j.geoderma.2004.03.006

Thornton, B., Martin, G., Procee, M., Miller, D. R., Coull, M., Yao, H., et al. (2015). Distributions of carbon and nitrogen isotopes in Scotland's topsoil: a national-scale study: stable isotopes in Scotland's topsoil. *Eur. J. Soil Sci.* 66, 1002–1011. doi: 10.1111/ejss.12289

Vandenberghe, J. (2013). Grain size of fine-grained windblown sediment: a powerful proxy for process identification. *Earth Sci. Rev.* 121, 18–30. doi: 10.1016/j.earscirev.2013.03.001

von Lützow, M., and Kögel-Knabner, I. (2009). Temperature sensitivity of soil organic matter decomposition—what do we know? *Biol. Fertil. Soils* 46, 1–15. doi: 10.1007/s00374-009-0413-8

von Lützow, M., Kögel-Knabner, I., Ekschmitt, K., Matzner, E., Guggenberger, G., Marschner, B., et al. (2006). Stabilization of organic matter in temperate soils: mechanisms and their relevance under different soil conditions - a review. *Eur. J. Soil Sci.* 57, 426–445. doi: 10.1111/j.1365-2389.2006.00809.x

Wang, D., and Anderson, D. W. (2000). Pedogenic carbonate in Chernozemic soils and landscapes of southeastern Saskatchewan. *Can. J. Soil Sci.* 80, 251–261. doi: 10.4141/S99-063

Wardle, D. A. (1992). A comparative assessment of factors which influence microbial biomass carbon and nitrogen levels in soil. *Biol. Rev.* 67, 321–358. doi: 10.1111/j.1469-185X.1992.tb00728.x

Weninger, B., and Jöris, O. (2008). A 14C age calibration curve for the last 60 ka: the Greenland-Hulu U/Th timescale and its impact on understanding the Middle to Upper Paleolithic transition in Western Eurasia. *J. Hum. Evol.* 55, 772–781. doi: 10.1016/j.jhevol.2008.08.017

West, L. T., Wilding, L. P., and Hallmark, C. T. (1988). Calciustolls in central Texas: II. Genesis of calcic and petrocalcic horizons. *Soil Sci. Soc. Am. J.* 52, 1731–1740. doi: 10.2136/sssaj1988.03615995005200060040x

Yakir, D., and Israeli, Y. (1995). Reduced solar irradiance effects on net primary productivity (NPP) and the δ13C and δ18O values in plantations of *Musa* sp., *Musaceae*. *Geochim. Cosmochim. Acta* 59, 2149–2151. doi: 10.1016/s0016-7037(99)80010-6

Zamanian, K., Pustovoytov, K., and Kuzyakov, Y. (2016). Pedogenic carbonates: forms and formation processes. *Earth Sci. Rev.* 157, 1–17. doi: 10.1016/j.earscirev.2016.03.003

Zech, M., Zech, R., and Glaser, B. (2007). A 240,000-year stable carbon and nitrogen isotope record from a loess-like palaeosol sequence in the Tumara Valley, Northeast Siberia. *Chem. Geol.* 242, 307–318. doi: 10.1016/j.chemgeo.2007.04.002

Zens, J., Zeeden, C., Römer, W., Fuchs, M., Klasen, N., and Lehmkuhl, F. (2017). The Eltville Tephra (Western Europe) age revised: integrating stratigraphic and dating information from different last glacial loess localities. *Palaeogeogr. Palaeoclimatol. Palaeoecol.* 466, 240–251. doi: 10.1016/j.palaeo.2016.11.033

Zerboni, A., Trombino, L., and Cremaschi, M. (2011). Micromorphological approach to polycyclic pedogenesis on the Messak Settafet plateau (central Sahara): formative processes and palaeoenvironmental significance. *Geomorphology* 125, 319–335. doi: 10.1016/j.geomorph.2010.10.015

Zheng, S., and Shangguan, Z. (2007). Spatial patterns of leaf nutrient traits of the plants in the Loess Plateau of China. *Trees* 21, 357–370. doi: 10.1007/s00468-007-0129-z

Conflict of Interest: The authors declare that the research was conducted in the absence of any commercial or financial relationships that could be construed as a potential conflict of interest.

frontiers in Earth Science

BRIEF RESEARCH REPORT
published: 23 October 2020
doi: 10.3389/feart.2020.561207

Thinking Outside the Box at Open-Air Archeological Contexts: Examples From Loess Landscapes in Southeast Romania

Kathryn E. Fitzsimmons[1,2]*, *Adrian Doboş*[3], *Mathias Probst*[4] and *Radu Iovita*[5,6,4,2]

[1] Research Group for Terrestrial Palaeoenvironments, Max Planck Institute for Chemistry, Mainz, Germany, [2] Department of Human Evolution, Max Planck Institute for Evolutionary Anthropology, Leipzig, Germany, [3] Institute of Archaeology "Vasile Pârvan", Romanian Academy, Bucharest, Romania, [4] MONREPOS Archaeological Research Centre and Museum, Römisch-Germanisches Zentralmuseum, Leibniz Institute for Archaeology, Schloss Monrepos, Neuwied, Germany, [5] Center for the Study of Human Origins, Department of Anthropology, New York University, New York, United States of America, [6] Early Prehistory and Quaternary Ecology, Eberhard Karls University of Tübingen, Tübingen, Germany

Stratified, well preserved sites preserving unambiguous geological and archeological data from which human-environmental interactions can be reconstructed, are rare. More commonly we must test our hypotheses based on extrapolation of the few available sites, particularly in regions with high sedimentation rates. Here we test the idea of aggregating "off-sites"—human traces which provide isolated evidence of activity in an area—to maximize the information which can meaningfully be extracted from Paleolithic open-air contexts. We present two case studies from the sediment-rich loess steppe of southeast Romania, Lipniţa and Dealul Peşterica. Both off-sites preserve low density, undiagnostic lithic assemblages which may otherwise be overlooked in favor of more impressive sites. We constrain the timing of occupation at these two localities to c. 61 and 34–41 ka at Lipniţa and Dealul Peşterica, and show that people were present near a river bank and on loess slopes respectively. Aggregation of data from the region suggests repeated visitation of riverine landscapes; additionally people likely ranged across landforms, particularly where raw material for making stone tools was plentiful. Our case studies demonstrate that empirical, incremental findings may still be generated from sites traditionally thought to be of little value. We argue that this approach is highly applicable to investigating the human implications for landscape context from archeological traces in sediment-rich, open-air situations.

Keywords: loess, archeological prospection, catena, Dobrogea, Romania, Danube

OPEN ACCESS

Edited by:
Verena E. Foerster,
University of Cologne, Germany

Reviewed by:
Andrea Zerboni,
University of Milan, Italy
Nadia Solovieva,
University College London, United Kingdom

***Correspondence:**
Kathryn E. Fitzsimmons
k.fitzsimmons@mpic.de

Specialty section:
This article was submitted to Quaternary Science, Geomorphology and Paleoenvironment, a section of the journal Frontiers in Earth Science

Received: *11 May 2020*
Accepted: *03 September 2020*
Published: *23 October 2020*

Citation:
Fitzsimmons KE, Doboş A, Probst M and Iovita R (2020) Thinking Outside the Box at Open-Air Archeological Contexts: Examples From Loess Landscapes in Southeast Romania. Front. Earth Sci. 8:561207. doi: 10.3389/feart.2020.561207

INTRODUCTION

In the investigation of interactions between people and their habitats over deep time, we seek a convergence of archives with which we can reconstruct past settings wherein ancient people lived, and gain insights into their survival strategies and adaptations under such conditions. This represents a manifold challenge. Sites may be rare, poorly preserved or fragmentary, evidence may be ambiguous, or sites may simply not yet have been discovered due to lack of survey efforts or challenging physical or political environments (Versaggi and Hohman, 2008; Verhagen et al., 2013; Iovita et al., 2014; Tourloukis, 2016). Optimal sites, which preserve uneroded, superposed

stratigraphic layers containing unambiguous geological and archeological data, occur seldom. All too often we are forced to test our hypotheses based on extrapolation from small numbers of key sites. This problem is particularly acute in regions with substantial sediment supply, where high sedimentation rates often obscure traces of human activity (e.g., Morgan et al., 2011; Romanowska, 2012; Krajcarz et al., 2016; Iovita et al., in press). The reconstruction of human-environmental interactions in such landscapes becomes a case of "finding a needle in the haystack"; conventional approaches involving the excavation, analysis and dating of previously identified or surveyed stratified deposits, are rarely feasible.

In cases when the information which can be extracted out of a landscape appears minimal or suboptimal, it pays to think "outside the box." Here we consider the idea of "off-sites" (Bintliff, 2000), human traces which provide scattered, isolated or non-permanent evidence of activity in an area, as an alternative way to extract data. This approach offers an unprejudiced means of interpreting evidence which may not be optimal but nevertheless provides aggregate archeological and paleoenvironmental datasets, so producing incremental discoveries.

There are often compelling reasons for exploring challenging sediment-rich contexts for the information they provide about the human past. The lower Danube River basin provides a case in point. The Danube is, and has long been, a conduit for human migration and trade, from the Orient Express railway to the Byzantine and Ottoman invasions (e.g., Babinger, 1961; Stephenson, 1999), to the Neolithic expansions of the Holocene (Davison et al., 2006). The role of the Danube as a corridor for prehistoric humans into Europe remains an intriguing hypothesis. However, this concept is based on a small handful of sites at geographic endpoints of the proposed route (Conard and Bolus, 2003; Chu, 2018), coupled with paleoenvironmental data suggesting that the region represented a relatively mild refuge during glacial phases (Fitzsimmons et al., 2012; Obreht et al., 2017). Substantial and widespread volcanic ash deposits in the lower Danube catchment (Anechitei-Deacu et al., 2014; Veres et al., 2013), deriving from the Campanian Ignimbrite eruption coeval with modern human arrival into Europe and projected Neandertal extinction (Fedele et al., 2008), have further sparked animated debate (Lowe et al., 2012; Fitzsimmons et al., 2013). Despite recent attempts to locate additional archeological sites in the Danube corridor (Richter et al., 2012; Sitlivy et al., 2012; Iovita et al., 2014; Chu, 2018; Hauck et al., 2018; Mihailović, 2020), optimal sites in the conventional sense have been few (Schmidt et al., 2013; Schmidt et al., 2020) and have added little to substantiate the Paleolithic corridor hypothesis.

The aim of this study is to examine whether aggregating data from off-sites provides a useful perspective on sites of apparent little value, adding aggregate data to our understanding of this highly strategic area. We focus on two localities in Dobrogea loess steppe, located east and south of the lower Danube **Figure 1B**. Rather than interpreting the sparse lithic assemblages occurring at these sites, we view the human implications for the landscape context of their traces, and constrain the timing of human presence.

MATERIALS AND METHODS

Localities, Survey and Test Pits

The two localities discussed here, Lipniţa and Dealul Peşterica (DP), represent examples of archeological surveys undertaken in a landscape with thick sediment cover (Iovita et al., 2014). Small test pits (sondages) were dug to test the prospectivity of individual localities.

Lipniţa is a new locality (Iovita et al., 2014), previously unknown in the archeological literature with the exception of Neolithic tumuli found within the village of the same name (Papasima, 1993). The locality is a north-facing loess quarry northeast of the village and immediately south of the presently dry lower catchment of the Suha Reka (Bulgarian: "dry river"), which at this point forms an ephemeral channel (Canaraua Fetii; Telteu and Zaharia, 2012) linking three lakes connected to the Danube River (**Figure 1A**). Lipniţa lies at c. 30 m above sea level and 20 vertical meters above the Danube. Surface survey at this site identified a c. 50 cm diameter block of sediment which had detached from the lower part of the quarry profile. Since the consolidated block comprised two identifiable sediment types, its stratigraphic context could be related to the *in situ* sequence, providing confidence in the setting of two lithic fragments excavated from the block (**Supplementary Figures 1 and 2**). No sondages were dug at Lipniţa since permits were not available.

DP is a previously reported site (Nicolăescu-Plopşor et al., 1959; Păunescu et al., 1972; Păunescu, 1999) located in central Dobrogea, close to the watershed of a tributary flowing west into the Danube and adjacent the village of Pestera (**Figure 1C**). The altitude of this location (c. 39 m above sea level) is comparable with that of Lipniţa 40 km west-southwest. The Lower Paleolithic workshop site of Dealul Guran, which contains evidence for Upper Paleolithic exploitation of surface-exposed limestone flints (Iovita et al., 2012), is located on the hill opposite. The DP locality encompasses the west-facing hillslope and is a complex of small rockshelters, sandstone and limestone bluffs overlain by mixed loess and colluvium of variable thickness. Since lithic assemblages had been documented at this site and sediment had been removed from most of the exposed rockshelters through recent use, our study focused on Paleolithic hominin traces within the sediments. Four sondages were excavated in a transect along the slope to document catenary change in the sediments, stratigraphic marker horizons such as the Campanian Ignimbrite tephra, and the occurrence of lithic artifacts.

Lithic Finds

In this study we are primarily interested in the incidence of artifacts as evidence of human presence in the landscape. We summarize what is known about the lithic assemblages at the two sites in *Sedimentary Context of the Lipniţa Locality, and Antiquity of the Lithic Fragments* and *Age and Sedimentary Context of the Dealul Peşterica Finds*.

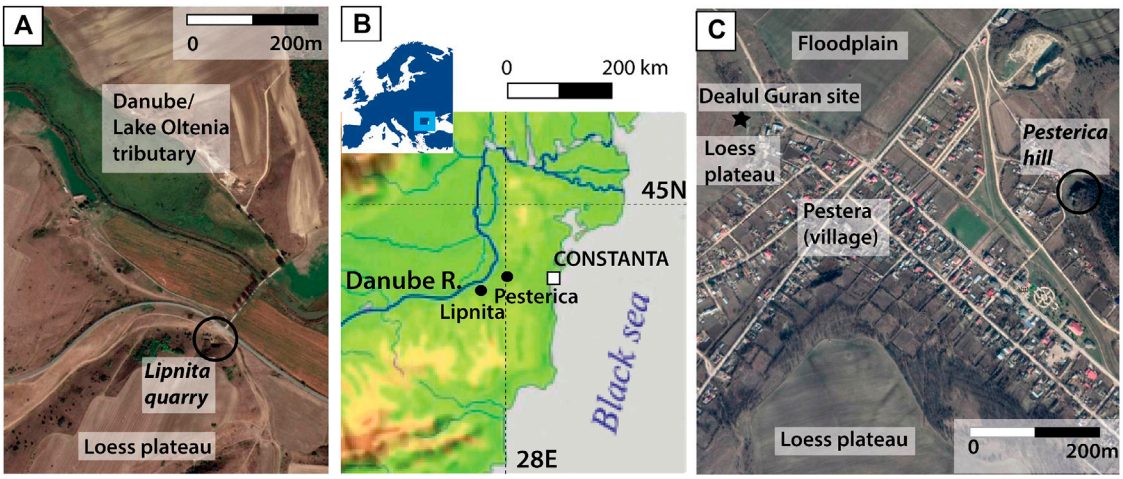

FIGURE 1 | Location and contexts of the two localities discussed in this study: **(A)**. Lipniţa quarry. **(B)**. Location of the Dobrogea region and the sites near the lower Danube river. **(C)**. Peşterica hill opposite the Lower Peolithic site of Dealul Guran.

At Lipniţa, only the two flakes found within the sediment block were identified. Both were embedded within red pedogenic sediment near the underlying contact with the basal fluvial gravels. Both lithics had relatively fresh surfaces, but were otherwise undiagnostic. No other lithics were found near the profile or on the surface of the loess plateau.

At DP, 187 lithic pieces (including 70 tools) collected from the surface by Păunescu (1999) were analyzed by Doboş (2010). Most of the retouched tools are non-cortical simple scrapers and thereby undiagnostic, although 3% bear similarity to Levallois technology. Artifacts found within the DP test excavations were recorded individually using measuring tape.

Luminescence Dating

Luminescence dating was undertaken to constrain the antiquity of the localities in question and, additionally at DP, to gain insight into the potential for relationships between artifacts along the catena. At DP, samples were collected by driving 10 cm long, 4 cm diameter stainless steel tubes horizontally into the excavated walls as close as possible to *in situ* lithics. The sediments in the shallow sondages three and four were unsuitable for dating due to bioturbation and were therefore not sampled. At Lipniţa, the block containing the lithic fragments was wrapped in plaster and transferred to the field station (**Supplementary Figures 1 and 2**), where the sediment was subsampled into blocks >10 cm in diameter for preparation in the laboratory. An additional, *in situ* tube sample was collected from the *in situ* lower red sediments directly in the profile at the stratigraphic equivalent of the block.

Samples were prepared for equivalent dose (D_e) measurement at the Max Planck Institute for Evolutionary Anthropology (Leipzig) under subdued red light. The sandy samples from Lipniţa were processed to extract the 180–212 μm quartz fraction for single-grain analysis according to published protocols (Fitzsimmons et al., 2014). The loessic DP sediments were processed to extract the 4–11 μm fine-grained fraction; the polymineral component was extracted following published protocols (Iovita et al., 2012), from which subsamples were etched to extract purified quartz (Timar et al., 2010). Further details relating to sample preparation and measurement can be found in the Supplementary. Dose rates were calculated based on beta counting, high resolution germanium gamma spectrometry (measured at VKTA in Dresden), published alpha dose-rate values (Rees-Jones and Tite, 1997) and cosmic ray dose rate formulae (Prescott and Hutton, 1994).

RESULTS

Luminescence Dating at Dealul Peşterica and Lipniţa

The quartz fine-grained samples from DP appear suitable for dating using the SAR protocol (**Supplementary Figures 6 and 7; Supplementary Table 1**) and yield OSL characteristics comparable with loess in the Dobrogea region (Timar et al., 2010; Fitzsimmons and Hambach, 2014; Constantin et al., 2015). By contrast, the polymineral fine-grained DP samples were less well suited to the pIR-IRSL protocol and likely subject to signal fading (further details in Supplementary). Consequently the pIR-IRSL age for the sondage one sample (EVA1192) is assumed to give a minimum estimate; quartz ages were used for the other DP samples (**Table 1**).

Sandy sediments from Dobrogea have rarely yielded reliable luminescence ages (Iovita et al., 2012; Anechitei-Deacu et al., 2014). However, the Lipniţa quartz sands produced good results (see **Supplementary Material**) which may be explained by a difference in sediment source from those investigated previously.

Table 1 summarizes the luminescence ages for the two localities. At DP, the age of the unit containing the lithic finds

TABLE 1 | Luminescence dating supporting data and age estimates for the sondages at Dealul Peşterica and both block and *in situ* samples from Lipniţa. Equivalent doses calculated using pIR-IRSL measurements on polymineral fine-grains (Buylaert et al., 2012) are shown in italics; those in plain text were measured using the SAR protocol on fine-grained quartz.

Sample code	Depth (m)	D_e (Gy)	Dose rates (attenuated; Gy/ka)				Age (ka)
			Beta	Gamma	Cosmic	Total	
Dealul Peşterica Sondage 1							
EVA1192	0.45 ± 0.05	*172 ± 9*	1.37 ± 0.14	0.99 ± 0.10	0.20 ± 0.03	3.33 ± 0.25	*51.6 ± 4.7*
Dealul Peşterica Sondage 2							
EVA1193	1.23 ± 0.05	142 ± 1	1.96 ± 0.20	1.27 ± 0.13	0.18 ± 0.01	3.91 ± 0.31	36.3 ± 2.9
EVA1194	0.87 ± 0.05	145 ± 2	1.99 ± 0.20	1.21 ± 0.12	0.19 ± 0.02	3.84 ± 0.28	37.8 ± 2.8
EVA1195	0.80 ± 0.05	145 ± 1	1.89 ± 0.19	1.22 ± 0.12	0.19 ± 0.02	3.76 ± 0.29	38.6 ± 3.0
Lipniţa							
EVA1196	3.57 ± 0.10	144 ± 13[a]	1.69 ± 0.17	1.03 ± 0.10	0.13 ± 0.01	3.28 ± 0.26	>44.0 ± 5.3*
EVA1197	3.57 ± 0.10	196 ± 21	1.77 ± 0.18	1.06 ± 0.11	0.13 ± 0.01	3.42 ± 0.28	57.4 ± 7.7
		221 ± 19					64.0 ± 7.6

[a]*Sample EVA1196 was calculated as a minimum age.*

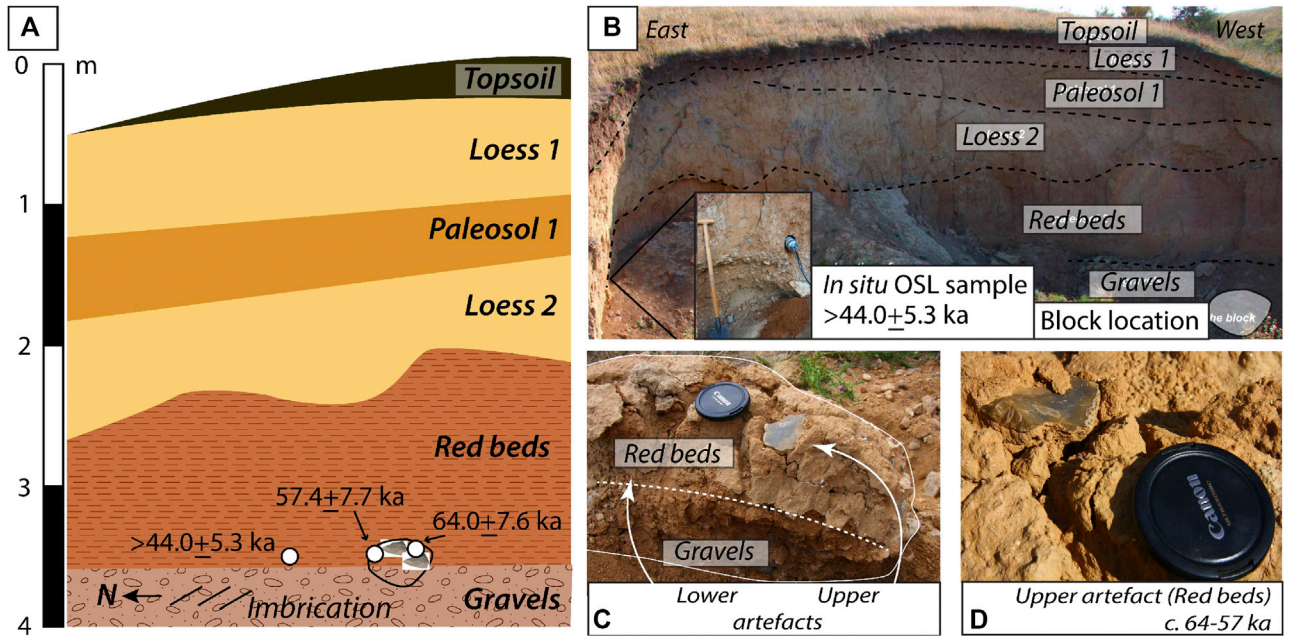

FIGURE 2 | Chronostratigraphic information for Lipniţa. **(A)**. Schematic overview of stratigraphy, dating and artifact context. **(B)**. View of the profile looking south. **(C)**. Sediment block with embedded artifacts. **(D)**. The upper artifact within the Red beds.

at sondage one is <51.6 ± 4.7 ka; at sondage two the deposition of lithics can be constrained to c. 34–41 ka (1σ). The Lipniţa artifacts are most likely c. 61 ka.

Sedimentary Context of the Lipniţa Locality, and Antiquity of the Lithic Fragments

Lipniţa is situated on the northern slope of a loess plateau adjacent the Suha Reka channel and its floodplain. Four major stratigraphic units, three of which include some degree of pedogenic development, are exposed within the profile (**Figures 2A,B**). Fluvial gravels at the base of the sequence include imbricated cobbles up to 7 cm diameter and indicate a northward flow direction, consistent with the present course of the Suha Reka. The size of larger clasts indicates a higher energy river than exists presently. Fluvial clasts are dominated by quartz and limestone, including flint-bearing calcareous material (Petrov and Yankov, 2017), infilled with a reddish clayey silt matrix similar to the overlying unit which may have been deposited during the initial stages of its deposition. We describe the overlying reddish clayey silts as "Red beds" (to disambiguate from the term paleosol used in Iovita et al., 2014). These unconformably overlie the basal gravels and comprise massive reddish clayey silts, minor sands, gravels and cobbles with some pedogenic development. The Red Beds are likely to be predominantly water-lain, with some eolian input, and may originally be derived from remobilization of

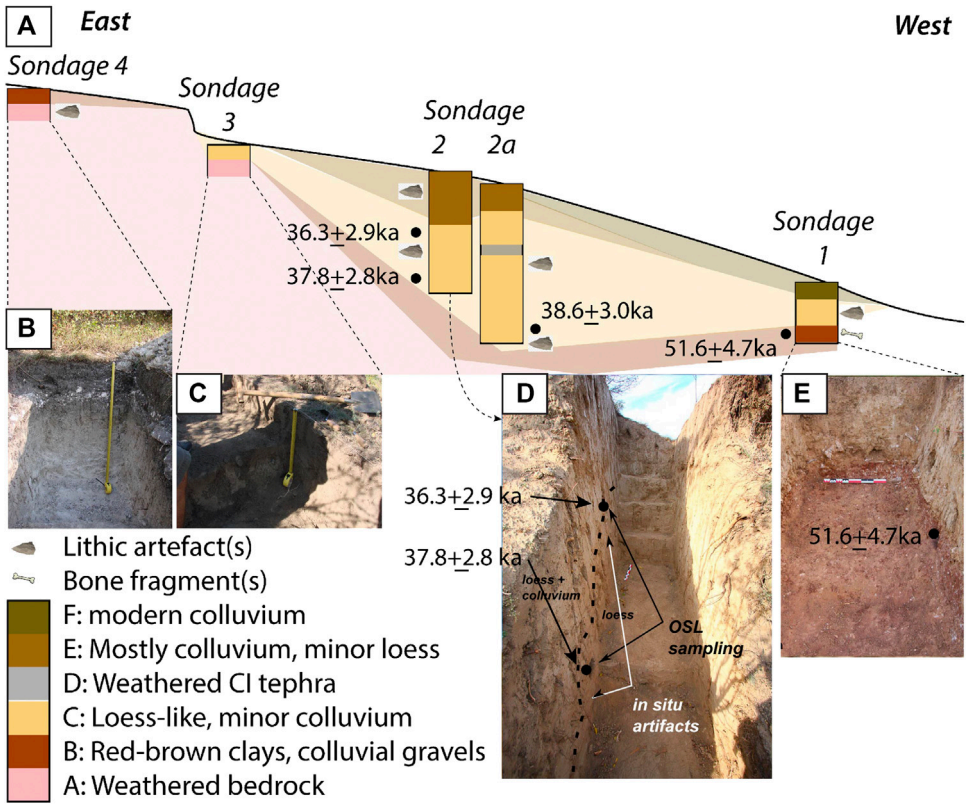

FIGURE 3 | Chronostratigraphic information for Dealul Peşterica. **(A)**. Overview of the stratigraphy and catenary relationships along the transect, including positions of artifacts and dating. **(B–E)**. Photographs of the four sondages.

Plio-Pleistocene clay-rich reposits found across the Danube Basin (Kovács et al., 2011). The Red Beds are unconformably overlain by two pale loess units, each with soil development, although there is nothing sufficiently distinctive about the loess or paleosols to justify correlation with the supra-regional stratigraphy (Fitzsimmons et al., 2012) without direct dating of the sediments. Unidentifiable bone fragments were observed at three places within the loess. The sequence at this locality indicates either progressive decrease in fluvial activity or lateral channel migration. The present-day ephemeral nature of the Suha Reka is due to deforestation within the catchment over 100 years ago; it now flows only during spring snow-melt or following major rainfall events (Telteu and Zaharia, 2012).

The two lithic fragments excavated from the block (**Figures 2C,D**) were found embedded within the Red beds just above the contact with the basal gravels. The profile sample yielded a minimum age of >44.0 ± 5.3 ka, whereas the two subsamples collected from the block produced ages of 57.4 ± 7.7 and 64.0 ± 7.6 ka (**Table 1**). These ages fall within error of one another and indicate an antiquity for the lithics of c. 61 ka.

Age and Sedimentary Context of the Dealul Peşterica Finds

The hillslope surface at DP comprises several catenary sequences which assist in piecing together both stratigraphy and context of the archeological traces. The DP stratigraphy can be grouped into six stratigraphic units (**Figure 3A**; **Supplementary Tables 5–9**).

The underlying bedrock, comprising Cretaceous calcareous sandstones and limestones (Avram et al., 1993), is exposed between sondages 3 and 4, and was observed in weathered form at both test pits (**Figures 3B,C**).

At the top and bottom of the hill, the bedrock is overlain by clays of varying color (unit B), most likely representing a still more weathered, unconsolidated component of *in situ* regolith. At the top of the hill, this unit is pale, with a higher proportion of sand derived from the glauconitic sandstones. By contrast, unit B at sondage 1 is reddish-brown, with a higher clay component and substantial inmixing of slope-deposited colluvium. Genetically, however, the two are related and can be linked in a catena downslope. Lithics and raw material are scattered on the surface and within unit B at the top of the slope. While flint chips are common in unit B at sondage 1, none could be clearly attributed to human agency. Two undiagnostic bone fragments

were also found in Unit B. This unit dates to at least 51.6 ± 4.7 ka (**Figure 3E**).

The mid-slope is dominated by pale, massive beige loess-like sediment, thicker on the northern slope than on the west and south, with colluvial clasts of flint and sandy limestone increasing in density downslope. This unit (C) dominates the sondages at position 2, and is thinner, and more colluvium-rich, in sondages 1 and 3 due to slope aspect and position along the slope. Flint fragments were found at low density within this unit, including five which could be confidently attributed to human activity at sondage 2, and four in sondage 1. Three ages, spanning 38.6 ± 3.0 to 36.3 ± 3.9 ka (**Figures 3A,D**), indicate rapid deposition of sediment at this time. At a side trench (sondage 2a), a thin, discontinuous weathered tephra was observed, interpreted to be the Campanian Ignimbrite; its known age (39.28 ± 0.11 ka; De Vivo et al., 2001) lies within uncertainty of the OSL ages.

Unit C is overlain at sondage 2 by a darker beige stratum (unit E) comprising a mix of colluvium and loess, dominated by the former. Two lithics attributed to human activity were observed within this unit, although evidence for substantial bioturbation in unit E prevented reliable luminescence sampling. The uneven contact between Units C and E suggests a short-lived erosional event followed by increasing dominance of slope deposition. Mass movement continues on the lower slopes as demonstrated by c. 20 cm of modern colluvium at Sondage 1.

DISCUSSION

Human use of Riverine Landscapes, but Not as Early as Thought: Lipniţa

According to conventional archeological thinking, the occurrence of two lithic artifacts at Lipniţa barely qualifies it as a site, although the actual artifact density could be much greater following future excavation. Through the unprejudiced perspective of off-sites, we may draw a number of conclusions from Lipniţa.

We may deduce that humans were present in the riparian landscape of the Suha Reka approximately c. 61 kyr ago. The artefact-bearing Red beds indicate a lower energy stream or swampy environment deposited during cool stadial conditions of marine isotope stage (MIS) 4, which succeeded a warm, wet interglacial. Transition from a high to lower energy stream is visible in the stratigraphy at Lipniţa, and is compatible with reduced hydrologic activity associated with the MIS4 stadial. In southeastern Romania, there is evidence at this time for spatially discontinuous peaks in loess accumulation (Timar-Gabor et al., 2011; Vasiliniuc et al., 2011; Constantin et al., 2014; Fitzsimmons, 2017), although dust deposition at Lipniţa initiated later.

The fresh surfaces of and lack of patina on the two lithics suggest that the artifacts were not fluvially transported but rather either discarded *in situ* (e.g., Delpiano et al., 2019), or transported only a very short distance. Given that flint cobbles up to 7 cm diameter are present in the basal gravels, it is possible that these provided the raw material for flake production, although flint outcrops are common in the karst gorge upstream.

The c. 61 ka age of the Lipniţa lithics is younger than anticipated. The paleosol preserved between the two loess units bears similarity to MIS5 interglacial loess soils (Fitzsimmons et al., 2012), and Iovita et al. (2014) surmised that deposition of the Red beds, and their artifacts predated MIS5. In this respect we can only emphasize the importance of direct dating.

We cannot infer much more about human behavior in this area without further excavation, however we can aggregate information about the distribution of people across the landscape at a given time. Another open-air locality of similar antiquity, yielding ca. 1,300 surface lithics, is Cuza Vodă E (Păunescu, 1999), 60 km northeast of Lipniţa. *In situ* lithic material at Cuza Vodă, also found at the contact with fluvial red beds, date to c. 95–55 ka (Iovita et al., 2014). Intriguingly, both environmental context and age are similar. Cuza Vodă site lies just north of the palaeo-Carasu River, another Dobrogea tributary of the Danube (Zaharia and Pisota, 2003). At this stage there are no other known localities of this age in Dobrogea, but incremental aggregation of datasets like these may eventually yield more useful information about human habitat preferences.

The Human Catena, and Life in Open-air Contexts: Dealul Peşterica

Unlike Lipniţa, DP is a reported site with at least 70 tools, albeit very few of which resemble known technocomplexes (Doboş, 2010). Our sondages confirmed a further nine lithics altered by human agency along the slope, further establishing human presence in the area in the deep past. Through an orthodox archeological lens, however, the density of lithics is low and more consistent with an off-site. Considering these traces nevertheless provides new avenues for understanding human use of the landscape.

Here we invoke the catena concept for understanding the stratigraphy at DP, its archeological traces, and their antiquity. A catena is a sequence of soil profiles of varying characteristics that occur down a slope, and sometimes contains Paleolithic finds (Łanczont et al., 2015). At least two catenas can be identified at DP: units B and C. Unit B is discontinuous, since it was observed only at the top and bottom of the slope. We conclude that the bone and lithic fragments in unit B at the base of the hill, dated to 51.6 ± 4.7 ka (or possibly slightly older), are likely the same age as those found in its equivalent on the hilltop. Although none of the artifacts found *in situ* within this unit are recognisable tools, and they are certainly lithic manuports, it is interesting that the timing of deposition of this unit closely postdates human presence at Lipniţa.

Greater meaning can be derived from in the overlying loessic unit C. The character of this unit likewise varies along slope, nevertheless its stratigraphic position remains consistent. We can argue that unit C dates to c. 41–34 ka, within interstadial MIS3. Furthermore, at least two visits by people—demonstrated by two lithics found below the tephra—shortly predate the Campanian Ignimbrite super-eruption which may have substantially impacted on people in the region (Fitzsimmons et al., 2013). As yet, there are few known archeological sites in Dobrogea dating to this time, with the exception of Cheia–La Izvor, which dates to c. 40 kcal BP (Păunescu, 1999). Most of the Paleolithic finds in Dobrogea

(>100 loci) derive from surface find spots, ranging from 1 to >100 pieces (Păunescu, 1999; Doboş et al., 2005; Iovita et al., 2014). The few sites with stratigraphy vary in assemblage size, depending on the site function. In the absence of ideal sites, an incremental approach which places human presence on the map (e.g., Delpiano et al., 2019) removes some uncertainty regarding human occupation at the gateway to Europe at this critical time.

Our approach allows tentative steps toward understanding the nature of Paleolithic mobility and taskscape (Ingold, 1993). The entire hillslope of DP yields evidence for human presence. Sub-millimeter air pockets within unit C at the mid-slope indicate rapid deposition; coupled with low artifact density, we may infer infrequent visitation of the area by people rather than continuous occupation. Examinations of vast surface records in Australia (Holdaway and Davies, 2019) and Egypt (Olszewski et al., 2010) have shown that many activities involving the use of stone tools takes place off-"site," although such loci of activity are rarely captured in environments with high sedimentation rates. One could argue that rather than confining themselves to a defined occupational area, people ranged over landscape scales, particularly where raw material for making stone tools was plentiful (e.g., Iovita et al., 2012). Such observations, while intuitive, are rarely supported by evidence (but see Zerboni et al., 2015; Delpiano et al., 2019, for a similar case in northern Italy). At DP, we may start to build a case for this hypothesis.

Applicability of Off-Sites to Geoarcheology in Challenging Open-air Situations

In reality, few sites provide all details sought for meaningful integration between paleoenvironmental and archeological datasets. However, in the search for localities, information from less impressive, ephemeral contexts may be overlooked (see also Foley, 1981; Glauberman, 2006). Here we argue for more careful consideration of the latter. Understanding Paleolithic mobility at landscape scales requires both nodes of dense interaction (sites) and networks of taskscape traces (Rezek et al., 2020).

Using case studies from the understudied, yet highly strategic region of Dobrogea, we demonstrate that empirical, incremental conclusions may still be drawn from sites typically thought to be of little value. Geochronology is an essential tool both for marking the presence of people at key times and for refuting chronologies inferred from regional correlations. Particularly in sediment-rich open-air contexts, people likely ranged over large areas particularly when raw material for making stone tools was widespread as in Dobrogea. We suggest that aggregating information from off-sites can further help us understand the human implications for landscape context through their traces.

DATA AVAILABILITY STATEMENT

The datasets generated by this study can be found in Edmond, the Open Access Data Repository of the Max Planck Society (https://edmond.mpdl.mpg.de).

AUTHOR CONTRIBUTIONS

KF conceived of the presented ideas in this study; RI developed the Lower Danube Survey for Paleolithic Sites project as a whole. RI and AD oversaw the archeological fieldwork, which was undertaken by AD, MP, and RI. Interpretation of the archeological results was undertaken by AD and RI. KF undertook the geological fieldwork and laboratory analyses. KF wrote the first draft of the manuscript. All authors contributed to manuscript revision, read and approved the submitted version.

FUNDING

The field and laboratory components of this study were funded by the Max Planck Institute for Evolutionary Anthropology as part of the Lower Danube Survey for Paleolithic Sites (LoDanS).

ACKNOWLEDGMENTS

The authors thank Professor J.-J Hublin and S. McPherron for their support of the Lower Danube Survey for Paleolithic sites project. Fieldwork was undertaken according to Romanian law and within the terms of permit 1/2011 granted by the Ministry of Culture of Romania (permit holders R. Dobrescu, V. V. Zirra, Institute of Archaeology "Vasile Pârvan" of the Romanian Academy), with German partners the Max Planck Institute for Evolutionary Anthropology and Römisch-Germanisches Zentralmuseum Mainz (RGZM-Monrepos). Thanks to S. Hesse for her assistance with luminescence dating sample preparation, and to students from the prehistory programme at the Johannes Gutenberg University Mainz for their assistance in the field.

SUPPLEMENTARY MATERIAL

The Supplementary Material for this article can be found online at: https://www.frontiersin.org/articles/10.3389/feart.2020.561207/full#supplementary-material

REFERENCES

Anechitei-Deacu, V., Timar-Gabor, A., Fitzsimmons, K., Veres, D., and Hambach, U. (2014). Multi-method luminescence investigations on quartz grains of different sizes extracted from a loess section in Southeast Romania interbedding the Campanian Ignimbrite ash layer. *Geochronometria* 41, 1–14. doi:10.2478/s13386-013-0143-4

Avram, E., Szasz, L., Antonescu, E., Baltreš, A., Iva, M., Melinte, M., et al. (1993). Cretaceous terrestrial and shallow marine deposits in northern South Dobrogea (SE Rumania). *Cretac. Res.* 14 (3), 265–305. doi:10.1006/cres.1993.1022

Bintliff, J. L. (2000). "The concepts of "site" and "off-site" archaeology in surface artefact survey," in *Non-destructive techniques applied to landscape Archaeology: The Archaeology of Mediterranean landscapes*. Editors M. Pasquinucci and F. Trément (Oxford, UK: Oxbow Books), Vol. 4, 200–215.

Buylaert, J.-P., Jain, M., Murray, A. S., Thomsen, K. J., Thiel, C., and Sohbati, R. (2012). A robust feldspar luminescence dating method for Middle and Late Pleistocene sediments. *Boreas* 41 (3), 435–451. doi:10.1111/j.1502-3885.2012.00248.x

Chu, W. (2018). The Danube corridor hypothesis and the Carpathian basin: geological, environmental and archaeological approaches to Characterizing Aurignacian dynamics. *J. World Prehist.* 31, 117–178. doi:10.1007/s10963-018-9115-1

Conard, N. J., and Bolus, M. (2003). Radiocarbon dating the appearance of modern humans and timing of cultural innovations in Europe: new results and new challenges. *J. Hum. Evol.* 44 (3), 331–371. doi:10.1016/s0047-2484(02)00202-6

Constantin, D., Begy, R., Vasiliniuc, S., Panaiotu, C., Necula, C., Codrea, V., et al. (2014). High-resolution OSL dating of the Costineşti section (Dobrogea, SE Romania) using fine and coarse quartz. *Quat. Int.* 334-335, 20–29. doi:10.1016/j.quaint.2013.06.016

Constantin, D., Cameniță, A., Panaiotu, C., Necula, C., Codrea, V., and Timar-Gabor, A. (2015). Fine and coarse-quartz SAR-OSL dating of last glacial loess in southern Romania. *Quat. Int.* 357, 33–43. doi:10.1016/j.quaint.2014.07.052

Davison, K., Dolukhanov, P., Sarson, G. R., and Shukurov, A. (2006). The role of waterways in the spread of the Neolithic. *J. Archaeol. Sci.* 33, 641–652. doi:10.1016/j.jas.2005.09.017

De Vivo, B., Rolandi, G., Gans, P. B., Calvert, A., Bohrson, W. A., Spera, F. J., et al. (2001). New constraints on the pyroclastic eruptive history of the Campanian volcanic Plain (italy). *Mineral. Petrol.* 73, 47–65.

Delpiano, D., Peresani, M., Bertola, S., Cremaschi, M., and Zerboni, A. (2019). Lashed by the wind: short-term middle palaeolithic occupations within the loess-palaeosoil sequence at Monte Netto (northern Italy). *Quat. Int.* 502, 137–147. doi:10.1016/j.quaint.2019.01.026

Doboş, A. (2010). *Paleoliticul mijlociu de pe teritoriul de la sud si sud-est de Carpati (Oltenia, Muntenia, Dobrogea) (in Romania)*. Bucharest, Romania: Institute of Archaeology "Vasile Pârvan", 289.

Doboş, A., Iacob, M., and Paraschiv, D. (2005). Paleolithic discoveries in northern Dobrogea. *Prehistoric Studies* 2, 215–219 [in Romanian, with English summary].

Doboş, A., and Iovita, R. (2016). "The lower paleolithic of Romania revisited: new evidence from the site of Dealul Guran," in *Paleoanthropology of the Balkans and Anatolia*. Editors K. Harvati and M. Roksandic (Dordrecht, Netherlands: Springer Netherlands), 171–186.

Fedele, F. G., Giaccio, B., and Hajdas, I. (2008). Timescales and cultural process at 40,000BP in the light of the Campanian ignimbrite eruption, Western Eurasia. *J. Hum. Evol.* 55 (5), 834–857. doi:10.1016/j.jhevol.2008.08.012

Fitzsimmons, K., Hambach, U., Veres, D., and Iovita, R. (2013). The Campanian Ignimbrite eruption: new data on volcanic ash dispersal and its potential impact on human evolution. *PloS One* 8 (6), e65839. doi:10.1371/journal.pone.0065839

Fitzsimmons, K. E. (2017). Reconstructing palaeoenvironments on desert margins: new perspectives from Eurasian loess and Australian dry lake shorelines. *Quat. Sci. Rev.* 171, 1–19. doi:10.1016/j.quascirev.2017.05.018

Fitzsimmons, K. E., and Hambach, U. (2014). Loess accumulation during the last glacial maximum: evidence from Urluia, southeastern Romania. *Quat. Int.* 334–335, 74–85. doi:10.1016/j.quaint.2013.08.005

Fitzsimmons, K. E., Marković, S. B., and Hambach, U. (2012). Pleistocene environmental dynamics recorded in the loess of the middle and lower Danube basin. *Quat. Sci. Rev.* 41, 104–118. doi:10.1016/j.quascirev.2012.03.002

Fitzsimmons, K. E., Stern, N., and Murray-Wallace, C. V. (2014). Depositional history and archaeology of the central Lake Mungo lunette, Willandra Lakes, southeast Australia. *J. Archaeol. Sci.* 41, 349–364. doi:10.1016/j.jas.2013.08.004

Foley, R. A. (1981). "Off-site archaeology: an alternative approach for the short-sited," in *Pattern of the past: studies in honour of David Clarke*. Editor N. Harmond (Cambridge, UK: Cambridge University Press), 157–183.

Glauberman, P. (2006). "Excavating surface sites, tapping a source of potential: the Middle Palaeolithic surface scatters of southern Limburg (NL) and the case study of Colmont-Ponderosa," in *Preserving the early past: investigation, selection and preservation of palaeolithic and mesolithic sites and landscapes, Nederlandse Archeologische Rapporten*. Editors E. Rensink and H. Peeters (Amersfoort, Netherlands: National Service for Archaeological Heritage), 87–106.

Hauck, T. C., Lehmkuhl, F., Zeeden, C., Bösken, J., Thiemann, A., and Richter, J. (2018). The Aurignacian way of life: Contextualizing early modern human adaptation in the Carpathian Basin. *Quat. Int.* 485, 150–166. doi:10.1016/j.quaint.2017.10.020

Holdaway, S. J., and Davies, B. (2019). Surface stone artifact scatters, settlement patterns, and new methods for stone artifact analysis. *Journal of Paleo. Arch.* 1–21. doi:10.1007/s41982-019-00030-8

Ingold, T. (1993). The temporality of the landscape. *World Archaeol.* 25, 152–174. doi:10.1080/00438243.1993.9980235

Iovita, R., Doboş, A., Fitzsimmons, K. E., Probst, M., Hambach, U., Robu, M., et al. (2014). Geoarchaeological prospection in the loess steppe: preliminary results from the lower Danube survey for paleolithic sites (LoDanS). *Quat. Int.* 351, 98–114. doi:10.1016/j.quaint.2013.05.018

Iovita, R., Fitzsimmons, K. E., Doboş, A., Hambach, U., Hilgers, A., and Zander, A., (2012). Dealul Guran: evidence for Lower Palaeolithic (MIS 11) occupation of the Lower Danube loess steppe. *Antiquity* 86, 973–989. doi:10.1017/s0003598x00048195

Iovita, R., Varis, A., Namen, A., Cuthbertson, P., Taimagambetov, Z., and Miller, C. E. (Forthcoming 2020). In search of a paleolithic silk road in Kazakhstan. *Quat. Int.* doi:10.1016/j.quaint.2020.02.023

Kovács, J., Fábián, S. Á., Varga, G., Újvári, G., Varga, G., and Dezso, J. (2011). Plio-Pleistocene red clay deposits in the Pannonian basin: a review. *Quat. Int.* 240 (1-2), 35–43. doi:10.1016/j.quaint.2010.12.013

Krajcarz, M. T., Kot, M., Pavlenok, K., Fedorowicz, S., Krajcarz, M., Lazarev, S. Y., et al. (2016). Middle Paleolithic sites of Katta Sai in western Tian Shan piedmont, Central Asiatic loess zone: Geoarchaeological investigation of the site formation and the integrity of the lithic assemblages. *Quat. Int.* 399, 136–150. doi:10.1016/j.quaint.2015.07.051

Łanczont, M., Madeyska, T., Sytnyk, O., Bogucki, A., Komar, M., Nawrocki, J., et al. (2015). Natural environment of MIS 5 and soil catena sequence along a loess slope in the Seret River valley: evidence from the Pronyatyn Palaeolithic site (Ukraine). *Quat. Int.* 365, 74–97.

Lowe, J., Barton, N., Blockley, S., Ramsey, C. B., Cullen, V. L., Davies, W., et al. (2012). Volcanic ash layers illuminate the resilience of Neanderthals and early modern humans to natural hazards. *Proc. Natl. Acad. Sci. Unit. States Am.* 109(34), 13532–13537. doi:10.1073/pnas.1204579109

Mihailović, D. (2020). Push-and-pull factors of the middle to upper paleolithic transition in the balkans. *Quat. Int.* 551, 47–62. doi:10.1016/j.quaint.2019.10.010

Morgan, C., Barton, L., Bettinger, R., Chen, F., and Dongju, Z. (2011). Glacial cycles and palaeolithic adaptive variability on China's Western Loess Plateau. *Antiquity* 85, 365–379. doi:10.1017/s0003598x00067818

Murray, A. S., and Wintle, A. G. (2000). Luminescence dating of quartz using an improved single-aliquot regenerative-dose protocol. *Radiat. Meas.* 32 (1), 57–73. doi:10.1016/s1350-4487(99)00253-x

Neagu, F. (1961). *Die Donau als Schicksalsstrom des Osmanenreiches*. (Munich, Germany: Südosteuropa-Jahrbuch), 5, 15–27 [in German].

Nicolăescu-Plopşor, C. S., Păunescu, A., and Bolomey, A. (1959). Raport preliminar asupra cercetarilor paleolitice din anul 1956. *Materiale si cercetari arheologice* 5, 15–43 [in Romanian]. doi:10.3406/mcarh.1959.1129

Obreht, I., Hambach, U., Veres, D., Zeeden, C., Bösken, J., Stevens, T., et al. (2017). Shift of large-scale atmospheric systems over Europe during late MIS 3 and implications for Modern Human dispersal. *Sci. Rep.* 7, 5848. doi:10.1038/s41598-017-06285-x

Olszewski, D. I., Dibble, H. L., McPherron, S. P., Schurmans, U. A., Chiotti, L., and Smith, J. R. (2010). Nubian Complex strategies in the Egyptian high desert. *J. Hum. Evol.* 59, 188–201. doi:10.1016/j.jhevol.2010.06.001

Papasima, T. (1993). *Cronica cercetărilor arheologice din românia, Campania 1983 - 1992*. Bucharest, Romania: CIMEC - institutul de Memorie Culturala.

Păunescu, A. (1999). *Paleoliticul si Mezoliticul de pe teritoriul Dobrodgei*. Bucharest, Romania: Editura Satya Sai [in Romanian].

Păunescu, A., Mogosanu, F., and Cârciumaru, M. (1972). Unele considerat¸ii privind paleoliticul mijlociu din Dobrogea. *Pontica* 5, 11–28 [in Romanian].

Petrov, G., and Yankov, R. (2017). ПРИМЕРЕН ГЕОГРАФСКИ ПОДЧОД ПРИ РАЗРАБОТВАНЕТО НА ПРОГНОЗЕН АРЧЕОЛОГИцЕСКИ МОДЕЛ (An exemplary geographic approach to developing a predicative archaeological model). ЕПОЧИ *(Epochs)* 1, 120–127 [in Bulgarian, with English summary].

Prescott, J. R., and Hutton, J. T. (1994). Cosmic ray contributions to dose rates for luminescence and ESR dating: large depths and long-term time variations. *Radiat. Meas.* 23, 497–500. doi:10.1016/1350-4487(94)90086-8

Rees-Jones, J., and Tite, M. S. (1997). Optical dating results for British archaeological sediments. *Archaeometry* 39, 177–187. doi:10.1111/j.1475-4754.1997.tb00797.x

Rezek, Z., Holdaway, S. J., Olszewski, D. I., Lin, S. C., Douglass, M., McPherron, S. P., et al. (2020). Aggregates, formational emergence, and the focus on practice in stone artifact archaeology. *J. Archaeol. Method Theor.* 1–42.

Richter, J., Hauck, T., Vogelsang, R., Widlok, T., Le Tensorer, J.-M., and Schmid, P. (2012). "Contextual areas" of early *Homo sapiens* and their significance for human dispersal from Africa into Eurasia between 200 ka and 70 ka. *Quat. Int.* 274, 5–24. doi:10.1016/j.quaint.2012.04.017

Romanowska, I. (2012). "Lower Palaeolithic of central and Eastern Europe: critical evaluation of the current state of knowledge," in *Unravelling the palaeolithic. 10 years of research at the Centre for the Archaeology of human origins (British archaeological Reports)*. Editors K. Ruebens, I. Romanowska, and R. Bynoe (Oxford, UK: Archaeopress), 1–12.

Schmidt, C., Anghelinu, M., Hambach, U., Veres, D., and Lehmkuhl, F. (2020). Reassessing the timeframe of upper palaeolithic deposits in the Ceahlău basin (Eastern Carpathians, Romania): Geochronological and archaeological implications. *Quat. Geochronol.* 55, 101020. doi:10.1016/j.quageo.2019.101020

Schmidt, C., Sitlivy, V., Anghelinu, M., Chabai, V., Kels, H., Uthmeier, T., et al. (2013). First chronometric dates (TL and OSL) for the Aurignacian open-air site of Românești-Dumbrăvița I, Romania. *J. Archaeol. Sci.* 40 (10), 3740–3753. doi:10.1016/j.jas.2013.04.003

Sitlivy, V., Chabai, V. P., Anghelinu, M., Uthmeier, T., Kels, H., Hilgers, A., et al. (2012). The earliest Aurignacian in Romania: new investigations at the open air site of Românești-Dumbrăvița I (Banat). *Quartär* 59, 85–130.

Stephenson, P. (1999). "The byzantine frontier at the lower Danube in the late tenth and eleventh Centuries," in *Frontiers in question: eurasian Borderlands, 700–1700*. Editors D. Power and N. Standen (London, UK: Macmillan Education UK), 80–104.

Telteu, C.-E., and Zaharia, L. (2012). Morphometrical and dynamical features of the South Dobrogea lakes, Romania. *Procedia Environmental Sciences* 14, 164–176. doi:10.1016/j.proenv.2012.03.016

Timar, A., Vandenberghe, D., Panaiotu, E. C., Panaiotu, C. G., Necula, C., Cosma, C., et al. (2010). Optical dating of Romanian loess using fine-grained quartz. *Quat. Geochronol.* 5 (2-3), 143–148. doi:10.1016/j.quageo.2009.03.003

Timar Gabor, A., Vandenberghe, D., Vasiliniuc, S., Panaiotu, C., Panaiotu, C., Dimofte, D., et al. (2011). Optical dating of Romanian loess: a comparison between silt-sized and sand-sized quartz. *Quat. Int.* 240 (1-2), 62–70. doi:10.1016/j.quaint.2010.10.007

Tourloukis, V. (2016). "On the spatio-temporal distribution of Mediterranean lower paleolithic sites: a Geoarchaeological perspective," in *Paleoanthropology of the Balkans and Anatolia: human evolution and its context, vertebrate paleobiology and paleoanthropology*. Editors K. Harvati and M. Roksandic (Dordrecht, Netherlands: Springer Netherlands), 303–323.

Vasiliniuc, Ş., Timar-Gabor, A., Vandenberghe, D. A. G., Panaiotu, C. G., Begy, R., and Cosma, C. (2011). A high resolution optical dating study of the Mostiștea loess-palaeosol sequence (SE Romania) using sand-sized quartz. *Geochronometria* 38 (1), 34–41.

Veres, D., Lane, C. S., Timar-Gabor, A., Hambach, U., Constantin, D., Szakács, A., et al. (2013). The Campanian Ignimbrite/Y5 tephra layer - a regional stratigraphic marker for isotope Stage 3 deposits in the Lower Danube region, Romania. *Quat. Int.* 293, 22–33. doi:10.1016/j.quaint.2012.02.042

Verhagen, P., Rensink, E., Bats, M., and Crombé, P. (2013). Establishing discovery probabilities of lithic artefacts in Palaeolithic and Mesolithic sites with core sampling. *J. Archaeol. Sci.* 40, 240–247. doi:10.1016/j.jas.2012.05.041

Versaggi, N. M., and Hohman, C. D. (2008). Small lithic sites: linking significance with context. Current approaches to the analysis and interpretation of small lithic sites in the northeast, 175–186.

Zaharia, L., and Pisota, I. (2003). "Apele dobrogei," in: *Geografie*. Bucharest, Romania: Analele Universitatii Bucuresti, 107–144 [in Romanian].

Zerboni, A., Trombino, L., Frigerio, C., Livio, F., Berlusconi, A., Michetti, A. M., et al. (2015). The loess-paleosol sequence at Monte Netto: a record of climate change in the Upper Pleistocene of the central Po Plain, northern Italy. *J. Soils Sediments* 15, 1329–1350. doi:10.1007/s11368-014-0932-2

Conflict of Interest: The authors declare that the research was conducted in the absence of any commercial or financial relationships that could be construed as a potential conflict of interest.

NOMENCLATURE

D_e equivalent dose

DP Dealul Peşterica (locality)

OSL Optically stimulated luminescence

pIR-IRSL Post-InfraRed InfraRed Stimulated Luminescence

frontiers in Earth Science

ORIGINAL RESEARCH
published: 03 December 2020
doi: 10.3389/feart.2020.585770

Holocene Hydroclimate Variability and Vegetation Response in the Ethiopian Highlands (Lake Dendi)

Andrea Jaeschke[1], Matthias Thienemann[1], Enno Schefuß[2], Jonas Urban[3], Frank Schäbitz[3], Bernd Wagner[1] and Janet Rethemeyer[1]*

[1]*Institute of Geology and Mineralogy, University of Cologne, Cologne, Germany,* [2]*MARUM-Center for Marine Environmental Sciences, University of Bremen, Bremen, Germany,* [3]*Institute of Geography Education, University of Cologne, Cologne, Germany*

Northern Africa's past climate is characterized by a prolonged humid period known as the African Humid Period (AHP), giving origin to the "Green Sahara" and supporting human settlements into areas that are now desert. The spatial and temporal extent of climate change associated with the AHP is, however, subject to ongoing debate. Uncertainties arise from the complex nature of African climate, which is controlled by the strength and interactions of different monsoonal systems, resulting in meridional shifts in rainfall belts and zonal movements of the Congo Air Boundary. Here, we examine a ~12,500-years record of hydroclimate variability from Lake Dendi located in the Ethiopian highlands based on a combination of plant-wax-specific hydrogen (δD) and carbon ($\delta^{13}C$) isotopes. In addition, pollen data from the same sediment core are used to investigate the response of the regional vegetation to changing climate. Our δD record indicates high precipitation during peak AHP (ca. 10 to 8 ka BP) followed by a gradual transition toward a drier late Holocene climate. Likewise, vegetation cover changed from predominant grassland toward an arid montane forest dominated by *Juniperus* and *Podocarpus* accompanied by a general reduction of understory grasses. This trend is corroborated by $\delta^{13}C$ values pointing to an increased contribution of C_3 plants during the mid-to late Holocene. Peak aridity occurred around 2 ka BP, followed by a return to a generally wetter climate possibly linked to enhanced Indian Ocean Monsoon strength. During the last millennium, increased anthropogenic activity, i.e., deforestation and agriculture is indicated by the pollen data, in agreement with intensified human impact recorded for the region. The magnitude of δD change (40‰) between peak wet conditions and late Holocene aridity is in line with other regional δD records of East Africa influenced by the CAB. The timing and pace of aridification parallels those of African and Indian monsoon records indicating a gradual response to local insolation change. Our new record combining plant-wax δD and $\delta^{13}C$ values with pollen highlights the sensitive responses of the regional vegetation to precipitation changes in the Ethiopian highlands.

Keywords: African Humid Period, Ethiopia, Lake Dendi, n-alkanes, δD, $\delta^{13}C$, pollen

OPEN ACCESS

Edited by:
David K. Wright,
University of Oslo, Norway

Reviewed by:
Nadia Solovieva,
University College London,
United Kingdom
Chengyu Weng,
Tongji University, China

****Correspondence:***
Andrea Jaeschke
andrea.jaeschke@uni-koeln.de

Specialty section:
This article was submitted to Quaternary Science, Geomorphology and Paleoenvironment, a section of the journal Frontiers in Earth Science

Received: *21 July 2020*
Accepted: *11 November 2020*
Published: *03 December 2020*

Citation:
Jaeschke A, Thienemann M, Schefuß E, Urban J, Schäbitz F, Wagner B and Rethemeyer J (2020) Holocene Hydroclimate Variability and Vegetation Response in the Ethiopian Highlands (Lake Dendi). Front. Earth Sci. 8:585770. doi: 10.3389/feart.2020.585770

1. INTRODUCTION

North Africa experienced extreme climatic variations during the Holocene with a prolonged humid period known as the African Humid Period (AHP), which had major consequences for terrestrial ecosystems and ancient civilizations (see recent review by Pausata et al., 2020). During this humid period, increased Northern Hemisphere (NH) summer insolation induced the northward extension and intensification of the tropical rainbelt (Gasse, 2000; Lézine et al., 2011a). Remains of large palaeo-lakes and -estuaries across northern Africa record the substantially altered hydroclimate during the AHP, which transformed the Saharan desert into an open grass savannah and allowed for widespread human occupation of nowadays mostly barren landscapes (Lézine et al., 1990; Kuper and Kröpelin, 2006; Kröpelin et al., 2008; Sereno et al., 2008; Tierney et al., 2017; Höpker et al., 2019). The subsequent return to arid climate is assumed to explain major societal shifts, including the demise of the Egyptian Old Kingdom, attributed to dramatic failure of annual Nile River floods driven by declining rainfall in the Ethiopian highlands (Stanley et al., 2003; Kuper and Kröpelin, 2006).

The timing and extent of the transition between the "Green Sahara" and today's hyperarid desert at the end of the AHP is, however, still highly debated. While many records suggest a gradual or time-transgressive transition (Kröpelin et al., 2008; Lézine et al., 2011b; Berke et al., 2012b; Foerster et al., 2012; Shanahan et al., 2015; Castañeda et al., 2016; Tierney et al., 2017) toward peak aridity at about 2–4 ka BP as a linear response to radiative forcing, others indicate an abrupt end of the AHP triggered by nonlinear biogeophysical feedback processes (DeMenocal et al., 2000; Claussen et al., 2013; Tierney and deMenocal, 2013; Collins et al., 2017). Uncertainties in the reconstructions arise from complex patterns of convergence and precipitation associated with both Atlantic and Indian Ocean climate dynamics as well as extratropical teleconnections shaping North African hydroclimate (Camberlin et al., 2001; Nicholson, 2017). Therefore, changes in the locations of the Intertropical Convergence Zone (ITCZ) and associated monsoonal rainfall belts as well as the Congo Air Boundary (CAB) may affect sedimentary archives differently, in particular in the easternmost sector of tropical Africa (Tierney et al., 2010; Tierney et al., 2011; Foerster et al., 2012; Costa et al., 2014; Junginger et al., 2014; Wagner et al., 2018). Further complications arise from the different sensitivity of individual hydroclimate proxies (Castañeda et al., 2016).

Because of their specificity as a plant biomarker, long-chain *n*-alkanes are well suited for reconstructing climate and ecosystem changes recorded in lacustrine sediments (e.g., Eglinton and Eglinton, 2008; Castañeda and Schouten, 2011). Sedimentary leaf-wax *n*-alkane δD values (δD_{wax}) have been frequently used to reconstruct past changes in the hydrological cycle (Schefuß et al., 2005; Tierney et al., 2010; Berke et al., 2012b; Kuechler et al., 2013; Costa et al., 2014; Castañeda et al., 2016; Collins et al., 2017). In tropical regions with only minor temperature variations, the most prominent factor influencing δD_{wax} is the amount effect (Bowen, 2008; Sachse et al., 2012). Apart from precipitation amounts, shifting wind regimes and associated variations in moisture sources have a strong control on δD_{wax} in East Africa (Levin et al., 2009; Costa et al., 2014; Castañeda et al., 2016). In addition, changes in vegetation type, carbon fixation pathways and relative humidity can exert secondary effects on δD_{wax} (Smith and Freeman, 2006; Sachse et al., 2012; Kahmen et al., 2013). Sedimentary $\delta^{13}C$ values ($\delta^{13}C_{wax}$) have also been shown to be sensitive to environmental conditions (i.e., temperature, rainfall) and are used as proxies for continental vegetation (C_3 vs. C_4 plant types) and climate change (Schefuß et al., 2003; Schefuß et al., 2005; Castañeda et al., 2009; Berke et al., 2012b; Kuechler et al., 2013; Dupont and Schefuß, 2018).

Previous studies from East African lakes using the same molecular approach (δD_{wax}, $\delta^{13}C_{wax}$) also exhibited significant differences in hydroclimate changes particularly in the timing of the AHP termination, i.e. abrupt vs. gradual (Tierney et al., 2010; Tierney et al., 2011; Berke et al., 2012b; Costa et al., 2014). This non-uniform hydroclimate response on a regional scale may relate to locally different precipitation regimes (bimodal vs. unimodal), humidity sources (Atlantic Ocean vs. Indian Ocean) modulated by the zonal movement of the CAB (Tierney et al., 2011; Costa et al., 2014; Junginger et al., 2014), and topography. Moreover, local vegetation structure may respond differently to regionally changing moisture balance (Lézine et al., 2011b; Berke et al., 2012b; Sachse et al., 2012; Kuechler et al., 2013). Information about vegetation composition is, however, missing in most of the previous investigations. In this study, we provide new insights into the termination of the AHP based on a sediment core from Lake Dendi located in the central Ethiopian highlands (2,836 m asl), where recent archaeological investigations indicated a long history of human occupation (Vogelsang et al., 2018). We use δD_{wax} to assess the regional precipitation history, and $\delta^{13}C_{wax}$ to examine the distribution of C_3 and C_4 vegetation in the catchment. In addition, we assess variations in pollen abundances to investigate the response of regional vegetation structure to changes in hydroclimate. A preceding study by Wagner et al. (2018) focused on sedimentological data to reconstruct erosion and rainfall dynamics in the lake catchment. According to this study, most arid conditions were reached at 3.9 ka BP but relatively stable climate conditions with low erosion and few rainfall events were indicated throughout the mid Holocene. The combination of molecular records with pollen data applied in this study allows a more differentiated perspective of environmental change at this high-altitude location over the past 12,500 years.

2. MATERIALS AND METHODS

2.1. Study Area and Climate Background

Lake Dendi is located on the central Ethiopian Plateau (8°50'N, 38°02'E; 2,836 m elevation) about 80 km to the west of Addis Ababa (**Figure 1A**). The lake is situated inside an ~8-km wide caldera of the dormant volcano Mount Dendi (**Figure 1B**). It comprises two basins connected via a shallow sill and has a maximum water depth of ~56 m in the eastern basin (Wagner

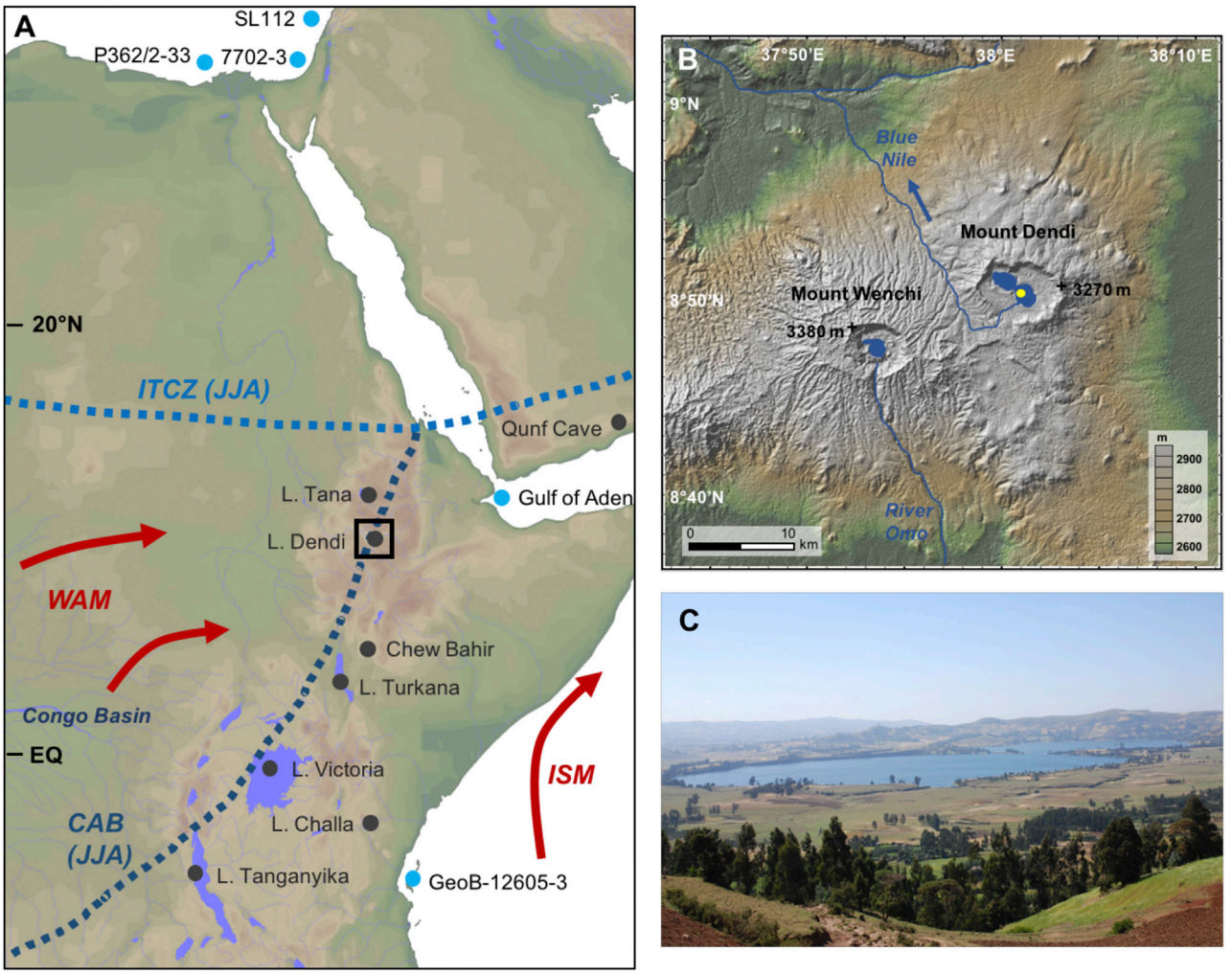

FIGURE 1 | (A) Map of Northeast Africa with the positions of terrestrial (black dots) and marine archives (blue dots) mentioned in the text. The black box denotes the Lake Dendi region. The approximate locations of the Intertropical convergence zone (ITCZ) and Congo Air Boundary (CAB) during northern hemisphere summer are indicated by blue dotted lines. Red arrows illustrate pathways of moisture advected from the Atlantic Ocean/Congo Basin and Indian Ocean during summer monsoon (WAM: West African Monsoon; ISM: Indian Summer Monsoon) **(B)** Close-up of the study area on the central Ethiopian Plateau showing the Dendi crater and coring location in the eastern lake (yellow dot). Lake Dendi seasonally contributes to the drainage system of the Blue Nile (indicated by blue arrow). Mount Wenchi is located about 12 km to the southwest. **(C)** The photograph shows the view from the northeastern crater rim on the two basins of Lake Dendi and the local vegetation, which is at present influenced by anthropogenic activity.

et al., 2018). The temperature of the upper 40 m of the oligotrophic lake ranges between 15° and 16°C (Degefu et al., 2014). Lake Dendi lacks permanent surface inlets but is fed by numerous small rivers and streams during the rainy season. The seasonally active outlet in the southwestern corner of the lake (**Figure 1B**) contributes to the drainage system of the Blue Nile (Degefu et al., 2014; Wagner et al., 2018). The lake catchment is part of the Lower Dega region, which is characterized by a sub-humid climate with moderate seasonal temperatures ranging from 14°C in winter to 17°C in summer (Mitchell and Jones, 2005).

The hydroclimate in the study area is controlled by the African rainbelt, which is closely associated with the ITCZ (**Figure 1A**). Both migrate seasonally between ca. 20°N (July) and ca. 20°S (January), following the movement of the insolation maximum (Nicholson, 2000). Another zone of convergence, the CAB, separates air masses containing moisture derived from the Atlantic and Indian Ocean (Mitchell and Jones, 2005; Degefu et al., 2014; Nicholson, 2017). Generation of rainfall and the seasonal shift of the African rainbelt are also closely linked to seasonally varying monsoon winds, which bring humid (dry) air on land during the summer (winter) months (Nicholson, 2000; Trenberth et al., 2000). A main rainy season from June to September is caused by movement of the rainbelt to its northernmost position. Highest rainfall (>250 mm/month) is observed during July and August, when the CAB allows moisture from westerly sources (i.e., Congo Basin) to reach the area (Mitchell and Jones, 2005; Levin et al., 2009). This

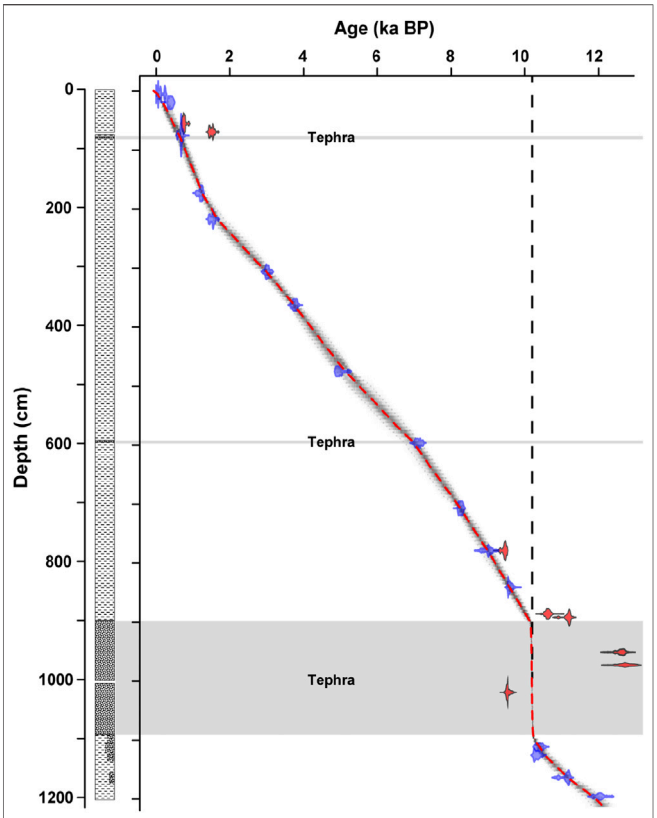

FIGURE 2 | Age model for Lake Dendi core composite. Bayesian age-depth modeling was based on 24 radiocarbon dates applying a reservoir correction of 329 years (Wagner et al., 2018). Radiocarbon ages in red were discarded from the calculation of the age depth curve. Gray bars indicate tephra horizons.

Congo Basin sourced precipitation is assumed to be more D-depleted compared to that from the Indian Ocean and may thus impact the isotopic composition of rainfall in Ethiopia (Levin et al., 2009; Costa et al., 2014). A relatively dry season (<50 mm/month) between October and February is characterized by predominant northeasterly winds. Rainfall during the short rain season in October-November is related to sea surface temperature (SST) anomalies, with intensified rains during periods of anomalous high SST in the western Indian Ocean (Nicholson, 2000; Ummenhofer et al., 2009). During February/March to May, prevailing easterly and southeasterly winds from the Indian Ocean cause the spring rainy season in the central Ethiopian highlands (Levin et al., 2009). Annual precipitation in the Dendi region averages ~1,200 mm (Mitchell and Jones, 2005; Degefu et al., 2014).

The natural vegetation in the catchment of Lake Dendi can be assigned to the "dry evergreen Afromontane forest" (Bekele, 1993; Friis et al., 2011), representing a mixture of open forest with dominant conifers, Juniper trees, and African redwood, interspersed with high-mountain grassland, mosses and lichens (Friis 1992; Bonnefille and Mohammed, 1994; Darbyshire et al., 2003). Today's landscape, however, is characterized by anthropogenic influence through deforestation and intensive agricultural activity that largely replaced the natural vegetation (**Figure 1C**) (Darbyshire et al., 2003; Hailu et al., 2015; Wagner et al., 2018). Archaeological investigations indicated human activity in the area of the Dendi caldera already more than 200 ka ago, and the crater lakes may have been important water reservoirs during more arid periods in the past, while the obsidian resource might have been important for the preparation of stone tools (Vogelsang et al., 2018).

Two sediment cores (DEN1: 08°50.178'N, 38°00.974'E and DEN2: 08°50.153'N, 38°01.075'E; **Supplementary Figure S1**) were obtained from the eastern twin-lake from a water depth of 50 and 54 m, respectively, in spring 2012. The cores were correlated based on optical and XRF analyses. Bayesian age-depth modeling used 24 radiocarbon (^{14}C) ages and provided a basal age of 12.19 cal ka BP for the correlated core (Wagner et al., 2018) (**Figure 2**). A reservoir correction of 329 years was applied to the entire set, consisting exclusively of bulk organic carbon samples. Sampling for molecular analyses was done with a resolution of ~200 years, and excluding the tephra. Detailed information on the age model can be found in Wagner et al. (2018).

2.2. Lipid Biomarker Extraction and Fractionation

Freeze dried sediment samples (ca. 2–7 g) were ultrasonically extracted with dichloromethane (DCM)/methanol (9:1, v/v) for 5 min repeated 3 times. The extracts were combined and the bulk of the solvent subsequently removed by rotary evaporation under vacuum. The resulting total lipid extracts (TLE) were saponified using 0.5 M aqueous potassium hydroxide (KOH) solution at 80°C for 2 h. Non-saponifiable lipids (neutral lipids) were extracted out of the basic solution using *n*-hexane. The neutral fractions were chromatographically separated using activated silica gel and *n*-hexane and DCM/methanol (1:1, v/v) to elute apolar and polar compounds, respectively. The apolar fractions were further separated into saturated and unsaturated compounds using $AgNO_3$-coated silica gel and *n*-hexane and DCM, respectively.

2.3. Sediment *n*-Alkane Analysis

n-Alkanes were analyzed using a gas chromatograph equipped with an on-column injector and a flame ionization detector (GC-FID; HP 5890). A fused silica capillary column (DB-5MS; 50 m × 0.2 mm, film thickness: 0.33 μm) was used with He as carrier gas. Samples were injected at 70°C and the GC oven temperature was subsequently raised to 150°C at a rate of 20°C/min, and then at 6°C/min to 320°C (held 40 min). Identification of *n*-alkanes was based on retention time in comparison with those of a standard solution (*n*-C_{21}–*n*-C_{40}). Analytical precision of the *n*-alkane quantifications based on replicate standard analyses was <5%.

To distinguish between contributions of higher plant wax and petrogenic sources, the carbon preference index (CPI; Bray and Evans, 1961) was calculated using the abundances of odd- and even-numbered *n*-alkane chain lengths from C_{27} to C_{33}:

$$CPI_{27-33} = 0.5 \times \left(\frac{nC_{27} + nC_{29} + nC_{31} + nC_{33}}{nC_{26} + nC_{28} + nC_{30} + nC_{32}} + \frac{nC_{27} + nC_{29} + nC_{31} + nC_{33}}{nC_{28} + nC_{30} + nC_{32} + nC_{34}} \right)$$

2.4. Compound-specific δD and $\delta^{13}C$ Analysis

δD analysis of the most abundant *n*-alkane homologues (*n*-C_{29} and *n*-C_{31}) was performed on a Thermo Trace GC coupled via a pyrolysis reactor to a Thermofisher MAT 253 mass spectrometer (GC/IR-MS) according to Jaeschke et al. (2018). The GC was equipped with a 30 m × 0.25 mm column (Restek Rxi-5ms, film thickness: 1.0 µm) and He was used as the carrier gas. The samples were injected via a PTV injector at 40°C and then transferred to the GC column. The GC temperature was programmed to increase from 120°C (2 min hold) to 200°C at 30°C/min and then at 4°C/min to 320°C (held 12.3 min). δD values were measured against calibrated reference gas using H_2 and are reported in ‰ relative to Vienna Standard Mean Ocean Water (VSMOW). The H_3-factor had a mean of 6.00 ± 0.02. An external standard mixture with known δD values was analyzed repeatedly in between samples and yielded a long-term precision of <3‰ and a mean deviation of <1‰ from reference values. All samples were analyzed in duplicate with an average standard deviation of 2‰.

$\delta^{13}C$ analysis of long chain *n*-alkanes was performed using a Trace GC instrument equipped with a 30 m × 0.25 mm column (Restek Rxi-5ms, film thickness: 0.25 µm) coupled via a combustion interface to a Thermofisher MAT 252 MS. He was used as carrier gas. The samples were injected via a PTV injector at 40°C and then transferred to the GC column. The GC oven was programmed from 60°C (3 min hold) to 150°C at 20°C/min, and then at 4°C/min to 320°C (held 10 min). Quantitative conversion of eluting compounds to CO_2 was conducted in a ceramic tube filled with Ni wires at 1,000°C using a trickle flow of O_2. CO_2 gas of known isotope composition was used as reference gas and $\delta^{13}C$ values are reported in ‰ relative to Vienna Peedee Belemnite (VPDB). Repeated analysis of an external *n*-alkane standard yielded long-term accuracy and precision of <0.1 and 0.3‰, respectively. All samples were analyzed in duplicate with an average standard deviation of 0.2‰.

2.5. Pollen Analysis

21 horizons, deriving from 64 cm equidistance core samples, were selected for pollen analysis. From each horizon, 2 cm^3 sediment material was used for laboratory preparation according to standard procedures including acetolysis (Faegri et al., 1989). Firstly, 10% HCl was added to remove $CaCO_3$. After washing with water and before sieving the remaining sample through a 112 µm wide mesh, 10% KOH was used to diminish organic material. Then 40% HF destroyed the sand grains before acetolysis (9 ml acetic anhydride and 1 ml concentrated sulfuric acid) decomposed cellulose. Finally, clay particles were washed out carefully in an ultrasonic bath. One drop of the remaining material was mounted on a microscope slide. The counting of the pollen grains was done under a Zeiss Primo Star light microscope using 400 to 1,000 times magnification until 300 individual grains were determined. To identify the taxonomic affiliation of each grain, photos, description and pollen atlases were used (Bonnefille 1971a; Bonnefille 1971b; Bonnefille and Riollet, 1980; Hamilton, 1982). The non-palynomorphes were identified with the help of Gelorini et al. (2011) and Van Geel et al. (2011). The concentration of spores was calculated using known numbers of *Lycopodium* markers in a tablet added to the samples before processing. The pollen diagram was constructed using the TILIA software, version 2.0.41 (Grimm, 2015). Cyperaceae were excluded from the pollen sum as they are generally limited to lake margins and thus not representative for the broader regional vegetation. For the zonation of the diagram, CONISS ("Constrained cluster analysis by sum-of-squares") analysis, was used including terrestrial pollen grains appearing at least once with more than 5%.

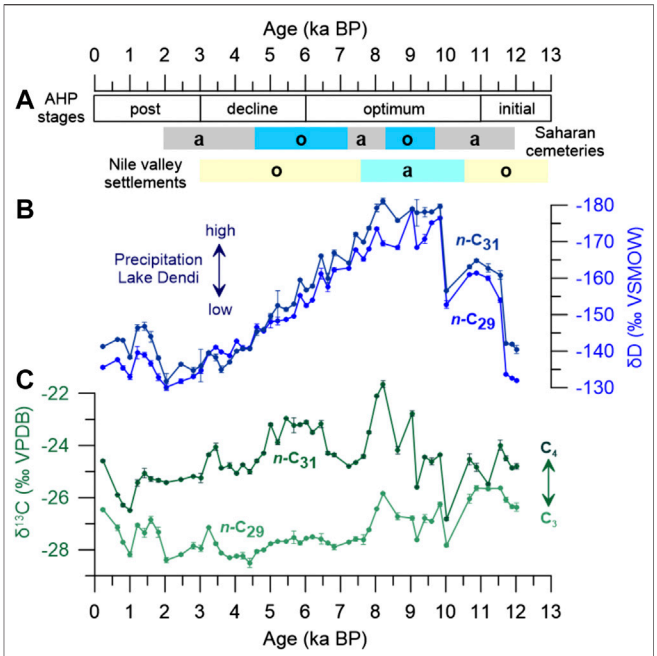

FIGURE 3 | Timing of the stages of the African Humid Period (AHP) based on paleohydrological records in northern Africa (10–25°N; Lézine et al., 2011a). Archaeological evidence for prehistoric human occupation of the Sahara (paleolake Gobero, Niger; Sereno et al., 2008) and the Nile valley (Kuper and Kröpelin, 2006; Weldeab et al., 2014). **(A)** Colored bars indicate phases of occupation (o) and abandonment (a), blue colours indicate humid phases. **(B)** δD values of the n-C_{29} (light blue) and n-C_{31} (dark blue) homologues from Lake Dendi sediment core. **(C)** $\delta^{13}C$ values of the n-C_{29} (light green) and n-C_{31} (dark green) homologues from Lake Dendi sediment core. Error bars represent analytical precision.

3. RESULTS

3.1. *n*-Alkane Distributions

The *n*-alkane distribution in all sediment samples shows a strong odd over even predominance with highest abundances of the *n*-C_{29} and *n*-C_{31} homologues. The C_{29} *n*-alkane is in general more

dominantly produced by trees and shrubs (C_3 photosynthesis), while the C_{31} *n*-alkane is more evenly produced by trees (C_3 plants) and grasses (C_4 plants in the study area). The sum of the long-chain *n*-alkanes (C_{27}-C_{33}) varies between 45 μg/g TOC and 260 μg/g TOC, showing the highest fluctuations in the early Holocene after 5.2 ka BP (**Supplementary Table S1**). CPI values are generally high and range between 7.6 and 4.8 (**Supplementary Table S1**), indicating no major contribution from fossil sources that might bias compound-specific δD and $\delta^{13}C$ values.

3.2. *n*-Alkane δD Values

δD values of the most abundant *n*-C_{29} and *n*-C_{31} plant wax homologues vary between –130 and –179‰ and thus exhibit a wide range of almost 50‰ (**Figure 3B**, **Supplementary Table S1**), which is comparable to the record of Lake Tana (~60‰; Costa et al., 2014). The similar δD evolution of the two homologues (r^2 = 0.95) suggests only a minor effect of vegetation changes (C_3 vs. C_4) on the climatic signal. We thus calculated δD_{wax} as the weighted average of both signals (**Supplementary Table S1**). The Younger Dryas (YD) is characterized by relatively positive δD_{wax} values (between –131 and –142‰). A rapid decrease of about 30‰ at 11.7 ka BP marks the abrupt termination of the YD. A second decrease of about 20‰ at 10 ka BP is followed by a ca. 2 kyr period with relatively stable δD values around –175‰. From ~8 ka BP, δD_{wax} values exhibit a long-term gradual increase to ca. 130‰ at about 2 ka BP. δD_{wax} values then decrease about 10‰ to the present, with some distinct fluctuations (**Figure 3B**). Late Holocene δD_{wax} values of Lake Dendi are comparable with modern δD_{wax} values reported for the Ethiopian highlands at a similar elevation (Jaeschke et al., 2018). In monsoon regions, variations in rainfall δD values are mainly controlled by the amount effect, with more negative δD values indicating more humid conditions. Different moisture sources potentially also influence precipitation δD values in the Ethiopian highlands (Rozanski et al., 1993; Levin et al., 2009). According to Costa et al. (2014), a contribution of 30% (modern) Congo-sourced moisture corresponds to a –4‰ change in δD, while in the most extreme case of 100% moisture derived from the Congo Basin could result in a δD change of –14‰. However, changes in the relative contribution of the different sources were proposed to be unrelated to the net annual precipitation amount (Costa et al., 2014). Here, we assume that δD_{wax} values primarily reflect the isotopic composition of local rainfall during the growing season (e.g., Schefuß et al., 2005) but also integrate the history of moisture transported to the Lake Dendi area, i.e., continental and Indian Ocean moisture.

3.3. $\delta^{13}C$ Values and Vegetation Types

n-Alkane $\delta^{13}C$ values range between –26.8 and –21.6‰ (*n*-C_{31}) and between –28.5 and 25.6‰ (*n*-C_{29}) (**Figure 3C**, **Supplementary Table S1**). The more ^{13}C-enriched values of the C_{31} *n*-alkane may be explained by the higher relative contribution of this homologue from C_4 grasses. $\delta^{13}C$ values of *n*-C_{29} generally show little variation but slightly ^{13}C-enriched values are observed during the early Holocene until about 8 ka BP and during the late Holocene starting at about 2 ka BP. $\delta^{13}C$ values of *n*-C_{31} are generally more ^{13}C enriched, especially from 9 to 8 ka BP and from 6.5 to 5 ka BP, resulting in a maximum isotopic spread of about 4‰ between *n*-C_{29} and *n*-C_{31} (**Figure 3C**). To estimate the relative contributions of C_4 and C_3 plants, which are dominantly controlled by aridity (Schefuß et al., 2003; Castañeda et al., 2009), a simplified two end-member mixing model is applied assuming end-member values for C_3 and C_4 vegetation of -34.7 and –21.4‰ for *n*-C_{29} and –35.2 and –21.7‰ for *n*-C_{31}, respectively (Castañeda et al., 2009; Berke et al., 2012b). Based on this assumption, the Lake Dendi region has a C_4-dominated (ca. 60–80%) vegetation (**Supplementary Table S1**). Uncertainties in the C_3/C_4 estimates of about 20%, however, have to be considered (Castañeda et al., 2009).

3.4. Pollen Stratigraphy

A total of 56 pollen and spore types was distinguished and percentages for the most abundant pollen taxa are summarized in **Figure 4**. Most important pollen groups indicating a C_4 plant origin are those of the grass (Poaceae) and sedge (Cyperaceae) families, while those from woody plants (*Podocarpus*, *Juniperus*) indicate a C_3 metabolism.

Poaceae pollen percentages are high throughout the record accounting for on average 62% during the YD, 53% throughout the AHP, and 32% during the late Holocene, (**Figure 4**). Cyperaceae pollen percentages range between 4 and 34%. Other herbaceous taxa include Asteraceae (av. 0.8–13.6%) and Amaranthaceae/Chenopodiaceae (av. 0.4–21.4%), Rosaceae (0.2–4.3%), Caryophyllaceae (0.2–5.3%), Solanaceae (0.2–2.5%), Apiaceae (0.2–2.6%), Fabaceae (0.2–2.5%) (**Figure 4**). High pollen percentages of Plantaginaceae (15–19%) are recorded only during the last 1,000 years (**Figure 4**) and may reflect the increasing anthropogenic influence in the Ethiopian highlands (Hamilton, 1982; Darbyshire et al., 2003; Umer et al., 2007; Hailu et al., 2015). Low pollen percentages of the dry Afromontane forest taxa *Podocarpus* are observed during both the YD and peak AHP (3–7%), while constantly increasing from ca. 7 ka BP to maximum values of 29% at 2.4 ka BP (**Figure 4**). Likewise, *Juniperus* pollen percentages increase over the course of the mid Holocene and reach a maximum of 19% at ca 3 ka BP, slightly leading those of *Podocarpus*. Other woody plant taxa are minor, i.e., Oleaceae (0.2–7%), Myricaceae (0.1–4%), Capparaceae (0.3–3%) (**Figure 4**).

The most distinct change in pollen distribution is observed above a ca. 2 m thick tephra layer, deposited at approximately 10.2 ka BP (**Figure 2**), and points to an extreme shift in plant community (**Figure 4**). This can be interpreted as the pioneer stage established after the volcanic eruption of Mount Wenchi located in close vicinity to Mount Dendi (**Figure 1B**) (Brown and Fuller, 2008; Wagner et al., 2018). Moreover, low pollen counts indicate sparse vegetation cover dominated by herbaceous plants. This extreme event may also have impacted the $\delta^{13}C$ and δD composition of the specific pioneer vegetation. Different photosynthetic pathways (C_3 vs. C_4 type) and diverse growth forms (e.g., trees, shrubs vs. herbaceous plants) vary in terms of stable carbon isotopic composition (Vogts et al., 2009; Jaeschke et al., 2018) and discriminate differently against deuterium during

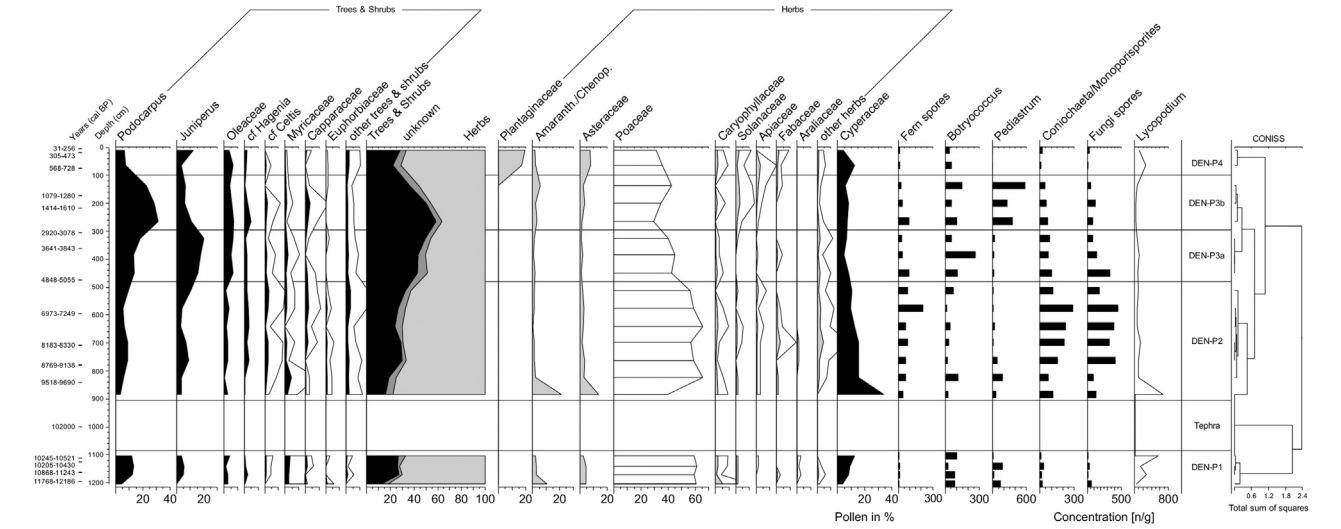

FIGURE 4 | Pollen diagram from Lake Dendi, showing percentage abundances of the principal taxa on a calibrated radiocarbon timescale. Percentages are calculated from the sum of all pollen grains (Cyperaceae excluded). The concentration of the palynomorphes was calculated based on the sediment dry weight.

lipid synthesis (Sachse et al., 2012). This may either amplify or reduce the signal. Both, $\delta^{13}C$ and δD values show abrupt shifts (**Figures 3B,C**) that coincide with the deposition of tephra at 10.2 ka BP and may thus not necessarily reflect a climatic signal.

4. DISCUSSION

4.1. Hydroclimate Changes at Lake Dendi and East Africa

The δD_{wax} record from Lake Dendi indicates that the Ethiopian highlands experienced major changes in hydroclimate during the past 12,500 years (**Figures 3B**, **5D**). Arid conditions during the YD documented at many Northeast and East African sites (Tierney et al., 2011; Foerster et al., 2012; Junginger et al., 2014; Castañeda et al., 2016) are confirmed at Lake Dendi by our δD_{wax} record (**Figure 5D**) and other sedimentological data (Wagner et al., 2018). Across tropical Africa, the termination of the YD was marked by an abrupt change in hydroclimate which involved major reorganization of monsoonal circulation across the continent and adjacent oceans (Talbot et al., 2007). Intense NH heating and an associated increase in thermal contrast between land and ocean resulted in a strengthening of the West African Monsoon (WAM) and the Indian Summer Monsoon (ISM) allowing the northward expansion of the tropical rainbelt (Nicholson, 2017; Pausata et al., 2020). The abruptness of change is thought to be related to the rapid resumption of the Atlantic Meridional Overturning Circulation (AMOC) (McManus et al., 2004; Weldeab et al., 2014). At Lake Dendi, the onset of the AHP and increasing rainfall at 11.7 ka BP are characterized by a large and abrupt shift in δD_{wax} of ~30‰ (**Figure 5D**). This abrupt decrease in δD_{wax} that points to increasing rainfall is in line with the abrupt strengthening of the WAM as indicated by the Ba/Ca time series from a marine sediment core of the Gulf of Guinea (Weldeab et al., 2007) (**Figure 5E**). A more gradual intensification of the monsoon circulation was indicated by Ba/Ca from a sediment core of the Levantine Sea and was proposed to reflect the influence of moisture from the Western Indian Ocean (Weldeab et al., 2014). Maximum monsoon rainfall at 9.9 ka BP and thus highest Nile river runoff based on Ba/Ca (**Figure 5C**) is in line with highest precipitation over the Blue Nile river basin as recorded in Lake Dendi δD_{wax} (**Figure 5D**). The timing of maximum rainfall at Lake Dendi is also in line with the abrupt intensification of the ISM based on the Qunf Cave $\delta^{18}O$ record from Oman (Fleitmann et al., 2003) (**Figure 5B**). The increased precipitation in the ISM domain corresponds to an enhanced atmospheric pressure gradient between East Africa and India (Camberlin, 1997; Junginger et al., 2014) that also leads to advection of D-depleted moisture from westerly sources, i.e. by an eastward shift of the CAB (Levin et al., 2009; Kebede and Travi, 2012; Costa et al., 2014). The incursion of humid air masses from the Congo Basin thus likely increased precipitation amount and decreased precipitation δD values in the Dendi area. Peak AHP conditions at Lake Dendi documented by strongly depleted δD_{wax} values of around −175‰ between 10 and 8 ka BP align with maximum NH insolation (Berger and Loutre, 1991) (**Figure 5A**) and highest monsoon intensity based on different archives (Fleitmann et al., 2003; Weldeab et al., 2007; Weldeab et al., 2014). This humid interval at the end of the early Holocene is also well-documented in other Northeast and East African hydroclimate records (Gasse, 2000; Tierney et al., 2011; Berke et al., 2012b; Foerster et al., 2012; Tierney and deMenocal, 2013; Costa et al., 2014; Castañeda et al., 2016), however, with locally different timing of onset and termination of the AHP (**Figure 6**). Intensified precipitation over the Blue Nile catchment area (**Figures 6D,E**) is also indicated by enhanced river discharge

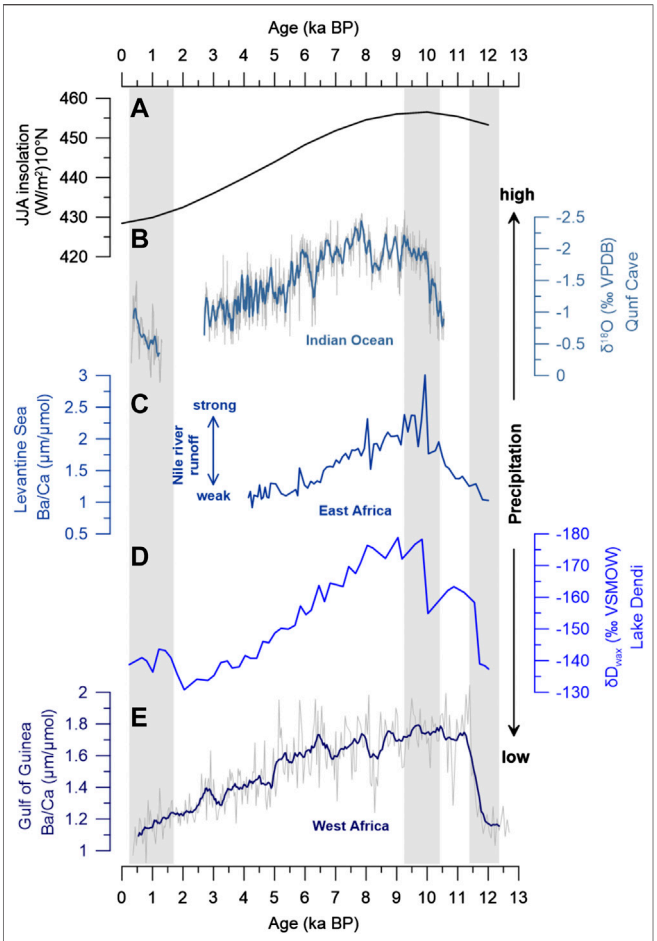

FIGURE 5 | Comparison with monsoon precipitation records. **(A)** Mean JJA insolation at 10°N (Berger and Loutre, 1991). **(B)** Stalagmite $\delta^{18}O$ record from Oman indicating changes in Indian Summer Monsoon (Fleitmann et al., 2003). **(C)** Ba/Ca record from the Levantine Basin indicating changes in Nile River discharge related to East African Monsoon rainfall (Weldeab et al., 2014). **(D)** Lake Dendi δD_{wax} record indicating changes in rainfall in the Ethiopian highlands (this study). **(E)** Ba/Ca record from the Gulf of Guinea indicating changes in river runoff draining the West African Monsoon area (Weldeab et al., 2007). Vertical gray bars mark abrupt changes in the monsoon systems based on the different proxies.

based on sedimentary records from the Nile deep-sea fan and eastern Mediterranean Sea (Blanchet et al., 2014; Castañeda et al., 2016). At the height of Nile River runoff, archaeological records indicate the abandonment of prehistoric human settlements in the Nile valley (Kuper and Kröpelin, 2006) while hydroclimate conditions were favourable for human occupation in the southern Sahara (Sereno et al., 2008) (**Figure 3A**).

After approximately 8 ka BP, the Lake Dendi δD_{wax} record shows a gradual aridification until ~2 ka BP, which is expressed in a progressive D-enrichment of ca. 45‰ (**Figure 5D**). The gradual decline in precipitation is in accordance with the long-term weakening of the African and Indian monsoon systems in response to decreasing NH summer insolation (Fleitmann et al., 2003; Weldeab et al., 2007; Weldeab et al., 2014) (**Figure 5**). This is supported by a general reduction in rainfall runoff based on sedimentological data at Lake Dendi (Wagner et al., 2018) and Lake Chew Bahir in southern Ethiopia (Foerster et al., 2012). A similar gradual trend in δD_{wax} is also observed in Lake Victoria, Kenya (Berke et al., 2012b) (**Figure 6F**) and in a sediment core from the eastern Mediterranean Sea (Castañeda et al., 2016) (**Figure 6B**), which received material from both, Blue and White Nile. Other δD_{wax} records from East Africa indicate continuous wet conditions during the AHP which ended abruptly at ~5 ka (Tierney et al., 2010; Tierney et al., 2011) (**Figures 6G,H**). Lakes Challa and Tanganyika located south of the equator experience a bimodal rainfall regime and may have benefited from enhanced short rains during autumn (Oct-Nov) related to SST anomalies in the Western Indian Ocean (Ummenhofer et al., 2009; Kuhnert et al., 2014). In contrast, the δD_{wax} record from Lake Tana, Ethiopia's largest lake, suggests an abrupt and early termination of the AHP at ~8.5 ka (Costa et al., 2014) (**Figure 6D**). The authors attributed this abrupt shift in δD_{wax} of about 60‰ to the westward retreat of the CAB and thus reduced moisture with a D-depleted signature derived from westerly sources (Congo Basin). Lake Dendi is located ~300 km to the south of Lake Tana, therefore, an abrupt shift of the CAB should have influenced δD_{wax} in a similar manner. We suspect locally different responses to changing hydroclimate associated with the 8.2 ka cold event in the North Atlantic (Alley and Ágústsdóttir, 2005). A distinct dry period between 8.5 and 7.8 ka has been documented by various archives throughout East Africa. Low lake levels were indicated in Lakes Ziway-Shala and Abhé (Gasse, 2000), Lakes Turkana and Suguta (Garcin et al., 2012; Junginger et al., 2014), Lake Tana (Marshall et al., 2011) and Chew Bahir (Foerster et al., 2012). Blanchet et al. (2014) suggested that this dry event marked a permanent modification of erosion dynamics and vegetation cover. Likewise, a decrease in Nile River runoff at 8.6–8.2 ka was reported based on Ba/Ca and Fe/Ca (Weldeab et al., 2014; Revel et al., 2010) and Sr isotopes (Blanchet et al., 2014) (**Figure 7A**). During this period, the southward migration of the rainbelt together with weakened monsoon precipitation in response to the 8.2 ka cold event may still have reached Lake Dendi, while Lake Tana dried out. In addition, a generally lower lake level of Lake Tana and lower elevation (i.e., implementing higher air temperature) would favor desiccation (drought stress) compared to Lake Dendi. Although not clearly visible from δD_{wax}, ^{13}C-enriched values of the *n*-alkanes may indicate the sensitive plant response to small changes in the local moisture balance at Lake Dendi during this interval (**Figure 3C**).

Late Holocene climate in East Africa is characterized by arid conditions in response to minimum NH summer insolation and a decrease in monsoon rainfall (**Figure 5**). According to the Lake Dendi δD_{wax} record, maximum aridity in the Ethiopian highlands is reached at ~2 ka BP (**Figures 3**, **6E**). This is in good agreement with the δD_{wax} record of Lake Tana (**Figure 6D**), the source of the Blue Nile (Costa et al., 2014). During the last 1,500 years, a trend toward slightly increasing humidity is indicated by a –15‰ shift in δD_{wax} (**Figure 5D**). This overall climatic rebound might be connected to a higher influence of precipitation from the Atlantic/Congo Basin as followed by a re-strengthening of the ISM (Fleitmann et al., 2003) (**Figure 5B**). The re-establishment of

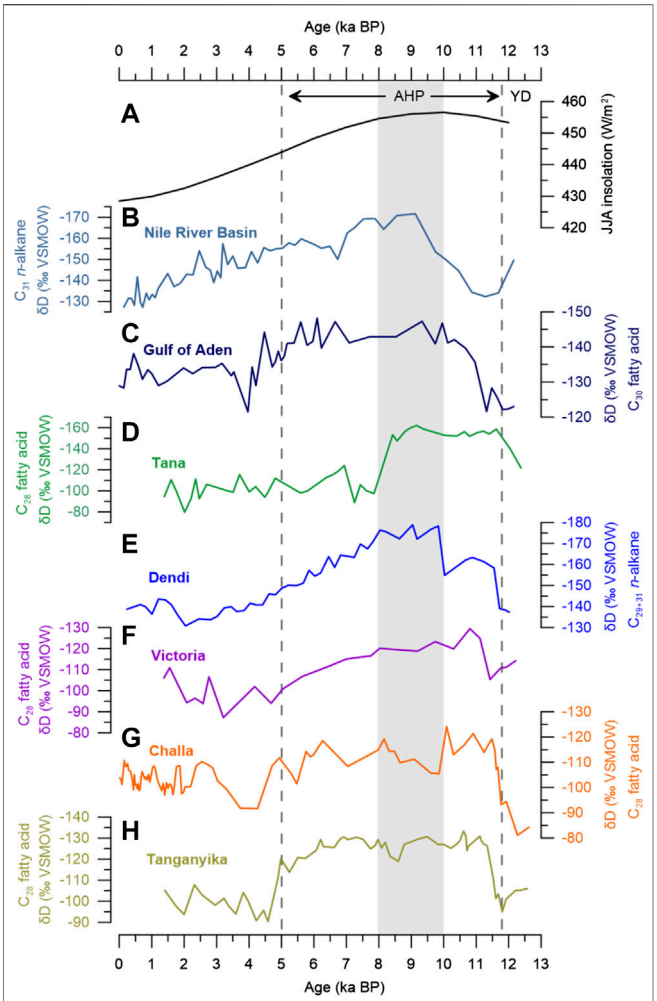

FIGURE 6 | Comparison with other East African δD_{wax} records. **(A)** Mean JJA insolation at 10°N (Berger and Loutre, 1991). **(B)** Nile River Basin (Castañeda et al., 2016). **(C)** Gulf of Aden (Tierney and deMenocal, 2013). **(D)** Lake Tana (Costa et al., 2014). **(E)** Lake Dendi (this study). **(F)** Lake Victoria (Berke et al., 2012b). **(G)** Lake Challa (Tierney et al., 2011). **(H)** Lake Tanganyika (Tierney et al., 2010). Vertical gray bar marks the optimum of the African Humid Period (AHP) at Lake Dendi. Black arrows indicate extent of the AHP in Africa.

seasonal rainfall in the Blue Nile source region is also indicated by enhanced Nile river discharge based on radiogenic Sr isotopes (**Figure 7A**), however with less vigorous floods compared to the early Holocene (Blanchet et al., 2014). The high fluctuations in rainfall runoff reported for Lake Dendi (**Figure 7B**) (Wagner et al., 2018) are also visible in the plant wax records (**Figure 3B**). These might be related to natural short-term environmental changes during the last millennium including the Medieval Warm Period (MWP) and the Little Ice Age. Thus, slightly enriched δD_{wax} values indicating a decrease in rainfall coincides with the MWP, which is frequently associated with a more arid climate in East Africa (Bonnefille and Mohammed, 1994; Verschuren et al., 2000; De Cort et al., 2013).

In conclusion, the timing and pace of hydroclimate evolution at Lake Dendi during the Holocene occurred in synchrony with the strength of the African and Indian monsoon systems and thus precipitation amount, pointing to orbitally induced gradual changes in NH summer insolation as the dominant forcing (Fleitmann et al., 2003; Renssen et al., 2006; Liu et al., 2007; Weldeab et al., 2007; Weldeab et al., 2014; Claussen et al., 2013). In East Africa, the variability in the amplitude of changes in δD_{wax} during the AHP compared to the late Holocene may be linked to a zonal gradient of hydroclimate anomaly patterns associated with the migration of the CAB (Tierney et al., 2011; Costa et al., 2014; Junginger et al., 2014). At Lake Dendi, this change of about 40‰ likely integrates the effects of both precipitation amount and water vapor transport, which is also seen in other East African δD_{wax} records (Tierney et al., 2010; Berke et al., 2012b; Castañeda et al., 2016).

4.2. Vegetation Response to Hydroclimate Changes at Lake Dendi

The pollen records of Lake Dendi provide evidence of distinct vegetation changes that accompanied the climate history in the region (**Figures 4**, **7E**,**F**). A sparse vegetation cover dominated by drought-tolerant C_4 grasses in combination with low total pollen counts suggests dry conditions at the end of the YD associated with low temperatures in the highlands and low CO_2 levels (Ehleringer et al., 1997). This is in line with other East African pollen records (Barker and Gasse, 2003), including Lake Tana (Lamb et al., 2007), Lake Victoria (Johnson et al., 1996), and Lake Garba Guracha in the Bale Mountains (Umer et al., 2007). The onset of more humid conditions during the AHP, as indicated by our δD_{wax} record, is accompanied by an increase in pollen counts but generally minor changes in vegetation composition, suggested by the predominance of Poaceae pollen between ca. 11.5 and 6 ka BP (**Figures 4**, **7F**). This is also reflected in ^{13}C-enriched values indicative of C_4 plants (**Figure 3C**) and in line with our $\delta^{13}C$-based estimation of vegetation types in the Dendi catchment (**Supplementary Table S1**). At ~10 ka BP, however, ca. 200 years after the volcanic eruption of Mount Wenchi (Brown and Fuller, 2008; Wagner et al., 2018), a distinct change in vegetation composition in combination with generally low pollen counts points to a pioneer stage developed after deposition of tephra in the catchment (**Figure 4**).

While the δD_{wax} record indicates gradual aridification between ca. 8 and 2 ka BP in response to weakening insolation forcing of the monsoon strength and thus precipitation amount (**Figures 5**, **7C**), increasing tree pollen percentages until ca. 2.4 ka BP indicate the expansion of a dry montane forest in the Dendi catchment (**Figures 4**, **7E**). A similar trend is also reported for the Bale Mountains, but culminates as early as about 4.5 ka BP (Umer et al., 2007). The climatic change to late Holocene aridity is well known throughout northern and eastern Africa (Kuper and Kröpelin, 2006; Lézine et al., 2011a). The resulting increase in the dry montane forest taxa (i.e., *Podocarpus*, *Juniperus*, Oleaceae; **Figure 4**) is also widely expressed in the central East African highlands, where a distinct dry season exists at present (Hamilton, 1982; Umer et al., 2007). Specifically, *Juniperus* is known to be more drought-resilient compared to *Podocarpus* and can tolerate extremely low precipitation amounts of ~200 mm/

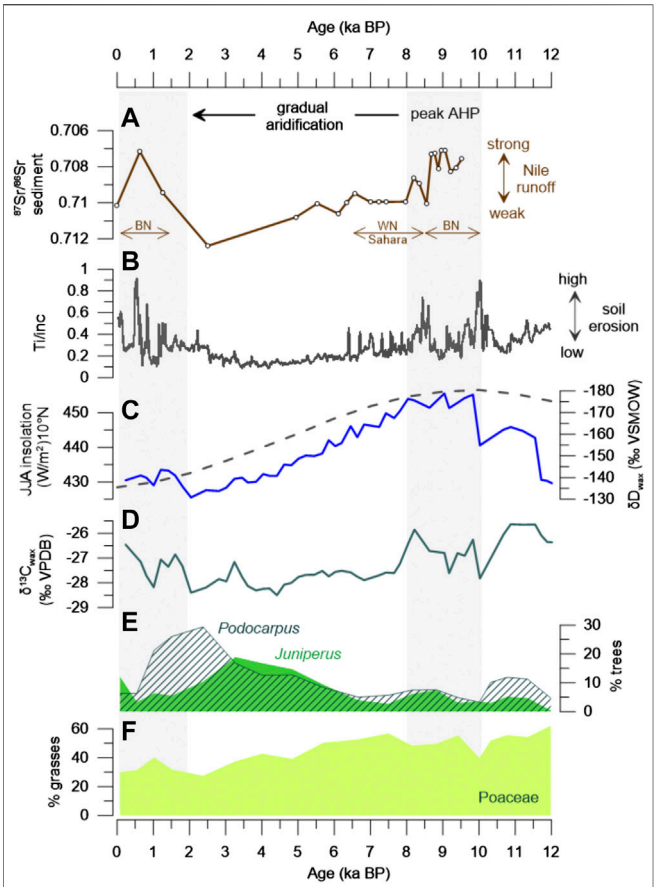

FIGURE 7 | Changes in precipitation and vegetation at Lake Dendi and river runoff in the Nile watershed during the Holocene. **(A)** Sediment sources from the Blue Nile (BN), White Nile (WN) and Sahara as estimated from the radiogenic Sr isotope signature in a marine sediment core from the Nile deep-sea fan (Blanchet et al., 2014). **(B)** Changes in catchment erosion at Lake Dendi based on Ti XRF-counts (Wagner et al., 2018). **(C)** Lake Dendi δD_{wax} record indicating changes in rainfall in the Ethiopian highlands (this study). Mean JJA insolation at 10°N (Berger and Loutre, 1991) is indicated as gray dashed line. **(D)** Lake Dendi $\delta^{13}C$ values of *n*-C_{29} indicate increasing contribution of C_3 vegetation (trees) from the late to the mid Holocene (this study). **(E)**, **(F)** Lake Dendi pollen percentages of predominant trees and grasses, respectively (this study). Vertical gray bars mark periods of enhanced Nile river runoff during high rainfall in the BN catchment.

year (Hall, 1984; Friis, 1992). Their increase, therefore, is believed to mark the establishment of the modern pattern of monsoonal rainfall seasonality (Umer et al., 2007).

Although the decline in insolation from its maximum during the early Holocene was gradual, many paleoclimatic records indicate an abrupt change to late Holocene aridity, explained as a triggering of vegetation albedo feedback mechanisms that provoke a nonlinear response to orbital forcing (DeMenocal et al., 2000; Renssen et al., 2006; Claussen et al., 2013). Vegetation is highly sensitive to the length of the dry season as well as the persistence of dry events (Lézine et al., 2011b). Specifically, length and intensity of the rainy season, dry spell occurrence and wind strength are of primary importance for plant distribution and pollen transport. However, the Lake Dendi pollen records show a gradual increase in both *Podocarpus* and *Juniperus* from ~6.5 ka BP onward (**Figures 4**, **7E**), which is in line with findings from the Bale Mountains (Umer et al., 2007). The gradual response may thus reflect the natural development of a dry Afromontane forest during the mid to late Holocene (Bonnefille and Hamilton, 1986; Darbyshire et al., 2003), related to the reduced precipitation in the region (**Figures 5**, **7C**). In combination with the pollen data we suggest that constantly decreasing $\delta^{13}C$ values of the *n*-C_{29} alkane (**Figure 7D**) may reflect the increasing contribution of C_3 woody plants. At the same time, the abundance of Poaceae pollen gradually decreased from 54% during the early to mid Holocene to 35% during the late Holocene (**Figure 7F**), pointing to a general reduction in understory grasses.

The maximum extent of trees and shrubs at Lake Dendi aligns with a minimum in precipitation amount in the source regions of the Blue Nile based on our δD_{wax} record (**Figures 6E**, **7C**) and that of Lake Tana (Costa et al., 2014) (**Figure 6D**). Most arid climate conditions in the Ethiopian highlands are corroborated by reduced catchment erosion at Lake Dendi (Wagner et al., 2018) (**Figure 7B**) and a strong reduction in Nile River discharge (Blanchet et al., 2014) (**Figure 7A**) as well as highest amounts of eolian dust detected in sediments of the Nile deep-sea fan (Blanchet et al., 2013). Increased dust transport during peak aridity may have facilitated eolian transport of *Podocarpus* pollen from additional extralocal sources (Hamilton, 1982) to the Dendi region (**Figure 7E**). On the other hand, highest pollen abundance of the more drought-tolerant *Juniperus* (**Figure 7E**), which are less susceptible to eolian transport, occurs earlier and aligns with the onset of full desert conditions at Lake Yoa at ~2.7 ka BP (Kröpelin et al., 2008). In East Africa, the late Holocene is characterized by increasing influence of human activity and a substantial land-cover change, which is also visible in the Ethiopian highlands (Hamilton, 1982; Friis, 1992; Darbyshire et al., 2003; Umer et al., 2007). At Lake Dendi, decreasing *Podocarpus* pollen percentages from about 1 ka BP point to tree clearance in favor of intensified agricultural use, which is indicated by high abundances of Plantaginaceae and Solanaceae pollen (**Figure 4**).

At high elevations, temperature is the main controlling factor allowing the growth of woody plants and for the establishment of open forest vegetation. Therefore, tropical warming during the Holocene may have extended the upper limit of trees toward higher altitudes in the Ethiopian highlands (Bonnefille and Mohammed, 1994; Wu et al., 2007). At Lake Dendi, the increase in pollen from drought-resilient taxa such as *Juniperus* and *Podocarpus* (**Figure 7E**) indicate the onset of forest development during the warm "Holocene Climate Optimum" (Wanner et al., 2011 and references therein). This pervasive mid Holocene warming is documented in lake sediment records from lower elevations in tropical East Africa (Powers et al., 2005; Tierney et al., 2010; Berke et al., 2012a). Distinct from most lowland savanna type vegetation that suffered degradation during the mid to late Holocene, the highlands received still sufficient moisture to support tree growth. A dense vegetation cover with more leaf litter and higher soil humus content may have restricted erosion of clastic minerals in the Dendi catchment (**Figure 7B**) (Wagner et al., 2018). In addition, high atmospheric CO_2

levels may have stabilized tropical forests by promoting tree growth, despite increased aridity (Shanahan et al., 2016). Our observations thus confirm model simulations by Claussen et al. (2013), that point to a substantial impact of plant diversity on the stability of the climate–vegetation system during the AHP transition. Our combined molecular and pollen records also indicate that vegetation evolution at Lake Dendi toward a dry montane forest is in line with the general trend in African hydroclimate evolution during the Holocene.

5. CONCLUSIONS

The Lake Dendi molecular and pollen records showed that Ethiopian highland vegetation was sensitive to moderate changes in moisture availability during the past 12,500 years. The gradual nature of hydroclimate change was related to weakening insolation forcing of the African and Indian Ocean monsoon intensities and thus precipitation amount. Based on our sedimentary δD_{wax} record, the onset of the AHP that followed YD aridity at Lake Dendi occurred in concert with the strengthening of the WAM at 11.7 ka BP. Peak AHP conditions were established at 10 ka BP, caused by the eastward shift of the CAB onto the central Ethiopian Plateau most likely due to an increase in ISM strength. After ca. 8 ka BP, the westward migration of the CAB resulted in a moderate decrease in precipitation amount, leading to a gradual transition out of the AHP. Peak aridity occurred around 2 ka BP, followed by a return to a generally wetter climate possibly linked to a re-strengthening of the ISM. The amplitude of change in δD_{wax} during the AHP compared to the late Holocene of about 40‰ is comparable to those of other East African δD_{wax} records influenced by the CAB. Parallel to the hydroclimate evolution, the vegetation structure at Lake Dendi changed gradually from a C_4-grass dominated vegetation toward the establishment of a dry montane forest characterized by *Juniperus*, *Podocarpus* and Oleaceae, which implies that moisture availability was not a limiting factor. At high elevations, rising temperatures and increasing atmospheric CO_2 levels during the Holocene may have initiated the growth of woody plants that once established, stabilized the vegetation cover, reduced soil erosion and sustained microclimate at Lake Dendi. During the last millennium, increasing anthropogenic activity is indicated by the pollen record pointing to deforestation and agriculture. Our results highlight that the nature of the transition out of the AHP seems to be controlled by complex interactions and shifts of wind regimes together with local insolation changes at different geographical positions. Finally, our multi-proxy approach showed that information on vegetation structure is important when interpreting plant wax-derived δD and $\delta^{13}C$ signatures.

DATA AVAILABILITY STATEMENT

All datasets generated in this study are included in the article and/or the Supplementary Files. Raw data are available in the PANGAEA repository (https://doi.pangaea.de/10.1594/PANGAEA.923143, https://doi.pangaea.de/10.1594/PANGAEA.923144).

AUTHOR CONTRIBUTIONS

FS and JR designed the research. FS and JU completed the sampling in Ethiopia. MT and ES carried out the lipid workup and compound-specific isotope analysis. JU carried out the pollen analysis. BW provided the age model. AJ completed data interpretation and served as primary author. All authors discussed the results and wrote the manuscript.

FUNDING

Funding for this study was provided by the German Research Foundation (DFG) within the scope of the CRC 806 ("Our way to Europe") - Project Number 57444011.

ACKNOWLEDGMENTS

We thank the editor and two reviewers for their helpful comments, which improved the quality of this manuscript. We would like to thank the whole coring team, Henry Lamb, Tamrat Endale, and Christian Tourney. Tamrat Endale and Asfawossen Asrat are thanked for logistic support during the field activities. We thank Ilona Steffen and Ralph Kreutz for help with sample preparation and isotope analysis.

SUPPLEMENTARY MATERIAL

The Supplementary Material for this article can be found online at: https://www.frontiersin.org/articles/10.3389/feart.2020.585770/full#supplementary-material.

REFERENCES

Alley, R. B. and Ágústsdóttir, A. M. (2005). The 8k event: cause and consequences of a major Holocene abrupt climate change. *Quat. Sci. Rev.* 24, 1123–1149. doi:10.1016/j.quascirev.2004.12.004

Barker, P. and Gasse, F. (2003). New evidence for a reduced water balance in East Africa during the Last Glacial Maximum: implication for model-data comparison. *Quat. Sci. Rev.* 22, 823–837. doi:10.1016/s0277-3791(03)00010-6

Bekele, T. (1993). "Vegetation ecology of remnant Afromontane forests on the central plateau of Shewa, Ethiopia," in *Acta phytogeographica Suecica*. Editor E. Sjörgen (Uppsala: Opulus Press AB), 3–64.

Berger, A. and Loutre, M. F. (1991). Insolation values for the climate of the last 10 million years. *Quat. Sci. Rev.* 10, 297–317. doi:10.1016/0277-3791(91)90033-q

Berke, M. A., Johnson, T. C., Werne, J. P., Schouten, S., and Sinninghe Damsté, J. S. (2012a). A mid-Holocene thermal maximum at the end of the African Humid Period. *Earth Planet Sci. Lett.* 351-352, 95–104. doi:10.1016/j.epsl.2012.07.008

Berke, M. A., Johnson, T. C., Werne, J. P., Grice, K., Schouten, S., and Sinninghe Damsté, J. S. (2012b). Molecular records of climate variability and vegetation response since the late pleistocene in the lake Victoria basin, east Africa. *Quat. Sci. Rev.* 55, 59–74. doi:10.1016/j.quascirev.2012.08.014

Blanchet, C. L., Frank, M., and Schouten, S. (2014). Asynchronous changes in vegetation, runoff and erosion in the Nile River watershed during the Holocene. *PloS One* 9 (12), e115958. doi:10.1371/journal.pone.0115958

Blanchet, C. L., Tjallingii, R., Frank, M., Lorenzen, J., Reitz, A., et al. (2013). High- and low-latitude forcing of the Nile River regime during the Holocene inferred from laminated sediments of the Nile deep-sea fan. *Earth Planet Sci. Lett.* 364, 98–110. doi:10.1016/j.epsl.2013.01.009

Bonnefille, R. (1971a). Atlas des pollens d'Ethiopie. Pollens actueles de la base vallée de l'Omo. *Adansonia* 2, 463–518.

Bonnefille, R. (1971b). Atlas des pollens d'Ethiopie. Principales espèces des forets de montagne. *Adansonia* 13, 15–72.

Bonnefille, R. and Hamilton, A. (1986). Quaternary and late tertiary history of Ethiopian vegetation. *Symb. Bot. Ups.* 26, 48–63.

Bonnefille, R. and Mohammed, U. (1994). Pollen-inferred climatic fluctuations in Ethiopia during the last 3000 years. *Palaeogeogr. Palaeoclimatol. Palaeoecol.* 109, 331–343. doi:10.1016/0031-0182(94)90183-x

Bonnefille, R. and Riollet, G. (1980). *Pollens des savanes d'Afrique orientale*. Paris, France:Editions du Centre National de la Recherche Scientifique, 140.

Bowen, G. J. (2008). Spatial analysis of the intra-annual variation of precipitation isotope ratios and its climatological corollaries. *J. Geophys. Res.* 113, D05113. doi:10.1029/2007JD009295

Bray, E. E. and Evans, D. E. (1961). Distribution of n-paraffins as a clue to recognition of source beds. *Geochem. Cosmochim. Acta* 22, 2–15. doi:10.1016/0016-7037(61)90069-2

Brown, F. H. and Fuller, C. R. (2008). Stratigraphy and tephra of the kibish formation, southwestern Ethiopia. *J. Hum. Evol.* 55, 366–403. doi:10.1016/j.jhevol.2008.05.009

Camberlin, P. (1997). Rainfall anomalies in the source region of the nile and their connection with the Indian summer monsoon. *J. Clim.* 10, 1380–1392. doi:10.1175/1520-0442(1997)010<1380:raitsr>2.0.co;2

Camberlin, P., Janicot, S., and Poccard, I. (2001). Seasonality and atmospheric dynamics of the teleconnection between African rainfall and tropical sea-surface temperature: Atlantic vs ENSO. *Int. J. Climatol.* 21, 973–1005.

Castañeda, I. S., Mulitza, S., Schefuß, E., Lopes Dos Santos, R., Sinninghe Damsté, J. S., and Schouten, S. (2009). Wet phases in the Sahara/Sahel region and human migration patterns in North Africa. *Proc. Natl. Acad. Sci. USA* 106, 20159–20163. doi:10.1002/joc.673

Castañeda, I. S. and Schouten, S. (2011). A review of molecular organic proxies for examining modern and ancient lacustrine environments. *Quat. Sci. Rev.* 30, 2851–2951. doi:10.1016/j.quascirev.2011.07.009

Castañeda, I. S., Schouten, S., Pätzold, J., Lucassen, F., Kasemann, S., Kuhlmann, H., et al. (2016). Hydroclimate variability in the Nile river basin during the past 28,000 years. *Earth Planet Sci. Lett.* 438, 47–56. doi:10.1016/j.epsl.2015.12.014

Claussen, M., Bathiany, S., Brovkin, V., and Kleinen, T. (2013). Simulated climate-vegetation interaction in semi-arid regions affected by plant diversity. *Nat. Geosci.* 6, 954–958. doi:10.1038/ngeo1962

Collins, J. A., Prange, M., Caley, T., Gimeno, L., Beckmann, B., Mulitza, S., et al. (2017). Rapid termination of the African Humid Period triggered by northern high-latitude cooling. *Nat. Commun.* 8, 1372. doi:10.1038/s41467-017-01454-y

Costa, K., Russell, J., Konecky, B., and Lamb, H. (2014). Isotopic reconstruction of the African humid period and Congo air boundary migration at Lake Tana, Ethiopia. *Quat. Sci. Rev.* 83, 58–67. doi:10.1016/j.quascirev.2013.10.031

Darbyshire, I., Lamb, H. F., and Umer, M. (2003). Forest clearance and regrowth in northern Ethiopia during the last 3000 years. *Holocene* 13, 537–546. doi:10.1191/0959683603hl644rp

De Cort, G., Bessems, I., and Keppens, E. (2013). Late-Holocene and recent hydroclimatic variability in the central Kenya Rift Valley: the sediment record of hypersaline lakes Bogoria, Nakuru and Elementeita. *Palaeogeogr. Palaeoclimatol. Palaeoecol.* 388, 69–80. doi:10.1016/j.palaeo.2013.07.029

Degefu, F., Herzig, A., Jirsa, F., and Schagerl, M. (2014). First limnological records of highly threatened tropical high-mountain crater lakes in Ethiopia. *Trop. Conserv. Sci.* 7 (3), 365–381. doi:10.1177/194008291400700302

DeMenocal, P., Ortiz, J., Guilderson, T., Adkins, J., Sarnthein, M., Baker, L., et al. (2000). Abrupt onset and termination of the African Humid Period: rapid climate responses to gradual insolation forcing. *Quat. Sci. Rev.* 19, 347–361. doi:10.1016/s0277-3791(99)00081-5

Dupont, L. M. and Schefuß, E. (2018). The roles of fire in Holocene ecosystem changes off West Africa. *Earth Planet Sci. Lett.* 481, 255–263. doi:10.1016/j.epsl.2017.10.049

Eglinton, T. I. and Eglinton, G. (2008). Molecular proxies for paleoclimatology. *Earth Planet Sci. Lett.* 275, 1–16. doi:10.1016/j.epsl.2008.07.012

Ehleringer, J. R., Cerling, T. E., and Helliker, B. R. (1997). C4 photosynthesis, atmospheric CO2, and climate. *Oecologia* 112, 285–299. doi:10.1007/s004420050311

Faegri, K., Kaland, P. E., and Krzywinski, K. (1989). *Textbook of pollen analysis*. 4th Edn. Chichester, United Kingdom: John Wiley & Sons, 328.

Fleitmann, D., Burns, S. J., Mudelsee, M., et al. (2003). Holocene forcing of the Indian monsoon recorded in a stalagmite from southern Oman. *Science* 300, 1737–1739. doi:10.1126/science.1083130

Foerster, V., Junginger, A., Langkamp, O., Gebru, T., Asrat, A., Umer, M., et al. (2012). Climatic change recorded in the sediments of the Chew Bahir basin, southern Ethiopia, during the last 45,000 years. *Quat. Int.* 274, 25–37. doi:10.1016/j.quaint.2012.06.028

Friis, I. (1992). *Forests & forest trees of Northeast tropical Africa – their natural habitats and distribution patterns in Ethiopia, Djibouti and Somalia*. (London, United Kingdom: Royal Botanic Gardens), 396.

Friis, I., Demissew, S., and van Breugel, P. (2011). *Atlas of the potential vegetation of Ethiopia*. Addis Ababa, Ethiopia: Addis Ababa University Press and Shama Books.

Garcin, Y., Melnick, D., Strecker, M. R., Olago, D., and Tiercelin, J. J. (2012). East African mid-Holocene wet–dry transition recorded in palaeo-shorelines of Lake Turkana, northern Kenya Rift. *Earth Planet Sci. Lett.* 331-332, 322–334. doi:10.1016/j.epsl.2012.03.016

Gasse, F. (2000). Hydrological changes in the African tropics since the last glacial maximum. *Quat. Sci. Rev.* 19, 189–211. doi:10.1016/s0277-3791(99)00061-x

Gelorini, V., Verbeken, A., van Geel, B., Cocquyt, C., and Verschuren, D. (2011). Modern non-pollen palynomorphs from East African lake sediments. *Rev. Palaeobot. Palynol.* 164, 143–173. doi:10.1016/j.revpalbo.2010.12.002

Grimm, M. (2015). Tilia 2.0.41. Available at: http://www.tiliait.com/.

Hailu, B. T., Maeda, E. E., Heiskanen, J., and Pellikka, P. (2015). Reconstructing pre-agricultural expansion vegetation cover of Ethiopia. *Appl. Geogr.* 62, 357–365. doi:10.1016/j.apgeog.2015.05.013

Hall, J. B. (1984). Juniperus excelsa in Africa: a biogeographical study of an Afromontane tree. *J. Biogeogr.* 11, 47–61. doi:10.2307/2844775

Hamilton, A. C. (1982). *Environmental history of East Africa*. London, United Kingdom: Academic Press.

Höpker, S. N., Wu, H. C., Müller, P., Barusseau, J.-P., Vernet, R., Lucassen, F., et al. (2019). Pronounced northwest African monsoon discharge during the mid- to late Holocene. *Front. Earth Sci.* 7, 314. doi:10.3389/feart.2019.00314

Jaeschke, A., Rethemeyer, J., Lappé, M., Schouten, S., Boeckx, P., and Schefuß, E. (2018). Influence of land use on the distribution of soil n-alkane D and brGDGTs along an altitudinal transect in Ethiopia: implications for (paleo) environmental studies. *Org. Geochem.* 124, 77–87.

Johnson, T. C., Scholz, C. A., Talbot, M. R., Kelts, K., Ricketts, R. D., Ngobi, G., et al. (1996). Late Pleistocene desiccation of Lake Victoria and rapid evolution of cichlid fishes. *Science* 273, 1091–1093.

Junginger, A., Roller, S., Olaka, L. A., and Trauth, M. H. (2014). The effects of solar irradiation changes on the migration of the Congo Air Boundary and water levels of paleo-Lake Suguta, Northern Kenya Rift, during the African Humid Period (15–5 ka BP). *Palaeogeogr. Palaeoclimatol. Palaeoecol.* 396, 1–16.

Kahmen, A., Schefuß, E., and Sachse, D. (2013). Leaf water deuterium enrichment shapes leaf wax n-alkane δD values of angiosperm plants I: experimental evidence and mechanistic insights. *Geochem. Cosmochim. Acta* 111, 39–49. doi:10.1016/j.gca.2012.09.003

Kebede, S. and Travi, Y. (2012). Origin of the δ18O and δ2H composition of meteoric waters in Ethiopia. *Quat. Bar Int.* 257, 4–12. doi:10.1016/j.quaint.2011.09.032

Kröpelin, S., Verschuren, D., Lézine, A. M., Eggermont, H., Cocquyt, C., Francus, P., et al. (2008). Climate-driven ecosystem succession in the Sahara: the past 6000 years. *Science* 320, 765–768. doi:10.1126/science.1154913

Kuechler, R. R., Schefuß, E., Beckmann, B., Dupont, L., and Wefer, G. (2013). NW African hydrology and vegetation during the Last Glacial cycle reflected in plant-wax- specific hydrogen and carbon isotopes. *Quat. Sci. Rev.* 82, 56–67. doi:10.1016/j.quascirev.2013.10.013

Kuhnert, H., Kuhlmann, H., Mohtadi, M., Meggers, H., Baumann, K. H., and Pätzold, J. (2014). Holocene tropical western Indian Ocean sea surface temperatures in covariation with climatic changes in the Indonesian region. *Paleoceanography* 29, 423–437. doi:10.1002/2013pa002555

Kuper, R. and Kröpelin, S. (2006). Climate-controlled Holocene occupation in the Sahara: motor of Africa's evolution. *Science* 313, 803–807. doi:10.1126/science.1130989

Lamb, H. F., Bates, C. R., Coombes, P. V., Marshall, M. H., Umer, M., Davies, S. J., et al. (2007). Late pleistocene desiccation of Lake Tana, source of the blue Nile. *Quat. Sci. Rev.* 26, 287–299. doi:10.1016/j.quascirev.2006.11.020

Levin, N. E., Zipser, E. J., and Cerling, T. E. (2009). Isotopic composition of waters from Ethiopia and Kenya: insights into moisture sources for eastern Africa. *J. Geophys. Res.* 114, D23306. doi:10.1029/2009JD012166

Lézine, A. M., Casanova, J., and Hillaire-Marcel, C. (1990). Across an early Holocene humid phase in Western Sahara: pollen and isotope stratigraphy. *Geology* 18, 264–267. doi:10.1130/0091-7613(1990)018<0264:aaehhp>2.3.co;2

Lézine, A.-M., Hély, C., Grenier, C., Braconnot, P., and Krinner, G. (2011a). Sahara and Sahel vulnerability to climate changes, lessons from Holocene hydrological data. *Quat. Sci. Rev.* 30, 3001–3012. doi:10.1016/j.quascirev.2011.07.006

Lézine, A. M., Zheng, W., Braconnot, P., and Krinner, G. (2011b). Late Holocene plant and climate evolution at Lake Yoa, northern Chad: pollen data and climate simulations. *Clim. Past* 7, 1351–1362.

Liu, Z., Wang, Y., Gallimore, R., Gasse, F., Johnson, T., de Menocal, P., et al. (2007). Simulating the transient evolution and abrupt change of Northern Africa atmosphere-ocean-terrestrial ecosystem in the Holocene. *Quat. Sci. Rev.* 26, 1818–1837. doi:10.1016/j.quascirev.2007.03.002

Marshall, M. H., Lamb, H. F., Huws, D., Davies, S. J., Bates, R., and Bloemendal, J. (2011). Late pleistocene and Holocene drought events at Lake Tana, the source of the blue Nile. *Global Planet. Change* 78, 147–161. doi:10.1016/j.gloplacha.2011.06.004

McManus, J. F., Francois, R., Gherardi, J. M., Keigwin, L. D., and Brown-Leger, S. (2004). Collapse and rapid resumption of Atlantic meridional circulation linked to deglacial climate changes. *Nature* 428, 834–837. doi:10.1038/nature02494

Mitchell, T. D. and Jones, P. D. (2005). An improved method of constructing a database of monthly climate observations and associated high-resolution grids. *Int. J. Climatol.* 25, 693–712. doi:10.1002/joc.1181

Nicholson, S. E. (2017). Climate and climatic variability of rainfall over eastern. *Africa. Rev. Geophys.* 55, 590–635. doi:10.1002/2016rg000544

Nicholson, S. E. (2000). The nature of rainfall variability over Africa on time scales of decades to millenia. *Global Planet. Change* 26, 137–158. doi:10.1016/s0921-8181(00)00040-0

Pausata, F. S. R., Gaetani, M., Messori, G., Berg, A., Maia de Souza, D., Sage, R. F., et al. (2020). The greening of the Sahara: past changes and future implications. *One Earth* 2, 235–250. doi:10.1016/j.oneear.2020.03.002

Powers, L. A., Johnson, T. C., Werne, J. P., Castañeda, I., Hopmans, E. C., Sinninghe Damsté, J. S., et al. (2005). Large temperature variability in the southern African tropics since the last glacial maximum. *Geophys. Res. Lett.* 32, L08706. doi:10.1029/2004GL022014

Renssen, H., Brovkin, V., Fichefet, T., and Goosse, H. (2006). Simulation of the Holocene climate evolution in northern Africa: the termination of the African humid period. *Quat. Int.* 15, 95–102. doi:10.1016/j.quaint.2005.01.001

Revel, M., Ducassou, E., Grousset, F. E., Bernasconi, S. M., Migeon, S., Revillon, S., et al. (2010). 100,000 Years of African monsoon variability recorded in sediments of the Nile margin. *Quat. Sci. Rev.* 29, 1342–1362. doi:10.1016/j.quascirev.2010.02.006

Rozanski, K., Araguás-Araguás, L., and Gonfiantini, R. (1993). "Isotopic patterns in modern global precipitation," in *Climate change in continental isotopic records*. Editors P. K. Swart, K. C. Lohmann, J. McKenzie, and S. Savin (Washington, Unites States: American Geophysics Union), 79–93.

Sachse, D., Billault, I., Bowen, G. J., Chikaraishi, Y., Dawson, T. E., Feakins, S. E., et al. (2012). Molecular paleohydrology: interpreting the hydrogen-isotopic composition of lipid biomarkers from photosynthesizing organisms. *Ann. Rev. Earth Planet. Sci.* 40, 221–249. doi:10.1146/annurev-earth-042711-105535

Schefuß, E., Schouten, S., Jansen, J. F., and Sinninghe Damsté, J. S. (2003). African vegetation controlled by tropical sea surface temperatures in the mid-Pleistocene period. *Nature* 422 (6930), 418–421. doi:10.1038/nature01500

Schefuß, E., Schouten, S., and Schneider, R. R. (2005). Climatic controls on central African hydrology during the past 20,000 years. *Nature* 437, 1003–1006. doi:10.1038/nature03945

Sereno, P. C., Garcea, E. A. A., Jousse, H., Stojanowski, C., Saliège, J. F., Maga, A., et al. (2008). Lakeside cemeteries in the Sahara: 5000 Years of Holocene population and environmental change. *PloS One* 3, e2995. doi:10.1371/journal.pone.0002995

Shanahan, T. M., Hughen, K. A., Mckay, N. P., Overpeck, J. T., Scholz, C. A., Gosling, W. D., et al. (2016). CO2 and fire influence tropical ecosystem stability in response to climate change. *Sci. Rep.* 6, 29587. doi:10.1038/srep29587

Shanahan, T. M., McKay, N. P., Hughen, K. A., Overpeck, J. T., Otto-Bliesner, B., Heil, C. W., et al. (2015). The time-transgressive termination of the African humid period. *Nat. Geosci.* 8, 140–144. doi:10.1038/ngeo2329

Smith, F. A. and Freeman, K. H. (2006). Influence of physiology and climate on δD of leaf wax n-alkanes from C3 and C4 grasses. *Geochem. Cosmochim. Acta* 70, 1172–1187. doi:10.1016/j.gca.2005.11.006

Stanley, J. D., Krom, M. D., Cliff, R. A., and Woodward, J. C. (2003). Short contribution: Nile flow failure at the end of the Old Kingdom, Egypt: strontium isotopic and petrologic evidence. *Geoarchaeology* 18 (3), 395–402. doi:10.1002/gea.10065

Talbot, M. R., Filippi, M. L., Jensen, N. B., and Tiercelin, J. J. (2007). An abrupt change in the African monsoon at the end of the younger Dryas. *G-cubed* 8, Q03005. doi:10.1029/2006GC001465

Tierney, J. E. and deMenocal, P. B. (2013). Abrupt shifts in horn of Africa hydroclimate since the last glacial maximum. *Science* 342, 843–846. doi:10.1126/science.1240411

Tierney, J. E., Pausata, F. S. R., and deMenocal, P. B. (2017). Rainfall regimes of the Green Sahara. *Sci. Adv.* 3, e1601503. doi:10.1126/sciadv.1601503

Tierney, J. E., Russell, J. M., and Huang, Y. (2010). A molecular perspective on Late Quaternary climate and vegetation change in the Lake Tanganyika basin, East Africa. *Quat. Sci. Rev.* 29, 787–800. doi:10.1016/j.quascirev.2009.11.030

Tierney, J. E., Russell, J. M., Sinninghe Damsté, J. S., Huang, Y., and Verschuren, D. (2011). Late quaternary behavior of the east African monsoon and the importance of the Congo air boundary. *Quat. Sci. Rev.* 30, 798–807. doi:10.1016/j.quascirev.2011.01.017

Trenberth, K. E., Stepaniak, D. P., and Caron, J. (2000). The global monsoon as seen through the divergent atmospheric circulation. *J. Clim.* 13, 3969–3993. doi:10.1175/1520-0442(2000)013<3969:tgmast>2.0.co;2

Umer, M., Lamb, H. F., Bonnefille, R., Tiercelin, J. J., Gibert, E., Cazet, J. P., et al. (2007). Late pleistocene and Holocene vegetation history of the Bale mountains, Ethiopia. *Quat. Sci. Rev.* 26, 2229–2246. doi:10.1016/j.quascirev.2007.05.004

Ummenhofer, C. C., Gupta, A. S., and England, M. H. (2009). Contributions of Indian Ocean sea surface temperatures to enhanced east Africa rainfall. *J. Clim.* 22, 993–1013. doi:10.1175/2008jcli2493.1

Van Geel, B., Gelorini, V., Lyaruu, A., Aptroot, A., Rucina, S., Marchant, R., et al. (2011). Diversity and ecology of tropical African fungal spores from a 25,000-year palaeoenvironmental record in southeastern Kenya. *Rev. Palaeobot. Palynol.* 164, 174–190. doi:10.1016/j.revpalbo.2011.01.002

Verschuren, D., Laird, K. R., and Cumming, B. F. (2000). Rainfall and drought in equatorial east Africa during the past 1,100 years. *Nature* 403, 410–414. doi:10.1038/35000179

Vogelsang, R., Bubenzer, O., Kehl, M., Meyer, S., Richter, J., and Zinaye, B. (2018). When hominins conquered highlands—an Acheulean site at 3000 m a.s.l. on Mount Dendi/Ethiopia. *J. Paleol. Archaeol* 1, 302–313. doi:10.1007/s41982-018-0015-9

Vogts, A., Moossen, H., Rommerskirchen, F., and Rullkötter, J. (2009). Distribution patterns and stable carbon isotopic composition of alkanes and alkan-1-ols from plant waxes of African rain forest and savanna C3 species. *Org. Geochem.* 40, 1037–1054. doi:10.1016/j.orggeochem.2009.07.011

Wagner, B., Wennrich, V., Viehberg, F., Junginger, A., Kolvenbach, A., Rethemeyer, J., et al. (2018). Holocene rainfall runoff in the central Ethiopian highlands and evolution of the River Nile drainage system as

revealed from a sediment record from Lake Dendi. *Global Planet. Change* 163, 29–43. doi:10.1016/j.gloplacha.2018.02.003

Wanner, H., Solomina, O., Grosjean, M., Ritz, S. P., and Jetel, M. (2011). Structure and origin of Holocene cold events. *Quat. Sci. Rev.* 30, 3109–3123. doi:10.1016/j.quascirev.2011.07.010

Weldeab, S., Lea, D. W., Schneider, R. R., and Anderson, N. (2007). 155,000 years of West African monsoon and ocean thermal evolution. *Science* 316, 1303–1307. doi:10.1126/science.1140461

Weldeab, S., Menke, V., and Schmiedl, G. (2014). The pace of East African monsoon evolution during the Holocene. *Geophys. Res. Lett.* 41, 2014GL059361. doi:10.1002/2014gl059361

Wu, H., Guiot, J., Brewer, S., Guo, Z., and Peng, C. (2007). Dominant factors controlling glacial and interglacial variations in the treeline elevation in tropical Africa. *Proc. Natl. Acad. Sci. USA* 104 (23), 9720–9724. doi:10.1073/pnas.0610109104

Conflict of Interest: The authors declare that the research was conducted in the absence of any commercial or financial relationships that could be construed as a potential conflict of interest.

frontiers in Earth Science

ORIGINAL RESEARCH
published: 14 January 2021
doi: 10.3389/feart.2020.611700

Stratigraphy and Chronology of Sodicho Rockshelter – A New Sedimentological Record of Past Environmental Changes and Human Settlement Phases in Southwestern Ethiopia

Elena A. Hensel[1]*, *Ralf Vogelsang*[2], *Tom Noack*[2] and *Olaf Bubenzer*[3]

[1]Institute of Geography, University of Cologne, Cologne, Germany, [2]Institute of Prehistoric Archaeology, University of Cologne, Cologne, Germany, [3]Institute of Geography and Heidelberg Center for the Environment (HCE), Heidelberg University, Heidelberg, Germany

OPEN ACCESS

Edited by:
Christian Zeeden,
Leibniz Institute for Applied Geophysics (LIAG), Germany

Reviewed by:
Alvise Barbieri,
University of Algarve, Portugal
Andrea Zerboni,
University of Milan, Italy

***Correspondence:**
Elena A. Hensel
elena.hensel@uni-koeln.de

Specialty section:
This article was submitted to Quaternary Science, Geomorphology and Paleoenvironment, a section of the journal Frontiers in Earth Science

Received: 29 September 2020
Accepted: 19 November 2020
Published: 14 January 2021

Citation:
Hensel EA, Vogelsang R, Noack T and Bubenzer O (2021) Stratigraphy and Chronology of Sodicho Rockshelter – A New Sedimentological Record of Past Environmental Changes and Human Settlement Phases in Southwestern Ethiopia. Front. Earth Sci. 8:611700. doi: 10.3389/feart.2020.611700

The preservation of archaeological remains and environmental information in a sediment accumulation can vary in caves and rockshelters, depending on external climatic conditions, and the circumstances within the shelter. Several sediment stratigraphies in the Horn of Africa are characterized by erosion layers, discordances and chronological gaps, that create uncertainties about the impact of climatic and environmental shifts on human settlements. Archaeological sites in Ethiopia that preserve information about human occupation during the Upper Pleistocene and Holocene often deal with major gaps during a period corresponding to MIS 2. In this study we present the first results of sedimentological, geochemical analyses and radiocarbon dating at Sodicho Rockshelter (1930 m above sea level) that provide evidence on high altitude settlement during this mentioned chronostratigraphic gap and subsequent time slices. This new archaeological site in the southwestern Ethiopian Highlands hosts a 2-m-long sediment record. So far, a stratigraphy has been excavated that dates back to ~27 ka, including several settlement phases of Late Pleistocene and Holocene hunter-gatherers and providing information on environmental changes. A multiproxy approach was chosen to establish a first general stratigraphy of the site and to disentangle the sediment composition as well as site formation processes. The results suggest a variation of allochthonous and autochthonous geogenic deposits, and anthropogenic accumulation processes. With the help of radiocarbon dating, anthropogenic layers were dated covering the arid Last Glacial Maximum (LGM, ~21 ± 2 ka). The occupation phases were interrupted in cause of environmental changes. The most prominent is the accumulation of reddish, archaeological sterile deposits that can be chronologically associated with the African Humid Period (AHP, ~15–5 ka BP). Geochemical records point to dry spells within this humid phase, suggesting correlations with regional climate signals of lacustrine sediments. These sediment accumulations of past wet conditions are covered by alternating layers of Holocene volcanic fallout and sediments with preserved cultural material. Our study

provides a preliminary impression of still poorly understood time periods of human occupation in the southwestern Ethiopian Highlands. The data obtained from Sodicho Rockshelter could validate the current state of knowledge and partially reduce the chronostratigraphic gap.

Keywords: geoarchaeology, stratigraphy, sedimentology, geochemistry, late pleistocene, holocene, african humid period, radiocabon dating

INTRODUCTION

The development of a sediment stratigraphy within a rockshelter setting is driven by diverse sediment origins and changing conditions of the regional environment, including human agency. The different sediment sources, e.g., geogenic (autochthonous and allochthonous), anthropogenic, and biogenic often result in a diverse, intermitted deposition. Like caves, rockshelters function as a sediment trap, however, they are often partly or completely exposed to weather conditions, which in turn explains the variability in deposition. The prehistoric humans used these places as natural shelters (Mentzer, 2017). The use of caves and rockshelters by prehistoric humans has been part of geoarchaeological research in several regions, such as southern and northern Africa, Europe or the Levant (Goldberg and Bar-Yosef, 1998; Goldberg et al., 2009; Marean et al., 2010; Miller et al., 2013; Kehl et al., 2014; Klasen et al., 2018; Inglis et al., 2018). The studies investigated the natural forces contributing to deposition of sediment and the active modification of sediment structures by human activities (e.g., fireplaces, trampling and bedding) (Goldberg et al., 2009; Miller et al., 2013). Deposits can be altered, masked or even erased from the sedimentary record by post-depositional processes, resulting in gaps of knowledge and uncertainties leading to rather short and discontinuous archaeological sequences (Kuehn and Dickson, 1999). In the Horn of Africa, especially in Ethiopia, these gaps in stratification are quite common. In most cases, they correlate with the transition from the Middle Stone Age (MSA) to the Late Stone Age (LSA) during the period of the MIS 2 (Tribolo et al., 2017). Several studies at sites such as Goda Buticha, the Ziway-Shala basin and Mochena Borago identified a stratigraphical and a chronological gap, spanning from ~38 ka and reaching into the Holocene (**Figure 1A**) (Tribolo et al., 2017).

Although terrestrial paleoenvironmental records are very scarce in Ethiopia, they provide a useful source for the reconstruction of past varying environmental conditions. Lacustrine sediments from Ethiopian and Kenyan lakes refer to hyper arid conditions during the Heinrich Events (H) and the Late Glacial Maximum (LGM, ~21 ± 2 ka), followed by overall moist conditions of the African Humid Period with intermediate dry spells (Mark and Osmaton, 2008; Junginger and Trauth, 2013; Foerster et al., 2015). Higher

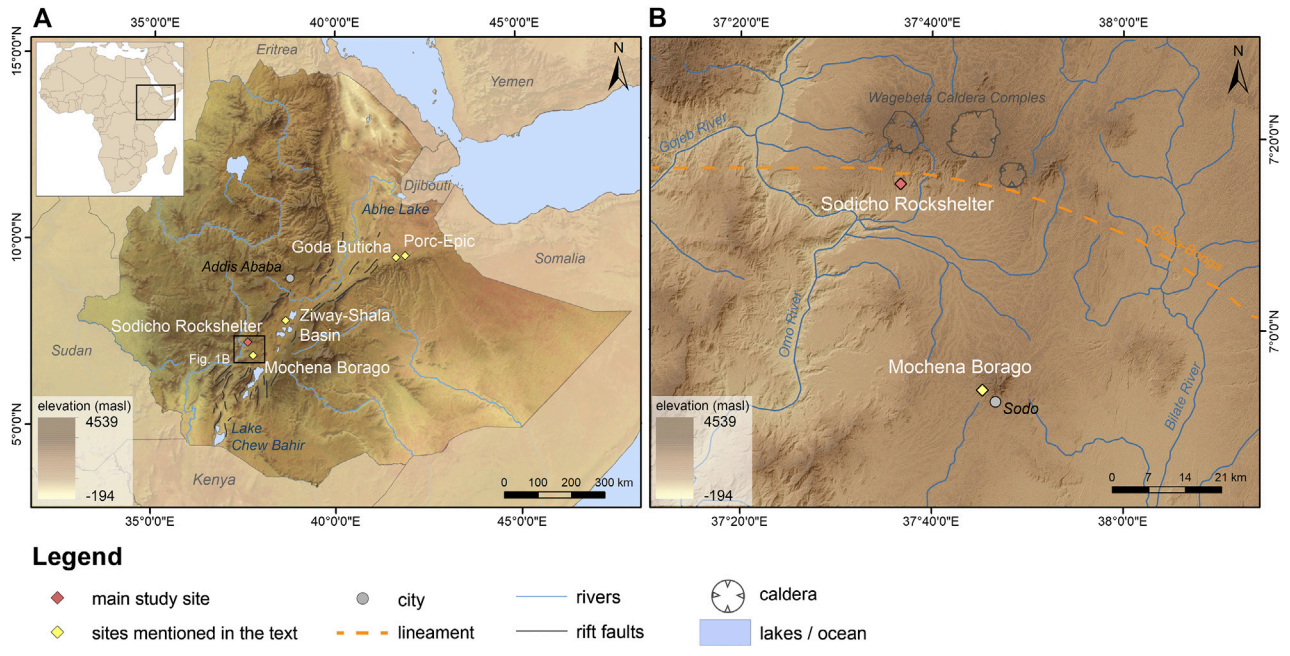

FIGURE 1 | (A) Map of the study area with locations and archaeological sites mentioned in the text. **(B)** Study area in the Southwestern Ethiopian Highlands (DEM data by ASTER GDEM and Natural Earth raster map data).

moisture availability in the highlands could have permitted the survival of vegetation, animals and humans during the arid phases. In this case, rockshelters in high altitude regions might have attracted hunter-gatherers, despite the challenging conditions for human physiology (Foerster et al., 2015; Vogelsang and Wendt, 2018).

Sodicho Rockshelter is located about 40 km NW from the aforementioned Mochena Borago Rockshelter site, which is one of the archaeological key-sites in northeastern Africa and shares a comparable well-structured sedimentological and archeological sequence (Brandt et al., 2017; Hensel et al., 2019). With this study we introduce preliminary results of geoarchaeological and archaeological investigations of Sodicho Rockshelter and relate the results to regional climatic records. We attempt to reconstruct geogenic and biogenic site formation processes and to compare them to the cultural induced processes. The aim of this study is 1) to determine the sediment composition, 2) to reconstruct the site formation processes in the shelter, 3) to develop a first ^{14}C chronology and 4) put the human occupation in the context of the geoarchaeological results.

BACKGROUNDS

Geoarchaeological Research

Until now, the most important rockshelter in the southwestern Ethiopian Highlands is Mochena Borago on Mount Damota. Since 1998, several research teams investigated almost 2 m of stratified Holocene and Late Pleistocene deposits. The latter preserved cultural remains dating between 36 and >50 ka (Gutherz et al., 2002; Fisher, 2010; Brandt et al., 2012; Brandt et al., 2017). In 2009 the Collaborative Research Center 806 (CRC 806, http://www.sfb806.uni-koeln.de) joint the investigations of Steven Brandt (Southwest Ethiopia Archaeological Project) at Mochena Borago. Geoarchaeological research at Mochena Borago aimed to reconstruct site formation processes with the help of geomorphological investigations and micromorphological observations (Brandt et al., 2017). During archaeological and geomorphological surveys in the surroundings, Sodicho Rockshelter was first visited in 2012 (Brandt et al., 2017; Vogelsang and Wendt, 2018; Hensel et al., 2019). Further research in the area focused on the exposure of archaeological records along the valleys of the Bilate River and its tributary the Bisare River, southwest of Mt. Damota. According to the studies, abundant archaeological material occurs in sediments, that are exposed by badland formation. These badlands are not older than 200 ka and hold mostly MSA and LSA obsidian artifacts. However, some sites also hold artifacts that show characteristics of the late Early Stone Age (ESA) (Benito-Calvo et al., 2007; De la Torre et al., 2007). Geomorphological–hydrological analyses around Mt. Damota and Mt. Sodicho revealed that the region is influenced by a very dynamic system of permanent and episodic river networks. The resulting soil erosion and the exposure and destruction of archaeological open-air sites and raw material outcrops emphasizes the importance of protected rockshelter stratigraphies and their potential to preserve archaeological deposits and environmental information (Hensel et al., 2019).

Geology, Geography, Climate and Vegetation of Study Area

Sodicho Rockshelter is located E 37°36'44 and N 7°15'21 in the southwestern Ethiopian Highlands. The cavity opens to the south and is situated at the slopes of Mount Sodicho at an elevation of about 1930 m above sea level (Hensel et al., 2019). The complex tectonic and volcanic structures of the Main Ethiopian Rift are situated to the west. To the east lies the deep canyon of the Omo River (**Figure 1B**). The mountain itself consists of a greyish to yellowish trachyte, and is part of a series of silicic domes, lavas and tephra that lie ~8 km south of the three circular Wagebeta Calderas. The past volcanic formations date back 3.6 to 4.2 Ma into the Pliocene and during the late phase of the rift system development in Ethiopia (WoldeGabriel et al., 1990; WoldeGabriel et al., 1992; Chernet, 2011; Hensel et al., 2019). The volcanic formations are aligned along the transverse east–west Goba-Bonga lineament, a depression that crosses the center of the Main Ethiopian Rift (Bonini et al., 2005; Corti, 2009; Corti et al., 2013). The present appearance of the area is shaped by Late Pleistocene to Holocene tectonic stress, climatic, and geomorphological changes (Benito-Calvo et al., 2007). A network of episodic and permanent streams drains down the slopes of Mt. Sodicho toward the Omo River, creating the mountain's characteristic irregular shape. The increased human influence during the last decades is visible by cleared slopes for cultivation and cattle farming (Hensel et al., 2019). The major soil type is the kaolinite rich, red colored Humic Nitisol, a fertile soil type, common in the humid tropics (Berhanu et al., 2013; IUSS Working Group WRB, 2014). The modern climate in the southwestern Ethiopian Highlands is a complex and variable system that is characterized by two rainy seasons with an average precipitation of about 2,000 mm per year. Over 50% of the annual rain in the SW Ethiopian Highlands falls in course of the "Kirmet", the main rainy season during the boreal summer (June to September). During the months November to February the region experiences the dry period with an average <50 mm per month, followed by a second weaker rainy season, the "Belg" (Fisher, 2010; Brandt et al., 2012; Hildebrand et al., 2019). These annual and inter-annual precipitation changes are connected to the interaction of the moist summer monsoon and the dry northeastern "Harmattan" wind system, resulting in changes of the north-south directed pressure gradient (Viste and Sorteberg, 2013; Nicholson, 2018). Further influences on the annual precipitation are associated with changes in sea surface temperature (SST) of the Indian Ocean, the northern shifting tropical rain belt, low-level convergences, and the Congo Air Boundary in lesser relevance (Griffiths, 1972; Segele et al., 2009; Tierney et al., 2011; Junginger and Trauth, 2013; Viste and Sorteberg, 2013; Nicholson, 2018).

Up to now, only the last 45 ka are analyzed from a drilling core in the Chew Bahir basin, which is situated ~300 km from Mount Sodicho. Its catchment area runs through the SW Highlands, which means that Chew Bahir was also affected by climatic

conditions prevailing in the highlands. According to sedimentological and geochemical investigations of these lake sediments, the past climate in the southwestern highlands has undergone arid and humid phases. A rather moist phase from 45 to 35 ka BP was followed by arid conditions (Foerster et al., 2012). During the cold and arid Marin Isotope Stage 2 (MIS 2, ~29–12 ka BP), lake levels and river catchments changed, which influenced the surrounding habitat of flora and fauna (Foerster et al., 2012; Foerster et al., 2015; Stewart and Jones, 2016). The aridity ended after 15 ka with an increase in humidity. This indicated the beginning of the Early Holocene African Humid Period, which stretched out until 5 ka and was interrupted by shorter dryer periods (Foerster et al., 2012; Foerster et al., 2015; Hildebrand et al., 2019; Trauth et al., 2019).

MATERIALS AND METHODS

Fieldwork and Archaeological Excavation

The excavations at Sodicho Rockshelter were conducted annually from 2015 to 2018. Of two 50 × 50 cm test pits in 2015, one was extended to an excavation trench with an area of four square meters, each split into 50 × 50 cm quadrants that were excavated individually (**Figure 2C**, F34/35 and G34/35). Big boulders stopped the extension of the second test pit (**Figure 2C**, E41), which was located in one of the cavities at the rear wall of the shelter. Both trenches are situated in backward areas that seem to be well protected from humidity, in terms of dripping water and trickle. Archaeological excavations followed natural stratigraphic boundaries, subdivided vertically into arbitrary spits with a maximum thickness of 5 cm. Spits never transversed natural stratigraphic boundaries, i.e. a spit definitely ended when visible sediment changes where observed during excavation. Specific archaeological features, such as hearths or pits, were excavated in the same way but separately from the surrounding matrix. No total station was available during the first fieldwork in 2015. Therefore, the grid system of the test pits was sat up with measuring tapes and leveling taken with a surveyor's level. Archaeological finds of the test pits were recovered via dry sieving in three stages, using mesh widths of 10, 5, and 2.5 mm. The closest spatial allocation of these finds is to one of the artificial spits. During the subsequent excavations all archaeological finds >5 mm were single plotted using a Leica TS02 total station and provenience information such as grid unit, depth, level and stratum, as well as material type (e.g., stone, bone, charcoal) were recorded. Each find was then bagged individually and assigned a unique identification number. The excavated sediments were dry sieved to recover smaller finds using 10-, 5-, and 2.5-mm mesh size. The total station was also employed to map each stratum, feature or natural disturbance as it was exposed, and forms recorded information on sedimentology, spatial and vertical configurations and other relevant data. In addition, plan views of each excavation spit and stratigraphic profiles were mapped on grid paper and recorded with digital photographs. The geoarchaeological fieldwork included on-site observation with an analysis of the sediment deposits (**Supplementary Table S1**) and a classification of the common lithological composition of the bedrock in the rockshelter itself. Furthermore, several half-day surveys along the mountain flanks of Mt. Sodicho were undertaken to identify lithological changes of bedrock and geomorphological conditions of the area.

Multiproxy Sediment Analyses

Bulk sediment samples were determined with a 2 cm resolution at the west facing profile from square F35 and the south facing profile from square G35 (**Figure 3**). Lower sediment samples were taken from square G35 because collapsed blocks in F35 hindered further sampling in this square. Both sample columns overlap by approximately 30 cm. The sample thickness was increased to 4 cm in layers of difficult access, e.g., around bigger rocks. As a pre-treatment the samples were dried at 40°C in a drying chamber and sieved to remove material >2 mm.

The granulometry was determined with a Laser Diffraction Particle Size Analyzer (Beckmann Coulter LS13 320, Beckmann Coulter, Inc.) and pretreated with hydrogen peroxide (H_2O_2 15%) to remove organic opal. In addition, several reference samples were treated with hydrochloric acid (HCl 10%) to remove organic and inorganic carbon. Prior to the measurements, Na_2PO_5 (46 g/L) was applied to all samples to avoid coagulation. The results were evaluated and statistically measured with the GRADISTAT software version 8 (Blott and Pye, 2001) and the parameters are based on Folk and Ward (1957).

Sediment color was measured with a VIS spectrophotometer (Konica Minolta CM-5) to determine the reflected wavelength from the sample in a visible range of 360–740 nm and converted into L*a*b* values (Eckmeier and Gerlach, 2012). The L*a*b* values express the extinction of light in the spectra from absolute black (L*0) to absolute white (L*100) and the color ranges from green to red (a* to $+a^*$) as well as from blue to yellow (b* to $-b^*$). The redness index (RI) was calculated applying the L*a*b* variables according to Barrón and Torrent (1986) $RI = \frac{a^*(a^{*2}+b^{*2})^{\frac{1}{2}}10^{10}}{b^*L^{*6}}$.

The mass specific magnetic susceptibility was determined by using a Bartington MS2 Magnetic Susceptibility System with a MS2k sensor and measured twice under laboratory conditions on the sieved and weighed in samples. For further geochemical investigations a part of the material was grinded with a vibrating zircon ball mill (Mixer Mill MM 400, Retsch). The total carbon content (TC) was measured with a vario EL cube (Elementar Analysensysteme GmbH). In addition, the total organic carbon (TOC) content was measured on a few reference samples after a pretreatment of HCl (10%).

For the determination of the major and trace elemental composition two methods using X-ray fluorescence (XRF) were applied. First, all grinded samples were measured with a handheld Niton™ XL3t XRF Analyzer (Thermo Scientific™) under laboratory conditions, viz. samples were pressed in pellets and measured twice in a test stand. This method has the advantage that many samples can be measured relatively quickly and easily after a relatively complex preparation. However, studies with a portable XRF devices (pXRF) have shown that the spectrometer cannot properly measure elements like phosphorous (Hunt and Speakman, 2015).

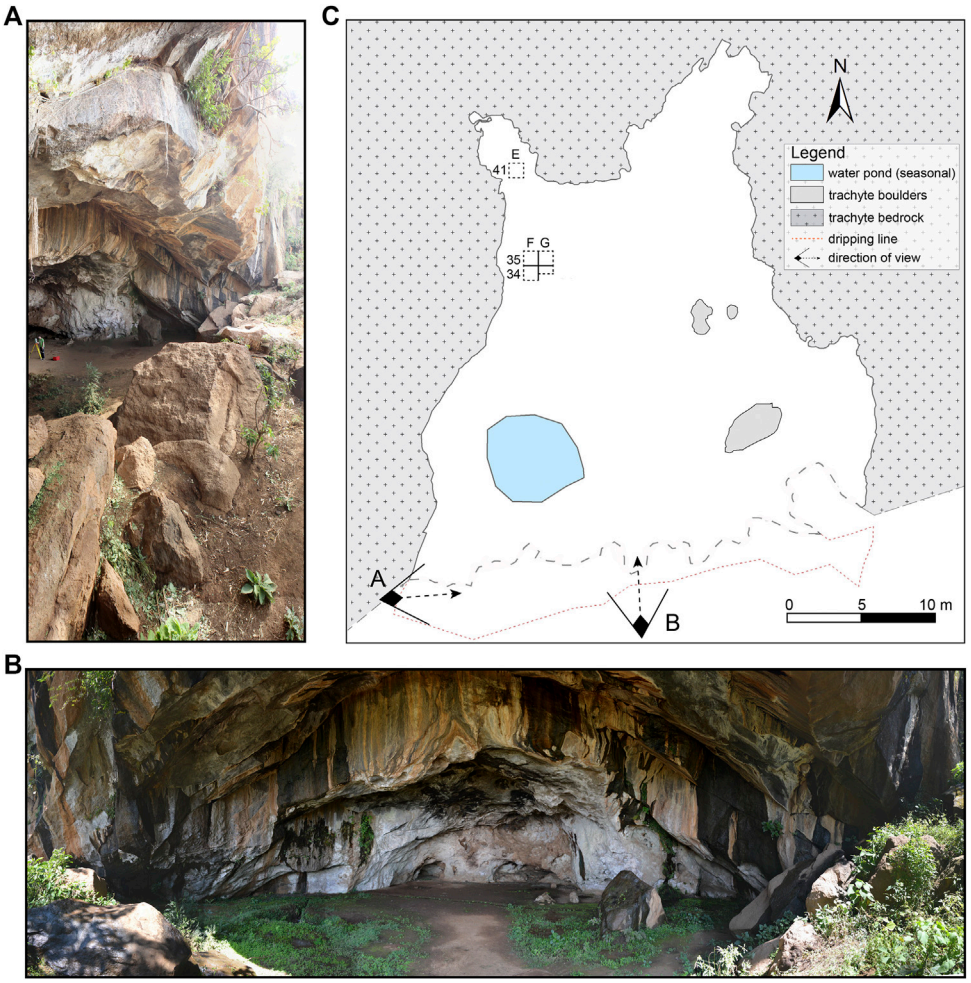

FIGURE 2 | (A) The collapsed overhang blocks the entrance. **(B)** Panoramic view into the shelter. Moisture becomes evident by the dark staining of the surface (photos by C. Schepers) **(C)** Plan of the Sodicho Rockshelter with the location of the excavation pits, an anthropogenic water pond and the location of the two photos.

Therefore, to verify the results of the pXRF analyzer, and to derive geochemical indicators for alteration and weathering a selection of the samples were measured at the Institute of Physical Geography and Geoecology at the RWTH Aachen. Here the grinded samples were also pressed to tablets and measured twice with the SPECTRO XEPOS energy dispersive X-ray fluorescence spectrometer (Spectro). The resulting elements and oxides were then chosen as representing indicators for depositional changes. A chemical index of alteration (CIA) was calculated according to the calculations of Nesbitt and Young (1982): $CIA = \left[\frac{Al_2O_3}{Al_2O_3+Na_2O+K_2O+CaO}\right] \times 100$·

Age Determination

A total of 31 samples were collected in the squares F34, F35, and G35 during the excavations in 2015 to 2018 (**Figure 2**). The radiocarbon AMS lab Beta Analytics Limited analyzed 28 samples of seeds and charcoal. Additionally, two charcoal and one soot sample, the latter scratched from the besmoked outer face of a cooking pot sherd, were measured at the AMS laboratory of the University of Cologne. The results were calibrated with Calib8.10. using the IntCal20.^{14}C curve (Reimer et al., 2020). A classic age depth model was established with the clam2.3.5 package in RStudio according to Blaauw (2010). In the model the radiocarbon ages were calibrated with the northern hemisphere terrestrial calibration curve IntCal20.^{14}C.

RESULTS

Field Observations at the Sodicho Rockshelter

The south facing opening of the rock shelter is almost completely protected by big trachytic boulders (2 diam.) that originate from the partial collapse of the originally larger front overhang (**Figure 2A**). This hinders the direct influence of precipitation and fluvial weathering into the flat shelter. However, the blocking rocks cause a slight downward slope into the shelter. The sediment accumulation therefore differs spatially, which in turn can influence the characteristics of certain sediment layers, like deposit thickness. The interior

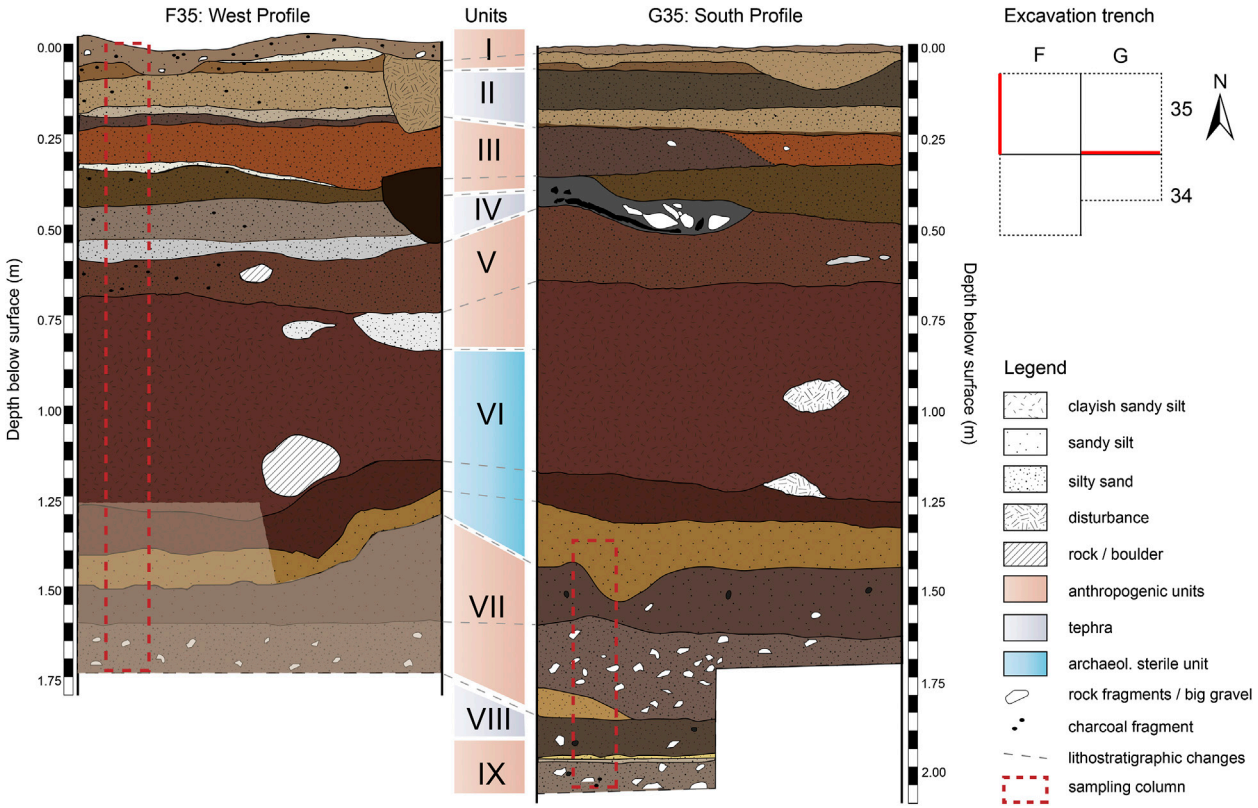

FIGURE 3 | Schematic excavation profiles of F35 **(left)** and G35 **(right)**. Sampling columns for sedimentological and geochemical analyses are marked in red. The course of layering in the brightened areas (F35) is assumed, since an exact pattern for this lower section could not be sketched in the field.

of Sodicho Rockshelter is characterized by the effects of moisture, which seeps through cracks in the ceiling and the walls, generating dark staining on the rock surface, and creating shallow pools and drip holes with stagnant water during wet seasons (**Figure 2**). A larger water pond in the western entrance area was dug by the local population living there. Big boulders and blocks in the south eastern corner are rounded by water dripping down the roof. Low growing plants and shrubs cover certain parts of the floor and grow along fissures at the rock shelter walls. During dry season the rock shelter can dry up almost completely. Apart from the dark staining at the walls and ceiling the trachyte differs in color, crystallization and softness within the shelter. The western wall is characterized by a pale gray trachyte with a rather crumbly matrix due to granular disintegration. Distinct alveolar weathering (honeycomb weathering) is common and parts of the walls show flaking of the rock surface and uneven exfoliation of the rock surface, which creates curve surfaced boulders. The color of the trachyte changes toward the eastern wall to a mustard yellow with well crystalized and colorless potassium feldspar minerals. Several overhangs along the rock shelter walls are darkened by soot caused by human induced burning. A low and narrow cavity in the north eastern back is extremely stained by fire activity. The lower ceiling has obtained a shiny, greasy surface due to the close fire exposure.

First observations during excavation revealed a complex stratigraphy with distinguishable sediment units and prominent boundaries. Some of the sediment units (Unit I, III, V, VII and IX) correspond to archaeological layers, that contain cultural material, such as obsidian artifacts and charcoal, and human made structures, such as pits and hearth. A 60 cm thick sterile sediment deposit roughly divides the deposits and associated human occupation phases into two parts. In the upper part of the stratigraphy, the anthropogenic units alternate with lighter colored geogenic units identified as tephra. The boundaries between these units are not uniform. Whereas the boundary between a cultural layer and an overlying tephra is sharp (e.g., between Units V and VI or between III and II), the transition between a cultural layer to a subjacent tephra seems gradual (e.g., between Units IV and III or between Units II and I). The tephra layers are exclusively of geogenic origin and therefore cultural remains are absent. Intermixing only occurs when the volcanic deposits have been relocated or disturbed by subsequent construction of pits or hearths. The lower part of the stratigraphy, below the thick sterile unit, is characterized a lager rockfall deposit, followed by anthropogenic deposits and geogenic deposits. The different layers in the lower section of the stratigraphy are difficult to distinguish, due to gradual or unclear layer boundaries and even mixing of the layers. Bioturbation can be recognized sporadically as insect or rodent

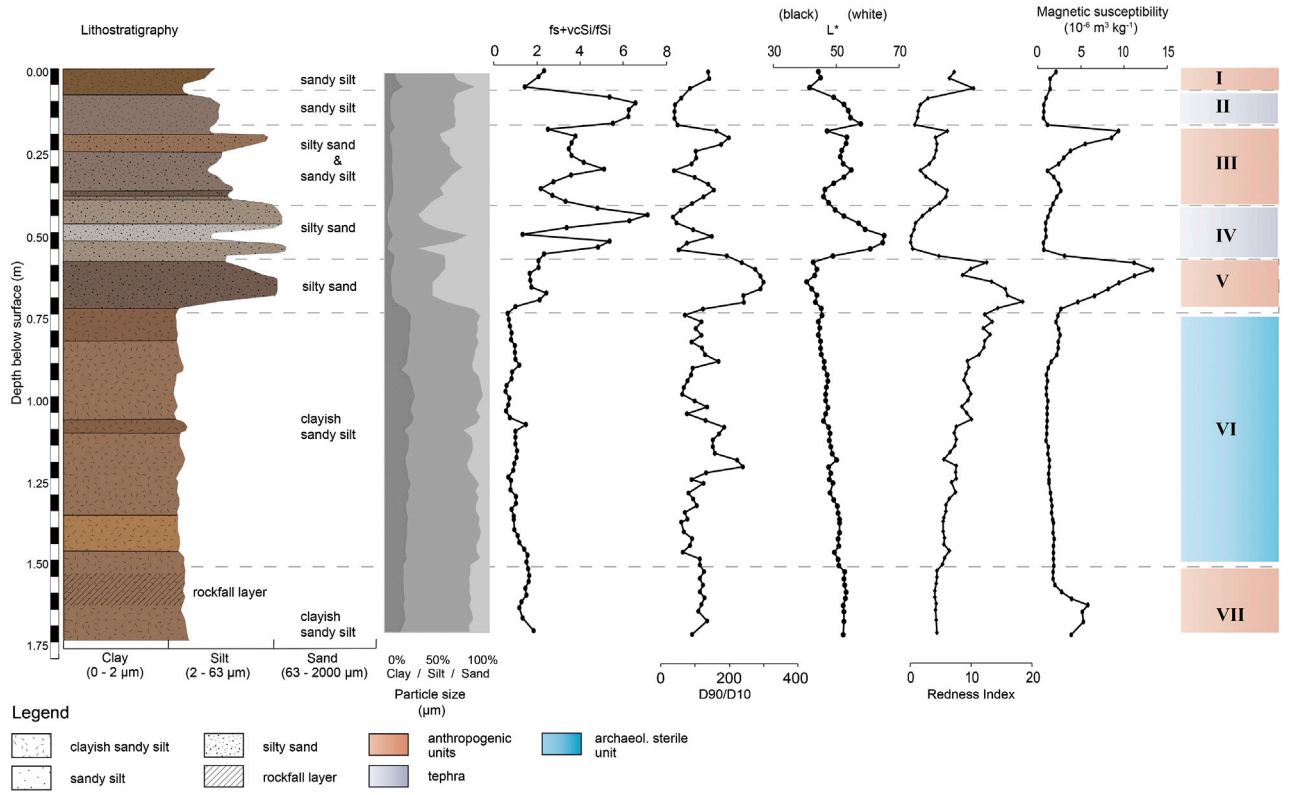

FIGURE 4 | Sedimentological properties of the profile F35: lithostratigraphy according to grain size analysis and sediment color measurement; grain size distribution; particle size parameter for aeolian transport; particle size parameter: 90th and 10th percentiles; CIELab color value L*; calculated Redness Index; magnetic susceptibility; sedimentological units.

borrows in all units. There is no macroscopic evidence of rooting by plants in the excavated stratigraphy. A detailed description of each unit, with its most important components can be found in the **Supplementary Table S1**.

Multiproxy Sediment Analyses

Macroscopic investigations of the 2 m stratigraphy revealed a complex interplay of cultural layers with light colored tephras and a 60 cm thick sterile sediment deposit. With the help of sedimentological and geochemical analysis nine sedimentological units (I–X) can be systematically differentiated.

Profile F35

We measured all sediment samples with a grain-size analyses to investigate changes in particle size distribution through the whole stratigraphy. It turns out that (sandy) medium to coarse silt is the omnipresent mean fraction, although the (silty) fine sand content is increased in several layers of the upper (0.00–0.73 m) profile section. The grain size peaks in Unit IV and V. The graph in **Figure 4** shows that the clay content increases suddenly within the sterile layer of Unit VI. According to the statistical analyses, the sample curves show a bi- and polymodal distribution and overall very poor sorting. The amount of the grain size fractions that corresponds to aeolian transport, e.g., fine sand and very coarse silt (40–125 µm), ranges from 9 to 41% with peaks in Unit II and IV. Within these layers the ratios of 90th to 10th percentiles are low, resulting in a better sorting (Kehl et al., 2014).

Comparing these results of the granulometric analyses with the samples in which the carbonate was previously destroyed (by means of HCl 10%), little change in the particle size distribution can be detected (**Supplementary Figure S1**). The peak within Unit V is also verified. Only the samples within the sterile Unit VI show a slightly different behavior to the samples which were exclusively sampled with H_2O_2. Nevertheless, the main grainsize fraction remains sandy medium silt to sandy coarse silt.

Using VIS spectrophotometer to analyze the color of the dried and powdered sediment, significant color changes in the upper part of the sediment column are obvious. Shades of dark brown alternate with lighter gray colors and more intense red-brown colors. In **Figure 4** the lighter shades of Units II and IV are particularly prominent, which are accompanied by an increase in the L* values and a decrease in the a* and b* values (**Supplementary Figure S1**). The a* value peaks in Unit V and in the upper part of Unit III, which could also be observed in the field. Especially this part of Unit III appeared brick-red under the prevailing lighting conditions inside the excavation trench. The values of the redness index (RI) corresponds to the a* values and the iron content within the sedimentary sequence. It also illustrates the decrease of iron oxides within Unit VI.

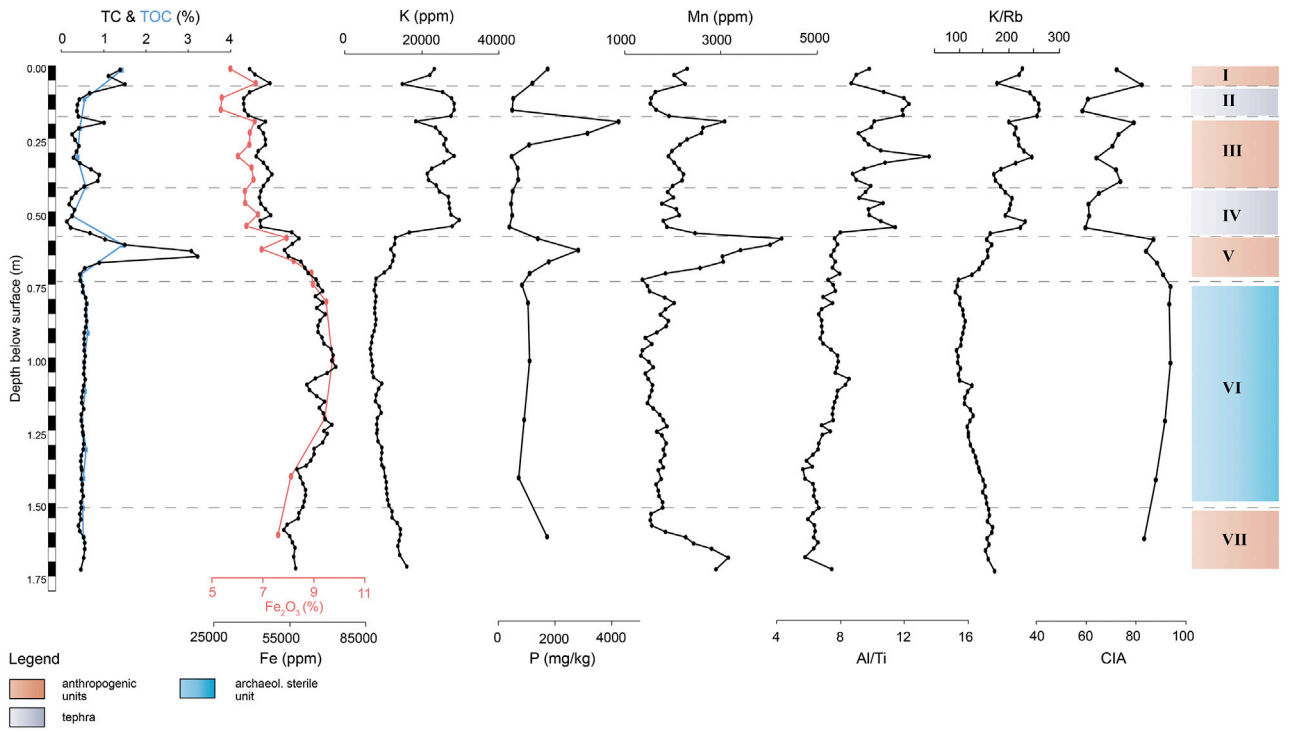

FIGURE 5 | Sedimentological and geochemical properties of the profile F35: carbon content (TC and TOC); element trends (Fe_2O_3, Fe, K, P, Mn); element ratios (Al/Ti, K/Rb), calculated index of alteration (CIA).

Magnetic susceptibility (MS) was measured in order to identify signals of human induced burning. The peak values are found in Unit III, V and VII, where archaeological finds are concentrated. Also, the darker color of the sediment, e.g., degreased values of the L* curve, correspond to higher magnetic susceptibility. The minimum values are found in Unit II, IV, VI and the lower part of Unit III.

The carbonate content in the samples varies strongly in the upper part of the profile and peaks within Units I, III and especially in Unit V. Within the lower section of the profile the amount remains relatively constant at around 0.5%. The measured TOC content shows minor deviations from the TC curve, thus it can be expected that little or no carbonate was precipitated after sedimentation (**Figure 5**).

An XRF analysis allows the detection of several counted elements present in the samples, but only a selection of the results is considered in this study. **Figure 5** illustrates that Iron (Fe), one of the most common trace elements on earth, shows relatively low values in the upper profile part. With the beginning of the Unit VI the Fe counts and the Iron (III) oxide (Fe_2O_3) percentage amount rise. The elements aluminum (Al) and titanium (Ti), often used as indicators for stronger weathering, show a similar course with enrichment in the sterile clayish Unit VI (**Supplementary Figure S1**). Diametrical to this are the curves of mobile alkali metal potassium (K), rubidium (Rb) and halogen chlorine (Cl), which are abruptly depleted in Unit VI. Peak values are found in Units II, IV and in the middle part of Unit III. The light element Silica (Si) is enriched within the same units in the upper part of the profile. The values of calcium (Ca), strontium (Sr), phosphorus (P) and manganese (Mn) are elevated in the Units III, V and VII which represent anthropogenic layers (**Figure 5**).

Selected element ratios, as Al/Ti and Fe/Al indicate major changes in the source areas of the deposits. Following the graphs in **Figure 5** and **Supplementary Figure S3** the Units II, IV and the middle of Unit III that can be characterized as volcanic ash with higher ratios of Al/Ti and Fe/Al. In contrast, Unit VI differs by very low values. According to the ratios of mobile to less mobile elements, e.g., between K/Ti and K/Rb, the lower section of the profile reflects changes into a regime with increased weathering (Brown, 2011; Arnaud et al., 2012; Kehl et al., 2014; Kehl et al., 2016). The calculated chemical index of alteration (CIA) peaks in the lower Unit VI of the profile. The resulting graph of the Mn/Fe ratio in **Supplementary Figure S3** shows an increase in the anthropogenic Units I, III and V.

Profile G35

The lower examined section in square G35 consists of the sedimentological Units VI to IX. The granulometric analyses and statistical analyses points to a tri- and polymodal grain size distribution as well as a very poor sorting throughout all the samples. (Sandy) medium silt is the dominant mean fraction within the whole sample column with variations of very fine sandy medium silt to medium and coarse silt. The exception

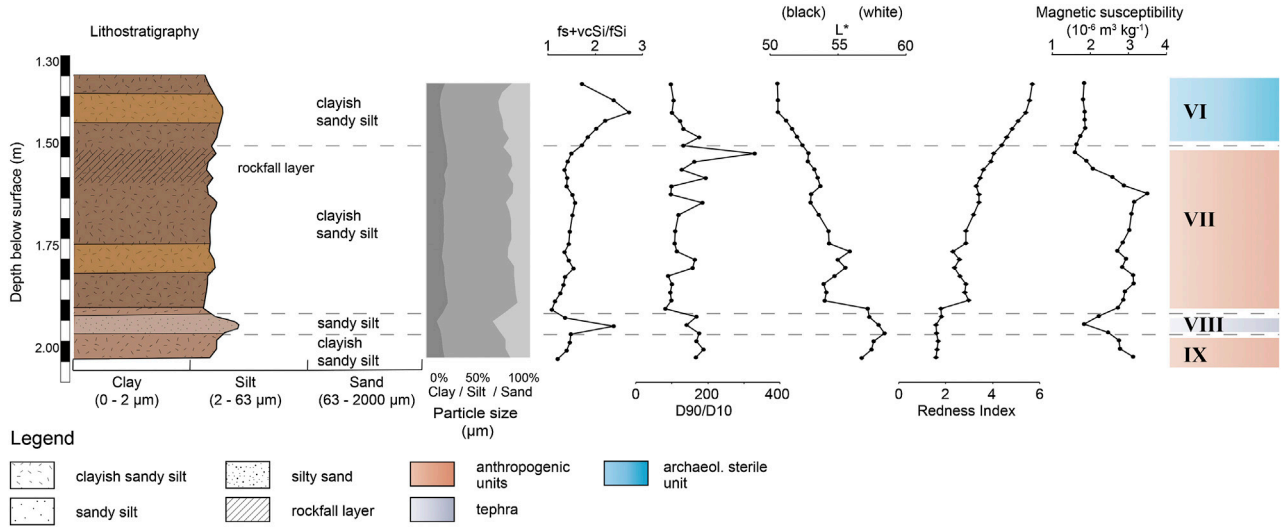

FIGURE 6 | Sedimentological properties of the profile G35: lithostratigraphy according to grain size analysis and sediment color measurement; grain size distribution; particle size parameter for aeolian transport; particle size parameter: 90th and 10th percentiles; CIELab color value L*; calculated Redness Index; magnetic susceptibility; sedimentological units.

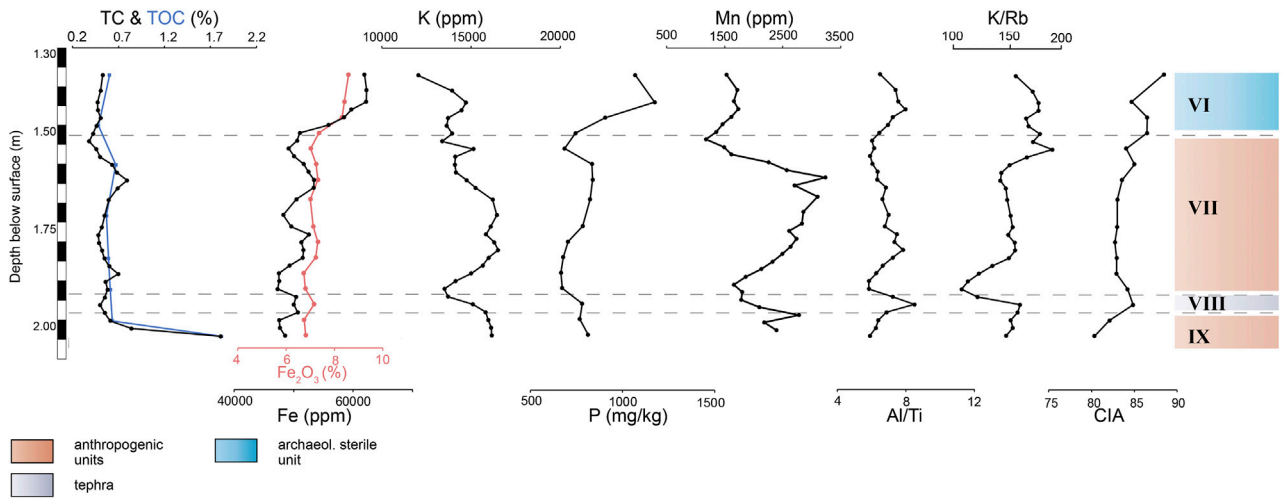

FIGURE 7 | Sedimentological and geochemical properties of the profile G35: carbon content (TC and TOC); element trends (Fe_2O_3, Fe, K, P, Mn); element ratios (Al/Ti, K/Rb), calculated index of alteration (CIA).

are two peaks within Unit VI and Unit VIII where the grain size is slightly higher. In addition, there is an increased proportion of the grain sizes fine sand and coarse silt (40–125 µm) which can be associated to an aeolian origin (**Figure 6**) (Kehl et al., 2014). The samples with this specific grain size range also show low ratios of the 90th and 10th percentiles and therefore a higher sorting.

The analyses of the sediment color show insignificant changes from brown to light brown. With increasing depth, the luminance (L*) increases and the red tones (a*) decrease (**Supplementary Figure S2**). During the field work the lower sediment sequences were described as reddish due to the limited daylight inside the shelter and the high moisture of the sediment. Actually, the calculated redness index in **Figure 6** illustrates a slow decrease of the values with increasing depth, which are synchronous to the Fe and Fe_2O_3 values.

The magnetic susceptibility shows increased values in the upper part of Unit VII and in the lower most Unit IX that is an anthropogenic layer. The values peak in the settlement layers, but generally less pronounced as in the profile F35.

TABLE 1 | Radiocarbon ages for samples from Sodicho Rockshelter, arranged by archaeological excavation units.

Lab code	Excavation unit (square-quarter-level)	Specimen	S.Unit	Conventional ^{14}C-date [BP]	Calibrated ^{14}C age range (2σ) [cal BP] IntCal20.14c	Prob. (%)	δ^{13} (‰)	Sample depth [cm b.s.]
Beta-449167	F34-SW-02	Charcoal	I	250 + 30	**270–322**	56	−27.9	8
Beta-449166	F34-NW-02	Charcoal	I (pit)	350 + 30	**315–411**	59	−24.8	11
COL3149.1.1	F35-SW-06	Soot	III	1944 ± 46	**1,741–1,948**	93	−26.1	excl.
COL3150.1.1	F35-SW-07	Charcoal	III	1806 ± 42	**1,685–1,824**	59	−24.1	excl.
Beta-449168	F34-NW-10	Charcoal	III (pit)	2,130 + 30	**1,999–2,153**	88	−25.7	48
Beta-486041	G34-NW-11	Charcoal	V (hearth)	3,860 ± 30	**4,227–4,407**	84	−25.0	44
Beta-449169	G35-NE-15	Charcoal	V	3,920 + 30	**4,242–4,424**	99	−26.4	56
COL3153.1.1	F35-SW-14	Charcoal	V	4,054 ± 45	**4,418–4,647**	88	−27.2	excl.
Beta-449170	G35-NE-18	Charcoal	V	4,060 + 30	**4,422–4,621**	92	−24.9	69
Beta-450067	F34-NE-18	Seed	V	4,190 + 30	**4,617–4,765**	74	−21.7	69
Beta-449171	G35-NE-19	Seed	V	4,130 + 30	**4,567–4,729**	64	−23.3	77
Beta-449175	G35-NE-20	Seed	V	4,160 + 30	**4,610–4,828**	94	−24.6	84
Beta-434190	G35-NE-23		VI	4,130 ± 30	**4,567–4,729**	64	−25.9	excl.
Beta-449172	G35		VI	9,540 ± 40	**10,695–10,897**	51	−22.3	150
Beta-449173	G35-NE-23	Charcoal	VII	11,620 ± 40	**13,401–13,521**	75	−22.1	excl.
Beta-481344	G35-SE-24	Charcoal	VII	12,560 ± 40	**14,812–15,122**	85	−25.1	159
Beta-523129	G35-NE-27	Org. Mat	VII	5,640 ± 30	**6,390–6,490**	78	−25.2	160
Beta-434191	G35-NE-28	Charcoal	VII	13,970 ± 50	**16,738–17,121**	100	−21.7	158
Beta-434192	G35-NE-28	Charcoal	VII	13,930 ± 50	**16,718–17,072**	100	−24.0	156
Beta-449174	G35-NE-28	Charcoal	VII	13,870 ± 50	**16,644–17,025**	100	−22.2	156
Beta-521542	F35-SE-26 B	Charcoal	VII	13,970 ± 50	**16,738–17,121**	100	−25.6	165
Beta-521541	F35-SE-26 a	Charcoal	VII	4,010 ± 30	**4,415–4,530**	99	−25.3	163
Beta-521539	F35-SE-27 a	Charcoal	VII	13,870 ± 40	**16,664–17,016**	100	−25.8	170
Beta-521540	F35-SE-27 B	Charcoal	VII	13,860 ± 50	**16,631–17,016**	100	−25.9	170
Beta-481345	G35-SE-31	Charcoal	VII	14,910 ± 50	**18,134–18,293**	100	−25.4	178
Beta-481347	G35-SE-37	Charcoal	IX	17,800 ± 60	**21,392–21,867**	100	−24.5	199
Beta-487731	G35-SE-37d	Sediment	IX	21,210 + 70	**25,292–25,749**	100	−24.3	203
Beta-486039	G35-SE-37C	Charcoal	IX	22,360 ± 80	**26,396–26,960**	100	−24.7	203
Beta-521544	G35-SE-38 a	Charcoal	IX	22,350 ± 80	**26,392–26,953**	100	−24.2	204
Beta-521545	G35-SE-38 B	Charcoal	IX	22,510 ± 80	**26,452–27,107**	100	−26.2	206
Beta-521547	G35-SE-39 B	Charcoal	IX	22,450 ± 70	**26,433–27,029**	100	−25.5	206

Roman numbers indicate sedimentological unit. The bold numbers represent the calibrated ^{14}C age range (2σ) in cal BP. Samples Beta-434190 and Beta-449172 were taken from the archaeologically sterile layer. Red numbering indicates sample depth that where defined by the excavation unit, "excl." illustrates samples that were excluded from the depth model.

The measured carbonate content in the samples also represents the TOC content as in the samples of profile F35, since the pretreatment with HCl (10%) did not show any significant changes in the values. Thus, the carbonate content of the samples can be addressed as organic carbon. A post-depositional formation of inorganic carbon, such as gypsum or carbonates is therefore insignificant. The carbonate content is expressed in three extreme peaks within the Units VII and IX.

The resulting curves of Si and Ti show similarities especially in the increased values within the anthropogenic Units VII and IX. The lowest values are found in the Units VI and VIII (**Supplementary Figure S2**). Ca and Mn are increased in Unit VII and IX, that is comparable with the peak values of magnetic susceptibility within the cultural layers. Especially Mn is marked by higher values in Unit VII (**Figure 7**). Rb and strontium also share the same minimum as Ti within Unit VII, although the resulting curve differs in Unit IX with slightly increasing values. The values of K on the other hand show a different pattern with minimum values in Unit VIII. In contrast the P, Cl values peak in Unit IV sand IX, following the increasing grain size. The graph of Al does not show as pronounced changes as in profile F35 but it displays a rising gradient of the values within the units with a higher mean grain size.

The ratios of Al/Ti and Fe/Al, that are often used to indicate changes in the source area of sediments during deposition (Kehl et al., 2014), show only slight variations within profile G35. In **Figure 7** and **Supplementary Figure S4** the low values of the ratios of K/Ti and K/Rb indicate a slightly increased influence of weathering on the deposits in Unit VII (Brown, 2011; Arnaud et al., 2012; Kehl et al., 2014; Kehl et al., 2016). These rather small changes can also be observed in the calculated CIA. As already observed in the profile F35, the Mn/Fe ratio is increased in the anthropogenic influenced layers VII and IX (**Supplementary Figure S4**).

Radiocarbon Chronology

According to the analyses, the stratigraphy can be roughly divided in five settlement phases, including the uppermost dated phase of recent times (**Table 1**). This proofs repeated occupation by humans since more than 20 thousand years. The radiocarbon samples originate predominantly from anthropogenically

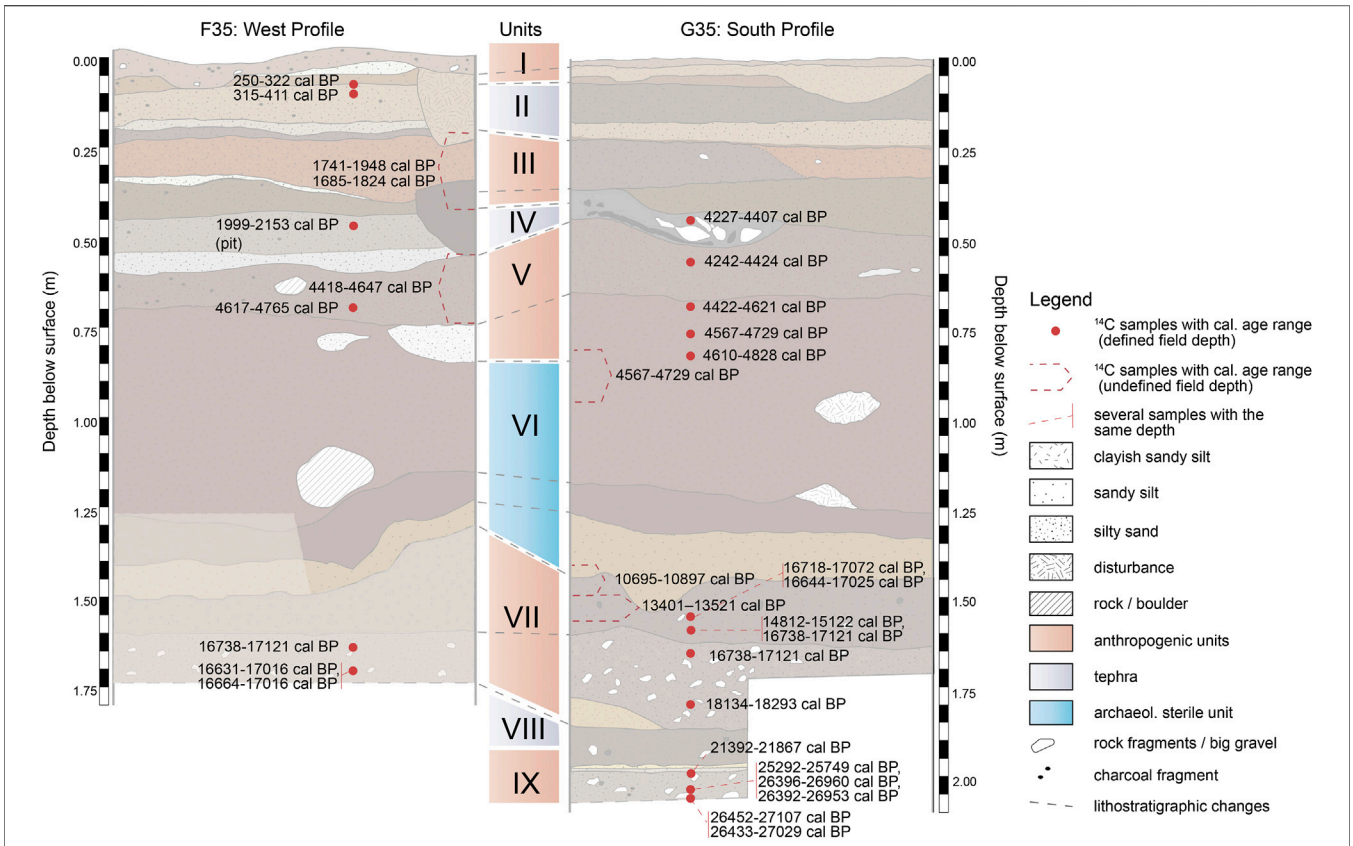

FIGURE 8 | Stratigraphy and the calibrated ^{14}C age range of the Sodicho Rockshelter. Red dots refer to radiocarbon samples with the measured field depth (defined field depth). Sieve finds that have not been calibrated are indicated next to the corresponding unit (undefined field depth).

influenced layers (**Figure 8**), with the exception of samples Beta-434190, Beta-449172 and Beta-481345, which originate from archaeologically sterile layers. The samples Beta-523129 and Beta-521541 show comparably younger radiocarbon ages to the samples of the same depth, which probably indicates post-depositional displacement or inconsistencies in the sampling procedure.

A modifiable classical age depth model was generated with the help of the clam2.3.5 package in RStudio. The model uses a linear interpolation technique with calculated accumulation rates to illustrate the changing deposition processes within the rockshelter. In **Figure 9** the mentioned human settlement phases accumulated relatively fast. The intermitted archaeological sterile layers deposited comparably slow. Despite these similarities between the calculated ages and the age-depth model, several calibrated age ranges cannot be considered in the model, which are highlighted as "excl." (**Table 1**). This includes the sample COL3149.1.1, COL3150.1.1, COL3153.1.1, which were taken during the test excavations of 2015 when no total station was available to record the exact location of the samples. The samples Beta-434190 and Beta-449173 are sieve finds and had to be excluded as well, since an exact field depth could not be measured. Samples that have been included in the model but clearly show a significant age deviation are marked as outliers. In **Figure 9**, a "plateau" is shown between 10.8 and 17 ka, which is due to the fact that the sample Beta-481344 is considered an outlier. If the Beta-481344 was included in the model, two other samples (Beta-449174 and Beta-434192) would have to be excluded to prevent a reverse chronology (**Figure 9**). This illustrates how variable the sediment deposition is within Sodicho Rockshelter and how difficult it is to develop a reliable model.

Archaeological Finds

The analysis of the archaeological finds is still ongoing and only preliminary results based on the analysis of artifacts from square F35 & G35 can be presented in this chapter. The preservation conditions for bones are extremely bad, due to the volcanic and moist environment of the shelter. The acid character of the sediments in combination with leakage water caused the destruction of any bones older than some hundred years. Pottery is also restricted to the recent surface layer and the youngest Stone Age occupation. This confirms the general picture of a late appearance of pottery in the southwestern Ethiopian Highlands around 2000 years ago (Gutherz et al., 2002; Hildebrand and Brandt, 2010; Schepers et al., 2020).

In all other cultural layers are stone artifacts the only cultural remains. The broad division of the stone artifact assemblages

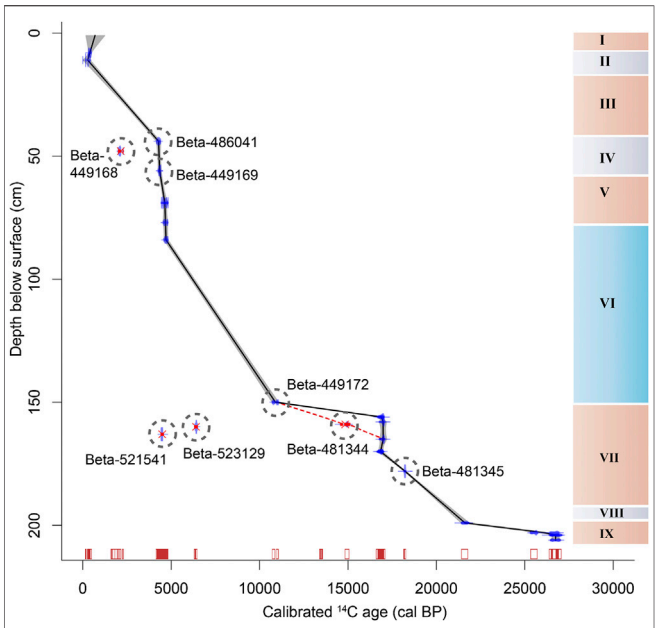

FIGURE 9 | Age-depth model with sediment units and probability distribution of the calibrated radiocarbon ages (red box plot). Possible course of a model that includes sample Beta-483144 is indicated by a red dashed line. Gray circles indicate outlier and samples that are discussed in the manuscript.

reflects the general sedimentological differentiation of an upper sediment package, which is separated by a sterile, reddish-brown deposit (Unit VI) from a basal sediment package. Chronologically, this division can be correlated with the Late Holocene and the Late Pleistocene, separated by a Middle to Early Holocene occupational gap.

Raw material for the production of stone tools is in all assemblages almost exclusively obsidian. First microprobe analysis results verify the exploitation of two local sources and of the large Bantuu outcrop, which was also used by the occupants of the rockshelter Mochena Borago. In addition, several up to now unknown raw-material sources have been used (pers. communication B. Nash). The two cultural layers in the upper part of the stratigraphy (Unit III and Unite V) are both characterized by microlithic stone tools, mainly backed tools, which are type forms of the African microlithic Later Stone Age (LSA). The main difference between the two assemblages is the number of artifacts. Only 69 pieces (without chips) from the upper LSA assemblage in square F35 stand in contrast to 531 pieces from the older LSA assemblage. The small number of stone artifacts of the upper LSA assemblage, which dates between ~1800 and ~2,100 cal BP, accounts for the low number of retouched tools. Despite two fragments of backed microliths that cannot be further classified, two segments are the only characteristic type-forms. The older assemblage, which dates between ~4,300 and ~4,800 cal BP, comprised 11 segments (**Figure 10**), seven micro-points and six double micro-points (following the definition of type-forms in Schepers et al., 2020). Single pieces are one scraper, one backed point and one drill. However, the percentage of retouched stone tools in comparison to the total number of stone artifacts is in both assemblages similar. The greater variation in type-forms of the older microlithic assemblage might be simply due to the higher total number of artifacts. Regarding the small sample size coming from a very restricted area of the shelter, further analysis has to verify, if the different spectrum of tools reflects any cultural or functional distinctions and if the number of finds reflects different settlement intensities.

A sediment package without any cultural remains (Unit VI) represents an occupational gap between these younger, microlithic assemblages and the Late Pleistocene assemblages. Repeated occupation of the shelter is testified between ~27,000 and ~13,500 cal BP. Preliminary analysis of the lithic assemblages shows a surprising uniformity of the stone artifacts. Obsidian is still the dominant raw-material for the production of stone tools, but also cryptocristalline silices were used in small numbers. All assemblages are dominated by the production of bladelets and the analyzed sample completely lacks any retouched tools (**Figure 11**). Settlement phases dating around 17 to 15 ka cal BP and 27 to 22 ka cal BP coincide with the arid or rather hyper-arid climatic phases of the Heinrich event 1 and 2 (H1, H2) (Hemming, 2004) and the Last Glacial Maximum (Mark and Osmaton, 2008).

DISCUSSION

Interpretation of Multiproxy Analyses

Our sedimentological and geochemical results revealed major changes of the sediment sources and indicate a combination of different geogenic and anthropogenic processes that influenced the deposits in the Sodicho Rockshelter. Our data revealed that the sedimentological units preserved within Sodicho Rockshelter accumulated in different depositional environments. Based on field observation and analyses we distinguished a total of nine sedimentological units, which can be grouped in four sediment facies:

Autochthonous geogenic deposits are mainly characterized by trachytic clasts and boulders, that could derive most likely from the rockshelter walls and the roof itself. This type of deposit is omnipresent in almost all sediment units. A rockfall layer located in the upper part of the Unit VII, right below the sterile Unit VI, consists of trachytic boulders with a maximum diameter of up to 70 cm (**Figure 4**). The upward facing surface of the boulders is rounded. This indicates that the boulders were not rapidly covered by sediment and persistent weathering dissolved the fine feldspar matrix.

Allochthonous geogenic deposits predominantly consist of well sorted volcanic tephra and ash, which were ejected during past volcanic eruptions in the region and deposited in the shelter by aeolian transport. These Units II, IV and VI are easily identifiable as thicker, light color sediment layers or lenses, with an increased mean grain size. The grainsize analyses revealed low ratios of the 90th and 10th percentiles and a higher amount of particle with the grain size that can be associated to an aeolian transport. These results and the field observation indicate major changes in sediment origin during

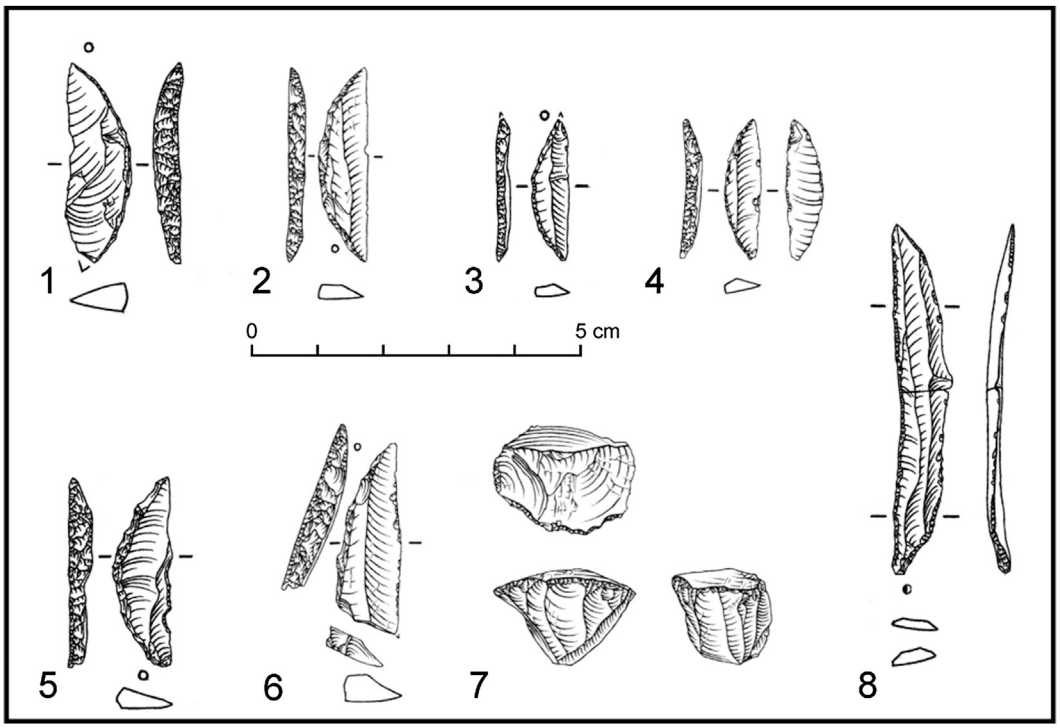

FIGURE 10 | Microlithic LSA lithics: Segments (1–5), backed point (6), prismatic bladelet core (7), broken bladelet with use-wear (8).

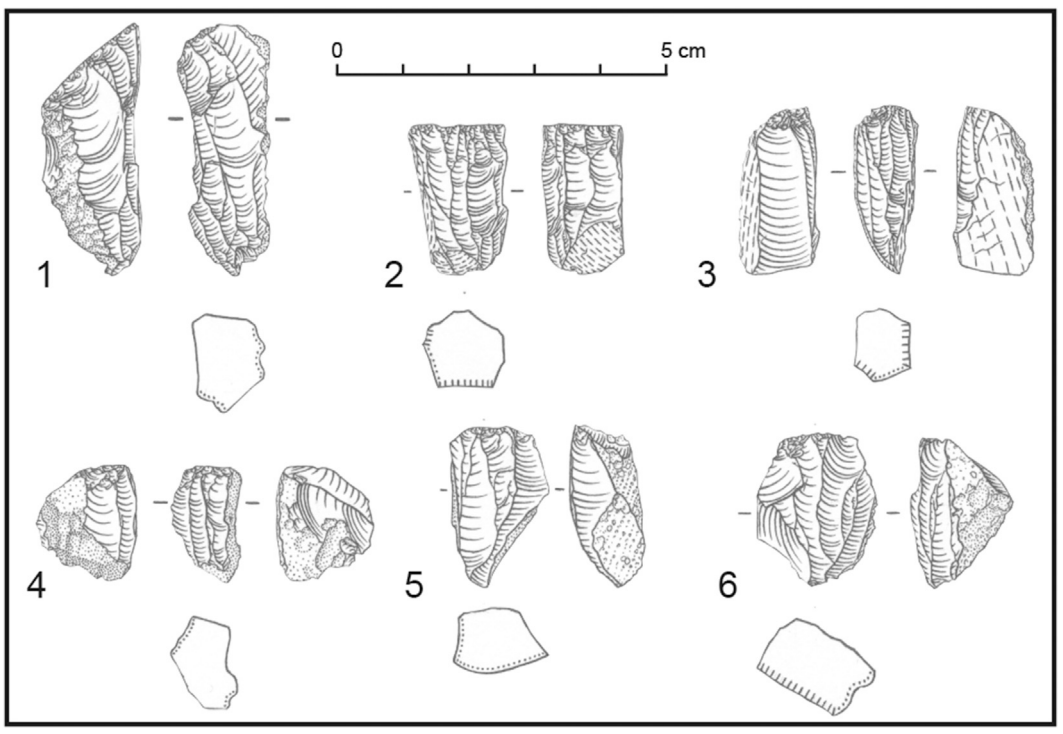

FIGURE 11 | Late Pleistocene lithics: Bladelet cores (1–6).

deposition with the highest aeolian input in Units II, IV, and partly in III. Geochemical analyses point to a potassium and chlorine enriched felsic tephra, that is distinguishable from the surrounding sediment. This geochemical fingerprint allows the identification of altered volcanic tephra within samples, as identified in Unit VI and VIII. The source volcanos of the tephra remain undefined, even though we identified the geochemical composition. It can be assumed that this type of allochthonous geogenic deposits of volcanic origin were deposited relatively abrupt, which is shown by the sharp boundaries to lower deposits.

Mixed autochthonous and allochthonous geogenic deposits are the result of weathering of the trachytic rock and water percolation through the sediment. This type is common in the sterile Unit VI, that differs from all the other sediment units in both sample columns. The poor sorting in these deposits indicate polygenic sediment origins. The high CIA index as well as low K/Ti, K/Rb values refer to increased (Kehl et al., 2014). The reddish-brown deposits are characterized by an increased clay content and peaks in the redness index that correspond with a higher Fe_2O_3 content (**Figure 5**). Particularly noticeable is the decrease in magnetic susceptibility and most other geochemical proxies. Nevertheless, Ti and Al content are increased since they are often bound to clay (Okrusch and Matthes, 2010). Based on its high Fe_2O_3, Ti and AL content, we argue that Unit VI originated from the weathering of the local bedrock in a moist environment, leading to the formation of authigenic clay minerals. Alternatively, the increased clay content and the different geochemical composition of this sediment could be the result of fine-grained soil material that was washed in the site through fissures in the ceiling of the rockshelter.

Anthropogenic deposits are identifiable by the concentration of archaeological finds, such as obsidian artifacts and charcoal from hearths, as observed in Units I, III, V, VII and IX. Moreover, the deposits have a certain sedimentological and geochemical fingerprint that is characterized by a poor sorting, high values of magnetic susceptibility and an increased content of Mn, P and TOC (**Figure 4–7**). Manganese and Phosphorous are released into the soil by the decay of deposited organic matter or inorganic compounds, as in phosphate minerals, that accumulate at the site by human occupation (Holliday and Gartner, 2007; Karkanas, 2017). Furthermore, the high percentage of TOC in Unit VII and IX can perhaps be explained by higher weathering of the lower levels of the stratigraphy and therefore the decomposing of the organic matter. The high values of the magnetic susceptibility most certainly derived from thermally alteration of the sedimentary substrate, due to burning activity. Chemical changes of magnetic minerals induce the development of ferrimagnetic mineral, such as maghemite that increases the magnetizability of the sediment (Le Borgne, 1955; Herrejón Lagunilla et al., 2019). Furthermore, manganese shows paramagnetic properties, which contributes to the relatively high ratios of magnetic susceptibility in the cultural layers. This means that randomly distributed magnetic dipoles interact with the external field of the magnetic susceptibility measurement, which orients the dipoles in one field direction, and amplifying the whole field (Ivers-Tiffée and von Münch, 2007). The Mn/Fe ratio is increased in the anthropogenic Units I, III and V (**Supplementary Figure S3**), suggesting increased manganese content under redox conditions in the upper part of the stratigraphy.

Although the sedimentological and elemental fingerprints show clear signs for human occupation, we cannot exclude that these layers underwent diagenetic processes such as dissolution or oxidation. This can bias results about environmental condition during human occupations in the shelter. By comparing the geochemical data of profile F35 with profile G35, it is noticeable that the values of the sedimentological and geochemical graphs of the basal sediment levels below the sterile unit are not as pronounced, which indicates stronger alteration. This may be caused by a higher influence of water infiltration during the deposition of the sterile layer that can be dated to the AHP (~15–5 ka BP) and a possible post depositional alteration.

Chronology and Human Occupation at the Rockshelter

We assigned the multiproxy results to the radiometric ages and via the age-depth model in order to understand site formation processes and to correlate them with the chronological succession of the cultural layer. Following the mentioned sedimentological and geochemical results we can distinguish nine sedimentological units, comprising of both natural and anthropogenic accumulations (**Figure 8**). The following chronological phases of human occupation are described in stratigraphic order. It is important to note that the calculated age-depth model cannot reflect the complete depositional conditions and their variations in the Sodicho Rockshelter, as these processes vary within the different excavation quadrants. The model is intended as a simplification to illustrate phases of human settlement.

Mount Sodicho is probably one of the silicic domes associated to the Wagebeta Caldera Complex that developed 3.6- to 4.2 Ma ago (WoldeGabriel et al., 1990; WoldeGabriel et al., 1992). The exact time for the formation of the Sodicho Rockshelter and the beginning of sediment deposition is not yet clear. Therefore, further investigations and excavations down to the bedrock are needed. The rockshelter increased in size as time progressed due to solution of silica in the trachytic rock by water that flowed in through fissures and cracks in the weathered rock shelter roof, which are still visible today.

As discussed above, the lowermost investigated Unit IX with an approximate age range of about ~27 to 22 ka cal PB represents an anthropogenic layer (**Figure 8**). Charcoal fragments and lithic artifacts as well as the characteristic anthropogenic deposits with increased magnetic susceptibility, higher manganese and phosphorus content indicate human occupation. The base of this layer has not been reached yet. The excavation unit GE35-SE-37 is represented only by a single date (Beta-481347) in the age-depth model, although two other samples (Beta-487731, Beta-486039) derive from this level (**Figure 9**). Their different age can be explained by the presence of a coarser-grained and lighter colored band in Unit VIII, with increased values of Al/Ti, which indicates a variation of the sediment source. The influence of post-depositional processes such as bioturbation cannot

be excluded, which has to be a focus of future micromorphological investigations.

Sediment Unit IX is covered by a brownish layer, representing a distinct anthropogenic unit (VII), which lies below the archaeological sterile unit. The lower part of the unit consists of a yellow brownish sediment with intermixed cultural findings. One radiocarbon sample that was collected from this section dates between 21,392 and 21,867 cal BP. The following settlement phase covers a period of about 17 to 15 ka cal BP. All radiocarbon samples were taken from sediment in-between and below the big trachytic boulders of the rockfall layer. Chronologically, the trachytic rock fall layer in the upper part of the unit cannot be assigned, as no datable material has been preserved directly above this layer. At the moment it is not possible to determine whether the collapse of the roof caused the end of this occupation phases or if the humans had already left the rockshelter. The stone artifact distribution in between and below the boulders points to a severe disturbance of the accumulated anthropogenic material. Another question is whether the larger rocks at the entrance of the rockshelter collapsed at the same time as the trachytic rocks in Unit VII, or if this was a different event. The absence of trachytic boulders in higher strata of the stratigraphy speaks for a simultaneous collapse of the rocks. Future analyses below the large rocks, blocking the entrance, could provide information about this. It can be assumed that the whole sedimentological unit has undergone post-depositional processes that let to disturbances and influenced the expression of some geochemical indicators. A possible influence of pedogenetic processes and temporary absence of human impact can be explained by the inconsistency of the magnetic susceptibility and the K/Rb ratio (Kehl et al., 2014). This indicates post-depositional disturbances and a possible displacement of radiocarbon samples. With this assumption in mind the two outliers (Beta-523129, Beta-521541) of this cultural phase, can be excluded from the model.

The following clayish Unit VI provides a unique indication for the prolonged absence of humans. Chronostratigraphically, this unit can be dated by one radiocarbon date (Beta-449172), that originates from the base of the unit, and by the dates of the cultural layer below and above it. Based on this, the dates of ~15 and 4.7 ka are the maximum, respectively minimum age of the deposition. This period can be assigned to the Early Holocene African Humid Period (Foerster et al., 2012; Foerster et al., 2015; Hildebrand et al., 2019). An exact dating of the deposits is not possible due to the lack of datable material within Unit VI (**Figure 8**). The duration of the deposition is unclear and it might have been a slow process over a long period or a rapid event. It can be assumed that there must have been fluctuations during the deposition. This is verified by the variations in the degree of sorting and by the distinctive yellowish, silty layer in the lower part of the unit.

The end of the archaeologically sterile Unit VI and thus the beginning of the anthropogenic unit V is verified by the presence of obsidian tools and charcoal, as well as by the abrupt change in sedimentological and geochemical features. In particular, the increased values of magnetic susceptibility, TOC, as well as the increase in manganese and phosphorus mark an intense re-occupation of the shelter by humans. Seed and charcoal samples date to an age range of about ~4.7–4.3 ka cal BP. Again, the accumulation rate of the anthropogenic impacted deposits in Unit V is higher than in the case of exclusively geogenic induced deposits in the Sodicho Rockshelter. Considering the sampling depth of the radiocarbon samples, the anthropogenic accumulations reach up to a field depth of 0.45 m. However, the samples Beta-486041 and Beta-449169, collected in excavation square G, are at the same depth as the sterile tephra of Unit IV in square F35, which is not visible in square G. These tephra layers can be geochemically identified by the coarser grain size, the increased potassium (K) amount and the maximum values of the Al/Ti proxies, which indicates a change in the sediment source (Kehl et al., 2014). In addition, sweeping and raking-out the surface may have been involved, as has already been observed in micromorphological studies at South African sites, like Sibudu Cave and Diepkloof Rock Shelter (Goldberg et al., 2009; Texier et al., 2010).

The radiocarbon sample Beta-449168 is marked as an outlier in the age-depth model because it was taken from a pit in excavation unit F34-NW-10 (**Figure 9**). Stratigraphically the sample is situated above sample Beta-486041 in Unit III (**Table 1**). This age discrepancy is the result of mixing and relocation of the sediment in the pit (Ossendorf et al., 2019). Nevertheless, the dated sample represents the anthropogenic Unit III, which is supported by cultural material and an increase in TOC and of manganese.

On the basis of the geochemical proxies alone, it can be assumed that the human occupation of the rockshelter was more pronounced in the periods above the sterile layer than in the stratigraphically older units. However, it should be pointed out that the proxies at the bottom of the sterile layer show weaker trends and were probably influenced by weathering. Considering the small size of the excavation trench, the artifact density might simply reflect differences in the spatial use of the shelter over time and is therefore an incidental result that cannot be considered as an indicator for settlement intensity.

Regional Paleoenvironmental Implications

The sedimentological results indicate changes in the depositional conditions over time. As discussed above, some of the results, e.g., archaeological finds, magnetic susceptibility and the Mn content show clear signs of human impact. By plotting elemental ratios against the calculated age-depth model, it is possible to model these first results in relation to regional paleoenvironmental changes during the last 27 kilo years (**Figure 12**), covering periods like the Last Glacial Maximum (LGM, 21 ± 2 ka) and the Early Holocene African Humid Period (AHP, ~15–5 ka). For the paleoenvironmental comparison we consider archaeological and sedimentological information from the rockshelter Mochena Borago, and paleoclimatic records from lacustrine sediments in Ethiopia. With our own data we observe local environmental fluctuations in sediment sources or weathering intensity caused by shifts in moisture availability.

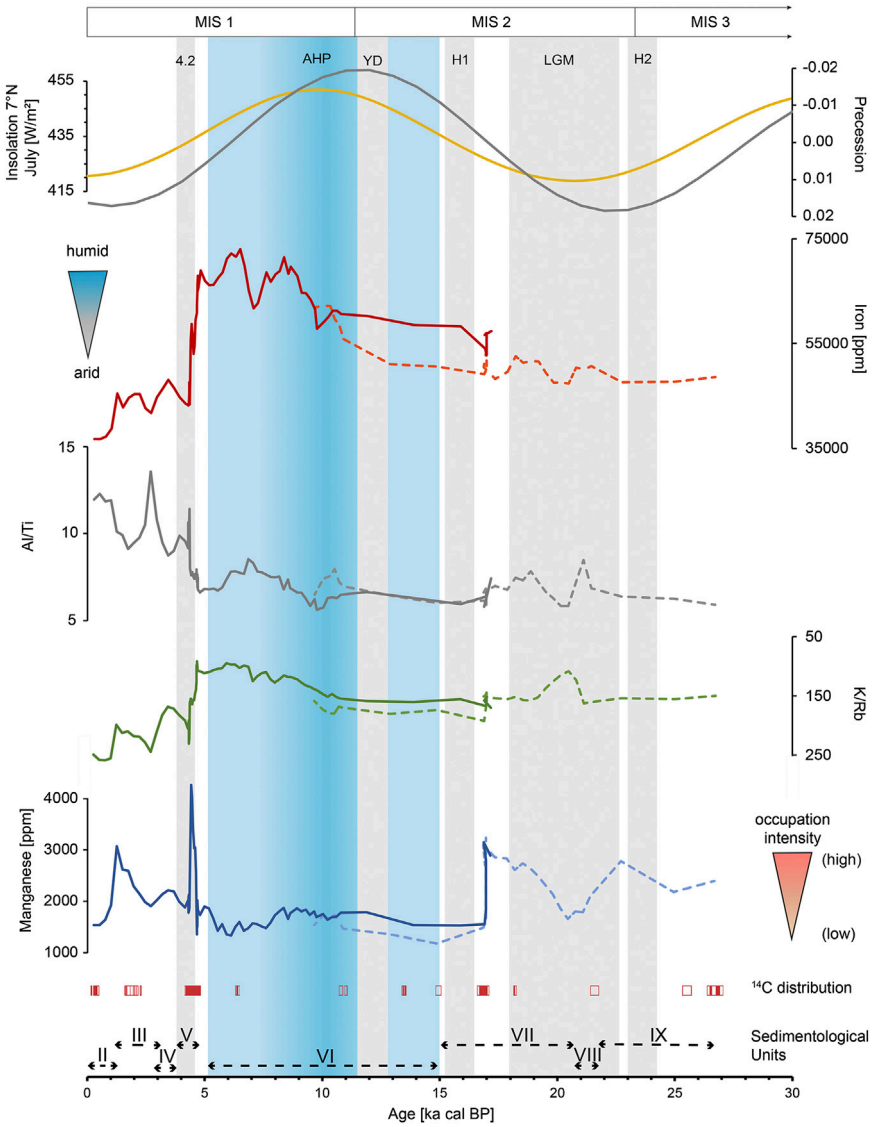

FIGURE 12 | Comparison of geochemical records with paleo-climate records (continous line = results F35, dotted line = results G35. Plotted from top to bottom: insolation variations 21st July, 7°N (Laskar et al., 2004); orbital precession (Laskar et al., 2004); Fe content with associated blue triangle shaped symbol (climate); K/Rb ratio (note reverse scale); Al/Ti; Mn content with associated orange triangle shaped symbol (occupation intensity); gray bars illustrate climatic dry events (4.2 event, Younger Dryas, Heinrich 1, Heinrich 2, Late Glacial Maximum); blue bar refers to African Humid Period; Reddish box plots illustrate ^{14}C distribution of Sodicho Rockshelter; roman numbers and bars illustrate sedimentological units.

Phase 3: Unit VII–IX, ~27–15 Ka

The short distance of about 40 km to Mochena Borago provides a suitable basis for a local comparison of the past conditions. Chronologically, the currently excavated and dated cultural layers from Sodicho cannot be connected to the Late Pleistocene deposits of Mochena Borago, since layers from this period have not been excavated yet. Nevertheless, we see similarities in the changes of the lithostratigraphic sequences. The basal Pleistocene deposits of the stratigraphy of Mochena Borago offers one of the most complete records from the timeframe of 60–30 ka in Eastern Africa. The main trench at Mochena Borago revealed three major lithostratigraphic units that preserved cultural remains dated between 36 and >50 ka (Brandt et al., 2017). The complex stratigraphy developed by multiphase, polygenetic accumulations of geogenic deposits, e.g., fluvial activities, volcanic eruptions, and anthropogenic depositional processes (Brandt et al., 2017). Several erosional activities resulted in a chronostratigraphic gap from ~36 to ~8 ka cal BP, erasing sedimentological history and possible cultural evidence until the Holocene (Brandt et al., 2012; Brandt et al., 2017). Although this archaeological and stratigraphic gap was recognized at other East African sites as well, e.g., Ziway-Shala basin and Goda Buticha (Tribolo et al., 2017), it is not found in Sodicho. In **Figure 12** the Mn record and the ^{14}C dates illustrate

two anthropogenic Units IX and VII that preserved cultural material ranging from ~27 to ~16 ka cal BP. This makes Sodicho Rockshelter the first site in Ethiopia that partially reduces the chronostratigraphic gap. The two anthropogenic units partly cover the global short-term Heinrich event 2 (H2) and the prolonged high-latitude LGM with a decrease of the Mn values around 21 ka (**Figure 12**). On a regional level, both time ranges are pronounced dry and cold phases, that can be tracked by a drop in the K record of the Chew Bahir basin core (Foerster et al., 2012). In contrast to the geoarchaeological evidence from Mochena Borago indicating that prehistoric humans frequented the rockshelter during more humid conditions (Vogelsang and Wendt, 2018), the sedimentological and archaeological results at Sodicho point to multiple occupations during humid and arid periods. In fact, Sodicho is the first evidence for the use of highlands as a refugium during times of severe environmental stress in the lowlands. In the Rift Valley, human occupation is not traceable during Late Pleistocene arid phases, even not in the surroundings of lakes, such as the Ziway-Shalla Basin (Bon et al., 2013). Thus, highlands might have been the only retreats. Paleoclimate simulations indicate higher annual precipitation in the Ethiopian highlands during arid phases than in lower elevated regions in Ethiopia, and suggest that these regions were part of a warm and temperate savanna and remained covered by low growing vegetations and scrubs during the glacial aridity of the LGM (Basell, 2008; Willmes et al., 2017). Residual water in the highlands could have attracted animals and humans (Basell, 2008). The Mn value of Unit VII peaks around ~17 ka cal BP, followed by a rather extreme drop of the values, which was not evident in the raw data of the geochemical analyses of the stratigraphy (**Figure 7**). This indicates the end of the cultural settlement phase. At the same time the Fe values show a rather gradual change to more humid conditions. The rapid changes of the records can be explained by the calculated sediment rate of the age model, which is increased in this section. In addition, post-depositional processes, the rockfall event of Unit VII, and the human impact has to be considered. A further explanation is the sample Beta-481344 (14,812–15,122 cal BP), which was marked as an outlier in the calculated age depth model. When this dating would have been included in the age-depth model, the geochemical data does not show such a strong trend around 17 ka (**Supplementary Figure S5**). Nevertheless, the geochemical values would steadily decrease from 17 ka. Another possible explanation are stepwise abrupt changes to increasing precipitation. This observation is also preserved in the Chew Bahir basin record between ~19 and 15 ka, and further paleoclimatic records on the northern African continent (for detailed descriptions and references to these records, see Foerster et al., 2012). Overall, our geochemical data from this period around 17 to ~15 ka cal BP should be regarded with caution, since the age data are influenced by the plateau in the ag-depth model (**Supplementary Figure S5**).

Phase 2: Unit VI, ~15–4.7 ka

As mentioned before in **Figure 12**, a phase of prolonged human absence correlates with a shift to more intense moisture, expressed in low Mn content and higher Fe content. The overall moist signal is recorded between a maximum age of ~17 ka cal BP and a minimum age of ~4.7 ka cal BP. Although Fe_2O_3 record has a comparable trend as Fe (**Figure 5**), the graph of Fe was chosen, due to the higher sample density and the more precise detection of fluctuations. This increased Fe trend, enhanced input of clay minerals and the lower K/Rb ratio corresponds to intensive weathering influence (**Figure 5**). As mentioned before this phase is known as the Early Holocene African Humid Period, that occurred during low orbital precession and associated higher insolation values (Laskar et al., 2004). Comparable conditions were observed in the increasing trend of the K record of the Chew Bahir basin (Foerster et al., 2012; Foerster et al., 2015). Our geochemical results in **Figure 12** show a gradual increase in humid conditions. In contrast, drier intervals like the Heinrich event 1 (H1, ~16 ka) and the Younger Dryas (YD, ~12 ka) are not visible in our geochemical record. This might be caused by one outlier sample that had to be excluded from our age model (see *Chronology and Human Occupation at the Rockshelter*). Nevertheless, a slight drop at 9.8 and 7 ka cal BP in the Fe values within the profile of F35 can be identified. These shifts can be explained by local changes in the sediment source region, as indicated by the fluctuations in the Al/Ti ratio. These intrusions correlate with a dry interval of 9.8–9.1 ka and a large-scale drought of around 7 ka observed at various sites throughout East Africa (Foerster et al., 2012). It is still unclear why the humans abandoned the rock shelter during the African Humid Period. Possibly the large lakes in the lowlands and Rift Valley offered preferred and easily accessible resources and the amount of energy needed to obtain food may have been lower there (Bon et al., 2013). Moreover, it can be assumed that the intense precipitation led to the formation of an extremely dense vegetation coverage, which impeded humans to live at the mountains slopes and use the highland ecosystems.

The termination of the AHP is a subject of current scientific discussions. These include the assumption of a slow gradual change to drier conditions (Kröpelin et al., 2008; Foerster et al., 2012) or a rather fast and relatively abrupt transition, which was also identified in several records, as according to water level reconstruction for the Turkana basin (Garcin et al., 2012). Furthermore, the role of humans as potential drivers for the end of the AHP is debated (Wright, 2017). These fundamental discussions go beyond the scope of this study that is based on a local data set. Regarding our analysis, after a maximum value of Fe around 6.5 ka cal BP a further weaker peak (4.8 ka cal BP) is followed by an abrupt drop in values, pointing to rather arid conditions. This abrupt change can also be seen in the other graphs of our figure. However, this is not an indication of the pace of termination of the AHP, since the sediment deposits at Sodicho are influenced by post-depositional processes. Furthermore, the deposition conditions in rockshelter settings are often somewhat more discontinuous, in comparison to other terrestrial or lacustrine deposits.

Phase 1: Unit V–I, ~ 4.7–0 ka

With the rapid decrease of the Fe values, the anthropogenic influenced Unit V emerges. Geochemically this can be clearly identified by increased MS and Mn values around 4.4 ka. This settlement phase and the associated deposition processes may have disturbed the sediment of the former walking horizon and thus partly explain the strong fluctuating Fe values. The dating of this cultural layer is of interest with regard to global climatic events, as it may cover

a time range that correlates with the so-called 4.2 ka event. This hyperarid event was mainly investigated in the Mediterranean (Kaniewski et al., 2018) or Chinese region (Xiao et al., 2018). Furthermore, a lacustrine record from Abhe Lake in northern Ethiopia indicates a drastic drop in lake levels between 4.5 and 3.7 ka, with an increase in aeolian accumulations indicating a drier climate (Khalidi et al., 2020). This could further confirm that humans lived in the Sodicho Rockshelter during arid periods with more favorable conditions in the montane forests (Hildebrand et al., 2019).

The tephra layers separating sedimentological Units I, III and V in excavation square F35 represent again a purely geogenic deposit and thus a temporary absence of humans within the rockshelter. The question whether humans were forced to abandon the site due to the volcanic eruptions and the consequential temporary environmental changes in the area cannot be answered on the base of the present results. Based on archaeological and chronological analyses at Mochena Borago, it is assumed that humans were influenced by rapid shifts in local or even regional environment that may have made it impossible to stay in the area (Brandt et al., 2012). The graphs in **Figures 4**, **6** of the sedimentological and geochemical analyses show that the deposition of the pyroclastic material occurred rapidly. Given the alternating tephra and cultural layers of the Sodicho stratigraphy, we can assume similar rapid changes influencing the surrounding landscape and the humans. In contrast we observe a rather slow change between Unit VII and the archaeologically sterile Unit VI. The geochemical analyses (slow decrease of MS and Mn content) may indicate that humans had already left the rockshelter.

CONCLUSION

The sediment record of Sodicho Rockshelter contains a 27 ka record of repeated human occupation and local paleoenvironmental proxies. The study presents a first stratigraphic and chronological framework for the Sodicho Rockshelter that is an important new site for studying prehistoric settlement in East Africa during critical time frames, such as the Last Glacial Maximum (LGM, ~ 21 ± 2 ka) or the African Humid Period (AHP, ~ 15–5 ka). Four sediment agents and the resulting site formation processes are identified. Purely geogenic accumulations differ significantly from anthropogenic induced deposits in terms of grain size distribution, sediment color and geochemical composition of the sediment. It is possible to indicate a higher intensity of human settlement phases during Unit V, according to the preliminary analyses of the lithic material, the results of magnetic susceptibility, and the content of Manganese and Phosphor. Archaeological sterile layers are identified with the help of sudden grain size variations and elemental ratios, like Al/Ti and K/Rb. These illustrate the deposition of volcanic fallout, changes of weathering intensity and shifts of major sediment sources. In particular, the Fe content reflects an increase in weathering caused by humid conditions between ~17 and 4.7 ka cal BP. Furthermore, the values also indicate short-term dry spells that may correlate with dated dry intervals of climatic records from the Chew Bahir basin, situated about 300 km southwest of the rockshelter but affected by the climatic conditions of the southwestern highlands. In total, our results verify human occupation in the highlands during humid and arid phases in the last 27 ka. This underlines the assumption that the highlands might have been used as part of larger settlement areas during times of favorable climatic conditions, but also as retreat under arid environmental conditions. However, a distinctive settlement gap is detected during the humid conditions of the AHP. Further excavations and investigations are needed to verify these first preliminary hypotheses. These would include micromorphological observations and the evaluation of phytoliths, which could offer a closer look into the microstratigraphical development of the site and the local paleo-vegetation. Nevertheless, the sediment record of the Sodicho Rockshelter reflects local environmental changes that correspond to the records of the Chew Bahir basin and to superregional climatic shifts. The sedimentological and archaeological records of Sodicho Rockshelter have the potential to be correlated to other archaeological and paleoenvironmental sites in eastern Africa and thus contribute to a supra-regional reconstruction of the settlement history and paleoenvironment. In particular, our study contributes to close the chronological gap of human occupation in north-eastern Africa around the times of the LGM.

DATA AVAILABILITY STATEMENT

The datasets analyzed for this study can be found at the CRC 806 Database, https://doi.org/10.5880/SFB806.55.

AUTHOR CONTRIBUTIONS

RV and OB developed the project framework within the CRC 806. RV and TN did archaeological excavation and preliminary stone tool analyze. EH performed sediment sampling in the field, sedimentological and geochemical analyses in the laboratory and developed the age-depth model with RStudio. EH developed the manuscript and figures. All co-authors contributed to, read, and approved the paper.

FUNDING

This research has been supported by the Deutsche Forschungsgemeinschaft (DFG, German Research Foundation) (grant No. 57444011 – SFB 806).

ACKNOWLEDGMENTS

We kindly thank the Authority for Research and Conservation of Cultural Heritage (ARCCH) of Ethiopia for their permission and general support, and the Ministry of Mines and Energy for the approval of our export permits. This study was conducted as a part of project A1 "Out of Africa – Late Pleistocene Rock Shelter Stratigraphies and Palaeoenvironments in Northeast Africa" in the framework of the Collaborative Research Center 806 (CRC 806) "Our way to Europe." We thank the team of Beta Analytic Inc. and

our colleagues from the radiocarbon AMS lab of the University of Cologne for radiocarbon dating. We thank Marianne Dohms and her colleagues from the Institute of Geography of the RWTH Aachen for their help and instructions for sediment color and XRF measurements. We are very grateful Thomas Albert, Degene Bado, Dejenne Degena, Mesfin Gete, Solomon Gitaw, Habir Mohammed Kebir, Mareike Röhl, Christian Schepers, Desta Sinajew, Mehdanit Tamerat, Fitsum Tefera, Minassie Tekelemariam and Thorben Thenbruck for their participation during various field seasons at Sodicho. Finally, we thank the local residents of Mt. Sodicho for their participation and support in field research.

SUPPLEMENTARY MATERIAL

The Supplementary Material for this article can be found online at: https://www.frontiersin.org/articles/10.3389/feart.2020.611700/full#supplementary-material.

REFERENCES

Arnaud, F., Révillon, S., Debret, M., Revel, M., Chapron, E., Jacob, J., et al. (2012). Lake Bourget regional erosion patterns reconstruction reveals Holocene NW European Alps soil evolution and paleohydrology. *Quat. Sci. Rev.* 51, 81–92. doi:10.1016/j.quascirev.2012.07.025

Barrón, V., and Torrent, J. (1986). Use of the kubelka–munk theory to study the influence of iron oxides on soil colour. *J. Soil Sci.* 37, 499–510. doi:10.1111/j.1365-2389.1986.tb00382.x

Basell, L. S. (2008). Middle Stone Age (MSA) site distributions in eastern Africa and their relationship to Quaternary environmental change, refugia and the evolution of Homo sapiens. *Quat. Sci. Rev.* 27 (27), 2484–2498. doi:10.1016/j.quascirev.2008.09.010

Benito-Calvo, A., De la Torre, I., Mora, R., Tibebu, D., Morán, N., and Martínez-Moreno, J. (2007). Geoarchaeological potential of the western bank of the Bilate River (Ethiopia). Analele Universităţii din Oradea XVIISeria Geographie), 99–104.

Berhanu, B., Melesse, A. M., and Seleshi, Y. (2013). GIS-based hydrological zones and soil geo-database of Ethiopia. *Catena* 104, 21–31. doi:10.1016/j.catena.2012.12.007

Blaauw, M. (2010). Methods and code for 'classical'age-modelling of radiocarbon sequences. *Quat. Geochronol.* 5 (5), 512–518. doi:10.1016/j.quageo.2010.01.002

Blott, S. J., and Pye, K. (2001). GRADISTAT: a grain size distribution and statistics package for the analysis of unconsolidated sediments. *Earth Surface Processes and Landforms.* 26 (11), 1237–1248. doi:10.1002/esp.261

Bon, F., Dessie, A., Bruxelles, L., Daussy, A., Douze, K., Fauvelle-Aymar, F., et al. (2013). Prehistory of the central main Ethiopian rift (Ziway-Shala basin): establishing the late stone age sequence in eastern Africa. *An. Ethiopie.* 28, 405–407. doi:10.3406/ethio.2013.1552

Bonini, M., Corti, G., Innocenti, F., Manetti, P., Mazzarini, F., Abebe, T., et al. (2005). Evolution of the Main Ethiopian Rift in the frame of Afar and Kenya rifts propagation. *Tectonics* 24, 1. doi:10.1029/2004TC001680

Brandt, S. A., Fisher, E. C., Hildebrand, E. A., Vogelsang, R., Ambrose, S. H., Lesur, J., et al. (2012). Early MIS 3 occupation of Mochena Borago rockshelter, southwest Ethiopian highlands: implications for late Pleistocene archaeology, paleoenvironments and modern human dispersals. *Quat. Int.* 274, 38–54. doi:10.1016/j.quaint.2012.03.047

Brandt, S., Hildebrand, E., Vogelsang, R., Wolfhagen, J., and Wang, H. (2017). A new MIS 3 radiocarbon chronology for Mochena Borago Rockshelter, SW Ethiopia: implications for the interpretation of Late Pleistocene chronostratigraphy and human behavior. *J. Archaeol. Sci. Report.* 11, 352–369. doi:10.1016/j.jasrep.2016.09.013

Brown, E. T. (2011). Lake Malawi's response to "megadrought" terminations: sedimentary records of flooding, weathering and erosion. *Palaeogeogr. Palaeoecol.* 303 (1-4), 120–125. doi:10.1016/j.palaeo.2010.01.038

Chernet, T. (2011). Geology and hydrothermal resources in the northern Lake Abaya area (Ethiopia). *J. Afr. Earth Sci.* 61 (2), 129–141. doi:10.1016/j.jafrearsci.2011.05.006, 2011

Corti, G. (2009). Continental rift evolution: from rift initiation to incipient break-up in the Main Ethiopian Rift, East Africa. *Earth Sci. Rev.* 96 (1-2), 1–53. doi:10.1016/j.earscirev.2009.06.005

Corti, G., Sani, F., Philippon, M., Sokoutis, D., Willingshofer, E., and Molin, P. (2013). Quaternary volcano-tectonic activity in the Soddo region, western margin of the Southern Main Ethiopian Rift. *Tectonics* 32 (4), 861–879. doi:10.1002/tect.20052

De la Torre, I., Benito-Calvo, A., Mora, R., Martínez-Moreno, J., Morán, N., and Tibebu, D. (2007). Stone age occurences in the western bank of the Bilate River (southern Ethiopia) - some preliminary results. *Nyame Akuma.* 67, 14–25.

Eckmeier, E., and Gerlach, R. (2012). Characterization of archaeological soils and sediments using VIS spectroscopy. *eTopoi. J. Ancient Stud.* 3, 285–290. doi:10.1002/gea.1004

Fisher, E. (2010). *Late Pleistocene technological change and hunter-gatherer behavior at moche Borago rockshelter, sodo-wolayta, Ethiopia: flaked stone artifacts from the early OIS 3 (60–43 ka) deposits.* Gainesville, FL: University of Florida.

Foerster, V., Junginger, A., Langkamp, O., Gebru, T., Asrat, A., Umer, M., et al. (2012). Climatic change recorded in the sediments of the Chew Bahir basin, southern Ethiopia, during the last 45,000 years. *Quat. Int.* 274, 25–37. doi:10.1016/j.quaint.2012.06.028

Foerster, V., Vogelsang, R., Junginger, A., Asrat, A., Lamb, H. F., Schaebitz, F., et al. (2015). Environmental change and human occupation of southern Ethiopia and northern Kenya during the last 20,000 years. *Quat. Sci. Rev.* 129, 333–340. doi:10.1016/j.quascirev.2015.10.026

Folk, R. L., and Ward, W. C. (1957). Brazos River bar [Texas]; a study in the significance of grain size parameters. *J. Sedim. Res.* 27 (1), 3–26. doi:10.1306/74d70646-2b21-11d7-8648000102c1865d

Garcin, Y., Melnick, D., Strecker, M. R., Olago, D., and Tiercelin, J.-J. (2012). East African mid-Holocene wet–dry transition recorded in palaeo-shorelines of Lake Turkana, northern Kenya Rift. *Earth Planet. Sci. Lett.* 331-332, 322–334. doi:10.1016/j.epsl.2012.03.016

Goldberg, P., and Bar-Yosef, O. (1998). "In site formation processes in kebara and hayonim caves and their significance in levantine prehistoric caves." in *Neandertals and modern humans in western Asia.* Editors T. Akazawa, K. Aoki, and O. Bar-Yosef (Boston, MA: Springer US), 107–125. doi:10.1007/0-306-47153-1_8

Goldberg, P., Miller, C. E., Schiegl, S., Ligouis, B., Berna, F., Conard, N. J., et al. (2009). Bedding, hearths, and site maintenance in the Middle Stone age of Sibudu cave, KwaZulu-Natal, South Africa. *Archaeol. Anthropo. Sci.* 1, 95–122. doi:10.1007/s12520-009-0008-1

Griffiths, J. (1972). "Ethiopian highlands,"in *World survey of climatology," in climates of Africa.* Editors H. Landsberg and N.L Amsterda (New York, NY: Elsevier), Vol. 10, 369–381.

Gutherz, X., Jallot, L., Lesur, J., Pouzolles, G., and Sordoillet, D. (2002). Annales d'Éthiopie, De Boc-card/Centre Français des Études Éthiopiennes. *Annales d'Ethiopie* 18, 181–190. doi:10.3406/ethio.2002.1019

Hemming, S. R. (2004). Heinrich events: massive late Pleistocene detritus layers of the north atlantic and their global climate imprint. *Rev. Geophys.* 42, RG1005. doi:10.1029/2003RG000128

Hensel, E. A., Bödeker, O., Bubenzer, O., and Vogelsang, R. (2019). Combining geomorphological– hydrological analyses and the location of settlement and raw material sites – a case study on understanding prehistoric human settlement activity in the southwestern Ethiopian Highlands. *E&G Quaternary Sci. J.* 68, 201–213. doi:10.5194/egqsj-68-201-2019

Herrejón Lagunilla, Á., Carrancho, Á., Villalaín, J. J., Mallol, C., and Hernández, C. M. (2019). An experimental approach to the preservation potential of magnetic signatures in anthropogenic fires. *PLoS One.* 14, e0221592. doi:10.1371/journal.pone.0221592

Hildebrand, E. A., and Brandt, S. A. (2010). An archaeological survey of the tropical highlands of Kafa, southwestern Ethiopia. *J. Afr. Archaeol.* 8 (1), 43–63. doi:10.3213/1612-1651-10152

Hildebrand, E. A., Brandt, S. A., Friis, I., and Demissew, S. (2019). "Paleoenvironmental reconstructions for the Horn of Africa: Interdisciplinary perspectives on strategy and significance," in *Trees, grasses and crops. People and plants in sub-saharan Africa and beyond*. Editors B. Eichorn and A. Höhn (Bonn, DE: Verlag Dr. Rudolf Habelt)), 187–210.

Holliday, V. T., and Gartner, W. G. (2007). Methods of soil P analysis in archaeology. *J. Archaeol. Sci.* 34 (2), 301–333. doi:10.1016/j.jas.2006.05.004

Hunt, A. M., and Speakman, R. J. (2015). Portable XRF analysis of archaeological sediments and ceramics. *J. Archaeol. Sci.* 53, 626–638. doi:10.1016/j.jas.2014.11.031

Inglis, R. H., French, C., Farr, L., Hunt, C. O., Jones, S. C., Reynolds, T., et al. (2018). Sediment micromorphology and site formation processes during the middle to later stone ages at the haua fteah cave, cyrenaica, Libya. *Geoarchaeology* 33 (3), 328–348. doi:10.1002/gea.21660

Iuss Working Group Wrb (2014). *World Reference Base for Soil Resources International soil classification system for naming soils and creating legends for soil maps in World soil resources report*. Rome: FAO, 106, 188.

Ivers-Tiffée, E., and von Münch, W. (2007). "Magnetische werkstoffe," in *Werkstoffe der Elektrotechnik*. Editors E. Ivers-Tiffée and W. von Münch (Wiesbaden (DE: B.G. Teubner Verlag) doi:10.1007/978-3-8351-9088-7_6

Junginger, A., and Trauth, M. H. (2013). Hydrological constraints of paleo-Lake Suguta in the Northern Kenya Rift during the African humid period (15–5 ka BP). *Global Planet. Change.* 111, 174–188. doi:10.1016/j.gloplacha.2013.09.005

Kaniewski, D., Marriner, N., Cheddadi, R., Joel, G., and Campo, E. (2018). The 4.2 ka BP event in the Levant. *Clim. Past.* 14, 1529–1542. doi:10.5194/cp-14-1529-2018

Karkanas, P. (2017). "Chemical alteration,," in *Encyclopedia of geoarchaeology. Encyclopedia of earth sciences series*. Editor A. S. Gilbert (Dordrecht, NL: Springer-Verlag) doi:10.1007/978-1-4020-4409-0_126

Kehl, M., Burow, C., Cantalejo, P., Domínguez-Bella, S., Durán, J. J., Henselowsky, F., et al. (2016). Site formation and chronology of the new Paleolithic site Sima de Las Palomas de Teba, southern Spain. *Quat. Res.* 85 (2), 313–331. doi:10.1016/j.yqres.2016.01.007

Kehl, M., Eckmeier, E., Franz, S., Lehmkuhl, F., Soler, J., Soler, N., et al. (2014). Sediment sequence and site formation processes at the Arbreda Cave, NE Iberian Peninsula, and implications on human occupation and climate change during the Last Glacial. *Clim. Past.* 10 (5), 1673–1692 doi:10.5194/cp-10-1673-2014

Khalidi, L., Mologni, C., Ménard, C., Coudert, L., Gabriele, M., Davtian, G., et al. (2020). 9000 years of human lakeside adaptation in the Ethiopian Afar: Fisher-foragers and the first pastoralists in the Lake Abhe basin during the African Humid Period. *Quat. Sci. Rev.* 243, 106459. doi:10.1016/j.quascirev.2020.106459

Klasen, N., Kehl, M., Mikdad, A., Brückner, H., and Weniger, G.-C. (2018). Chronology and formation processes of the Middle to Upper Palaeolithic deposits of Ifri n'Ammar using multi-method luminescence dating and micromorphology. *Quat. Int.* 485, 89–102. doi:10.1016/j.quaint.2017.10.043

Kröpelin, S., Verschuren, D., Lézine, A.-M., Eggermont, H., Cocquyt, C., Francus, P., et al. (2008). Climate-driven ecosystem succession in the Sahara: the past 6000 years. *Science* 320, 765–768. doi:10.1126/science.1154913.5877

Kuehn, D. D., and Dickson, D. B. (1999). Stratigraphy and noncultural site formation at the shurmai rockshelter (GnJm1) in the mukogodo hills of north-Central Kenya. *Geoarchaeology: Int. J.* 14 (1), 63–85. doi:10.1002/(SICI)1520-6548.199901)14:1<63::AID-GEA5>3.0.CO;2-F

Laskar, J., Robutel, P., Joutel, F., Gastineau, M., Correia, A. C. M., and Levrard, B. (2004). A long-term numerical solution for the insolation quantities of the Earth. *A&A* 428 (1), 261–285. doi:10.1051/0004-6361:20041335

Le Borgne, E. (1955). Susceptibilité magnétique anormale du sol superficiel. *Ann. Geophys.* 11, 399–419.

Marean, C. W., Bar-Matthews, M., Fisher, E., Goldberg, P., Herries, A., Karkanas, P., et al. (2010). The stratigraphy of the middle stone age sediments at pinnacle point cave 13B (mossel bay, western cape province, South Africa). *J. Hum. Evol.* 59 (3-4), 234–255. doi:10.1016/j.jhevol.2010.07.007

Mark, B. G., and Osmaton, H. A. (2008). Quaternary glaciation in Africa: key chronologies and climatic implications. *J. Quat. Sci.* 23, 589–608. doi:10.1002/jqs.1222

Mentzer, S. M. (2017). "Rockshelter settings," in *Encyclopedia of geoarchaeology. Encyclopedia of earth sciences series*. Editor A. S. Gilbert (Dordrecht (NL): Springer-Verlag) doi:10.1007/978-1-4020-4409-0_159

Miller, C. E., Goldberg, P., and Berna, F. (2013). Geoarchaeological investigations at diepkloof rock shelter, western Cape, South Africa. *J. Archaeol. Sci.* 40 (9), 3432–3452. doi:10.1016/j.jas.2013.02.014

Nesbitt, H., and Young, G. (1982). Early Proterozoic climates and plate motions inferred from major element chemistry of lutites. *Nature* 299 (5885), 715–717. doi:10.1038/299715a0

Nicholson, S. E. (2018). The ITCZ and the seasonal cycle over equatorial Africa. *Bull. Am. Meteorol. Soc.* 99 (2), 337–348. doi:10.1175/BAMS-D-16-0287.1

Okrusch, M., and Matthes, S. (2010). *Mineralogie*. Berlin, Germany: Springer-Verlag

Ossendorf, G., Groos, A. R., Bromm, T., Tekelemariam, M. G., Glaser, B., Lesur, J., et al. (2019). Middle Stone Age foragers resided in high elevations of the glaciated Bale Mountains, Ethiopia. *Science* 365 (6453), 583–587. doi:10.1126/science.aaw8942

Reimer, P., Austin, W., Bard, E., Bayliss, A., Blackwell, P., Bronk Ramsey, C., et al. (2020). The IntCal20 northern hemisphere radiocarbon age calibration curve (0–55 cal kBP). *Radiocarbon* 62 (4), 725–757. doi:10.1017/RDC.2020.41

Schepers, C., Lesur, J., and Vogelsang, R. (2020). Hunter-gatherers of the high-altitude afromontane forest – the Holocene occupation of Mount dendi, Ethiopia. *Azania* 55 (3), 329–359. doi:10.1080/0067270X.2020.1792709

Segele, Z. T., Lamb, P. J., and Leslie, L. M. (2009). Large-scale atmospheric circulation and global sea surface temperature associations with Horn of Africa June–September rainfall. *Int. J. Climatol.* 29 (8), 1075–1100. doi:10.1002/joc.1751

Stewart, B. A., and Jones, S. C. (2016). "Africa from MIS 6-2: the florescence of modern humans," in Africa from MIS 6-2: population dynamics and paleoenvironments. Editors S. C. Jones and B. A. Stewart (Dordrecht: Springer Netherlands), 1–20. doi:10.1007/978-94-017-7520-5_1

Texier, P. J., Porraz, G., Parkington, J., Rigaud, J. P., Poggenpoel, C., Miller, C., et al. (2010). From the Cover: a Howiesons Poort tradition of engraving ostrich eggshell containers dated to 60,000 years ago at Diepkloof Rock Shelter, South Africa. *Proc. Natl. Acad. Sci. USA.* 107, 6180–6185. doi:10.1073/pnas.0913047107

Tierney, J. E., Lewis, S. C., Cook, B. I., LeGrande, A. N., and Schmidt, G. A. (2011). Model, proxy and isotopic perspectives on the east african Humid Period. *Earth Planet Sci. Lett.* 307 (1-2), 103–112. doi:10.1016/j.epsl.2011.04.038

Trauth, M. H., Asrat, A., Duesing, W., Foerster, V., Kraemer, K. H., Marwan, N., et al. (2019). Classifying past climate change in the Chew Bahir basin, southern Ethiopia, using recurrence quantification analysis. *Clim. Dynam.* 53 (5-6), 2557–2572. doi:10.1007/s00382-019-04641-3

Tribolo, C., Asrat, A., Bahain, J. J., Chapon, C., Douville, E., Fragnol, C., et al. (2017). Across the gap: geochronological and sedimentological analyses from the Late Pleistocene-Holocene sequence of Goda Buticha, southeastern Ethiopia. *PLos One.* 12 (1), e0169418. doi:10.1371/journal.pone.0169418

Viste, E., and Sorteberg, A. (2013). Moisture transport into the Ethiopian highlands. *Int. J. Climatol.* 33, 249–263. doi:10.1002/joc.3409

Vogelsang, R., and Wendt, K. P. (2018). Reconstructing prehistoric settlement models and land use patterns on Mt. Damota/SW Ethiopia. *Quat. Int.* 485, 140–149. doi:10.1016/j.quaint.2017.06.061

Willmes, C., Becker, D., Brocks, S., Hütt, C., and Bareth, G. (2017). High resolution köppen-geiger classifications of paleoclimate simulations. *Trans. GIS.* 21, 57–73. doi:10.1111/tgis.12187

WoldeGabriel, G., James, L. A., and Robert, C. W. (1990). Geology, geochronology, and rift basin development in the central sector of the Main Ethiopian Rift. *Geol. Soc. Am. Bull.* 102 (4), 439–485. doi:10.1130/0016-7606 (1990)102<0439:GGARBD>2.3.CO;2

WoldeGabriel, G., Walter, R. C., Aronson, J. L., and Hart, W. K. (1992). Geochronology and distribution of silicic volcanic rocks of Plio-Pleistocene age from the central sector of the Main Ethiopian Rift. *Quat. Int.* 13, 69–76. doi:10.1016/1040-6182(92)90011-P

Wright, D. K. (2017). Humans as agent in the termination of the african Humid Period. *Front. Earth Sci.* 5, 4. doi:10.3389/feart.2017.00004

Xiao, J., Zhang, S., Fan, J., Wen, R., Zhai, D., Tian, Z., et al. (2018). The 4.2 ka BP event: multi-proxy records from a closed lake in the northern margin of the East Asian summer monsoon. *Clim. Past.* 14 (10), 1417–1425. doi:10.5194/cp-14-1417-2018

Conflict of Interest: The authors declare that the research was conducted in the absence of any commercial or financial relationships that could be construed as a potential conflict of interest.

frontiers in Earth Science

ORIGINAL RESEARCH
published: 15 January 2021
doi: 10.3389/feart.2020.598448

Chronological Assessment of the Balta Alba Kurgan Loess-Paleosol Section (Romania) – A Comparative Study on Different Dating Methods for a Robust and Precise Age Model

Stephanie Scheidt[1], Sonja Berg[1], Ulrich Hambach[2,3], Nicole Klasen[4], Stephan Pötter[5], Alexander Stolz[6], Daniel Veres[7], Christian Zeeden[8], Dominik Brill[4], Helmut Brückner[4], Stephanie Kusch[9], Christian Laag[8,10], Frank Lehmkuhl[5], Martin Melles[1], Florian Monnens[1], Lukas Oppermann[4], Janet Rethemeyer[1] and Janina J. Nett[5]*

[1]Institute of Geology and Mineralogy, Faculty of Mathematics and Natural Sciences, University of Cologne, Cologne, Germany, [2]Chair of Geomorphology, Faculty of Biology, Chemistry, and Earth Sciences, University of Bayreuth, Bayreuth, Germany, [3]Bayreuth Center for Ecology and Environmental Research, University of Bayreuth, Bayreuth, Germany, [4]Cologne Luminescence Laboratory, Institute of Geography, Faculty of Mathematics and Natural Sciences, University of Cologne, Cologne, Germany, [5]Chair of Physical Geography and Geoecology, Department of Geography, RWTH Aachen University, Aachen, Germany, [6]Institute for Nuclear Physics, Faculty of Mathematics and Natural Sciences, University of Cologne, Cologne, Germany, [7]Institute of Speleology, Romanian Academy, Cluj-Napoca, Romania, [8]Rock Physics and Borehole Geophysics, Leibniz Institute for Applied Geophysics, Hannover, Germany, [9]CologneAMS-Centre—Centre for Accelerator Mass Spectrometry, University of Cologne, Cologne, Germany, [10]Université de Paris, Institut de Physique du Globe de Paris, CNRS, Paris, France

OPEN ACCESS

Edited by:
Amanda Owen, University of Glasgow, United Kingdom

Reviewed by:
Zhixiong Shen, Coastal Carolina University, United States
Gabor Ujvari, Hungarian Academy of Sciences (MTA), Hungary

***Correspondence:**
Stephanie Scheidt
stephanie.scheidt@uni-koeln.de

Specialty section:
This article was submitted to Sedimentology, Stratigraphy and Diagenesis, a section of the journal Frontiers in Earth Science

Received: *24 August 2020*
Accepted: *06 November 2020*
Published: *15 January 2021*

Citation:
Scheidt S, Berg S, Hambach U, Klasen N, Pötter S, Stolz A, Veres D, Zeeden C, Brill D, Brückner H, Kusch S, Laag C, Lehmkuhl F, Melles M, Monnens F, Oppermann L, Rethemeyer J and Nett JJ (2021) Chronological Assessment of the Balta Alba Kurgan Loess-Paleosol Section (Romania) – A Comparative Study on Different Dating Methods for a Robust and Precise Age Model. Front. Earth Sci. 8:598448. doi: 10.3389/feart.2020.598448

Loess-paleosol sequences (LPSs) are important terrestrial archives of paleoenvironmental and paleoclimatic information. One of the main obstacles for the investigation and interpretation of these archives is the uncertainty of their age-depth relationship. In this study, four different dating techniques were applied to the Late Pleistocene to Holocene LPS Balta Alba Kurgan (Romania) in order to achieve a robust chronology. Luminescence dating includes analysis of different grain-size fractions of both quartz and potassium feldspar and the best results are obtained using fine-grained quartz blue-stimulated and polymineral post-infrared infrared-stimulated luminescence measurements. Radiocarbon (^{14}C) dating is based on the analysis of bulk organic carbon (OC) and compound-specific radiocarbon analysis (CSRA). Bulk OC and leaf wax-derived *n*-alkane ^{14}C ages provide reliable age constraints for the past c. 25–27 kyr. CSRA reveals post-depositional incorporation of roots and microbial OC into the LPS limiting the applicability of ^{14}C dating in older parts of the sequence. Magnetic stratigraphy data reveal good correlation of magnetic susceptibility and the relative paleointensity of the Earth's magnetic field with one another as well as reference records and regional data. In contrast, the application of paleomagnetic secular variation stratigraphy is limited by a lack of regional reference data. The identification of the Campanian Ignimbrite/Y-5 tephra layer in the outcrop provides an independent time marker against which results from the other dating methods have been tested. The most accurate age constraints from each method are used for two Bayesian age-depth modeling approaches. The systematic comparison of the individual results exemplifies the advantages and disadvantages of the respective methods. Taken as a whole, the two age-depth models

agree very well, our study also demonstrates that the multi-method approach can improve the accuracy and precision of dating loess sequences.

Keywords: loess-paleosol sequences, optically stimulated luminescence dating, magnetic stratigraphy, compound-specific radiocarbon analysis, tephrochronology, age-depth modeling, Romania, late Pleistocene-Holocene

INTRODUCTION

Loess-paleosol sequences (LPSs) are widely spread across Central Eastern Europe (**Figure 1**) and provide archives of paleoclimate information crucial for the reconstruction of the Pleistocene environmental evolution (e.g., Marković et al., 2015). In addition to semi-continuous dust input, the formation of LPSs is closely linked to changes in climate and environmental conditions, which are controlled by interglacial-glacial cycles (Gallet et al., 1996; Kohfeld and Harrison, 2003; Svensson et al., 2008; Újvári et al., 2010; Obreht et al., 2017; Zeeden et al., 2018b). Beyond reconstructing Milankovitch-scale climatic variations, LPSs also allow sub-millennial climatic fluctuations to be identified (Moine et al., 2017; Újvári et al., 2017; Zeeden et al., 2018c; Veres et al., 2018). In LPSs of the last glacial cycle, the imprint of past climatic fluctuations is preserved as a succession of weakly developed paleosols or pedogenetically overprinted loess layers, which often gradually turn into adjacent loess beds. These imprints of orbital to millennial climatic variations provide the backbone for chronostratigraphic correlations (at least) on hemispheric scales and interpretation of deposits across environmental boundaries (e.g., Rousseau et al., 2020). In paleoclimatology, this approach was used even before absolute dating techniques became available (e.g., Emiliani, 1955). Nevertheless, to unambiguously link the characteristic paleoclimatic imprints in sedimentary archives to a precisely defined chronostratigraphic interval, time anchors (tie points) are essential (Govin et al., 2015). In their absence, the chronologies of precisely dated archives (e.g., ice core records, speleothems) and even chronologies derived using astrochronological approaches remain speculative (e.g., Lowe and Walker, 2014). Hence, one of the main obstacles for the investigation and interpretation of climatic and environmental information preserved in sedimentary archives is the uncertainty of the age-depth relationship. Most analytical dating techniques applicable to LPSs have age uncertainties that exceed

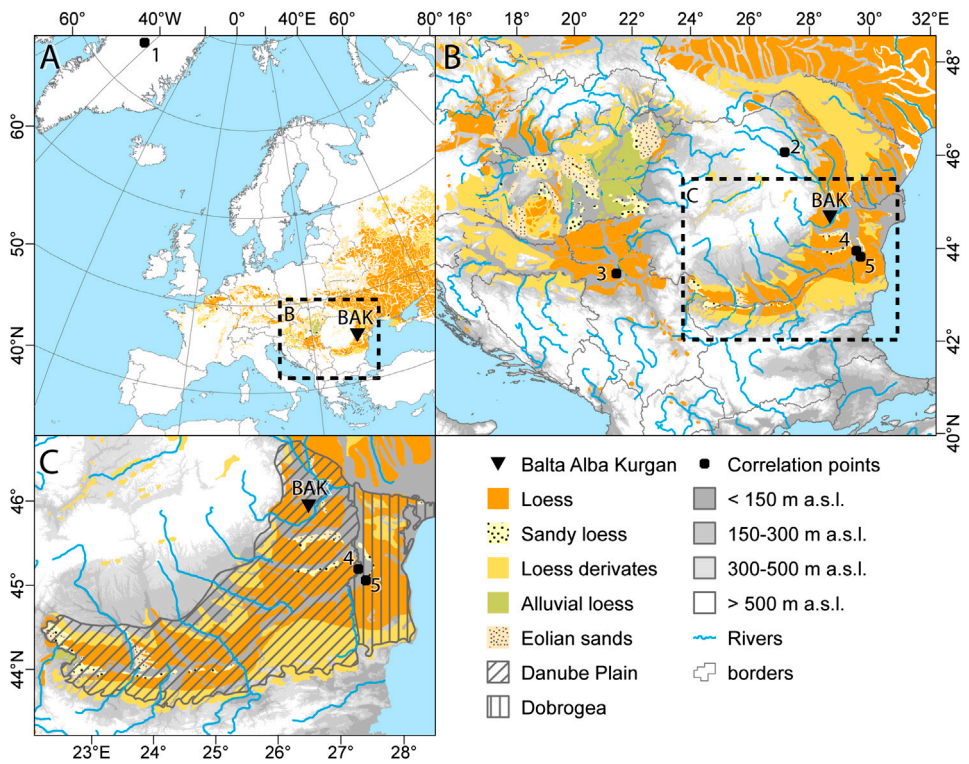

FIGURE 1 | Location of the study area and distribution of eolian sediments (according to Haase et al. (2007), modified). **(A)** Europe. **(B)** Southeast Europe. **(C)** The Lower Danube Basin with landscape units (according to Jipa (2014), modified). Black circles indicate the correlation sites for magnetic stratigraphy as described in *Magnetic Stratigraphy*. 1) NGRIP, 2) Poiana Ciresului, 3) Batajnica, 4) Vlasca, 5) Rasova. Elevation contours (based on JAXA, 2016) are shown to illustrate the natural altitudinal boundaries of loess distributions.

millennial-to-centennial-scale resolution. Thus, the exact timing and duration of individual short-term climatic fluctuations can be difficult to establish (e.g., Zeeden et al., 2018c). However, good age control of these events is of particular importance in understanding broad-scale atmospheric circulation patterns, climatic feedback mechanisms and possibly offsets in timing between different regions and deposit types. Therefore, in this study we combine absolute dating techniques (optically stimulated luminescence, radiocarbon) with correlative dating (tephrochronology, relative magnetic paleointensity, magnetic susceptibility correlation) and integrate the results in a robust absolute age model.

Optically stimulated luminescence (OSL) dating is the most commonly used absolute dating technique in loess chronological research (Roberts, 2008). Sediment accumulation is dated directly by measuring a signal that builds up over time in buried quartz and feldspar grains and resets during particle transport. The use of different grain-sizes and mineral extracts and measurement protocols has been well established (Murray and Wintle, 2000; Murray and Wintle, 2003; Timar-Gabor et al., 2011; Buylaert et al., 2012). The ubiquity of suitable sample material in loess, favorable conditions for signal resetting during eolian transport and a dating range covering at least the last interglacial-glacial cycle are the main advantages of this methods for dating LPSs (e.g., Lauer et al., 2016; Bösken et al., 2017; Timar-Gabor et al., 2017; Bösken et al., 2019; Constantin et al., 2019; Lomax et al., 2019; Fenn et al., 2020a). However, the age uncertainties of luminescence methods are on the order of thousands of years, and significant age offsets have also been reported between different mineral fractions dated as well as different protocols applied. In comparison, the age uncertainty of radiocarbon (^{14}C) analysis of carbonaceous and organic materials is substantially lower allowing centennial-scale resolution chronologies in LPS records (e.g., Song et al., 2012; Újvári et al., 2014c; Song et al., 2015). The method uses the radioactive decay of naturally occurring ^{14}C in organic matter or carbonates to calculate the time since the last equilibration with atmospheric CO_2 or other carbon pools (e.g., dissolved inorganic carbon in aquatic environments). Due to the half-life of ^{14}C and analytical limitations, maximum ages of 50–60 ka can typically be resolved with this approach for regular-sized (~1 mg) samples. Since the atmospheric ^{14}C content has changed in the past, ^{14}C ages are calibrated against reference curves to obtain absolute ages (e.g., Reimer et al., 2020). Nonetheless, the application of ^{14}C analysis to loess is frequently limited by the absence/scarcity of suitable remains such as wood, charcoals, bones and carbonate fossils (e.g., Haesaerts et al., 2010; Pigati et al., 2013; Újvári et al., 2014c; Moine et al., 2017). Moreover, ^{14}C ages obtained on bulk organic carbon (OC) can be biased by relocation of organic matter in loess, which may result in an underestimation of sedimentation ages (e.g., Hatté et al., 2001). In contrast to OSL and ^{14}C analyses, magnetic stratigraphy is an indirect and correlative dating approach and includes age uncertainties that are not easily quantified. The method can be used for sediments accumulated beyond the dating limit of radiocarbon and luminescence techniques and is best applied to (several meter) long sequences (Heil et al., 2010; Song et al., 2018a; Zeeden et al., 2018b; Pfeifer et al., 2020; Zeeden et al., 2020). In general, age control is achieved by "wiggle-matching", i.e., tying significant features of paleo- and rock magnetic parameters to independently dated master curves (Maher, 1999; Hambach et al., 2008). The signals used are typically the magnetic susceptibility and, to a lesser extent, the direction and/or relative paleointensity (RPI) of the Earth's magnetic field. If unequivocal correlations are not possible, potential correlations need to be verified using other dating techniques, which may result in an iterative process. While magnetic stratigraphy is a powerful chronostratigraphic tool for LPSs, it should be noted that ages can be younger than the deposition of the respective LPS (Liu et al., 2015), because soils develop on and into accumulated sediments post-depositionally.

The motivation for this study was to compare the results of the individual dating methods and obtain a robust absolute chronology for the LPS Balta Alba Kurgan (in Romanian: Balta Albă Kurgan; hereafter BAK; **Figure 1**). In this LPS, a well constrained tephra layer is included and forms an independent time marker. We apply luminescence dating, radiocarbon dating and magnetic stratigraphy. In addition to the standard (bulk OC) ^{14}C analysis, we also test the applicability of compound-specific radiocarbon analysis (CSRA) of leaf wax lipids for age determination of loess, a method that has been rarely applied to LPSs (Häggi et al., 2014). We also use an extended set of OSL dating protocols to validate the OSL age assignment, including one for coarse-grain feldspar that is typically not applied to loess in this region. Furthermore, we combine the results with statistical age-depth modeling to obtain a robust chronology of the BAK loess profile. Our approach illustrates the potentials and limitations of each individual method for dating loess sequences and may help to gain a better understanding of the advantages and disadvantages of the individual methods in dating of LPSs. Our observations and conclusions are highly relevant for future studies that focus on the interpretation of loess sequences to study the paleoclimatic and paleoenvironmental evolution in south-eastern Europe and elsewhere.

REGIONAL SETTING AND STUDY SITE

The Lower Danube Basin (LDB) in southeast Romania (**Figure 1**) is characterized by vast Pleistocene sedimentary deposits of considerable thickness, which are mostly of eolian and fluvial origin. The deposits are incised by broad valleys and alluvial plains of the Danube and its major tributaries. These broad alluvial valleys acted as the major dust source for the coarse components of the loess formed during the Pleistocene (Buggle et al., 2008; Jipa, 2014). The loess deposits of the LDB reach thicknesses of more than 50 m. The thickness and the mean grain size of these loess deposits decrease with distance from potential source areas, i.e., especially the river beds (Smalley and Leach, 1978; Smalley et al., 2009; Jipa, 2014). The most intensively studied LPSs within the LDB are found on the Dobrogea plateau (**Figure 1**; e.g., Buggle et al., 2009; Buggle et al., 2013; Fitzsimmons and Hambach, 2014; Obreht et al., 2017), along the shores of the Black Sea (e.g., Necula et al., 2015) and along river

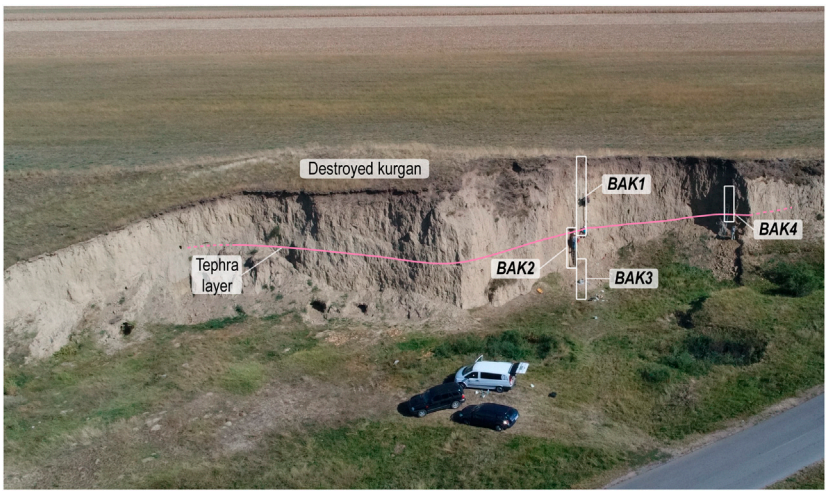

FIGURE 2 | Aerial view of the BAK site looking southeast. The location of the kurgan as well as the stratigraphic position of the tephra layer (pink line) are indicated. The sampled sub-profiles are shown with white rectangles.

cuts of the Danube and its tributaries across the Danube Plain (Constantin et al., 2014; Obreht et al., 2017; Antoine et al., 2019; **Figure 1**). These sections often exhibit several loess-soil couplets representing glacial-interglacial-cycles. The forelands of the Eastern Carpathians, however, are severely underrepresented in loess research, although the area is covered by vast loess deposits. The BAK LPS (45°16'40"N, 27°17'27"E, ca. 46 m above mean sea level, **Figure 1**) is located in this area, approx. 40 km east of the foothills of the Carpathian Bend. It is exposed at a road cut of road DC13 dissecting the northern slope of a loess plateau between the rivers Râmnicul Sărat and Buzău. The Carpathian foothills to the West comprise thick Neogene deposits. The loess plateau frames a basin that includes the alkaline lake Balta Alba, located approximately 2 km east of the section. Lake Balta Alba formed during the Holocene due to neotectonic subsidence in a paleo-channel of the Râmnicul Sărat (ILEC, 2019).

The sampled BAK sequence is ~15.4 m thick. Several large pit-grave burial mounds (kurgans) are preserved in the vicinity of the sampling site. The majority of these tumuli in the Lower Danube area most likely date to the Late Neolithic-Early Bronze Age transition (~3 ka B.C.; Frînculeasa et al., 2015). Our sampled profiles are located close to the margin of a kurgan (**Figures 2**, **3**). The uppermost 0.78 m of the profile formed after kurgan construction as indicated by the preservation of a non-ploughed topmost horizon of a chernozem. Between 0.78 and 1.55 m depth, the sediments in the BAK profile consist of disturbed anthropogenic infill of the grave mound. Between 1.55 m and 2.10 m depth, the in-situ lower part of the primary Holocene chernozem (S0, nomenclature according to Marković et al., 2015) overlies bioturbated loess with a leopard skin pattern. From 2.10 m to 7.40 m depth, the sediment is a typical loess including pedogenetically overprinted intervals between 4.30–5.92 m and 6.40–6.95 m. A strongly bioturbated paleosol occurs between 7.40 m and 8.06 m depth. At 8.06–8.10 m depth a macroscopically visible tephra layer has been identified as laterally continuous loose pinkish-whitish patches of coarse silt, resembling other tephra occurrences within the Lower Danube loess (Veres et al., 2013; Obreht et al., 2017; Zeeden et al., 2018c). Below the tephra, up to 8.70 m depth, the loess is carbonate-rich as well as bioturbated and strongly overprinted by pedogenesis. Underneath, a dark reddish paleosol with two to three distinct pedogenetic horizons is present down to 9.85 m depth. Other (weakly developed) paleosols can be found between 10.0 m and 10.2 m depth, as well as between 10.8 m and 11.4 m depth and are intercalated with carbonate-rich loess. The underlying loess reaches down to 13.2 m depth. A clay-rich, dark greyish to blackish paleosol resembling vertisol features with vertical cracks lies underneath, atop a carbonate-rich loess, which becomes increasingly reddish towards a depth of around 14 m. The paleosol between 14.0 m and 14.5 m depth exhibits chernozem-like characteristics. It overlies a carbonate-rich loess horizon, which turns into loess with sub-mm sized pores filled with organic material at 14.7 m depth. At the base of the section, waterlogged, hydromorphic loess and sands are present.

MATERIALS AND METHODS

Sampling

For our multidisciplinary dating approach, four subsections (BAK1 to BAK4) were defined along the BAK sequence (**Figures 2**, **3**). The composite profile comprises BAK1 (0–8.50 m), BAK2 (8–12 m) and BAK3 (11.5–15.4 m), which are directly adjacent to one another (thus forming a vertical sampling line) and located slightly to the South of the center of the kurgan. BAK4 is situated approximately 10 m to the South of the main profile (BAK1-3) and spans 3.66 m. Prior to sampling, the outcrops were thoroughly cleaned to obtain fresh and unweathered sediments. Samples for tephrochronological analyses were collected from the visible volcanic ash layer.

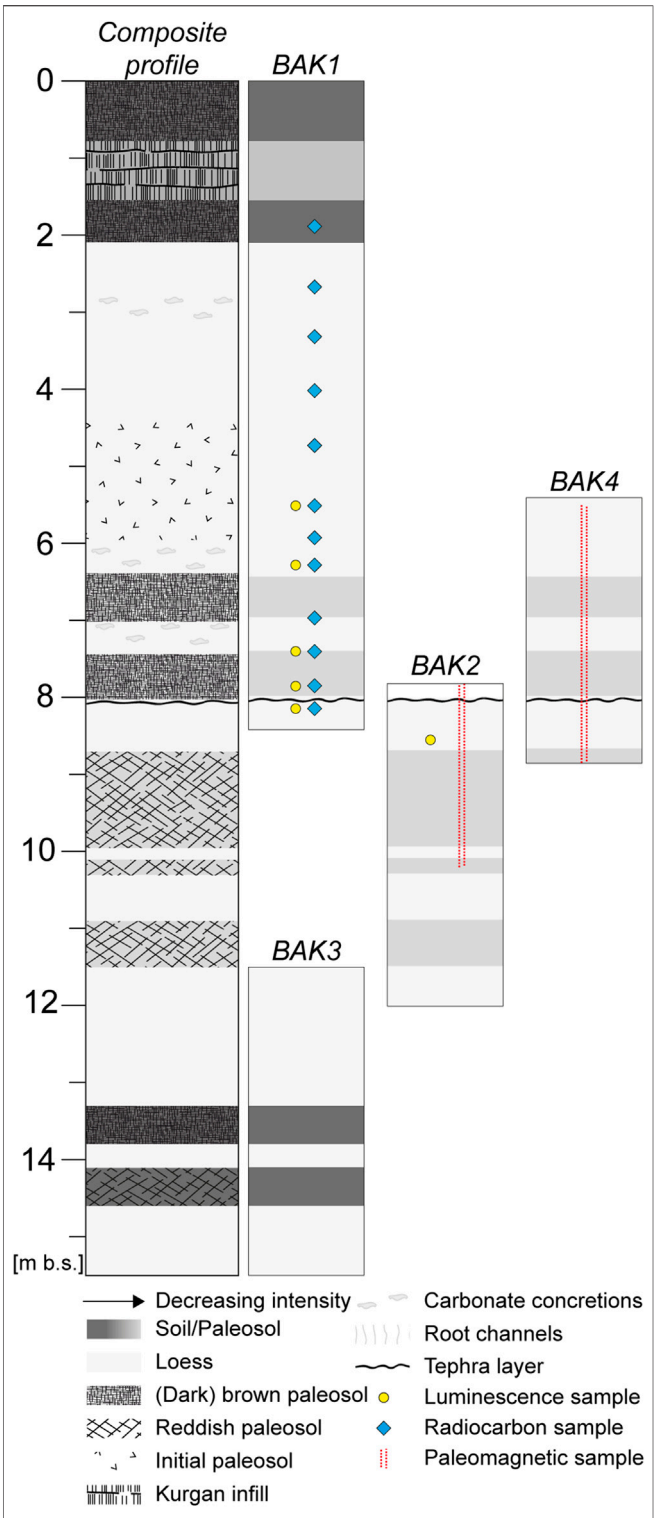

FIGURE 3 | Stratigraphic composite profile of Balta Alba Kurgan. Subsections BAK1 to BAK4 are shown with stratigraphic overlap and simplified stratigraphic information. The depth is given in meters below the surface (m b.s.) of the main profile (BAK1-BAK3).

Samples for OSL dating were taken using 20 cm long metal tubes. Additionally, a sample of the surrounding 30 cm of sediment was taken for radionuclide analysis (i.e., approximate penetration depth of γ-radiation). In total, six samples were analyzed in this study. For ^{14}C analysis, twelve samples of 6 cm thickness (~20 kg of sediment each) adjacent to OSL samples were taken from the BAK1 profile. Oriented paleomagnetic samples were obtained from subsections BAK2 and BAK4 (**Figure 2**). These subsections allow for cross-correlation with an overlap of approximately 85 cm, which includes the tephra layer. Sampling was performed by inserting square brass tubes of 2 cm edge length through an orientation frame into the wall. Full spatial orientation was provided by means of magnetic compass measurements combined with an inclinometer to define the dip of the frame. The resulting sediment prisms were subsequently carefully pushed from the tubes into cubic plastic boxes of 8 cm^3 volume to retain orientation. The vertical space between the center of the samples is ~2.1 cm. Overall 304 specimens were obtained: 120 from the BAK2 profile and 184 from the BAK4 profile. Twelve additional samples from the BAK1 and BAK2 subsections were selected for mineral magnetic analyses.

Tephra Geochemical Analysis

Bulk samples collected from the volcanic ash bed identified at BAK were subjected to glass-shard geochemical analyses at the Bayerisches GeoInstitut, University of Bayreuth, Germany. Measurements were performed on thin sections of volcanic glass shards containing sediment embedded in epoxy using a JXA8200 microprobe (JEOL, JP) and single-grain, wavelength-dispersive electron microprobe analysis (WDS-EPMA). Measurements were performed using an accelerating voltage of 15 keV and a 6 nA beam current. Peak counting times were 10 s for Na, 30 s for Si, Al, K, Ca, Fe and Mg, 40 s for Ti and Mn and 60 s for P. Precision is estimated at <1–6% (2σ) and 10–25% (2σ) for major and minor element concentrations, respectively. Geochemical results are summarized in **Supplementary Table 6** and an image of the analyzed glass shards is provided in **Supplementary Figure 15** of **Supplementary Section 4**.

Luminescence Dating

Polymineral fine-grained samples (4–11 µm) were prepared for luminescence dating using conventional preparation techniques (Frechen et al., 1996). A separate batch of the fine-grained fraction was etched in 34% H_2SiF_6 for one week to extract fine-grained quartz. Laboratory treatment of sand-sized samples included sieving to isolate the 63–90 µm fraction, chemical treatment with HCl (10%), H_2O_2 (10%) and $Na_2C_2O_4$ (0.01N) to remove carbonates, organic material and clay, respectively, as well as density separation (ρ = 2.58 g cm^{-3}, ρ = 2.62 g cm^{-3} and ρ = 2.68 g cm^{-3}) to isolate potassium feldspar and quartz. We used an automated Risø TL/OSL DA 20 reader equipped with a calibrated ^{90}Sr beta source for equivalent dose determination. All samples were prepared and measured in the Cologne Luminescence Laboratory (CLL, University of Cologne, DE).

Blue light emitting diodes at 470 nm (FWHM = 20 nm) were used for the stimulation of the quartz samples and the luminescence signal was detected through a Hoya U-340 filter (blue stimulated luminescence (BSL); Murray and Wintle, 2000; Murray and Wintle, 2003). The initial 0.8 s of the signal minus a background of the last 4 s were used. Laboratory experiments included preheat plateau tests using a series of preheat temperatures between 180°C and 280°C and dose recovery tests. For the dose recovery test, the samples were illuminated with blue light emitting diodes for 100 s at room temperature and a laboratory dose in the range of the natural dose was given to the samples. Equivalent doses were calculated using the arithmetic mean.

Post-infrared infrared stimulated luminescence measured at 290°C (p-IR $IRSL_{290}$ or $pIRIR_{290}$; Thiel et al., 2011) and infrared stimulated luminescence measured at 50°C (IR_{50}; Wallinga et al., 2000) were used to measure the polymineral fine-grained samples and the sand-sized potassium feldspar samples. Stimulation was carried out with infrared diodes (870 nm, FWHM = 40 nm) and the signals were detected through an interference filter (410 nm). The initial 4 s of the signal minus a background of the last 20 s were used. Laboratory experiments included prior-IR stimulation temperature tests (Buylaert et al., 2012) using a range of temperatures from 50° to 220°C and dose recovery tests. For the dose recovery tests, the samples were illuminated for 24 h in a Hönle SOL2 solar simulator and a laboratory dose in the range of the natural dose was applied to the samples. Equivalent doses were calculated using the arithmetic mean. Fading tests (Auclair et al., 2003) were carried out for all samples for the IR_{50} measurement protocol. IR_{50} ages were corrected for fading following the approach of Huntley (2006).

For the determination of the environmental dose rate, radionuclide concentrations of ^{238}U, ^{232}Th and ^{40}K were measured using high-resolution gamma-ray spectrometry. The dose rate was calculated with the open access web-based program DRAC v.1.2 (Durcan et al., 2015), using conversion factors reported by Guérin et al., 2011, alpha-efficiency values of 0.10 ± 0.014 ($pIRIR_{290}$; Schmidt et al., 2018), 0.07 ± 0.02 (IR_{50}) and 0.04 ± 0.01 (BSL) and a water content of 25 ± 10% for samples with clay and fine silt contents of about 25–30% and 15 ± 10% for samples with clay and fine silt contents of about 20%. Additionally, the gravimetric water content was determined by weighing before and after drying the dosimetry samples in the oven at 50°C. The internal beta dose rate contribution of the polymineral and the feldspar samples was calculated assuming a potassium content of 12.5 ± 0.5% (Huntley and Baril, 1997). The cosmic dose rate was calculated following Prescott and Hutton (1994). We refer to the **Supplementary Section 1** for further details.

Radiocarbon Analysis

Sediment samples for ^{14}C analysis were oven-dried at 40°C. For bulk OC ^{14}C analysis, root remains were removed by hand-picking prior to subsequent chemical treatment with a standard acid-alkali-acid (AAA) protocol. The purified bulk OC was converted to graphite using an automated graphitization system and analyzed at the CologneAMS facility at the University of Cologne, DE (Rethemeyer et al., 2019). Due to the low OC content of the samples, which produced 0.30 to 0.63 mg C (less than 1 mg C needed for the routine measurement), we determined the background of this specific suite of samples with size matched standards at 42,700 ± 590 ^{14}C years ($F^{14}C$ = 0.0049 ± 0.0004, fraction modern, Reimer et al., 2004).

For CSRA, ~1 kg of the dried sediment was ground in an agate mortar. The total lipid extract (TLE) was sequentially extracted by ultrasonication using methanol (MeOH), MeOH: dichloromethane (DCM, 1:1, v/v) and DCM: hexane (Hex, 1:1, v/v). The TLE was saponified with 0.5 M KOH in MeOH and water (9:1, v/v) at 80°C for 2 h. After addition of water, neutral lipids (including *n*-alkanes) were removed by liquid-liquid phase separation using DCM. For extraction of *n*-alkanoic acids, the remaining KOH mixture was acidified to pH 1 and the acid-fraction was extracted with DCM. *n*-Alkanes were eluted over SiO_2 columns with Hex. *n*-Alkanoic acids were methylated with MeOH and 12 M HCl (95:5, v/v) using MeOH of known ^{14}C isotopic composition ($F^{14}C_{MeOH}$ = 0.0002) to form fatty acid methyl esters (FAMEs).

Individual *n*-alkane and *n*-alkanoic acid homologs were isolated using a 7680 Agilent gas chromatograph (GC, Agilent Technologies, United States) equipped with a CIS 4 injection system (Gerstel, DE) and coupled to a preparative fraction collector (PFC; Gerstel, DE). Trapping of individual compounds was achieved at room temperature. For subsequent processing, individual compounds were flushed from the glass traps with 1 ml DCM. The purity of each isolated compound was determined by GC-FID (Agilent 7890B, Agilent Technologies, United States) and compounds with purities >98% were processed further. Two molecular standards C_{18} *n*-alkane (Fluka, Prod. No. 74691-5g, Lot. 0001448903 with an $F^{14}C$ value of <0.0008) and squalane (C_{30} isoprenoid; Fluka, Prod. No. 85629–50 ml, Lot. 0001418796 with an $F^{14}C$ value of 1.0187 ± 0.0033) were also processed to detect extraneous carbon (blank C) introduced during sample handling and PCGC purification.

Compounds were transferred into tin capsules for combustion and ^{14}C analysis with the EA-GIS (elemental analyzer coupled to a gas injection system) periphery at CologneAMS (Stolz et al., 2019). Due to the small and variable sample sizes of the lipid biomarker compounds used for ^{14}C analysis (9–42 µg C, see **Supplementary 2, Supplementary Table 2**), the extraneous C introduced during combustion in tin capsules and analysis with the EA-GIS set-up was also quantified. Following the procedure described in Hanke et al. (2017) a constant contamination of 1.0 ± 0.1 µg C with an $F^{14}C$ value of 0.44 ± 0.05 was determined (see **Supplementary Section 2.2** for further details). To assess if the ^{14}C age of a sample is distinguishable from background, the mass-dependent detection limit was calculated following Hanke et al. (2017). For example, the mass-dependent detection limit of a sample with a mass of 16 µg C (Col6363) was $F^{14}C$ = 0.015, corresponding to ~38,000 ^{14}C yr BP (**Supplementary Figure 7**). $F^{14}C$ values of all compound samples were corrected for the PCGC processing blank ($F^{14}C$ = 0.25 ± 0.017 and 0.6 ± 0.3 µg C)

and FAMEs for the addition of one methyl group added during transesterification using mass balance.

Magnetic Stratigraphy

For age determination using magnetic stratigraphy, the variations of the relative paleointensity (RPI) of the Earth's magnetic field recorded in the loess sequence and the magnetic susceptibility of the sediment were used. Magnetic measurements were conducted in different laboratories. A list of the devices used in the individual labs is given in **Supplement 2** (**Supplementary Table 4**). The measurements performed include determination of the mass and the magnetic susceptibility (given as mass specific magnetic susceptibility χ) and frequency dependence of magnetic susceptibility (κ_{FD}) of the oriented samples. The measurement of the natural remanent magnetization (NRM) was followed by progressive alternating field (AF) demagnetization in 12 steps up to 80 mT. The data was plotted in orthogonal vector diagrams (Zijderveld, 1967) and analyzed using the program Remasoft 3.0 (Chadima and Hrouda, 2006). The characteristic remanent magnetization (ChRM) was isolated using principal component analysis (Kirschvink, 1980) embedded in the Remasoft 3.0 software (Chadima and Hrouda, 2006). For most samples the ChRM was determined between the 15 mT and the 40 mT AF step. In every second sample, an anhysteretic remanent magnetization (ARM) was imparted by superposition of a 100 μT DC field and 100 mT alternating field. Subsequently the ARM was demagnetized in a 25 mT alternating field. The RPI was determined as suggested by Levi and Banerjee (1976), i.e., dividing the remanence of the sample measured after 25 mT AF demagnetization by the remanence of the ARM after the 25 mT AF demagnetization. The value of 25 mT was chosen to ensure magnetic cleaning of viscose remanence, whilst a reasonable amount of magnetization is still preserved. Furthermore, mineral magnetic investigations were performed on 12 selected samples to ascertain whether the sediment had preserved paleomagnetic information over geological time scales. Besides determination of the hysteresis parameters, the temperature dependence of the magnetic susceptibility (κ_{TD}) was measured.

To provide chronostratigraphic constraints by magnetic stratigraphy we correlate the magnetic properties of the BAK site to those of independently dated reference records. We visually align our RPI data with the upgraded version of the high-resolution global paleointensity stack GLOPIS-75 (Laj et al., 2004) and GLOPIS-GICC05 (Laj and Kissel, 2015). Additionally, we compare the data with the RPI values gained from the archaeological site of Poiana Ciresului in northeastern Romania (**Figure 1**; Zeeden et al., 2009; Zeeden et al., 2011). To reduce noise, the RPI of the BAK profile is smoothed with a three-point running average. Please note that the original age model of Poiana Ciresului (Zeeden et al., 2009; Zeeden et al., 2011; Zeeden et al., 2020; Zeeden and Hambach, 2020) is based on an RPI correlation for which the Laschamp geomagnetic excursion is set at 38.5 ka BP instead of 41 ka BP (Laj and Kissel 2015). We therefore show an adjusted age model in this study that correlates the four tie points used in Zeeden et al. (2009) with GLOPIS-GICC05. We also compare the magnetic susceptibility data of the BAK pmag composite to the NGRIP $\delta^{18}O$ record (Andersen et al., 2004) and to different loess records from the region (**Figure 1**). As for the RPI correlation, the individual tie points result from wiggle matching of prominent fluctuations. For the time interval of interest, we use the data of the loess sites Rasova (**Figure 1**; Zeeden et al., 2016; Zeeden et al., 2018c; Zeeden et al., 2019) and Vlasca in Romania (**Figure 1**; Obreht et al., 2017). Please note that the magnetic susceptibility of Vlasca below the Campanian Ignimbrite/Y-5 tephra layer includes new data for which the age model is preliminary only. Additionally, we correlate BAK to the magnetic susceptibility record of the Batajnica site in Serbia (**Figure 1**; Marković et al., 2009; Basarin et al., 2014) for which OSL ages have recently been published (Avram et al., 2020). An overview of the data used for the age models at the respective loess sites used for correlation with the BAK site is shown in **Supplementary Table 3**.

The age models resulting from the paleomagnetic dating approaches arise from linear interpolation between age tie points. The age-depth relationship was linearly extended to include the top and the bottom of the sequence.

Age Modeling

To combine the age information of the individual dating methods, we used two different Bayesian age-depth modeling approaches. The Bchron software (Parnell et al., 2008; Parnell, 2018) runs in the R environment (R Core Team, 2020). The BChron age-depth modeling approach relies on an increasing sediment column and a gamma distribution as prior information for a sediment accumulation model. The ages and their uncertainties are assumed to be correct. We also apply the ADMin approach (Zeeden et al., 2018a), which is originally tailored to luminescence ages. Here, we apply this model to the combination of ages from different dating methods. Initially, it reconstructs a probability density for the random and systematic parts of uncertainty, which represent unsystematic random effects and a possibly systematic offset, respectively. It then uses the random part for modeling and re-combines the model results with systematic uncertainty. This model defines no priors about sedimentation rates, but resamples ages and uncertainty 'as is' and uses combinations, which represent chronological order.

After careful inspection of the results, individual age data for each method were selected as described below (*Luminescence dating, Radiocarbon Analysis and Magnetic Stratigraphy*). ^{14}C ages are calibrated using the IntCal20 dataset (Reimer et al., 2020) and reported using the 2σ uncertainty ranges (**Table 2**). When multiple ^{14}C ages were included from individual layers, they were combined by averaging calibrated age ranges. An uncertainty of 10% is assigned to the ages resulting from magnetic stratigraphy in order to provide a conservative estimate. Reported OSL ages are given with 1σ uncertainty, which is considered as such in the age model. The tephra layer identified as the Campanian Ignimbrite/Y-5 (see *Tephrochronology*) is embedded in the age model using its reported $^{40}Ar/^{39}Ar$ age of 39.85 ± 0.14 ka (Giaccio et al., 2017). Please note, calibrated radiocarbon ages refer to AD 1950, while there is no reference date for luminescence dating and

TABLE 1 | Luminescence dating results showing sampling depths, radionuclide concentrations, fading g-values, dose rates, equivalent doses (De) and ages (1σ uncertainty) for all applied measurement protocols. IR50 ages are corrected for fading.

Lab Code	Sample ID	Depth (m b.s.)	Radionuclide concentration			IR_{50} g value	IR_{50} dose rate (Gy/ka)	BSL dose rate (Gy/ka)	$pIRIR_{290}$ dose rate (Gy/ka)	IR_{50} De (Gy)	BSL De (Gy)	$pIRIR_{290}$ De(Gy)	IR_{50} Age (ka) Fading corr.	BSL Age (ka)	$pIRIR_{290}$ Age (ka) uncorr.
	Grain size		U (ppm)	Th (ppm)	K (%)										
C-L 4884	BAK1-6 4–11 µm	5.59	3.05 ± 0.17	9.93 ± 0.61	1.66 ± 0.02	3.86 ± 0.52	3.81 ± 0.22	—	4.16 ± 0.20	64.7 ± 3.2	—	113.7 ± 5.7	31.7 ± 2.9	—	28.2 ± 2.5
C-L 4883	BAK1-5 4–11 µm	6.35	2.86 ± 0.13	9.55 ± 0.48	1.61 ± 0.03	1.23 ± 0.80	3.61 ± 0.21	3.23 ± 0.14	3.94 ± 0.19	67.1 ± 3.4	95.0 ± 7.4	108.9 ± 5.4	22.6 ± 2.1	30.3 ± 3.2	28.5 ± 2.5
C-L 4881	BAK1-3 4–11 µm	7.47	3.10 ± 0.17	10.58 ± 0.62	1.77 ± 0.02	3.28 ± 0.49	3.98 ± 0.23	3.57 ± 0.16	3.98 ± 0.23	85.3 ± 4.3	114.0 ± 6.6	134.0 ± 6.2	48.0 ± 4.3	36.3 ± 3.2	38.3 ± 3.4
C-L 4880	BAK1-2 4–11 µm	7.93	2.98 ± 0.14	10.69 ± 0.53	1.61 ± 0.03	2.69 ± 0.82	3.80 ± 0.22	3.39 ± 0.15	4.15 ± 0.20	89.1 ± 4.5	113.6 ± 6.0	140.0 ± 7.0	40.8 ± 3.6	38.1 ± 3.2	38.5 ± 3.2
C-L 4880	BAK1-2 63–90 µm	7.93	2.98 ± 0.14	10.69 ± 0.53	1.61 ± 0.03	1.30 ± 0.55	3.40 ± 0.16	—	3.49 ± 0.14	80.2 ± 4.5	—	137.0 ± 6.9	31.5 ± 3.1	—	44.0 ± 3.4
C-L 4879	BAK1-1 4–11 µm	8.23	3.01 ± 0.16	10.81 ± 0.66	1.70 ± 0.02	2.20 ± 0.62	3.90 ± 0.22	—	4.25 ± 0.20	92.0 ± 4.6	—	149.5 ± 7.5	43.9 ± 3.9	—	40.1 ± 3.3
C-L 4879	BAK1-1 63–90 µm	8.23	3.01 ± 0.16	10.81 ± 0.66	1.70 ± 0.02	1.33 ± 0.50	3.50 ± 0.14	—	3.59 ± 0.14	93.0 ± 4.7	—	142.1 ± 7.1	35.8 ± 3.1	—	44.4 ± 3.4
C-L 4895	BAK2-7 4–11 µm	8.63	2.90 ± 0.13	10.16 ± 0.50	1.64 ± 0.03	—	—	—	4.07 ± 0.19	—	—	148.8 ± 7.9	—	—	41.7 ± 3.5

magnetic stratigraphy. For modeling, we did not adjust ages to a common reference point in time, since the offset of c. 70 years is well within the uncertainty ranges of the respective methods and also falls within the temporal resolution of our sampling intervals (which is ~100 yr for magnetic stratigraphy and ~200 yr for OSL and ^{14}C dating). Therefore, adjusting the age scales in this study would imply a degree of precision that is not appropriate. The R script for age-depth modeling and data interpolation is available in the **Supplements 5 and 6**.

RESULTS

Tephrochronology

Analyses of glass shards from the visible tephra show homogeneous SiO_2 concentrations averaging 60.76 wt%, associated with 18.41 wt% Al_2O_3, 2.77 wt% FeO, 0.40 wt% TiO_2, 1.69 wt% CaO, 5.97 wt% Na_2O and 7.02 wt% K_2O (for full details on analytical data see **Supplement 4, Supplementary Tables 6 and 7**). The typical phonolite to trachyte composition of glass shards suggests that the tephra layer at BAK pertains to the Campanian Ignimbrite/Y-5 tephra (CI/Y5). This volcanic ash layer has been visually and geochemically identified in many loess sequences throughout the Lower Danube Basin (Constantin et al., 2012; Fitzsimmons et al., 2013; Veres et al., 2013; Anechitei-Deacu et al., 2014; Obreht et al., 2017), where it forms an important stratigraphic marker horizon and chronological tie-point (Zeeden et al., 2018c) with an $^{40}Ar/^{39}Ar$ age of 39.85 ± 0.14 ka (Giaccio et al., 2017).

Luminescence Dating

The fine-grained quartz samples showed bright BSL signals with a fast signal decay (**Supplement 1, Supplementary Figure 1**). Preheat plateau tests for quartz sample BAK1-2 revealed no dependency of the equivalent dose with temperatures between 180 and 280°C. For sample BAK1-5, we did not observe a dependency of the equivalent dose with temperatures between 180 and 200°C (**Supplementary Figure 2A**). Dose recovery tests for samples BAK1-2, BAK1-3 and BAK1-5 showed that the laboratory given dose was recovered within <5% of unity for the three samples (**Supplementary Figure 3**). We have calculated equivalent doses with an arithmetic mean to 95.0 ± 7.4 Gy (BAK1-5; 6.35 m depth), 114.0 ± 6.6 Gy (BAK1-3; 7.47 m depth) and 113.6 ± 6.0 Gy (BAK1-2; 7.93 m depth). Dose rates range from 3.23 ± 0.14 Gy/ka to 3.57 ± 0.16 Gy/ka. The quartz luminescence ages were calculated to 30.3 ± 3.2 ka (BAK1-5), 36.3 ± 3.2 ka (BAK1-3) and 38.1 ± 3.2 ka (BAK1-2; **Table 1**). All OSL ages are depicted in **Figure 4**.

Typical IR50 and pIRIR290 signals are depicted in **Supplementary Figure 1**. First IR stimulation temperature tests showed no dependency of the equivalent dose on the stimulation temperature, which indicates signal stability (Buylaert et al., 2012; **Supplementary Figure 2B**). Dose recovery tests indicate that laboratory given doses were recovered within <5% of unity for the IR_{50} and $pIRIR_{290}$ signals of potassium feldspars and polymineral fine-grained samples BAK1-3 (7.47 m), BAK1-2 (7.93 m) and BAK2-7

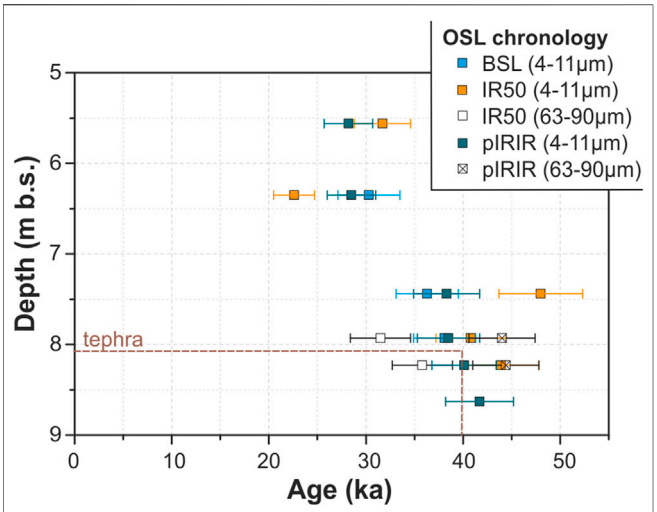

FIGURE 4 | Luminescence ages depicted in an age-depth plot. The location of the tephra layer is shown with a dashed line. OSL ages are given as average and error bars show standard error (1σ).

(8.63 m; **Figure 3**). We measured fading rates between 1.30 ± 0.55% g_{2days} and 3.86 ± 0.52 g_{2days} for the IR_{50} signals and between −2.01 ± 0.37% g_{2days} and −0.06 ± 0.06% g_{2days} for the $pIRIR_{290}$ signals. Mean equivalent doses are lower for IR_{50} measurements ranging from 64.7 ± 3.2 Gy to 93.0 ± 4.7 Gy for IR_{50} and from 108.9 ± 5.4 Gy to 149.5 ± 7.5 Gy for $pIRIR_{290}$ (**Table 1**). Dose rates are between 3.40 ± 0.16 Gy/ka and 3.98 ± 0.23 Gy/ka for IR_{50} and between 3.49 ± 0.14 Gy/ka and 4.25 ± 0.2 Gy/ka for $pIRIR_{290}$, respectively. This results in fading corrected IR_{50} ages between 22.6 ± 2.1 ka and 43.9 ± 3.9 ka (**Figure 4**). Post-$IRIR_{290}$ ages for the corresponding samples are between 28.2 ± 2.5 ka and 44.4 ± 3.4 ka (**Figure 4**). The pIRIR ages were not fading corrected due to the low values measured. The calculated ages of both sample sets are in good agreement for 50% of the samples and results differ for those samples with low fading rates (~1.3% g_{2days}) as well as for sample BAK1-3 (7.47 m depth; **Table 1**).

Radiocarbon Dating

Twelve bulk OC ^{14}C ages were obtained for subsection BAK1 (**Figure 3**). In the following, conventional ^{14}C ages are reported. The uppermost sample collected from the Holocene soil at 1.90 m depth provided an age of 6,440 ± 60 ^{14}C yr BP (**Table 2**; **Figure 5**). Up to 7.05 m depth, ^{14}C ages increase with depth and appear in stratigraphic order (28,400 ± 280 ^{14}C yr BP at 7.05 m). Below 7.05 m depth, ^{14}C ages range from 27,300 ± 220 to 29,100 ± 220 ^{14}C yr BP and are either reversed or agree in consecutive depth intervals (**Figure 5**).

Compound-specific ^{14}C ages of *n*-alkanes and *n*-alkanoic acids were analyzed for four depths (**Table 2**; **Figure 5**). In general, the ^{14}C ages of *n*-alkanoic acids increase with increasing molecular weight (chain length). At 3.35 m depth, $n\text{-}C_{16}$ alkanoic acid has an age of 2,430 ± 110 ^{14}C yr BP, while $n\text{-}C_{26}$ and $n\text{-}C_{28+30}$ alkanoic acids have ^{14}C ages of 14,300 ± 230 and 15,100 ± 230 ^{14}C yr BP, respectively. The $n\text{-}C_{29+31}$ alkanes are slightly older than the $n\text{-}C_{28+30}$ alkanoic acids (15,950 ± 170 ^{14}C yr BP). At 4.77 m depth, one ^{14}C age could be obtained for $n\text{-}C_{24+26}$ alkanoic acids (18,700 ± 190 ^{14}C yr BP). Concurrent $n\text{-}C_{29}$ and $n\text{-}C_{31}$ alkanes are older (21,600 ± 290 ^{14}C yr BP and 22,000 ± 310 ^{14}C yr BP, respectively) than the $n\text{-}C_{24+26}$ alkanoic acids. At 6.35 m depth, a total of 5 compounds could be analyzed. Analogous to the sample from 3.35 m depth, ^{14}C ages increase with increasing chain length: $n\text{-}C_{16}$ alkanoic acid has an age of 3,190 ± 115 ^{14}C yr BP, $n\text{-}C_{24}$ alkanoic acid (17,850 ± 230 ^{14}C yr BP) and $n\text{-}C_{26}$ alkanoic acid (22,500 ± 370 ^{14}C yr BP) are younger than $n\text{-}C_{28+30}$ alkanoic acids (25,000 ± 350 ^{14}C yr BP). The value obtained for the $n\text{-}C_{29+31}$ alkanes shows the highest ^{14}C age (29,200 ± 570 ^{14}C yr BP). At 7.47 cm depth, $n\text{-}C_{24+26}$ alkanoic acids (23,100 ± 290 ^{14}C yr BP) are younger than $n\text{-}C_{29+31+33}$ alkanes (28,400 ± 420 ^{14}C yr BP) in agreement with the age patterns observed in the overlying samples.

Magnetic Stratigraphy

The paleomagnetic samples of subsections BAK2 and BAK4 were combined into a composite profile by aligning their magnetic susceptibility curves (**Supplement 3, Supplementary Figure 8**). The depth scale of this BAK pmag composite corresponds to the depth scale of the main profile (BAK1-3). Overall, 236 oriented samples are included, of which the upper 109 and lower 127 originate from the BAK4 and the BAK2 profile, respectively. The magnetic properties are reported and discussed in **Supplementary Section 3** (*Mineral Magnetic analyses and paleomagnetic evidence*).

In contrast to the absolute dating techniques used in this study, the ages obtained via correlation of the magnetic evidence of the BAK site with reference records (**Supplementary Table 3**) are a result of correlative interpretation (see *Magnetic Stratigraphy*). Because of the scarcity of high resolution paleomagnetic records from the region for the relevant time range, the directional data do not contribute to the magnetic stratigraphy in this study. However, directional data of the ChRM of the BAK pmag composite are available in the **Supplementary Section 3.3**, including a comparison with the inclination and the declination determined at the Poiana Ciresului site.

DISCUSSION

Luminescence Dating

Dating of quartz (BSL) is often deemed to be the most reliable luminescence technique, because quartz signals bleach quickly during transport allowing the signal to build up from zero after deposition. In contrast, feldspar and polymineral IR_{50} signals bleach at a lower rate, but might suffer from signal loss (anomalous fading) after deposition (Wintle, 1973). Feldspar and polymineral pIRIR signals show the slowest bleaching rates, but are supposedly less prone to anomalous fading (Buylaert et al., 2012). The signal loss can be corrected for, but fading correction requires various assumptions (Thomsen et al., 2008; Guérin et al., 2015). Due to the different bleaching rates, similar ages for three different signals of the same sample are a reliable indicator of complete resetting of the luminescence signal prior to deposition (Murray et al., 2012; Klasen et al., 2018).

TABLE 2 | Radiocarbon isotope data and ages obtained on bulk organic carbon (bulk OC) and *n*-alkanes and *n*-alkanoic acids (alk. acids). Calibrated ages are given as 2σ uncertainty ranges.

Depth (m b.s.)	Sample ID	AMS ID	Dated material	$F^{14}C$	^{14}C age (year BP)	Age (year cal BP)
1.9	BAK1-11	Col6033	Bulk OC	0.4483 ± 0.0033	6,440 ± 60	7,255–7,432
2.69	BAK1-10	Col6034	Bulk OC	0.2356 ± 0.0025	11,600 ± 90	13,299–13,612
3.35	BAK1-9	Col6035	Bulk OC	0.1212 ± 0.0019	16,950 ± 130	20,178–20,835
		Col6355	*n*-C_{29+31} alkane	0.1370 ± 0.0029	15,950 ± 170	18,883–19,588
		Col6359	*n*-C_{16} alk. acid	0.7387 ± 0.0097	2,430 ± 110	2,302–2,754
		Col6360	*n*-C_{26} alk. acid	0.1684 ± 0.0047	14,300 ± 230	16,869–18,166
		Col6361	*n*-C_{28+30} alk. acid	0.1526 ± 0.0042	15,100 ± 230	17,903–18,852
4.05	BAK1-8	Col6036	Bulk OC	0.0870 ± 0.0012	19,600 ± 110	23,267–23,846
4.77	BAK1-7	Col6037	Bulk OC	0.0582 ± 0.0012	22,800 ± 160	26,467–27,457
		Col6356	*n*-C_{29} alkane	0.0680 ± 0.0024	21,600 ± 290	25,234–26,429
		Col6357	*n*-C_{31} alkane	0.0644 ± 0.0025	22,000 ± 310	25,801–27,059
		Col6362	*n*-C_{24+26} alk. acid	0.0972 ± 0.0022	18,700 ± 190	22,324–22,997
5.59	BAK1-6	Col6038	Bulk OC	0.0495 ± 0.0011	24,100 ± 180	27,856–28,707
5.94	BAk1-5b	Col6039	Bulk OC	0.0438 ± 0.0012	25,100 ± 210	28,968–29,951
6.35	BAK1-5	Col6040	Bulk OC	0.0345 ± 0.0011	27,000 ± 240	30,831–31,632
		Col6358	*n*-C_{29+31} alkane	0.0264 ± 0.0019	29,200 ± 570	31,953–34,612
		Col6363	*n*-C_{16} alk. acid	0.6723 ± 0.0092	3,190 ± 115	3,076–3,691
		Col6364	*n*-C_{24} alk. acid	0.1083 ± 0.0030	17,850 ± 230	20,988–22,226
		Col6365	*n*-C_{26} alk. acid	0.0606 ± 0.0026	22,500 ± 370	25,967–27,416
		Col6366	*n*-C_{28+30} alk. acid	0.0446 ± 0.0019	25,000 ± 350	27,704–29,053
7.05	BAK1-4	Col6041	Bulk OC	0.0290 ± 0.0010	28,400 ± 280	31,768–33,502
7.47	BAK1-3	Col6042	Bulk OC	0.0334 ± 0.0009	27,300 ± 220	31,082–31,694
		Col6663	*n*-$C_{29+31+33}$ alkane	0.0291 ± 0.0015	28,400 ± 420	31,575–33,819
		Col6664	*n*-C_{24+26} alk. acid	0.0563 ± 0.0020	23,100 ± 290	26,515–27,840
7.93	BAK1-2	Col6043	Bulk OC	0.0271 ± 0.0008	28,900 ± 240	32,322–34,198
8.23	BAK1-1	Col6044	Bulk OC	0.0266 ± 0.0007	29,100 ± 220	33,099–34,248

Ideally, we can distinguish a partially bleached signal from a completely bleached signal by comparison of the fading corrected IR_{50} with the $pIRIR_{290}$ signal and the BSL signal. We applied this approach to samples from three depth intervals. For sample BAK1-2 (4–11 μm; 7.93 m depth), the obtained ages are similar for all three protocols and we conclude that fading correction of the IR_{50} signal was successful and the luminescence signal was completely reset prior to deposition. A complete reset would be expected for eolian sediments. For this sample, all three protocols appear to be equally suitable for dating. For sample BAK1-5 (4–11 μm, 6.35 m depth), BSL and $pIRIR_{290}$ ages are in good agreement, while the IR_{50} age is younger. This is likely due to the low fading rate of 1.23 ± 0.8%. For sample BAK1-3 (4–11 μm, 7.47 m depth), BSL and $pIRIR_{290}$ ages agree well ruling out incomplete bleaching, while the IR_{50} age is significantly older (**Table 1**). For two of the three samples, the IR_{50} luminescence signal in combination with fading correction results in different age estimates, which is most likely due to the IR_{50} fading correction and the underlying assumptions included in the modeling approach (Thomsen et al., 2008; King et al., 2018). Therefore, for dating the BAK profile we regard the fading corrected IR_{50} ages to be less robust than the $pIRIR_{290}$ ages obtained on the polymineral fine grain fraction. As outlined above, the BSL and $pIRIR_{290}$ protocols provide equally robust age estimates for the BAK profile. However, we focused on $pIRIR_{290}$ dating for the lowermost samples, because we did not want to rely solely on quartz dating for ongoing measurements of older samples (not presented here) as it was shown that quartz signals are problematic for doses above 150 Gy (fine-grain) and 250 Gy (coarse-grain), respectively (Avram et al., 2020). Nevertheless, the corresponding quartz and $pIRIR_{290}$ ages of samples BAK1-2, BAK1-3 and BAK1-5 are a good indicator that $pIRIR_{290}$ is a suitable dating protocol for the section.

Part of the uncertainty related to the luminescence age calculation is the estimation of the paleo-water content. Most studies use an average water content value for the entire period between sediment accumulation and sampling. For most samples, this period covers different paleoclimatic conditions, suggesting that sediment water contents are not constant. For the BAK samples we measured water contents between 1 and 30%, but it is possible that samples dried out during transport if sample containers were not completely air tight. Therefore, we use the grain size composition of each sample to estimate a paleo-water content (see **Supplement 1, Supplementary Figure 4**) of 25 ± 10% for samples with a fine silt and clay content above 25% and 15 ± 10% for samples below this value.

The fine-grain (4–11 μm) $pIRIR_{290}$ and BSL ages of BAK1-1 (8.23 m depth) and BAK1-2 (7.93 m depth), which bracket the CI/Y-5 tephra agree well with its established $^{40}Ar/^{39}Ar$ age of 39.85 ± 0.14 ka (Giaccio et al., 2017), while coarse-grain (63–90 μm) $pIRIR_{290}$ ages at 8.23 m and 7.93 m depth seem to overestimate the tephra age slightly (~1 ka when 1σ error is considered; **Figure 4**). The older coarse-grain feldspar ages may be explained by contributions of coarse-grained tephra particles that were not removed completely during sample

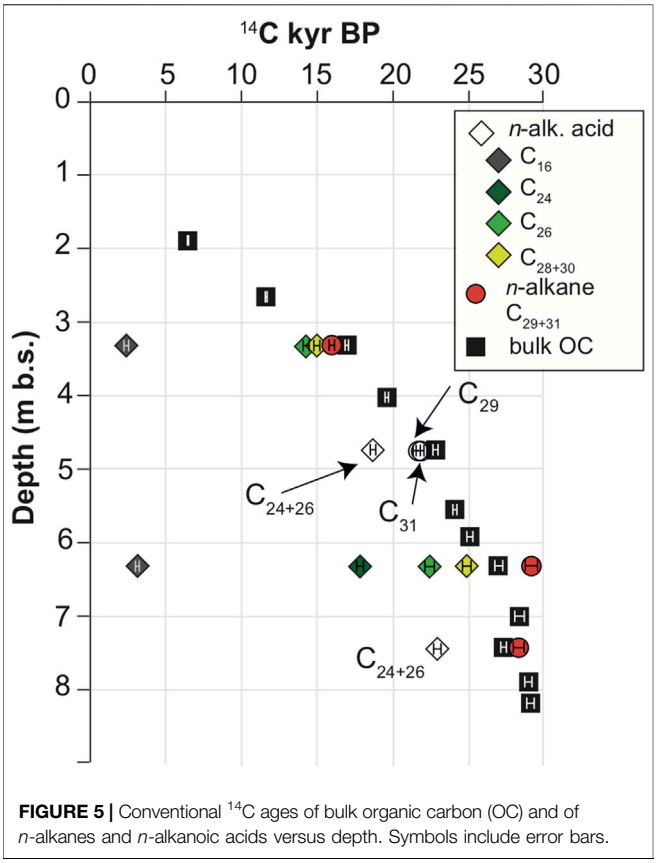

FIGURE 5 | Conventional ^{14}C ages of bulk organic carbon (OC) and of *n*-alkanes and *n*-alkanoic acids versus depth. Symbols include error bars.

preparation. Dating tephra deposits using luminescence techniques is not always straightforward, even when the surrounding sediments are dated (cf. Bösken and Schmidt, 2020). Independent of the dated grain-size range, samples taken in close proximity to the tephra layer are particularly critical, since fresh geologic deposits are prone to relocation of radioelements leading to an incorrect ascertainment of dose rates (Krbetschek et al., 1994; Biswas et al., 2013; Bösken and Schmidt, 2020). In the Middle and Lower Danube Basins, loess layers embedding the CI/Y-5 tephra have been often dated using luminescence dating methods (Constantin et al., 2012; Fitzsimmons et al., 2013; Veres et al., 2013; Anechitei-Deacu et al., 2014; Bösken et al., 2017; Obreht et al., 2017; Zeeden et al., 2018c): depending on the specific dose rate of the profiles, equivalent doses of loess layers above the CI/Y-5 tephra range from 114 ± 7 Gy to 200 ± 4 Gy for fine-grained quartz and 104 ± 6 Gy to 221 ± 12 Gy for fine-grained polymineral $pIRIR_{290}$ measurements, respectively, while values below the tephra layer range from 136 ± 6 Gy to 286 ± 9 Gy (fine-grained quartz) and from 172 ± 12 Gy to 193 ± 4 Gy (fine-grained polymineral $pIRIR_{290}$), respectively. These values result in ages between 26–44 ka above and 39–57 ka below the tephra. In the BAK sequence, equivalent doses and ages are in the same age range as reported in those studies. This highlights the consistency of luminescence ages among the BAK site and other loess sites in the region. Given the fact that fine-grain $pIRIR_{290}$ results seem to provide the most accurate age around the tephra, we only use the fine-grain $pIRIR_{290}$ ages for our integrated age-depth model.

Radiocarbon Analysis

Sedimentary bulk OC contains a mix of organic matter (OM) from different sources with different ^{14}C isotope signatures that may either be deposited syn-depositionally or introduced post-depositionally. For example, OM reworked from older deposits (e.g., eroded from bedrock or soils in the source area of the dust) may have a ^{14}C isotope signal, which is older than the actual age of loess deposition or potentially radiocarbon-dead. In contrast, OM introduced after sediment deposition, e.g., leaching by percolating pore water, may be younger than the sediment (e.g., Hatté et al., 2001). Typically, aboveground biomass is preferably used for dating terrestrial sediments, since roots can extend up to several meters below the surface introducing modern C into deeper layers of the loess profile. In addition to macroscopic plant remains, epicuticular leaf wax lipids such as long-chain *n*-alkanes (*n*-C_{27} to *n*-C_{35}) and *n*-alkanoic acids (*n*-C_{24} to *n*-C_{32}) are preserved in sedimentary records. As done by us in the BAK profile, these lipids have previously been tested as target OC for loess ^{14}C chronologies (e.g., Häggi et al., 2014; Haas et al., 2017; Zech et al., 2017; Bliedtner et al., 2020). In the following we will discuss to what extent the ^{14}C ages of bulk OC and of leaf wax lipids provide a representative estimate of the actual age of sediment deposition in the BAK profile.

Above 7.05 m depth, bulk OC ^{14}C ages successively increase with depth, suggesting that bulk OC may provide meaningful age information (**Figure 5**). Below this depth, ^{14}C ages do not increase continually, which could be due to very high sedimentation rates in this part of the profile. However, an age reversal at 7.47 m depth indicates that mixing with younger OM (e.g., by bioturbation) likely influences ^{14}C ages in this part of the profile (**Figures 2**, **5**). This interpretation is strongly supported by the presence of the independent age marker (CI/Y-5 tephra layer, 39.85 ± 0.14 ka) at ~8 m depth, since the calibrated bulk OC ^{14}C age from below this depth yields 32.71–33.87 cal ka BP (**Table 2**). Analogous to soils, loess deposits are not closed systems and the ^{14}C isotope signature of bulk OC or individual compounds is determined by their intrinsic turnover times determined by input vs. output flux (e.g., Trumbore, 2009). Soils are also prone to physical disturbance such as bioturbation by roots, which penetrate into deeper horizons and admix younger OM into older sediments (e.g., Zech et al., 2017). Similar to leaves, roots contain some proportion of *n*-alkanoic acids, with dominance of the *n*-C_{24} homolog (e.g., Wiesenberg et al., 2012). In the BAK profile, *n*-C_{24} alkanoic acid is less ^{14}C-depleted than bulk OC, suggesting the presence of "younger" root-derived material in the older BAK sediments (**Figure 5**). Evidence for admixture of younger OC throughout the loess sequence also comes from the two ^{14}C ages obtained on *n*-C_{16} alkanoic acids from 3.35 and 6.35 m depth. Both alkanoic acids are significantly younger than the other analyzed OC fractions from the same sediment samples with offsets of >25 kyr. Short-chain *n*-C_{16} and *n*-C_{18} alkanoic acids are produced by plants (leaves and roots, e.g., Wiesenberg et al., 2012) but also derive from microbial sources (e.g., phospholipid *n*-alkanoic acids in soils; Zelles, 1999). Admixture of OC from roots and microbes with "younger" ^{14}C isotope signatures has particularly large effects on

relatively old samples and likely limits the applicability of bulk OC ^{14}C dating in loess deposits to sediments <25 ^{14}C ka, which per mass balance are less biased by such contributions. Similar results from LPS sequences in Central Asia (Song et al., 2018b) indicate that this is likely characteristic for LPS deposits in general and not a feature inherent to the BAK site.

For dating loess deposits, OM sub-pools that are less prone to admixture of younger material, likely provide a more accurate age assignment. The ^{14}C ages of the other epicuticular leaf wax lipids in BAK sediments are older than the age of the *n*-C_{24} alkanoic acid (**Figure 5**), with *n*-C_{29} and *n*-C_{31} alkanes consistently providing the oldest ages and being in good agreement with bulk OC ^{14}C ages. However, the systematic depletion in ^{14}C of *n*-C_{29} and *n*-C_{31} alkanes relative to the corresponding *n*-C_{28+30} alkanoic acids in all investigated samples indicates that different biogeochemical processes affect ^{14}C signatures of individual compounds and compound classes. The *n*-alkanoic acids show a systematic increase in age with increasing chain length (**Figure 5**), an observation that is well known from marine sediments (e.g., Kusch et al., 2010), but data from soils are limited (van der Voort et al., 2017). In addition to compound source variability, this observation is also considered an effect of selective degradation leading to relative ^{14}C enrichment of the short-chain *n*-alkanoic acid pool relative to the long-chain homologs (e.g., Matsumoto et al., 2007). The older ages of long-chain *n*-alkanoic acids relative to short-chain *n*-alkanoic acids as well as *n*-alkanes relative to long-chain *n*-alkanoic acids likely also reflect a fast turnover of short-chain *n*-alkanoic acids and slow turnover of *n*-alkanes in the loess (e.g., Wiesenberg et al., 2008; van der Voort et al., 2017). In addition, *n*-alkanes in sediments may also contain some proportion derived from geological (^{14}C-free) sources resulting in bias towards ^{14}C ages that are older than the actual sedimentation age (e.g., Bliedtner et al., 2020). In subsection BAK1, however, the chain lengths distribution of *n*-alkanes is similar to that found in grasses and herbs implying negligible contribution of *n*-alkanes from petrogenic sources (cf. **Supplement 2**). In summary, *n*-alkane ages closely correspond to bulk OC ^{14}C ages and we conclude that both *n*-alkanes and bulk OC reflect the best sediment age estimates in this study. For the age-depth model we therefore use *n*-alkanes and bulk OC ^{14}C ages. However, ^{14}C ages from 7.05 m depth and below are not considered in age-depth modeling, since these ages are biased by admixture of "younger" OC resulting in significant underestimation of actual sedimentation ages.

Magnetic Stratigraphy

The paleomagnetic chronostratigraphic framework for the BAK pmag composite profile is essentially based on the correlation of the smoothed RPI values with the GLOPIS-GICC05 data set. The RPI of loess sequences is not widely used for age determination even though a number of studies gained reasonable results (e.g., Liu et al., 2005; Zeeden et al., 2009; Rolf et al., 2014; Li et al., 2020). At the BAK site, the basic requirement of homogeneity of magnetic properties is fulfilled as shown in the mineral magnetic assessment (**Supplementary Section 3.3**). The BAK pmag composite and GLOPIS-GICC05 show greater similarities in the upper than in the lower part, but allow for correlation of significant features in both cases (**Figure 6**). However, various confounding factors introduce uncertainties when aligning different records. The record of the past variability of the intensity and direction of the Earth's magnetic field in sediments depends to a large extent on the accumulation rate and the complex remanence acquisition processes. Additionally, hiatuses, bioturbation and chemical overprinting may influence the record (Evans and Heller, 2001; Roberts and Winklhofer, 2004; Jin and Liu, 2010). Therefore, not all highs and lows of the RPI reference record may be similarly expressed in the BAK profile. In fact, only when considering the stratigraphic position and age of the CI/Y-5 tephra layer, six tie points (1–6, **Table 3**) can be determined for visual correlation of the two RPI records (**Figure 6**). Additional tie points would be ambiguous. Thus, we limit the number of tie points, but acknowledge that this approach may average out possible variations in accumulation rate. The age-depth data resulting from the correlation (**Table 3**) imply that the BAK pmag composite profile comprises two magnetic excursions, Mono Lake and Laschamp. The Mono Lake excursion (Channell et al., 2020) may correspond to the RPI low in the BAK profile between tie points 2 and 3 (**Figure 6**). We decided not to tie this RPI low to the GLOPIS-GICC05 curve, because the sections above and below would be substantially stretched and clinched, respectively. It is still under debate whether the Mono Lake geomagnetic excursion occurs globally synchronous, asynchronous, or may be a series of excursions across a given time interval (Korte et al., 2019). From the correlation applied in **Figure 6**, the putative Mono Lake excursion is dated at 33.2 ka BP. Despite the offset to the Mono Lake excursion in GLOPIS-GICC05, dated at 34.15 ka BP, it is within the time interval associated with the excursion in other parts of the world (Channell et al., 2020). The second geomagnetic excursion is the Laschamp with an age of ~41 ka (Channell et al., 2020). It is recorded only as a minor decrease of

TABLE 3 | Tie points of RPI correlation (1–6, cf. **Figure 6**) assigned to the ages resulting from correlation with GLOPIS-GICC05. Tie points resulting from correlation of magnetic susceptibility data (A-H, cf. **Figure 6**) are shown as mean ages and their age variation. These values do not represent confidence intervals.

Tie point	Depth (m b.s.)	Age (ka)
1	5.83	26.08
2	6.51	31.73
3	7.39	35.76
4	8.22	40.97
5	8.67	43.63
6	9.59	51.92
A	5.83	25.84 ± 0.65
B	6.17	27.63 ± 0.11
C	6.39	28.71 ± 0.09
D	7.11	32.80 ± 0.08
E	7.61	35.88 ± 0.02
F	8.55	43.43 ± 0.89
G	9.36	47.75 ± 0.92
H	9.75	53.99 ± 0.01

the RPI in the BAK composite, but is supported by the stratigraphic position just below the CI/Y-5 tephra layer (**Figure 6**). Thus, this excursion defines tie point 4 (8.22 m). Using this tie point, the BAK record can be directly linked to the RPI record of Poiana Ciresului. However, even though Mono Lake and Laschamp can be distinguished at the Poiana Ciresului site (Zeeden et al., 2009), the magnetic record is partly corrupted due to the high number of archeological layers (Nițu et al., 2019) and a visual side-by-side comparison is difficult. Because the RPI record of the Poiana Ciresului site does not extend below the Laschamp geomagnetic excursion, a comparison with BAK is not possible for the complete BAK pmag composite profile. In the lowermost part of the BAK pmag composite, the RPI record shows a similar trend matching two different sections of the GLOPIS-GICC05 record, i.e., at 51.9 ka and 46.9 ka. Considering the thickness of the BAK LPS and the lack of macroscopic evidence suggesting an increase of the accumulation rate such as sandy layers or a general increase in grain size, we tentatively

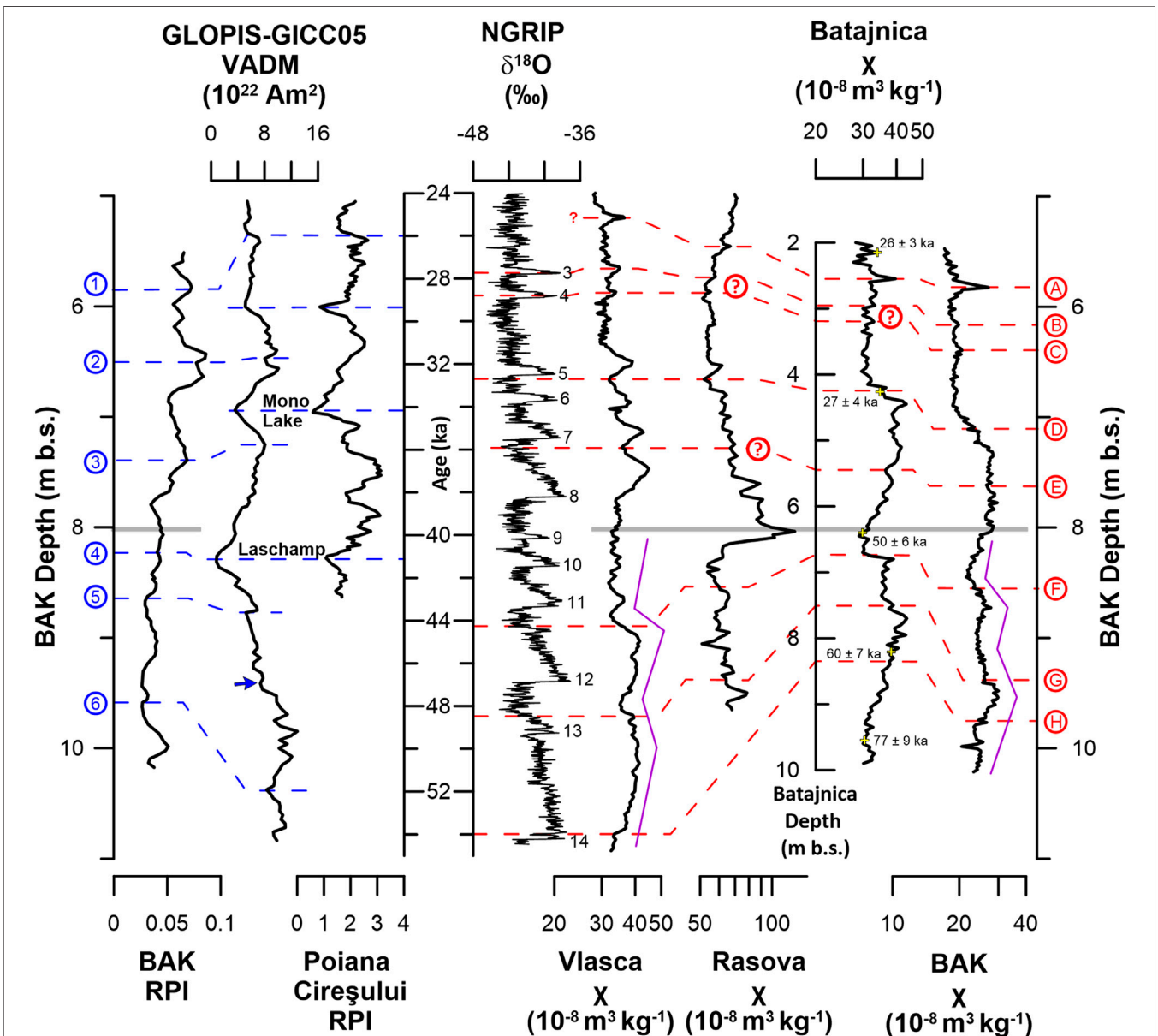

FIGURE 6 | Correlation of the BAK pmag composite. The position of the CI/Y-5 tephra is indicated as a grey horizontal line. RPI of BAK vs. depth is correlated (blue lines) with GLOPIS-GICC05 vs. age and compared to the RPI vs. age of the Poiana Ciresului site. The tie points are shown by blue numbers (1-6, cf. **Table 3**). The positions of geomagnetic excursions are noted. The blue arrow is described in the text. The χ vs. depth curve of BAK is correlated (red lines) with the χ vs. age curves of the sites Rasova and Vlasca, the χ vs. depth curve of Batajnica (note different scale) and the NGRIP $\delta^{18}O$ (Greenland interstadials are numbered). Tie points of the magnetic susceptibility correlation are labeled A to H (cf. **Table 3**). Examples of stylized representations of the trend of the magnetic susceptibility in the lower part are shown with purple lines next to Vlasca and BAK. Tie points labeled with question marks are ambiguous and not considered for age modeling.

favor the correlation that leads to an age of 51.9 ka instead of 46.9 ka (blue arrow in **Figure 6**). This solution results in a moderate decrease of accumulation that could be explained by hiatuses, while the alternative would require a sudden and extreme increase of sediment deposition rates.

The second magnetic dating approach is based on correlation of the magnetic susceptibility. This technique was first proven to be useful by Heller and Liu (1986) and is widely applied since then. We correlate eight tie points of the magnetic susceptibility curve of the BAK pmag composite profile (labeled A to H from top to bottom) to selected loess records of the region (**Figure 6**), as well as to the NGRIP $\delta^{18}O$ isotope record. The ages obtained using this method depend either on the age models of the reference records or the relationship of the fluctuations of the magnetic susceptibility to the interplay of interstadial-stadial events expressed in the NGRIP record. In both cases, the results should only be used with caution. On the one hand, the age models of the selected loess records are partly compiled from multiple dating approaches, including radiocarbon and luminescence dating (**Supplementary Table 3**). Given that we also aim at testing the feasibility of different dating methods, the use of these data may result in a vicious circle. On the other hand, the magnetic susceptibility is biased by non-climatic factors such as grain-size distribution and local dust influx. The characteristic features of the magnetic susceptibility curve of a section may therefore not coincide with those of the NGRIP record, although they may look similar. Furthermore, a delayed response of the loess properties to climate change may have occurred (Újvári et al., 2014a). Nevertheless, we apply the correlation of the magnetic susceptibility in order to provide a comparison to the RPI derived age model.

Tie point A (5.83 m) is a characteristic peak that is recognized in all reference records (**Figure 6**). At the BAK site, it is a horizon rich in organic matter, which could be a small pedogenic horizon. Because of its thinness, it might be a short-term regional signal; thus, we did not correlate the peak to the NGRIP record. The small peaks defined as tie points B (6.17 m) and C (6.39 m) correspond to Greenland interstadials (GI) 3 and 4 in the NGRIP curve. They are also easily identified in the magnetic susceptibility curve of Vlasca, but not unequivocally recognizable at Batajnica and Rasova. In contrast, tie points D (7.11 m) and E (7.61 m) are based on a striking resemblance of the shape of the BAK curve with Batajnica. The further correlation of D is based on the correlation of Batajnica with Rasova, which show clear similarities in the range between C and D. By comparison, the Vlasca record shows higher similarity to the NGRIP curve than to the BAK curve. However, the position of E in Batajnica can be correlated very well with Vlasca. The identification of tie point E in the Rasova profile is more complicated since characteristic features are missing.

The CI/Y-5 tephra is found between tie points E and F (8.55 m) in the BAK, Vlasca and Rasova profiles. The correlation of the curves in the profile section below this marker horizon is less obvious than above, which might be due to regional differences in the intensity of pedogenetic overprinting. A general trend consisting of multiple changes between moderate decreases and fast increases of the magnetic susceptibility towards larger depth can be recognized more or less clearly in all magnetic susceptibility records. Stylized representations of this trend are visualized with purple lines along the Vlasca and BAK curves in **Figure 6**. Based on this observation, the tie points F, G (9.36 m) and H (9.75 m) are defined. F and G are located within an increase of magnetic susceptibility, H is positioned in a small minimum above a stronger decrease of magnetic susceptibility, which is interpreted to reflect the beginning of GI 14. It should be noted from the tie lines that the age model resulting from the correlation of the site Rasova with NGRIP (Zeeden et al., 2016; Zeeden et al., 2018c; Zeeden et al., 2019) is different to the correlation we suggest in this study. Accordingly, the positions of the tie point within the Rasova record provide minimum age estimates for the magnetic susceptibility age model of BAK. In contrast, the polymineral $pIRIR_{225}$ ages of Batajnica in this part of the section appear slightly too old (shown in **Figure 6**) and will not be further discussed in this study.

The BAK age models derived from correlation of RPI and magnetic susceptibility include all tie points (**Figure 7**) that are not denoted with a question mark in **Figure 6**. All used tie points are equally weighted and considered in the integrating age model (*Integrating Age Models*). According to the age models based on magnetic susceptibility and RPI correlation, the sediment at the depth of the CI/Y-5 tephra was deposited 39.3 and 40.6 kyr ago, respectively. Due to the good agreement with the known age of 39.85 ± 0.14 ka (Giaccio et al., 2017), the models appear robust. Overall the models resulting from magnetic dating agree well. In the upper part, the age models diverge slightly, because tie points C, D and E do not correspond to tie points 2 and 3. As a consequence, the age models shift between 5.8 and 8.2 m depth with a maximum age offset of 2.3 ka. In general, ages that are younger than expected might be explained (to a certain degree) by a lock-in effect, which causes the sediment to carry the magnetic signal of a younger time interval than that of sediment deposition. The lock-in depths of paleomagnetic signals in LPSs strongly depend on the syn-depositional water availability as well as at the degree of diagenesis and pedogenesis (e.g., Liu et al., 2015) and are therefore difficult to estimate. However, the BAK profile is characterized by good preservation of subtle sedimentological structures such as the CI/Y-5 tephra layer and macroscopically visible layers of fine sands within unaltered loess as well as in interstadial soils. Thus, an overprinting of the primary depositional signal by post-depositional processes (bioturbation, pedogenesis) seems minimal. A conservative estimate of the potential temporal offset can be calculated assuming a lock-in depth of 0.1–0.15 m in unaltered loess and a slightly higher lock-in depth in interstadial soils. This leads to a potential temporal offset of ~1 kyr for the average accumulation rate of the BAK pmag composite profile. However, the ages resulting from RPI correlation, which are also based on the magnetic properties, exclude a significant bias from a lock-in effect. Thus, the age discrepancies may rather arise from a mismatch during correlation. In the lower part of the BAK profile, tie point G causes a different shape of the age-depth plot of the susceptibility/NGRIP based model (**Figure 7**). This difference can be explained

by the different frequency of tie points. Irrespective, the age constraints provided by the magnetic stratigraphy approaches overall suggest rather consistent accumulation rates over time.

Integrating Age Models

Age-depth models are used for constraining the chronological age assuming that samples in stratigraphic order must have chronological order (e.g., Buck et al., 1996; Bronk Ramsey, 2009). Age-depth modeling generally allows for reducing uncertainty of the age estimates when uncertainties of individual ages overlap. This approach has been previously employed to loess deposits in the Danube catchment (e.g., Fenn et al., 2020a; Fenn et al., 2020b; Sümegi et al., 2020). In this study, we select the most accurate ages obtained with each method for age-depth modeling (for details see discussion of individual methods). Hence, age information for the upper half of the BAK profile is provided by ^{14}C data, while the lower part is covered by results of luminescence dating and magnetic stratigraphy (**Figure 8A**). Unfortunately, while we were aiming at high data coverage allowing cross-method validation, robust OSL and radiocarbon ages overlap only at 5.59 and 6.35 m depth.

We apply two age-depth models, one of which is conservative in reducing uncertainty (ADMin; **Figure 8C**) and the other interpolates ages between the dated horizons (BChron; **Figure 8B**). Both models use ages and their respective 2-sigma uncertainty. We compare the model outputs in a similar fashion as the data to discuss the chronology of the BAK profile using dating and modeling approaches; model output is available in the supplementary materials (**Supplementary Tables 8–10**). The BChron model (**Figure 8B**) shows an age span of ~6 to ~54 ka BP for the uppermost 9–10 m of the BAK profile. In the upper half of the profile, the sedimentation model produces increasing uncertainties between individual ages. This is due to relatively few age control points in this section and the gamma-distribution based sedimentation model inherent to this method. At ~6 m depth, the model is clearly constrained by the ^{14}C ages and uncertainty is confined by the high precision of the ^{14}C ages. Around the CI/Y-5, uncertainty is strongly reduced by this well-dated marker bed. For the oldest three samples, the model provides the best fit using the younger ages included in the 95% uncertainty interval. This is probably due to the sedimentation model, which forces the results towards a constant accumulation rate. The ADMin model (**Figure 8C**) does not interpolate ages, but only produces model ages for dated depths. Up to ~5.5 m depth, both the BChron and the ADMin model results are similar; below this depth, the ADMin model results include higher uncertainty between several ^{14}C-dated layers at ~6 m depth. In general, since the random portion (not shared portion) of uncertainty is used in the model, it reduces the uncertainty of the age model less. In this study, the random component makes up an average of about 60%. Analogous to BChron, the ADMin age models best fit is shifted towards younger ages for the lowermost three ages, but not as much as the BChron model.

Overall, the BChron and the ADMin models are in good agreement (**Figure 8D**). The age-depth models based on magnetic and luminescence data are in excellent agreement and are supported by the age of the CI/Y-5 tephra. Both models have their strengths. The BChron model interpolates ages and directly constructs a chronology for the whole sedimentary sequence. The ADMin model deliberately does not do this to avoid potential incorrect interpolation (cf. Telford et al., 2004; Trachsel and Telford, 2017). Because of their similarity we do not consider one model better than the other. Further constraints of the BChron and ADMin Bayesian models are based on a suite of assumptions about the sedimentation process itself and on the correctness of both ages and uncertainties. The uncertainties of magnetic and luminescence ages may be over- or underestimated, which may influence the age-depth models. Especially for magnetic dating, uncertainties are not easy to calculate, since they include uncertainties that are associated with each stage of paleomagnetic analysis (Tauxe et al., 2010; Heslop and Roberts, 2020). In case of the magnetic data set of the BAK site, we only estimate uncertainty, i.e., we have a component of random uncertainty (e.g., through proxy data) and also systematic effects from correlation with a possibly biased reference chronology. We acknowledge that such an uncertainty should not be used for modeling *per se* (Zeeden et al., 2018c), but in the absence of alternative quantifiable methods this is a common approach. In this case, we argue that the mean modeled age should be correct within ~±10% of the real age, because this would account for

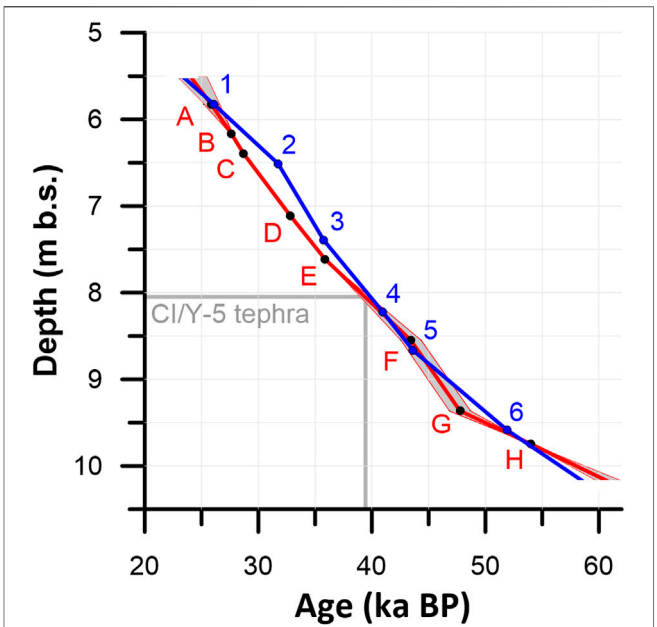

FIGURE 7 | Age models derived from RPI (blue) and magnetic susceptibility/NGRIP correlation (red). Because different ages arise from the correlation of most tie points by magnetic susceptibility correlation, the mean value is given by the red line framed by a shaded area confined by the minimum and maximum ages. This area does not represent the confidence interval. The tephra layer is indicated in grey at 39.85 ka (Giaccio et al., 2017).

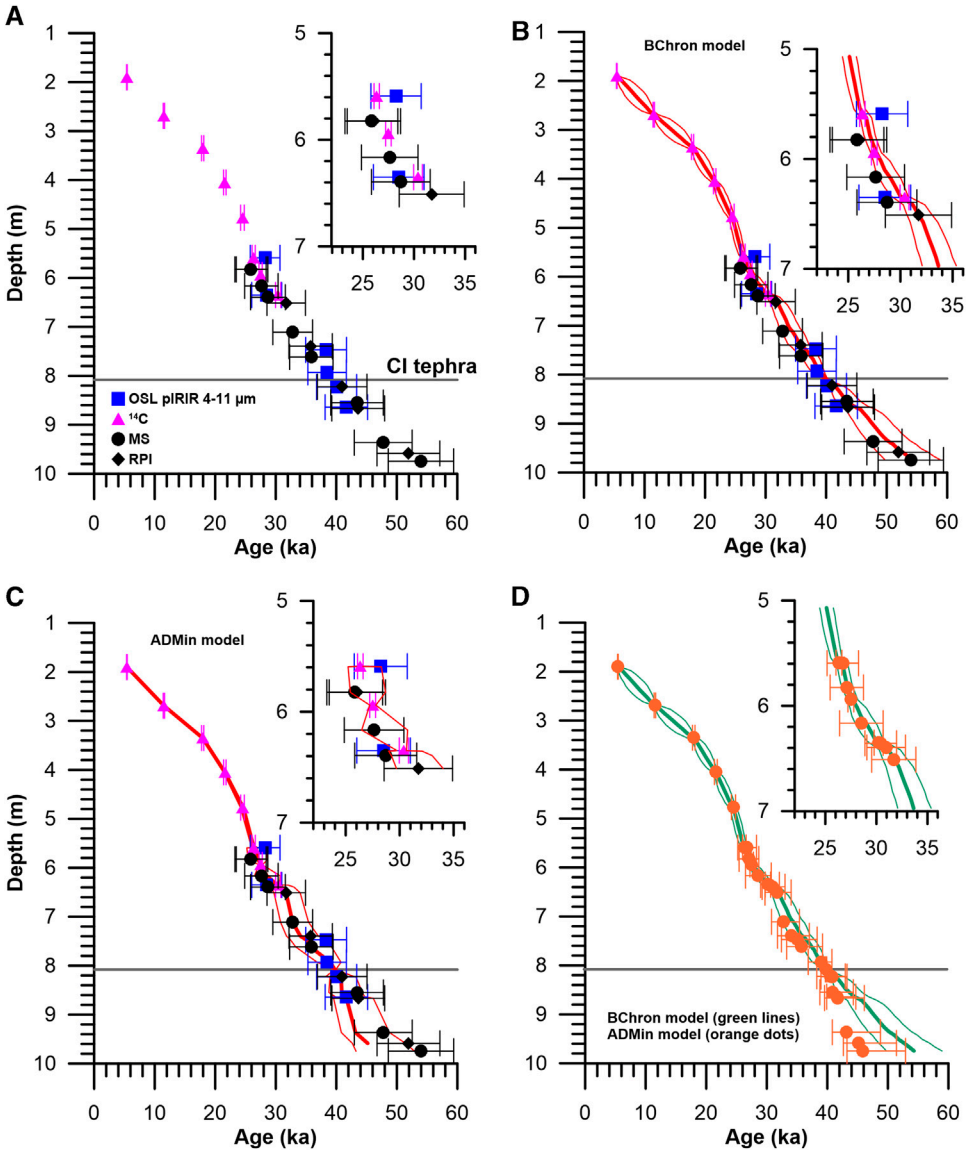

FIGURE 8 | Age models for the BAK profile. The legend is included in **(A)**. **(A)** Cross plot of age vs. depth used for modeling, where calibrated ^{14}C ages and OSL ages (pIRIR 4–11 µm) are given as magenta triangles and blue squares, respectively. For several depths (3.35 m, 4.77 m, 6.35 m), all reliable ^{14}C ages were calibrated and then averaged. Ages obtained by magnetic stratigraphy (black) distinguish between magnetic susceptibility-based data (circles) and RPI based data (diamonds). **(B)** The result of the BChron model including a 95% confidence interval. **(C)** The results of the ADMin model including a 95% confidence interval. **(D)** Comparison of results from the ADMin (orange) and Bchron (green) models. The uncertainty range of the BChron model is shown as green circles to facilitate comparison. Note that these are in very good agreement in the upper part, but deviate below ~5.5 m depth. For clarity, the insets show a close-up of the data around 6 m depth.

possibly systematic parts of uncertainty and possibly uncertainty sources which were not accounted for by radiometric dating. Another problem is the confined uncertainty at ~6 m depth with an age of ~30 ka, which may not be a realistic model outcome as it relies on the assumption that the ^{14}C age is unambiguous. Finally, due to the good agreement of the BChron and ADMin age models, we do not favor one model over the other. In both models, the composite section of the BAK LPS analyzed in this study comprises an age of ~56 ka (with a difference of ~2 ka). The age-depth trend reflects semi-constant sediment accumulation similar to existing records from the region (e.g., Tecsa et al., 2020; Zeeden et al., 2020).

Evaluation of the Multi-Method Approach and Implications for Future Studies

Most studies of LPSs combine OSL dating with either ^{14}C analysis or magnetic stratigraphy to gain age control (e.g., Novothny et al., 2011; Song et al., 2012; Újvári et al., 2014a; Újvári et al., 2014b; Song et al., 2015; Song et al., 2018b; Zhang et al., 2018), while a

combination of ^{14}C analysis and magnetic stratigraphy is less commonly used (Zeeden et al., 2011). Only in a very few cases all three methods have been applied in concert (e.g., Zeeden et al., 2009; Li et al., 2020). However, none of these studies compared the results of different dating approaches systematically against each other or investigated the effects of age-depth models. In this respect, we provide a unique case study for comparison and integration of the three dating methods most commonly used in loess research. Above, we illustrate that each of the methods provides reasonable age constraints, even though all individually are subject to method-specific biases and limitations. In the following, we compare the results of the BAK section between ~5.6 and ~8.7 m depth in a stratigraphic context to evaluate the multi-method approach. To allow us to directly compare magnetic stratigraphy at those depths constrained by luminescence and/or radiocarbon ages, we use linear interpolation between tie points (the respective age values are marked with an asterix).

The ages obtained using the different methods show a considerable spread of up to ~15 ka at 6.35 m depth and >25 ka at 7.47 m depth (**Figure 9**). However, some ^{14}C and OSL ages were identified to be biased by post-depositional processes (*n*-alkanoic acids with chain lengths <28) and uncertainty in the correction procedure for anomalous fading (IR_{50} 4–11 μm and 63–90 μm) and will, thus, not be discussed further. Ages obtained by IR_{50} deviate substantially from the age constraints provided by magnetic stratigraphy, radiocarbon chronology and the other OSL ages (**Figure 9**). This indicates that IR_{50} measurements are less suitable for many geochronological questions – at least at the BAK LPS – due to reduced accuracy. The remainder of the data cluster in variable groups over depth. At 5.59 m depth, bulk OC ^{14}C and OSL ($pIRIR_{290}$ 4–11 μm) ages are in very good agreement (29.9 ± 0.7 ka and 28.2 ± 2.5 ka, respectively). The $pIRIR_{290}$ (4–11 μm) protocol was identified as the most reliable OSL protocol for this profile (setting), which is supported by the overlap with bulk OC ^{14}C ages. In contrast, the results of magnetic stratigraphy seem to be too young in the uppermost section. Down to 6.35 m depth, the magnetic stratigraphy correlation shows an offset of ~2,000 years relative to the bulk OC ^{14}C ages. At 6.35 m depth, OSL ($pIRIR_{290}$ 4–11 μm) and ^{14}C (n-C_{28+30} alkanoic acids) ages as well as magnetic stratigraphy correlation (28.5* ka) range between 28.5 ± 2.5 ka and 30.6 ± 0.7 ka, while OSL (BSL 4–11 μm), ^{14}C (bulk OC and *n*-alkanes) and RPI correlation (30.4* ka) age estimates range between 30.3 ± 3.2 ka and 32.3 ± 1.8 ka. Because the latter group includes those ages identified as the most accurate for ^{14}C and magnetic stratigraphy and we regard BSL and pIRIR as equally suitable we favor the older age assignment here. Although the bulk OC ^{14}C age at 7.05 m depth (32 ± 0.8 ka) is in very good agreement with the age obtained by magnetic stratigraphy correlation (31.7* ka), it probably underestimates the sedimentation age due to the contribution of younger OC from overlying strata or roots. A bias towards young ^{14}C ages is also evident for the section below implying that ^{14}C ages do not reliably reflect sediment ages older than ~30–32 ka BP in the BAK section. As a consequence, the age of magnetic stratigraphy tie point D (7.11 m) is likely also too young. In contrast, the RPI correlation shows a better fit with the overall trend and likely provides appropriate results. At 7.47 m depth and below, the ages obtained by $pIRIR_{290}$ (4–11 μm), BSL (4–11 μm) and magnetic stratigraphy overlap within the analytical uncertainty of the OSL ages. In contrast, the coarse-grain $pIRIR_{290}$ ages seem to overestimate the time of deposition at the BAK site. Around 8 m, the presence of the CI/Y-5 tephra supports the ages obtained by OSL and the magnetic susceptibility based magnetic stratigraphy. Please note that the RPI based magnetic stratigraphy uses the tephra to adjust the complete correlation; thus, we cannot conclude that the tephra supports the RPI based ages.

Direct comparison of the methods allows us to discern details that otherwise may not be recognized. The consistent results of certain OSL ages with the ^{14}C results and magnetic stratigraphy reveal that OSL may provide accurate ages if a suitable measurement protocol is chosen. As shown above, we suggest to refrain from using the conventional IR_{50} protocol as this might lead to less precise ages. In future studies, we suggest comparing at least two different luminescence protocols and/or grain-size fractions. It might also be interesting to further investigate coarse-grain feldspar and single-grain measurements. Our ^{14}C analyses of bulk OC and leaf wax lipids support previous findings that show biogeochemical processes inherent to loess deposits may bias bulk or molecular level ^{14}C ages. For this specific LPS profile we conclude that sediments can be reliably ^{14}C-dated up to a maximal age of 30 ka. This age limit may be higher or lower in other LPS, depending on the proportion of younger (e.g., root-derived) OM relative to contemporaneous OM. With respect to magnetic stratigraphy, both magnetic susceptibility and RPI correlations seem to result in valuable age constraints. Whether preference should be given to one of these methods in future studies, depends on the aim of the study. It has been shown that the correlation to δ^{18}O isotope records such as NGRIP alone can be quite complicated and that comparison with local records helps determining tie points. Thus, if additional records from the region are available, the use of magnetic susceptibility is less time-consuming when establishing chronologies. However, a higher availability of RPI and directional data of LPSs is desirable. The RPI would enable deducing the regional field behavior of the Earth's magnetic field and the directional data could potentially provide an additional tool for correlation. Finally, we recommend the use of a carefully selected modeling approach that fits both the specific conditions for a given site and the specific age data generated by the chosen methods. However, we do not advise a specific modeling approach, since the model selection criteria are typically subjective.

The overall good agreement of the individual age data obtained with different methods at BAK is a rare observation in LPS studies and highlights the significance of the study (cf. Li et al., 2020). Especially the use of the tephra in the BAK profile offered the unique possibility of comparing the dating methods against a well-defined time marker. We propose to use this approach in other geochronological

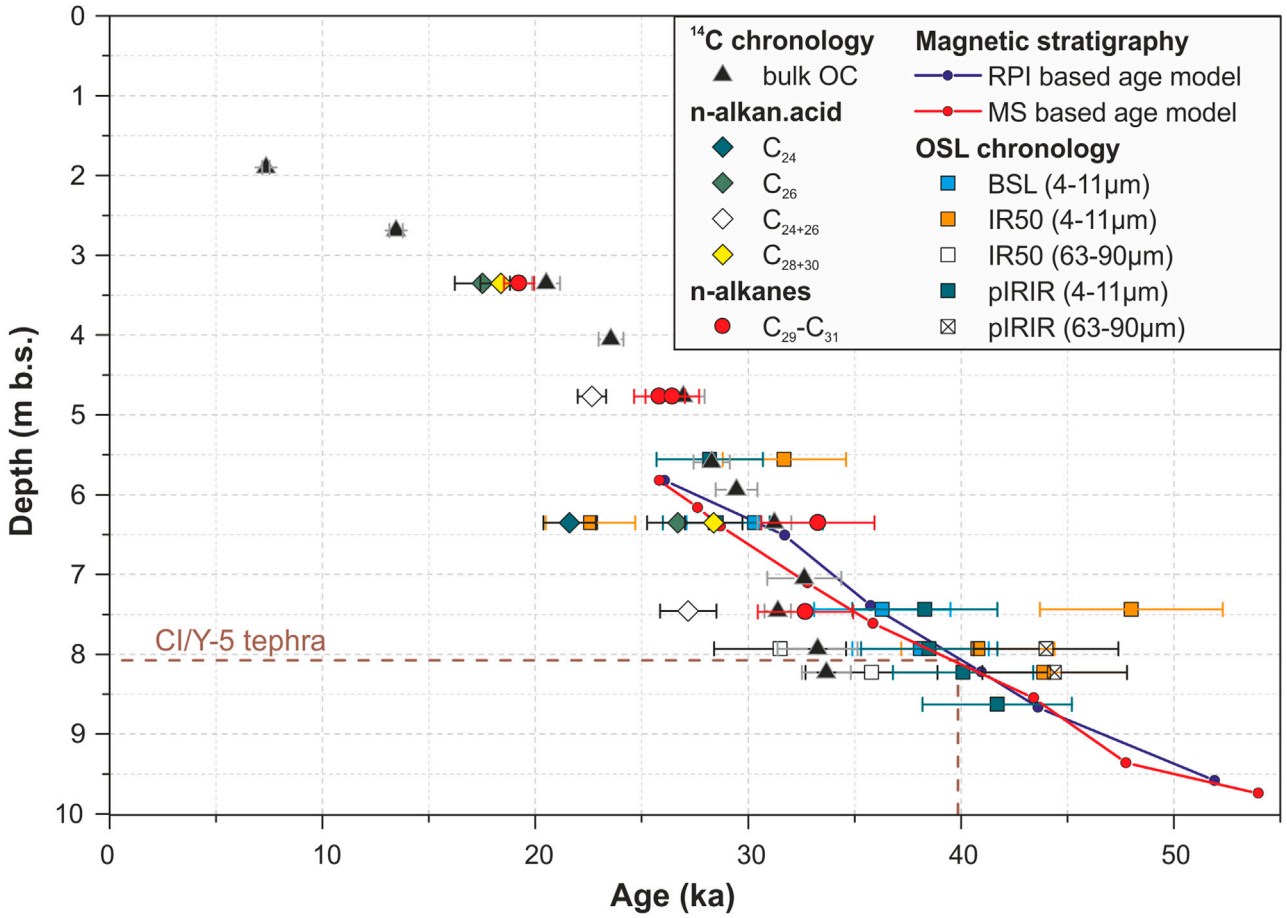

FIGURE 9 | Ages determined for BAK using the different methods. Outliers are not shown. For better visibility, *n*-alkane ^{14}C ages are not distinguished based on chain length and only the mean age of the tie points of the magnetic stratigraphy-based age model are shown. OSL data error bars reflect 1σ uncertainty. Calibrated ^{14}C ages are presented with 95% (2σ) confidence intervals. The age-depth relationship of the tephra layer is depicted as a dashed line.

studies that test dating methods against each other. The results highlight that ages from LPSs should be obtained using at least two independent yet complementary dating methods to allow verification of individual results. However, higher data density and age validation using additional techniques seem to substantially increase the reliability of LPS age models. The increased accuracy of the BAK age-depth models may enable correlation of BAK paleoclimatic proxy information to archives with better age control such as speleothems, marine sediments or ice cores (e.g., Svensson et al., 2008; Govin et al., 2015; Staubwasser et al., 2018; Zhang et al., 2019). At best, a resolution beyond the capability of the discussed methods may be achieved, which may in turn allow comparison of paleoclimate trends across regions and archives. This work may assist future studies to find a suitable combination of dating methods and special techniques to obtain accurate and precise chronologies for loess-paleosol sequences. Due to the variability of LPS (e.g., differences in lithology, grain sizes, carbon contents, mineral compositions, vegetation influences), it remains to be tested whether our conclusions regarding the applicability of each method in the BAK profile can be transferred to other LPSs. We regard our current study as a first step to a generalization to facilitate obtaining high quality age models for LPSs.

DATA AVAILABILITY STATEMENT

All ^{14}C datasets presented in this study are included in the article and the **Supplementary Material** and are also uploaded in the PANGAEA data repository (Berg, 2020). The data sets of OSL (i.e., DRAC files for age calculation) are available in the CRC806 database (Nett et al. 2020). The magnetic stratigraphy data sets generated for this study are available in the PANGAEA data repository (Scheidt et al., 2020) and in the data repository of the CRC 806. The raw data of the mineral magnetic analyses supporting the conclusions of this article and the data of the sites Vlasca, Batajnica, Poiana Ciresului will be made available by the authors, without undue reservation.

AUTHOR CONTRIBUTIONS

DB, HB, FL, NK, MM and JR initialized the project. NK suggested the study. UH, JN, DV suggested the site and the investigation approach. SS coordinated the work at the manuscript. JN provided the OSL part, with help from NK, DB, HB, LO: JN (sampling, data interpretation, writing), NK (measurements, data interpretation, writing), DB (review and editing), HB (review and editing), LO (sample preparation, measurements, review and editing). SB provided the ^{14}C part with help from AS, SK, JR: SB (data interpretation, writing), AS (measurements, data interpretation, writing), SK (data interpretation, review and editing), JR (data interpretation, review and editing). SS provided the magnetic stratigraphy part with help from UH, CL, FM: SS (sampling, measurements, data interpretation, writing), UH (sampling, data interpretation, review and editing), CL (measurements, review and editing), FM (Master's thesis: measurements, preliminary data interpretation; review and editing). DV provided the tephrochronology part with help of UH: DV (data interpretation, writing), UH (measurements, review and editing). CZ provided the age modeling (calculation, interpretation, writing). SP provided the regional information with help of FL, MM: SP (sampling, field survey, interpretation, writing), FL and MM (interpretation, review and editing). The final language check was provided by SK.

FUNDING

The study was funded by the Deutsche Forschungsgemeinschaft (DFG, German Research Foundation) – Project number 57444011 – CRC 806 "Our Way to Europe." DV's work on tephrochronology of BAK was supported through a fellowship provided by the Alexander von Humboldt Foundation.

ACKNOWLEDGMENTS

The study is part of the CRC 806 which aims at understanding routes and timing of anatomically modern humans' migration from Africa to Europe. We thank all colleagues who make this CRC successful. We thank A. Zander of the Cologne Luminescence Laboratory for measuring the radionuclide concentrations of the dosimetry samples. We thank D. Haase for sharing the shapefiles of the loess distribution for **Figure 1**. This is IPGP contribution number 4178.

SUPPLEMENTARY MATERIAL

The Supplementary Material for this article can be found online at: https://www.frontiersin.org/articles/10.3389/feart.2020.598448/full#supplementary-material.

REFERENCES

Andersen, K. K., Azuma, N., Barnola, J. M., Bigler, M., Biscaye, P., Caillon, N., et al. (2004). High-resolution record of Northern Hemisphere climate extending into the last interglacial period. *Nature* 431 (7005), 147–151. doi:10.1038/nature02805

Anechitei-Deacu, V., Timar-Gabor, A., Fitzsimmons, K., Veres, D., and Hambach, U. (2014). Multi-method luminescence investigations on quartz grains of different sizes extracted from a loess section in Southeast Romania interbedding the Campanian Ignimbrite ash layer. *Geochronometria* 41 (1), 1–14. doi:10.2478/s13386-013-0143-4

Antoine, P., Rousseau, D.-D., Degeai, J.-P., Moine, O., Lagroix, F., Fuchs, M., et al. (2013). High-resolution record of the environmental response to climatic variations during the Last Interglacial–Glacial cycle in Central Europe: the loess-palaeosol sequence of Dolní Věstonice (Czech Republic). *Quat. Sci. Rev.* 67, 17–38. doi:10.1016/j.quascirev.2013.01.014

Antoine, P., Lagroix, F., Jordanova, D., Jordanova, N., Lomax, J., Fuchs, M., et al. (2019). A remarkable late Saalian (MIS 6) loess (dust) accumulation in the lower Danube at Harletz (Bulgaria). *Quat. Sci. Rev.* 207, 80–100. doi:10.1016/j.quascirev.2019.01.005

Auclair, M., Lamothe, M., and Huot, S. (2003). Measurement of anomalous fading for feldspar IRSL using SAR. *Radiat. Meas.* 37 (4-5), 487–492. doi:10.1016/s1350-4487(03)00018-0

Avram, A., Constantin, D., Veres, D., Kelemen, S., Obreht, I., Hambach, U., et al. (2020). Testing polymineral post-IR IRSL and quartz SAR-OSL protocols on middle to late Pleistocene loess at Batajnica, Serbia. *Boreas* 49 (3), 615–633. doi:10.1111/bor.12442

Basarin, B., Buggle, B., Hambach, U., Marković, S. B., Dhand, K. O. H., Kovačević, A., et al. (2014). Time-scale and astronomical forcing of Serbian loess–paleosol sequences. *Global Planet. Change.* 122, 89–106. doi:10.1016/j.gloplacha.2014.08.007

Berg, S. (2020). Radiocarbon data determined on sediments from loess paleosol sequence BAK. *PANGAEA*. doi:10.1594/PANGAEA.925059

Biswas, R., Williams, M., Raj, R., Juyal, N., and Singhvi, A. (2013). Methodological studies on luminescence dating of volcanic ashes. *Quat. Geochronol.* 17, 14–25. doi:10.1016/j.quageo.2013.03.004

Bliedtner, M., von Suchodoletz, H., Schäfer, I. K., Welte, C., Salazar Quintero, G. A., Szidat, S., et al. (2020). Age and origin of leaf wax *n*-alkanes in fluvial sediment–paleosol sequences and implications for paleoenvironmental reconstructions. *Hydrol. Earth Syst. Sci.* 24 (4), 2105–2120. doi:10.5194/hess-24-2105-2020

Bösken, J. J. and Schmidt, C. (2020). Direct and indirect luminescence dating of tephra: a review. *J. Quat. Sci.* 35 (1-2), 39–53. doi:10.1002/jqs.3160

Bösken, J., Klasen, N., Zeeden, C., Obreht, I., Marković, S. B., Hambach, U., et al. (2017). New luminescence-based geochronology framing the last two glacial cycles at the southern limit of European Pleistocene loess in Stalać (Serbia). *Geochronometria* 44 (1), 150–161. doi:10.1515/geochr-2015-0062

Bösken, J., Obreht, I., Zeeden, C., Klasen, N., Hambach, U., Sümegi, P., et al. (2019). High-resolution paleoclimatic proxy data from the MIS3/2 transition recorded in northeastern Hungarian loess. *Quat. Int.* 502, 95–107. doi:10.1016/j.quaint.2017.12.008

Bronk Ramsey, C. (2009). Bayesian analysis of radiocarbon dates. *Radiocarbon* 51 (1), 337–360. doi:10.1017/S0033822200033865

Buck, C. E., Cavanagh, W. G., and Litton, C. D. (1996). *Bayesian approach to interpreting archaeological data. Chichester*.

Buggle, B., Glaser, B., Zöller, L., Hambach, U., Marković, S., Glaser, I., et al. (2008). Geochemical characterization and origin of southeastern and eastern European loesses (Serbia, Romania, Ukraine). *Quat. Sci. Rev.* 27 (9-10), 1058–1075. doi:10.1016/j.quascirev.2008.01.018

Buggle, B., Hambach, U., Glaser, B., Gerasimenko, N., Marković, S., Glaser, I., et al. (2009). Stratigraphy and spatial and temporal paleoclimatic trends in Southeastern/Eastern European loess–paleosol sequences. *Quat. Int.* 196 (1-2), 86–106. doi:10.1016/j.quaint.2008.07.013

Buggle, B., Hambach, U., Kehl, M., Marković, S. B., Zöller, L., and Glaser, B. (2013). The progressive evolution of a continental climate in southeast-central European lowlands during the Middle Pleistocene recorded in loess paleosol sequences. *Geology* 41 (7), 771–774. doi:10.1130/g34198.1

Buylaert, J. P., Jain, M., Murray, A. S., Thomsen, K. J., Thiel, C., and Sohbati, R. (2012). A robust feldspar luminescence dating method for Middle and Late Pleistocene sediments. *Boreas* 41 (3), 435–451. doi:10.1111/j.1502-3885.2012.00248.x

Chadima, M. and Hrouda, F. (2006). Remasoft 3.0 - a user-friendly paleomagnetic data browser and analyzer. *Travaux Géophysiques* 27, 20–21.

Channell, J. E., Singer, B. S., and Jicha, B. R. (2020). Timing of Quaternary geomagnetic reversals and excursions in volcanic and sedimentary archives. *Quat. Sci. Rev.* 228, 106114. doi:10.1016/j.quascirev.2019.106114

Constantin, D., Timar-Gabor, A., Veres, D., Begy, R., and Cosma, C. (2012). SAR-OSL dating of different grain-sized quartz from a sedimentary section in southern Romania interbedding the Campanian Ignimbrite/Y5 ash layer. *Quat. Geochronol.* 10, 81–86. doi:10.1016/j.quageo.2012.01.012

Constantin, D., Begy, R., Vasiliniuc, S., Panaiotu, C., Necula, C., Codrea, V., et al. (2014). High-resolution OSL dating of the Costineşti section (Dobrogea, SE Romania) using fine and coarse quartz. *Quat. Int.* 334, 20–29. doi:10.1016/j.quaint.2013.06.016

Constantin, D., Veres, D., Panaiotu, C., Anechitei-Deacu, V., Groza, S. M., Begy, R., et al. (2019). Luminescence age constraints on the Pleistocene-Holocene transition recorded in loess sequences across SE Europe. *Quat. Geochronol.* 49, 71–77. doi:10.1016/j.quageo.2018.07.011

Durcan, J. A., King, G. E., and Duller, G. A. (2015). DRAC: dose rate and age calculator for trapped charge dating. *Quat. Geochronol.* 28, 54–61. doi:10.1016/j.quageo.2015.03.012

Emiliani, C. (1955). Pleistocene temperatures. *J. Geol.* 63 (6), 538–578. doi:10.1086/626295

Evans, M. E. and Heller, F. (2001). Magnetism of loess/palaeosol sequences: recent developments. *Earth Sci. Rev.* 54 (1), 129–144. doi:10.1016/s0012-8252(01)00044-7

Fenn, K., Durcan, J. A., Thomas, D. S., and Banak, A. (2020a). A 180 ka record of environmental change at Erdut (Croatia): a new chronology for the loess–palaeosol sequence and its implications for environmental interpretation. *J. Quat. Sci.* 35 (4), 582–593. doi:10.1002/jqs.3201

Fenn, K., Durcan, J. A., Thomas, D. S., Millar, I. L., and Marković, S. B. (2020b). Re-analysis of late Quaternary dust mass accumulation rates in Serbia using new luminescence chronology for loess–palaeosol sequence at Surduk. *Boreas* 49 (3), 634–652. doi:10.1111/bor.12445

Fitzsimmons, K. E. and Hambach, U. (2014). Loess accumulation during the last glacial maximum: evidence from Urluia, southeastern Romania. *Quat. Int.* 334, 74–85. doi:10.1016/j.quaint.2013.08.005

Fitzsimmons, K. E., Hambach, U., Veres, D., and Iovita, R. (2013). The Campanian Ignimbrite eruption: new data on volcanic ash dispersal and its potential impact on human evolution. *PLoS One* 8 (6), e65839. doi:10.1371/journal.pone.0065839

Frechen, M., Schweitzer, U., and Zander, A. (1996). Improvements in sample preparation for the fine grain technique. *Ancient TL* 14 (2), 15–17

Frînculeasa, A., Preda, B., and Heyd, V. (2015). Pit-graves, yamnaya and kurgans along the lower Danube: disentangling IVth and IIIrd millennium BC burial customs, equipment and chronology. *Praehistorische Zeitschrift* 90 (1-2), 45–113. doi:10.1515/pz-2015-0002

Gallet, S., Jahn, B.-m., and Torii, M. (1996). Geochemical characterization of the Luochuan loess-paleosol sequence, China, and paleoclimatic implications. *Chem. Geol.* 133 (1-4), 67–88. doi:10.1016/s0009-2541(96)00070-8

Giaccio, B., Hajdas, I., Isaia, R., Deino, A., and Nomade, S. (2017). High-precision ^{14}C and ^{40}Ar/^{39}Ar dating of the Campanian Ignimbrite (Y-5) reconciles the time-scales of climatic-cultural processes at 40 ka. *Sci. Rep.* 7 (1), 1–10. doi:10.1038/srep45940

Govin, A., Capron, E., Tzedakis, P. C., Verheyden, S., Ghaleb, B., Hillaire-Marcel, C., et al. (2015). Sequence of events from the onset to the demise of the last interglacial: evaluating strengths and limitations of chronologies used in climatic archives. *Quat. Sci. Rev.*, 129, 1–36. doi:10.1016/j.quascirev.2015.09.018

Guérin, G., Frouin, M., Talamo, S., Aldeias, V., Bruxelles, L., Chiotti, L., et al. (2015). A multi-method luminescence dating of the palaeolithic sequence of La Ferrassie based on new excavations adjacent to the La Ferrassie 1 and 2 skeletons. *J. Archaeol. Sci.* 58, 147–166. doi:10.1016/j.jas.2015.01.019

Guérin, G., Mercier, N., and Adamiec, G. (2011). Dose-rate conversion factors: update. *Ancient TL* 29 (1), 5–8.

Haas, M., Bliedtner, M., Borodynkin, I., Salazar, G., Szidat, S., Eglinton, T. I., et al. (2017). Radiocarbon dating of leaf waxes in the loess-paleosol sequence Kurtak, central Siberia. *Radiocarbon* 59 (1), 165–176. doi:10.1017/rdc.2017.1

Haase, D., Fink, J., Haase, G., Ruske, R., Pécsi, M., Richter, H., et al. (2007). Loess in Europe—its spatial distribution based on a European loess map, scale 1: 2,500,000. *Quat. Sci. Rev.* 26 (9-10), 1301–1312. doi:10.1016/j.quascirev.2007.02.003

Haesaerts, P., Borziac, I., Chekha, V. P., Chirica, V., Drozdov, N. I., Koulakovska, L., et al. (2010). Charcoal and wood remains for radiocarbon dating upper pleistocene loess sequences in eastern Europe and central Siberia. *Palaeogeogr. Palaeoclimatol. Palaeoecol.* 291 (1), 106–127. doi:10.1016/j.palaeo.2010.03.034

Häggi, C., Zech, R., McIntyre, C. P., Zech, M., and Eglinton, T. I. (2014). On the stratigraphic integrity of leaf-wax biomarkers in loess paleosols. *Biogeosciences* 11 (9), 2455–2463. doi:10.5194/bg-11-2455-2014

Hambach, U., Rolf, C., and Schnepp, E. (2008). Magnetic dating of Quaternary sediments, volcanites and archaeological materials: an overview. *Eiszeitalt. Ggw. Quat. Sci. J.* 57 (2), 25–51. doi:10.3285/eg.57.1-2.2

Hanke, U. M., Wacker, L., Haghipour, N., Schmidt, M. W. I., Eglinton, T. I., and McIntyre, C. P. (2017). Comprehensive radiocarbon analysis of benzene polycarboxylic acids (BPCAs) derived from pyrogenic carbon in environmental samples. *Radiocarbon* 59 (4), 1103–1116. doi:10.1017/RDC.2017.44

Hatté, C., Pessenda, L. C., Lang, A., and Paterne, M. (2001). Development of accurate and reliable ^{14}C chronologies for loess deposits: application to the loess sequence of Nussloch (Rhine valley, Germany). *Radiocarbon* 43 (2B), 611–618. doi:10.1017/s0033822200041266

Heil, C. W., Jr, King, J. W., Zárate, M. A., and Schultz, P. H. (2010). Climatic interpretation of a 1.9 Ma environmental magnetic record of loess deposition and soil formation in the central eastern Pampas of Buenos Aires, Argentina. *Quat. Sci. Rev.* 29 (19-20), 2705–2718. doi:10.1016/j.quascirev.2010.06.024

Heller, F. and Liu, T.-S. (1986). Palaeoclimatic and sedimentary history from magnetic susceptibility of loess in China. *Geophys. Res. Lett.* 13, 1169–1172. doi:10.1029/gl013i011p01169

Heslop, D. and Roberts, A. P. (2020). Uncertainty propagation in hierarchical paleomagnetic reconstructions. *J. Geophys. Res.* 125 (6). doi:10.1029/2020JB019488

Huntley, D. (2006). An explanation of the power-law decay of luminescence. *J. Phys. Condens. Matter.* 18 (4), 1359. doi:10.1088/0953-8984/18/4/020

Huntley, D. J. and Baril, M. (1997). The K content of the K-feldspars being measured in optical dating or in thermoluminescence dating. *Ancient TL* 15 (1), 11–13.

ILEC (2019). Lake Balta Alba. Available at: https://wldb.ilec.or.jp/Lake/EUR-41. Date of access: 2020/07/20.

JAXA (2016). *ALOS global digital surface model "ALOS world 3D - 30m (AW3D30)"*.

Jin, C. and Liu, Q. (2010). Reliability of the natural remanent magnetization recorded in Chinese loess. *J. Geophys. Res. Solid Earth* 115 (B4), B04103. doi:10.1029/2009jb006703

Jipa, D. C. (2014). The conceptual sedimentary model of the Lower Danube loess basin: sedimentogenetic implications. *Quat. Int.* 351, 14–24. doi:10.1016/j.quaint.2013.06.008

King, G. E., Burow, C., Roberts, H. M., and Pearce, N. J. (2018). Age determination using feldspar: evaluating fading-correction model performance. *Radiat. Meas.* 119, 58–73. doi:10.1016/j.radmeas.2018.07.013

Kirschvink, J. (1980). The least-squares line and plane and the analysis of palaeomagnetic data. *Geophys. J. Int.* 62 (3), 699–718. doi:10.1111/j.1365-246x.1980.tb02601.x

Klasen, N., Kehl, M., Mikdad, A., Brückner, H., and Weniger, G.-C. (2018). Chronology and formation processes of the middle to upper palaeolithic deposits of Ifri n'Ammar using multi-method luminescence dating and micromorphology. *Quat. Int.* 485, 89–102. doi:10.1016/j.quaint.2017.10.043

Kohfeld, K. and Harrison, S. (2003). Glacial-interglacial changes in dust deposition on the Chinese loess plateau. *Quat. Sci. Rev.* 22 (18-19), 1859–1878. doi:10.1016/s0277-3791(03)00166-5

Korte, M., Brown, M. C., Panovska, S., and Wardinski, I. (2019). Robust characteristics of the Laschamp and Mono Lake geomagnetic excursions: results from global field models. *Front. Earth Sci.* 7 (86), 1–21. doi:10.3389/feart.2019.00086

Krbetschek, M., Rieser, U., Zöller, L., and Heinicke, J. (1994). Radioactive disequilibria in palaeodosimetric dating of sediments. *Radiat. Meas.* 23 (2-3), 485–489. doi:10.1016/1350-4487(94)90083-3

Kusch, S., Rethemeyer, J., Schefuβ, E., and Mollenhauer, G. (2010). Controls on the age of vascular plant biomarkers in Black Sea sediments. *Geochim. Cosmochim. Acta* 74, 7031–7047. doi:10.1016/j.gca.2010.09.005

Laj, C. and Kissel, C. (2015). An impending geomagnetic transition? Hints from the past. *Front. Earth Sci.* 3 (61), 1–10. doi:10.3389/feart.2015.00061

Laj, C., Kissel, C., and Beer, J. (2004). High resolution global paleointensity stack since 75 kyr (GLOPIS-75) calibrated to absolute values. *Geophys. Monogr.* 145, 255–265. doi:10.1029/145gm19

Lauer, T., Frechen, M., Vlaminck, S., Kehl, M., Sharifi, J., Rolf, C., et al. (2016). *The Agh Band loess-palaeosol sequence in Northern Iran - a detailed archive for climate and environmental change during the last and penultimate glacial-interglacial cycles*. Vienna Austria: 2016EGUGA..18.2488L.

Levi, S. and Banerjee, S. K. (1976). On the possibility of obtaining relative paleointensities from lake sediments. *Earth Planet Sci. Lett.* 29 (1), 219–226. doi:10.1016/0012-821x(76)90042-x

Li, G., Xia, D., Appel, E., Lu, H., Wang, Y., Jia, J., et al. (2020). Characteristics of a relative paleointensity record from loess deposits in arid central Asia and chronological implications. *Quat. Geochronol.* 55, 101034. doi:10.1016/j.quageo.2019.101034

Liu, Q., Banerjee, S. K., Jackson, M. J., Deng, C., Pan, Y., and Zhu, R. (2005). Inter-profile correlation of the Chinese loess/paleosol sequences during Marine Oxygen Isotope Stage 5 and indications of pedogenesis. *Quat. Sci. Rev.* 24, 195–210. doi:10.1016/j.quascirev.2004.07.021

Liu, Q., Jin, C., Hu, P., Jiang, Z., Ge, K., and Roberts, A. P. (2015). Magnetostratigraphy of Chinese loess–paleosol sequences. *Earth Sci. Rev.* 150, 139–167. doi:10.1016/j.earscirev.2015.07.009

Lomax, J., Fuchs, M., Antoine, P., Rousseau, D. D., Lagroix, F., Hatté, C., et al. (2019). A luminescence-based chronology for the Harletz loess sequence, Bulgaria. *Boreas* 48 (1), 179–194. doi:10.1111/bor.12348

Lowe, J. J. and Walker, M. J. (2014). *Reconstructing quaternary environments*: London and New York: Routledge.

Maher, B. A. (1999). "Palaeomonsoons I: the magnetic record of palaeoclimate in the terrestrial loess and palaeosol sequences," in *Quaternary climates, environments and magnetism*. Editors B.-A. Maher and R. Thompson (Cambridge University Press), 81–125.

Marković, S. B., Hambach, U., Catto, N., Jovanović, M., Buggle, B., Machalett, B., et al. (2009). Middle and late Pleistocene loess sequences at Batajnica, Vojvodina, Serbia. *Quat. Int.* 198 (1-2), 255–266. doi:10.1016/j.quaint.2008.12.004

Marković, S. B., Fitzsimmons, K. E., Sprafke, T., Gavrilović, D., Smalley, I. J., Jović, V., et al. (2016). The history of Danube loess research. *Quat. Int.* 399, 86–99. doi:10.1016/j.quaint.2015.09.071

Marković, S. B., Stevens, T., Kukla, G. J., Hambach, U., Fitzsimmons, K. E., Gibbard, P., et al. (2015). Danube loess stratigraphy — towards a pan-European loess stratigraphic model. *Earth Sci. Rev.* 148, 228–258. doi:10.1016/j.earscirev.2015.06.005

Matsumoto, K., Kawamura, K., Uchida, M., and Shibata, Y. (2007). Radiocarbon content and stable carbon isotopic ratios of individual fatty acids in subsurface soil: implication for selective microbial degradation and modification of soil organic matter. *Geochem. J.* 41 (6), 483–492. doi:10.2343/geochemj.41.483

Moine, O., Antoine, P., Hatté, C., Landais, A., Mathieu, J., Prud'homme, C., et al. (2017). The impact of last glacial climate variability in West-European loess revealed by radiocarbon dating of fossil earthworm granules. *Proc. Natl. Acad. Sci. U.S.A.* 114 (24), 6209–6214. doi:10.1073/pnas.1614751114

Murray, A. S., Thomsen, K. J., Masuda, N., Buylaert, J. P., and Jain, M. (2012). Identifying well-bleached quartz using the different bleaching rates of quartz and feldspar luminescence signals. *Radiat. Meas.* 47 (9), 688–695. doi:10.1016/j.radmeas.2012.05.006

Murray, A. S. and Wintle, A. G. (2000). Luminescence dating of quartz using an improved single-aliquot regenerative-dose protocol. *Radiat. Meas.* 32 (1), 57–73. doi:10.1016/s1350-4487(99)00253-x

Murray, A. S. and Wintle, A. G. (2003). The single aliquot regenerative dose protocol: potential for improvements in reliability. *Radiat. Meas.* 37 (4), 377–381. doi:10.1016/s1350-4487(03)00053-2

Necula, C., Dimofte, D., and Panaiotu, C. (2015). Rock magnetism of a loess-palaeosol sequence from the western Black Sea shore (Romania). *Geophys. J. Int.* 202 (3), 1733–1748. doi:10.1093/gji/ggv250

Nett, J., Oppermann, L., and Klasen, N. (2020). OSL data of the Balta Alba Kurgan loess-paleosol sequence, Romania. *CRC806-Database*. doi:10.5880/SFB806.54

Niţu, E.-C., Cârciumaru, M., Nicolae, A., Cîrstina, O., Lupu, F. I., and Leu, M. (2019). Mobility and social identity in the Mid Upper Paleolithic: new personal ornaments from Poiana Cireşului (Piatra Neamţ, Romania). *PLoS One.* 14 (4), e0214932. doi:10.1371/journal.pone.0214932

Novothny, Á., Frechen, M., Horváth, E., Wacha, L., and Rolf, C. (2011). Investigating the penultimate and last glacial cycles of the Süttő loess section (Hungary) using luminescence dating, high-resolution grain size and magnetic susceptibility data. *Quat. Int.* 234 (1-2), 75–85. doi:10.1016/j.quaint.2010.08.002

Obreht, I., Hambach, U., Veres, D., Zeeden, C., Bösken, J., Stevens, T., et al. (2017). Shift of large-scale atmospheric systems over Europe during late MIS 3 and implications for Modern Human dispersal. *Sci. Rep.* 7 (1), 5848. doi:10.1038/s41598-017-06285-x

Parnell, A. (2018). *Bchron: radiocarbon dating, age-depth modelling, relative sea level rate estimation and non-parametric phase modelling*.

Parnell, A. C., Haslett, J., Allen, J. R., Buck, C. E., and Huntley, B. (2008). A flexible approach to assessing synchroneity of past events using Bayesian reconstructions of sedimentation history. *Quat. Sci. Rev.* 27 (19-20), 1872–1885. doi:10.1016/j.quascirev.2008.07.009

Pfeifer, L. S., Hinnov, L., Zeeden, C., Rolf, C., Laag,, C., and Soreghan, G. S. (2020). Rock magnetic cyclostratigraphy of permian loess in eastern equatorial pangea (Salagou formation, South-Central France). *Front. Earth Sci.* 8 (241). doi:10.3389/feart.2020.00241

Pigati, J. S., McGeehin, J. P., Muhs, D. R., and Bettis, E. A., III (2013). Radiocarbon dating late Quaternary loess deposits using small terrestrial gastropod shells. *Quat. Sci. Rev.* 76, 114–128. doi:10.1016/j.quascirev.2013.05.013

Prescott, J. R. and Hutton, J. T. (1994). Cosmic ray contributions to dose rates for luminescence and ESR dating: large depths and long-term time variations. *Radiat. Meas.* 23 (2-3), 497–500. doi:10.1016/1350-4487(94)90086-8

R Core Team (2020). *R: a language and environment for statistical computing*: R Core Team.

Reimer, P. J., Brown, T. A., and Reimer, R. W. (2004). Discussion: reporting and calibration of post-bomb ^{14}C data. *Radiocarbon* 46 (3), 1299–1304. doi:10.1017/s0033822200033154

Reimer, P. J., Austin, W. E. N., Bard, E., Bayliss, A., Blackwell, P. G., Bronk Ramsey, C., et al. (2020). The INTCAL20 northern hemisphere radiocarbon age calibration curve (0–55 cal kBP). *Radiocarbon* 62 (4), 725–757. doi:10.1017/rdc.2020.41

Rethemeyer, J., Gierga, M., Heinze, S., Stolz, A., Wotte, A., Wischhöfer, P., et al. (2019). Current sample preparation and analytical capabilities of the radiocarbon laboratory at CologneAMS. *Radiocarbon* 61 (5), 1449–1460. doi:10.1017/RDC.2019.16

Roberts, A. P. and Winklhofer, M. (2004). Why are geomagnetic excursions not always recorded in sediments? Constraints from post-depositional remanent magnetization lock-in modelling. *Earth Planet Sci. Lett.* 227 (3-4), 345–359. doi:10.1016/j.epsl.2004.07.040

Roberts, H. M. (2008). The development and application of luminescence dating to loess deposits: a perspective on the past, present and future. *Boreas* 37 (4), 483–507. doi:10.1111/j.1502-3885.2008.00057.x

Rolf, C., Hambach, U., Novothny, Á., Horváth, E., and Schnepp, E. (2014). Dating of a last glacial loess sequence by relative geomagnetic palaeointensity: a case study from the middle Danube basin (Süttő, Hungary). *Quat. Int.* 319, 99–108. doi:10.1016/j.quaint.2013.08.050

Rousseau, D.-D., Antoine, P., Boers, N., Lagroix, F., Ghil, M., Lomax, J., et al. (2020). Dansgaard–Oeschger-like events of the penultimate climate cycle: the loess point of view. *Clim. Past.* 16 (2), 713–727. doi:10.5194/cp-16-713-2020

Scheidt, S., Hambach, U., Laag, C., and Monnens, F. (2020). [Dataset]: Paleomagnetic and mineral magnetic data of the loess paleosol record Balta Alba Kurgan. *PANGAEA*. https://doi.org/10.1594/PANGAEA.922831

Schmidt, C., Bösken, J., and Kolb, T. (2018). Is there a common alpha-efficiency in polymineral samples measured by various infrared stimulated luminescence protocols? *Geochronometria* 45 (1), 160–172. doi:10.1515/geochr-2015-0095

Smalley, I. J. and Leach, J. A. (1978). The origin and distribution of the loess in the Danube basin and associated regions of East-Central Europe - a review. *Sediment. Geol.* 21 (1), 1–26. doi:10.1016/0037-0738(78)90031-3

Smalley, I., O'Hara-Dhand, K., Wint, J., Machalett, B., Jary, Z., and Jefferson, I. (2009). Rivers and loess: the significance of long river transportation in the complex event-sequence approach to loess deposit formation. *Quat. Int.* 198 (1), 7–18. doi:10.1016/j.quaint.2008.06.009

Song, Y., Li, C., Zhao, J., Cheng, P., and Zeng, M. (2012). A combined luminescence and radiocarbon dating study of the Ili loess, central Asia. *Quat. Geochronol.* 10, 2–7. doi:10.1016/j.quageo.2012.04.005

Song, Y., Lai, Z., Li, Y., Chen, T., and Wang, Y. (2015). Comparison between luminescence and radiocarbon dating of late Quaternary loess from the Ili basin in central Asia. *Quat. Geochronol.* 30, 405–410. doi:10.1016/j.quageo.2015.01.012

Song, Y., Guo, Z., Marković, S., Hambach, U., Deng, C., Chang, L., et al. (2018a). Magnetic stratigraphy of the Danube loess: a composite Titel-Stari Slankamen

loess section over the last one million years in Vojvodina, Serbia. *J. Asian Earth Sci.* 155, 68–80. doi:10.1016/j.jseaes.2017.11.012

Song, Y., Luo, D., Du, J., Kang, S., Cheng, P., Fu, C., et al. (2018b). Radiometric dating of late Quaternary loess in the northern piedmont of South Tianshan Mountains: implications for reliable dating. *Geol. J.* 53 (S2), 417–426. doi:10.1002/gj.3129

Staubwasser, M., Drăguşin, V., Onac, B. P., Assonov, S., Ersek, V., Hoffmann, D. L., et al. (2018). Impact of climate change on the transition of Neanderthals to modern humans in Europe. *Proc. Natl. Acad. Sci. U.S.A.* 115 (37), 9116–9121. doi:10.1073/pnas.1808647115

Stolz, A., Dewald, A., Heinze, S., Altenkirch, R., Hackenberg, G., Herb, S., et al. (2019). Improvements in the measurement of small $^{14}CO_2$ samples at CologneAMS. *Nucl. Instrum. Methods Phys. Res. Sect. B Beam Interact. Mater. Atoms.* 439, 70–75. doi:10.1016/j.nimb.2018.12.008

Sümegi, P., Gulyás, S., Molnár, D., Szilágyi, G., Sümegi, B. P., Törőcsik, T., et al. (2020). ^{14}C dated chronology of the thickest and best resolved loess/paleosol record of the LGM from SE Hungary based on comparing precision and accuracy of age-depth models. *Radiocarbon* 62 (2), 403–417. doi:10.1017/RDC.2019.154

Svensson, A., Andersen, K. K., Bigler, M., Clausen, H. B., Dahl-Jensen, D., Davies, S. M., et al. (2008). A 60 000 year Greenland stratigraphic ice core chronology. *Clim. Past.* 4 (1), 47–57. doi:10.5194/cp-4-47-2008

Tauxe, L. (2010). *Essentials of paleomagnetism*. University of California Press, Berkeley.

Tecsa, V., Gerasimenko, N., Veres, D., Hambach, U., Lehmkuhl, F., Schulte, P., et al. (2020). Revisiting the chronostratigraphy of late Pleistocene loess-paleosol sequences in southwestern Ukraine: OSL dating of Kurortne section. *Quat. Int.* 542, 65–79. doi:10.1016/j.quaint.2020.03.001

Telford, R. J., Heegaard, E., and Birks, H. J. B. (2004). All age–depth models are wrong: but how badly? *Quat. Sci. Rev.* 23 (1), 1–5. doi:10.1016/j.quascirev.2003.11.003

Thiel, C., Buylaert, J.-P., Murray, A., Terhorst, B., Hofer, I., Tsukamoto, S., et al. (2011). Luminescence dating of the Stratzing loess profile (Austria) – Testing the potential of an elevated temperature post-IR IRSL protocol. *Quat. Int.* 234 (1-2), 23–31. doi:10.1016/j.quaint.2010.05.018

Thomsen, K. J., Murray, A. S., Jain, M., and Bøtter-Jensen, L. (2008). Laboratory fading rates of various luminescence signals from feldspar-rich sediment extracts. *Radiat. Meas.* 43 (9), 1474–1486. doi:10.1016/j.radmeas.2008.06.002

Timar-Gabor, A., Vandenberghe, D. A. G., Vasiliniuc, S., Panaoitu, C. E., Panaiotu, C. G., Dimofte, D., et al. (2011). Optical dating of Romanian loess: a comparison between silt-sized and sand-sized quartz. *Quat. Int.* 240 (1), 62–70. doi:10.1016/j.quaint.2010.10.007

Timar-Gabor, A., Panaiotu, C., Vereș, D., Necula, C., and Constantin, D. (2017). "The lower Danube loess, new age constraints from luminescence dating, magnetic proxies and isochronous tephra markers," in *Landform dynamics and evolution in Romania*. Editors M. Radoane and A. Vespremeanu-Stroe (Cham: Springer International Publishing), 679–697.

Trachsel, M. and Telford, R. J. (2017). All age–depth models are wrong, but are getting better. *Holocene* 27 (6), 860–869. doi:10.1177/0959683616675939

Trumbore, S. (2009). Radiocarbon and soil carbon dynamics. *Annu. Rev. Earth Planet Sci.* 37, 47–66. doi:10.1146/annurev.earth.36.031207.124300

Újvári, G., Kovács, J., Varga, G., Raucsik, B., and Marković, S. B. (2010). Dust flux estimates for the Last Glacial Period in East Central Europe based on terrestrial records of loess deposits: a review. *Quat. Sci. Rev.* 29 (23), 3157–3166. doi:10.1016/j.quascirev.2010.07.005

Újvári, G., Kovács, J., Varga, G., Molnár, M., and Novothny, Á. (2014a). Late Pleistocene millennial scale cycles of aeolian sedimentation in the Dunaszekcső loess record, south Hungary: preliminary data and interpretations. *Sci. Annals Stefan cel Mare Univ. Suceava Geography Ser.* 24 (2), 168–169. doi:10.4316/GEOREVIEW.2014.0.0.244

Újvári, G., Molnár, M., Novothny, A., and Kovacs, J. (2014b). *Lessons from the AMS ^{14}C and OSL/IRSL-dating of the Dunaszekcső loess record*. Hungary.

Újvári, G., Molnár, M., Novothny, Á., Páll-Gergely, B., Kovács, J., and Várhegyi, A. (2014c). AMS ^{14}C and OSL/IRSL dating of the Dunaszekcső loess sequence (Hungary): chronology for 20 to 150 ka and implications for establishing reliable age–depth models for the last 40 ka. *Quat. Sci. Rev.* 106, 140–154. doi:10.1016/j.quascirev.2014.06.009

Újvári, G., Stevens, T., Molnár, M., Demény, A., Lambert, F., Varga, G., et al. (2017). Coupled European and Greenland last glacial dust activity driven by North Atlantic climate. *Proc. Natl. Acad. Sci. U.S.A.* 114 (50), E10632–E10638. doi:10.1073/pnas.1712651114

van der Voort, T. S., Zell, C. I., Hagedorn, F., Feng, X., McIntyre, C. P., Haghipour, N., et al. (2017). Diverse soil carbon dynamics expressed at the molecular level. *Geophys. Res. Lett.* 44 (11840–11), 850. doi:10.1002/2017gl076188

Veres, D., Lane, C. S., Timar-Gabor, A., Hambach, U., Constantin, D., Szakács, A., et al. (2013). The Campanian Ignimbrite/Y5 tephra layer – a regional stratigraphic marker for Isotope Stage 3 deposits in the Lower Danube region, Romania. *Quat. Int.* 293, 22–33. doi:10.1016/j.quaint.2012.02.042

Veres, D., Tecsa, V., Gerasimenko, N., Zeeden, C., Hambach, U., and Timar-Gabor, A. (2018). Short-term soil formation events in last glacial east European loess, evidence from multi-method luminescence dating. *Quat. Sci. Rev.* 200, 34–51. doi:10.1016/j.quascirev.2018.09.037

Wallinga, J., Murray, A., and Duller, G. (2000). Underestimation of equivalent dose in single-aliquot optical dating of feldspars caused by preheating. *Radiat. Meas.* 32 (5-6), 691–695. doi:10.1016/s1350-4487(00)00127-x

Wiesenberg, G. L., Schmidt, M., and Schwark, L. (2008). Plant and soil lipid modifications under elevated atmospheric CO_2 conditions: I. Lipid distribution patterns. *Org. Geochem.* 39 (1), 91–102. doi:10.1016/j.orggeochem.2007.09.005

Wiesenberg, G. L., Schneckenberger, K., Schwark, L., and Kuzyakov, Y. (2012). Use of molecular ratios to identify changes in fatty acid composition of *Miscanthus × giganteus* (Greef et Deu.) plant tissue, rhizosphere and root-free soil during a laboratory experiment. *Org. Geochem.* 46, 1–11. doi:10.1016/j.orggeochem.2012.01.010

Wintle, A. G. (1973). Anomalous fading of thermo-luminescence in mineral samples. *Nature* 245 (5421), 143–144. doi:10.1038/245143a0

Zech, M., Kreutzer, S., Zech, R., Goslar, T., Meszner, S., McIntyre, C., et al. (2017). Comparative ^{14}C and OSL dating of loess-paleosol sequences to evaluate post-depositional contamination of n-alkane biomarkers. *Quat. Res.* 87, 180–189. doi:10.1017/qua.2016.7

Zeeden, C., Dietze, M., and Kreutzer, S. (2018a). Discriminating luminescence age uncertainty composition for a robust Bayesian modelling. *Quat. Geochronol.* 43, 30–39. doi:10.1016/j.quageo.2017.10.001

Zeeden, C., Hambach, U., Obreht, I., Hao, Q., Abels, H. A., Veres, D., et al. (2018b). Patterns and timing of loess-paleosol transitions in Eurasia: constraints for paleoclimate studies. *Global Planet. Change.* 162, 1–7. doi:10.1016/j.gloplacha.2017.12.021

Zeeden, C., Hambach, U., Veres, D., Fitzsimmons, K., Obreht, I., Bösken, J., et al. (2018c). Millennial scale climate oscillations recorded in the Lower Danube loess over the last glacial period. *Palaeogeogr. Palaeoclimatol. Palaeoecol.* 509, 164–181. doi:10.1016/j.palaeo.2016.12.029

Zeeden, C. and Hambach, U. (2020). [Dataset]: Paleomagnetic of Poiana Ciresului/Romania. *PANGAEA*. https://doi.org/10.1594/PANGAEA.918106

Zeeden, C., Hambach, U., Steguweit, L., Fülling, A., Anghelinu, M., and Zöller, L. (2009). Using the relative intensity variation of the Earth's magnetic palaeofield as correlative dating technique: a case study from loess with Upper Palaeolithic cultural layers at Poiana Cireşului, Romania. *Quartär* 56, 175–185. doi:10.7485/QU56_10

Zeeden, C., Hambach, U., Steguweit, L., and Anghelinu, M. (2011). Loess stratigraphy using palaeomagnetism: application to the Poiana Cireșului archaeological site (Romania). *Quat. Int.* 240 (1-2), 100–107. doi:10.1016/j.quaint.2010.08.018

Zeeden, C., Hambach, U., Veres, D., Fitzsimmons, K., Obreht, I., Bösken, J., et al. (2019). Corrigendum to "Millennial scale climate oscillations recorded in the Lower Danube loess over the last glacial period". *Palaeogeogr. Palaeoclimatol. Palaeoecol.* 509, 15–117. doi:10.1016/j.palaeo.2019.01.026

Zeeden, C., Hambach, U., Veres, D., Fitzsimmons, K., Obreht, I., Bösken, J., et al. (2016). [Dataset]: Physical properties and fine fraction from Loess at Rasova/lower Danube. *PANGAEA*. https://doi.org/10.1594/PANGAEA.870532

Zeeden, C., Obreht, I., Veres, D., Kaboth-Bahr, S., Hošek, J., Marković, S. B., et al. (2020). Smoothed millennial-scale palaeoclimatic reference data as unconventional comparison targets: application to European loess records. *Sci. Rep.* 10 (1), 5455. doi:10.1038/s41598-020-61528-8

Zelles, L. (1999). Fatty acid patterns of phospholipids and lipopolysaccharides in the characterisation of microbial communities in soil: a review. *Biol. Fertil. Soils* 29 (2), 111–129. doi:10.1007/s003740050533

Zhang, H., Ait Brahim, Y., Li, H. Z., Jingyao, G., Tian, Y., Baker, J., et al. (2019). The Asian summer monsoon: teleconnections and forcing mechanisms — A review from Chinese speleothem $\delta^{18}O$ records. *Quaternary* 2, 26. doi:10.3390/quat2030026

Zhang, J., Rolf, C., Wacha, L., Tsukamoto, S., Durn, G., and Frechen, M. (2018). Luminescence dating and palaeomagnetic age constraint of a last glacial loess-palaeosol sequence from Istria, Croatia. *Quat. Int.* 494, 19–33. doi:10.1016/j.quaint.2018.05.045

Zijderveld, J. (1967). "AC demagnetization of rocks: analysis of results," in *Methods in paleomagnetism*. Editors D. Collinson, K. Creer, and S. Runcorn (New York: Elsevier), 254–286.

Conflict of Interest: The authors declare that the research was conducted in the absence of any commercial or financial relationships that could be construed as a potential conflict of interest.

frontiers in Earth Science

REVIEW
published: 27 January 2021
doi: 10.3389/feart.2020.607183

The Main Nile Valley at the End of the Pleistocene (28–15 ka): Dispersal Corridor or Environmental Refugium?

Alice Leplongeon[1,2]*

[1]Department of Archaeology, KU Leuven, Leuven, Belgium, [2]UMR 7194 Histoire Naturelle de l'Homme Préhistorique (HNHP), Muséum National d'Histoire Naturelle, Université de Perpignan Via Domitia, CNRS, Paris, France

Under present environmental conditions, the Nile Valley acts as a 'natural' route between Africa and Eurasia, and is often considered as a corridor for dispersals out of and back into Africa in the past. This review aims to address the role played by the Nile Valley at the end of the Pleistocene (28-15 ka) in the context of post-'Out of Africa' modern human dispersals. Genetic studies based on both modern and ancient DNA suggest pre-Holocene dispersals 'back into Africa' as well as genetic interactions between modern humans across Africa and the Levant. During the Last Glacial, the lowering, or even complete desiccation of major eastern African lakes, including Lake Victoria, reduced the White Nile to a highly seasonal river, depriving the main Nile from its most important tributary in the dry season. This had major consequences, the specifics of which are still debated, on the behavior of the main Nile and the landscape around the Nile Delta. Despite this shift to more arid conditions, there is abundant evidence for human occupation in the main Nile Valley. Combining available geological, palaeoenvironmental, anthropological, genetic and archaeological data, this article discusses problems encountered when trying to reconcile results from different fields, the current limitations of the available data and research perspectives to further address the role of the Nile Valley as a dispersal corridor or an environmental refugium at the end of the Pleistocene.

Keywords: North-Eastern Africa, prehistory, human dispersals, late palaeolithic, human-environment interactions

OPEN ACCESS

Edited by:
Annett Junginger, University of Tubingen, Germany

Reviewed by:
Nick Blegen, University of Connecticut, United States
Huw Groucutt, Max Planck Institute for Chemical Ecology, Germany

***Correspondence:**
Alice Leplongeon
alice.leplongeon@kuleuven.be

Specialty section:
This article was submitted to Quaternary Science, Geomorphology and Paleoenvironment, a section of the journal Frontiers in Earth Science

Received: *16 September 2020*
Accepted: *30 November 2020*
Published: *27 January 2021*

Citation:
Leplongeon A (2021) The Main Nile Valley at the End of the Pleistocene (28–15 ka): Dispersal Corridor or Environmental Refugium?. Front. Earth Sci. 8:607183. doi: 10.3389/feart.2020.607183

INTRODUCTION

The Last Glacial (Marine Isotope Stages (MIS) 4-2, 73.5-14.7 ka) is marked by abrupt climatic oscillations of irregular periodicity. In particular, MIS 2 (27.8-14.7 ka – Sanchez Goñi and Harrison, 2010), which includes the Last Glacial Maximum (LGM, 23-19 ka – Waelbroeck et al., 2009) and Heinrich Stadial 1[1] (HS 1, 19-14.6 ka – Stanford et al., 2011), is generally characterized by drier conditions and lower temperatures than the present day, with some abrupt arid-humid transitions in northern and equatorial Africa (Gasse, 2000). The impact of these rapid climatic fluctuations on Palaeolithic hunter-gatherer populations in Africa, although undeniable, remains not well understood. MIS 2 may have been a period of contraction of populations (toward environmental refugia), which may have been significant in shaping the variability in human

[1]In this review paper, Heinrich Stadial is used rather than Greenland Stadial (Rasmussen et al., 2014), as it follows recent regional palaeoenvironmental studies (e.g., Stager et al., 2011; Revel et al., 2015; Castañeda et al., 2016).

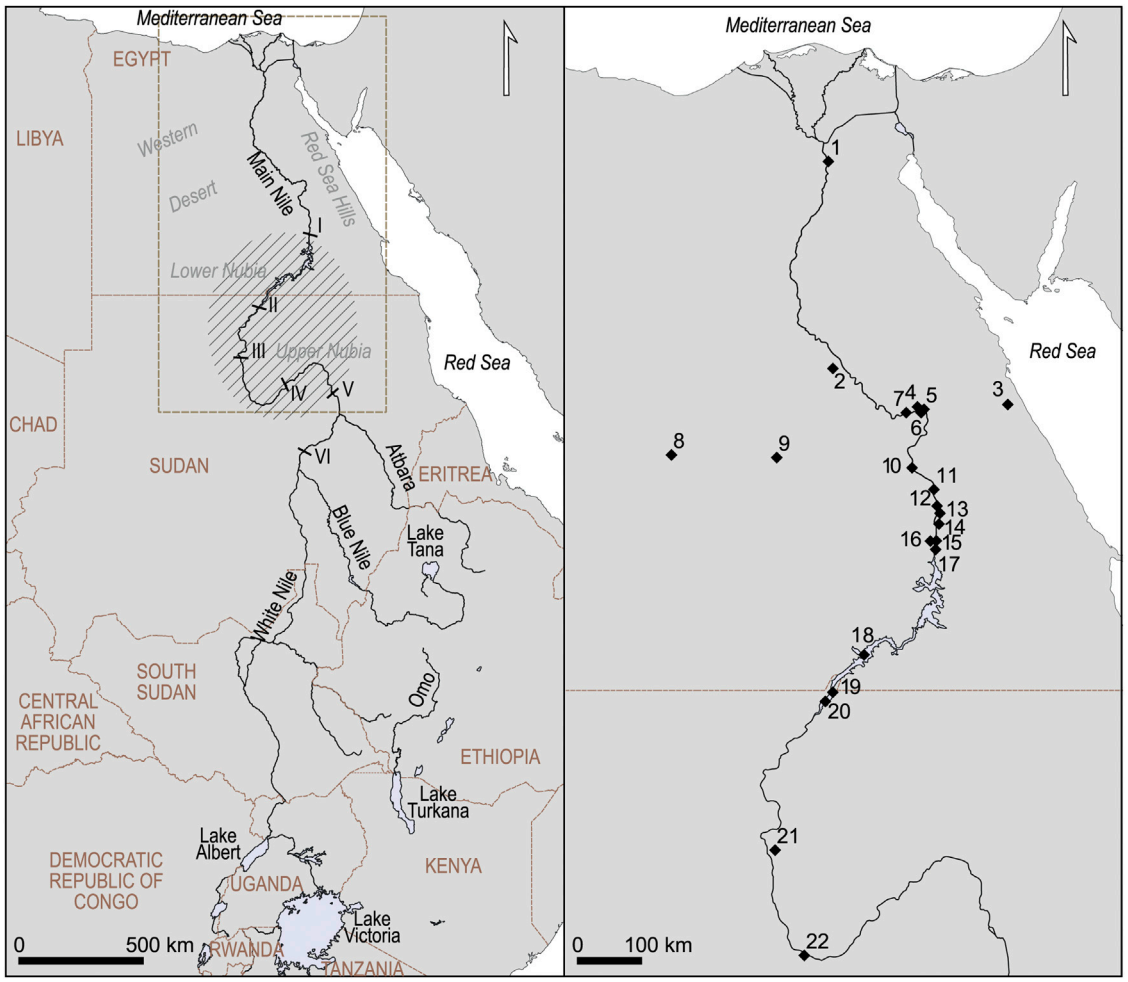

FIGURE 1 | Map of the Nile Basin **(left)** and the Main Nile Basin **(right)**. Created in QGIS v. 3.15 (QGIS Development Team, 2017) using Natural Earth Data. Hatched area: broad geographical extent of Nubia. Numbers: geographical locations discussed in the text; 1, Helwan; 2, Nazlet Khater; 3, Sodmein Cave; 4, Makhadma; 5, Qena; 6, Taramsa; 7, Dishna; 8, Dakhleh Oasis; 9, Kharga Oasis; 10, Esna; 11, Edfu; 12, El Hosh; 13, Qurta; 14, Kom Ombo; 15, Wadi Abu Subeira; 16, Wadi Kubbaniya; 17, Aswan; 18, Tushka; 19, Jebel Sahaba; 20, Wadi Halfa; 21, El Barga; 22, Ed-Debba.

populations that we know today (e.g., Mirazón Lahr, 2016). However, at the same time, genetic data indicate the occurrence of gene flow between human populations in northern Africa, the Levant and south of the Sahara before 15 ka BP (Van de Loosdrecht et al., 2018).

This paper investigates the role that the main Nile Valley (i.e., the northern end of the Nile Valley corresponding to the main Nile, **Figure 1**) may have had for human populations during MIS 2. In the context of a hyper-arid Sahara (e.g., Pachur and Hoelzmann, 2000), the Nile Valley may have constituted an environmental refugium for human populations and / or it may have acted as a dispersal corridor. Numerous archaeological sites dating to MIS 2 are known in the Nile Valley in southern Egypt and northern Sudan. While several reviews of the archaeological record already exist (e.g., Schild and Wendorf, 2010; Vermeersch and Van Neer, 2015; Usai, 2019; Garcea, 2020; Vermeersch, 2020), the aim here is to take a multidisciplinary approach and review recent advances in palaeoenvironmental, anthropological, genetic and archaeological research in order to shed new light on human-environment interactions and in particular the potential role of the main Nile Valley as an environmental refugium or dispersal corridor during MIS 2.

This article focuses on the northern end of the Nile Valley and particularly on southern Egypt, northern (= Lower) and southern (= Upper) Nubia during MIS 2. This geographical focus is mainly guided by the availability of archaeological data for this period. The definition and geographical extent of Nubia has varied through time, in particular regarding its southern boundary. In a broad sense, Nubia is located between the First Cataract near Aswan with a southern boundary fluctuating between the Fourth and the Sixth Cataract north of Khartoum (**Figure 1**). Northern Nubia corresponds to the area between the First and

TABLE 1 | General expectations under a refugium or dispersal corridor model.

	Palaeoenvironmental data	Human fossil and genetic data	Archaeological data
The Nile Valley is an environmental refugium	Suitable environmental conditions for continuous human occupation over the period (e.g., availability of water) Areas adjacent to the Nile Valley unsuitable for human occupation	In a long-term isolation model, development of unique biological characteristics that differ from human remains in other regions and biological continuity over the refugial period	Abundant archaeological evidence (based on archaeological radiocarbon data) in the Nile Valley, but not in adjacent areas
The Nile Valley is a dispersal corridor	Suitable environmental conditions for continuous human occupation over the period (e.g., availability of water), restricted to the Nile Valley Areas at either end of the Nile Valley suitable for human occupation	Evidence for past gene flow between different areas Evidence for biological similarities in all adjacent areas	Abundant archaeological evidence (based on archaeological radiocarbon data) in the Nile Valley, in the Levant, in North and in eastern Africa Possible but not required: Evidence for horizontal cultural transmission in the archaeological record between the Nile Valley, the Levant, North Africa and eastern Africa consistent with contact between populations

Second Cataract, whereas southern Nubia corresponds to the area upstream from the Second cataract (Adams, 1977, 13–17; Hassan, 2007; Auenmüller, 2019).

The concept of 'refugia' comes from the field of biogeography in the context of studies focusing on changing spatial distributions of plant and animal species linked to climatic and environmental fluctuations (Bennett and Provan, 2008; Sommer and Zachos, 2009; Stewart et al., 2010). Refugia therefore refer to areas where, for example, temperate animal or plant species can survive during unfavourable environmental conditions (in this case Glacial periods). Refugia areas are thus necessarily restricted compared to the full range distribution of these species under different environmental conditions (Interglacial). Most of these studies concern Eurasian species during the Last Glacial Maximum, where the distribution range of temperate species was restricted to southern Europe. Because population contraction to refugia often imply reduced population size, the concept of refugia is closely linked to the genetic concept of a 'bottleneck,' a drastic decrease in population followed by a phase of expansion (Bennett and Provan, 2008). Genetic studies have indeed shown for several species that refugia areas during the LGM were the source of subsequent major expansions of the distribution of these species after the LGM and also included speciation processes (see Hewitt, 1996; and review in Bennett and Provan, 2008).

Refugia models have been used in archaeological studies as well, in particular as a possible framework to explain the population history of Western Europe at the end of the Pleistocene (e.g., Gamble et al., 2005), modern human expansions within and out of Africa, as well as population substructure (Basell, 2008; Stewart and Stringer, 2012; Mirazón Lahr and Foley, 2016; Mirazón Lahr, 2016; Scerri et al., 2018). In the context of this paper, a (n environmental) refugium for human populations is defined as an area that human populations inhabited during phases of unfavourable environmental conditions which restricted their distribution range over a given time interval. Refugial phases therefore correspond to periods when populations are in isolation. While some definitions specify that these areas must have been inhabited during an entire glacial / interglacial cycle (e.g., Stewart and Stringer, 2012, or 'long-term refugium' as defined in Stewart et al., 2010), this should not necessarily be the case (Stewart et al., 2010).

A dispersal corridor indicates a restricted geographical area characterized by environmental conditions suitable for allowing movements of faunal or floral species (and specifically in this paper, of human populations) from one region to another.

The definitions used for each of these concepts imply that at a given time the Nile Valley can only be a refugium area or a dispersal corridor. However, the period considered spans nearly 15 millennia and the Nile Valley may have been alternately a refugium area and a dispersal corridor. An alternative scenario to the refugium / dispersal corridor dichotomy is that the Nile Valley may have not been suitable for human occupation at all during periods of MIS 2. Because most of the Sahara was hyper-arid during MIS 2 and there is no evidence for human occupation of the Sahara during MIS 2, we can dismiss the last alternative scenario that the Nile Valley was only part of a wider area occupied by human populations (and not a restricted area) during MIS 2.

The multidisciplinary approach adopted here will address the complex issue of the role that the main Nile Valley may have had for human populations during MIS 2 from different perspectives. General expectations of what we may find from a palaeoenvironmental, human fossil and genetic, and archaeological perspectives under each of the two models (refugium model and dispersal corridor model) are summarized in **Table 1** and will provide a broad framework for the ensuing discussion.

PALAEOENVIRONMENTAL DATA

General Data on the River Nile

The Nile Basin is one of the largest basins in the world–*ca.* 3.3 million km^2, from 4°S to 31°N–with three principal tributaries for the main (or desert) Nile: the White Nile, the Blue Nile and the Atbara (**Figure 1**). It encompasses several climatic zones. In Equatorial East Africa where the White Nile, Blue Nile and

TABLE 2 | Characteristics of cultural entities of the Late Palaeolithic in the Lower Nile Valley.

Cultural entity	Location*	Lithic characteristics**	Other characteristic finds
Idfuan/Shuwikhatian	A	Blade production using opposed platform cores and crested products; denticulates, burins, endscrapers[a]	
Levallois Idfuan	A	Blade production using opposed platform cores, use of Levallois and Halfa methods; notches, denticulates are dominant	
Fakhurian	A	Blade and bladelet production, single and opposed platform cores; backed bladelets largely dominant, retouched pieces and perforators	
Gemaian	B	Halfan and Nubian-like cores; denticulates and notches	Bone tool (N = 1)
Halfan	B	Microlithic aspect; Halfan and Levallois cores; Ouchtata and backed bladelets	
Kubbaniyan	A	Flake and bladelet production, use of single and opposed platform cores, occasional use of Levallois and Halfa methods; Ouchtata and backed bladelets, burins. Egyptian variant of the Halfan?	Grinding implements, bone tools and ostrich eggshell beads
Ballanan-Silsilian	A, B	Sometimes includes the use of exotic raw materials; mainly oriented toward the production of short elongated blanks (blade/let) with single and opposed platform cores; backed pieces, truncations, proximally retouched blade (let)s and notched tools, occasional use of the microburin technique[b]	
Qadan	Mostly B, one site in a (Wadi Kubbaniya)	Small dimensions of the artefacts; mainly oriented toward flake production with single and opposed platform cores, several cores reminiscent of the Levallois methods for Qadan point production, bladelet production documented in some but not all sites; Qadan points, burins, small scrapers and backed pieces (the latter only at some sites)[c]	Rare bone tools, grinding implements
Afian	A	Mainly oriented toward the production of wide and small elongated products, planimetric conception of debitage with high frequencies of faceted platforms; truncations, backed bladelets and geometrics[d]	Grinding stones (Kom Ombo area), bone tools (Makhadma 4)
Sebilian	A, B	Discoidal and Levallois cores for the production of flakes; truncated and backed flakes, use of the microburin technique	
Isnan	A	Production of flakes and rare blades from single and opposed platform cores; high percentage of endscrapers, followed by notches and denticulates, rare backed pieces	Grinding implements
Arkinian (excl. El Adam Variant)	B	Bladelet and flake production from single and opposed platform cores, presence of bipolar reduction, stone anvils; numerous backed pieces and endscrapers	Grinding implements, bone spatula

After Schild and Wendorf (2010), A = southern Egypt between Sohag and the first cataract, see also **Figures 1, **3** (N.B. Schild and Wendorf, 2010 use Dishna as the northern limit); B = Egyptian and Sudanese Nubia between the first and the second cataract.*

***After Schild and Wendorf (2010) except when mentioned otherwise.*

[a]Characteristics after Vermeersch (2020). These characteristics, associated with minimal ages around 25 ka led to an attribution to the later Upper Palaeolithic, rather than the Late Palaeolithic (Vermeersch, 2020).

[b]Characteristics after Smith (1966) and Leplongeon (2017).

[c]Characteristics after Usai (2020).

[d]Characteristics after Leplongeon (2017). Note that in Leplongeon (2017), the attribution of Makhadma 4 to the Afian is questioned.

Atbara headwaters are located, precipitation is mostly driven by the East African monsoon system, a complex interplay of seasonal migrations of the Intertropical Convergence Zone (ITCZ) and the Congo Air Boundary (CAB) (Gasse, 2000; Gasse et al., 2008). At the northern end of the Nile Valley, a Mediterranean dry-summer climate predominates and precipitation is mostly brought by the Western westerlies in winter (Gasse, 2000; Williams, 2019). Regional environmental responses to global climatic events are thus very diverse across the Nile Basin.

The contribution of tributaries to the main Nile can be divided into two main types: flood discharge and sediment discharge. Regarding flood discharge, two main periods are distinguished: high flow months and low flow months. Prior to the building of the main dams, the Blue Nile and Atbara rivers provided most of the flood discharge during high flow months (respectively 68 and 22%), whereas the White Nile provided most of it (83%) during low flow months. The White Nile flood discharge was therefore critical for maintaining a perennial flow of the Nile (Williams, 2020; Williams, 2019). Regarding sediment discharge, most of the total sediment load of the Nile comes from the Blue Nile (61%) and Atbara (36%) (Williams, 2019).

This brief summary of the characteristics of the Nile Basin shows that reconstructions of past environments along the northern end of the Nile Valley cannot be understood without the support of information on environmental changes in White Nile, Blue Nile and Atbara.

Palaeoenvironments in the Main Nile Valley During MIS 2

General Data on the Late Pleistocene Main Nile and Its Tributaries

Major comprehensive reviews for the late Quaternary environmental changes in the Nile Basin have been recently

published (e.g., Woodward et al., 2007; Williams, 2019; Williams, 2020). The aim here is to briefly review the available and most recent palaeoenvironmental data relevant for a study of human occupation and population dynamics in the northern end of the Nile Valley during MIS 2.

MIS 2 was generally drier and colder than present in the Nile Basin, with peaks of aridity during the LGM and HS 1. The Late Pleistocene Blue Nile was a highly seasonal river, similar to the modern Atbara, and was characterized by a reduced annual discharge while keeping a high carrying capacity and transporting coarse sand and gravels until its alluvial fan in Central Sudan (Williams, 2020; Williams, 2019, 93). In the Atbara headwaters region, the small cirque glaciers on the highest mountains associated with lower temperatures caused the river to be even more seasonal than nowadays, transporting coarse debris. Regarding the White Nile, very high floods are documented at *ca.* 27 ka (Williams et al., 2010; Williams, 2019, 113). However, for most of MIS 2 and until 14.7 ka, the White Nile was cut off from its main source, Lake Victoria (Johnson et al., 1996; Talbot et al., 2000; Williams et al., 2006; Williams et al., 2015), and may have virtually ceased to flow during the LGM (Williams, 2020; Williams, 2019, chapter 14). Because the water discharge of the main Nile during low flow months is dependent on the contribution of the White Nile, perennial flow throughout the year of the main Nile during MIS 2, and particularly during the LGM, was probably jeopardised.

At the other end of the Nile Basin, the Nile Delta Project within the Mediterranean Basin (MEDIBA) project has conducted intensive geological coring across the northern Delta and documented subsurface (located from 3 to 45 m deep) Late Pleistocene deposits dated to >35–12 ka (Stanley et al., 1996, **Table 2**). These deposits are interpreted as sands of alluvial, aeolian or shallow marine origins, interfingered with thin and localized floodplain and playa muds (Stanley and Warne, 1993; Warne and Stanley, 1993). While different origins have been identified for these Late Pleistocene muds, most of them are interpreted as relating to deposits occurring in seasonally flooded depressions in the vicinity of the Nile channels, in a context of low sea levels (Chen and Stanley, 1993). Radiocarbon ages (n = 46) associated with Late Pleistocene muds span the entirety of MIS 2 with their deposition generally occurring >34 ka, *ca.* 28-22 ka and *ca.* 16->10 ka uncal BP, whereas evidence for deposition during the interval between 16 and 22 ka uncal BP is limited (Chen and Stanley, 1993, 560 and fig. 12). Similarly, sand deposits dated to >35–11 ka uncal BP are interpreted as braided river deposits (Chen et al., 1992) but the (dis)continuity of their deposition throughout MIS 2 remains difficult to evaluate, as are their implications and relationship with what happens upstream from the Nile Delta (Butzer, 1997, 167). Late Pleistocene deposits have since been identified in drilling projects in northern Egypt focusing on the Holocene (e.g., Hamdan et al., 2019).

Geological cores in the eastern Mediterranean show that sediment input from the Nile during the LGM, while present, is highly reduced compared to previous periods (e.g., Revel et al., 2010). These data are consistent with a Nile that continued to flow during MIS 2, but possibly only seasonally or during major flood events. Element analyses of core sediments from the eastern Mediterranean confirm a negligible input from the White Nile, vs. an input from the Blue Nile and Atbara, and indicates an increase of Saharan dust input during the LGM (Revel et al., 2010; Revel et al., 2015). A recent high-resolution multi-proxy study of a sediment core from the eastern Mediterranean (Castañeda et al., 2016) documents the most severe period of aridity in the Nile Basin in the past 28,000 years, after the LGM, during the second phase of HS 1, ca. 16-14.5 ka (HS 1b).

From 14.5 ka, the Mediterranean sea level starts to rise again and several proxies, such as pollen data and lake levels, indicate wetter conditions over at least some areas of eastern Africa, in two phases *ca.* 14.5 and *ca.* 11.6 ka (e.g., Williams et al., 2006; Gasse et al., 2008; Foerster et al., 2012). In particular, the abrupt return of precipitation over eastern Africa *ca.* 14.5 ka led to an overflow of Lake Victoria into Lake Albert, the Ugandan headwaters of the White Nile, which triggered high floods in the White Nile Valley as well as at the northern end of the Nile Valley (Williams et al., 2006). These data are mirrored by data from the Delta, indicating a marked increase in the sedimentary input of the Blue Nile and Atbara in Delta sediment cores (Ducassou et al., 2009; Revel et al., 2015), with evidence for high floods in the Delta *ca.* 15–10 ka (Ducassou et al., 2007; Ducassou et al., 2009). However, millennial-scale episodes of aridity are noted, such as one *ca.* 13-12 ka before a return to humid conditions *ca.* 12 ka (Revel et al., 2015). Maximum Nile flow is documented in the Delta at that time leading to the deposition of an organic-rich dark layer known as Sapropel 1 in the Delta *ca.* 9.5-7 ka (Ducassou et al., 2007).

The Late Pleistocene Main Nile in Southern Egypt and Nubia

The late Pleistocene geological evolution of the main Nile, in Egypt and Nubia in particular, has been the subject of major work (e.g., Said, 1981; Said, 1993; Hamimi et al., 2020). At the regional scale, research projects conducted in numerous districts of Nubia (Sandford and Arkell, 1929; Sandford and Arkell, 1933; de Heinzelin, 1968), in the mouth of Wadi Kubbaniya (Schild et al., 1989; Wendorf and Schild, 1989), in the Kom-Ombo plain (Butzer and Hansen, 1968; Butzer, 1980), in the El Kihl (north of Edfu) and Esna areas (Wendorf and Schild, 1976) and in the Sohag area in Middle Egypt (Paulissen and Vermeersch, 1989; Vermeersch et al., 1989; Vermeersch, 2000; Vermeersch, 2002a), enabled reconstruction of the geology of the Egyptian Nile Valley during the Pleistocene (see also reviews in Paulissen and Vermeersch, 1987; Wendorf and Schild, 1989; Butzer, 1997). However, the general chronology is not well known, as many radiocarbon dates are considered too young (Wendorf et al., 1979). In addition, correlations between the geological formations of the different parts of the Nile Valley remain problematic (see **Figure 2** and discussions in Paulissen and Vermeersch, 1987; Schild et al., 1989; Butzer, 1997).

Two main models are currently proposed for the Late Pleistocene main Nile based on geological data from southern Egypt. The first model suggests the presence of a slowly aggrading highly seasonal braided river, and is hereafter referred to as the braided river model (Schild et al., 1989; Wendorf and Schild, 1989; Schild and Wendorf, 2010). The second model suggests that

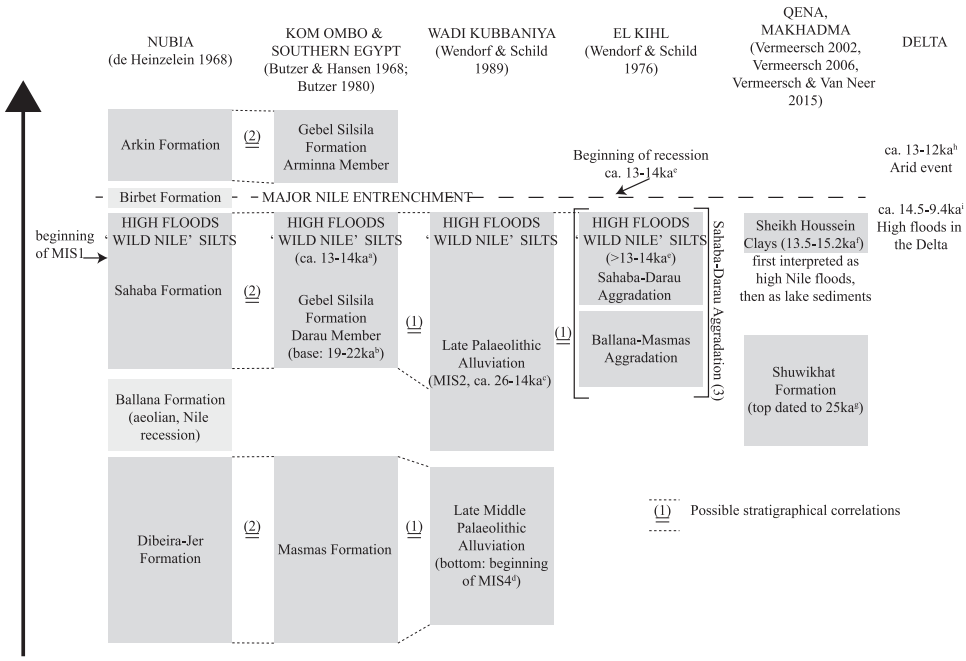

FIGURE 2 | Overview of main geological formations and their proposed correlations in the Lower Egyptian Nile Valley. All dates in the figure are in cal BP and were calibrated with two sigma ranges using Intcal20 (Reimer et al., 2020) for terrestrial or Marine20 (Heaton et al., 2020) for marine samples and Calib v. 8.1.0 (Stuiver and Reimer, 1993) 1) Correlations proposed in Wendorf and Schild (1989) 2) Correlations proposed in Butzer and Hansen (1968) and Butzer (1980) 3) Proposed name in Paulissen and Vermeersch, 1987, 46 [a]Dark silts at New Ballana I dated to 11,720 ± 195 BP (Hv-1264) and 12,000 ± 120 BP (Y-1446) (Butzer and Hansen, 1968), 115) but they are uncorrected for fractionation and may be too young (Butzer, 1997), 161) [b]Date of the base of the Gebel Silsila Formation at Kom Ombo, dated to 17,000 ± 600 BP (I-297) (Butzer and Hansen, 1968), 114) [c]The base of the Late Palaeolithic Alluviation at Wadi Kubbaniya is dated to 20,690 ± 280 BP (SMU-1037) and the top to 12,430 ± 100 BP (SMU-1032) (Haas, 1989) [d]The chronological attribution of the Late Middle Palaeolithic Alluviation is discussed in detail in (Schild et al., 2020) eThe beginning of the recession of the Nile at the site E71P5 (Late Isnan) at El Kihl is dated to 11,560 ± 180 BP (I-3760) (Wendorf and Schild, 1976, 179), which means that the preceding high floods documented at the area must be older [f]The Sheikh Houssein Clays (Paulissen and Vermeersch, 2000; Van Neer et al., 2000) are dated between 12,570 ± 80 BP (GrN-12033) and 12,060 ± 280 BP (GrN-12029). [g]Burnt clay from the Shuwikhat Formation (Paulissen and Vermeersch, 2000) was dated by thermoluminescence (Vermeersch et al., 2000) to 25,000 ± 2500 BP (Ox85TLi), which is considered as a minimum age (Vermeersch, 2020).[h]Isotope data from marine core MS27PT indicating an arid episode between 10,835 ± 40 BP (corrected age, SacA16516) and 11,495 ± 40 BP (corrected age, SacA16517) (Revel et al., 2015). NB: these ages were calibrated using the Marine20 curve. [i]Sedimentary features in cores from the Nile deep-sea turbidite system indicate high Nile floods during early MIS1. The chronological range given is based on two dates from core 84MD637 (Ducassou et al., 2007; Ducassou et al., 2009); 12,670 ± 50 BP (corrected age, SacA004998) and 8,800 ± 35 BP (corrected age, SacA004997). NB: these ages were calibrated using the Marine20 curve.

the Nile was dammed by sand dunes at several places along the Nile Valley, thus creating large lakes favourable for human occupation, hereafter referred to as the lake model (Vermeersch and Van Neer, 2015). These models and their different implications for human groups living in the Nile Valley are briefly summarized below.

The braided river model is extensively described in the second and third volume of *The Prehistory of Wadi Kubbaniya* (Schild et al., 1989; Wendorf and Schild, 1989). The data on which the model relies result from several years of archaeological and geological fieldwork at Wadi Kubbaniya. MIS 2 (or Late Palaeolithic) deposits at Wadi Kubbaniya lie in disconformity above MIS 4 (or Late Middle Palaeolithic) deposits (Schild et al., 2020). MIS 2 deposits in the mouth of Wadi Kubbaniya can be described as follows (after Schild et al., 2020; Schild et al., 1989; Wendorf and Schild, 1989):

- A series of silts (Lower Kubbaniyan silts) interfingering and interstratified with aeolian sands (Dunes). These are interpreted as evidence for a dune encroachment creating a dune barrier across the mouth of the wadi that favored accumulation of Nilotic overbank silts.
- The wadi floor is characterized by a flat silty plain (Fronting Plain), probably made of Lower Kubbaniyan clayey silts and clays. Above these silts and a vertisol, there is a bed of clayey lacustrine silts which is interpreted as having formed in a temporary pond within an interdunal basin.
- At several localities of the mouth of Wadi Kubbaniya (main Dune field, embayment, bay area), a series of white-to-grey silts, marls and diatomites (Upper Lacustrine Series) is observed. They are interpreted as lacustrine sediments, relating to a lake that would have formed when the expansion of the dune field completely closed the wadi mouth before 13 ka BP (or before 15 ka cal BP).
- A series of silts (Upper Kubbaniyan silt) interpreted as Nilotic overbank silts deposited in the context of exceptional high floods overlie the Upper Lacustrine Series. A correlation with the high floods documented at

the beginning of MIS 1 (or 'Wild Nile', Butzer, 1980) is proposed.
- A lack of evidence for wadi run-off during MIS 2 suggests that the wadi was not active and that the desert was hyper-arid during the whole period.

Based on these data, Schild et al. (1989) and Wendorf and Schild (1989) develop a model according to which the main Nile during MIS 2 was a seasonal braided river with a reduced stream competence and an increased sediment load. Renewed precipitation during the rainy season in the Nile headwaters would be responsible for high floods in southern Egypt and would lead to the deposition of the overbank silts identified at Wadi Kubbaniya. This model is consistent with the data available from the Delta, suggesting a continuous albeit very reduced sediment input from the Nile during MIS 2 (Revel et al., 2015). A correlation based on petrological compositions has additionally been proposed between the Late Pleistocene aggradation (Sahaba-Darau corresponding to the Late Palaeolithic Alluviation at Wadi Kubbaniya, see **Figure 2**) and some Late Pleistocene deposits from the Nile Delta, which are interpreted as evidence for the presence of a seasonal braided river in the Delta plain (Chen et al., 1992, 568–569; Stanley and Warne, 1993, 631). However, the exact relationship between the Late Pleistocene Delta sequence and the Nile River system upstream of the Delta is unclear (Butzer, 1997). In particular, sea level variation is an important geological factor in the development of Delta sequences (e.g., Warne and Stanley, 1995), and their relatively coarse chronological resolution for the Late Pleistocene (>35-11 ka uncal BP, see Stanley et al., 1996, **Table 2**) makes direct chronological correlation difficult.

The lake model was first described by Vermeersch and colleagues (2006) and further detailed by Vermeerch and Van Neer (2015). They argue that the aeolian and Nilotic deposits in the main Nile Valley can be interpreted in terms of a lake model. The lake model hypothesizes that enhanced dune activity associated with reduced Nile flow during MIS 2, and especially during the LGM, would have favored the presence of dune dams over the Nile, creating large lakes. Such lakes would have offered a favourable environment for human occupation all-year round (Vermeersch and Van Neer, 2015). The authors' main objections to the braided river model is that there is no evidence for major alluvial deposits in the Nile Valley such as those expected in the braided river model, and that there is no evidence for channel deposits at Wadi Kubbaniya (Schild et al., 1989, 91). Damming of water courses by sand dunes are well-documented in similar contexts (e.g., in the Negev, Goring-Morris and Goldberg, 1990 and see below; or at Wadi Kubbaniya itself, see above and Schild et al., 1989), and satellite images show that similar processes may have occurred at different locations along the Nile Valley (Vermeersch and Van Neer, 2015; **Supplementary Information 3**). Dune activity would have been possible due to strong winds, lack of vegetation and abundant sand supply (e.g.,, from the Delta area, which was at the time a sparsely-vegetated plain, Vermeersch and Van Neer, 2015; or from previous high floods of the Nile, leading to the transport of large quantities of sand and subsequent evaporative events, as is documented in the White Nile Valley, Williams, 2019, 113). Data from fish 'ear-stones' (otoliths) found at the archaeological site of Makhadma 4 indicate that hydroclimatic conditions during MIS 2 were different from both modern and expected pre-Aswan dam Nile conditions and would be consistent with the lake model (Dufour et al., 2018).

In the context of the lake model, deposits in the area of Makhadma (Sheikh Houssein Clays, see **Figure 2**), interpreted as high Nile deposits are re-interpreted as suspension deposits, that would have occurred in the setting of a lake environment. Schild and Wendorf (2010) have objected to this model arguing that deposits at Makhadma are not typical of lacustrine deposits, as they are lacking calcareous marls or diatomites. Vermeersch and Van Neer (2015) responded to this by indicating that their model implies a dynamic landscape. The lakes were not permanent lakes *per se* and the dune dams were occasionally breached by a stronger Nile flood, but would have reformed quickly afterward, recreating a lake at a slightly different location. Such a process is not favourable to the formation of calcareous marls or diatomites. Vermeersch and Van Neer (2015) propose that the geological data at other locations (near Esna, or at Wadi Kubbaniya) may also be reinterpreted in terms of the lake model (Vermeersch and Van Neer, 2015).

This model would also be consistent with available data from the Delta, if we consider that the reduced sediment input documented in geological cores in the eastern Mediterranean (Revel et al., 2015) and part of the Late Pleistocene sequences documented in the Delta (Stanley and Warne, 1993; Warne and Stanley, 1995) were deposited during occasional major floods that would have breached the sand dune dams.

Further field data are thus needed to confirm one or the other model. However, because both models are connected to evidence for human occupation, they imply availability of fresh water and habitability of the main Nile Valley during MIS 2. In addition, both models suggest similar mechanisms of water courses dammed by encroaching sand dunes. They differ in that the braided river model implies that sand dunes did not dam the Nile but rather only specific locations such as the mouth of wadis (e.g., at Wadi Kubbaniya), whereas the lake model implies damming of the Nile itself. The braided river model implies that the floodplain become inaccessible during the flood season, whereas the lake model implies habitability in restricted–but dynamic–zones (lakes) in an overall more stable environment. Nonetheless, because the Nile would have been a seasonal river in the braided river model, or would have resumed its course only during major Nile floods in the lake model, it can be inferred from both models that dammed lakes or seasonally filled depressions on the floodplain would have been attractive and predictable environments for human groups, particularly during the dry season.

After MIS 2, evidence for major floods (or 'Wild Nile', Butzer, 1980) corresponding to the overflow of eastern African lakes *ca.* 14.5 ka cal BP are documented at several locations along the Nile Valley (**Figure 2**). These floods would have created important environmental changes and may have been catastrophic for human populations living in the Nile Valley (Connor and Marks, 1986; Kuper and Kröpelin, 2006; Schild and Wendorf,

2010; Vermeersch and Van Neer, 2015). However, Butzer (1997) suggests that it is the subsequent incision of the Nile (**Figure 2**), broadly coeval with the Younger Dryas (*ca.* 12.8-12 ka), rather than the high floods, that would have presented a major adaptation challenge to human groups living in the Nile Valley.

Palaeoenvironments in the Main Nile Valley and Neighboring Regions During MIS 2: Indirect Evidence for Environmental Refugia or Dispersal Corridor?

In order to consider the hypotheses of the main Nile Valley as an environmental refugium or corridor for dispersals during MIS 2, the palaeoenvironmental data from neighboring regions must also be considered (see **Table 1**). In particular, the available records from northern Egypt, the southern Levant, and the deserts adjacent to the Nile Valley will be reviewed below in order to discuss whether the Delta, Sinai and Negev or eastern Sahara could have been crossed by human populations at the end of the Pleistocene.

When looking at local and regional palaeoenvironmental records, few well-dated records are available but several indicate that some areas were wetter than today during part of MIS 2. For example, fine-grained valley fills in the Sinai suggest that low-energy stream channels during times of prolonged but gentle winter rains existed in the Sinai during the late Pleistocene (Williams, 2019), whereas spring-fed tufa deposits are documented in the Eastern Desert of Egypt and Sinai during the late Pleistocene until *ca.* 22 ka (Hamdan and Brook, 2015). Wetter conditions are also suggested at Sodmein Cave, in the Red Sea Mountains, *ca.* 25 ka (D layer, Moeyersons et al., 2002). The Negev desert was characterized by arid (in the northern part) to hyper-arid (in the southern part) conditions (Enzel et al., 2008). A major phase of dune activity, probably related to the high-velocity winds generated by deep Cyprus Lows over the Eastern Mediterranean (Enzel et al., 2008), is documented in the northwestern Negev in the second part of MIS 2 (23-11.5 ka), with three distinct episodes broadly coeval to the LGM, HS1 and the Younger Dryas (YD) (Goring-Morris and Goldberg, 1990; Roskin and Tsoar, 2017). Dune encroachment sometimes led to damming wadis and the creation of seasonal ponds, creating environments favourable for vegetation growth, attracting animals and thus human groups (Goring-Morris, 2017).

During MIS 2, the lowering of the sea level led to an incision of the Nile starting around Qena (nick point, Sandford, 1936; Wendorf and Schild, 1989). No archaeological evidence dated to MIS 2 is available from the northern part of Egypt (north of Dishna). Geological deposits from this period and associated archaeological remains are thus either absent or buried under several meters of sediments accumulated by the Nile in parallel with the rise of the sea level. One main issue when discussing whether the Nile Valley acted as a corridor during MIS 2 is whether the Nile Delta was habitable. However, it is important to consider that the sea shore during most of MIS 2 was several kilometres northwards, and up to 50 km to the north during the LGM and maximum sea low stand (Stanley and Warne, 1993). Late Pleistocene deposits dated to MIS 2 documented in what is today the Nile Delta, was thus located well upstream from the sea shore. They show evidence for Nile floods and the presence of seasonal ponds, but the evidence is limited for the LGM in particular (Chen and Stanley, 1993; Stanley and Warne, 1993). Based on the characteristics of the mud deposits and their distribution in the Nile Delta, Chen and Stanley (1993) and Stanley and Warne (1993) suggest that the region during the Late Pleistocene was mostly a minimally-vegetated plain with seasonally active braided channels and ephemeral ponds in a generally arid environment. In addition, the composition of the Late Pleistocene Nile deposits in the Delta are consistent with the hypothesis that the Delta constituted the primary source of sand for the Negev-Sinai erg (Muhs et al., 2013). Punctuated human occupation of what is now the Nile Delta in the Late Pleistocene may therefore have been possible but it remains to be confirmed, particularly during the LGM.

West of the Nile Valley, the eastern Sahara was hyper-arid during MIS 2 and until after the Younger Dryas (i.e., after 12.8 ka, Kuper and Kröpelin, 2006). However, at Kharga and Dakhleh, in the Western Desert of Egypt, the presence of tufa deposits and lacustrine sediments where freshwater snails (which can only survive in abundant fresh water lakes) are found, are past evidence for several phases where surface water was present in the now hyper-arid Western Desert of Egypt (Nicoll et al., 1999; Skinner et al., 2013). Tufa deposits were formed during times of alkaline spring discharge, the latter likely linked to a high groundwater table in the Nubian Sandstone Aquifer (Nicoll et al., 1999; Skinner et al., 2013). Electron Spin Resonance (ESR) dates on shells and mammalian teeth suggest the presence of surface water in Kharga and Dakhleh during several phases of the Late Pleistocene, including during MIS 2 (Blackwell et al., 2012; Blackwell et al., 2017; Skinner et al., 2013; Kleindienst et al., 2016; Kleindienst et al., 2020). These MIS 2 dates are consistent with evidence for groundwater recharge of the Nubian Sandstone Aquifer during late MIS 3 / the first part of MIS 2 (pre-LGM) (e.g., Pachur and Hoelzmann, 1991; Abouelmagd et al., 2014). Isotopic composition of older (>MIS 3) fossil water in the Western Desert has been linked to precipitation brought by westerly winds (Sultan et al., 1997). Westerly winds may be dominant across the northern Sahara during glacial periods (Williams, 2019, 244), and a similar origin may be hypothesized for the groundwater recharge of the Nubian Sandstone Aquifer during MIS 2.

Despite a reduced flow and its possible transformation into a more seasonal river, this short review shows that the main Nile never ceased to flow for a long period of time. Survival during the dry season and dry periods of MIS 2 may have been possible around lakes created by the damming of the Nile by sand dunes or interdunal ponds. Favourable conditions for human occupation therefore existed in at least part of the Lower Nile Valley during MIS 2 as well as in several other localized areas over northeastern Africa and the southern Levant (e.g., around lakes fed by wadis or local springs). These localized environmental refugia occur in an otherwise hyper-arid environment, which characterizes the Sahara during MIS 2 as well as probably what is nowadays the Nile Delta. However, based on palaeoenvironmental data alone, the available geographical and chronological resolution of the

data does not yet allow us to determine whether the Nile Valley facilitated a free passage to the Sinai-Negev or the rest of northern Africa at that time.

ARCHAEOLOGICAL EVIDENCE FOR HUMAN OCCUPATION OF THE NILE VALLEY DURING MIS 2

General Data on the Late Palaeolithic of the Main Nile Valley

Numerous archaeological sites are dated to MIS 2 in the main Nile Valley, most of which are surface occurrences of bone fragments and lithic artefacts. Based on the characteristics of the lithic artefacts, i.e., the production of flakes and elongated products (blade/lets) of small dimensions associated with a toolkit including high proportions of backed tools, they are attributed to the Late Palaeolithic. The Late Palaeolithic (*ca.* 25-12 ka) in north-eastern Africa follows the Upper Palaeolithic (with scarce sites dated to *ca.* 50-25 ka), and precedes the Epipalaeolithic in the Egyptian Nile Valley and Egyptian Eastern Desert (with sites dated from *ca.* 9 ka cal BP, Vermeersch, 2012), the Early Neolithic in the Western and Eastern Desert of Egypt (from *ca.* 10 ka cal BP, Wendorf et al., 2001; Gatto, 2012) and the Mesolithic in the Sudan (from *ca.* 11 ka cal BP, Honegger, 2019). The Late Palaeolithic in north-eastern Africa is coeval with the Epipalaeolithic in the Levant, the Iberomaurusian/Later Stone Age in northern Africa and the Later Stone Age in other African regions. This constellation of terminologies and the use of the same terms to designate different periods in different regions make comparisons at the macro-regional scale difficult.

Late Palaeolithic sites in north-eastern Africa are located mostly in southern Egypt and Nubia. Most sites were discovered during prehistoric investigations as part of the Nubia Campaign which began in 1961–1962, (Schild and Wendorf, 2002) and archaeological expeditions that followed, until the end of the 1980s. This leads to a record biased toward certain geographical areas (in particular, the location of the Aswan Dam in northern Nubia), although geomorphological reasons also explain why virtually no Late Palaeolithic sites are known north of Qena (see also *The Late Pleistocene main Nile in southern Egypt and Nubia* section). The only possible occurrences of Late Palaeolithic assemblages in northern Egypt are in the region of Helwan, near Cairo, where P. Bovier-Lapierre at the beginning of the 20th century (Bovier-Lapierre, 1926) and F. Debono in 1936 (Debono, 1948; Debono and Mortensen, 1990, 9–11) noted several surface occurrences or 'stations' of material that they attribute to the end of the Palaeolithic. In a later reassessment of Debono's surface collections, Schmidt (1996) attributed Debono site 7 'ostrich' to the Late Upper Palaeolithic and published two dates on ostrich eggshell fragments of *ca.* 18 ka BP (or *ca.* 21–23 ka cal BP). Schmidt (1996) also mentions several localities with microlithic artefacts that he attributes to the Epipalaeolithic, although it is unclear whether this refers to the Epipalaeolithic or Late Palaeolithic. Recent research in the Nile Delta has also reported the presence of Epipalaeolithic assemblages (Rowland and Tassie, 2014; Tassie, 2014). However, with the exception of the two dates on ostrich eggshell fragments which must be considered with caution as these are surface finds, the Late Palaeolithic or Epipalaeolithic surface occurrences in the Nile Delta are poorly dated and may not in fact date to MIS 2 (see discussion below).

In southern Egypt and Nubia, where most Late Palaeolithic sites are found, the archaeological record shows evidence for variability in subsistence behaviors, which may correspond to different seasons of the year. Many sites document subsistence based on fishing, with numerous fish remains, mainly belonging to the Clariidae (e.g., *Clarias* sp.) and Cichlidae (e.g., tilapias) families that prefer shallow waters and could be fished at the beginning and end of the flood season, or even after the flood season when some fish can survive in residual pools that remain on the floodplain (Van Neer et al., 2000). A variety of fishing methods may have been used depending on the season, and in particular there is archaeological evidence for the use of small double-pointed bone hooks (Van Neer and Gautier, 1989; Van Neer et al., 2000). In addition, at Makhadma 4 (Van Neer et al., 2000), the association of high densities of fish bones with black archaeological layers showing an abundance of charcoal and the occurrence of post-holes may suggest the use of curing strategies such as fish smoking at the site. Other sites document subsistence based on large-game hunting. The most common hunted species are hartebeest, aurochs and (Dorcas) gazelles (Linseele and Van Neer, 2010; Coudert, 2013; Yeshurun, 2018). Occasionally, hippopotamus hunting is documented (e.g., on the Kom Ombo plain), and this high-risk hunting may have been related to activities other than strictly subsistence-based ones (Yeshurun, 2018). There is also archaeological evidence for plant (tubers) processing, through the use of grinding implements, e.g., at Wadi Kubbaniya (Roubet, 1989a; Roubet, 1989b).

Beyond subsistence-based behaviors, several rock art panels attributed to the Late Palaeolithic have been documented in localities near Kom Ombo, in Qurta and Abu Tanqura Bahari at el-Hosh (Huyge et al., 2007; Huyge et al., 2011; Huyge, 2009; Huyge and Claes, 2015) and near Aswan, in Wadi Abu Subeira (Storemyr et al., 2008; Kelany, 2012; Graff and Kelany, 2013; Kelany, 2014; Kelany et al., 2015). These rock art panels had previously been noticed in 1962–1963 by the Canadian Prehistoric Expedition (e.g., Smith, 1967; Smith et al., 1985) during the investigation of Late Palaeolithic sites on the Kom Ombo plain. Rock art at these localities comprises a very homogeneous group of panels characterized by the use of hammering and incision to represent large animal figures in a naturalistic style. Bovid (aurochs) figures are dominant, followed by birds, hippopotami, gazelle, fish and hartebeest. Highly stylized human figures are also present in Qurta and Abu Tanqura Bahari (Huyge, 2009; Huyge, 2018). Because these representations are very different in style from what is known for later periods (e.g., Huyge, 2005), and because they are characterized by a dark patina and rock varnish associated with intense weathering, a Late Pleistocene age was proposed (Huyge et al., 2007) and later confirmed by the OSL (Optically-Stimulated Luminescence) dating of sediments covering rock art panels at Qurta II (Huyge et al., 2011). These suggest a minimal

age of 15 ka. Due to the vicinity of the Qurta localities to several Late Palaeolithic sites in the Kom Ombo area, Huyge and colleagues (2007, 2011) suggest an association with a particular entity of the Late Palaeolithic, the Ballanan-Silsilian (**Table 2**). It is also interesting to note that these sites are located not far (on the opposite bank of the Nile) from one of the main Late Palaeolithic site clusters, Wadi Kubbaniya (Wendorf et al., 1989).

Finally, several cemeteries are attributed to the end of the Late Palaeolithic; one of the best documented is site 117 in Jebel Sahaba (Wendorf, 1968). These cemeteries are well-known for showing evidence for inter-personal violence, several individuals bearing marks consistent with parry fractures or with lithic artifacts still embedded in their bones (Wendorf, 1968; Greene and Armelagos, 1972). Evidence from these cemeteries is detailed further in *Human fossil and genetic data: evidence for a return to Africa during MIS 2?* section.

Geographical and Chronological Patterns of Human Occupation in the Lower Nile Valley During the Late Palaeolithic

Although a few well-preserved archaeological contexts enable us to have a glimpse of Late Palaeolithic lifeways in the main Nile Valley, most of the archaeological record consists of surface occurrences of stone artefacts. The variability observed in lithic assemblages has led to their grouping into different basic cultural taxonomic entities or industries (see **Table 2** and Schild and Wendorf, 2010). Most of these entities were defined in the 1960s–1970s based on typological characteristics (types of cores and finished tools) and were thought to represent different adaptations by different groups to the Nilotic environment (e.g., Schild and Wendorf, 2010, 116). A few recent studies aiming to study lithic variability in the Late Palaeolithic from a technological perspective have questioned the characteristics of some of these entities or the integrity of the assemblages used to define them (e.g., Paulissen and Vermeersch, 1987; Vermeersch, 2000; Usai, 2008; Usai, 2020; Leplongeon, 2017). However, the validity of the use of this chrono-cultural system for the Late Palaeolithic in the Nile Valley and its implications for reconstructing past human behaviors or human interactions has rarely been called into question. In the current research context aiming to contribute to the reconstruction of past population dynamics both from an archaeological and genetic perspective, evaluating the relevance of the current cultural taxonomic system in use is a fundamental step that remains to be done, as is the case for (most) other regions (e.g., the Upper and Late Palaeolithic in Europe; Reynolds and Riede, 2019; Riede et al., 2019).

Keeping in mind this caveat, a systematic literature review was conducted in order to investigate geographical and chronological patterns of human occupation in the Lower Nile Valley during the Late Palaeolithic, with the aim of creating an inventory of all published sites attributed to this period (**see Supplementary Information 1a–d**). The attribution of sites to specific entities or industries was kept in order to provide an overview of the archaeological record as it is currently classified.

This inventory was undertaken in parallel with the creation of the database for the 'Big Dry' Project, coordinated by Prof. François Bon and funded by the French National Research Agency (ANR). All data used in this paper are presented in the supplementary information (**see Supplementary Information 1a–d**). The definition of a 'site,' particularly when dealing with surface material in desert areas, is a matter of debate (see discussion in Phillips et al., 2017). In the context of this paper, the designation used by the excavators was retained. Only in cases where different areas of a site (localities) were assigned to different taxonomic entities were these areas considered as separate sites. For example, site 8,905 is divided into several localities but all are attributed to the Qadan, and it was thus considered as a single site. Conversely, site E71P1, located in the Edfu area (Wendorf and Schild, 1976), consisted of material collected at four arbitrarily-defined localities, two of which were later attributed to the Kubbaniyan and two others to the Levallois Idfuan, therefore E71P1 is considered here as two sites. Only sites with an–even limited–description of the context (location, geological description) were included in the database. This resulted in the exclusion of the surface occurrences in the Nile Delta surveyed in the first part of the 20th century and mentioned above, since no description of the geological setting of the sites is available. Similarly, and despite the presence of geological descriptions, the seminal work of Vignard (1928); Vignard (1955) on the plain of Kom Ombo could not be included in the database as Vignard's survey methods do not allow the identification of sites. Sites where only surface and limited subsurface material was found (usually less than 10 cm below the surface) were considered as having only one 'archaeological' layer. Only in the case of sites with stratified evidence for multiple layers were sites divided into two or more archaeological layers. Absolute dates associated with the archaeological layers were also systematically collected in the database. All of the steps and arguments used to retain or reject each date are described in the supplementary material (**Supplementary Information 1a–d**).

The detailed literature review shows that a total of 151 sites located in southern Egypt and Egyptian and Sudanese Nubia–corresponding to 168 archaeological layers–are attributed to the Late Palaeolithic (see **Table 3**). Their distribution (see **Figure 3**) shows clear concentrations within southern Egypt and Nubia, which reflect the history of research in the area.

The most common Late Palaeolithic industries (based on the number of archaeological layers attributed to them, see **Table 3**) are the Qadan, Kubbaniyan, Sebilian, Isnan, Ballanan-Silsilian and Halfan. Only a limited number of absolute dates are available (i.e., 120 dates), including 23 dates that are likely minimum or maximum ages, coming from 41 archaeological sites and two geological localities (see **Table 3**). Among the different industries defined for the Late Palaeolithic, only the Kubbaniyan is well-dated, with 47 dates coming from eight archaeological sites. This represents more than a third of all available dates for the Late Palaeolithic in the Nile Valley.

Other reasonably dated industries are the Afian, Isnan and to a lesser extent the Halfan. The Qadan is associated with a relatively

TABLE 3 | Number of sites, archaeological layers and dates for each industry for the Late Palaeolithic of the Lower Nile Valley.

Industry	Number of sites where the industry is represented	Number of archaeological layers	Number of sites with dates (incl. geological locations)	Number of dates (incl. minimum or maximum ages)**	Chronological range (this study)***
Shuwikhatian/Idfuan	6	6	2	4 (4)	Min age of ca. 25 ka
Fakhurian	8	8	4 (1)	4 (1)	23–25.6 ka cal BP
Levallois Idfuan	3	3	1	4	19.7–22 ka cal BP
Gemaian	5	5	0	0	Undated
Kubbaniyan	16	25	8	47	**19.3–23.5 ka cal BP**
Halfan	15	15	5	6	**19–24 ka cal BP**
Ballanan-Silsilian	15	16	3	3 (1)	16.3–20.8 ka cal BP
Qadan[a]	22	22	3	13 (9)	**12–20.2 ka cal BP**
Afian	5	5	2	10	**14–16.8 ka cal BP**[b]
Isnan	19	19	6 (1)	9 (2)	**13.2–16.6 ka cal BP**
Sebilian	18	19	2	5	12.6–16.9 ka cal BP
Arkinian (excl. El Adam)	1	2	1	2	11.9–12.8 ka cal BP
Late Palaeolithic – Miscellaneous	23	23	6	13 (6)	11.2–23.9 ka cal BP
TOTAL	**156***	**168**	**43 (2)***	**120 (23)**	

These totals differ from the total number of archaeological sites. The total of 156 correspond to 151 archaeological sites including five sites where two industries are represented. 43 dated locations correspond to 41 dated sites plus two geological localities. ** the number of dates does not include dates that were rejected by the authors or for which the association with archaeological material was not sustained on stratigraphic grounds. * Only radiocarbon dates with error margins <1,000 and which did not represent minimum or maximum ages were taken into account. In bold are chronological ranges based on more than five dates.*

[a]Sites 34C, 605 and 621 were removed from the count of Qadan sites since these present clear signs of admixture (see review in Usai, 2008; Usai, 2020). It is probable that other sites attributed to the Qadan also represent mixed contexts (Usai, 2020).

[b]Although doubts were cast on the association of the site of Makhadma 4 to the Afian (Leplongeon, 2017), in the absence of detailed comparative analysis that would confirm or refute this association, in the context of this review, the site is attributed to the Afian.

high number of dates (N = 15), but most of them are minimum ages and come from one site, site 117 (Zazzo, 2014). The association of the cemetery at site 117 with the Qadan industry has been questioned (Usai, 2020). The Qadan lithic assemblages remain poorly described and several doubts have been raised about the mixed nature of some of the sites (e.g., discussion in Usai, 2008; Usai, 2020).

Previous studies (Vermeersch and Van Neer, 2015; Vermeersch, 2020) have shown two main periods of human occupation in the main Nile Valley during MIS 2, *ca.* 23-20 ka cal BP and ca. 16-14 ka cal BP. They correspond to the LGM and the second phase of H1, identified by Castañeda et al., 2016 as the most arid phase of MIS 2 in north-eastern Africa. These studies showed that virtually no human occupation is known after 14 ka cal BP in the Egyptian Nile Valley (Vermeersch and Van Neer, 2015; Vermeersch, 2020), but the picture is less clear in Sudanese Nubia (e.g., Butzer, 1997). The period 14-11 ka cal BP corresponds to major environmental changes that may have been catastrophic for human populations living in the Nile Valley (Butzer, 1997; Kuper and Kröpelin, 2006; Vermeersch and Van Neer, 2015).

To build on these studies (see also Nicoll, 2001, for radiocarbon dates of the Western Desert during the Holocene) and in order to explore the distribution of radiocarbon dates and associated Late Palaeolithic human occupations, a subset of the date database was created, where only dates directly associated with archaeological material were considered (i.e., minimum or maximum ages for human occupations were removed). In addition, dates with an error margin greater than 1,000 years were also removed (e.g., following Vermeersch, 2020 and see **Supplementary Information 1a,c**). The remaining dates (N = 91), all of which are radiocarbon dates, were then calibrated with two sigma ranges using the INTCAL20 calibration curve (Reimer et al., 2020) and Calib 8.1 (Stuiver and Reimer, 1993). To summarize the data and explore the temporal density of the available dates, a Kernel Density Estimate (KDE) was calculated, using the Rowcal package (McLaughlin, 2019) in R (R Core Team, 2020). The Rowcal KDE method uses a bootstrap method in order to take into account the error margin caused by the calibration process (McLaughlin, 2019, 481). KDE is one of the most effective ways to summarize radiocarbon dates and is particularly useful for exploring radiocarbon data when there is little information on the relative stratigraphic locations of the dates (e.g., Bronk Ramsey, 2017; McLaughlin, 2019). Because of the timespan considered (*ca.* 15,000 years) and the fact that the radiocarbon dates included in the dataset are mostly conventional dates with relatively large standard deviations, a bandwidth of 200 years was used in the model.

Figure 4 shows the resulting density graph. Unsurprisingly, as it is based on similar datasets to the ones used in previous studies (compare **Figure 4** with Vermeersch and Van Neer, 2015; **Figure 3**; Vermeersch, 2020; fig. 6.4 and Butzer, 1997; **Figure 2**), it shows similar results, with higher densities of dates during the LGM as well as during the second part of H1 (HS1b). However, it should be noted that the peak in dates corresponding to the LGM is mostly due to the numerous dates available for the Kubbaniyan, which represent more than half of the sample considered here (N = 47/91). The peak in dates between 15 and 14 ka cal BP is mostly associated with Afian and Isnan occupations. Because of the nature of our radiocarbon dataset, which includes an over-representation of the Kubbaniyan, and to a lesser extent the Afian and Isnan

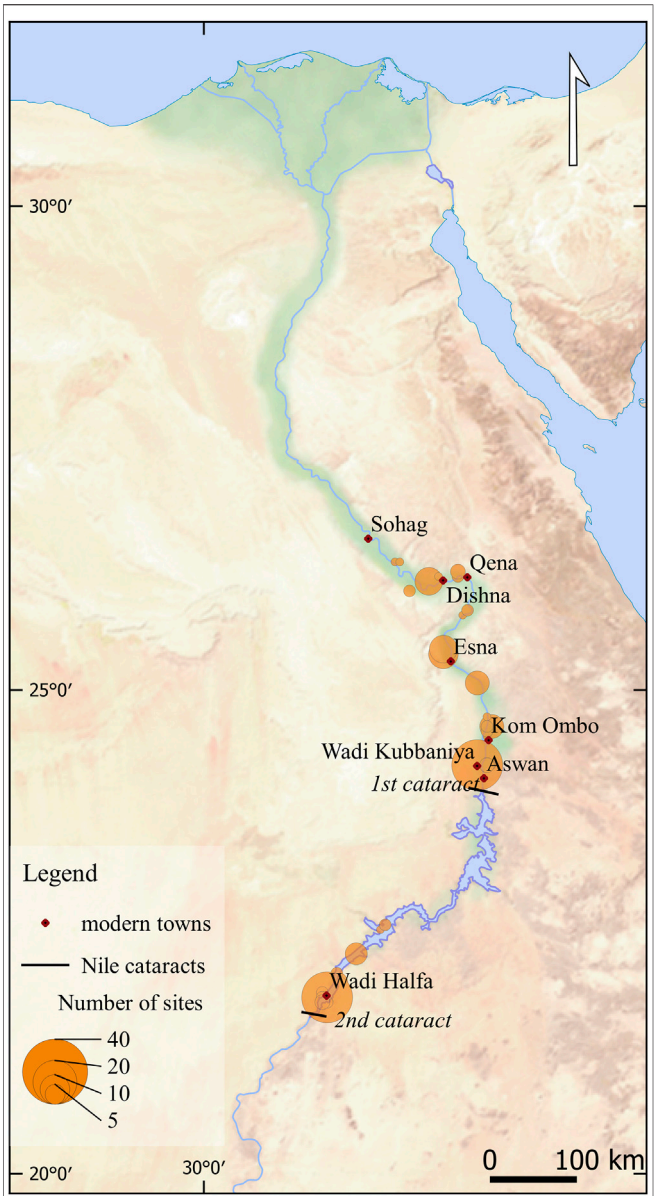

FIGURE 3 | Geographic distribution of Late Palaeolithic sites in the main Nile Valley. Number of sites were counted using a square grid with each square side measuring ca. 5 kms. Created in QGIS v. 3.15 (QGIS Development Team, 2017) using Natural Earth Data.

compared to the other industries (see **Table 3**), and because of the characteristics of the method chosen (KDE), these peaks show evidence for human occupation during these times but the low densities of dates between the two peaks cannot be interpreted as reflecting lower frequencies of human occupation in-between the LGM and the end of H1. Additional dates from other industries are needed in order to test this hypothesis.

In addition, the KDE graph shows that some dates fall within the range of 14-11 ka cal BP. When looking at the raw data (see **Figure 5**), this corresponds to 11 dates, coming from Qadan (8,905 – Tushka), Sebilian (1024A–Wadi Halfa and possibly Sebil VII–Kom Ombo), Isnan (Makhadma 2, El Abadiya 3 – Qena; E71P5 – Edfu) and Arkinian (DIW 1 – Wadi Halfa) sites, plus two sites (Makhadma 1, Qena; WK26, Wadi Kubbaniya) which were attributed to the Late Palaeolithic. In order to interpret the significance of these dates for the presence of human occupation in the Nile Valley in early MIS 1, it is useful to briefly review their geological context.

Only very limited information is available from Sebil VII (Smith, 1967), but most of the calibrated range of the date falls before 14 ka cal BP. The dated material from the sites of Makhadma 1, 2 and El Abadiya come from levels stratigraphically located within the Sheikh Houssein Clays (Paulissen and Vermeersch, 2000; Vermeersch et al., 2006). The site of WK26 (Banks et al., 2015) is located within the Upper Kubbaniyan silts (Schild et al., 1989). Both the Sheikh Houssein Clays and the Upper Kubbaniyan silts may relate to the same phase of high Nile floods at the very beginning of MIS 1. The stratigraphic location of the dated material thus suggests a probable age close to 14 ka cal BP and the date of El Abadiya 3 may be too young. In addition, the charcoal dated to 12,060 ± 50 BP (Beta-319442) at site WK26 was collected during a preliminary survey of the site in 2012, and differs significantly from the three other dates obtained during the 2014 excavations (PRI-14-041-1, PRI-14-041-2 and PRI-14-041-3 clustering *ca.* 13–13.5 ka BP or 15.5–17 ka cal BP). This may indicate two distinct periods of occupation at the site, or that the first date may be too recent.

Similarly, site 8,905 is associated with the top of the Sahaba Formation (Wendorf, 1968), which suggests a probable end-of-MIS 2 age (see **Figure 2**), and therefore that the date obtained from WSU-415b is too young, particularly when considering the other date available for the site, WSU-315 (14,500 ± 490 BP) which has a calibrated range between 16.3 and 18.7 ka cal BP (**Figure 5**; **Supplementary Information 1c**). The stratigraphic position of site 1024A is uncertain, but may relate to the end of the Sahaba Formation or the beginning of the Birbet Formation (Marks, 1968, 488 and see **Figure 2**). Similarly, E71P5, near Edfu, is associated with the incision (Birbet) immediately following the deposit of the Sahaba Formation (Wendorf and Schild, 1976; Wendorf et al., 1979 and see **Figure 2**). The site of Dibeira West 1 (DIW 1), near Wadi Halfa, is associated with the Arkin Formation, a short aggradational event following the Birbet Incision (Schild et al., 1968 and see **Figure 2**). Only these three sites (E71P5, 1020 A and DIW 1) have dates than can be linked with some certainty to the interval after 14 ka cal BP. This seems very few but all three sites are associated with rich lithic material, and in the case of DIW 1, it shows evidence for repeated occupation episodes (Schild et al., 1968). This suggests that human occupation may have occurred during early MIS 1 in the main Nile Valley in southern Egypt and Nubia.

Previous studies (Vermeersch and Van Neer, 2015; Vermeersch, 2020) have suggested that the lack of evidence for human occupation in the Egyptian Nile Valley after 14 ka cal BP may be related to profound environmental changes at that time. In the context of the lake model, these include high floods occurring at the beginning of MIS 1, leading to high lake levels and subsequent breaching of the sand dune dams that were responsible for the presence of the lakes. Here, the small

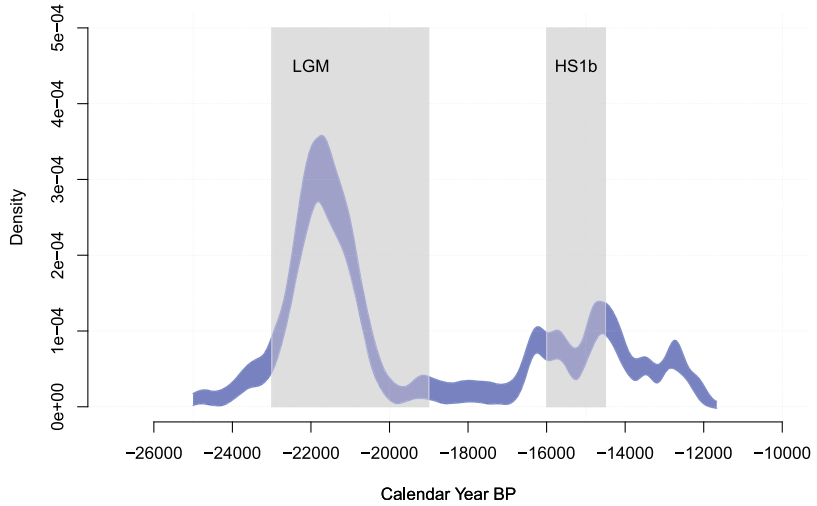

FIGURE 4 | Kernel Density Estimates for all available radiocarbon dates associates with human occupation attributed to the Late Palaeolithic (see **Supplementary Information c**). Created using the Rowcal package in R (McLaughlin, 2019).

number of dates falling in the range of 14-11 ka cal BP can be explained by the inclusion of additional dates from Nubian sites compared to the above-mentioned studies, as well as differences in the method used to calibrate and summarize the radiocarbon dataset. The presence of these dates may suggest 1), a geographical (i.e., north of southern Egypt vs. Nubia), pattern in the distribution of radiocarbon dates, or 2), that currently identified gaps in human occupation, such as the one after 14 ka cal BP in Upper Egypt, are the product of available radiocarbon dates that are biased toward some industries and, perhaps, toward certain periods of time. In the first scenario, the hypothesis of human groups moving toward the south at the beginning of MIS 1, during a period of profound environmental changes seems particularly appealing. This is especially the case in light of the evidence for high levels of inter-personal violence in the Nubian cemeteries, for which available dates indicate use at the end of MIS 2 or beginning of MIS 1. However, the biases identified in the dataset and the fact that it includes only ten dates (N = 10/91) for Sudanese Nubia, force us to also consider the second scenario.

As previous studies have already shown (Vermeersch and Van Neer, 2015; Vermeersch, 2020), the available dated archaeological material presented here shows strong evidence for human occupation during MIS 2 in the Lower Egyptian Nile Valley, and in particular during the periods documented regionally as the driest of the end of the Pleistocene (i.e., the LGM and H1, Castañeda et al., 2016). This stands in agreement with the hypothesis of the Nile Valley as an environmental refugium during MIS 2. However, the present study also shows that the available dated archaeological evidence presents major geographical (concentration of sites within southern Egypt and Nubia) and chronological (only some industries are well dated) biases. While the available data may indicate different clusters of human occupation in time and space, consistent with the hypothesis of the existence of several discontinuous refugia areas along the Nile Valley during MIS 2, this remains to be tested on a larger and more representative set of radiocarbon dates. The implementation of systematic dating programmes of Late Palaeolithic materials stored in museums using recent dating method protocols that target materials other than charcoal or bone collagen (such as apatite, e.g., Zazzo, 2014; ostrich eggshell, e.g., Tryon et al., 2018; terrestrial shells, e.g., Douka, 2017) may be a suitable research avenue to further enlarge the dataset.

Variability in the Late Palaeolithic in the Main Nile Valley: Evidence for Local Developments or External Influences?

Inferring past human population interactions from the lithic record relies on the assumption that lithic assemblages include information on past socio-cultural groups. Under this assumption, discussing human dispersals based on the lithic record amounts to identify cultural transmission across space (e.g., Tostevin, 2012, 80). However, dispersals in the genetic sense, i.e., with gene flow, may have occurred without cultural transmission. Conversely, cultural transmission across space may occur without gene flow. Once similarities in the lithic record have been identified across space, an additional challenge is to be able to distinguish between cultural diffusion (with or without gene flow) and convergence, i.e., similar forms of material culture independently produced (e.g., Groucutt et al., 2015). Determining the conditions for similarities between lithic assemblages to be interpreted as indicators for cultural transmission across space, which would be consistent with dispersal hypotheses, thus requires a well-defined theoretical framework, high-resolution archaeological and palaeoenvironmental record, as well as robust cultural taxonomies (For recent reviews on this topic, see for example Tostevin, 2012; Groucutt et al., 2015; Riede et al., 2019).

While a commonly-accepted view considers the main Nile Valley as being mostly isolated during MIS 2, several external

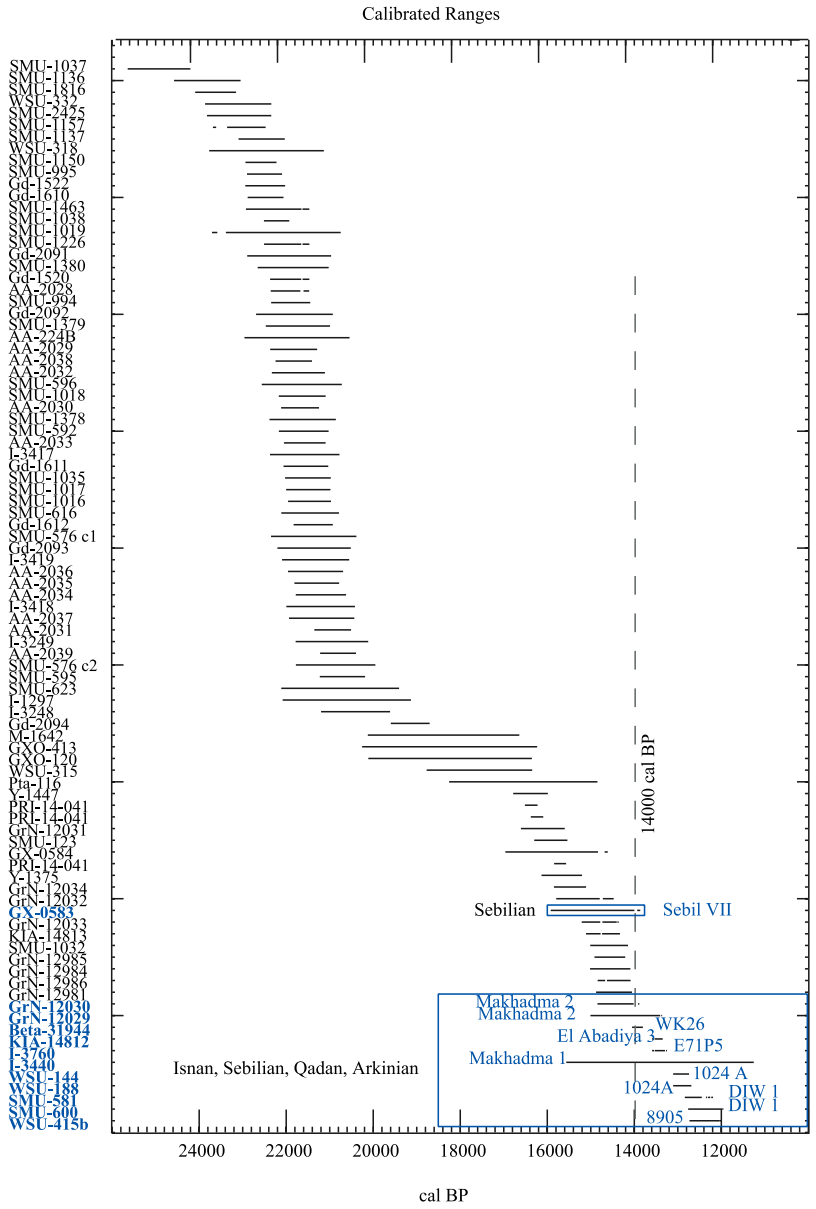

FIGURE 5 | Barplots of all two-sigma calibrated ranges of radiocarbon dates considered in the paper (N = 91). Created using Intcal20 (Reimer et al., 2020) and Calib 8.1 (Stuiver and Reimer, 1993).

influences have also been suggested (e.g., Schild and Wendorf, 2010, 116). Links with the south, toward eastern Africa, have been suggested for earlier periods, in the Middle Stone Age (e.g., Goder-Goldberger, 2013), but there is currently no supporting evidence for such contacts during MIS 2 (e.g., see discussion in Leplongeon et al., 2020). Several authors have also proposed connections between the Nile Valley and north-western Africa or the Levant during MIS 2 based on similarities in the lithic record.

Evidence for lithic similarities that have been argued to indicate contacts between the Nile Valley and the Levant at the end of the Pleistocene is mainly based on the sparse data from the Nile Delta. The unsystematic collections of microlithic artefacts by F. Debono near Helwan (see above, Debono, 1948; Schmidt, 1996; Tassie, 2014) includes tool types that are more similar to Epipalaeolithic industries from the southern Levant (e.g., Mushabian, Ramonian, dated to *ca.* 18-15 ka cal BP, Goring-Morris, 2017), than from known industries in the Nile Valley (Schmidt, 1996; **Figures 3**, **4**). Given their geographical location, they might correspond to a westward expansion of the 'territory' of the Mushabian and Ramonian, that are well attested to in the Sinai (Bar-Yosef and Phillips, 1977) rather than contacts between two different populations. However, in the absence of numbers and context, it is not possible to further interpret these similarities. In addition, a detailed comparative analysis

between the Afian and Ballanan-Silsilian from sites in Upper Egypt, and Epipalaeolithic assemblages of the Negev desert in Israel failed to highlight any similarities important enough to be interpreted as indicating contacts between these two regions (Leplongeon, 2017; Leplongeon and Goring-Morris, 2018). Detailed investigation and dating of the recently found material in the Delta region (Rowland and Tassie, 2014), will be critical to discussing the place of the Nile Delta in interregional population interactions at the end of the Pleistocene.

Links between some Nile Valley Late Palaeolithic industries and the North African LSA/Iberomaurusian were suggested based on typological similarities referring to attributes such as the type (e.g., Ouchtata) or side of the retouch for backed bladelets (Schild et al., 1968; Phillips, 1972; Phillips, 1973; Close, 1978; Close, 2002). If typological similarities are evident between some Nile Valley industries and the North African LSA, their interpretation is challenging. Interpreting these typological similarities in terms of socio-cultural relationships would be an over-simplification (e.g., Close, 1978, 235). Furthermore, there is no strict contemporaneity between the Late Palaeolithic in the Nile Valley and the Iberomaurusian in North Africa. As shown above, the Late Palaeolithic in the Nile Valley broadly corresponds to MIS 2, with several sites dated to the LGM, whereas if the earliest dates for the Iberomaurusian are *ca.* 25-23 ka cal BP, the evidence remains limited for its initial phase and most of the sites are dated from *ca.* 16-15 ka cal BP (Potì and Weniger, 2019). Systematic comparisons including technological and typological aspects of the assemblages as well as an evaluation of their chronometric dating would be critical in confirming or rejecting hypotheses of contacts between the Nile Valley and north-western Africa at the end of the Pleistocene.

From a non-lithic point of view, similarities have been noted in rock art between Late Pleistocene depictions of human figures ('headless women') from Qurta and el Hosh with depictions found in a rock shelter in the Sinai Desert (Zboray, 2012; Huyge, 2018). The rock art in Sinai remains undated, and the fauna associated with the human figures there is different from what is found in the Nile Valley (e.g., equines and (non-domesticated?) camel figures are dominant). However, similarities in human figures are striking. The presence of similar headless figures in European Magdalenian art also led Huyge (2018) to suggest that it may represent potential out of or back into Africa dispersals. However, as unsettling as these similarities may seem, further dated evidence is needed to consider such a (bold) scenario.

Nonetheless, *ca.* 25 ka cal BP in North Africa, the Nile Valley and the Levant, blade/let industries with a toolkit dominated by backed pieces are documented. The significance of the presence of these broad lithic characteristics in all three regions at the same time is unclear. The emergence of these industries may reflect earlier connections between the regions (see also discussion in Vermeersch, 2020). However, beyond these similar traits, each region seems to be characterized by its own development of industries with different technological and typological characteristics. The rare systematic comparative analyses between these regions focusing on both technological and typological traits, in addition to the difficulties of interpreting lithic data in terms of socio-cultural relationships, make it currently impossible to highlight some kind of 'information sharing' between these regions during MIS 2. Currently available archaeological data therefore do not support any intensive contact between human groups in North Africa, the Levant and the Nile Valley, although this does not exclude the possibility of movement of people without cultural transmission.

HUMAN FOSSIL AND GENETIC DATA: EVIDENCE FOR A RETURN TO AFRICA DURING MIS 2?

Some General Considerations

The evolutionary history of modern humans was a complex process involving alternations between phases of expansion and contraction of populations. Mirazón Lahr (2016) identifies the period corresponding to the end of MIS 3 and MIS 2 as a period of structuring of human diversity. The environmental changes occurring during this period led to the fragmentation, or even extinction, of some populations, and thus to a loss of inter-group diversity, whereas the expansion of some groups during the Holocene led to a subsequent increase of overall diversity (Mirazón Lahr, 2016, 9). The MIS 2 African fossil record is relatively limited but recent paleoanthropological research indicates that past biological variation was greater than in extant human populations (e.g., Tryon et al., 2015; Crevecoeur et al., 2016) and that past human populations were highly structured (e.g., Scerri et al., 2018).

To test whether the Nile Valley acted as a dispersal corridor or an environmental refugium based on the human fossil record, a simple model of isolation *vs.* connection with other regions may be proposed (see **Table 1**). For isolated populations, we would expect a record showing distinct characteristics compared to the record of other regions (e.g., North African and the Levant), whereas if population interactions were maintained, we would expect to find shared variability between human groups from different regions. This model would only be valid if populations were isolated for enough time to develop distinct biological characteristics; however, how much time is necessary for the latter is difficult to evaluate.

Since the fossil record is generally limited, such hypotheses are often formulated through genetic studies, where we would expect to find evidence for population bottlenecks in the isolation hypothesis, or evidence for admixture in the contact hypothesis. Genetic studies relying on modern DNA cannot answer questions related to the precise provenance of past human populations, and distinguishing recent vs. ancient gene flow, as well as estimating the age of new gene flow, is often complex. However, ancient DNA studies can help to mitigate these problems and several recently published results show their potential to better understand human interactions in Africa in the past (e.g., Gallego-Llorente et al., 2015; Skoglund et al., 2017; Fregel et al., 2018; Van de Loosdrecht et al., 2018; Prendergast et al., 2019; Wang et al., 2020).

Here, the contribution of the currently available human fossil and genetic data to the discussion of whether the Nile Valley

TABLE 4 | List of human fossils dated to MIS 2 from the Nile Valley.

Site name and location	Geological settings	Date	Chrono-cultural attribution	Number of individuals identified	References
Site E71K1, Deir el Fakhuri, Esna	Eroding out on the surface of Ballana Dune	MIS 2?	Fakhurian	2 (burials)	Butler (1974); Lubell (1974)
Site 8905, Tushka	Top of Sahaba formation	MIS 2?	Qadan	19 (cemetery)	Schild et al. (1968)
Site GS-2B-I[a], Kom-Ombo	Within level characterized by silty coarse sand and concretionary pebbles (interpreted as a channel), probably derived from older site upstream	MIS 2	Late Palaeolithic	1 (scattered fragments of one or more human calvaria, plus a large fragment of frontal bone)	Reed (1965); Butzer and Hansen (1968)
Site E-82-6, Wadi Kubbaniya	Surface find	MIS 2?	Late Palaeolithic	1 (skeleton)	Wendorf and Schild (1986)
Site 6B28, Wadi Halfa	Surface find	MIS 2?	Halfan?	1 (fossilized mandible)	Armelagos (1964); Irwin et al. (1968)
Site 6B36, Wadi Halfa	Surface	MIS 2?	Qadan	38 (cemetery)	Hewes et al. (1964); Greene and Armelagos (1972)
Site ANE-1, Wadi Halfa	Surface, eroded sandstone bedrock	MIS 2?	Qadan?	2 (skull fragments)	Shiner (1968)
Site 117, Jebel Sahaba	Base of a Nubian sandstone inselberg, with an elevation of 160 m above sea level (asl), which is above the Sahaba silts (140 m asl) in the area	MIS 2?b	Qadan?	62 (cemetery)	Anderson (1968); Wendorf (1968)

[a]*Reed (1965) reports (I believe incorrectly) the frontal bone as coming from the site GS-2A but the preliminary report (Reed et al., 1967) as well as the detailed account by Butzer and Hansen (1968, 168) clearly places the human bone as coming from level 1 of site GS-2B-I. Contrary to what Reed (1965) states, there is no date directly associated with the level where the human bone was found.*

[b]*Nine minimum ages (radiocarbon dates on human bone apatite (Zazzo, 2014) from 8,000 to 13,600 cal BP and one radiocarbon date 13,750 ± 600 BP (from 15,000 to 18,350 cal BP; Pta-116).*

could have acted as an environmental refugium or a dispersal corridor during MIS 2 is summarised.

Human Fossil Data

Table 4 lists sites where human fossils attributed to MIS 2 have been recovered in the Lower Nile Valley. The record is divided into two categories of sites with human remains: isolated finds and cemeteries. Isolated finds are often from the surface or reworked levels, the chronological attribution of which relies on their geological context and an (often uncertain) association with archaeological sites in the immediate vicinity. In all cemeteries, as well as in some of the isolated finds, there is evidence for 'aggressive-defensive trauma' including parry fractures and instances of stone artefacts embedded in bones. Unfortunately, very few sites are well-dated, and for the sites that do have absolute dates, their calibrated chronology places them between the end of MIS 2 and early MIS 1. Only the cemetery of site 117 (Jebel Sahaba) possesses several direct dates on human bones, but most are radiocarbon dates on apatite and they likely represent minimum ages (Zazzo, 2014). Five dates are available for site 8,905 (Schild et al., 1968), of which three can be considered unreliable. WSU-415a was rejected as too young and a second count from the same sample (WSU-415b) gave an older age (Wendorf, 1968). WSU-417-442 was not taken into consideration here as it is a date on a combined charcoal sample from two different localities at the site. Finally, WSU-444 is also considered unreliable as it is on carbonate sample (see Dal Sasso et al., 2018 for a discussion on radiocarbon dating carbonate). The two remaining dates, from the same locality, place the site between 12,030 and 18,760 cal BP, indicating either two distinct periods of occupation or contamination problems (**see Supplementary Information 1c, d**). The attribution of these human remains to MIS 2 is therefore in most cases tentative and relies on their association with Late Palaeolithic industries, some of which are also poorly dated (see *Archaeological evidence for human occupation of the Nile Valley during MIS 2* section). Nonetheless, the geological location of some of the human remains is consistent with a chronological attribution to the end of MIS 2 or early MIS 1 (see **Table 4**).

All human remains listed in **Table 4** are characterized by a robust morphology and fall within the same range of variation, which has been interpreted as evidence that they represent closely related populations (e.g., Armelagos, 1964; Hewes et al., 1964; Anderson, 1968; Wendorf, 1968; Greene and Armelagos, 1972; Butler, 1974; Wendorf and Schild, 1986), despite differences in the ways the bodies were buried (Wendorf, 1968).

Pre-MIS 2 modern human remains in the Nile Valley consist of few individuals, namely the child of Taramsa 1 and the two skeletons of Nazlet Khater 2. These three individuals were found in contexts interpreted as burials within or in close proximity to raw material extraction sites.

Several OSL dates are available for the child burial of Taramsa 1 (Van Peer et al., 2010). Sand deposits from three extraction pits, including the one where the burial was dug, gave OSL ages consistent with other dates available for human occupation at the extraction site (ranging from 60 to 110 ka, Van Peer et al.,

2010, table 10.2 p. 223). OSL dating from sand samples from within the skull gave an average of about 24 ka BP, but the excavators favor an earlier date for the burial (in particular, OSL date TAR-3, 68.6 ± 8 ka BP of sand deposits located above the burial). Recent reviews have questioned this chronological attribution, arguing that the sediment within the skull would give the most likely age for the burial (e.g., Grine, 2016, 354; Groucutt, 2020, 67). Based on the OSL dates, only a broad chronological range from MIS 4-2 can be proposed for the human burial of Taramsa 1. However, Van Peer et al. (2010, 223) associate the young MIS 2 dates with the fill of desiccation cracks, one of which was observed in stratigraphy just above the skull. They propose that these desiccation cracks formed during the arid conditions of MIS 2 and that a large amount of aeolian sand filled the cracks as well as the skull at that time. In addition, the burial was sealed by an undisturbed layer of extracted cobbles, which stratigraphically is covered by dump deposits of other Middle Palaeolithic extraction pits (Vermeersch et al., 1998). The archaeological evidence associated with the deposits surrounding the burial are attributed to the Late Middle Palaeolithic and have absolute dates corresponding to the first half of the Upper Pleistocene. Accepting a MIS 2 chronology for the burial would require explaining why older dates were obtained from deposits surrounding the burial. Finally, despite the poor preservation of the remains, and although these results must be taken cautiously as the analysis was carried out on photographs, the apparent absolute dimensions of the teeth would set the Taramsa child apart from the 'small-toothed' modern humans of the end of the Pleistocene in northern Africa (Vermeersch et al., 1998, 481). Unfortunately, the poor preservation of the human remains, the fact that a detailed morphological description was not possible, and the young age of the individual, prevent its inclusion in detailed comparisons with MIS 2 human remains.

The two burials discovered at Nazlet Khater 2 (NK2) are dated to 37,570 +350 -310 BP (39,400 cal BP, GrA-20145, Vermeersch, 2020; Vermeersch, 2002a) and have been extensively studied (Pinhasi and Semal, 2000; Vermeersch, et al., 2002b; Crevecoeur, 2008; Crevecoeur, 2012). Only the remains from one male individual were well-preserved and could be analyzed in detail. They are associated with the contemporaneous Upper Palaeolithic raw material extraction site of Nazlet Khater 4 (NK4), dated to ca. 38-34,000 cal BP (Vermeersch, 2002a). The presence of pathologies, particularly in the cervical vertebrae and the hands, are consistent with raw material extraction activities, such as heavy load-carrying with forehead straps or repeated impact on the hand while using extraction tools (Crevecoeur, 2012, 216). In addition, the NK2 individual was buried with a bifacial axe of a similar type to those found at NK4 and interpreted as extraction tools (Vermeersch, et al., 2002b). A detailed descriptive and comparative analysis of these remains shows that the NK2 individual presents a unique mosaic of features, which places him at the edge of extant variation and distinguishes him from any other known past or recent modern humans (Pinhasi and Semal, 2000; Crevecoeur, 2008; Crevecoeur, 2012). This is consistent with a growing body of evidence suggesting that Late Pleistocene human variation in Africa was much greater than current variation (e.g., Tryon et al., 2015; Crevecoeur et al., 2016; Pearson et al., 2020). Furthermore, the characteristics of the inner ear structure place the NK2 individual closer to early modern humans and European Upper Palaeolithic individuals than to recent humans. It does not present obvious similarities with MIS 2 modern humans, other than a general robust morphology.

Post-MIS 2 human remains, particularly from the Early and Middle Holocene, are known from Nubia in the context of Mesolithic or Neolithic burials (e.g., Usai, 2016; Honegger, 2019). While the hypothesis of population continuity has previously been proposed for Nubian populations from MIS 2 until the Middle Holocene (e.g., Greene, 1982), several recent studies have refuted this hypothesis (Crevecoeur et al., 2012; Galland et al., 2016; Benoiston et al., 2018). In Sudan, two cemeteries were found at El Barga (Honegger 2019), one attributed to the Mesolithic (7,800-6,900 BC) and the other to the Early Neolithic (6,000-5,500 BC). Preliminary analysis of the human remains associated with these two cemeteries show important differences between the two populations, both in terms of funerary practices and biological characteristics; the early Holocene Mesolithic individuals are extremely robust, while the Neolithic sample is more gracile (Crevecoeur et al., 2012). The Mesolithic individuals from El Barga show close affinities in their mandibular attributes and dental remains with MIS 2 Nubian populations, and are clearly separated from the Neolithic individuals (Crevecoeur et al., 2012, 27–28; Benoiston et al., 2018). Similar results were obtained when comparing dental features (Irish, 2005) and cranial and mandibular morphology (Galland et al., 2016) in a comparative analysis of human remains from Nubia, from the Late Palaeolithic to the Christian era. These results show a drastic shift in cranial, mandibular and dental morphologies and suggest a major population replacement in Nubia during the Holocene some time before the final Neolithic.

Comparisons between MIS 2 human remains from the Nile Valley and from northern Africa (Iberomaurusian) and the Levant (Epipalaeolithic / Natufian) suggest some similarities, such as in their robust morphologies and cranial features (e.g., Anderson, 1968; Greene and Armelagos, 1972; Butler, 1974) whereas other studies highlight several differences (see review in Irish (2000)). Extreme divergence in dental traits between Iberomaurusians and Late Palaeolithic Nubians were highlighted by Irish (2000), which would suggest that these populations are not closely related. In a study about regional variation in the postcranial robusticity of Late Upper Palaeolithic humans, Shackelford (2007) mentions that because of significant differences in body size, body proportion and robusticity, the Nile Valley (Nubian) and Mediterranean (North Africa and Levant) samples were treated as two different groups. In a study of the Jebel Sahaba (site 117) human remains, Holliday (2015) also highlights differences in body shape between the Jebel Sahaba individuals and contemporary North African and Levantine human remains. Nonetheless, in the comparative analysis of mandibular morphology between samples from the Mesolithic and Neolithic (Holocene) from El Barga, from Jebel Sahaba, Wadi Halfa, Taforalt (Iberomaurusian) and from the Levant (Natufian), only the Neolithic sample stands apart, while

the Late Pleistocene and early Holocene populations show close results (Crevecoeur et al., 2012, figure 19).

In sum, the available data suggest the following:

- All Late Pleistocene (MIS 2/early MIS 1) human remains from the Lower Nile Valley present similarities, which is consistent with the hypothesis that they belong to the same or closely-related population(s).
- From a socio-cultural point of view, there is evidence for high levels of interpersonal violence during MIS 2 in the Lower Nile Valley and high diversity of burial practices.
- Pre-MIS 2 data from the Lower Nile Valley are too sparse to indicate (dis)continuity of human populations.
- Comparisons between Late Palaeolithic and Early Holocene human remains show similarities, but their interpretation in terms of population continuity throughout MIS 2 and 1 is hampered by the poor chronological resolution of human remains attributed to MIS 2 (see **Table 4**).
- Post-MIS 2 data from Nubia indicate a strong population discontinuity (replacement of the population?) occurring after the early Holocene and before the middle Holocene.
- If MIS 2 human remains from the Nile Valley share some general characteristic with contemporaneous human remains from other regions, and particularly from North Africa and the Levant, there is also evidence that they represent distinct human populations/groups.

Distinguishing between refugial and dispersal corridor models based on human fossil data alone is challenging (see **Table 1**). Assessing how much time is necessary for isolated populations to be characterized by distinct physical characteristics and how different two contemporaneous human groups from adjacent regions should be to demonstrate isolation is extremely complex. The limited number of human remains from the Nile Valley and their coarse chronological resolution therefore results in a human fossil record that may appear consistent with both models. This depends on whether the emphasis is put on the fact that there is some evidence for the presence of distinct human groups in the Nile Valley and adjacent regions (refugial model), or that there also is some evidence for the presence of shared characteristics (dispersal corridor model).

Genetic Data

Recent developments in genetic studies using modern or ancient DNA have been crucial in testing and proposing new hypotheses of population interactions and dispersals in prehistory. Because of their location, north-eastern Africa and the Nile Valley in particular hold a special place in the debates surrounding modern human dispersals out of and back into Africa. One particular debate concerns the occurrence of major dispersals back into Africa during the Pleistocene and potentially via the Nile Valley (e.g., Hodgson et al., 2014 and references therein). In north-eastern Africa, Eurasian admixture during a recent (*ca.* 700 BP) major back-into Africa expansion has been documented, but its impact is different in the north and south of the region (e.g., Hollfelder et al., 2017). When working with modern DNA, such recent events may contribute to hiding the signatures of more ancient (particularly Pleistocene) back-flows from Eurasia into Africa. Ancient DNA studies can contribute to overcoming this issue. For example, ancient DNA from ancient Egyptian mummies dated to between 3,000 and 1,600 cal BP showed that ancient Egyptians before the major admixture event identified above already had a strong near-eastern component, found in Levantine Neolithic individuals, suggesting an earlier influx of near-eastern ancestry (Schuenemann et al., 2017). However, all the samples analyzed in this study come from a single site, Abusir-el Melek in Middle Egypt, and results may be related more to the location of the site and the local history, rather than reflecting general trends that can be applied to all of Ancient Egypt (Schuenemann et al., 2017, 8).

Outside north-eastern Africa, in Morocco, analyses of ancient DNA from human remains dated to *ca.* 15 ka (Iberomaurusian) at Taforalt (Van de Loosdrecht et al., 2018), *ca.* 7 ka (Early Neolithic) at Ifri n'Amr and *ca.* 5 ka (Late Neolithic) at Kelif el Boroud (Fregel et al., 2018) highlight complex population dynamics in North Africa at the end of the Pleistocene and Holocene. Later Stone Age and Early Neolithic individuals appear similar from a genetic point of view, and both groups are distantly related to Levantine Natufian hunter-gatherers, indicating both a Levantine intrusion into North Africa during the Late Pleistocene and a certain degree of population continuity in northern Africa between the Late Pleistocene and Holocene. Data from Kelif el Boroud suggest that its population (Late Neolithic) results from admixture between populations related to Early Neolithic populations and European Neolithic groups from across the Mediterranean. Available data therefore point to population interactions, at least along the Mediterranean coast of Africa, in the Pleistocene before 15 ka.

Pagani and Crevecoeur (2019) discuss the potential implications of these recent genetic data on the African genetic diversity in the form of two 'entirely speculative' (their words) scenarios. Because the second of these scenarios is particularly relevant for our topic, it is briefly summarized here. It hypothesizes a fragmentation of populations during the arid Late Glacial period (MIS 4-2) in north-eastern Africa. Small subgroups of these fragmented populations would have expanded west along the North African coast and east toward Eurasia. Under this hypothetical scenario, which considers the Nile Valley as the main route out of Africa (e.g., Pagani et al., 2015), the genetic bottleneck characterizing all non-African groups, and generally linked to an out of Africa expansion of a small group during favourable environmental conditions would instead be related to the closing of the 'Nile corridor'. The fragmentation of populations would have lasted until the reopening of the Nile Valley during the Holocene, where admixture between the isolated local groups and Levantine or north-western groups would have occurred. This would be consistent with the available fossil evidence (e.g., see *Geographical and chronological patterns of human occupation in the Lower Nile Valley 447 during the Late Palaeolithic* section and Pagani and Crevecoeur, 2019), in particular the uniqueness of the human fossil from NK2, and the persistence of robust phenotypes in Nubia until the emergence of more gracile

morphologies, possibly related to a population replacement when the Nile Valley reopens, after 8 ka).

Currently available genetic data, including Late Pleistocene and early Holocene ancient DNA, highlight a particularly complex history of human interactions in North Africa during the end of the Pleistocene. Although further evidence is needed to support it, the scenario proposed by Pagani and Crevecoeur (2019) seems consistent with the human fossil data from the Nile Valley and Nubia in particular, and would imply that during MIS 2 and until after 8 ka, the Nile Valley was not a dispersal corridor. Ancient DNA studies applied to the Late Palaeolithic or Mesolithic/Neolithic Nubian human remains–if DNA extraction were possible–would be critical to confirm or deny such a hypothesis.

SUMMARY AND RESEARCH PERSPECTIVES

Available palaeoenvironmental, human fossil, genetic and archaeological data all present their own limitations and offer contrasting views when considering the question of whether the Nile Valley acted as a corridor for dispersal or environmental refugium during MIS 2. Improved chronological and geographical resolution is needed in order to bring definitive support to one or the other hypothesis (or both). Nonetheless, the available evidence seems to suggest that the Nile Valley acted primarily as an environmental refugium during MIS 2. Indirect evidence from palaeoenvironmental data show that several locations at least in the Nile Valley were suitable for human occupation during MIS 2. This is supported by archaeological evidence showing human occupation during the driest episodes of MIS 2. Human occupation might also have been possible in some areas of the adjacent deserts, at least in an intermittent manner. Similarly, human fossil data suggest that human groups from the Nile Valley are different from adjacent regions, which is consistent with a scenario involving the isolation of human groups into environmental refugia (e.g., Pagani and Crevecoeur, 2019).

The hypothesis of the Nile Valley as a dispersal corridor during MIS 2 receives little support. Palaeoenvironmental data suggest that the deserts adjacent to the Nile Valley were hyper-arid over most of the period, and connectivity between the different areas identified as potential environmental refugia remains to be demonstrated. In particular, acquiring further archaeological data from the Nile Delta is critical to elucidate whether the area was inhabitable for none, part or all of MIS 2. Human fossil and archaeological records show little-to-no evidence for contacts between human groups, other than very broad similarities at the macro-regional scale. Genetic studies based on ancient DNA suggest gene flow between human groups located in the Levant and North Africa before 15 ka, but this may indicate interactions along the Mediterranean coast, without involving the Nile Valley. Other genetic studies, based on both ancient and modern DNA, suggest gene flow from Eurasia to eastern Africa, but this may have occurred before or after MIS 2. Ancient DNA studies involving samples from MIS 2 human remains from the Nile Valley would be extremely important to help elucidate the population dynamics of this region during MIS 2.

Most of the known Late Palaeolithic sites of the main Nile Valley are now destroyed. Their location, close to the Nile, makes them particularly vulnerable to the building of dams, expansion of irrigation systems and urbanization in Egypt and Sudan. Despite major Palaeolithic work in the region in the second half of the 20th century, very few fieldwork projects focusing on the end of the Palaeolithic are currently on-going in the main Nile Valley. Both renewed archaeological and geological fieldwork in areas where Late Pleistocene deposits are preserved, and reinvestigation of archival and artefact collections in museums, many of which remain only partly published, will allow us to shed further light on human-environment interactions in the Nile Valley and neighboring regions at the end of the Pleistocene.

AUTHOR CONTRIBUTIONS

AL conceived and designed the study, collected the data, performed the analysis and wrote the paper.

FUNDING

This research has received funding from the Research Foundation – Flanders (FWO) in the frame of a postdoctoral fellowship (FWO file # 12U9220N) and from the French National Research Agency (ANR) 'Big Dry'Project (Project No. ANR-14-CE31-0023, coordinated by Prof. François Bon).

ACKNOWLEDGMENTS

I thank V. Foerster, A. Junginger, N. Klasen, and C. Zeeden for inviting me to present my research in the session 'Integrating stratigraphy, sedimentology, palaeontology and paleoclimate in human evolution and dispersal studies - from early hominins to the Holocene' at EGU 2019 in Vienna and for organizing this special issue of Frontiers in Earth Sciences. I thank R. McLaughlin for his help and advice in using the Rowcal package. Finally, I sincerely thank P. Vermeersch, R. Schild (in particular regarding discussions on the role of the Arkinian), M. Williams, I. Crevecoeur, and Philip Van Peer for numerous discussions and helpful comments on earlier versions of the manuscript. I thank the reviewers for their constructive comments that helped improve the manuscript. Finally, I would also like to thank E. Hallinan for her help with the English editing of this manuscript.

SUPPLEMENTARY MATERIAL

The Supplementary Material for this article can be found online at: https://www.frontiersin.org/articles/10.3389/feart.2020.607183/full#supplementary-material.

REFERENCES

Abouelmagd, A., Sultan, M., Sturchio, N. C., Soliman, F., Rashed, M., Ahmed, M., et al. (2014). Paleoclimate record in the Nubian Sandstone Aquifer, Sinai Peninsula, Egypt. *Quatern. Res.* 81, 158–167. doi:10.1016/j.yqres.2013.10.017

Adams, W. Y. (1977). Nubia, corridor to Africa. Princeton, NJ: Princeton University Press.

Anderson, F. (1968). "Late paleolithic skeletal remains from Nubia," in *The prehistory of Nubia*. Editor F. Wendorf (Dallas: Fort Burgwin Research Center; SMU Press), 996–1040.

Armelagos, G. J. (1964). A fossilized mandible from near Wadi Halfa, Sudan. *Man* 64, 12–13. doi:10.2307/2797558

Auenmüller, J. (2019). "Topography and regional geography of Nubia: River, Cataract and Desert Landscapes," in Handbook of Ancient Nubia, Editor D. Raue (Berlin Munich Boston: De Gruyter), 39–61. doi:10.1515/9783110420388-003

Banks, W. E., Signe Snortland, J., Scott Cummings, L., Gatto, M. C., and Usai, D. (2015). The terminal late palaeolithic in Wadi Kubbaniya, Egypt. Antiquity Project Gallery 89, Available at: https://antiquity.ac.uk/projgall/banks346 (Accessed January 4, 2021).

Basell, L. S. (2008). Middle Stone Age (MSA) site distributions in eastern Africa and their relationship to Quaternary environmental change, refugia and the evolution of *Homo sapiens*. *Quat. Sci. Rev.* 27, 2484–2498. doi:10.1016/j.quascirev.2008.09.010

Bar-Yosef, O. and Phillips, J. L. (1977). *Prehistoric investigations in Gebel Maghara, Northern Sinai*. Jerusalem: The Hebrew University of Jerusalem.

Bennett, K. D., and Provan, J. (2008). What do we mean by 'refugia'?. *Quat. Sci. Rev.* 27, 2449–2455. doi:10.1016/j.quascirev.2008.08.019

Benoiston, A.-S., Bayle, P., and Crevecoeur, I. (2018). "Biological affinity of the Mesolithic and Neolithic populations from El-Barga, Sudan: the dental remains," in *Nubian archaeology in the XXIst century*. Editor M. Honegger (Leuven Paris Bristol: Peeters), 806–816.

Blackwell, B. A. B., Skinner, A. R., Mashriqi, F., Deely, A. E., Long, R. A., Gong, J. J. J., et al. (2012). Challenges in constraining pluvial events and hominin activity: examples of ESR dating molluscs from the Western Desert, Egypt. *Quat. Geochronol.* 10, 430–435. doi:10.1016/j.quageo.2012.01.005

Blackwell, B. A. B., Skinner, A. R., Smith, J. R., Hill, C. L., Churcher, C. S., Kieniewicz, J. M., et al. (2017). ESR analyses for herbivore teeth and molluscs from Kharga, Dakhleh, and Bir Tarfawi Oases: constraining water availability and hominin paleolithic activity in the Western Desert, Egypt. *J. Afr. Earth Sci.* 136, 216–238. doi:10.1016/j.jafrearsci.2017.07.007

Bovier-Lapierre, P. (1926). "Stations préhistoriques des environs du Caire," in *Compte Rendu du Congrès international de géographie, Avril 1925*. (Le Caire: Institut française d'archéologie orientale du Caire), 298–308.

Bronk Ramsey, C. (2017). Methods for summarizing radiocarbon datasets. *Radiocarbon*. 59, 1809–1833. doi:10.1017/RDC.2017.108

Butler, B. (1974). "Skeletal remains from a late paleolithic site near Esna," in *The fakhurian: a late paleolithic industry from upper Egypt geological survey of Egypt paper*. Editor D. Lubell (Cairo: The Geological Survey of Egypt), 176–183.

Butzer, K. W. (1980). "Pleistocene history of the Nile valley in Egypt and lower Nubia," in *The Sahara and the Nile*. Editors M. A. J. Williams and H. Faure (Rotterdam: Balkema), 253–280.

Butzer, K. W. (1997). Late Quaternary problems of the Egyptian Nile : stratigraphy, environments, prehistory. *Paleo.* 23, 151–173. doi:10.3406/paleo.1997.4658

Butzer, K. W., and Hansen, C. L. (1968). *Desert and river in Nubia: geomorphology and prehistoric environments at the Aswan reservoir*. Madison: University of Wisconsin Press.

Castañeda, I. S., Schouten, S., Pätzold, J., Lucassen, F., Kasemann, S., Kuhlmann, H., et al. (2016). Hydroclimate variability in the Nile River Basin during the past 28,000 years. *Earth Planet Sci. Lett.* 438, 47–56. doi:10.1016/j.epsl.2015.12.014

Chen, Z., and Stanley, D. J. (1993). Alluvial stiff muds (late pleistocene) underlying the lower nile delta plain, Egypt: petrology, stratigraphy and origin, *J. Coast. Res.* 9, 539–576. Available at: https://www.jstor.org/stable/4298107 (Accessed January 4, 2021).

Chen, Z., Warne, A. G., and Stanley, D. J. (1992). Late quaternary evolution of the Northwestern nile delta between the Rosetta Promontory and Alexandria. *Egypt. J. Coast. Res.* 8, 527–561.

Close, A. E. (2002). "Backed bladelets are a foreign country," in *Thinking small: global perspectives on microlithization archeological papers of the American anthropological association*. Editors S. L. Kuhn and R. G. Elston (Arlington, Virginia: American Anthropological Association), 31–44.

Close, A. E. (1978). The identification of style in lithic artefacts. *World Archaeol.* 10, 223–237. doi:10.1080/00438243.1978.9979732

Connor, D. R., and Marks, A. E. (1986). "The terminal Pleistocene on the Nile: the final Nilotic adjustment". in The end of the Paleolithic in the old world, Editor L. G. Straus (Oxford: British Archaeological Reports), 171–99.

Coudert, L. (2013). Les stratégies d'acquisition des ressources animales à la fin du Pléistocène et au début de l'Holocène : synthèse documentaire.

Crevecoeur, I. (2008). "Etude anthropologique du squelette du Paléolithique supérieur de Nazlet Khater 2 (Égypte)," in *Apport à la compréhension de la variabilité des hommes modernes*. (Leuven: Leuven University Press).

Crevecoeur, I. (2012). "The upper paleolithic human remains of Nazlet Khater 2 (Egypt) and past modern human diversity," in *Modern origins vertebrate paleobiology and paleoanthropology*. Editors J.-J. Hublin and S. P. McPherron (Dordrecht: Springer Netherlands), 205–219.

Crevecoeur, I., Brooks, A., Ribot, I., Cornelissen, E., and Semal, P. (2016). Late stone age human remains from Ishango (Democratic Republic of Congo): new insights on late Pleistocene modern human diversity in Africa. *J. Hum. Evol.* 96, 35–57. doi:10.1016/j.jhevol.2016.04.003

Crevecoeur, I., Desideri, J., Chaix, L., and Honegger, M. (2012). "First anthropological insights on the Early Holocene funerary assemblages from El-Barga". in *Kerma, Documents de la mission archéologique suisse au Soudan*. Editor M. Honegger (Neuchâtel: Université de Neuchâtel), 19–28.

Dal Sasso, G., Zerboni, A., Maritan, L., Angelini, I., Compostella, C., Usai, D., et al. (2018). Radiocarbon dating reveals the timing of formation and development of pedogenic calcium carbonate concretions in Central Sudan during the Holocene. *Geochem. Cosmochim. Acta.* 238, 16–35. doi:10.1016/j.gca.2018.06.037

de Heinzelin, J. (1968). "Geological history of the Nile Valley in Nubia," Editor F. Wendorf (Dallas: Fort Burgwin Research Center, SMU Press), 19–55.

Debono, F. (1948). Le paléolithique final et le mésolithique à Hélouan. *Annales du Service des Antiquités de l'Egypte*. 48, 629–637.

Debono, F., and Mortensen, B. (1990). El Omari: a neolithic settlement and other sites in the vicinity of Wadi Hof, Helwan. Mainz am Rhein: von Zabern.

Douka, K. (2017). "Radiocarbon dating of marine and terrestrial shell," in *Molluscs in archaeology methods, approaches and applications*. Editor M. J. Allen (Oxford, PA: Oxbow Books), 381.

Ducassou, E., Capotondi, L., Murat, A., Bernasconi, S. M., Mulder, T., Gonthier, E., et al. (2007). Multiproxy Late Quaternary stratigraphy of the Nile deep-sea turbidite system—towards a chronology of deep-sea terrigeneous systems. *Sediment. Geol.* 200, 1–13. doi:10.1016/j.sedgeo.2007.01.023

Ducassou, E., Migeon, S., Mulder, T., Murat, A., Capotondi, L., Bernasconi, S. M., et al. (2009). Evolution of the Nile deep-sea turbidite system during the Late Quaternary: influence of climate change on fan sedimentation. *Sedimentology*. 56, 2061–2090. doi:10.1111/j.1365-3091.2009.01070.x

Dufour, E., Van Neer, W., Vermeersch, P. M., and Patterson, W. P. (2018). Hydroclimatic conditions and fishing practices at Late paleolithic Makhadma 4 (Egypt) inferred from stable isotope analysis of otoliths. *Quat. Int.* 471, 190–202. doi:10.1016/j.quaint.2017.09.026

Enzel, Y., Amit, R., Dayan, U., Crouvi, O., Kahana, R., Ziv, B., et al. (2008). The climatic and physiographic controls of the eastern Mediterranean over the late Pleistocene climates in the southern Levant and its neighboring deserts. *Global Planet. Change*. 60, 165–192. doi:10.1016/j.gloplacha.2007.02.003

Foerster, V., Junginger, A., Langkamp, O., Gebru, T., Asrat, A., Umer, M., et al. (2012). Climatic change recorded in the sediments of the Chew Bahir basin, southern Ethiopia, during the last 45,000 years. *Quat. Int.* 274, 25–37. doi:10.1016/j.quaint.2012.06.028

Fregel, R., Méndez, F. L., Bokbot, Y., Martín-Socas, D., Camalich-Massieu, M. D., Santana, J., et al. (2018). Ancient genomes from North Africa evidence prehistoric migrations to the Maghreb from both the Levant and Europe. *Proc. Natl. Acad. Sci. U. S. A.* 115, 6774–6779. doi:10.1073/pnas.1800851115

Galland, M., Van Gerven, D. P., Von Cramon-Taubadel, N., and Pinhasi, R. (2016). 11,000 years of craniofacial and mandibular variation in Lower Nubia. *Sci. Rep.* 6, 31040. doi:10.1038/srep31040

Gallego Llorente, M., Jones, E. R., Eriksson, A., Siska, V., Arthur, K. W., Arthur, J. W., et al. (2015). Ancient Ethiopian genome reveals extensive Eurasian admixture throughout the African continent. *Science*. 350, 820–822. doi:10.1126/science.aad2879

Gamble, C., Davies, W., Pettitt, P., Hazelwood, L., and Richards, M. (2005). The archaeological and genetic foundations of the European population during the late glacial: implications for 'agricultural thinking. *Camb. Archaeol. J.* 15, 193–223. doi:10.1017/S0959774305000107

Garcea, E. A. A. (2020). The prehistory of the Sudan. Cham, Switzerland: Springer International Publishing. doi:10.1007/978-3-030-47185-9

Gasse, F. (2000). Hydrological changes in the African tropics since the last glacial maximum. *Quat. Sci. Rev.* 19, 189–211. doi:10.1016/S0277-3791(99)00061-X

Gasse, F., Chalié, F., Vincens, A., Williams, M. A. J., and Williamson, D. (2008). Climatic patterns in equatorial and southern Africa from 30,000 to 10,000 years ago reconstructed from terrestrial and near-shore proxy data. *Quat. Sci. Rev.* 27, 2316–2340. doi:10.1016/j.quascirev.2008.08.027

Gatto, M. C. (2012). "The holocene prehistory of the Nubian Eastern Desert," in *The history of the peoples of the Eastern Desert*. Editors H. Barnard and K. Duistermaat (Los Angeles: Cotsen Institute of Archaeology, University of California), 42–57.

Goder-Goldberger, M. (2013). The khormusan: evidence for an MSA East African industry in Nubia. *Quat. Int.* 300, 182–194. doi:10.1016/j.quaint.2012.11.031

Goring-Morris, A. N. (2017). "Loess, dunes, and human activities," in *Quaternary of the levant. Environments, climate change, and humans*. Editors Y. Enzel and O. Bar-Yosef (Cambridge: Cambridge University Press), 493–504.

Goring-Morris, A. N., and Goldberg, P. (1990). Late quaternary dune incursions in the southern levant: archaeology, chronology and palaeoenvironments. *Quat. Int.* 5, 115–137. doi:10.1016/1040-6182(90)90031-X

Graff, G., and Kelany, A. (2013). "Paysages gravés: la longue continuité du Wadi Abu Subeira (région d'Assouan, Egypte)," in Art as a source of history, Editor E. Anati (Paris: Unesco), 315–324.

Greene, D. L., and Armelagos, G. (1972). *The Wadi Halfa mesolithic population*. Amherst: University of Massachusetts.

Greene, D. L. (1982). Discrete dental variations and biological distances of nubian populations. *Am. J. Phys. Anthropol.* 58, 75–79. doi:10.1002/ajpa.1330580109

Grine, F. E. (2016). "The late quaternary hominins of Africa: the skeletal evidence from MIS 6-2," in *Africa from MIS 6-2: population dynamics and paleoenvironments vertebrate paleobiology and paleoanthropology*. Editors S. C. Jones and B. A. Stewart (Dordrecht: Springer Netherlands), 323–381.

Groucutt, H. S. (2020). "Culture and convergence: the curious case of the Nubian complex," in *Culture history and convergent evolution: can we detect populations in prehistory? Vertebrate paleobiology and paleoanthropology*. Editor H. S. Groucutt (Cham, Switzerland: Springer).

Groucutt, H. S., Petraglia, M. D., Bailey, G., Scerri, E. M., Parton, A., Clark-Balzan, L., et al. (2015). Rethinking the dispersal of *Homo sapiens* out of Africa. *Evol. Anthropol.* 24, 149–164. doi:10.1002/evan.21455

Haas, H. (1989). "The radiocarbon dates from Wadi Kubbaniya," in *The prehistory of Wadi Kubbaniya, vol 2, stratigraphy, paleoeconomy, and environment*. Editors F. Wendorf, R. Schild, and A. Close (Dallas: Southern Methodist University Press), 274–279.

Hamimi Z., El-Barkooky A., Frías J. M., Fritz H., and El-Rahman Y. A. Editors (2020). *The geology of Egypt*. Chambéry: Springer International Publishing.

Hamdan, M. A., and Brook, G. A. (2015). Timing and characteristics of Late Pleistocene and Holocene wetter periods in the Eastern Desert and Sinai of Egypt, based on 14C dating and stable isotope analysis of spring tufa deposits. *Quat. Sci. Rev.* 130, 168–188. doi:10.1016/j.quascirev.2015.09.011

Hamdan, M. A., Hassan, F. A., Flower, R. J., Leroy, S. A. G., Shallaly, N. A., and Flynn, A. (2019). Source of Nile sediments in the floodplain at Saqqara inferred from mineralogical, geochemical, and pollen data, and their palaeoclimatic and geoarchaeological significance. *Quater. Int.* 501, 272–288. doi:10.1016/j.quaint.2018.02.021

Hassan, F. A. (2007). The Aswan high dam and the International rescue Nubia campaign. *Afr. Archaeol. Rev.* 24, 73–94. doi:10.1007/s10437-007-9018-5

Heaton, T. J., Köhler, P., Butzin, M., Bard, E., Reimer, R. W., Austin, W. E. N., et al. (2020). Marine20—the marine radiocarbon age calibration curve (0–55,000 cal BP). *Radiocarbon*. 62, 779–820. doi:10.1017/RDC.2020.68

Hewes, G. W., Irwin, H., Papworth, M., and Saxe, A. (1964). A new fossil human population from the Wadi Halfa Area, Sudan. *Nature*. 203, 341. doi:10.1038/203341a0

Hewitt, G. M. (1996). Some genetic consequences of ice ages, and their role in divergence and speciation. *Biol. J. Linn. Soc.* 58, 247–276. doi:10.1111/j.1095-8312.1996.tb01434.x

Hodgson, J. A., Mulligan, C. J., Al-Meeri, A., and Raaum, R. L. (2014). Early back-to-Africa migration into the horn of Africa. *PLoS Genet*. 10, e1004393. doi:10.1371/journal.pgen.1004393

Hollfelder, N., Schlebusch, C. M., Günther, T., Babiker, H., Hassan, H. Y., and Jakobsson, M. (2017). Northeast African genomic variation shaped by the continuity of indigenous groups and Eurasian migrations. *PLoS Genet*. 13, e1006976. doi:10.1371/journal.pgen.1006976

Holliday, T. W. (2015). Population affinities of the Jebel Sahaba skeletal sample: limb proportion evidence. *Int. J. Osteoarchaeol.* 25, 466–476. doi:10.1002/oa.2315

Honegger, M. (2019). "The Holocene prehistory of upper Nubia until the rise of the Kerma Kingdom," in *Handbook ofAncient Nubia*. Editor D. Raue (Berlin, Boston: De Gruyter), 217–238.

Huyge, D. (2009). Late palaeolithic and epipalaeolithic rock art in Egypt: qurta and El-Hosh. *Archéo-Nil.* 19, 109–120. Available at: https://www.archeonil.fr/images/revue%202008%202010/AN2009-08-Huyge.pdf (Accessed January 4, 2021).

Huyge, D. (2005). The fish hunters of El-Hosh: rock art research and archaeological investigations in upper Egypt (1998–2004). *Meded. der Zittingen van de K. Acad. voor Overzeese Wet./Bull. Seances Acad. R. Sci. Outre-Mer*. 51, 231–249.

Huyge, D. (2018). The 'headless women' of Qurta (Upper Egypt): the earliest anthropomorphic images in northern-African rock art," in *What ever happened to the people? Humans and anthropomorphs in the rock art of northern Africa*. Editors D. Huyge and F. Van Noten (Brussels: Royal Academy of Overseas Sciences), 419–430.

Huyge, D., and Claes, W. (2015). Art rupestre gravé paléolithique de Haute Egypte : El-Hosh et Qurta. *Bull. de l'Assoc. Sci. Liégeoise pour la Rech. Archéologique*. 28, 21–40.

Huyge, D., Aubert, M., Barnard, H., Claes, W., Darnell, J. C., De Dapper, M., et al. (2007). "Lascaux along the Nile": late Pleistocene rock art in Egypt. Antiquity project gallery 81. Available at: https://www.antiquity.ac.uk/projgall/huyge313/. (Accessed June 22, 2020).

Huyge, D., Vandenberghe, D. A. G., Dapper, M. D., Mees, F., Claes, W., and Darnell, J. C. (2011). First evidence of Pleistocene rock art in North Africa: securing the age of the Qurta petroglyphs (Egypt) through OSL dating. *Antiquity*. 85, 1184–1193. doi:10.1017/S0003598X00061998

Irish, D. J. D. (2005). Population continuity vs. discontinuity revisited: dental affinities among late paleolithic through Christian-era Nubians. *Am. J. Phys. Anthropol.* 128, 520–535. doi:10.1002/ajpa.20109

Irish, J. D. (2000). The Iberomaurusian enigma: North African progenitor or dead end?. *J. Hum. Evol.* 39, 393–410. doi:10.1006/jhev.2000.0430

Irwin, H. T., Irwin, L. F., and Wheat, J. B. (1968). *University of Colorado investigations of paleolithic and epipaleolithic sites in the Sudan, Africa*. Salt Lake City: University of Utah Press.

Johnson, T. C., Scholz, C. A., Talbot, M. R., Kelts, K., Ricketts, R. D., Ngobi, G., et al. (1996). Late Pleistocene desiccation of Lake Victoria and rapid evolution of cichlid fishes. *Science*. 273, 1091–1093. doi:10.1126/science.273.5278.1091

Kelany, A. (2014). Late palaeolithic rock art sites at Wadi Abu Subeira and el-'Aqaba el-Saghira, Upper Egypt. *Cahier de l'AARS*. 17, 105–115.

Kelany, A. (2012). More late palaeolithic rock art at Wadi Abu Subeira, Upper Egypt. *Bull. des Musées Royaux d'Art et d'Hist.* 83, 5–22.

Kelany, A., Tohami, A., Harby, H., Mokhtar, M., Elhomosany, S., Badawy, M., et al. (2015). "Surveying work at Wadi Abu Subeira, season 2012," in *From the delta to the cataract*, Editors J. Jiménez-Serrano and C. von Pilgrim (Leiden: Brill), 98–107.

Kleindienst, M. R., Blackwell, B. A. B., Skinner, A. R., Churcher, C. S., Kieniewicz, J. M., Smith, J. R., et al. (2016). Assessing long-term habitability at an eastern Sahara oasis: ESR dating of molluscs and herbivore teeth at Dakhleh Oasis, Egypt. *Quat. Int.* 408, 106–120. doi:10.1016/j.quaint.2015.11.045

Kleindienst, M. R., McDonald, M. M. A., Skinner, A. R., Blackwell, B. A. B., and Wiseman, M. F. (2020). "Evidence for pleistocene habitability and occupations in the Western Desert of Egypt, MIS 4 through early MIS 2," in *Not just a corridor. Human occupation of the Nile Valley and neighbouring regions*

between 75,000 and 15,000 years ago. Editors A. Leplongeon, M. Goder-Goldberger, and D. Pleurdeau (Paris: Muséum national d'histoire naturelle), 39–69.

Kuper, R., and Kröpelin, S. (2006). Climate-controlled Holocene occupation in the Sahara: motor of Africa's evolution. *Science*. 313, 803–807. doi:10.1126/science.1130989

Leplongeon, A. (2017). Technological variability in the late Palaeolithic lithic industries of the Egyptian Nile Valley: the case of the silsilian and afian industries. *PLOS ONE*. 12, e0188824. doi:10.1371/journal.pone.0188824

Leplongeon, A., and Goring-Morris, A. N. (2018). Terminal Pleistocene lithic variability in the Western Negev (Israel): is there any evidence for contacts with the Nile Valley? *J. Lithic Stud*. 5. doi:10.2218/jls

Leplongeon, A., Ménard, C., Douze, K., Habte, B., Bon, F., and Pleurdeau, D. (2020). "The Horn of Africa at the end of the Pleistocene (75–12 ka) in its macroregional context," in *Not just A CorridorHuman occupation of the Nile Valley and neighbouring regions between 75,000 and 15,000 years ago*. Editors A. Leplongeon, M. Goder-Goldberger, and D. Pleurdeau (Paris: Muséum national d'Histoire naturelle), 269–283.

Linseele, V., and Van Neer, W. (2010). "Exploitation of desert and other wild game in ancient Egypt: the archaeozoological evidence from the Nile Valley," in *Exploitation of desert and other wild game in ancient Egypt*. Editors H. Riemer, F. Förster, M. Herb, and N. Pöllath (Köln: Heinrich Barth Institute), 47–78.

Lubell, D. (1974). *The fakhurian: a late paleolithic industry from upper Egypt*. Cairo: The Geological Survey of Egypt.

Marks, A. E. (1968). "The Sebilian industry of the second cataract," in The Prehistory of Nubia, Editor F. Wendorf (Dallas: Southern Methodist University Press), 461–531.

McLaughlin, T. R. (2019). On applications of space–time modelling with open-source 14C age calibration. *J. Archaeol. Method Theor*. 26, 479–501. doi:10.1007/s10816-018-9381-3

Mirazón Lahr, M. (2016). The shaping of human diversity: filters, boundaries and transitions. *Philos. Trans. R. Soc. Lond. B Biol. Sci*. 371, 20150241. doi:10.1098/rstb.2015.0241

Mirazón Lahr, M., and Foley, R. A. (2016). "Human evolution in late quaternary Eastern Africa," in *Africa from MIS 6-2: population dynamics and paleoenvironments vertebrate paleobiology and paleoanthropology*.Editors S. C. Jones and B. A. Stewart (Dordrecht: Springer Netherlands), 215–231.

Moeyersons, J., Vermeersch, P. M., and Van Peer, P. (2002). Dry cave deposits and their palaeoenvironmental significance during the last 115 ka, Sodmein Cave, Red Sea Mountains, Egypt. *Quat. Sci. Rev*. 21, 837–851. doi:10.1016/S0277-3791(01)00132-9

Muhs, D. R., Roskin, J., Tsoar, H., Skipp, G., Budahn, J. R., Sneh, A., et al. (2013). Origin of the Sinai–Negev erg, Egypt and Israel: mineralogical and geochemical evidence for the importance of the Nile and sea level history. *Quat. Sci. Rev*. 69, 28–48. doi:10.1016/j.quascirev.2013.02.022

Nicoll, K. (2001). Radiocarbon chronologies for prehistoric human occupation and hydroclimatic change in Egypt and Northern Sudan. *Geoarchaeology* 16, 47–64. doi:10.1002/1520-6548(200101)16:1

Nicoll, K., Giegengack, R., and Kleindienst, M. (1999). Petrogenesis of artifact-bearing fossil-spring tufa deposits from Kharga Oasis, Egypt. *Geoarchaeology*. 14, 849–863. doi:10.1002/(SICI)1520-6548

Pachur, H.-J., and Hoelzmann, P. (2000). Late Quaternary palæoecology and palæoclimates of the eastern Sahara. *J. Afr. Earth Sci*. 30, 929–939. doi:10.1016/S0899-5362(00)00061-0

Pachur, H.-J., and Hoelzmann, P. (1991). Paleoclimatic implications of late quaternary lacustrine sediments in Western Nubia, Sudan. *Quat. Res*. 36, 257–276. doi:10.1016/0033-5894(91)90002-M

Pagani, L., and Crevecoeur, I. (2019). "What is Africa? A human perspective," in *Modern human origins and dispersal words, bones, genes, tools: DFG center for advanced studies series*. Editors Y. Sahle, H. Reyes-Centeno, and C. Bentz (Tübingen: Kerns Verlag).

Pagani, L., Schiffels, S., Gurdasani, D., Danecek, P., Scally, A., Chen, Y., et al. (2015). Tracing the route of modern humans out of Africa by using 225 human genome sequences from Ethiopians and Egyptians. *Am. J. Hum. Genet*. 96, 986–991. doi:10.1016/j.ajhg.2015.04.019

Paulissen, E., and Vermeersch, P. (1989). Le comportement des grands fleuves allogènes: l'exemple du Nil durant le Quaternaire Supérieur. *Bull. de la Soc. Géol. de France*, 73–83. doi:10.2113/gssgfbull.V.1.73.

Paulissen, E., and Vermeersch, P. M. (1987). "Earth, man and climate in the Egyptian Nile Valley during the Pleistocene," in *Prehistory of arid North Africa : essays in honor of fred Wendorf*. Editor A. E. Close (Dallas: SMU Press), 29–68.

Paulissen, E., and Vermeersch, P. M. (2000). "Stratigraphical context of the Palaeolithic sites in the Makhadma area," in *Palaeolithic living sites in upper and middle Egypt*. Editor P. M. Vermeersch (Leuven: Leuven University Press), 75–90.

Pearson, O. M., Hill, E. C., Peppe, D. J., Van Plantinga, A., Blegen, N., Faith, J. T., et al. (2020). A late Pleistocene human humerus from Rusinga Island, Lake Victoria, Kenya. *J. Hum. Evol*. 146, 102855. doi:10.1016/j.jhevol.2020.102855

Phillips, J. L. (1972). North Africa, the Nile Valley, and the problem of the late paleolithic. *Curr. Anthropol*, 587–590.

Phillips, J. L. (1973). *Two final paleolithic sites in the Nile Valley and their external relations*. Cairo: Ministry of Petroleum and Mineral Wealth, Geological Survey of Egypt and Mining Authority.

Phillips, R., Holdaway, S. J., Ramsey, R., Wendrich, W., and Emmitt, J. (2017). "Approaches to paleoenvironment and landscape use," in *The desert fayum reinvestigated. The early to mid-holocene landscape archaeology of the fayum north shore, Egypt monumenta archaeologica*. Editors S. J. Holdaway and W. Wendrich (Los Angeles: UCLA Cotsen Institute of Archaeology Press), 17–50.

Pinhasi, R., and Semal, P. (2000). The position of the Nazlet Khater specimen among prehistoric and modern African and Levantine populations. *J. Hum. Evol*. 39, 269–288. doi:10.1006/jhev.2000.0421

Potì, A., and Weniger, G.-C. (2019). "Human occupation of Northern Morocco at the Last Glacial Maximum," in Human Adaptations to the Last Glacial Maimum: the Solutrean and its neighbors, Editors I. Schmidt, J. Cascalheira, N. Bicho, and G.-C. Weniger (Newcastle upon Tyne: Cambridge Scholars Publishing), 44–64.

Prendergast, M. E., Lipson, M., Sawchuk, E. A., Olalde, I., Ogola, C. A., Rohland, N., et al. (2019). Ancient DNA reveals a multistep spread of the first herders into sub-Saharan Africa. *Science*. 365, eaaw6275. doi:10.1126/science.aaw6275

QGIS Development Team (2017). QGIS geographic information system. Open source geospatial foundation project. Available at: http://qgis.osgeo.org (Accessed January 4, 2021).

R Core Team (2020). *R: a language and environment for statistical computing*. Vienna, Austria: R Foundation for Statistical Computing. Available at: https://www.R-project.org.

Rasmussen, S. O., Bigler, M., Blockley, S. P., Blunier, T., Buchardt, S. L., Clausen, H. B., et al. (2014). A stratigraphic framework for abrupt climatic changes during the Last Glacial period based on three synchronized Greenland ice-core records: refining and extending the INTIMATE event stratigraphy. *Quat. Sci. Rev*. 106, 14–28. doi:10.1016/j.quascirev.2014.09.007

Reed, C. A. (1965). A human frontal bone from the Late Pleistocene of the Kom Ombo Plain, Upper Egypt. *Man*. 65, 101–104. doi:10.2307/2797442

Reed, C. A., Baumhoff, M. A., Butzer, K. W., and Boloyen, D. S. (1967). "Preliminary report on the archaeological aspects of the research of the yale university prehistoric expedition to Nubia (Kom-Ombo) 1962–1963," in *Fouilles en Nubie: 1961–1963 International Campaign to Save the Monuments of Nubia (Le Caire: organisme général des impressions gouvernementales)*, 145–156.

Reimer, P. J., Austin, W. E. N., Bard, E., Bayliss, A., Blackwell, P. G., Ramsey, C. B., et al. (2020). The Intcal20 northern Hemisphere radiocarbon age calibration curve (0–55 cal kBP). *Radiocarbon*. 62, 1–33. doi:10.1017/RDC.2020.41

Revel, M., Ducassou, E., Grousset, F. E., Bernasconi, S. M., Migeon, S., Revillon, S., et al. (2010). 100,000 years of African monsoon variability recorded in sediments of the Nile margin. *Quat. Sci. Rev*. 29, 1342–1362. doi:10.1016/j.quascirev.2010.02.006

Revel, M., Ducassou, E., Skonieczny, C., Colin, C., Bastian, L., Bosch, D., et al. (2015). 20,000 years of Nile River dynamics and environmental changes in the Nile catchment area as inferred from Nile upper continental slope sediments. *Quat. Sci. Rev*. 130, 200–221. doi:10.1016/j.quascirev.2015.10.030

Reynolds, N., and Riede, F. (2019). House of cards: cultural taxonomy and the study of the European Upper Palaeolithic. *Antiquity*. 93, 1350–1358. doi:10.15184/aqy.2019.49

Riede, F., Hoggard, C., and Shennan, S. (2019). Reconciling material cultures in archaeology with genetic data requires robust cultural evolutionary taxonomies. *Palgrave Commun*. 5, 1–9. doi:10.1057/s41599-019-0260-7

Roskin, J., and Tsoar, H. (2017). "Late quaternary chronologies of the Northern Sinai/Northwestern Negev dunefield and their palaeoclimatic and palaeoenvironmental implications," in *Quaternary of the levant: environments, climate change, and humans*. Editors Y. Enzel and O. Bar-Yosef (Cambridge University Press), 505–520.

Roubet, C. (1989a). "Report on site E-82-1: a workshop for the manufacture of grinding stones at Wadi Kubbaniya," in *The prehistory of Wadi Kubbaniya*. Editors F. Wendorf, R. Schild, and A. E. Close (Dallas, Texas: SMU Press), 588–610.

Roubet, C. (1989b). "The grinding stones of site E-78-3, Wadi Kubbaniya," in *The prehistory of Wadi Kubbaniya*. Editors F. Wendorf, R. Schild, and A. E. Close (Dallas: SMU Press), Vol. 3, 473–489.

Rowland, J., and Tassie, G. J. (2014). Prehistoric sites along the edge of the Western Nile Delta: report on the results of the imbaba prehistoric survey 2013–14. *J. Egypt. Archaeol.* 100, 49–65. doi:10.1177/030751331410000104

Said, R. (1981). *The geological evolution of the river Nile*. New York: Springer-Verlag.

Said, R. (1993). *The river Nile. Geology, hydrology and utilization*. Oxford: Pergamon Press.

Sanchez Goñi, M. F., and Harrison, S. P. (2010). Millennial-scale climate variability and vegetation changes during the Last Glacial: concepts and terminology. *Quat. Sci. Rev.* 29, 2823–2827. doi:10.1016/j.quascirev.2009.11.014

Sandford, K. S. (1936). Problems of the Nile valley. *Am. Geogr. Soc.* 26, 67–76. doi:10.2307/209464

Sandford, K. S., and Arkell, W. J. (1929). On the relation of palaeolithic man to the history and geology of the Nile Valley in Egypt. *Man*. 29, 65–69. doi:10.2307/2790452

Sandford, K. S., and Arkell, W. J. (1933). *Paleolithic man and the Nile Valley in Nubia and upper Egypt: a study of the region during pliocene and pleistocene times*. Chicago: University of Chicago press.

Scerri, E. M. L., Thomas, M. G., Manica, A., Gunz, P., Stock, J. T., Stringer, C., et al. (2018). Did our species evolve in subdivided populations across Africa, and why does it matter?. *Trends Ecol. Evol.* 33, 582–594. doi:10.1016/j.tree.2018.05.005

Schild, R., and Wendorf, F. (2002). Forty years of the combined prehistoric expedition. *Archaeologia Polona*. 40, 5–22.

Schild, R., and Wendorf, F. (2010). "Late palaeolithic hunters-gatherers in the Nile Valley of Nubia and Upper Egypt," in *South-eastern mediterranean peoples between 130,000 and 10,000 years ago*. Editor E. A. A. Garcea (Oxford and Oakville: Oxbow Books), 89–125.

Schild, R., Chmielewska, M., and Wieckowska, H. (1968). "The arkinian and shamarkian industries," in *The prehistory of Nubia*. Editor F. Wendorf (Dallas: Fort Burgwin Research Center; SMU Press), 651–767.

Schild, R., Hill, C. L., and Bluszcz, A. (2020). "Age of the late middle paleolithic nile aggradation, the Khormusan and the Atmur El Kibeish Aterian," in *Not just a corridor. Human occupation of the Nile Valley and neighbouring regions between 75,000 and 15,000 years ago*. Editors A. Leplongeon, M. Goder-Goldberger, and D. Pleurdeau (Paris: Muséum national d'histoire naturelle), 71–91.

Schild, R., and Wendorf, F. (1989). "The late Pleistocene Nile in Wadi Kubbaniya," in *The prehistory of Wadi Kubbaniya, volume 2. stratigraphy, paleoeconomy, and environment*. Editors F. Wendorf, R. Schild, and A. E. Close (Dallas: Southern Methodist University Press), 15–100.

Schmidt, K. (1996). "Helman in Egypt-a PPN site?," in *Neolithic chipped stone industries of the fertile crescent, and their contemporaries in adjacent regions studies in early near eastern production, subsistence, and environment*. Editors S. K. Kozlowski and H. G. Gebel (Berlin: Ex Oriente), 127–136.

Schuenemann, V. J., Peltzer, A., Welte, B., van Pelt, W. P., Molak, M., Wang, C. C., et al. (2017). Ancient Egyptian mummy genomes suggest an increase of Sub-Saharan African ancestry in post-Roman periods. *Nat. Commun.* 8, 15694. doi:10.1038/ncomms15694

Shackelford, L. L. (2007). Regional variation in the postcranial robusticity of late upper paleolithic humans. *Am. J. Phys. Anthropol.* 133, 655–668. doi:10.1002/ajpa.20567

Shiner, J. L. (1968). "Miscellaneous sites," in *The prehistory of Nubia*. Editor F. Wendorf (Dallas: Fort Burgwin Research Center; SMU Press), 630–650.

Skinner, A. R., Blackwell, B. A. B., Kleindienst, M. R., Smith, J. R., Kieniewicz, J. M., Adelsberger, K. A., et al. (2013). "Reconstructing paleoenvironments in the Western Desert, Egypt: ESR dating freshwater Molluscs from Kharga Oasis," in *Archaeological chemistry VIII ACS symposium series*. Editors R. A. Armitage and J. H. Burton (Washington, DC: American Chemical Society), 321–364. doi:10.1021/bk-2013-1147.ch019

Skoglund, P., Thompson, J. C., Prendergast, M. E., Mittnik, A., Sirak, K., Hajdinjak, M., et al. (2017). Reconstructing prehistoric African population structure. *Cell.* 171, 59–71.e21. doi:10.1016/j.cell.2017.08.049

Smith, P. E. L. (1966). *A revised view of the later palaeolithic of Egypt. La Préhistoire: problèmes et Tendances*. Paris: CERS, 391.

Smith, P. E. L. (1967). "Canadian prehistoric expedition to Nubia. A preliminary report on the recent prehistoric investigations near Kom Ombo, Upper Egypt," in *Fouilles en nubie: 1961–1963. International campaign to save the monuments of Nubia*. (Le Caire: Organisme Général des Impressions Gouvernementales), 195–208.

Smith, P. E. L. (1985). "An enigmatic frieze from Upper Egypt: a problem in Nilotic rock art," in *Studi di paletnologia in onore di Salvatore*. Editors M. Puglisi, M. Liverani, A. Palmieri, and R. Peroni (Roma: Universita di Roma), 359–368.

Sommer, R. S., and Zachos, F. E. (2009). Fossil evidence and phylogeography of temperate species: 'glacial refugia' and post-glacial recolonization. *J. Biogeogr.* 36, 2013–2020. doi:10.1111/j.1365-2699.2009.02187.x

Stager, J. C., Ryves, D. B., Chase, B. M., and Pausata, F. S. (2011). Catastrophic drought in the Afro-Asian Monsoon region during Heinrich event 1. *Science*. 331, 1299–1302. doi:10.1126/science.1198322

Stanford, J. D., Rohling, E. J., Bacon, S., Roberts, A. P., Grousset, F. E., and Bolshaw, M. (2011). A new concept for the paleoceanographic evolution of Heinrich event 1 in the North Atlantic. *Quat. Sci. Rev.* 30, 1047–1066. doi:10.1016/j.quascirev.2011.02.003

Stanley, D. J., McRea, J. E., and Waldron, J. C. (1996). Nile Delta drill core and sample database for 1985–1994: Mediterranean Basin (MEDIBA) Program. Washington: Smithsonian Institution Press.

Stanley, D. J., and Warne, A. G. (1993). Nile Delta: recent geological evolution and human impact. *Science* 260, 628–634. doi:10.1126/science.260.5108.628

Stewart, J. R., Lister, A. M., Barnes, I., and Dalén, L. (2010). Refugia revisited: individualistic responses of species in space and time. *Proc. Biol. Sci.* 277, 661–671. doi:10.1098/rspb.2009.1272

Stewart, J. R., and Stringer, C. B. (2012). Human evolution out of Africa: the role of refugia and climate change. *Science*. 335, 1317–1321. doi:10.1126/science.1215627

Storemyr, P., Kelany, A., Negm, M. A., and Tohami, A. (2008). More "Lascaux along the Nile"? Possible late palaeolithic rock art in Wadi Abu Subeira, Upper Egypt. *Sahara*. 19, 155–158.

Stuiver, M., and Reimer, P. J. (1993). Extended 14C data base and revised CALIB 3.0 14C age calibration program. *Radiocarbon*. 35, 215–230. doi:10.1017/S0033822200013904

Sultan, M., Sturchio, N., Hassan, F. A., Hamdan, M. A. R., Mahmood, A. M., Alfy, Z. E., et al. (1997). Precipitation source inferred from stable isotopic composition of Pleistocene groundwater and carbonate deposits in the Western Desert of Egypt. *Quaternary Res.* 48, 29–37. doi:10.1006/qres.1997.1907

Talbot, M. R., Williams, M. a. J., and Adamson, D. A. (2000). Strontium isotope evidence for late Pleistocene reestablishment of an integrated Nile drainage network. *Geology*. 28, 343–346. doi:10.1130/0091-7613(2000)28<343:SIEFLP>2.0

Tassie, G. J. (2014). *Prehistoric Egypt: socioeconomic transformations in Northeast Africa from the last glacial maximum to the neolithic, 24,000 to 6,000 cal BP*. London: Golden House Publications.

Tostevin, G. B. (2012). *Seeing lithics: a middle-range theory for testing for cultural transmission in the Pleistocene*. Oxford: Oxbow Books.

Tryon, C. A., Crevecoeur, I., Faith, J. T., Ekshtain, R., Nivens, J., Patterson, D., et al. (2015). Late Pleistocene age and archaeological context for the hominin calvaria from GvJm-22 (Lukenya Hill, Kenya). *Proc. Natl. Acad. Sci. U.S.A.* 112, 2682–2687. doi:10.1073/pnas.1417909112

Tryon, C. A., Lewis, J. E., Ranhorn, K. L., Kwekason, A., Alex, B., Laird, M. F., et al. (2018). Middle and later stone age chronology of kisese II rockshelter (UNESCO world heritage kondoa rock-art sites), Tanzania. *PLOS One*. 13, e0192029. doi:10.1371/journal.pone.0192029

Usai, D. (2016). *A picture of prehistoric Sudan*. Oxford Handbooks Online. doi:10.1093/oxfordhb/9780199935413.013.56

Usai, D. (2008). "Lunates and micro-lunates, cores and flakes: the lithic industry of R12," in *A neolithic cemetery in the Northern Dongola reach (Sudan): excavation at site R12 BAR international series*. Editors S. Salvatori and D. Usai (Oxford: Archaeopress), 33–52.

Usai, D. (2019). "The palaeolithic / stone age," in Handbook of ancient Nubia, Editor D. Raue (Berlin/Boston: De Gruyter). 155–170. doi:10.1515/9783110420388-008

Usai, D. (2020). The Qadan, the Jebel Sahaba cemetery and the lithic collection. *Archaeol. Polona*. 58, 99–119. doi:10.23858/APa58.2020.006

Van de Loosdrecht, M., Bouzouggar, A., Humphrey, L., Posth, C., Barton, N., Aximu-Petri, A., et al. (2018). Pleistocene North African genomes link near Eastern and sub-Saharan African human populations. *Science*. 360, 548–552. doi:10.1126/science.aar8380

Van Neer, W., Paulissen, E., and Vermeersch, P. M. (2000). Chronology, subsistence and environment at the Late Palaeolithic fishing sites of Mahatma 2 and 4" in *Palaeolithic living sites in Upper and Middle Egypt*. (Leuven: Leuven University Press), 271–288.

Van Neer, W., and Gautier, A. (1989). "Animal remains from the late paleolithic sequence at Wadi Kubbaniya" in *The prehistory of Wadi Kubbaniya, volume 2. Stratigraphy, paleoeconomy, and environment*. Editors. F. Wendorf, R. Schild, and A. E. Close (Dallas: Southern Methodist University Press), 119–161.

Van Peer, P., Vermeersch, P. M., and Paulissen, E. (2010). *Chert quarrying, lithic technology and a modern human burial at the palaeolithic site of Taramsa 1, Upper Egypt*. Leuven: Leuven University Press.

Vermeersch, P. M. (2012). "Contributions to the prehistory of the Eastern Desert in Egypt," in *The history of the peoples of the Eastern Desert*. Editors H. Barnard and K. Duistermaat (Los Angeles: Cotsen Institute of Archaeology, University of California), 24–41.

Vermeersch, P. M., Editor (2000). *Palaeolithic living sites in Upper and Middle Egypt*. Leuven: Leuven University Press.

Vermeersch, P. M. (2020). "Human occupation density in the lower Nile Valley (75,000–15,000 years ago)," in *Not just a corridor. Human occupation of the Nile Valley and neighbouring regions between 75,000 and 15,000 years ago*. Editors A. Leplongeon, M. Goder-Goldberger, and D. Pleurdeau (Paris: Muséum National d'Histoire Naturelle), 139–157.

Vermeersch, P. M. (2002a). "Two upper palaeolithic burials at Nazlet Khater," in *Palaeolithic quarrying sites in upper and middle Egypt Egyptian prehistory monographs*. Editor P. M. Vermeersch (Leuven: Leuven University Press), 273–282.

Vermeersch, P. M., and Van Neer, W. (2015). Nile behaviour and late palaeolithic humans in upper Egypt during the late Pleistocene. *Quat. Sci. Rev*. 130, 155–167. doi:10.1016/j.quascirev.2015.03.025

Vermeersch, P. M., Gijselings, G., and Paulissen, E. (2000). "Shuwikhat 2, a silsilian site," in *Palaeolithic living sites in Upper and Middle Egypt*. Editor P. M. Vermeersch (Leuven: Leuven University Press), 201–210.

Vermeersch, P. M., Paulissen, E., Peer, P. V., Stokes, S., Charlier, C., Stringer, C., et al. (1998). A middle palaeolithic burial of a modern human at Taramsa Hill, Egypt. *Antiquity*. 72, 475–484. doi:10.1017/S0003598X00086919

Vermeersch, P. M., Paulissen, E., and Vanderbeken, T. (2002b). "Nazlet Khater 4, an upper palaeolithic underground chert mine," in *Palaeolithic quarrying sites in Upper and Middle Egypt*. Editor P. M. Vermeersch (Leuven: Leuven University Press), 211–272.

Vermeersch, P., Paulissen, E., and Van Neer, W. (1989). "The late Palaeolithic Makhadma sites (Egypt): environment and subsistence". in *Late Prehistory of the Nile Basin and the Sahara*. Editors L. Krzyzaniak and M. Kobusiewicz (Poznan: Poznan Archaeological Museum), 87–114. doi:10.11588/propylaeum.194.259

Vermeersch, P., Van Neer, W., and Gullentops, F. (2006). "El Abadiya 3, Upper Egypt, a Late Palaeolithic site on the shore of a large Nile Lake," in *Archeaology of Early Northeastern Africa Studies in African Archaeology*, Editors K. Kroeper, M. Chlodnicki, and M. Kobusiewicz (Poznan: Poznan Archaeological Museum), 375–424. doi:10.11588/propylaeum.218.287

Vignard, E. (1955). Les stations et industries Sébiliennes du Burg el Makkazin: Région de Kom-Ombo (Haute-Egypte). *Bull. de la Soc. Préhist. de Fr*. 52, 437–452. Available at: http://www.jstor.org/stable/27915064 (Accessed January 4, 2021).

Vignard, E. (1928). Une nouvelle industrie lithique: le Sébilien. *Bull. de la Soc. Préhist. de Fr*. 25, 200–220.

Waelbroeck, C., Paul, A., Kucera, M., Rosell-Melé, A., Weinelt, M., Schneider, R., et al. (2009). Constraints on the magnitude and patterns of ocean cooling at the last glacial maximum. *Nat. Geosci*. 2, 127–132. doi:10.1038/ngeo411

Wang, K., Goldstein, S., Bleasdale, M., Clist, B., Bostoen, K., Bakwa-Lufu, P., et al. (2020). Ancient genomes reveal complex patterns of population movement, interaction, and replacement in sub-Saharan Africa. *Sci. Adv*. 6, eaaz0183. doi:10.1126/sciadv.aaz0183

Warne, A. G., and Stanley, D. J. (1993). Late quaternary evolution of the Northwest Nile Delta and adjacent coast in the alexandria region, Egypt. *J. Coast Res*. 9, 26–64. Available at: https://journals.flvc.org/jcr/article/view/78957 [Accessed January 4, 2021].

Warne, A. G., and Stanley, D. J. (1995). Sea-level change as critical factor in development of basin margin sequences: new evidence from late quaternary record. *J. Coast. Res*. 17, 231–240. Available at https://www.jstor.org/stable/25735649 (Accessed January 4, 2021)

Wendorf, F. (1968). "Site 117: a nubian final paleolithic graveyard near Jebel Sahaba, Sudan," in *The prehistory of Nubia*. Editor F. Wendorf (Dallas: Fort Burgwin Research Center, SMU Press), 954–995.

Wendorf, F., and Schild, R. (1976). *Prehistory of the Nile Valley*. New: Academic Press.

Wendorf, F., and Schild, R. (1989). "Summary and synthesis," in *The prehistory of Wadi Kubbaniya*. Editors F. Wendorf, R. Schild, and A. E. Close (Dallas: SMU Press), 768–824.

Wendorf, F., and Schild, R. (1986). *The Wadi Kubbaniya skeleton: a late paleolithic burial from Southern Egypt*. Dallas: Southern Methodist University Press.

F. Wendorf, R. Schild, and A. E. Close Editors (1989). *The prehistory of Wadi Kubbaniya*. Dallas: SMU Press.

Wendorf, F., and Schild, R. (2001). *Holocene settlement of the Egyptian Sahara*. New York: Kluwer Academic Publishers/Plenum Publishers.

Wendorf, F., Schild, R., and Haas, H. (1979). A new radiocarbon chronology for prehistoric sites in Nubia. *J. Field Archaeol*. 6, 219–223. doi:10.1179/009346979791489311

Williams, M. A. J. (2020). "Ice, wind and water. Late Pleistocene environments in the main Nile, Atbara, Blue and White Nile basins (75,000–15,000 years ago)," in *Not just a corridor. Human occupation of the Nile Valley and neighbouring regions between 75,000 and 15,000 years ago*. Editors A. Leplongeon, M. Goder-Goldberger, and D. Pleurdeau (Paris: Muséum National d'histoire Naturelle), 19–37.

Williams, M. (2019). *The Nile basin quaternary geology, geomorphology and prehistoric environments*. Cambridge: Cambridge University Press.

Williams, M. A. J., Duller, G. A. T., Williams, F. M., Woodward, J. C., Macklin, M. G., El Tom, O. A. M., et al. (2015). Causal links between Nile floods and eastern Mediterranean sapropel formation during the past 125 kyr confirmed by OSL and radiocarbon dating of Blue and White Nile sediments. *Quat. Sci. Rev*. 130, 89–108. doi:10.1016/j.quascirev.2015.05.024

Williams, M. A. J., Talbot, M. R., Aharon, P., Abdl Salaam, Y., Williams, F., and Brendeland, K. I. (2006). Abrupt return of the summer monsoon 15,000 years ago: new supporting evidence from the lower White Nile valley and Lake Albert. *Quat. Sci. Rev*. 25, 2651–2665. doi:10.1016/j.quascirev.2005.07.019

Williams, M. A. J., Williams, F. M., Duller, G. A. T., Munro, R. N., El Tom, O. A. M., Barrows, T. T., et al. (2010). Late Quaternary floods and droughts in the Nile valley, Sudan: new evidence from optically stimulated luminescence and AMS radiocarbon dating. *Quat. Sci. Rev*. 29, 1116–1137. doi:10.1016/j.quascirev.2010.02.018

Woodward, J. C., Macklin, M. G., Krom, M. D., and Williams, M. A. J. (2007). "The Nile: evolution, quaternary river environments and material fluxes," in *Large rivers: geomorphology and management*. Editor A. Gupta (Chichester, West Sussex: John Wiley & Sons, Ltd), 261–292.

Yeshurun, R. (2018). Taphonomy of old archaeofaunal collections: new site-formation and subsistence data for the Late paleolithic Nile Valley. *Quat. Int*. 471, 35–54. doi:10.1016/j.quaint.2017.06.027

Zazzo, A. (2014). Bone and enamel carbonate diagenesis: a radiocarbon prospective. *Palaeogeogr. Palaeoclimatol. Palaeoecol*. 416, 168–178. doi:10.1016/j.palaeo.2014.05.006

Zboray, A. (2012). An unpublished shelter with prehistoric engravings of a possible late Pleistocene date in the North-central Sinai (Egypt). *Sahara* 23, 163–166.

Conflict of Interest: The author declares that the research was conducted in the absence of any commercial or financial relationships that could be construed as a potential conflict of interest.

frontiers in Earth Science

ORIGINAL RESEARCH
published: 12 February 2021
doi: 10.3389/feart.2020.599491

Magnetic Susceptibility Properties of Loess From the Willendorf Archaeological Site: Implications for the Syn/Post-Depositional Interpretation of Magnetic Fabric

Christian Zeeden[1,2]* *and Ulrich Hambach*[2]

[1]Leibniz Institute for Applied Geophysics, Hannover, Germany, [2]BayCEER and Chair of Geomorphology, University of Bayreuth, Bayreuth, Germany

At the Willendorf site Upper Paleolithic archeological layers associated to early Aurignacian cultures were found. The environmental conditions of the associated society, potentially co-existing with Neanderthal groups, is still not fully understood. Here, we report on environmental magnetic analyses including anisotropy of the magnetic susceptibility (AMS) carried out on loessic aeolian sediments at the Willendorf site. Data on lineation, foliation and the degree of anisotropy were used to assess depositional and post-depositional magnetic fabric properties and to deduce site-specific environmental processes. Overall, the loess is of aeolian origin and shows magnetic enhancement and magnetic fabric properties similar to those of other European loess geoarchives, but the magnetic mineralogy differs from many 'dry' loess sites, insofar as it shows a higher susceptibility during heating. We infer an enhanced neoformation of magnetite during heating due to the presence of organic matter. While at face value the AMS properties are indicative of pure aeolian loess consistent with previous studies, imbrication suggests post-depositional slope movement toward the Danube, which obscures inferences on palaeo-wind direction. It is well possible that these post-depositional magnetic fabric alterations occur at other localities with similar geomorphological settings.

Keywords: environmental magnetism, geoarchaeology, sedimentology, loess, magnetic fabric (AMS), magnetic fabric and anisotropy, rock magnetic analyses

OPEN ACCESS

Edited by:
Barbara Mauz,
University of Salzburg, Austria

Reviewed by:
Chris Oldknow,
University of Liverpool,
United Kingdom
Maodu Yan,
Institute of Tibetan Plateau Research (CAS), China

***Correspondence:**
Christian Zeeden
christian.zeeden@leibniz-liag.de

Specialty section:
This article was submitted to Sedimentology, Stratigraphy and Diagenesis, a section of the journal Frontiers in Earth Science

Received: *27 August 2020*
Accepted: *16 December 2020*
Published: *12 February 2021*

Citation:
Zeeden C and Hambach U (2021) Magnetic Susceptibility Properties of Loess From the Willendorf Archaeological Site: Implications for the Syn/Post-Depositional Interpretation of Magnetic Fabric. Front. Earth Sci. 8:599491. doi: 10.3389/feart.2020.599491

INTRODUCTION

Loess deposits provide the longest continuous terrestrial record of paleoclimatic change still accumulating today, and cover large parts of Eurasia. These sediments originate from settled dust of dominantly silty composition. Generally, fine and predominantly silty material can be derived directly from vast drylands or high mountain ranges, and is in the latter case transported first by river systems, and later on by wind (e.g., Cowie, 1964; Smalley, 1972; Mason, 2001; Smalley et al., 2009; Lancaster, 2020). In western Eurasia and especially in the surroundings of glaciated areas and river floodplains of (braided) rivers, silt-size mineral dust typically accumulates in sediment-traps close to the major rivers systems, where they contribute the substrate for loess-paleosol-sequences (LPS; e.g., Smalley, 1972; Smalley et al., 2009; Jipa, 2014; Lehmkuhl et al., 2016; Lehmkuhl et al., 2018). This may include the slopes of surrounding mountains. While aeolian sedimentation rates and pedogenetic

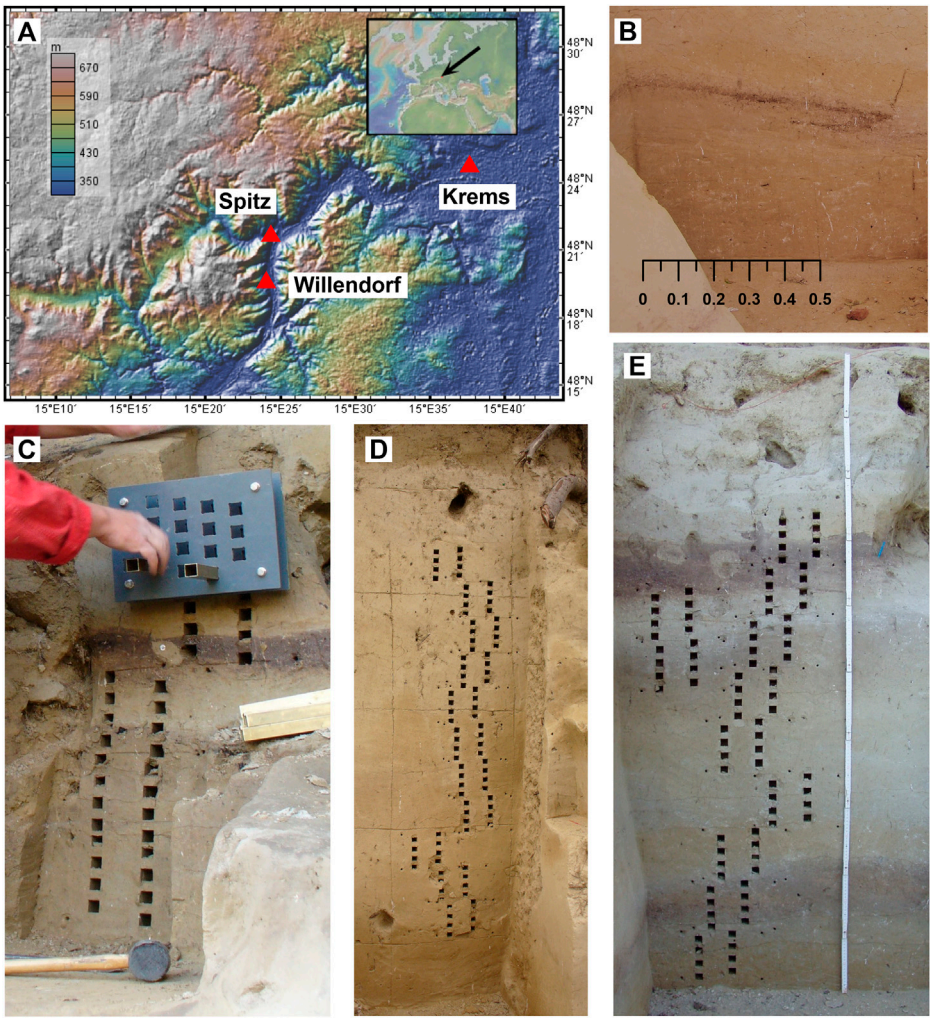

FIGURE 1 | Location of the Willendorf Site in Lower Austria [**(A)**; top] in the vicinity of the cities Spitz and Krems, and field photos of sediment movement **(B)**, including a scale of 0.5 m, **(C)** the right profile #5, **(D)** the left profile #4, and **(E)** profile #1. Note that images **(B–D)** were taken into the wall, where **(E)** is taken perpendicular to the wall. Photographs were taken in daylight and partly under a tent, therefore illumination is imperfect.

overprinting of accumulated dust may differ with climatic conditions, LPS often constitute high-resolution geoarchives of past environmental conditions where other archives are sparse or even absent (e.g., Derbyshire, 2003; Shi et al., 2003; Rousseau et al., 2007; Yang and Ding, 2014; Haesaerts et al., 2019). Therefore, numerous loess sites in Europe are considered valuable archives for past climate and environments (e.g., Shi et al., 2003; Antoine et al., 2009; Krauß et al., 2016; Moine et al., 2017; Obreht et al., 2017; Zeeden et al., 2018). This includes specifically archaeological sites imbedded in loess in Austria (e.g., Hambach et al., 2008; Händel et al., 2009; Sprafke et al., 2013; Terhorst et al., 2013, Terhorst et al., 2015; Zeeden et al., 2015; Meyer-Heintze et al., 2018; Sprafke et al., 2020). Notably in western Eurasia, loess hosts and preserves a wealth of archaeological materials due to its naturally high carbonate content which ensures not only bone preservation but generally buffers pervasive chemical weathering (Händel et al., 2009; Neugebauer-Maresch et al., 2014).

Sedimentological and rock magnetic analyses are used in geoarchaeological research in order to investigate the intensity and type of deposition, pedogenesis and post-depositional alterations (e.g., Hambach et al., 2008; Antoine et al., 2009; Zeeden et al., 2009; Bösken et al., 2018). The homogeneity of a sediment source may be determined from grain size-, geochemical- and rock magnetic properties (e.g., Cheng et al., 2019; Obreht et al., 2019). The intensity of pedogenesis may be derived from geochemical weathering indices (e.g., Buggle et al., 2011; Újvári et al., 2014; Obreht et al., 2019), the neoformation of clay (Schulte and Lehmkuhl, 2018) and also magnetic enhancement (e.g., Heller and Tung-Sheng, 1986; Forster et al., 1994; Forster et al., 1996; Hambach et al., 2008; Bradák et al., 2011; Zeeden et al., 2016). Post-depositional alteration through water logging may be derived from the depletion of magnetic minerals if present (e.g., Bábek et al., 2011; Baumgart et al., 2013; Gocke et al., 2014; Taylor et al., 2014; Krauß et al., 2016). In addition, the translocation of

fine magnetic particles may play a role (e.g., Oldknow et al., 2020).

At Willendorf, the sediment is described to be of local aeolian origin due to its grain size distribution properties (Haesaerts, 1990). The sediment exhibits clear features of slope movement (Haesaerts, 1990; Haesaerts and Teyssandier, 2003; Nigst, 2006; Nigst et al., 2008; Nigst et al., 2014), also **Figure 1B**. The loess shows stratigraphical consistency of bleaching, pedogenesis of different intensity, and charcoal indicative of (human?) burning. To assess in which manner the loess is suitable for paleoenvironmental reconstructions, we conducted an environmental magnetic study. Several rock magnetic parameters were measured to assess the type of magnetic enhancement or depletion, and to roughly characterize the minerals contributing to the magnetic susceptibility. Most relevant, the anisotropy of the magnetic susceptibility (AMS) was measured for a suite of samples to gain insight into magnetic fabric and either depositional or post-depositional processes. In order to account for possible spatial differences, several profiles were sampled. The AMS describes the spatial anisotropy of the magnetic fabric. In sediments, oblate fabrics often dominate due to the settling of, among others, clay minerals; the resulting oblateness is commonly called foliation (F). A preferential alignment, called lineation (L), may be interpreted in terms of transport direction, and/or may give insight into post-depositional processes, especially slope movement. Importantly, the AMS can give insight different depositional processes, such as aeolian loess and water-lain material (Liu et al., 1988; Bradák and Kovács, 2014). However, the values reported in Liu et al. (1988) are not ubiquitously applicable (Bradák and Kovács, 2014; Cheng et al., 2019). Further, preferential alignment directions of magnetic particles can be used to investigate the direction in which deposition took place (Jordanova et al., 2007b; Zeeden et al., 2015) and also the effects of post-depositional alteration (e.g., Bradák and Kovács, 2014; Taylor and Lagroix, 2015; Bradák et al., 2019a).

Here we present a rock magnetic study on the Willendorf site in Austria, which is famous for reports on the oldest Aurignacian technology in Central Europe (Nigst et al., 2008; Nigst et al., 2014). The key aim is to understand the primary (post) depositional and pedogenic processes.

SETTING

The archaeological site of Willendorf is famous for the "Venus of Willendorf" (Antl-Weiser, 2009). It is one of a suite of archaeological sites preserved in loess along the Danube in the area since 2006, systematic excavations were conducted by an interdisciplinary team (Nigst, 2006; Nigst et al., 2008; Nigst et al., 2014), from which one of the earliest modern human tool assemblages in western Europe was identified. The excavation studied here is commonly referred to as "Willendorf II." The Willendorf II section is located in the Danube valley west of Vienna (Austria) in the Wachau area (**Figure 1**). The exposure is located on a terrace c. 15 above and c. 300 m west of the present Danube river at 48°19′23.5″ latitude and 15°24′15.2″ longitude.

Along with the archaeological excavations, sedimentological investigations and detailed ^{14}C dating have been carried out. Several publications divide the site into sedimentological Units A (top) to E (bottom) (Haesaerts, 1990; Haesaerts et al., 1996; Haesaerts and Teyssandier, 2003, and references therein). We sampled the Units C and D in order to gain information on the site formation and post-depositional processes. Unit D is characterized as "thick stony heterogeneous brown loam" (Haesaerts and Teyssandier, 2003). Abundant molluscs, a polyedric structure and biogalleries filled with carbonates are reported from the top of Unit D. It was ^{14}C dated to ~41,700 and ~39,500 BP. Layers (C9 to C2) represent a suite of yellow to gray loess intercalated with several humic horizons. The uppermost humic soil horizon (at the top of the interval C9 to C2; **Figure 2**) is expressed as strongest soil. Especially as the lower part is reported to be stretched by solifluction, and contains stripes of ash. Subunit C1 represents a tundra gley and represents a marker between the middle and late Pleniglacial at ~28,000 BP (Haesaerts, 1990; Haesaerts and Teyssandier, 2003). The layers at the archaeological site are inclined toward the Danube valley (Haesaerts et al., 1996; their **Figure 1**) and show, at least in part, signs of solifluction (Haesaerts, 1990; Haesaerts et al., 1996; Haesaerts and Teyssandier, 2003; Nigst et al., 2008; Nigst et al., 2014). Grain size distributions of the Willendorf stratigraphy are reported in Haesaerts (1990), and show the highest contributions of silt in the ~10–80 μm range. An additional coarse component (>150 μm) contributes up to ~10% in Unit D, but less than 5% to samples from Unit C. Haesaerts (1990) interprets the grain size data (in context of field observations) as indicative aeolian transported fluvial sediments from the Danube River floodplain.

Here we report on the sedimentological findings from environmental magnetic investigations, and contextualize these regarding selected loess geoarchives. Sedimentological descriptions of Willendorf were done by Haesaerts and Teyssandier (2003) and the references therein. Especially the paper by Haesaerts and Teyssandier (2003) provides comprehensive sedimentological descriptions of loess, loam and different soil types. In addition, their work and the paper by Haesaerts (1990) place the Willendorf into the stratigraphic context of other archaeological sites from the Danube Valley and Moravia.

METHODS

Oriented specimens were taken using brass tubes and an orientation holder. The samples are cubes with an edge length of 2 cm each, giving 8 cm^3 sample volume. Full spatial orientation was provided by means of magnetic compass measurements. The vertical spacing of sample centers was ~2.1 cm. Stratigraphic heights are given in cm as relative to the profile base.

Once in the laboratory, samples were stored in a μ-metal box until measurements began. Measurements were carried out in the Laboratory for Paleo- and Environmental Magnetism, Bayreuth. Anhysteric remanent magnetisations (ARMs) were produced along one spatial axis, and were induced with a 50 μT static

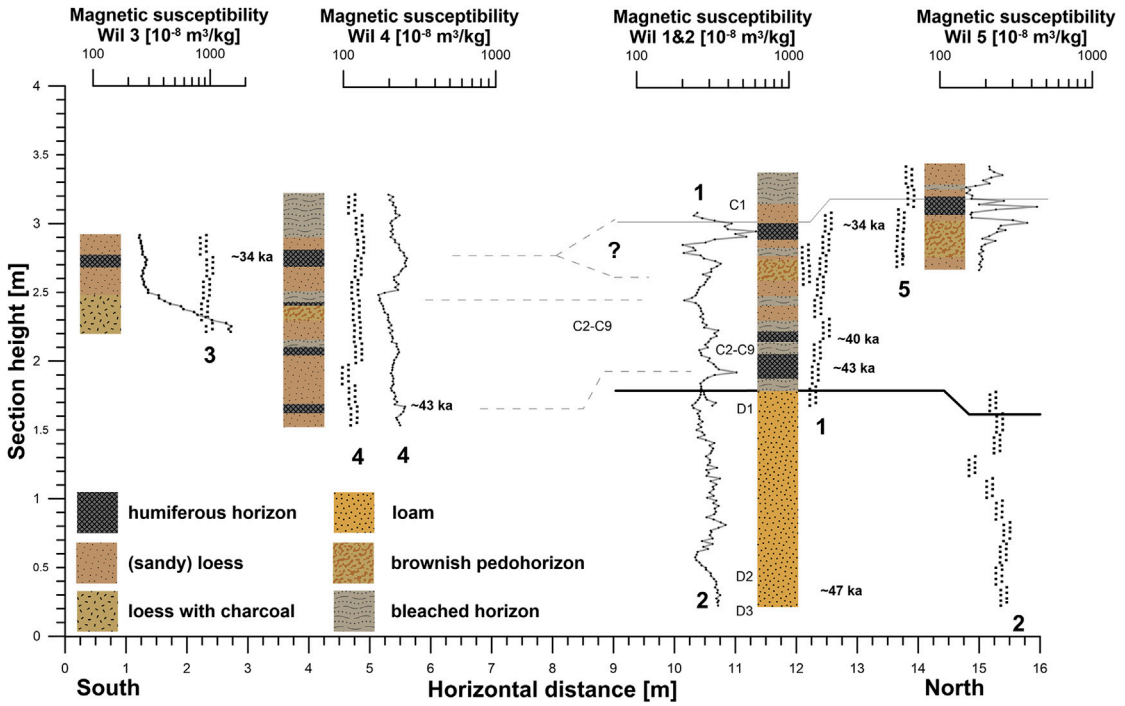

FIGURE 2 | Sampling scheme for magnetic measurements at Willendorf as sampling spurs. The magnetic susceptibility profiles (one to five, where one and two are plotted together) are plotted with simplified stratigraphies. Several geological layer numbers (from Nigst et al., 2008) are included here (C1-D3). Ages are taken from the correlation to Greenland ice core proxy data by (Nigst et al., 2014) and have been applied to equivalent depths of our profiles. Lines correlate different profiles (own interpretation).

field and 100 mT alternating field amplitude using a Magnon AFD 300 (**Figure 3**). Isothermal remanent magnetisations (IRMs) were induced with fields up to 2.5 T using a MAGNON PM II pulse magnetizer. Back-field IRMs were produced to determine the coercivity of remanence (Bcr). The magnetisations resulting from imprinting ARMs and IRMs were measured using an AGICO JR-6A spinner magnetometer.

The mass-specific magnetic low-field susceptibility (MS) and AMS measurements were made with an AGICO KLY-3S kappabridge at a frequency of 875 kHz and a magnetic field intensity of 300 A/m. The temperature dependent susceptibility (κ-T) was determined with this bridge and the CS-3 furnace under an Argon atmosphere. Data were corrected for a nine-point moving average smoothed dataset of the empty holder, and were scaled to the mass-normalized room temperature susceptibility using the CUREVAL software supplied by AGICO. The frequency dependent susceptibility (χfd%) was measured for profiles one to three. A MAGNON VFSM was used with frequencies of 300 Hz and 3 kHz and a field of 300 A/m. χ_{fd}% is defined as (χ300 Hz–χ3 kHz)/χ300 Hz × 100, Δχ represents the difference χ300 Hz–χ3 kHz (**Figure 4**).

The AMS was measured for every 8th/5th sample. The AMS is defined by a symmetric tensor with three principal axes (k1 > k2 > k3). k1 is the main MS axis of a 3-dimensional ellipsoid and represents the magnetic lineation direction. k3 is perpendicular to the magnetic foliation which represents a plain through k1 and k2 (e.g., Ferré et al., 2003). The principal susceptibility angles were corrected for the sampling angles, and were calculated together with AMS parameters using the AGICO software Anisoft 5.0. The determination and interpretation of AMS is a useful tool to determine the alignment of para- and ferromagnetic particles. Both the intensity of alignment and its direction can give insight into syn- and post-depositional sedimentary processes. However, a single sample may not be representative for a past environment, and commonly multiple samples are being investigated for a well-founded interpretation (Tarling and Hrouda, 1993). The AMS parameters lineation (L), foliation (F) and the degree of anisotropy (P) are plotted in **Figure 3** with corresponding depths. These are defined as L = ($k1$–$k2$)/kmean, F = ($k2$–$k3$)/kmean and P = $k1$/$k3$ (Tarling and Hrouda, 1993, and references therein).

RESULTS AND DISCUSSION

Rock Magnetic Properties as Indicators of Lithology

The reported rock magnetic datasets, in depth, consist of the magnetic susceptibility, its frequency dependency, and the ARM. In addition, AMS, κ-T and IRM data have been measured for selected samples (**Figures 3**, **5**-**7**). An overview of the sampling scheme is given in **Figure 2**, with MS data plotted for all samples. **Figure 3** depicts several rock magnetic properties (left) and also the AMS properties: Lineation and Foliation (right). The

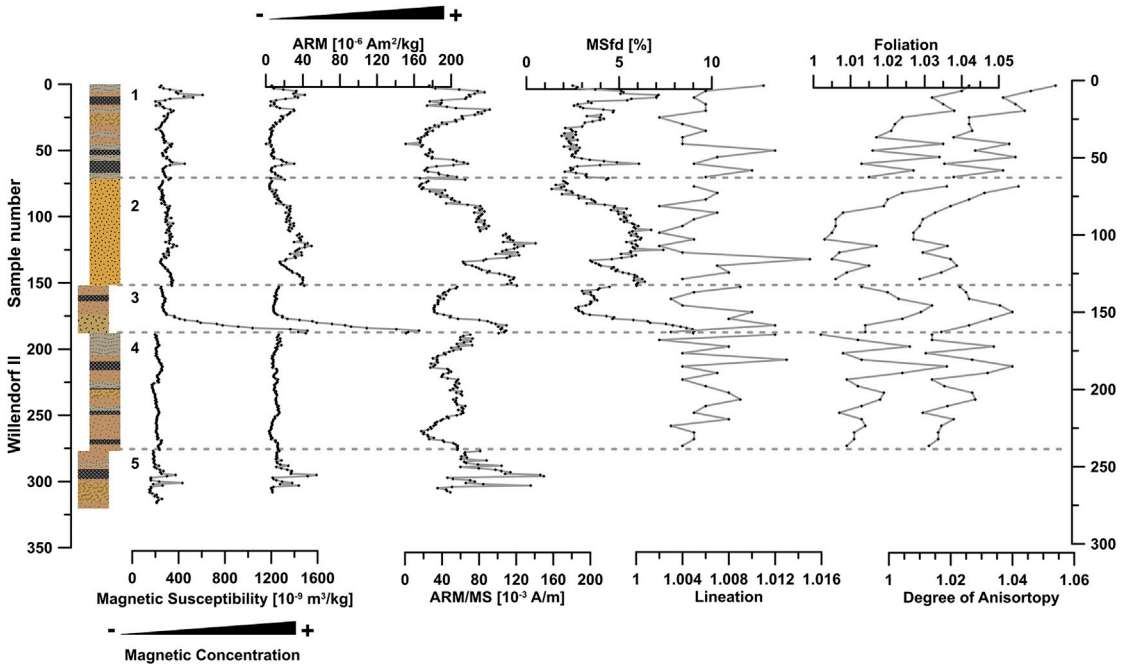

FIGURE 3 | Rock magnetic parameters for the five profiles (from **Figure 2**; plotted on top of each other against lithology on the left), and their interpretation regarding magnetic concentration and grain size for the magnetic susceptibility (MS), anhysteretic remeanent magnetisation (ARM) and the ARM/MS ratio. The frequency dependent magnetic susceptibility (χ_{fd}%) may be regarded as representing a combination of magnetic concentration and grain size. Note that the ordinate is not representing a continuous stratigraphy.

magnetic parameters ARM, ARM/MS and χfd%, indicative of magnetic concentration and grain size, roughly follow the lithology. Increased values of the MS, χfd%, and ARM occur in soil formation phases and cultural layers. The mean MS is 29.5 $\times 10^{-8}$ m^3/kg, the mean χfd% is 4%, and the mean ARM is 18.63 $\times$ 10^{-8} Am/kg.

Mineral magnetic parameters have been recognized as relevant paleoclimate proxies in loess research. MS and χfd% provide highly sensitive proxies in particular for humidity during dust accumulation and loess formation (e.g., Buggle et al., 2014 and references therein). This is based on the assumption that the original loess can be regarded as homogenous, and the neoformation of magnetic minerals (mainly magnetite and maghemite) is driven by pedogenesis. Increasingly intense pedogenesis enhances the mineral magnetic signals. The MS of any mineral magnetic assemblage in loess-paleosol sequences is also determined by the physical grain size distribution and magnetic mineralogy. The highest values in MS and χfd% can occur in intervals with higher concentrations of ultra-fine magnetic particles, but may in theory also be dependent on dust source and wind intensity (Song et al., 2010). Such fine particles precipitate dominantly from weathering solutions, and their abundance is a sensitive sediment/soil humidity proxy (e.g., Balsam et al., 2011; Maher, 2011). The MS is mainly an indicator of bulk concentration of magnetic minerals, while the χfd% is mainly driven by magnetic grain size. Increased χfd% indicates fine-viscous (VF herein) magnetic grain sizes in the transition from Stable Single Domain (SSD) and Superparamagnetic (SP) states (e.g., Zheng et al., 1991; Yu and Oldfield, 1993; Deng et al., 2006).

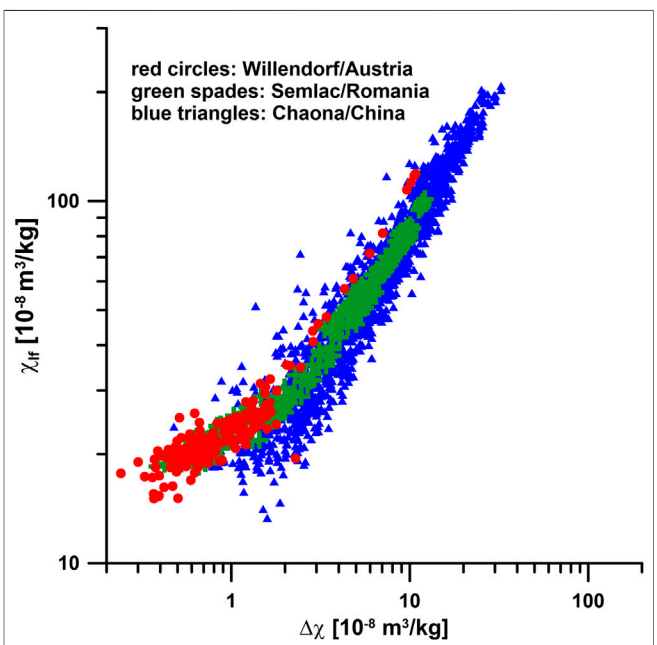

FIGURE 4 | Magnetic enhancement at Willendorf, compared with Semlac in the Middle Danube Basin (Zeeden et al., 2016) and Chinese loess from Chaona (Song et al., 2007). Note that this is a double logarithmic plot.

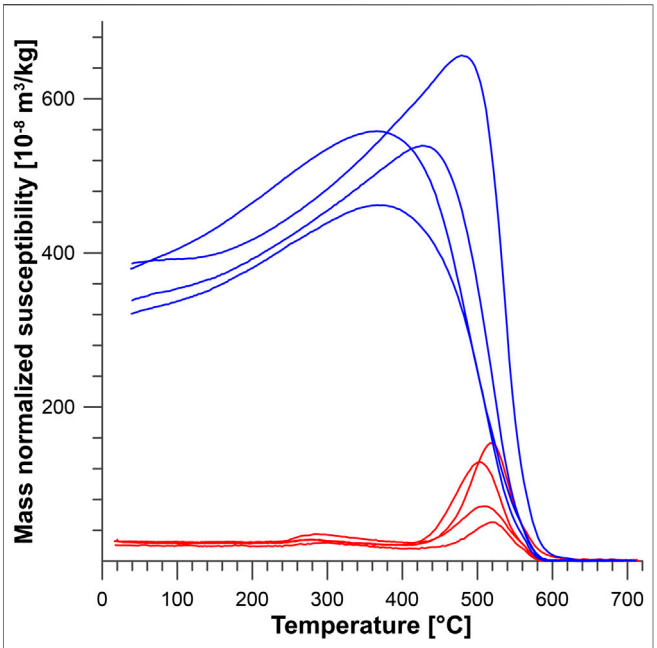

FIGURE 5 | Temperature dependent magnetic susceptibility of four selected samples. Heating is plotted in red, cooling is depicted in blue. Note the increase at ~300°C, and decrease at ~580°C indicative of a magnetite contribution.

The IRM acquisition curves show the dominance of magnetically soft minerals (**Figure 7**), here probably magnetite and maghemite. A hard component, which is not fully saturated at 2.5 T, is also present, and is interpreted to represent (goethite and/or) hematite. The ARM signal is considered to be driven by the concentration of ferromagnetic particles. Thereby, ARM reflects mainly Stable Single Domain (SSD) magnetite and maghemite, for which MS is relatively low. Consequently, the ARM/MS ratio is related to magnetic grain size, with higher ARM contributions (and thus a higher ARM/MS ratio) referring to magnetic grain sizes of SSD and small PSD range (c. 0.03–0.2 μm; Liu et al., 2012). This relationship between ARM contribution and grain size is highlighted by the pattern similarity of the ARM and the χfd%, which is also related to magnetic grain size. The information from both proxies characterize the enhancement of fine magnetic grain size populations at the SP-SSD boundary, which is increasing with pedogenetic overprinting of unaltered aeolian dust accumulation.

Although the frequency dependency of the magnetic susceptibility is relatively low on average, a magnetic enhancement similar to other Eurasian profiles can be observed (**Figure 4**). For example, the magnetic enhancement at Willendorf is similar to the enhancement at Semlac (eastern Middle Danube Basin; Zeeden et al., 2016) and Chaona (Chinese Loess Plateau; Song et al., 2007). The highest MS and Δχ data from Willendorf are likely related to a contribution of magnetic minerals created during burning in an archaeological and pedo-horizon in sub-profile three (vgl. **Figure 2**). In the enhancement plot (**Figure 4**), data from Willendorf show a higher increase of MS than of Δχ. This property suggests a higher proportion of SSD and MD particles with high MS but limited VF particles. This may also be an influence of higher hematite concentrations; its presence is indicated by the hard IRM component.

Magnetic Mineralogy Derived from Temperature Dependent Magnetic Susceptibility

To gain insight into the magnetic mineralogy of the Willendorf site, high-temperature susceptibility experiments were carried out. **Figure 5** shows the results of high-temperature susceptibility measurements (normalized to the initial susceptibility) from selected samples. The results are similar for the four investigated samples and are therefore discussed together.

Little change can be observed in the magnetic susceptibility during heating up to ~240°C, but an increase in the magnetic susceptibility is present from ~250 to ~280°C. This pattern is followed by an MS decrease up to ~400°C, a strong increase to ~500–520°C, and a final decrease in the susceptibilities at ~580–600°C (**Figure 5**). Oches and Banerjee (1996) discuss an increase in the magnetic susceptibility at ~300°C as related to a "transition of weakly-magnetic Fe-hydroxides (e.g., lepidocrocite) to maghemite or some other higher susceptibility phase". The decrease between ~300 and 400°C has been interpreted as the alteration of maghemite to hematite (Gao et al., 2019 and references therein). The increase from ~400 up to ~510°C is interpreted as formation of magnetite from several other iron bearing minerals (Hunt et al., 1995; Oches and Banerjee, 1996; Deng et al., 2001; Liu et al., 2005; Deng et al., 2006). The sample with the highest MS also shows an increase beyond this temperature, which may be a contribution of the Hopkinson effect (Dunlop, 2014). However, due to the decrease in MS before ~550°C and a strong increase of the MS during heating we consider the Hopkinson effect a contributor, but not the dominant control on MS above ~450°C (following Deng et al., 2000). Also the increased MS during cooling speaks for the neo-formation of magnetite, and against the dominance of the Hopkinson effect. Here, the final decrease of the susceptibility at ~580°C is interpreted to represent the Curie temperature of magnetite. While it is clear from these data that magnetite dominates the magnetic susceptibility, the size of the potential contribution from hematite is uncertain in this case. The fact that magnetite did only partly oxidize to maghemite during seasonal dry phases may be interpreted as annually mostly wet soil and sediment conditions, possibly due to periglacial conditions. Note that our κ-T results are similar to the κ-T data obtained from loess from the last glacial at the Krems-Wachtberg archaeological site about 20 km north-east of Willendorf (Zeeden et al., 2015), a loess-paleosol sequence in the Czech Republic (Oches and Banerjee, 1996), and the Poiana Cireşului site in eastern Romania (Zeeden et al., 2009, Zeeden et al., 2011); and as such, indicates similarities in terms of magnetic mineralogy. However, in other studies of European loess distinctly different temperature dependent susceptibility patterns have been observed in the drier parts of the Middle and Lower Danube Basins (Jordanova et al., 2007a; Necula and Panaiotu, 2012; Bradák et al., 2019b). In particular, the strong

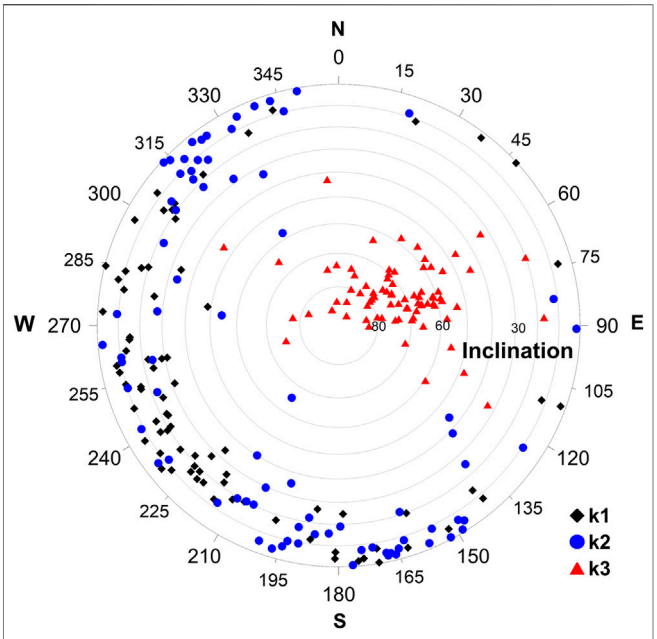

FIGURE 6 | Directions of the anisotropy of the magnetic susceptibility, plotted as stereographic projection on the upper hemisphere. Red triangles represent Kmin directions pointing predominantly to the east (northeast), black spades stand for Kmax directions and blue circles represent Kint directions.

increase in MS from ~450 to 580°C is not present in loess preserved within arid and steppe environments. This increase in MS from ~450 to 580°C may be related to a higher amount of organic matter in the sediment at Willendorf (Campbell et al., 1997).

A relevant contribution of water logging processes would lead to an increase in the amount of fine particles through grain size reduction. This would be visible as increasing $\Delta\chi$ and decreased MS in **Figure 4** (Baumgart et al., 2013; Zeeden et al., 2018). However, this has not been observed in our results. Water logging can also increase magnetic grain size through preferential dissolution of small grains (e.g., Oldknow et al., 2020). This would lead to decreasing $\Delta\chi$ with decreasing MS, which does not seem a relevant factor either compared to reference data (**Figure 4**).

AMS Properties

Phyllosilicates (here probably micas and clay minerals), generally have oblate AMS ellipsoids (e.g., Borradaile and Werner, 1994; Martín-Hernández and Hirt, 2003). Under gravity these will settle preferentially in a horizontal plane, imprinting an oblate magnetic fabric in the bedding plane. Also compaction plays a role and increases F (Zhu et al., 2004). Since the AMS of most samples from Willendorf is oblate due to the higher foliation than lineation (**Figure 3**), and only few samples show strong lineations, the AMS may be dominated by phyllosilicates and potentially by super-fine ferrimagnetic particles incorporated in and attached to those minerals (Hyodo et al., 2020).

Here, the measures of anisotropy (P, L, F) show no obvious trends and relations to archaeological layers and pedo-horizons. Generally, the anisotropy of samples is low, mean values for P, L and F are 1.006, 1.017 and 1.023, respectively. The P and F data correlate with a correlation coefficient of 0.98, whereas the correlation between the L and F is only 0.01. The F and L are independent variables, and therefore may have different physical and genetic origins. Foliation is commonly found parallel to the bedding plane due to gravitational forces and compaction (Hus, 2003), and is generally interpreted to be the result of sedimentation of oblate particles. Wang and Løvlie (2010) suggest that the foliation is mainly acquired during (initial) wetting of freshly aeolian deposited loess.

The lineation of the magnetic fabric may be related to a preferential aeolian wind or deposition direction (e.g., Tarling and Hrouda, 1993; Lagroix and Banerjee, 2002; Zeeden et al., 2015), or can originate from post-depositional processes (e.g., slope movement processes; Reinders and Hambach, 1995). At Willendorf, slope movement toward the Danube valley is evident in the field (**Figure 1B**). The imbrication of the k3 axis in the north-east direction (**Figure 6**) may be related to either deposition on a slope, or to post-depositional changes due to down-slope sediment movement. Because the magnetic foliation is mainly acquired through gravitational forces during initial wetting (Wang and Løvlie, 2010), we consider the imbrication as originating from post-depositional slope movement in the direction of the Danube valley. The k1 direction is aligned in the downslope direction with the imbrication of the k3 inclination. We therefore interpret the k1 direction as indicative of the direction of the windblown loess, while the imbrication as representing post-depositional slope processes, the latter dominating the AMS at Willendorf.

The degree of anisotropy has been suggested to reflect the depositional environment of loess and loess-like deposits, where aeolian loess has been shown to obtain a lower foliation relative to loess redistributed by water or as water-saturated mud [mostly <1.02, (Liu et al., 1988; Bradák and Kovács, 2014); mostly <1.03 (Wang and Løvlie, 2010)]. Comparing the Willendorf data (mean Foliation F of 1.023 and mean Lineation L of 1.017) to the data of Bradák and Kovács (2014), Liu et al., (1988), and Wang and Løvlie (2010), the loess at Willendorf is of aeolian origin, and not re-deposited on the slope by periglacial or other slope processes. This contradicts our interpretation of a post-depositional imbrication. In addition, the loess was deposited on a slope which makes the absence of post-depositional relocation unlikely, especially also regarding potential sediment dynamics under a periglacial climate. Therefore, this study shows that the low foliations may not always be representative of "purely" aeolian loess. We hypothesize that the values of AMS properties are influenced by the grain size distribution, which is in this case rather coarse. Especially the addition of quartz sand can be expected to decrease the AMS and lead to a lower foliation than caused by finer silt- and clay-sized (and more often platy) particles.

While fine magnetic particles formed during *in-situ* pedogenesis may dominate the MS signal, the originally deposited carriers of MS are relevant for interpreting the AMS. This may be a large or small proportion, depending on the original contribution of grain sizes. Numerous studies have

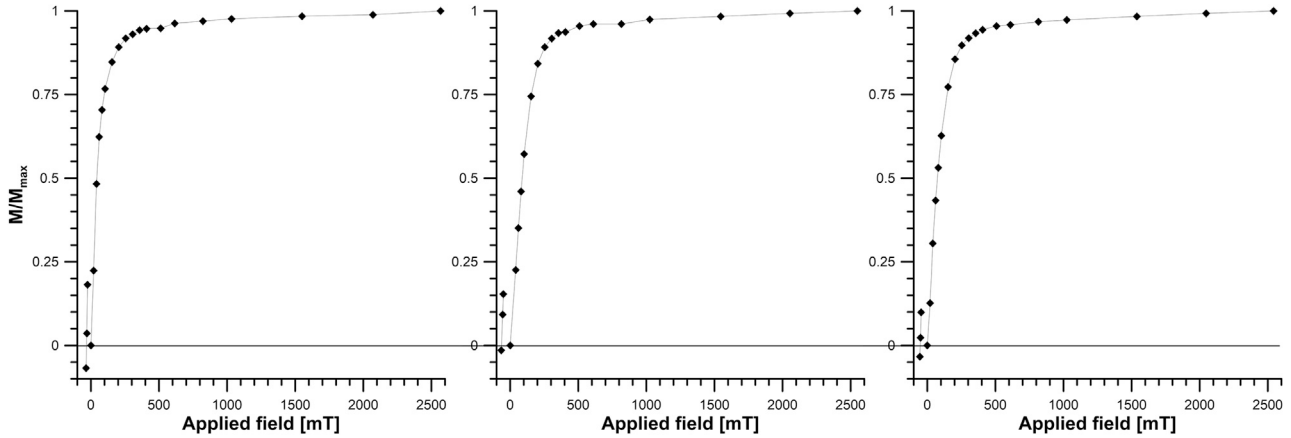

FIGURE 7 | Acquisition and back-field curves of the Isotherman Remanent Magnetisation (IRM) for three samples. The ordinate denotes the magnetisation over the maximal magnetisation at the highest applied field. Note that magnetisation increases steeply with the applied field until ~300 mT, and increases slowly thereafter. The field necessary to reduce the net remanence to zero lies between 32 and 64 mT.

shown a relationship between particle size and magnetic grain size, with detrital magnetic grains being SSD or coarser. These tend to reside in coarser particle size fractions—and therefore, are less liable to translocation. Larger detrital (magnetic) grains are unlikely to be moved within the sediment, while small grains may move downward in the sediment column. In addition, illuviation of fine particles (as fine clay), which may be relevant carriers of fine magnetic particles, can be excluded here because the sediment has a high carbonate content throughout, preventing any illuviation processes (e.g., Kühn et al., 2018).

CONCLUSION

Based on the magnetic properties of the loess sediment at Willendorf, we draw the following conclusions on the sedimentation and post-depositional alteration.

Grain size data demonstrated the loess to be of aeolian origin. The loess is partly overprinted by pedogenesis, but interstadial soils are much more weakly developed than interglacial soils from the reference data, in agreement with chronological information. The magnetic sediment properties do not show magnetic depletion due to waterlogging and/or permafrost action which is surprising in light of the presence of leached horizons, but may have resulted from the presence of high carbonate content which could have buffered dissolution reactions.

Despite evidence for colluvial slope processes in the field, these do not result in enhanced foliation values. Rather, the relatively low foliation values observed are controlled by the grain size of the loess, provenanced from deflation of the nearby Danube floodplain. We imply that AMS is to be seen in the context of grain size of the investigated material, and that general distinctions between aeolian and water-lain fabric can only be made for specific grain size distributions. The lineation in the southwest/northeast direction is interpreted as indicative for deposition on a gentle slope inclined toward the Danube. In particular, we interpret the clear imbrication in the same direction as the result of post-depositional processes moving the sediment toward the valley, presumably under a periglacial climate with seasonal freezing and thawing cycles.

DATA AVAILABILITY STATEMENT

The original data presented in the study are included in the article/**Supplementary Material**, further inquiries can be directed to the corresponding author.

AUTHOR CONTRIBUTIONS

UH designed the study; CZ and UH took the samples; CZ carried out measurements and carried out the study. Both authors jointly interpreted data. CZ wrote the manuscript with input from UH.

FUNDING

Funding for measurements were provided by the DFG under grant number 5370964.

ACKNOWLEDGMENTS

We thank the archaeological team under P. Nigst and B. Violá for access to the Site and for providing local assistance. We appreciate the helpful and constructive feedback from three reviewers.

SUPPLEMENTARY MATERIAL

The Supplementary Material for this article can be found online at: https://www.frontiersin.org/articles/10.3389/feart.2020.599491/full#supplementary-material.

REFERENCES

Antl-Weiser, W. (2009). The time of the Willendorf figurines and new results of Palaeolithic research in lower Austria. *Anthropologie.* 47, 131–141.

Antoine, P., Rousseau, D.-D., Fuchs, M., Hatté, C., Gauthier, C., Marković, S. B., et al. (2009). High-resolution record of the last climatic cycle in the southern Carpathian Basin (Surduk, Vojvodina, Serbia). *Quat. Int.* 198, 19–36. doi:10.1016/j.quaint.2008.12.008

Bábek, O., Chlachula, J., and Grygar, T. M. (2011). Non-magnetic indicators of pedogenesis related to loess magnetic enhancement and depletion: examples from the Czech Republic and southern Siberia. *Quat. Sci. Rev.* 30, 967–979. doi:10.1016/j.quascirev.2011.01.009

Balsam, W. L., Ellwood, B. B., Ji, J., Williams, E. R., Long, X., and El Hassani, A. (2011). Magnetic susceptibility as a proxy for rainfall: worldwide data from tropical and temperate climate. *Quat. Sci. Rev.* 30, 2732–2744. doi:10.1016/j.quascirev.2011.06.002

Baumgart, P., Hambach, U., Meszner, S., and Faust, D. (2013). An environmental magnetic fingerprint of periglacial loess: records of Late Pleistocene loess–palaeosol sequences from Eastern Germany. *Quat. Int.* 296, 82–93. doi:10.1016/j.quaint.2012.12.021

Borradaile, G. J., and Werner, T. (1994). Magnetic anisotropy of some phyllosilicates. *Tectonophysics* 235, 223–248. doi:10.1016/0040-1951(94)90196-1

Bösken, J., Sümegi, P., Zeeden, C., Klasen, N., Gulyás, S., and Lehmkuhl, F. (2018). Investigating the last glacial Gravettian site 'Ságvár Lyukas Hill' (Hungary) and its paleoenvironmental and geochronological context using a multi-proxy approach. *Palaeogeogr. Palaeoclimatol. Palaeoecol.* 509, 77–90. doi:10.1016/j.palaeo.2017.08.010

Bradák, B., and Kovács, J. (2014). Quaternary surface processes indicated by the magnetic fabric of undisturbed, reworked and fine-layered loess in Hungary. *Quat. Int.* 319, 76–87. doi:10.1016/j.quaint.2013.02.009

Bradák, B., Kovács, J., and Magyari, Á. (2019a). The origin and significance of some 'irregular' loess magnetic fabric found in the Paks succession (Hungary). *Geophys. J. Int.* 217, 1742–1754. doi:10.1093/gji/ggz117

Bradák, B., Seto, Y., Csonka, D., Végh, T., and Szeberényi, J. (2019b). The hematite–goethite enhancement model of loess and an 'irregular' case from Paks, Hungary. *J. Quat. Sci.* 34, 299. doi:10.1002/jqs.3101

Bradák, B., Thamó-Bozsó, E., Kovács, J., Márton, E., Csillag, G., and Horváth, E. (2011). Characteristics of Pleistocene climate cycles identified in Cérna Valley loess–paleosol section (Vértesacsa, Hungary). *Quat. Int.* 234, 86–97. doi:10.1016/j.quaint.2010.05.002

Buggle, B., Glaser, B., Hambach, U., Gerasimenko, N., and Marković, S. (2011). An evaluation of geochemical weathering indices in loess–paleosol studies. *Quat. Int.* 240, 12–21. doi:10.1016/j.quaint.2010.07.019

Buggle, B., Hambach, U., Müller, K., Zöller, L., Marković, S. B., and Glaser, B. (2014). Iron mineralogical proxies and quaternary climate change in SE-European loess–paleosol sequences. *Catena.* 117, 4–22. doi:10.1016/j.catena.2013.06.012

Campbell, A. S., Schwertmann, U., and Campbell, P. A. (1997). Formation of cubic phases on heating ferrihydrite. *Clay Miner.* 32, 615–622. doi:10.1180/claymin.1997.032.4.11

Cheng, L., Song, Y., Sun, H., Bradák, B., Rustam, O., Zong, X., et al. (2019). Pronounced changes in paleo-wind direction and dust sources during MIS3b recorded in the Tacheng loess, northwest China. *Quat. Int.* 552, 122–134. doi:10.1016/j.quaint.2019.05.002

Cowie, J. D. (1964). Loess in the Manawatu district, New Zealand. *N. Z. J. Geol. Geophys.* 7, 389–396. doi:10.1080/00288306.1964.10420185

Deng, C., Shaw, J., Liu, Q., Pan, Y., and Zhu, R. (2006). Mineral magnetic variation of the Jingbian loess/paleosol sequence in the northern Loess Plateau of China: implications for Quaternary development of Asian aridification and cooling. *Earth Planet Sci. Lett.* 241, 248–259. doi:10.1016/j.epsl.2005.10.020

Deng, C., Zhu, R., Jackson, M. J., Verosub, K. L., and Singer, M. J. (2001). Variability of the temperature-dependent susceptibility of the Holocene eolian deposits in the Chinese loess plateau: a pedogenesis indicator. *Phys. Chem. Earth Part Solid Earth Geod.* 26, 873–878. doi:10.1016/S1464-1895(01)00135-1

Deng, C., Zhu, R., Verosub, K. L., Singer, M. J., and Yuan, B. (2000). Paleoclimatic significance of the temperature-dependent susceptibility of Holocene loess along a NW-SE transect in the Chinese loess plateau. *Geophys. Res. Lett.* 27, 3715–3718. doi:10.1029/2000GL008462

Derbyshire, E. (2003). Loess, and the dust indicators and records of terrestrial and marine palaeoenvironments (DIRTMAP) database. *Quat. Sci. Rev.* 22, 1813–1819. doi:10.1016/S0277-3791(03)00209-9

Dunlop, D. J. (2014). High-temperature susceptibility of magnetite: a new pseudo-single-domain effect. *Geophys. J. Int.* 199, 707–716. doi:10.1093/gji/ggu247

Ferré, E. C., Teyssier, C., Jackson, M., Thill, J. W., and Rainey, E. S. G. (2003). Magnetic susceptibility anisotropy: a new petrofabric tool in migmatites. *J. Geophys. Res. Solid Earth.* 108, 2086. doi:10.1029/2002JB001790

Forster, T., Evans, M. E., and Heller, F. (1994). The frequency dependence of low field susceptibility in loess sediments. *Geophys. J. Int.* 118, 636–642. doi:10.1111/j.1365-246X.1994.tb03990.x

Forster, Th., Heller, F., Evans, M. E., and Havliček, P. (1996). Loess in the Czech Republic: magnetic properties and paleoclimate. *Studia Geophys. Geod.* 40, 243–261. doi:10.1007/BF02300741

Gao, X., Hao, Q., Oldfield, F., Bloemendal, J., Deng, C., Wang, L., et al. (2019). New high-temperature dependence of magnetic susceptibility-based climofunction for quantifying paleoprecipitation from Chinese loess. *G-cubed.* 20, 4273–4291. doi:10.1029/2019GC008401

Gocke, M., Hambach, U., Eckmeier, E., Schwark, L., Zöller, L., Fuchs, M., et al. (2014). Introducing an improved multi-proxy approach for paleoenvironmental reconstruction of loess–paleosol archives applied on the Late Pleistocene Nussloch sequence (SW Germany). *Palaeogeogr. Palaeoclimatol. Palaeoecol.* 410, 300–315. doi:10.1016/j.palaeo.2014.06.006

Haesaerts, P. (1990). Nouvelles recherches au gisement de Willendorf (Basse Autriche). *Bull. L'Institut R. Sci. Nat. Belg. Sci. Terre.* 60, 203–218.

Haesaerts, P., Damblon, F., Bachner, M., and Trnka, G. (1996). Revised stratigraphy and chronology of the Willendorf II sequence, Lower Austria. *Archaeol. Austriaca.* 80, 25–42.

Haesaerts, P., Gerasimenko, N., Damblon, F., Yurchenko, T., Kulakovska, L., Usik, V., et al. (2019). The Upper Palaeolithic site Doroshivtsi III: a new chronostratigraphic and environmental record of the Late Pleniglacial in the regional context of the Middle Dniester-Prut loess domain (Western Ukraine). *Quat. Int.* 546, 196. doi:10.1016/j.quaint.2019.12.018

Haesaerts, P., and Teyssandier, N. (2003). "The early Upper Paleolithic occupations of Willendorf II (Lower Austria): a contribution to the chronostratigraphic and cultural context of the beginning of the Upper Paleolithic in Central Europe." in The chronology of the Aurignacian and of the transitional technocomplexes: dating, stratigraphies, cultural implications. proceedings of symposium, 2–8 September 2-8, 2001.

Hambach, U., Zeeden, C., Hark, M., and Zöller, L. (2008). Magnetic dating of an Upper Palaeolithic cultural layer bearing loess from the Krems-Wachtberg site (Lower Austria). *Abh. Geol. Bundesanst.* 62, 153–157.

Händel, M., Simon, U., Einwögerer, T., and Neugebauer-Maresch, C. (2009). Loess deposits and the conservation of the archaeological record—the Krems-Wachtberg example. *Quat. Int.* 198, 46–50. doi:10.1016/j.quaint.2008.07.005

Heller, F., and Tung-sheng, L. (1986). Palaeoclimatic and sedimentary history from magnetic susceptibility of loess in China. *Geophys. Res. Lett.* 13, 1169–1172. doi:10.1029/GL013i011p01169

Hunt, C. P., Banerjee, S. K., Han, J., Solheid, P. A., Oches, E., Sun, W., et al. (1995). Rock-magnetic proxies of climate change in the loess-palaeosol sequences of the western Loess Plateau of China. *Geophys. J. Int.* 123, 232–244. doi:10.1111/j.1365-246X.1995.tb06672.x

Hus, J. J. (2003). The magnetic fabric of some loess/palaeosol deposits. *Phys. Chem. Earth, Parts A/B/C.* 28, 689–699. doi:10.1016/S1474-7065(03)00128-1

Hyodo, M., Sano, T., Matsumoto, M., Seto, Y., Bradák, B., Suzuki, K., et al. (2020). Nanosized authigenic magnetite and hematite particles in mature-paleosol phyllosilicates: new evidence for a magnetic enhancement mechanism in loess sequences of China. *J. Geophys. Res. Solid Earth.* 125, e2019JB018705. doi:10.1029/2019JB018705

Jipa, D. C. (2014). The conceptual sedimentary model of the Lower Danube loess basin: sedimentogenetic implications. *Quat. Int.* 351, 14–24. doi:10.1016/j.quaint.2013.06.008

Jordanova, D., Hus, J., and Geeraerts, R. (2007a). Palaeoclimatic implications of the magnetic record from loess/palaeosol sequence Viatovo (NE Bulgaria): palaeoclimatic implications of the magnetic record. *Geophys. J. Int.* 171, 1036–1047. doi:10.1111/j.1365-246X.2007.03576.x

Jordanova, D., Jordanova, N., Henry, B., Hus, J., Bascou, J., Funaki, M., et al. (2007b). Changes in mean magnetic susceptibility and its anisotropy of rock samples as a result of alternating field demagnetization. *Earth Planet Sci. Lett.* 255, 390–401. doi:10.1016/j.epsl.2006.12.025

Krauß, L., Zens, J., Zeeden, C., Schulte, P., Eckmeier, E., and Lehmkuhl, F. (2016). A multi-proxy analysis of two loess-paleosol sequences in the northern Harz foreland, Germany. *Palaeogeogr. Palaeoclimatol. Palaeoecol.* 461, 401–417. doi:10.1016/j.palaeo.2016.09.001

Kühn, P., Aguilar, J., Miedema, R., and Bronnikova, M. (2018). "Chapter 14-textural pedofeatures and related horizons," in *Interpretation of micromorphological features of soils and regoliths*. 2nd Edn, Editors F. Mees, G. Stoops, and V. Marcelino (Elsevier), 377–423.

Lagroix, F., and Banerjee, S. K. (2002). Paleowind directions from the magnetic fabric of loess profiles in central Alaska. *Earth Planet Sci. Lett.* 195, 99–112. doi:10.1016/S0012-821X(01)00564-7

Lancaster, N. (2020). On the formation of desert loess. *Quat. Res.* 96, 1–18. doi:10.1017/qua.2020.33

Lehmkuhl, F., Bösken, J., Hošek, J., Sprafke, T., Marković, S. B., Obreht, I., et al. (2018). Loess distribution and related quaternary sediments in the Carpathian Basin. *J. Maps.* 14, 673–682. doi:10.1080/17445647.2018.1526720

Lehmkuhl, F., Zens, J., Krauß, L., Schulte, P., and Kels, H. (2016). Loess-paleosol sequences at the northern European loess belt in Germany: distribution, geomorphology and stratigraphy. *Quat. Sci. Rev.* 153, 11–30. doi:10.1016/j.quascirev.2016.10.008

Liu, Q., Deng, C., Yu, Y., Torrent, J., Jackson, M. J., Banerjee, S. K., et al. (2005). Temperature dependence of magnetic susceptibility in an argon environment: implications for pedogenesis of Chinese loess/palaeosols. *Geophys. J. Int.* 161, 102–112. doi:10.1111/j.1365-246X.2005.02564.x

Liu, Q., Roberts, A. P., Larrasoaña, J. C., Banerjee, S. K., Guyodo, Y., Tauxe, L., et al. (2012). Environmental magnetism: principles and applications. *Rev. Geophys.* 50, 1–50. doi:10.1029/2012RG000393

Liu, X., Xu, T., and Liu, T. (1988). The Chinese loess in Xifeng, II. A study of anisotropy of magnetic susceptibility of loess from Xifeng. *Geophys. J. Int.* 92, 349–353. doi:10.1111/j.1365-246X.1988.tb01147.x

Maher, B. A. (2011). The magnetic properties of Quaternary aeolian dusts and sediments, and their palaeoclimatic significance. *Aeolian Res.* 3, 87–144. doi:10.1016/j.aeolia.2011.01.005

Martín-Hernández, F., and Hirt, A. M. (2003). The anisotropy of magnetic susceptibility in biotite, muscovite and chlorite single crystals. *Tectonophysics* 367, 13–28. doi:10.1016/S0040-1951(03)00127-6

Mason, J. A. (2001). Transport direction of peoria loess in Nebraska and implications for loess sources on the central great plains. *Quat. Res.* 56, 79–86. doi:10.1006/qres.2001.2250

Meyer-Heintze, S., Sprafke, T., Schulte, P., Terhorst, B., Lomax, J., Fuchs, M., et al. (2018). The MIS 3/2 transition in a new loess profile at Krems-Wachtberg East—a multi-methodological approach. *Quat. Int.* 464, 370–385. doi:10.1016/j.quaint.2017.11.048

Moine, O., Antoine, P., Hatté, C., Landais, A., Mathieu, J., Prud'homme, C., et al. (2017). The impact of Last Glacial climate variability in west-European loess revealed by radiocarbon dating of fossil earthworm granules. *Proc. Natl. Acad. Sci. U.S.A.* 114, 6209. doi:10.1073/pnas.1614751114

Necula, C., and Panaiotu, C. (2012). Rock magnetic properties of a loess-paleosols complex from Mircea Voda (Romania). *Rom. Rep. Phys.* 64, 516–527.

Neugebauer-Maresch, C., Hambach, U., and Anghelinu, M. (2014). Loess and the record of upper palaeolithic cultures in the Danube Basin. *Quat. Int.* 351, 1–4. doi:10.1016/j.quaint.2014.10.041

Nigst, P. R. (2006). "The first modern humans in the middle Danube area?: new evidence from Willendorf II (eastern Austria)," in *When neanderthals and modern humans met.* (Kerns), 269–304.

Nigst, P. R., Haesaerts, P., Damblon, F., Frank-Fellner, C., Mallol, C., Viola, B., et al. (2014). Early modern human settlement of Europe north of the Alps occurred 43,500 years ago in a cold steppe-type environment. *Proc. Natl. Acad. Sci. U.S.A.* 111, 14394–14399. doi:10.1073/pnas.1412201111

Nigst, P. R., Viola, T. B., Haesaerts, P., Blockley, S., Damblon, F., Frank, C., et al. (2008). New research on the Aurignacian of Central Europe: a first note on the 2006 fieldwork at Willendorf II. *Quartar.* 55, 9–15. doi:10.7485/QU55_01

Obreht, I., Hambach, U., Veres, D., Zeeden, C., Bösken, J., Stevens, T., et al. (2017). Shift of large-scale atmospheric systems over Europe during late MIS 3 and implications for Modern Human dispersal. *Sci. Rep.* 7, 5848. doi:10.1038/s41598-017-06285-x

Obreht, I., Zeeden, C., Hambach, U., Veres, D., Marković, S. B., and Lehmkuhl, F. (2019). A critical reevaluation of palaeoclimate proxy records from loess in the Carpathian Basin. *Earth Sci. Rev.* 190, 498–520. doi:10.1016/j.earscirev.2019.01.020

Oches, E. A., and Banerjee, S. K. (1996). Rock-magnetic proxies of climate change from loess -paleosol sediments of the Czech Republic. *Stud. Geophys. Geod.* 40, 287–300. doi:10.1007/BF02300744

Oldknow, C. J., Oldfield, F., Carr, A. S., Hooke, J. M., Biggin, A., Boyle, J. F., et al. (2020). Palustrine wetland formation during the MIS 3 interstadial: implications for preserved alluvial records in the South African Karoo. *Sediment. Geol.* 405, 105698. doi:10.1016/j.sedgeo.2020.105698

Reinders, J., and Hambach, U. (1995). A geomagnetic event recorded in loess deposits of the Tönchesberg (Germany): identification of the Blake magnetic polarity episode. *Geophys. J. Int.* 122, 407–418. doi:10.1111/j.1365-246X.1995.tb07004.x

Rousseau, D.-D., Sima, A., Antoine, P., Hatté, C., Lang, A., and Zöller, L. (2007). Link between European and North Atlantic abrupt climate changes over the last glaciation. *Geophys. Res. Lett.* 34, L22713. doi:10.1029/2007GL031716

Schulte, P., and Lehmkuhl, F. (2018). The difference of two laser diffraction patterns as an indicator for post-depositional grain size reduction in loess-paleosol sequences. *Palaeogeogr. Palaeoclimatol. Palaeoecol.* 509, 126–136. doi:10.1016/j.palaeo.2017.02.022

Shi, C., Zhu, R., Glass, B. P., Liu, Q., Zeman, A., and Suchy, V. (2003). Climate variations since the last interglacial recorded in Czech loess. *Geophys. Res. Lett.* 30, 1562. doi:10.1029/2003GL017251

Smalley, I., O'Hara-Dhand, K., Wint, J., Machalett, B., Jary, Z., and Jefferson, I. (2009). Rivers and loess: the significance of long river transportation in the complex event-sequence approach to loess deposit formation. *Quat. Int.* 198, 7–18. doi:10.1016/j.quaint.2008.06.009

Smalley, I. J. (1972). The interaction of great rivers and large deposits of primary loess. *Trans. N. Y. Acad. Sci.* 34, 534–542.

Song, Y., Fang, X., Torii, M., Ishikawa, N., Li, J., and An, Z. (2007). Late Neogene rock magnetic record of climatic variation from Chinese eolian sediments related to uplift of the Tibetan Plateau. *J. Asian Earth Sci.* 30, 324–332. doi:10.1016/j.jseaes.2006.10.004

Song, Y., Shi, Z., Fang, X., Nie, J., Naoto, I., Qiang, X., et al. (2010). Loess magnetic properties in the ili basin and their correlation with the Chinese Loess Plateau. *Sci. China Earth Sci.* 53, 419–431. doi:10.1007/s11430-010-0011-5

Sprafke, T., Schulte, P., Meyer-Heintze, S., Händel, M., Einwögerer, T., Simon, U., et al. (2020). Paleoenvironments from robust loess stratigraphy using high-resolution color and grain-size data of the last glacial Krems-Wachtberg record (NE Austria). *Quat. Sci. Rev.* 248, 106602. doi:10.1016/j.quascirev.2020.106602

Sprafke, T., Terhorst, B., Peticzka, R., and Thiel, C. (2013). Paudorf locus typicus (Lower Austria) revisited–The potential of the classic loess outcrop for Middle to Late Pleistocene landscape reconstructions. *Quat. Sci. J. EG.* 62, 59–72. doi:10.3285/eg.62.1.06

Tarling, D., and Hrouda, F. (1993). *Magnetic anisotropy of rocks*. London, Glasgow, New York, Tokyo, Melbourne, Madras: Springer Science and Business Media.

Taylor, S. N., and Lagroix, F. (2015). Magnetic anisotropy reveals the depositional and postdepositional history of a loess-paleosol sequence at Nussloch (Germany). *J. Geophys. Res. Solid Earth.* 120, 2859–2876. doi:10.1002/2014JB011803

Taylor, S. N., Lagroix, F., Rousseau, D.-D., and Antoine, P. (2014). Mineral magnetic characterization of the Upper Pleniglacial Nussloch loess sequence (Germany): an insight into local environmental processes. *Geophys. J. Int.* 199, 1463–1480. doi:10.1093/gji/ggu331

Terhorst, B., Kühn, P., Damm, B., Hambach, U., Meyer-Heintze, S., and Sedov, S. (2013). Paleoenvironmental fluctuations as recorded in the loess-paleosol sequence of the Upper Paleolithic site Krems-Wachtberg. *Quat. Int.* 351, 67. doi:10.1016/j.quaint.2013.03.045

Terhorst, B., Sedov, S., Sprafke, T., Peticzka, R., Meyer-Heintze, S., Kühn, P., et al. (2015). Austrian MIS 3/2 loess–palaeosol records—key sites along a west–east transect. *Palaeogeogr. Palaeoclimatol. Palaeoecol.* 418, 43–56. doi:10.1016/j.palaeo.2014.10.020

Újvári, G., Varga, A., Raucsik, B., and Kovács, J. (2014). The Paks loess-paleosol sequence: a record of chemical weathering and provenance for the last 800ka in the mid-Carpathian Basin. *Quat. Int.* 319, 22–37. doi:10.1016/j.quaint.2012.04.004

Wang, R., and Løvlie, R. (2010). Subaerial and subaqueous deposition of loess: experimental assessment of detrital remanent magnetization in Chinese loess. *Earth Planet Sci. Lett.* 298, 394–404. doi:10.1016/j.epsl.2010.08.019

Yang, S., and Ding, Z. (2014). A 249 kyr stack of eight loess grain size records from northern China documenting millennial-scale climate variability. *G-cubed.* 15, 798–814. doi:10.1002/2013GC005113

Yu, L., and Oldfield, F. (1993). Quantitative sediment source ascription using magnetic measurements in a reservoir-catchment system near Nijar, S.E. Spain. *Earth Surf. Process. Landforms.* 18, 441–454. doi:10.1002/esp.3290180506

Zeeden, C., Hambach, U., and Händel, M. (2015). Loess magnetic fabric of the Krems-Wachtberg archaeological site. *Quat. Int.* 372, 188–194. doi:10.1016/j.quaint.2014.11.001

Zeeden, C., Hambach, U., Steguweit, L., and Anghelinu, M. (2011). Loess stratigraphy using palaeomagnetism: application to the Poiana Cireşului archaeological site (Romania). *Quat. Int.* 240, 100–107. doi:10.1016/j.quaint.2010.08.018

Zeeden, C., Hambach, U., Steguweit, L., Fülling, A., Anghelinu, M., and Zöller, L. (2009). Using the relative intensity variation of the Earth's magnetic palaeofield as correlative dating technique: a case study from loess with Upper Palaeolithic cultural layers at Poiana Cireşului, Romania. *Quartar.* 56, 175–185. doi:10.7485/QU56_10

Zeeden, C., Hambach, U., Veres, D., Fitzsimmons, K., Obreht, I., Bösken, J., et al. (2018). Millennial scale climate oscillations recorded in the Lower Danube loess over the last glacial period. *Palaeogeogr. Palaeoclimatol. Palaeoecol.* 509, 164–181. doi:10.1016/j.palaeo.2016.12.029

Zeeden, C., Kels, H., Hambach, U., Schulte, P., Protze, J., Eckmeier, E., et al. (2016). Three climatic cycles recorded in a loess-palaeosol sequence at Semlac (Romania)—implications for dust accumulation in south-eastern Europe. *Quat. Sci. Rev.* 154, 130–142. doi:10.1016/j.quascirev.2016.11.002

Zheng, H., Oldfield, F., Yu, L., Shaw, J., and An, Z. (1991). The magnetic properties of particle-sized samples from the Luo Chuan loess section: evidence for pedogenesis. *Phys. Earth Planet. In.* 68, 250–258. doi:10.1016/0031-9201(91)90044-I

Zhu, R., Liu, Q., and Jackson, M. J. (2004). Paleoenvironmental significance of the magnetic fabrics in Chinese loess-paleosols since the last interglacial (<130 ka). *Earth Planet Sci. Lett.* 221, 55–69. doi:10.1016/S0012-821X(04)00103-7

Conflict of Interest: The authors declare that the research was conducted in the absence of any commercial or financial relationships that could be construed as a potential conflict of interest.

frontiers in Earth Science

ORIGINAL RESEARCH
published: 26 February 2021
doi: 10.3389/feart.2021.599986

The Early Upper Paleolithic Site Crvenka-At, Serbia–The First Aurignacian Lowland Occupation Site in the Southern Carpathian Basin

Janina J. Nett[1], Wei Chu[2], Peter Fischer[3], Ulrich Hambach[4], Nicole Klasen[5], Christian Zeeden[1,6], Igor Obreht[1,7], Lea Obrocki[3], Stephan Pötter[1], Milivoj B. Gavrilov[8], Andreas Vött[3], Dušan Mihailović[9], Slobodan B. Marković[8] and Frank Lehmkuhl[1]*

[1]Department of Geography, Physical Geography and Geoecology, RWTH Aachen University, Aachen, Germany, [2]Institute of Prehistoric Archeology, University of Cologne, Cologne, Germany, [3]Institute for Geography, Natural Hazard Research and Geoarchaeology, Mainz, Germany, [4]BayCEER & Chair of Geomorphology, University of Bayreuth, Bayreuth, Germany, [5]Cologne Luminescence Laboratory, Institute of Geography, University of Cologne, Cologne, Germany, [6]Department of Rock Physics and Borehole Geophysics, Leibniz Institute for Applied Geophysics, Hannover, Germany, [7]Organic Geochemistry Group, MARUM-Center for Marine Environmental Sciences and Department of Geosciences, University of Bremen, Bremen, Germany, [8]Chair for Physical Geography, Faculty of Science, University of Novi Sad, Novi Sad, Serbia, [9]Department of Archeology, Faculty of Philosophy, University of Belgrade, Belgrade, Serbia

OPEN ACCESS

Edited by:
David K. Wright,
University of Oslo, Norway

Reviewed by:
Kaja Fenn,
University of Oxford, United Kingdom
Theodoros Karampaglidis,
Research Centre and Museum for Human Behavioural Evolution, Germany

***Correspondence:**
Janina J. Nett
Janina.boesken@geo.rwth-aachen.de

Specialty section:
This article was submitted to Quaternary Science, Geomorphology and Palaeoenvironment, a section of the journal Frontiers in Earth Science

Received: 28 August 2020
Accepted: 21 January 2021
Published: 26 February 2021

Citation:
Nett JJ, Chu W, Fischer P, Hambach U, Klasen N, Zeeden C, Obreht I, Obrocki L, Pötter S, Gavrilov MB, Vött A, Mihailović D, Marković SB and Lehmkuhl F (2021) The Early Upper Paleolithic Site Crvenka-At, Serbia–The First Aurignacian Lowland Occupation Site in the Southern Carpathian Basin. Front. Earth Sci. 9:599986. doi: 10.3389/feart.2021.599986

The Carpathian Basin is a key region for understanding modern human expansion into western Eurasia during the Late Pleistocene because of numerous early hominid fossil find spots. However, the corresponding archeological record remains less understood due to a paucity of well dated, contextualized sites. To help rectify this, we excavated and sampled Crvenka-At (Serbia), one of the largest Upper Paleolithic sites in the region to obtain radiometric ages for the archeological artifacts and evaluate their depositional context and subsequent site formation processes. Our results confirm that this locality represents a multiple-occupation Aurignacian site that dates to 36.4 ± 2.8 ka based on modeling of luminescence ages. Electrical resistivity tomography measurements indicate that the site formed on a sandy-gravelly fill terrace covered by overbank deposits. Complex grain size distributions further suggest site formation in contrasting depositional environments typically occurring alongside fluvial channels, at lakeshores, in alluvial fan or delta settings. The site is thus the closest (ca. 50 km) known Aurignacian site to the earliest undisputed modern human remains in Europe at the Peştera cu oase and some intervals of the occupation may therefore have been contemporaneous with them. This suggests that modern humans, during their initial settlement of Europe, exploited a wider range of topographic and ecological settings than previously posited. Our findings indicate that lowland areas of the Carpathian Basin are an important part of understanding the early settlement patterns of modern humans in Europe.

Keywords: late pleistocene, MIS 3, middle danube basin, luminescence dating, aurignacian, paleoenvironment, modern human, banat

INTRODUCTION

While it is generally accepted that the initial dispersal of modern humans into western Eurasia originated in Africa, the timing, trajectory and conditions of this spread are still not fully understood (e.g., Davies et al., 2015; Obreht et al., 2017; Staubwasser et al., 2018; Teyssandier and Zilhão, 2018; Bösken, 2020; Hublin et al., 2020). An often-discussed potential trajectory of human migration into Central Europe is along the Danube, where river valleys and/or piedmonts have been suggested as possible ecological corridors (Kozłowski, 1992; Zilhão et al., 2007; Conard and Bolus, 2008; Hauck et al., 2018; Chu, 2018). Central to this discussion is the Banat, a geographically and environmentally diverse region in the southeastern Carpathian Basin shared by Romania, Serbia and Hungary. This region holds a key geographical position immediately northwest of the Iron Gates, the only hydrological connection between Central and Southeastern European continental drainage systems (Schwarz, 2014; Krézsek and Olariu, 2020).

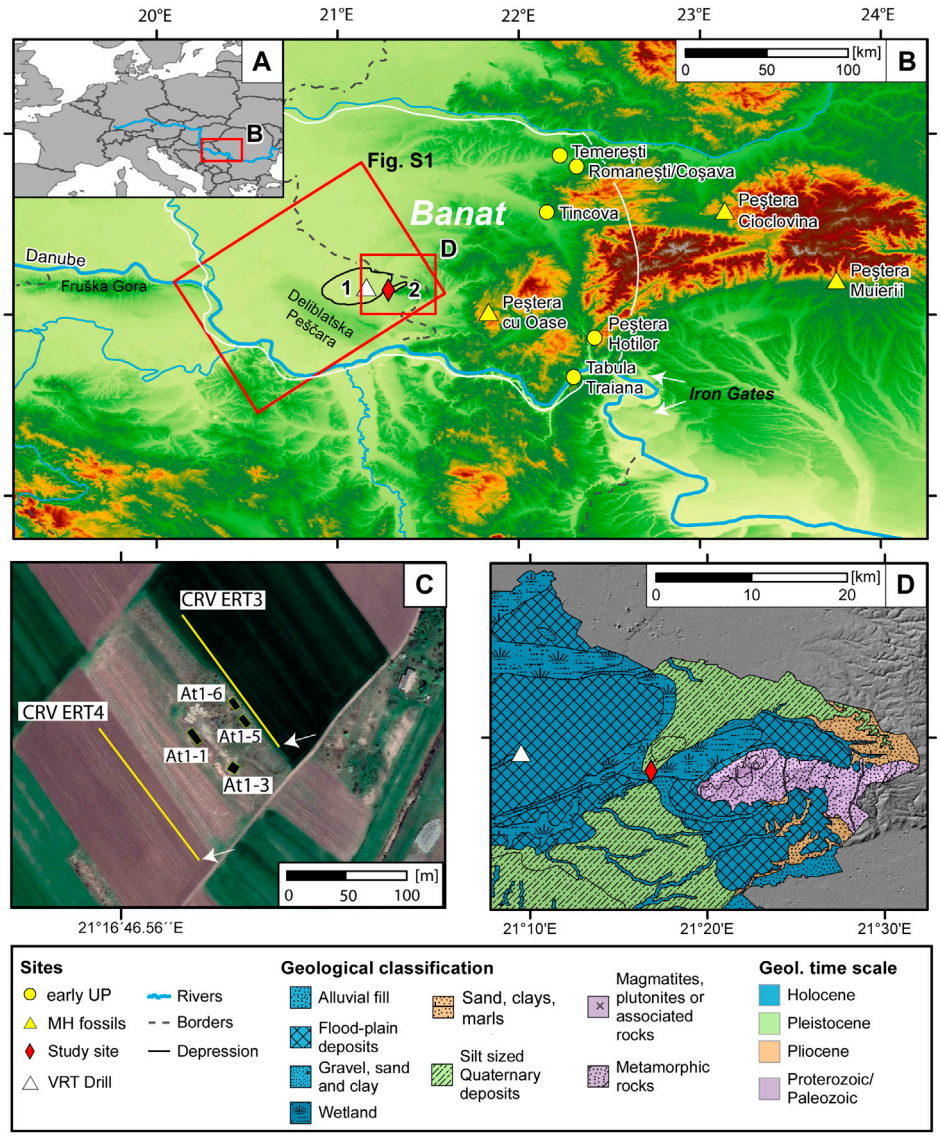

FIGURE 1 | Location **(A–C)** and geology **(D)** of the research site Crvenka-At (red diamond) east of the Deliblatska Peščara dune field and the Alibunar Depression (1) and west of the Vršac Mountains (2; map **B)**. The site is located at the border to two morphological depressions (black lines). Several sites that contain early Upper Palaeolithic artifacts are indicated (yellow circles). Caves containing early modern human remains are marked with yellow triangles. Furthermore, the location of the Vršac borehole is shown (white triangle; Zeeden et al., 2021). The ALOS Global Digital Surface Model (AW3D30) builds the basemap for the surface elevation ©JAXA (JAXA EORC, 2016). The extend of **Figure S1** is indicated (red rectangle). The Banat region is located within the white lines. Map **(C)** shows a close-up of the At I site including the ERT transects and the excavation trenches. The arrows indicate electrodes 48 of each transect. The google base map (Bilder © 2020 CNES/Airbus, Maxar Technologies, Kartendaten ©) shows a satellite photo. The geological map in D uses the map provided by the Geological Institute of Serbia, 2009.

Archeological interest in the Banat area increased after the discovery of early modern human remains at the Peștera cu oase (ca. 42–37 ka cal BP; Trinkaus et al., 2003a; Trinkaus et al., 2003b; Trinkaus et al., 2012). The conspicuous absence of accompanying archeological artifacts stimulated the re-investigation of the open-air sites of Românești, Coşava and Tincova (**Figure 1**) that highlight the archeological importance of the Banat during the early Upper Paleolithic (e.g., Anghelinu et al., 2012; Sitlivy et al., 2012; Kels et al., 2014; Sitlivy et al., 2014; Chu et al., 2016b). Furthermore, abundant, nearby loess archives have augmented our understanding of the prevailing palaeoenvironmental conditions during the Late Pleistocene (e.g., Schmidt et al., 2013; Kels et al., 2014; Schulte et al., 2014; Obreht et al., 2015; Zeeden et al., 2016; Gavrilov et al., 2018; Pötter et al., 2020).

Many open-air archeological sites from the early Upper Paleolithic in the Banat (and many sites within the wider Carpathian Basin) have been recovered in an approximate altitudinal belt of 200–300 m above mean sea level (AMSL; Hauck et al., 2018) where artifacts have been mainly excavated in pedogenic complexes that developed in the Carpathian foothills during Marine Isotope Stage (MIS) 3 (Kels et al., 2014). Research has thus far focused on archeological sites along the western foothills of the Carpathian Mountains. However, those sites are characterized by short sections (<3 m) of Upper Pleistocene sediments thereby hindering high-resolution dating and palaeoenvironmental analyses (e.g., Kels et al., 2014; Chu et al., 2016b; Chu et al., 2019). On the other hand, other geomorphological settings (e.g., lower altitudes) of the Carpathian Basin have received little attention, thereby limiting a broader understanding of how modern humans interacted with the landscape (Dobos and Chu, 2019). This may be related to either a true absence of archeological sites, problematic sedimentological archives with high deposition rates that obscure archeological findings (Tourloukis, 2016) or limited systematic research (Fitzsimmons et al., 2012; Iovita et al., 2014; Chu et al., 2016b; Mihailović, 2020).

To examine the latter possibility, a re-excavation campaign was undertaken at Crvenka-At in the vicinity of Vršac, in northern Serbia, between 2014 and 2015. The site was chosen for proximity to the Peștera cu oase, its unique topographic position and its well attributed stratified Aurignacian assemblages that remained undated by absolute dating methods. The aim of the study was to extend our knowledge of early modern human occupation in the lowland areas of the Carpathian Basin by investigating its timing and environmental context.

BACKGROUND

Research Site and Site History

Crvenka-At (45°08.104′ N, 21°16.853′ E) is an archeological site complex comprising at least two separate localities (Crvenka and At) and other find spots located approximately 3 km north of the town of Vršac (northeastern Serbia) in the southeastern part of the Carpathian Basin (**Figure 1**). Both localities are situated within a ridge (top ~93 m AMSL; At I ~87 m AMSL; At II ~86 m AMSL; bottom of depressions ~76–82 m AMSL) separating depressions north of Vršac and east of Alibunar The Alibunar Depression (**Figure 1B**) was described as a *morass* (i.e., mire/mud/swamp) in the map of 1769 but was later drained at the turn of the 18th century (Müller, 1769; Timár et al., 2008). The depression is bounded by the Deliblatska/Banatska Peščara loess and dune fields to the west and the Vršac Mountains to the east. Middle and Upper Paleolithic artifacts from the northern foothills of the Vršac Mountains were first discovered during sand extraction in the 19th century. More systematic collection at the Crvenka-At sites was undertaken by R. Rašajski (1952–1978) that highlighted the technological homogeneity of the recovered artifacts (Mihailović et al., 2011). A test excavation in 1984 identified three separate archeological levels containing 19 flints and several dozen quartz artifacts (Radovanović, 1986). These were later attributed to "typical" Aurignacian (IIa at At and IIb at Crvenka) and "Krems" style Aurignacian assemblages (Layer IIb at Crvenka; Mihailović, 1992) based on their typological characteristics. Against this background, the site was relocated through a series of trench excavations and its sedimentary and environmental contexts were investigated through chronostratigraphical dating and sedimentological analyses (cf. Chu et al., 2014; Chu et al., 2016a).

Geological and Geomorphological Setting

The area of the Vršac Mountains is part of the southeastern margin of the Carpathian Basin that tectonically formed during the Neogene and Quaternary periods (Matenco and Radivojević, 2012; Sušić et al., 2016; Bartha et al., 2018; Rundić et al., 2019). The present-day landscape in the Carpathian Basin is also strongly affected by neo-tectonic processes, with the youngest tectonic deformations characterized by positive and negative vertical motions (Toljić et al., 2013). The central and southeastern part of the basin, where the research area is located, is dominated by northeast-southwest and northwest-southeast oriented strike-slip faults (Marović et al., 2007; Sušić et al., 2016). This tectonic regime resulted beside rapidly uplifting blocks (e.g., Vršac Mtns.) in the development of the Alibunar Depression (**Figure 1**), which was filled with fluvial sediments as it is connected to a river system, something that is typical for such structural depressions. The geological map in **Figure 1D** depicts the ridges as Pleistocene silts (green) and the basins as Holocene wetland and floodplain deposits (blue). This underlines the ongoing subsidence of the basin. The Vršac Mountains as push-up structure contain crystalline basement rocks of Paleoproterozoic–Paleozoic age (purple) covered by Pliocene marls, sands and silts (orange). Further information on the dynamic landscape evolution can be found in the Supplementary Material (cf. **Supplementary Figure S1**).

MATERIALS AND METHODS

Excavation and Sampling

In 2015, eight test trenches were prepared at the edge of two pre-existing sand extraction pits (At I and At II). The first trench was

excavated to locate the 1984 excavation trench by Radovanović (At II). Seven other trenches were excavated at the margins of an adjacent sand pit (At I) to clarify the sedimentary setting and to correlate the stratigraphy of At I and At II with the Crvenka locality (see Chu et al., 2014; Chu et al., 2016a). Here, we focus on two of these trenches: trench 3 and 5. All finds and the excavation areas were piece-provenienced in a local coordinate system using both traditional analogue methods and a total station.

Eight luminescence samples and corresponding radionuclide concentration samples were extracted at two trench profiles (At I-3B and At I-5) with the highest artifact density in order to chronostratigraphically constrain the archeological levels. In addition, sediment samples were collected for grain size analyses and color measurements in 2 cm intervals to investigate the palaeoenvironmental setting of the site. **Supplementary Figure S2** shows photographs of the sampled profiles.

Electrical Resistivity Tomography

Electrical resistivity tomography (ERT) was conducted to detect stratigraphic differences within the near-surface deposits and to map the underlying bedrock topography. A Syscal R1+ Switch 48 device (Iris Instruments) and a Wenner-Schlumberger electrode array with 3 m electrode spacing were used allowing for an investigation depth of approximately 18 m below surface. The elevation and geographical position of each electrode were measured using a differential GPS (type Topcon HiPerPRO). GPS altitudes were corrected to m AMSL based on known altitudes from topographical fixed points at the excavation site. Data were then inverted incorporating the topography using the Res2Dinv inversion program (Geotomo Software).

Optically Stimulated Luminescence Dating of Sediments

Samples were separated into 100–150 and 150–200 µm fractions. Only for sample C-L4241, grain sizes between 100 and 250 µm were used due to a low amount of sample material. Both quartz and potassium feldspar grains were extracted. Further sample preparation and measurement facilities are described in detail in the **Supplementary Material**. A single aliquot regenerative dose (SAR) protocol (Murray and Wintle, 2000; Murray and Wintle, 2003) was applied for quartz. A preheat plateau test (Murray and Wintle, 2000) and a dose recovery test (DRT, e.g., Murray and Wintle, 2003) were performed on sample C-L4240 before D_e (equivalent dose) measurements to assess the proper measurement settings.

For potassium feldspar measurements, post-infrared infrared stimulated luminescence ($pIRIR_{290}$ and $pIRIR_{225}$) protocols were tested (Buylaert et al., 2009; Thiel et al., 2011). Prior infrared (IR) stimulation temperature tests were performed (Buylaert et al., 2012). Furthermore, DRTs using bleached samples (24 h Hönle Sol2 solar simulator) were conducted. These tests were carried out on samples C-L4239–C-L4242. Finally, the equivalent dose was determined on a minimum of 28 aliquots per sample using an arithmetic mean. Residual doses were assessed after bleaching the aliquots for 24 h in a solar simulator. Fading tests were conducted on sample C-L4240 using three aliquots per tested protocol and pause times of 6,000, 12,000, 24,000, and 48,000 s.

For the determination of dose rates, radionuclide concentrations were measured on a high-purity germanium gamma-ray spectrometer. Additionally, the saturation water content of one sample representative for the sand layer (unit C in **Figure 2**) was determined by centrifuging and adding water until the sediment reached its maximum absorption capacity (following the example of Nelson and Rittenour, 2015). The dose rates and ages were calculated using the Adele software (Kulig, 2005).

The luminescence dating results were further analyzed using the Bayesian ADMin model (Zeeden et al., 2018) to build an age-depth model. The model runs in the R environment (R Core Team, 2020). The corresponding R script can be found in the **Supplementary Material** (Section 4). Prior to modeling, the pIR ages of both profiles were combined by transferring the depths of samples in trench 3B into the depth scale of trench 5.

Grain Size Analysis

All grain size samples were prepared following the methods described in Nottebaum et al. (2015) and Schulte et al. (2016). Grain size was measured with a Laser Diffraction Particle Size Analyzer (Beckman Coulter LS 13 320) calculating the percentaged size frequency of 116 classes within a size range of 0.04–2,000.00 µm (2% uncertainty). The measurement accuracy was increased by measuring each sample four times in two different concentrations. The grain size distributions were determined using the Mie theory (ISO, 2009; Fluid RI: 1.33; Sample RI: 1.55; Imaginary RI: 0.1; Özer et al., 2010; cf.; Schulte et al., 2016).

Spectrophotometric Analysis

The colorimetric properties of the sediments were determined as described in e.g., Eckmeier et al. (2013) and Vlaminck et al. (2016) using a Konica Minolta CM-5 spectrophotometer after the samples were homogenized and dried. The L*a*b* values indicate the extinction of light, on a scale from L* 0 (absolute black) to L* 100 (absolute white) and express color as chromaticity coordinates on red-green (a*) and blue-yellow (b*) scales. Measured colors were plotted in *R* using the 'drawProfile.R' script (Sprafke, 2016; Zeeden et al., 2017).

RESULTS

Stratigraphy

The stratigraphic succession of At I trench 5 started with fine white sands showing a fining up trend as coarser sands and mica flitters occur at the profile base (4.45–4.20 m depth; see **Figure 2**; **Supplementary Figure S2**; description follows ISO 11277, 2009). At a depth of 4.20 m, some organic material was present, potentially from rootlets. On top of this, layered orange, beige, and white sands with fine gravels with diameters up to 4 mm accumulated (4.20–4.06 m). Above, from 4.06 to 3.95 m, beige sands with occasional fine gravels (within the sandy matrix) were deposited. These were overlain by a homogeneous bed of beige

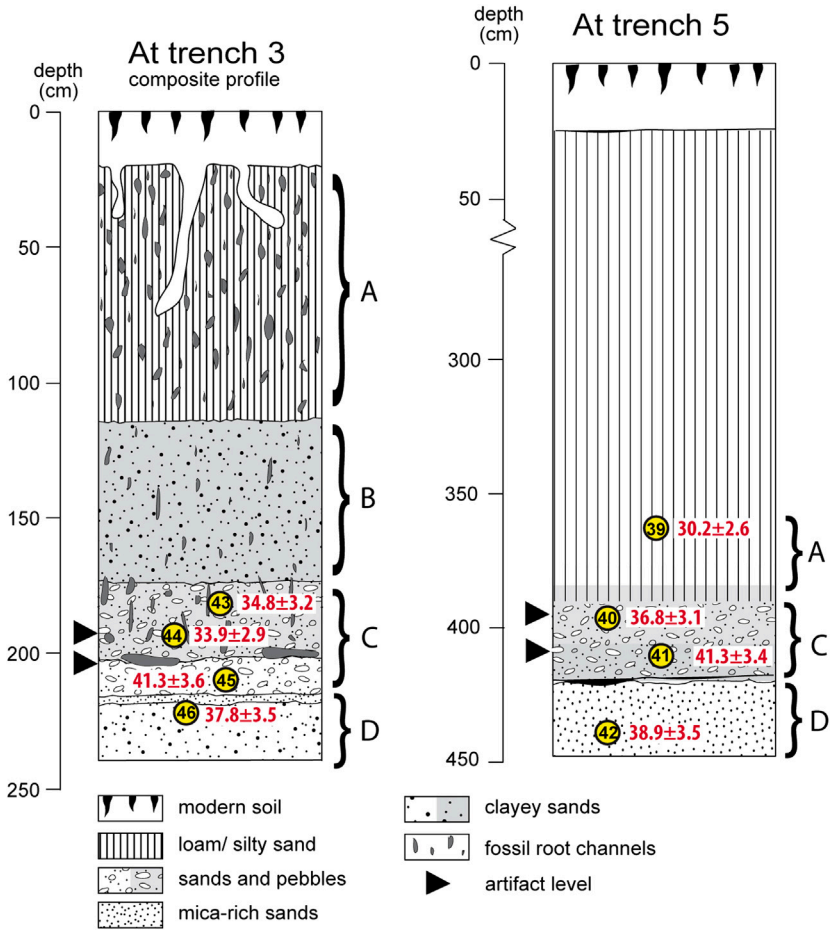

FIGURE 2 | Profile sketches show a composite of At trench 3A and 3B on the left and trench 5 on the right. The artifact find levels are shown with black triangles. For trench 3 these include the faunal remains. Location of luminescence samples are illustrated and labeled with the last two digits of the laboratory numbers in yellow circles. Luminescence ages are shown in red next to these. Letters A–D indicate the different units as used in **Figure 7**.

silty sands (3.95–3.85 m). At a depth of 3.85 m, dark brown organic material with bedding-parallel orientation was present. The horizon from 3.85 to 3.60 m consisted of dark brown sands and silts that fined upwards. Numerous rootlets were also present. The upper ~3.60 m of the profile belonged to the same stratigraphic unit as the dark brown silts, but were not investigated in detail. **Figure 2** shows the stratigraphical column of the section.

In trench 3, two profiles were investigated (cf. **Figure 2**; **Supplementary Figure S2**). Their stratigraphy was similar to trench 5, but contained rootlet channels throughout the profiles. A composite profile for trench 3 was made using both profile descriptions and the grain size data for correlation (**Figure 2**). The profile descriptions of the sub-profiles is found in the **Supplementary Material**. The composite profile At I-3 has a depth of 2.40 m. The sequence started with a layer of mica-bearing (loamy) sands (2.20–2.40 m), followed by mica-rich golden sands (2.17–2.20 m). Above, a clast-supported layer of white sands and fine gravels accumulated (2.03–2.17 m). This was overlain by a matrix-supported ash-gray (reductimorphic) bed of intercalated coarse sands and very fine gravels (1.74–2.03 m) that contained humic rootlet channels and was overlain by matrix-supported clayey sands with orange mottles (redoximorphic features; 1.15–1.74 m). The upper part of the sequence was characterized by an ochre-gray, bioturbated and inhomogeneous bed of sandy loam (0.15–1.15 m) containing occasional fine gravels. The top unit comprised the recent brown humic soil (0.15 m to the top). Approximately 1.6 m of sediment was missing on top due to agricultural activities (deduced from the maximum height measured at the outcrop using the total station).

Excavation

Trenches installed at the margins of the sandpits preserved deposits dating to the Neolithic Vinča (ca. 5500–4500 BCE) and Starčevo (ca. 6200 BCE and 5500 BCE) cultures (Chapman, 2000, 237–239; Chu et al., 2016a), followed by sterile sediments overlaying two layers of early Upper Paleolithic artifacts, corresponding in raw material and form to those collected throughout the 20th century now in museum

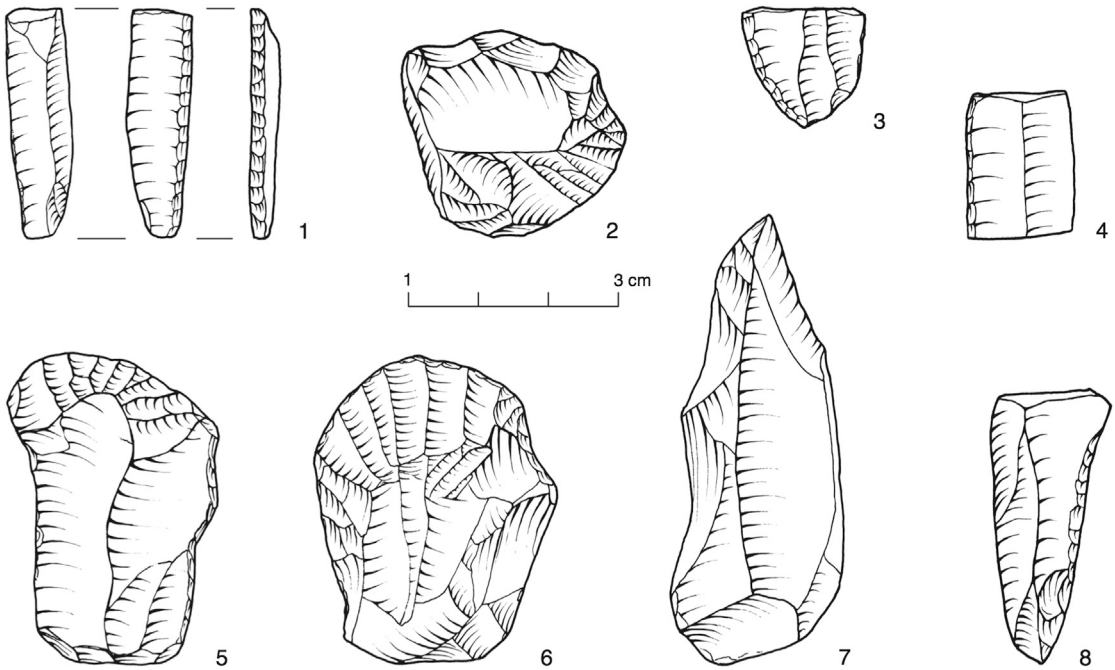

FIGURE 3 | Selected lithic artifacts from the Crvenka-At 2015 excavations (from Chu et al., 2016a).

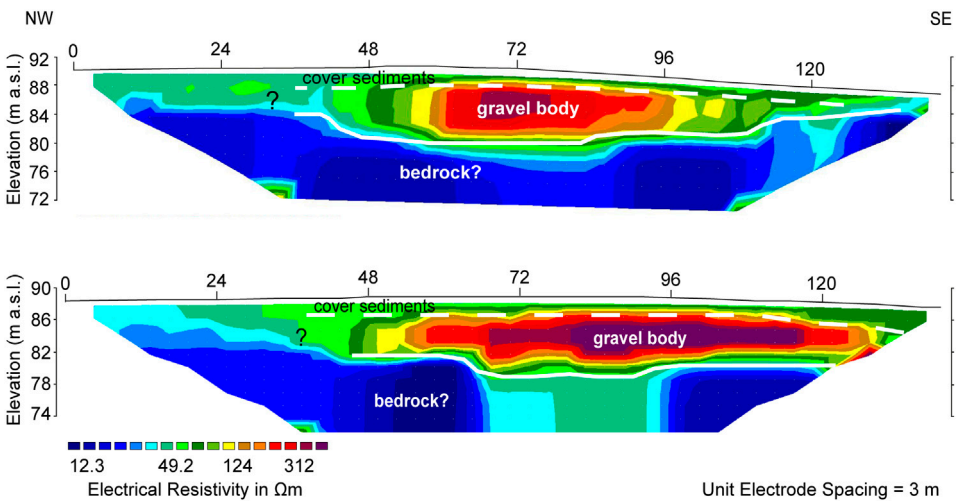

FIGURE 4 | Inversion models of ERT-transects CRV ERT 3 **(upper)** and CRV ERT 4 **(lower)**. The coarse-grained sediments that were found at the bottom of the excavation trenches are depicted by a unit of high resistivity values while overlying cover sediments show significantly lower resistivity values. The shape of these units indicates the presence of a fill terrace with overlying cover sediments. The base suggests incision into underlying strata at identical elevation AMSL. Stratigraphic information for the underlying units that are characterized by low resistivity values rising toward the northwest is not available. The location of the transects is depicted in **Figure 1C**.

collections. The artifacts were found in a relative depth of ~1.90 and ~2.05 m in trench 3 and ~3.90 m and ~4.10 m in trench 5 (~83 m AMSL). Excavations uncovered early Upper Paleolithic Aurignacian lithic artifacts (usually placed around 43–35 ka), including several bladelet cores (e.g., thick endscrapers, nosed endscrapers), blades and endscrapers (**Figure 3**). Most or all of the blades come from single-platform cores and the high blade-to-flake ratio of the lithic assemblage made primarily from so-called *Banat flint* (Ciornei et al., in press) that is technologically consistent with the Aurignacian artifacts from the open air sites of the Romanian Banat (Anghelinu et al., 2012; Sitlivy et al., 2012; Sitlivy et al., 2014; Chu et al., 2016b; Chu et al., 2019). Some of the

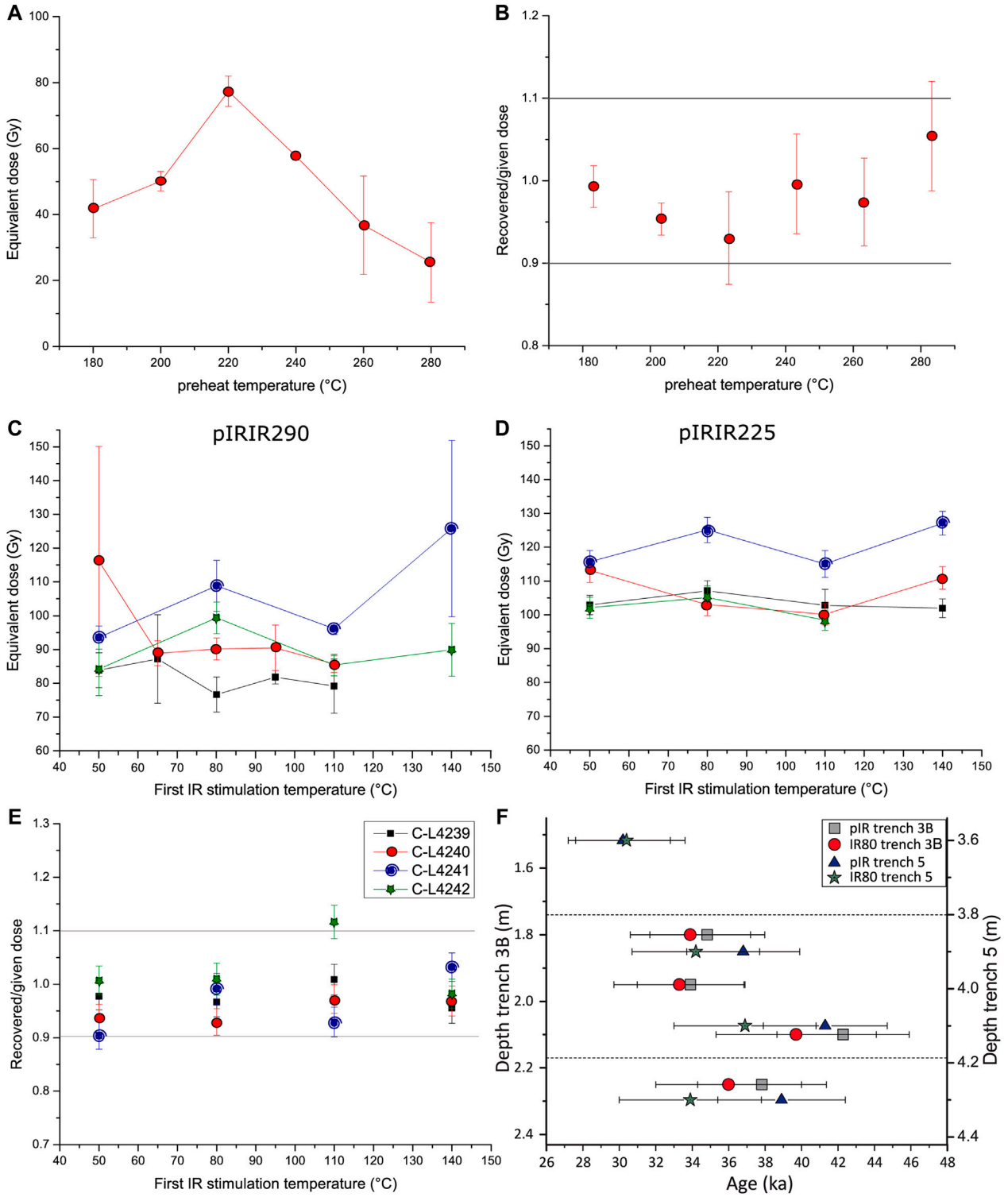

FIGURE 5 | Luminescence dating results from Crvenka-At. Preheat plateau test **(A)** and dose recovery test **(B)** of the quartz fraction of sample C-L4240; first IR stimulation temperature tests using the $pIRIR_{290}$ **(C)** and $pIRIR_{225}$ **(D)** protocols, dose recovery test **(E)** of the feldspar fractions of samples C-L4239–C-L4242, and age-depth plot showing the age data of the $pIRIR_{225}$ and the IR_{80} signals of all samples **(F)**.

lithics in the upper layer were recovered in sandy deposits and showed fine-grained fluvial abrasion (*sensu* Chu, 2016, p. 123), while others were found in fresher condition within finer-grained deposits. Bone preservation from these levels was infrequent and poor, however identified species include *Bos primigenius* and *Equus* sp. that were found in the find layers in trench 3. None of the remains retained suitable collagen for ^{14}C-dating.

Electrical Resistivity Tomography

ERT transects CRV ERT 3 and CRV ERT 4 (**Figure 4**) were conducted to obtain information on the near-surface stratigraphy of the site and its surroundings. In both transects, the lowest unit is characterized by low resistivity values sloping upward toward the northwest. On top, a unit of higher resistivity values is limited to the central and southeastern parts of the transects (from 48 m toward the end) showing a sharp lower boundary and a gradual transition to the overlying unit of lower resistivities. In the excavation area, the find layers occur within and on top of sandy gravels below a layer of finer sandy and silty sediments. The transition between these layers is marked by a gradual decrease of resistivities in both transects. The sharp lower boundary was not disclosed in the profile sections, thus no information on the strata characterized by low resistivities is available.

Luminescence Dating

The quartz fraction results were variable with some aliquots (2–8 mm) approaching saturation and exhibiting a small IR signal, although no feldspars were detected under the microscope. The measurements focused on the 100–150 µm grain size fraction. The preheat plateau test of sample C-L4240 did not show a plateau, but the dose recovery test behaved satisfactorily with recovered/given dose ratios between 0.95 ± 0.02 and 1.05 ± 0.07 (**Figures 5A,B**). The different characteristics of the single aliquots are demonstrated in **Supplementary Figure S3** that show shine down and dose response curves of three quartz aliquots from sample C-L4240. D_e measurements were performed with a preheat temperature of 240°C. However, the Abanico plot in **Supplementary Figure S4** demonstrates a large spread in the D_e data, as only 43.6% of the data points lie in a 2σ range. Due to this problematic behavior, the quartz fraction was not further measured.

For the potassium feldspar fraction of samples C-L4239–C-L4243, a first IR stimulation temperature test was conducted using the $pIRIR_{225}$ and the $pIRIR_{290}$ protocols (see **Figures 5C,D**). For the latter, no plateau region could be identified, but the $pIRIR_{225}$ showed less scatter with a first IR stimulation temperature plateau between all tested temperatures. Therefore, a dose recovery test was applied using solely the $pIRIR_{225}$ protocol. **Figure 5E** shows recovered/given dose ratios between 0.96 ± 0.03 and 1.12 ± 0.03. Fading measurements indicate low fading rates of g_{2days} = 0.08 ± 0.77% ($pIR_{50}IR_{225}$), g_{2days} = 0.01 ± 0.77% ($pIR_{80}IR_{225}$) and g_{2days} = 0.21 ± 0.78% ($pIR_{110}IR_{225}$; given as average and standard deviation; see **Supplementary Figure S5**). Due to the satisfactory behavior of the measurements using the $pIR_{80}IR_{225}$ protocol within the first IR stimulation temperature test, dose recovery test and fading experiment, the D_e measurements were also carried out with this protocol. **Supplementary Figures S6** and **S7** present shine down and growth curves for all measured samples from both trenches, which show bright luminescence signals. **Supplementary Figures S8** and **S9** depict the corresponding Abanico plots. There is variability in the data, but this is likely from the small aliquot sizes (2 mm) derived from coarse-grained sediments possibly transported by fluvial processes. A summary of the luminescence and age data is given in **Table 1** and the dose rate data of the sediment layers is given in **Table 2**. The saturation water content measurements indicate a value of ~24% for the sandy layer (unit C in **Figure 2**). To account for a range (50%) of possible moisture conditions, a water content of 12 ± 6% was used for all samples in the age calculations. A higher water content of 20 ± 8% was assumed for C-L4242 and C-L4246 from unit D, because the measured water contents were higher than within the other samples.

To further investigate the luminescence results, the IR_{80} signals contained in the $pIR_{80}IR_{225}$ measurements were analyzed (**Supplementary Figure S10**). Dose recovery ratios were satisfactory for all tested samples (average: 0.95 ± 0.04, **Supplementary Figure S11**). Equivalent doses were between 100 and 144 Gy. The fading rate for sample C-L4240 was with g_{2days} = 0.65 ± 0.70% slightly higher than for the pIRIR measurements (cf. **Supplementary Figure S12**). This value was used to correct the IR_{80} ages of all samples. The resulting fading corrected mean ages were all slightly younger than the corresponding pIRIR ages, but age estimates agreed within 1σ uncertainty (**Figure 5F**). A summary of the IR_{80} luminescence data is provided in **Supplementary Table S1**. **Figure 5F** shows an age-depth plot of the two profiles At I-3B and At I-5 and highlights the consistency between the obtained ages.

The age model places the sediment deposition of the dated samples between 38.9 ± 3.0 and 32.6 ± 2.5 ka (1σ; **Figure 6**, Tab. S2). The Aurignacian artifacts were found between samples C-L4240 and C-L4241 and C-L4244 and C-L4245, indicating the deposition of the find-bearing sediments according to the OSL data between 44.1 ± 3.4 and 33.9 ± 2.9 ka (1σ; cf. **Table 1**, **Supplementary Figure S13**). It should be noted that the timing can be pinpointed more precisely at At I-5, but more artifacts were found at At I-3B. Considering the age model, which incorporates the stratigraphic information (i.e., order of the samples), the sediments of the upper artifact level deposited at 35.3 ± 3.6 ka (2σ), while the lower level deposited between 35.3 ± 3.6 ka (2σ) and 37.8 ± 4.2 ka (2σ). Averaging all the modeled ages within the archeological context, gives an overall modeled average timing of 36.4 ± 2.8 ka (2σ).

Grain Size Analysis

Grain sizes were clustered into four units related to their stratigraphy and textural characteristics (see **Figure 7**). The most completely sampled trench 3A (**Figure 7A**) shows a well-sorted pattern in all units. The upper unit (0.00–1.20 m) depicts a bimodal grain size distribution (GSD) with a minor peak in coarse silt and a distinct peak in medium sand. A shoulder in medium and coarse clay can be also observed. Unit B (1.20–1.75 m) shows a similar pattern, but here the sand

TABLE 1 | Summary of the luminescence data of the potassium feldspar samples from At trench 5 and trench 3B. The used grain size (GS), depth considering erosion of ~1.6m, number of accepted (n) and measured (N) aliquots measured (W_m) and used (W_{used}) water contents, cosmic (D_{cos}) and total dose rates (D_{total}), residual doses, equivalent doses (D_e) and ages are shown.

Code C-L	GS (μm)	Depth (m)	*n/N*	W_m (%)	W_{used} (%)	D_{cos} (mGy/ka)	D_{total} (Gy/ka)	Residual (Gy)	D_e (Gy)	Age (ka)
4239	150–200	3.6	28/34	8	12 ± 6	143	3.33 ± 0.34	1.4 ± 0.1	100.62 ± 5.25	30.2 ± 2.6
4240	150–200	3.9	43/46	3	12 ± 6	139	2.81 ± 0.28	1.3 ± 0.2	103.60 ± 5.67	36.8 ± 3.1
4241	100–250	4.1	28/34	1	12 ± 6	136	2.85 ± 0.28	1.3 ± 0.1	118.00 ± 6.11	41.3 ± 3.4
4242	150–200	4.3	30/31	20	20 ± 8	133	2.57 ± 0.27	1.4 ± 0.1	100.04 ± 5.12	38.9 ± 3.5
4243	150–200	3.1	36/37	8.3	12 ± 6	150	3.25 ± 0.35	1.3 ± 0.2	113.1 ± 6.83	34.8 ± 3.2
4244	150–200	3.3	39/40	3.8	12 ± 6	148	3.25 ± 0.33	1.4 ± 0.1	110.05 ± 5.96	33.9 ± 2.9
4245	150–200	3.5	51/55	5.7	12 ± 6	144	3.85 ± 0.41	1.4 ± 0.1	158.84 ± 9.24	41.3 ± 3.6
4246	150–200	3.7	32/34	13.4	20 ± 8	142	3.13 ± 0.34	1.3 ± 0.1	118.23 ± 6.45	37.8 ± 3.5

TABLE 2 | Summary of the dose rate data shown for the individual stratigraphic layers of At trench 5 and trench 3B.

Layer	U (Bq/kg)	Th (Bq/kg)	K (Bq/kg)
At1-5A	20.71 ± 1.01	25.34 ± 1.31	636.29 ± 9.46
At1-5B	4.93 ± 0.43	6.96 ± 0.51	647.13 ± 9.49
At1-5C	5.51 ± 0.42	6.66 ± 0.48	686.17 ± 9.98
At1-5D	4.58 ± 0.35	5.85 ± 0.46	645.46 ± 9.52
At1-3B A	20.91 ± 1.07	23.97 ± 1.30	613.94 ± 9.15
At1-3B	12.43 ± 0.72	15.67 ± 0.94	713.57 ± 10.38
At1-3B C	6.62 ± 0.54	10.12 ± 0.71	1,024.52 ± 14.37
At1-3B D	12.68 ± 0.73	17.89 ± 1.02	712.63 ± 10.49

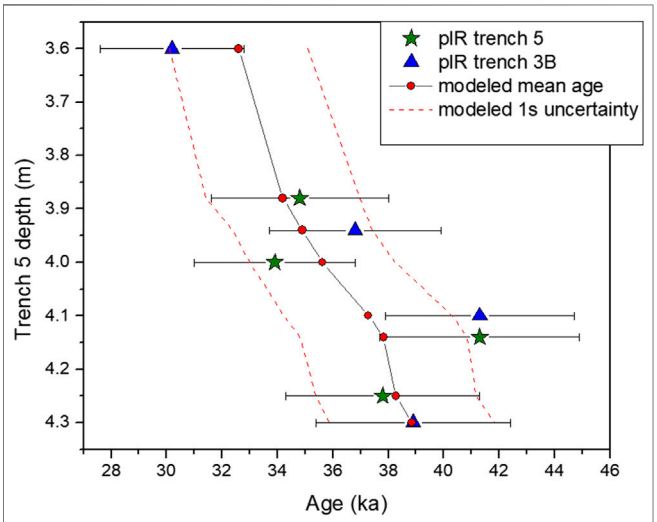

FIGURE 6 | Age-depth plot showing the pIR ages (green stars, blue triangles), the modeled mean ages (red circles), and their upper and lower 1σ of credibility (dashed red lines).

fraction is divided into two peaks at ca. 245 and 567 μm. The clay content of Unit C (1.75–2.08 m) is lower than in units A and B and three local maxima are found at 35, 200, and 517 μm. Unit D (2.08–2.3 m) is composed of fine and medium sand with a bimodal distribution that peaks around 170–180 and 567 μm as well as negligible amounts of clay and silt.

Despite its proximity to profile 3A (ca. 1.5 m), profile 3B shows a different pattern (**Figure 6B**). The GSD is poorly-sorted and the sediments are generally coarser than in profile 3A. While the GSD of units A and B (0.90–1.56 m) show minor contributions of clay and silt, these are absent in units C (1.50–1.78 m) and D (1.78–2.14 m). All units are primarily comprised of coarse sands, but also show high values of fine and medium sand.

Grain sizes of profile 5 show a well-sorted distribution (**Figure 7C**). Unit A (3.60–3.87 m) is characterized by a trimodal distribution with peaks in coarse silt (ca. 35 μm), fine (ca. 200 μm) and medium sand (517–623 μm). Unit B cannot be clearly identified, but the upper part of unit C (3.87–4.03 m) shows small amounts of silt and medium sand (623 μm) and may be contemporary to unit B. The rest of unit C shows a GSD that generally peaks in medium and coarse sand (684–993 μm). The GSD of the lowermost sample (only representative of unit D in this profile) peaks in fine sand (140 μm) with a shoulder in medium sand.

Sediment profiles 3A and 3B were correlated based on stratigraphy and grain size data. The mode of the grain size shows good agreement between the profiles (see Fig. S14). Further details on the in-depth variations are depicted in **Figures 8**, **9**.

Spectrophotometric Analysis

The color data of trenches 3A and B follow the same pattern with high L*, a* and b* values in unit D and decreased values in unit C. a* and b* are elevated again in unit B and fluctuate slightly in unit A. L* is slightly lower in unit B than A and decreases at the top of profile 3A. Mean values are 59/62 (L*), 2/1 (a*) and 17/15 (b*) for trenches 3A and 3B, respectively (**Figure 8**).

The color data of trench 5 shows less fluctuations than in trench 3. L* has a decreasing trend in the lower 10 cm, which is followed by a gradual increase. At ~490 cm, values drop sharply to be followed by a gradual increase again. The mean L* value is 63. a* and b* show a similar pattern with local maxima at 396 and 418 cm. The upper 36 cm have an increasing trend in b*. Mean a* and b* values are 2 and 18. See **Figure 9** for full details.

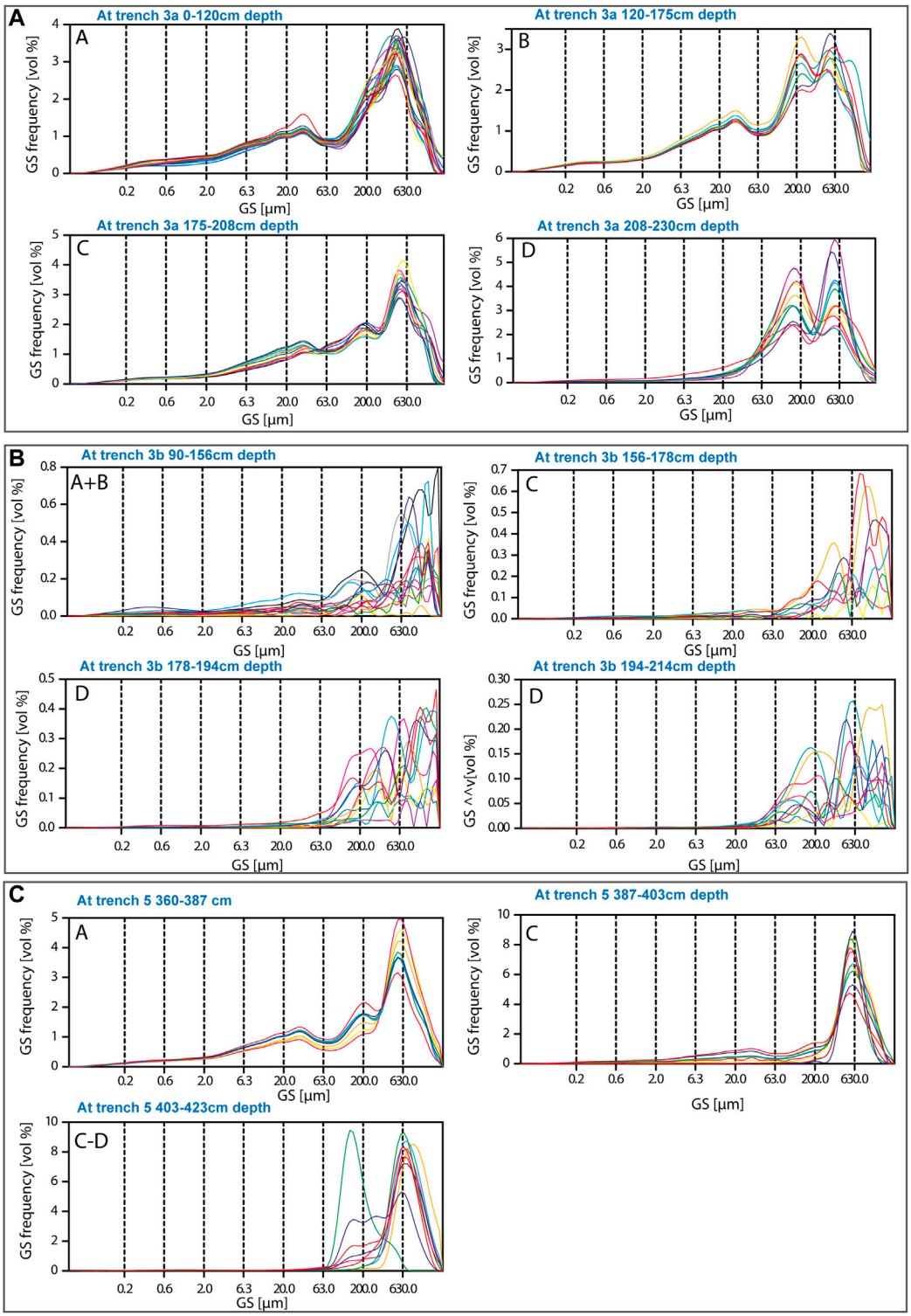

FIGURE 7 | Grain size distribution of At trench 3A **(A)**, trench 3B **(B)**, and trench 5 **(C)**. Position according to stratigraphy is indicated by **A–D**; see **Figure 2**. In trench 5 only one sample represents the fine white sands of unit D because sampling did not continue further down. Random colors are used to differentiate between the single samples.

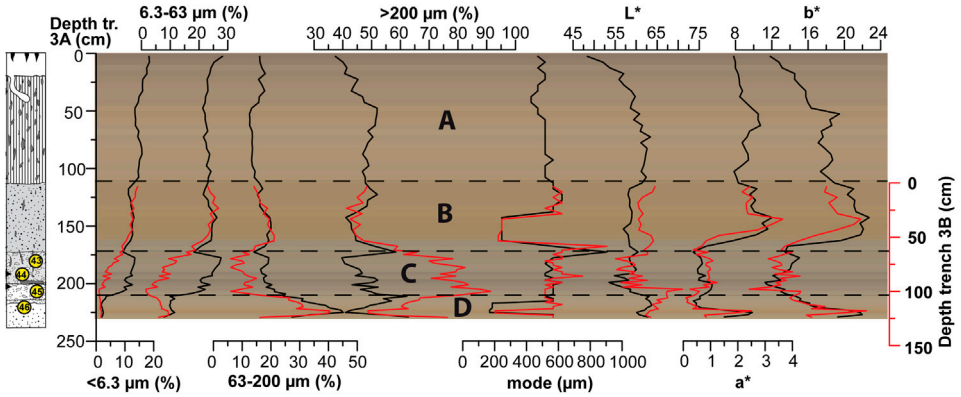

FIGURE 8 | Proxy data of At trench 3A (black line) and 3B (red line) show the grain size distribution in classes <6.3, 6.3–63, 63–200, and >200 µm, and the mode. Further, spectrophotometric color data (L, a*, b*) is shown. Measured colors are plotted in the background using the 'drawProfile.R' R script (Sprafke, 2016; Zeeden et al., 2017). A simplified sketch of the stratigraphy is shown on the left and the stratigraphic units are indicated by A–D (see legend in **Figure 2**).

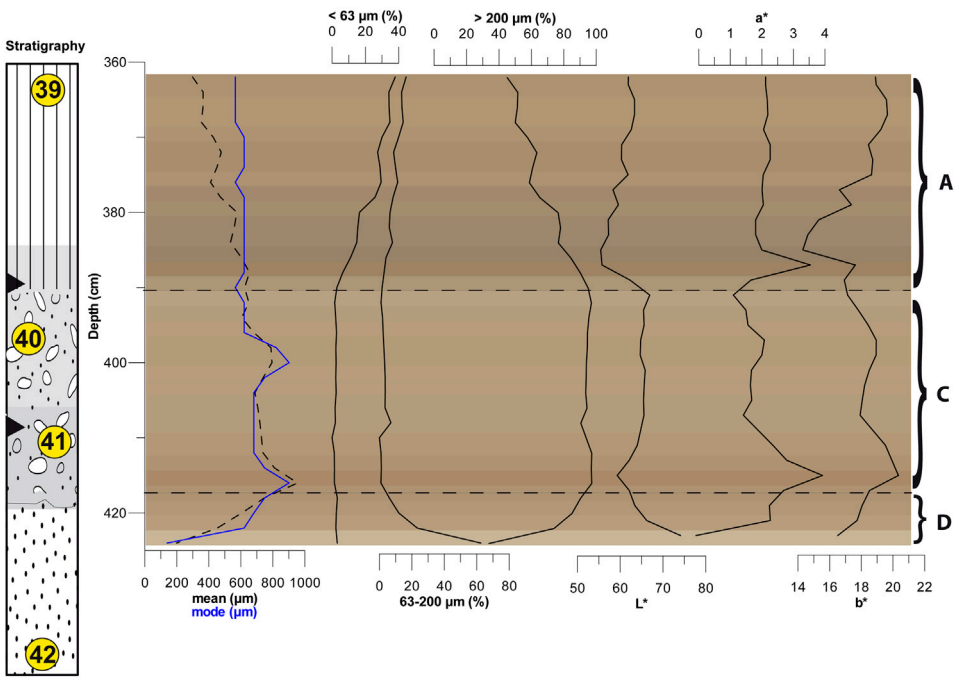

FIGURE 9 | Proxy data of At trench 5 showing the mean and mode, grain size distribution in classes <63, 63–200, and >200 µm and the spectrophotometric color data (L, a*, b*). Measured colors are plotted in the background using the 'drawProfile.R' R script (Sprafke, 2016; Zeeden et al., 2017). A simplified sketch of the stratigraphy is shown on the left and the stratigraphic units are indicated by A–D (see legend in **Figure 2**).

DISCUSSION

Geochronology

After thorough investigation of the quartz and potassium feldspar luminescence characteristics, it was shown that the $pIR_{80}IR_{225}$ protocol using potassium feldspars is most suitable for D_e measurements. The problematic behavior of the quartz fraction (i.e. approaching saturation, IR signal, wide scatter, no preheat plateau) might be due to metamorphic source rocks, which are fairly abundant in the Vršac Mountains. Additionally, the OSL samples contained a high amount of muscovite, which were difficult to remove during sample preparation. While quartz crystals sourced from metamorphic rocks reportedly are affected by problematic luminescence behavior (cf. Nelson et al., 2015), the occurrence of IR signals might also point to feldspar inclusions within the quartz crystals, but this was not investigated further. Popov et al. (2012) who investigated late glacial fluvial terrace deposits of the Tisza River in northern

Serbia encountered complex luminescence characteristics in their quartz samples. Most of their aliquots exhibit an IR signal, which they tried to remove using a double-SAR protocol (Banerjee et al., 2001), prior to the D_e measurements. However, even then large variability between aliquots and shine down curve shapes as well as poor recycling ratios were observed. In a later study, this complex behavior was not encountered, but overestimated dose recovery ratios led the authors to caution the quartz OSL results (Vandenberghe et al., 2018).

The potassium feldspar samples, however, showed excellent luminescence characteristics. Our samples exhibit no laboratory fading, even though fading rates have been reported in literature (Vasiliniuc et al., 2012). Residual doses are <1.5 Gy. Also the IR_{80} signal shows little fading and the fading corrected ages agree within 1σ uncertainty with the $pIRIR_{225}$ ages. The difference between both sets of ages is slightly higher in samples C-L4240–C-L4242 and C-L4245, which may be due to a minor degree of incomplete bleaching (cf. Murray et al., 2012; Klasen et al., 2018) or the fading correction (cf. Thomsen et al., 2008; Guérin et al., 2015). Further uncertainty is likely introduced by the estimation of the moisture content. Therefore, the saturation water content was determined to achieve a better estimate of the average moisture conditions since deposition. Nevertheless, some uncertainty remains because this was only done for one sample. This uncertainty might also explain why in both profiles, the lowermost samples from layer D have slightly younger mean ages than the samples above. Here, also the measured water content was higher than within the other samples. Of course, one might also argue that the age estimates of samples C-L4241 and C-L4245 are overestimated, but this seems unlikely considering that their ages are identical. Nevertheless, when the Bayesian age model is applied, it shifts these ages to their lower uncertainty limit (cf. **Figure 6**).

Although the luminescence tests (first IR stimulation temperature tests, dose recovery tests and fading experiments) were only carried out on the samples of At I-5, the geochronologies of both profiles agree. This further supports the robustness of the luminescence ages. Nevertheless, the Abanico plots (**Supplementary Figures S8** and **S9**) show more scatter in the D_e distributions of the samples from At I-3B, which is likely connected to post-depositional mixing due to rootlet penetration (as observed in the field) and/or may be linked to the unsorted grain size distributions (**Figure 7**). However, most D_e distributions resemble a normal distribution and only samples C-L4240 and C-L4245 show a skewed distribution toward higher D_e values. Nevertheless, this does not significantly affect the average D_e and only a few outliers are present (cf. **Supplementary Figures S8** and **S9**). Our investigation shows that potassium feldspars at Crvenka-At can be successfully dated using the $pIRIR_{225}$ protocol. This shows potential for other studies on coarse-grained feldspars in the Carpathian Basin, as was already suggested for the deposits of the paleo Tisza River (cf. Popov et al., 2012; Vandenberghe et al., 2018). Nevertheless, it should be noted that the dated grain size fraction does not reflect the dominant sedimentological grain size (cf. **Figure 7**).

Age modeling of the luminescence age data reduced the overall uncertainty and evened out some age estimates (**Figure 6**). For example, the ages of samples C-L4239 and C-L4244 are modeled to be slightly older, while the ages of samples C-L4241 and C-L4245 are modeled to be younger. It also allowed for more precise age estimates for the artifact layers.

Environmental and Geomorphological Evolution

The results from the ERT-measurements characterized the sedimentary composition of the shallow subsurface at the study site, allowing the identification of the broader stratigraphic context. The find-bearing layers occur in sand-dominated, in parts gravelly, deposits that are depicted by relatively high resistivity values (up to 300 Ωm in CRV ERT 3; **Figure 4**). The sharply developed lower boundary of this unit probably indicates an erosional phase cutting into the underlying strata followed by an accumulation of sand and gravel (as evident in the trenches). Shape and distribution are indicative of a fill terrace. Remarkably, the deepest incision does not occur downslope but in the center of the ERT-transects. Thus, it is possible that erosion and accumulation of the coarser grained material was related to fluvial (channeled) runoff evidenced by high resistivity values followed by the accumulation of overbank deposits. There are no other ERT studies conducted in this region, but the observed values compare well to the cover sediments on top of fluvial terraces in the Rhine area (Gerlach, 2019; Fischer et al., 2021).

Based on the sediment characteristics (**Figures 7–9**), the drainage patterns and the overall geomorphology, one can presume that the sediments were related to fluvial deposition close to a river mouth draining into a paleolake in the Alibunar Depression. This is similar to the morass mapped by Müller (1769) and will be investigated in a forthcoming publication (Zeeden et al., 2021). Additionally, a differentially compaction may have influenced the bedding inclination toward finer grained sedimentary units as they undergo higher compaction than sandy and gravelly units (e.g., Bjørlykke, 2015).

Similar to the ERT-measurements, the grain size data shows coarser sandy and gravelly deposits in units C and D and finer deposits in units A and B. The GSD of trench 3A, with its peaks in coarse silt and medium sand, can be interpreted as reworked sand (cf. Chu et al., 2019). The GSD of trench 3B points to fluvial sand deposits, shown by high amounts of poorly-sorted fine to coarse sands. Variations in grain sizes in unit C and the clast-supported appearance point to higher transport velocities during deposition in comparison to unit D, where the mode of the grain size decreases in both trenches. The grain size differences within trench 3 can be interpreted as contrasting depositional environments typically occurring alongside fluvial channels, at lakeshores or in alluvial fan or delta settings (cf. Xiao et al., 2012; Brooke et al., 2018; Vandenberghe et al., 2018). The absence of finer material such as silt in units C–D of trench 5 highlights that the fluvial sedimentary system was complex, even at a local scale. The relatively well sorted GSD, especially GSD, especially in unit A of trench 5, might point to an eolian origin of these sediments, while the GSD of this unit in trench 3 is more turbulent, possibly confirming the interpretation of overbank deposits.

The consistency of bleaching/graying as seen in the field and imprinted in decreased L* and b* values (unit C; **Figures 7**, **8**) is interpreted as post-depositional hydromorphic alteration of the sediments. It implies phases of water saturation at least in trench 3 (compare color data in **Figures 8**, **9**). This might be related to high groundwater tables or slack water conditions in the vicinity of a water body and close to a groundwater table little below the land surface. Moreover, elevated a* and b* values in unit B indicate preservation or subsequent formation of iron (hydr-) oxides such as hematite (tentatively indicated by a*) and goethite (tentatively indicated by b*) due to *in situ* weathering (Barron and Torrent, 1986). The fine material in units B and A suggests a low energy deposition that might have occurred in a less fluvial and possibly (episodic) overbank or lacustrine environment. Additional eolian sediment input might have been possible. These sediments were subsequently heavily bioturbated, which is especially evident in trench 3.

Additionally, the observed bones of *Bos primigenius* and *Equus sp.* found in the artifact levels of trench 3 may suggest a general limnic/fluvial woodland environment: *Bos primigenius* preferred floodplain habitats in river valleys, river deltas and bogs (Tikhonov, 2008) and the occurrence of *Equus sp.* suggests a grass-dominated habitat in proximity. While this needs to be considered with caution, as only two identifiable faunal fragments were found, it matches well with our sedimentological interpretation of a river stream (units D, C) changing toward a floodplain or lakeshore environment (units B, A). From a sequence stratigraphic point this change in time will apply to space as well, inferring overbank or lakeshore sediments in the vicinity.

Changes in fluvial systems in this complex setting (see *Geological and Geomorphological Setting section*) do not readily correlate to climatic changes (cf. Starkel et al., 2015) and we can expect that large rivers, oxbow lakes or lakes were likely always present in tectonic depressions such as Alibunar Nevertheless, the timing of fluvial sediment deposition (~42–31 ka; units D-C) coincides with the formation of Middle Pleniglacial (MIS 3) paleosols and pedocomplexes of the southern Carpathian Basin (e.g., Fuchs et al., 2008; Antoine et al., 2009; Schmidt et al., 2010; Zeeden et al., 2016; Avram et al., 2020). This suggests a phase of warmer and moister climatic conditions with higher fluvial discharge velocities, although the southern parts of the Carpathian Basin were generally arid (e.g., Obreht et al., 2019). For unit A and B, only one date of 30.2 ± 2.6 ka is available, thus, we cannot infer much. It is possible that the upper non-investigated parts of the trenches were formed during MIS 2, when loess sedimentation is reported in the region (e.g., Marković et al., 2014; Obreht et al., 2015; Marković et al., 2018; Perić et al., 2019; Perić et al., 2020). This might be connected to enhanced eolian sand and silt input at Crvenka-At as suggested by the well-sorted GSDs (trench 5), but needs further investigation.

Archeological and Paleoanthropological Implications

The results indicate that Aurignacian artifacts at Crvenka-At were found in sediments that accumulated 36.4 ± 2.8 ka (2σ modeled ages). With this, the assemblages are firmly ascribed to MIS 3 and correspond with the nearby early modern human remains from the Peştera cu oase (ca. 42–37 ka cal BP[1]; Trinkaus et al., 2003a; Trinkaus et al., 2012), the Peştera Muierii (ca. 35 ka cal BP; Soficaru et al., 2006) and the Peştera Cioclovina (ca. 35.5 ka cal BP; Soficaru et al., 2007). If the full range of the OSL ages is considered, these additionally overlap with other dated Aurignacian sites in the Banat at Românești (40.6 ± 1.5 ka; Schmidt et al., 2013), the small (<15 artifacts) assemblages from the Baranica Cave (layer 4b; 40.76 ± 0.73 ka cal BP, Mihailović et al., 2011), Tabula Traiana Cave (Layer 207; 41.3 ka cal BP to 34.5 ka cal BP; Borić et al., 2012; Mandić and Borić, 2015) and the poorly-contextualized Peştera Hoţilor (30.90 ± 0.37 ka cal BP; Anghelinu and Niţă, 2014; Păunescu, 2001, p. 142).

Crvenka-At's main interest is its lowland setting; an outlier in the Carpathian Basin's Aurignacian record. While lowland Aurignacian sites are occasionally encountered elsewhere in Europe (e.g., Masières Canal; Miller, 2014), it has previously been suggested that the occurrence of Aurignacian sites in short stratigraphic sequences in the Carpathian Basins foothills, between 43 and 30 ka BP are a genuine reflection of modern human behavioral preference for this specific biome (Hauck et al., 2018). Our results provide a first direct indication that modern humans made use of riparian landscapes possibly to avoid mountainous regions as a result of late Neanderthal territoriality until c. 39 ka cal BP in the Central Balkans (Alex, 2016, 112; Marín-Arroyo and Mihailović, 2017; Alex et al., 2019; Mihailović, 2020). In the Banat however, the situation may have been more nuanced given the recent Neanderthal/modern human hybridization at the Peştera cu oase in the nearby Anina Mountains indicating territorial and temporal overlap (Fu et al., 2015).

Our results also suggest that fluviolacustrine environments were exploited by early modern humans potentially even representing a favorable location in the landscape where vital aquatic food sources rich in micronutrients could be harvested (Brown et al., 2013). Two technologically analogous layers at At along the wider Crvenka-At complex suggest multiple site visits or at least a more sustained occupation of the area. This is in agreement with isotopic findings from the region's early Upper Paleolithic human record that have high δ^{15}N values, suggesting higher consumption of freshwater foods compared to previous indigenous populations (Richards and Trinkaus, 2009; Trinkaus et al., 2009).

Excavation results thus document the site formation processes of Crvenka-At and interpret the site as a palimpsest of a series of hominin visits of short duration captured within fine-grained, water-lain sediments. This highlights the potential for finding large, well-preserved Late Pleistocene archeological sites within the Carpathian Basin lowlands that may provide important archaeological context (Fitzsimmons et al., 2020) and recommends further (geo)archeological work in these environs to fill the current

research gap. All radiocarbon ages were calibrated using Calpal2007-Hulu (Weninger et al., 2008)

CONCLUSION

We confirm and date the Aurignacian site of Crvenka-At in the Banat region of the southeastern Carpathian Basin using luminescence dating of potassium feldspars. The Aurignacian artifacts were found in sediments with a modeled age of 36.4 ± 2.8 ka (2σ). This age range agrees with other dated Aurignacian findings in the Banat region and further confirms the early chronological position of the Aurignacian in the Carpathian Basin. Moreover, it is suggested that the site served for repeated/sustained hominin visits as evidenced by numerous multi-layered find spots within the sand ridge. The combination of ERT and sedimentological analyses confirm a position of the site within a complex fluviolacustrine environment. Shape and distribution of the ERT-transects suggest an interpretation as sandy-gravelly fill terrace and also the diverse grain-size distribution of the investigated trenches support a formation within fluvial channels, at lakeshores or in alluvial fan or delta settings. Subsequent weathering and phases of water saturation further altered the deposited sediments. Further association to a potential paleolake needs to be investigated in future studies. Our study demonstrates that not only the upland regions, but also lowland areas were attractive to early modern human hunter-gatherers and demonstrates the need for more comprehensive geoarcheological investigations including the analyses of different sedimentary archives.

DATA AVAILABILITY STATEMENT

Granulometric and colorimetric data analyzed for this study are reposited in the CRC806 Database (https://doi.org/10.5880/SFB806.62). For luminescence data, please consult the **Supplementary Material**. Further inquiries can be directed to the corresponding author.

AUTHOR CONTRIBUTIONS

JN, WC, CZ, PF, UH, and FL contributed conception and design of the study. JN, CZ, UH, IO, PF, and LO conducted sediment sampling and ERT measurements. WC and DM undertook archeological excavation and interpretation. PF, LO and AV analyzed and interpreted the ERT data. JN undertook OSL sample preparation, measurements and analysis with support and discussion by NK. JN analyzed and interpreted the grain size and color data with support and discussion by SP and IO. JN wrote the first draft of the manuscript. PF and WC wrote sections of the manuscript. All authors were involved with the regional discussion and interpretation. All authors contributed to manuscript revision, read and approved the submitted version.

FUNDING

The investigations were carried out in the frame of the CRC 806 "Our Way to Europe", subproject B1 "The Eastern Trajectory": "Last Glacial Palaeogeography and Archaeology of the Eastern Mediterranean and of the Balkan Peninsula", funded by the Deutsche Forschungsgemeinschaft (DFG, German Research Foundation)–Projektnummer 57444011-SFB 806. The work of DM was supported by Ministry of Culture and Information and the Ministry of Education, Science and Technological Development of the Republic of Serbia (project no. 177023).

ACKNOWLEDGMENTS

We thank Ivana Pantović, Nadine Nolde, Dragan Jovanović for their gracious help in the field and laboratory; Anja Zander for the dosimetry measurements and support in the Cologne Luminescence Laboratory, Marianne Dohms and the PGG team for the measurements of the grain size and color data and Philipp Schulte for support in the analysis of the grain size data. We thank Jens Weise for his work on **Figure 1**; **Supplementary Figure S1**, Thomas Albert on **Figure 1C** and Anja Rüschmann and Sofija Dragosavac for drawing **Figure 3**.

SUPPLEMENTARY MATERIAL

The Supplementary Material for this article can be found online at: https://www.frontiersin.org/articles/10.3389/feart.2021.599986/full#supplementary-material.

REFERENCES

Alex, B. (2016). Establishing contexts of encounters: radiocarbon dating of archaeological assemblages with implications for Neanderthal-modern human interactions. Doctoral dissertation: Cambridge: Harvard University.

Alex, B., Mihailović, D., Milošević, S., and Boaretto, E. (2019). Radiocarbon chronology of middle and upper paleolithic sites in Serbia, central Balkans. *J. Archaeol. Sci. Rep.* 25, 266–279. doi:10.1016/j.jasrep.2019.04.010

Anghelinu, M., Niță, L., Sitlivy, V., Uthmeier, T., and Băltean, I. (2012). Looking around Peştera Cu Oase: the beginnings of upper paleolithic in Romania. *Quat. Int.* 274, 136–157. doi:10.1016/j.quaint.2012.01.012

Anghelinu, M., and Niță, L. (2014). What's in a name: the Aurignacian in Romania. *Quat. Int.* 351, 172–192. doi:10.1016/j.quaint.2012.03.013

Antoine, P., Rousseau, D.-D., Fuchs, M., Hatté, C., Gauthier, C., Marković, S. B., et al. (2009). High-resolution record of the last climatic cycle in the southern Carpathian Basin (Surduk, Vojvodina, Serbia). *Quat. Int.* 198, 19–36. doi:10.1016/j.quaint.2008.12.008

Avram, A., Constantin, D., Veres, D., Kelemen, S., Obreht, I., Hambach, U., et al. (2020). Testing polymineral post-IR IRSL and quartz SAR-OSL protocols on Middle to Late Pleistocene loess at Botanica, Serbia. *Boreas* 49, 12442. doi:10.1111/bor.12442

Banerjee, D., Murray, A. S., Bøtter-Jensen, L., and Lang, A. (2001). Equivalent dose estimation using a single aliquot of polymineral fine grains. *Radiat. Meas.* 33, 73–94. doi:10.1016/S1350-4487(00)00101-3

Barron, V., and Torrent, J. (1986). Use of the Kubelka—munk theory to study the influence of iron oxides on soil colour. *J. Soil Sci.* 37, 499–510. doi:10.1111/j.1365-2389.1986.tb00382.x

Bartha, A., Balázs, A., and Szalay, Á. (2018). On the tectono-stratigraphic evolution and hydrocarbon systems of extensional back-arc basins: inferences from 2D basin modelling from the Pannonian Basin. *Acta Geod. Geophys.* 53, 369–394. doi:10.1007/s40328-018-0225-0

Bjørlykke, K. (2015). "Compaction of sedimentary rocks: shales, sandstones and carbonates," in *Petroleum geoscience* (Berlin, Heidelberg: Springer), 351–360.

Borić, D., Dimitrijević, V., White, D., Lane, C., French, C., and Cristiani, E. (2012). Early modern human settling of the danube corridor: the middle to upper palaeolithic site of tabula traiana cave in the danube gorges (Serbia). *Antiq. Proj. Gallery* 86 (334).

Bösken, J. J. (2020). Luminescence dating of eolian and fluvial archives in the middle and lower danube catchment and the palaeoenvironmental implications. *E&G Quat. Sci. J.* 69, 89–92. doi:10.5194/egqsj-69-89-2020

Brooke, S. A. S., Whittaker, A. C., Armitage, J. J., D'Arcy, M., and Watkins, S. E. (2018). Quantifying sediment transport dynamics on alluvial fans from spatial and temporal changes in grain size, Death Valley, California. *J. Geophys. Res. Earth Surf.* 123, 2039–2067. doi:10.1029/2018JF004622

Brown, A. G., Basell, L. S., Robinson, S., and Burdge, G. C. (2013). Site distribution at the edge of the Palaeolithic world: a nutritional niche approach. *PLoS One* 8, e81476. doi:10.1371/journal.pone.0081476

Buylaert, J.-P., Jain, M., Murray, A. S., Thomsen, K. J., Thiel, C., and Sohbati, R. (2012). A robust feldspar luminescence dating method for Middle and Late Pleistocene sediments: feldspar luminescence dating of Middle and Late Pleistocene sediments. *Boreas* 41, 435–451. doi:10.1111/j.1502-3885.2012.00248.x

Buylaert, J. P., Murray, A. S., Thomsen, K. J., and Jain, M. (2009). Testing the potential of an elevated temperature IRSL signal from K-feldspar. *Radiat. Meas.* 44, 560–565. doi:10.1016/j.radmeas.2009.02.007

Chapman, J. (2000). *Fragmentation in Archaeology: people, places, and broken objects in the prehistory of south eastern Europe*. London; New York: Routledge.

Chu, W. (2016). *Fluvial processes in the Pleistocene of northern Europe*. Oxford: British Archaeological Reports.

Chu, W., Hauck, T., and Mihailović, D. (2014). "Crvenka-At– preliminary results from a lowland Aurignacian site in the Middle danube catchment," in *Palaeolithic and mesolithic research in the central Balkans*. Editors D. Mihailovic (Belgrade, Serbia: Serbian Archaeological Society), 69–75.

Chu, W., Mihailović, D., Pantović, I., Zeeden, C., Hauck, T., and Lehmkuhl, F. (2016a). Archaeological excavations at the site of at (Vršac, Serbia). *Antiq. Proj. Gallery* 90 (352).

Chu, W., Pötter, S., Doboș, A., Albert, T., Klasen, N., Ciornei, A., et al. (2019). Geoarchaeology and geochronology of the Upper Palaeolithic site of Temereşti Dealu Vinii, Banat, Romania: site formation processes and human activity of an open-air locality. *Quartär* 66, 111–134. doi:10.7485/QU66_5

Chu, W. (2018). The danube corridor hypothesis and the Carpathian Basin: geological, environmental and archaeological approaches to characterizing aurignacian dynamics. *J. World Prehist.* 31, 117–178. doi:10.1007/s10963-018-9115-1

Chu, W., Zeeden, C., and Petrescu, S. (2016b). The early upper paleolithic of the Banat and recent research at the paleolithic site of Tincova. *Banatica* 26, 51–72.

Ciornei, A., Chu, W., Maris, I., and Dobos, A. *(in press) Lithic raw material patterns at the Upper Palaeolithic site of Românești-Dumbrăvița* (Southwestern Romania). Dacia.

Conard, N. J., and Bolus, M. (2008). Radiocarbon dating the late middle paleolithic and the aurignacian of the swabian jura. *J. Hum. Evol.* 55, 886–897. doi:10.1016/j.jhevol.2008.08.006

Davies, W., White, D., Lewis, M., and Stringer, C. (2015). Evaluating the transitional mosaic: frameworks of change from neanderthals to *Homo sapiens* in eastern Europe. *Quat. Sci. Rev.* 118, 211–242. doi:10.1016/j.quascirev.2014.12.003

Doboș, A., and Chu, W. (2019). Between the woods and the water: the early Upper Palaeolithic from the Romanian karst. *Analele Banatului* 26, 17–34. Essays in honor of Alexandru Szentmiklosi.

Eckmeier, E., Mavris, C., Krebs, R., Pichler, B., and Egli, M. (2013). Black carbon contributes to organic matter in young soils in the Morteratsch proglacial area (Switzerland). *Biogeosciences* 10, 1265–1274. doi:10.5194/bg-10-1265-2013

Fischer, P., Jöris, O., Fitzsimmons, K. E., Vinnepand, M., Prud'homme, C., Schulte, P., et al. (2021). Millennial-scale terrestrial ecosystem responses to upper Pleistocene climatic changes: 4D-reconstruction of the Schwalbenberg loess-palaeosol-sequence (Middle Rhine Valley, Germany). *Catena* 196, 104913. doi:10.1016/j.catena.2020.104913

Fitzsimmons, K. E., Doboș, A., Probst, M., and Iovita, R. (2020). Thinking outside the box at open-air archeological contexts: examples from loess landscapes in southeast Romania. *Front. Earth Sci.* 8, 561207. doi:10.3389/feart.2020.561207

Fitzsimmons, K. E., Marković, S. B., and Hambach, U. (2012). Pleistocene environmental dynamics recorded in the loess of the middle and lower danube Basin. *Quat. Sci. Rev.* 41, 104–118. doi:10.1016/j.quascirev.2012.03.002

Fu, Q., Hajdinjak, M., Moldovan, O. T., Constantin, S., Mallick, S., Skoglund, P., et al. (2015). An early modern human from Romania with a recent Neanderthal ancestor. *Nature* 524, 216–219. doi:10.1038/nature14558

Fuchs, M., Rousseau, D.-D., Antoine, P., Hatté, C., Gauthier, C., Marković, S., et al. (2008). Chronology of the last climatic cycle (upper Pleistocene) of the surduk loess sequence, Vojvodina, Serbia. *Boreas* 37, 66–73. doi:10.1111/j.1502-3885.2007.00012.x

Gavrilov, N. B., Marković, S. B., Schaetzl, R. J., Tošić, I. A., Zeeden, C., Obreht, I., et al. (2018). Prevailing surface winds in Northern Serbia in the recent and past time periods; modern- and past dust deposition. *Aeolian Res.* 31, 117–129. doi:10.1016/j.aeolia.2017.07.008

Geological Institute of Serbia (2009). *Basic geological map of Serbia 1: 100000, Vršac Sheet number L34-103*. Belgrade: Faculty of Mining and Geology, University of Belgrade. Available at: http://geoliss.mre.gov.rs/OGK/RasterSrbija/.

Gerlach, R., Fischer, P., Meurers-Balke, J., Mirschenz, M., Röbke, A., Hadler, H., Willershäuser, T., and Vött, A. (2019). Römische Hafenstandorte: Standortbedingungen und Flussdynamik am niedergermanischen Rheinlimes von Königswinter bis Kleve-Rindern. Bonner Beiträge zur Vor- und Frühgeschichtlichen Archäologie, 22, 17–77.

Guérin, G., Frouin, M., Talamo, S., Aldeias, V., Bruxelles, L., Chiotti, L., et al. (2015). A multi-method luminescence dating of the Palaeolithic sequence of La Ferrassie based on new excavations adjacent to the La Ferrassie 1 and 2 skeletons. *J. Archaeol. Sci.* 58, 147–166.

Hauck, T. C., Lehmkuhl, F., Zeeden, C., Bösken, J., Thiemann, A., and Richter, J. (2018). The Aurignacian way of life: contextualizing early modern human adaptation in the Carpathian Basin. *Quat. Int.* 485, 150–166. doi:10.1016/j.quaint.2017.10.020

Hublin, J. J., Sirakov, N., Aldeias, V., Bailey, S., Bard, E., Delvigne, V., et al. (2020). Initial upper palaeolithic *Homo sapiens* from bacho kiro Cave, Bulgaria. *Nature* 581, 299–302. doi:10.1038/s41586-020-2259-z

Iovita, R., Doboș, A., Fitzsimmons, K. E., Probst, M., Hambach, U., Robu, M., et al. (2014). Geoarchaeological prospection in the loess steppe: preliminary results from the Lower danube survey for Paleolithic sites (LoDanS). *Quat. Int.* 351, 98–114. doi:10.1016/j.quaint.2013.05.018

ISO (2009). *Soil quality–Determination of particle size distribution in mineral soil material–Method by sieving and sedimentation*. Berlin: Beuth, 11277.

Kels, H., Protze, J., Sitlivy, V., Hilgers, A., Zander, A., Anghelinu, M., et al. (2014). Genesis of loess-like sediments and soils at the foothills of the Banat Mountains, Romania – examples from the paleolithic sites românești and coșava. *Quat. Int.* 351, 213–230. doi:10.1016/j.quaint.2014.04.063

Klasen, N., Kehl, M., Mikdad, A., Brückner, H., and Weniger, G.-C. (2018). Chronology and formation processes of the Middle to Upper Palaeolithic deposits of Ifri n'Ammar using multi-method luminescence dating and micromorphology. *Quat. Int.* 485, 89–102.

Kozłowski, J. (1992). The Balkans in the middle and upper palaeolithic: the gate to Europe or a cul-de-sac? *Proc. Prehist. Soc.* 58, 1–20.

Krézsek, C., and Olariu, C. (2020). Filling of sedimentary basins and the birth of large rivers: the lower danube network in the Dacian Basin, Romania. *Glob. Planet. Change* 197, 103391. doi:10.1016/j.gloplacha.2020.103391

Kulig, G. (2005). Erstellung einer Auswertesoftware zur altersbestimmung mittels Lumineszenzverfahren unter spezieller Berücksichtigung des Einflusses radioaktiver Ungleichgewichte in der 238-U-Zerfallsreihe. Bakkalaureusarbeit Network Computer TU Freib.

Mandić, M., and Borić, D. (2015). "Pećina kod trajanove table," in *In pećina kod trajanove table*. Editor J. Ćalić (Belgrade: Public Enterprise "Djerdap National Park), 84–89.

Marín-Arroyo, A. B., and Mihailović, B. (2017). The chronometric dating and subsistence of late Neanderthals and early anatomically modern humans in the central Balkans: insights from Šalitrena Pećina (Monica, Serbia). *J. Anthropol. Res.* 73, 413–447. doi:10.1086/693054

Marković, S. B., Sümegi, P., Stevens, T., Schaetzl, R. J., Obreht, I., Chu, W., et al. (2018). The Crvenka loess-paleosol sequence: a record of continuous grassland domination in the southern Carpathian Basin during the Late Pleistocene. *Palaeogeogr. Palaeoclimatol. Palaeoecol.* 509, 33–46. doi:10.1016/j.palaeo.2018.03.019

Marković, S. B., Timar-Gabor, A., Stevens, T., Hambach, U., Popov, D., Tomić, N., et al. (2014). Environmental dynamics and luminescence chronology from the Orlovat loess-Paleosol sequence (Vojvodina, Northern Serbia). *J. Quat. Sci.* 29, 189–199.

Marović, M., Toljić, M., Rundić, L., and Milivojević, J. (2007). *Neoalpine tectonics of Serbia*. Belgrade, Serbia: Serbian Geological Society.

Matenco, L., and Radivojević, D. (2012). On the formation and evolution of the Pannonian Basin: constraints derived from the structure of the junction area between the Carpathians and Dinarides. *Tectonics* 31, 1–31. doi:10.1029/2012TC003206

Mihailović, D. (1992). *Aurignacian flint industry from the site Crvenka-At near Vršac*. Belgrade: Centre for Archaeological Research: Faculty of Philosophy in Belgrade.

Mihailović, D., Mihailović, B., and Lopičić, M. (2011). "The palaeolithic in northern Serbia," in *The prehistory of Banat: the palaeolithic and mesolithic*. Editors N. Tasić, F. Drașovean, and B. Jovanović (Bucharest: Publishing House of the Romanian Academy), 77–93.

Mihailović, D. (2020). Push-and-pull factors of the middle to upper paleolithic transition in the Balkans. *Quat. Int.* 551, 47–62. doi:10.1016/j.quaint.2019.10.010

Miller, R. (2014). "Maisières-Canal: an open-air Aurignacian workshop" in *Encyclopedia of global Archaeology*. Editor C. Smith (New York, NY: Springer) doi:10.1007/978-1-4419-0465-2_1986

Müller, I. (1769). Mappa geographica novissima regni hungariae. Available at: https://maps.hungaricana.hu/hu/MOLTerkeptar/11272/view/?pg=6&bbox=4590%2C-3664%2C8209%2C-1572 (Accessed October 24, 2019).

Murray, A. S., Thomsen, K. J., Masuda, N., Buylaert, J. P., and Jain, M. (2012). Identifying well-bleached quartz using the different bleaching rates of quartz and feldspar luminescence signals. *Radiat. Meas.* 47 (9), 688–695. doi:10.1016/j.radmeas.2012.05.006

Murray, A. S., and Wintle, A. G. (2000). Luminescence dating of quartz using an improved single-aliquot regenerative-dose protocol. *Radiat. Meas.* 32, 57–73. doi:10.1016/S1350-4487(99)00253-X

Murray, A. S., and Wintle, A. G. (2003). The single aliquot regenerative dose protocol: potential for improvements in reliability. *Radiat. Meas.* 37, 377–381. doi:10.1016/S1350-4487(03)00053-2

Nelson, M. S., Gray, H. J., Johnson, J. A., Rittenour, T. M., Feathers, J. K., and Mahan, S. A. (2015). User guide for luminescence sampling in archaeological and geological contexts. *Adv. Archaeol. Pract.* 3, 166–177. doi:10.7183/2326-3768.3.2.166

Nelson, M. S., and Rittenour, T. M. (2015). Using grain-size characteristics to model soil water content: application to dose-rate calculation for luminescence dating. *Radiat. Meas.* 81, 142–149. doi:10.1016/j.radmeas.2015.02.016

Nottebaum, V., Stauch, G., Hartmann, K., Zhang, J., and Lehmkuhl, F. (2015). Unmixed loess grain size populations along the northern Qiqian Shan (China): relationships between geomorphologic, sedimentologic and climatic controls. *Quat. Int.* 372, 151–166. doi:10.1016/j.quaint.2014.12.071

Obreht, I., Hambach, U., Veres, D., Zeeden, C., Bösken, J., Stevens, T., et al. (2017). Shift of large-scale atmospheric systems over Europe during late MIS 3 and implications for modern human dispersal. *Sci. Rep.* 7, 5848. doi:10.1038/s41598-017-06285-x

Obreht, I., Zeeden, C., Hambach, U., Veres, D., Marković, S. B., and Lehmkuhl, F. (2019). A critical reevaluation of palaeoclimatic proxy records from loess in the Carpathian Basin. *Earth-Sci. Rev.* 190, 498–520. doi:10.1016/j.earscirev.2019.01.020

Obreht, I., Zeeden, C., Schulte, P., Hambach, U., Eckmeier, E., Timar-Gabor, A., et al. (2015). Aeolian dynamics at the Orlovat loess–paleosol sequence, northern Serbia, based on detailed textural and geochemical evidence. *Aeolian Res.* 18, 69–81. doi:10.1016/j.aeolia.2015.06.004

Özer, M., Orhan, M., and Işik, N. S. (2010). Effect of particle optical properties on size distribution of soils obtained by laser diffraction. *Environ. Eng. Geosci.* 16, 163–173. doi:10.2113/gseegeosci.16.2.163

Perić, Z., Adophi, E. L., Buylaert, J. P., Stevens, T., Újvári, G., Marković, S. B., et al. (2019). Quartz OSL dating of late Quaternary Chinese and Serbian loess: a cross Eurasian comparison of dust and mass accumulation rates. *Quat. Int.* 509A, 30–44. doi:10.1016/j.quaint.2018.01.010

Perić, Z., Marković, S. B., Sipos, Gy., Gavrilov, M. B., Thiel, C., Zeeden, C., et al. (2020). A post-IR IRSL chronology and dust mass accumulation rates of the Novak loess-paleosol sequence in northeastern Serbia. *Boreas* 49, 841–857. doi:10.1111/bor.12459

Popov, D., Vandenberghe, D. A. G., and Marković, S. B. (2012). Luminescence dating of fluvial deposits in Vojvodina, N Serbia: first results. *Quat. Geochronol.* 13, 42–51. doi:10.1016/j.quageo.2012.08.002

Pötter, S., Schmitz, A., Lücke, A., Schulte, P., Obreht, I., Zech, M., et al. (2021). Middle to Late Pleistocene environments based on stableorganic carbon and nitrogen isotopes of loess-palaeosol sequences from the Carpathian Basin. *Boreas* 50, 184–204. doi:10.1111/bor.12470

Păunescu, A. (2001). *Paleoliticul și mezoliticul din spațiul transiliac*. Bucharest: Agir.

R Core Team (2020). *R: a language and environment for statistical computing*. Available at: http://www.R-project.org/. Date of access: 2020/12/08.

Radovanović, I. (1986). Vršac-At, palaeolitsko nalazište. *Arheol. Pregl.* 25, 11–12.

Richards, M. P., and Trinkaus, E. (2009). Out of Africa: modern human origins special feature: isotopic evidence for the diets of European Neanderthals and early modern humans. *Proc. Natl. Acad. Sci. U.S.A.* 106, 16034–16039. doi:10.1073/pnas.0903821106

Rundić, L., Ganic, M., Knezevic, S., Radivojevic, D., and Radonjic, M. (2019). Stratigraphic implications of the mio-pliocene geodynamics in the area of Mt. Avala: new evidence from torlak hill and beli potok (Belgrade, Serbia). *Geol. Croat.* 72, 109–128. doi:10.4154/gc.2019.11

Schmidt, C., Sitlivy, V., Anghelinu, M., Chabai, V., Kels, H., Uthmeier, T., et al. (2013). First chronometric dates (TL and OSL) for the Aurignacian open-air site of Românești-Dumbrăvița I, Romania. *J. Archaeol. Sci.* 40, 3740–3753. doi:10.1016/j.jas.2013.04.003

Schmidt, E. D., Machalett, B., Marković, S. B., Tsukamoto, S., and Frechen, M. (2010). Luminescence chronology of the upper part of the Stari Slankamen loess sequence (Vojvodina, Serbia). *Quat. Geochronol.* 5, 137–142. doi:10.1016/j.quageo.2009.09.006

Schulte, P., Lehmkuhl, F., Kels, H., Loibl, C., Klasen, N., and Hauck, T. (2014). Environmental change indicated by grain-size variations and trace elements: examples from two different sections - the sandy-loess sediments from the Doroshivtsy site (Ukraine) and the loess section Semlac (Romania). *Proscience* 1, 106–112. doi:10.14644/dust.2014.017

Schulte, P., Lehmkuhl, F., Steininger, F., Loibl, D., Lockot, G., Protze, J., et al. (2016). Influence of HCl pretreatment and organo-mineral complexes on laser diffraction measurement of loess–paleosol-sequences. *Catena* 137, 392–405. doi:10.1016/j.catena.2015.10.015

Schwarz, U. (2014). "Hydromorphology of the danube," in *The danube river basin* (Berlin, Heidelberg: Springer), 469–479.

Sitlivy, V., Chabai, V., Anghelinu, M., Uthmeier, T., Kels, H., Hilgers, A., et al. (2012). The earliest Aurignacian in Romania: new investigations at the open air site of Românești-Dumbrăvița I (Banat). *Quartär* 59, 85–130.

Sitlivy, V., Nită, L., Băltean, I., Anghelinu, M., Uthmeier, T., Hilger, A., et al. (2014). "Placing the aurignacian from Banat (southwestern Romania) into the European early upper paleolithic context," in *Modes de Contactes et de Deplacements au Paléolithique Eurasiatique*. Editors M. Otte and F. le (Brun-Ricalens Liége: ERAUL), 243–277.

Soficaru, A., Dobos, A., and Trinkaus, E. (2006). Early modern humans from the pestera Muierii, baia de Fier, Romania. *Proc. Natl. Acad. Sci. U.S.A.* 103, 17196–17201. doi:10.1073/pnas.0608443103

Soficaru, A., Petrea, C., Doboș, A., and Trinkaus, E. (2007). The human cranium from the Peștera Cioclovina uscată, Romania. *Curr. Anthropol.* 48, 611–619. doi:10.1086/519915

Sprafke, T. (2016). *Löss in Niederösterreich – archiv quartärer Klima- und Landschaftsveränderungen (Loess in Lower Austria - archive of Quaternary climate and landscape development)*. Würzburg: Würzburg University Press.

Starkel, L., Michczunska, D. J., Gebica, P., Kiss, T., Panin, A., and Persoiu, I. (2015). Climatic fluctuations reflected in the evolution of fluvial systems of Central-Eastern Europe (60-80 ka cal BP). *Quat. Int.* 388, 97–118. doi:10.1016/j.quaint.2015.04.017

Staubwasser, M., Drăguşin, V., Onac, B. P., Assonov, S., Ersek, V., Hoffmann, D. L., et al. (2018). Impact of climate change on the transition of Neanderthals to modern humans in Europe. *Proc. Natl. Acad. Sci. U.S.A.* 115, 9116. doi:10.1073/pnas.1808647115

Sušić, Z., Toljić, M., Bulatović, V., Ninkov, T., and Stojadinović, U. (2016). Present-day horizontal mobility in the Serbian part of the Pannonian Basin; inferences from the geometric analysis of deformations. *Acta Geophys.* 64, 1626–1654. doi:10.1515/acgeo-2016-0074

Teyssandier, N., and Zilhão, J. (2018). On the entity and antiquity of the Aurignacian at Willendorf (Austria): implications for modern human emergence in Europe. *J. Paleolit. Archaeol.* 1, 107–138. doi:10.1007/s41982-017-0004-4

Thiel, C., Buylaert, J.-P., Murray, A., Terhorst, B., Hofer, I., Tsukamoto, S., et al. (2011). Luminescence dating of the Stratzing loess profile (Austria) – testing the potential of an elevated temperature post-IR IRSL protocol. *Quat. Int.* 234, 23–31. doi:10.1016/j.quaint.2010.05.018

Thomsen, K. J., Murray, A. S., Jain, M., and Bøtter-Jensen, L. (2008). Laboratory fading rates of various luminescence signals from feldspar-rich sediment extracts. *Radiat. Meas.* 43 (9), 1474–1486. doi:10.1016/j.radmeas.2008.06.002

Tikhonov, A. (2008). The IUCN red list of threatened species 2008: e.T136721A4332142. *Bos Primigenius*, 7 doi:10.2305/IUCN.UK.2008.RLTS.T136721A4332142.en

Timár, G., Székely, B., Molnár, G., Ferencz, C., Kern, A., Galambos, C., et al. (2008). Combination of historical maps and satellite images of the Banat region—re-appearance of an old wetland area. *Glob. Planet. Change* 62, 29–38. doi:10.1016/j.gloplacha.2007.11.002

Toljić, M., Matenco, L., Ducea, M. N., Stojadinović, U., Milivojević, J., and Đerić, N. (2013). The evolution of a key segment in the Europe–Adria collision: the Fruška Gora of northern Serbia. *Glob. Planet Change* 103, 39–62. doi:10.1016/j.gloplacha.2012.10.009

Tourloukis, V. (2016). "On the spatio-temporal distribution of mediterranean lower paleolithic sites: a geoarchaeological perspective," in *Paleoanthropology of the Balkans and anatolia: human evolution and its context*. Editors K. Harvati and M. Roksandic (Dordrecht: Springer), 303–323.

Trinkaus, E., Milota, S., Rodrigo, R., Mircea, G., and Moldovan, O. (2003a). Early modern human cranial remains from the Peştera cu Oase, Romania. *J. Hum. Evol.* 45, 245–253. doi:10.1016/j.jhevol.2003.08.003

Trinkaus, E., Moldovan, O., Milota, S., Bîlgăr, A., Sarcina, L., Athreya, S., et al. (2003b). An early modern human from the Peştera cu Oase, Romania. *Proc. Natl. Acad. Sci. U.S.A.* 100, 11231–11236. doi:10.1073/pnas.2035108100

Trinkaus, E., Constantin, S., and Zilhão, J. (2012). *Life and death at the Peştera cu Oase: a setting for modern human emergence in Europe*. New York: Oxford University Press.

Trinkaus, E., Soficaru, A., Doboş, A., Constantin, S., Zilhão, J., and Richards, M. (2009). Stable isotope evidence for early modern human diet in southeastern Europe: peştera cu Oase, Peştera muierii and peştera cioclovina uscată. *Mater. Cercetări Arheolog.* 5, 4–14.

Vandenberghe, J., Kasse, C., Popov, D., Markovic, S. B., Vandenberghe, D., Bohncke, S., et al. (2018). Specifying the external impact on fluvial lowland evolution: the Last Glacial Tisza (Tisa) catchment in Hungary and Serbia. *Quaternary* 1, 14. doi:10.3390/quat1020014

Vasiliniuc, Ş., Vandenberghe, D. A. G., Timar-Gabor, A., Panaiotu, C., Cosma, C., and van den Haute, P. (2012). Testing the potential of elevated temperature post-IR IRSL signals for dating Romanian loess. *Quat. Geochronol.* 10, 75–80. doi:10.1016/j.quageo.2012.02.014

Vlaminck, S., Kehl, M., Lauer, T., Shahriari, A., Sharifi, J., Eckmeier, E., et al. (2016). Loess-soil sequence at toshan (northern Iran): insights into late Pleistocene climate change. *Quat. Int.* 399, 122–135. doi:10.1016/j.quaint.2015.04.028

Weninger, B., Joris, O., and Danzeglocke, U. (2008). *CalPal-2007. Cologne, radiocarbon calibration & palaeoclimate research package*. Available at: http://www.calpal.de.

Xiao, J., Chang, Z., Fan, J., Zhou, L., Zhai, D., Wen, R., et al. (2012). The link between grain-size components and depositional processes in a modern clastic lake: grain-size components of Hulun Lake sediments. *Sedimentology* 59, 1050–1062. doi:10.1111/j.1365-3091.2011.01294.x

Zeeden, C., Dietze, M., and Kreutzer, S. (2018). Discriminating luminescence age uncertainty composition for a robust Bayesian modelling. *Quat. Geochron.* 43, 30–39. doi:10.1016/j.quageo.2017.10.001

Zeeden, C., Hambach, U., Klasen, N., Fischer, P., Schulte, P., Nett, J. J., et al. (2021). Sedimentology of a late Quaternary lacustrine record from the south-eastern Carpathian Basin. *J. Quat. Sci.*

Zeeden, C., Kels, H., Hambach, U., Schulte, P., Protze, J., Eckmeier, E., et al. (2016). Three climatic cycles recorded in a loess-paleosol sequence at Semlac (Romania) – implications for dust accumulation in south-eastern Europe. *Quat. Sci. Rev.* 154, 130–142. doi:10.1016/j.quascirev.2016.11.002

Zeeden, C., Krauß, L., Kels, H., and Lehmkuhl, F. (2017). Digital image analysis of outcropping sediments: comparison to photospectrometric data from quaternary loess deposits at Şanovița (Romania) and Achenheim (France). *Quat. Int.* 429, 100–107. doi:10.1016/j.quaint.2016.02.047

Zilhão, J., Trinkaus, E., Constantin, S., Milota, S., Gherase, M., Sarcina, L., et al. (2007). "The Peştera cu Oase people, Europe's earliest modern humans," in *Rethinking the human revolution: new behavioural and biological perspectives on the origin and dispersal of modern humans*. Editors P. Mellars, K. Boyle, O. Bar-Yosef, and C. Stringer (Cambridge, UK: McDonald Institute for Archaeological Research), 249–262.

Conflict of Interest: The authors declare that the research was conducted in the absence of any commercial or financial relationships that could be construed as a potential conflict of interest.

frontiers in Earth Science

METHODS
published: 04 March 2021
doi: 10.3389/feart.2021.594047

Multiband Wavelet Age Modeling for a ~293 m (~600 kyr) Sediment Core From Chew Bahir Basin, Southern Ethiopian Rift

*Walter Duesing[1], Nadine Berner[2], Alan L. Deino[3], Verena Foerster[4], K. Hauke Kraemer[1,5], Norbert Marwan[5] and Martin H. Trauth[1]**

[1]Institute of Geoscience, University of Potsdam, Potsdam, Germany, [2]Safety Analyses Department, Gesellschaft für Anlagen- und Reaktorsicherheit (GRS) GmbH, Forschungszentrum, Garching, Germany, [3]Berkeley Geochronology Center, Berkeley, CA, United States, [4]Institute of Geography Education, University of Cologne, Cologne, Germany, [5]Potsdam Institute for Climate Impact Research, Potsdam, Germany

The use of cyclostratigraphy to reconstruct the timing of deposition of lacustrine deposits requires sophisticated tuning techniques that can accommodate continuous long-term changes in sedimentation rates. However, most tuning methods use stationary filters that are unable to take into account such long-term variations in accumulation rates. To overcome this problem we present herein a new multiband wavelet age modeling (MUBAWA) technique that is particularly suitable for such situations and demonstrate its use on a 293 m composite core from the Chew Bahir basin, southern Ethiopian rift. In contrast to traditional tuning methods, which use a single, defined bandpass filter, the new method uses an adaptive bandpass filter that adapts to changes in continuous spatial frequency evolution paths in a wavelet power spectrum, within which the wavelength varies considerably along the length of the core due to continuous changes in long-term sedimentation rates. We first applied the MUBAWA technique to a synthetic data set before then using it to establish an age model for the approximately 293 m long composite core from the Chew Bahir basin. For this we used the 2nd principal component of color reflectance values from the sediment, which showed distinct cycles with wavelengths of 10–15 and of ~40 m that were probably a result of the influence of orbital cycles. We used six independent 40Ar/39Ar ages from volcanic ash layers within the core to determine an approximate spatial frequency range for the orbital signal. Our results demonstrate that the new wavelet-based age modeling technique can significantly increase the accuracy of tuned age models.

Keywords: orbital forcing, african climate, age modeling, cyclostratigraphy, lake sediments

OPEN ACCESS

Edited by:
David K. Wright,
University of Oslo, Norway

Reviewed by:
Huaichun Wu,
China University of Geosciences, China
Shiyong Yu,
Jiangsu Normal University, China

****Correspondence:***
Martin H. Trauth
wduesing@uni-potsdam.de

Specialty section:
This article was submitted to Quaternary Science, Geomorphology and Paleoenvironment, a section of the journal Frontiers in Earth Science

Received: *13 August 2020*
Accepted: *14 January 2021*
Published: *04 March 2021*

Citation:
Duesing W, Berner N, Deino AL, Foerster V, Kraemer KH, Marwan N and Trauth MH (2021) Multiband Wavelet Age Modeling for a 293 m (600 kyr) Sediment Core From Chew Bahir Basin, Southern Ethiopian Rift. Front. Earth Sci. 9:594047. doi: 10.3389/feart.2021.594047

INTRODUCTION

When investigating paleoclimate records derived from lake cores, the reliability of the age model used is crucial. This reliability depends largely on the density of independent age-control points, which should ideally be evenly distributed along the entire length of the core. Such age-control points are derived from radiometric age determinations obtained by, for example, 40Ar/39Ar dating of volcanic ash layers, 14C dating of organic material, or luminescence dating of feldspar and quartz crystals. Datable material is,

however, often scarce in sediment cores. Cyclostratigraphy can be used in such cases to add additional age control points, evenly distributed in time. This method has been applied since the mid-1970s to marine records that extend beyond the range of the radiocarbon dating technique (e.g., Hays et al., 1976; Imbrie and Imbrie, 1980; Pisias et al., 1984; Martinson et al., 1987; Tiedemann et al., 1994; Grant et al., 2017). Orbital tuning has often been used to increase the temporal resolution between radiometric age control points, more commonly in paleoceanography than in paleolimnology (e.g., Grant et al., 2017).

Traditional tuning techniques first assume a maximum age for the base of the core (the base age), which is typically derived from existing radiometric dating and/or magnetostratigraphy, to derive a preliminary linear age model assuming constant sedimentation rates. (e.g., Hays et al., 1976; Pisias et al., 1984; Martinson et al., 1987; Tiedemann et al., 1994). The next step involves using a bandpass filter to reduce the proxy data to a single orbital frequency, which should match that of the tuning target (TT). The TT is a reference time series used during tuning, whose exact time course is known and whose frequency is also expressed in the proxy data. The final step is then to align the peaks of the filtered time series with those of the TT (fine tuning the preliminary age model) and to interpolate all core data to the new tuned age model.

Variants of this technique use frequency shifts by applying a moving-window Fourier technique Meyers et al., 2001), a method that tracks the dominant harmonic in the data series (Park and Herbert, 1987), an average spectral misfit method (Meyers and Sageman, 2007), a method that identifies the time scale that simultaneously optimizes eccentricity amplitude modulation of the precession band (Meyers, 2015), or a spectral moment approach (Sinnesael et al., 2018), to establish an age model (Hinnov, 2013, and references therein). Some published applications of the method have been criticized for over tuning (e.g. Tiedemann et al., 1994; Raymo et al., 1997) which is why Muller and MacDonald (2002) proposed the use of *minimal tuning*, for which only a few age control points are required (for example ages obtained from magnetic field reversals or radiometric ages) obtained from within the core. One of the main assumptions of the minimal tuning methods is a relatively constant sedimentation rate, which allows a stationary bandpass filter to be used. This tuning method, which is increasingly popular in paleolimnology (e.g., Wagner et al., 2019), consequently needs to be adapted in order to be applicable to lake environments, where the sedimentation rate is unlikely to be constant.

In this paper we present a new tuning technique that is suitable for use with paleoclimate records that have few radiometric age determinations but show significant orbital cyclicity. The fundamental difference between this new technique and other tuning techniques is that instead of a fixed bandpass filter we use a new adaptive filtering method that takes into account continuous long-term changes in sedimentation rates. The multiband wavelet age modeling (MUBAWA) approach uses a continuous wavelet spectral analysis to identify and trace the orbital signal within a user-defined range of possible base ages for the core.

We first used a synthetic example to demonstrate the advantages of the new method compared to a traditional method of cyclostratigraphy similar to the minimal tuning approach of Muller and MacDonald (2002). We then applied the technique to a 292.87 m composite core collected from the Chew Bahir basin in southern Ethiopia. The results demonstrate how this method can be used to further improve orbital tuning as an age-modeling technique and facilitate its use in a broad range of applications.

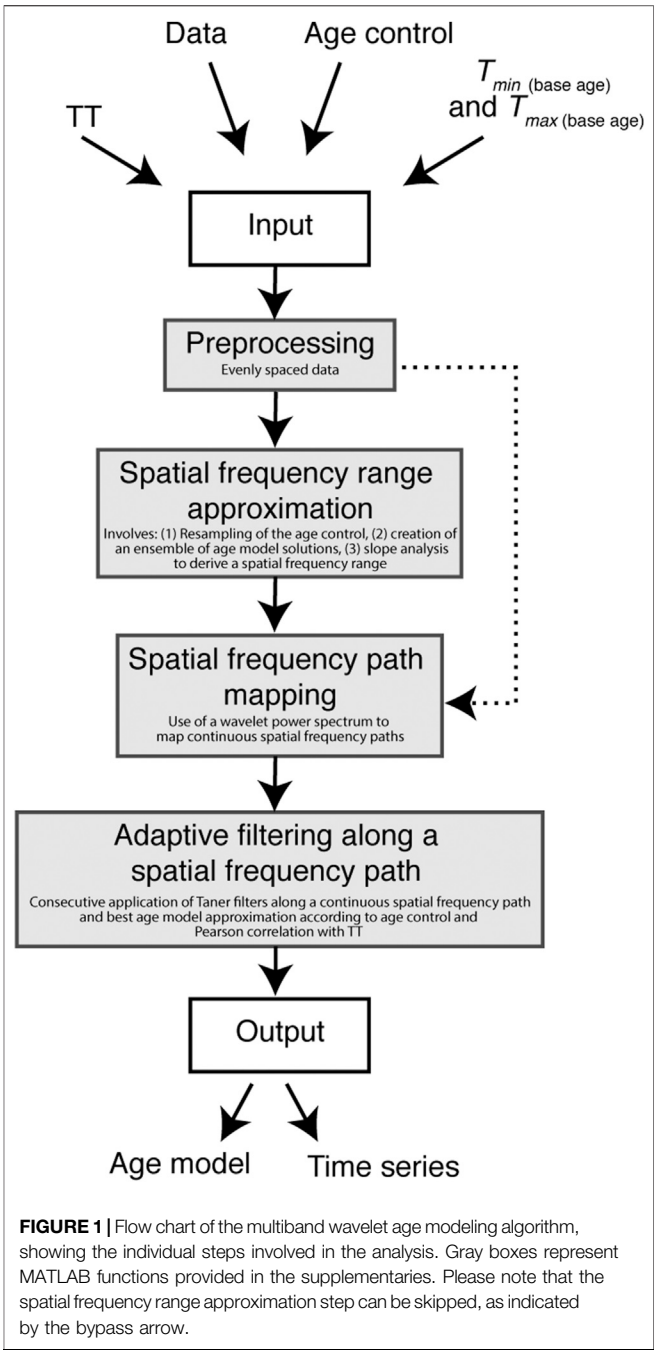

FIGURE 1 | Flow chart of the multiband wavelet age modeling algorithm, showing the individual steps involved in the analysis. Gray boxes represent MATLAB functions provided in the supplementaries. Please note that the spatial frequency range approximation step can be skipped, as indicated by the bypass arrow.

METHODS

The Principle of the MUBAWA Approach

The MUBAWA approach is based on the application of a continuous wavelet transformation (CWT) to a depth series,

with the aim of generating a tuned age model. We use the CWT to track variations in the spatial frequency of the astronomical component with depth (which we refer to as the spatial frequency path), in order to be able to adaptively bandpass filter the astronomical component from the proxy data. The MUBAWA technique is specifically designed for lacustrine depositional environments such as that of the Chew Bahir basin, with their continuous, long-term changes in sedimentation rates, whereas methods using stationary filters are not suitable for such complex depositional environments.

The MUBAWA algorithm consists of several modular functions, which are wrapped in a MATLAB live script and are available in the **Supplementary material**. The algorithm is divided into the following four steps (**Figure 1**). Step 1: preprocessing, which involves resampling and evenly spacing the input data defined by the frequency of the TT and the maximum possible base age (*tmax*). Step 2: spatial frequency range approximation (SFRA), which is an optional step that uses the available age control to approximate the spatial frequency range of the targeted orbital component, Step 3: spatial frequency path mapping, which involves determining spatial frequencies using a CWT and applying a weighting function to prevent the inclusion of unrealistic sedimentation rates, and Step 4: identification of the best continuous spatial frequency path, adaptive filtering by the consecutive application of Taner filters along this spatial frequency path, and identification of the best age model solution.

Preprocessing

The filter methods used in this method, as well as the CWT, require evenly spaced data and the sample size should be restricted in order to avoid long computation times. We chose a sample size that did not exceed 20 data points for each cycle occurring in the TT within the time interval between t_0 and t_{max}. We then established an evenly spaced depth vector to match the new sampling rate and interpolated the proxy values in order to obtain an evenly spaced subsampled data set. The resulting computed depth series was then used in all of the subsequent steps.

Spatial Frequency Range Approximation (SFRA)

In this step we use the age control points and their corresponding uncertainties to estimate a spatial frequency range, which is defined by the frequency of the TT and the maximum and minimum slopes of the ensemble of age model solutions for each depth point. This procedure is based on the assumption that every age model solution results in a particular spatial frequency path for each depth point, depending on the frequency of the TT and the slope of the age model solution. This procedure can help to find tuned age model solutions that conform with the age control points (within their respective uncertainties). This is an optional procedure that is not essential for the determination of a frequency path, but it provides an auxiliary strategy with which to improve the chances of approximating a path that will yield results that conform with the age control points, within their uncertainty ranges.

This resampling-based approach involves obtaining random samples from the normal distribution of the available age control points and computing an age model for each set of random samples. A piecewise cubic Hermite interpolating polynomial (PCHIP; Fritsch and Carlson, 1980) is used to interpolate between the resampled age control points. Using a PCHIP yields solutions that tend not to have any strong fluctuations, since the interpolations are generally more gradual and do not deviate markedly from each other in the way that they do with other methods, such as the classic cubic spline interpolation method.

The maximum and minimum slopes of the age models derived from the resampling of the age control points, are then computed for each depth point. Only monotonically increasing solutions are accepted, in order to avoid any solutions that describe time reversals. The slopes are converted into a spatial frequency range with respect to the TT. Two depth series are then generated in which the maximum slope values lead to a depth series with a low spatial frequency limit, and the minimum slope values to a depth series with a high spatial frequency limit.

The spatial frequency limits are then used to adaptively bandpass filter the regularly sampled depth series obtained from the preprocessing, using Taner filters (Taner 1992).

Spatial Frequency Path Mapping

The following steps use either the adaptively filtered depth series obtained from the SFRA or, if the SFRA has not been used, the preprocessed depth data.

A continuous power spectrum (CWT) resolves the evolution of frequencies through time or space. Throughout this paper we focus on the perspective of spatial frequencies, since we are dealing with depth series. A spatial frequency path can be obtained by analyzing the frequency evolution of a CWT-based wavelet power spectrum of the input depth series. Further on in this section, we describe how we identify these paths. We then use the identified spatial frequency paths to adjust bandpass filter center points for each point in the depth series, thus creating an adaptive filter.

A wavelet is the basis function used for the wavelet transformation (WT) and can be thought of a specific wave defined by its frequency and amplitude, with the amplitude decaying to zero toward either end. Since wavelets can be stretched and translated in both frequency and space, with a flexible resolution, they can easily map changes in the spatial frequency domain (**Figures 2A,B**). We define β as the depth variable such that $y(\beta)$ is the signal under consideration (i.e. the climate proxy data as a function of the core depth β). A continuous wavelet transformation (CWT) mathematically decomposes $y(\beta)$ into the elementary functions $\Psi_{a,b}(\beta)$, derived from a mother wavelet $\Psi(\beta)$ by dilation and translation (Addison, 2017). The dilation indicates a compressing or stretching of the mother wavelet $\Psi(\beta)$,

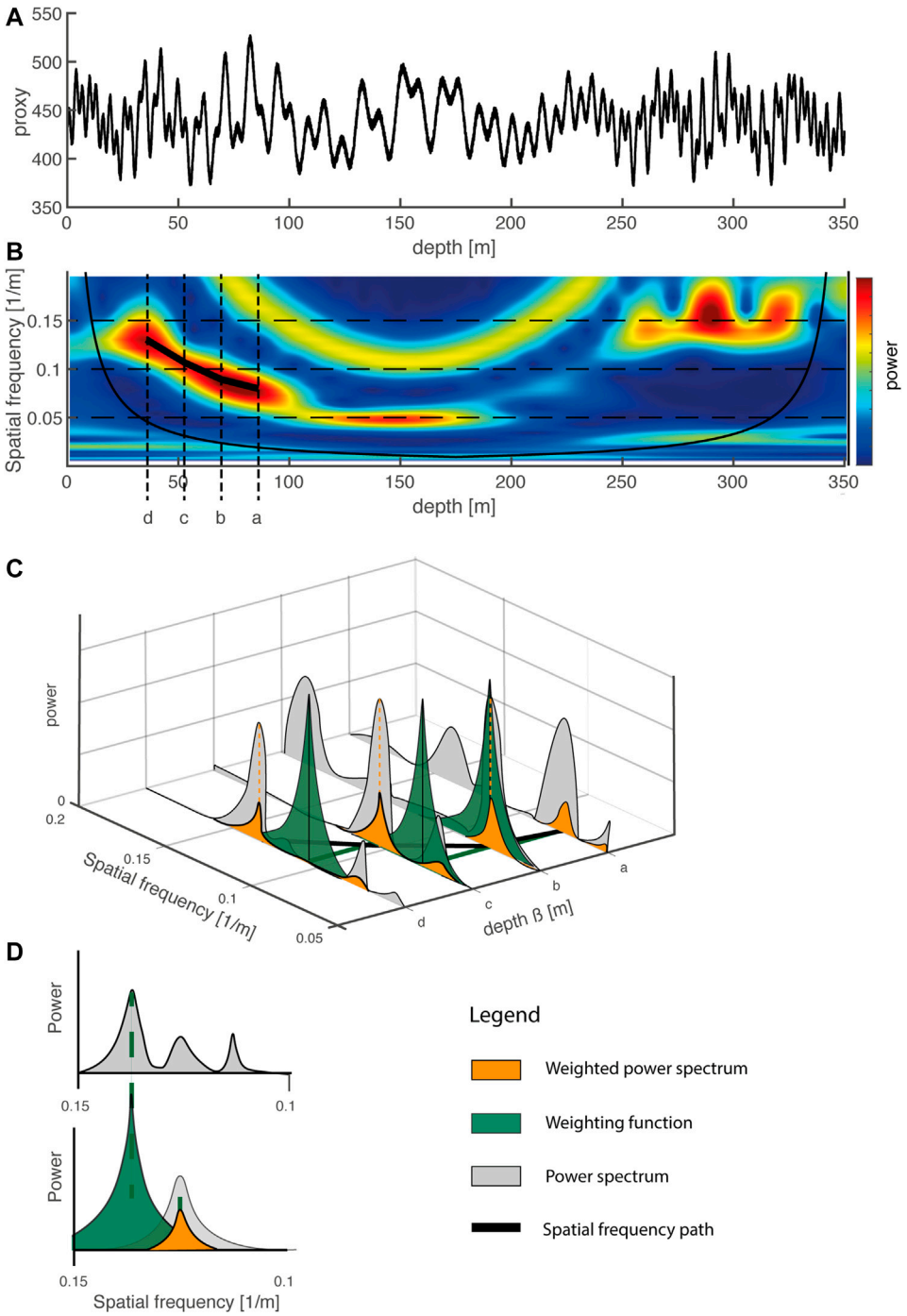

FIGURE 2 | (A) To illustrate how to map spatial frequency paths we generated a demonstration depth series consisting of an insolation signal (from Laskar et al., 2004) and superimposed sinusoids. The result was a depth series that had been stretched and compressed by variations in the sedimentation rate. **(B)** We computed a CWT from the depth series and plotted the results in a wavelet power spectrum. Note that the frequency evolution followed curved paths. We extracted four profiles from the CWT, labeled **a, b, c, and d**. **(C)** Showing how continuous spatial frequency paths are mapped along the profiles **a, b, c, and d**. **(D)** Showing how a peak is detected and how the power spectrum of the next profile is weighted by application of the green weighting function. The gray peak is weighted and forms the orange weighted power spectrum.

resulting in a variation in its frequency, controlled by the scale parameter a. The spatial resolution of the CWT follows the translation of the mother wavelet $\Psi(\beta)$ along the depth β and is controlled by the translation parameter b (Lau and Weng, 1995). The wavelet transform of the signal $y(\beta)$ is then defined as the convolution integral

$$\mathrm{CWT}_{\Psi}(a,b) = \frac{1}{\sqrt{a}} \int \Psi^{*}\left(\frac{\beta - b}{a}\right) y(\beta) d\beta \tag{1}$$

in which the asterisk indicates the complex conjugate of the mother wavelet Ψ and the factor $1/\sqrt{a}$ ensures the preservation of energy. By varying b for a range of values for the scale parameter a, the final wavelet power spectrum and the corresponding scalogram can be obtained (**Equation 4**; **Figure 2B**).

The CWT can be computed for a broad spectrum of different mother wavelets. In geoscience, however, the complex Morlet wavelets are most widely used because they can be more easily adapted to capture oscillatory behavior (Torrence and Compo, 1998):

$$\Psi_{\mathrm{Morlet}}(\beta) = \frac{1}{\pi^{1/4}} e^{i2\pi f_0 \beta} e^{-\beta^2/2} \tag{2}$$

from which the elementary functions

$$\Psi_{a,b}(\beta) = \frac{1}{\pi^{1/4}} e^{\left(i2\pi f_0 \frac{\beta - b}{a}\right)} e^{-\left(\frac{\beta - b}{\sqrt{2}\, a}\right)^2} \tag{3}$$

are derived and then used in **Equation 1**. Computing the CWT of the spatial data results in a complex spatial frequency output, of which the absolute value represents a wavelet power spectrum for a particular (a,b)-parameter configuration:

$$E(a,b) = |\mathrm{CWT}(a,b)|^2 \tag{4}$$

This is called a *scalogram*, representing the energy density surface of the fast Fourier transform, analogous to a *spectrogram* (Addison 2017). Mapping $E(a,b)$ for a variety of (a,b)-parameter value pairs yields a three-dimensional frequency map (**Figure 2B**) in which the x-values represent core depth-values β (related to the dilation parameter b in **Equations 1**, **3**, **4**, the y-values represent frequencies (related to the scale parameter a in **Equations 1**, **3**, **4**), and the color coded z-values represent the power of the (spatial) frequencies at each given β/b-value, $E_b(a)$ (**Equation 1**). We refer to this as the wavelet power spectrum throughout this paper. Finally the relationship between the scale parameter a and a spatial frequency f, at depth β, is

$$a = \frac{f_c}{f} \tag{5}$$

where f_c is the *center frequency* of the Morlet wavelet used and is chosen automatically, depending on the energy spread of the wavelet in spatial frequency and depth (MathWorks, 2020a).

The wavelet power spectrum (**Figure 2B**) allows us to map frequency paths by following the β-axis along a high energy ridge (represented by a continuous color band and reflecting sufficiently high energies), remaining at the highest local energy level, following changes in spatial frequency without jumping from one ridge to another (**Figure 2C**). These ridges are referred to as spatial frequency paths. They represent continuous changes in the spatial frequencies within a certain power range of the signal (e.g. a color range of a band in **Figure 2B**). To map a spatial frequency path we need to set starting points in the wavelet transform plot, which are derived from the absolute value of the first complex spatial frequency output $E_{b_{first}}(a)$ (**Equation 4**) and its respective maxima in spatial frequency, where each maximum represents a starting point. Since we can in theory start our spatial frequency path tracking from either end of the wavelet transform plot, starting points are derived from maxima of the absolute value of the complex frequency output of the CWT, $E_{b_{first}}(a)$, from either end of the core (i.e. where $\beta = 0$ and $\beta = \max.$):

$$\text{Starting point } = \zeta_{\beta_{first}} = \max_{a} E_{b_{first}}(a)$$

In the application presented herein, in which spatial frequency paths are used to derive cutoff frequencies for adaptive filtering of the depth series, jumps in the spatial frequency paths represent abrupt changes in the sedimentation rate. These need to be avoided because the resolution of our method is limited to one cycle of the TT, and it is therefore unable to detect such abrupt changes. We therefore assume that any changes in spatial frequency occur continuously. This is achieved by introducing a weighting function that penalizes any sudden fluctuations in spatial frequency, e.g., when going from $E_{b=\beta_0}(a)$ at depth β_0 to the next point in the path $E_{b=\beta_1}(a)$ at depth β_1 (**Equation 6**, **7**). For an illustration of such a path through slices $E_b(a)$ of the wavelet transform plot see **Figures 2C,D**, in which the weighting function is highlighted in green. The weighting procedure prevents sudden jumps in the spatial frequency when following along a spatial frequency path and avoids the inclusion of a neighboring cycles. A suitable weighting function is a negative exponential function with a decay parameter $\kappa = 20$, which we place at the location of the previous spatial frequency point in the wavelet transform plot (ξ_{β_0}) before determining the next point (ξ_{β_1}):

$$\begin{aligned} \xi_0 &= max\left(E_{b=\beta_0}(a)\right) \\ \xi_1 &= max\left(E_{b=\beta_1}(a) \cdot f_{\mathrm{weighting}}\right) \end{aligned} \tag{6}$$

with

$$f_{\mathrm{weighting}} = e^{-\kappa \cdot |a - \xi_1|} \tag{7}$$

The frequency path analysis is sensitive to the directionality of the weighting strategy, i.e. to whether the weighting is applied top-down or bottom-up along the core. Our age model is based on spatial frequency paths that are computed bottom-up, which we interpret as the physically correct approach, assuming that the preceding spatial frequency point contains information about the subsequent spatial frequency point, proceeding along a positive time scale.

Completing this step of the algorithm typically yields a number of continuous frequency paths from which the best approximation to the orbital component needs to be identified in the following final step.

Adaptive Filtering Along the Spatial Frequency Path

For our adaptive filter approach we use a series of Taner filters (Taner, 1992; Zeeden et al., 2018). These filters have decisive

advantages over the widely used Butterworth filters due to their steep roll off rates for narrow bandpass configuration. On the other hand, the longer computation times compared to Butterworth filters are an obvious disadvantage. The method proposed herein uses continuous spatial frequency paths, identified by spatial frequency mapping, to design adaptive bandpass filters for use on the depth series along these paths, assuming that one of these paths approximates the orbital component that we ultimately want to tune. Adapting the cutoff frequencies used in the filtering process allows continuous variations in sedimentation rates, which ultimately cause changes in the wavelength of the orbital component, to be taken into account.

The spatial frequency path mapping usually yields a number of possibly suitable paths. The following steps are performed with all of the spatial frequency paths that resulted from the previously described spatial frequency mapping. Each frequency path is first smoothed using a 20 data point Gaussian filter, in order to avoid abrupt changes in frequency. Both forward and reverse filtering are used to avoid phase shifts. The frequency paths are then converted into a lower cutoff depth series and an upper cutoff depth series. (For the lower cutoff frequency we subtracted one sixth of the frequency of the spatial frequency path and for the upper cutoff frequency we added one sixth: these values were found to be practicable for our purposes.) The result is a frequency tube enclosing the frequency path used.

Each data point in the entire time series is then filtered separately using Taner filters. From the results of the filtering a new adaptively filtered composite depth series is created in which each value is the result of an individual bandpass filter setting that was derived from a particular spatial frequency path. To reduce any noise that can derive from the adaptive filtering, the resulting composite depth series is filtered with a Taner filter. The upper cutoff frequency is set to the maximum cutoff frequency of the spatial frequency path that was used for the adaptive filtering and the lower cutoff frequency to the minimum cutoff frequency.

The set of maxima appearing in each of the adaptively filtered depth series is then determined. The first and last maxima of the adaptively filtered depth series are rejected in order to avoid edge effects at either end of the wavelet power spectrum. An age model can be obtained for each of the spatial frequency paths by assigning the remaining maxima in the adaptively filtered depth series to the minima of the TT, translating each adaptively filtered depth series into a time series. Each age model is applied to the filtered time series and an adaptively filtered time series thus obtained.

In order to identify the most suitable age model on the basis of its agreement with age control points and the TT, each age model is ranked using the following procedure. For each age control point (and uncertainty) that is included, the age model corresponding to the time series is assigned a score of one point. Pearson correlation coefficients between each of the adaptively filtered time series and the TT are also used to provide an indication of the degree of correlation. The age model corresponding to the time series that has the highest degree of correlation gains an additional point. The age model and its corresponding time series that has the highest final score is rated as the best age model. The full data set is then interpolated using the best age model approximation and the maximum sampling rate, as defined by the length of the original data set.

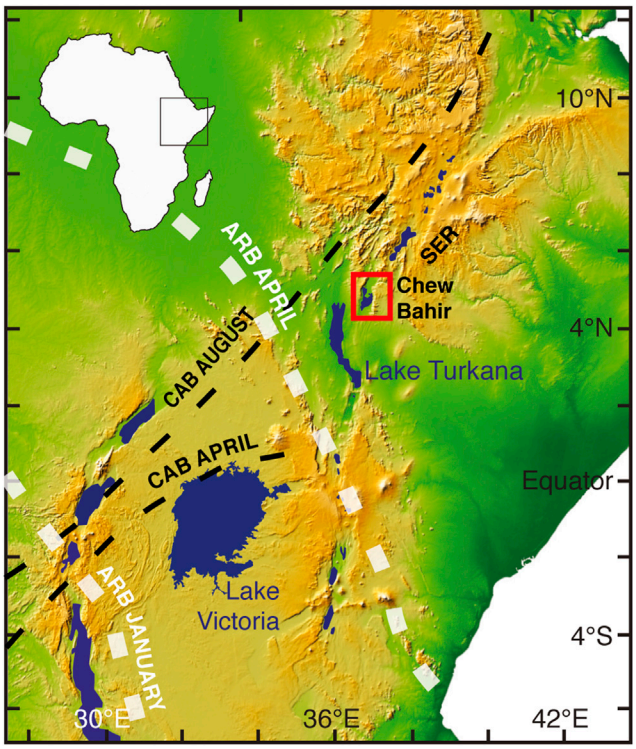

FIGURE 3 | Location of the study area. The Chew Bahir basin is located in southern Ethiopia, within the southern Ethiopian rift (indicated by the red box). Rainfall in the area is determined by the annual migration of the tropical rain belt (TRB), and on inter annual time scales by the migration of the Congo air boundary (CAB). On millennial time scales rainfall shows a strong correlation with orbital precession cycles.

Traditional Tuning

We compared the MUBAWA tuning technique with an established tuning technique widely used in paleoceanography (e.g., Hays et al., 1976; Imbrie and Imbrie, 1980). In contrast to the MUBAWA method, established tuning approaches use a preliminary estimate for the basal age of the core (e.g. from magnetostratigraphy) and interpolate an environmental proxy (such as benthic oxygen isotopes) to a preliminary age scale, before then bandpass filtering and tuning this proxy to an orbital cycle (e.g. Earth's precession cycle) as the TT. The maxima of the filtered time series are then interpolated to the minima of orbital precession based, for example, on the solution by Laskar et al. (2004). Both time series are then in phase and the age model is complete.

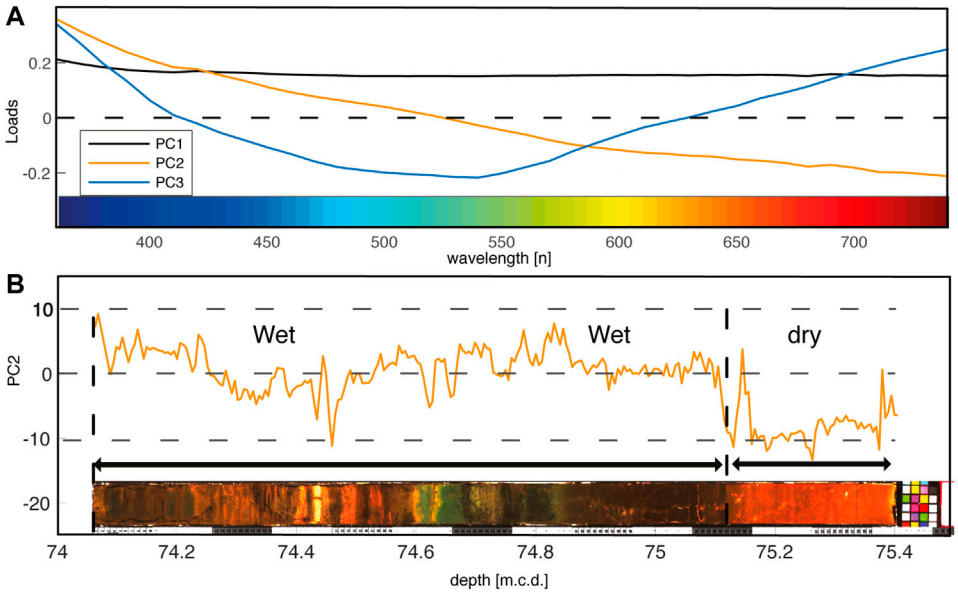

FIGURE 4 | (A) To extract the environmental signal from the 39 band color reflectance data set we used a principal component analysis (PCA). The first three principal components explained 99.88% of the total variance. We used the 2nd principal component (PC2) as an environmental indicator, with positive values indicating wet periods. **(B)** The PC2 corresponds to red blue green color shifts that are characteristic for the sediments of the Chew Bahir core displayed at the bottom of the diagram. The colors of the core have been photographically enhanced.

MATERIALS

Synthetic Data for Testing

To test the MUBAWA algorithm we produced synthetic data using an insolation signal for 4°N and 35°E from Laskar et al. (2004), covering the past 800 kyrs with a sampling interval of 100 years. In addition to the insolation signal, we added a distinct 10-kyr cycle and a distinct 100-kyr cycle as two sine waves. Adding extra cycles to the quasi monochromatic insolation signal produced synthetic data that was closer to real climate data, in which multiple continuous frequencies can occur. We created an artificial age model that was characterized by a continuous increase in sedimentation rates down core from 0.3 to 0.9 m/kyr, transferred the time series into a space series, and added white noise. For age control points we generated randomly distributed ages that were resampled from the time series, simulating, for example, the presence of Argon-dated volcanic ash layers in the core. The result was a synthetic depth series that was derived from a time series and in which the sediment deposition rate varied with time, simulating a climate proxy record.

The Chew Bahir Data

The Chew Bahir sediment cores described herein were collected from the Chew Bahir paleolake basin in the southern Ethiopian Rift (4.1–6.3°N, 36.5–38.1°E; **Figure 3**), a segment of the East African Rift System (EARS). The Chew Bahir record discussed in this work is a composite record from duplicate sediment cores, HSPDP-CHB14-2A and HSPDP-CHB14-2B[1]. In the following sections we use meter composite depth [m.c.d.] as our unit for depth.

Rainfall in the area is determined by the migration of the tropical rain belt, which in turn follows the zenith of the Sun and results in two rainy seasons (Nicholson, 2017). During the Pleistocene, African climatic changes on millennial time scales are thought to have been caused by periodic (23–19 kyr) variations in insolation resulting from Earth's orbital precession (e.g., Kutzbach and Street-Perrott, 1985; Berger et al., 2006). Due to the geometry of precession, changes in summer solar radiation are anti-phased between hemispheres, resulting in maximum monsoonal circulation and maximum precipitation every 19–23 kyrs in northern and southern Africa (Partridge, 1997; Trauth et al., 2003; Berger et al., 2006). In contrast, periods of increased humidity in equatorial East Africa occurred at 10–11 kyr intervals following maximum equatorial insolation in March and September (Trauth et al., 2003; Berger et al., 2006).

For this study, with its focus on calculating an age model by orbital tuning, we used the 39 band color reflectance data, which show distinct continuous cycles at ~10–15 and ~40 m depth intervals. Past variations in rainfall are reflected in the color of the sediments of the Chew Bahir basin, with blue-green colors during wet episodes and reddish-brown colors during dry episodes (Foerster et al., 2012). The sediment color can be primary, resulting from direct detrital sediment input, or secondary, due to diagenesis of the deposited sediments by, for example, redox processes at the sediment-water boundary under lacustrine conditions (Giosan et al., 2002 and references therein). Color reflectances within the blue green spectrum suggest reactions at the sediment-water boundary as a result

[1]Foerster, et al. submitted.

of H2S production, fueled by organic matter and its consumption by sulfate reducing bacteria. H2S in the anoxic zone at the water-sediment boundary reacts with iron hydroxides, reducing any Fe^{3+} that is attached to clay minerals, bound in iron-hydroxides, or present in aqueous solution. During this process mono-sulphides and pyrite form on the lake floor and within the uppermost centimeters of sediment (Giosan et al., 2002), resulting in a spectral shift toward green/blue reflectances.

Organic matter input can derive from algal blooms within the lake and from plant material washed into the lake from the Chew Bahir catchment area. Algal blooms are in turn driven by nutrient and iron influx to the lake system (Storch and Dunham, 1986). Dissolved iron (Fe) and iron hydroxide may originate from the catchment areas at the upper eastern edge of the Chew Bahir basin, from the Teltele Plateau, and from the northeastern part of the catchment, where volcanic rocks are exposed to weathering (Foerster et al., 2012). Wind-blown dust from more distant sources may also have contributed to the nutrient and iron flux into the lake (Foerster et al., 2012). In the absence of oxygen the reduced minerals retain their diagenetic signatures and associated color reflectances until they are eventually sealed off from the lake water and possible chemical alteration by subsequent sedimentation.

We used a principal component analysis (PCA) (Pearson, 1901) to unmix the environmental factors controlling sediment color and to increase the signal-to-noise ratio, as well as to assist in interpreting the multivariate data set. The first principal component (PC1) showed similar loadings for all color bands; it was interpreted to represent the total reflectance of the sediment and was not used in this method. We Instead used PC2 (3.4% of the total variance), with positive loadings within the short wavelengths (blue reflected light), as a proxy for precipitation within the catchment area (**Figures 4A,B**). Complete linear unmixing was, however, not possible because the intensity values within individual wavelength bands were not perfectly Gaussian distributed.

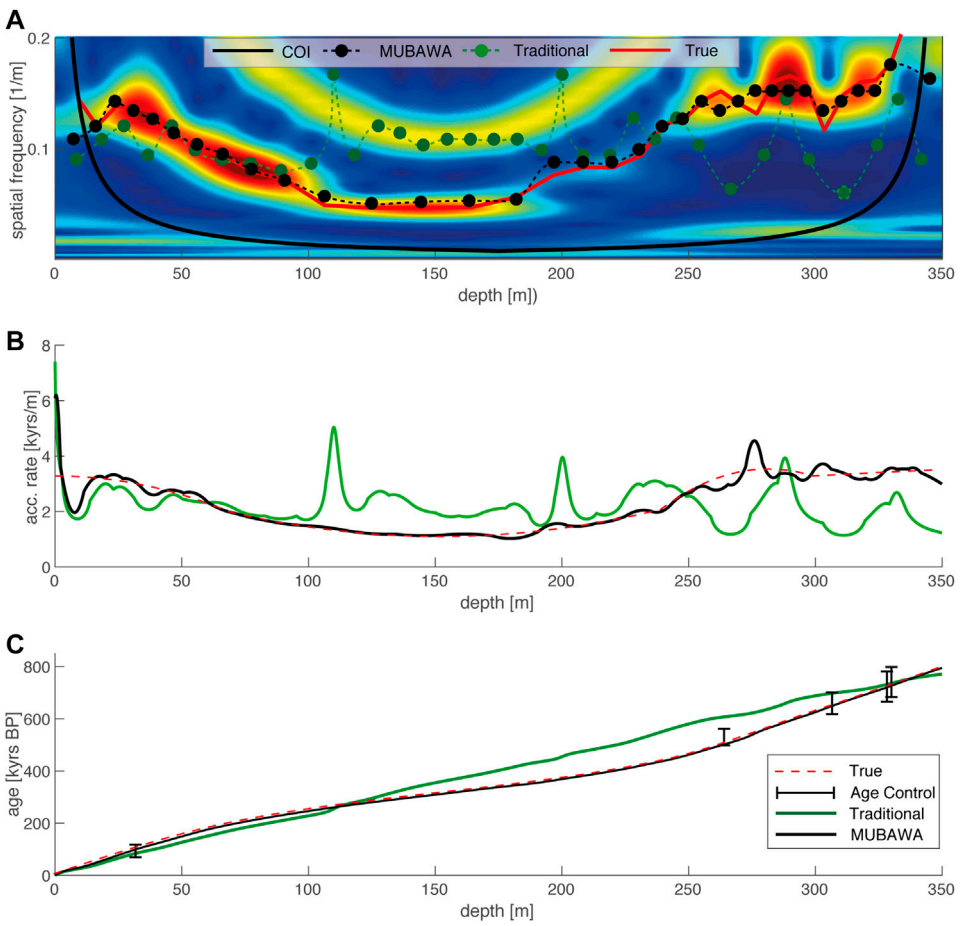

FIGURE 5 | (A) The wavelet power spectrum that resulted from the CWT of the synthetic depth data demonstrates the frequency shift that has been applied by the continuous sedimentation rate changes induced by the synthetic age model. Blue colors refer to low power and red colors to high power. The green dots represent the peak distances of the filtered linear interpolated time series from the first step of the traditional tuning method. Note that where the peak distances do not follow a continuous frequency path, the traditional tuning method failed to reconstruct the synthetic sedimentation rate shown in **(B)**. **(C)** The depth-age plot shows that even though the traditional method failed to reconstruct the correct sedimentation history, it yielded a similar base age.

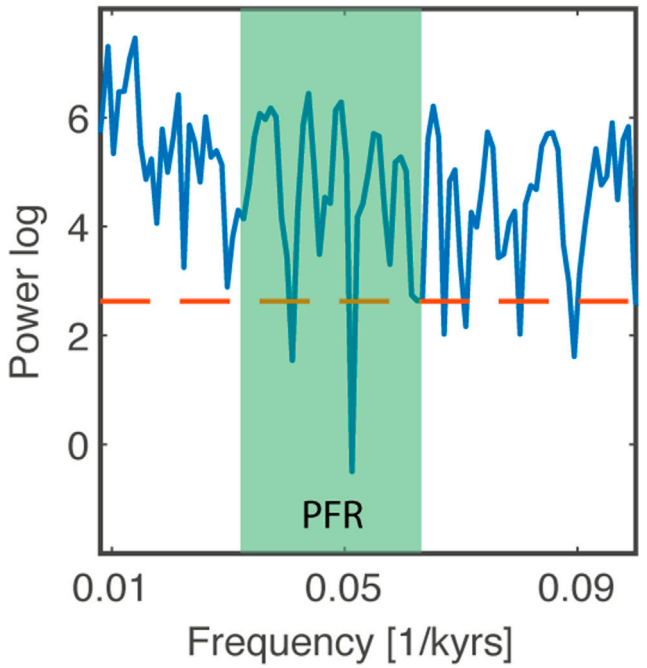

FIGURE 6 | Lomb-Scargle power spectrum derived from a simple linear age model. The green color represents the precession frequency range (PFR) within which the precession frequencies can be expected to occur. The red line indicates the 95% detection probability. Frequencies within the PFR are above the detection probability suggesting that there is enough power within the precession band to run the multiband wavelet age modeling approach.

We also used six Argon ages, which date the sediment at the bottom of the core to 629 ± 11 kyrs BP (one sigma error) (Roberts et al., submitted).

RESULTS

Synthetic Data Results

We first applied the new MUBAWA technique, including the SFRA, to the synthetic data set. To visualize the frequency evolution of the synthetic data we computed a wavelet power spectrum (**Figure 5A**). We used the time series of orbital precession between −1.0 and 0 Ma BP from Laskar et al. (2004) as the TT and the synthetic ages as the age control points for our hypothetical core. We selected a minimum base age of 550 kyrs BP (t_{min}) and a maximum base age of 850 kyrs BP (t_{max}).

The reconstructed accumulation rates calculated using MUBAWA age modeling largely correspond to the *true* (synthetic) accumulation rates (**Figure 5C**). A closer look at the results reveals minor deviations of the modeled accumulation rate from the true accumulation rate. The maximum age of the core determined from the synthetic data by MUBAWA age modeling, agrees well with the true maximum age.

In order to compare the results obtained from the MUBAWA method with those obtained using established tuning methods, we reconstructed the accumulation rate of the synthetic data using a traditional tuning method. We first

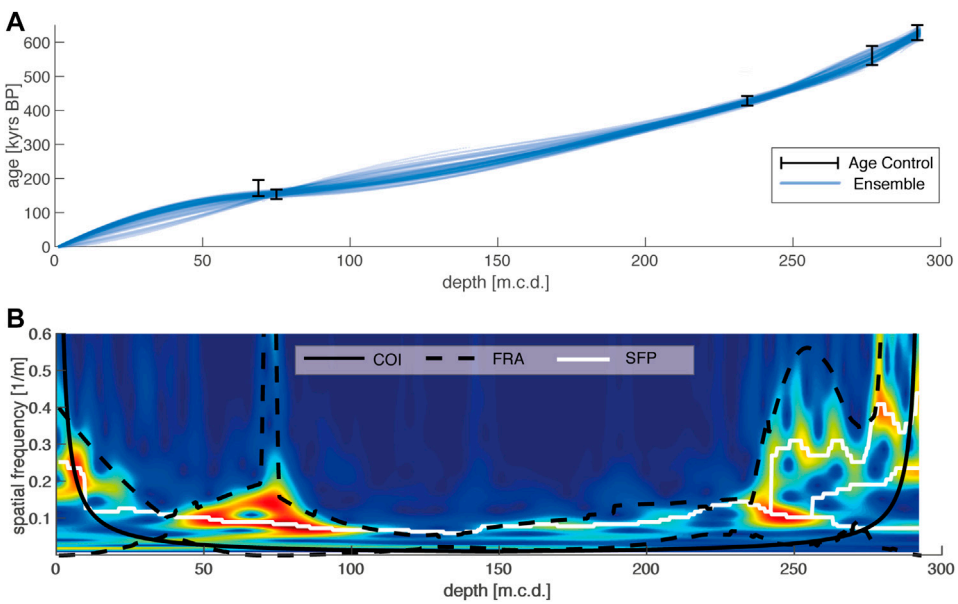

FIGURE 7 | Results of the SFRA. **(A)** We computed 100,000 realizations **(blue lines)** between the randomly resampled age control points to approximate a spatial frequency range depending on the frequency of the TT and the minimum and maximum slopes of the age model ensemble. **(B)** The wavelet power spectrum of the adaptively filtered PC2, with blue colors indicating low power and red colors high power. The SFRA resulted in the black dashed lines that have been used to adaptively filter the depth series. The white lines are spatial frequency paths that resulted from the spatial frequency mapping. Note that we left out the age at 230 m.c.d. from the SFRA because it was very close to a better dated age with less uncertainty (close ages expand the SFRA).

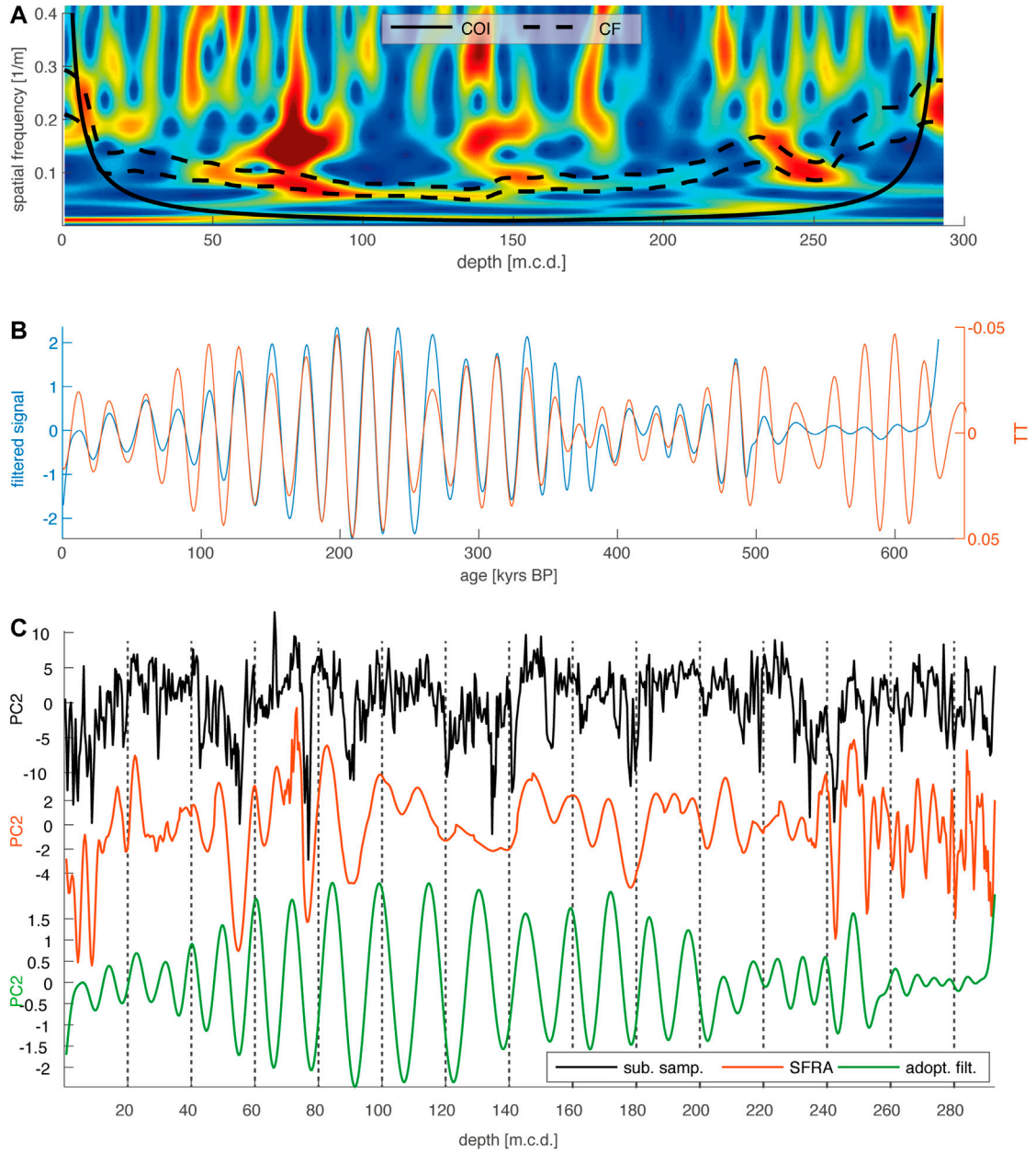

FIGURE 8 | (A) Each frequency path was converted into an upper and lower cutoff frequency to adaptively filter along the spatial frequency path. The cutoff frequencies that resulted in the best age model are shown as black dashed lines. **(B)** The peaks of the adoptively filtered signal were consecutively projected onto the peaks of the tuning target (TT) to generate an age model. **(C)** The results of each processing step are shown from top to bottom, starting with the sub sampled PC2, the results of the SFRA, and the adoptively filtered depth series.

transformed the space series into a time series with a maximum age of 800 kyrs BP. We then bandpass filtered the signal to extract the 19–23 kyr cycle that we wanted to use as the TT. Since we knew that the time series had been compressed and stretched by varying sedimentation rates, we chose a relatively wide passband with cutoff frequencies of 1/15 and 1/30 kyr^{-1} for the filter. Finally, we aligned the maxima of the filtered time series with the minima of the TT.

Although the traditional tuning method found the correct base age for the synthetic data, it did not reconstruct the accumulation rates of the synthetic example correctly. In order to visualize which spatial frequencies resulted in the final traditionally tuned age model we used peak distances, these being the distances between each of the peaks in the filtered depth series. The variations in these distances ultimately determine the age model. A projection of the inverse of the peak distances into a wavelet power spectrum reveals which of the spatial frequencies

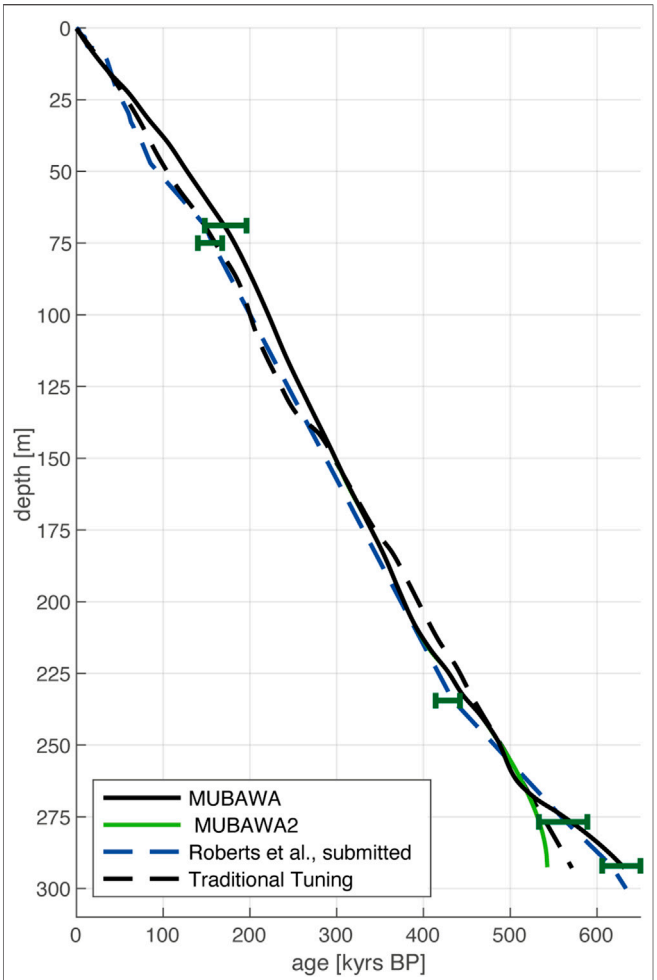

FIGURE 9 | Two additional age models have been developed for the Chew Bahir project: a direct-dated age model (Roberts et al., submitted.) and a traditionally tuned age model. Note that the multiband wavelet age modeling (MUBAWA) age model is in strong agreement with the age controls. MUBAWA2 represents an additional age model that has resulted from one of the frequency paths, but was ranked second.

the tuned age model is based on. The projection of the inverse of the peak distances into the wavelet power spectrum showed that the traditional method generated an age model on the basis of different spatial frequency paths from our original insolation signal. The reconstructed accumulation rates diverged from the "true" accumulation rates where the peak distances projected into the wavelet power spectrum failed to follow the continuous spatial frequency evolution of our initial insolation signal (**Figures 5A–C**). The result obtained using the traditional tuning method cannot be considered satisfactory, indicating the need for a different strategy that avoids such a failure. The MUBAWA approach, which clearly follows a continuous spatial frequency path, provides such an alternative strategy.

Chew Bahir Data Results

We first created a linear age model by extrapolating through the age control at 240 m (400 kyrs). We used this age because a similar age has been obtained from the same depth in the parallel core (Roberts et al., submitted). The age model yielded a base age of 570 kyrs. We calculated a Lomb-Scargle power spectrum for the time series and computed the detection probability limit (Lomb, 1976; Scargle, 1982) (**Figure 6**). We found power above the detection probability limit within the precession frequency range (PFR). The possible precession cycles indicated by the simple linear age model suggested that the cycles already observed in the depth scale were indeed related to orbital precession.

We then used the MUBAWA algorithm to calculate an orbitally tuned age model for the Chew Bahir composite core. We used PC2 from the color reflectance data, an orbital precession (according to Laskar et al., 2004) of between −1 and 0 Ma BP as the TT, and the Argon ages (together with their uncertainties) as age control points. We rejected the Argon age at a depth at 234.066 m.c.d. because of its large uncertainty and its proximity to the age date at 234.048 m.c.d., which had a smaller uncertainty. We chose 850 kyrs as the maximum base age (t_{max}) and 550 kyrs as the minimum base age (t_{min}). Preprocessing with the MUBAWA function resulted in a sampling rate of 0.3661 m^{-1}. The resulting evenly spaced subsampled data set contained 800 data points.

We then used the SFRA to approximate the frequency range that corresponded to the age control (within their uncertainty ranges) by randomly resampling the age control points to create an age model ensemble (**Figure 7A**). The SFRA resulted in a relatively broad frequency range in the top and bottom sections of the core, where more radiometric ages were available, and a narrower range in between (**Figure 7B**).

We used Taner filters to adaptively bandpass filter the y-values using the upper and lower frequency limits from the SFRA, thus obtaining an adaptively filtered depth series. We performed the spatial frequency path mapping using the data from the SFRA. Ten different spatial frequency paths were mapped. All paths had different starting positions but merged after a certain depth (**Figure 7B**). We adaptively filtered along the frequency paths by adjusting the cutoff frequencies of the Taner filters according to the values of each individual frequency path.

Each frequency path resulted in an adaptively filtered depth series. We computed the maxima of the depth series and the minima of the TT, as negative precession resulted in an increase in monsoon strength within the study area. The interpolation points were then arranged in chronological order so that the second maximum of the filtered time series and the second minimum of the TT were assigned to each other, until the penultimate maxima of the filtered time series. We omitted the first and last maxima to avoid any edge effect of the wavelet power spectrum.

We then used a PCHIP to interpolate between the new tie-points, derived by assigning the maxima of the adaptive filtered depth series to the minima of the TT, and generated an age model for each spatial frequency path. We used the agreement between the age models resulting from the interpolation and the age control points (within their uncertainties) to evaluate the age models. We also used the Pearson correlation coefficient to rate the age models. The cutoff frequencies that eventually led to the best age model are shown in **Figure 8A**. The adaptively filtered

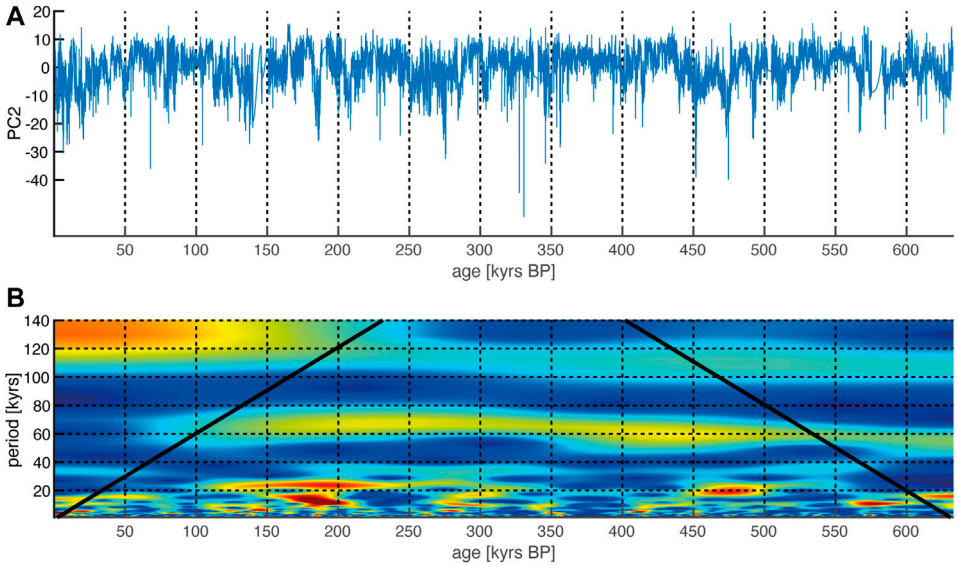

FIGURE 10 | (A) Resulting time series. The multiband wavelet age modeling age model was used to convert PC2 depth series into a time series, as shown. **(B)** Wavelet power spectrum, with the age along the *x*-axis and the period along the *y*-axis. The colors indicate the power of the cycle, with red colors for high power and blue colors for low power. The wavelet power spectrum computed from the PC2 time series shows the anticipated precession cycles, since the age model was tuned to that cycle. The continuity of the longer wavelength periods at 60 and 100 kyrs shows that the tuning has been successful.

time series then correlated with the TT (**Figure 8B**). The individual steps and their results that were applied to the depth series are shown in **Figure 8C**. This analysis resulted in an age model that was in agreement with most of the age control points (within their two sigma errors) and indicated a maximum age for the base of the core of 632.62 kyrs BP (**Figure 9**). We applied our MUBAWA-based age model to the PC2 of the 39 band color reflectance record (**Figure 10A**).; the wavelet power spectrum of the resulting time series showed significant orbital cycles with periods of 100, 60, 19–25, 10–15, and 5 kyrs (**Figure 10B**).

In order to further compare our MUBAWA approach with the traditional method we also applied the previously described traditional tuning method to the Chew Bahir data. For this we first assumed a preliminary base age of 500 kyrs. We generated a time series based on this simple linear preliminary model and then applied a relatively wide bandpass filter with cutoff frequencies of 1/28 and 1/16 kyr^{-1}. Both methods can be seen from the peak distances to operate in the same frequency domain (**Figure 11A**). The accumulation rates show a strong correlation with the peak distances (**Figure 11B**). The age-depth gradients differ only slightly and remain within the uncertainties of the Argon ages (**Figure 11C**).

DISCUSSION

We have developed a new age modeling technique that is specifically suited to climate records with distinct orbital cycles and limited age control. The approach involves statistical analysis of an age model ensemble to delimit the spatial frequency range of the targeted orbital frequency. It uses a wavelet power spectrum derived from the CWT to trace the evolution of the orbital frequency and ultimately adapt the bandpass filter to its variations, allowing for continuous long-term changes in sedimentation rates. This new technique is in improvement on traditional tuning techniques that use a single bandpass filter to tune paleoclimate records. The method depends on a number of parameters that may need to be adjusted when using data sets other than those presented herein. These include the amount of weighting, the sampling rate, and the bandwidth of the adaptive filter.

By applying a traditional tuning method to synthetic data we have shown that when the data to be tuned are characterized by continuous long-term changes in sedimentation rates, jumps occur in the spatial frequency that lead to misinterpretation of the spectral data and ultimately to a false age model. We have shown that such misinterpretation of the data set can be detected by plotting the peak distances of the filtered, but untuned, time series into a wavelet power spectrum of the untuned raw spatial data. If the peak distances correspond to a continuous frequency evolution, the traditional tuning method will produce accurate results. If, however, the peak distances show no match with a continuous frequency evolution the method will fail to deliver accurate results. It is specifically for cases resembling the synthetic data, which are common in nature, that we have developed the MUBAWA method. The MUBAWA technique has demonstrated its ability to handle such special circumstances by correctly solving the synthetic example.

Application of the MUBAWA approach to the Chew Bahir record and using PC2 from its color reflectance data set has produced a tuned age model that is in strong agreement with

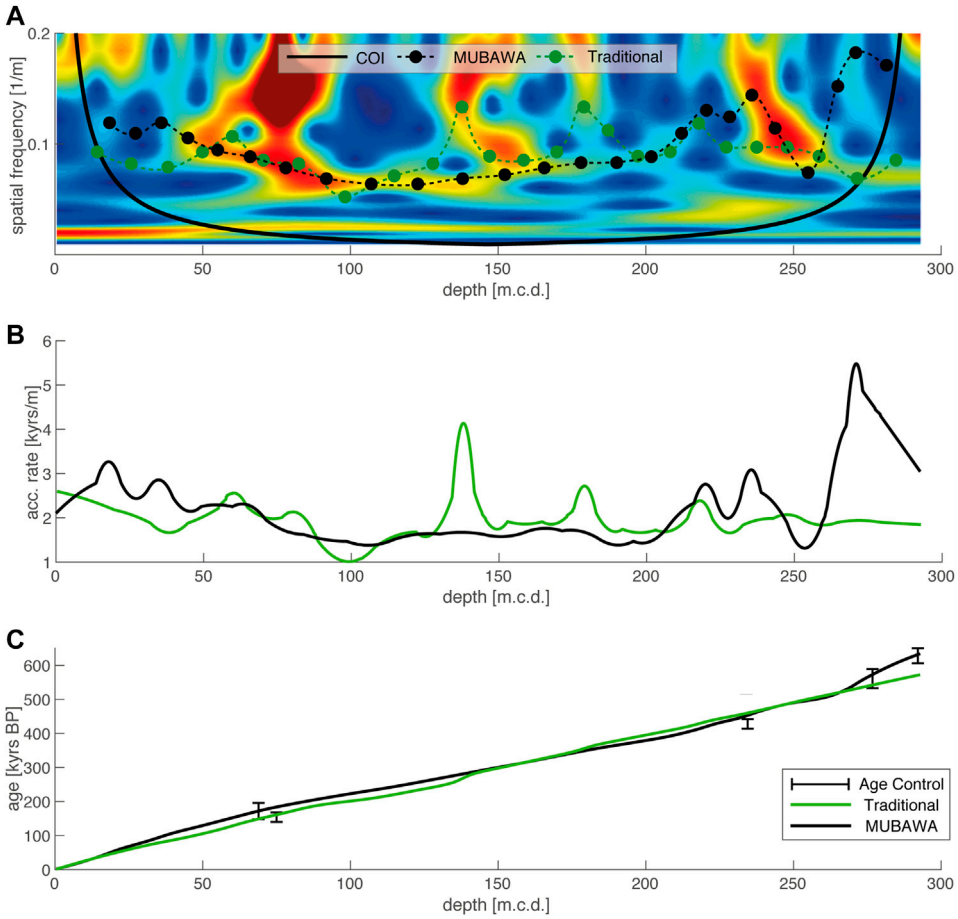

FIGURE 11 | (A) Wavelet power spectrum, with frequency along the *y*-axis and depth along the *x*-axis. The power is indicated by color, with red colors for high power and blue colors for low power. The peak distances can be used to compare the traditional approach with the new multiband wavelet age modeling (MUBAWA) approach. Both methods follow approximately the same cycle until 230 m.c.d., after which they show marked differences. **(B)** Where the peak distances differ in **(A)**, the accumulation rates are significantly different. **(C)** The two age models only vary insignificantly in the depth age plot. However, the MUBAWA model tracks to higher frequencies below 250 m.c.d. on, which allows it to reach the argon age at the base of the composite core.

independent age controls and shows continuous orbital cycles in the wavelet power spectrum. As expected, the tuning revealed particularly distinct cycles corresponding to frequencies contained in the TT. Furthermore, a set of higher frequencies with periods of ~5 kyr that, according to Berger et al. (2006), are attributable to fundamental harmonics, can be identified in the tuned time series. The occurrence of a distinct ~10–15 kyr cycle suggests half precessional forcing of the Chew Bahir environmental conditions, as previously suggested by Berger et al. (2006), Berger et al. (1997), and Trauth et al. (2003). We also identified a distinct continuous 63 kyr cycle. Its occurrence can possibly be attributed to heterodynes, as described by Clemens et al. (2010), Clemens et al. (2018) and recently identified in South Asian precipitation records (Gebregiorgis et al., 2018). We also recognized a continuous 100 kyr cycle that can be ascribed to eccentricity in the earth's orbit (**Figure 10**).

We also created a traditional tuned age model (according to common practice) using the Chew Bahir data, for comparison with the MUBAWA age model. The result again revealed a strong agreement with the age control points (**Figure 11C**), with the exception of the oldest age at the base of the composite core. This model would certainly be a satisfactory result for users of established tuning methods. To compare the resulting filtered depth series of the MUBAWA approach with the traditionally tuned filtered depth series we plotted the peak distances of the traditionally tuned filtered depth series and the peak distances of the MUBAWA filtered depth series into the wavelet power spectrum (**Figure 11A**), as demonstrated previously for the synthetic example.

The peak distance analysis revealed that, despite the agreement with the age control points and the increase in the power of the eccentricity cycle, a discontinuous spatial frequency evolution had been used through parts of the composite core. The synthetic data example showed that such jumps in spatial frequency can lead to misinterpretations (**Figure 11A**). Although real data are far more complex and the exact sedimentation history of such data is largely unknown, we believe that the continuity assumption in our MUBAWA

approach enables it to make an important contribution to tuning-based age modeling.

CONCLUSION

We have demonstrated in our synthetic example that tuning methods using stationary bandpass filters have difficulty reconstructing the correct accumulation history, whereas the MUBAWA algorithm presented herein, using the CWT to track a continuous frequency evolution, yielded the correct solution. Application of the MUBAWA approach to the Chew Bahir record and the PC2 of its color reflectance data revealed that the method is also applicable to real climate data sets. A comparison with traditional tuning showed that, whereas the traditional tuning method is limited to rather linear age models, the MUBAWA approach is capable of detecting and taking into account continuous long-term changes in sedimentation rates. Not only was the MUBAWA-generated age model in good agreement with the available age control points (within their uncertainties), but it was also able to reconstruct continuous orbital cycles, as shown in the wavelet power spectrum. We recommend the MUBAWA approach for use with a wide range of climate data sets that require sophisticated tuning methods.

DATA AVAILABILITY STATEMENT

The original contributions presented in the study are included in the article/**Supplementary Material**, further inquiries can be directed to the corresponding author.

AUTHOR CONTRIBUTIONS

WD is the lead author of the publication and was involved in all crucial steps from initiation of the first ideas, implementation of the statistical analysis, and the writing process. KH and NB were mainly involved in supporting the development of the methods section. MT, as well as NM have accompanied the entire process and supported the development of the work on numerous issues ranging from code implementation to the interpretation of climate processes. AD provided the radiometric ages.

FUNDING

Support for HSPDP has been provided by the National Science Foundation (NSF) grants and the International Continental Drilling Program (ICDP). Support for CBDP has been provided by Germany Research Foundation (DFG) through the Priority Program SPP 1006 ICDP (SCHA 472/13 and /18, TR 419/8, /10 and /16) and the CRC 806 Research Project "Our way to Europe" Project Number 57444011. Support has also been received from the UK Natural Environment Research Council (NERC, NE/K014560/1, IP/1623/0516). We also thank the Ethiopian permitting authorities to issue permits for drilling in the Chew Bahir basin. We also thank the Hammar people for the local assistance during drilling operations. We thank DOSECC Exploration Services for drilling supervision and Ethio Der pvt. Ltd. Co. for providing logistical support during drilling. Initial core processing and sampling were conducted at the US National Lacustrine Core Facility (LacCore) at the University of Minnesota. S.K.B. has received further financial support from the University of Potsdam Open Topic Postdoc Program.

ACKNOWLEDGMENTS

We thank Christopher Bronk Ramsey, Melissa Chapot, Christine S. Lane, Helen M. Roberts and Céline Vidal for discussions on the geochronology and age modeling. This is publication ## of the Hominin Sites and Paleolakes Drilling Project.

SUPPLEMENTARY MATERIAL

The Supplementary Material for this article can be found online at: https://www.frontiersin.org/articles/10.3389/feart.2021.594047/full#supplementary-material.

REFERENCES

Addison, P. S. (2017). *The illustrated wavelet transform handbook: introductory theory and applications in science, engineering, medicine and finance*. 2nd Ed. India: CRC Press.

Berger, A., Loutre, M. F., and Mclntyre, A. (1997). Intertropical latitudes and precessional and half-precessional cycles. *Science* 278 (5342), 1476–1478. doi:10.1126/science.278.5342.1476

Berger, A., Loutre, M. F., and Mélice, J. L. (2006). Equatorial insolation: from precession harmonics to eccentricity frequencies. *Clim. Past* 2 (2), 131–136. doi:10.5194/cp-2-131-2006

Campisano, F. A., Drake, A. J., Floyd, M. S., Hui, D. T., Owczarczyk, P., Tiner, M. D., et al. (2017). U.S. Patent Application No. 14/879,269.

Cheung, W. H., Senay, G. B., and Singh, A. (2008). Trends and spatial distribution of annual and seasonal rainfall in Ethiopia. *Int. J. Climatol.* 28 (13), 1723–1734. doi:10.1002/joc.1623

Clemens, S. C., Holbourn, A., Kubota, Y., Lee, K. E., Liu, Z., Chen, G., et al. (2018). Precession-band variance missing from East Asian monsoon runoff. *Nat. Commun.* 9 (1), 3364. doi:10.1038/s41467-018-05814-0

Clemens, S. C., Prell, W. L., and Sun, Y. (2010). Orbital - scale timing and mechanisms driving Late Pleistocene Indo - Asian summer monsoons: reinterpreting cave speleothemδ18O. *Paleoceanography* 25 (4). doi:10.1029/2010pa001926

Cohen, A., Campisano, C., Arrowsmith, R., Asrat, A., Behrensmeyer, A. K., Deino, A., et al. (2016). The Hominin Sites and Paleolakes Drilling Project: inferring the environmental context of human evolution from eastern African rift lake deposits. *Sci. Drill.* 21, 1–16. doi:10.5194/sd-21-1-2016

Davidson, A. (1983). The Omo River project: reconnaissance geology and geochemistry of parts of Ilubabor, Kefa, Gemu Gofa and Sidamo. Ethiopian Institute of Geological Surveys Bulletin 2, 1e89.

Ebinger, C. J., Yemane, T., Harding, D. J., Tesfaye, S., Kelley, S., and Rex, D. C. (2000). Rift deflection, migration, and propagation: linkage of the Ethiopian and Eastern rifts, Africa. *Geol. Soc. Am. Bull.* 112 (2), 163–176. doi:10.1130/0016-7606(2000)112<163:rdmapl>2.0.co;2

Foerster, V., Junginger, A., Langkamp, O., Gebru, T., Asrat, A., Umer, M., et al. (2012). Climatic change recorded in the sediments of the Chew Bahir basin, southern Ethiopia, during the last 45,000 years. *Quat. Int.* 274, 25–37. doi:10.1016/j.quaint.2012.06.028

Fritsch, F. N., and Carlson, R. E. (1980). Monotone piecewise cubic interpolation. *SIAM J. Numer. Anal.* 17 (2), 238–246. doi:10.1137/0717021

Gebregiorgis, D., Hathorne, E. C., Giosan, L., Clemens, S., Nürnberg, D., and Frank, M. (2018). Southern Hemisphere forcing of South Asian monsoon precipitation over the past ~1 million years. *Nat. Commun.* 9 (1), 4702. doi:10.1038/s41467-018-07076-2

Giosan, L., Flood, R. D., and Aller, R. C. (2002). Paleoceanographic significance of sediment color on western North Atlantic drifts: I. Origin of color. *Mar. Geol.* 189 (1-2), 25–41. doi:10.1016/s0025-3227(02)00321-3

Grant, K. M., Rohling, E. J., Westerhold, T., Zabel, M., Heslop, D., Konijnendijk, T., et al. (2017). A 3 million year index for North African humidity/aridity and the implication of potential pan-African Humid periods. *Quat. Sci. Rev.* 171, 100–118. doi:10.1016/j.quascirev.2017.07.005

Hays, J. D., Imbrie, J., and Shackleton, N. J. (1976a). Variations in the earth's orbit: pacemaker of the ice ages. *Science* 194, 1121–1132. doi:10.1126/science.194.4270.1121

Hays, J. D., Imbrie, J., and Shackleton, N. J. (1976b). *Variations in the Earth's orbit: pacemaker of the ice ages*. Washington, DC: American Association for the Advancement of Science.

Hinnov, L. A. (2013). Cyclostratigraphy and its revolutionizing applications in the earth and planetary sciences. *Geol. Sci. Am. Bull.* 125 (11–12), 1703–1734. doi:10.1130/b30934.1

Hotelling, H. (1933). Analysis of a complex of statistical variables into principal components. *J. Educ. Psychol.* 24 (6), 417–441. doi:10.1037/h0071325

Imbrie, J., and Imbrie, J. Z. (1980). Modeling the climatic response to orbital variations. *Science* 207 (4434), 943–953. doi:10.1126/science.207.4434.943

Kutzbach, J. E., and Street-Perrott, F. A. (1985). Milankovitch forcing of fluctuations in the level of tropical lakes from 18 to 0 kyr BP. *Nature* 317 (6033), 130–134. doi:10.1038/317130a0

Laskar, J., Robutel, P., Joutel, F., Gastineau, M., Correia, A. C. M., and Levrard, B. (2004). A long-term numerical solution for the insolation quantities of the Earth. *Astron. Astrophys.* 428, 261–285. Available at: http://vo.imcce.fr/insola/earth/online/earth/online/. doi:10.1051/0004-6361:20041335

Lau, K.-M., and Weng, H. (1995). Climate signal detection using wavelet transform: how to make a time series sing. *Bull. Am. Meteorol. Soc.* 76 (12), 2391–2402. doi:10.1175/1520-0477(1995)076<2391:csduwt>2.0.co;2

Lomb, N. R. (1976). Least-squares frequency analysis of unequally spaced data. *Astrophys. Space Sci.* 39 (2), 447–462. doi:10.1007/bf00648343

Martinson, D. G., Pisias, N. G., Hays, J. D., Imbrie, J., Moore, T. C., and Shackleton, N. J. (1987). Age dating and the orbital theory of the ice ages: development of a high-resolution 0 to 300,000-year chronostratigraphy. *Quat. res.* 27 (1), 1–29. doi:10.1016/0033-5894(87)90046-9

MathWorks (2020a). *MATLAB signal processing toolbox – User's guide*. Natick, MA: The MathWorks, Inc.

Meyers, S. R., Sageman, B. B., and Hinnov, L. A. (2001). Integrated quantitative stratigraphy of the Cenomanian-Turonian Bridge Creek Limestone Member using evolutive harmonic analysis and stratigraphic modeling. *J. Sediment. Res.* 71 (4), 628–644. doi:10.1306/012401710628

Meyers, S. R., and Sageman, B. B. (2007). Quantification of deep-time orbital forcing by average spectral misfit. *Am. J. Sci.* 307 (5), 773–792. doi:10.2475/05.2007.01

Meyers, S. R. (2015). The evaluation of eccentricity-related amplitude modulation and bundling in paleoclimate data: an inverse approach for astrochronologic testing and time scale optimization. *Paleoceanography* 30 (12), 1625–1640. doi:10.1002/2015pa002850

Muller, R. A., and MacDonald, G. J. (2002). *Ice ages and astronomical causes: data, spectral analysis and mechanisms*. London, UK: Springer Science & Business Media.

Nicholson, S. E. (2017). Climate and climatic variability of rainfall over eastern Africa. *Rev. Geophys.* 55 (3), 590–635. doi:10.1002/2016rg000544

Park, J., and Herbert, T. D. (1987). Hunting for paleoclimatic periodicities in a geologic time series with an uncertain time scale. *J. Geophys. Res.* 92 (B13), 14027–14040. doi:10.1029/jb092ib13p14027

Partridge, T. C. (1997). Cainozoic environmental change in southern Africa, with special emphasis on the last 200 000 years. *Prog. Phys. Geogr. Earth Environ.* 21 (1), 3–22. doi:10.1177/030913339702100102

Pearson, K. (1901). LIII. On lines and planes of closest fit to systems of points in space. *The London, Edinburgh, and Dublin Philos. Mag. J. Sci.* 2 (11), 559–572. doi:10.1080/14786440109462720

Pik, R., Marty, B., Carignan, J., Yirgu, G., and Ayalew, T. (2008). Timing of East African Rift development in southern Ethiopia: implication for mantle plume activity and evolution of topography. *Geology* 36 (2), 167–170. doi:10.1130/g24233a.1

Pisias, N. G., Martinson, D. G., Moore, T. C., Jr, Shackleton, N. J., Prell, W., Hays, J., et al. (1984). High resolution stratigraphic correlation of benthic oxygen isotopic records spanning the last 300,000 years. *Mar. Geol.* 56 (1–4), 119–136. doi:10.1016/0025-3227(84)90009-4

Raymo, M. E., Oppo, D. W., and Curry, W. (1997). The Mid-Pleistocene climate transition: a deep sea carbon isotopic perspective. *Paleoceanography* 12 (4), 546–559. doi:10.1029/97pa01019

Roberts, et al. (2020). Interactive comment on "New analytical and data evaluation protocols to improve the reliability of U-Pb LA-ICP-MS carbonate dating" by Marcel Guillong et al. *Geochronol. Dis.* C1–C7. doi:10.5194/gchron-2019-20-sc1

Saji, N. H., Goswami, B. N., Vinayachandran, P. N., and Yamagata, T. (1999). A dipole mode in the tropical Indian Ocean. *Nature* 401 (6751), 360–363. doi:10.1038/43854

Scargle, J. D. (1982). Studies in astronomical time series analysis. II - statistical aspects of spectral analysis of unevenly spaced data. *Astrophys. J.* 263, 835–853. doi:10.1086/160554

Segele, Z. T., Richman, M. B., Leslie, L. M., and Lamb, P. J. (2015). Seasonal-to-interannual variability of Ethiopia/horn of Africa monsoon. Part II: statistical multimodel ensemble rainfall predictions. *J. Clim.* 28 (9), 3511–3536. doi:10.1175/jcli-d-14-00476.1

Seleshi, Y., and Zanke, U. (2004). Recent changes in rainfall and rainy days in Ethiopia. *Int. J. Climatol.* 24 (8), 973–983. doi:10.1002/joc.1052

Sinnesael, M., Zivanovic, M., De Vleeschouwer, D., and Claeys, P. (2018). Spectral moments in cyclostratigraphy: advantages and disadvantages compared to more classic approaches. *Paleoceano. Paleoclimatol.* 33 (5), 493–510. doi:10.1029/2017pa003293

Storch, T. A., and Dunham, V. L., (1986). Iron-mediated changes in the growth of lake erie phytoplankton and axenic algal cultures. *J. Phycol.* 22 (2), 109–117. doi:10.1111/j.1529-8817.1986.tb04152.x

Taner, M. T. (1992). *Attributes revisted. Technical Report*. Rock solid images, Inc. Available at: http://www.rocksolidimages.com/attributes-revisited/#_Toc328470897.

Tiedemann, R., Sarnthein, M., and Shackleton, N. J. (1994). Astronomic timescale for the pliocene atlantic Î´18O and dust flux records of ocean drilling program site 659. *Paleoceanography* 9 (4), 619–638. doi:10.1029/94pa00208

Torrence, C., and Compo, G. P. (1998). A practical guide to wavelet analysis. *Bull. Am. Meteorol. Soc.* 79 (1), 61–78. doi:10.1175/1520-0477(1998)079<0061:apgtwa>2.0.co;2

Trauth, M. H., Deino, A. L., Bergner, A. G., and Strecker, M. R. (2003). East African climate change and orbital forcing during the last 175 kyr BP. *Earth Planet Sci. Lett.* 206 (3–4), 297–313. doi:10.1016/s0012-821x(02)01105-6

Wagner, B., Vogel, H., Francke, A., Friedrich, T., Donders, T., Lacey, J. H., et al. 2019). Mediterranean winter rainfall in phase with African monsoons during the past 1.36 million years. *Nature* 573, 256–260. doi:10.1038/s41586-019-1529-0

Woldegabriel, G., Aronson, J. L., and Walter, R. C. (1990). Geology, geochronology, and rift basin development in the central sector of the Main Ethiopia Rift. *Geol. Soc. Am. Bull.* 102 (4), 439–458. doi:10.1130/0016-7606(1990)102<0439:ggarbd>2.3.co;2

Zeeden, C., Kaboth, S., Hilgen, F. J., and Laskar, J. (2018). Taner filter settings and automatic correlation optimisation for cyclostratigraphic studies. *Comput. Geosci.* 119, 18–28. doi:10.1016/j.cageo.2018.06.005

Conflict of Interest: The authors declare that the research was conducted in the absence of any commercial or financial relationships that could be construed as a potential conflict of interest.

frontiers in Earth Science

ORIGINAL RESEARCH
published: 26 March 2021
doi: 10.3389/feart.2021.611687

Lithological and Topographic Impact on Soil Nutrient Distributions in Tectonic Landscapes: Implications for Pleistocene Human-Landscape Interactions in the Southern Kenya Rift

S. Kübler[1], S. Rucina[2], D. Aßbichler[1], E. Eckmeier[3] and G. King[4]*

[1]Department of Earth and Environmetal Sciences, Ludwig Maximilian University of Munich, Munich, Germany, [2]National Museums of Kenya, Nairobi, Kenya, [3]Department of Geography, Ludwig Maximilian University of Munich, Munich, Germany, [4]UMR7154, Institut De Physique Du Globe De Paris (IPGP), Paris, France

Tectonically active regions are characterized by complex landscapes comprising soils with heterogeneous physicochemical properties. Spatial variability of nutrient sources enhances landscape biodiversity and creates heterogeneous habitats potentially attractive for animals and humans. In this study, we analyze the role of geological processes in the distributions of soil nutrients in the southern Kenya Rift, a key region in the interpretation of early human-landscape interactions. Our aim is to determine how spatial variations in rock chemistry, as well as topographic gradients and localized zones of rock fracturing from tectonic faulting determine the distributions of plant-available soil nutrients in soils. We hypothesize that present-day soil nutrient levels reflect the long-term chemical and geomorphological characteristics of the landscape and underlying parent material, and that regions with high nutrient availability occur along pathways correlating with locations of hominin fossil sites. Analyses of 91 topsoil samples from the main geological units show that Calcium (Ca) deficiencies predominately occur in shallow soils developed on trachytic volcanic rocks and granitic gneisses, while high Ca levels are associated with basaltic parent material and sedimentary deposits of mixed sources. XRF analysis of rock samples confirms that CaO levels in trachyte rocks are significantly lower than those in basalts, and Ca mobilization in basalt is more effective than in trachyte. Along two toposequences in densely faulted basaltic and trachytic rocks, we observed slope dependent soil nutritional gradients and a systematic increase of the concentrations of Ca, Mg and SOC in topsoils of colluvial sediments downslope of active normal faults. Known hominin sites in the region are located either along corridors of long-term Ca availability or at short-term nutrient hotspots potentially related to active CO_2 degassing along active fault zones. This implies a strategic advantage of Ca-rich regions for hominin subsistence strategies, such as provision of predictable constraints on the distribution and mobility of grazing animals in complex tectonic landscapes. Our study implies that geological processes impact nutrient distributions in the southern Kenya Rift. Results of this study have further implications for understanding the role of soils in the interpretation of hominin-landscape interactions in the early stages of human evolution.

Keywords: rock-soil interface, tectonic geomorphology, east african rift system, plant-available soil nutrients, human-landscape interactions

OPEN ACCESS

Edited by:
Verena E. Foerster, University of Cologne, Germany

Reviewed by:
Emily J. Beverly, University of Houston, Houston, United States
Felix Bachofer, German Aerospace Center, Weßling, Germany

****Correspondence:***
S. Kübler
s.kuebler@lmu.de

Specialty section:
This article was submitted to Quaternary Science, Geomorphology and Paleoenvironment, a section of the journal Frontiers in Earth Science

Received: *29 September 2020*
Accepted: *08 February 2021*
Published: *26 March 2021*

Citation:
Kübler S, Rucina S, Aßbichler D, Eckmeier E and King G (2021) Lithological and Topographic Impact on Soil Nutrient Distributions in Tectonic Landscapes: Implications for Pleistocene Human-Landscape Interactions in the Southern Kenya Rift. Front. Earth Sci. 9:611687. doi: 10.3389/feart.2021.611687

INTRODUCTION

Soils in landscapes characterized by tectonic and volcanic activity can exhibit a large variability in the distribution and availability of nutrients vital for plant growth and animal nutrition. Topographic complexity and lithological diversity leads to catchment-to-landscape-scale variations in soil nutritional characteristics. Knowledge on the long-term status of soil chemical properties can be gained by detailed and quantitative analysis of geological factors and processes at the rock-soil interface influencing the release and distribution of soil nutrients. While short-term variations in soil properties and vegetation dynamics are often associated with climatic factors, recent studies have shown that geological factors such as bedrock chemistry (Hahm et al., 2014) and topographic gradients (Weintraub et al., 2015; Chadwick and Asner, 2016; Calitri et al., 2019) play an important role in influencing the long-term nutritional fate of soils.

From a geological point of view, the morphological characteristics of a landscape, particularly hillslope steepness and related erosional and depositional processes, are important drivers in soils that can counteract the effect of nutrient depletion through chemical weathering, as enhanced erosion along steep slopes locally rejuvenates the soil parent material in downslope deposits through provision of freshly eroded rocks (Li and Lindstrom, 2001; Porder et al., 2005). This is of particular importance in high rainfall tropical and equatorial regions where long-term exposure (10^5–10^6 years) of stable land surfaces are prone to deep-seated weathering processes and the formation of nutrient-depleted lateritic soils (Tardy, 1997).

Stark contrasts between geochemical properties of neighboring rock units, e.g., the occurrence of ultramafic rocks in regions of magmatic rocks of intermediate geochemical characteristics, can lead to the formation of azonal vegetation cover and barren landscapes (Kruckeberg, 2004). But also more subtle geochemical variations can lead to noticeable changes in the soil nutritional status of a region, sometimes severe enough to impact the health of grazing animals (Maskall and Thornton, 1996).

In the East African Rift, volcanism has influenced greatly the nature of soils and the geochemistry of ground and surface waters (Maskall and Thornton, 1996; Davies, 2008). Strong heterogeneities in rock chemistry and intense tropical weathering result in variations in the availability of soil nutrients, with zones of severe nutrient deficiencies in contrast to zones of excessive nutrient levels that can both be critical for human and animal health. A general lack of rock-derived calcium in soils developed on acidic and intermediate volcanic rocks of the East African Rift restricts plant growth and leads to widespread deficiencies of this macronutrient in wildlife and livestock (Abate, 1988; Gachuiri et al., 2012). Long-term Ca-deficiencies manifest as nutritional diseases such as hypocalcemia or rickets in grazing animals (Maskall and Thornton, 1996; Davies, 2013). Deficiency of plant available phosphorus is also a widespread issue in East African soils, leading to limited plant growth and reduced reproductive rates in grazing animals (Howard, 1963; Abate, 1988; Margenot et al., 2016). The Lake Nakuru region in the central Kenya Rift Valley is located about 50 km north of our study region, and is well known for geochemically induced cattle diseases. In the ground and surface waters of this region, as well as in the Lake Baringo region, the Kerio river valley and in northern and central Tanzania, fluoride levels are up to 20 times higher than the upper levels defined by the World Health Organization (Gaciri and Davies, 1993; D'Alessandro, 2006; Ghiglieri et al., 2012; Gevera et al., 2019). As a result, dental and skeletal fluorosis are a widespread problem for humans and animals (Gaciri and Davies, 1993; Moturi et al., 2002; Davies, 2008). Also, cattle diseases related to nutrient deficiencies are reported for the Nakuru region (Maskall and Thornton, 1996). Low levels of copper and cobalt cause a cattle disease locally known as nakuruitis, that eventually leads to starvation of ruminants because their enteric bacteria need cobalt to process food (e.g., Howard, 1963). Indications of mineral deficiencies in East African pastures can indirectly be observed by the widespread phenomena of wildlife and livestock practising geophagia (eating of soils and sediments), particularly along exposed salt-rich lakebeds and volcanic ash deposits in the East African Rift (Davies, 2013).

Understanding the factors that determine variations in soil nutrient levels is important, not only for agricultural and livestock research, but also for other disciplines including ecology and paleoanthropology, which can exploit knowledge of the long-term distribution and availability of soil nutrients. This helps to better understand paleoecological conditions in regions of early human presence, and deduce regional-scale mobility patterns of animals and humans in past and present (Sturdy and Webley, 1988; McNaughton, 1990; Murray, 1995; Sturdy et al., 1997; Devès et al., 2014; Devès et al., 2015; Kübler et al., 2015; Kübler et al., 2016; Kübler et al., 2019; Eckmeier et al., 2020; Junginger and Kübler, 2020; Kübler et al., 2020).

Interactions between geological, topographic and pedological processes have rarely been considered, especially regarding the long-term soil nutritional status of soils at a regional scale. Further, the implementation of knowledge on local-to-regional scale variations on soil nutrients in archeological and paleoanthropological studies is lacking in most regions. Considering results of pedological and CRITICAL ZONE studies on the long-term influence of geological factors on soils in paleoanthropological research can improve interpretations related to how our ancestors have strategically exploited beneficial landscape elements and may further lead to new methods in discovering hominin fossil sites in other regions in the world.

The main objective in this study was to provide a geological perspective on the various drivers of soil nutrient distributions in a complex, tectonically active landscape with special focus on: 1) identifying spatial variations in soil chemical properties in the southern Kenya Rift, with emphasis on soil organic carbon (SOC), calcium (Ca), magnesium (Mg) and plant available phosphorus (P); 2) correlating soil nutrient levels with the chemistry of underlying volcanic and metamorphic rocks, and different sedimentary deposits; 3) correlating soil nutrient levels with topographic gradients and regions of erosion and deposition created by active extensional tectonics; 4) correlating potential

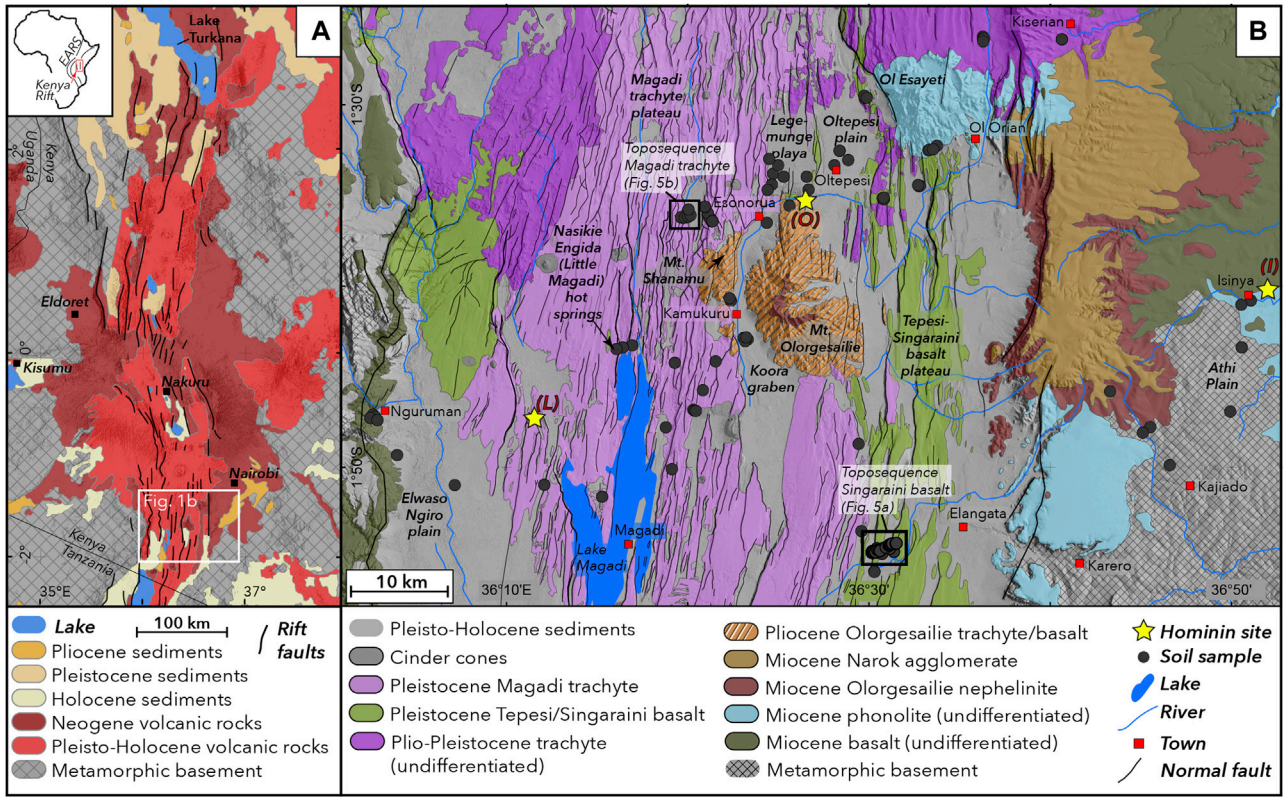

FIGURE 1 | Geological setting of the study region. **(A)** Geological frameworkof the Kenya Rift depicting the main lithological and tectonic features. **(B)** Geological framework and sampling locations of the study region in the southern Kenya Rift (geological data from Guth et al., 2013). Black boxes depict locations of two toposequences shown in **Figure 5**; yellow stars indicate locations of hominin fossil sites: (I) Isinya, (L) Lainyamok, (O) Olorgesaile.

soil nutritional corridors with the location of hominin sites in the study region.

SETTING OF THE STUDY REGION

Geology and Soils

The study region is located in the southern sector of the Kenya Rift, an integral part of the eastern part of the East African Rift System (**Figure 1A**), and extends from the Magadi trachyte plateau in the north to the southern shores of Lake Magadi in the south (**Figure 1B**). The region is characterized by extensive volcanism and associated tectonic activity from late Miocene to present. Pleistocene extensional tectonics have formed a complex system of grid faults in the rift center that hosts a series of tectonically controlled lake basins.

The oldest geological units are exposed at the uplifted rift shoulders at the eastern and western parts of the study area, comprising a series of Precambrian metamorphic basement rocks including granitic gneiss, quartzites and schists (Baker et al., 1971). Basement rocks are overlain by a series of Miocene basalt, phonolite and nephelinite (**Figure 1B**). The rift shoulders are characterized by the effects of long-term surface uplift and subtle tilting perpendicular from the rift axes. The Athi Plain on the eastern rift shoulder reflects long-term eastward tilt and forms a complex dendritic fluvial network oriented eastwards.

Mt. Olorgesailie, a prominent topographic feature located in the center of the rift valley, is a late Pliocene rift volcano (Baker et al., 1971) comprising trachytic, basaltic and nephelinitic lavas and pyroclastic deposits. The rift valley floor surrounding Mt Olorgesailie is extensively covered with Early to Mid Pleistocene lavas forming extensive plateaus, which resulted from widespread fissure eruptions of the Magadi trachyte (1.4–0.7 Ma BP: Baker et al. (1971); (Crossley, 1979)) in the north and west, as well as the Tepesi-Singaraini basalt plateau, comprising the Ol Tepesi (1.65–1.4 Ma BP), Ol Keju Nero (1.79–1.65) and Singaraini (2.31–2.33 Ma BP) olivine basalts in the eastern and southeastern segments of the study region (Baker and Mitchell, 1976). Due to their mineralogical similarities and for simplicity, we use in this study for the Pleistocene basalt series the combined term "Tepesi-Singaraini basalts". The Mid Pleistocene volcanic units along with associated sedimentary deposits were subjected to complex and densely spaced extensional tectonic faulting in the Mid to Late Pleistocene (**Figure 1B**).

The most prominent sedimentary basins of the study area are 1) the Olorgesailie basin north of Mt. Olorgesailie comprising the alkaline Legemunge plain to the west and the Oltepesi alluvial plain to the east, 2) the Koora Graben west and south of Mt.

Olorgesailie, 3) the Lake Magadi basin, and 4) the Ewaso Ngiro Plain (**Figure 1B**). Lake Magadi is characterized by high salinity, widespread exposures of trona deposits, and frequent water recharge by saline hot springs along the northwestern and southern lake shores. Normal faults in the Lake Magadi region are among the most active tectonic structures in the otherwise seismically relatively quiescent Kenya rift. Present seismicity in the region is characterized by high-frequency low-magnitude seismic swarms (Ibs-von Seht et al., 2001), and individual stronger events of magnitudes up to 4.2 accompanied by extensional surface fissures in the epicentral region (Atmaoui and Hollnack, 2003).

To describe soils in the study region (**Supplementary Figure S1**), we use the soil classification provided by the World reference base for Soil Resources (WRB, 2015). Playa deposits of the Lengemunge playa and alluvial sediments of the Oltepesi plain, are characterized by high soluble salt accumulations and are dominated by soil types haplic solonchak and associated haplic solonetz. Clay rich sediments in the Koora Graben comprise eutric cambisols and eutric fluvisols and associated chromic and pellic vertisols. Alluvial plain deposits in the Ewaso Ngiro plain and other smaller alluvial plains comprise predominantly eutric fluvisols and eutric cambisols. The densely faulted landscape of the Magadi plateau is characterized by an alternation of shallow soils comprising rhodic nitisols, and associated calcaric regosols and chromic luvisols along the fault ridges and steep slopes, and eutric cambisols on the alluvial deposits in the fault-bounded basins. The Singaraini-Tepesi basalt plateau comprises haplic luvisols and associated chromic luvisols along the fault ridges. Soils on basaltic rocks and associated alluvial deposits at the western rift shoulder predominately comprise gleyic solonchaks, eutric planosols, haplic phaeozems and associated haplic calcisols. The eastern rift shoulder is characterized by luvic phaeozem and associated vertic luvisols developed on Pliocene volcanic rocks, and eutric vertisols and chromic luvisols on metamorphic basement rocks (Touber, 1977).

Besides extensive soda ash mining in the Lake Magadi region, traditional Maasai livestock grazing is the main anthropogenic and agricultural activity in this region, which is otherwise only scarcely settled and influenced by human impact.

Topography, Climate and Vegetation

The landscape of the southern Kenya Rift is characterized by steep topographic gradients from the eastern and western rift shoulders situated above 1500 m asl to the rift center that lies at 600 m asl in the Lake Magadi basin. While the rift shoulders, particularly in the east, are dominated by wide and gently sloping plains and a generally low relief, the rift center is much more complex and characterized by a low-topography high-relief landscape as a result of densely spaced extensional faulting.

Climate in the study region can be classified between humid climate in regions above 2000 m, semi-arid to sub-humid climate in regions between 1000 and 2000 m asl, and arid climate in the low lying parts of the rift center below 1000 m asl (Köppen, 1900; Thornthwaite, 1948; Pratt et al., 1966). Major parts of the study region are characterized by aridity and seasonal large-scale rainfall patterns controlled by the East African monsoonal system and locally modified by topography (Vincens and Casanova, 1987). Lowest rainfall (<750 mm/yr) and highest mean potential evaporation (>2400 mm/yr) in the study region are observed in the Lake Magadi basin, leading to widespread exposure of evaporites and very sparse vegetation cover.

Regional scale vegetation patterns in the study area closely follow topographic and climatic gradients leading to widespread distribution of semi-desert shrubland in the low lying lake basins between 600–900 m asl, *Acacia commiphora* dominated woodland in widespread regions below 1500 m asl, and mosaic evergreen and semi-evergreen bushland in regions above 1500 m asl (Mworia et al., 1988). On a local scale, vegetation varies most significantly with hydrology and relief. In the densely faulted landscape of the plateau-like landscape dominated by Magadi trachyte and Tepesi-Singaraini basalt (**Figure 1B**), vegetation systematically varies with hillslope, and the associated distribution of colluvial and alluvial sediments. Uplifted surfaces on horst structures are dominated by open *Acacia commiphora* woodland, while alluvial plains next to active faults are dominated by open grassland frequently scattered with bushes of different species including *Acacia melifera* and *Acacia tortilis*. Vegetation density along colluvial deposits downslope of active fault scarps is systematically higher than on adjacent uplifted horst structures. Vegetation on colluvium comprises *Acacia commiphora*, densely interspersed with other shrubs and small trees including *Grewia similis*, *Grewia bicolour*, *Balanicis egyptiaca*, and *Maerua* sp. Steep fault scarps are dominated by bedrock exposure and scattered grass tussocks, as well as sporadic occurrence of *Acacia melifera* and *Acacia tortilis* (Mworia et al., 1988).

In recent years, the southern Kenya Rift is further affected by rapid invasion of *Prosopis juliflora* (Kyuma et al., 2016), an invasive subaerial plant species originating from Central and South America, which predominately occupies extensive regions on floodplain deposits in the Koora Graben, and along hillslopes in the Lake Magadi basin and Ewaso Ngiro plain.

Fossil Sites

The southern Kenya rift is a key region for studying Pleistocene hominin and archeological sites (Isaac, 1977; Potts, 1989; Behrensmeyer et al., 2002; Behrensmeyer et al., 2018). The most significant is Olorgesailie, located in diatomaceous lakebeds of the Legemunge Plain north of Mt. Olorgesailie. It is famous for its abundant Acheulean stone stools and fossil mammals spanning 1.2–0.5 Ma (Potts, 1989; Potts et al., 1999; Potts et al., 2004) and Middle Stone Age artifacts spanning 320 to ca. 36 ka–(Behrensmeyer et al., 2018; Deino et al., 2018). Other sites bearing evidence for Pleistocene hominins include the Isinya site (>0.98 Ma) on the eastern rift shoulder (Roche et al., 1988; Durkee and Brown, 2014), and Lainyamok (0.7–0.56 Ma) located north of Lake Magadi (Shipman et al., 1983). The latter site is interpreted as a locality of minor hominin activity (Potts et al., 1988).

METHODS

We have carried out an integrated geopedological analysis in order to decipher the influence of lithology and topography on

the nutrient status of soils in the southern Kenya Rift. We have used a combination of remote sensing and field-based analysis to identify rock and soil sample locations along a lithosequence comprising the main geological units exposed in the study area, which covers a 70 × 40 km large region, as well as two toposequences across the faulted Magadi trachyte and Tepesi-Singaraini basalt plateaus (**Figure 1B**). The main objective of field sampling and analysis was to determine the regional and local variations in physicochemical soil properties and their association with bedrock chemistry and topographic gradients created by tectonic activity. Soil transects were chosen to be located perpendicular to the strike of well-preserved normal faults vertically displacing volcanic bedrock. Fault erosion along the transects is dominated by gravity-driven slope processes forming colluvial deposits downslope of the fault exposures. We have mapped the geology and geomorphology in the vicinity of the transects and carefully chosen sample sites to avoid locations overprinted by the effects of local heterogeneities in sediment transport and nutrient redistribution due to e.g. alluvial processes, localized springs and groundwater seepage as well as local soil disturbances from burrowing animals.

Remote Sensing and Topographic Analysis

We have performed detailed topographic and optical analyses of satellite remote sensing datasets including high resolution digital elevation models of the TanDEM-X mission (Krieger et al., 2013), and multispectral Sentinel-2 datasets. We combined our observations with geological and pedological datasets of the region (Touber, 1977; Sombroek et al., 1982; Guth and Wood, 2013). The aim of the remote sensing work was to identify geological and geomorphological features that could potentially influence soil formation processes, such as tectonic fault scarps and volcanic deposits, as well as river networks, and local scale erosional features. Based on this analysis, we selected preliminary soil sampling sites on volcanic and meatamorphic bedrock, as well as on different sedimentary deposits, and the locations of two toposequences in Pleistocene volcanic rocks.

To analyze the relationship between vegetation growth and soil nutrient levels, we have produced a one-year average Normalized Differential Vegetation Index (NDVI) map of the study region from January 2017 to January 2018. To do so, we have selected one Sentinel-2 scene per month and calculated the mean NDVI using *ArcGIS Raster Calculator* (D'Allestro and Parente, 2015).

Rock Analysis

The objective of rock analysis was to identify weathering processes and related element mobilization in the volcanic rocks of the study region, and to compare the results with those of the analyzed soils developed on the selected rock types. We collected rock samples from several locations in the study region and along the Magadi and Tepesi-Singaraini transects and produced thin sections for polarized microscopic analysis as well as powder and glass beads for XRF analysis.

Polished thin sections were produced and analyzed by polarized light microscopy and scanning electron microscope (SEM). Microscopic pictures were taken by a Keyence Microscope (Mineralogische Staatssammlung München, SNSB), using a polarizing filter. Back scattered electron images (BSE) were taken by a Zeiss scanning electron microscope at the Department of Earth- and Environmental Sciences at the Ludwig Maximilian University Munich (LMU). WD-XRF analysis of the whole-rock composition were measured with a Philips, MagiX Pro WD-XRF spectrometer at the LMU, Department of Earth- and Environmental Sciences. Sample powders were dried at 110°C for more than 6 h and subsequently ignited at 1050°C for more than 2 h to determine the loss on ignition (LOI). Major and minor elements were measured using glass beads prepared by fusion of 1 g ignited sample powder and 9 g SPECTROMELT A12 (66% di-lithium tetraborate, 34% lithium metaborate) in a PANalytical Eagon 2 furnace fusion system. SO_3 was measured by XRF analysis of powder tablets; these were prepared by mixing 8 g of the sample powder with 2 g of Merck Hoechst wax C micropowder ($C_{38}H_{76}N_2O_2$). Powder tablets were homogenized and pressed with $p = 15$ bar for >1 min. The calibration was done using international certified standards. Analytical quality was ensured by analyzing reference materials by the US Geological Survey as unknowns (Flanagan, 1969).

Soil Analysis

The main objective of soil analysis was to collect data on the variability and distribution of key soil nutrients in soils developed on the individual rock units and sedimentary deposits exposed in the study region. A sampling location usually consists of three to five soil samples. Composite topsoil samples were taken in a 5 × 5 m square from the uppermost 25 cm of a soil profile, to capture the portion of the soil profile most relevant for nutrient uptake by grassroots. In regions of deep soils additional sampling was carried out along depth profiles, and samples were taken from the individual soil horizons. Along a ~60-km-wide lithosequence we sampled topsoil at 91 locations located on six different bedrock units and three different sedimentary units. To capture the effect of thermal activity and active CO_2 degassing, three sample locations are in the vicinity of active hot springs at Nasikie Engida (Little Magadi: **Figure 1B**). We also sampled depth profiles at three locations on the Legemunge Plain, Oltepesi plain and a river terrace of the Ol Keju Nero river, respectively. To analyze the effect of topography and tectonics, we sampled 51 topsoils at 17 locations across a 3 km long toposequence in tectonically faulted Tepesi-Singaraini basalt, and 21 topsoils at 7 locations across a 750 m long toposequence in tectonically faulted Magadi trachyte. Originally, we intended to take a similar amount of samples along both toposequences, however, for security reasons, we had to prematurely terminate field work in the Magadi region.

Soil samples were tested for a wide range of macronutrients and trace elements. We will show here only the results for Ca, Mg, and plant available P, as previous studies carried out in the wider vicinity of the study region have documented deficiencies and related health problems for humans and animals in relation to those nutrients (McNaughton, 1990; Maskall and Thornton, 1996; Davies, 2013; Kübler et al., 2015; Kübler et al., 2019).

Soil analysis was carried out by the soil chemistry laboratories of the Kenyan National Agricultural and Livestock Research Organization (KALRO-Kabete) and the National Museums of

Kenya. Before analysis, samples were air dried and sieved through a 2 mm sieve. Organic carbon was oxidized with concentrated H_2SO_4 and K_2CrO_7 and determined calorimetrically (Anderson and Ingram, 1993). Available P was determined using the method by Olsen (1954); Exchangeable cations were extracted using 1N ammonium acetate at pH 7.0, followed by flame photometry for the determination of Na, K, Mg and Ca, using an A2 flow analyser. Determinations of low, moderate and high nutrient levels follow recommendations by Shand (2007) and Hengl et al. (2017).

RESULTS

Tectonic Geomorphology of the Study Region

The study region is characterized by the typical geomorphological features of an asymmetric continental rift system with uplifted and slightly tilted rift flanks away from the rift axes along the Athi Plains to the east and Nguruman escarpment to the west (**Figure 1B**) (Baker and Mitchell, 1976; Birt et al., 1997; Chorowicz, 2005). Extensional tectonics are manifested in large N-S trending border faults at the eastern and western rift shoulder, and a more complex system of N-S and NNE-SSW trending normal faults in the rift center. Mt. Olorgesailie in the rift center is subject to strong fluvial erosion and incision by the Ol Keju Nero river and its tributaries, forming the up to 6-km wide Koora Graben and separating Mt. Olorgesailie from Mt. Shanamu (**Figure 1B**). Fault scarps in the study region display different stages of erosion suggesting preservation of faults of different ages, as well as variations in the erosional behaviour of the fault structures due to material differences. Faults developed in trachytic volcanic rocks along the northern Magadi trachyte plateau are typically characterized by a stronger degree of erosion and fault scarp degradation than those exposed in the southern Koora Graben and Lake Magadi region, suggesting a gradual N-S shift in faulting activity over time (Owen et al., 2018b; Owen et al., 2019).

The landscapes of the Magadi trachyte and Tepesi-Singaraini basalt plateaus comprise a diverse suite of tectonic landforms created by extensional faulting such as north-south trending successions of horst and graben structures dissected by sub-vertical fault scarps in volcanic bedrock dominated by lavas and pyroclastic deposits. The uplifted fault ridges and horst surfaces are subject to frequent surface runoff and pronounced soil erosion leading to a patchwork of shallow and rocky soils and exposed volcanic bedrock. Bedrock fault scarps are well preserved as sub-vertical cliffs and commonly display strong coating by desert varnish. Downslope of the steep fault cliffs the transition from the uplifted footwall to the fault zone is expressed by an increase of fracture density in the exposed bedrock (fault core). Here, densely fractured fault breccias and clastic dykes are exposed. Fault breccias are frequently cemented with light-colored Ca and Na-rich carbonates. Colluvial deposits at the footslope of the fault cliffs are commonly densely vegetated–with the exception of the little vegetated faulted margins of Lake Magadi and Nasikie Engida–and characterized by a large range of grain sizes including meter-sized angular blocks of volcanic rocks. Basin fill in the tectonic grabens are a wide range of alluvial and lacustrine deposits. The Magadi transect exposes gravelly fluvial terraces in the center, and fine fluvial sands and playa deposits in the easternmost graben. The Tepesi-Singaraini transect exposes clay-rich gravely alluvial plain deposits at the westernmost graben, coarse sand and gravel-rich alluvial and playa deposits in the center, and a mixture of fine-grained sand-rich fluvial deposits and poorly sorted slope wash deposits in the easternmost graben.

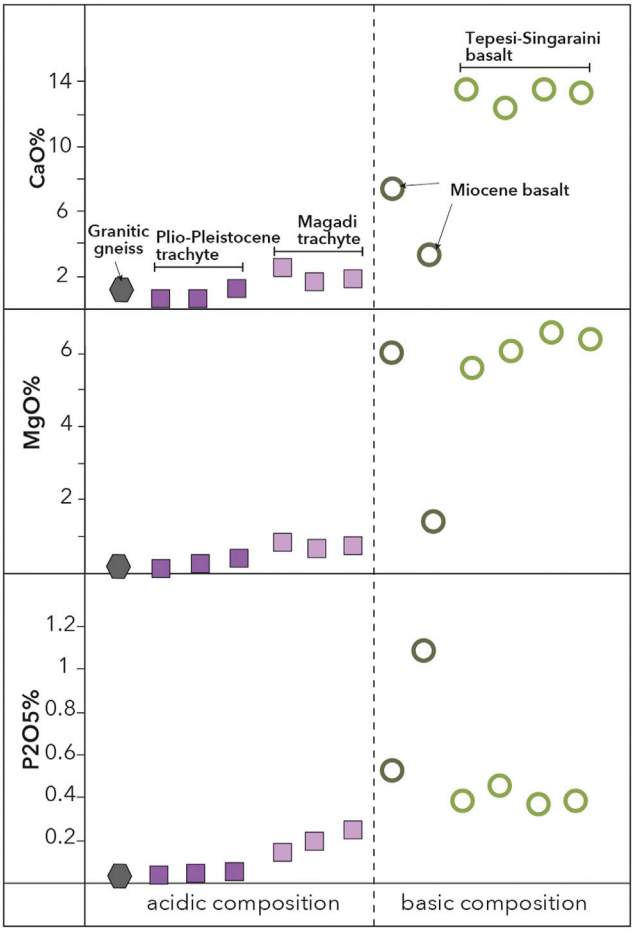

FIGURE 2 | Results of XRF whole rock analysis of the representative samples comprising basaltic, trachytic and subordinate granitic lithologies. Different lithological units are represented by varying symbols and colors. Dashed vertical line depicts separation between basic and acidic geochemical compositions.

Results of XRF and Microscopic Rock Analysis

Whole Rock Composition

The lithology in the study area consists of basaltic and trachytic volcanic rocks and subordinate granitic gneiss. In this study, five rock types were selected as representatives: the Tepesi-

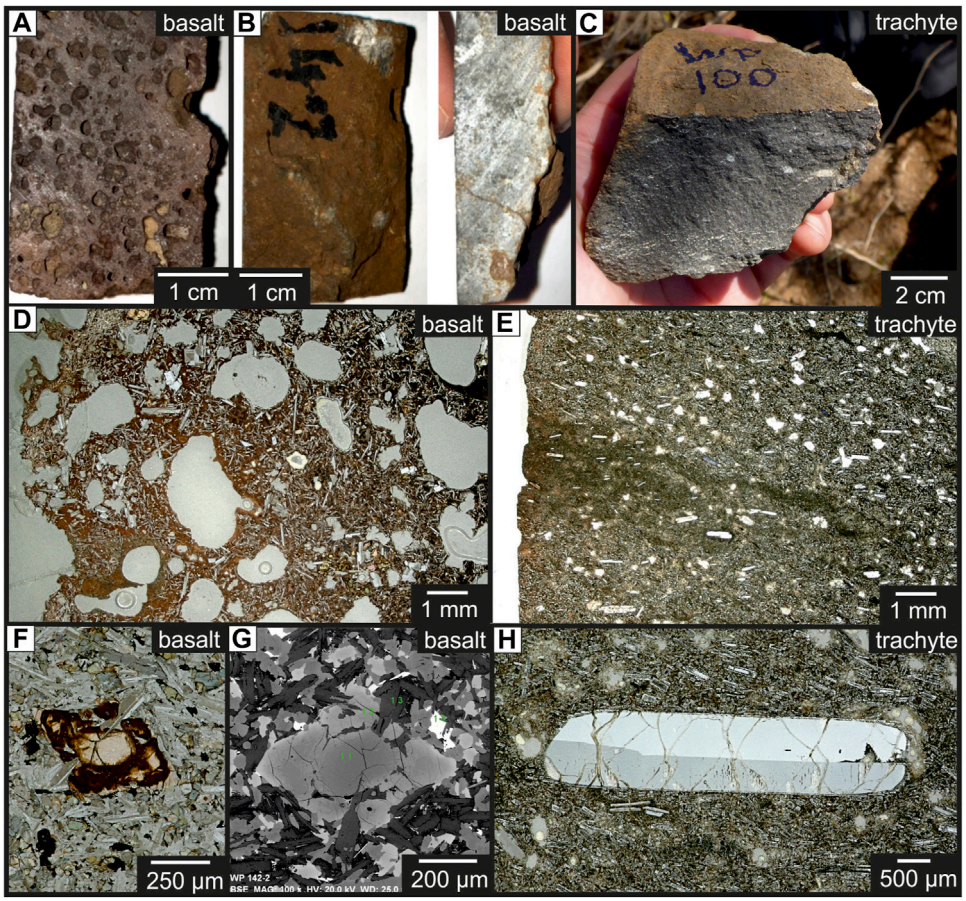

FIGURE 3 | (**A–C**) Photos of hand samples of **(A)** a bubble rich, completely weathered basalt, **(B)** a compact, strongly weathered basalt in top view **(left)** and along a section **(right)**, **(C)** a compact trachyte with a thin brown weathering crust. **(D–H)** Microscopic images of **(D)** a strongly weathered, bubble-rich basalt with a high proportion of white needle-shaped feldspar in a reddish-brown altered matrix, **(E)** trachyte containing elongated feldspar crystals in a very fine-grained groundmass, with a thin, near-surface, brown weathering crust **(left)** and in the middle a greenish-brown area indicating the course of a fluid path running from the left (surface of the rock) into deeper (several mm) parts of the rock. Olivine within a moderately weathered basalt, **(F)** showing strong alteration (dark brown areas) along the grain boundaries and along the cracks (thin section) and **(G)** a BSE-image of the same olivine crystal; the darker gray area represents the primary olivine with Mg-rich composition and the brighter gray parts of the crystals indicates Fe-enrichment within the altered section of the mineral. **(H)** One large feldspar crystals within trachyte with weak alteration specifically along the cracks.

Sagaraini basalt, Miocene basalt, the Magadi trachyte and Plio-Pleistocene trachyte as well as a granitic gneiss. These rocks can be divided chemically into two major groups. Primitive (basic), mafic basalts with high concentrations of CaO, MgO and P_2O_5 and more evolved (acidic) and alkaline granitic gneiss and trachyte with low concentrations of CaO, MgO and P_2O_5 (**Figure 2**). CaO is highest in the Tepesi-Singaraini basalt with values ranging between 12.3 and 13.5 wt% and intermediate values of 3.3–7.5 wt% in the Miocene basalts. CaO concentration in Plio-Pleistocene trachyte is always <1.2 wt% and it is slightly elevated in the Magadi trachyte (1.6–2.7 wt%). MgO is also highest in the Tepesi-Singaraini basalt with values ranging between 5.6 and 6.5 wt%. In Miocene basalts, MgO concentrations are highly variable ranging between 1.4 and 6.0 wt%, while in granitic gneiss the contents are always <0.8 wt%. P_2O_5 concentrations are highest in Pliocene basalt at 0.6–1.1 wt%, whereas concentrations are moderate in Tepesi-Singaraini basalt at about 0.4 wt%. P_2O_5 concentrations in trachyte and granitic gneiss are always low, with maximal contents in Magadi trachyte (0.2 wt%).

Mineralogy of the Rock Samples

The whole rock composition reflects the mineralogy of the respective rocks (**Figure 3**). Basalt consist mainly of Ca-rich plagioclase (50–60 vol%) and Mg-bearing olivine (20–30 vol%) and minor proportions of melt blobs containing primary (magmatic) Ca- and Mg carbonates. Trachytes consist mainly of K-rich alkali feldspar (60–70 vol%) and only subordinate Ca-containing mineral phases like carbonate and clinopyroxene.

Influence of Weathering

The basalt and trachyte rocks show significant differences in weathering behavior (**Figures 3A–C**). The two basalt types in this

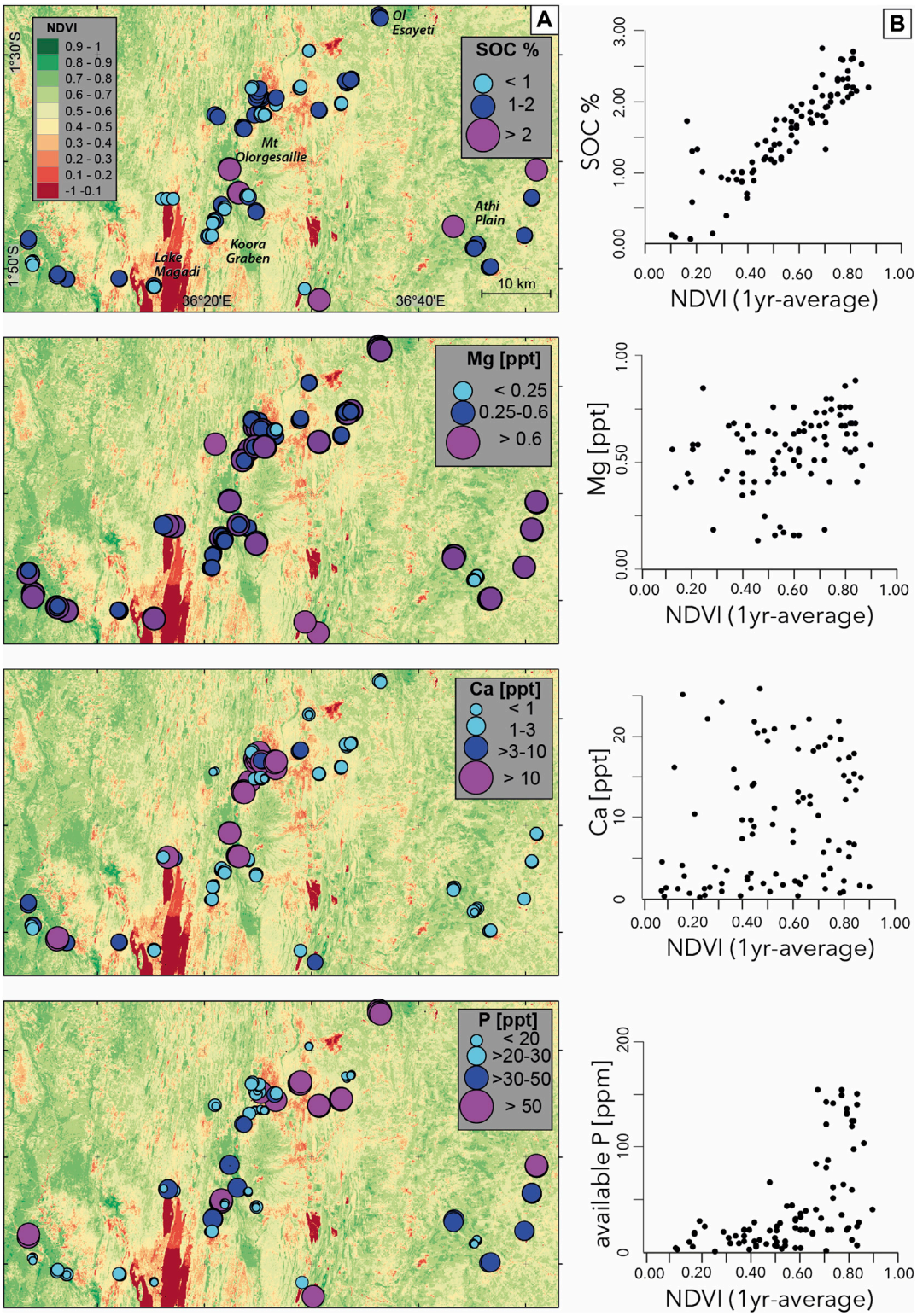

FIGURE 4 | SOC, NDVI and soil nutrient distributions; **(A)** variations in SOC and soil nutrient levels in topsoil samples of the study area, sample locations are represented by colored circles, backround map shows distribution of healthy vegetation using a 1-year average NDVI dataset, derived from Sentinel 2 data. **(B)** diagrams showing the relationship between SOC and soil nutrients vs. NDVI.

region are always fine-grained and often show different degrees of porosity, with some of the basalts being highly vesicular. As the porosity of the basalts increases, the degree of weathering generally increases. Accordingly, basalts are often coated with thick (0.5 - > 1 cm) weathering crusts (denser varieties, **Figure 3B**) up to completely weathered varieties (bubble-rich varieties, **Figures 3A,D**). In contrast, trachyte exposed along the toposequence is more compact and therefore more resistant to weathering. Weathering crusts are thin (<1 mm) and present near the surface (**Figures 3C,E**). Only occasionally, greenish-brown areas were identified, representing fluid pathways (**Figure 3E**). However, these fluid paths are always limited to a maximum of several millimeters from the surface into the rock (**Figure 3E**).

Fresh Tepesi-Singaraini Basalts and Magadi trachyte with the weathered samples were analyzed for rock chemistry and mineralogy to determine the consequences of the weathering process.

The weathered parts of Tepesi-Singaraini basalt are depleted in Na, Mg and Ca, which reflect the alteration and dissolution of strongly weathered olivine (releasing Mg) and *in-situ* crystallization of Fe-rich varieties (**Figures 3F,G**) and plagioclase (releasing Ca, Na). In contrast, P, Fe, Ti and K are enriched in the weathered part. The newly formed minerals consist mainly of Fe-Ti-rich mineral phases, such as Fe-Ti-oxides or clay minerals among others (**Figures 3D,F,G**), which dominate strongly altered rock specimens, in some cases up to complete replacement of the primary feldspathic groundmass (**Figure 3D**).

The comparison of the whole-rock composition of fresh and weathered Magadi trachyte showed only a slight enrichment of Mg, Ca, Na and P in the weathering crusts. Microscopic investigations showed that the primary minerals, such as feldspars, are only slightly altered along the grain boundaries and cracks (**Figure 3H**). Primary carbonates have been observed in both rock types and are believed to reflect carbonate melt blobs (size range 100–500 μm). Microscopic observations showed that in both rocks these carbonates are only weakly altered along the grain boundaries. Fine-grained secondary carbonates within the rocks indicate that they precipitated *in situ*. In general, the enrichment of Mg, Ca, Na and P in the weathered parts indicates a fixation of these elements in secondary minerals within the weathered crust of trachytes, whereas the respective elements in basalts are depleted in the weathered areas and therefore released to the soils and groundwater.

Results of Soil Analysis

Soil Organic Carbon and Normalized Differential Vegetation Index

SOC values vary significantly in the study region (**Figure 4A**) between 0.11% in soils developed on saline lakebeds at the Lake Magadi shore and 2.76% on the Pliocene Narok Agglomerate at higher elevations on the eastern rift shoulder. NDVI values vary between 0.12 and 0.97 in the study area, with lowest NDVI values found on soils derived from volcanic ash exposures south of Mt Suswa in the northern segment of the study region, as well as on exposed lacustrine sediments of Lake Magadi. Highest values were observed on swampy and densely vegetated fluvial deposits in the Koora Graben to the north and east of Kamukuru village (**Figure 1B**). NDVI strongly correlates with SOC (**Figure 4B**), indicating that plant biomass production plays an important role in the accumulation of carbon stocks across the entire study region. SOC and NDVI values do not show a clear correlation with particular lithologies, but correlate positively with altitude, as values are on average higher on the uplifted rift flanks (Athi Plain, Ol Eyaseti, Narok, Nguruman). In the densely faulted landscape of the rift center, SOC and NDVI values are systematically higher on the hanging wall sediments compared to lower values on uplifted fault ridges. Generally, high SOC and NDVI values occur in regions that are characterized by the presence of groundwater and/or surface water.

Soil Nutrient Levels

Calcium

Variations in Ca concentrations were driven by both topographic location and chemistry of parent material. Ca levels vary significantly between 0.54 ppt on granitic gneiss and 24.6 ppt on fluvial sediments in the Koora Graben (**Figure 4A**). Highest Ca levels (>25 ppt) occur in alkaline soils developed on lacustrine sediments of the Legemunge Playa and on fluvial sediments of the Koora Graben. Soils on alluvial plains display more heterogeneous Ca levels, potentially reflecting differences in sedimentary composition or catchment sizes and lithologies; the highest Ca levels are found on soils of the Ol Tepesi plain, lowest levels are found on alluvial deposits dominated by quartzite and granitoid clasts south of Nguruman, in the western sector of the study region.

Soils developed on Limuru Trachyte, Eyasi Phonolite, and Narok Agglomerate have systematically low to very low Ca levels. Shallow soils on Magadi trachyte generally contain low to very low amounts, with the exception of soils sampled in the vicinity of the Magadi hot springs at Little Magadi Lake, which have adequate to high Ca levels. Soils on hanging wall sediments in the faulted landscape of the Magadi trachyte display slightly higher Ca levels than the shallow and rocky soils developed on top of the fault scarps. Ca levels in soils developed on the Athi plain on metamorphic basement rocks are generally low to very low, lowest values are found in shallow rocky soils developed on granitic gneiss south of Kaijado, an area characterized by widespread sheet erosion negatively affecting soil productivity (Sindiga, 1984). Shallow basaltic soils North of Mt Olorgesailie are characterized by adequate to high Ca levels, shallow soils on basalts northeast of Mt Olorgesailie display low Ca levels. Highest amounts of Ca in shallow soils are found on basaltic rocks in the western sector of the study area at Nguruman.

Soils developed on the sedimentary deposits surrounding Mt Olorgesailie contain adequate to high amounts of Ca. Highest levels are found in soils on lakebeds of the Legemunge Plain and in the Koora Graben on river sediments of Ol Keju Nero River. Ca levels in Fluvisols on river deposits in the western sector of the study area are adequate to high, whereas soils on alluvial fan deposits sourced from metamorphic basement rocks (phyllites and granites) have low to very low Ca levels. Unlike SOC, Ca contents in the study region do not show a clear correlation with NDVI values (**Figure 4B**).

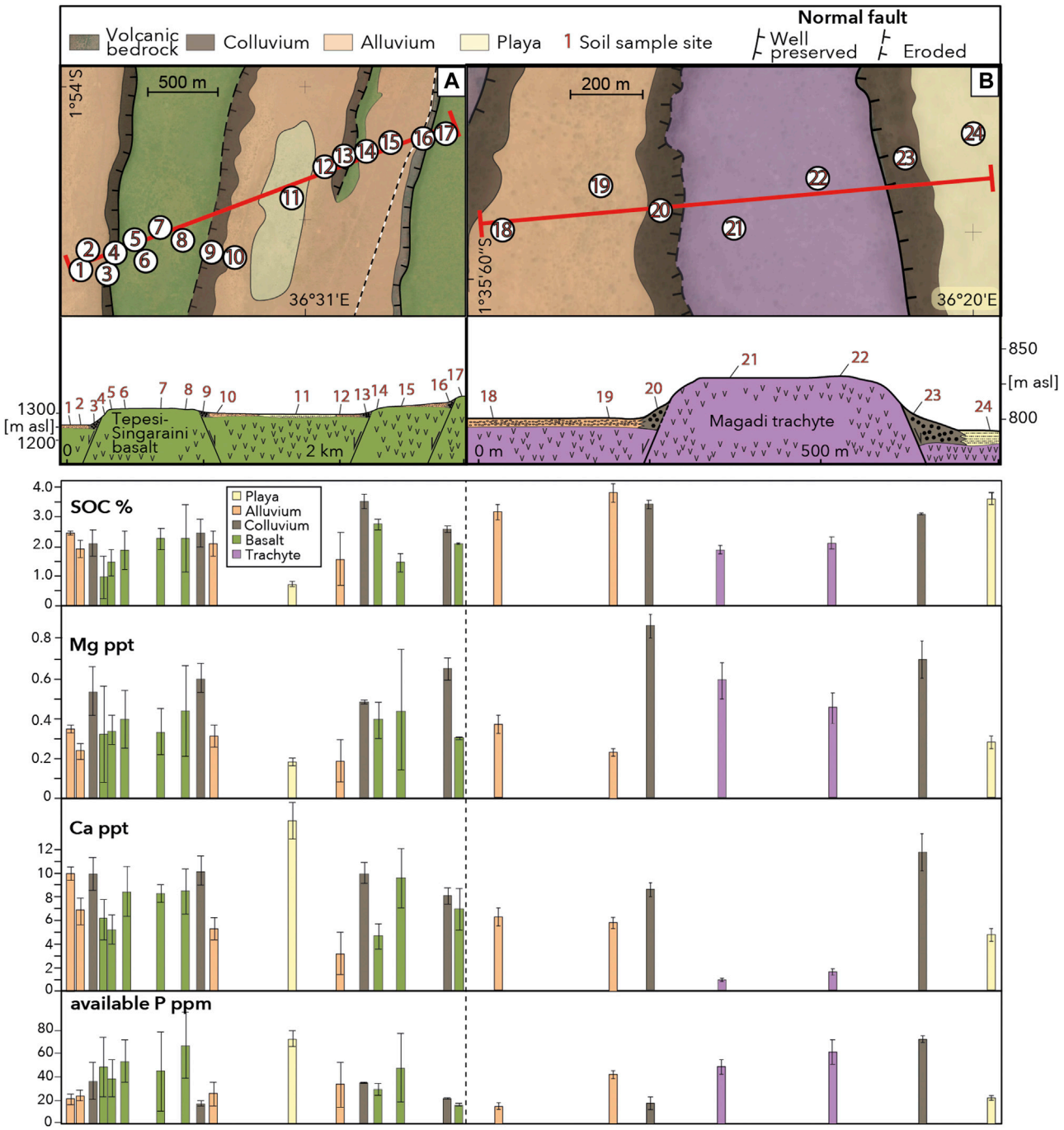

FIGURE 5 | Soil nutrient and SOC variations along two toposequnces crossing **(A)** the Tepesi-Singaraini basalt plateau, and **(B)** the Magadi trachyte plateau. Red lines depict the locations of topographic profiles; numbers represent locations of a soil sampling site that usually consists of 3-5 individual soil samples; colored bars represent differences in parent material.

Soils along the Tepesi-Singaraini basalt toposequence (**Figure 5A**) have consistently moderate to high Ca levels; highest Ca levels are found in playa sediments in the middle of the transect, lowest in alluvial soils east of the playa. Ca distribution shows a systematic correlation with hillslope location, and proximity to steep fault ridges, respectively. In colluvial deposits Ca levels in soils are systematically higher compared to those located upslope on fault ridges and plateaus. Highest Ca variations are in soils developed on alluvial plains and fluvial deposits.

Compared to soils along the Tepesi-Singaraini transect, Ca levels are on average lower along the Magadi trachyte

toposequence (**Figure 5B**). However, the 5 to 7-fold increase of Ca in soils on colluvial deposits at the base of fault scarps vs. those in shallow soils on fault ridges and the uplifted plateau is much more distinct in trachytic soils compared to that observed in basaltic soils (1.5 to 2-fold increase).

Magnesium

Mg levels in the study region vary relatively little between and only weakly correlate with the different lithologies (**Figure 4A**). Low levels are found in a few soils developed on granitic gneiss and at one sample location on the Legemunge playa. At all other sample locations the soils contained moderate (0.25–0.6 ppt) to high (>0.6 ppt) amounts. Mg is highest in soils developed on trachytic and phonolitic parent material and thus negatively correlates with Ca, which is lowest in these soils. Mg levels along the Tepesi-Singaraini and Magadi toposequences vary in a similar pattern to Ca (**Figure 5**). Soils on fault colluvium are systematically higher in Mg than those on ridges and plateaus. Mg levels on the uplifted Magadi plateau negatively correlate with Ca, a pattern we have also observed in other soils on trachytic and phonolitic parent material. Mg levels in the study region do not show a clear correlation with NDVI values (**Figure 4B**).

Plant-Available Phosphorus

Available P levels in the study area vary significantly between 1 ppm on granitic gneiss and 155 ppm on Narok agglomerate. Highest P levels occur in soils located on the eastern rift shoulder (**Figure 4A**) that has been subjected to agricultural use, which is why the use of phosphate fertilizer cannot be excluded as an explanation for high P values. Soils with high P that were not affected by cropping occur on sediments in the footwall of fault ridges on Tepesi-Singaraini basalt, as well as basaltic soils in the vicinity of Nguruman. P levels of soils in the Koora Graben and Legemunge playa vary significantly and correlate negatively with Ca levels. Variations in P across the study area show a weak positive correlation with NDVI (**Figure 4B**), and regions with high P (>50 ppm) are located in regions with NDVI >0.6; P levels <50 ppm are less clearly correlated with NDVI. This suggests that biochemical processes such as root-soil interactions or the presence of grazing animals may play a dominant role in the release of plant available P levels in such regions (Mathews et al., 1994; Richardson et al., 2009).

P levels along the Tepesi-Singaraini and Magadi toposequences vary strongly with proximity to hillslopes and show a trend opposite to Ca and Mg. P levels are systematically higher on flat terrain compared to steep slopes. Highest P values occur in regions subject to intensive animal grazing on playa deposits and the top of the westernmost fault plateau, which suggests additional P input from biological sources.

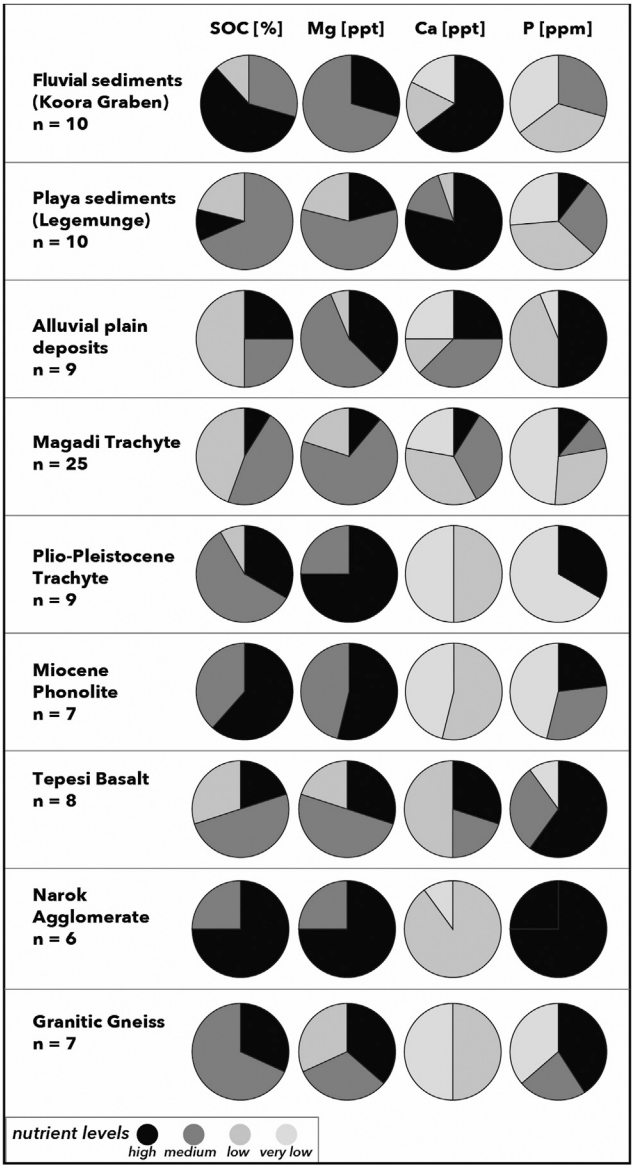

FIGURE 6 | Distributions of soil nutrient levels and SOC attributed to the main lithological and sedimentological units of the study area; SOC: low <1%, moderate <2%, high >2%; Mg: low <0.25 ppt, moderate 0.25–0.6 ppt, high >0.6 ppt; Ca: very low <1 ppt, low 1–3 ppt, moderate > 3–10 ppt, high >10 ppt; available P: very low <20 ppm, low 20–30 ppm, moderate >30–50 ppm, high >50 ppm.

DISCUSSION

Geological Factors in Soil Nutrient Distributions

The availability of soil nutrients in ecosystems and natural landscapes depends on a combination of climate, topography, parent material, biota and time, and the interplay of these factors can be very complex and our understanding of their relative significance remains limited (Mage and Porder, 2013). While climatic and biological activity can vary drastically over short time scales and may change some soil properties on time scales of a few decades, factors like the chemistry of parent material and the topographic setting of a tectonically quiescent region can potentially control soil properties for much longer time scales of 10^3–10^6 years. However, in dynamic landscapes controlled by e.g., volcanism and earthquake activity and

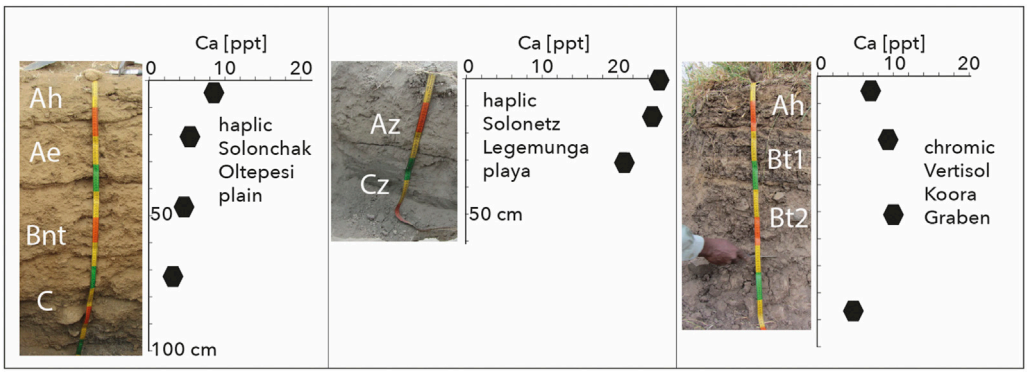

FIGURE 7 | Soil profiles and Ca variations with depth; **(A)** haplic Solonchak from soil pit on Oltepesi plain; **(B)** haplic Solonetz exhibiting strong salinification features from soil pit on Legemunge playa north of Olorgesailie site; **(C)** chromic Vertisol from road cut in floodplain deposits of the Koora graben, SW of Mt. Olorgesailie.

associated hillslope processes, both topographic and lithological factors can change drastically during single events, as well as continuously over long time periods. Single events can include: 1) volcanic eruptions and related widespread deposition of volcanic ash over several days or weeks as recently and historically documented for the Serengeti plains in northern Tanzania (Murray, 1995; Quigley et al., 2017; Eckmeier et al., 2020); 2) surface rupturing by large earthquakes and related dissection and uplift of the landscape leading to drastic readjustments of the landscape such as transient river damming (e.g., King and Vita-Finzi, 1981), as well as enhanced erosion and slope failure processes along uplifted fault escarpments (e.g., Hermanns et al., 2001). Long-term processes may include drainage rearrangement by river capture and river gorge development in steadily uplifting regions (Bishop, 1995; Stokes et al., 2008). To understand how soil nutrient variations determine ecosystem processes and human-landscape interactions over long periods of time, we need to carefully consider the whole range of processes influencing the availability and distributions of soil nutrients, as well as the temporal variability of such processes in our studied region.

Rock Chemistry and Soil Properties

Base cation concentrations in soils have commonly been attributed to *in-situ* mineral weathering, suggesting that high levels of Ca, Mg, Na, and K can be directly attributed to the mineralogical and sedimentological composition of the parent material. Due to high solubility of these base cations in the soil solution, frequent provision of freshly weathered minerals is necessary to prevent leaching losses (Bern et al., 2005). In our study area, we observed strong variations in Ca, available P and SOC levels over the entire study area as well as across both toposequences. While Ca, P and SOC levels all vary with topography and relief, only Ca can systematically be correlated with the composition of the parent material. Low Ca levels in soils occur on trachyte, phonolite and granitic gneiss (**Figure 6**)–the lithologies with the lowest amounts of CaO in the study region (**Figure 2**).

Excessive Ca levels (>10 ppt) are found in soils on playa and alluvial deposits characterized by high alkalinity (**Figures 4**, **5A**), which suggests an enrichment of Ca in the form of $CaCO_3$ as a component of calcretes, dust or lacustrine sediments. It can accumulate in the topsoil through evapotranspiration (e.g., Alonso-Zarza, 2003) or deposition of carbonate rich materials such as dust or volcanic ash. This hypothesis is supported by soil profiles analyzed on the Legemunge and Oltepesi plains. Here, Ca levels are highest in the topsoil and systematically decrease with depth, while clay rich vertisols in the Koora Graben show an increase of Ca with depth, potentially due to leaching processes in near surface horizons (**Figure 7**). Our observations suggest that while geological data in general can provide useful information on the long-term availability of Ca in soils, locations of high alkalinity may display drastic differences in near-surface Ca levels under wetter climates.

In contrast to Ca, levels of available P are scattered over different lithologies (**Figure 6**), suggesting minor influence of mineral-bound P in the parent material on available P in soils. In alkaline soils of the Legemunge playa and Lake Magadi basin available P levels are consistently low and negatively correlated with Ca levels (**Figure 8**). Calcium is known to cause P fixation in high pH soils (Hemwall, 1957). We observe a threshold of Ca > 10 ppt above which available P is suppressed (**Figure 8**). This observation suggests that under stable climatic conditions, the studied soils in arid locations on playa deposits subjected to high evaporation rates and excess soil Ca levels are likely to be characterized by long-term deficient available P. This in turn implies that present day P levels are not necessarily a reliable proxy for the long term nutritional soil status, as P fixation might have been drastically different under wetter climatic conditions as reported for the study region in Pleistocene and early Holocene times (Trauth et al., 2005; Owen et al., 2018a; Owen et al., 2019).

We did not observe a clear correlation between SOC and lithology (**Figure 6**), which suggests that parent material does not primarily influence biomass production, as reported from regions interspersed with e.g. ultramafic rocks or in limestone landscapes (Kruckeberg, 2004). However, SOC systematically follows topographic gradients and related vegetation patterns, as

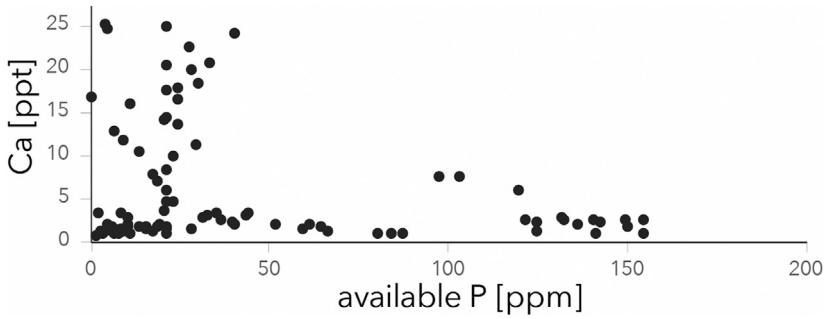

FIGURE 8 | Relationship between soil Ca and plant available P in the study region. Note the ~10 ppt threshold of Ca concentrations supressing available P in topsoil samples.

shown in the strong correlation between NDVI and SOC (**Figure 4A**).

The major rock types occurring in the study area, trachyte and basalt, show differences in weathering behavior. In comparison to the fine-grained and often highly porous (vesicular) basalts, trachyte is more resistant to weathering processes because it is more compact and therefore resist better the penetration of fluids into the rock. Macroscopic and microscopic observations showed that trachyte shows predominately near-surface alteration rims of millimeter to centimeter in size, whereas basalts are mostly characterized by deep to complete alteration (**Figure 3**).

Microscopic examinations revealed a specific resistivity of the minerals present in the assemblages, with olivine < plagioclase < pyroxene; this trend corresponds to the observations of Eggleton et al. (1987). Accordingly, olivine and plagioclase, the main components of basalts, show strong weathering effects and are replaced by secondary minerals, such as Fe-Ti oxides. The observed enrichment of Fe and Ti and a depletion of Mg, Ca and Na in the whole rock composition of the weathered parts of basalt compared to fresh samples means that Fe and Ti are mineralogically bound within the weathering crusts of the rocks and Mg, Ca and Na are released into the soil, and groundwater–if present. In contrast, weathering of trachyte is limited to an alteration of clinopyroxene, which induces a mobilization of Ca and Mg. However, the whole rock composition shows an accumulation of these elements in the weathered parts of the trachyte. This indicates limited mobilization and mineralogical fixation of Mg and Ca in secondary minerals, such as carbonates, within the rock. Consequently, these elements are not available for overlying soils.

Puzzling are high Ca concentrations of soils developed on colluvial deposits in both basaltic and in trachytic areas, with significant increase of Ca concentrations in soils on trachytic colluvium in comparison to the original fresh rock. Primary carbonates, which are present in trachytes and in basalts, represent carbonatitic melt blobs, which can theoretically be a source of Ca and Mg in soils. However, microscopic observations showed that these carbonatite blobs are generally only slightly altered along grain boundaries and are replaced *in situ* as fine-grained secondary carbonates. Therefore, the availability of Ca and Mg from these carbonates for soils is limited.

Petrological investigation of a soil-rock (basalt)-profile from Sahand volcano (NW Iran), located in an area of active CO_2 degassing, has shown a preferential mobilization of Ca from the host rock and precipitation of carbonates along cracks and at the interface between rock and soil (Aßbichler et al., in preparation). Correspondingly, preliminary results of leaching experiments carried out at the geological laboratories at the Department of Earth and Environmental Sciences, LMU Munich, showed that the addition of CO_2 gas generally improves the leachability of Ca from minerals and thus enhances the mobilization of divalent elements such as Ca and Mg (Aßbichler et al., in preparation). Previous studies carried out in the Lake Magadi and Lake Natron regions (Lee et al., 2016; De Cort et al., 2019) have shown that generally fault zones provide perfect pathways for mantle gases such as CO_2 (diffusive soil gas).

High Ca contents in trachytic soils can not only be found on the colluvial deposits, but also at the northern shore of Nasikie Engida in the vicinity of the Little Magadi hot springs (**Figures 1B**, **4A**), suggesting an influence of CO_2 degassing on Ca mobilization. In this context, one would also expect travertine or other secondary carbonate formations at the hot springs. Thicker carbonate formations at the hot springs are, however, only fossil (Pleistocene) calcretes (>30 cm) north of Nasikie Engida (Renaut et al., 2020, in press). In addition, the recent saline spring fluids are characterized by low dissolved Ca- and Mg- concentration and precipitates are dominated by Na-(hydro)-carbonates (Renaut et al., 2020, in press), indicating that nowadays Ca mobilization by the fluids of the hot springs does not play a major role. In this context, two things have to be considered: 1) At the warm temperature of the hot springs fluids, Ca-carbonate hardly dissolves in water. Even at room temperature, Ca-bearing water immediately precipitates carbonates in the presence of CO_2 (e.g. Dodson and Standing, 1944). The carbonate solubility decreases with increasing temperature, and in consequence water with low Ca (and Mg) concentrations remains. In the Magadi basin, the effect of early precipitation of calcite and Mg-calcite in subsurface flow paths has been observed by (Owen et al., 2019) for the Lake Magadi

brines. 2) At the presence of water, leaching of Ca is expected to be enhanced due to the formation of carbonic acid compared to "dry" (water-free) conditions, leading to a faster leaching of Ca from the exposed trachytes. The occurrence of Pleistocene carbonate precipitates and carbonates at the bedrock interface indicates that Ca mobilization has occurred within a limited period in the past. Trachytes in the Magadi area have low Ca contents (<2.7 wt% CaO), while Na- and K- concentrations are significantly higher (e.g. >5 wt% Na_2O). It is therefore reasonable, that after most of the Ca has already been leached from the exposed trachytes, the conditions shifted to more Na- (and K-) rich conditions, which are now present at the hot springs. Correspondingly, a study of samples from Laacher See volcano has shown that under CO_2 rich conditions Ca is preferentially leached, followed by the leaching of Na from the primary minerals (Aßbichler, 2020).

The soil and rock samples in our study were taken from areas in which water is likely to play only a subordinate role, particularly along the Magadi toposequence (**Figure 5**), where no groundwater influence on soil formation has been observed. Assuming a "dry" diffusive CO_2 soil degassing, in which water is only a subordinate reaction partner, leaching and dissolution reaction via CO_2 is to be expected to be much slower, but continuous. This contributes to a constant, low level-mobilization of Ca from the rocks to the surface, and consequently to a continuous enrichment of Ca in the soils, and at the interface between rock and soil. We therefore assume that ascending mantle gases may be an overlooked factor in mobilizing Ca ± Mg from deeper parts of the rock profile and may contribute to the accumulation of Ca in the colluvial soil and areas close to the hot springs.

Tectonic Faulting and Soil Nutrient Redistribution

Nutrient distributions in soils are controlled by two main factors 1) release and vertical transport through *in situ* mineral weathering and soil profile development in residual soils 2) lateral transport through mass flux along topographic gradients or airborne accessions of dust and/or volcanic ash (Simonson, 1995; Calitri et al., 2019).

Extensional tectonics led to a horst-and-graben landscape characterized by a complex patchwork of uplifted and eroding surfaces. This promoted the formation of residual soils, and down-dropped basins constantly subjected to deposition of freshly eroded material, as well as redeposition of soil cover and sediments through slope failure and alluvial processes (Tucker and Bras, 1998; Roering et al., 2001; Pelletier and Rasmussen, 2009).

Along both toposequences, we observe a systematic increase of Ca and Mg in soils from uplifted fault ridges, to colluvial deposits downslope of active fault structures. This suggests that primary weathering of freshly eroded minerals releases sufficient amounts of Ca and Mg-bearing minerals to rejuvenate soils in these locations. Alluvial soils in the valleys are often depleted in Ca and Mg, either because of fast weathering and dissolution of Ca and Mg-bearing minerals or lateral translocation of sediments through alluvial processes. Systematic increase of Ca, as well as other nutrients including Mg and K downslope along steep convex hillslopes has already been reported in other studies (e.g., Chadwick and Asner, 2016). Our field observations and laboratory analyses suggest that Ca enrichment in downslope deposits occurs through a combination of accumulation of freshly eroded rocks in colluvial deposits and *in-situ* alteration of rejuvenated soils, potentially enhanced by the effect of diffusive CO_2 degassing along the fault zones (Lee et al., 2016).

Levels of available P are lower in colluvial deposits than on flat surfaces, suggesting that slope and topographic position influences available P levels in a different way than Ca and Mg. While earlier studies showed that parent material and topographic position have a strong influence on the levels of total P in soils (Mage and Porder, 2013; Chadwick and Asner, 2016), the controls on plant available P appear to be different. In our study area along the Singaraini toposequence, flat terrain is frequently visited by herds of grazing animals. This suggests that the sources of plant available P might be related to other biological P sources such as animal manure. Also, the effects from burrowing animals or termites in soil redistribution and P sorption and availability, as well as the role of eolian input by dust or volcanic ash in providing extra amounts of various minerals may play a role in this context and need further attention (Chadwick et al., 1999; Seymour et al., 2014). Particularly the potential role of carbonatitic volcanic ash on the distribution of exchangeable cations could be of interest for future studies in the area, as there are three volcanic centers of in the vicinity of the study region (Pleistocene volcanos Suswa and Shombole and the currently active Ol Doinyo Lengai) exposing carbonatitic eruption phases. Studies in the Serengeti-Mara ecosystem have shown that frequent input of Na- and Ca-rich carbonatitic ash from recent eruptions of Ol Doinyo Lengai volcano has had a strong effect on the distribution of Na and Ca in the topsoils of the Serengeti Plains (Jager, 1982; Murray, 1995; Eckmeier et al., 2020).

SOC variations along both toposequences correlate with vegetation density suggesting coupling between soil carbon storage and total biomass production. This observation is consistent with SOC levels of the entire study area, which strongly correlate with average annual NDVI values (**Figure 4A**). In the southern Kenya Rift, stripes of dense vegetation systematically occur along colluvial sediments deposited adjacent to active normal faults, a phenomena common for tectonic landscapes worldwide as fault zones are often characterized by structurally controlled hydrology and vegetation cover. Footwall sediments adjacent to active fault ridges are likely situated in favorable hydrological conditions as fault zones promote water infiltration and storage, as well as zones of localized water discharge. Therefore, wetlands and other regions of stable vegetation cover are often associated with active fault zones (Forsberg et al., 2000; Reynolds et al., 2011). The correlation between SOC and average NDVI throughout the study area further implies that topsoils in regions of seasonally stable vegetation cover are significantly more effective in building up SOC stocks than regions dominated by dry vegetation and short green vegetation periods during the rainy seasons. Less precipitation or even drought inhibit plant growth and soil

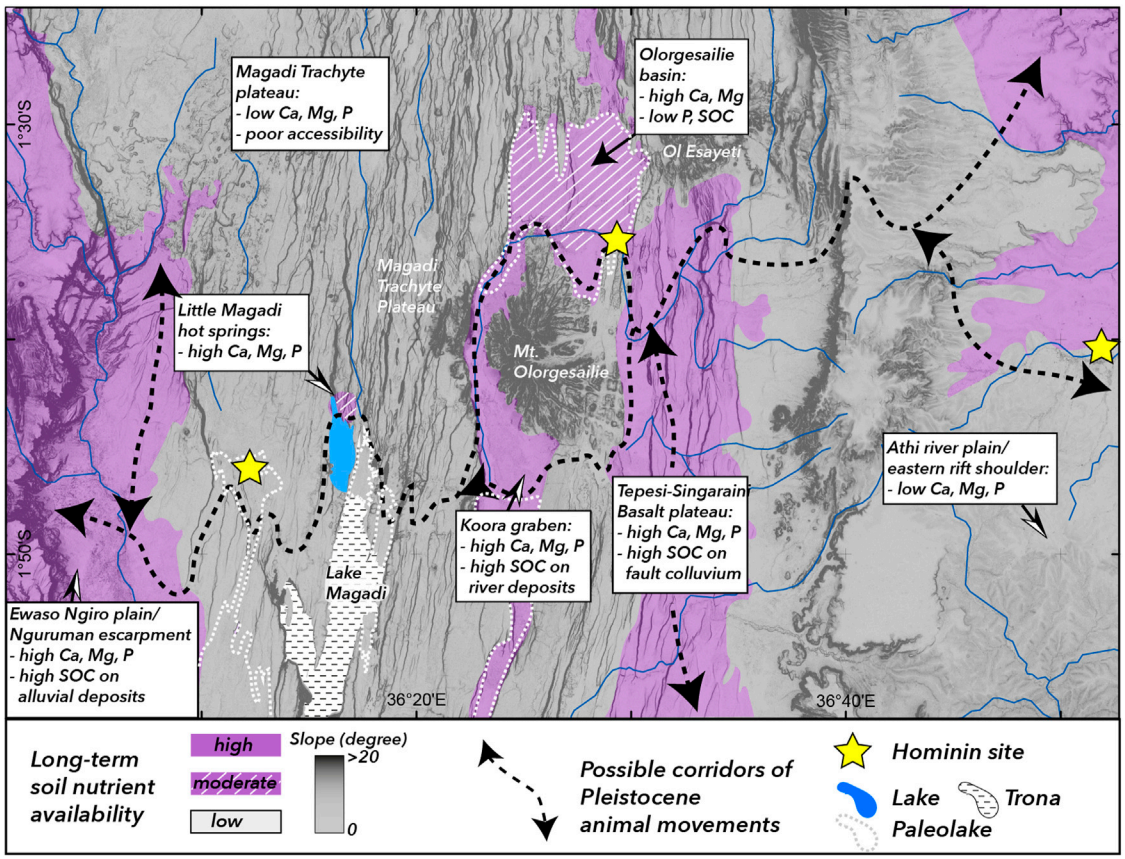

FIGURE 9 | Soil nutritional corridors and Pleistocene human-animal-landscape interactions. Regions colored in gray are characterized by low long-term soil nutrient availability and/or poor accessibility due to topographic barriers such as fault scarps and complex terrain, purple regions represent possible soil nutritional corridors and paleo-migration routes for animal herds that could have been exploited by early hominins. Purple regions with white cross patterns depict regions of moderate nutrient availability (e.g., high Ca, but low P or SOC) potentially representing locations of transitional or short-term grazing. Steep slopes are potential migration barriers in regions of high landscape complexity and are indicated by dark gray shading. Yellow stars indicate locations of hominin fossil sites: (I) Isinya, (L) Lainyamok, (O) Olorgesaile. Potential paleolake extents (dashed white lines) are derived from geological and pealeoenvironmetal datasets (Guth and Wood, 2013; Muiruri, 2017; Owen et al., 2019).

biota activity, which results in lower production of soil organic matter or SOC (e.g., McSherry and Ritchie, 2013).

Soil Nutrients and Hominin-Landscape Interactions

While the importance of soils to influence the growth and annual dynamics of vegetation is well studied in plant ecology and evolution (Kruckeberg, 2004; Rajakaruna and Boyd, 2019), the ability of soil parameters to drive other ecosystem dynamics such animal grazing patterns and human subsistence strategies is less well known. Studies on the mobility of present-day ungulate herds in the Serengeti-Mara ecosystem, in northern Tanzania, have provided first insights in the interplay between the nutrient status of soils on a regional scale and related seasonal movements (McNaughton, 1990; Murray, 1995; Eckmeier et al., 2020). Results of these studies suggest that rock-soil interactions and frequent input of weatherable minerals from volcanism, particularly carbonatitic ash from nearby Ol Doinyo Lengai volcano, as well as spatially limited tectonic activity play a role in driving and maintaining the long-term movement of large animal herds from one nutritional hot spot to another. Regions of high soil nutrient availability represent seasonally stationary grazing areas, while regions of low soil nutrient availability serve as short-term or transitional grazing (Murray, 1995). In contrast to the landscape in the Serengeti-Mara ecosystem, characterized by relatively low relief and - with the exception of the Utimbaru-Isuria fault system (Kabete et al., 2012)–little tectonic activity, the Southern Kenya Rift is highly complex and dominated by the long-term effects of extensional faulting volcanic activity. Wildlife dynamics as responses to soil nutritional gradients in a relatively flat Serengeti-type landscape lead to wide corridors of animal movements distributed over a large region. In complex tectonic landscapes such as the southern Kenya Rift, animal movements are likely channeled through narrow corridors along soil nutritional and/or topographical pathways (King et al., 1994; King and Bailey, 2006; Devès et al., 2014; Kübler et al., 2019). In our study region, during Pleistocene lake-level high stands such migration corridors would have likely lead along narrow strips of exposed lake sediments or

the northern or southern footslopes of Mt. Olorgesailie (**Figure 9**).

In a paleoanthropological context, the study of landscape complexity and related heterogeneity on soil parameters derived from long-term geological processes can serve as proxy for long-term environmental variability–a factor that has been identified as key element in human evolution studies (Potts, 1996; Potts, 1998; Potts, 2013; Potts et al., 2018). Geologically controlled and topographically accessible corridors of reliable vegetation cover and soils high in vital nutrients thus represent potential paleo-migration corridors of grazing animal herds (Devès et al., 2014; Kübler et al., 2015; Kübler et al., 2016) and regions of importance for hominin subsistence strategies and enhanced hominin mobility over long periods of time (**Figure 9**).

The Olorgesailie site is located at a narrow corridor, extending from the Oltepesi plain to the southern Koora Graben, characterized by spatially consistent high Ca-levels and variable P-levels in a wider region deficient of these important macronutrients. The possibility that such conditions can be extended to paleoenvironmental settings depends on the supply of rock-derived nutrients to the Olorgesailie basin and their temporal and spatial variability. The extremely high Ca levels on Legemunge playa and Oltepesi plain at present-day likely result from superficial evapotranspiration processes under semi-arid conditions, potentially combined with periodic eolian input of Ca-rich dust and/or volcanic ash, and would have likely been less pronounced during more humid climate periods. Higher soil moisture contents in the past environment around Olorgesailie site would have had two likely consequences: first, Ca levels in topsoils would have overall been lower and likely closer to those observed at present in the Koora Graben or at higher altitudes; second, fixation of available P through excessive Ca would have been less pronounced, and P levels would have likely been higher in soils. Under moister conditions, the overall coverage of seasonally stable green vegetation would likely be higher than today. Our results on the correlation between SOC and NDVI (**Figure 4**) imply that regions of short green vegetation periods are not well reflected in the topsoil's SOC stocks, we argue that the present-day distribution of topsoil SOC is a not a suitable proxy for past vegetation patterns.

To better understand the changing sources of nutrients for the Olorgesailie site and surrounding region from Mid Pleistocene to present, it is important to take a closer look at the development of the fluvial system supplying the Olorgesailie basin (**Figure 1B**). The Ol Keju Nero river is characterized by a widespread network of different tributaries draining through various different lithological units and therefore provides a wide range of nutrients from various mineral sources. Reconstructions of Mid Pleistocene to recent depositional cycles show that from ~1.2–0.5 Ma BP the Olorgesailie basin was characterized by an extensive lake located north of Mt. Olorgesailie and south-westward drainage by the ancestral Ol Keju Nero river (Isaac, 1977; Behrensmeyer et al., 2018). Sediment input was dominated by transport of volcanic sediments from proximal sources, primarily consisting of Ol Tepesi Basalt and Magadi trachyte ridges surrounding the basin (Behrensmeyer et al., 2018). After 0.5 Ma, a series of tectonic and/or volcanic events (Kübler et al., 2015) led to the disappearance of the extensive lake and incision of Ol Keju Nero river in lacustrine sediments. A northern tributary draining from the northern rift center and northeastern rift shoulder into the basin was established after ~320 ka BP and included sediments from carbonatitic lavas and ash deposits derived from Mt Suswa after ~240 ka BP. The modern course of Ol Keju Nero river with main drainage from the east was established after ~45 ka BP.

Despite the modifications in river networks since the Middle Pleistocene that lead to various changes of the catchment sizes and tributaries draining into Olorgesailie basin (Behrensmeyer et al., 2018), sediments were persistently characterized by a mixture of different volcanic and metamorphic rock sources likely providing a wide range of weatherable minerals to the depositional system. Thus, it is reasonable to assume that soils in the vicinity of Olorgesailie site would have had sufficient soil nutrient levels under different paleoclimatic conditions since the Mid Pleistocene. The location of Olorgesailie site proximal to the lakeshores and reliable soil nutrient levels providing attractive animal grazing grounds has likely promoted the long-term attractiveness of this location for hominin subsistence strategies.

Isinya site is the first Acheulean site excavated in the highlands on the eastern rift shoulder (**Figures 1B**, **9**) and represents in contrast to the long-lived Olorgesailie site a location where only one time period of site inhabitance (>0.96 Ma BP) can be resolved (Durkee and Brown, 2014). The site is located in fluvio-lacustrine deposit at the transition between phonolitic rocks to the south and basaltic rocks to the north (Roche et al., 1988; Guth and Wood, 2013). Given the limited amount of artifacts and relatively short time span of site occupation, reasons for hominin presence at Isinya site is poorly understood. However, the proximity to water as well as workable stones from phonolitic and basaltic sources, and reliable nutrient provision from soils developed on basaltic parent material have likely played a role in hominin inhabitance around Isinya site.

Lainyamok site is located north of Lake Magadi in the densely faulted Magadi trachyte plateau. Unlike at the other two sites, the site likely represents a location of hominin bone deposition from proximal sources through debris flows and redistribution from carnivore activity (Potts et al., 1988). The poor soil nutrient status of the surrounding region would support the interpretation that Lainyamok represents a region promoting short-term or transitional landuse and high hominin mobility between several small-scale nutritional hot spots like the one identified at Little Magadi hot springs (**Figures 1B**, **4A**, **9**) rather than long-term occupation of one location.

In summary, our results show that integrating information from pedological and geological analysis provided additional information to interpret the long-term attractiveness for grazing animals and human subsistence of the southern Kenya Rift with regard to its soil nutritional status.

CONCLUSION

Soil chemical properties in the southern Kenya Rift are strongly variable and controlled by geochemical as well as topographic

factors. SOC is coupled with vegetation density, which in turn is controlled by topography and tectonic activity. Stable vegetation cover in the rift center is predominately fault controlled and occurs along colluvial sediments downslope of active normal faults.

Chemical properties of the parent material represent an important constraint on the distribution of soil nutrients, particularly of Ca, in topsoils. Granitic and trachytic rocks are systematically lower in CaO compared to basaltic rocks sampled in the study region, resulting in low Ca levels in regions dominated by soils developed on felsic and intermediate parent material. Locally enhanced Ca levels in soils proximal to the Little Magadi hot springs represent a striking anomaly compared to the surrounding region possibly results from CO_2 degassing, which suggests that localities of high seismicity and related thermal activity may provide sufficient nutrients for a limited amount of time. Ca levels correlate with hillslope position and are consistently high on colluvial deposits downslope of active faults, suggesting higher CO_2-induced Ca mobilization from the substrate rock through enhanced weathering and/or tectonic degassing (Lee et al., 2016). The potential role of CO_2 in the precipitation of Ca is a novel aspect of our analysis and requires additional systematic studies in the future. Improved knowledge on this process may have implications for other research fields such as ecosystem and agricultural sciences. In contrast to Ca, correlation between lithology, relief and plant available P is less obvious, which implies that P availability is controlled by other factors such as P fixation through Ca in alkaline soils and additional biological and/or eolian P sources.

Known hominin sites in the region are located either along corridors of long-term Ca availability (Olorgesailie, Isinya) or in proximity to short-term nutrient hotspots (Lainyamok) potentially related to active CO_2 degassing along active fault zones. The correlation between locations of hominin activity and the long-term soil nutrient availability in the study region suggests that knowledge of the long-term soil nutrient availability of a region can improve paleoenvironmental and paleoanthropological interpretations related to how hominins have strategically exploited beneficial elements of complex landscapes and provide important information on the interpretation of hominin subsistence strategies. Further, integrated geopedological studies in a paleoanthropological context can become a new tool in discovering hominin fossil sites in other tectonically active regions in the world.

DATA AVAILABILITY STATEMENT

The original contributions presented in the study are included in the article/**Supplementary Material**, further inquiries can be directed to the corresponding author.

AUTHOR CONTRIBUTIONS

SK supervised the project and designed the field study. SK, SR, GK have carried out field sampling and mapping; DA has carried out chemical and microscopic analysis of rock samples; EE has interpreted soil data. SK wrote the manuscript with support from DA and EE. All authors provided critical feedback and helped shape the research, analysis and manuscript.

FUNDING

Research was carried out under a permit (NACOSTI/P/16/8491/7891) by the National Commission for Science, Technology and Innovation of Kenya, and was supported by the European Research Council through ERC Advanced Grant 269686 DISPERSE, granted to GK (IPGP) and G. Bailey (University of York). SK received financial support from a postdoctoral fellowship of the German Science Foundation (DFG grant No. KU 3512/2-1) and provision of high-resolution Satellite data (TanDEM-X mission) from the Helmholtz Alliance EDA. Additional financial support for field work and sample analysis was granted by the Carl Friedrich von Siemens Fellowship from the Alexander von Humboldt Foundation.

ACKNOWLEDGMENTS

We are grateful to Peter Owenga and Maurice Obunga for assistance during field work as well as soil sampling and soil laboratory work, and to Daniel Lohner and Nikolai Rauchberger (University of Munich) for thin section and XRF preparation and technical support.

SUPPLEMENTARY MATERIAL

The Supplementary Material for this article can be found online at: https://www.frontiersin.org/articles/10.3389/feart.2021.611687/full#supplementary-material.

REFERENCES

Abate, A. (1988). Effect of pasture mineral levels on extensive cattle production in Kenya. *Afr. Forage Plant Genet. Resour. Eval. Forage Germplasm Extensive Livestock Prod. Syst.* 449.

Alonso-Zarza, A. M. (2003). Palaeoenvironmental significance of palustrine carbonates and calcretes in the geological record. *Earth-Science Rev.* 60 (3-4), 261–298. doi:10.1016/s0012-8252(02)00106-x

J. M. Anderson and J. S. Ingram (1993). *Tropical soil biology and fertility: a handbook of methods*. Wallingford: CAB International.

Atmaoui, N., and Hollnack, D. (2003). Neotectonics and extension direction of the southern Kenya rift, Lake Magadi area. *Tectonophysics* 364 (1), 71–83. doi:10.1016/s0040-1951(03)00051-9

Aßbichler, D. (2020). *Impact of CO2 on alkali-rich explosive volcanism*. München: lmu.

Baker, B. H., and Mitchell, J. G. (1976). Volcanic stratigraphy and geochronology of the Kedong-Olorgesailie area and the evolution of the South Kenya rift valley. *J. Geol. Soc.* 132 (5), 467–484. doi:10.1144/gsjgs.132.5.0467

Baker, B. H., Williams, L. A. J., Miller, J. A., and Fitch, F. J. (1971). Sequence and geochronology of the Kenya rift volcanics. *Tectonophysics* 11 (3), 191–215. doi:10.1016/0040-1951(71)90030-8

Behrensmeyer, A. K., Potts, R., Deino, A., and Ditchfield, P. (2002). Olorgesailie, Kenya: a million years in the life of a rift basin. *Soc. Sediment. Geology. Spec. Publ. No.* 73, 97–106. doi:10.2110/pec.02.73.0097

Behrensmeyer, A. K., Potts, R., and Deino, A. (2018). The Oltulelei Formation of the southern Kenyan Rift Valley: a chronicle of rapid landscape transformation over the last 500 ky. *GSA Bull.* 130 (9-10), 1474–1492. doi:10.1130/b31853.1

Bern, C. R., Townsend, A. R., and Farmer, G. L. (2005). Unexpected dominance of parent-material strontium in a tropical forest on highly weathered soils. *Ecology* 86 (3), 626–632. doi:10.1890/03-0766

Birt, C., Maguire, P., Khan, M., Thybo, H., Keller, G. R., and Patel, J. (1997). The influence of pre-existing structures on the evolution of the southern Kenya Rift Valley—evidence from seismic and gravity studies. *Tectonophysics* 278 (1-4), 211–242. doi:10.1016/s0040-1951(97)00105-4

Bishop, P. (1995). Drainage rearrangement by river capture, beheading and diversion. *Prog. Phys. Geogr. Earth Environ.* 19 (4), 449–473. doi:10.1177/030913339501900402

Calitri, F., Sommer, M., Norton, K., Temme, A., Brandová, D., Portes, R., et al. (2019). Tracing the temporal evolution of soil redistribution rates in an agricultural landscape using $^{239+}$ ^{240}Pu and ^{10}Be. *Earth Surf. Process. Landforms* 44 (9), 1783–1798. doi:10.1002/esp.4612

Chadwick, K. D., and Asner, G. P. (2016). Tropical soil nutrient distributions determined by biotic and hillslope processes. *Biogeochemistry* 127 (2-3), 273–289. doi:10.1007/s10533-015-0179-z

Chadwick, O. A., Derry, L. A., Vitousek, P. M., Huebert, B. J., and Hedin, L. O. (1999). Changing sources of nutrients during four million years of ecosystem development. *Nature* 397 (6719), 491–497. doi:10.1038/17276

Chorowicz, J. (2005). The east African rift system. *J. Afr. Earth Sci.* 43 (1-3), 379–410. doi:10.1016/j.jafrearsci.2005.07.019

Crossley, R. (1979). The Cenozoic stratigraphy and structure of the western part of the rift valley in southern Kenya. *J. Geol. Soc.* 136 (4), 393–405. doi:10.1144/gsjgs.136.4.0393

D'Alessandro, W. (2006). Human fluorosis related to volcanic activity: a review. *Environ. Toxicol.* 1, 21–30. doi:10.2495/ETOX060031

Davies, T. C. (2013). Geochemical variables as plausible aetiological cofactors in the incidence of some common environmental diseases in Africa. *J. Afr. Earth Sci.* 79, 24–49. doi:10.1016/j.jafrearsci.2012.11.002

Davies, T. (2008). Environmental health impacts of East African rift volcanism. *Environ. Geochem. Health* 30 (4), 325–338. doi:10.1007/s10653-008-9168-7

De Cort, G., Mees, F., Renaut, R. W., Sinnesael, M., Van der Meeren, T., Goderis, S., et al. (2019). Late-Holocene sedimentation and sodium carbonate deposition in hypersaline, alkaline Nasikie Engida, southern Kenya Rift Valley. *J. Paleolimnol* 62 (3), 279–300. doi:10.1007/s10933-019-00092-2

Deino, A. L., Behrensmeyer, A. K., Brooks, A. S., Yellen, J. E., Sharp, W. D., and Potts, R. (2018). Chronology of the acheulean to middle stone age transition in eastern africa. *Science* 360 (6384), 95–98. doi:10.1126/science.aao2216

Devès, M. H., Reynolds, S., King, G. C. P., Küebler, S., Sturdy, D., and Godet, N. (2015). Insights from Earth Sciences into human evolution studies: the example of prehistoric landscape use in africa and the levant. *Comptes Rendus Geosci.* 347 (4), 201–211. doi:10.1016/j.crte.2015.02.012

Devès, M., Sturdy, D., Godet, N., King, G. C., and Bailey, G. N. (2014). Hominin reactions to herbivore distribution in the lower palaeolithic of the southern levant. *Quat. Sci. Rev.*

Dodson, C., and Standing, M. (1994). "Pressure-volume-temperature and solubility relations for natural-gas-water mixtures", in Paper presented at the Drilling and production practice, New York, January 1, 1994 (American Petroleum Institute).

Durkee, H., and Brown, F. H. (2014). Correlation of volcanic ash layers between the early pleistocene acheulean sites of Isinya, kariandusi, and Olorgesailie, Kenya. *J. archaeological Sci.* 49, 510–517. doi:10.1016/j.jas.2014.06.006

D'Allestro, P., and Parente, C. (2015). GIS application for NDVI calculation using Landsat 8 OLI images. *Int. J. Appl. Eng. Res.* 10 (21), 42099–42102.

Eckmeier, E., Kübler, S., Meya, A., and Mathai Rucina, S. (2020). "The role of geology and climate in soil nutrient variability-potential drivers for large ungulate migrations in the Serengeti ecosystem (Northern Tanzania, East Africa)," in EGU General Assembly Conference Abstracts, May 4-8, 2020. 13969.

Eggleton, R. A., Foudoulis, C., and Varkevisser, D. (1987). Weathering of basalt: changes in rock chemistry and mineralogy. *Clays Clay Miner.* 35 (3), 161–169.

Flanagan, F. J. (1969). U.S. Geological Survey standards-II. First compilation of data for the new U.S.G.S. rocks. *Geochimica et Cosmochim. Acta* 33 (1), 81–120. doi:10.1016/0016-7037(69)90094-5

Forsberg, B. R., Hashimoto, Y., Rosenqvist, Å., and Pellon de Miranda, F. (2000). Tectonic fault control of wetland distributions in the Central Amazon revealed by JERS-1 radar imagery. *Quat. Int.* 72 (1), 61–66. doi:10.1016/s1040-6182(00)00021-5

Gachuiri, C., Lukuyu, M., Lusweti, C., and Mwendia, S. W. (2012). Feeding dairy cattle in east Africa," in *East africa dairy development project*. Editors Lukuyu, B., and Gachuiri, C.

Gaciri, S. J., and Davies, T. C. (1993). The occurrence and geochemistry of fluoride in some natural waters of Kenya. *J. Hydrol.* 143 (3), 395–412. doi:10.1016/0022-1694(93)90201-j

Gevera, P., Mouri, H., and Maronga, G. (2019). Occurrence of fluorosis in a population living in a high-fluoride groundwater area: Nakuru area in the Central Kenyan Rift Valley. *Environ. Geochem. Health* 41 (2), 829–840. doi:10.1007/s10653-018-0180-2

Ghiglieri, G., Pittalis, D., Cerri, G., and Oggiano, G. (2012). Hydrogeology and hydrogeochemistry of an alkaline volcanic area: the NE Mt. Meru slope (East African Rift - northern Tanzania). *Hydrol. Earth Syst. Sci.* 16 (2), 529–541. doi:10.5194/hess-16-529-2012

Guth, A., and Wood, J. (2013). *Geological maps of the southern Kenya rift (nairobi, Suswa, Magadi)Michigan technical university. Digital map and chart series DMCH016*. Boulder, Colorado: USGS.

Hahm, W. J., Riebe, C. S., Lukens, C. E., and Araki, S. (2014). Bedrock composition regulates mountain ecosystems and landscape evolution. *Proc. Natl. Acad. Sci. USA* 111 (9), 3338–3343. doi:10.1073/pnas.1315667111

Hemwall, J. B. (1957). The fixation of phosphorus by soils. *Adv. Agron.* 9, 95–112. doi:10.1016/S0065-2113(08)60110-8

Hengl, T., Leenaars, J. G. B., Shepherd, K. D., Walsh, M. G., Heuvelink, G. B. M., Mamo, T., et al. (2017). Soil nutrient maps of Sub-Saharan Africa: assessment of soil nutrient content at 250 m spatial resolution using machine learning. *Nutr. Cycl Agroecosyst* 109 (1), 77–102. doi:10.1007/s10705-017-9870-x

Hermanns, R. L., Niedermann, S., Garcia, A. V., Sosa Gomez, J., and Strecker, M. R. (2001). Neotectonics and catastrophic failure of mountain fronts in the southern intra-Andean Puna Plateau, Argentina. *Geol* 29 (7), 619–622. doi:10.1130/0091-7613(2001)029<0619:nacfom>2.0.co;2

Howard, D. A. (1963). Notes on animal diseases XXIII - mineral deficiency diseases. *East Afr. Agric. For. J.*28 (April), 191–194. doi:10.1080/00128325.1963.11661872

Ibs-von Seht, M., Blumenstein, S., Wagner, R., Hollnack, D., and Wohlenberg, J. (2001). Seismicity, seismotectonics and crustal structure of the southern Kenya Rift-new data from the Lake Magadi area. *Geophys. J. Int.* 146 (2), 439–453. doi:10.1046/j.0956-540x.2001.01464.x

Isaac, G. L. (1977). *Olorgesailie: archaeological studies of a middle Pleistocene lake basin in Kenya*. Chicago: University of Chicago Press.

Jager, T. (1982). *Soils of the Serengeti woodlands, Tanzania*. Dissertation. Pudoc Wageningen.

Junginger, A., and Kübler, S. (2020). "One million years of human-landscape interaction in the Ethiopian and Kenyan rift-system," in EGU General assembly conference abstracts, May 4-8, 2020. 9748.

Kabete, J. M., Groves, D. I., McNaughton, N. J., and Mruma, A. H. (2012). A new tectonic and temporal framework for the Tanzanian Shield: implications for gold metallogeny and undiscovered endowment. *Ore Geology. Rev.* 48, 88–124. doi:10.1016/j.oregeorev.2012.02.009

King, G., Bailey, G., and Sturdy, D. (1994). Active tectonics and human survival strategies. *J. Geophys. Res.* 99 (B10), 20063–20078. doi:10.1029/94jb00280

King, G., and Bailey, G. (2006). Tectonics and human evolution. *Antiquity* 80 (308), 265–286. doi:10.1017/s0003598x00093613

King, G. C. P., and Vita-Finzi, C. (1981). Active folding in the Algerian earthquake of 10 October 1980. *Nature* 292 (5818), 22–26. doi:10.1038/292022a0

Köppen, W. (1900). Versuch einer Klassifikation der Klimate, vorzugsweise nach ihren Beziehungen zur Pflanzenwelt. *Geographische Z.*, 6 (11), 593–611.

Krieger, G., Zink, M., Bachmann, M., Bräutigam, B., Schulze, D., Martone, M., et al. (2013). TanDEM-X: a radar interferometer with two formation-flying satellites. *Acta Astronautica* 89, 83–98. doi:10.1016/j.actaastro.2013.03.008

Kruckeberg, A. R. (2004). *Geology and plant life: the effects of landforms and rock types on plants*. University of Washington Press.

Kübler, S., Owenga, P., Reynolds, S. C., Rucina, S. M., and King, G. C. (2015). Animal movements in the Kenya Rift and evidence for the earliest ambush hunting by hominins. *Sci. Rep.* 5, 14011. doi:10.1038/srep14011

Kübler, S., Rucina, S., Reynolds, S., Owenga, P., Bailey, G., and King, G. (2016). Edaphic and topographic constraints on exploitation of the Central Kenya rift by large mammals and early hominins. *Open Quat.* 2, 5. doi:10.5334/oq.21

Kübler, S., King, G. C., Devès, M. H., Inglis, R. H., and Bailey, G. N. (2019). "Tectonic geomorphology and soil edaphics as controls on animal migrations and human dispersal patterns," in *Geological setting, palaeoenvironment and archaeology of the red sea*. Editors N. M. A. Rasul and I. C. F. Stewart (Cham: Springer), 653–673.

Kübler, S., Bailey, G., Rucina, S., Devès, M., and King, G. C. P. (2020). Rift dynamics and archaeological sites:. *Archaeopress Archaeology*, 42–63. doi:10.2307/j.ctvx5w983.8

Kyuma, R. K., Wahome, R. G., Kinama, J. M., and Waonga, V. O. (2016). Temporal relationship between climate variability, Prosopis juliflora invasion and livestock numbers in the drylands of Magadi, Kenya. *Afr. J. Environ. Sci. Technol.* 10 (4), 129–140. doi:10.5897/ajest2015.2034

Lee, H., Muirhead, J. D., Fischer, T. P., Ebinger, C. J., Kattenhorn, S. A., Sharp, Z. D., et al. (2016). Massive and prolonged deep carbon emissions associated with continental rifting. *Nat. Geosci* 9 (2), 145–149. doi:10.1038/ngeo2622

Li, Y., and Lindstrom, M. J. (2001). Evaluating soil quality-soil redistribution relationship on terraces and steep hillslope. *Soil Sci. Soc. Am. J.* 65 (5), 1500–1508. doi:10.2136/sssaj2001.6551500x

Mage, S. M., and Porder, S. (2013). Parent material and topography determine soil phosphorus status in the Luquillo Mountains of Puerto Rico. *Ecosystems* 16 (2), 284–294. doi:10.1007/s10021-012-9612-5

Margenot, A. J., Singh, B. R., Rao, I. M., and Sommer, R. (2016). "Phosphorus fertilization and management in soils of Sub-Saharan Africa," in *Soil phosphorus* (Boca Raton: CRC Press), 151–208.

Maskall, J., and Thornton, I. (1996). The distribution of trace and major elements in Kenyan soil profiles and implications for wildlife nutrition. *Geol. Soc. Lond. Spec. Publications* 113 (1), 47–62. doi:10.1144/gsl.sp.1996.113.01.05

Mathews, B. W., Sollenberger, L. E., Nair, V. D., and Staples, C. R. (1994). Impact of grazing management on soil nitrogen, phosphorus, potassium, and sulfur distribution. *J. Environ. Qual.* 23 (5), 1006–1013. doi:10.2134/jeq1994.00472425002300050022x

McNaughton, S. J. (1990). Mineral nutrition and seasonal movements of African migratory ungulates. *Nature* 345 (6276), 613–615. doi:10.1038/345613a0

McSherry, M. E., and Ritchie, M. E. (2013). Effects of grazing on grassland soil carbon: a global review. *Glob. Chang Biol.* 19 (5), 1347–1357. doi:10.1111/gcb.12144

Moturi, W. K., Tole, M. P., and Davies, T. C. (2002). The contribution of drinking water towards dental fluorosis: a case study of Njoro Division, Nakuru District, Kenya. *Environ. Geochem. Health* 24 (2), 123–130. doi:10.1023/a:1014204700612

Muiruri, V. M. (2017). Late quaternary diatom and palynomorph stratigraphies and palaeoenvironments of the Koora graben and Lake Magadi basin, Kenya rift valley. Open Access Theses and Dissertations. 461.

Murray, M. G. (1995). Specific nutrient requirements and migration of wildebeest," in *Serengeti II:dynamics, management, and conservation of an ecosystem*. Editors A. R. E. Sinclair and P. Arcese (Chicago: University of Chicago Press), 231–256.

Mworia, J., Dallmeijer, A., and Jacobs, B. (1988). Vegetation and modern pollen rain at Olorgesailie, Kenya. *Utafiti* 1 (1), 1–22.

Olsen, S. R. (1954). *Estimation of available phosphorus in soils by extraction with sodium bicarbonate*. Washington, DC: US Department of Agriculture.

Owen, R. B., Muiruri, V. M., Lowenstein, T. K., Renaut, R. W., Rabideaux, N., Luo, S., et al. (2018a). Progressive aridification in East Africa over the last half million years and implications for human evolution. *Proc. Natl. Acad. Sci. USA* 115 (44), 11174–11179. doi:10.1073/pnas.1801357115

Owen, R. B., Renaut, R. W., and Lowenstein, T. K. (2018b). Spatial and temporal geochemical variability in lacustrine sedimentation in the East African Rift System: evidence from the Kenya Rift and regional analyses. *Sedimentology* 65 (5), 1697–1730. doi:10.1111/sed.12443

Owen, R. B., Renaut, R. W., Muiruri, V. M., Rabideaux, N. M., Lowenstein, T. K., McNulty, E. P., et al. (2019). Quaternary history of the lake Magadi basin, southern Kenya rift: tectonic and climatic controls. *Palaeogeogr. Palaeoclimatol. Palaeoecol.* 518, 97–118.

Pelletier, J. D., and Rasmussen, C. (2009). Quantifying the climatic and tectonic controls on hillslope steepness and erosion rate. *Lithosphere* 1 (2), 73–80. doi:10.1130/l3.1

Porder, S., Asner, G. P., and Vitousek, P. M. (2005). Ground-based and remotely sensed nutrient availability across a tropical landscape. *Proc. Natl. Acad. Sci. USA* 102 (31), 10909–10912. doi:10.1073/pnas.0504929102

Potts, R., Behrensmeyer, A. K., Deino, A., Ditchfield, P., and Clark, J. (2004). Small mid-pleistocene hominin associated with East African acheulean Technology. *Science* 305, 75–78. doi:10.1126/science.1097661

Potts, R., Behrensmeyer, A. K., and Ditchfield, P. (1999). Paleolandscape variation and early pleistocene hominid activities: members 1 and 7, Olorgesailie formation, Kenya. *J. Hum. Evol.* 37, 747–788. doi:10.1006/jhev.1999.0344

Potts, R., Behrensmeyer, A. K., Faith, J. T., Tryon, C. A., Brooks, A. S., Yellen, J. E., et al. (2018). Environmental dynamics during the onset of the middle stone age in eastern africa. *Science* 360 (6384), 86–90. doi:10.1126/science.aao2200

Potts, R. (1989). Olorgesailie: new excavations and findings in Early and Middle Pleistocene contexts, southern Kenya rift valley. *J. Hum. Evol.* 18 (5), 477–484. doi:10.1016/0047-2484(89)90076-6

Potts, R. (1996). Evolution and climate variability. *Science* 273 (5277), 922. doi:10.1126/science.273.5277.922

Potts, R. (1998). Environmental hypotheses of hominin evolution. *Am. J. Phys. Anthropol.* 107 (27), 93–136. doi:10.1002/(sici)1096-8644(1998)107:27+<93::aid-ajpa5>3.0.co;2-x

Potts, R. (2013). Hominin evolution in settings of strong environmental variability. *Quat. Sci. Rev.* 73 (0), 1–13. doi:10.1016/j.quascirev.2013.04.003

Potts, R., Shipman, P., and Ingall, E. (1988). Taphonomy, paleoecology, and hominids of Lainyamok, Kenya. *J. Hum. Evol.* 17 (6), 597–614. doi:10.1016/0047-2484(88)90087-5

Pratt, D. J., Greenway, P. J., and Gwynne, M. D. (1966). A classification of East African rangeland, with an appendix on terminology. *J. Appl. Ecol.* 3, 369–382. doi:10.2307/2401259

Quigley, K. M., Donati, G. L., and Anderson, T. M. (2017). Variation in the soil 'silicon landscape'explains plant silica accumulation across environmental gradients in Serengeti. *Plant and Soil* 410 (1-2), 217–229. doi:10.1007/s11104-016-3000-4

Rajakaruna, N., and Boyd, R. S. (2019). "Edaphic Factor," in *Reference module in earth systems and environmental sciences*. Editor S. A. Elias (Oxford, United Kingdom: Elsevier).

Renaut, R. W., Owen, R. B., Lowenstein, T. K., De Cort, G., Mcnulty, E., Scott, J. J., et al. (2020). The role of hydrothermal fluids in sedimentation in saline alkaline lakes: evidence from Nasikie Engida, Kenya Rift Valley. *Sedimentology* 68 (1), 108–134. doi:10.1111/sed.12778

Reynolds, S. C., Bailey, G., and King, G. C. (2011). Landscapes and their relation to hominin habitats: case studies from Australopithecus sites in eastern and southern Africa. *J. Hum. Evol.* 60, 281–298. doi:10.1016/j.jhevol.2010.10.001

Richardson, A. E., Hocking, P. J., Simpson, R. J., and George, T. S. (2009). Plant mechanisms to optimise access to soil phosphorus. *Crop Pasture Sci.* 60 (2), 124–143. doi:10.1071/cp07125

Roche, H., Brugal, J.-P., Lefevre, D., Ploux, S., and Texier, P.-J. (1988). Isenya: état des recherches sur un nouveau site acheuléen d'Afrique orientale. *Afr. Archaeol Rev.* 6 (1), 27–55. doi:10.1007/bf01117111

Roering, J. J., Kirchner, J. W., and Dietrich, W. E. (2001). Hillslope evolution by nonlinear, slope-dependent transport: steady state morphology and equilibrium adjustment timescales. *J. Geophys. Res.* 106 (B8), 16499–16513. doi:10.1029/2001jb000323

Seymour, C. L., Milewski, A. V., Mills, A. J., Joseph, G. S., Cumming, G. S., Cumming, D. H. M., et al. (2014). Do the large termite mounds of Macrotermes concentrate micronutrients in addition to macronutrients in nutrient-poor African savannas?. *Soil Biol. Biochem.* 68, 95–105. doi:10.1016/j.soilbio.2013.09.022

Shand, C. (2007). "Plant nutrition for food security. A guide for integrated nutrient management," in *Experimental agriculture*. Editors R. N. Roy, A. Finck, G. J. Blair, and H. L. S. Tandon (Rome: Food and Agriculture Organization of the United Nations 2006), 348, 43 (1), 132.

Shipman, P., Potts, R., and Pickford, M. (1983). Lainyamok, a new middle Pleistocene hominid site. *Nature* 306 (5941), 365–368. doi:10.1038/306365a0

Simonson, R. W. (1995). Airborne dust and its significance to soils. *Geoderma* 65 (1-2), 1–43. doi:10.1016/0016-7061(94)00031-5

Sindiga, I. (1984). Land and population problems in kajiado and Narok, Kenya. *Afr. Stud. Rev.* 27 (1), 23–39. doi:10.2307/523948

Sombroek, W. G., Braun, H., and Van der Pouw, B. (1982). *Exploratory soil map and agro-climatic zone map of Kenya,* 1980. *Scale 1: 1,000,000*. Nairobi: Kenya Soil Survey.

Stokes, M., Mather, A. E., Belfoul, A., and Farik, F. (2008). Active and passive tectonic controls for transverse drainage and river gorge development in a collisional mountain belt (Dades Gorges, High Atlas Mountains, Morocco). *Geomorphology* 102 (1), 2–20. doi:10.1016/j.geomorph.2007.06.015

Sturdy, D. A., and Webley, D. P. (1988). Palaeolithic geography: or where are the deer?. *World Archaeology* 19 (3), 262–280. doi:10.1080/00438243.1988.9980041

Sturdy, D., Webley, D., and Bailey, G. (1997). "The palaeolithic geography of Epirus," in *Klithi: palaeolithic settlement and quaternary landscapes in northwest Greece*. Editor G. Bailey (Cambridge: McDonald Institute for Archaeological Research), 2, 587–614.

Tardy, Y. (1997). *Petrology of laterites and tropical soils*. Rotterdam, Netherlands: AA Balkema.

Thornthwaite, C. W. (1948). An approach toward a rational classification of climate. *Geographical Rev.* 38 (1), 55–94. doi:10.2307/210739

Touber, L. (1977). *Soil map of kajiado district (rift valley province, Kenya), current land suitability for extensive cattle range*. Nairobi: National Soil Maps (EUDASM), 24.

Trauth, M. H., Maslin, M. A., Deino, A., and Strecker, M. R. (2005). Late cenozoic moisture history of East Africa. *Science* 309 (5743), 2051–2053. doi:10.1126/science.1112964

Tucker, G. E., and Bras, R. L. (1998). Hillslope processes, drainage density, and landscape morphology. *Water Resour. Res.* 34 (10), 2751–2764. doi:10.1029/98wr01474

Vincens, A., and Casanova, J. (1987). Modern background of Natron-Magadi basin (Tanzania-Kenya) : physiography, climate, hydrology and vegetation. Contexte actuel du bassin Natron-Magadi (Tanzanie-Kenya): physiographie, climat, hydrologie et végétation. *Sci. Geol. Bull. Mem.* 40 (1), 9–21. doi:10.3406/sgeol.1987.1747

Weintraub, S. R., Taylor, P. G., Porder, S., Cleveland, C. C., Asner, G. P., and Townsend, A. R. (2015). Topographic controls on soil nitrogen availability in a lowland tropical forest. *Ecology* 96 (6), 1561–1574. doi:10.1890/14-0834.1

WRB, I. W. G. (2015). *World reference base for soil resources 2014, update 2015: international soil classification system for naming soils and creating legends for soil maps*. Rome: Fao.

Conflict of Interest: The authors declare that the research was conducted in the absence of any commercial or financial relationships that could be construed as a potential conflict of interest.

frontiers in Earth Science

ORIGINAL RESEARCH
published: 20 April 2021
doi: 10.3389/feart.2021.600010

Disentangling Sedimentary Pathways for the Pleniglacial Lower Danube Loess Based on Geochemical Signatures

Stephan Pötter[1], Daniel Veres[1,2], Yunus Baykal[3], Janina J. Nett[1], Philipp Schulte[1], Ulrich Hambach[4] and Frank Lehmkuhl[1]*

[1]Department of Geography, Chair of Physical Geography and Geoecology, RWTH Aachen University, Aachen, Germany, [2]Romanian Academy, Institute of Speleology, Cluj-Napoca, Romania, [3]Department of Earth Sciences, Uppsala University, Uppsala, Sweden, [4]BayCEER and Chair of Geomorphology, University of Bayreuth, Bayreuth, Germany

The source of aeolian sediments such as loess has been investigated since decades. Reliable knowledge on potential dust sources is crucial to understand past climatic and environmental conditions accompanying the dispersal of early modern humans (EMH) into Europe. Provenance studies are usually performed on small sample sets and most established methods are expensive and time-consuming. Here, we present the results of high-resolution geochemical analyses performed on five loess-palaeosol sequences from the Lower Danube Basin (LDB), a region, despite its importance as a trajectory for EMH, largely underrepresented in loess provenance studies. We compare our results with geochemical data of loess-palaeosol sequences from Austria, Hungary, Serbia, and Ukraine. Based on published literature, we thus evaluate five plausible sedimentary pathways for the LDB loess: 1) the Danube alluvium (DA) pathway, which constrains the transport and re-deposition of detrital material by the Danube and its tributaries; 2) the Carpathian Bending (CB) pathway, where sediment is mainly transported from the Cretaceous to Neogene flysch of the Eastern Carpathian Bending; 3) the Eastern Carpathian (EC) pathway, in which sediment is eroded from the flysch of the Outer Eastern Carpathians, transported by rivers, and deflated by northwesterly to westerly winds; 4) the glaciofluvial (GF) pathway, where dust is deflated from glacial outwash plains in nowadays Ukraine, and 5) the Black Sea (BS) pathway, where dust originates from the exposed shelf of the Black Sea. Based on geochemical data, we consider the DA pathway to be the major sediment trajectory for loess in the LDB. Especially the sequences located close to the Danube and the Dobrogea show similarities to sites in Central and Northeast Hungary as well as Northern Serbia. For the northeastern part of the LDB, we demonstrate that dust input is mainly sourced from primary material from the Eastern Carpathians. Mineralogical estimations and geochemical data render the CB pathway as an additional substantial source of detrital material for the loess of this area. We consider the influence of the GF pathway in the LDB as negligible, whereas some minor influences of the BS pathway cannot be ruled out based on geochemical data.

Keywords: loess provenance, aeolian sediments, Southeastern Europe, geochemistry, sedimentary pathways

OPEN ACCESS

Edited by:
Annett Junginger, Department of Geosciences, University of Tubingen, Germany

Reviewed by:
Mingrui Qiang, South China Normal University, China
Roberto Adrián Scasso, University of Buenos Aires, Argentina

****Correspondence:***
Stephan Pötter
stephan.poetter@geo.rwth-aachen.de

Specialty section:
This article was submitted to Quaternary Science, Geomorphology and Paleoenvironment, a section of the journal Frontiers in Earth Science

Received: *28 August 2020*
Accepted: *18 February 2021*
Published: *20 April 2021*

Citation:
Pötter S, Veres D, Baykal Y, Nett JJ, Schulte P, Hambach U and Lehmkuhl F (2021) Disentangling Sedimentary Pathways for the Pleniglacial Lower Danube Loess Based on Geochemical Signatures. Front. Earth Sci. 9:600010. doi: 10.3389/feart.2021.600010

INTRODUCTION

Since the earliest days of loess research, the origin and source of aeolian sediments such as loess have been a matter of debate. Richthofen (1882), a pioneer in loess research, named non-vegetated deserts and desiccated lake beds as potential source areas for loess in China. Throughout the decades, the definition of loess as well as its sources and origin have been subjects of debate in numerous studies (see Smalley et al., 2001; Marković et al., 2016; Sprafke and Obreht, 2016 and references therein). However, most studies agree that the formation of dust (i.e., silt-sized particles) essentially involves a series of sedimentary processes prior to aeolian transport and loess formation (Smalley and Smalley, 1983; Pécsi, 1990; Pye, 1995; Muhs and Bettis, 2003; Badura et al., 2013; Sprafke and Obreht, 2016). The knowledge of the sedimentary pathways, thus the transport chains from the initial production of silt-sized particles to its final deposition and loess formation, is crucial to understand past environmental and climatic systems in varying geographical settings (Muhs, 2018). The reconstruction of atmospheric circulation patterns and climatic gradients is crucial to understand past environmental constraints on the spread of early modern humans (Obreht et al., 2017; Staubwasser et al., 2018), especially in areas which are believed to be important trajectories for their migration into Europe (Anghelinu and Niţă, 2014; Chu, 2018; Fitzsimmons et al., 2020).

The steps involved in dust production can be generalised and summarised in the pathways of desert and glacial loess genesis (Tsoar and Pye, 1987; Wright, 2001; Muhs, 2013; Muhs et al., 2014; Lancaster, 2020 and references therein). The main differences of these two pathways are the processes of dust formation, thus the production of silt-sized particles. Silt-sized particles of desert loess are mainly generated by physical weathering in high altitude areas and desert basins. This mode of genesis is constrained to the margins of drylands in low- to mid-latitudes as well as extreme continental regions (Wright, 2001; Lancaster, 2020). For glacial loess, however, grinding by mountain glaciers and continental ice sheets (CIS) as well as frost shattering of periglacial mountainous areas are the main dust formation processes (Smalley and Smalley, 1983; Smalley et al., 2014). Furthermore, various authors highlighted the general significance of rivers as agents of reworking and storage of silt-sized particles, respectively (Smalley and Leach, 1978; Smalley et al., 2009; Badura et al., 2013; Lehmkuhl et al., 2018a, 2018b). The distinction between dust formation by CIS and processes in the high mountain areas was recently postulated by Li et al. (2020), who differentiated between the continental glacier-river transport (CR) mode and the mountain provenance-river transport (MR) mode of loess genesis.

The two glacial modes of loess genesis can be assumed as the main sedimentary pathways of European loess (**Figure 1**; Li et al., 2020). Loess deposits in northern Central Europe, roughly extending over southern England, France, Germany, Poland, Belarus, and Ukraine, are believed to partially originate from glacially ground material derived from the Fennoscandian and British-Irish ice sheets (Antoine et al., 2009; Skurzyński et al., 2019, 2020; Stevens et al., 2020). In Central and Southeastern Europe, silt particles forming loess deposits were subjected to a multi-step transport, essentially involving river transport of silt particles generated by intensive physical weathering and/or glacial activity in the adjacent mountain ranges (Smalley and Leach, 1978; Buggle et al., 2008; Smalley et al., 2009; Újvári et al., 2012).

However, global models of loess genesis simplify transport processes and atmospheric circulation patterns, which hampers their (supra-) regional application. Regions can be influenced by several dust sources, which correspond to both modes of loess genesis. In Eastern Europe for example, the boundary between the two modes is roughly parallel to the Eastern Carpathians (Smalley et al., 2009; Li et al., 2020; Pańczyk et al., 2020; Skurzyński et al., 2020). Hence, the Lower Danube Basin (LDB) is located near the boundary between these two modes and thus it represents a transitional depositional zone, where a mixing of several potential source areas occurs (Buggle et al., 2008).

Therefore, the aim of this study is to evaluate potential source areas for the loess of the LDB and to refine our understanding of the modes of loess genesis in the region. We hypothesise five possible regional sedimentary pathways that may account for loess formation in the LDB and asses their importance alongside results of high-resolution geochemical analyses of five loess-palaeosol sequences (LPS) distributed throughout the basin. First, geochemical compositions are compared in order to evaluate signatures of each loess-palaeosol sequence that may reflect commonalities and differences in terminal dust sources. The continuous sampling in equidistant intervals allows us to reliably assess shifts in sediment provenance over time. Second, the elemental compositions and respective ratios are compared to loess records from reference regions upstream the Danube in Lower Austria, Central and Northeastern Hungary, and the Vojvodina region in Northern Serbia as well as loess deposits from the shore of the Black Sea in Ukraine. After establishing commonalities and differences of the different loess regions, the results are compared with findings from published provenance studies from the reference regions.

REGIONAL SETTING AND STUDY SITES

The Lower Danube Basin

The LDB is the last depositional segment of the Danube River catchment, spanning between the Iron Gates and the Danube Delta (**Figures 1**, **2**). The Lower Danube drainage basin *sensu stricto* covers large parts of the Transylvanian Basin, most of the Romanian Carpathians as well as the north facing slopes of the Balkan Mountains (**Figure 2**). The LDB *sensu* Jipa (2014), who defined it as a loess sedimentary basin, only covers the lowlands of the Danube Plain (Romanian/Wallachian Plain and Bulgarian Plain, hereafter combined as Danube Plain) as well as the plateau of the Dobrogea. The basin is bounded by the Carpathians to the north and west, the Balkans to the west and south, and opens toward the Black Sea in the east. The Moldavian Plateau adjoins in the northeast (**Figure 2**). The basin is mainly covered by detrital Late Neogene to Pleistocene/Holocene deposits of predominantly marine, fluvial, and aeolian origin (Krézsek and

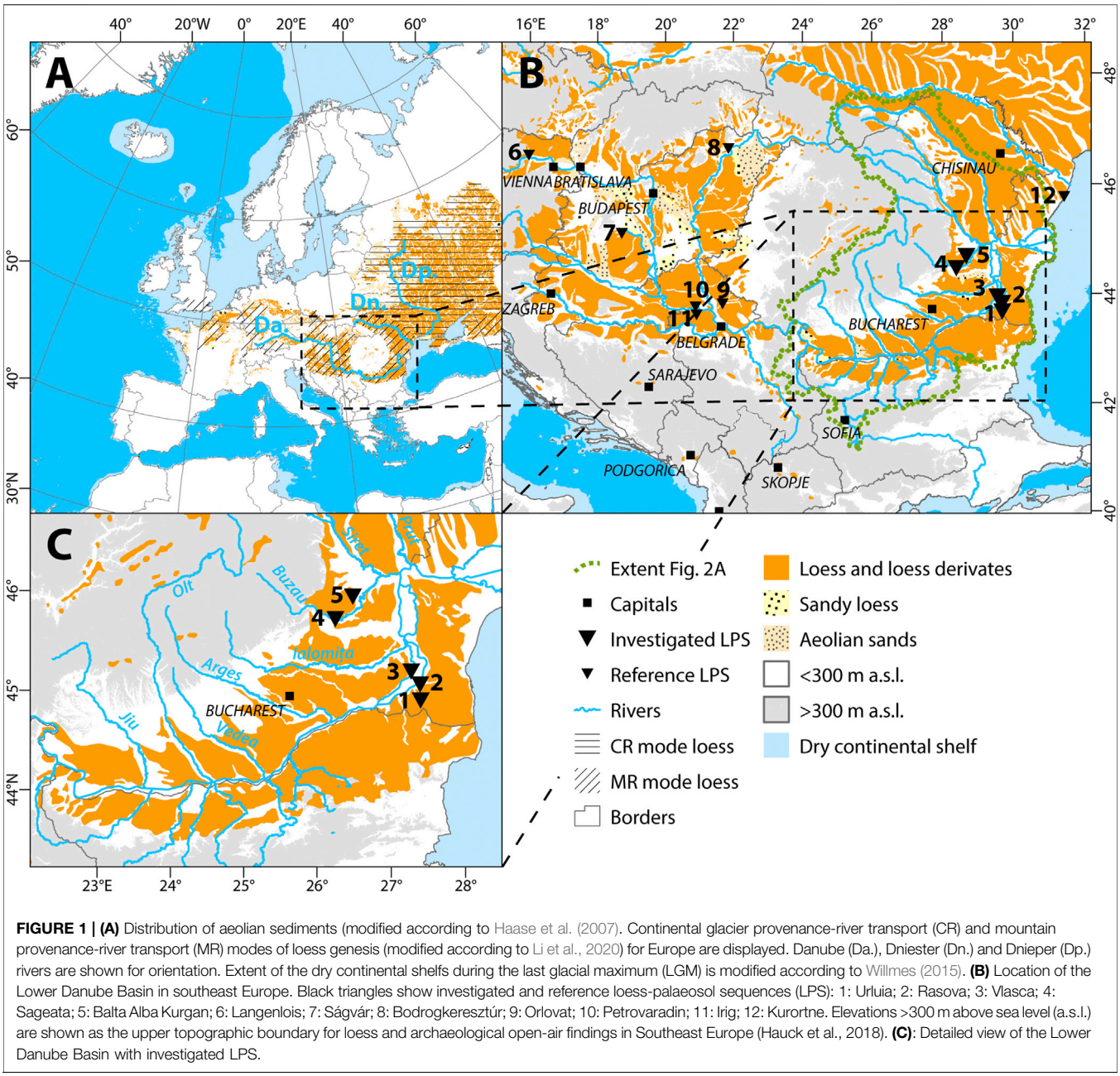

FIGURE 1 | (A) Distribution of aeolian sediments (modified according to Haase et al. (2007). Continental glacier provenance-river transport (CR) and mountain provenance-river transport (MR) modes of loess genesis (modified according to Li et al., 2020) for Europe are displayed. Danube (Da.), Dniester (Dn.) and Dnieper (Dp.) rivers are shown for orientation. Extent of the dry continental shelfs during the last glacial maximum (LGM) is modified according to Willmes (2015). **(B)** Location of the Lower Danube Basin in southeast Europe. Black triangles show investigated and reference loess-palaeosol sequences (LPS): 1: Urluia; 2: Rasova; 3: Vlasca; 4: Sageata; 5: Balta Alba Kurgan; 6: Langenlois; 7: Ságvár; 8: Bodrogkeresztúr; 9: Orlovat; 10: Petrovaradin; 11: Irig; 12: Kurortne. Elevations >300 m above sea level (a.s.l.) are shown as the upper topographic boundary for loess and archaeological open-air findings in Southeast Europe (Hauck et al., 2018). **(C)**: Detailed view of the Lower Danube Basin with investigated LPS.

Olariu, 2021). The aeolian sediments consist of loess, sandy loess, and Pleistocene to Holocene sand dunes, particularly in the western part of the basin, and essentially loess and loess derivates in the central and eastern part (Lehmkuhl et al., 2021).

The loess deposits in the LDB are among the thickest in Europe and laterally continuous over large areas (Haase et al., 2007; Fitzsimmons et al., 2012; Jipa, 2014; Marković et al., 2015). The landscape of the basin is diverse and allows for its division into seven subunits. The Carpathian foothills are intersected by a multitude of Danube tributaries such as Jiu, Olt, Argeş, Ialomiţa, and Buzău (**Figure 1C**). The Bulgarian Plain is characterized by a hilly landscape with short, steep tributaries discharging into the Danube that incises into mainly Mesozoic sediments underlying the Late Neogene to Quaternary mantles of the plain (**Figure 2**; Krézsek and Olariu, 2021). The Wallachian Plain is dominated by a flat topography, gently inclined toward the south. The left-side tributaries of the Danube, draining the Carpathians and their foothills, are sediment laden and show braided river characteristics. Therefore, they intersect the widespread Late Neogene to Quaternary deposits in broad, alluvial valleys, leaving vertical bluffs which often expose thick loess sequences. The topography of the Dobrogea plateau shows many ephemeral valleys, draining the area towards the Danube and the Black Sea. The Moldavian Plateau, which adjoins to the northeast, is dissected by the broad valleys of the Siret and the Prut, large tributaries of the Danube which are

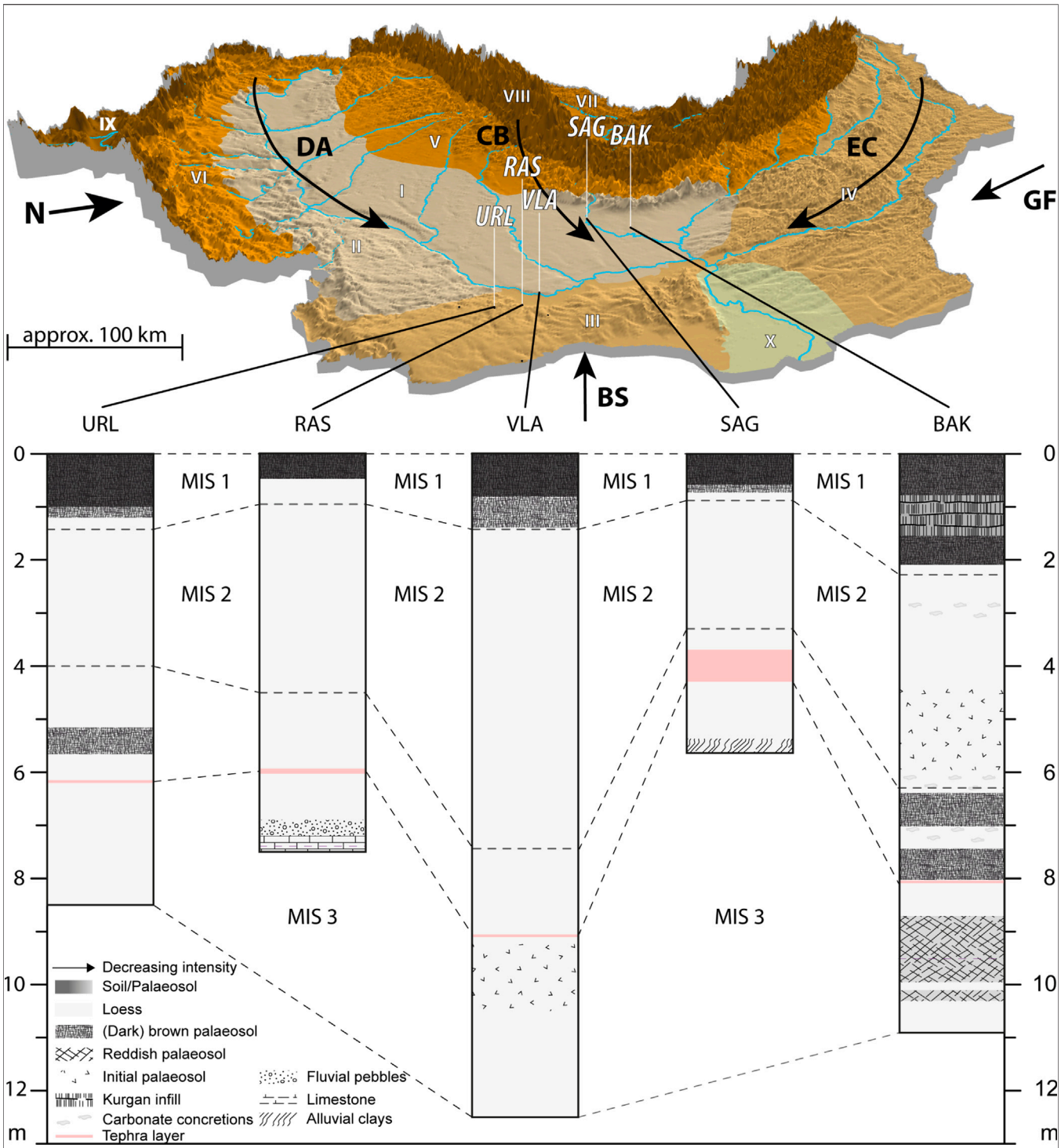

FIGURE 2 | (A) Perspective view of the LDB, looking from the southeast. Extents are indicated in **Figure 1**. Shaded areas indicate landscape units within the LDB: I: Wallachian Plain; II: Bulgarian Plain; III: Dobrogea; IV: Moldavian Plateau; V: Subcarpathians; VI: Pryedbalkans; VII: Transylvanian Basin; VIII: Carpathians; IX: Balkans; X: Danube Delta. Hypothesised sedimentary pathways are shown as black arrows (DA: Danube Alluvium pathway; CB: Carpathian Bending pathway; BS: Black Sea pathway; GF: Glaciofluvial pathway). Note that the scale bar is only accurate in the front part of the figure, due to the perspective view **(B)** Stratigraphic sketches for the investigated sections with correlation scheme.

draining the Eastern Carpathian flysch. Additionally, the plateau is deeply dissected by a dense dendritic network of tributary systems.

Study Sites

The investigated loess sections are located along a south-north transect of the eastern part of the LDB in different geomorphological settings (**Figure 2**).

1) The Urluia (URL) LPS is located in an abandoned limestone quarry on the limestone plateau of the Dobrogea (Fitzsimmons et al., 2013; Fitzsimmons and Hambach, 2014; Obreht et al., 2017). The outcrop preserves five loess-palaeosol couplets reaching to the Middle Pleistocene. In this study, we focus on the uppermost 8.5 m, spanning from Marine Isotope Stage (MIS) 3 to 1. The Campanian Ignimbrite (CI) tephra, which is an important isochron in the area (Fitzsimmons et al., 2013; Veres et al., 2013), can be found in a stratigraphic depth of approximately 6 m at the studied profile. At the sampling site, tephra particles are syn-depositionally mixed into the loess and are exposed in an approx. 10 cm thick characteristic bed (Obreht et al., 2017). The tephra layer is dated in its source region of the Phlegrean Fields in Italy to an age of roughly 39–40 ka (De Vivo et al., 2001; Giaccio et al., 2017). The URL LPS was additionally dated by luminescence dating. The results were incorporated into a correlative age model (Obreht et al., 2017). This age model dates the uppermost 8.5 m of the section to a time span reaching back to ca. 55 ka.
2) The Rasova (RAS) sequence is exposed in a small valley on the right bank of the Dunarea Veche branch of the Danube bordering the Dobrogea to the west. The section is 7.2 m thick and overlies weathered Cretaceous limestone (Zeeden et al., 2018). The CI tephra is found at a depth of around 6 m and was confirmed by geochemical evidence and by luminescence dating (Anechitei-Deacu et al., 2014). The tephra is preserved as a thick bed of pure volcanic ash, with glass shards also incorporated into the overlying loess. Furthermore, the chronology of RAS relies on luminescence dating and a correlative age model (Zeeden et al., 2018) linked to the NGRIP $\delta^{18}O$ record (North Greenland Ice Core Project members, 2004). The resulting age model dates the base of the sequence to ca. 47 ka.
3) The Vlasca (VLA) LPS is exposed at the left bank of the Braţul Borcea branch of the Danube River bordering the Wallachian Plain toward the east (Obreht et al., 2017). The loess bluff has a length of more than 2 km and a height of approx. 30–40 m above the current Danube level. The investigated part of the outcrop, covering MIS 3 to 1, is 12.5 m thick and the CI tephra is situated at a depth of 9.1 m. The tephra is preserved as a lateral continuous bed, several centimetres in thickness. The section was dated by a correlative approach to URL and Greenland ice core data (Obreht et al., 2017), which led to an age model with a maximum age of ca. 44 ka in a depth of 10.72 m. Furthermore, the underlying 1.8 m of the here investigated section were correlated to the published proxy data from URL covering the entire MIS 3 (**Supplementary Material 3**).
4) The section Sageata (SAG) is situated on the left bank of the Buzău River and is 5.5 m thick. The LPS consists of sandy loess sediments and overlies river pond loams, which developed in the floodplain of the Buzău River. A more than 50 cm thick layer of pure ash, assigned to the CI tephra, is intercalated in the sequence. The section was not directly dated yet but correlated to the other LPS records using the CI tephra and the Holocene topsoil as tie points (**Supplementary Material 3**).
5) The Balta Alba Kurgan (BAK) site is situated 1.5 km west of the alkaline Balta Alba lake in the northern Danube Plain. The section is exposed in a road cut opening the edge of a loess plateau. Within the upper 2 m of the section, remains of a Neolithic to Bronze Age tumulus can be found. Below the tumulus, the sequence consists of loess with several intercalated interstadial palaeosols and weakly pedogenically overprinted horizons. The CI tephra lies at a depth of 8.06 m and is preserved as a horizontal bed of patchy tephra lenses. The investigated section is 10.9 m thick. The chronological framework for this section is based on an integrative age model, using luminescence dating, radiocarbon dating as well as (palaeo-) magnetic correlation (Scheidt et al., 2021). The resulting model shows a maximum age of ca. 53 ka at a depth of 9.8 m.

All investigated LPS were correlated using proxy data and their respective age models revealing a set of records covering the timeframe from MIS 3 to MIS 1.

Possible Sedimentary Pathways of the Lower Danube Loess

The loess deposits of the LDB are located in the transitional zone between the East European loess zone and the Caspian-Black Sea loess zone (Stephens et al., 2002). The provenance of the Danube alluvium (DA) in the Lower Danube Basin is diverse, including sediments derived from the upper reaches of the river in Central Europe but also more locally derived material carried by its main tributaries within the basin. The DA is regarded as the main source area for loess deposits within the LDB (Buggle et al., 2008; Jipa, 2014). The Carpathian Bending (CB), narrowly defined here as the flysch area, drained by the Buzău and Ialomiţa rivers consists mainly of Cretaceous and Neogene flysch deposits, as well as unconsolidated but uplifted Pliocene to Quaternary marine to brackish sediments evolving into lacustrine deposits and locally interfingered with fluvial and alluvial fan deposits (e.g, Krézsek and Olariu, 2021 and references therein). The sediment yields of these rivers are among the largest in Europe and their carrying capacities are strongly reduced when entering the basin. Their river flow regime changes from an intra-mountainous, hence erosive, to a depositional fluvial system. These rivers built up large alluvial fan systems and even nowadays show braided river characteristics (Rădoane et al., 2003; Floroiu, 2011). These sedimentary cascades are also influenced by complicated local tectonics (Matenco et al., 2016; Krézsek and

Olariu, 2021). The strong tectonic subsidence in the Lower Danube area, that comprises several km thick Quaternary marine to brackish, lacustrine, and fluvial deposits (Matenco and Andriessen, 2013; Matenco et al., 2016; Krézsek and Olariu, 2021) coupled with uplifting in the Carpathian Bending area (Necea et al., 2013; Krézsek and Olariu, 2021) considerably influence the riverine morphocharacteristics and sediment yield. Thus, the exposed large valley plains act as deflation areas within and in the foreland of the Carpathian Bending area (Jipa, 2014). The third pathway, which similarly to the DA and CB pathways corresponding to the MR mode (Li et al., 2020), is the drainage of the Eastern Carpathians (EC). This mode is mainly fed by eroded Cretaceous and Neogene flysch sediments, as well as widespread unconsolidated fluvial, aeolian, and shallow marine deposits of Late Miocene to Quaternary age covering the Eastern European Platform. These areas are drained by the Danube River system with its tributaries Siret and Prut, as well as the Dniester River that discharges into the Black Sea. This sediment pathway was identified as an important dust source for loess deposits in Poland and (southwestern) Ukraine (Nawrocki et al., 2018; Pańczyk et al., 2020). The glaciofluvial outwash plains of Central and Northern Ukraine pose a major dust source for Ukrainian loess-palaeosol sequences (Nawrocki et al., 2006, 2019; Buggle et al., 2008; Pańczyk et al., 2020). This pathway, hereafter called glaciofluvial (GF) pathway, can be related to the CR mode (Li et al., 2020). Another potential sediment pathway is the dust entrainment from exposed sediments on the shelf of the Black Sea (BS) during low sea level stands. This pathway cannot be directly linked to any loess genesis mode *sensu* Li et al. (2020), since the catchment of the Black Sea between southern Ukraine and Bulgaria covers riverine input from several mode domains, including the DA. For example, the sediment yield of the Danube corresponds to the MR mode, whereas the sediment yield of the Bug, Dnieper, and Don is derived from the CR mode. Since the BS pathway is assumed to be an important dust source area for loess deposits in Bulgaria (Avramov et al., 2006; Jordanova et al., 2007), it is considered as a potential pathway for the LDB loess.

SAMPLING AND LABORATORY ANALYSES

Methodological Background of Loess Provenance Studies

The range of methodological approaches used in loess provenance research is broad. Conceptual research assessed dust sources based on the geographical and geomorphological situation of loess deposits (Smalley and Leach, 1978; Leger, 1990; Smalley et al., 2009; Badura et al., 2013; Lehmkuhl et al., 2016, 2018b) or prevailing atmospheric regimes favoring dust transport and deposition (Antoine et al., 2001, 2009; Vandenberghe et al., 2006). Spatial variability in grain size distributions can be used as a proxy for the distance from the source area (Frazee et al., 1970; Jipa, 2014; Schaetzl et al., 2018). More complex statistical analyses of grain size data, e.g. based on end member models, have been used to unmix grain size distributions and to constrain transport processes, pathways, as well as potential source areas (Prins and Vriend, 2007; Bokhorst et al., 2011; Nottebaum et al., 2015). The imbrication of grains in sediments, recorded by the anisotropy of magnetic susceptibility (AMS) allows the reconstruction of palaeowind directions and thus dust transport pathways (Lagroix and Banerjee, 2002; Nawrocki et al., 2006, 2018; Bradák, 2009; Bradák et al., 2020; Zeeden and Hambach, 2021). Heavy mineral assemblage data can be used to fingerprint loess deposits and compare them to potential source sediments. However, using heavy mineral distribution assemblages as a provenance proxy may bear the drawback of mixing multiple distinct sources (Mikulčić Pavlaković et al., 2011; Römer et al., 2016; Meng et al., 2019; Wolf et al., 2019). Recently, the advent of single-grain provenance techniques such as detrital zircon U-Pb dating allowed disentangling multiple dust sources and potentially sign specific proto-source terranes (Stevens et al., 2010; Újvári et al., 2012; Fenn et al., 2018; Pańczyk et al., 2020). However, the aeolian system is subjected to well-known gravitative distance sorting processes, potentially leading to an over- or underrepresentation of proximal sources, depending on the sample location (Schaetzl et al., 2018).

Loess geochemical provenance proxies circumvent misinterpretations of proximal and distal dust sources by including sedimentary components representative for all grain size classes and mineralogical components (Buggle et al., 2008; Skurzyński et al., 2020). Despite the aforementioned mixing of sources, distinct geochemical differences between loess sequences provide information about the detrital background of the sediment and therefore allow the interpretation of dust sources (Muhs, 2018). Usually, the geochemical compositions of loess deposits are compared to those of potential source areas to determine geochemical commonalities (Buggle et al., 2008; Obreht et al., 2016). Despite methodological limitations (Buggle et al., 2008; Schatz et al., 2015a), geochemical signatures provide a tool which is neither time-consuming nor expensive. Its application has enabled for example to distinguish dust sources of the Chinese Loess Plateau and loess deposits in southern China (Hao et al., 2010) and to exclude local sources for aeolian silt mantles on the Californian Channel Islands (Muhs et al., 2007, 2008). Campodonico et al. (2019) confirmed the dominance of Andean detritus as source material for Pampean loess deposits of Central Argentina, based on bulk geochemical evidence.

Due to its complex formation, loess represents a geological and lithological mixture of its source areas. The different mineralogical components of loess deposits are prone to a multitude of methodological issues and sensible to, e.g., instrumentation or pretreatment of samples (Goff et al., 2020). Differences between different geochemical analysis techniques, such as inductively coupled plasma mass spectrometry (ICP-MS) and x-ray fluorescence analyses (XRF) can account to up to 10% of the measured contents (Miyazaki et al., 2016). To exclude such biases (Demir et al., 2006), we only use XRF data from samples pretreated and measured at the Physical Geography Laboratory of the RWTH Aachen University (Germany).

Sampling

Sampling of all sections was conducted in a continuous sampling line. Before sampling, several decimetres of sediment were removed from the vertical face of the loess wall to avoid

contamination from freshly weathered exposed loess or downslope relocated material. Samples were taken contiguously in 2 cm increments for URL, RAS, VLA, and BAK and in 10 cm increments for SAG. The reference sections discussed in our regional comparison were sampled in 3–10 cm resolution (Table with sampling resolution and number of samples is provided in **Supplementary Table S1**). Sampling was conducted with cleaned tools and samples were packed into sterile plastic bags.

Geochemical Analyses

All samples were analysed by means of an energy dispersive x-ray fluorescence (EDPXRF, hereafter XRF) analysis using a Spectro Xepos. The samples were sieved to the silt fraction (<63 μm) and dried at 105 °C for 12 h. A subsample of 8 g for each sample was mixed with 2 g Fluxana Cereos wax and homogenised in a shaker. The admixture was pressed to a pellet with a pressure of 19.2 MPa for 120 s. The measurements were conducted by means of a pre-calibrated method. Each sample was measured in duplicate and the pellets were rotated by 90° between measurements to avoid matrix effects. The results of every sample were averaged. Conspicuous samples with striking differences between both measurements were remeasured in duplicate to avoid analytical artifacts. Major elements are given in oxide form (%; Na_2O, Al_2O_3, SiO_2, K_2O, TiO_2, Fe_2O_3), whereas trace elements are expressed in mg/kg (V, Cr, Ni, Rb, Sr, Y, Zr, Ba, Th). A similar analytical procedure was applied for all other studies used in this comparison (Obreht et al., 2015; Bösken et al., 2018, 2019; Marković et al., 2020; Tecsa et al., 2020).

The results were visualised in bi- and depth plots to investigate differences and similarities in space and time. To visualise the relations between soluble and insoluble elements and therefore interpret post-depositional alterations of sediments due to weathering, the Al_2O_3-CaO*+Na_2O-K_2O (molar proportions) ternary (A–CN–K) diagram (Nesbitt and Young, 1984) was plotted for the investigated LPS to display commonalities and differences between the sites. CaO* reflects the content of Ca in silicates. The ratio of the total Ca content (CaO) and Na_2O in silicates is assumed to never exceed a value of 1. Therefore, when CaO content is higher than the Na_2O, the siliceous Ca content (CaO*) is set to the content of Na_2O (McLennan, 1993; Buggle et al., 2011).

Grain Size Analyses

For grain size analyses, the samples were dried at 35 °C, sieved to the fine earth fraction (<2 mm), and two subsets of each sample (between 0.1 and 0.3 g) were pretreated with 0.7 ml H_2O_2 (30%) at 70 °C for 12 h. This process was repeated until a bleaching of the material was visible (Allen and Thornley, 2004), but not longer than three days. To keep the particles dispersed during the analysis, samples were treated with 1.25 ml $Na_4P_2O_7$ (0.1 mol*L^{-1}) in an overhead shaker for 12 h. The grain size was determined with a Beckman Coulter LS 13320 laser diffractometer using the Mie-theory (Fluid RI: 1.33, Sample RI: 1.55, Imaginary RI: 0.1; Özer et al., 2010; Nottebaum et al., 2015; Schulte et al., 2016). The results of grain size analyses are visualised as heatmaps. This visualisation allows interpretations of shifts in grain size distributions with depth (Schulte et al., 2016; Schulte and Lehmkuhl, 2018). From each loess sequence, an interval of 30 cm apparently unaffected by post-depositional processes such as weathering or pedogenesis was chosen. These intervals were determined using the grain size distributions and magnetic susceptibility. Over each of these intervals, the average of the mean grain size was calculated as representative for undisturbed loess of the respective section.

Environmental Magnetic Analyses and Correlative Age Model

Samples for environmental magnetic analyses were dried, ground using a porcelain mortar, and packed into plastic boxes. The samples were fixed with cotton wool to avoid movement of particles during transport and measurement. The volumetric magnetic susceptibility was measured at two frequencies (300 and 3,000 Hz) in a static field of 300 mA/m, using a Magnon International VSFM at Bayreuth University (Germany). The results were corrected for drift and the weak diamagnetism of the sample boxes and normalised for density. Environmental magnetic data was used for correlation of the investigated LPS to create a tentative regional age model (**Supplementary Material 3, Figure S1**).

A correlative age model (**Supplementary Material 3, Figure S1**) was established based on published age models for the investigated LPS URL and VLA (Obreht et al., 2017), RAS (Zeeden et al., 2018), and BAK (Scheidt et al., 2021). SAG was correlated based on tephrochronological evidence and trends in magnetic susceptibility. The LPS were correlated on the MIS scale spanning from MIS 3 to 1. To ensure comparability to the reference regions, only (parts of) sections covering the same or comparable time frames were used (Marković et al., 2007, 2020; Obreht et al., 2015; Bösken et al., 2018, 2019; Tecsa et al., 2020; Pötter et al., 2021).

RESULTS

Geochemistry

Within the geochemical data set, the tephra layers show the largest fluctuations in their geochemical composition compared to the surrounding sediments, especially for RAS and SAG (see below). However, to ensure the full integrity of the presented records, the data of the samples affected by the tephra are presented together with other samples, but not included into the discussion. The same applies for samples where volcanic glass shards are incorporated into the sediment in considerable amounts, influencing the geochemical signature noticeably. In the data visualisations, extreme outliers caused by tephra particles are displayed together and additionally marked.

The geochemical compositions of the investigated LPS exhibit broad variations (**Supplementary Table S2**). Mean values for the Na_2O content vary between 0.92% for URL and 1.34% in SAG. The latter shows the highest values within the CI tephra layer (max.: 4.84%). Mean Al_2O_3 contents spread between 10.28% for URL and 12.01% for SAG. BAK shows the highest variability of SiO_2 contents, spanning from 39.84 to 66.72%, with an average of

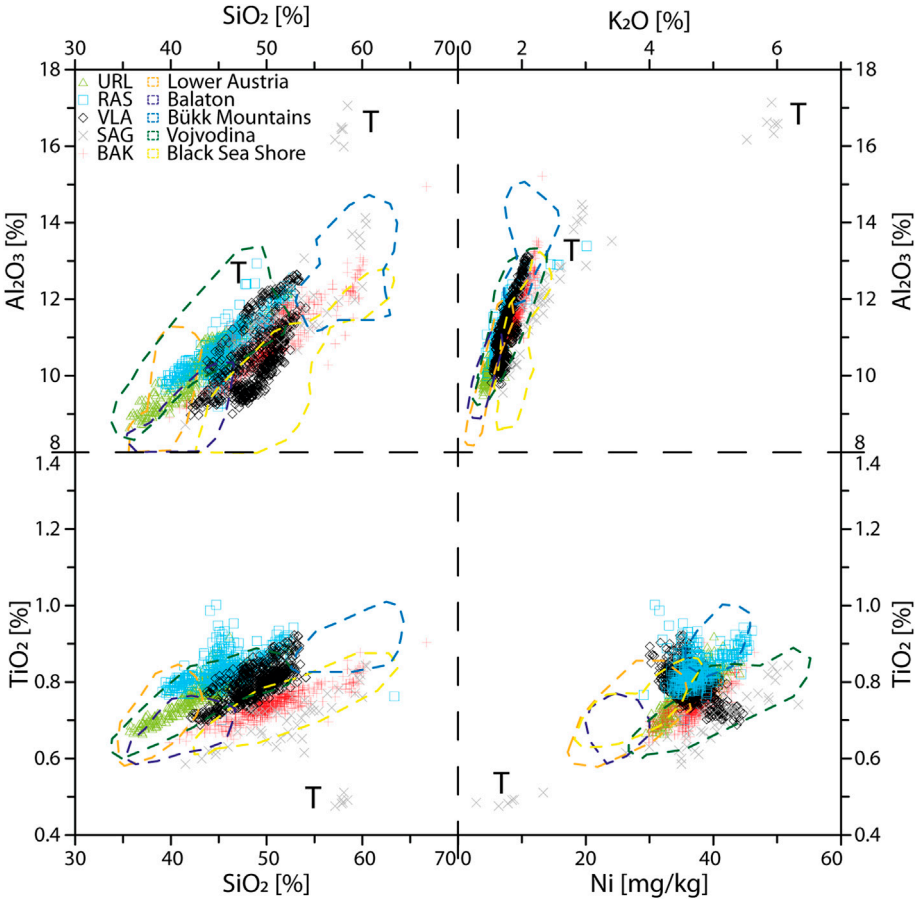

FIGURE 3 | Bi-plots of major element composition for all investigated sections and reference regions. Symbols represent the here investigated loess-palaeosol sequences (Urluia (URL): green; Rasova (RAS): blue; Vlasca (VLA): black; Sageata (SAG): gray; Balta Alba Kurgan (BAK): red. Extreme outliers from the CI tephra layers and mixed loess-tephra samples are indicated by the letter T. The dashed lines show the geochemical composition of the reference regions: Lower Austria = orange; Lake Balaton (Central Hungary) = purple; Bükk Mountains (Northeast Hungary) = blue; Vojvodina = green; Black Sea Shore (Ukraine) = yellow (for location of the reference sections, see **Figure 1**). Note that extreme outliers for the reference regions are excluded.

50.41%. The other sections, with exception of SAG (mean: 52.78%) exhibit lower contents (URL: 43.46%; RAS: 45.61%; VLA: 48.73%). The mean content of K_2O of the southern sites of URL (1.68%), RAS (1.75%), and VLA (1.74%) are generally lower than those of the northern sites of BAK (1.89%) and SAG (2.71%). The high values in SAG again occur in the thick CI tephra bed. TiO_2 values for SAG again show the broadest spread (min.: 0.48%; max.: 0.84%), whereas the mean value (0.68%) is the lowest of the investigated LPS (URL: 0.78%; RAS: 0.83%; VLA: 0.79%; BAK: 0.74%). The range of mean Fe_2O_3 contents of 0.16% for all sections is narrow (VLA: 4.05%; RAS: 4.21%). The trace element compositions as well as the data for the reference section can be found in **Supplementary Table S2**.

The bi-plot visualisations of element contents and ratios show distinct patterns when comparing the investigated LPS. The ratios of major elements (**Figures 3**, **4**) overlap between the sites. This is especially the case in the Al_2O_3/K_2O ratio (**Figure 3**). In this ratio as well as the Al_2O_3/SiO_2 ratio, URL and RAS show very similar trends. Especially URL is characterised by the lowest values for both elements, and the point clouds of both sites are roughly parallel to the diagonal of the plot. VLA shows higher SiO_2 contents compared to URL and RAS, especially in samples with lower Al_2O_3 values. The overlap of these three sites is generally quite large, whereas BAK and SAG are characterised by higher SiO_2, K_2O, and Al_2O_3 contents. The TiO_2 values are depleted for these two sites. For SAG, the CI tephra layer is visible in all major elements with either extremely elevated or depleted values. The TiO_2/Ni plot, adapted from Újvári et al. (2008), shows different trends within the five sites. BAK, SAG, and URL show elongated point clouds with a trend parallel to a positive correlation between Ti and Ni. VLA, however, shows a more circular point cloud with a trend roughly perpendicular to BAK and URL. The pattern of RAS shows both, a circular and a linear component in its pattern.

The Na_2O/Al_2O_3 vs. K_2O/Al_2O_3 diagram shows a large overlap between URL, RAS, VLA, and most of the BAK record (**Figure 4**). The rest of BAK as well as the majority of SAG are shifted toward higher K_2O/Al_2O_3 and lower Na_2O/Al_2O_3 ratios. In RAS and SAG, the CI tephra layer is clearly visible in strongly elevated values. The distinction between the investigated LPS is more evident in the other major element ratios. Especially the SiO_2/TiO_2 vs. K_2O/Al_2O_3

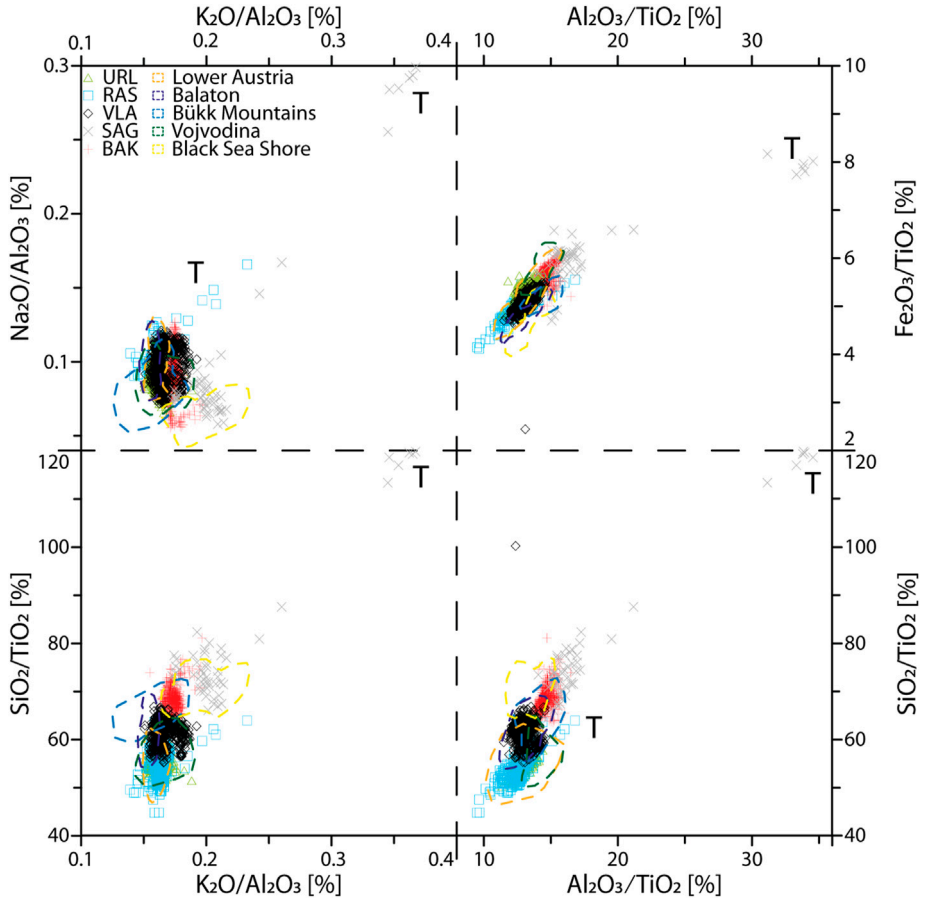

FIGURE 4 | Bi-plots of major element ratios for all investigated sections and reference regions. Legend according to **Figure 3**. Note that extreme outliers for the reference regions are excluded.

diagram shows a clear differentiation between most sites. RAS and URL again are overlapping, whereas VLA is characterised by higher SiO_2/TiO_2 ratios. BAK shows a narrow range, with similar K_2O/Al_2O_3 and elevated SiO_2/TiO_2 ratios. The range of the SAG data, even when the tephra samples are not included, is quite high for both ratios. Whereas the SiO_2/TiO_2 is comparable to BAK, with higher maximum values, the K_2O/Al_2O_3 ratio shows a spread of 0.17 to more than 0.25. The Al_2O_3/TiO_2 and to lesser extent the Fe_2O_3/TiO_2 ratio show a similar pattern.

Trace element compositions vary strongly between the five LPS (**Figure 5**). Whereas URL and VLA overlap in large parts, RAS shows elevated Zr/Ni and Zr/V ratios. The samples from the tephra layer in SAG have, similarly to RAS, extremely high values in these ratios. The loess layers are characterised by depleted values. The Cr/V vs. Y/Ni diagram shows a trend subparallel to the *x*-axis. Here, SAG exhibits the lowest Y/Ni values, but the CI tephra samples again show very high values for VLA, BAK, and SAG compared to the other LPS. With the samples covering the CI tephra excluded, the Cr/V ratios for these three LPS vary between 0.5 and 1.5. RAS and URL show a large spread, from values around 1 to more than 4. The Ba/Sr vs. Rb/Sr diagram depicts an almost linear trend between these two ratios for most of the sample. BAK is slightly shifted toward lower Rb/Sr ratios. SAG, which shows the largest spread in both ratios, also has an almost horizontal trend.

The A–CN–K diagram shows point clouds subparallel to the CN joint for all sections (**Figure 6**). Whereas this is the case for all samples from URL, VLA, and BAK, RAS and SAG have a strong vertical component in their pattern. The point clouds of the respective sections have relative offsets to each other. VLA shows the largest spread on the Al_2O_3 joint, whereas RAS is shifted toward the CN joint, and BAK and especially SAG are shifted toward the K_2O apex. The point clouds of VLA and BAK have very similar starting points trending toward the composition of the upper continental crust (UCC).

Grain Size Analyses

The results of the granulometric analyses for the investigated LPS are depicted in **Figure 7**. All five sites are dominated by strong modes of coarse silt (20–63 μm). However, the five sites show distinguished patterns of grain size distributions. The base of the investigated section at URL is characterised by a distinct mode of coarse silt, with a slightly fining tendency up-section (**Figure 7A**). Between 7 and 6 m below surface (b.s.), the contents of finer

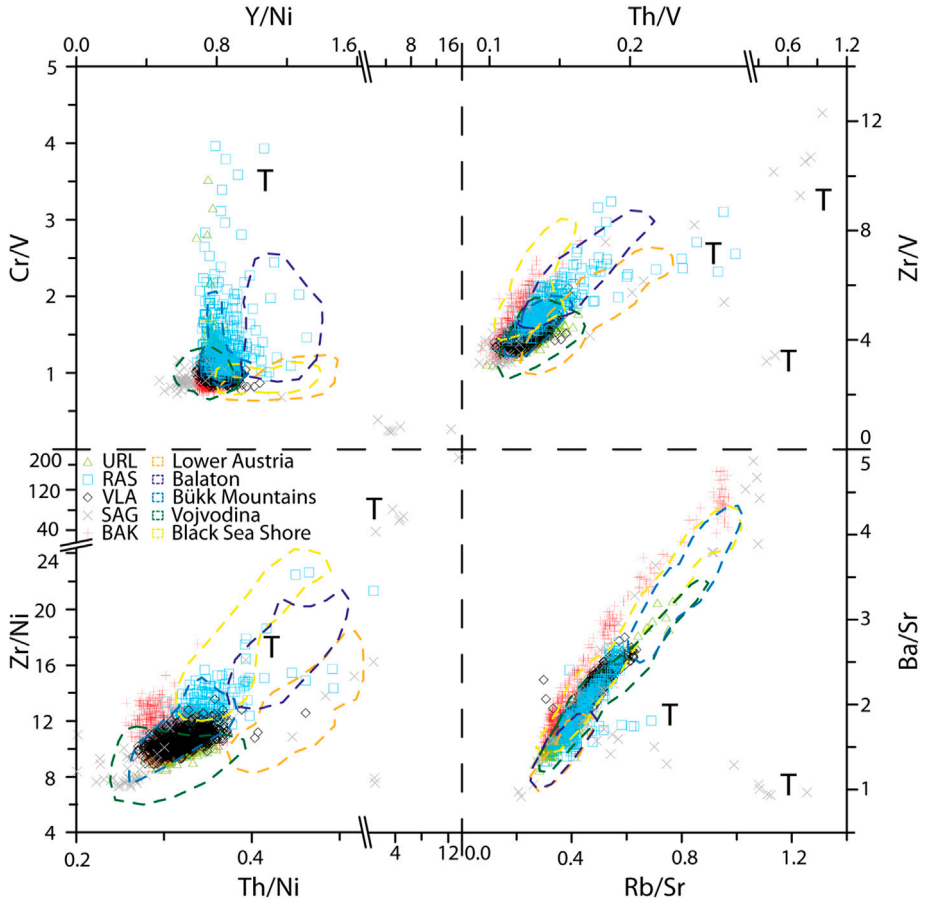

FIGURE 5 | Bi-plots of trace element composition for all investigated sections and reference regions. Legend according to **Figure 3**. Note that extreme outliers for the reference regions are excluded.

particles, particularly fine silt, increase. Around the CI tephra layer (approx. 6 m b.s.), a thin but distinct peak in finer particles occurs. The mode of coarse silt is less well expressed but still visible. Above the tephra, the sediment becomes coarser until 5 m depth and the mode of coarse silt as well as fine sand contents increase. Between 4 and 3 m b.s., two coarser layers with increased amounts of sand occur. Above 3 m, a decreasing trend in grain size can be seen toward the top. Generally, the grain size distributions are well sorted.

RAS generally shows a coarser distribution than URL, as the main mode is between coarse silt and fine sand (**Figure 7B**). The basal part is characterised by a strong mode of these two grain size classes. The CI tephra is clearly visible as a strong distinct peak of coarse grain sizes, with a strong mode in fine sand and increased middle sand contents. Above the tephra, the strong mode continues until a depth of around 5.5 m. Within the 50 cm above, two distinct coarse peaks are visible. Above that, the grain size distribution is well sorted, with a fining trend toward the top. Despite this trend, no major variations are visible.

The mode of coarse silt is also visible in VLA, where the basal part shows high percentages of this class (**Figure 7C**). Between 11.5 m b.s and the CI tephra at a depth of 9.1 m, increased proportions of medium and fine silt occur. The coarse silt mode dominates with increased grain size between 7 and 6 m b.s.. Above that, the distributions remain rather consistent until a depth of around 2 m, where the fine silt and especially the clay contents increase toward the top of the profile. The loess packages with a prominent mode in coarse silt are very well sorted.

The grain size distribution of SAG is very complex (**Figure 7D**). The base of the section, which overlies alluvial loams, shows no clear sorting. Within the thick tephra bed, a prominent mode within the fine sand fraction is visible. This continues above the ash layer, until a depth of around 3.1 m. Between three and 2.5 m b.s., the sediment fines up and shows a mode between coarse silt and fine sand. Above, the sediment is coarser and less well sorted. Between 1.7 and 1 m, the sediment is relatively well sorted and the mode ranges in the coarse silt fraction. Above 1 m b.s., middle clay contents increase.

The mode of the grain size distribution of BAK is from the base to approx. 7 m b.s rather constant, ranging in the coarse silt grain size (**Figure 7E**). Within this package, however, there are four layers of increased clay content as well as a coarser interval. Above that, a slight coarsening of the sediments texture is noticeable, with a more pronounced coarse silt mode. The

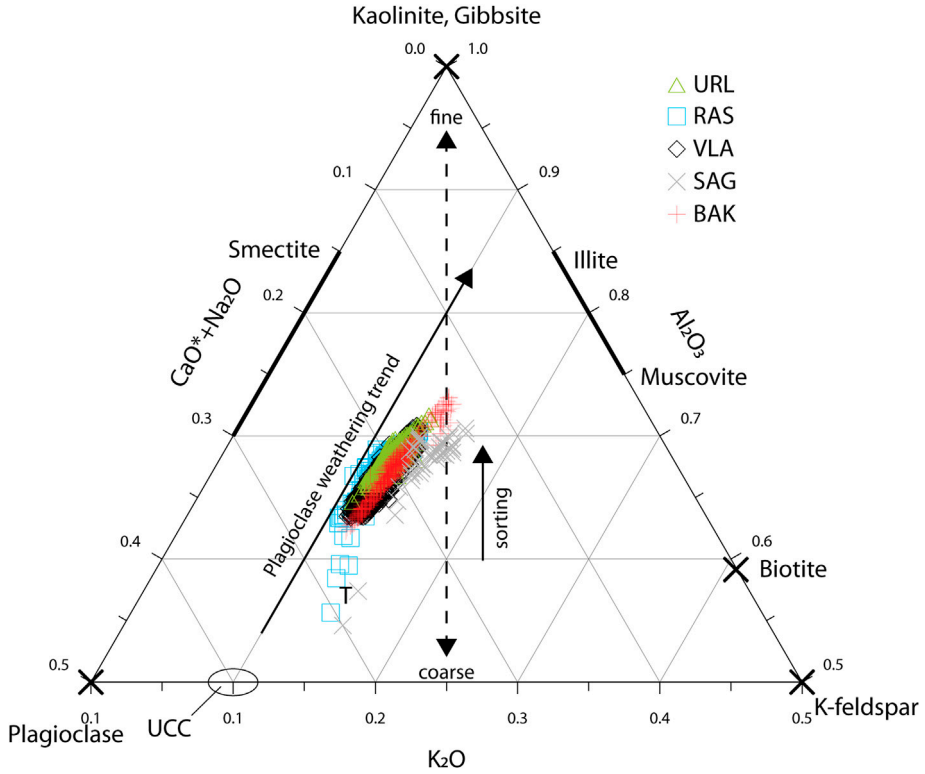

FIGURE 6 | A–CN–K plot for the investigated sections (URL: Urluia; RAS: Rasova; VLA: Vlasca; SAG: Sageata, BAK: Balta Alba Kurgan). Compositions of minerals as well as grain size, weathering and sorting trends are modified according to Buggle et al. (2008). UCC = Upper Continental Crust. Extreme outliers from the CI tephra layers and mixed loess-tephra samples are indicated by the letter T.

sediment is generally very well sorted. Until 4 m b.s., four coarser layers are intercalated. Between 4 and 3 m, a coarsening trend is visible, whereas between 3 and 2 m, the clay content increases. The uppermost 2 m of the profile exhibit a mode of coarse silt to fine sand, with varying clay contents. However, since this is the anthropogenic infill of the kurgan, it is not included in the provenance discussion.

The mean grain size distributions for unaltered loess intervals are shown in **Figure 7F**. The distributions of URL and BAK show almost identical unimodal courses, with a prominent peak in the coarse silt fraction. Both sites also exhibits shoulders in coarse clay, as well as fine sand. The peak in VLA is shifted slightly toward coarser grain sizes, whereas the clay and fine silt contents are lower than in URL and BAK. The mode for RAS lies on the boundary between coarse silt and fine sand, and the content of fine sand is higher than at the other sites. The most complex distribution is found in SAG, where the mode is less expressed and not as narrow as for the other sites. The content of fine sand is considerably higher than, e.g., in BAK. SAG also shows the highest contents of clay, especially in the coarse and middle clay fraction.

DISCUSSION

The Geochemical Imprint of the Campanian Ignimbrite Tephra

Tephra layers alter the chemical composition of the sediment in which they are incorporated (e.g., Obreht et al., 2016). The CI tephra, which is used here as a chronostratigraphic marker horizon (Constantin et al., 2012; Fitzsimmons et al., 2013; Veres et al., 2013; Obreht et al., 2017), leaves a clear geochemical signature compared to the embedding loess. Due to its trachytic characteristics the CI tephra can be identified using geochemical proxies of bulk sediment samples even when present as cryptotephra (see Obreht et al., 2016). The influence of the CI tephra on the geochemical composition of the embedding loess varies strongly between the investigated sections. In BAK and URL, where the CI tephra is only preserved in patchy lenses or mixed with loess, respectively, the geochemical composition of the embedding loess samples seems less affected (e.g., **Figures 8**, **9**). Contrary, for VLA the Zr/V and Zr/Ni ratio for example are increased since the ash layer is preserved as a laterally continuous stratum of several cm thickness (**Figure 10**, **Supplementary Figure S3**). The strongest and most prominent peaks in Zr/V can be seen in RAS (30 cm thick tephra) and SAG, where the tephra bed consists of pure pyroclastic material. Especially in SAG, where the CI tephra is more than 50 cm thick, parts of the layer consist of pure ash beds, which strongly influence the geochemical signal of the analysed samples. Since volcanic glass shards are usually incorporated into subsequently deposited dust (Obreht et al., 2017), the geochemical effects of the tephra can be found even some cm to dm above the actual layer forming a

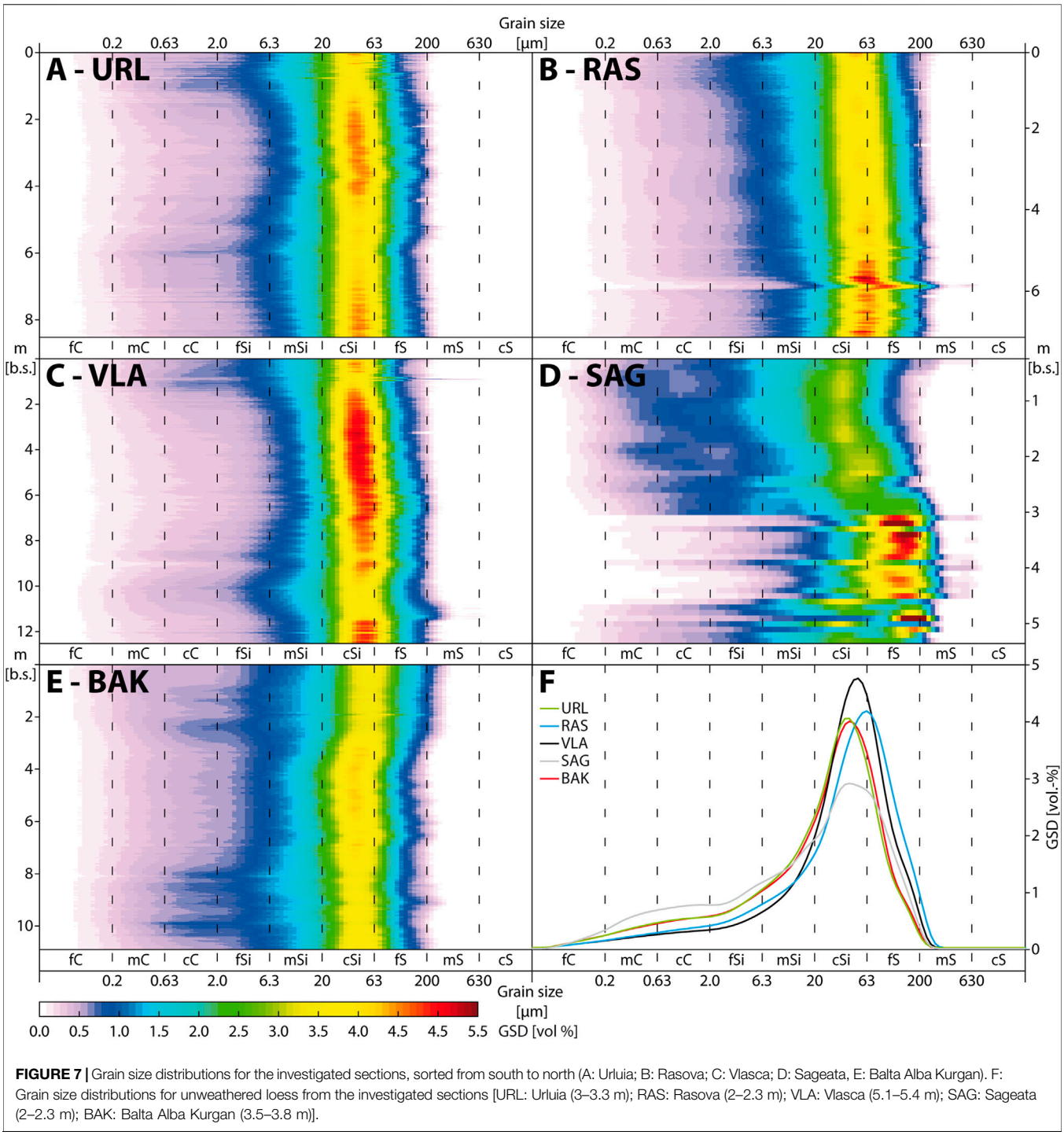

FIGURE 7 | Grain size distributions for the investigated sections, sorted from south to north (A: Urluia; B: Rasova; C: Vlasca; D: Sageata, E: Balta Alba Kurgan). F: Grain size distributions for unweathered loess from the investigated sections [URL: Urluia (3–3.3 m); RAS: Rasova (2–2.3 m); VLA: Vlasca (5.1–5.4 m); SAG: Sageata (2–2.3 m); BAK: Balta Alba Kurgan (3.5–3.8 m)].

gradual transition to the overlying loess. Geochemical proxy data, especially those based on diagnostic elements, can be easily used to detect volcanic material in loess sequences. In the here investigated LPS, the tephra layers show typical characteristics imprinted in the geochemical data. The Al_2O_3/TiO_2 ratio in RAS, e.g., shows a rapid increase at the lower boundary of the tephra and a gentle decline toward the above-lying loess, indicating incorporation of volcanic glass shards into the sediment. In other localities, such as BAK where the tephra is preserved as a patchy layer, the geochemical influences up-profile of the tephra are reduced (**Figure 10**). However, these large variations originating from the volcanic ash, both in samples of pure ash beds as well as varying amounts of glass shards in the sediment, cannot be interpreted as true loess provenance signals but must be kept in mind when discussing transport pathways of contemporaneous dust deposition.

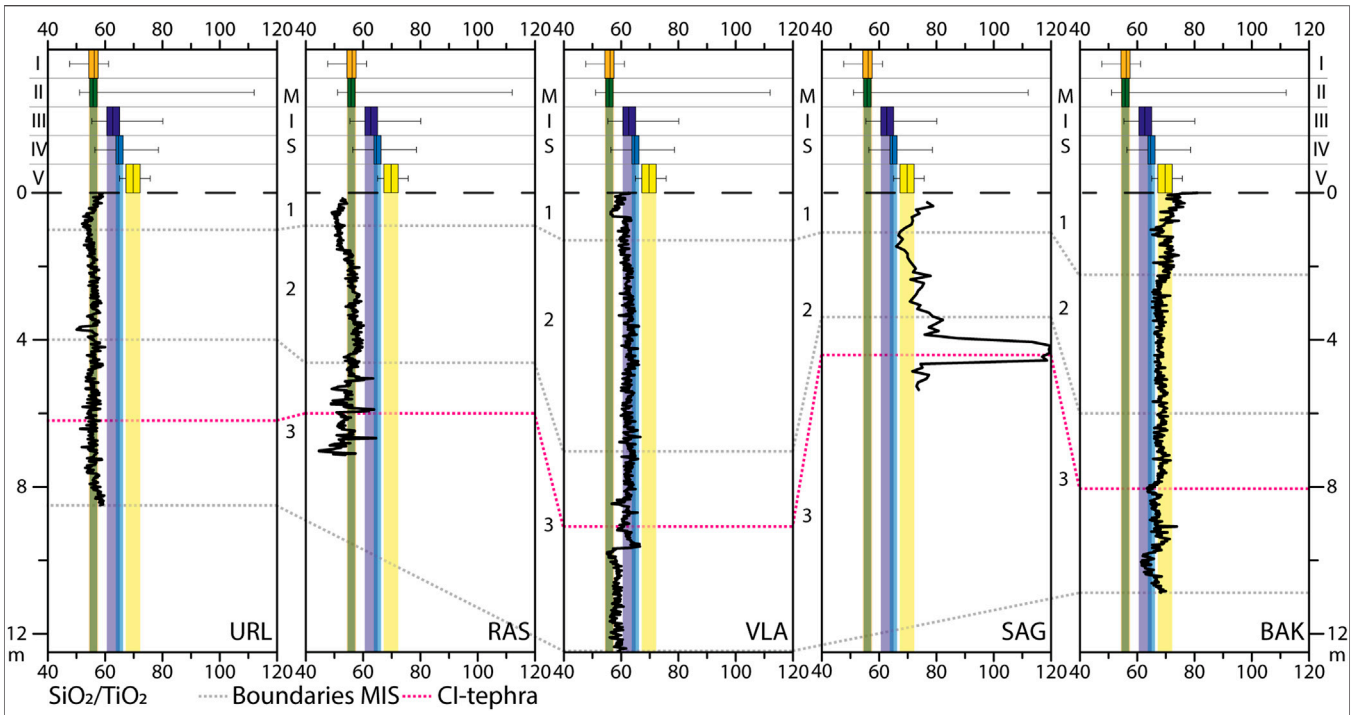

FIGURE 8 | Depth variations of the SiO_2/TiO_2 ratios for the investigated loess-palaeosol sequences, sorted from south to north (URL: Urluia; RAS: Rasova; VLA: Vlasca; SAG: Sageata, BAK: Balta Alba Kurgan). The box-whisker plots on top show the composition of the sections from the reference regions: I: Lower Austria; II: Vojvodina; III: Balaton (Central Hungary); IV: Bükk Mountains (Northeast Hungary) and V: Black Sea Shore (Ukraine). The interquartile area (between 25 and 75% quartile) are shown as shaded boxes. The correlative age model as well as the CI tephra are shown for temporal comparison.

Geochemical Signature and Mineralogical Composition of the Lower Danube Loess

Some mineralogical approximations can be made based on loess geochemical data (Muhs, 2018). Generally high SiO_2 contents show the predominance of quartz in the mineralogical composition of all five LPS. The varying contents, both between and within the LPS, are mainly governed by differences in the mineralogical compositions and grain size distributions (**Figure 8**, **Supplementary Figure S2**). The clear positive relationship between Al_2O_3 and SiO_2 (**Figure 3**) indicates the presence of aluminosilicates such as mica or feldspars in all LPS investigated here. This is supported by the positive relation between Al_2O_3 and K_2O, which suggests that the aluminum content is mainly bound to phyllosilicates or K-feldspars. The presence of Ti-bearing phyllosilicates is also supported by the weak positive correlation between Ti and Ni (Újvári et al., 2008), since Ni tends to be enriched in these minerals. This is, to varying degrees, visible in all sections (**Figure 3**).

The A–CN–K ternary diagram developed by Nesbitt and Young (1984) has been widely applied to LPS from varying environments to investigate influences of chemical weathering and mineralogical compositions on the geochemical composition of sediments (e.g., Yang et al., 2004; Schatz et al., 2015b; Vlaminck et al., 2018; Skurzyński et al., 2019). All investigated LPS show a trend of plagioclase weathering (**Figure 6**). This trend indicates a rather stable ratio of K-feldspar and albite for most of the samples. The (sub-) parallel point clouds of especially URL is characteristic for loess deposits of the Dobrogea, such as the Mircea Voda (Buggle et al., 2008) or the Costinești LPS (Tugulan et al., 2016). The shifts of BAK and especially SAG toward the right edge of the plot indicates either increased feldspar weathering or different mineralogical composition of source areas compared to the other sites (Vlaminck et al., 2018). In the latter case, it can be interpreted to reflect more K-feldspar rich parent material (Újvári et al., 2008). The abundance of K-bearing minerals, such as K-feldspars, muscovite, or illite is indicated for all sections by the shift toward the K-apex in the A–CN–K ternary diagram (**Figure 6**) and a strong correlation between the Rb/Sr and Ba/Sr ratio (**Figure 5**; Újvári et al., 2008). High Ba/Sr ratios also show the presence of plagioclase, as indicated by the A–CN–K plot. However, the shifts of SAG and BAK toward higher Rb/Sr and Ba/Sr values, as well as their extreme values, can be interpreted as Sr depletion due to leaching processes during soil formation (Újvári et al., 2008).

The geochemical and mineralogical compositions of loess and palaeosols is not solely determined by the composition of the parent material. In subaerial deposits such as loess, post-depositional processes including weathering or pedogenesis frequently alter the material's geochemical composition (Vlaminck et al., 2018; Bösken et al., 2019; Skurzyński et al., 2020). As seen in the A–CN–K plot (**Figure 6**), the majority of the samples show a discernible plagioclase weathering trend.

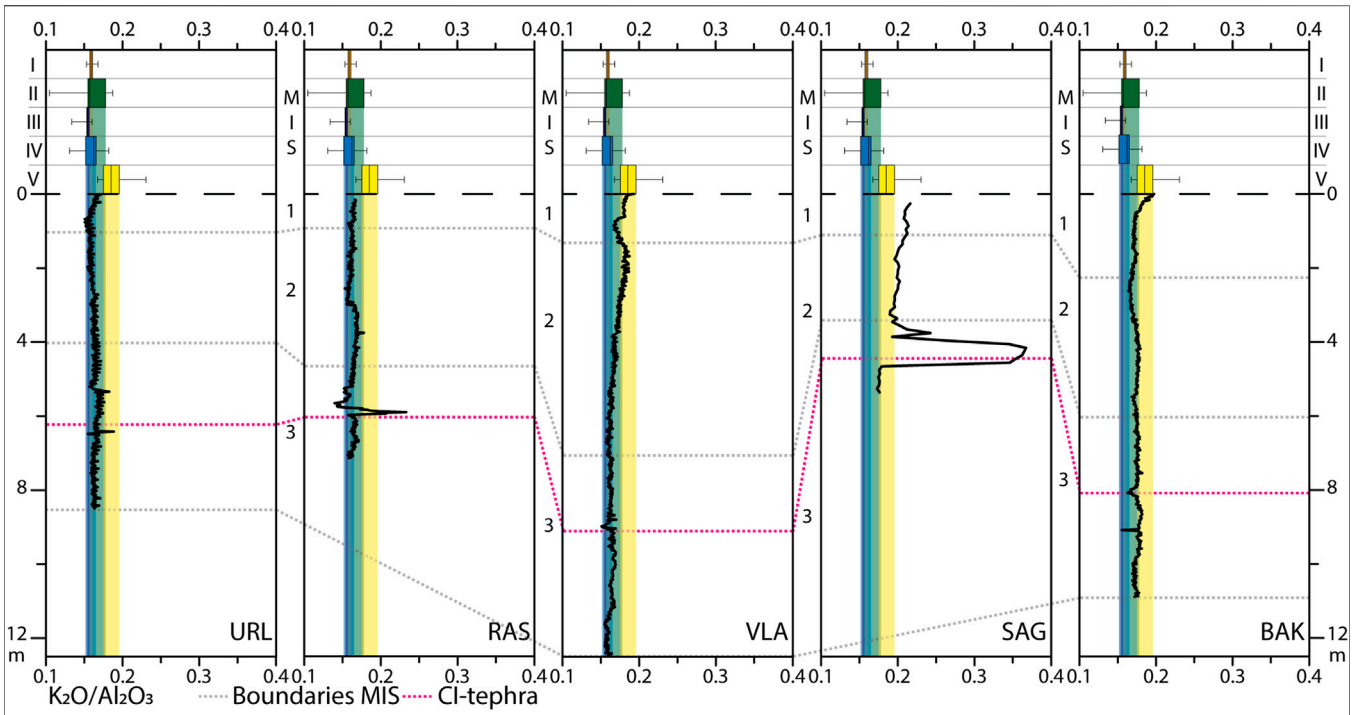

FIGURE 9 | Depth variations of the K_2O/Al_2O_3 ratios for the investigated loess-palaeosol sequences, sorted from south to north (URL: Urluia; RAS: Rasova; VLA: Vlasca; SAG: Sageata, BAK: Balta Alba Kurgan). The box-whisker plots on top show the composition of the sections from the reference regions: I: Lower Austria; II: Vojvodina; III: Balaton (Central Hungary); IV: Bükk Mountains (Northeast Hungary) and V: Black Sea Shore (Ukraine). The interquartile area (between 25 and 75% quartile) are shown as shaded boxes. The correlative age model as well as the CI tephra are shown for temporal comparison.

Especially soluble or easily weathered compounds and minerals are prone to depletion by leaching. The Ba/Sr and the Rb/Sr ratios, e.g., are used in loess research as weathering indices, since Sr is easily leached during carbonate dissolution while Ba and Rb are rather immobile elements, which are relatively enriched during leaching (Chen et al., 1999; Buggle et al., 2011). When discussing loess provenance based on geochemistry, palaeosol samples are often excluded to overcome issues of geochemical alteration during pedogenesis (Buggle et al., 2008; Újvári et al., 2008; Schatz et al., 2015a). However, a clear distinction between loess, pedogenically overprinted loess and fully developed palaeosols is not always straightforward in semi-arid environments. Therefore, we included all samples and plotted provenance proxies as depth functions to complement the bi-plot visualisations. In these plots (**Figures 8–13**), data from the reference regions are displayed as box-whisker plots on top of the graphs. The interquartile ranges are indicated as shaded boxes of the respective color in the depth plots. The effects of solution and weathering can be seen in a variety of element contents and ratios. The Na_2O/Al_2O_3 ratio is depleted in the recent topsoil at URL, VLA, and BAK, and increased and/or constant in the loess intervals (**Supplementary Figure S4**). Post-depositional alterations by weathering or pedogenesis are also expressed by the (neo-)formation of (aluminous) clay minerals or iron oxides. As the former may lead to a relative enhancement of aluminum oxides (**Figure 11**, **Supplementary Figure S2**), the latter leads to an increase in iron contents in the affected sediment (**Figure 12**). Since the formation if these minerals is usually linked to pedogenesis, the elevated Al and Fe contents can be related to the clay content (**Supplementary Figure S2**). The Al_2O_3/TiO_2 ratio plotted as a depth function (**Figure 11**) as well as the direct comparison between the Al content and the grain size (**Supplementary Figure S2**) reflects this issue and must therefore be carefully discussed. Shifts in these ratios, such as those observed below the CI tephra in VLA, cannot be interpreted as provenance signal as they are of post-depositional nature.

Since trace elements such as Ni and V are compatible elements within igneous systems, they can be used as indicators for the provenance of rocks and sediments (Újvári et al., 2014; Obreht et al., 2016). Ratios based on these trace elements reveal striking similarities between URL and VLA (**Figures 3**, **5**). RAS shows large overlaps with the two sites in, e.g., the Th/Ni or Th/V ratios (**Figure 5**). However, the Zr based provenance ratios vary substantially between those sites. These differences can be explained by the enrichment of zircon minerals in RAS; in detrital sediments Zr is almost entirely bound to zircons. These heavy minerals can be enriched in loess by selective deflation of less dense particles. This so-called hydraulic sorting (Malusà et al., 2016) causes enrichment of zircons which in turn leads to elevated Zr contents in the geochemical screening of such samples. Therefore, the elevated Zr/Ni and Zr/V ratios can be interpreted as an indicator of sorting processes (**Figure 5**; Újvári et al., 2008).

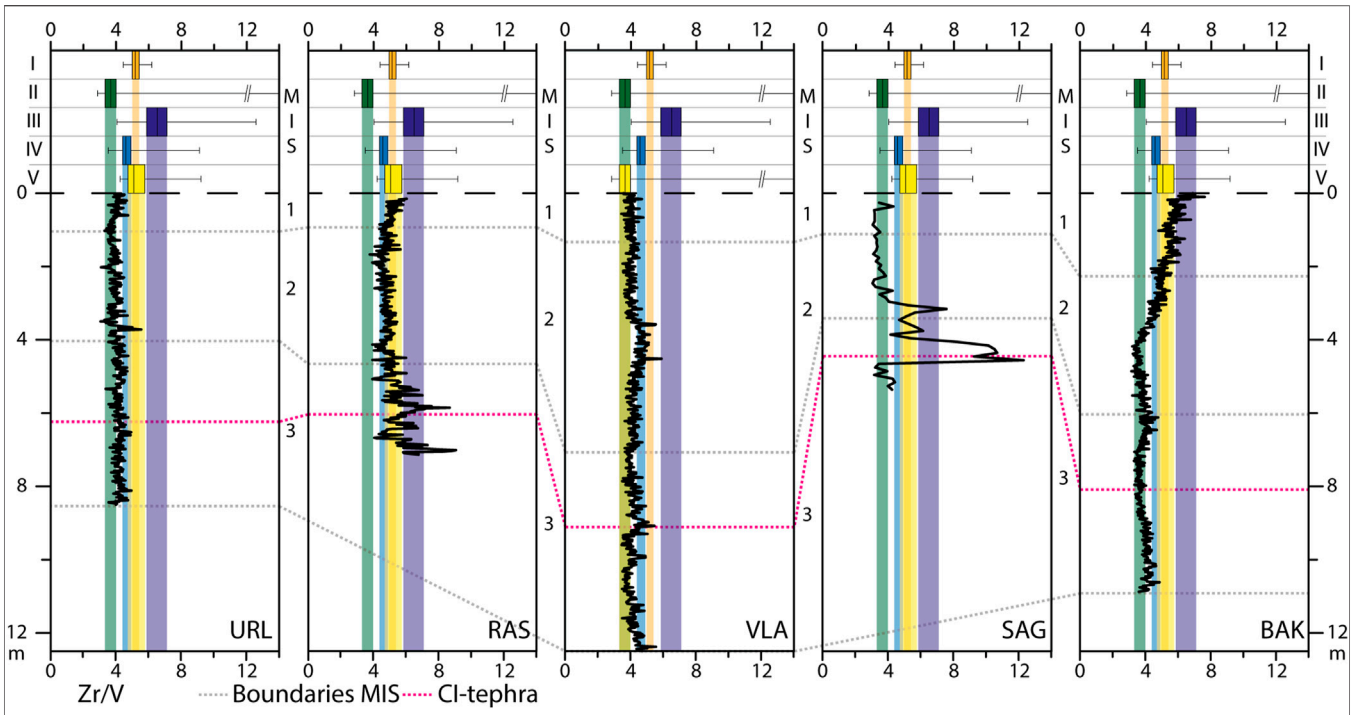

FIGURE 10 | Depth variations of the Zr/V ratios for the investigated loess-palaeosol sequences, sorted from south to north (URL: Urluia; RAS: Rasova; VLA: Vlasca; SAG: Sageata, BAK: Balta Alba Kurgan). The box-whisker plots on top show the composition of the sections from the reference regions: I: Lower Austria; II: Vojvodina; III: Balaton (Central Hungary); IV: Bükk Mountains (Northeast Hungary) and V: Black Sea Shore (Ukraine). The interquartile area (between 25 and 75% quartile) are shown as shaded boxes. The correlative age model as well as the CI tephra are shown for temporal comparison.

The hydraulic sorting of minerals by water or air not only affects the trace element geochemistry, such as the Zr content of loess deposits, but is also expressed in other geochemical proxies (Ohta, 2004). The position and the shape of the point cloud of a sample set in the A–CN–K plot can be indicative for such sorting processes. Due to the abundance of Al in aluminous clay minerals, finer, often weathered sediments tend to plot close to the Al_2O_3 apex of the diagram, whereas coarser sediments show a contrary trend (Nesbitt and Young, 1996; Nesbitt et al., 1996). When the grain size differences within a LPS are solely driven by (plagioclase) weathering, point clouds plot (sub-) parallel to the CaO*–Na_2O join (see Vlaminck et al., 2018; Bösken et al., 2019; Skurzyński et al., 2019). However, when hydraulic sorting skews the grain size distribution, point clouds in the A–CN–K plot tend to develop (sub-)vertical shapes, trending toward the Al_2O_3 apex (Ohta, 2004; Buggle et al., 2008). For BAK and URL, the point clouds sub-parallel to the CaO*–Na_2O join indicate no major influence of hydraulic sorting processes. VLA shows a similar pattern, but the point cloud shows a slightly stronger vertical component (**Figure 6**). The strongest evidence for sorting processes can be found in RAS and SAG, with strong vertical components. The direct vicinity of RAS and SAG to the recent courses of the Danube and the Buzău might be the main reason for these sorting processes. The high intensity of these processes in RAS can be explained by enhanced fluvial activity of small Danube tributaries acting as dust sources, as this section is exposed in the recent dry valley of such a tributary and its base shows a sharp fluvial erosional contact (Zeeden et al., 2018). The pre-aeolian setting is therefore fluvial as it is in SAG. This section lies on top of alluvial loams, which were presumably deposited in river ponds in the floodplain of the palaeo-Buzău. Therefore, the general high fluvial activity strongly influenced the formation of these loess deposits during the Late Pleistocene. The alluvial deposits near the sites of RAS and SAG, and to a lesser extent of VLA, acted as local sources for coarse material deposited in direct vicinity while finer particles were transported over longer distances. The grain size distributions also reflect these processes, since the three sites show generally coarser distributions than URL and BAK (**Figure 7**).

Generally, the investigated LPS show striking similarities in some of the presented provenance proxies. Especially the sites from the Dobrogea, URL and RAS, show significant common variabilities, indicating geochemically similar parent material as expressed in the Cr/V ratios (**Figures 5**, **13**). This ratio serves as a good indicator for the contributions of detrital material derived from mafic to ultramafic rocks since Cr is almost entirely bound to mafic strata (Zimmermann and Bahlburg, 2003; Mikes et al., 2006; Újvári et al., 2008). For the other sites, the values of this ratio are in a rather narrow spectrum without large variations. However, data from URL and RAS exhibit large scatter of this ratio with maximum values of >4. This feature is in accordance with elevated Cr contents compared to the UCC established in

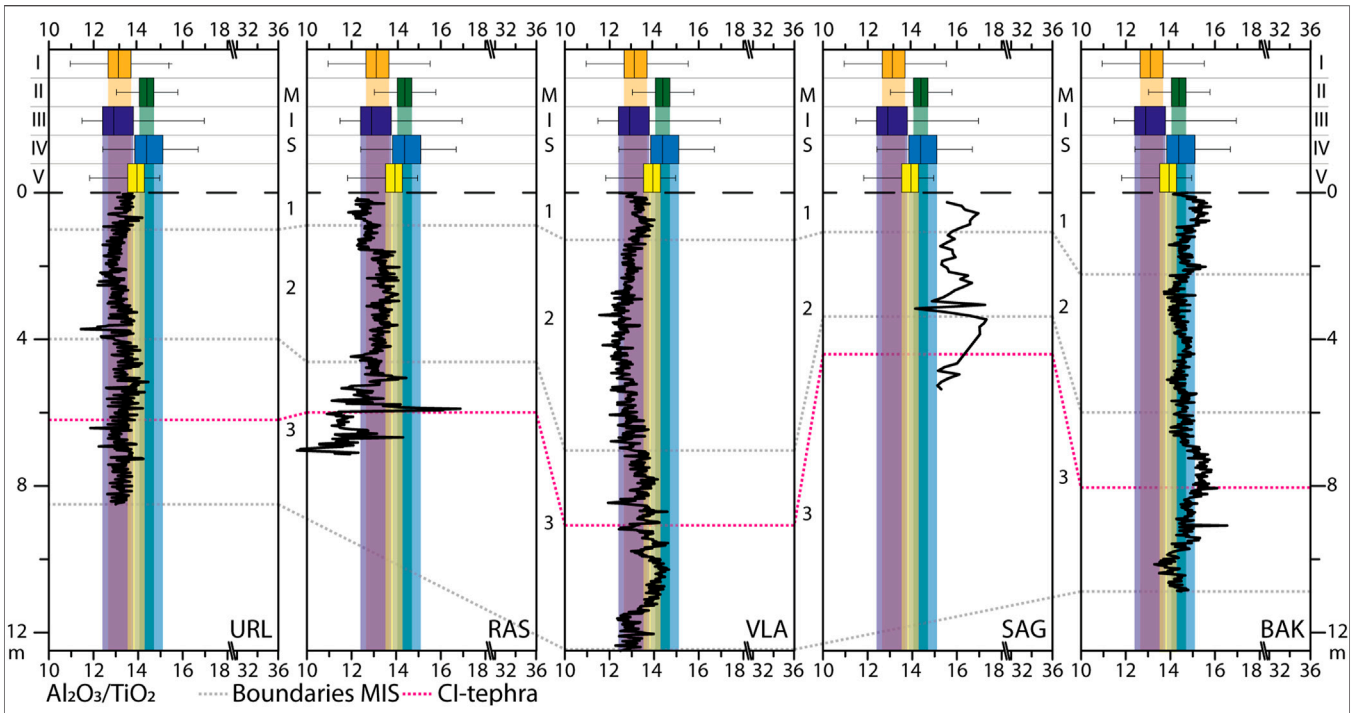

FIGURE 11 | Depth variations of the Al_2O_3/TiO_2 ratios for the investigated loess-palaeosol sequences, sorted from south to north (URL: Urluia; RAS: Rasova; VLA: Vlasca; SAG: Sageata, BAK: Balta Alba Kurgan). The box-whisker plots on top show the composition of the sections from the reference regions: I: Lower Austria; II: Vojvodina; III: Balaton (Central Hungary); IV: Bükk Mountains (Northeast Hungary) and V: Black Sea Shore (Ukraine). The interquartile area (between 25 and 75% quartile) are shown as shaded boxes. The correlative age model as well as the CI tephra are shown for temporal comparison.

loess sequences from the southern Dobrogea (Tugulan et al., 2016), which indicates the influence of distinct sources for the loess deposits of the area (**Figure 5**, **Supplementary Figure S7**).

VLA shows similarities to URL in several of the presented geochemical provenance proxies. The correspondence with URL is evident for example in the Na_2O/Al_2O_3 vs. K_2O/Al_2O_3 and the Al_2O_3/TiO_2 vs. SiO_2/TiO_2 plot (**Figure 4**), suggesting similar sourced material contributed to both records. RAS, however, shows some overlap with URL, but also exhibits a distinct pattern, e.g., in the Al_2O_3/TiO_2 ratio, which is depleted compared to the other sites. Besides the general commonalities identified within the studied LPS, significant variations are also discernible. It is noteworthy that the variations in the K_2O/Al_2O_3 vs. SiO_2/TiO_2 diagram tend to plot closer to the data from BAK, with which VLA also has large overlaps. SAG, however, shows some commonalities to BAK, but is distinguishable from the other sites, indicating a substantial contribution from a different dust source area. Therefore, we propose similar dominant source areas for the URL, RAS, and VLA sequences, with a more diverse input from multiple sources for the latter. For SAG, different and especially local sources, such as the proximal input from the Carpathian Bending can be assumed while BAK represents a more mixed provenance signal of different sources. While the use of multiple insightful bulk geochemical proxies has enabled us to sufficiently differentiate loess deposits in the Lower Danube Basin, further reference data is needed to assign the respective dust sources.

Estimations of Sedimentary Pathways of the Lower Danube Loess

As stated previously, at this stage of research we compare our results with geochemical data obtained using the same instrumentation and pretreatment from other loess deposits in Central and Southeastern Europe (i.e., the Middle Danube Basin (MDB) and Ukraine), where previous multi-proxy provenance studies have constrained potential dust sources (**Supplementary Table S1**). This comparison potentially allows to indirectly assign potential sources to the loess deposits in the Lower Danube Basin, a region yet largely underrepresented in loess provenance studies. The discussed provenance studies were chosen according to their proximity to the reference sections from Austria, Hungary, the Vojvodina, and Ukraine. However, local and regional differences in deflation and accumulation cannot be excluded. Therefore, only a tentative identification of potential source areas can be postulated in addition to the discussed geochemical characterisation. An overview of the discussed and additional provenance (**Supplementary Table S3**) and palaeowind direction studies (**Supplementary Table S4**) can be found in the **Supplementary Material**.

The Danube Alluvium (DA) Sedimentary Pathway

The large overlap of especially URL, RAS, and VLA with the geochemical compositions of some of the reference sites in Lower Austria, Central Hungary, and the Vojvodina, indicates similar

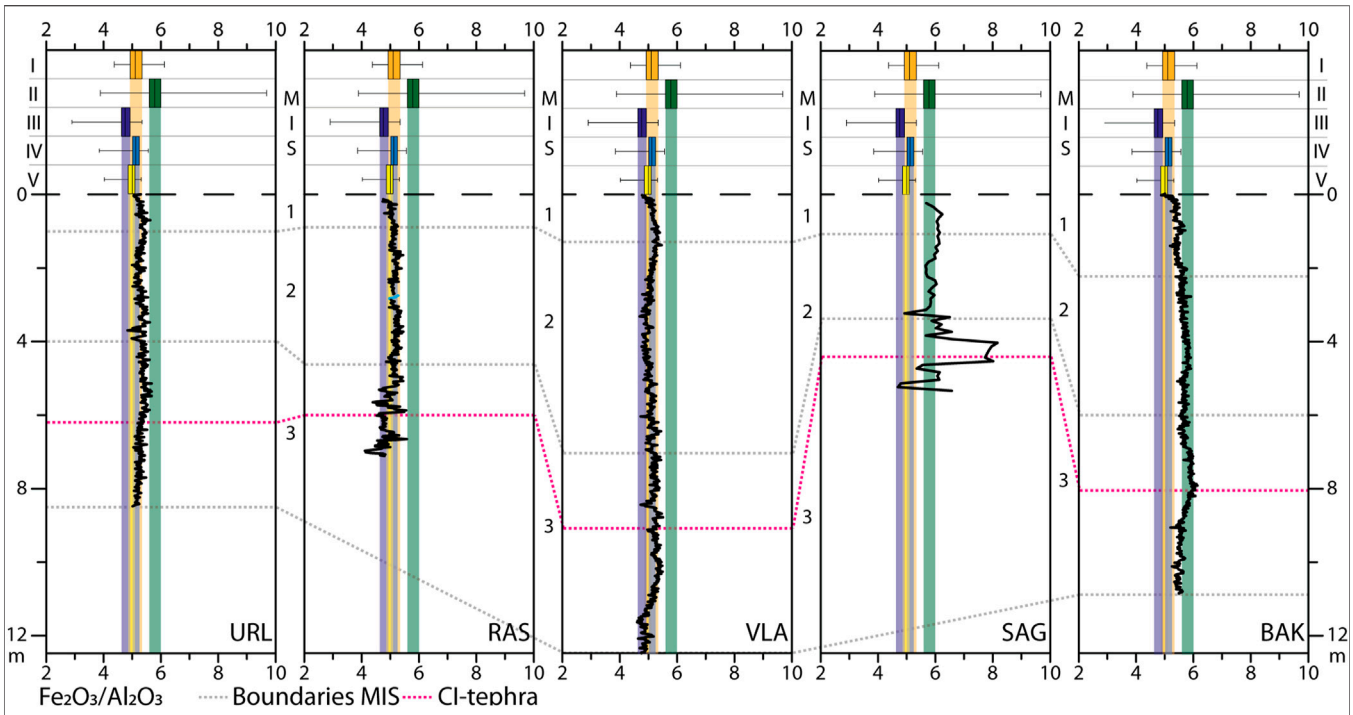

FIGURE 12 | Depth variations of the Fe_2O_3/TiO_2 ratios for the investigated loess-palaeosol sequences, sorted from south to north (URL: Urluia; RAS: Rasova; VLA: Vlasca; SAG: Sageata, BAK: Balta Alba Kurgan). The box-whisker plots on top show the composition of the sections from the reference regions: I: Lower Austria; II: Vojvodina; III: Balaton (Central Hungary); IV: Bükk Mountains (Northeast Hungary) and V: Black Sea Shore (Ukraine). The interquartile area (between 25 and 75% quartile) are shown as shaded boxes. The correlative age model as well as the Cl tephra are shown for temporal comparison.

geochemical signatures of the dust sources to the respective loess deposits (**Figures 8**, **9**, **Supplementary Figure S4**). The alluvial sediments of the MDB are recognized as the main source for the loess deposits in the area (Újvári et al., 2012; Obreht et al., 2019). This is in accordance with findings from Buggle et al. (2008), who demonstrated geochemical similarities between the Mircea Voda site in the LDB and the Batajnica/Stari Slankamen composite sequence of the Vojvodina. The authors interpreted these similarities as an indicator for the importance of the Danube alluvium (DA) as the main sediment supplier and dust source in the LDB, corresponding to the MR mode of loess genesis (Li et al., 2020). However, the geochemical composition of the alluvial sediment changes laterally, as major tributaries in the MDB contribute to the sediment load of the Danube (Nenadić et al., 2016; Vandenberghe et al., 2018; Mitrinović et al., 2020). The influence of other local to sub-regional source areas for the loess of the Middle Danube Basin is evident in the range in the geochemical data of the reference sections from the MDB. The importance of this influence increases with distance from the course of the Danube (Basarin et al., 2011; Obreht et al., 2014, 2016, 2019). Accordingly, the loess deposits of Northeast Hungary, which cover the upper to middle reaches of the Tisa catchment (Schatz et al., 2015a; Bösken et al., 2019), show different geochemical signatures as expressed in the K_2O/Al_2O_3 vs. SiO_2/TiO_2 diagram (**Figure 4**). These patterns are also evident for other LPS of the area, which show considerable geochemical differences to deposits in direct proximity to the Danube (Schatz et al., 2015a). Enhanced contributions from other local sources, such as the Bohemian Massif for Austrian loess (Újvári et al., 2013; Újvári and Klötzli, 2015), exposed local sandstones in Hungary (Újvári et al., 2008, 2012; Sebe, 2013) or from the Deliblatska Peščara sand field in Serbia (Obreht et al., 2015) were detected using various methods. However, for most loess deposits in the Carpathian Basin, the Danube alluvium appears to be the main dust source. The large overlap between the geochemical compositions of especially VLA, RAS, and URL with sections from the Middle Danube Basin indicates that the Danube alluvium in the LDB area is geochemically similar to the upper reaches of the river and acted as the dominant regional source area for dust deflation and ultimately, loess formation. Geochemical differences are either due to local sources within the LDB, but can also be attributed to palaeoclimatic gradients (Buggle et al., 2008).

The Eastern Carpathian (EC) Sedimentary Pathway

The SiO_2/TiO_2 ratio also shows a good agreement between BAK and SAG and the reference section of Kurortne (Black Sea Shore) in southwest Ukraine (Tecsa et al., 2020), which is visible in the K_2O/Al_2O_3 vs. SiO_2/TiO_2 diagram as well (**Figures 4**, **8**). In general, two sediment pathways were reconstructed for Ukrainian loess covers. On the one hand, the loess deposits of Central Ukraine are linked to the glaciofluvial (GF) sedimentary pathway (Buggle et al., 2008). These deposits, *inter alia* located in the catchment of the Dnieper River (Veres et al., 2018), consist of

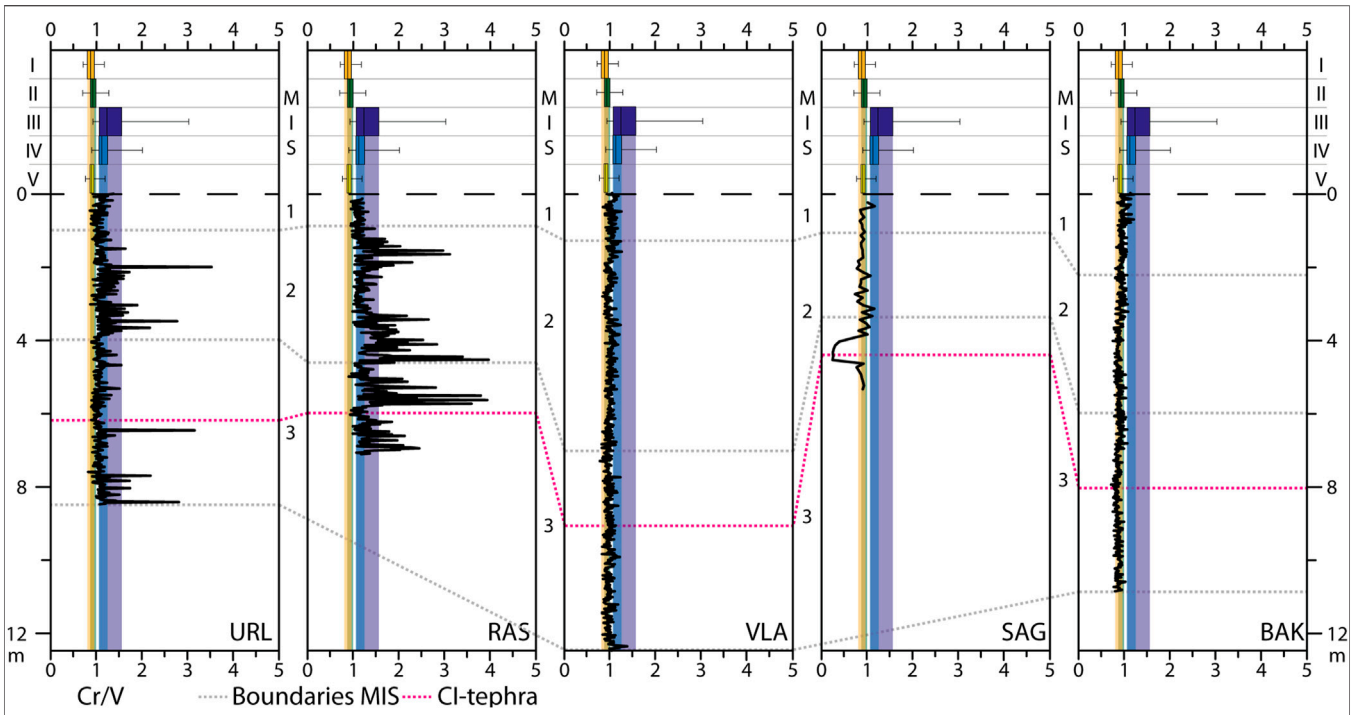

FIGURE 13 | Depth variations of the Cr/V ratios for the investigated loess-palaeosol sequences, sorted from south to north (URL: Urluia; RAS: Rasova; VLA: Vlasca; SAG: Sageata, BAK: Balta Alba Kurgan). The box-whisker plots on top show the composition of the sections from the reference regions: I: Lower Austria; II: Vojvodina; III: Balaton (Central Hungary); IV: Bükk Mountains (Northeast Hungary) and V: Black Sea Shore (Ukraine). The interquartile area (between 25 and 75% quartile) are shown as shaded boxes. The correlative age model as well as the CI tephra are shown for temporal comparison.

aeolian dust entrained from the glaciofluvial outwash plains by strong northerly winds (Buggle et al., 2008; Nawrocki et al., 2019). On the other hand, the loess deposits of southern Ukraine rather correspond to the Eastern Carpathian (EC) sedimentary pathway sourced from the sediments of the Dniester River and its tributaries. Northwesterly palaeowinds have been reconstructed for dust transport in this region (Nawrocki et al., 2006, 2018; Pańczyk et al., 2020). Although the GF pathway cannot be ruled out completely for Kurortne, its location on the southern Ukrainian shore of the Black Sea (**Figure 1**; Tecsa et al., 2020) close to the Dniester estuary suggests the EC pathway to account for loess deposits in this area. Therefore, the striking overlap with especially BAK suggests similar source areas for both sections and agrees with the reconstructed strong and consistent N-NW palaeowinds in the area. This is supported by residual forms of loess dunes, so-called gredas (Rozycki, 1967; Leger, 1990; Mason et al., 1999), which can be found in the entire eastern foreland of the Carpathians, and which are usually oriented NW-SE (**Figure 14**; Rozycki, 1967; cited in Leger, 1990). Although detrital material derived from the Carpathians has a strong influence on the sediment yield of the Danube, the sediments of tributaries draining the (Outer) Eastern Carpathians can be distinguished by geochemistry (Buggle et al., 2008) and detrital zircon age assemblages (Ducea et al., 2018). Therefore, the differences between BAK and loess deposits further south in the LDB such as VLA and URL can be linked to the dominance of the EC sedimentary pathway for the BAK area.

The Carpathian Bending (CB) Sedimentary Pathway

Another potential mode of origin for loess at SAG and BAK is the Carpathian Bending (CB) sedimentary pathway, with primary material being eroded from the bending sector of the Eastern Carpathians and transported by rivers like Buzău or Ialomița. This pathway corresponds to the MR mode of loess genesis (Li et al., 2020). There are no direct provenance studies on loess deposits from this region, but the floodplains of the rivers draining the Southern Carpathians to the west of the CB were detected as potential source areas based on heavy mineral composition data (Jipa, 2014). Decreasing zircon concentrations toward the Danube plain can be linked to the decreasing influence of sediment input from the Carpathians where detrital material is enriched in zircons. The opposing trend in hornblende contents was interpreted as the transport direction of dust deflated from the Danube alluvium, as the hornblende minerals are enriched in the deposits of the Danube (**Figure 14B**; Andar and Codarcea, 1981; cited in Jipa, 2014). **Figure 14B** shows that BAK and SAG are located in a transitional area, where the influence of the Eastern Carpathians is strong, but also some amount of hornblende can be found within the loess deposits, pointing to the Danube alluvium as a potential source area. The EC pathway is supported by high zirconium concentrations for both sites but especially in SAG (**Supplementary Table S2**). As stated above, the inferred zircon enrichment is indeed an indicator for sorting processes at this site. However, the fact that according to the A–CN–K plot (**Figure 6**) not all samples of the SAG section are affected by sorting, the

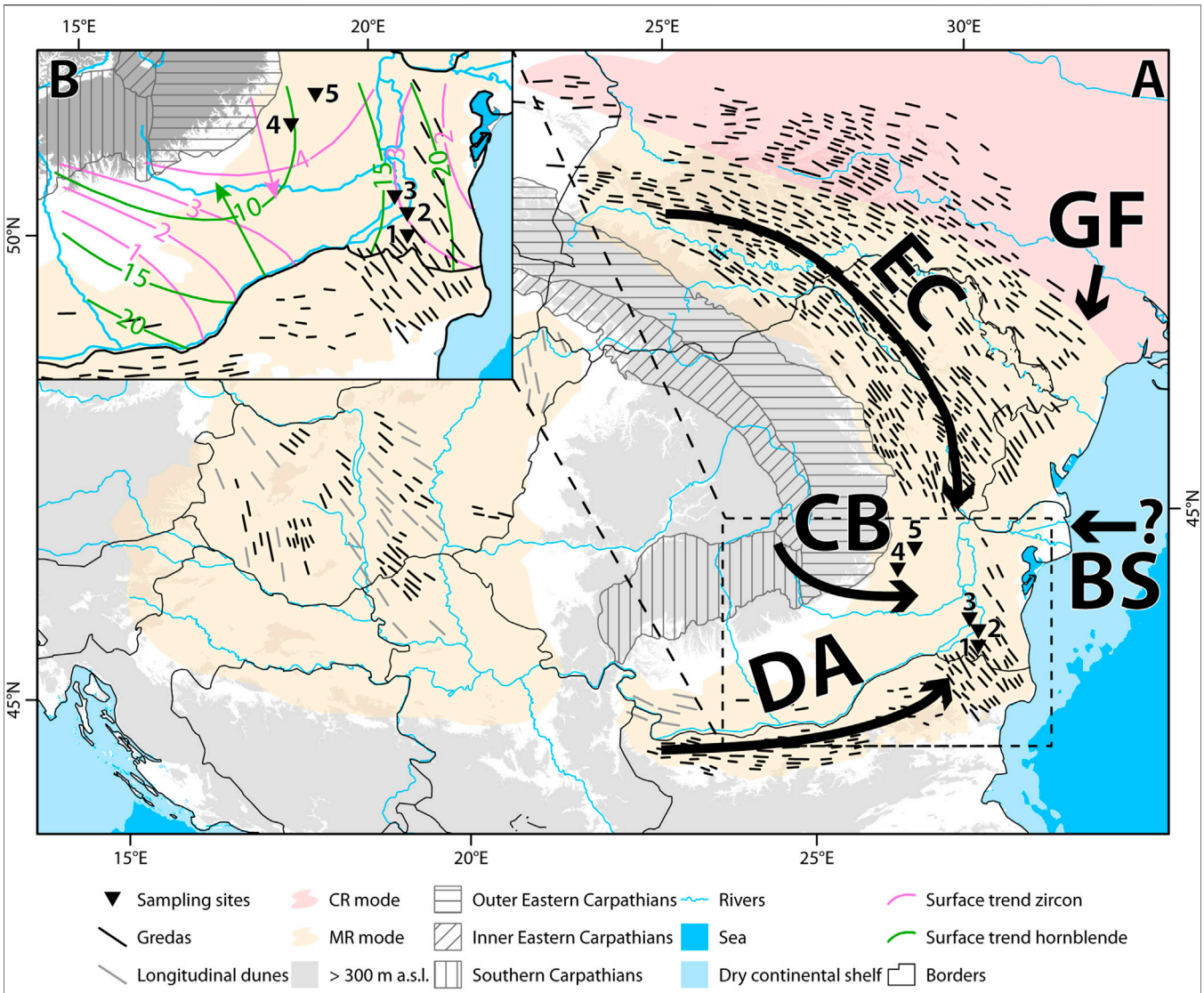

FIGURE 14 | A: potential sedimentary pathways for loess deposits in the Lower Danube Basin (DA: Danube alluvium; CB: Carpathian Bending; BS: Black Sea; EC: Eastern Carpathians; GF: glaciofluvial). Modes of loess genesis according to Li et al. (2020). Residual forms of gredas and longitudinal dunes in the Middle and Lower Danube Basin are adapted from (Rozycki 1967; cited in Leger, 1990). The division of the Carpathians is given to demonstrate different (proto-) source areas such as the flysch terrains of the Outer Eastern Carpathians, the volcanic chains of the Inner Eastern Carpathians or the crystalline and metamorphic bed rocks of the Southern Carpathians. The study sites are shown as triangles. **B:** surface trends for zircons (pink) and hornblende minerals (green). The isolines represent surface concentrations (in %) and are derived from statistical computation of mineralogical analyses of hundreds of surface samples (Andar and Codarcea, 1981; cited in; Jipa, 2014). The arrows indicate reconstructed transport directions (pink: towards Danube; green: towards Carpathians), based on the heavy mineralogical evidence.

generally high values could be a sign for the input of detrital material from the Carpathians for these loess deposits. The overlap with data from northeast Hungary in proxies such as the Al_2O_3/TiO_2 ratio (**Figures 4**, **11**) or the elevated Zr contents (**Figure 5** and **Supplementary Table S2**) support the influence of detrital material from the Carpathians, as northeast Hungary is strongly controlled by the Tisa and its tributaries (Thamó-Bozsó et al., 2014; Schatz et al., 2015a). Therefore, these areas experience a strong input from the Inner Eastern Carpathians and their extensive volcaniclastic forelands, which are also drained by the upper reaches of some main tributaries of the Danube in the LDB such as the Olt River.

The Black Sea (BS) and Glaciofluvial (GF) Sedimentary Pathways

The main characteristics of the BS and GF sedimentary pathways cannot be illustrated in detail due to the lack of reference data. However, the importance of these pathways has been discussed for loess deposits of the LDB and adjacent areas. Especially the BS pathway was linked to the formation of loess deposits in Bulgaria (Avramov et al., 2006; Jordanova et al., 2007). The complexity of the sedimentological composition of the Black Sea shelf, caused by multiple large rivers discharging into the basin, hinders a clear link to this pathway based on geochemistry. Large amounts of the

sediments building the Black Sea shelf were, e.g., deposited by the palaeo-Danube, indicating similar geochemical and mineralogical compositions to the DA pathway (Ducea et al., 2018). The GF pathway was reconstructed for LPS in Poland and Ukraine (Buggle et al., 2008; Skurzyński et al., 2019, 2020; Pańczyk et al., 2020) and was mainly driven by enhanced aeolian activities of katabatic winds influenced by fluctuations of the Eurasian CIS (Nawrocki et al., 2019). Pańczyk et al. (2020) constrained a divide of dust provinces based on detrital zircon ages, which divides the GF from the EC mode in Poland and Ukraine. In combination with the reconstruction of atmospheric circulations for the last glacial (Meyer and Kottmeier, 1989; Obreht et al., 2017), a major input of entrained dust from the GF pathway seems unlikely, especially for the southern part of the LDB.

Spatial and Temporal Provenance Variations of Lower Danube Loess and Palaeoclimatic Implications

The provenance of Lower Danube loess deposits varies spatially. While the sites from the Dobrogea plateau and the Danube plain seem to be linked mainly to sediment input via the Danube alluvium, sites in the northern part of the LDB are influenced by a mixture of potential source areas, including the DA, the EC, and the CB sedimentary pathways.

The hypothesized sedimentary pathways for the Lower Danube loess highlight the importance of proximal dust sources, as previously stated for the Middle Danube Basin (Obreht et al., 2019). However, far traveled dust originating from, e.g., the Sahara Desert can contribute especially to the fine silt fraction of aeolian deposits (Stuut et al., 2009). Although the importance of these distal sources for Southeastern European dust records was discussed for interglacial periods (Longman et al., 2017), the proposed contribution to glacial loess is of minor importance (see Varga et al., 2013).

Changes of dust source areas over time are potentially linked to palaeoclimatic fluctuations driving dust source expansion and/or changes in dust transport pathways (Zhang et al., 2018; Nawrocki et al., 2019; Pańczyk et al., 2020; Skurzyński et al., 2020). For MIS 3, URL, VLA, and BAK show some variation in the zirconium-based provenance proxies (**Figure 10**, **Supplementary Figure S3**). Especially in VLA, the Zr/Ni and Zr/V ratios show a decreasing trend from the bottom of the investigated section towards the CI tephra, whereas above it the values remain rather constant. The same trend but to lesser extent is visible in BAK. Since the grain size and especially the median grain size do not show large variations during this period (**Figure 7**), zircon enrichment due to sorting seems unlikely. The decreasing ratios are rather an indicator for the weakening of the influence of the Eastern Carpathians as a source area during this period. The weakened input of material derived from the Eastern Carpathians can be explained by shifts of atmospheric patterns during this time. During the middle MIS 3, westerlies reached Southeastern Europe on a NW-SE trajectory (see also Staubwasser et al., 2018). During the late MIS 3, the Siberian High pressure system intensified, leading to a shift of westerlies southwards (Obreht et al., 2017). Local maxima in the Zr based ratios in VLA suggest temporally increased input of Carpathian detrital material, indicating short-term fluctuations in source material. In URL, the Cr/V record is clearly divided during MIS 3 (**Figure 13**). Below the CI tephra, some oscillations occur indicating the input of detrital material potentially originating from more mafic sources. Above the tephra, these oscillations decrease and are within the interquartile range of the reference regions upstream. In RAS, the Cr/V proxy shows large variations throughout the whole profile, with exceptions during mid-MIS 2 and MIS 1, indicating an almost constant influence of mafic sources for these intervals. The pattern during MIS 2 is similar to URL, but the values are generally higher. Accumulation effects can explain the higher values and the large variations through time. Cr rich material was eroded in the Dobrogea and transported via small rivers toward the Danube Plain. The sediment was accumulated near RAS, deflated and deposited as aeolian dust (Zeeden et al., 2018).

The early MIS 2 was generally characterized by stable source areas for the investigated LPS. URL, RAS and VLA are clearly dominated by the DA sedimentary pathway during this period, whereas BAK shows large overlaps with the EC pathway (e.g., **Figure 8**). In the middle of MIS 2, however, the geochemical evidence shows changes in all sequences, e.g., in the K_2O/Al_2O_3 ratio (**Figure 9**). URL, RAS, and BAK show a noticeable decline in this proxy, whereas VLA and SAG show increasing values. These changes could be explained by the shift toward prevailing easterlies in large parts of Europe during the LGM (Schaffernicht et al., 2020). This would imply that the Black Sea (BS) sedimentary pathway, or long-range transport of material deflated even further to the east, becomes progressively more important throughout MIS 2, possibly contributing dust into the aeolian system of the LDB more significantly than hitherto considered. This coincides with sea level low stands of the Black Sea during the LGM (Constantinescu et al., 2015). However, since no reference data from sediments of the Black Sea shelf is available for this study, this hypothesis remains tentative. The same applies for long-range dust transport from the Caspian Basin further east, which was postulated for southwestern Ukraine especially for glacial periods (Stephens et al., 2002).

Methodological Limitations and Potential for Further Research

The general limitations of this methodological approach, such as the averaging of input from multiple dust sources, must be considered when discussing geochemical source estimations. The admixture of material from different proto-sources in a large sedimentary system such as the Danube Basin, can complicate the interpretation of distinct dust sources. When using bulk sediment (<63 μm) geochemistry as a provenance tool, signatures of multiple sources may be averaged out and assigning distinct sources might not be feasible (Bird et al., 2015). To identify specific dust (proto-)sources, it is essential that future research complements this method with further analyses, preferably single grain techniques that allow for more

conclusive discrimination between potential source sediments of similar geochemical composition (Stevens et al., 2010; Fenn et al., 2018). Nevertheless, the geochemical composition of bulk sediments can be used to either rule out sources or to assess the main variability in loess provenance based on the varying contents of diagnostic elements and identifiable geochemical similarities or differences (Buggle et al., 2008; Újvári et al., 2008), as presented here for a transect of records from the Lower Danube loess.

SUMMARY AND CONCLUSIONS

Our high-resolution geochemical study on several loess-palaeosol sequences from the Lower Danube Basin is among the first multi-record analyses contributing to the understanding of loess provenance and major sedimentary pathways in different sectors of the basin. Based on the presented data, we subdivide the basin into two major domains of loess geochemical signatures. The southern part of the basin including the southern Wallachian Plain and the Dobrogea with the LPS of Urluia, Rasova, and Vlasca can be distinguished from the northern Wallachian Plain with the LPS of Sageata and Balta Alba Kurgan. The boundary between these two domains appears to be transitional rather than a sharp contact.

The comparison with reference sections from Austria, Hungary, the Vojvodina, and Ukraine reveals that the Urluia, Rasova, and Vlasca records show striking geochemical similarities with loess records from the Middle Danube Basin. Since these similarities can be seen in many provenance proxies, a similar dominant geochemical signature of source areas in the Middle and Lower Danube Basin can be assumed. Furthermore, the geochemical composition of the Balta Alba Kurgan LPS rather resembles the one of Kurortne in Ukraine, pointing to similar source areas for these regions. Lastly, Sageata, situated in the floodplain of the Buzău River, shows rather unique geochemical patterns compared to the other sections, despite some overlaps with Balta Alba Kurgan.

The link of these geochemical findings with published provenance studies from the reference regions allows a tentative identification of potential source areas for the Lower Danube loess. It confirms the previous perception that the alluvial sediments of the Danube and its major tributaries act as a main storage and as source areas for dust deflation in the basin. The comparison to loess deposits in the middle and upper reaches of the Danube supports the Danube alluvium pathway hypothesis, especially for the southern sites of Urluia, Rasova, and Vlasca. Further to the north, other sources gain more importance. For Sageata, detrital material eroded from the Carpathian Bending area and redeposited by sediment-laden rivers such as the proximal Buzău River plays a major role as a local dust source. For Balta Alba Kurgan, the Eastern Carpathian sedimentary pathway is of particular importance. Here, material is deflated from the riverbeds draining the northern slopes of the Carpathians. Therefore, the dominant mode of loess genesis here is the mountain provenance-river transport loess *sensu* Li et al. (2020). The input of material deflated from the glaciofluvial outwash plains of Ukraine can neither be confirmed nor ruled out. However, we consider this sedimentary pathway, corresponding to the continental glacier provenance-river transport mode *sensu* Li et al. (2020) to be of minor importance, especially for the southern Lower Danube Basin. Our study confirms the general assumptions of prevailing northwesterly to westerly winds during the Pleniglacial in the area. These findings should be complemented using single grain techniques such as detrital zircon U-Pb ages to illuminate the sedimentary pathways accounting for dust deposition in the Lower Danube Basin in greater detail.

DATA AVAILABILITY STATEMENT

The raw data supporting the conclusions of this article will be made available by the authors, without undue reservation.

AUTHOR CONTRIBUTIONS

SP, PS, and UH designed the study. SP compiled the figures and wrote the first draft of the manuscript. SP, DV, PS, and UH defined the methodology. PS supervised the laboratory work and generated the discussed data. SP, DV, JN, UH, PS, and FL among others conducted fieldwork. All authors discussed the data, visualisations, and text.

FUNDING

The investigations were carried out in the frame of the CRC 806 "Our way to Europe," subproject B1 "The Eastern Trajectory": "Last Glacial Palaeogeography and Archaeology of the Eastern Mediterranean and of the Balkan Peninsula," funded by the Deutsche Forschungsgemeinschaft (DFG, German Research Foundation)—Projektnummer 57444011-SFB 806.

ACKNOWLEDGMENTS

We thank Marianne Dohms and her team for the laboratory framework. Alina Blume and Bruno Boemke helped vectorising parts of **Figures 1**, **14**. We thank Dagmar Haase for providing the shapefiles of loess distribution for **Figure 1**. We thank Jacek Skurzyński for his input on the methodological discussion. DV' work on the tephrochronology of investigated sequences was supported through a fellowship provided by Alexander von Humboldt Foundation. We thank Annett Junginger for the editorial work and MQ and RS for their helpful comments, which improved the manuscript substantially.

SUPPLEMENTARY MATERIAL

The Supplementary Material for this article can be found online at: https://www.frontiersin.org/articles/10.3389/feart.2021.600010/full#supplementary-material.

REFERENCES

Allen, J. R. L., and Thornley, D. M. (2004). Laser granulometry of Holocene estuarine silts: effects of hydrogen peroxide treatment. *The Holocene* 14, 290–295. doi:10.1191/0959683604hl681rr

Andar, P., and Codarcea, V. (1981). Analiza statisticaă a variabilităaţt¸ ii mineralelor grele din loessurile şs¸ i depozitele loessoide din Dobrogea şs¸ i Câmpia Română Occidentală (Statistical analysis of the variability of heavy minerals in the loess and loess deposits from Dobrogea and the Western Romanian Plain). *Dari Seama Institutul Geol. Geofiz.* LXVI, 15–41.

Anechitei-Deacu, V., Timar-Gabor, A., Fitzsimmons, K., Veres, D., and Hambach, U. (2014). Multi-method luminescence investigations on quartz grains of different sizes extracted from a loess section in Southeast Romania interbedding the Campanian Ignimbrite ash layer. *Geochronometria* 41, 1–14. doi:10.2478/s13386-013-0143-4

Anghelinu, M., and Niţă, L. (2014). What's in a name: the Aurignacian in Romania. *Quat. Int.* 351, 172–192. doi:10.1016/j.quaint.2012.03.013

Antoine, P., Rousseau, D.-D., Moine, O., Kunesch, S., Hatté, C., Lang, A., et al. (2009). Rapid and cyclic aeolian deposition during the Last Glacial in European loess: a high-resolution record from Nussloch, Germany. *Quat. Sci. Rev.* 28, 2955–2973. doi:10.1016/j.quascirev.2009.08.001

Antoine, P., Rousseau, D.-D., Zöller, L., Lang, A., Munaut, A.-V., Hatté, C., et al. (2001). High-resolution record of the last Interglacial–glacial cycle in the Nussloch loess–palaeosol sequences, Upper Rhine Area, Germany. *Quat. Int.* 76–77, 211–229. doi:10.1016/S1040-6182(00)00104-X

Avramov, V. I., Jordanova, D., Hoffmann, V., and Roesler, W. (2006). The role of dust source area and pedogenesis in three loess-palaeosol sections from North Bulgaria: a mineral magnetic study. *Stud. Geophys. Geod.* 50, 259–282. doi:10.1007/s11200-006-0015-y

Badura, J., Jary, Z., and Smalley, I. (2013). Sources of loess material for deposits in Poland and parts of Central Europe: the lost Big River. *Quat. Int.* 296, 15–22. doi:10.1016/j.quaint.2012.06.019

Basarin, B., Vandenberghe, D. A. G., Marković, S. B., Catto, N., Hambach, U., Vasiliniuc, S., et al. (2011). The Belotinac section (Southern Serbia) at the southern limit of the European loess belt: initial results. *Quat. Int.* 240, 128–138. doi:10.1016/j.quaint.2011.02.022

Bird, A., Stevens, T., Rittner, M., Vermeesch, P., Carter, A., Andò, S., et al. (2015). Quaternary dust source variation across the Chinese Loess Plateau. *Palaeogeogr. Palaeoclimatol. Palaeoecol.* 435, 254–264. doi:10.1016/j.palaeo.2015.06.024

Bokhorst, M. P., Vandenberghe, J., Sümegi, P., Łanczont, M., Gerasimenko, N. P., Matviishina, Z. N., et al. (2011). Atmospheric circulation patterns in central and eastern Europe during the Weichselian Pleniglacial inferred from loess grain-size records. *Quat. Int.* 234, 62–74. doi:10.1016/j.quaint.2010.07.018

Bösken, J., Obreht, I., Zeeden, C., Klasen, N., Hambach, U., Sümegi, P., et al. (2019). High-resolution paleoclimatic proxy data from the MIS3/2 transition recorded in northeastern Hungarian loess. *Quat. Int.* 502, 95–107. doi:10.1016/j.quaint.2017.12.008

Bösken, J., Sümegi, P., Zeeden, C., Klasen, N., Gulyás, S., and Lehmkuhl, F. (2018). Investigating the last glacial Gravettian site 'Ságvár Lyukas Hill' (Hungary) and its paleoenvironmental and geochronological context using a multi-proxy approach. *Palaeogeogr. Palaeoclimatol. Palaeoecol.* 509, 77–90. doi:10.1016/j.palaeo.2017.08.010

Bradák, B. (2009). Application of anisotropy of magnetic susceptibility (AMS) for the determination of paleo-wind directions and paleo-environment during the accumulation period of Bag Tephra, Hungary. *Quat. Int.* 198, 77–84. doi:10.1016/j.quaint.2007.11.005

Bradák, B., Seto, Y., Chadima, M., Kovács, J., Tanos, P., Újvári, G., et al. (2020). Magnetic fabric of loess and its significance in Pleistocene environment reconstructions. *Earth-sci. Rev.* 210, 103385. doi:10.1016/j.earscirev.2020.103385

Buggle, B., Glaser, B., Hambach, U., Gerasimenko, N., and Marković, S. (2011). An evaluation of geochemical weathering indices in loess–paleosol studies. *Quat. Int.* 240, 12–21. doi:10.1016/j.quaint.2010.07.019

Buggle, B., Glaser, B., Zöller, L., Hambach, U., Marković, S., Glaser, I., et al. (2008). Geochemical characterization and origin of Southeastern and Eastern European loesses (Serbia, Romania, Ukraine). *Quat. Sci. Rev.* 27, 1058–1075. doi:10.1016/j.quascirev.2008.01.018

Campodonico, V. A., Rouzaut, S., and Pasquini, A. I. (2019). Geochemistry of a Late Quaternary loess-paleosol sequence in central Argentina: implications for weathering, sedimentary recycling and provenance. *Geoderma* 351, 235–249. doi:10.1016/j.geoderma.2019.04.024

Chen, J., An, Z., and Head, J. (1999). Variation of Rb/Sr ratios in the loess-paleosol sequences of Central China during the last 130,000 Years and their implications for monsoon paleoclimatology. *Quat. Res.* 51, 215–219. doi:10.1006/qres.1999.2038

Chu, W. (2018). The Danube corridor hypothesis and the Carpathian Basin: geological, environmental and archaeological approaches to characterizing Aurignacian dynamics. *J. World Prehistory* 31, 117–178. doi:10.1007/s10963-018-9115-1

Constantin, D., Timar-Gabor, A., Veres, D., Begy, R., and Cosma, C. (2012). SAR-OSL dating of different grain-sized quartz from a sedimentary section in southern Romania interbedding the Campanian Ignimbrite/Y5 ash layer. *Quat. Geochronol.* 10, 81–86. doi:10.1016/j.quageo.2012.01.012

Constantinescu, A. M., Toucanne, S., Dennielou, B., Jorry, S. J., Mulder, T., and Lericolais, G. (2015). Evolution of the Danube deep-sea fan since the last glacial maximum: new insights into Black Sea water-level fluctuations. *Mar. Geol.* 367, 50–68. doi:10.1016/j.margeo.2015.05.007

De Vivo, B., Rolandi, G., Gans, P. B., Calvert, A., Bohrson, W. A., Spera, F. J., et al. (2001). New constraints on the pyroclastic eruptive history of the Campanian volcanic Plain (Italy). *Mineral. Petrol.* 73, 47–65. doi:10.1007/s007100170010

Demir, F., Budak, G., Baydaş, E., and Şahin, Y. (2006). Standard deviations of the error effects in preparing pellet samples for WDXRF spectroscopy. *Nucl. Instrum. Methods Phys. Res. Sect. B Beam Interact. Mater.* 243, 423–428. doi:10.1016/j.nimb.2005.09.019

Ducea, M. N., Giosan, L., Carter, A., Balica, C., Stoica, A. M., Roban, R. D., et al. (2018). U-PB detrital zircon geochronology of the lower Danube and its tributaries: implications for the geology of the Carpathians. *Geochem. Geophys. Geosystems* 19, 3208–3223. doi:10.1029/2018GC007659

Fenn, K., Stevens, T., Bird, A., Limonta, M., Rittner, M., Vermeesch, P., et al. (2018). Insights into the provenance of the Chinese Loess Plateau from joint zircon U-Pb and garnet geochemical analysis of last glacial loess. *Quat. Res.* 89, 645–659. doi:10.1017/qua.2017.86

Fitzsimmons, K. E., Doboş, A., Probst, M., and Iovita, R. (2020). Thinking outside the box at open-air archeological contexts: examples from loess landscapes in southeast Romania. *Front. Earth Sci.* 8, 561207. doi:10.3389/feart.2020.561207

Fitzsimmons, K. E., and Hambach, U. (2014). Loess accumulation during the last glacial maximum: evidence from Urluia, southeastern Romania. *Quat. Int.* 334–335, 74–85. doi:10.1016/j.quaint.2013.08.005

Fitzsimmons, K. E., Hambach, U., Veres, D., and Iovita, R. (2013). The Campanian Ignimbrite eruption: new data on volcanic ash dispersal and its potential impact on human evolution. *PLoS ONE* 8, e65839. doi:10.1371/journal.pone.0065839

Fitzsimmons, K. E., Marković, S. B., and Hambach, U. (2012). Pleistocene environmental dynamics recorded in the loess of the middle and lower Danube basin. *Quat. Sci. Rev.* 41, 104–118. doi:10.1016/j.quascirev.2012.03.002

Floroiu, I. (2011). Types of riverbed along the lower course of the Buzău River. *Forum Geogr.* X, 91–98. doi:10.5775/fg.2067-4635.2011.022.i

Frazee, C. J., Fehrenbacher, J. B., and Krumbein, W. C. (1970). Loess distribution from a source. *Soil Sci. Soc. Am. J.* 34, 296–301. doi:10.2136/sssaj1970.03615995003400020032x

Giaccio, B., Hajdas, I., Isaia, R., Deino, A., and Nomade, S. (2017). High-precision 14C and 40Ar/39Ar dating of the Campanian Ignimbrite (Y-5) reconciles the time-scales of climatic-cultural processes at 40 ka. *Sci. Rep.* 7, 45940. doi:10.1038/srep45940

Goff, K., Schaetzl, R. J., Chakraborty, S., Weindorf, D. C., Kasmerchak, C., and Bettis, E. A. (2020). Impact of sample preparation methods for characterizing the geochemistry of soils and sediments by portable X-ray fluorescence. *Soil Sci. Soc. Am. J.* 84, 131–143. doi:10.1002/saj2.20004

Haase, D., Fink, J., Haase, G., Ruske, R., Pécsi, M., Richter, H., et al. (2007). Loess in Europe—its spatial distribution based on a European Loess Map, scale 1: 2,500,000. *Quat. Sci. Rev.* 26, 1301–1312. doi:10.1016/j.quascirev.2007.02.003

Hao, Q., Guo, Z., Qiao, Y., Xu, B., and Oldfield, F. (2010). Geochemical evidence for the provenance of middle Pleistocene loess deposits in southern China. *Quat. Sci. Rev.* 29, 3317–3326. doi:10.1016/j.quascirev.2010.08.004

Hauck, T. C., Lehmkuhl, F., Zeeden, C., Bosken, J., Thiemann, A., and Richter, J. (2018). The Aurignacian way of life: Contextualizing early modern human adaptation in the Carpathian Basin. *Quat. Int.* 485, 150–166. doi:10.1016/j.quaint.2017.10.020

Jipa, D. C. (2014). The conceptual sedimentary model of the Lower Danube loess basin: sedimentogenetic implications. *Quat. Int.* 351, 14–24. doi:10.1016/j.quaint.2013.06.008

Jordanova, D., Hus, J., and Geeraerts, R. (2007). Palaeoclimatic implications of the magnetic record from loess/palaeosol sequence Viatovo (NE Bulgaria): palaeoclimatic implications of the magnetic record. *Geophys. J. Int.* 171, 1036–1047. doi:10.1111/j.1365-246X.2007.03576.x

Krézsek, C., and Olariu, C. (2021). Filling of sedimentary basins and the birth of large rivers: the lower Danube network in the Dacian Basin, Romania. *Glob. Planet. Change* 197, 103391. doi:10.1016/j.gloplacha.2020.103391

Lagroix, F., and Banerjee, S. K. (2002). Paleowind directions from the magnetic fabric of loess profiles in central Alaska. *Earth Planet. Sci. Lett.* 195, 99–112. doi:10.1016/s0012-821x(01)00564-7

Lancaster, N. (2020). On the formation of desert loess. *Quat. Res.* 96, 105–122. doi:10.1017/qua.2020.33

Leger, M. (1990). Loess landforms. *Quat. Int.* 7–8, 53–61. doi:10.1016/1040-6182(90)90038-6

Lehmkuhl, F., Bösken, J., Hošek, J., Sprafke, T., Marković, S. B., Obreht, I., et al. (2018a). Loess distribution and related quaternary sediments in the Carpathian Basin. *J. Maps* 14, 661–670. doi:10.1080/17445647.2018.1526720

Lehmkuhl, F., Nett, J. J., Pötter, S., Schulte, P., Sprafke, T., Jary, Z., et al. (2021). Loess landscapes of Europe - mapping, geomorphology, and zonal differentiation. *Earth-sci. Rev.* 215, 103496. doi:10.1016/j.earscirev.2020.103496

Lehmkuhl, F., Pötter, S., Pauligk, A., and Bösken, J. (2018b). Loess and other quaternary sediments in Germany. *J. Maps* 14, 330–340. doi:10.1080/17445647.2018.1473817

Lehmkuhl, F., Zens, J., Krauß, L., Schulte, P., and Kels, H. (2016). Loess-paleosol sequences at the northern European loess belt in Germany: distribution, geomorphology and stratigraphy. *Quat. Sci. Rev.* 153, 11–30. doi:10.1016/j.quascirev.2016.10.008

Li, Y., Shi, W., Aydin, A., Beroya-Eitner, M. A., and Gao, G. (2020). Loess genesis and worldwide distribution. *Earth-sci. Rev.* 201, 102947. doi:10.1016/j.earscirev.2019.102947

Longman, J., Veres, D., Ersek, V., Salzmann, U., Hubay, K., Bormann, M., et al. (2017). Periodic input of dust over the Eastern Carpathians during the Holocene linked with Saharan desertification and human impact. *Clim. Past* 13, 897–917. doi:10.5194/cp-13-897-2017

Malusà, M. G., Resentini, A., and Garzanti, E. (2016). Hydraulic sorting and mineral fertility bias in detrital geochronology. *Gondwana Res.* 31, 1–19. doi:10.1016/j.gr.2015.09.002

Marković, S. B., Fitzsimmons, K. E., Sprafke, T., Gavrilović, D., Smalley, I. J., Jović, V., et al. (2016). The history of Danube loess research. *Quat. Int.* 399, 86–99.

Marković, S. B., Oches, E. A., McCoy, W. D., Frechen, M., and Gaudenyi, T. (2007). Malacological and sedimentological evidence for "warm" glacial climate from the Irig loess sequence, Vojvodina, Serbia. *Geochem. Geophys. Geosystems* 8, Q09008. doi:10.1029/2006GC001565

Marković, S. B., Stevens, T., Kukla, G. J., Hambach, U., Fitzsimmons, K. E., Gibbard, P., et al. (2015). Danube loess stratigraphy — towards a pan-European loess stratigraphic model. *Earth-sci. Rev.* 148, 228–258. doi:10.1016/j.earscirev.2015.06.005

Marković, S. B., Vandenberghe, J., Stevens, T., Mihailović, D., Gavrilov, M. B., Radaković, M. G., et al. (2020). Geomorphological evolution of the Petrovaradin fortress paleolithic site (novi sad, Serbia). *Quat. Res.* 14, 33. 10.1017/qua.2020.88

Mason, J. A., Nater, E. A., Zanner, C. W., and Bell, J. C. (1999). A new model of topographic effects on the distribution of loess. *Geomorphology* 28, 223–236. doi:10.1016/S0169-555X(98)00112-3

Matenco, L., and Andriessen, P. (2013). Quantifying the mass transfer from mountain ranges to deposition in sedimentary basins: source to sink studies in the Danube Basin–Black Sea system. *Glob. Planet. Change* 103, 1–18. doi:10.1016/j.gloplacha.2013.01.003

Matenco, L., Munteanu, I., ter Borgh, M., Stanica, A., Tilita, M., Lericolais, G., et al. (2016). The interplay between tectonics, sediment dynamics and gateways evolution in the Danube system from the Pannonian Basin to the western Black Sea. *Sci. Total Environ.* 543, 807–827. doi:10.1016/j.scitotenv.2015.10.081

McLennan, S. M. (1993). Weathering and global denudation. *J. Geol.* 101, 195–303.

Meng, X., Liu, L., Zhao, W., He, T., Chen, J., and Ji, J. (2019). Distant Taklimakan Desert as an important source of aeolian deposits on the Chinese Loess Plateau as evidenced by carbonate minerals. *Geophys. Res. Lett.* 46, 4854–4862. doi:10.1029/2018GL081551

Meyer, H.-H., and Kottmeier, C. (1989). Die atmosphärische Zirkulation in Europa im Hochglazial der Weichsel-Eiszeit—abgeleitet von Paläowind-Indikatoren und Modellsimulationen. *Eampg Quat. Sci. J.* 39, 10–18. doi:10.3285/eg.39.1.02

Mikes, T., Dunkl, I., Frisch, W., and von Eynatten, H. (2006). Geochemistry of Eocene flysch sandstones in the NW external Dinarides. *Acta Geol. Hung.* 49, 103–124. doi:10.1556/AGeol.49.2006.2.2

Mikulčić Pavlaković, S., Crnjaković, M., Tibljaš, D., Šoufek, M., Wacha, L., Frechen, M., et al. (2011). Mineralogical and geochemical characteristics of Quaternary sediments from the Island of Susak (Northern Adriatic, Croatia). *Quat. Int.* 234, 32–49. doi:10.1016/j.quaint.2010.02.005

Mitrinović, D., Zarić, J., Anđelković, O., Sipos, G., Polomčić, D., and Dimkić, M. (2020). Dating of alluvial sediments from borehole at the lower course of the Sava river and indications of the connection between their genesis and climate changes in the Pleistocene. *Quat. Int.* 547, 75–85. doi:10.1016/j.quaint.2019.09.028

Miyazaki, T., Kimura, J.-I., and Katakuse, M. (2016). Geochemical records from loess deposits in Japan over the last 210 kyr: lithogenic source changes and paleoclimatic indications. *Geochem. Geophys. Geosystems* 17, 2745–2761. doi:10.1002/2016GC006322

Muhs, D. R., and Bettis, A. E. (2003). "Quaternary loess-Paleosol sequences as examples of climate-driven sedimentary extremes," in *Extreme depositional environments: mega end members in geologic time*. Editors M. A. Chan and A. W. Archer (Boulder: Geological Society of America). doi:10.1130/0-8137-2370-1.53

Muhs, D. R., Budahn, J., Reheis, M., Beann, J., Skipp, G., and Fisher, E. (2007). Airborne dust transport to the eastern pacific ocean off southern California: evidence from san clemente island. *J. Geophys. Res. Atmospheres* 112, 2006JD007577. doi:10.1029/2006JD007577

Muhs, D. R., Budahn, J. R., Johnson, D. L., Reheis, M., Beann, J., Skipp, G., et al. (2008). Geochemical evidence for airborne dust additions to soils in Channel Islands National Park, California. *Geol. Soc. Am. Bull.* 120, 106–126. doi:10.1130/B26218.1

Muhs, D. R., Cattle, S. R., Crouvi, O., Rousseau, D.-D., Sun, J., and Zárate, M. A. (2014). *"Loess records," in Mineral Dust*. Editors P. Knippertz and J.-B. W. Stuut (Dordrecht: Springer Netherlands), 411–441. doi:10.1007/978-94-017-8978-3_16

Muhs, D. R. (2018). The geochemistry of loess: asian and North American deposits compared. *J. Asian Earth Sci.* 155, 81–115. doi:10.1016/j.jseaes.2017.10.032

Muhs, D. R. (2013). The geologic records of dust in the Quaternary. *Aeolian Res.* 9, 3–48. doi:10.1016/j.aeolia.2012.08.001

Nawrocki, J., Bogucki, A. B., Gozhik, P., Łanczont, M., Pańczyk, M., Standzikowski, K., et al. (2019). Fluctuations of the Fennoscandian Ice Sheet recorded in the anisotropy of magnetic susceptibility of periglacial loess from Ukraine. *Boreas* 48, 940–952. doi:10.1111/bor.12400

Nawrocki, J., Gozhik, P., Łanczont, M., Pańczyk, M., Komar, M., Bogucki, A., et al. (2018). Palaeowind directions and sources of detrital material archived in the Roxolany loess section (southern Ukraine). *Palaeogeogr. Palaeoclimatol. Palaeoecol.* 496, 121–135. doi:10.1016/j.palaeo.2018.01.028

Nawrocki, J., Polechońska, O., Boguckij, A., and Łanczont, M. (2006). Palaeowind directions recorded in the youngest loess in Poland and western Ukraine as derived from anisotropy of magnetic susceptibility measurements. *Boreas* 35, 266–271. doi:10.1080/03009480600584907

Necea, D., Fielitz, W., Kadereit, A., Andriessen, P. A. M., and Dinu, C. (2013). Middle Pleistocene to Holocene fluvial terrace development and uplift-driven valley incision in the SE Carpathians, Romania. *Tectonophysics* 602, 332–354. doi:10.1016/j.tecto.2013.02.039

Nenadić, D., Gaudenyi, T., Bogićević, K., and Tošović, R. (2016). Stratigraphic and lithologic characteristics of Pleistocene fluvial deposits in the Danube and Sava riparian area near Belgrade (Serbia). *Stratigr. Geol. Correl.* 24, 427–437. doi:10.1134/S0869593816040055

Nesbitt, H. W., Young, G. M., McLennan, S. M., and Keays, R. R. (1996). Effects of chemical weathering and sorting on the petrogenesis of siliciclastic sediments, with implications for provenance studies. *J. Geol.* 104, 525–542. doi:10.1086/629850

Nesbitt, H. W., and Young, G. M. (1984). Prediction of some weathering trends of plutonic and volcanic rocks based on thermodynamic and kinetic

considerations. *Geochim. Cosmochim. Acta* 48, 1523–1534. doi:10.1016/0016-7037(84)90408-3

Nesbitt, H., and Young, G. (1996). Petrogenesis of sediments in the absence of chemical weathering: effects of abrasion and sorting on bulk composition and mineralogy. *Sedimentology* 43, 341–358. doi:10.1046/j.1365-3091.1996.d01-12.x

North Greenland Ice Core Project Members. (2004). High-resolution record of Northern Hemisphere climate extending into the last interglacial period. *Nature* 431, 147–151. doi:10.1038/nature02805

Nottebaum, V., Stauch, G., Hartmann, K., Zhang, J., and Lehmkuhl, F. (2015). Unmixed loess grain size populations along the northern Qilian Shan (China): relationships between geomorphologic, sedimentologic and climatic controls. *Quat. Int.* 372, 151–166. doi:10.1016/j.quaint.2014.12.071

Obreht, I., Buggle, B., Catto, N., Marković, S. B., Bösel, S., Vandenberghe, D. A. G., et al. (2014). The Late Pleistocene Belotinac section (southern Serbia) at the southern limit of the European loess belt: environmental and climate reconstruction using grain size and stable C and N isotopes. *Quat. Int.* 334, 10–19. doi:10.1016/j.quaint.2013.05.037

Obreht, I., Hambach, U., Veres, D., Zeeden, C., Bösken, J., Stevens, T., et al. (2017). Shift of large-scale atmospheric systems over Europe during late MIS 3 and implications for Modern Human dispersal. *Sci. Rep.* 7, 5848. doi:10.1038/s41598-017-06285-x

Obreht, I., Zeeden, C., Hambach, U., Veres, D., Marković, S. B., Bösken, J., et al. (2016). Tracing the influence of Mediterranean climate on Southeastern Europe during the past 350,000 years. *Sci. Rep.* 6, 36334. doi:10.1038/srep36334

Obreht, I., Zeeden, C., Hambach, U., Veres, D., Marković, S. B., and Lehmkuhl, F. (2019). A critical reevaluation of palaeoclimate proxy records from loess in the Carpathian Basin. *Earth-sci. Rev.* 190, 498–520. doi:10.1016/j.earscirev.2019.01.020

Obreht, I., Zeeden, C., Schulte, P., Hambach, U., Eckmeier, E., Timar-Gabor, A., et al. (2015). Aeolian dynamics at the Orlovat loess–paleosol sequence, northern Serbia, based on detailed textural and geochemical evidence. *Aeolian Res.* 18, 69–81. doi:10.1016/j.aeolia.2015.06.004

Ohta, T. (2004). Geochemistry of Jurassic to earliest Cretaceous deposits in the Nagato Basin, SW Japan: implication of factor analysis to sorting effects and provenance signatures. *Sediment. Geol.* 171, 159–180. doi:10.1016/j.sedgeo.2004.05.014

Özer, M., Orhan, M., and Işik, N. S. (2010). Effect of particle optical properties on size distribution of soils obtained by laser diffraction. *Environ. Eng. Geosci.* 16, 163–173. doi:10.1016/s0012-821x(01)00564-7

Pańczyk, M., Nawrocki, J., Bogucki, A. B., Gozhik, P., and Łanczont, M. (2020). Possible sources and transport pathways of loess deposited in Poland and Ukraine from detrital zircon U-Pb age spectra. *Aeolian Res.* 45, 100598. doi:10.1016/j.aeolia.2020.100598

Pécsi, M. (1990). Loess is not just the accumulation of dust. *Quat. Int.* 7, 1–21.

Pötter, S., Schmitz, A., Lücke, A., Schulte, P., Obreht, I., Zech, M., et al. (2021). Middle to Late Pleistocene environments based on stable organic carbon and nitrogen isotopes of loess-palaeosol sequences from the Carpathian Basin. *Boreas* 50, 184–204. doi:10.1111/bor.12470

Prins, M. A., and Vriend, M. (2007). Glacial and interglacial eolian dust dispersal patterns across the Chinese Loess Plateau inferred from decomposed loess grain-size records. *Geochem. Geophys. Geosystems* 8, Q07Q05. doi:10.1029/2006GC001563

Pye, K. (1995). The nature, origin and accumulation of loess. *Quat. Sci. Rev.* 14, 653–667. doi:10.1016/0277-3791(95)00047-X

Rădoane, M., Rădoane, N., and Dumitriu, D. (2003). Geomorphological evolution of longitudinal river profiles in the Carpathians. *Geomorphology* 50, 293–306. doi:10.1016/S0169-555X(02)00194-0

Richthofen, B. F. (1882). II.—on the mode of origin of the loess. *Geol. Mag.* 9, 293–305. doi:10.1017/S001675680017164X

Römer, W., Lehmkuhl, F., and Sirocko, F. (2016). Late Pleistocene aeolian dust provenances and wind direction changes reconstructed by heavy mineral analysis of the sediments of the Dehner dry maar (Eifel, Germany). *Glob. Planet. Change* 147, 25–39. doi:10.1016/j.gloplacha.2016.10.012

Rozycki, S. Z. (1967). Le sens des vents portant la poussière de loess à la lumière de l'analyse des formes d'accumulation du loess en Bulgarie et en Europe Centrale. *Rev. Géomorphologie Dyn.* 1–9, 33.

Schaetzl, R. J., Bettis, E. A., Crouvi, O., Fitzsimmons, K. E., Grimley, D. A., Hambach, U., et al. (2018). Approaches and challenges to the study of loess—introduction to the LoessFest special issue. *Quat. Res.* 89, 563–618. doi:10.1017/qua.2018.15

Schaffernicht, E. J., Ludwig, P., and Shao, Y. (2020). Linkage between dust cycle and loess of the last glacial maximum in Europe. *Atmos. Chem. Phys.* 20, 4969–4986. 10.5194/acp-20-4969-2020

Schatz, A.-K., Qi, Y., Siebel, W., Wu, J., and Zöller, L. (2015a). Tracking potential source areas of Central European loess: examples from Tokaj (HU), Nussloch (D) and Grub (AT). *Open Geosci.* 7, 678–720. doi:10.1515/geo-2015-0048

Schatz, A.-K., Scholten, T., and Kühn, P. (2015b). Paleoclimate and weathering of the Tokaj (Hungary) loess–paleosol sequence. *Palaeogeogr. Palaeoclimatol. Palaeoecol.* 426, 170–182. doi:10.1016/j.palaeo.2015.03.016

Scheidt, S., Berg, S., Hambach, U., Klasen, N., Pötter, S., Stolz, A., et al. (2021). Chronological assessment of the Balta Alba Kurgan loess-paleosol section (Romania)—a comparative study on different dating methods for a robust and precise age model. *Front. Earth Sci.* 14, 312. 10.3389/feart.2020.598448

Schulte, P., Lehmkuhl, F., Steininger, F., Loibl, D., Lockot, G., Protze, J., et al. (2016). Influence of HCl pretreatment and organo-mineral complexes on laser diffraction measurement of loess–paleosol-sequences. *CATENA* 137, 392–405. doi:10.1016/j.catena.2015.10.015

Schulte, P., and Lehmkuhl, F. (2018). The difference of two laser diffraction patterns as an indicator for post-depositional grain size reduction in loess-paleosol sequences. *Palaeogeogr. Palaeoclimatol. Palaeoecol.* 509, 126–136. doi:10.1016/j.palaeo.2017.02.022

Sebe, K. (2013). Ventifacts in the Mecsek region (SW Hungary) – climatic interpretation and tectonic implications. *Z. Für Geomorphol.* 57, 305–323. doi:10.1127/0372-8854/2013/0103

Skurzyński, J., Jary, Z., Kenis, P., Kubik, R., Moska, P., Raczyk, J., et al. (2020). Geochemistry and mineralogy of the Late Pleistocene loess-palaeosol sequence in Złota (near Sandomierz, Poland): implications for weathering, sedimentary recycling and provenance. *Geoderma* 375, 114459. doi:10.1016/j.geoderma.2020.114459

Skurzyński, J., Jary, Z., Raczyk, J., Moska, P., Korabiewski, B., Ryzner, K., et al. (2019). Geochemical characterization of the late Pleistocene loess-palaeosol sequence in Tyszowce (Sokal Plateau-Ridge, SE Poland). *Quat. Int.* 502, 108–118. doi:10.1016/j.quaint.2018.04.023

Smalley, I., Jefferson, I. F., Dijkstra, T. A., and Derbyshire, E. (2001). Some major events in the development of the scientific study of loess. *Earth-Sci. Rev.* 54, 5–18. doi:10.1016/s0012-8252(01)00038-1

Smalley, I. J., and Smalley, V. (1983). Loess material and loess deposits: formation, distribution and consequences. *Dev. Sedimentol.* 38, 51–68. doi:10.1016/S0070-4571(08)70788-X

Smalley, I., and Leach, J. A. (1978). The origin and distribution of the loess in the Danube basin and associated regions of East-Central Europe—a review. *Sediment. Geol.* 21, 1–26. doi:10.1016/0037-0738(78)90031-3

Smalley, I., O'Hara-Dhand, K., and Kwong, J. (2014). China: materials for a loess landscape. *CATENA* 117, 100–107. doi:10.1016/j.catena.2013.11.016

Smalley, I., O'Hara-Dhand, K., Wint, J., Machalett, B., Jary, Z., and Jefferson, I. (2009). Rivers and loess: the significance of long river transportation in the complex event-sequence approach to loess deposit formation. *Quat. Int.* 198, 7–18. doi:10.1016/j.quaint.2008.06.009

Sprafke, T., and Obreht, I. (2016). Loess: rock, sediment or soil – what is missing for its definition?. *Quat. Int.* 399, 198–207. doi:10.1016/j.quaint.2015.03.033

Staubwasser, M., Drăguşin, V., Onac, B. P., Assonov, S., Ersek, V., Hoffmann, D. L., et al. (2018). Impact of climate change on the transition of Neanderthals to modern humans in Europe. *Proc. Natl. Acad. Sci.* 115, 9116–9121. doi:10.1073/pnas.1808647115

Stephens, M., Krzyszkowsku, D., Ivchenko, A., and Majewski, M. (2002). Palaeoclimate and pedosedimentary reconstruction of a Middle to Late Pleistocene loess-palaeosol sequence, Prymorske, SW Ukraine. *Stud. Quat.* 19, 3–17.

Stevens, T., Palk, C., Carter, A., Lu, H., and Clift, P. D. (2010). Assessing the provenance of loess and desert sediments in northern China using U-Pb dating and morphology of detrital zircons. *Geol. Soc. Am. Bull.* 122, 1331–1344. doi:10.1130/B30102.1

Stevens, T., Sechi, D., Bradák, B., Orbe, R., Baykal, Y., Cossu, G., et al. (2020). Abrupt last glacial dust fall over southeast England associated with dynamics of

the British-Irish ice sheet. *Quat. Sci. Rev.* 250, 106641. doi:10.1016/j.quascirev.2020.106641

Stuut, J.-B., Smalley, I., and O'Hara-Dhand, K. (2009). Aeolian dust in Europe: african sources and European deposits. *Quat. Int.* 198, 234–245. doi:10.1016/j.quaint.2008.10.007

Tecsa, V., Gerasimenko, N., Veres, D., Hambach, U., Lehmkuhl, F., Schulte, P., et al. (2020). Revisiting the chronostratigraphy of Late Pleistocene loess-paleosol sequences in southwestern Ukraine: OSL dating of Kurortne section. *Quat. Int.* 542, 65–79. doi:10.1016/j.quaint.2020.03.001

Thamó-Bozsó, E., Kovács, L. Ó., Magyari, Á., and Marsi, I. (2014). Tracing the origin of loess in Hungary with the help of heavy mineral composition data. *Quat. Int.* 319, 11–21. doi:10.1016/j.quaint.2013.04.030

Tsoar, H., and Pye, K. (1987). Dust transport and the question of desert loess formation. *Sedimentology* 34, 139–153. doi:10.1111/j.1365-3091.1987.tb00566.x

Tugulan, L. C., Duliu, O. G., Bojar, A.-V., Dumitras, D., Zinicovskaia, I., Culicov, O. A., et al. (2016). On the geochemistry of the Late Quaternary loess deposits of Dobrogea (Romania). *Quat. Int.* 399, 100–110. doi:10.1016/j.quaint.2015.06.062

Újvári, G., Klötzli, U., Kiraly, F., and Ntaflos, T. (2013). Towards identifying the origin of metamorphic components in Austrian loess: insights from detrital rutile chemistry, thermometry and U–Pb geochronology. *Quat. Sci. Rev.* 75, 132–142. doi:10.1016/j.quascirev.2013.06.002

Újvári, G., and Klötzli, U. (2015). U–Pb ages and Hf isotopic composition of zircons in Austrian last glacial loess: constraints on heavy mineral sources and sediment transport pathways. *Int. J. Earth Sci.* 104, 1365–1385. doi:10.1007/s00531-014-1139-x

Újvári, G., Varga, A., and Balogh-Brunstad, Z. (2008). Origin, weathering, and geochemical composition of loess in southwestern Hungary. *Quat. Res.* 69, 421–437. doi:10.1016/j.yqres.2008.02.001

Újvári, G., Varga, A., Ramos, F. C., Kovács, J., Németh, T., and Stevens, T. (2012). Evaluating the use of clay mineralogy, Sr–Nd isotopes and zircon U–Pb ages in tracking dust provenance: an example from loess of the Carpathian Basin. *Chem. Geol.* 304–305, 83–96. doi:10.1016/j.chemgeo.2012.02.007

Újvári, G., Varga, A., Raucsik, B., and Kovács, J. (2014). The Paks loess-paleosol sequence: a record of chemical weathering and provenance for the last 800ka in the mid-Carpathian Basin. *Quat. Int.* 319, 22–37. doi:10.1016/j.quaint.2012.04.004

Vandenberghe, J., Kasse, C., Popov, D., Markovic, S. B., Vandenberghe, D., Bohncke, S., et al. (2018). Specifying the external impact on fluvial lowland evolution: the last glacial tisza (Tisa) catchment in Hungary and Serbia. *Quaternary* 1, 14. doi:10.3390/quat1020014

Vandenberghe, J., Renssen, H., van Huissteden, K., Nugteren, G., Konert, M., Lu, H., et al. (2006). Penetration of atlantic westerly winds into Central and East Asia. *Quat. Sci. Rev.* 25, 2380–2389. doi:10.1016/j.quascirev.2006.02.017

Varga, G., Kovács, J., and Újvári, G. (2013). Analysis of saharan dust intrusions into the Carpathian Basin (central Europe) over the period of 1979–2011. *Glob. Planet. Change* 100, 333–342. doi:10.1016/j.gloplacha.2012.11.007

Veres, D., Lane, C. S., Timar-Gabor, A., Hambach, U., Constantin, D., Szakács, A., et al. (2013). The Campanian Ignimbrite/Y5 tephra layer–A regional stratigraphic marker for Isotope Stage 3 deposits in the Lower Danube region, Romania. *Quat. Int.* 293, 22–33.

Veres, D., Tecsa, V., Gerasimenko, N., Zeeden, C., Hambach, U., and Timar-Gabor, A. (2018). Short-term soil formation events in last glacial east European loess, evidence from multi-method luminescence dating. *Quat. Sci. Rev.* 200, 34–51. doi:10.1016/j.quascirev.2018.09.037

Vlaminck, S., Kehl, M., Rolf, C., Franz, S. O., Lauer, T., Lehndorff, E., et al. (2018). Late Pleistocene dust dynamics and pedogenesis in Southern Eurasia – detailed insights from the loess profile Toshan (NE Iran). *Quat. Sci. Rev.* 180, 75–95. doi:10.1016/j.quascirev.2017.11.010

Willmes, C. (2015). LGM sealevel change (HiRes), CRC806 database, collaborative research centre 806.Available at:http://crc806db.uni-koeln.de/dataset/show/lgm-sealevel-change-hires1436532921 [Accessed March 9, 2016].

Wolf, D., Ryborz, K., Kolb, T., Zapata, R. C., Vizcaino, J. S., Zöller, L., et al. (2019). Origins and genesis of loess deposits in central Spain, as indicated by heavy mineral compositions and grain-size variability. *Sedimentology* 66, 1139–1161. doi:10.1111/sed.12539

Wright, J. S. (2001). "Desert" loess versus "glacial" loess: quartz silt formation, source areas and sediment pathways in the formation of loess deposits. *Geomorphology* 36, 231–256. doi:10.1016/S0169-555X(00)00060-X

Yang, S. Y., Li, C. X., Yang, D. Y., and Li, X. S. (2004). Chemical weathering of the loess deposits in the lower Changjiang Valley, China, and paleoclimatic implications. *Quat. Int.* 117, 27–34. doi:10.1016/S1040-6182(03)00113-7

Zeeden, C., and Hambach, U. (2021). Magnetic susceptibility properties of loess from the Willendorf archaeological site: implications for the syn/post-depositional interpretation of magnetic fabric. *Front. Earth Sci.* 8 .10.3389/feart.2020.599491

Zeeden, C., Hambach, U., Veres, D., Fitzsimmons, K., Obreht, I., Bösken, J., et al. (2018). Millennial scale climate oscillations recorded in the Lower Danube loess over the last glacial period. *Palaeogeogr. Palaeoclimatol. Palaeoecol.* 509, 164–181. doi:10.1016/j.palaeo.2016.12.029

Zhang, H., Lu, H., Stevens, T., Feng, H., Fu, Y., Geng, J., et al. (2018). Expansion of dust provenance and aridification of asia since ~7.2 ma revealed by detrital zircon U-Pb dating. *Geophys. Res. Lett.* 45. doi:10.1029/2018GL079888

Zimmermann, U., and Bahlburg, H. (2003). Provenance analysis and tectonic setting of the Ordovician clastic deposits in the southern Puna Basin, NW Argentina. *Sedimentology* 50, 1079–1104. doi:10.1046/j.1365-3091.2003.00595.x

Conflict of Interest: The authors declare that the research was conducted in the absence of any commercial or financial relationships that could be construed as a potential conflict of interest.

frontiers in Earth Science

ORIGINAL RESEARCH
published: 30 April 2021
doi: 10.3389/feart.2021.607695

Modern Sedimentation and Authigenic Mineral Formation in the Chew Bahir Basin, Southern Ethiopia: Implications for Interpretation of Late Quaternary Paleoclimate Records

Daniel Gebregiorgis[1], Daniel M. Deocampo[1], Verena Foerster[2], Fred J. Longstaffe[3], Jeremy S. Delaney[4], Frank Schaebitz[2], Annett Junginger[5], Monika Markowska[6], Stephan Opitz[7], Martin H. Trauth[8], Henry F. Lamb[9,10] and Asfawossen Asrat[11]*

[1] Department of Geosciences, Georgia State University, Atlanta, GA, United States, [2] Institute of Geography Education, University of Cologne, Cologne, Germany, [3] Department of Earth Sciences, The University of Western Ontario, London, ON, Canada, [4] Department of Earth and Planetary Sciences, Rutgers University, Piscataway, NJ, United States, [5] Department of Geosciences, University of Tübingen, Tübingen, Germany, [6] Department of Climate Geochemistry, Max Planck Institute for Chemistry, Mainz, Germany, [7] Institute of Geography, University of Cologne, Cologne, Germany, [8] Institute of Geosciences, University of Potsdam, Potsdam, Germany, [9] Department of Geography and Earth Sciences, Aberystwyth University, Aberystwyth, United Kingdom, [10] Botany Department, School of Natural Sciences, Trinity College, Dublin, Ireland, [11] School of Earth Sciences, Addis Ababa University, Addis Ababa, Ethiopia

OPEN ACCESS

Edited by:
Gary E. Stinchcomb, Murray State University, United States

Reviewed by:
Steven L. Forman, Baylor University, United States
Dhananjay Anant Sant, Maharaja Sayajirao University of Baroda, India

***Correspondence:**
Daniel Gebregiorgis
dgebregiorgis@gsu.edu

Specialty section:
This article was submitted to Quaternary Science, Geomorphology and Paleoenvironment, a section of the journal Frontiers in Earth Science

Received: 17 September 2020
Accepted: 24 March 2021
Published: 30 April 2021

Citation:
Gebregiorgis D, Deocampo DM, Foerster V, Longstaffe FJ, Delaney JS, Schaebitz F, Junginger A, Markowska M, Opitz S, Trauth MH, Lamb HF and Asrat A (2021) Modern Sedimentation and Authigenic Mineral Formation in the Chew Bahir Basin, Southern Ethiopia: Implications for Interpretation of Late Quaternary Paleoclimate Records. Front. Earth Sci. 9:607695. doi: 10.3389/feart.2021.607695

We present new mineralogical and geochemical data from modern sediments in the Chew Bahir basin and catchment, Ethiopia. Our goal is to better understand the role of modern sedimentary processes in chemical proxy formation in the Chew Bahir paleolake, a newly investigated paleoclimatic archive, to provide environmental context for human evolution and dispersal. Modern sediment outside the currently dry playa lake floor have higher SiO_2 and Al_2O_3 (50–70 wt.%) content compared to mudflat samples. On average, mudflat sediment samples are enriched in elements such as Mg, Ca, Ce, Nd, and Na, indicating possible enrichment during chemical weathering (e.g., clay formation). Thermodynamic modeling of evaporating water in upstream Lake Chamo is shown to produce an authigenic mineral assemblage of calcite, analcime, and Mg-enriched authigenic illitic clay minerals, consistent with the prevalence of environments of enhanced evaporative concentration in the Chew Bahir basin. A comparison with samples from the sediment cores of Chew Bahir based on whole-rock MgO/Al_2O_3, Ba/Sr and authigenic clay mineral $\delta^{18}O$ values shows the following: modern sediments deposited in the saline mudflats of the Chew Bahir dried out lake bed resemble paleosediments deposited during dry periods, such as during times of the Last Glacial Maximum and Younger Dryas stadial. Sediments from modern detrital upstream sources are more similar to sediments deposited during wetter periods, such as the early Holocene African Humid Period.

Keywords: oxygen isotopes in authegenic clay minerals, X-ray core scanning, paleoclimate proxy formation and interpretation, whole-rock and clay mineralogy, geochemical modeling, the Chew Bahir K record

INTRODUCTION

The field of sedimentary geochemistry is at the forefront of both outcrop- and core-based paleoclimate research. Aided by the introduction of X-ray fluorescence (XRF) core scanning techniques, down-core patterns of element intensities and ratios in both marine and lake sediments are routinely applied as proxies of past climate changes (e.g., Croudace et al., 2006, 2019; Lyons et al., 2015; Gebregiorgis et al., 2020b). Although the link between the chemistry of deposited weathering products and climate is complex, the distribution of mobile versus immobile elements in sediment likely varies in accordance with climate variables (e.g., temperature, precipitation; e.g., Harriss and Adams, 1966; Nesbitt, 1979; Chesworth et al., 1981; Middelburg et al., 1988). Element intensities (e.g., Zr, Ti, K) and ratios (e.g., K/Zr, K/Ti, K/Al, and K/Rb) are routinely used to trace a wide range of climate-related processes such as changes in rainfall amount (e.g., Foerster et al., 2012; Hendy et al., 2015) and intensity of weathering processes (e.g., Burnett et al., 2011; Tian et al., 2011; Clift et al., 2014) within lake catchments.

The application of XRF-generated elemental proxies in paleoclimatology, however, is not without its pitfalls. Depositional variability, hiatuses and erosion, diagenesis, and pedogenesis commonly work together to obscure or overprint primary geochemical signals preserved in sediments. Authigenic mineral formation can also control lake sediment geochemistry, particularly in saline lakes (Deocampo and Jones, 2014). Indeed, in many African lakes, clay minerals rich in Al, or zeolites rich in Ca or K, have been shown to alter in saline and alkaline lakes to produce Mg-rich authigenic clay minerals and Na-rich analcime (e.g., Surdam and Eugster, 1976; Singer and Stoffers, 1980; Trauth et al., 2001; Deocampo, 2004, 2015). As a result, large discrepancies between lake records remain unresolved, leading to difficulties in interpreting proxy records of climate (e.g., Trauth et al., 2003). These challenges are in large part due to an incomplete understanding of proxy formation and are particularly relevant in paleolimnology, where down-core variability of selected elements in the sediment may have little direct relation with the rate and intensity of weathering of the surrounding catchment, but might rather reflect post-depositional hydrochemical conditions.

The potassium (K) record of the Chew Bahir basin provides an excellent example demonstrating the complexity of interpreting highs and lows in K content in the sediment as past water balance changes in the catchment (Foerster et al., 2012; Fischer et al., 2020). Foerster et al. (2018) considered multiple hypotheses to explain the K record, concluding that K enrichment in the sediment could not entirely indicate episodes of enhanced detrital input, but rather incipient low temperature K-fixation during illitization associated with Mg uptake and clay mineral layer charge increase (Deocampo and Tactikos, 2010; Deocampo, 2015). It is worth noting that the temporal variability of the K record is remarkably consistent with half a dozen well-dated proxy records from continental Africa (e.g., Brown et al., 2007; Junginger and Trauth, 2013; Tierney and deMenocal, 2013; Otto-Bliesner et al., 2014; Shanahan et al., 2015).

The present study takes its impetus from Foerster et al. (2018) and has three main objectives. The study's core objective is to describe the major input and alteration processes utilizing new geochemical data in modern sediments collected from the Chew Bahir basin. Second, by comparing the new geochemical data from the modern sediments with PHREEQC geochemical modeling, where the acronym PHREEQC stands for PH (pH), RE (redox), EQ (equilibrium), and C (program written in C), of local waters, the study aims to improve our understanding of relevant hydrogeochemical processes in the Chew Bahir catchment. Third, the study aims to further refine interpretations of the Chew Bahir K record using clay mineralogical and geochemical analysis of modern sediments collected from the Chew Bahir catchment. Within this framework, this study is aimed at advancing our understanding of such climate proxies, and the development of a reliable high-resolution environmental context for the newly investigated site of Chew Bahir. A preliminary attempt is made to investigate whether oxygen-isotope measurements of authigenic clay minerals covering notable warm/wet (e.g., the early-middle Holocene) and cold/dry intervals (e.g., the Last Glacial Maximum, LGM) suggest similar changes in wet and dry conditions inferred from the Chew Bahir K record.

GEOMORPHOLOGY OF THE CHEW BAHIR BASIN

The Chew Bahir basin is a hydrographic and sedimentary system located at the southern sector of the Main Ethiopian Rift, northeast of the Omo-Turkana basin of southern Ethiopia and northern Kenya (**Figures 1a–d**). It forms part of a ∼250 km wide broadly rifted zone, mainly composed of Pliocene-Holocene sediment-filled basins underlying strongly uplifted Precambrian blocks (e.g., Ebinger et al., 2000). Oligocene basalts and subordinate rhyolites, trachytes, tuffs and ignimbrites cover the Precambrian basement units near the northeastern, northern and northwestern parts of the catchment. The Teltele plateau, which consists of Miocene basalts and rhyolite, trachyte and felsic tuff, is located in the eastern part of the Chew Bahir catchment (**Figure 1d**; see also Davidson, 1983). The northern part of the Teltele plateau extends to the Konso upland, which is drained by the Segen River, one of the major rivers draining to the Weyto River, and then to the Chew Bahir basin (Fischer et al., 2020).

The Chew Bahir basin is a deep tectonic basin, where a nearly flat, ∼30 km wide and ∼100 km long playa surface is bounded by a ∼500 m high tectonic escarpments to its west and east. Formation of shallow but wide alluvial fans, the biggest of which is a 20 km by 10 km fan located just west of the Chew Bahir coring sites, has been the major geomorphological features at the borders between the basin and the adjacent highland graben shoulders. The Weyto River flows in a north-south direction, forming a wide and shallow deltaic system before it disappears into the playa wetland (**Figure 1c**). The northern part of the flat basin is covered by relatively dense grassland vegetation mostly inhibiting aeolian geomorphological processes. Only on the vegetation-free, strongly desiccated southernmost (∼20 km long) part of the basin can local aeolian deflation, remobilization and sedimentation of

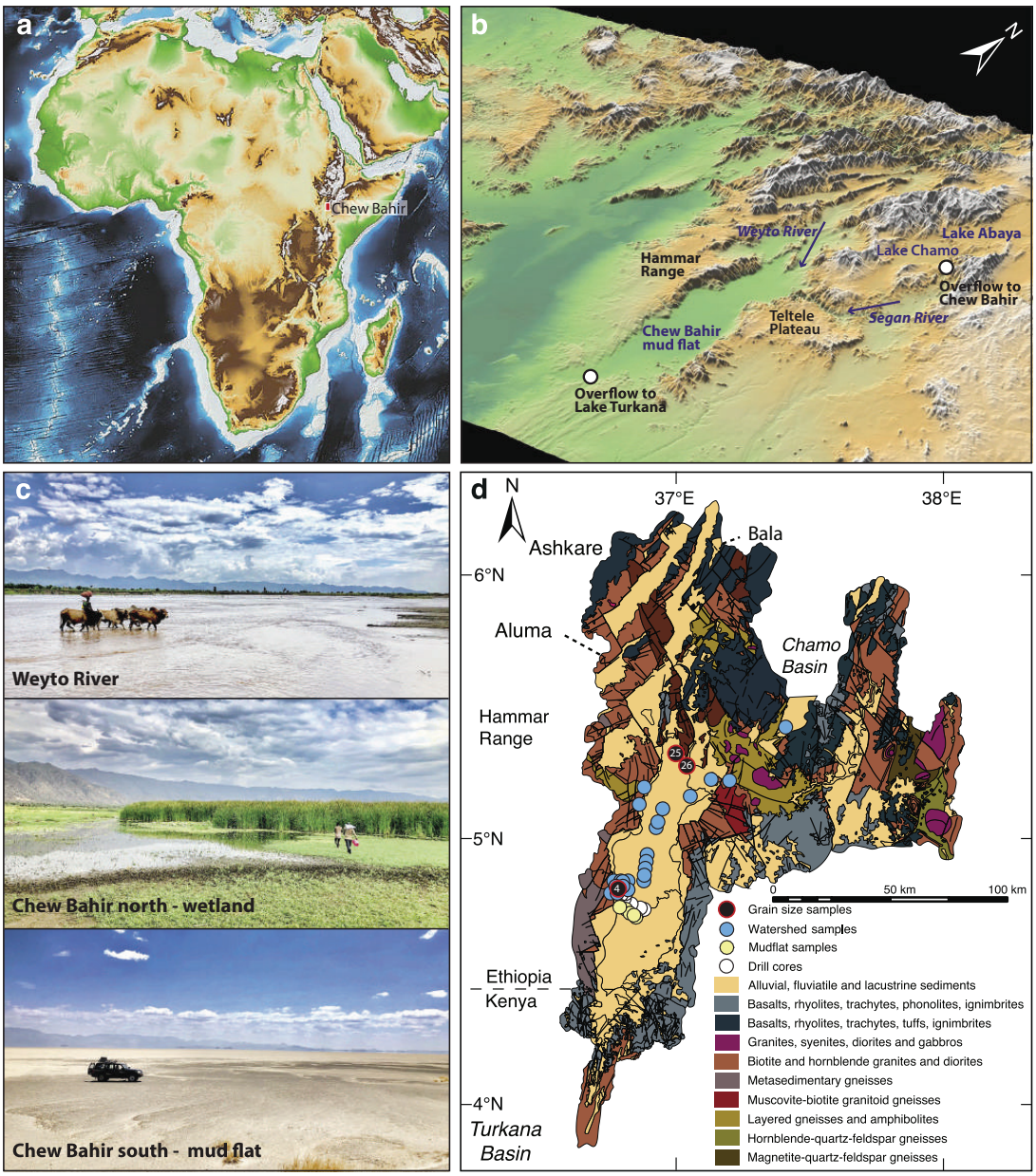

FIGURE 1 | Elevation map of **(a)** eastern Africa with **(b)** 3D, **(c)** field, and **(d)** geologic representation of the Chew Bahir basin. Filled blue and yellow-green circles in **(d)** show sampling locations for modern watershed (WS) and mudflat (MF) samples, respectively. Filled black circles in **(d)** show locations of samples collected from the Chew Bahir catchment for grain size analysis.

fine sediments by "dust-devils" or dust storms be observed. In the extreme southern part of the Chew Bahir basin, small aeolian geomorphological features like "kupsten" dunes appear close to the recent "coastline."

The Chew Bahir tectonic basin, which has an elevation of ∼500 masl, lies on the southeastern side of the western Ethiopian highlands, which are greater than ∼2,500 masl (**Figures 1a,b**). The deep basin is thus located on the lee of potential dust sources, especially the Sahara. Likewise, the ∼1,800 m high Teltele plateau, which gently descends to the east, blocks potential dust plumes from reaching the southeastern Ethiopian lowlands. The paleo-lake 'periodically fills with water (up to 2 m in depth) supplied primarily via the Weyto River. Modern dust input in the form of local short events of "dust-devils" occurs during remobilization and deposition of dust from the loose playa sediments on the strongly desiccated surface in the extreme southern part of the basin.

In sum, the Hammar Range to the west and the highlands to the north and northeast, consisting of Late Proterozoic granite and gneiss, are therefore the primary sediment sources to the Chew Bahir basin (Foerster et al., 2012). All surface samples were therefore collected between sub-watersheds from riverbeds or the

desiccated lake floor to help improve our understanding of proxy formation in this region (see sampling locations in **Figure 1d** and methods). However, it should be noted that our study cannot be considered an exhaustive survey of all geomorphological processes active in the larger Chew Bahir catchment.

HYDROGEOLOGICAL AND CLIMATIC FEATURES OF THE CHEW BAHIR CATCHMENT

Today the Chew Bahir basin and catchment area has two rainy seasons, during boreal spring and autumn, owing to the North–South migration of the tropical African rain belt (**Figures 2a–c**). The tropical African rain belt is commonly referred to as the intertropical convergence zone (ITCZ) but the twice-yearly passing of the tropical African rain belt may not necessarily be synchronized with the annual cycle of insolation (e.g., Nicholson, 2018). Catchment wide mean annual rainfall is in the order of 900–1,000 mm, and the boreal spring rainy season (i.e., March–May) accounts for >50% of the annual total (Fischer et al., 2020).

Water balance model estimates for paleo-lake Chew Bahir, based on the Surface Energy Balance Algorithm for Land, estimate an actual evaporation rate for the catchment of 847 mm/a (Fischer et al., 2020). Although mesoscale convective processes and topography also play an important role in the development of rain-bearing systems in eastern Africa (e.g., Hession and Moore, 2011), aridity in the catchment area is linked to large-scale divergence in the lower troposphere (Nicholson, 2016). The prevailing aridity in northern Kenya and southern Ethiopia is also associated with the Turkana Jet, which flows at low levels with highest wind speeds at the 850 mb pressure level; maximum aridity over the region occurs when the Turkana Jet is at minimum speed (Nicholson, 2016). There is also a negative correlation between the strength of the Turkana Jet and low level divergence, and rainfall over that region (e.g., Sun et al., 1999). On a broader scale, rainfall patterns in eastern Africa are also sensitive to sea surface temperature variability in both the Indian and Pacific Oceans (e.g., Gebregiorgis et al., 2019).

During the last African Humid Period (AHP), 20–30% more precipitation led to lake level rises of Lake Abaya-Chamo (Fischer et al., 2020). At that time, overflow spilled into the Chew Bahir basin forming paleo-lake Chew Bahir, which in turn overspilled into Lake Turkana after reaching the overflow sill at 543 masl (Fischer et al., 2020).

MATERIALS AND METHODS

Sampling

Thirty-four surface samples from the main catchment areas of paleo-lake Chew Bahir were collected in October 2018 for mineralogical, and major, minor and trace element analyses (**Table 1**). Twenty-eight of these surface samples were collected between watersheds from riverbeds (henceforth referred to as watershed samples or WS samples). Six samples were collected from the desiccated lake floor (henceforth referred to as mudflat samples or MF samples). Twelve samples from the Chew Bahir pilot drill core CB-01 were analyzed from selected wetter and drier intervals of the late Pleistocene and Holocene based on the Chew Bahir K record (**Figure 3**; Foerster et al., 2012, 2018). Samples collected from wetter intervals (henceforth referred to as WI) include 6 samples from the AHP interval, ∼15–5 ka (Demenocal et al., 2000; Shanahan et al., 2015). Samples collected from drier intervals (henceforth referred as DI) include 2 samples each from the LGM (∼21 ka BP; Clark et al., 2009), Younger

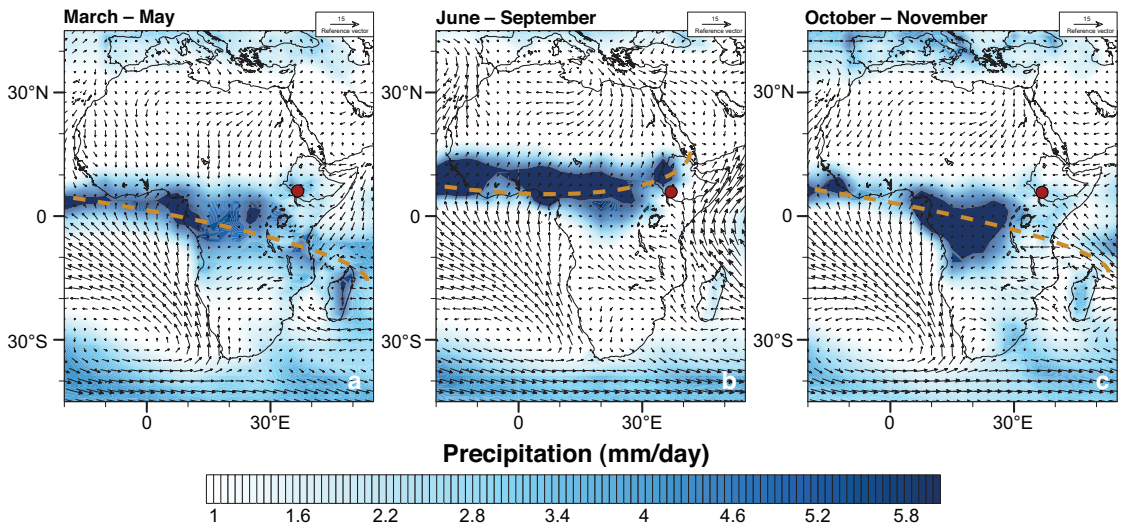

FIGURE 2 | Seasonal precipitation (mm/day) patterns in eastern Africa during **(a)** March–May, **(b)** June–September, and **(c)** October–November; mean precipitation for the period 1979–2015 at 1,000 hPa geopotential height (gph) fields. Global Precipitation Climatology Centre (GPCC) monthly precipitation data is acquired from the National Oceanic and Atmospheric Administration (NOAA) and can be accessed at https://www.esrl.noaa.gov/psd/. Thick, dashed, brown lines indicate the approximate location of the tropical African rain belt. Red circle indicates the location of the drill site.

TABLE 1 | Major/minor (wt. %) and trace (including rare earth) (ppm) element compositions of modern and down-core Chew Bahir samples.

Legend	WS1	WS2	WS3	WS4	WS5	WS6	WS7	WS8	WS9	WS10	WS11	WS12	WS13	WS14	WS15	WS16
SiO_2†	68.7	64.4	62.2	59.4	60.9	56.5	61.3	60.3	58.3	55.1	54.8	68.2	61.1	56.4	56.5	60.3
Al_2O_3†	14.0	15.3	15.3	14.3	15.6	14.8	14.7	16.4	16.9	16.7	15.9	13.1	16.4	16.5	16.2	15.9
CaO†	3.9	4.4	4.8	5.9	4.6	5.0	4.7	4.6	4.7	6.4	5.2	2.7	5.1	4.7	4.3	4.1
Fe_2O_3†	4.7	5.4	6.4	7.5	7.3	11.3	9.4	7.1	6.9	6.9	7.2	5.1	6.6	7.5	6.5	7.5
K_2O†	1.8	2.1	1.9	1.9	2.3	1.9	1.9	2.2	2.3	2.2	2.1	2.7	2.0	2.3	2.2	2.0
MgO†	1.5	1.7	2.2	2.5	2.2	2.8	2.2	2.4	2.5	3.3	3.0	1.4	2.3	3.4	2.1	2.0
Na_2O†	3.4	3.4	3.4	3.0	3.5	3.2	3.3	3.6	3.7	3.7	3.6	3.3	4.0	3.2	3.9	4.1
TiO_2†	0.5	0.7	1.0	1.0	1.0	1.7	1.3	0.9	1.0	1.0	1.0	0.6	0.9	1.1	1.0	1.2
Ba	837	833	686	741	857	673	689	876	880	789	761	804	775	840	719	565
Ce	36	52	54	57	62	81	68	62	84	79	77	61	60	77	61	63
Co	9	11	15	15	15	22	17	16	17	20	20	9	15	24	17	19
Cr	40	50	50	80	60	90	80	60	70	80	80	40	60	90	60	70
Dy	3.5	5.5	5.3	5.8	5.3	7.0	5.7	5.5	6.5	6.7	6.6	7.0	5.4	6.4	5.1	6.3
Er	2.2	3.0	3.1	3.3	2.9	4.0	3.3	3.1	3.5	3.9	3.6	3.4	3.1	3.6	2.8	3.4
Eu	1.2	1.7	1.8	1.6	1.8	1.9	1.7	1.8	2.0	2.2	2.2	2.2	1.8	2.1	1.8	1.7
Ga	14.0	16.0	18.0	17.0	18.0	21.0	19.0	19.0	21.0	21.0	21.0	19.0	19.0	21.0	20.0	20.0
Gd	3.4	5.0	5.5	5.6	5.7	7.5	6.0	5.7	7.3	7.1	6.9	7.1	5.4	7.1	5.4	6.0
Hf	3.1	4.2	4.8	4.5	4.8	7.9	7.2	7.0	10.6	8.2	6.6	4.8	6.6	6.6	5.1	6.3
Ho	0.7	1.0	1.1	1.1	1.0	1.3	1.1	1.1	1.2	1.2	1.3	1.3	1.1	1.2	0.9	1.2
La	17.9	26.6	26.3	27.3	29.7	37.0	31.7	29.7	39.6	37.5	36.3	29.3	28.5	37.0	30.0	29.3
Lu	0.4	0.5	0.5	0.5	0.4	0.6	0.5	0.4	0.5	0.5	0.6	0.5	0.5	0.5	0.4	0.5
Nb	3.0	6.0	6.0	6.0	6.0	11.0	8.0	8.0	11.0	9.0	8.0	4.0	6.0	9.0	14.0	16.0
Nd	18	26	29	28	32	40	34	31	41	41	40	35	31	39	30	32
Rb	28	37	34	36	44	37	32	47	48	52	46	51	34	52	46	33
Sc	12	15	14	19	14	20	16	15	16	18	17	10	14	20	13	14
Sm	3.9	5.9	6.4	6.5	7.1	8.4	7.4	6.8	9.1	8.6	8.7	8.5	6.4	8.6	6.4	7.4
Sr	482	456	491	504	473	429	436	457	526	584	542	315	522	452	538	433
Tb	0.6	0.9	0.9	1.0	0.9	1.2	1.0	0.9	1.1	1.1	1.1	1.2	0.9	1.1	0.9	1.0
Th	2.6	3.8	3.2	4.3	4.2	5.9	5.2	4.1	5.1	3.5	3.6	4.7	3.6	5.4	3.3	3.2
Tm	0.3	0.5	0.4	0.5	0.4	0.6	0.5	0.4	0.5	0.5	0.5	0.5	0.4	0.5	0.4	0.5
U	0.4	0.7	0.5	0.7	0.5	0.7	0.6	0.6	0.8	0.7	0.7	0.5	0.5	0.7	0.6	0.8
V	82	88	101	148	119	213	175	107	107	112	119	61	107	134	95	122
Yb	2.1	3.0	2.8	3.4	2.6	3.8	3.2	2.7	3.2	3.4	3.5	3.0	2.8	3.3	2.5	3.2
Zr	126	182	186	168	197	306	282	270	410	316	264	215	259	270	200	251
CIA	60	61	60	57	60	60	60	61	61	57	59	60	60	62	61	61
Eu/Eu*	1.01	0.91	0.89	0.76	0.81	0.72	0.74	0.88	0.73	0.82	0.83	0.82	0.91	0.80	0.92	0.77

(Continued)

TABLE 1 | Continued

Legend	WS17	WS18	WS19	WS20	WS21	WS22	WS23	WS24	WS25	WS26	WS27	WS28	MF1	MF2	MF3
SiO_2†	67.0	55.5	55.4	56.2	56.5	61.8	65.2	59.4	60.1	54.4	58.3	44.9	42.4	28.9	31.4
Al_2O_3†	14.0	16.1	15.6	15.0	16.6	15.7	12.0	14.1	15.1	14.7	15.1	14.2	12.1	8.6	9.4
CaO†	3.4	7.2	4.6	6.2	4.8	4.5	4.1	5.3	7.3	9.9	7.2	8.3	8.0	14.7	15.6
Fe_2O_3†	6.2	9.5	7.6	7.5	7.7	7.1	5.4	8.8	8.1	9.0	10.1	17.2	9.3	6.4	6.9
K_2O†	2.1	1.5	2.3	2.6	2.5	2.1	2.2	2.0	1.4	0.4	0.5	1.0	2.2	1.5	1.6
MgO†	1.3	3.1	2.5	2.6	2.9	1.7	1.3	2.9	1.8	6.8	3.7	3.7	5.1	3.1	3.4
Na_2O†	3.7	3.9	3.3	3.4	4.0	4.2	2.7	3.1	3.3	2.9	2.6	2.8	4.9	11.6	6.7
TiO_2†	0.9	1.3	1.0	0.9	1.1	1.0	0.8	1.6	0.6	0.7	0.7	3.0	1.1	1.1	1.1
Ba	738	470	696	754	766	711	542	776	855	170	209	523	371	485	524
Ce	57	44	68	65	66	49	68	50	61	31	17	77	83	95	105
Co	11	22	21	19	20	13	12	23	20	24	50	36	25	16	18
Cr	50	120	80	80	90	50	50	230		770	24	100	60	50	50
Dy	4.2	5.0	6.5	5.7	6.0	4.5	5.5	4.8	5.7	5.1	4.0	6.9	7.8	8.5	8.9
Er	2.3	2.8	3.5	3.1	3.3	2.5	3.1	2.7	3.4	3.0	2.3	3.4	4.1	4.4	4.8
Eu	1.5	1.5	1.8	1.8	2.1	2.0	1.6	1.7	1.6	1.7	1.1	2.7	2.3	2.6	2.9
Ga	17.0	19.0	20.0	20.0	22.0	19.0	17.0	18.0	16.0	18.0	14.0	23.0	19.0	13.0	14.0
Gd	4.4	4.9	6.6	5.7	6.1	4.7	6.1	4.8	6.4	5.2	3.5	7.7	8.2	8.9	9.8
Hf	5.7	4.4	5.0	4.7	6.3	5.1	6.4	9.5	2.3	1.6	0.9	5.6	5.4	3.6	4.0
Ho	0.8	1.0	1.3	1.1	1.2	0.9	1.0	0.9	1.1	1.0	0.8	1.3	1.5	1.6	1.7
La	28.3	20.2	32.4	32.2	30.6	23.6	32.4	22.9	30.1	12.4	7.2	38.5	48.7	55.1	59.3
Lu	0.3	0.4	0.5	0.4	0.5	0.4	0.4	0.5	0.5	0.4	0.3	0.5	0.6	0.6	0.7
Nb	9.0	10.0	12.0	12.0	12.0	8.0	17.0	15.0	5.0	4.0	1.0	37.0	31.0	26.0	26.0
Nd	28	23	36	32	33	25	34	26	31	21	13	40	45	52	55
Rb	34	22	48	58	55	35	43	43	17	2	6	16	42	27	31
Sc	9	24	17	17	18	13	10	18	23	41	39	28	17	15	18
Sm	5.4	5.3	8.1	7.2	7.6	5.5	7.1	5.6	7.0	5.5	3.4	8.7	9.7	11.1	11.8
Sr	501	510	418	479	524	561	319	537	723	714	209	462	498	860	917
Tb	0.7	0.8	1.1	0.9	1.0	0.7	1.0	0.8	1.0	0.8	0.6	1.2	1.3	1.4	1.5
Th	4.0	2.4	3.5	3.5	3.4	2.6	4.6	4.5	0.2	0.2	0.1	3.8	5.7	5.7	6.4
Tm	0.3	0.4	0.5	0.4	0.5	0.4	0.4	0.4	0.5	0.5	0.3	0.5	0.6	0.7	0.7
U	0.5	0.5	0.7	0.7	0.7	0.4	1.2	1.8	0.2	0.1	0.1	1.2	0.8	5.0	1.8
V	96	191	111	113	128	114	79	177	90	212	1	344	134	126	119
Yb	2.0	2.7	3.4	2.7	3.0	2.4	2.8	2.9	3.4	2.8	2.2	3.1	3.6	4.1	4.1
Zr	229	171	196	175	239	199	238	357	81	50	17	228	211	147	156
CIA	60	56	60	55	60	59	57	58	56	53	60	54	44	24	28
Eu/Eu*	0.90	0.85	0.71	0.81	0.89	1.15	0.70	0.96	0.71	0.93	0.93	0.97	0.76	0.77	0.78

(Continued)

TABLE 1 | Continued

Legend	MF4	MF5	MF6	DI1	DI2	DY3	DI4	DI5	DI6	WI1	WI2	WI3	WI4	WI5	WI6
SiO_2†	37.2	39.7	45.4	35.6	40.9	40.9	41.9	44.8	42.5	44.3	43.8	49.5	41.6	45.5	36.7
Al_2O_3†	12.3	12.8	15.1	9.7	10.1	10.7	11.3	11.2	10.5	11.1	11.5	11.0	10.7	10.4	8.2
CaO†	10.5	8.6	6.1	13.4	5.4	9.5	5.8	2.6	6.2	5.2	5.2	2.0	7.8	3.3	11.6
Fe_2O_3†	8.8	9.0	9.7	7.0	8.6	8.7	9.1	10.0	8.5	8.7	9.5	8.8	8.6	8.1	6.5
K_2O†	1.7	1.8	1.8	2.3	2.9	2.4	2.4	2.8	2.3	1.9	1.6	1.3	1.3	1.6	1.1
MgO†	3.5	3.6	3.5	5.1	7.1	5.5	6.5	6.1	4.9	5.1	3.4	2.5	2.8	3.2	2.9
Na_2O†	6.0	6.5	2.7	4.6	5.0	4.3	5.5	6.0	5.8	4.9	5.0	6.3	5.4	8.4	7.8
TiO_2†	1.4	1.3	1.4	0.9	1.0	1.0	1.1	0.9	1.0	0.9	1.0	0.9	0.9	0.9	0.7
Ba	459	469	502	514	281	381	345	204	288	279	330	236	345	308	304
Ce	104	92	91	75	44	68	66	62	69	59	81	71	103	55	69
Co	24	25	26	18	24	21	23	28	23	23	23	24	20	17	14
Cr	60	70	90	60	50	50	70	90	50	60	70	70	70	50	60
Dy	9.9	8.1	7.8	6.2	3.7	5.4	4.8	4.3	5.3	4.9	6.2	5.7	7.4	4.4	5.0
Er	5.0	4.3	4.0	3.2	2.0	3.0	2.5	2.3	2.9	2.7	3.3	3.2	3.9	2.3	2.6
Eu	3.1	2.5	2.4	1.7	1.0	1.5	1.4	1.1	1.5	1.4	1.6	1.6	1.9	1.2	1.4
Ga	19.0	19	22	14	15	15	16	18	16	16	17	18	16	12	12
Gd	10.5	8.4	8.4	7.0	4.1	6.0	5.3	4.4	6.0	5.5	6.7	6.4	7.9	4.7	5.6
Hf	5.1	4.6	5.8	3.7	4.5	4.8	4.0	6.0	5.0	4.7	4.3	5.1	4.2	3.5	3.2
Ho	1.8	1.5	1.4	1.2	0.7	1.0	0.9	0.9	1.0	0.9	1.2	1.1	1.4	0.9	0.9
La	61.3	51	47	38	23	31	31	25	32	30	36	37	44	27	31
Lu	0.7	0.6	0.6	0.5	0.3	0.4	0.4	0.3	0.4	0.4	0.5	0.4	0.6	0.3	0.4
Nb	32.0	30	30	21	25	26	25	32	28	24	24	27	26	19	19
Nd	61	48	45	37	22	31	30	24	31	29	36	36	43	26	29
Rb	39	43	49	52	56	44	60	56	47	57	64	54	55	41	42
Sc	18	19	22	15	14	18	15	18	21	18	20	17	17	16	13
Sm	12.9	10.3	9.6	7.7	4.4	6.4	6.0	4.9	6.6	6.2	7.5	7.4	8.8	5.4	6.0
Sr	645	516	410	778	356	536	449	169	372	259	211	129	284	197	397
Tb	1.7	1.3	1.4	1.1	0.6	0.9	0.8	0.7	0.9	0.8	1.1	1.0	1.2	0.8	0.9
Th	6.9	6.4	6.4	5.7	3.8	5.2	5.5	5.6	5.2	5.3	6.1	6.0	8.3	4.6	5.3
Tm	0.7	0.6	0.6	0.4	0.3	0.4	0.3	0.4	0.4	0.4	0.5	0.5	0.6	0.3	0.4
U	1.3	2.3	1.4	2.1	1.0	1.0	2.5	1.7	2.2	1.4	1.3	1.9	2.3	3.3	4.4
V	165	145	160	103	97	121	142	302	108	146	117	145	104	120	101
Yb	4.4	3.8	3.6	3.1	1.9	2.7	2.3	2.3	2.7	2.4	2.9	3.0	3.8	2.2	2.4
Zr	187	179	214	150	190	208	162	278	208	208	198	200	182	161	131
CIA	40	43	59	32	43	40	45	50	42	48	49	54	42	44	28
Eu*	0.78	0.78	0.81	0.70	0.72	0.74	0.72	0.69	0.71	0.70	0.69	0.70	0.69	0.68	0.70

†*Given in wt. %; Eu/Eu* = (2Eu/Eu$_{chondrite}$)/(Sm/Sm$_{chondrite}$ + Gd/Gd$_{chondrite}$).*

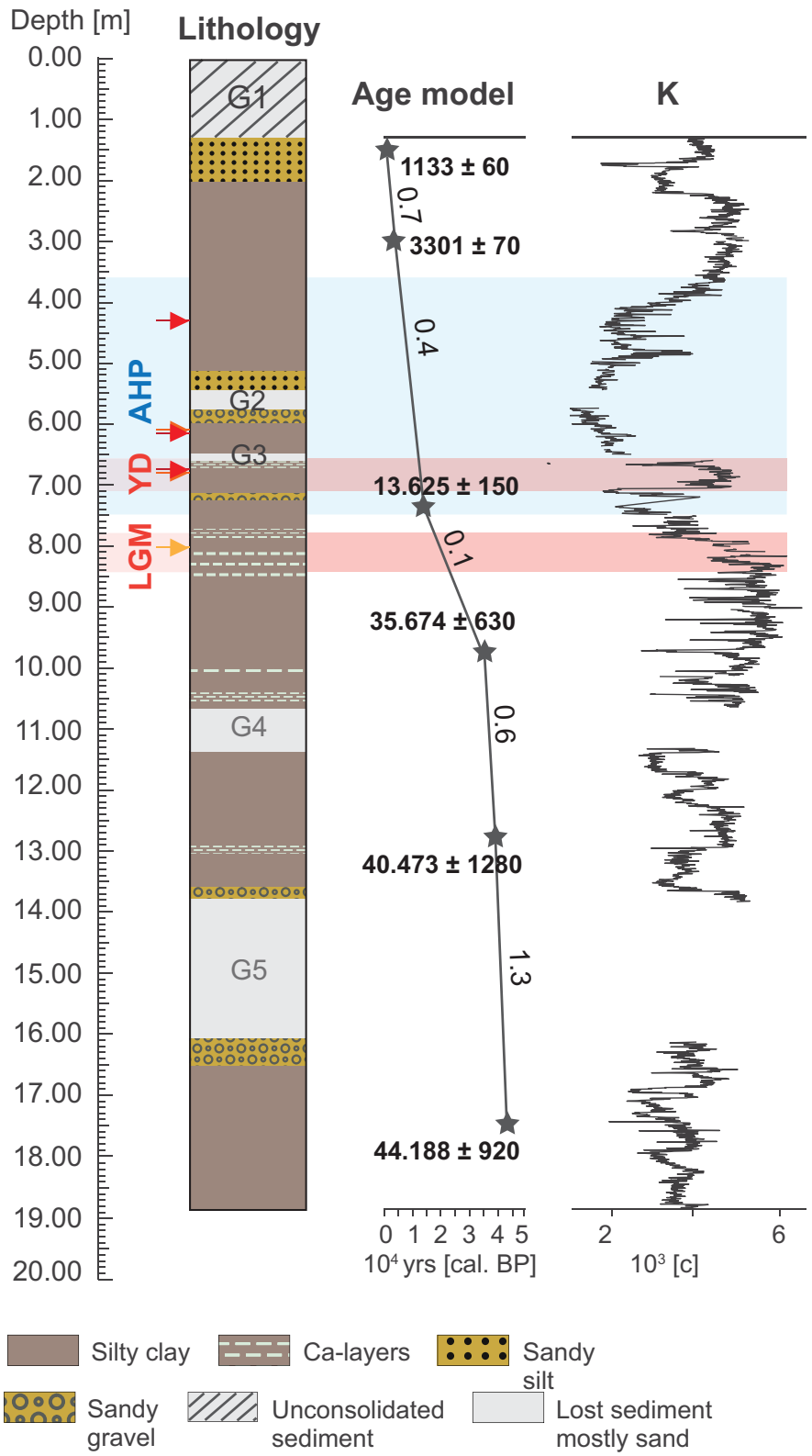

FIGURE 3 | Core lithology, age-depth model, and the Chew Bahir K record over the past ~45 kyrs.

Dryas (YD; ∼12.9–11.7 ka BP; Roberts et al., 1993) and Late Holocene (representing the last ∼2 ka BP of the record; **Figure 3**). Three samples (i.e., W4, W25, and W26) were collected in November 2018 for grain size analysis (**Figure 1**). W25 and W26 were collected from the Weyto River catchment entering into the Chew Bahir basin. W26 was collected from a freshly accumulated riverbank, while W25 represents an alluvial fan accumulation site between Weyto town and Weyto River. W4 was collected from a deep incised river at the foot of the Hammar range in the southern part of the Chew Bahir basin (see **Figure 1** for sample locations).

X-Ray Diffraction, Electron Microprobe and Grain Size Analysis

The mineralogical composition of powdered bulk sediments and oriented mounts of clay particles (<2 μm) were analyzed using X–ray powder diffraction (XRD) at the Department of Geosciences, Georgia State University. The clay fractions were extracted according to Stokes' settling velocity principle in 1,000 ml glassware. Randomly-oriented, powdered bulk samples were analyzed using Cu-Kα radiation (45 kV, 40 mA) from 5 to 70° 2θ, with a 0.02° 2θ step and 60 s per step, to identify a suite of non-clay minerals. Preferred-oriented samples of the <2 μm size fraction were analyzed in both air-dried (AD) and ethylene glycol-solvated (EG) states from 3 to 35° 2θ with a 0.02° 2θ step at 60 s per step, following the principles of Moore and Reynolds (1997).

The octahedral cation ratios [(Mg/(Al + Fe)] of the <0.1 μm size-fractions were determined using the JEOL-8200 electron microprobe at Rutgers University. The analyses were performed at 15 Kv accelerating voltage and 15 mA beam current, using a suite of in-house standards, including several hydroxyl-bearing sheet silicates, and derived from multiple sources. Data corrections were done using ZAF procedures. Since the samples are intrinsically fine-grained powders, normal polishing procedures could not be used and instead the samples had the form of compressed pellets that were sufficiently smooth to permit analysis. The presence of unquantified inter-grain voids reduces the overall density of the samples and, together with unanalyzed hydroxyl fractions, prevents the analysis totals reaching the nominal 100%.

Grain size analysis was carried out at the laboratory of the Geographic Institute, University of Cologne. Analysis was conducted in 116 channels from 0.04 to 2,000 mm with a Laser Diffraction Particle Size Analyzer (LS 13320 Beckmann CoulterTM), using the Fraunhofer optical model. Before analysis, organic and carbonate content was removed using 15% H2O2 and 10% HCL, respectively. Grain-size parameters are based on Folk and Ward (1957) and were calculated by GRADISTAT software version 8 (Blott and Pye, 2001).

Quantitative Multi-Element and Oxygen-Isotope Analysis

A total of 46 samples were analyzed for major, minor and trace elements at the Activation Laboratories Ltd. in Ontario, Canada following the analytical procedure termed "Code 4LITHO Major Elements Fusion ICP (WRA)/Trace Elements Fusion ICP/MS." Major, minor and trace element data were acquired by ICP-OES fusion and ICP-MS, respectively. Samples were analyzed in a batch system with each batch containing a method reagent blank, certified reference material and duplicates. Samples were analyzed for major oxides and selected trace elements (Code 4B) using Perkin Elmer Sciex ELAN 6000, 6100, or 9000 ICP/MS, providing a precision of ±5% and 10% for major and minor oxides, and trace elements at 100x the detection limit, respectively. Seven USGS and CANMET certified reference materials were used for calibration and one of the 7 standards was analyzed for every group of 10 samples. Three blanks and duplicates were analyzed per group of samples and every 15 samples, respectively.

The chemical index of alteration (CIA) was calculated on the basis of major element chemistry following Nesbitt and Young (1982) as follows:

$$CIA = [Al_2O_3/(Al_2O_3 + Na_2O + K_2O + CaO)] \times 100 \quad (1)$$

Six samples (3 each from DI and WI) were selected for clay mineral purification and subsequent oxygen-isotope analysis. Ultrafine clay size-fractions (<0.1 μm) were separated from the bulk sediments following routine centrifugation protocols (Moore and Reynolds, 1997) for XRD analysis. Samples were analyzed in both AD and EG states from 3 to 35° 2θ. Oxygen-isotope analyses were performed on the same samples at the Laboratory for Stable Isotope Science at the University *of* Western Ontario following Libbey et al. (2013) and references therein. The results are presented in the normal δ-notation relative to the VSMOW-SLAP calibrated scale in parts per thousand (‰). Reproducibility was better than ±0.2‰. VSMOW-SLAP calibrated standards analyzed as unknowns returned $\delta^{18}O$ = + 11.54 ± 0.2‰ (quartz; n = 2) and +10.18 ± 0.01‰ (carbon dioxide; n = 2), which compares well with their accepted values of +11.5‰ and +10.25‰, respectively (Huggett et al., 2017).

Geochemical Modeling

Geochemist's Workbench® (Bethke et al., 2019) was used to model the evaporative concentration of water with a dissolved solid composition equivalent to Lake Chamo, a freshwater lake that drains through the Segen River to the Chew Bahir basin (**Table 2**; Ayenew, 2005). Equilibrium reactions were modeled iteratively to dryness, assuming equilibrium gas exchange with the atmosphere. Equilibrium precipitation-dissolution was assumed with respect to gibbsite, and the precipitation of dolomite, talc, chrysotile, and mica were all suppressed as reaction kinetics likely do not favor these authigenic phases (Deocampo, 2010; Deocampo and Jones, 2014).

RESULTS

Mineralogy and Grain Size Distribution

The mineralogical assemblage of the WS samples is composed primarily of sand- and silt-size particles containing a higher fraction of non-clay mineral silicate phases than the MF samples,

TABLE 2 | Chemical composition of Lake Chamo water used for geochemical modeling.

Solute	Concentration (mg/L)
Na	265
K	14.1
Ca	2.2
Mg	3.8
Cl	64.9
SO_4	4.1
HCO_3	573
pH = 8.9	

which comprised mostly clay minerals. In addition to illite, smectite, and kaolinite, the <2 μm size-fraction of the WS samples also contain quartz and feldspar, and trace amounts of calcite and analcime (**Figure 4**). Analcime content increases in the MF samples that are transitional to the desiccated lake floor of the Chew Bahir basin. The <2 μm size-fraction of the MF samples contains illite, smectite and kaolinite (**Figure 4**).

Grain-size data of three samples are shown in **Supplementary Figure 2**. Two of the three samples (i.e., W26 and W4) show unimodal features, while one (W25) shows multimodal features (**Supplementary Figure 2**). All samples contained relatively little material in the 2–50 μm aeolian size range (**Supplementary Figure 2**). The amount of material within the 2–50 μm fraction in W26 and W4, and W25 samples is ∼14% and 36.8%, respectively.

Whole-Rock and Authigenic Clay Mineral Geochemistry

Major and trace element concentrations of the different sample groups show clear intergroup differences in the enrichment and depletion of certain major elements (**Table 1**). WS samples have higher SiO_2 (50–70 wt.%) contents compared to the MF samples (**Figure 5** and **Table 1**). In WS samples, as SiO_2 content increases, most other element abundances decrease, suggesting their association with non-quartz minerals. K_2O contents, however, remain relatively constant as SiO_2 varies. In MF samples, major element contents increase with increasing SiO_2, except for CaO, which strongly decreases. On the A–CN–K diagram (**Figure 6a**), WS samples are richest in Al_2O_3 (∼50–70%); CaO + Na_2O contents in MF samples trend toward the cluster of WS samples while their K_2O contents remain at ≤10%. On the A–CNK–FM diagram (**Figure 6b**), the CaO + Na_2O + K_2O content of some MF samples increases to ∼50% approaching the cluster of WS samples. CIA values (**Table 1**) range between 24 and 62 with WS samples consistently yielding higher values. Mean CIA values for WS and MF samples are 59 and 40, respectively. Mean CIA values for WI and DI samples are 44 and 42, respectively.

Upper Continental Crust-normalized (McLennan, 2001) chemical compositions of the sediments show that MF samples, on average, are enriched in elements such as Mg, Ca, Ce, Nd, and Na, and depleted of elements such as Ba and Zr relative to WS samples (**Figures 7a,b**). DI samples, on average, are enriched in Mg and depleted of K relative to WS samples (**Figures 7c,d**). Chondrite-normalized REE patterns reveal minor differences between the WS and MF samples (**Figure 8**). WS samples [e.g., mean $(La/Sm)_N$ = 2.61] are slightly depleted of Light REE (LREE) compared to MF samples [e.g., mean $(La/Sm)_N$ = 3.07] (**Figure 8**). Similarly, no significant differences are observed between Heavy REE (HREE) in WS [e.g., average $(Gd/Yb)_N$ = 1.61] and MF [e.g., average $(Gd/Yb)_N$ = 1.86] samples. No preferential removal of LREE or HREE is observed for either DI or WI samples (**Figure 8**). Eu anomalies in WS (mean Eu/Eu^* = 0.85), MF (mean Eu/Eu^* = 0.78), DI (mean Eu/Eu^* = of 0.71), and WI (mean Eu/Eu^* = 0.69) samples are also virtually identical (**Table 1**).

Whole-rock Ba/Sr ratios, a widely used proxy for weathering intensity (e.g., Buggle et al., 2011), show WS and WI samples generally having higher Ba/Sr ratios compared to MF and DI samples (**Figure 9a**). On average, MF samples have higher MgO/Al_2O_3 ratios (mean = 0.3) than WS samples (mean = 0.15), but both DI and WI samples have higher MgO/Al_2O_3 ratios compared to MF samples (**Figures 9a,b**). MgO/Al_2O_3 and Ba/Sr ratios in WS and MF samples show a somewhat higher degree of correlation (R^2 = 0.64) than in WI and DI samples (R^2 = 0.52; **Figure 9a**). MgO/Al_2O_3 and K_2O/Al_2O_3 ratios in DI and WI samples similarly show a high degree of correlation (R^2 = 0.64; **Figure 10a**), and this relationship is the same for MgO and K_2O.

Oxygen-isotope measurements of authigenic clay minerals ($\delta^{18}O_{illite-smectite}$ = + 22.44 to + 25.32‰) show that, except for one sample, the DI samples have higher $\delta^{18}O_{illite-smectite}$ compared to WI samples (**Figures 10b,c** and **Table 3**). The oxygen-isotope results for the <0.1 μm size-fraction also correlate well with the octahedral Mg/(Al + Fe) ratios determined by electron microprobe analysis (**Figure 10b** and **Table 3**).

Geochemical Modeling

Model results (**Figure 11**) show the immediate precipitation of calcite, reflecting the near-saturation of most surface waters in the region with respect to calcium carbonate. Evaporative concentration increases the amount of calcite precipitation and is also associated with analcime formation (Foerster et al., 2018). The next phase to reach supersaturation in the system is analcime ($NaAlSi_2O_6 \bullet H_2O$). Although solid phase analcime is stable in these surface waters, only a small mass of mineral was predicted to precipitate. The final phase to reach supersaturation is sepiolite [$Mg_4(Si_6O_{15})(OH)_2 \bullet 6H_2O$].

DISCUSSION

Weathering, Early Diagenesis and Authigenesis in Chew Bahir Sediments

The sedimentary deposits comprised in the Chew Bahir cores are primarily derived from Precambrian metamorphic rocks of the Hammar Range and the volcanic rocks at the northern and northeastern parts of the catchment via erosion and physical weathering of the source rock, which also facilitates chemical weathering. The CIA, first introduced by Nesbitt and Young (1982), has proved useful for quantifying progressive chemical weathering of the source rock, with higher

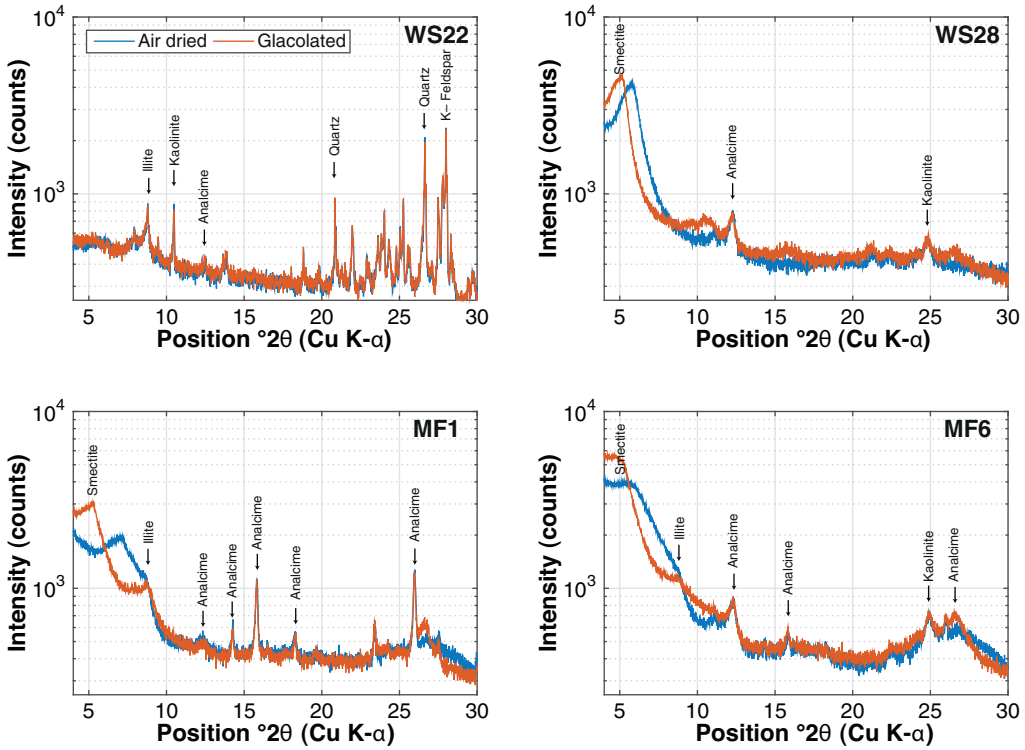

FIGURE 4 | XRD patterns of preferred-oriented, air-dried and glycolated mounts of the <2 μm size-fraction for four (4) WS and MF samples of modern Chew Bahir sediments. WS, modern watershed; and MF, modern mudflat. XRD patterns for air-dried samples are shown in blue, and those for samples treated with ethylene glycol, red.

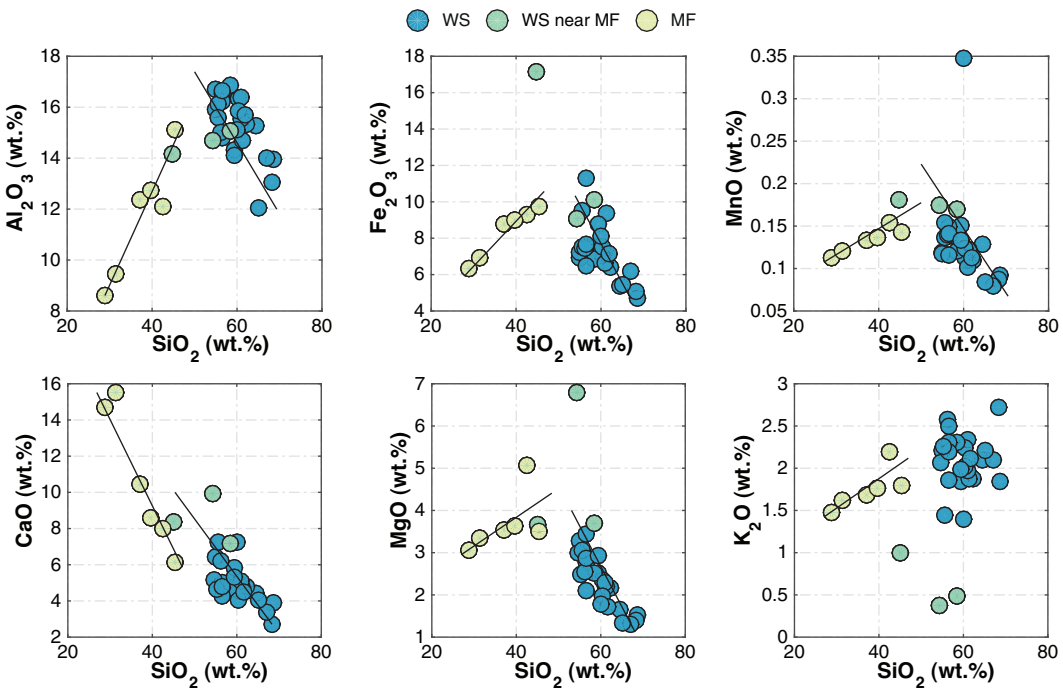

FIGURE 5 | Relationships between major element oxide and SiO_2 contents in WS and MF samples. WS, modern watershed; and MF, modern mudflat.

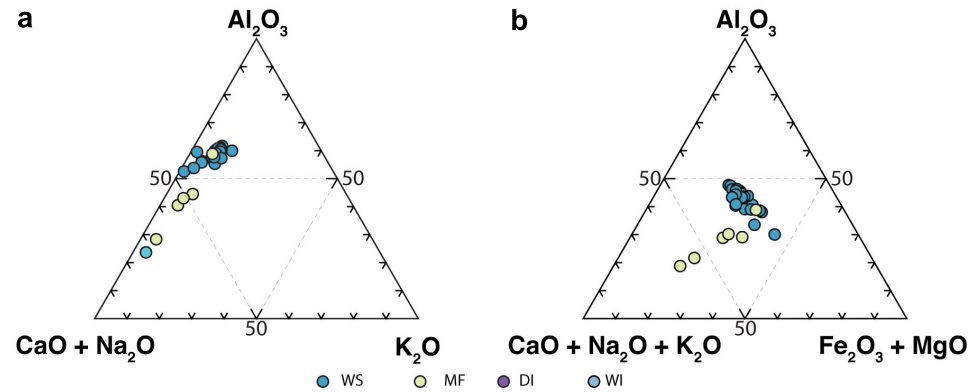

FIGURE 6 | Ternary plots of **(a)** A-CN-K, and **(b)** A-CNK-FM illustrating the degree of alteration in WS, MF, WI, and DI samples. WS, modern watershed sample; and MF, modern mudflat sample.

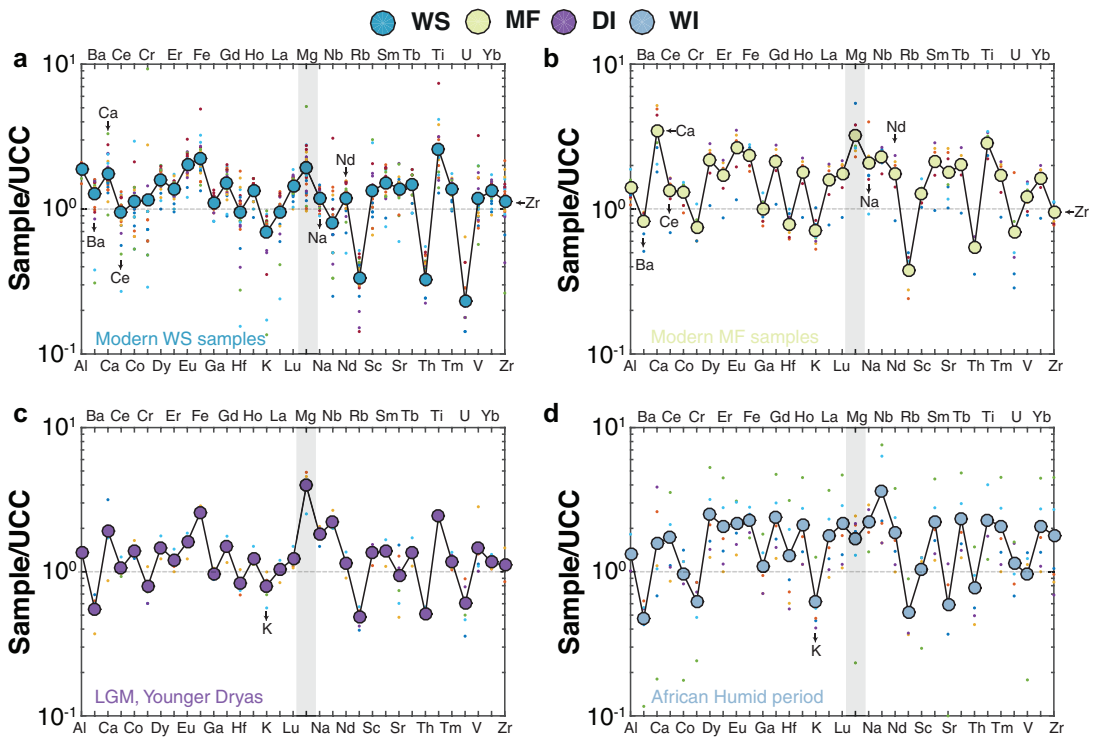

FIGURE 7 | Upper Continental Crust (UCC)-normalized (McLennan, 2001) chemical composition in **(a)** WS, **(b)** MF, **(c)** DI, and **(d)** WI samples. Colored dots show the individual averages for each sample group. WS, modern watershed; MF, modern mudflat; MF, modern mudflat; DI, late Quaternary dry interval; and WI, late Quaternary wet interval.

values indicating stronger weathering. In the case of WS samples, both physical weathering of the source rock material (i.e., metamorphosed granitic and gneissic rocks) and progressive chemical weathering are likely at play. The presence of authigenic carbonates, abundant in MF samples, however, complicates application of the CIA when endeavoring to capture the true extent of weathering (e.g., Cullers, 2000; Buggle et al., 2011; Garzanti et al., 2014). The Fe_2O_3, MnO, and K_2O contents of both WS and MF samples are about the same but the CaO content is generally higher in MF samples (**Figure 5**). Solving Equation 1 excluding CaO provides higher CIA values for WS samples (i.e., mean CIA = 74) than MF samples (i.e., mean CIA = 60), indicating stronger weathering in WS samples than MF samples. Although the unavailability of a systematic dust record is a key limitation, the conclusion that sedimentary deposits comprised in the Chew Bahir cores are primarily derived from Precambrian metamorphic rocks of the Hammar Ranis is consistent with the inferences made from XRD and grain size data (**Supplementary Figures 1**, **2**). The XRD data do not show evidence for windblown or distant aeolian-transported

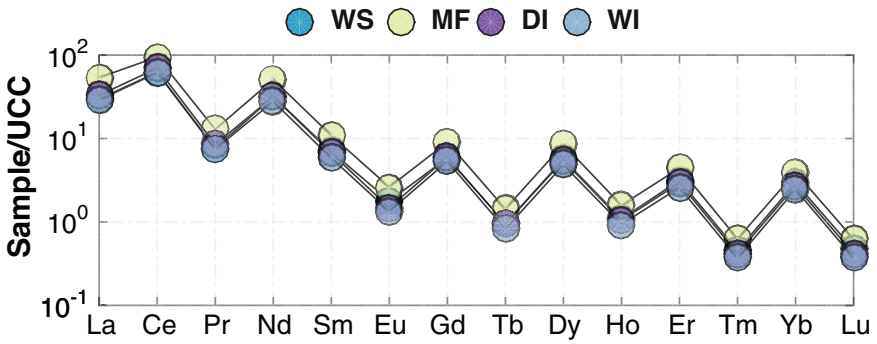

FIGURE 8 | REE patterns normalized to chondrite (McDonough and Sun, 1995) in MF (yellow-green), DI (purple), WI (light blue), and WS (blue) samples. WS, modern watershed; MF, modern mudflat; DI, late Quaternary dry interval; and WI, late Quaternary wet interval.

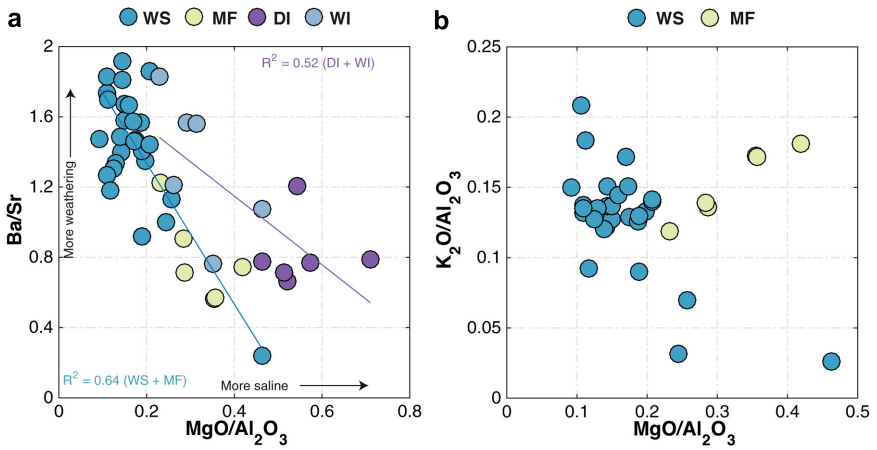

FIGURE 9 | Comparison between **(a)** Ba/Sr and MgO/Al_2O_3 for WS, MF, DI, and WI samples and **(b)** K_2O/Al_2O_3 and MgO/Al_2O_3 for WS and MF samples. WS, modern watershed; MF, modern mudflat; DI, late Quaternary dry interval; and WI, late Quaternary wet interval. The R^2 values shown in the lower left corner of **(b)** are for Ba/Sr versus MgO/Al_2O_3 in WS and MF (blue), and WI and DI (purple) samples, respectively. Arrows in **(b)** show direction of increase in weathering intensity and salinity inferred from the Ba/Sr and MgO/Al_2O_3 ratios, respectively.

dust sources, which are commonly associated with clay minerals such as palygorskite (see, for example, Ehrmann et al., 2017 and **Supplementary Figure 1**). Two of the three samples (i.e., W26 and W4) collected for grain size analysis derived from freshly transported material of recent riverbeds show unimodal features and very little material in the 2–50 μm aeolian size range (**Supplementary Figure 2**). W25 collected from an alluvial fan accumulation is a mixture of different grain-size fractions with multimodal features, suggesting strong local fluvial reworking (**Supplementary Figure 2**). The amount of material in the 2–50 μm size range is also much higher in W25 (∼36. 8%) than in W26 and W4 (∼14.4%), and lends further support for the aforementioned interpretations vis-à-vis the source of Chew Bahir sediments. We concede, however, that the above interpretations need to be independently verified using dust traps.

As described in the Results section, notable differences in major and minor whole-rock geochemistry exist between MF and WS samples (**Figure 5** and **Table 1**). Differences also include significant enrichment of MF samples compared to WS samples in some mobile elements (e.g., Na and Mg), which may have been introduced externally from saline, alkaline pore waters (**Figures 7a,b**). Na contents in WI and DI samples, however, are not significantly different (**Figure 7c,d**). The decreasing trend in Al_2O_3, Fe_2O_3, MnO, and MgO contents with increasing SiO_2 in the WS samples reflects the process involved in the formation of the source granitic rocks by a simple fractional crystallization (e.g., Asrat and Barbey, 2003). However, the MF samples also show an increase in MgO, which indicates its possible enrichement during chemical weathering (e.g., clay formation; **Figure 5**).

The true extent of early diagenetic control on the elemental composition of Chew Bahir sediments is amplified in their clay mineralogy. The modern MF samples mostly contain illite, Mg-rich smectite and some kaolinite (**Figure 4**). The Mg enrichment observed in clay minerals from MF samples is similar to late Quaternary DI samples and most likely reflects authigenic clay mineral formation from the alteration of feldspathic glass

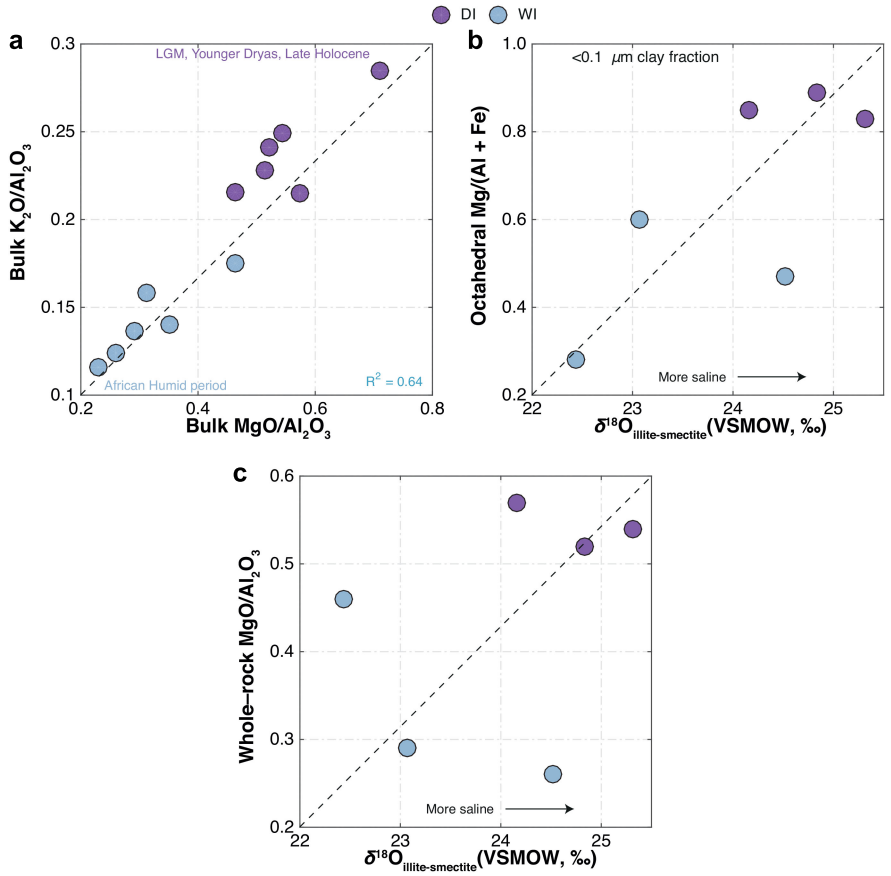

FIGURE 10 | Comparison for DI and WI samples between **(a)** bulk K_2O/Al_2O_3 and MgO/Al_2O_3, **(b)** octahedral Mg/(Al + Fe) versus $\delta^{18}O$ of authigenic illite-smectite (<0.1 μm size-fraction), and **(c)** bulk MgO/Al_2O_3 versus $\delta^{18}O$ of authigenic illite-smectite (<0.1 μm size-fraction). Arrows in **(b,c)** show direction of increase in salinity deduced from $\delta^{18}O_{illite-smectite}$.

TABLE 3 | $\delta^{18}O$ values and octahedral cation ratios for illite-smectite from late Quaternary samples.

Samples	Timing (Sample group)	$\delta^{18}O_{illite-smectite}$ (‰)*	Oct Mg	Oct Fe	Oct Al	Oct Mg/(Fe + Al)*
CB- 05- 2010- 478	LGM (DI)	+25.32	0.44	0.73	0.81	0.87
CB- 01- 2009-658	AHP (WI)	+23.07	0.80	0.64	0.68	0.65
CB- 03- 2010- 468	AHP (WI)	+24.52	0.99	0.75	0.46	0.47
CB- 01- 2009-730	YD (DI)	+24.83	1.06	0.74	0.46	0.95
CB- 03- 2010- 570	YD (DI)	+24.16	0.98	0.79	0.37	1.08
CB- 01- 2009- 450	AHP (WI)	+22.44	0.64	0.59	0.76	0.32

<0.1 μm size-fraction.

(Deocampo and Jones, 2014; Deocampo, 2015), a precursor phase present in abundant quantities in the Chew Bahir basin (Foerster et al., 2018).

Watershed samples also show a slightly higher degree of LREE and HREE fractionation compared to MF samples, while all sample groups also have negative Eu anomalies with no clear differences between WS and MF samples (average Eu/Eu* of 0.85 versus 0.78, respectively; **Table 1**) or WI and DI samples (average Eu/Eu* of 0.71 versus 0.69, respectively; **Table 1**). Assuming Eu concentration is not affected by weathering, a negative Eu anomaly is an indication of strong plagioclase fractionation in the source rocks; notably, the Proterozoic granitic and gneissic rocks of the Hammar Range show strong negative Eu anomalies (Asrat and Barbey, 2003). It also suggests that the bulk sediment source rock remained very similar through time. In short, the REE data suggest that the detrital sediment load is predominantly derived from the Hammar Range.

Consistent with the CIA, intergroup comparisons between MgO/Al_2O_3 and K_2O/Al_2O_3 or Ba/Sr for the bulk sediments suggest that the intensity of weathering, inferred from Ba/Sr data, is (and was) highest in late Quaternary WI and modern WS samples (**Figure 9a**). Although the link between weathering

and geochemical proxy formation is known to be more complex, Ba/Sr ratios are routinely used as a weathering proxy. The power of this proxy is provided by the selective removal of more mobile Sr coupled with the relative immobility of Ba, which is readily adsorbed by clay minerals during weathering (e.g., Nesbitt and Markovics, 1980; Middelburg et al., 1988; Deocampo et al., 2010). By comparison, DI samples have consistently higher MgO/Al_2O_3, while $K_2O/Al2O_3$ in MF samples holds constant (**Figure 10b**). A strong positive relationship between MgO/Al_2O_3 and K_2O/Al_2O_3 (also between MgO and K_2O) within the mudflat samples indicates the effect of greater exposure to salinity and alkalinity on the mudflats, with octahedral Mg substitution and K-uptake due to incipient illitization (Deocampo, 2015; **Figure 9b**). The presence of both smectite and illite-smectite (the latter formed by low temperature illitization of smectite; e.g., Eberl et al., 1986) is reminiscent of similar differences observed between the late Quaternary WI and DI samples. The geochemistry of MF samples is most likely constrained by diagenesis and authigenic mineral formation, rather than solely representing the end product of weathering. Indeed, neoformation of clay minerals in alkaline solutions is termed "inverse weathering" as it is chemically the opposite of silicate hydrolysis, which produces authigenic alkaline silicate minerals (Deocampo and Jones, 2014; Deocampo, 2015).

The presence of analcime, a precursor zeolite formed under conditions of increasing lake water salinity and alkalinity, is noteworthy in all MF samples and WS samples collected near the desiccated lake floor (**Figure 4**). Analcime is also present in cores collected from the center of the Chew Bahir basin (e.g., Viehberg et al., 2018). Analcime can form under diverse physical, chemical and geological settings including marine and hydrothermal alteration, but it is much more common in saline and alkaline lake deposits (e.g., Hay and Sheppard, 2001). We have considered a range of possibilities to explain diagenetic formation of analcime in the Chew Bahir basin. In some other eastern African lakes such as Lake Magadi, analcime is thought to form by reaction of precursor zeolites, volcanic glass, hydrous sodium aluminosilicate gels or a combination of all three phases in saline alkaline solutions (e.g., Surdam and Eugster, 1976). In other eastern African rift lakes such as Lake Bogoria, authigenic analcime has been shown to form from poorly crystalline smectite clay minerals reacting with saline, alkaline pore fluids (e.g., Renaut, 1993).

Hydrogeochemical Processes in the Chew Bahir Basin

The Geochemist's Workbench[§] model results indicate that evaporative concentration increases the amount of calcite precipitation, eventually eliminating calcium from evolved waters (Deocampo and Jones, 2014). The next phase to reach supersaturation in the model system is analcime ($NaAlSi_2O_6 \bullet H_2O$; **Figure 11**). This reflects the high alkalinity of the waters in the presence of reactive aluminosilicates (Hay, 1978). Although analcime is stable in these modeled waters, however, only a small mass of mineral was predicted to precipitate. This suggests that the significant accumulations of analcime observed in the Chew Bahir sediments (e.g., Foerster et al., 2018) result not only from evaporative concentration, but also from alteration of locally abundant volcanic glass in alkaline waters (Hay and Sheppard, 2001).

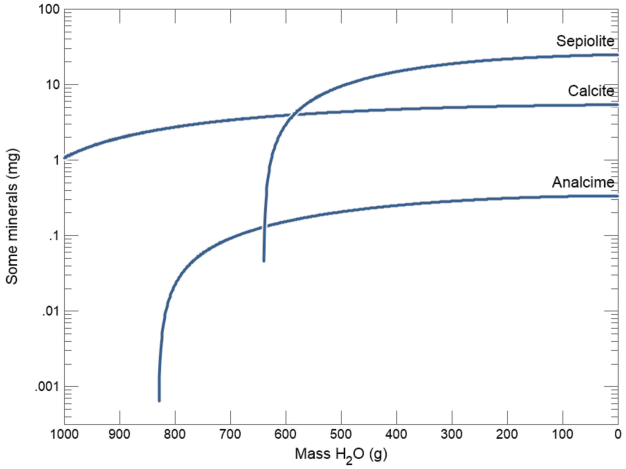

FIGURE 11 | Modeled hydrochemical evolution and mineral reaction pathways in the Chew Bahir basin showing the immediate precipitation of calcite, and followed by analcime and sepiolite, calculated based on Lake Chamo dissolved solid composition (**Table 2**; Ayenew, 2005).

Sepiolite [$Mg_4(Si_6O_{15})(OH)_2 \bullet 6H_2O$] is the final phase to reach supersaturation in the modeled system (**Figure 11**). Although sepiolite has not been observed locally and is not expected to precipitate in this setting, we can use its thermodynamics to model the behavior of Mg-silicates more generally (Deocampo, 2005, 2015). Abundant aluminous detrital clay minerals in fluvio-lacustrine environments provide reactive substrates with low kinetic barriers for precipitation of Mg-rich interstratifications rather than pure Mg-silicate such as sepiolite (Deocampo, 2015). The model prediction of sepiolite precipitation shows the potential for Mg-rich authigenic clay minerals to form, which is well known as an indicator of elevated salinity in lake deposits in the region (Deocampo et al., 2017; Foerster et al., 2018).

In sum, thermodynamic modeling of evaporating Lake Chamo water produces an authigenic mineral assemblage typical of both modern lake mudflats in the Chew Bahir basin and Late Quaternary sediments recovered from cores (Foerster et al., 2018). These data suggest that the mineral assemblage of calcite, analcime, and Mg-enriched authigenic illitic clay minerals is indicative of environments of enhanced evaporative concentration in the basin.

Refining Interpretation of the Chew Bahir K Record Using Whole-Rock and Clay Mineral Geochemistry

Foerster et al. (2018) demonstrated that K content in the Chew Bahir sediments is likely derived from enhanced K-fixation during dry high-salinity episodes. Salinity in the hydrologically closed paleo-Lake Chew Bahir was controlled by the amount of

TABLE 4 | Arid and humid phases identified based on multi-proxy indicators.

Chew Bahir proxies	Arid	Humid
K concentration (counts)	↑	↓
Clay mineralogy (Illite versus smectite)	Illite ↑	Smectite ↑
Zeolite mineralogy	Analcime ↑	Analcime ↓
Oxygen isotopes	↑	↓
Ba/Sr ratios	↓	↑

paleo-precipitation in the catchment and the rate of evaporation in the paleolake. It is therefore conceivable that the chemical composition of the paleolake significantly impacted the crystal chemistry of authigenic minerals present in the sediment, including the progress of K-fixation in clay minerals (Foerster et al., 2018). Like many other eastern African rift lakes, aridity and the prevalence of hypersaline conditions facilitate authigenic illitization of smectite (e.g., Singer and Stoffers, 1980; Deocampo et al., 2009) and consequently K-enrichment in Chew Bahir sediments. The major element geochemistry of the late Quaternary DI and WI samples establishes a clear relationship between K-enrichment in Chew Bahir sediments and hypersaline conditions in the basin (**Figure 10a**). It should also be noted that sediments deposited during humid episodes (e.g., during the AHP) had whole-rock MgO/Al_2O_3 ratios ranging from ∼0.2 to 0.4, whereas those deposited during arid episodes (e.g., at LGM and YD times) had MgO/Al_2O_3 ratios ranging from ∼0.5 to 0.7, indicating higher salinity (**Figure 10a**). These results show that ancient sediments deposited during dry periods most similarly resemble modern saline mudflats in dry-Lake Chew Bahir today and had Ba/Sr values ranging from ∼0.6 to 1.2 (**Figure 9a**). Conversely, sediments deposited during relatively wetter periods, such as the AHP, have sources similar to those found presently in upstream locations, e.g., WS samples.

The proposed relationship between basin aridity and K uptake in the sediment is compared with oxygen-isotope analysis of authigenic illite-smectite. The oxygen−isotope composition of authigenic clay minerals formed in lake water at isotopic equilibrium is controlled primarily by clay mineral composition, structure, and water temperature (Savin and Lee, 1988). Once formed, oxygen in the tetrahedral and octahedral sheets does not undergo isotopic exchange with pore fluids in the absence of dissolution−precipitation reactions. In the current study, the $\delta^{18}O_{illite-smectite}$ has been determined by the oxygen-isotope composition of the incoming waters draining through the Weyto River (**Figures 1b,c**) and the extent of lake-water evaporation (e.g., Gebregiorgis et al., 2020a). Lake-water $\delta^{18}O$ is certainly influenced by the isotopic composition of the prevailing source (i.e., Lake Chamo; see **Figure 1b**) during periods of rapid lake level change. This signal, however, is likely overprinted in a system like Chew Bahir, where the extent of lake-water ^{18}O-enrichment was largely driven by evaporation.

The $\delta^{18}O$ of authigenic illite-smectite in the late Quaternary WI and DI samples range from +22.4 to +24.5‰ (average + 23.3‰), and +24.1 to +25.3‰ (average + 24.77‰), respectively (**Figures 10b,c**). Notably wet (i.e., during the AHP) and dry (e.g., at LGM and YD times) periods of the late Quaternary have been identified from the Chew Bahir K record, which are now largely confirmed independently by these oxygen-isotope measurements. The authigenic illite-smectite is generally most enriched in ^{18}O during periods of regional aridity, which also coincides with significant Mg enrichment (**Figure 10b** and **Table 3**) and low-temperature illitization suggestive of enhanced evaporative concentration in the basin (**Figure 11** and **Table 4**). Collectively, our results confirm that, in closed-basin lake deposits not overly diluted by detrital or biogenic sediments, subtle changes in water balance can be detected using both elemental and oxygen-isotope analysis of submicron authigenic clay minerals. Our first attempt to reproduce the climate signals recorded in the Chew Bahir K record using oxygen-isotope measurements of authigenic illite-smectite from notable warm/wet (e.g., during the Mid-Holocene) and cold/dry intervals (e.g., during the LGM) has proven to be successful.

CONCLUSION

New mineralogical and geochemical data from modern and ancient sediments in the Chew Bahir basin shed light on the role of sedimentary processes in chemical proxy formation. The data presented here show that the geochemistry of the modern saline mudflats in dry Lake Chew Bahir today resemble ancient sediments deposited during dry periods. Conversely, the geochemistry of modern detrital upstream sources can be compared to sediments deposited during relatively wetter periods, such as the AHP. This study demonstrates that interpretation of such geochemical datasets is complex and highly site-specific, and careful evaluation of any seemingly straightforward relationship between sediment composition and climate is required. This knowledge is critical for understanding proxy formation in playa sites and sedimentary records from semi-arid regions of the world.

DATA AVAILABILITY STATEMENT

All data generated or analyzed during this study are included in this published article.

AUTHOR CONTRIBUTIONS

DG, DD, VF, and AA designed the project. DD conducted the geochemical modeling. FL provided and acquired funding for the oxygen-isotope analyses. AA, FS, HL, and MT acquired the funding, designed, and directed the Chew Bahir Drilling Project as part of the Hominin Sites and Paleolakes Drilling Project, directed by A. Cohen of the University of Arizona. FS, AA, HL, and VF did the coring at Chew Bahir. JD carried out electron probe microanalyses of samples. VF, FS, AJ, MM, and HL added modern samples to this study. SO carried out grain size analysis of samples. DG led sample collection, data analysis, and wrote the manuscript with contributions from all co-authors. All authors revised the manuscript.

FUNDING

This research was supported by NSF grant (NSF 1349651) to DD. The oxygen-isotope measurements were supported by a Natural Sciences and Engineering Research Council Discovery Grant of Canada and the Canada Research Chairs Program (FL). FS acknowledges further funding from the DFG through grants SCHA 472/13 and SCHA 472/18. MT acknowledges funding from the DFG through grants TR 419/8, TR 419/9, and TR 419/16. In addition, FS acknowledges funding from the CRC 806 Research Project "Our way to Europe" – Project Number 57444011. HL was funded by grant NE/K014560/1 from the UK Natural Environment Research Council. This was Western's Laboratory for Stable Isotope Science Contribution #385.

SUPPLEMENTARY MATERIAL

The Supplementary Material for this article can be found online at: https://www.frontiersin.org/articles/10.3389/feart.2021.607695/full#supplementary-material

REFERENCES

Asrat, A., and Barbey, P. (2003). Petrology, geochronology and Sr–Nd isotopic geochemistry of the konso pluton, south-western ethiopia: implications for transition from convergence to extension in the mozambique belt. *Int. J. Earth Sci.* 92, 873–890. doi: 10.1007/s00531-003-0360-9

Ayenew, T. (2005). Major ions composition of the groundwater and surface water systems and their geological and geochemical controls in the ethiopian volcanic terrain. *SINET Ethiopian J. Sci.* 28, 171–188.

Bethke, C. M., Farrell, B., and Yeakel, S. (2019). *GWB essentials guide*. Champaign, Illinois: Aqueous Solutions, LLC.

Blott, S. J., and Pye, K. (2001). GRADISTAT: a grain size distribution and statistics package for the analysis of unconsolidated sediments. *Earth Surface Processes Landforms* 26, 1237–1248. doi: 10.1002/esp.261

Brown, E., Johnson, T., Scholz, C. A., Cohen, A., and King, J. (2007). Abrupt change in tropical african climate linked to the bipolar seesaw over the past 55,000 years. *Geophys. Res. Lett.* 34:20702. doi: 10.1029/2007GL031240

Buggle, B., Glaser, B., Hambach, U., Gerasimenko, N., and Marković, S. (2011). An evaluation of geochemical weathering indices in loess–paleosol studies. *Quaternary Int.* 240, 12–21. doi: 10.1016/j.quaint.2010.07.019

Burnett, A. P., Soreghan, M. J., Scholz, C. A., and Brown, E. T. (2011). Tropical east african climate change and its relation to global climate: a record from lake tanganyika, tropical east africa, over the past 90+ kyr. *Palaeogeogr. Palaeoclimatol. Palaeoecol.* 303, 155–167. doi: 10.1016/j.palaeo.2010.02.011

Chesworth, W., Dejou, J., and Larroque, P. (1981). The weathering of basalt and relative mobilities of the major elements at belbex, france. *Geochimica et Cosmochimica Acta* 45, 1235–1243. doi: 10.1016/0016-7037(81)90147-2

Clark, P. U., Dyke, A. S., Shakun, J. D., Carlson, A. E., Clark, J., Wohlfarth, B., et al. (2009). The last glacial maximum. *Science* 325, 710–714.

Clift, P. D., Wan, S., and Blusztajn, J. (2014). Reconstructing chemical weathering, physical erosion and monsoon intensity since 25 ma in the northern south china sea: a review of competing proxies. *Earth Sci. Rev.* 130, 86–102. doi: 10.1016/j.earscirev.2014.01.002

Croudace, I. W., Löwemark, L., Tjallingii, R., and Zolitschka, B. (2019). Current perspectives on the capabilities of high resolution XRF core scanners. *Quaternary Int.* 514, 5–15. doi: 10.1016/j.quaint.2019.04.002

Croudace, I. W., Rindby, A., and Rothwell, R. G. (2006). "ITRAX: description and evaluation of a new multi-function X-ray core scanner," in *New techniques in sediment core analysis*, ed. R. G. Rothwell (London, UK: Geological Society of London), 51–63.

Cullers, R. L. (2000). The geochemistry of shales, siltstones and sandstones of pennsylvanian–permian age, colorado, USA: implications for provenance and metamorphic studies. *Lithos* 51, 181–203. doi: 10.1016/S0024-4937(99)00063-8

Davidson, A. (1983). The omo river project: reconnaissance geology and geochemistry of parts of Ilubabor, kefa, gemu gofa and sidamo. *Ethiopian Instit. Geol. Surv. Bull.* 2, 1–89.

Demenocal, P., Ortiz, J., Guilderson, T., Adkins, J., Sarnthein, M., Baker, L., et al. (2000). Abrupt onset and termination of the african humid period: rapid climate responses to gradual insolation forcing. *Quaternary Sci. Rev.* 19, 347–361. doi: 10.1016/S0277-3791(99)00081-5

Deocampo, D., Cuadros, J., Wing-Dudek, T., Olives, J., and Amouric, M. (2009). Saline lake diagenesis as revealed by coupled mineralogy and geochemistry of multiple ultrafine clay phases: pliocene olduvai gorge, tanzania. *Am. J. Sci.* 309, 834–868. doi: 10.2475/09.2009.03

Deocampo, D. M. (2004). Authigenic clays in east africa: regional trends and paleolimnology at the plio–pleistocene boundary, olduvai gorge, tanzania. *J. Paleolimnol.* 31, 1–9. doi: 10.1023/B:JOPL.0000013353.86120.9b

Deocampo, D. M. (2005). Evaporative evolution of surface waters and the role of aqueous CO2 in magnesium silicate precipitation: lake eyasi and ngorongoro crater, northern tanzania. *South Afric. J. Geol.* 108, 493–504. doi: 10.2113/108.4.493

Deocampo, D. M. (2010). The geochemistry of continental carbonates. *Dev. Sedimentol.* 62, 1–59. doi: 10.1016/S0070-4571(09)06201-3

Deocampo, D. M. (2015). Authigenic clay minerals in lacustrine mudstones. *Geol. Soc. Am. Spl. Papers* 515, SE503–SE515.

Deocampo, D. M., Behrensmeyer, A. K., and Potts, R. (2010). Ultrafine clay minerals of the pleistocene olorgesailie formation, southern kenya rift: diagenesis and paleoenvironments of early hominins. *Clays Clay Minerals* 58, 294–310. doi: 10.1346/CCMN.2010.0580301

Deocampo, D. M., Berry, P. A., Beverly, E. J., Ashley, G. M., and Jarrett, R. E. (2017). Whole-rock geochemistry tracks precessional control of pleistocene lake salinity at olduvai gorge, tanzania: a record of authigenic clays. *Geology* 45, 683–686. doi: 10.1130/G38950.1

Deocampo, D. M., and Jones, B. F. (2014). "Geochemistry of saline lakes," in *Treatise on Geochemistry*, Second Edn, eds H. D. Holland and K. K. Turekian (Amsterdam: Elsevier), 437–469.

Deocampo, D. M., and Tactikos, J. C. (2010). Geochemical gradients and artifact mass densities on the lowermost Bed II eastern lake margin (˜ 1.8 Ma), olduvai gorge, tanzania. *Quaternary Res.* 74, 411–423. doi: 10.1016/j.yqres.2010.09.004

Eberl, D. D., Środoń, J., and Northrop, H. R. (1986). "Potassium fixation in smectite by wetting and drying," in *Geochemical Processes at Mineral Surfaces*, eds J. A. Davies and K. F. Hayes (Washington, DC: American Chemical Society Symposium), 296–326.

Ebinger, C., Yemane, T., Harding, D., Tesfaye, S., Kelley, S., and Rex, D. (2000). Rift deflection, migration, and propagation: linkage of the ethiopian and eastern rifts, africa. *Geol. Soc. Am. Bull.* 112, 163–176. doi: 10.1130/0016-76062000112<163:RDMAPL<2.0.CO;2

Ehrmann, W., Schmiedl, G., Beuscher, S., and Krüger, S. (2017). Intensity of african humid periods estimated from saharan dust fluxes. *PloS one* 12:e0170989. doi: 10.1371/journal.pone.0170989

Fischer, M. L., Markowska, M., Bachofer, F., Foerster, V. E., Asrat, A., Zielhofer, C., et al. (2020). Determining the pace and magnitude of lake level changes in southern ethiopia over the last 20,000 years using lake balance modelling and SEBAL. *Front. Earth Sci.* 8:197. doi: 10.3389/feart.2020.00197

Foerster, V., Deocampo, D. M., Asrat, A., Günter, C., Junginger, A., Krämer, K. H., et al. (2018). Towards an understanding of climate proxy formation in the chew bahir basin, southern ethiopian rift. *Palaeogeogr. Palaeoclimatol. Palaeoecol.* 501, 111–123. doi: 10.1016/j.palaeo.2018.04.009

Foerster, V., Junginger, A., Langkamp, O., Gebru, T., Asrat, A., Umer, M., et al. (2012). Climatic change recorded in the sediments of the chew bahir basin, southern ethiopia, during the last 45,000 years. *Quaternary Int.* 274, 25–37. doi: 10.1016/j.quaint.2012.06.028

Folk, R. L., and Ward, W. C. (1957). Brazos river bar: a study in the significance of grain size parameters. *J. Sediment. Petrol.* 27, 3–26. doi: 10.1306/74D70646-2B21-11D7-8648000102C1865D

Garzanti, E., Padoan, M., Setti, M., López-Galindo, A., and Villa, I. M. (2014). Provenance versus weathering control on the composition of tropical river mud (southern africa). *Chem. Geol.* 366, 61–74. doi: 10.1016/j.chemgeo.2013.12.016

Gebregiorgis, D., Deocampo, D. M., Longstaffe, F. J., Simpson, A., Ashley, G. M., Beverly, E. J., et al. (2020a). Oxygen isotopes in authigenic clay minerals: Toward building a reliable salinity proxy. *Geophys. Res. Lett.* 47:e2019GL085576. doi: 10.1029/2019GL085576

Gebregiorgis, D., Giosan, L., Hathorne, E. C., Anand, P., Nilsson-Kerr, K., Plass, A., et al. (2020b). What can we learn from X-ray fluorescence core scanning data? A paleomonsoon case study. *Geochem. Geophys. Geosyst.* 21:e2019GC008414. doi: 10.1029/2019GC008414

Gebregiorgis, D., Rayner, D., and Linderholm, H. W. (2019). Does the IOD independently influence seasonal monsoon patterns in northern ethiopia? *Atmosphere* 10:432. doi: 10.3390/atmos10080432

Harriss, R. C., and Adams, J. A. (1966). Geochemical and mineralogical studies on the weathering of granitic rocks. *Am. J. Sci.* 264, 146–173. doi: 10.2475/ajs.264.2.146

Hay, R. L. (1978). "Geologic occurrence of zeolites," in *Natural zeolites: Occurrence, properties, use*, eds L. B. Sand and F. A. Mumpton (Elmsford, NY: Pergamon Press), 135–143.

Hay, R. L., and Sheppard, R. A. (2001). Occurrence of zeolites in sedimentary rocks: an overview. *Rev. Mineral. Geochem.* 45, 217–234. doi: 10.2138/rmg.2001.45.6

Hendy, I. L., Napier, T. J., and Schimmelmann, A. (2015). From extreme rainfall to drought: 250 years of annually resolved sediment deposition in santa barbara basin, california. *Quaternary Int.* 387, 3–12. doi: 10.1016/j.quaint.2015.01.026

Hession, S. L., and Moore, N. (2011). A spatial regression analysis of the influence of topography on monthly rainfall in east africa. *Int. J. Climatol.* 31, 1440–1456. doi: 10.1002/joc.2174

Huggett, J., Adetunji, J., Longstaffe, F., and Wray, D. (2017). Mineralogical and geochemical characterisation of warm-water, shallow-marine glaucony from the tertiary of the london basin. *Clays Clay Minerals* 52, 25–50. doi: 10.1180/claymin.2017.052.1.02

Junginger, A., and Trauth, M. H. (2013). Hydrological constraints of paleo-lake suguta in the northern kenya rift during the african humid period (15–5 ka BP). *Global Planetary Change* 111, 174–188. doi: 10.1016/j.gloplacha.2013.09.005

Libbey, R. B., Longstaffe, F. J., and Flemming, R. L. (2013). Clay mineralogy, oxygen isotope geochemistry, and water/rock ratio estimates, Te Mihi area, Wairakei geothermal field, new zealand. *Clays Clay Minerals* 61, 204–217. doi: 10.1346/CCMN.2013.0610304

Lyons, R. P., Scholz, C. A., Cohen, A. S., King, J. W., Brown, E. T., Ivory, S. J., et al. (2015). Continuous 1.3-million-year record of east african hydroclimate, and implications for patterns of evolution and biodiversity. *Proc. Natl. Acad. Sci.* 112, 15568–15573. doi: 10.1073/pnas.1512864112

McDonough, W. F., and Sun, S. S. (1995). The composition of the earth. *Chem. Geol.* 120, 223–253. doi: 10.1016/0009-2541(94)00140-4

McLennan, S. M. (2001). Relationships between the trace element composition of sedimentary rocks and upper continental crust. *Geochem. Geophys. Geosyst.* 2:1021. doi: 10.1029/2000GC000109

Middelburg, J. J., van der Weijden, C. H., and Woittiez, J. R. (1988). Chemical processes affecting the mobility of major, minor and trace elements during weathering of granitic rocks. *Chem. Geol.* 68, 253–273. doi: 10.1016/0009-2541(88)90025-3

Moore, D., and Reynolds, R. (1997). *X-ray Diffraction and the Identification and Analysis of Clay Minerals*, Second Edn. Oxford, England: Oxford University Press.

Nesbitt, H., and Young, G. (1982). Early Proterozoic climates and plate motions inferred from major element chemistry of lutites. *Nature* 299, 715–717. doi: 10.1038/299715a0

Nesbitt, H. W. (1979). Mobility and fractionation of rare earth elements during weathering of a granodiorite. *Nature* 279, 206–210. doi: 10.1038/279206a0

Nesbitt, H. W., and Markovics, G. (1980). Chemical processes affecting alkalis and alkaline earths during continental weathering. *Geochim. et Cosmochim. Acta* 44, 1659–1666. doi: 10.1016/0016-7037(80)90218-5

Nicholson, S. (2016). The turkana low-level jet: mean climatology and association with regional aridity. *Int. J. Climatol.* 36, 2598–2614. doi: 10.1002/joc.4515

Nicholson, S. E. (2018). The ITCZ and the seasonal cycle over equatorial africa. *Bull. Am. Meteorol. Soc.* 99, 337–348. doi: 10.1175/BAMS-D-16-0287.1

Otto-Bliesner, B. L., Russell, J. M., Clark, P. U., Liu, Z., Overpeck, J. T., Konecky, B., et al. (2014). Coherent changes of southeastern equatorial and northern african rainfall during the last deglaciation. *Science* 346, 1223–1227. doi: 10.1126/science.1259531

Renaut, R. (1993). Zeolitic diagenesis of late quaternary fluviolacustrine sediments and associated calcrete formation in the lake bogoria basin, kenya rift valley. *Sedimentology* 40, 271–301. doi: 10.1111/j.1365-3091.1993.tb01764.x

Roberts, N., Taieb, M., Barker, P., Damnati, B., Icole, M., and Williamson, D. (1993). Timing of the younger dryas event in east africa from lake-level changes. *Nature* 366, 146–148. doi: 10.1038/366146a0

Savin, S., and Lee, M. (1988). Isotopic studies of phyllosilicates. *Rev. Mineral. Geochem.* 19, 189–223.

Shanahan, T. M., McKay, N. P., Hughen, K. A., Overpeck, J. T., Otto-Bliesner, B., Heil, C. W., et al. (2015). The time-transgressive termination of the african humid period. *Nat. Geosci.* 8, 140–144. doi: 10.1038/ngeo2329

Singer, A., and Stoffers, P. (1980). Clay mineral diagenesis in two east african lake sediments. *Clays Clay Minerals* 15, 291–307. doi: 10.1180/claymin.1980.015.3.09

Sun, L., Semazzi, F. H., Giorgi, F., and Ogallo, L. (1999). Application of the NCAR regional climate model to eastern africa: 1. Simulation of the short rains of 1988. *J. Geophys. Res. Atmospheres* 104, 6529–6548. doi: 10.1029/1998JD200051

Surdam, R. C., and Eugster, H. P. (1976). Mineral reactions in the sedimentary deposits of the lake magadi region, kenya. *Geol. Soc. Am. Bull.* 87, 1739–1752. doi: 10.1130/0016-7606197687<1739:MRITSD<2.0.CO;2

Tian, J., Xie, X., Ma, W., Jin, H., and Wang, P. (2011). X-ray fluorescence core scanning records of chemical weathering and monsoon evolution over the past 5 Myr in the southern south china sea. *Paleoceanography* 26,

Tierney, J. E., and deMenocal, P. B. (2013). Abrupt shifts in horn of africa hydroclimate since the last glacial maximum. *Science* 342, 843–846. doi: 10.1126/science.1240411

Trauth, M. H., Deino, A., Bergner, A. G. N., and Strecker, M. R. (2003). East african climate change and orbital forcing during the last 175 kyr BP. *Earth Planetary Sci. Lett.* 206, 297–313. doi: 10.1016/S0012-821X(02)01105-6

Trauth, M. H., Deino, A., and Strecker, M. R. (2001). Response of the east african climate to orbital forcing during the last interglacial (130-117 kyr BP) and the early last glacial (117-60 kyr BP). *Geology* 29, 499–502. doi: 10.1130/0091-76132001029<0499:ROTEAC<2.0.CO;2

Viehberg, F. A., Just, J., Dean, J. R., Wagner, B., Franz, S. O., Klasen, N., et al. (2018). Environmental change during MIS4 and MIS 3 opened corridors in the horn of africa for homo sapiens expansion. *Quat. Sci. Rev.* 202, 139–153. doi: 10.1016/j.quascirev.2018.09.008

Conflict of Interest: The authors declare that the research was conducted in the absence of any commercial or financial relationships that could be construed as a potential conflict of interest.

frontiers in Earth Science

ORIGINAL RESEARCH
published: 25 May 2021
doi: 10.3389/feart.2021.600086

A Detailed Paleoclimate Proxy Record for the Middle Danube Basin Over the Last 430 kyr: A Rock Magnetic and Colorimetric Study of the Zemun Loess-Paleosol Sequence

Christian Laag[1,2,3], Ulrich Hambach[3,4], Christian Zeeden[1], France Lagroix[2], Yohan Guyodo[2], Daniel Veres[5], Mladjen Jovanović[6] and Slobodan B. Marković[6,7]*

[1] Section 5: Rock Physics and Borehole Geophysics, Leibniz Institute for Applied Geophysics (LIAG), Hanover, Germany, [2] Université de Paris, Institut de Physique du Globe de Paris (IPGP), CNRS, Paris, France, [3] Chair of Geomorphology, University of Bayreuth, Bayreuth, Germany, [4] Bayreuth Center of Ecology and Environmental Research (BayCEER), University of Bayreuth, Bayreuth, Germany, [5] Institute of Speleology, Romanian Academy, Cluj-Napoca, Romania, [6] Chair of Physical Geography, Faculty of Sciences, University of Novi Sad, Novi Sad, Serbia, [7] Serbian Academy of Sciences and Arts, Belgrade, Serbia

OPEN ACCESS

Edited by:
Julie Fosdick, University of Connecticut, United States

Reviewed by:
Giancarlo Scardia, São Paulo State University, Brazil
Jinbo Zan, Institute of Tibetan Plateau Research (CAS), China
Chenglong Deng, Institute of Geology and Geophysics, Chinese Academy of Sciences (CAS), China

***Correspondence:**
Christian Laag
laag@ipgp.fr

Specialty section:
This article was submitted to Sedimentology, Stratigraphy and Diagenesis, a section of the journal Frontiers in Earth Science

Received: *28 August 2020*
Accepted: *20 April 2021*
Published: *25 May 2021*

Citation:
Laag C, Hambach U, Zeeden C, Lagroix F, Guyodo Y, Veres V, Jovanović M and Marković SB (2021) A Detailed Paleoclimate Proxy Record for the Middle Danube Basin Over the Last 430 kyr: A Rock Magnetic and Colorimetric Study of the Zemun Loess-Paleosol Sequence. Front. Earth Sci. 9:600086. doi: 10.3389/feart.2021.600086

In mid-latitude Eurasia, loess-paleosol sequences (LPS) provide the most widespread sedimentary records of Quaternary paleoenvironmental evolution. In the Middle Danube Basin (MDB), these archives cover at least the last million years of climate history, and occasionally contain archeological findings. The studied Zemun LPS is located on the right bank of the Danube in Northern Serbia. The site was declared as a protected site, based on Paleolithic artifacts found on the riverbank and stemming from unknown stratigraphic levels of the loess cliffs exposed along the Danube. The present study aims to provide a stratigraphic, paleoenvironmental, and temporal context for the Zemun LPS by means of environmental magnetic and colorimetric methods. Our investigations result in a chronostratigraphic scheme allowing direct comparison with other well-established reference records in the MDB and elsewhere. Two potential tephra layers tentatively assigned to the so-called L2 and Bag tephras, which are both widespread in the MDB and beyond were investigated for their bulk magnetic properties. The resulting integrated age model suggests that the Zemun LPS records a detailed history of a quasi-continuous accumulation of mineral dust from Marine Oxygen Isotope Stage (MIS) 11–5a (c. 430–60 ka). The outcome of our integrative approach indicates a continuous aridification over the last four interglacial/glacial cycles and we discuss potential changes in seasonality over time.

Keywords: loess-paleosol sequences, environmental magnetism, diffuse reflectance spectrometry, stratigraphy, paleoclimate dynamics

INTRODUCTION

Over the past decades, many loess-paleosol sequences (LPSs) have been investigated predominantly in the extensive northern hemisphere loess belt (Marković et al., 2015; Schaetzl et al., 2018; Lehmkuhl et al., 2021). Unlike lake and other terrestrial records, which are rather sparsely distributed, the spatial continuity of LPSs makes them valuable archives of past environmental

change in the prevailing climatic past regimes that sustained loess formation and preservation (e.g., Basarin et al., 2014; Marković et al., 2015). Glacial and interglacial cycles, usually associated with shifts in humidity and temperature resulting from long-term variations in orbital parameters of eccentricity, obliquity, and precession driving ice volume (Imbrie and Imbrie, 1980; Heslop et al., 2000; Lisiecki and Raymo, 2005; Sun et al., 2006; Abe-Ouchi et al., 2013), are recorded through the alternation of loess and paleosol horizons, respectively. The paleoclimatic relevance of the quasi-cyclic alternation of loess and paleosols in LPSs of the Chinese Loess Plateau (CLP) was demonstrated in the 1980s through the correlation of magnetostratigraphically dated susceptibility records to the marine oxygen isotope records (Heller and Liu, 1982, 1986), and similarly in the 1990s based on long-term variability in grain size distribution (e.g., Ding et al., 1994). Most of the early work relied on analyses of rock-magnetic parameters, often limited to magnetic susceptibility (Ding et al., 1993) and its frequency dependence. However, quantitative analyses of loess color spectra are also valuable indicators of shifts in mineralogical assemblages, as well as in organic matter content (Ding et al., 2002b; Lukić et al., 2014). Studies of LPSs from the CLP (Ji et al., 2002) and the Danube Basin (Lukić et al., 2014; Obreht et al., 2016) demonstrated the strength of combining magnetic and colorimetric parameters. While many multi-proxy studies have been performed on archives covering the last glacial cycle, investigations of European LPSs spanning multiple glacial–interglacial cycles are fewer (e.g., Jordanova et al., 2007; Necula et al., 2013; Basarin et al., 2014; Marković et al., 2015; Zeeden et al., 2016; Sümegi et al., 2018; Antoine et al., 2019; Obreht et al., 2019). In this study, we extend colorimetric data to about 430 kyr with the Zemun LPS record from the Middle Danube Basin (MDB), spanning from Marine Isotope Stage (MIS) 11 to MIS 5a.

Besides a dominating amount of quartz, feldspar, phyllosilicate and carbonate grains, comprising the average composition of the upper continental crust, Eurasian loess consists of heavy minerals and measurable relevant ferromagnetic (s.l.) particles such as a broad variety of iron oxides (Maher, 2016). Rock magnetic investigations allow differentiating magnetic particles formed *in-situ* via pedogenic processes from the initial detrital content of magnetic particles in wind-blown loess. Relevant iron oxides for deciphering between loess and paleosol-units, which are readily detectable and relative concentrations quantifiable by room-temperature magnetic investigations, consists of magnetite, maghemite and hematite (Heller and Evans, 1995). Pedogenesis takes place under relatively warm and humid conditions (Maher, 2016), involving various abiotic and bio-mediated chemical reactions not yet completely understood (e.g., Torrent et al., 2007; sections 2.5.2 and 2.6 in Lagroix et al., 2016) and resulting in the neo-formation of ultra-fine magnetic minerals (Maher and Taylor, 1988; Dearing et al., 1996; Maher, 1998; Torrent et al., 2007; Hu et al., 2013). Pedogenetically neo-formed magnetite/maghemite have magnetic grains sizes ranging from unstable single domain [superparamagnetic (SP)] to stable single domain (SD) sizes, where the SP/SD particle size threshold at room temperature is about 30 nm (e.g., Peters and Dekkers, 2003). SP particles display a frequency dependence of susceptibility, which can be used to quantify their relative concentration and help discriminate between paleosols (high SP concentration) and loess (low to SP concentration). Weathering of loess can also occur under glacial conditions (Maher, 2011), but it is generally less intense due to increased aeolian sediment accumulation rates and generally drier conditions (Kohfeld and Harrison, 2003). Such weak glacial pedogenic alterations can also be detected by rock magnetic investigations (e.g., Taylor et al., 2014).

In most Eurasian LPSs, magnetic susceptibility values of paleosols are enhanced with respect to loess units (e.g., Maher, 1998, 2016; Marković et al., 2009, 2015) from which a first order (chrono)stratigraphy can be established. For example, Marković et al. (2015) proposed a composite loess stratigraphy nomenclature scheme for the Danube loess belt region to facilitate pan-Eurasian LPS comparisons based on trends in magnetic susceptibility and other chronostratigraphic constrains. The stratigraphic system is based on the "S" (for soil) and "L" (for loess) labeling without any specific regional prefixes as is well established for the Chinese loess stratotype sections (Kukla and An, 1989). In the present study, the proposed composite stratigraphy is used to compare magnetic susceptibility variations of the Zemun LPS, evolving under non-monsoonal controlled (paleo-) climate with that of a monsoonal-dominated loess-paleosol sequence from the CLP (Luochuan, e.g., Hao et al., 2012).

The Zemun site hosts a variety of Middle and Late Paleolithic, and Neolithic artifacts found on the river bank nearby the LPS outcrop and upstream to the northwest (Šarić, 2008). The stratigraphic position within the Zemun LPS of these artifacts is, to date, unknown. However, providing a chronological framework for the protected loess site and establishing a range of environmental conditions these settlements may have been subjected to is important and will be beneficial to future archeological work.

Establishing a reliable chronology for LPSs remains challenging when absolute dating techniques such as luminescence reach their dating limits. Correlative age models are a mean to partly overcome this challenge. For LPS, correlative age models rely on the key process of pedogenic alteration, which induces variations in physical parameters and consequently records the environmental impact of interglacial/glacial cycles. In this study, magnetic susceptibility measurements coupled to diffuse reflectance spectrometry (DRS) analyses provide insights into past changes in environmental conditions. Rock-magnetic parameters provide insight into the source of variations in magnetic susceptibility, and together trace changes in the strength of pedogenesis along the Zemun LPS. Lastly, the developed correlative age model provides a mean to compare DRS and magnetism-based indicators of pedogenesis with global climate stacks (here the LR04 stack; Lisiecki and Raymo, 2005).

Volcanic ashes are often identified in European loess units, but in most cases, these tephras are mixed within aeolian loess or occur as crypto-tephras invisible to the naked eye. As most widespread tephras stem from highly explosive silicic magmas they are rather dominated by volcanic glass instead of by minerals or rock fragments (e.g., Lowe et al., 2017). Therefore, tephra layers are expected to have magnetic grain sizes similar to

rapidly cooled magmatic rocks, characterized by dominantly SD and pseudo-single domain (PSD) particles, representing "frozen" magma at the time of eruption (e.g., Till et al., 2011). Both the magnetic grain size and composition of magnetic minerals contained in the tephra are also expected to contrast with that of the loess in which they are embedded. In the Zemun LPS, two tephra layers were identified through distinguishing magnetic properties similar to previous reports (Marković et al., 2015, 2018). Despite the lack of geochemical and mineralogical constraints, they are tentatively assigned to the so-called L2 and Bag tephra, both widespread regional marker-horizons.

PROFILE SETTING AND STRATIGRAPHY

The Zemun LPS (N 44.9246°, E 20.3197°) is located in the southern part of the Middle Danube Basin and is exposed by the escarpment of a landslide scar developed in the high cliffs on the right bank of the Danube at the northwestern border of the Belgrade conurbation (Šarić, 2008). The profile belongs to the Srem loess plateau, which is delimited to the East and Northeast by the Danube and to the South by the Sava (**Figure 1A**). The Zemun LPS reveals several loess-paleosol couplets, reflecting warm/humid (interglacial) and cool/dry (glacial) past environmental conditions. The Zemun LPS shows similar litho- and pedo-stratigraphic features as neighboring profiles at Batajnica (Marković et al., 2009) and within the Titel loess plateau (Marković et al., 2015).

Parallel to sampling, the lithology of the sequence was described in the field focusing on loess structure, pedogenic features, and sediment color. Additionally, sediment samples were investigated under the binocular microscope in order to estimate mineralogical compositions and degree of roundness of grains. In loess deposits, aeolian origin is assumed when single grains predominantly show little rounding due to direct source to sink transport, whereas well-rounded grains reflect complex sediment recycling, long term transport and/or fluvial processes. Soil units were described following the *World reference base for soil resources* (IUSS Working Group WRB, 2015[1]), even though we are fully aware that this system is not designed to classify buried soils also referred to as paleosols. Additionally, we follow the concept of accretionary soil formation characteristic of aeolian landscapes of western Eurasian dry steppe regions (Hambach et al., 2019; Jordanova and Jordanova, 2020; Lehmkuhl et al., 2021). These observations combined with results of laboratory analyses (colorimetric and magnetic parameters) form the base for a genetic interpretation of sediment formation.

Field observation of the vertically exposed outcrop wall recognizes four major lithofacies units (**Figure 1**): loess (L4, L3, L2LL1, L2, L1), interstadial-type (embryonic) paleosol (L2SS1), interglacial-type paleosols (S4, S3, S2, S1), and a brownish to blackish, sandy-silty well-bedded unit (marshy floodplain sediment, MFS) outcropping between the lower two interglacial paleosols.

[1]http://www.fao.org/soils-portal/data-hub/soil-classification/world-reference-base/en/

Sampling for sedimentological analysis started at the transition from a basal brownish-yellowish loess unit to the lowermost exposed interglacial pedocomplex (S4) characterized by humus infiltrations in ancient root channels, carbonate concretions (up to 5 cm in diameter) and hydromorphic features, such iron coatings and iron/manganese oxide patches (**Figure 1C**). The basal red-brownish fossil pedocomplex (24.35–22.30 m relative profile depth) is c. 2.05 m thick and can be classified as a Cambisol typical of forest-steppe environments. A gradual transition is observed to the overlying loess unit (L4, 22.25–21.90 m). From 21.85 to 21.70 m, a 0.20 m thick bed of loosely cemented loess can be recognized. At 21.65 m depth, a drastic change in sediment toward sandier material is observed and referred hereafter as marshy floodplain sediment (MFS) (see section "Integrated Stratigraphy"). The MFS persists from 21.65 to 16.50 m with alternation of sandy iron-stained and sandy-silty beds with dark humus rich partly clayey beds dominating.

The subsequent polygenetic light reddish-brown paleosol (S3, 16.45–18.80 m) can be classified as a Phaeozem typical of steppe environments with mild and relatively humid winters. It is built from the bottom to the top by a lower pedogenetically overprinted unit. This is followed by a thin, lightly colored horizon with carbonate nodules and numerous krotovinas likely representing a pedogenetically overprinted loess unit overlain by a pedogenetic horizon with again many krotovinas. A gradual transition to the overlying c. 2.65 m thick yellowish-grayish loess (L3, 13.75–11.10 m) is observed.

The contact between L3 and the pedocomplex above is massively bioturbated and interspersed with carbonate concretions of sub-centimeter to decimeter size. This interglacial-type pedocomplex is c. 3.50 m thick and comprises in its lower part a brownish-blackish to dark grayish c. 2.00 m thick paleosol unit (S2, 11.05–8.70 m), which is classified as a polygenetic steppe soil of Kastenozem to Chernozem type typical of cool mid-latitude steppe environments. The lower strongly developed darker horizon has many carbonate pseudomycelia. Krotovinas are scattered throughout the middle lighter colored horizon and the upper weakly developed interstadial-type paleosol horizon (L2SS1, 8.40–7.35 m). S2 and L2SS1 are separated a thin (∼25 cm) pale yellowish loess unit (L2LL1, 8.65–8.45 m), which is bioturbated in its uppermost part transitioning into L2SS1 interstadial paleosol. The overlying pale-yellowish to partly yellowish-grayish loess unit (L2, 7.30–3.60 m) is c. 4.00 m thick and shows numerous fine lamina consisting of sandy loess beds in its middle part. At c. 5.8 m, a 2–3 cm reddish to brownish loose loess layer was observed.

The contact between L2 and the uppermost interglacial pedocomplex (S1, 3.55–0.60 m) is also characterized by massive carbonate concretions and krotovinas. The S1 pedocomplex is c. 2.95 m thick, composed of a lower dark brownish-grayish paleosol overlain by lighter paleosols marking variable degrees of pedogenesis during continued dust deposition. The entire complex can be characterized as a typical Chernozem soil with decreasing intensity of pedogenesis with time. The uppermost horizon of the S1 pedocomplex is rather weakly developed and contains numerous krotovinas.

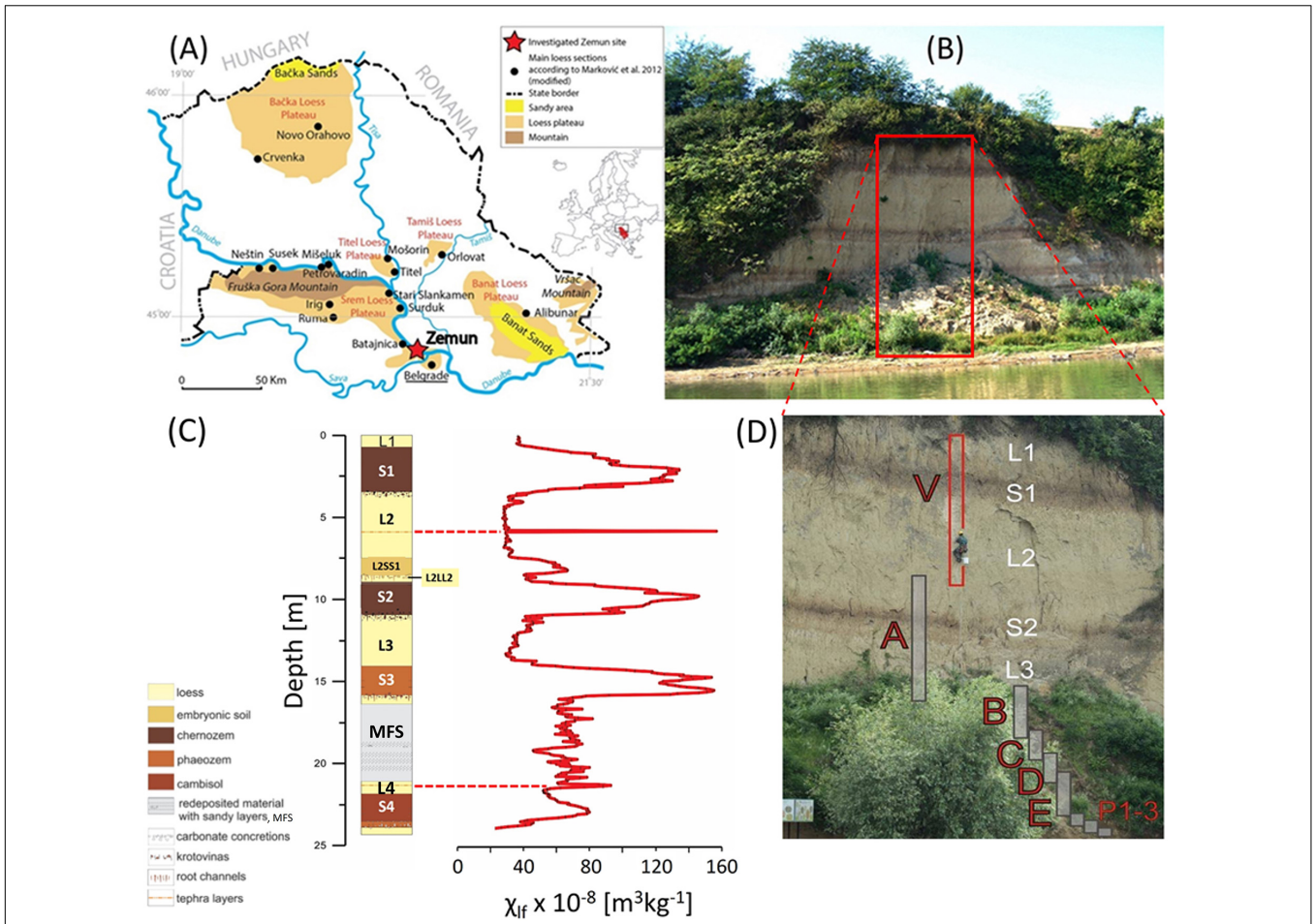

FIGURE 1 | (A) Regional map with the loess distribution of northern Serbia (southern Middle Danube Basin) and neighboring key-profiles, adapted from Gavrilović et al. (2020). The Zemun LPS is indicated with a red star. **(B)** Photo of the studied Zemun LPS. Brownish layers are buried soils (paleosols). The studied section has a thickness of approximately 25 m. **(C)** Schematic drawing of the Zemun profile and the corresponding low-frequency magnetic susceptibility (χ_{lf}) record highlighting (dashed lines) the anomalously high values associated to two tephra layers. **(D)** Sampling strategy with indicated sub-sections mentioned in the text.

The uppermost layer of the studied Zemun LPS is composed of pale porous sandy loess (L1, 0.60–0.00 m), which is loosely cemented with a few thin laminated beds of sandy-silt.

With the exception of the MFS sand dominated unit between 21.65 and 16.50 m, the entire sequence consists of coarse primary eolian silt with alternating contributions of fine sand in the pure loess and medium to fine silt in the paleosol units. Similar stratigraphic features can be observed in LPSs close to the Zemun LPS, e.g., from Batajnica (Marković et al., 2009), and the Titel-Stari Slankamen composite profile (Marković et al., 2011, 2015).

MATERIALS AND METHODS

Sampling

Sampling was performed from abseiling the wall (subsections V, A) and in dug trenches (subsections B, C, D, E, P 1–3). Subsections V and A cover the uppermost c. 15 m and are c. 2 m apart, whereas subsections B, C, D, E, and P 1–3 are located between c. 6 and 10 m upstream to the northwest (**Figure 1D**). All subsections overlap and provide the basis for the construction of the composite profile. After thorough cleaning of the profile, bulk samples were taken with 5 cm spacing for a total of 479 sampling depths. For laboratory analyses described in following section "Room Temperature Susceptibility Measurements", bulk samples were dried at 30°C for 48 h, homogenized and compressed into non-magnetic 6.4 cm^3 plastic boxes (n = 479) and ∼1.1 cm^3 gelatin capsules (n = 262). Masses of bulk samples within boxes and capsules were measured and recorded.

Room Temperature Susceptibility Measurements

Magnetic susceptibility measurements were carried out in 2017 at the Environmental and Palaeomagnetic laboratory at the University of Bayreuth. Measurements of low-field mass normalized magnetic susceptibility (χ), performed on all 479 box-samples, were obtained with a Magnon kappa bridge (Magnon, Dassel, Germany—VFSM) operating with a 320 A/m

applied field at low frequency (300 Hz, χ_{lf}) and high frequency (3,000 Hz, χ_{hf}). The absolute frequency dependence of magnetic susceptibility $\Delta\chi$ is determined from:

$$\Delta\chi = \chi_{lf} - \chi_{hf}[m^3kg^{-1}]$$

and the percent increase (χ_{fd}) with respect to χ_{lf} from:

$$\chi_{fd} = \left(\frac{\chi_{lf} - \chi_{hf}}{\chi_{lf}}\right) \times 100\%$$

(Mullins and Tite, 1973; Dearing et al., 1996; Eyre, 1997).

Hysteresis Measurements

Hysteresis measurements were performed with a Princeton Measurements Corporation Model 3900 Vibrating Sample Magnetometer (VSM) at the Institut de Physique du Globe de Paris (Paleomagnetism Research Group). A total of 262 samples were investigated across sub-sections of the Zemun profile covering the interval from 12.05 m depth (L3) to the top of the profile continuously (n = 240), an interval from 22.25 to 21.50 m continuously (n = 16) and 6 other discontinuous intervals within the sandy MFS (**Figure 1**).

For 6 of 10 samples stemming from the MFS sample preparation required modification to prevent grain movement favored by the higher sand content during hysteresis, FORC and IRM acquisition measurements on the VSM. The preparation consisted in piercing a hole at the base of the capsule to allow air to be released during the filling process. A thin layer of diamagnetic cotton was inserted to prevent single grains to fall through the air-release hole. Between 120 and 170 mg of the coarse grain sediment was added to the capsule and the net-weight measured. Grains were immobilized by adding neoprene gel glue, verified to be diamagnetic (c. -3×10^{-8} m^3kg^{-1}). Complete saturation with glue was confirmed by leaking glue through the air-release hole. The lid was also filled with neoprene glue before sealing the capsules with the temperature resistant tape (see **Supplementary Figure 1**). Samples were dried overnight.

Prior to hysteresis measurements, the χ of each sediment-filled capsule was determined with an AGICO KLY-3 kappabridge operating in a 300 A/m applied field at a frequency of 875 Hz. These low-field susceptibility measurements were used to (1) test whether the gelatine capsule subsamples are representative of the larger box samples, and (2) calculate the ferrimagnetic component of susceptibility (χ_{ferri}) by calculating the difference of the KLY3 bulk low-field susceptibility and the calculated high-field susceptibility (χ_{hifi}) from the slope of the high-field linear segment of the hysteresis loop:

$$\chi_{ferri} = \chi_{lf\ KLY3} - \chi_{hifi}$$

Three experiments were conducted with the VSM. (1) Hysteresis loops were measured in maximum applied fields of ± 1.5 T over 100 ms measurement times at each applied field step. The applied field increment was set to 5 mT. Experiments began at positive maximum field following a 1 s pause. The following parameters were derived from each hysteresis loop: coercivity (Hc), saturation magnetization (Ms), saturation remanent magnetization (Mrs) and high-field magnetic susceptibility (χ_{hifi}), calculated from the linear high-field slope of the magnetization above 1.05 T. The ratio between χ_{ferri} and Ms can be used to track variations in relative concentration of superparamagnetic (SP) particles assuming a constant magnetic mineral assemblage. (2) The coercivity of remanence (Hcr) was determined from backfield direct current demagnetization of the forward maximum field (1.5 T) isothermal remanent magnetization (IRM). 70 backfield steps were logarithmically spaced over the 0–500 mT range. (3) Backfield direct current demagnetization of the forward maximum field (1.5 T) IRM was also measured using linear 100 mT backfield steps from 0 to 1.5 T. From these data, relative contributions to the total $IRM_{1.5T}$, such as the S-ratio are determined, as well as absolute contributions to the total $IRM_{1.5T}$ within various coercivity windows, such as HIRM, are quantified. The S-ratio was calculated after King and Channell (1991) as follows:

$$S - ratio = \frac{IRM_{-0.3T}}{IRM_{-1.5T}}$$

resulting in values possibly ranging from −1 to +1, where values decrease from 1 as the relative contribution of hard magnetic minerals (defined here as having a coercivity of remanence greater than 300 mT) to the total $IRM_{1.5T}$ increases. The hard isothermal remanent magnetization (HIRM) was calculated from the difference in magnetization between the 0.3 T and 1.5 T backfield steps following a forward field magnetization in 1.5 T (e.g., Taylor and Lagroix, 2015; Liu et al., 2016):

$$HIRM = IRM_{-0.3T} - IRM_{-1.5T}$$

The ratios of Hcr/Hc and Mrs/Ms (indicative of a samples mean magnetic grain size) were plotted on a modified Day-Dunlop plot (Day et al., 1977; Dunlop, 2002a,b), tracing differences in loess/paleosol samples and potentially tephra-bearing samples, the latter expected to contain higher PSD and SD content than loess.

First Order Reversal Curve (FORC) Investigations

FORC investigations were carried out for six samples using the VSM. Specifically, FORCs were acquired on two samples suspected to contain tephra material (ZV 117, 5.80 m profile depth, containing the L2 tephra) and ZP1 001 (21.70 m, containing the Bag tephra, and reflecting the highest magnetic susceptibility signal out of 4 samples (ZP1 001- ZP1 004). To identify differences in magnetic grain size and possible differences in magnetic interactions, FORCs were also carried out on samples representative of loess units bracketing the suspected L2 and Bag tephra occurrences ZV 112 (5.55 m), ZV 126 (6.25 m), ZE 047 (21.65 m), and ZP1 016 (22.45 m). ZE 047 marks the base of the MFS and is hydromorphically overprinted but it is the sample immediately above the suspected Bag tephra sample analyzed (ZP1 001). Samples were exposed to a saturating field of 500 mT, Hu (min, max) were selected after initial test-measurements to ± 80 mT, and Hc (min, max) to 0 and 100 mT. Averaging

time was set to 300 ms, reducing measurement noise. For each diagram, 150 FORCs were acquired at a field increment of ca. 1.9 mT. For weak samples originating from loess units, 2–9 series of FORC measurements were measured and averaged. The number of FORCs averaged for each sample is reported as *n*-values in **Figure 6**.

FORC data analyses were carried out using FORCinel version 3.06 (Harrison and Feinberg, 2008). The main pre-processing consisted in drift and high-field slope corrections, first point removal, and lower-branch subtraction. FORCs of loess samples, for which multiple FORC were measured, were averaged in FORCinel. FORC diagrams were improved by color rescaling selecting a rectangle area around the central ridge and using the "Autoscale" option. Smoothing was conducted according to the VARIFORC approach (Egli, 2013) with the following smoothing factors: vertical ridge Sc0 = 4, central ridge Sb0 = 3, horizontal smoothing Sc1 = 7, vertical smoothing Sb1 = 7, horizontal and vertical lambdas 0.1, output grid = 1 and central ridge offset = 0. Horizontal profiles were extracted using FORCinextras.

High-Resolution IRM Acquisition

Complementary to FORC measurements, high-resolution stepwise isothermal remanent magnetizations (IRM) were acquired on the same samples using the VSM. Samples were demagnetized before IRM acquisition. The initial field was set to 15 μT, the final field to 1.5 T, using 300 logarithmically spaced measurement steps.

Tentative un-mixing of the IRM acquisition curves was carried out with aid of the MAX UnMix RShiny web-application (Maxbauer et al., 2016). Smoothing factors were set between 0.5 and 0.6, depending on measurement noise. Before using MAX UnMix, first derivatives of the raw IRM acquisition data were calculated, distributions of suspected tephra and bracketing loess samples compared to determine roughly the number and characteristics of geologically realistic components. These components were used in the fitting panel of MAX Unmix, and then refined in the optimization panel by minimizing the residual sum of squares (RSS). Final determination of the components characteristics were obtained in the Error Analysis panel, providing mean values and uncertainties based on 100 Monte-Carlo random re-samplings of 95% of the data.

Colorimetric Measurements

Initial colorimetric measurements were carried out at the Environmental and Palaeomagnetic laboratory at the University of Bayreuth. Colorimetric analyses have been done in the past decades by visual identification of Munsell color charts (e.g., Tsatskin et al., 1998; Günster et al., 2001; Machalett et al., 2006), but its importance for paleoclimatic reconstruction remained little explored for a long time. These color charts provide alphanumerical indices for each sample by comparing the sampling material with a single-color rectangle. This procedure has some disadvantages (Post et al., 2015) such as subjective evaluation by a researcher and dependence on specific moisture and lighting. Spectrophotometers eliminate these uncertainties (Sun et al., 2011) and provide objective numerical values of luminance (L*), redness (a*) and blueness (b*). L* ranges from 0 (black) to 100 (white), whereas a* ranges from negative (green) to positive (red) and b* from negative (blue) and positive (yellow). The redness a* is commonly interpreted as reflecting weathering intensity (Yang and Ding, 2003). These three parameters span a 3-dimensional color sphere and derived Lab-values can be transformed to RGB colors to make their real colors visible (as conducted in **Figure 3**). Furthermore, spectrophotometers provide backscattered intensities of wavelengths each 10 nm from the visible light spectrum (here 400 to 700 nm only). These backscattered spectra are capable of tracing distinct minerals out of a heterogeneous bulk-sample mineral assemblage. An additional advantage is the fast (∼2 s per sample) and non-destructive nature of the measurement.

Diffuse Reflective Spectroscopy (DRS) measurements were carried out in 2020 at the Leibniz Institute for Applied Geophysics (LIAG, Grubenhagen) with a Konica Minolta CM 700d spectrophotometer, in 10° observer angle and using the D65 norm-light calibration. An oculus width was obtained with a 0.8 cm open adapter. Backscattered reflectance spectra were converted into 1st derivative values with a newly developed R-script. 1st derivative values were used to calculate the hematite/goethite ratio (HGR), following the same approach described in Wu et al. (2018). HGR was calculated from the ratio of backscattered intensities (I) at 565 nm, associated to hematite, and 435 nm, associated to goethite, so that $HGR = I_{565\ nm} / I_{435\ nm}$ (Barranco et al., 1989; Deaton and Balsam, 1991; Debret et al., 2011). The backscattered intensity bands were selected based on peaks in the 1st derivative spectrum (**Figure 2**). For the transformation of Lab values into RGB colors, a modified R-script (R Core Team, 2020) was used (Zeeden et al., 2017).

Generation of the Age Model

The age model (**Figure 9**) was constructed by correlating $\Delta\chi$ variations and the LR04 stack (Lisiecki and Raymo, 2005), reflecting mainly global ice volume by benthic $\delta^{18}O$. Tie-points were selected based on (1) variations in magnetic parameters interpreted to fluctuate predominantly as a function of pedogenic intensity, and (2) similarities in fluctuation and amplitude of magnetic parameters when compared to the LR04 stack and Imbrie and Imbrie ice model (Imbrie and Imbrie, 1980). Identified tephra layers provide additional tie-points. This approach resulted in 13 tie-points (**Table 1**). Two additional tie-points constrain the age model stemming from the two potential tephra layers identified magnetically and compatible with sedimentological observations in the field. For the age model construction, the "astrochron" package version 0.9 (Meyers, 2014) was used for linear interpolation.

RESULTS

Magnetic Susceptibility Parameters and Stratigraphical Assignment

Based on the record of magnetic susceptibility with depth, a general pattern with low-frequency susceptibility (χ_{lf}) values being generally low in loess units, and high in paleosols can be observed for the Zemun LPS (**Figure 3** and **Table 2**).

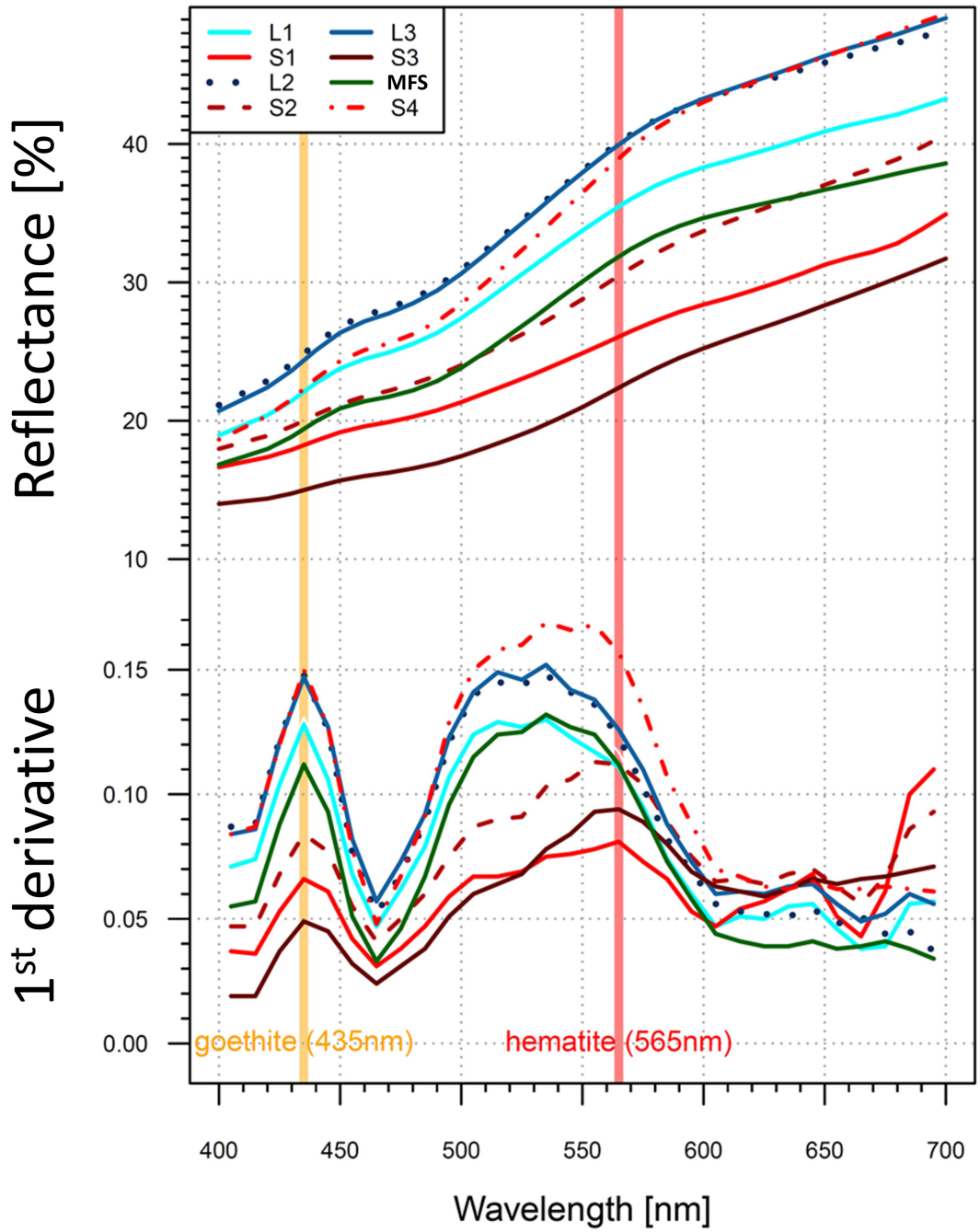

FIGURE 2 | DRS analysis of selected representative samples from different stratigraphical units of the Zemun LPS. Upper plot displays raw backscattered intensities of wavelengths ranging between 400 and 700 nm in 10 nm intervals. Lower plot displays the first derivatives of backscattered wavelengths. Assumed contributions of hematite and goethite at distinct wavelengths are indicated as orange and red vertical bands, respectively. MFS is the abbreviation for marshy floodplain sediments.

Such a pattern is well known from Eurasian LPS and predominantly reflects past environmental changes between glacials and interglacials during the Pleistocene. Following the stratigraphic nomenclature introduced by Marković et al. (2015), results reveal that the sampled profile extends from a basal S4 pedo-complex, assigned to MIS 11 to the oldest part of the L1 directly overlaying the last interglacial-early glacial pedo-complex S1. Beside distinct elevated magnetic susceptibilities in interglacial paleosols, the highest χ_{lf} value (157×10^{-8} m^3kg^{-1}) is observed as a sharp peak at 5.80 m depth within the L2 unit. This peak coincides with the field description of a 2–3 cm reddish to brownish loose loess layer and is stratigraphically and magnetically consistent with the L2 tephra layer described in other LPS regionally (e.g., Laag et al., 2018; Antoine et al., 2019). Mean χ_{lf} values of paleosols S3 to S1 decrease slightly from ~115 to 100 to 90 $\times 10^{-8}$ m^3kg^{-1},

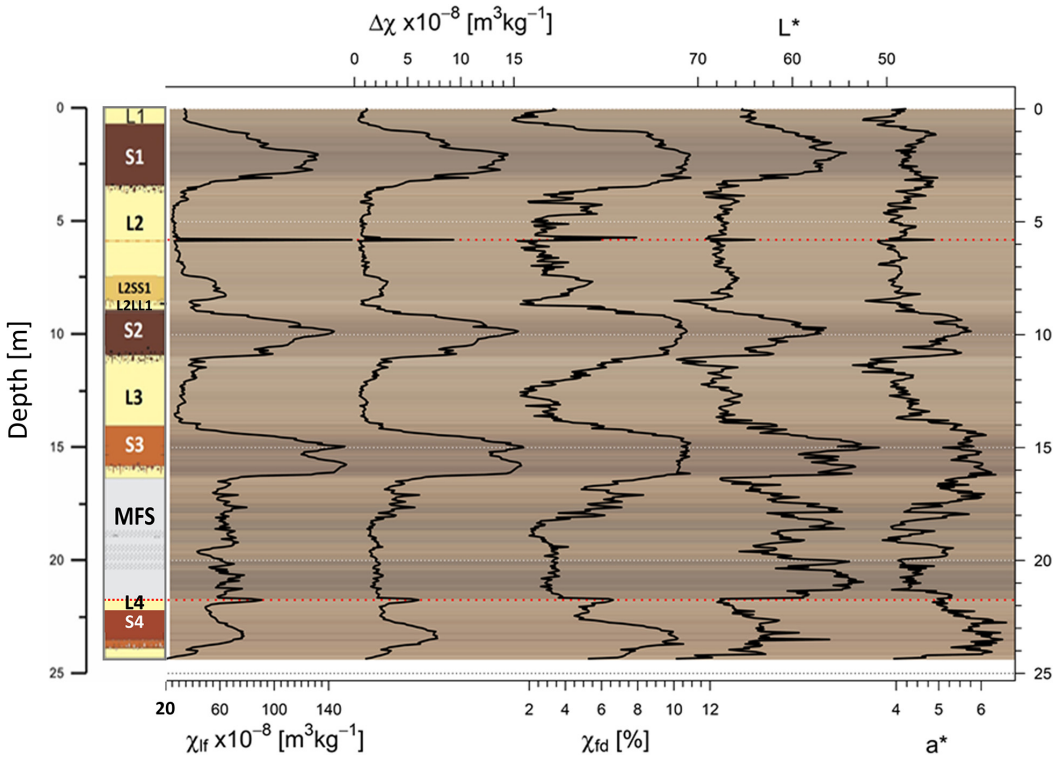

FIGURE 3 | Stratigraphic view of magnetic susceptibility parameters χ_{lf}, $\Delta\chi$, χ_{fd} [%], and selected colorimetric parameters L* and a*. The variability of magnetic susceptibility parameters with depth reflects the pacing of interglacial (S4–S1) and glacial (L4–L1) cycles. Potential tephra layers (red dotted lines) are referred to as the L2 tephra and to as the Bag tephra. Note that the scale for L* is inversed. Lab color values are transformed to RGB colors for each sample and plotted in the background.

TABLE 1 | Selected tiepoints for age model calculation.

Zemun depth [m]	Age [ka]	Comment
0.50	60.0	LR04
0.50	66.0	LR04
1.65	108.0	LR04
2.70	123.0	LR04
5.80	160.6	L2 tephra / Vico Ignimbrite B
7.65	171.5	LR04
8.55	180.1	LR04
9.90	215.0	LR04
10.85	239.0	LR04
13.80	268.5	LR04
14.95	308.0	LR04
15.85	330.9	LR04
21.80	367.5	Bag Tephra / TF-85
22.60	391.0	LR04
23.45	406.0	LR04

respectively (**Table 2** and **Figure 3**). Mean values of $\Delta\chi$ also decrease from S3 to S1. The S4 pedocomplex displays mean values of χ_{lf}, $\Delta\chi$ and χ_{fd} % that are much lower than S3–S1. Finally the MFS layer has moderately high χ_{lf} values, greater than S4 but less than S3-S1, which fluctuate over short depth intervals. $\Delta\chi$ and χ_{fd} % values of the MFS are low comparable to loess units.

The magnetic enhancement of the paleosol is readily observable on the $\Delta\chi$ vs. χ_{lf} bi-plot shown in **Figure 5A**. Depth intervals within the MFS and containing tephra material plot above the main trend line. Two populations are distinctively identified along this trend with one predominantly represented by samples showing no magnetic enhancement characterized by nearly all samples within loess units, and a second reflecting pedogenesis (higher $\Delta\chi$ and χ_{lf}) are all stemming from paleosol units. The strongest enhancement is expressed in paleosol S3, while S1 and S4 pedocomplexes spread over a wide range of $\Delta\chi$ and χ_{lf}. A background low-frequency magnetic susceptibility of 24.6×10^{-8} m^3kg^{-1} is obtained by fitting a linear regression line through the data excluding the MFS and tephra intervals. This background value is higher than what is observed in Central Asia and China ($17 \pm 2 \times 10^{-8}$ m^3kg^{-1} Forster et al., 1994) or at Semlac in Romania (10×10^{-8} m^3kg^{-1} Zeeden et al., 2016) but similar to LPS north of Prague in the Czech Republic (22×10^{-8} m^3kg^{-1} for Sedlec and 23×10^{-8} m^3kg^{-1} for Zemechy Forster et al., 1996).

Hysteresis Parameters

Hysteresis loop derived parameters are summarized in **Table 3** and plotted in **Figures 4**, **5**. Combining data sets acquired on

TABLE 2 | Minima, Maxima and Mean values for the different stratigraphic units.

Unit	n	$\Delta\chi$ × 10^{-8} [m^3kg^{-1}]			χ_{lf} × 10^{-8} [m^3kg^{-1}]			χ_{fd} [%]		
		Min	Max	Mean	Min	Max	Mean	Min	Max	Mean
L1	13	0.372	1.19	0.7197	33.50	36.10	34.87	1.073	3.473	2.078
S1	60	0.676	14.40	8.3990	36.20	132.00	88.90	1.766	10.929	8.843
L2*	73	0.360	2.38	0.9840	24.50	29.22	36.70	1.353	7.928	3.355
L2SS1	20	0.912	3.12	2.3450	33.70	64.40	55.16	2.709	5.497	4.228
L2LL1	5	0.624	1.35	0.8484	37.70	50.80	41.64	1.525	2.661	2.005
S2	48	1.090	15.40	9.2760	38.80	144.00	95.54	2.399	10.715	9.233
L3	51	0.471	3.48	1.4100	26.80	49.80	35.52	1.507	7.118	3.813
S3	50	1.020	15.90	10.21	30.20	153.00	103.6	3.365	10.911	9.130
MFS	103	1.200	6.09	2.544	43.40	79.70	63.08	2.010	8.305	4.027
L4	8	2.370	3.280	2.758	49.50	59.90	52.27	4.772	5.617	5.264
S4	42	1.090	7.79	4.599	20.50	77.60	56.89	4.508	10.523	7.813
L2 tephra	1		9.310			157.00			5.935	
Bag tephra	4	4.620	6.030	5.383	74.40	90.70	83.58	6.206	6.643	6.429
Total	479	0.360	15.90	4.540	20.50	157.00	63.98	1.073	10.929	5.872

the box and gelatin capsules subsamples was validated and is demonstrated in the **Supplementary Material** (**Supplementary Figure 2**) by KLY3 χ_{lf} vs. VFSM χ_{lf} measurements defining a linear fit with an r of 0.99.

The commonly used magnetic proxy for pedogenic intensity is $\Delta\chi$, which increases with increasing degree of pedogenesis is compared to χ_{ferri}/Ms, Hc, HIRM and S-ratio in **Figure 4A** through D, respectively. The χ_{ferri}/Ms ratio, like $\Delta\chi$, track relative changes in SP particle concentration, assuming the mineral assemblage contributing is monomineralic or that proportions between mineral components are constant. The data acquired clearly shows that the magnetic mineral assemblage is not monomineralic but that the soft ferrimagnetic component dominates both Ms (**Figure 5C**) and χ_{ferri} (**Figure 5G**). The magnetic mineral assemblage of the MFS and tephra samples do differ in terms of composition, concentration and magnetic grain size with respect to the loess and paleosol units, thus falling off the main trend line correlating ($r = 0.9$) χ_{ferri}/Ms and $\Delta\chi$. At higher pedogenic intensities, χ_{ferri}/Ms increases less rapidly than $\Delta\chi$ suggesting an increased contribution to Ms of a mineral, likely hematite, with a lower saturation magnetization than magnetite and maghemite. **Figure 5I** shows HIRM increasing as $\Delta\chi$ increases in paleosols corroborating the previous observation. In **Figure 4B**, $\Delta\chi$ and Hc are displayed, showing for all samples (tephra layers excluded) a negative exponential behavior. Loess and MFS samples reflect the highest coercivities with low amounts of pedogenetically formed SP particles. The tephra samples reflect a diametral behavior, indicating the presence of SP particles but at similar SP concentrations the tephra samples have a higher bulk coercivity due to either a higher proportion of SD and PSD grains and/or of high coercivity minerals. **Figure 4C** confirms the latter and results presented in section "FORC Analysis" supports the former. HIRM and $\Delta\chi$ correlate positively with a weaker coefficient ($r = 0.69$) than for soft remanence-bearing ferrimagnetic ($IRM_{-100\,mT}$) component (**Figure 5F**, $r = 0.92$), indicating that high-coercivity minerals present are also in paleosols and their concentration increases with increasing pedogenic intensity (**Figure 4C**). Interestingly, samples from the MFS, L2SS1 and samples stemming from the L4 loess unit also define a linear trend but with a much higher slope where increases in HIRM are associated with only small increases of $\Delta\chi$. **Figure 4D** correlates $\Delta\chi$ and the S-ratio. S-ratio values equal to 1 indicate the presence of only soft magnetic minerals like maghemite and magnetite, whereas reduced values underline the presence of high-coercivity minerals like hematite and goethite. The relative proportion of hard-magnetic minerals contributing to the $IRM_{1.5T}$ is greater in Zemun loess, especially L2, than in paleosols units. The highest S-ratio values are observed for samples stemming from the MFS and the tephra samples. Excluding MFS and tephra samples, the S-ratio correlates positively with $\Delta\chi$ with $r = 0.79$ (**Figure 4D**) indicating that the relative proportion of soft-magnetic minerals contributing to $IRM_{1.5T}$ increases with increasing degree of pedogenesis. At the same time, absolute concentrations of both soft remanence-bearing (**Figure 5F**) and hard (**Figure 4C**) magnetic mineral components increase individually with increasing pedogenesis.

Finally, hysteresis data presented on a modified Day-Dunlop plot (**Supplementary Figure 3**) reveals that all loess and paleosol samples fall within the PSD range as mean domain size, but samples stemming from the MFS as well as the tephra samples indicate a higher amount of SD particles.

FORC Analysis

FORC diagrams and extracted horizontal profiles (Hu = 0) of the six samples are shown in **Figure 6**. The three samples from the 5.55 to 6.25 m interval (ZV112, ZV117, ZV126) and the 21.65–22.45 m interval (ZE047, ZP1001, ZP1016) are presented separately because there main sediment compositions differ.

FORC diagrams and central ridge profiles of the bracketing loess for each subset interval, are very similar (**Figures 6A,C,D,F**). Samples ZV112 and ZV126 display a FORC diagram globally expected for PSD assemblages, in accordance with hysteresis parameters (Hcr/Hc = 3.18 and 3.29, Mrs/Ms = 0.14 and 0.13). The horizontal profiles are

TABLE 3 | Summary of derived hysteresis parameters and calculated ratios.

Stratigraphic unit		L1	S1	L2	L2SS1	L2LL1	S2	L3	MFS	L4	L2 tephra	Bag tephra
n samples		13	60	73	20	5	48	20	10	8	1	4
Ms × 10^{-3} [Am^2/kg]	Min	21.81	18.16	14.67	19.56	19.44	20.42	19.09	45.65	28.18	100.2	40.88
	Max	27.92	45.92	20.79	36.06	27.49	48.24	27.46	111.85	37.87		46.84
	Mean	24.39	33.45	17.71	30.05	21.87	35.79	22.81	67.40	30.37		44.35
Mrs × 10^{-3} [Am^2/kg]	Min	3.137	2.501	2.120	2.941	3.117	2.976	2.766	7.785	4.519	17.71	6.763
	Max	3.749	6.615	3.111	5.358	4.038	7.233	3.958	18.2	6.003		7.866
	Mean	3.432	4.769	2.573	4.358	3.338	5.274	3.424	12.04	5.014		7.488
Hc × 10^{-3} [T]	Min	11.93	7.931	11.97	11.52	11.84	8.377	10.87	13.85	13.03	13.71	11.75
	Max	13.40	11.991	15.09	13.85	13.17	12.338	13.60	17.65	14.07		12.37
	Mean	12.78	9.107	13.78	12.02	12.50	9.409	12.29	15.23	13.44		12.09
Hcr × 10^{-3} [T]	Min	35.91	21.84	38.27	34.22	36.30	23.20	32.46	31.91	36.08	33.03	30.50
	Max	40.86	39.06	46.61	40.41	39.04	37.40	39.90	43.12	39.94		32.15
	Mean	38.35	27.56	42.37	35.90	37.55	28.30	36.87	37.73	37.96		31.33
χ_{lfKLY3} × 10^{-8} [m^3/kg]	Min	26.27	27.58	18.31	25.61	30.12	31.82	29.82	46.48	37.94	115.4	53.01
	Max	29.92	94.70	29.83	49.13	40.39	104.72	40.48	77.05	48.35		63.01
	Mean	27.80	64.76	22.53	41.59	33.26	68.74	34.08	52.16	41.09		58.46
χ_{hifi} × 10^{-8} [m^3/kg]	Min	4.340	4.020	4.090	5.000	4.450	3.880	3.770	2.820	4.800	5.660	4.980
	Max	4.860	6.050	5.150	5.630	5.140	6.400	4.890	4.290	5.150		5.130
	Mean	4.637	5.250	4.553	5.441	4.676	5.460	4.511	3.548	4.889		5.055
χ_{ferri} × 10^{-8} [m^3/kg]	Min	21.60	23.40	14.00	20.60	25.70	27.00	25.30	42.20	33.10	110.00	48.00
	Max	25.20	88.90	25.20	43.70	35.30	98.60	36.20	73.60	43.20		57.90
	Mean	23.16	59.51	17.97	36.16	28.60	63.28	29.57	48.60	36.20		53.40
Mrs/Ms	Min	0.1325	0.1326	0.1264	0.1389	0.1469	0.1383	0.1371	0.1484	0.1581	0.1767	0.1654
	Max	0.1509	0.1518	0.1578	0.1523	0.1604	0.1528	0.1574	0.2076	0.1762		0.1719
	Mean	0.1408	0.1424	0.1452	0.1451	0.1532	0.1472	0.1500	0.1808	0.1653		0.1688
Hcr/Hc	Min	2.807	2.664	2.878	2.909	2.879	2.769	2.887	2.278	2.724	2.41	2.561
	Max	3.163	3.257	3.434	3.127	3.077	3.285	3.156	2.648	2.890		2.611
	Mean	3.003	3.019	3.078	2.987	3.005	3.006	3.002	2.475	2.824		2.591
S-ratio	Min	0.9159	0.9153	0.8890	0.9080	0.9143	0.9187	0.9131	0.9491	0.9279	0.9659	0.9472
	Max	0.9394	0.9476	0.9255	0.9327	0.9272	0.9458	0.9339	0.9744	0.9383		0.9518
	Mean	0.9266	0.9346	0.9052	0.9238	0.9201	0.9362	0.9233	0.9642	0.9317		0.9495
HIRM × 10^{-5} [Am^2/kg]	Min	21.24	20.86	18.65	25.71	22.58	21.67	21.81	34.05	31.58	58.57	35.16
	Max	26.52	35.35	29.39	40.00	30.88	40.92	28.20	46.01	36.78		38.07
	Mean	24.39	28.70	23.69	31.94	25.81	31.01	25.21	39.81	33.49		36.66
χ_{ferri}/Ms × 10^{-6} [m/A]	Min	8.650	11.10	8.770	10.50	12.80	12.90	10.90	5.810	11.40	11.00	11.60
	Max	10.300	21.20	12.400	12.90	13.60	20.70	14.80	9.910	12.50		12.40
	Mean	9.518	17.43	10.114	12.01	13.08	17.27	13.02	7.533	11.94		12.03

characterized by one main coercivity peak around 10 mT, and a second peak close to Hc = 0, along with a broad distribution up to about 80–100 mT. The PSD character of the FORC diagrams of samples ZE047 and ZP1016 is less pronounced and also reflected by the main hysteresis parameters (Hcr/Hc = 2.62 and 2.72, Mrs/Ms = 0.17 and 0.17). For these samples, the horizontal profiles are also characterized by a peak around 10 mT, but lack the very low-coercivity peak, probably due to a lesser content in grains either close to the superparamagnetic threshold or in the multidomain range. Sample ZV117 (Hcr/Hc = 2.46, Mrs/Ms = 0.17) displays a FORC diagram with a main distribution more elongated along the central ridge axis and shifted to higher Hc values, making the diagram appear more SD-like than those of the bracketing loess samples (**Figure 6B**). A similar observation can be made from sample ZP1001 (Hcr/Hc = 2.66, Mrs/Ms = 0.16), although it is not as prominent as for sample ZV117 (compare **Figures 6E,B**). This is also seen in the horizontal profiles, where the main distribution peak are broadened and shifted to slightly higher values by 5–10 mT. This indicates the input of additional and non-loessic material.

High Resolution IRM Acquisition

Detailed IRM acquisitions can provide alternative insights on the coercivity distributions because focusing on remanent magnetizations instead of direct in-field measurements, which is the case for FORCs.

These are therefore differently affected by magnetic particle sizes (for instance, superparamagnetic particles do not carry a remanent magnetization). IRM acquisition curves were obtained for the same six samples that underwent FORC

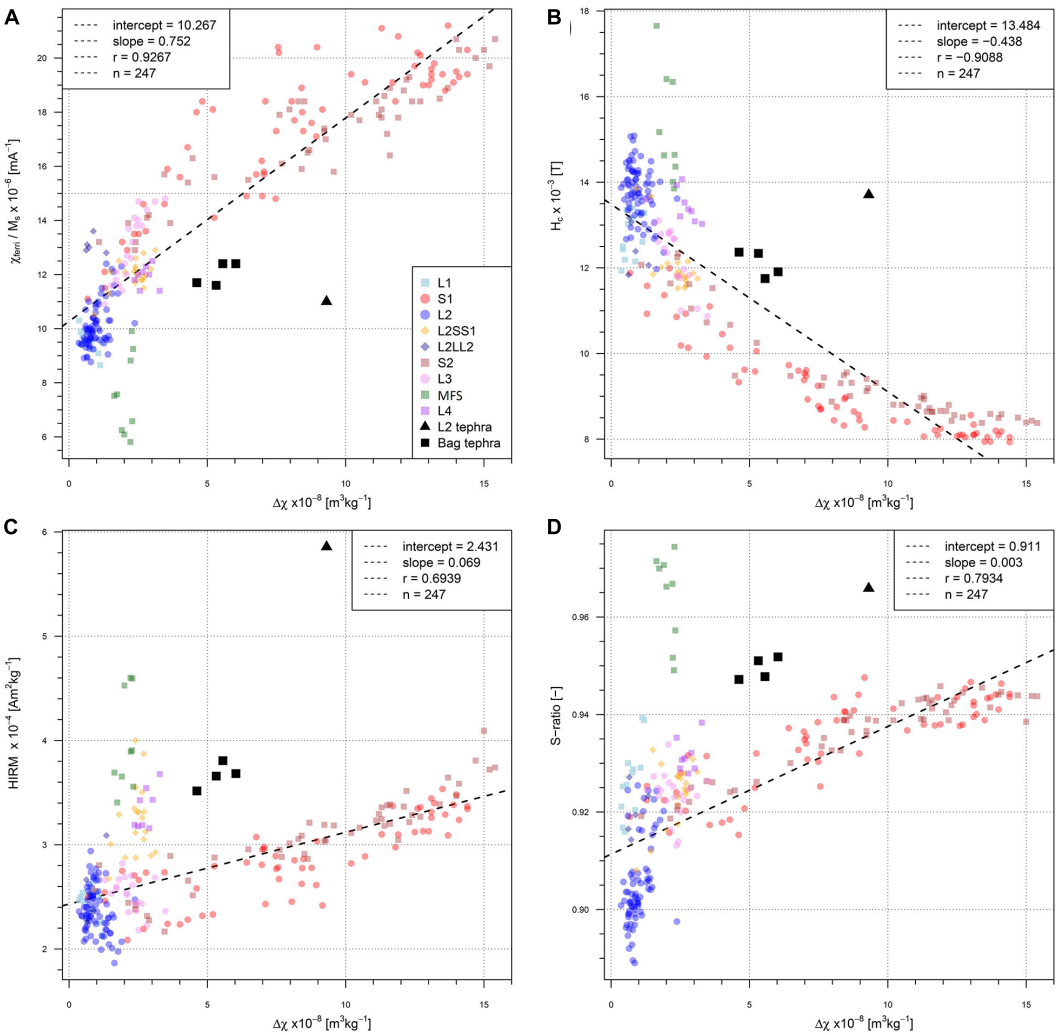

FIGURE 4 | Correlation of different magnetic parameters [χ_{ferri}/Ms, **(A)**; Hc, **(B)**; HIRM, **(C)**; and S-ratio, **(D)**] and inter-parametric ratios compared to $\Delta\chi$ for the units and samples summarized in **Table 3**. For correlation coefficients and regression fits, samples from the MFS, and the tephra layers were excluded.

as shown in **Figures 7A,F**. All six samples fail to saturated by 1.5T, indicating the presence of high-coercivity minerals. Raw coercivity distributions of samples ZV112 and ZV126 (**Figure 7G**) are nearly identical, as expected from both hysteresis parameters and FORC diagrams. Samples ZE047 and ZP1016 are also very similar (**Figure 7G**). The coercivity distribution of all four bracketing loess samples is characterized by two main peaks at about 20–30 mT (1.3–1.5 in log scale) and 60–100 mT (1.8–2.0 in log scale) (**Figures 7C,E,H,J**). The distribution of sample ZV117 (**Figure 7D**) differs significantly from that of samples ZV112 and ZV126 and is dominated by a peak around 45 mT (1.65 in log scale). For sample ZP1001, the distinction with its bracketing loess samples is less marked (**Figure 7I**), similar to observations made from FORC measurements. However, a small additional peak around 35 mT (1.55 in log scale) can be observed. These observations were used as first inputs for the MAX Unmix program. To these, we added a small amount of high-coercivity component to account for the unsaturated IRM. Results of the unmixing are depicted in **Figures 7C–E,H–J**. Taken separately, each sub-set of loess samples (ZV112 and ZV126; ZE047 and ZP1016) are characterized by similar distribution components. The IRM acquisitions of samples ZV117 and ZP1001 are compatible with models involving the same distribution components as those of the surrounding loess samples, with the addition of the fourth component. As in the case of the FORC measurements, this is more evident for sample ZV117.

Colorimetric/DRS Analysis

L* values are generally higher in light loess units meaning brighter colors due to higher amounts of quartz and carbonates than in paleosols, where clays and organic matter decrease the luminance (**Figure 3** and **Table 4**). The highest L* value (72.5) is found in the L2SS1 and the lowest L* value (50.8) in the S3 pedocomplex. Luminance values follow stratigraphic units from the S3 pedocomplex to the L1 loess at the top of the profile. Below

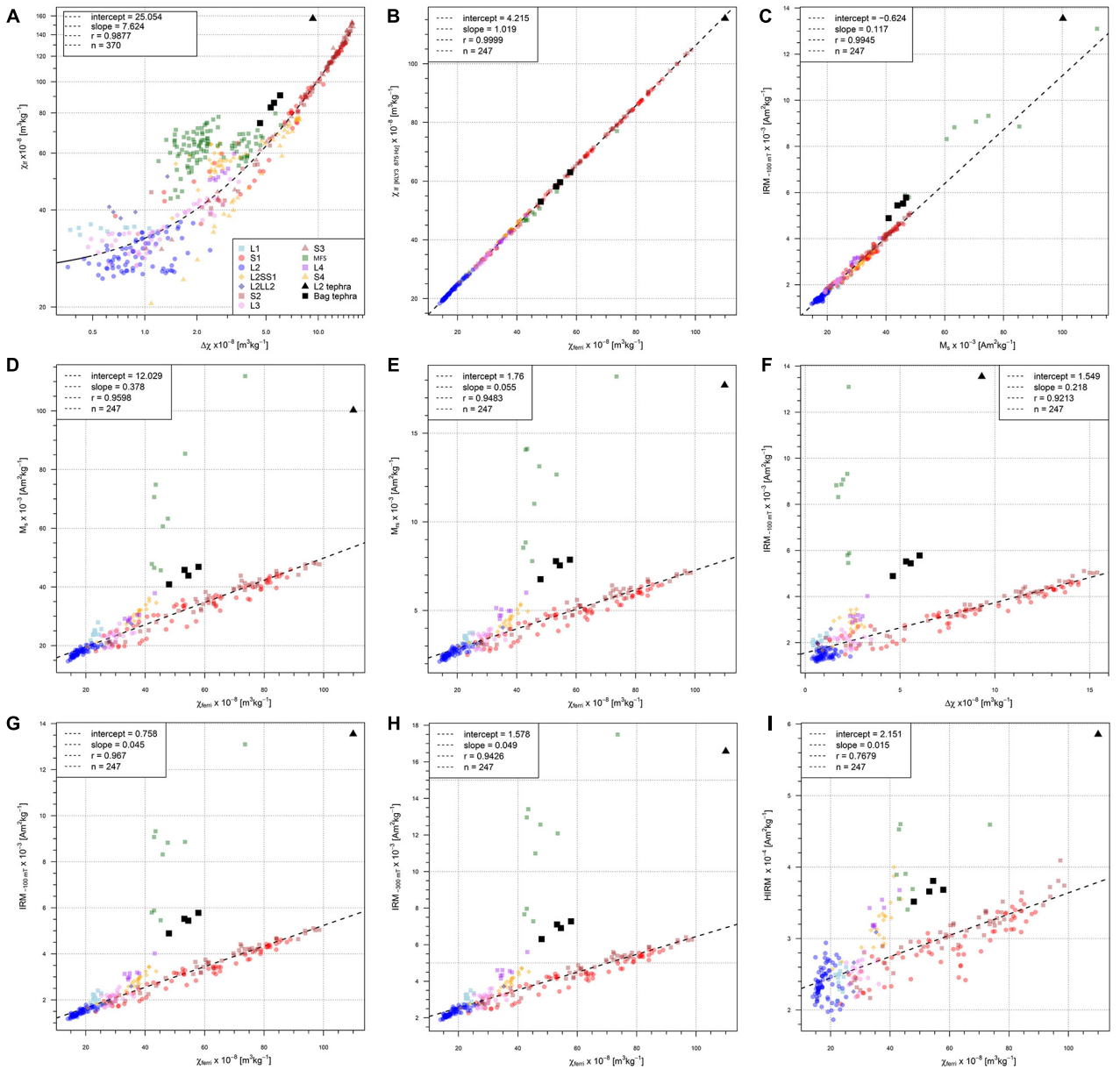

FIGURE 5 | Scatterplots of environmental magnetic data. Low frequency susceptibility (χ_{lf}) plotted against $\Delta\chi$ in **(A)** shows the characteristics of magnetic enhancement for the Zemun LPS. Samples stemming from the MFS (marshy floodplain sediments) and the tephra layers are excluded for calculated regression fit and correlation coefficient, resulting in 370 samples out of a total of 479 for **(A)** and 247 samples out of a total of 262 for **(B–I)**.

S3, the correlation of L* with the stratigraphy is more complex. The pedocomplex S4 is weakly expressed in the Zemun LPS characterized by a broad range of L* values. S4 can be considered as brighter than the other pedocomplexes with brightest values in the lower part at the base of the profile, possibly as a result of carbonate precipitation.

Similar to luminance (L*) values, redness values (a*) also reflect alternations between loess and paleosols (**Figure 3**). However, a clear separation between loess and paleosols is not as obvious for all paleosols from a* data. In the L1 loess unit, a* values vary between 3.2 and 4.2. Compared to the mean a* from the S1 pedocomplex, redness is reduced in L1 (3.8, in S1 4.4). The mean a* of L3 is similar to L2 (4.2) and relatively low with respect to S1. Higher a* values are reached in the S3 pedocomplex (mean = 5.7), but the highest a* values are reached in the S4 pedocomplex with a mean of 5.8 and a maximum of 6.6. Over the entire profile, a decreasing trend from S4 to S1 samples can be observed with even lower a* values for the weakly developed interstadial L2SS1 paleosol. Blueness (b*) values, which are inverse to yellow, are generally low in paleosols and high in loess units. The lowest b* values are found in the pedocomplex S1 and the highest b* values in the S4 pedocomplex. However, the

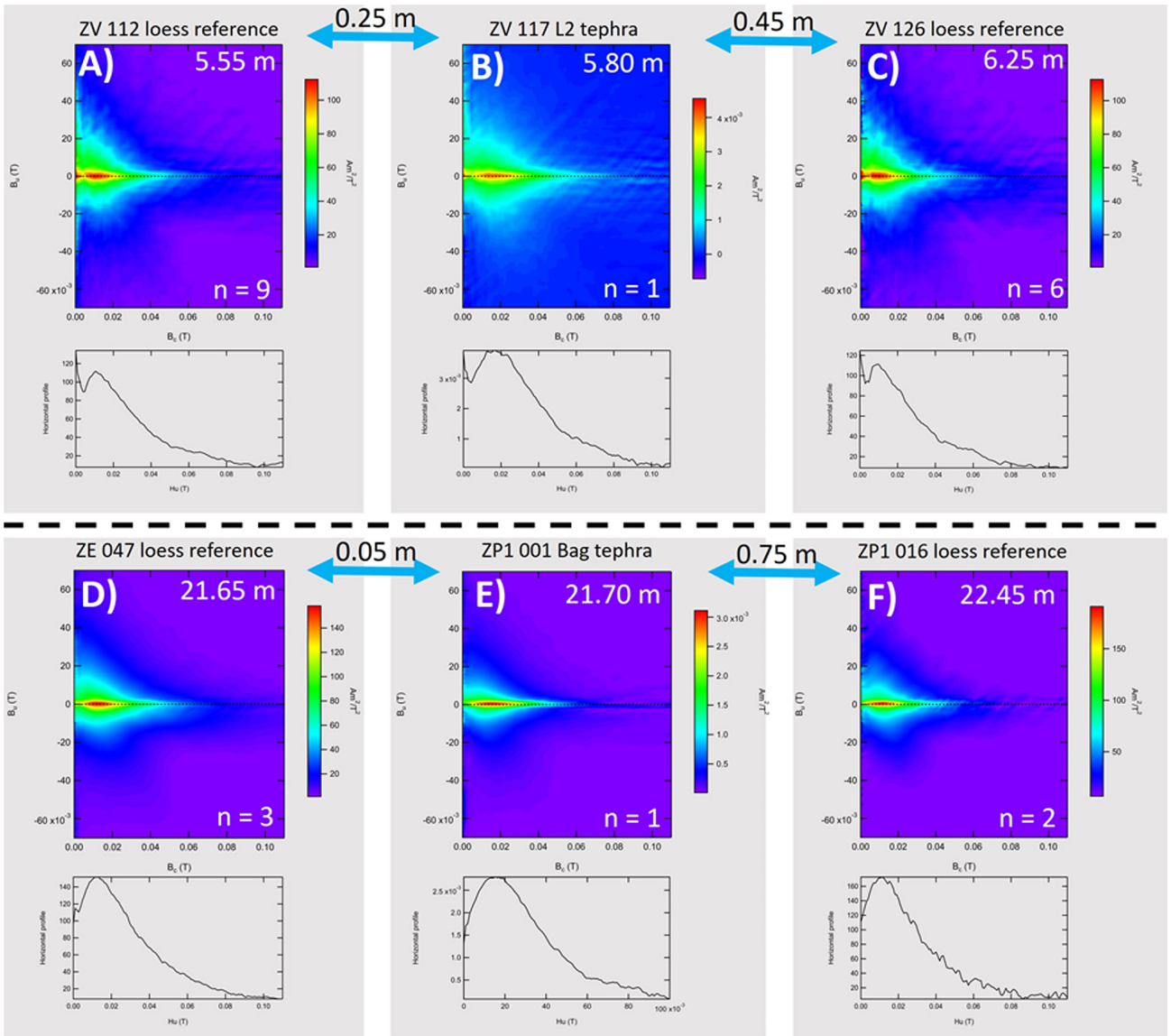

FIGURE 6 | FORC plots and related central ridge profiles of the tephra samples [ZV117, **(B)** for L2 tephra and ZP1001 for the Bag tephra, **(E)**] and neighboring reference loess samples [**(A,C)** for the bracketing loess samples of the L2 tephra and **(D,F)** for bracketing loess samples of the Bag tephra]. Blue arrows between the plots indicate the stratigraphical distance between the samples.

pedocomplex S2 (compared to the other pedocomplexes) does not show these well-expressed low values of b*. In summary, a*, a commonly used pedogenic indicator suggest the highest intensity of pedogenesis is found in S4 which contradicts interpretations based on magnetic proxies and field observations.

DRS derived goethite- and hematite concentrations (1st derivatives of intensities at 435 and 565 nm; I_{435} and I_{565}) and the ratio of hematite to goethite (HGR) mainly follow glacial/interglacial cyclicity. Both $I_{435\ nm}$ and $I_{565\ nm}$ values are reduced in paleosol complexes and are high in loess units with the exception of S4, which has values characteristic of the loess units (**Table 4**). HGR values are maximum in paleosols and like magnetic susceptibility parameters decrease from S3 to S1. Luminance (L*) and redness (a*) correlate with $r \sim -0.3$, while L* and blueness (b*) correlate positively with r∼0.78. HGR correlates with L* with r∼–0.82, with a* r∼0.76, and b* with r∼–0.5.

Additionally, selected colorimetric parameters are tested against magnetic indicators of relative concentration of SP-particles ($\Delta\chi$ and χ_{ferri}/Ms) and of high-coercive minerals (Hcr and S-ratio) (**Figure 8**). In **Figures 8A–C** test the correlation of $\Delta\chi$ vs. I_{435}, I_{565} and HGR. I_{435} correlates strongly negative with $\Delta\chi$ ($r = -0.92$), indicating a higher amount of goethite in loess units than paleosol units. A weaker but still present negative correlation to I_{565} ($r = -0.54$) indicates a higher amount of hematite in loess units as well. A strong and positive

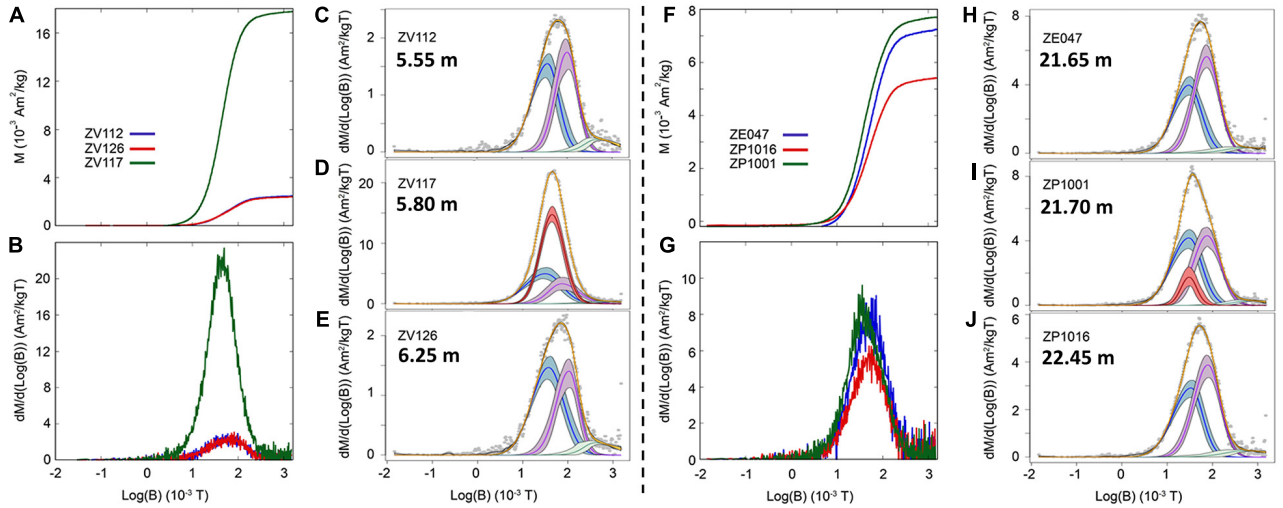

FIGURE 7 | IRM acquisition coercivity distribution and unmixing of coercivity spectra. Values are given in log scale. **(A,F)** compare IRM acquisition curves for samples measured for FORCs. **(B,G)** are comparisons of the first derivatives of the IRM acquisitions. **(C–E)** and **(H–J)** display the different results of the unmixing.

TABLE 4 | Summary of colorimetric parameters. HGR is the calculated hematite/goethite ratio.

Unit	n	L*			a*			b*			$I_{435\ nm}$			$I_{565\ nm}$			HGR		
		Min	Max	Mean	Min	Max	Mean	Min	Max	Mean	Min	Max	Mean	Min	Max	Mean	Min	Max	Mean
L1	12	63.87	65.47	64.60	3.220	4.220	3.832	13.88	15.62	14.85	0.1220	0.1330	0.1281	0.0900	0.1170	0.1061	0.6923	0.9032	0.8285
S1	60	54.31	67.98	59.80	3.560	4.970	4.402	10.01	16.86	12.66	0.0540	0.1530	0.08835	0.07300	0.13700	0.09708	0.8362	1.3750	1.1395
L2	74	65.11	69.38	67.49	3.570	4.690	4.057	14.89	17.47	16.12	0.1360	0.1660	0.1514	0.1130	0.1370	0.1237	0.7419	0.9412	0.8177
L2SS1	20	65.68	68.56	66.79	3.830	4.560	4.061	14.17	15.70	15.16	0.1260	0.1430	0.1353	0.1090	0.1250	0.1177	0.8429	0.9542	0.8703
L2LL1	5	68.50	72.49	70.42	3.280	4.090	3.726	14.31	15.56	15.00	0.1490	0.1700	0.1586	0.1170	0.1330	0.1248	0.7059	0.8418	0.7882
S2	48	56.46	71.43	62.78	3.740	5.760	5.008	12.67	16.04	14.12	0.06500	0.15400	0.10283	0.1030	0.1340	0.1183	0.7987	1.6154	1.2022
L3	51	65.37	72.24	67.72	2.980	4.780	4.072	13.71	16.84	15.42	0.1340	0.1690	0.1471	0.1000	0.1330	0.1216	0.6815	0.9366	0.8283
S3	50	50.81	67.70	58.66	4.760	6.340	5.635	10.25	17.22	14.02	0.04100	0.14800	0.08246	0.07600	0.15200	0.11432	0.9122	1.9600	1.4843
MFS	103	52.49	66.39	59.17	3.680	6.070	4.726	10.28	17.85	14.08	0.05000	0.14000	0.09303	0.0700	0.1480	0.1041	0.8911	1.4035	1.1421
L4	8	64.04	67.24	66.12	4.960	5.840	5.201	16.19	17.01	16.42	0.1190	0.1410	0.1331	0.1380	0.1450	0.1409	0.9929	1.2185	1.0610
S4	42	56.07	72.26	64.09	3.950	6.590	5.791	13.57	18.36	16.40	0.0620	0.1920	0.1193	0.1170	0.1610	0.1442	0.7292	1.8871	1.2460
L2 tephra	1		64.00			4.87			17.1			0.122			0.12			0.9836	
Bag tephra	4	67.23	67.96	67.63	4.860	5.130	5.013	16.30	16.68	16.57	0.1390	0.1460	0.1427	0.1400	0.1450	0.1422	0.9658	1.0288	0.9970

correlation of $\Delta\chi$ with HGR ($r = 0.87$) reflects a relatively higher amount of hematite than goethite in paleosol samples. This is supported by correlations based on magnetic indicators for hard magnetic minerals like hematite and goethite (high Hcr and low S-ratio values) for loess samples reflecting positive correlations for hematite and goethite and a negative correlation with HGR. This underlines the presence of hematite and goethite in loess samples and a relatively higher presence of hematite compared to goethite in paleosol samples. Overall, the variation of HGR and I_{565} is high in paleosols and low in loess units. I_{435} varies distinctively less in loess and paleosol samples. The luminance L* reflects toward younger samples a continuous evolution of brighter paleosols, where the S3 is the darkest (**Figure 3**). a* decreases as well, even more than L*, for all paleosols from S4 to S1 (**Figure 3**). With respect to the hematite/goethite ratio (HGR), the decreasing trend is most obvious. While there is a general increase of the colorimetric properties with increasing $\Delta\chi$, these are clearly non-linear.

Age Model

The age model (**Figure 9**) was constructed based on 15 tie-points listed in **Table 1** and shown as dotted lines in **Figure 10**. Thirteen tie-points are based on synchronizing variations in $\Delta\chi$ and benthic $\delta^{18}O$ values from the LR04 stack (Lisiecki and Raymo, 2005). In total, fifteen tie-points were used including the two identified tephra layers (L2 and Bag tephras). Two additional tie-points correspond to tephra layers demonstrated to be present based on magnetic properties presented in sections "Magnetic Susceptibility Parameters and Stratigraphical Assignment" through "High Resolution IRM Acquisition",

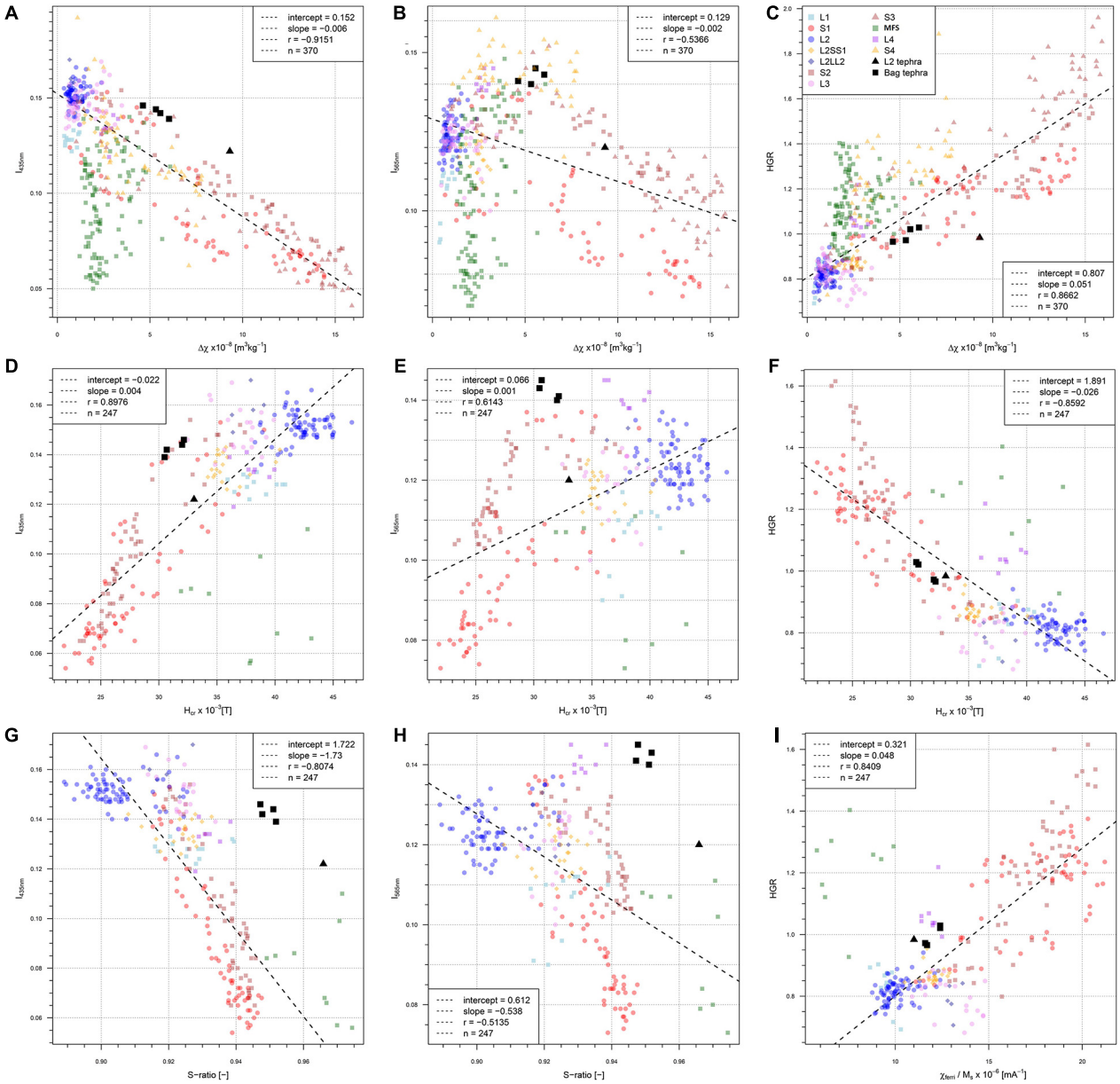

FIGURE 8 | Scatterplots of integrated magnetic and colorimetric data from the Zemun LPS. Note, that samples stemming from the MFS (marshy floodplain sediments) and the tephra layers are excluded for calculated regression fit and correlation coefficient, resulting in 370 samples out of a total of 479 for **(A–C)** and 247 samples out of a total of 262 for **(D–I)**.

especially evidenced by FORC analysis and IRM unmixing, and compatible with field-based sedimentological observations described in section "Profile Setting and Stratigraphy".

The L2 tephra is a widespread tephra occurrence within southeastern European loess records (Laag et al., 2018; Avram et al., 2020). Based on its stratigraphic position in several other well-dated profiles, like the neighboring Batajnica LPS (Avram et al., 2020), and the Harletz LPS in Bulgaria (Antoine et al., 2019), the L2 tephra can potentially be correlated to the Vico-Ignimbrite B eruption, dated to 160.6 ± 2.0 ka (Mannella et al., 2019). However, uncertainty remains with the age assignment, because (1) no geochemical evidence is to our knowledge available to trace back the L2 tephra to a specific eruption and (2) the archives of Lake Ohrid (Wagner et al., 2019) and Fucino Basin (Leicher et al., 2016; Giaccio et al., 2017, 2019) exhibit several prominent tephra layers during MIS 6, which may be assigned to the L2 tephra with ages spanning 150–168 ka. For the present study, we anchored the L2 tephra at 160.6 ka (**Table 1**) following the hypothesis of a correlation with the Vico Ignimbrite B eruption and the age provided by Mannella et al. (2019).

The Bag tephra, demonstrated to be contained in the Zemun LPS in 4 samples between 21.85 and 21.70 m depth, has been

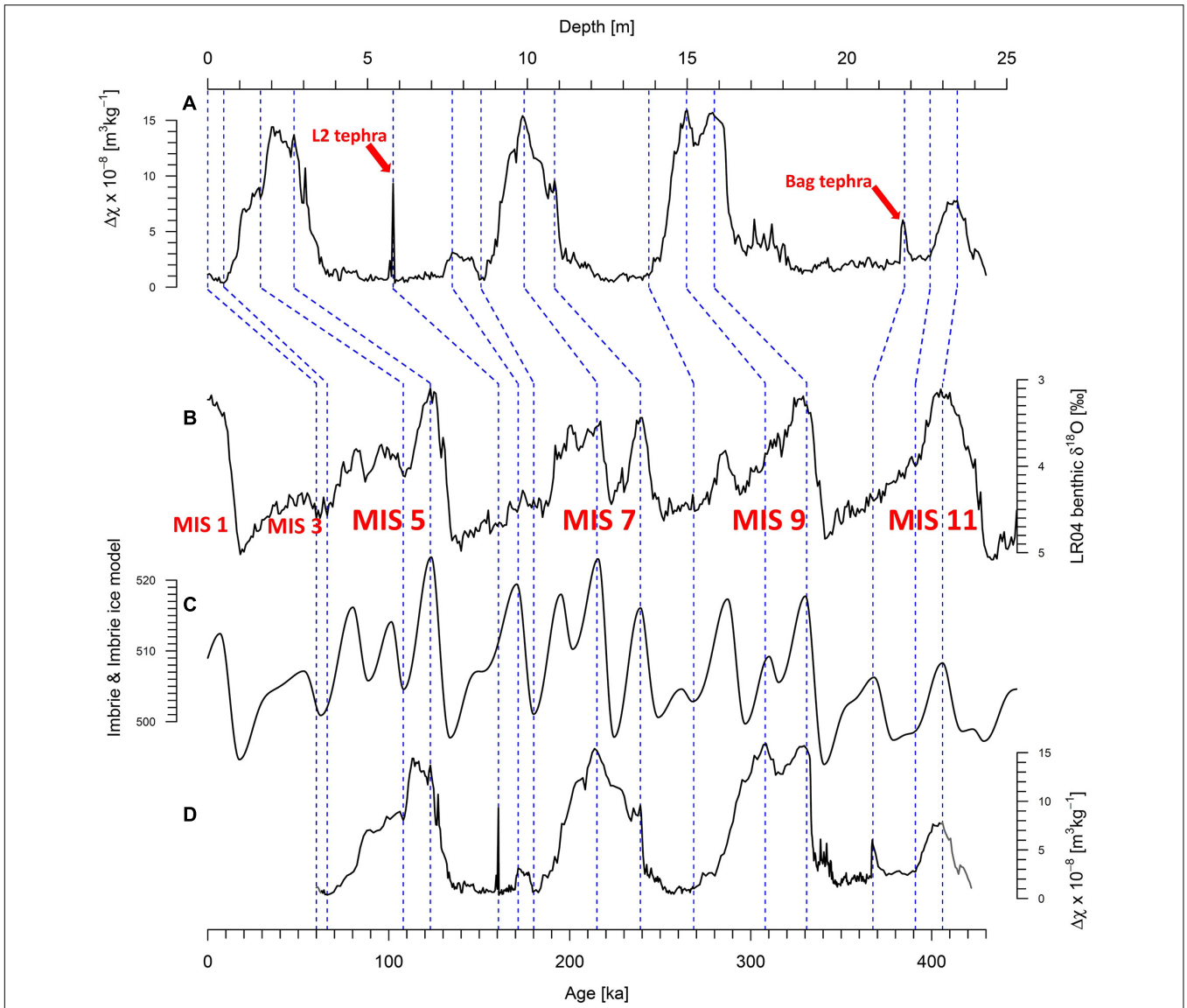

FIGURE 9 | Age model based on the correlation of absolute frequency dependent magnetic susceptibility values ($\Delta\chi$) with LR04 (Lisiecki and Raymo, 2005) and Imbrie and Imbrie Ice model (Imbrie and Imbrie, 1980). **(A)** $\Delta\chi$ as function of stratigraphy. **(B)** Extract of the LR04 stack (last 430 ka). **(C)** Imbrie and Imbrie ice model (last 430 ka). **(D)** The age-tuned $\Delta\chi$ record based on the 15 tie-points, indicated by dashed lines (see **Table 1**).

associated elsewhere to an eruption originating from the Alban Hill Volcanic region and dated to 350–360 ka (Pouclet et al., 1999; Marković et al., 2015). A corresponding tephra layer can be found in the Fucino Basin record (TF-85), which is dated to 367 ± 1.6 ka (Marra et al., 2009, 2019; Giaccio et al., 2012) and thought to originate from the Colli Albani Villa Senni eruption (Marković et al., 2015). We tentatively use this age estimate for the tie-point represented by the Bag tephra at Zemun (**Table 1** and **Figure 9**).

Attempts to extrapolated ages for samples depths above and below the youngest and oldest tie-points lead to an age of 50 ka corresponding to MIS 3 interglacial, which is not contained in the Zemun LPS and therefore too young for the top of the profile. Based on magnetic susceptibility variations, the loess at the top of the profile was likely deposited during the early MIS 4 (∼60 ka). The uncertainty in age extrapolation at the base of the profile is highlighted by the gray shading in **Figure 9**.

DISCUSSION

Integrated Stratigraphy

The Zemun LPS comprises four interglacial paleosol complexes, S4 (Cambisol), S3 (forest-steppe soil), and S2 and S1, both considered as steppe soils (Marković et al., 2011; Obreht et al., 2016). Our correlative age model (**Figure 9**) suggests that the Zemun loess profile covers the time interval from MIS 11 to MIS 5/4, which is additionally constrained by the identification of two widespread tephra layers of known stratigraphic position within

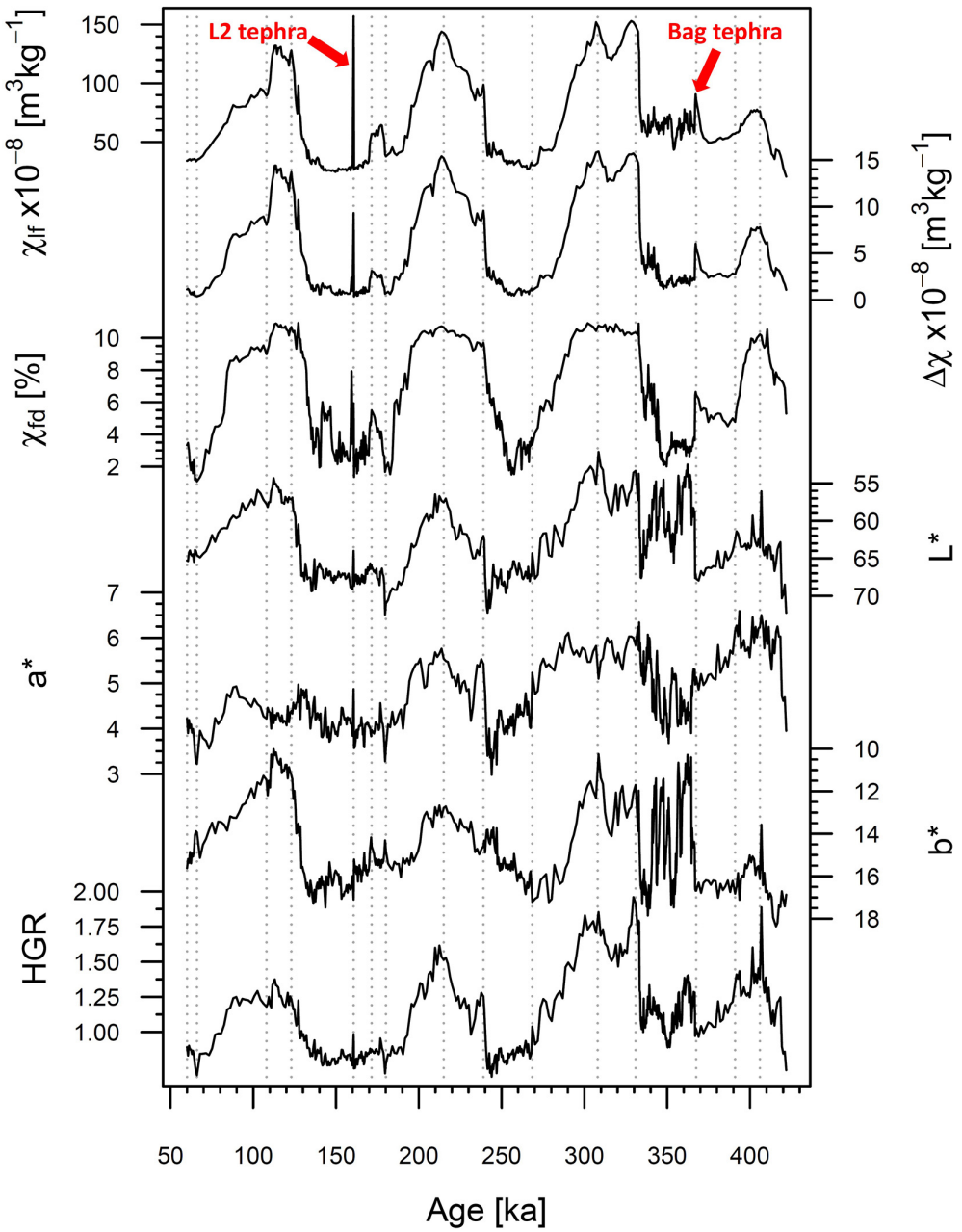

FIGURE 10 | Magnetic susceptibility parameters χ_{lf}, $\Delta\chi$, χ_{fd} [%], and the hematite/goethite ratio (HGR) as function of age. Note that the axes for L* and b* are inverted. The gray dotted lines indicate the tie-point-ages from **Table 1**.

other Danube loess sequences (Marković et al., 2015, 2018). However, the selected correlative tie-points (**Table 1**) include the tephra layers, but do not account for the colorimetric data. The general stratigraphy of loess and intercalated paleosols at the Zemun LPS is in good agreement with independently dated records in the southern MDB, based on luminescence dating and paleomagnetism (Marković et al., 2009, 2011, 2015; Basarin et al., 2014; Song et al., 2018; Avram et al., 2020). It is noteworthy, that uncertainties of the direct correlation of $\Delta\chi$ to the LR04 stack exist (Zeeden et al., 2018), mainly because of uncertainty in the exact position of tie points and correlation targets. The stacked LR04 record provides ages for the last 1 Ma with 4 kyr uncertainty (Lisiecki and Raymo, 2005).

The fluvial sediment facies (MFS unit) below S3 is widespread in the southern MDB and is interpreted as an intercalation of marshy floodplain sediments (MFS) consisting of an alternation of sandy iron-stained and sandy-silty beds with dark humus rich partly clayey beds (e.g., Marković-Marjanović, 1970; Gaudenyi et al., 2015). The MFS unit represents overbank deposits of a river system flowing through a steppe/forest steppe landscape laterally

interfingering with aeolian loess. They probably represent relatively short-term intervals of aquatic deposits formed after prominent flooding events. The loess unit L4 in which the MFS are intercalated measures ∼ 1.1 m at the neighboring section Batajnica (Marković et al., 2009) and is generally relatively thin in the entire MDB (Marković et al., 2015) and across Eurasia (Song et al., 2018).

Magnetic susceptibility parameters of the Zemun LPS convincingly track the environmental impact of interglacials and glacials during the Middle to Late Pleistocene (**Figure 9**). All four paleosols (S4–S1) are characterized by elevated values of χ_{lf}, $\Delta\chi$, and χ_{fd} indicative of higher concentration of magnetic minerals and specifically superparamagnetic particles formed *in-situ* during pedogenesis (Maher and Taylor, 1988). Based on χ_{lf}, $\Delta\chi$ and χ_{fd} parameters, the intensity of pedogenesis increases from S4 (MIS 11) to S1 (MIS 5), to S2 (MIS 7) to S3 (MIS 9).

Colorimetric parameters are used to quantify hematite and goethite (e.g., Scheinost, 1998). The assumption that the HGR reflects changes in goethite remains questionable. Studies from Liu et al. (2008) and Jiang et al. (2018) show that goethite does not play a crucial role for LPS and additionally the process of the neo-formation of goethite is different from processes related to pedogenesis. In contrary, Bilardello et al. (2020) demonstrate in their experimental simulations that a simultaneous neoformation of goethite, hematite and magnetite is possible, and they add further evidence that biogeochemical conditions are a key-controller of the proportions of the neo-formed minerals. Our good correlation of magnetic parameters (**Figure 8**) like the S-ratio and remanence of coercivity (indicating the presence of hard magnetic minerals) with 1st derivative intensity band values for goethite ($I_{435\ nm}$) indicate the presence of goethite. However, the good correlation of HGR with the pedogenesis indicators (χ_{ferri}/Ms and $\Delta\chi$) indicates an overall higher presence of hematite over goethite in the paleosols of the Zemun LPS. This said, the magnetic experiments conducted in the present study do not readily permit the identification of goethite, which is facilitated in low-temperature magnetic experiments (e.g., Lagroix and Guyodo, 2017). Following that, we consider for the Zemun LPS, that the HGR can reflect changes in goethite and/or hematite. Our quantitative colorimetric data show variations that are related to the different soil types. S3, the forest-steppe soil and the most mature paleosol based on magnetic susceptibility parameters and χ_{ferri}/M_s has the lowest luminance, which would result from high amounts of mineralized organic matter. With decreasing precipitation, the predominant soils are chernozems, which are represented by S1 and S2. Cambisols are brighter, which is reflected by S4 and its increased luminance (L^*).

Paleoclimatic Implications for the Zemun LPS

The stratigraphic interpretations of both rock magnetic and colorimetric data in combination with the correlative age model provide insights into the environmental evolution of the southern Middle Danube Basin for the last 430 kyr.

All susceptibility parameters (χ_{lf}, $\Delta\chi$, and χ_{fd} [%]) reflect large and quasi-cyclic fluctuations, generally recording changes between warm and humid (interglacial), and cool and dry (glacial) conditions (**Figure 10**). Remarkably, for MIS 9 (paleosol S3) to MIS 5 (paleosol S1) the susceptibility parameters show a similar range of amplitude, whereas in MIS 11 (paleosol S4) $\Delta\chi$ and χ_{lf} are only weakly expressed. For S4, however, the amplitudes of χ_{fd} [%] are comparable with S1–S3.

This would suggest that for S4 the intensity of pedogenesis was weaker compared to S3–S1, which is not supported by the general pedogenetic trend in the MDB and Western Eurasia (e.g., Marković et al., 2015, and references therein). Colorimetric data of redness (a^*), an indicator for weathering intensity (Yang and Ding, 2003), leads to the opposite conclusion. The a^* parameter is highest in S4 paleosol (**Table 4**) suggesting it has the highest intensity of pedogenesis, which is in line with the general paleoenvironmental evolution in the Eurasian loess belt (e.g., Buggle et al., 2013, 2014) and our pedologic interpretation. Both $I_{435\ nm}$ and $I_{565\ nm}$ 1st derivative intensities are highest in S4 (**Figure 8**) shows that both high coercivity goethite and hematite are important mineral components in S4. Both are magnetically weak, with mass specific magnetic susceptibilities 3–4 orders of magnitude less than magnetite and maghemite (Hunt et al., 1995). While the absolute concentration of SP particles in S4 is half that of S1 and one third of S3, χ_{fd} varies significantly less being 8.2% for S4, 8.9% for S1 and 9.8% for S3 (**Table 2**). The lower χ_{lf} and $\Delta\chi$ for S4 may simply result from the mineralogy of the neo-formed pedogenic iron mineral, paleoclimate and local biogeochemical conditions favored the formation of hematite and goethite or at least their preservation.

Progressively reduced precipitation and temperature characterize the general climatic trend over the last 430 kyr at Zemun when considering the colorimetric data, gradually leading to more arid climate conditions. A fundamental factor for reduced weathering intensity, indicated by decreasing a^* values, may be the general aridification as proposed by Marković et al. (2009) and Buggle et al. (2013) for the Middle and Lower Danube Basins. Buggle et al. (2013) proposed the progressive uplift of the Carpathians, Dinarides, and Eastern Alps during the Pleistocene as main cause of this of the aridification trend.

Since, at Zemun, magnetic susceptibility is dominated by ferrimagnetic minerals, maghemite and magnetite (**Figure 5B**), and colorimetric analyses by hematite, an integrative view of the results from both methods is needed and beneficial. Regarding the formation of magnetite in LPS, the preferred climatic conditions are seasonally alternating wet (reducing) and dry (oxidizing) conditions controlling pedogenetic processes subsequently leading to higher susceptibilities (Maher, 1998). Differences in relative amounts of maghemite and hematite are probably caused by distinct characteristics and seasonality of climatic periods (Maher, 2011). A climate characterized by warm and dry summers in combination with mild and humid winters leads to relatively higher amounts of hematite (Balsam et al., 2004; Liu et al., 2008; Jiang et al., 2018). The interpretation of our results are in good agreement with interpretations from other studies focusing on the Lower and Middle Danube Basin (Buggle et al., 2013, 2014). With regard to the paleosols, a decreasing HGR is associated with a lower seasonality of precipitation and/or a reduction of temperature (Balsam et al., 2004). Based on our

results, we assign HGR as an index for increased heat and dryness during estival periods. With respect to the susceptibility parameters, in interglacial periods the mean precipitation over the year cannot be that different. A similar trend from MIS 9 to MIS 5 is reported by Obreht et al. (2016) from the Stalać LPS, who interpret this as changing influence of different climate systems over western Eurasia.

Comparison of the Zemun LPS With Titel-Stari Slankamen and Luochuan

Thick loess-paleosols sequences are spread over the northern hemisphere, located in different geomorphological settings which are influenced by diverse prevailing climate regimes (see Schaetzl et al., 2018; Lehmkuhl et al., 2021). To detect similarities and differences in magnetic and colorimetric properties conserved in loess-paleosol sequences, we compare the Zemun LPS with two well-known reference profiles. The Titel-Stari Slankamen LPS (Serbia) covers the last million years and the interval from MIS 11 to present is archived in c. 38 m.

The Luochuan record from the CLP (Hao et al., 2012) covers approximately the last 1.1 million years and the interval MIS 11 to present in c. 30 m of loess/paleosol couplets. For comparison, the low-frequency magnetic susceptibility data (the only data set available for all three LPSs) are shown on an age scale (**Figure 11**). Generally, the Zemun LPS's long-term χ_{lf} variability reflecting interglacial/glacial alternations are in excellent agreement with Titel-Stari Slankamen and Luochuan, even though the latter is located in a monsoon prevailing climate. Indeed, it is well known that different prevailing climate regimes and primary sediment sources affect the χ_{lf} values (Maher, 2016; Schaetzl et al., 2018), which are nearly 60% higher in Luochuan than in the both Serbian LPSs. More than doubled $\Delta\chi$ values in Luochuan compared to Titel-Stari Slankamen (Song et al., 2018) and Zemun indicate that the neo-formation of magnetite/maghemite SP particles during pedogenesis was enhanced at Luochuan, potentially due to more moisture during interglacials. The S4 paleosol at Titel-Stari Slankamen and Zemun shows-compared to the S3 paleosol – less prominent values for χ_{lf} and $\Delta\chi$ (**Figure 11**). In all records, the S3 paleosol appears in the χ_{lf} data as a double peak. The timing of onset and demise of the corresponding interglacial MIS 9 (S3) is in better agreement between Zemun and Luochuan than between Zemun and Titel-Stari Slankamen. Variations in χ_{lf} for paleosol S2 (MIS 7) are similar for both Zemun and Titel-Stari Slankamen, but the χ_{lf} values are 2–3 times higher at Zemun. The S2 pedocomplex at Luochuan displays a clear three folded paleosol based on χ_{lf}. Song et al. (2018) correlated the two older paleosols of MIS 7 with the S2 and L2SS1 horizons at Titel-Stari Slankamen. However, comparing Zemun and Titel-Stari Slankamen, a correlation of the S2 pedocomplex with the older two paleosols of Luochuan and a further correlation of the Zemun L2SS1 with the youngest MIS 7 paleosol seems more plausible. Similar to Titel-Stari Slankamen, the S1 of Zemun shows two pedogenetic horizons, a lower strongly expressed paleosol, and a younger, weakly expressed paleosol. This feature is also observable in Titel-Stari Slankamen but differently expressed in Luochuan, where the pedogenic intensity remains fairly constant throughout the S1 pedocomplex. Age differences for the onsets and demises of the paleosols might result from the applied dating techniques. For Zemun, the correlative age model is based on fluctuation in $\Delta\chi$ and two tephra marker horizons. For Titel-Stari Slankamen, composite record ages were provided by tuning with aid of an astronomical target, correlating peaks in χ_{lf} with June perihelia (Basarin et al., 2014). Ages for the Luochuan LPS were determined by direct correlations of the fluctuations in χ_{lf} and isotopic data from deep-sea sediments (Ding et al., 2002a; Sun et al., 2006).

Tephra Layers as Widespread Marker Horizons Using Magnetic Proxies to Highlight the Presence of Tephra Layers in Loess

In tephrochronology (Lowe, 2011) ash layers of known age and origin can be used as reliable dating tools and correlation targets. This approach plays an increasingly important role in Quaternary stratigraphy (see Abbott et al., 2020 and references therein) as for example, the accuracy of luminescence numerical dating, the choice of method of dating the emplacement time of loess deposits is still impacted by many limiting factors such as large offsets between the different methods currently applied on the same sample (Avram et al., 2020), or even between different grain-size aliquots (e.g., Timar-Gabor et al., 2011; Veres et al., 2018). The most prominent tephra layer preserved in Eastern European loess and archeological deposits is the Campanian Ignimbrite/Y5 tephra (Veres et al., 2013; Giaccio et al., 2017). Dated to c. 40 ka BP, it provides an exceptional tie-point for linking records within MIS 3 and in testing the accuracy of luminescence and radiocarbon dating for loess records (Constantin et al., 2012; Fitzsimmons et al., 2013; Anechitei-Deacu et al., 2014; Obreht et al., 2016, 2017; Scheidt et al., 2021). However, several more tephra layers have been identified in south-eastern European loess profiles (see Marković et al., 2015, 2018) which, if well assessed, not only chronologically but also by their bulk sediment geochemical (see Pötter et al., 2021) and magnetic properties (this work) may serve as important anchor points for more secure lateral stratigraphic correlations (Zeeden et al., 2018). At present, glass shard geochemical data are not available for the two tephra layers identified at Zemun (and elsewhere in the wider region) because all attempts of geochemical fingerprinting have failed due to the strong weathering and alteration of the volcanic products.

Indeed, our integrated approach combining high-resolution FORC analysis and IRM unmixing provide magnetic evidence for the presence of volcanogenic material not only for the L2 tephra, but also for the Bag tephra (**Figures 6**, **7**). Both ZV 117 (L2 tephra) and ZP1 001 (Bag tephra) samples are characterized by a higher relative content of SD and PSD grains than the bracketing loess as well as a distinctive coercivity distribution not present in the bracketing loess. As most volcanic ashes identified in European loess units are mixed with loess or occur as cryptotephra, our approach may provide an excellent screening potential for assessing the tephrostratigraphic potential of loess records beyond the classical glass-shard geochemical analyses.

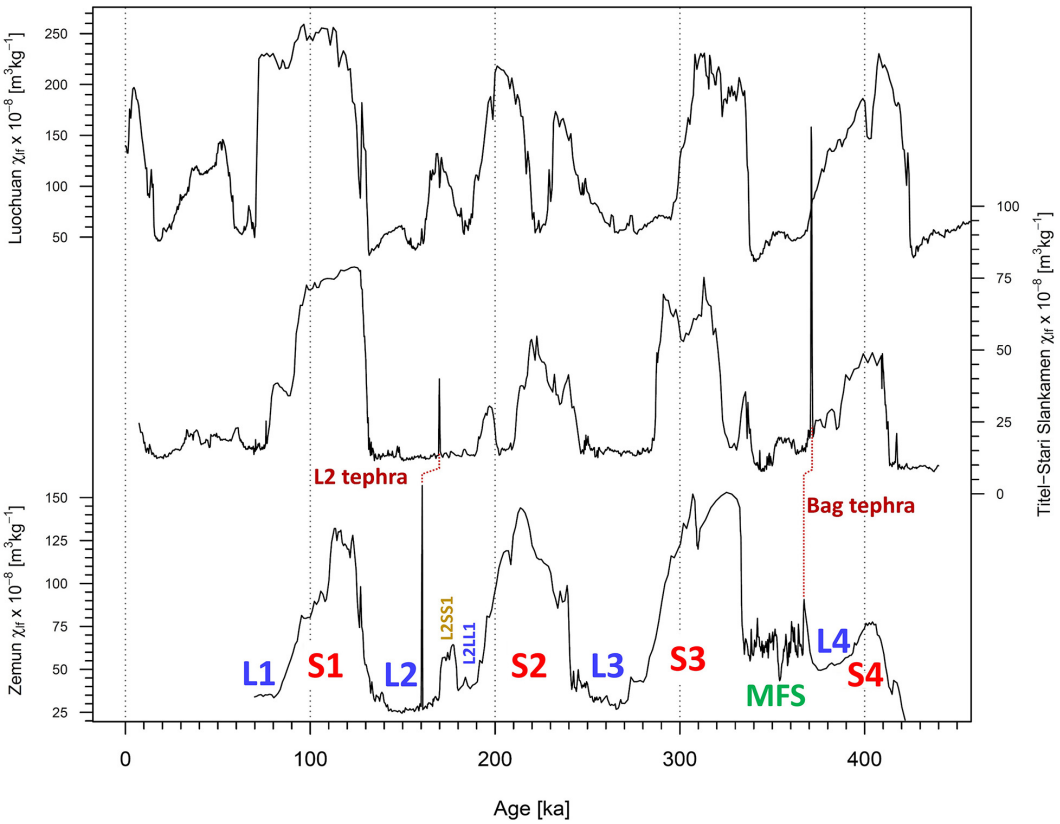

FIGURE 11 | Comparison of the χ_{lf} record from the LPS at Zemun, Titel-Stari Slankamen, and Luochuan on their individual age scales. Note the very similar chronostratigraphic depiction of the potential tephra layers at Zemun and Titel-Stari Slankamen. Differences in onsets and demises of different paleosol units may result from different age models and applied indirect (correlative) dating. Details are discussed in the text.

CONCLUSION AND SUMMARY

In this study, we present a new high-resolution loess-paleosol paleoclimate record from the Middle Danube Basin based on the application of environmental magnetic and colorimetric techniques for the last four-interglacial-to-glacial cycles spanning from MIS 11 to MIS 4. Data stemming from the S2 pedocomplex reveals different stages of environmental change during an interglacial, reflected by different coercivities, magnetic grain sizes, and different magnetic mineralogies. The combination of rock-magnetic and colorimetric data for the Zemun loess profile confirms the proposed aridification trend by Marković et al. (2009), Buggle et al. (2013), and Obreht et al. (2016). Furthermore, our HGR dataset indicates a general decreasing summer heat or dryness over the last 430 kyr in the Middle Danube Basin. Our study shows tracking only the soft ferrimagnetic (magnetite/maghemite) content may not provide a clear interpretation of changes in pedogenic intensity between interglacials, and that colorimetric data, providing insight into hematite and goethite content (high coercivity minerals) in addition are important for reconstructing summer conditions in addition to mean annual soil moisture. For loess samples stemming from the younger L3, L2, and L1 units, both hysteresis data and colorimetric data provide evidence for higher relative concentrations of high-coercivity magnetic minerals (like hematite and goethite) than in paleosols. The hematite/goethite ratio reflects a relatively higher amount of hematite compared to goethite in paleosol layers. Additionally, the investigation and comparison of FORC and highly resolved IRM acquisitions of potentially tephra bearing and pure loess samples provides further evidence of the deposition of volcanic ashes. Even when volcanic glass shards are too weathered for geochemical investigations, the remaining magnetic signal (increased PSD and SD particles in combination with reduced magnetic interactions) can be clearly identified and used as individual anchor points for future comparison and stratigraphy in the MDB and beyond.

DATA AVAILABILITY STATEMENT

The original contributions presented in the study are included in the article/**Supplementary Material**, further inquiries can be directed to the corresponding author/s.

AUTHOR CONTRIBUTIONS

CL, UH, and SM designed the study. CL measured all magnetic and parts of the colorimetric parameters, did the data analysis and interpretation with close advice from CZ, FL, YG, DV, and

UH, and programmed all analytical R-scripts for this study. MJ conducted the sampling. CL, UH, CZ, FL, DV, and YG wrote the manuscript with close advice from all co-authors. All authors contributed significantly to the article.

ACKNOWLEDGMENTS

We want to thank the Zemun sampling team. We want to thank Kathrin Worm (LIAG Grubenhagen) for the additional colorimetric measurements and Eva Meier (University of Bayreuth) for language improvements of this manuscript. DV was supported through a fellowship provided by Alexander von Humboldt Foundation. All data will be made available on the Pangaea Data Repository. This is IPGP contribution 4210.

SUPPLEMENTARY MATERIAL

The Supplementary Material for this article can be found online at: https://www.frontiersin.org/articles/10.3389/feart.2021.600086/full#supplementary-material

REFERENCES

Abbott, P. M., Jensen, B. J. L., Lowe, D. J., Suzuki, T., and Veres, D. (2020). Crossing new frontiers: extending tephrochronology as a global geoscientific research tool. *J. Quat. Sci.* 35, 1–8. doi: 10.1002/jqs.3184

Abe-Ouchi, A., Saito, F., Kawamura, K., Raymo, M. E., Okuno, J., Takahashi, K., et al. (2013). Insolation-driven 100,000-year glacial cycles and hysteresis of ice-sheet volume. *Nature* 500, 190–193. doi: 10.1038/nature12374

Anechitei-Deacu, V., Timar-Gabor, A., Fitzsimmons, K., Veres, D., and Hambach, U. (2014). Multi-method luminescence investigations on quartz grains of different sizes extracted from a loess section in Southeast Romania interbedding the Campanian Ignimbrite ash layer. *Geochronometria* 41, 1–14. doi: 10.2478/s13386-013-0143-4

Antoine, P., Lagroix, F., Jordanova, D., Jordanova, N., Lomax, J., Fuchs, M., et al. (2019). A remarkable Late Saalian (MIS 6) loess (dust) accumulation in the Lower Danube at Harletz (Bulgaria). *Quat. Sci. Rev.* 207, 80–100. doi: 10.1016/j.quascirev.2019.01.005

Avram, A., Constantin, D., Veres, D., Kelemen, S., Obreht, I., Hambach, U., et al. (2020). Testing polymineral post−IR IRSL and quartz SAR-OSL protocols on Middle to Late Pleistocene loess at Batajnica, Serbia. *Boreas* 49, 615–633. doi: 10.1111/bor.12442

Balsam, W., Ji, J., and Chen, J. (2004). Climatic interpretation of the Luochuan and Lingtai loess sections, China, based on changing iron oxide mineralogy and magnetic susceptibility. *Earth Planet. Sci. Lett.* 223, 335–348. doi: 10.1016/j.epsl.2004.04.023

Barranco, F. T., Balsam, W. L., and Deaton, B. C. (1989). Quantitative reassessment of brick red lutites: evidence from reflectance spectrophotometry. *Mar. Geol.* 89, 299–314. doi: 10.1016/0025-3227(89)90082-0

Basarin, B., Buggle, B., Hambach, U., Marković, S. B., Dhand, K. O., Kovačević, A., et al. (2014). Time-scale and astronomical forcing of Serbian loess–paleosol sequences. *Glob. Planet. Change* 122, 89–106. doi: 10.1016/j.gloplacha.2014.08.007

Bilardello, D., Banerjee, S. K., Volk, M. W. R., Soltis, J. A., and Penn, R. L. (2020). Simulation of natural iron oxide alteration in soil: conversion of synthetic ferrihydrite to hematite without artificial dopants, observed with magnetic methods. *Geochem. Geophys. Geosyst.* 21:e2020GC009037. doi: 10.1029/2020GC009037

Buggle, B., Hambach, U., Kehl, M., Markovic, S. B., Zoller, L., and Glaser, B. (2013). The progressive evolution of a continental climate in southeast-central European lowlands during the Middle Pleistocene recorded in loess paleosol sequences. *Geology* 41, 771–774. doi: 10.1130/G34198.1

Buggle, B., Hambach, U., Müller, K., Zöller, L., Marković, S. B., and Glaser, B. (2014). Iron mineralogical proxies and Quaternary climate change in SE-European loess–paleosol sequences. *CATENA* 117, 4–22. doi: 10.1016/j.catena.2013.06.012

Constantin, D., Timar-Gabor, A., Veres, D., Begy, R., and Cosma, C. (2012). SAR-OSL dating of different grain-sized quartz from a sedimentary section in southern Romania interbedding the Campanian Ignimbrite/Y5 ash layer. *Quat. Geochronol.* 10, 81–86. doi: 10.1016/j.quageo.2012.01.012

Day, R., Fuller, M., and Schmidt, V. A. (1977). Hysteresis properties of titanomagnetites: grain size and composition dependence. *Phys. Earth Planet. Interiors* 13, 260–267.

Dearing, J. A., Dann, R. J. L., Hay, K., Lees, J. A., Loveland, P. J., Maher, B. A., et al. (1996). Frequency-dependent susceptibility measurements of environmental materials. *Geophys. J. Int.* 124, 228–240. doi: 10.1111/j.1365-246X.1996.tb06366.x

Deaton, B. C., and Balsam, W. L. (1991). Visible spectroscopy; a rapid method for determining hematite and goethite concentration in geological materials. *J. Sediment. Res.* 61, 628–632. doi: 10.1306/D4267794-2B26-11D7-8648000102C1865D

Debret, M., Sebag, D., Desmet, M., Balsam, W., Copard, Y., Mourier, B., et al. (2011). Spectrocolorimetric interpretation of sedimentary dynamics: the new "Q7/4 diagram." *Earth Sci. Rev.* 109, 1–19. doi: 10.1016/j.earscirev.2011.07.002

Ding, Z., Rutter, N., and Liu, T. (1993). Pedostratigraphy of Chinese loess deposits and climatic cycles in the last 2.5 Myr. *CATENA* 20, 73–91. doi: 10.1016/0341-8162(93)90030-S

Ding, Z., Yu, Z., Rutter, N. W., and Liu, T. (1994). Towards an orbital time scale for chinese loess deposits. *Quat. Sci. Rev.* 13, 39–70. doi: 10.1016/0277-3791(94)90124-4

Ding, Z. L., Derbyshire, E., Yang, S. L., Yu, Z. W., Xiong, S. F., and Liu, T. S. (2002a). Stacked 2.6-Ma grain size record from the Chinese loess based on five sections and correlation with the deep-sea δ^{18}O record: STACKED QUATERNARY CLIMATE RECORD FROM CHINESE LOESS. *Paleoceanography* 17, 5–1. doi: 10.1029/2001PA000725

Ding, Z. L., Ranov, V., Yang, S. L., Finaev, A., Han, J. M., and Wang, G. A. (2002b). The loess record in southern Tajikistan and correlation with Chinese loess. *Earth Planet. Sci. Lett.* 200, 387–400. doi: 10.1016/S0012-821X(02)00637-4

Dunlop, D. J. (2002a). Theory and application of the Day plot (Mrs /Ms versus Hcr/Hc 1. Theoretical curves and tests using titanomagnetite data. *J. Geophys. Res.* 107:2056. doi: 10.1029/2001JB000486

Dunlop, D. J. (2002b). Theory and application of the Day plot (Mrs /Ms versus Hcr/ Hc 2. Application to data for rocks, sediments, and soils. *J. Geophys. Res.* 107:2057. doi: 10.1029/2001JB000487

Egli, R. (2013). VARIFORC: an optimized protocol for calculating non-regular first-order reversal curve (FORC) diagrams. *Glob. Planet. Change* 110, 302–320. doi: 10.1016/j.gloplacha.2013.08.003

Eyre, J. K. (1997). Frequency dependence of magnetic susceptibility for populations of single-domain grains. *Geophys. J. Int.* 129, 209–211. doi: 10.1111/j.1365-246X.1997.tb00951.x

Fitzsimmons, K. E., Hambach, U., Veres, D., and Iovita, R. (2013). The campanian ignimbrite eruption: new data on volcanic ash dispersal and its potential impact on human evolution. *PLoS One* 8:e65839. doi: 10.1371/journal.pone.0065839

Forster, T., Evans, M. E., and Heller, F. (1994). The frequency dependence of low field susceptibility in loess sediments. *Geophys. J. Int.* 118, 636–642. doi: 10.1111/j.1365-246X.1994.tb03990.x

Forster, T., Heller, F., Evans, M. E., and Havliėek, P. (1996). Loess in the Czech Republic: magnetic properties and paleoclimate. *Stud. Geophys. Geod.* 40, 243–261. doi: 10.1007/BF02300741

Gaudenyi, T., Nenadić, D., Stejić, P., Jovanović, M., and Bogićević, K. (2015). The stratigraphy of the Serbian Pleistocene Corbicula beds. *Quat. Int.* 357, 4–21. doi: 10.1016/j.quaint.2014.07.050

Gavrilović, B., Sümegi, P., Ćirić, M., Radaković, M. G., Gavrilov, M. B., Mlaqan,., et al. (2020). The middle and late pleniglacial (Weichselian) malacofauna of the Zemun loess-paleosol sequence, Serbia. *PalZ* 94, 519–531.

Giaccio, B., Galli, P., Messina, P., Peronace, E., Scardia, G., Sottili, G., et al. (2012). Fault and basin depocentre migration over the last 2 Ma in the L'Aquila 2009 earthquake region, central Italian Apennines. *Quat. Sci. Rev.* 56, 69–88. doi: 10.1016/j.quascirev.2012.08.016

Giaccio, B., Leicher, N., Mannella, G., Monaco, L., Regattieri, E., Wagner, B., et al. (2019). Extending the tephra and palaeoenvironmental record of the Central Mediterranean back to 430 ka: a new core from Fucino Basin, central Italy. *Quat. Sci. Rev.* 225:106003. doi: 10.1016/j.quascirev.2019.106003

Giaccio, B., Niespolo, E. M., Pereira, A., Nomade, S., Renne, P. R., Albert, P. G., et al. (2017). First integrated tephrochronological record for the last ∼190 kyr from the Fucino Quaternary lacustrine succession, central Italy. *Quat. Sci. Rev.* 158, 211–234. doi: 10.1016/j.quascirev.2017.01.004

Günster, N., Eck, P., Skowronek, A., and Zöller, L. (2001). Late Pleistocene loess and their paleosols in the Granada Basin, Southern Spain. *Quat. Int.* 7, 241–245. doi: 10.1016/S1040-6182(00)00106-3

Hambach, U., Veres, D., Constantin, D., Zeeden, C., Pötter, S., Baykal, Y., et al. (2019). "Interglacial, Holocene and recent dust accretion in the Danube Basin and beyond: evidence for uninterrupted dust accumulation in Eurasian dry steppe regions," in *International Workshop on Loess and Archeology: GEOARCHEOLOGICAL and Paleoenvironmental Research in European Loess-scapes: Abstract Book / Herausgeber: Prof. Dr. Frank Lehmkuhl*, ed. J. Bösken (Aachen: Lehrstuhl für Physische Geographie und Geoökologie), 25–27. doi: 10.18154/RWTH-2019-10413

Hao, Q., Wang, L., Oldfield, F., Peng, S., Qin, L., Song, Y., et al. (2012). Delayed build-up of Arctic ice sheets during 400,000-year minima in insolation variability. *Nature* 490, 393–396. doi: 10.1038/nature11493

Harrison, R. J., and Feinberg, J. M. (2008). FORCinel: an improved algorithm for calculating first-order reversal curve distributions using locally weighted regression smoothing: FORCINEL ALGORITHM. *Geochem. Geophys. Geosyst.* 9:Q05016. doi: 10.1029/2008GC001987

Heller, F., and Evans, M. E. (1995). Loess magnetism. *Rev. Geophys.* 33:211. doi: 10.1029/95RG00579

Heller, F., and Liu, T. (1982). Magnetostratigraphical dating of loess deposits in China. *Nature* 300, 431–433. doi: 10.1038/300431a0

Heller, F., and Liu, T. (1986). Palaeoclimatic and sedimentary history from magnetic susceptibility of loess in China. *Geophys. Res. Lett.* 13, 1169–1172. doi: 10.1029/GL013i011p01169

Heslop, D., Langereis, C. G., and Dekkers, M. J. (2000). A new astronomical timescale for the loess deposits of Northern China. *Earth Planet. Sci. Lett.* 184, 125–139. doi: 10.1016/S0012-821X(00)00324-1

Hu, P., Liu, Q., Torrent, J., Barrón, V., and Jin, C. (2013). Characterizing and quantifying iron oxides in Chinese loess/paleosols: implications for pedogenesis. *Earth Planet. Sci. Lett.* 369–370, 271–283. doi: 10.1016/j.epsl.2013.03.033

Hunt, C. P., Moskowitz, B. M., and Banerjee, S. K. (1995). "Magnetic properties of rocks and minerals," in *AGU Reference Shelf*, ed. T. J. Ahrens (Washington, DC: American Geophysical Union), 189–204. doi: 10.1029/RF003p0189

Imbrie, J., and Imbrie, J. Z. (1980). Modeling the climatic response to orbital variations. *Science* 207, 943–953. doi: 10.1126/science.207.4434.943

Ji, J., Balsam, W., Chen, J. U., and Liu, L. (2002). Rapid and quantitative measurement of hematite and goethite in the chinese loess-paleosol sequence by diffuse reflectance spectroscopy. *Clays Clay Minerals* 50, 208–216. doi: 10.1346/000986002760832801

Jiang, Z., Liu, Q., Roberts, A. P., Barrón, V., Torrent, J., and Zhang, Q. (2018). A new model for transformation of ferrihydrite to hematite in soils and sediments. *Geology* 46, 987–990. doi: 10.1130/G45386.1

Jordanova, D., Hus, J., and Geeraerts, R. (2007). Palaeoclimatic implications of the magnetic record from loess/palaeosol sequence Viatovo (NE Bulgaria): palaeoclimatic implications of the magnetic record. *Geophys. J. Int.* 171, 1036–1047. doi: 10.1111/j.1365-246X.2007.03576.x

Jordanova, D., and Jordanova, N. (2020). Diversity and peculiarities of soil formation in eolian landscapes – insights from the mineral magnetic records. *Earth Planet. Sci. Lett.* 531:115956. doi: 10.1016/j.epsl.2019.115956

King, J. W., and Channell, J. E. T. (1991). SEDIMENTARY MAGNETISM, ENVIRONMENTAL MAGNETISM, AND MAGNETOSTRATIGRAPHY. *Rev. Geophys.* 29, 358–370. doi: 10.1002/rog.1991.29.s1.358

Kohfeld, K., and Harrison, S. P. (2003). Glacial-interglacial changes in dust deposition on the Chinese Loess Plateau. *Quat. Sci. Rev.* 22, 1859–1878. doi: 10.1016/S0277-3791(03)00166-5

Kukla, G., and An, Z. (1989). Loess stratigraphy in Central China. *Palaeogeogr. Palaeoclimatol. Palaeoecol.* 72, 203–225. doi: 10.1016/0031-0182(89)90143-0

Laag, C., Hambach, U. F., Botezatu, A., Baykal, Y., Veres, D., Schönwetter, T., et al. (2018). "The geographical extent of the "L2-Tephra": a widespread marker horizon for the penultimate glacial (MIS 6) on the Balkan Peninsula," in *Abstract book, INQUA-INTAV International Field Conference and Workshop - Crossing New Frontiers - Tephra Hunt in Transylvania*, eds U. Hambach and D. Veres (Romania: INQUA-INTAV), 111–112. doi: 10.13140/RG.2.2.29686.96325

Lagroix, F., Banerjee, S. K., and Jackson, M. J. (2016). "Geological occurrences and relevance of iron oxides," in *Iron Oxides: From Nature to Applications*, ed. D. Faivre (Weinheim: Wiley-VCH), 9–29.

Lagroix, F., and Guyodo, Y. (2017). A new tool for separating the magnetic mineralogy of complex mineral assemblages from low temperature magnetic behavior. *Front. Earth Sci.* 5:61. doi: 10.3389/feart.2017.00061

Lehmkuhl, F., Nett, J. J., Pötter, S., Schulte, P., Sprafke, T., Jary, Z., et al. (2021). Loess landscapes of Europe – mapping, geomorphology, and zonal differentiation. *Earth Sci. Rev.* 215:103496. doi: 10.1016/j.earscirev.2020.103496

Leicher, N., Zanchetta, G., Sulpizio, R., Giaccio, B., Wagner, B., Nomade, S., et al. (2016). First tephrostratigraphic results of the DEEP site record from Lake Ohrid (Macedonia and Albania). *Biogeosciences* 13, 2151–2178. doi: 10.5194/bg-13-2151-2016

Lisiecki, L. E., and Raymo, M. E. (2005). A Pliocene-Pleistocene stack of 57 globally distributed benthic δ18O records. *Paleoceanography* 20:A1003. doi: 10.1029/2004PA001071

Liu, Q., Barrón, V., Torrent, J., Eeckhout, S. G., and Deng, C. (2008). Magnetism of intermediate hydromaghemite in the transformation of 2-line ferrihydrite into hematite and its paleoenvironmental implications. *J. Geophys. Res.* 113:B01103. doi: 10.1029/2007JB005207

Liu, Q., Zhang, C., Torrent, J., Barrón, V., Hu, P., Jiang, Z., et al. (2016). Factors controlling magnetism of reddish brown soil profiles from calcarenites in Southern Spain: dust input or in-situ pedogenesis? *Front. Earth Sci.* 4:51. doi: 10.3389/feart.2016.00051

Lowe, D. J. (2011). Tephrochronology and its application: a review. *Quat. Geochronol.* 6, 107–153.

Lowe, D. J., Pearce, N. J. G., Jorgensen, M. A., Kuehn, S. C., Tryon, C. A., and Hayward, C. L. (2017). Correlating tephras and cryptotephras using glass compositional analyses and numerical and statistical methods: review and evaluation. *Quat. Sci. Rev.* 175, 1–44. doi: 10.1016/j.quascirev.2017.08.003

Lukić, T., Basarin, B., Buggle, B., Marković, S. B., Tomović, V. M., Ralјič, J. P., et al. (2014). A joined rock magnetic and colorimetric perspective on the Late Pleistocene climate of Orlovat loess site (Northern Serbia). *Quat. Int.* 334–335, 179–188. doi: 10.1016/j.quaint.2014.03.042

Machalett, B., Frechen, M., Hambach, U., Oches, E. A., Zöller, L., and Marković, S. B. (2006). The loess sequence from Remisowka (northern boundary of the Tien Shan Mountains, Kazakhstan)—Part I: luminescence dating. *Quat. Int.* 15, 192–201. doi: 10.1016/j.quaint.2005.12.014

Maher, B. A. (1998). Magnetic properties of modern soils and Quaternary loessic paleosols: paleoclimatic implications. *Palaeogeogr. Palaeoclimatol. Palaeoecol.* 137, 25–54.

Maher, B. A. (2011). The magnetic properties of Quaternary aeolian dusts and sediments, and their palaeoclimatic significance. *Aeolian Res.* 3, 87–144. doi: 10.1016/j.aeolia.2011.01.005

Maher, B. A. (2016). Palaeoclimatic records of the loess/palaeosol sequences of the Chinese Loess Plateau. *Quat. Sci. Rev.* 154, 23–84. doi: 10.1016/j.quascirev.2016.08.004

Maher, B. A., and Taylor, R. M. (1988). Formation of ultrafine-grained magnetite in soils. *Nature* 336, 368–370.

Mannella, G., Giaccio, B., Zanchetta, G., Regattieri, E., Niespolo, E. M., Pereira, A., et al. (2019). Palaeoenvironmental and palaeohydrological variability of mountain areas in the central Mediterranean region: a 190 ka-long chronicle from the independently dated Fucino palaeolake record (central Italy). *Quat. Sci. Rev.* 210, 190–210. doi: 10.1016/j.quascirev.2019.02.032

Marković, S. B., Hambach, U., Catto, N., Jovanović, M., Buggle, B., Machalett, B., et al. (2009). Middle and Late Pleistocene loess sequences at Batajnica, Vojvodina, Serbia. *Quat. Int.* 198, 255–266. doi: 10.1016/j.quaint.2008.12.004

Marković, S. B., Hambach, U., Stevens, T., Kukla, G. J., Heller, F., McCoy, W. D., et al. (2011). The last million years recorded at the Stari Slankamen (Northern Serbia) loess-palaeosol sequence: revised chronostratigraphy and long-term environmental trends. *Quat. Sci. Rev.* 30, 1142–1154. doi: 10.1016/j.quascirev.2011.02.004

Marković, S. B., Stevens, T., Kukla, G. J., Hambach, U., Fitzsimmons, K. E., Gibbard, P., et al. (2015). Danube loess stratigraphy — towards a pan-European loess stratigraphic model. *Earth Sci. Rev.* 148, 228–258. doi: 10.1016/j.earscirev.2015.06.005

Marković, S. B., Stevens, T., Mason, J., Vandenberghe, J., Yang, S., Veres, D., et al. (2018). Loess correlations – between myth and reality. *Palaeogeogr. Palaeoclimatol. Palaeoecol.* 509, 4–23. doi: 10.1016/j.palaeo.2018.04.018

Marković-Marjanović, J. (1970). Data concerning the stratigraphy and the fauna of the lower and middle pleistocene of Yugoslavia. *Palaeogeogr. Palaeoclimatol. Palaeoecol.* 8, 153–163. doi: 10.1016/0031-0182(70)90008-8

Marra, F., Bahain, J.-J., Jicha, B. R., Nomade, S., Palladino, D. M., Pereira, A., et al. (2019). Reconstruction of the MIS 5.5, 5.3 and 5.1 coastal terraces in Latium (central Italy): a re-evaluation of the sea-level history in the Mediterranean Sea during the last interglacial. *Quat. Int.* 525, 54–77. doi: 10.1016/j.quaint.2019.09.001

Marra, F., Karner, D. B., Freda, C., Gaeta, M., and Renne, P. (2009). Large mafic eruptions at Alban Hills Volcanic District (Central Italy): chronostratigraphy, petrography and eruptive behavior. *J. Volcanol. Geothermal Res.* 179, 217–232. doi: 10.1016/j.jvolgeores.2008.11.009

Maxbauer, D. P., Feinberg, J. M., and Fox, D. L. (2016). MAX UnMix: a web application for unmixing magnetic coercivity distributions. *Comp. Geosci.* 95, 140–145. doi: 10.1016/j.cageo.2016.07.009

Meyers, S. R. (2014). *astrochron: An R Package for Astrochronology. Version 0.8*. Available online at: http://www.geology.wisc.edu/~{}smeyers (accessed June 17, 2020).

Mullins, C. E., and Tite, M. S. (1973). Magnetic viscosity, quadrature susceptibility, and frequency dependence of susceptibility in single-domain assemblies of magnetite and maghemite. *J. Geophys. Res.* 78, 804–809. doi: 10.1029/JB078i005p00804

Necula, C., Panaiotu, C., Heslop, D., and Dimofte, D. (2013). Climatic control of magnetic granulometry in the Mircea Vodă loess/paleosol sequence (Dobrogea, Romania). *Quat. Int.* 293, 5–14. doi: 10.1016/j.quaint.2012.03.043

Obreht, I., Hambach, U., Veres, D., Zeeden, C., Bösken, J., Stevens, T., et al. (2017). Shift of large-scale atmospheric systems over Europe during late MIS 3 and implications for Modern Human dispersal. *Sci. Rep.* 7:5848. doi: 10.1038/s41598-017-06285-x

Obreht, I., Zeeden, C., Hambach, U., Veres, D., Marković, S. B., Bösken, J., et al. (2016). Tracing the influence of Mediterranean climate on Southeastern Europe during the past 350,000 years. *Sci. Rep.* 6:36334. doi: 10.1038/srep36334

Obreht, I., Zeeden, C., Hambach, U., Veres, D., Marković, S. B., and Lehmkuhl, F. (2019). A critical reevaluation of palaeoclimate proxy records from loess in the Carpathian Basin. *Earth Sci. Rev.* 190, 498–520. doi: 10.1016/j.earscirev.2019.01.020

Peters, C., and Dekkers, M. J. (2003). Selected room temperature magnetic parameters as a function of mineralogy, concentration and grain size. *Phys. Chem. Earth Parts A/B/C* 28, 659–667. doi: 10.1016/S1474-7065(03)00120-7

Post, D. F., Bryant, R. B., Batchily, A. K., Huete, A. R., Levine, S. J., Mays, M. D., et al. (2015). "Correlations between field and laboratory measurements of soil color," in *SSSA Special Publications*, eds J. M. Bigham and E. J. Ciolkosz (Madison, WI: Soil Science Society of America), 35–49. doi: 10.2136/sssaspecpub31.c3

Pötter, S., Veres, D., Baykal, Y., Nett, J. J., Schulte, P., Hambach, U., et al. (2021). Disentangling sedimentary pathways for the Pleniglacial Lower Danube loess based on geochemical signatures. *Front. Earth Sci.* 9:600010.

Pouclet, A., Horvath, E., Gabris, G., and Juvigné, E. (1999). The Bag Tephra, a widespread tephrochronological marker in Middle Europe: chemical and mineralogical investigations. *Bull. Volcanol.* 61, 265–272. doi: 10.1007/s004450050275

R Core Team (2020). *R: A Language and Environment for Statistical Computing*. Vienna: R Foundation for Statistical Computing.

Šarić, J. (2008). Paleolithic and mesolithic finds from profile of the Zemun loess. *Starinar* 9–27. doi: 10.2298/STA0858009S

Schaetzl, R. J., Bettis, E. A., Crouvi, O., Fitzsimmons, K. E., Grimley, D. A., Hambach, U., et al. (2018). Approaches and challenges to the study of loess—introduction to the LoessFest Special Issue. *Quat. Res.* 89, 563–618. doi: 10.1017/qua.2018.15

Scheidt, S., Berg, S., Hambach, U., Klasen, N., Pötter, S., Stolz, A., et al. (2021). Chronological assessment of the balta alba kurgan loess-paleosol section (Romania) – a comparative study on different dating methods for a robust and precise age model. *Front. Earth Sci.* 8:598448. doi: 10.3389/feart.2020.598448

Scheinost, A. C. (1998). Use and limitations of second-derivative diffuse reflectance spectroscopy in the visible to near-infrared range to identify and quantify Fe oxide minerals in soils. *Clays Clay Minerals* 46, 528–536. doi: 10.1346/CCMN.1998.0460506

Song, Y., Guo, Z., Marković, S., Hambach, U., Deng, C., Chang, L., et al. (2018). Magnetic stratigraphy of the Danube loess: a composite Titel-Stari Slankamen loess section over the last one million years in Vojvodina, Serbia. *J. Asian Earth Sci.* 155, 68–80. doi: 10.1016/j.jseaes.2017.11.012

Sümegi, P., Gulyás, S., Molnár, D., Sümegi, B. P., Almond, P. C., Vandenberghe, J., et al. (2018). New chronology of the best developed loess/paleosol sequence ofHungary capturing the past 1.1 ma: implications for correlation andproposed pan-Eurasian stratigraphic schemes. *Quat. Sci. Rev.* 191, 144–166.

Sun, Y., Clemens, S. C., An, Z., and Yu, Z. (2006). Astronomical timescale and palaeoclimatic implication of stacked 3.6-Myr monsoon records from the Chinese Loess Plateau. *Quat. Sci. Rev.* 25, 33–48. doi: 10.1016/j.quascirev.2005.07.005

Sun, Y., He, L., Liang, L., and An, Z. (2011). Changing color of Chinese loess: geochemical constraint and paleoclimatic significance. *J. Asian Earth Sci.* 40, 1131–1138. doi: 10.1016/j.jseaes.2010.08.006

Taylor, S. N., and Lagroix, F. (2015). Magnetic anisotropy reveals the depositional and postdepositional history of a loess-paleosol sequence at Nussloch (Germany): AMS OF NUSSLOCH LOESS-PALEOSOL SEQUENCE. *J. Geophys. Res. Solid Earth* 120, 2859–2876. doi: 10.1002/2014JB011803

Taylor, S. N., Lagroix, F., Rousseau, D.-D., and Antoine, P. (2014). Mineral magnetic characterization of the Upper Pleniglacial Nussloch loess sequence (Germany): an insight into local environmental processes. *Geophys. J. Int.* 199, 1463–1480. doi: 10.1093/gji/ggu331

Till, J. L., Jackson, M. J., Rosenbaum, J. G., and Solheid, P. (2011). Magnetic properties in an ash flow tuff with continuous grain size variation: a natural reference for magnetic particle granulometry: SUPERPARAMAGNETIC GRAINS IN TUFF. *Geochem. Geophys. Geosyst.* 12:Q07Z26. doi: 10.1029/2011GC003648

Timar-Gabor, A., Ivascu, C., Vasiliniuc, S., Daraban, L., Ardelean, I., Cosma, C., et al. (2011). Thermoluminescence and optically stimulated luminescence properties of the 0.5P2O5–xBaO–(0.5-x)Li2O glass systems. *Appl. Radiation Isotopes* 69, 780–784. doi: 10.1016/j.apradiso.2011.01.015

Torrent, J., Liu, Q., Bloemendal, J., and Barrón, V. (2007). Magnetic Enhancement and Iron Oxides in the Upper Luochuan Loess-Paleosol Sequence, Chinese Loess Plateau. *Soil Sci. Soc. Am. J.* 71, 1570–1578. doi: 10.2136/sssaj2006.0328

Tsatskin, A., Heller, F., Hailwood, E. A., Gendler, T. S., Hus, J., Montgomery, P., et al. (1998). Pedosedimentary division, rock magnetism and chronology of the loess/palaeosol sequence at Roxolany (Ukraine). *Palaeogeogr. Palaeoclimatol. Palaeoecol.* 143, 111–133. doi: 10.1016/S0031-0182(98)00073-X

Veres, D., Lane, C. S., Timar-Gabor, A., Hambach, U., Constantin, D., Szakács, A., et al. (2013). The Campanian Ignimbrite/Y5 tephra layer – a regional stratigraphic marker for Isotope Stage 3 deposits in the Lower Danube region, Romania. *Quat. Int.* 293, 22–33. doi: 10.1016/j.quaint.2012.02.042

Veres, D., Tecsa, V., Gerasimenko, N., Zeeden, C., Hambach, U., and Timar-Gabor, A. (2018). Short-term soil formation events in last glacial east European loess, evidence from multi-method luminescence dating. *Quat. Sci. Rev.* 200, 34–51. doi: 10.1016/j.quascirev.2018.09.037

Wagner, B., Vogel, H., Francke, A., Friedrich, T., Donders, T., Lacey, J. H., et al. (2019). Mediterranean winter rainfall in phase with African monsoons during the past 1.36 million years. *Nature* 573, 256–260. doi: 10.1038/s41586-019-1529-0

WRB 2014/2015. *IUSS Working Group World Reference Base for Soil Resources 2014, Update 2015. International Soil Classification System for Naming Soils and Creating Legends for Soil Maps. World Soil Resources, Reports No. 106.* Rome: FAO.

Wu, Y., Qiu, S., Fu, S., Rao, Z., and Zhu, Z. (2018). Pleistocene climate change inferred from multi-proxy analyses of a loess-paleosol sequence in China. *J. Asian Earth Sci.* 154, 428–434. doi: 10.1016/j.jseaes.2017.10.007

Yang, S. L., and Ding, Z. L. (2003). Color reflectance of Chinese loess and its implications for climate gradient changes during the last two glacial−interglacial cycles. *Geophys. Res. Lett.* 30:GL018346. doi: 10.1029/2003GL018346

Zeeden, C., Hambach, U., Obreht, I., Hao, Q., Abels, H. A., Veres, D., et al. (2018). Patterns and timing of loess-paleosol transitions in Eurasia: constraints for paleoclimate studies. *Glob. Planet. Change* 162, 1–7. doi: 10.1016/j.gloplacha.2017.12.021

Zeeden, C., Kels, H., Hambach, U., Schulte, P., Protze, J., Eckmeier, E., et al. (2016). Three climatic cycles recorded in a loess-palaeosol sequence at Semlac (Romania) – implications for dust accumulation in south-eastern Europe. *Quat. Sci. Rev.* 154, 130–142. doi: 10.1016/j.quascirev.2016.11.002

Zeeden, C., Krauß, L., Kels, H., and Lehmkuhl, F. (2017). Digital image analysis of outcropping sediments: comparison to photospectrometric data from Quaternary loess deposits at Şanoviţa (Romania) and Achenheim (France). *Quat. Int.* 429, 100–107. doi: 10.1016/j.quaint.2016.02.047

Conflict of Interest: The authors declare that the research was conducted in the absence of any commercial or financial relationships that could be construed as a potential conflict of interest.

frontiers in Earth Science

ORIGINAL RESEARCH
published: 23 June 2021
doi: 10.3389/feart.2021.606588

Advanced Hyperspectral Analysis of Sediment Core Samples from the Chew Bahir Basin, Ethiopian Rift, in the Spectral Range from 0.25 to 17 µm: Support for Climate Proxy Interpretation

Gabriele E. Arnold[1,2]*, *Verena Foerster*[3], *Martin H. Trauth*[2], *Henry Lamb*[4,5], *Frank Schaebitz*[3], *Asfawossen Asrat*[6,7], *Claudia Szczech*[1,2] *and Christina Günter*[2]

[1]*Institute of Planetary Research, German Aerospace Center (DLR), Berlin, Germany,* [2]*Institute of Geosciences, University of Potsdam, Potsdam, Germany,* [3]*Institute of Geography Education, University of Cologne, Cologne, Germany,* [4]*Department of Geography and Earth Sciences, Aberystwyth University, Aberystwyth, United Kingdom,* [5]*Botany Department, Trinity College Dublin, Dublin, Ireland,* [6]*School of Earth Sciences, Addis Ababa University, Addis Ababa, Ethiopia,* [7]*Department of Mining and Geological Engineering, Botswana International University of Science and Technology, Palapye, Botswana*

OPEN ACCESS

Edited by:
Matthias Prange,
University of Bremen, Germany

Reviewed by:
Christopher Scholz,
Syracuse University, United States
Rik Tjallingii,
Helmholtz Centre Potsdam, Germany

***Correspondence:**
Gabriele E. Arnold
gabriele.arnold@dlr.de

Specialty section:
This article was submitted to Quaternary Science, Geomorphology and Paleoenvironment, a section of the journal Frontiers in Earth Science

Received: *15 September 2020*
Accepted: *07 June 2021*
Published: *23 June 2021*

Citation:
Arnold GE, Foerster V, Trauth MH, Lamb H, Schaebitz F, Asrat A, Szczech C and Günter C (2021) Advanced Hyperspectral Analysis of Sediment Core Samples from the Chew Bahir Basin, Ethiopian Rift, in the Spectral Range from 0.25 to 17 µm: Support for Climate Proxy Interpretation. Front. Earth Sci. 9:606588. doi: 10.3389/feart.2021.606588

Establishing robust environmental proxies at newly investigated terrestrial sedimentary archives is a challenge, because straightforward climate reconstructions can be hampered by the complex relationship between climate parameters and sediment composition, proxy preservation or (in)sufficient sample material. We present a minimally invasive hyperspectral bidirectional reflectance analysis on discrete samples in the wavelength range from 0.25 to 17 µm on 35 lacustrine sediment core samples from the Chew Bahir Basin, southern Ethiopia for climate proxy studies. We identified and used absorption bands at 2.2 µm (Al–OH), at 2.3 µm (Mg–OH), at 1.16 µm (analcime), and at 3.98 µm (calcite) for quantitative spectral analysis. The band depth ratios at 2.3/2.2 µm in the spectra correlate with variations in the potassium content of the sediment samples, which also reflect periods of increased Al-to-Mg substitution in clay minerals during drier climatic episodes. During these episodes of drier conditions, absorption bands diagnostic of the presence of analcime and calcite support this interpretation, with analcime indicating the driest conditions. These results could be compared to qualitative analysis of other characteristic spectral properties in the spectral range between 0.25 and 17 µm. The results of the hyperspectral measurements complement previous sedimentological and geochemical analyses, allowing us in particular to resolve more finely the processes of weathering in the catchment and low-temperature authigenic processes in the sediment. This enables us to better understand environmental changes in the habitat of early humans.

Keywords: Ethiopian Rift, Chew Bahir Basin, sediment cores, paloclimate, VIS/IR spectroscopy

INTRODUCTION

Reliable and precise climate indicators (proxies) are essential for reconstructing paleoenvironmental conditions from sedimentary archives. The development of robust climate proxies is a challenge due to the complex and often highly site-specific relationship between various potential indicators (such as, geochemical or physical composition, micro- or macro fossils that are typically found in terrestrial climate archives) and actual climate conditions of the past (Mann, 2002; Huntley, 2012; Chevalier and Chase, 2016; Wilke et al., 2016; Foerster et al., 2018). Paleoenvironmental studies are often hampered by constraints on sufficient sample material, discontinuous preservation of proxy carriers through the record, or missing contextualization of data sets. Efforts to link geochemical high-resolution X-ray fluorescence data (XRF) with mineralogical X-ray diffraction data (XRD) from lacustrine sediments of the Chew Bahir Basin, south Ethiopia, have shown that the establishment of new climate proxies necessitates a multi-dimensional understanding of processes in the catchment that control the ultimate composition of the sediments, including the relative impact of weathering and erosion, transport and deposition, and post-depositional processes (Foerster et al., 2018; Viehberg et al., 2018).

A profound understanding of the nature and amplitude of past hydroclimatic variations has become increasingly important to the growing debate on the role of climate in the evolution, cultural development and dispersal of *Homo sapiens* (e.g., Roberts and Stewart, 2018; Mounier and Lahr, 2019; Stewart et al., 2019). As a contribution toward an enhanced understanding of human-climate interactions, the Hominin Sites and Paleolakes Drilling Project (HSPDP) has cored five fluvio-lacustrine archives covering the last ~3.5 Ma of climate change in eastern Africa. All five sites in Ethiopia and Kenya are adjacent to key paleoanthropological research areas encompassing diverse milestones in human evolution, and times of dispersal and technological and cultural innovation (Cohen et al., 2016; Campisano et al., 2017; Owen et al., 2018, 2019; Potts et al., 2018). In late 2014, the Chew Bahir Drilling Project (CBDP), addressing one of the key HSPDP sites, recovered a ~293 m-long composite sediment core from Chew Bahir (CHB), a tectonically-bound basin (4°45′40.5″N, 36°46′1.0″E) in the southern Ethiopian Rift (**Figure 1**). The ~620 ka Chew Bahir record covers recent phases of hominin evolution, a time interval marked by intense climatic changes and including milestones, such as, the transition from the Acheulean to the Middle Stone Age and the emergence of archaic and modern *H. sapiens* in Africa, as well as the dispersal of this species (e.g., Stringer, 2016; Stringer and Galway-Witham, 2017; Roberts et al., submitted).

As part of the Chew Bahir Drilling Project, X-ray diffractometric investigations were carried out on a set of over 1,000 samples (Foerster et al., 2018). The results provided information through time on the sediment origin, potential transport mechanisms, post-depositional conditions and inferred precipitation distributions. Micro-X-ray fluorescence analyses (μXRF) showed that potassium content of the CHB sediment appears to be a reliable proxy for aridity (Foerster et al., 2012; Trauth et al., 2015, 2018, 2019; Viehberg et al., 2018). K-fixation in the sediment smectites was found to be enhanced by changes in octahedral occupancy of clay minerals. These results suggest that the most likely process linking climate with potassium concentrations is authigenic illitization of smectites during periods of higher alkalinity and salinity in the closed-basin lake of CHB, due to a drier climate (Foerster et al., 2018; Fischer et al., 2020).

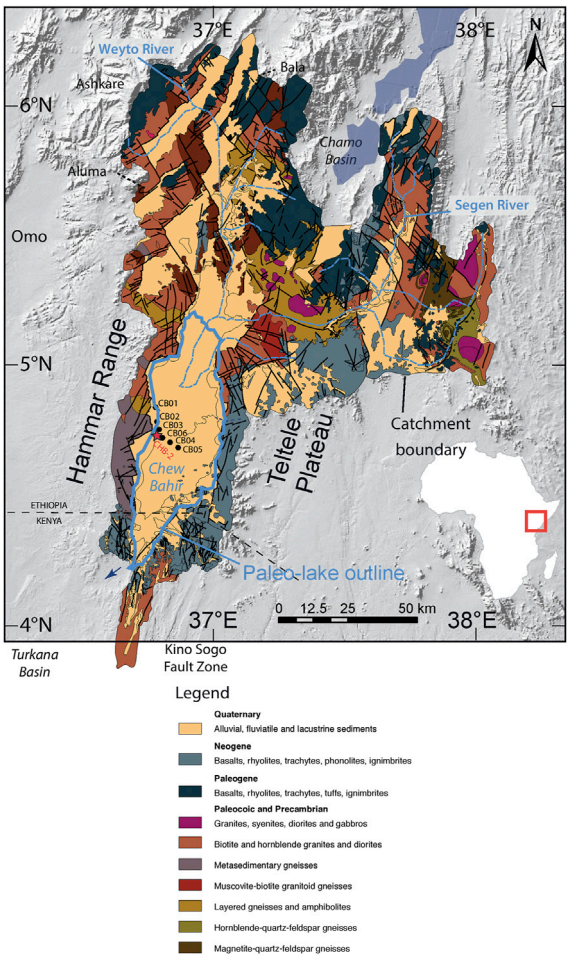

FIGURE 1 | Geologic map of the Chew Bahir Basin based on Omo River Project Map (Davidson, 1983), Geology of the Sabarei Area (Key, 1987), Geology of the Yabello Area (Hailemeskel and Fekadu, 2004), and Geology of the Agere Maryam Area (Hassen et al., 1997). The red star marks the location of CHB14-2 coring site.

Hydrochemical processes of authigenic clay alteration can readily be tracked by means of visible and infrared spectral investigation methods. This paper reports the results of a study that applied advanced hyperspectral analysis to support the non-destructive study of CHB sediment core samples. We examine the relationship between the derived mineralogical and geochemical properties of selected samples to test their linkage to the hydroclimate history of the CHB region. Visual and infrared reflectance spectroscopy (VIR) is a well-known and remote sensing evaluated method for composition analysis (e.g., Clark

et al., 1999). In sedimentology, methods for visual and near infrared (VNIR) spectral characterization in the range of 0.35–2.5 μm have been applied, e.g., by Grosjean et al. (2014), Butz et al. (2015, 2017) and Körting et al. (2015).

In contrast to these earlier analyses, a very wide spectral range of 0.2–17 μm was used for the CHB samples investigated. The wide wavelength coverage allows use of both the absorption bands of electronic solid state processes in the ultraviolet/visual (UV, VIS) spectral range, and the fundamental lattice vibration absorption bands in the mid infrared (MIR), as well as their overtone and combination tone vibration bands in the short wavelength infrared (SWIR). Synergy in the use of the overall complex of compositional and textural information resulting from these spectral surveys will ensure improved and unambiguous mineralogical analysis. Aspects of this method have already been partly tested in planetary remote sensing (e.g., Christensen et al., 2003; Bibring et al., 2006; Bishop et al., 2008) and are being extended here for the analysis of CHB samples. Our goal is to characterize wet and dry climate phases based on the spectral properties of the CHB samples and to compare them with the results of previous XRF and XRD analyses, and thus to contribute to improvements in climate proxy interpretation.

GEOGRAPHIC AND GEOLOGIC SETTING OF THE CHEW BAHIR BASIN

Study Site

Chew Bahir is a deep tectonically-bound basin (4.1–6.3°N; 36.5–38.1°E) in the southern Ethiopian Rift. It holds an extensive saline playa mudflat, but was repeatedly filled with paleolake Chew Bahir during pronounced pluvial phases (Foerster et al., 2012; Viehberg et al., 2018; Fischer et al., 2020) (**Figure 1**). The north-south trending rift basin is separated from the Turkana Basin to the west by the Hammar Range and bound to the east by the eastern Rift escarpment, the Teltele Plateau, part of the Teltele-Konso Range. The Hammar Range is underlain by Neo-Proterozoic basement rocks dominantly composed of granitic and mafic gneisses with minor occurrences of meta-sedimentary rocks. The basement rocks are partially covered by largely Oligocene to Quaternary volcanic rocks. The Teltele range on the other hand is predominantly composed of Miocene basaltic lava flows with subordinate rhyolite-trachyte and felsic tuff intercalations. The northeastern, northern and northwestern parts of the catchment comprise basalt flows with subordinate rhyolites, trachytes, tuffs and ignimbrites in most cases overlying the Precambrian basement (Davidson, 1983; Foerster et al., 2012, 2018).

Various feldspars and micas with different degrees of resistance to weathering, and volcanic glass in volcanic terrain have been characterized as precursors of the sediments in the Chew Bahir Basin. Metamorphic rocks of the Hammar Range are the most probable source of primary feldspars, such as, albite, anorthite and orthoclase (Pawar et al., 2008; Sak et al., 2010; Locsey et al., 2012; Foerster et al., 2012, 2018). They are also potential suppliers of potassium and the basis for the formation of smectite by aqueous weathering which in turn is the starting point for further alteration processes of the sediments. Therefore the deposits transported into the Chew Bahir Basin contain, among feldspars, mica and quartz, clay minerals (smectite, illite), zeolites (analcime) and carbonates (calcite) (Navarre-Stichler and Brantley, 2007; Vebel and Loisak, 2008; Navarre-Stichler et al., 2009; Sak et al., 2010; Ehlmann Mc et al., 2012; Foerster et al., 2012; Viehberg et al., 2018). Alternatively, the smectites could have resulted from weathering of basalts in the eastern and northeastern part of the CHB or silicate hydrolysis during wet climate conditions and diagenetic reactions (Renaut, 1993; Hay and Kyser, 2001; Foerster et al., 2018). Post-depositional processes have been shown to alter detrital deposits within the Chew Bahir Basin, mostly driven by the extreme hydrochemistry of the lake and paleolake. Saline and alkaline paleolake brines alter the octahedral composition of deposited minerals, while samples associated with wet phases reflect di-octahedral Al-rich phases. Mg-rich minerals dominate the spectra during arid intervals and an increase of trioctahedral phases has been observed (Foerster et al., 2018).

The 32,400 km^2 catchment is drained by the perennial rivers Segen and Weyto in the northeast and northwest, respectively (**Figure 1**). The endorheic Chew Bahir Basin is a terminal sink for detrital weathering products from the wider catchment and surrounding rift flanks. It was hydrologically connected to lakes Chamo and Abaya to the north via overflow from lake highstands during pluvial phases (Fischer et al., 2020). Paleolake Chew Bahir reached the overflow sill to Lake Turkana in the south during maximum lake-level high stands at ~45 m above the basin floor. The extensive alluvial fans along the escarpment, draining the Hammar Range to the west and the Teltele Plateau to the east, become seasonally and episodically reactivated after strong rainfall events, when they contribute coarser fluvial sediment flux into the basin (Foerster et al., 2012).

Silt-sized aeolian sediments are deposited mainly during predominantly drier conditions and are of more distal origin, mostly from the south of the catchment. Evidence of pyroclastic components in the Chew Bahir core is scarce, mainly due to intense alteration processes after deposition. The Konso Silver Tuff (154 ± 7 ka, Clark et al., 2003) as a tuffaceous marker (Silver Vitric Tuff, SVT) could be identified at ~75 mcd in the Chew Bahir core (Roberts et al., submitted). The at least ~2.5 km deep Chew Bahir Basin infill, representing predominantly Miocene to Quaternary fluvio-lacustrine sedimentary deposits, has been largely undisturbed by tectonic processes because rifting declined after the formation of the Chew Bahir rift (Pik et al., 2008). However, the sediments have been subject to intense post-sedimentary authigenic alteration processes that are indicative of paleohydrochemical variations of paleolake and porewaters (Foerster et al., 2018).

Modern Climate

The present-day climate in eastern and northeastern Africa is influenced by a number of major air streams and convergence zones, with their effects superimposed on regional influences associated with topography, large lakes, and the nearby oceans. Rainfall in the area is associated with the seasonal migration of the

tropical rain belt, resulting in bimodal rainy seasons in March-May and October-November (Nicholson, 2017, 2018). However, Chew Bahir is adjacent to regions of unimodal and trimodal rainfall distributions, which may have shifted in the course of long-term climate change (Nicholson, 2017, 2018). Inter-annual rainfall intensity also strongly depends on Atlantic and Indian Ocean sea-surface temperature (SST) variations caused by the Indian Ocean Dipole (IOD) and the El Niño-Southern Oscillation (ENSO) (Viste and Sorteberg, 2013).

MATERIAL, XRD AND XRF METHODS AND DATA

Coring, Sampling and Core Processing

From the western margin of the Chew Bahir Basin, duplicate cores CHB-2A and CHB-2B (hereafter in summary also referred to as CHB14-2) were retrieved, to 278.58 and 266.38 m below surface (mbs), respectively, with the parallel coring sites being ~20 m part (Cohen et al., 2016; **Figure 1**). The Chew Bahir long cores consist of more than 115 sections each, which all sum up to nearly 3 t of lacustrine sediment. All core sections were opened, lithologically described, processed, photographed, measured and sampled (~32 cm routine resolution) according to the HSPDP laboratory protocols at the U.S. National Lacustrine Core Facility (LacCore), the University of Minnesota. The two CHB14-2 cores 2A and 2B were subsequently spliced together on a common depth scale (meters composite depth = mcd). The merged CHB profile comprises 292.87 m in composite depth (mcd) and is with ~90% near continuous. (Cohen et al., 2016; Campisano et al., 2017; Roberts et al., submitted). The standard core analyses included Multi Sensor Core Logger (MSCL)-based color reflectance values from 360 to 740 nm in 10 nm steps, magnetic susceptibility, gamma-ray density and p-wave velocity, X-ray fluorescence (XRF) scanning and entailed a detailed multi-proxy campaign, including geochemical, biological, physical analyses on ~14,000 discrete samples.

X-ray Data

XRF Scanning Data

To determine the varying elemental composition of the CHB sediment profile, X-ray fluorescence (XRF) core scanning was performed at 5 mm resolution at the Large Lake Observatory (LLO) of the University of Minnesota following HSPDP protocols (Campisano et al., 2017). The Itrax core scanner (https://www.coxsys.se) was used with a chromium (Cr) tube as radiation source, a tube voltage of 30 kV, current of 30 mA and scanning time of 10 s. For normalization, and compensation of the aging of the Cr tube (Schlolaut et al., 2018), the element counts were divided by coherence scattering and multiplied by a correction factor (c.f.), that was determined for all XRF data by dividing the week's measurements by long-term average values of a set of SRM (Standard Reference Materials). Finally, all compositional data sets have been cleaned sub-cm wise by a quality flag system, avoiding coring artifacts, such as, cracks and voids (Trauth et al., 2020).

CHB Aridity Proxy: Potassium

The potassium (K) content of the sediment has been established as a reliable proxy for dry climate phases in the Chew Bahir Basin, corresponding to increased evaporation, reduced vegetation cover and a lower lake level (Foerster et al., 2012; Trauth et al., 2015, 2018, 2020; Fischer et al., 2020). **Figure 2** displays the variations in potassium (K) content of the composite CHB14-2 core (in normalized counts per second) plotted against age and core depth.

Increased influx of detrital K-rich weathering products may be associated with arid phases, when the extensive, sparsely-vegetated alluvial fans became activated during rare and short-lived strong rainfall events, transporting weathered feldspar and mica from the potassium-rich gneisses and granites of the adjacent Hammar Range into the basin (Foerster et al., 2012, 2015; Trauth et al., 2018). In addition, high K abundances in the Chew Bahir sediment cores are linked to an increase in alkalinity and salinity of the paleolake and porewater favoring so-called reverse weathering processes, such as, the low-temperature authigenic illitization of smectites. The hydrochemistry can be shown to control the degree of mineral alteration in the sedimentary deposits, and in the case of K-concentrations, Al-to-Mg substitutions lead to excess octahedral layer charge, which in turn further enhances K fixation in smectites (Foerster et al., 2018).

X-ray Diffraction

Mineral compositions of 1,040 discrete samples at 32 cm resolution along the composite core was determined applying X-ray diffraction (XRD). All samples were processed and analyzed at the University of Potsdam following the principles of Moore and Reynolds (1997) on an EMPYREAN X-ray diffractometer (PANalytical) using CuKα radiation. HighScore Plus version 4.0 (including the PDF reference data base) was used as analytical reference software for phase identification following the protocols developed for the Chew Bahir short cores (Foerster et al., 2018). Selected clay separates were further treated by air drying (N), ethylene glycol (EG) solvation and heating (H) at 550 °C for 1 h for phase identification. Analcime occurrences in the Chew Bahir sediment cores are markers for pronounced arid conditions with increased evaporation, pH and salinity (Renaut, 1993; Foerster et al., 2012, 2018; Viehberg et al., 2018). For smectites, variations in semi-quantitative abundances downcore were determined by a PCA that clustered similar diffraction patterns into clusters 0–10. To see tentative shifts in analcime occurrences downcore, the 112 analcime peak intensities (Bravais Miller index) of XRD patterns were used in counts and normalized by baseline correction.

Chronology

For age-depth control, a Bayesian stratigraphic age model was applied to independent directly dated chronometers including radiocarbon dating of ostracodes, OSL dating of quartz, $^{40}Ar/^{39}Ar$ dating of K-feldspar grains from tuffaceous zones, and geochemical correlation of the Konso Silver Tuff (Silver Vitric Tuff, SVT) to a visible tephra unit in the core (Brown and Fuller,

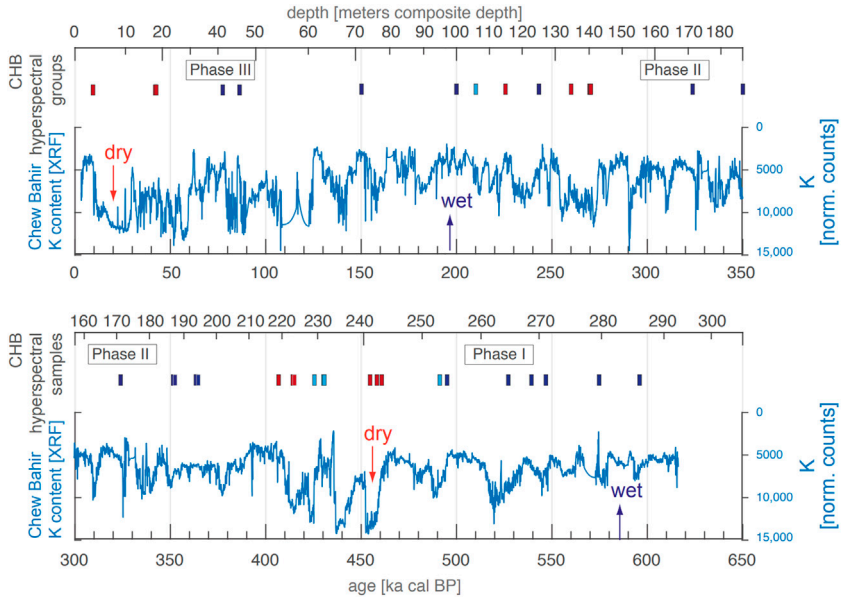

FIGURE 2 | Variation in the potassium (K) content of the composite CHB14-2 core from the Chew Bahir Basin (in normalized counts per second) (Trauth et al., 2020) plotted against age (Roberts et al., submitted) and core depth. The potassium content is an established aridity proxy for the CHB sediments (Foerster et al., 2018). The bars and the phases refer to the results of the hyperspectral analyses as discussed in "**Conclusion**" section (red: dry-climate sediment; light blue: wet-to-dry-transition-climate sediment; blue: wet-climate sediment).

2008; Clark et al., 2003; Brown et al., 2012; Roberts et al., submitted). With a basal age of ~617 ka BP, and a spatial resolution for XRF elemental proxies of 0.5 cm, the temporal resolution of the CHB14-2 K record averages ~10 years per data point (Trauth et al., 2020; Roberts et al., submitted)[1].

REFLECTANCE SPECTROSCOPY OF THE CHB CORE SAMPLES

Experimental Setup and Sample Preparation

The spectral measurements were carried out in DLR's Planetary Spectral Laboratory (Maturilli et al., 2018). PSL is a multi-country access facility that operates two identical Bruker Vertex 80V Fourier Transform Interferometers (FTIR) among other instruments. They allow measurements in the ultraviolet (UV), visible (VIS), near infrared (NIR) and mid infrared (MIR) spectral range. With a Bruker 513 accessory the bi-directional reflectance of samples with variable angles of incidence and emergence between 13° and 85° can be measured. The reflectance measurements are calibrated by comparison with spectroscopic measurements of well characterized standard references. These references are certificated standards of $BaSO_4$ for the UV range, spectralon for the VIS and NIR and a rough gold surface standard for the MIR spectral range. A GaP diode detector was used in the UV, a Si diode in the VIS and an MCT detector in the MIR part of the electromagnetic spectrum.

Thirty-five CHB samples from core CHB14-2, previously prepared for XRD and quantitative XRF analyses including fine-grain fractionation, were selected for spectral measurement (Foerster et al., 2018). All 35 samples have equal and homogeneous particle-size distributions. Sample selection was primarily based on covering the range of XRF-determined potassium content of the core, because K- content has been shown to be a proxy for hydroclimate (Davies et al., 2015; Foerster et al., 2018). In selecting the CHB14-2 samples, importance was attached to sampling different drilling depths and thus different chronological intervals (**Table 1**).

Spectral measurements were performed at atmospheric pressure between 0.25 and 17 µm, at room temperature, at 15° incident and emergence angles, and with a spectral resolution of ≥4 cm^{-1}. Standardized measurement procedures and data handling as well as a detailed error analyses for the entire measurement procedure at the PSL guarantee standardized and reliable measurement results, which make the obtained spectral data comparable with those of other international databases (Maturilli et al., 2018).

For spectral measurements, the samples were filled into aluminum sample cups according to a standardized procedure and placed in the Bruker 513 accessory for the measurement of the bi-directional reflectance. The filling of sample dishes ensures a constant packing texture by testing constant density for

[1]Roberts, H., Bronk Ramsey, C., Chapot, M., Deino, A., Lane, C., Vidal, C., et al. (2021). Using multiple chronometers to establish a long, directly-dated lacustrine record: constraining >600,000 years of environmental change at Chew Bahir, Ethiopia. Quater. Sci. Rev., Submitted.

TABLE 1 | Overview of all spectrally measured CHB14-2 samples with information on sample ID, core depth (midpoint) in meters composite depth (mcd), and potassium counts (normalized counts per 10 s) (Trauth et al., 2020) and interpolated sediment age in ka cal BP (Roberts et al., submitted).

No.	HSPDP No	Depth (mcd)	K (norm. Counts)	Age (ka cal BP)
1	HSPDP-CHB14-2B-2E-1	3,286	96,521	9.6
2	HSPDP-CHB14-2B-7H-1	18,971	64,855	43.5
3	HSPDP-CHB14-2B-7H-2	19,208	69,745	43.7
4	HSPDP-CHB14-2B-20H-1	41,979	31,075	78.2
5	HSPDP-CHB14-2B-22H-1	47,399	49,152	85.9
6	HSPDP-CHB14-2B-36E-1	71,246	33,767	151.5
7	HSPDP-CHB14-2A-48Q-2	99,524	54,893	199.4
8	HSPDP-CHB14-2B-58Q-2	106,194	82,058	211.0
9	HSPDP-CHB14-2B-61Q-2	115,230	42,795	226.7
10	HSPDP-CHB14-2B-64Q-2	124,220	54,465	242.3
11	HSPDP-CHB14-2B-68Q-2	134,506	90,396	260.2
12	HSPDP-CHB14-2B-70Q-1	139,637	109068	269.1
13	HSPDP-CHB14-2B-70Q-2	139,957	75,027	269.7
14	HSPDP-CHB14-2A-65Q-1	140,625	110765	270.9
15	HSPDP-CHB14-2A-75Q-2	170,966	62,388	323.6
16	HSPDP-CHB14-2A-80Q-2	187,205	69,610	351.8
17	HSPDP-CHB14-2B-86Q-1	187,693	63,456	352.7
18	HSPDP-CHB14-2A-82Q-1	193,132	60,818	362.1
19	HSPDP-CHB14-2A-82Q-2	193,775	59,540	363.2
20	HSPDP-CHB14-2B-96Q-1	219,133	48,049	407.3
21	HSPDP-CHB14-2A-93Q-2	223,374	101099	414.7
22	HSPDP-CHB14-2A-93Q-3	224,014	95,633	415.8
23	HSPDP-CHB14-2B-100Q-1	230,980	62,104	427.9
24	HSPDP-CHB14-2A-96Q-1	232,652	67,831	430.8
25	HSPDP-CHB14-2A-96Q-2	232,967	55,257	431.3
26	HSPDP-CHB14-2B-103Q-1	240,861	128597	453.7
27	HSPDP-CHB14-2A-99Q-3	242,462	85,497	458.7
28	HSPDP-CHB14-2A-99Q-3	243,102	64,241	460.6
29	HSPDP-CHB14-2B-107Q-1	252,746	82,888	490.4
30	HSPDP-CHB14-2B-107Q-2	254,028	48,760	494.4
31	HSPDP-CHB14-2B-110Q-3	265,201	82,769	528.8
32	HSPDP-CHB14-2A-108Q-2	268,633	66,275	539.4
33	HSPDP-CHB14-2A-109Q-3	271,624	59,976	548.7
34	HSPDP-CHB14-2A-112Q-1	279,670	69,719	574.4
35	HSPDP-CHB14-2A-115Q-2	286,218	70,780	596.4

comparison. After each sample measurement, the reference standard is measured under identical environmental conditions. The quotient of both radiances is the bi-directional reflectivity, which is subsequently referred to as reflectance (R). This quantity is in the UV to NIR spectral range directly comparable with measurement results of spectral remote sensing and in the MIR with $R = 1 - \varepsilon$, where ε is the directional emissivity.

Results: Spectral Features and Climate Indicators

Figure 3 shows three CHB14-2 spectra obtained for samples with variable potassium content and core depth. The upper part (A) shows the total reflectance spectra between 0.25 and 17 µm, while B and C (centre) enhance the spectral information in the wavelength ranges between 0.25–5 and 7–17 µm, respectively. In addition, spectra B and C are shown with an offset for better clarity. The UV–VIS spectral part of the spectra is dominated by weaker absorption bands due to different electronic processes (Burns, 1993). The overall strong slope from the UV to the VIS is due to an $Fe^{3+} \rightarrow O^{2-}$ charge transfer that results in a strong absorption band at around 0.27 µm. Superimposed on the long wavelength flank of this band absorption bands near 0.44 and 0.63 µm can appear that are caused by crystal field transitions. Absorption bands at about 1 µm can be caused by Fe^{2+} crystal field transitions (see spectrum 21). Features between 0.4 and 0.8 µm can be excited by Fe^{3+}, intervalence charge transfer transitions between Fe^{2+} and Fe^{3+} generate bands between 0.55 and 0.8 µm. These absorption bands provide useful information on transition metal ions in minerals.

In the range of wavelengths longer than 1 µm, overtones and combination tones of the mineral lattice vibration bands occur in the NIR. This wavelength range is particularly suitable for the investigation of hydrochemically weathered minerals and rocks. The molecules of the hydroxyl and the H_2O group embedded during aqueous weathering cause characteristic absorption bands near 1.4 and 1.9 µm, which are clearly visible in the CHB spectra. The strong band near 1.9 µm is a combination of the H–O–H bend and the asymmetric O–H stretch and thus indicative for molecular water. Absorption bands at 1.4 µm are caused by an O–H stretch in molecular water and structural OH. The simultaneous appearance of both absorption bands is a spectral indication of phyllosilicates with a three-layer

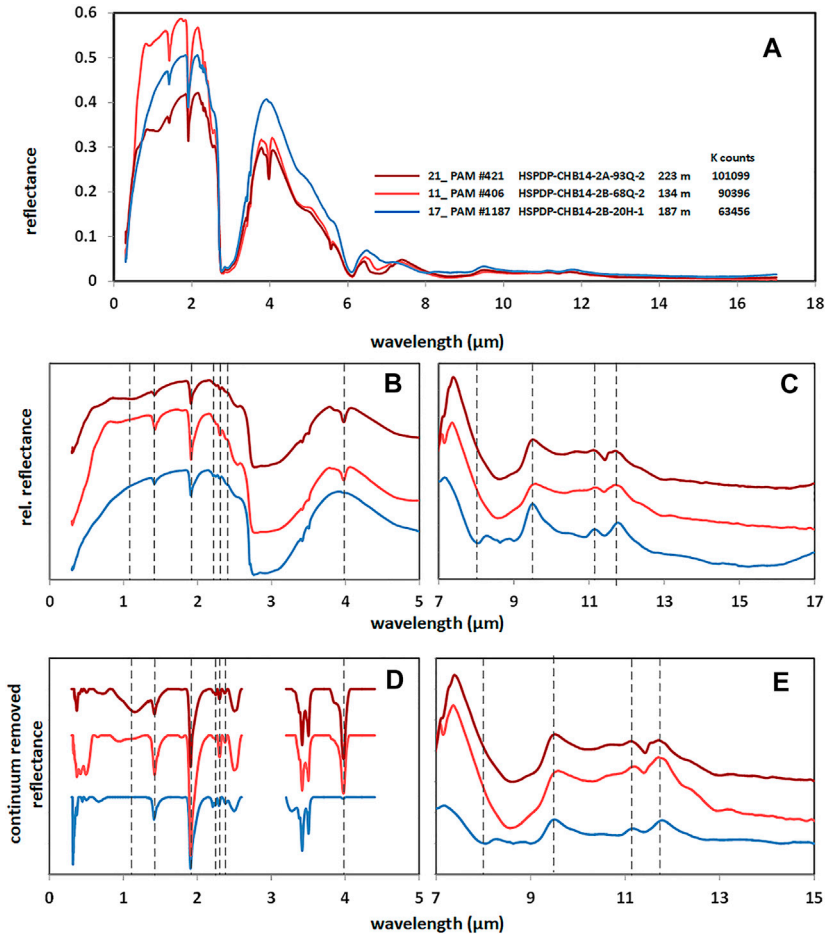

FIGURE 3 | (A) Typical reflectance spectra of three selected CHB14-2 drill core samples in the wavelength range from 0.3 to 7 µm. **(B, C)** Detailed view of the 0.3–5 µm and the 7–17 µm range. **(D, E)** Continuum removed spectra between 0.25 and 5 µm and between 7 and 17 µm. For reasons of clarity, the spectra are presented with an offset in reflectance (left and right offsets are different).

structure, such as, smectites. These clay minerals are dioctahedral smectites with, primarily Al, but also Mg and Fe ions in octahedral coordination with oxygen and hydroxyl in a sheet-like structure. These layers are loosely bond to each other with cations (e.g., Ca and Na) and variable amount of water in the interlayer (Grim, 1968; Singer, 1982).

Spectra of smectites are known to form weak absorption bands in the spectra between 2 and 2.5 µm. These absorption bands can be attributed to combination overtones of structural hydroxyl stretches with lattice modes. The exact wavelength position depends on the cation present. An Al–OH vibration results in an absorption band near 2.2 µm and is therefore typical for montmorillonite. Magnesium, on the other hand, causes a corresponding absorption band at 2.3 µm, as occurs for saponite (Gaffey et al., 1993). Al–Mg mixing stages and contributions of other metal ions can influence the variability of the band positions between 2 and 2.5 µm. The exact positions and spectra of the CHB sample within this range are shown in **Figure 5** in more detail. The X-ray examinations of the CHB samples suggest that during dry climate episodes, an illitization of the CHB smectites and an octahedral Al-to-Mg substitution takes place. The authigenic enrichment of Mg in clays has been observed in several other saline and alkaline lakes, such as, Paleolake Olduvai and is diagnostic for the intense clay mineral alteration under increasingly saline and alkaline conditions (Deocampo et al., 2009; Deocampo and Tactikos, 2010; Foerster et al., 2018). Therefore, especially the investigation of these absorption bands should provide valuable information about these processes.

Figure 4 shows spectra of possible CHB mineral endmembers in the 0.25–5 µm range (kaolinite, analcime, saponite, illite, Ca- and Na-montmorillonite). **Figure 4** can directly be compared to **Figure 3B**. The kaolinite belongs to the phyllosilicate type with two-layer structure. It primarily bonds OH not H_2O, which is shown in the spectra by an only weakly pronounced water absorption band at 1.9 µm. Analcime can be discriminated among the possible sediment candidates by an absorption band at 1.16 µm. Montmorillonites and saponite can be distinguished using the 2–2.5 µm band positions. While the montmorillonite spectra are characterized by an Al–OH band

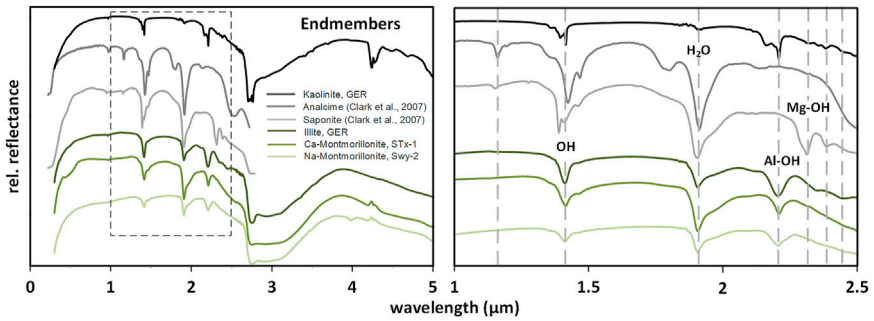

FIGURE 4 | Left–Relative reflectance spectra between 0.25 and 5 µm of possible mineral endmembers for comparison to CHB. Right—Detailed view of the spectral range between 1 and 2.5 µm with marking of characteristic absorption bands: 1.16 µm—analcime, 1.4 µm—OH, 1.9 µm—H_2O, 2.2 µm—Al–OH, 2.3 µm—Mg–OH and bands at 2.4 and 2.5 µm which can be assigned to illite. The positions of the absorption bands of the structural H_2O and OH as well as those of the Al–OH and Mg–OH absorption bands are marked in the plot.

near 2.2 µm in the absence of other absorption bands in this region, the saponite spectra show an Mg–OH absorption band at 2.3 µm and no absorption band near 2.2 µm. Illite spectra, on the other hand, show several absorption bands of variable band depth close to 2.2, 2.3, and 2.38 µm depending on the Al/Mg ratio.

With increasing wavelength (**Figure 3**) the first fundamental lattice vibration bands occur at about 2.7 µm and close to 6 µm, which can be assigned to the OH complex and the bond water. These bands are strong and nearly saturated. They are also significantly overlaid by adsorbed water bands, which are not indicative of the crystal structure of the CHB sediments (**Figure 3**). The long-wave flank of the 2.7 µm absorption band is superimposed by low-contrast bands in the 3.4 µm range. These absorption bands are associated with organic components. Of particular interest is an absorption band in the vicinity of 4 µm. It is clearly visible in the CHB spectra that are also marked by high potassium values (see **Figures 3A,B**). This feature can be attributed to calcite (Clark et al., 1999; Arnold et al., 2020). This absorption band thus also proves to be an important spectral paleoclimate indicator, as it can be a measure of evaporative concentration of the lake water during dry periods.

In the MIR the fundamental vibration bands of silicates and other minerals occur in the reflectance spectra. Low-contrast double structure occurs in the CHB spectra around 11 µm together with an absorption band at ~9.5 µm (see **Figure 3C**). This behavior is consistent with smectites, predominately montmorillonites. The depth of the MIR absorption bands is reduced due to the fine particle size structure of the samples (Arnold 1991). The double structured band around 11 µm is a result of an Al–Fe–OH vibration (~11.1 µm) and an Al–Mg–OH vibration (~11.7 µm). The band at ~9.5 µm is from a Si–O stretching and bending vibration. Weaker absorption bands, which are hardly discernible in the spectra of **Figure 3C** (sample spectrum 17, blue color), occur at ~8.25 and ~12.35 µm. The 8.25 µm band is due to SiO_2 and the 12.35 µm absorption band is produced by an Mg–Fe–OH vibration (Farmer and Russel, 1964; Bishop et al., 1994, 2008). In addition, a local reflectance minimum appears at ~8 µm in the spectrum of sample 17 (**Figure 3C**, blue color). This is the Christiansen Feature (CF) (Salisbury, 1993), which is a result of the optical properties of the mineral grains and their environment (air). At the specific wavelength of the CF the optical properties of the mineral and the medium surrounding it are very similar. This results in a reflectance minimum, which is diagnostic for the mineral as well. However, CF can only be used for spectra of CHB samples with low calcite concentration. As **Figure 3C** demonstrates, the presence of calcite masks the spectral properties of spectra 11 and 21 (red color) in the 8 µm spectral range.

Overall, the simultaneous use of the spectral indicators in the wavelength ranges from the UV to the MIR allows a comprehensive evaluation of the aqueous weathering processes of the CHB sediments. For further discussion and quantitative data evaluation, the use of the defined spectral indicators next requires a continuum correction of the spectra. The spectral continuum is defined as a series of linear progressions and then the continuum-correlated reflectance spectrum is calculated. This common method ensures the exact determination of the wavelength positions of absorption bands and allows the calculation of band depths. Since all 35 CHB samples have the same particle size distribution, particle size effects due to grain size variations need not be considered. **Figures 3D,E** show the results of the continuum correction for CHB samples 11, 17, and 21. The continuum-corrected reflectance spectra form the basis for further data handling.

DISCUSSION: SPECTRAL PROPERTIES OF CLIMATE PROXIES

Hyperspectral Properties

We used the spectral properties of climate-relevant indicators near 1.16, 2.2, 2.3, 2.4, and 3.98 µm to quantify climate-related dependencies and to analyze cross-correlations with the X-ray data. Other spectral indicators mentioned above are discussed as qualitative indicators.

The CHB14-2 sample reflectance spectra show that the sediment core samples are mainly composed of smectites, with

a dominance of montmorillonites. In addition, calcite is present in samples with high potassium content (see **Figure 3A**, red spectra). At low K content of the samples, pronounced Al-OH absorption bands near 2.2 μm appear in the reflectance spectra while the calcite band near 3.98 μm does not occur or is only weakly pronounced (see **Figure 3A**, blue spectrum). In contrast, spectra of samples with high calcium content show absorption bands near 2.3 and 2.38 μm due to an Mg–OH stretch while the 2.2 μm absorption band either disappears completely or is only weakly pronounced. Simultaneously, strong calcite absorption bands at 3.98 μm are observed to be correlating with high K values. At the highest potassium contents, an additional absorption band at 1.16 μm appears in the spectra, which indicates the presence of analcime. Furthermore, there are differences in the characteristics of absorption bands in the UV–NIR range, of organic constituents that occur on the long-wave flank of the 2.7 μm band and some variations of the strength of MIR absorption bands. In the UV–NIR spectral range, differences in mean reflectance must also be considered. These differences can be caused by materials that can act as gray body reflectors without producing selective absorption bands (dark agents). Such dark materials can reduce the spectral contrasts of the other absorption bands, an effect that is stringently considered in quantitative data evaluation of the 2.2 and 2.3 μm bands by the use of spectral ratios.

Figure 5 displays continuum removed reflectance spectra of the 35 CHB14-2 samples in the spectral ranges between 1 and 1.25 μm (left), 2.15 and 2.45 μm (middle) and between 3.7 and 4.3 μm (right). The spectra are shown with a vertical offset to illustrate the evolution of the sediment composition over time (samples down-core). The left diagram of **Figure 5** displays the variation of the 1.16 μm absorption band characteristic for analcime. The middle diagram shows three groups of spectra. Spectra in dark blue color have clearly visible and dominant Al–OH absorption bands near 2.2 μm with larger band contrasts, and moderately pronounced bands at 2.3 and 2.38 μm. In the light blue spectra (group 2) the absorption bands are weaker near 2.2 μm. In the third group (red spectra 1–3, 11–14, 21, 22, and 26–28), contrasts of the absorption band near 2.2 μm are either very small or the band disappears completely. On the other hand, the Mg-OH absorption band near 2.3 μm is clearly visible and can completely dominate the red spectra in individual cases. These spectra in red correspond to those samples for which higher potassium contents were determined from the XRF measurements whereas the spectra in blue belong to samples with lower potassium content. Spectra of samples with high potassium content (red) have distinct calcite absorption bands at 3.98 μm (**Figure 5**, right, red spectra). The appearance of absorption bands at 1.16 μm, near 2.2 and 2.3 μm and at 3.98 μm correlates with the trend potassium contents and can be used to evaluate the degree of mineral alteration in the course of varying pore water alkalinity and salinity. Consistently, this means that during humid climate episodes the formation of aluminum-rich montmorillonites is favored. In dry climate periods, however, aluminum is replaced by magnesium resulting in an enhanced K-fixation and formation of a trioctahedral phase under alkaline and saline conditions (Foerster et al., 2018). This is consistent with authigenic illitization and at the same time a higher alkalinity and salinity in the closed lake of CHB, due to the drier climate, which can be associated with the calcite enrichment of the high potassium samples.

In this argument, it is possible to divide the spectra into groups that can be assigned to (a) dry-climate sediments, (b) wet-to-dry-transition-climate sediments, and (c) wet-climate sediments. This is done in **Figure 5** by assigning a color: (a)—red spectra, (b)—light blue spectra and (c)—blue spectra. Only the spectra of samples 27 and 28 show a deviation from the general trend in the range around 3.98 μm (**Figure 5**, right), which is manifested by the fact that despite the absence of the 2.2 μm band and a clear band at 2.3 μm, no or only a weakly contrasted calcite band occurs. These spectra are shown in black on the right side of **Figure 5**. This could possibly be related to the fact that during the corresponding short dry period between the longer humid climate episodes an Al-to-Mg substitution was initiated, but the period was too short to deposit significant amounts of calcite for spectral detection. With these results a general picture of the temporal sequence of weathering within the alternating humid and dry climate phases in the CHB Basin is obtained.

Relation of Indicative Band Depths to X-ray Values

Figure 6 shows a comparison of XRF and XRD results for the selected 35 samples in this study with indicative band depths near 2.2 and 2.3 μm caused by Al and/or Mg inclusions in the minerals of the CHB14-2 samples vs. their core depth. The first column (A) in **Figure 6** shows the elemental variations in between samples for Al (scanning XRF data in normalized counts per second). The second column (B) indicates the variations in smectite abundances, determined in groups 0–10 according to diagnostic variations in diffractograms (XRD results). The third, middle column (C) displays the variation in the potassium (K) content among CHB14-2 samples, each displayed data point representing an average of 5 data points, determined by X-ray fluorescence (XRF) core scanning in 5 mm resolution in normalized counts per second (cps). Each discrete sample equals a 2 cm increment. A clear inverse relationship between K-values and smectite abundances (reflecting illitization at the expense of smectites) is apparent. The aluminum content of the samples follows this trend showing that primarily montmorillonites dominate the mineral spectrum during wet phases as products of aqueous weathering. Smectites in CHB are weathering products and poor in potassium. Inverse correlation of K contents and smectite abundances supports the hypothesis that K concentration is largely controlled by the K-fixation in smectites altering them into low-temperature authigenic illite. Thus, high potassium contents correlate with dry climate periods whereas wet episodes are characterized by lower potassium values. Under dry climatic conditions and with increasing evaporation, octahedral Al-to-Mg substitution in the phyllosilicates leads to an increase in the layer charge, which facilitates potassium fixation (Deocampo et al., 2009; Foerster

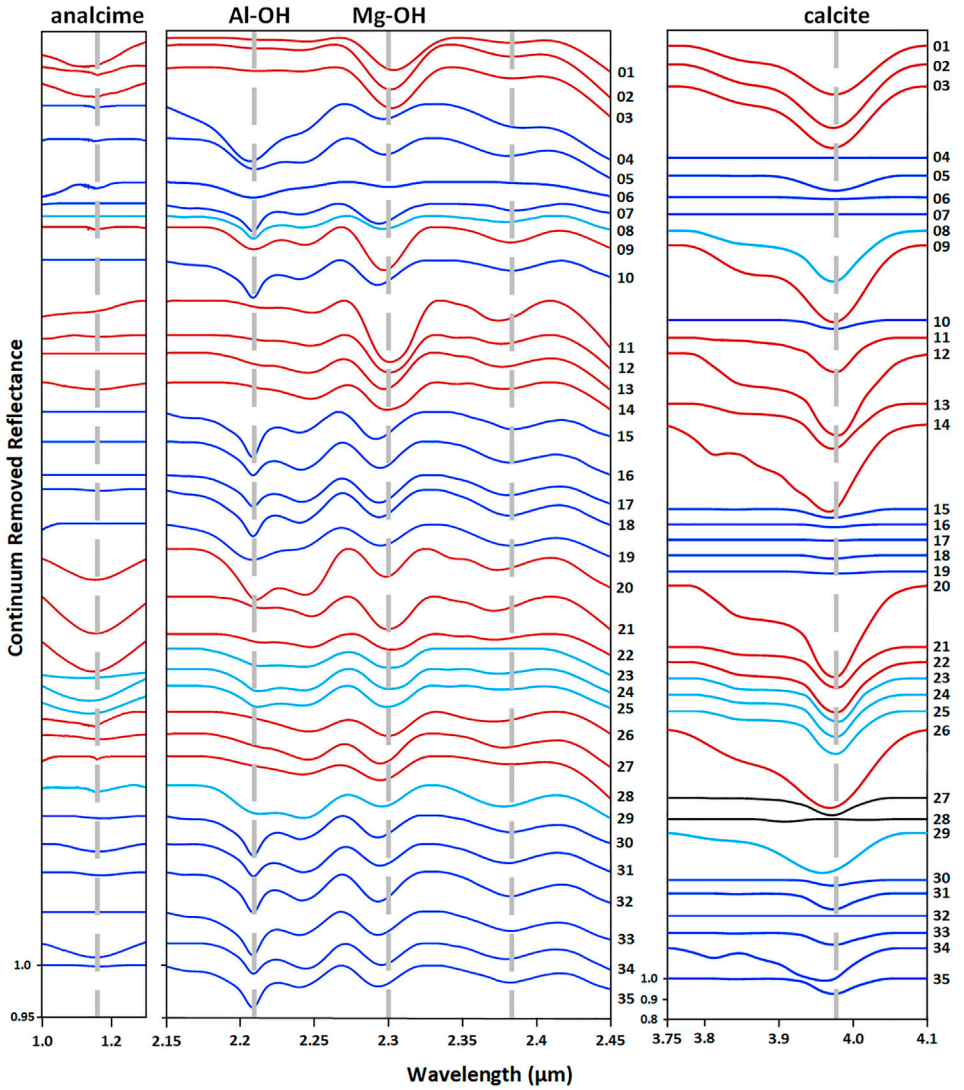

FIGURE 5 | Continuum removed reflectance spectra of all 35 CHB14-2 samples. Left—Spectral range between 1.0 and 1.25 µm (analcime). Middle—2.15 and 2.45 µm. Right—Spectral range from 3.7 to 4.3 µm (calcite). All spectra are offset relative to the spectrum of sample 35. For information on sample depth and age see **Table 1**.

et al., 2018). Therefore, the potassium content is a direct indicator for paleohydrological conditions in the Chew Bahir Basin.

The following three columns D–F in **Figure 6** show the ratios of the band depths at 2.2 and 2.3 µm divided by those at 1.4 µm and the ratio of the two band depths at 2.3 µm against 2.2 µm from left to right. The use of ratios for the comparison takes into account the possible influence of variable dark agents of the different samples. In addition, rationing to 1.4 µm enables to control significant variation of molecular water and structural OH by comparing the single sample spectra with each other. The colored crossbars in the three right-hand columns are based on the results of the discussion in **Figure 5**. Red crossbars correspond to dry-climate sediments, light blue to wet-to-dry-transition-climate sediments and blue ones to wet-climate sediments.

The analysis of the spectral indicators (absorption bands near 2.2 and at 2.3 µm) shown in the right part of **Figure 6** are in full agreement with these previous X-ray measurement results. Column D with the depth of the 2.2 µm band, which is generated by an Al–OH stretch, shows higher values mainly for wet-climate samples. Thus, higher aluminum contents correspond to lower absorption bands at 2.2 µm. The diagram in column D is therefore highly correlated with the smectite XRD results and anticorrelated with the XFR potassium values. The opposite is the case for the vibration band caused by Mg–OH at 2.4 µm, whose depth is presented in column E. Column E in **Figure 6** confirms that during dry climate phases more Mg is incorporated and the 2.3 µm absorption band increases in depth. The comparison of diagrams 4 and 5 clearly demonstrates that the incorporation of Mg takes place by substitution of Al.

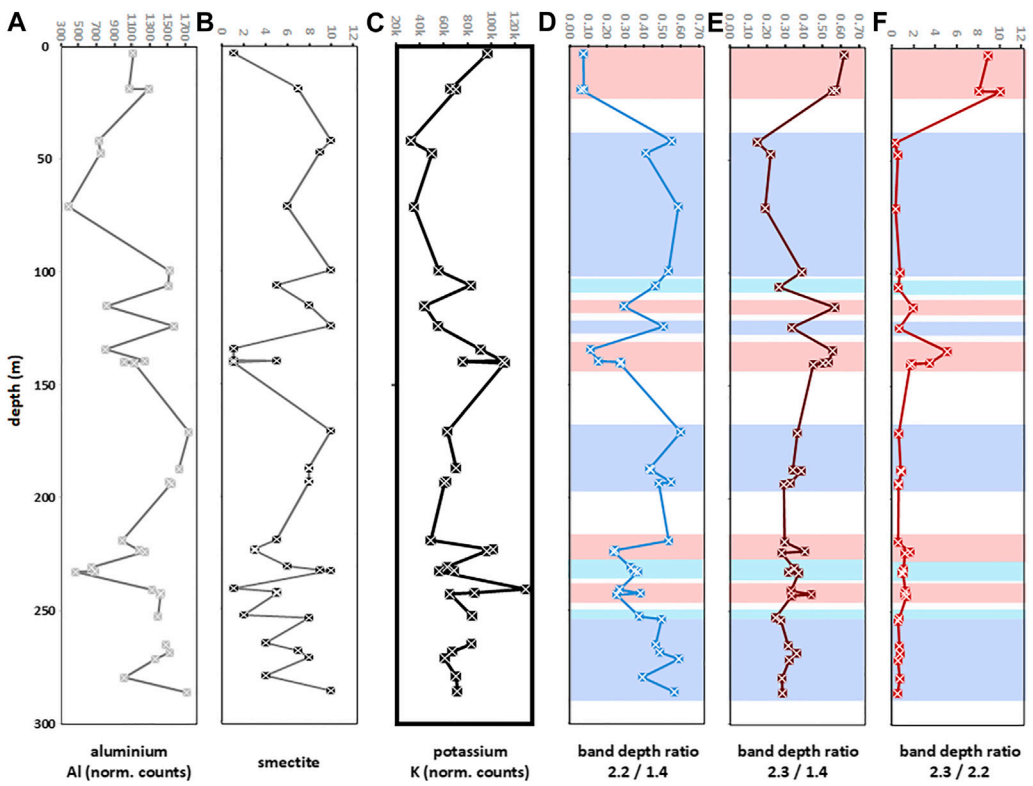

FIGURE 6 | Comparison of absorption band ratios at 2.2/1.4, 2.3/1.4 and 2.3/2.2 (hyperspectral analysis) **(D–F)** for the CHB14-2 samples with elemental variations (XRF, **A, C**) and semi quantitative phase abundances (XRD, **B**) of analyzed samples downcore. **(A)** Aluminum, **(B)** smectite, **(C)** potassium, **(D)** 2.2/1.4 band depth ratio, **(E)** 2.3/1.4 band depth ratio, and **(F)** 2.3/2.2 band depth ratio. CHB potassium values (K) (scanning XRF, in normalized counts per second) show an inverse correlation with smectite abundances (XRD) in corresponding samples. Al content (scanning XRF, in normalized counts per second) largely follow smectite abundances (XRD) that are typically rich in Al. Color shading indicates inferred hydroclimate: red: dry-climate sediment; light blue: wet-to-dry-transition-climate sediment; blue: wet-climate sediment, derived from spectral analysis.

Consequently, both diagrams are clearly anticorrelated. The last column (diagram F, **Figure 6**) summarizes the result as a ratio of both band depths at 2.3 µm relatively to 2.2 µm confirming this inverse relationship. The local maxima of this ratio can be clearly assigned to dry climate episodes. Moreover, it shows the degree of Mg substitution, which is mostly higher for samples with high potassium content. Maxima of this ratio occur in younger time periods <45 ka BP (core depths <20 m) and around 270 ka BP (~140 m). But the hyperspectral measurements are also sensitive to weaker changes in the ratio of these absorption band depths. Local weaker maxima almost always coincide with a higher potassium content and thus with drier climate phases. Examples are spectra of the dry-climate sediment samples 9, 21, 22, 26, 27, 28 (see core depth and age date from **Table 1**).

These findings are consistent with the model according to Foerster et al. (2018), and with surface sediment samples from the CHB catchment. The results are also a methodologically independent test of the weathering model based on short core results (Foerster et al., 2018). Beyond this confirmation of authigenic processes evident on shorter timescales applying also on longer timescales, the hyperspectral data reveal new capacities for climate-relevant studies. In the spectral range between 1 and 2.5 µm it is possible under controlled laboratory conditions not only to prove Al-substitution by Mg and low-temperature illitization, but also to perform semi-quantitative analyses with the help of these spectral indicators and their relationships to each other. This provides valuable and more detailed information about the degree of weathering processes, their duration and their correlated fine structure; crucial information for the reliable establishment, validation and advanced understanding of paleoclimatic proxies.

Figure 7 compares the shifts in 112 analcime peak intensities, indicative for varying abundances of analcime in discrete samples (XRD results, column A) and the potassium content from XRF data (column B) with further hyperspectral indicators that complete these studies. These spectral indicators are an absorption band at 1.16 µm, which can be attributed to analcime and a band at 3.98 µm caused by calcite. Columns C and D in **Figure 7** display the band depth variation at 1.16 and 3.98 µm (right two columns) against the core depth in meters (mcd). The shifts of analcime abundances, indicated in variations of XRD peak intensities of the 112 analcime peak, are consistent with high potassium values (see columns 1 and 2). The analcime absorption band at 1.16 µm (column C) is not observed in most of the CHB14-2 sample spectra or it is characterized by a very low spectral contrast. It is only found in the spectra of CHB14-2

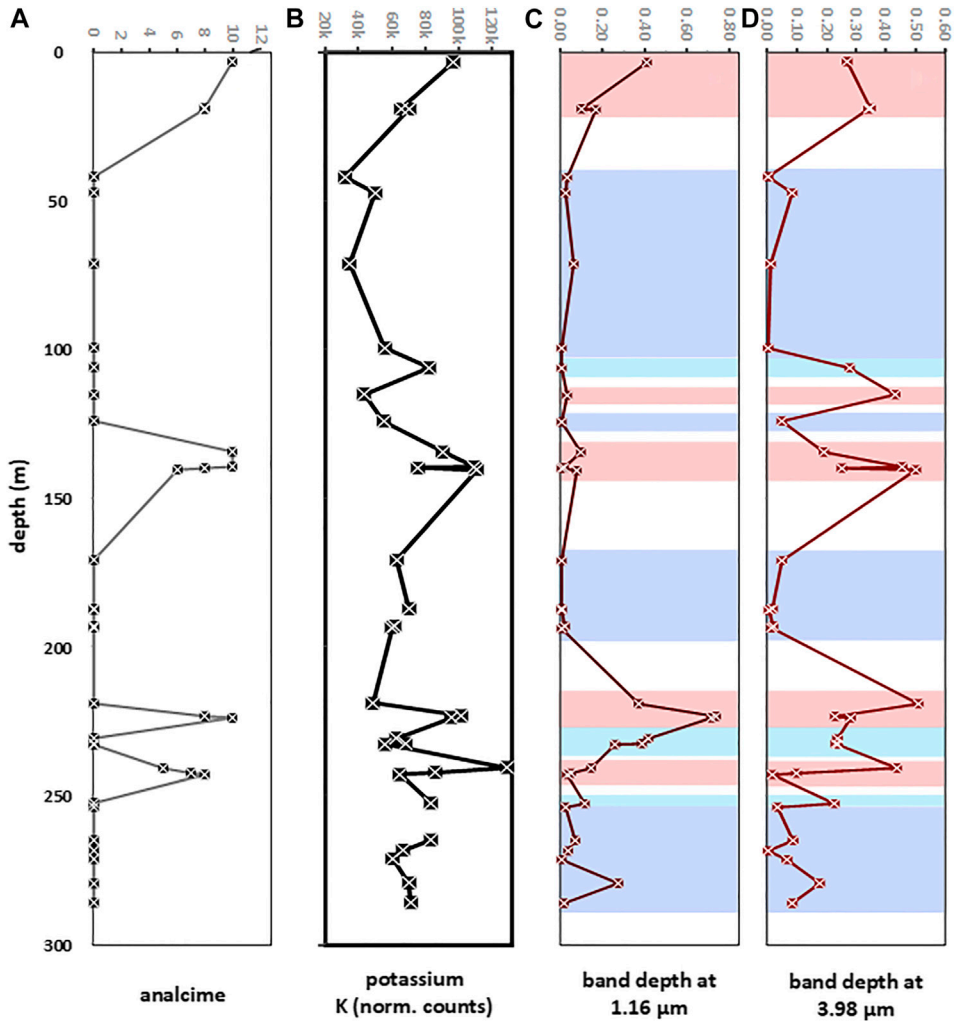

FIGURE 7 | Comparison of absorption band depths at 1.16 µm (characteristic for analcime) and at 3.98 µm (calcite) with K values (scanning XRF, normalized counts per second) and analcime intensities (XRD, normalized). **(A)** Analcime, **(B)** potassium, **(C)** band depth at 1.16 µm, and **(D)** band depth at 3.98 µm. Color shading indicates inferred hydroclimate: red: dry-climate sediment; light blue: wet-to-dry-transition-climate sediment; blue: wet-climate sediment, derived from spectral analysis.

sediment samples with the highest potassium contents corresponding to pronounced dry climate phases. Although one of the maximum values of XRD data for analcime in sediment samples from a core depth of 134.5–139 mcd (samples 11 and 12) corresponds to a weaker band depth at 1.16 µm, the band is clearly identifiable in the spectrum of the 134.5 mcd sample and is also increased in contrast to spectra of samples with low potassium levels. The maximum depth of the 1.16 µm absorption band is observed in the spectrum of sediment samples from depths of ~224 mcd (samples 21 and 22), which correlates with a high potassium abundances and dry climate conditions. Further consistency between high analcime and potassium values and the band contrast at 1.16 µm is shown for younger sediment samples (1–3) from depths 3 and 20 m and for sample 26 from ~241 m.

Of particular interest is that even for sediment samples for which the XRD method could not provide analcime detection, 1.16 µm bands could be recorded with the hyperspectral method. The corresponding depths of this absorption band follow, apart from some already discussed deviations, the course of the potassium content determined by XRF methods to a large extent (compare **Figure 5**, 2nd and 3rd column). This opens up the possibility of refining the sediment investigations for the detection of analcime with hyperspectral methods for future analysis.

Diagram D in **Figure 7** shows the corresponding depths of the absorption band at 3.98 µm. As this band is indicative for calcite, it enables a link to be established to the salinity of the samples, which in turn is also an important marker in CHB sediments for the change from humid to dry climate conditions. High band contrasts are an evidence of high calcite concentrations. Their occurrence correlates to dry climate episodes that could be typically connected with increased salinity. The curve of the band depth as a function of the core depth of the samples

follows the corresponding curve of the potassium content (column B). Maximum potassium contents are consistent with high band contrasts of the 3.98 μm band. This applies to almost all samples investigated except for sample 9 (~115-m core depth), which has a relatively high band depth compared to the determined potassium content. The correlations between analcime and calcite band contrasts must also be considered. Here, too, apart from the spectra of samples 9, 11, and 12, we see a high degree of agreement in the tendencies for the corresponding band depths. The synergetic use of both bands therefore also offers the potential to investigate the weathering paths in dry periods more precisely by means of hyperspectral data.

The finding of analcime and high calcite abundances in dry-climate samples is in line with the results of the X-ray analyses and supports the model of Foerster et al. (2018). Since the composition of the authigenic minerals are characteristic of past and present hydrological conditions, all spectral indicators discussed in this chapter are suitable proxies to track the climate of the Chew Bahir region over the past ~620 ka. This is further supported by UV, VIS and MIR spectral features, which in turn support the presence of smectites, calcite and analcime, and can also enable further and more refined mineralogical analyses.

The UV–VIS absorption bands (see **Figure 3D**) offer the possibility of detecting the involvement of certain transition metal ions in the mineralogical solid state lattice and thus to draw connections to the origin and nature of the initial products of weathering. Absorption bands close to 3.4 μm (see **Figure 3D**) are of organic origin and can in future also be used to study the type of organic matter and its variations in the sediment as a function of past environmental factors. Finally, the semi-quantitative evaluation of spectral indicators in the mid-infrared offers additional possibilities, e.g., to narrow down the silicate components of the sediments more distinctly. Thus, in the spectra of the calcite-free or calcite-poor sediment samples, such as, the spectrum of sample 17 (blue spectrum) shown in **Figure 3E**, spectral signatures like the minimum reflectance at 8 μm or the silicate fundamental vibration bands near 11 μm can be extracted, which can be assigned to the phyllosilicate dominant in the sample and which in the case of sample 17 clearly indicate montmorillonite. This will be the subject of additional future quantitative analysis of these hyperspectral data.

The 0.25–17 μm reflectance spectroscopy is a minimally invasive, fast and inexpensive analytical method for studying the chemical-mineralogical composition of sediments. In the case of the drill core samples from the Chew Bahir Basin, the method is shown to be a valuable tool in establishing correlations between spectral information on the mineralogy of the samples and climatic indicators. Thus, hyperspectral spectroscopy is a suitable and independent method for studying paleoclimatic weathering processes in the Chew Bahir Basin. This is especially valid for the study of the alternating processes of aqueous and dry weathering, processes that commonly influenced sediments of the Chew Bahir region in the past 620 ka. The spectral measurements have shown that the CHB sediment mineralogy is dominated by smectites with variable Al and/or Mg incorporation. In addition, calcite is the major carbonate component present. The calcite content is highest in samples that can be assigned to dry climate phases. Samples that can be attributed to the driest climate phases contain the zeolite analcime.

The hyperspectral studies show a clear positive correlation of absorption band depth ratios 2.3/2.2 μm with the potassium (K) content of the samples. The absorption band ratio corresponds to increases in K values and thus reflects the increased incorporation of Mg into Al montmorillonite during episodes of an arid climate. The analyses support the conclusion that the illitization of the Chew Bahir clay minerals with increasing evaporation is enhanced by octahedral Al-to-Mg substitution in the clay minerals, with the resulting increase in layer charge facilitating potassium fixation. This confirms the model of authigenic illitization of smectites under more arid conditions during episodes of higher alkalinity and salinity in the closed-basin lake of Chew Bahir as proposed by Foerster et al. (2018). In comparison and in addition to the results of the XRF/XRD analyses, however, the hyperspectral investigations also go well beyond these former results. The high sensitivity of the absorption band depths near 2.2, 2.3, and 2.35 μm for the Al-to-Mg substitution and the associated illitization allows a re-tuning of the wet and dry environmental sequences in the course of the alteration.

Furthermore, it is possible to track analcime and calcite in dry periods by using hyperspectral analysis close to 1.16 and 3.98 μm. The salinity of the Chew Bahir sediments is strongly correlated to the 3.98 μm absorption band depth of calcite in the samples. During wet climate periods the carbonate is precipitated from solution. The drier the environmental condition, the more calcite is formed. Variable band contrasts at 3.98 μm indicate this. The highest band depth values occur at the highest potassium abundances and in the driest climatic phases. Only within these highly arid periods can analcime be detected in the sediment spectra as authigenic formation by reverse weathering of clay minerals. Since the formation of analcime requires high alkalinity and salinity of the paleolake water, linked to desiccation in terminal lakes, the synchronous finding of high calcite content and analcime is conclusive.

CONCLUSION

Based on the spectral investigations presented here, a climatic record can be built, comprising the following phases: ~600–500 ka wet phase, ~460–454 ka dry episode, ~431–428 ka weak humid phase, ~415–407 ka dry conditions, ~363–324 wet phase, ~270–260 ka dry episode, ~242 ka short humid phase, ~227 ka short dry phase, ~211–78 ka wet episode and since ~44 ka dry conditions. These results are shown as colored shading in **Figure 2** and can be directly compared with the geochemical analyses of variations in potassium content as a function of core depth and sample age. This record is largely consistent with the wet-dry variations as suggested by the aridity-proxy K (Trauth et al., 2020). Those wet-dry variations can be discerned into three phases with similarities in the central tendency and dispersion: a long-term drying trend in Phase I (~620–413 ka BP), a generally wetter but increasingly fluctuating

Phase II (~413–195 ka BP) and finally a long-term drying trend that is marked by rapid climate oscillations from ~195 ka BP on (Phase III).

The results of the spectral analyses presented here can also further qualify the degree of past aridity/humidity, which has important implications for understanding environmental influence on past human populations. Climatic fluctuations may have had a critical impact in shaping human habitats (Campisano et al., 2017; Owen et al., 2018; Mounier and Lahr, 2019). The oscillating environmental extremes in the final part of Phase I may have been strongly selective in driving evolutionary and cultural change, including the abandonment of Acheulean technology (e.g., Potts et al., 2018). The hyperspectral results support the aridity-proxy record (**Figure 2**) but suggest that there were also narrower time windows where the climate was neither fully humid nor arid, but moderately humid, which would have had an impact on the connectivity of potential corridors of population dispersal. Favorable humid conditions during Phase II, pulsed by short arid excursions, interpreted as having played a key role in the emergence of *Homo sapiens*, are confirmed by the results presented here. Similarly, the results confirm the occurrence of short-term oscillations in Phase III, which may have played a role in the timing of migration events out of Africa (Stringer and Galway-Witham, 2017; Stewart et al., 2019).

In summary, the hyperspectral reflectance measurements show that for the continuum-corrected spectra obtained under well-defined laboratory conditions in terms of sample preparation and measurement performance, four spectral indicators can be clearly defined that can be reliably correlated directly with the climatic conditions under which the sediments were formed. These are absorption bands at 1.16, near 2.2, near 2.3 and at 3.98 μm and their band depths. It could be demonstrated in this paper that the synergetic use of these climate-relevant spectral indicators offers a complementary and enhancing contribution to previous climate proxy studies in the Chew Bahir Basin (e.g., Foerster et al., 2018; Trauth et al., 2020). Overall there is very good agreement between the geochemical and hyperspectral mineralogical results.

Further spectral signatures are currently being tested for semi-quantitative climate proxy studies. These include the UV/VIS absorption bands caused by electronic processes on transition metal ions, features due to organic matter near 3.4 μm, the MIR reflectance minima on the short-wave flank of the silicate reststrahlen bands and the fundamental vibration bands themselves. They have the potential to provide further information from the entire wavelength range from 0.25 to 17 μm in order to extract additional climate-relevant information in future studies. To the extent that the number of climate-relevant spectral indicators can be expanded and the method can be extended to a larger number of drill core samples, statistical methods up to machine learning algorithms can be used in the future to further professionalize climate proxy studies with hyperspectral analyses and potentially apply these methodological findings to other coring sites and environmental archives. Finally, the hyperspectral reflectance spectroscopy method allows a direct comparison with spectral remote sensing data and thus a combination of investigations of the current surface composition in the Chew Bahir Basin and its connection to past climate data.

DATA AVAILABILITY STATEMENT

The raw data supporting the conclusions of this article will be made available by the authors, without undue reservation.

AUTHOR CONTRIBUTIONS

Each named author has substantially contributed to conducting the underlying research and drafting this manuscript.

ACKNOWLEDGMENTS

Support for HSPDP has been provided by the National Science Foundation (NSF) Grants and the International Continental Drilling Program (ICDP). Support for CBDP has been provided by Germany Research Foundation (DFG) through the Priority Program SPP 1006 ICDP (FS 472/13 and /18, MHT: TR 419/8, /10 and /16, FO 734/2) and the CRC 806 Research Project "Our way to Europe" (Project Number 57444011). Support has also been received from the UK Natural Environment Research Council (NERC, NE/014K560/1, IP/1623/0516). We thank the Ethiopian authorities for permits for drilling in the Chew Bahir Basin, and the Hammar people for local assistance during drilling operations. Logistic support and supervision of drilling was provided by DOSECC Exploration, in co-operation with Ethio Der pvt. Ltd. Co. Initial core processing and sampling were conducted at the US National Lacustrine Core Facility (LacCore) at the University of Minnesota. The authors would like to thank DLR's Institute of Planetary Research, Berlin-Adlershof, for use of the laboratory and for their support in the spectral investigations. This is publication HSPDP#39 of the Hominin Sites and Paleolakes Drilling Project.

REFERENCES

Arnold, G., Szczech, C., Asrat, A., Cohen, A. S., Foerster, V., Schäbitz, F., et al. (2020). Advanced Hyperspectral Analysis of Sediment Core Samples from the Chew Bahir Basin, Ethiopian Rift in the Spectral Range from 0.25 to 17 Mm: Support for Climate Proxy Information. *EGU Gen. Assembly* 2020, 5233. doi:10.5194/egusphere-egu2020-5233

Arnold, G. (1991). Measurements of the Spectral Emittance of Particulate Minerals and Some Remote Sensing Implications. *Vibrational Spectrosc.* 2, 245–249. doi:10.1016/0924-2031(91)85032-i

Bibring, J.-P., Langevin, Y., Mustard, J. F., Poulet, F., Arvidson, R., Gendrin, A., et al. (2006). Global Mineralogical and Aqueous Mars History Derived from OMEGA/Mars Express Data. *Science* 312, 5772, 400–404. doi:10.1126/science.1122659

Bishop, J. L., Pieters, C. M., and Edwards, J. O. (1994). Infrared Spectroscopic Analyses on the Nature of Water in Montmorillonite. *Clay and Clay Minerals* 42, 702–716. doi:10.1346/ccmn.1994.0420606

Bishop, J. L., Noe Dobrea, E. Z., McKeown, N. K., Parente, M., Ehlmann, B. L., Michalski, J. R., et al. (2008). Phyllosilicates Diversity and Past Aqueous Activity Revealed at Mawrth Vallis, Mars. *Science* 321 (5890), 830–833. doi:10.1126/science.1159699

Brown, F. H., and Fuller, C. R. (2008). Stratigraphy and Tephra of the Kibish Formation, Southwestern Ethiopia. *J. Hum. Evol.* 55, 366–403. doi:10.1016/j.jhevol.2008.05.009

Brown, F. H., McDougall, I., and Fleagle, J. G. (2012). Correlation of the KHS Tuff of the Kibish Formation to Volcanic Ash Layers at Other Sites, and the Age of Early Homo sapiens (Omo I and Omo II). *J. Hum. Evol.* 63, 577–585. doi:10.1016/jhevol.2015.05.014

Burns, R. G. (1993). "Origin of Electronic Spectra of Minerals in the Visible to Near-Infrared Region," in *Remote Geochemical Analysis: Elemental and Mineralogical Composition 4*. Editors C. M. Pieters and P. A. J. Englert (Cambridge: Cambridge University Press), 3–29.

Butz, C., Grosjean, M., Wunderle, S., Tylmann, W., and Rein, B. (2015). Hyperspectral Imaging Spectroscopy: a Promising Method for the Biochemical Analysis of lake Sediments. *J. Appl. Remote Sens.* 9, 1–20. doi:10.1117/1.JRS.9.096031

Butz, C., Grosjean, M., Goslar, T., and Tylmann, W. (2017). Hyperspectral Imaging of Sedimentary Bacterial Pigments: a 1700-year History of Meromixis from Varved Lake Jaczno, Northeast Poland. *J. Paleolimnology* 58, 57–72. doi:10.1007/s10933-017-9955-1

Campisano, C. J., Cohen, A. S., Arrowsmith, J. R., Asrat, A., Behrensmeyer, A. K., Brown, E. T., et al. (2017). The Hominin Sites and Paleolakes Drilling Project: High-Resolution Paleoclimate Records from the East African Rift System and Their Implications for Understanding the Environmental Context of Hominin Evolution. *PaleoAnthropology* 14, 1–43. doi:10.4207/PA.2017.ART104

Chevalier, M., and Chase, B. M. (2016). Determining the Drivers of Long-Term Aridity Variability: a Southern African Case Study. *J. Quat. Sci.* 31, 143–151. doi:10.1002/jps.2850

Christensen, P.R., Bandfield, J.L., Bell, J.F., III, Gorelick, N., Hamilton, V.E., Ivanov, A., et al. (2003). Morphology and composition of the surface of Mars: Mars Odyssey THEMIS results. *Science* 330(5628), 2056–2061. doi:10.1126/science.1080885

Clark, J., Beyene, Y., WoldeGabriel, G., Hart, W. K., Renne, P. R., Gilbert, H., et al. (2003). Stratigraphic, Chronological and Behavioural Contexts of Pleistocene Homo sapiens from Middle Awash, Ethiopia. *Nature* 423, 747–752. doi:10.1038/nature01670

Clark, R. N. (1999). "Chapter 1: Spectroscopy of Rocks and Minerals, and Principles of Spectroscopy," in *Manual of Remote Sensing, Volume 3, Remote Sensing for the Earth Sciences*. Editor A.N. Rencz (New York: John Wiley & Sons), 3–58.

Cohen, A. S., Campisano, C., Arrowsmith, R., Asrat, A., Behrensmeyer, A. K., Deino, A., et al. (2016). The Hominin Sites and Paleolakes Drilling Project: Inferring the Environmental Context of Human Evolution from Eastern African Rift Lake Deposits. *Scientific Drilling* 21, 1–16. doi:10.5194/sd-21-1-2016

Davidson, A. (1983). The Omo River Project: Reconnaissance Geology and Geochemistry of Parts of Ilubabor, Kefa, Gemu Gofa and Sidamo. *Ethiopian Inst. Geol. Surv. Bull.* 2, 1–89.

Davies, S. J., Lamb, H. F., and Roberts, S. J. (2015). "Micro-XRF Core Scanning in Palaeolimnology: Recent Developments," in MicroXRF Studies of Sediment Cores, in *Developments In Paleoenvironmental Research 17*. Editors I. W. Croudace and R. G. Rothwell (New York: John Wiley & Sons). doi:10.1007/978-94-017-9849-5_7

Deocampo, D. M., and Tactikos, J. C. (2010). Geochemical Gradients and Artifact Mass Densities on the Lowermost Bed II Eastern lake Margin (~1.8 Ma), Olduvai Gorge, Tanzania. *Quat. Res.* 74, 411–423. doi:10.1016/j.yqres.2010.09.004

Deocampo, D. M., Cuadros, J., Wing-Dudek, T., Olives, J., and Amouric, M. (2009). Saline lake Diagenesis as Revealed by Coupled Mineralogy and Geochemistry of Multiple Ultrafine clay Phases: Pliocene Olduvai Gorge. *Am. J. Sci.* 309, 834–868. doi:10.2475/09.2009.03

Ehlmann Mc, B. L., Bish, D. L., Ruff, S. W., and Mustard, J. F. (2012). Mineralogy and Chemistry of Altered Icelandic Basalts: Application to clay mineral Detection and Understanding Aqueous Environments on Mars. *J. Geophys. Res.* 117 (E11), E00J16. doi:10.1029/2012JE004156

Farmer, V., and Russel, J. (1964). The Mid-infrared Spectra of Layer Silicates. *Spectrochim. Acta* 20, 1149–1173. doi:10.1016/0371-1951(64)80165-x

Fischer, M. L., Markowska, M., Bachofer, F., Foerster, V., Asrat, A., Zielhofer, C., et al. (2020). Determining the Pace and Magnitude of Lake Level Changes in Southern Ethiopia over the Last 20,000 Years Using Lake Balance Modeling and SEBAL. *Front. Earth Sci.* 8, 197. doi:10.3389/feart.2020.00197

Foerster, V., Junginger, A., Langkamp, O., Gebru, T., Asrat, A., Umer, M., et al. (2012). Climatic Change Recorded in the Sediments of the Chew Bahir Basin, Southern Ethiopia, during the Last 45,000 Years. *Quat. Int.* 274, 25–37. doi:10.1016/j.quaint.2012.06.028

Foerster, V., Vogelsang, R., Junginger, A., Asrat, A., Lamb, H. F., Schaebitz, F., et al. (2015). Environmental Change and Human Occupation of Southern Ethiopia and Northern Kenya during the Last 20,000 Years. *Quat. Sci. Rev.* 129, 333–340. doi:10.1016/j.quascirev.2015.10.026

Foerster, V., Deocampo, D. M., Asrat, A., Günter, C., Junginger, A., Kraemer, H., et al. (2018). Towards an Understanding of Climate Proxy Formation in the Chew Bahir Basin, Southern Ethiopian Rift. *Palaeogeogr. Palaeoclimatol. Palaeoecol.* 501, 111–123. doi:10.1016/j.palaeo.2018.04.009

Gaffey, S. J., McFadden, L. A., Nash, D., and Pieters, C. M. (1993). "Ultraviolet, Visible, and Near-Infrared Reflectance Spectroscopy: Laboratory Spectra of Geologic Materials," in *Remote Geochemical Analysis: Elemental and Mineralogical Composition 4*. Editors C. M. Pieters and P. A. J. Englert (Cambridge University Press), 43–77.

Grim, R. E. (1968). Clay Mineralogy. *International Series in the Earth and Planetary Sciences*, 2. New York: McGraw-Hill.

Grosjean, M., Amann, B., Butz, C., Rein, B., and Tylmann, W. (2014). Hyperspectral Imaging: a Novel, Nondestructive Method for Investigating Sub-annual Sediment Structures and Composition. *Past Glob. Changes Mag.* 22 (1), 1–11. doi:10.22498/pages.22.1.10

Hailemeskel, A., and Fekadu, H. (2004). *Geological Map of Yabello*. Addis Ababa: Geological Survey of Ethiopia.

Hassen, N., Yemane, T., and Genzebu, W. (1997). *Geology of the Agere Maryam Area*. Addis Ababa: Geological Survey of Ethiopia.

Hay, R. L., and Kyser, T. K. (2001). Chemical Sedimentology and Paleoenvironmental History of Lake Olduvai, a Pliocene lake in Northern Tanzania. *GSA Bull.* 113, 1505–1521. doi:10.1130/0016-7606(2001)113<1505:csapho>2.0.co;2

Huntley, B. (2012). Reconstructing Palaeoclimates from Biological Proxies: Some Often Overlooked Sources of Uncertainty. *Quat. Sci. Rev.* 31, 1–16. doi:10.1016/j.quascirev.2011.11.006

Key, R. M. (1987). *Geology of the Sabarei Area: Degree Sheets 3 and 4, with Coloured 1:250 000 Geological Map and Results of Geochemical Exploration (Report)*. Nairobi, Kenya: Ministry of Environment and Natural Resources, Mines and Geology Dept.

Körting, F., Rogass, C., Kaempf, H., Lubitz, C., Harms, U., Schudack, M., et al. (2015). Drill core mineral analysis by means of the hyperspectral imaging spectrometer HySpex, XRD and ASD in proximity of the Mytina MaarR, Czech Republic. The International Archives of the Photogrammetry, *Remote Sensing and Spatial Information Sciences* 21, 417–424. doi:10.5194/isprsarchives-XL-1-W5-417–2015

Locsey, K. L., Grigorescu, M., and Cox, M. E. (2012). Water-rock Interactions: an Investigation of Relationships between Mineralogy and Groundwater Composition and Flow in a Subtropical basalt Aquifer. *Aquat. Geochem.* 18, 45–75. doi:10.1007/s10498-011-9148-x

Mann, M. E. (2002). The Value of Multiple Proxies. *Science* 297, 1481–1482. doi:10.1126/science.10743110.1126/science.1074318

Maturilli, A., Helbert, J., D'Amore, M., Varatharajan, I., and Rosas Ortiz, Y. (2018). "The Planetary Spectroscopy Laboratory (PSL): Wide Spectral Range, Wider Sample Temperature Range, SPIE," in Infrared Remote Sensing and Instrumentation XXVI, San Diego, USA, 19 – 23 August 2018. doi:10.1117/12.2319944

Moore, D. M., and Reynolds, R. C. (1997). *X-Ray Diffraction and the Identification and Analysis of Clay Minerals*. 2nd ed, XVII. Oxford, New York: Oxford University Press, 378.

Mounier, A., and Lahr, R. (2019). M.M. Deciphering African Late Middle Pleistocene Hominin Diversity and the Origin of Our Species. *Nat. Commun.* 10, 34061–34113. doi:10.1038/s41467-019-11213-w

Navarre-Stichler, A., and Brantley, S. (2007). Basalt Weathering across Scales. *Earth Planet. Sci. Lett.* 261, 321–334. doi:10.1016/j.epsl.2007.07.010

Navarre-Stichler, A., Steefel, C., Yang, L., and Brantley, S. (2009). Evolution of Porosity Diffusivity during Chemical Weathering of basalt Clast. *J. Geophys. Res. Earth* 114, F02016. doi:10.1029/2008JF001060

Nicholson, S. E. (2017). Climate and Climatic Variability of Rainfall over Eastern Africa. *Rev. Geophys.* 55 (3), 590–663. doi:10.1002/2016RG000544

Nicholson, S. E. (2018). The ITCZ and the Seasonal Cycle over Equatorial Africa. *Bull. Am. Meteorol. Soc.* 99, 337–348. doi:10.1175/BAMS-D-16-0287.1

Owen, R. B., Muiruri, V. M., Lowenstein, T. K., Renaut, R. W., Rabideaux, N., Luo, S., et al. (2018). Progressive Aridification in East Africa over the Last Half Million Years and Implications for Human Evolution. *Proc. Natl. Acad. Sci.* 115, 11174–1117. doi:10.1073/pnas.1801357115

Owen, R. B., Renaut, R. W., Muiruri, V. M., Rabideaux, N. M., Lowenstein, T. K., McNulty, E. P., et al. (2019). Quaternary History of the Lake Magadi Basin, Southern Kenya Rift_ Tectonic and Climatic Controls. *Palaeogeogr. Palaeoclimatol. Palaeoecol.* 518, 97–118. doi:10.1016/j.palaeo.2019.01.017

Pawar, N. J., Pawar, J. B., Kumar, S., and Supekar, A. (2008). Geochemical Eccentricity of Ground Water Allied to Weathering Basalts from the Deccan Volcanic Province, India: Insinuation on CO_2 Consumption. *Aquat. Geochem.* 14, 41–71. doi:10.1007/s10498-007-9025-9

Pik, R., Marty, B., Carignan, J., Yirgu, G., and Ayalew, T. (2008). Timing of East African Rift Development in Southern Ethiopia: Implication for Mantle Plume Activity and Evolution of Topography. *Geology* 36, 167–170. doi:10.1130/G24233A.1

Potts, R., Behrensmeyer, A. K., Faith, J. T., and Tryon, C. A. (2018). Environmental Dynamics during the Onset of the Middle Stone Age in Eastern Africa. *Science* 360 6384, 86–90. doi:10.1126/science.aao2200

Renaut, R. W. (1993). Zeolitic Diagenesis of Late Quaternary Fluviolacustrine Sediments and Associated Calcrete Formation in Lake Bogoria Basin, Kenya Rift Valley. *Sedimentology* 40, 271–301. doi:10.1111/j.1365-3091.1993.tb01764.x

Roberts, P., and Stewart, B. A. (2018). Defining the "Generalist Specialist" Niche for Pleistocene *Homo sapiens*. *Nat. Hum. Behav.* 2, 542–550. doi:10.1038/s41562-018-0394-4

Roberts, H.M., Bronk Ramsey, C., Chapot, M.S., Deino, A., Lane, C.S., Vidal, C., et al. (2021). Using multiple chronometers to establish a long, directly-dated lacustrine record: constraining >600,000 years of environmental change at Chew Bahir, Ethiopia. *Quater. Sci. Rev., submitted.*

Sak, P. B., Navarre-Stichler, A. K., Miller, C. E., Daniel, C. C., Geillardt, J., Buss, H. L., et al. (2010). Controls on Rind Thickness on Basaltic Andesite Clasts Weathering in Guadeloupe. *Chem. Geol.* 276, 129–143. doi:10.1016/j.chemgeo.2010.05.002

Salisbury, J. W. (1993). "Mid-infrared Spectroscopy: Laboratory Data,". *Remote Geochemical Analysis: Elemental and Mineralogical Composition 4*. Editors C.M. Pieters and P.A.J. Englert (Cambridge University Press), 79–98.

Schlolaut, G., Staff, R. A., Brauer, A., Lamb, H. F., Marshall, M. H., Bronk Ramsey, C., et al. (2018). An Extended and Revised Lake Suigetsu Varve Chronology from ~50 to ~10 Ka BP Based on Detailed Sediment Micro-facies Analyses. *Quat. Sci. Rev.* 200, 351–366. doi:10.1016/j.quascirev.2018.09.021

Singer, R. B. (1982). Spectral Evidence for the Mineralogy of High-Albedo Soils and Dust on Mars. *J. Geophys. Res.* 87 (B12)), 10159. doi:10.1029/jb087ib12p10159

Stewart, M., Louys, J., Price, G. J., Drake, N. A., Groucutt, H. S., and Petraglia, M. D. (2019). Middle and Late Pleistocene Mammal Fossils of Arabia and Surrounding Regions: Implications for Biogeography and Hominin Dispersals. *Quat. Int.* 515, 12–29. doi:10.1016/j.quaint.2017.11.052

Stringer, C., and Galway-Witham, J. (2017). On the Origin of Our Species. *Nature* 546, 212–214. doi:10.1038/546212a

Stringer, C. (2016). The Origin and Evolution of Homo sapiens. *Phil. Trans. R. Soc. B* 371, 20150237. doi:10.1098/rstb.2015.0237

Trauth, M. H., Bergner, A. G. N., Foerster, V., Junginger, A., Maslin, M. A., and Schaebitz, F. (2015). Episodes of Environmental Stability and Instability in Late Cenozoic Lake Records of Eastern Africa. *J. Hum. Evol.* 87, 21–31. doi:10.1016/j.jhevol.2015.03.011

Trauth, M. H., Foerster, V., Junginger, A., Asrat, A., Lamb, H. F., and Schaebitz, F. (2018). Abrupt or Gradual? Change Point Analysis of the Late Pleistocene-Holocene Climate Record from Chew Bahir, Southern Ethiopia. *Quat. Res.* 90 (2), 321–330. doi:10.1017/qua.2018.30

Trauth, M. H., Asrat, A., Duesing, W., Foerster, V., Kraemer, K. H., Marwan, N., et al. (2019). Classifying Past Climate Change in the Chew Bahir Basin, Southern Ethiopia, Using Recurrence Quantification Analysis. *Clim. Dyn.* 53 (5-6), 2557–2572. doi:10.1007/s00382-019-04641-3

Trauth, M. H., Asrat, A., Cohen, A. S., Duesing, W., Foerster, V., Kaboth-Bahr, S., et al. (2020). Recurring Types of Variability and Transitions in the ~620 Kyr Record of Climate Change from the Chew Bahir basin, Southern Ethiopia. *Quat. Sci. Rev.* 11, 121. doi:10.1016/j.quascirev.2020.106777

Vebel, M. A., and Losiak, A. I. (2008). Influence of Surface-Area Estimation on Rates of Plagioclase Weathering Determined from Naturally Weathered 3400 Y Old Hawaiian basalt. *Mineral. Mag.* 72, 91–94. doi:10.1180/minmag.2008.072.1.91

Viehberg, F. A., Just, J., Dean, J. R., Wagner, B., Franz, S. O., Klasen, N., et al. (2018). Environmental Change during MIS4 and MIS 3 Opened Corridors in the Horn of Africa for Homo sapiens Expansion. *Quat. Sci. Rev.* 202, 139–153. doi:10.1016/j.quascirev.2018.09.008

Viste, E., and Sorteberg, A. (2013). The Effect of Moisture Transport Variability on Ethiopian Summer Precipitation. *Int. J. climatology* 33 (15), 3106–3123. doi:10.1002/joc.3566

Wilke, T., Wagner, B., Van Bocxlaer, B., Albrecht, C., Ariztegui, D., Delicado, D., et al. (2016). Scientific Drilling Projects in Ancient Lakes: Integrating Geological and Biological Histories. *Glob. Planet. Change* 143, 118–151. doi:10.1016/j.gloplacha.2016.05.005

Conflict of Interest: The authors declare that the research was conducted in the absence of any commercial or financial relationships that could be construed as a potential conflict of interest.

frontiers in Earth Science

ORIGINAL RESEARCH
published: 01 July 2021
doi: 10.3389/feart.2021.668445

Lake-Level Changes and Their Paleo-Climatic Implications at the MIS12 Lower Paleolithic (Middle Pleistocene) Site Marathousa 1, Greece

Ines J. E. Bludau[1,2], Penelope Papadopoulou[3], George Iliopoulos[3], Max Weiss[1], Ellen Schnabel[1], Nicholas Thompson[1,4], Vangelis Tourloukis[1,4], Charlotte Zachow[1], Styliani Kyrikou[1,4], George E. Konidaris[1,4], Panagiotis Karkanas[5], Eleni Panagopoulou[6], Katerina Harvati[1,2,4] and Annett Junginger[1,2]**

[1]Department of Geosciences, Eberhard Karls University Tuebingen, Tuebingen, Germany, [2]Senckenberg Centre for Human Evolution and Palaeoenvironment (S-HEP), Tuebingen, Germany, [3]Department of Geology, University of Patras, Rio Patras, Greece, [4]Paleoanthropology, Institute for Archaeological Sciences, Eberhard Karls University of Tübingen, Tübingen, Germany, [5]The Malcolm H. Wiener Laboratory for Archaeological Science, American School of Classical Studies at Athens, Athens, Greece, [6]Ephoreia of Paleoanthropology-Speleology of Greece, Athens, Greece

OPEN ACCESS

Edited by:
Matthias Prange,
University of Bremen, Germany

Reviewed by:
Li Wu,
Anhui Normal University, China
Steffen Mischke,
University of Iceland, Iceland

***Correspondence:**
Annett Junginger
annett.junginger@uni-tuebingen.de
Ines J. E. Bludau
bludau.ines@gmail.com

Specialty section:
This article was submitted to Quaternary Science, Geomorphology and Paleoenvironment, a section of the journal Frontiers in Earth Science

Received: 16 February 2021
Accepted: 18 May 2021
Published: 01 July 2021

Citation:
Bludau IJ E, Papadopoulou P, Iliopoulos G, Weiss M, Schnabel E, Thompson N, Tourloukis V, Zachow C, Kyrikou S, Konidaris GE, Karkanas P, Panagopoulou E, Harvati K and Junginger A (2021) Lake-Level Changes and Their Paleo-Climatic Implications at the MIS12 Lower Paleolithic (Middle Pleistocene) Site Marathousa 1, Greece. Front. Earth Sci. 9:668445. doi: 10.3389/feart.2021.668445

Lithics and cut-marked mammal bones, excavated from the paleo-lake Marathousa 1 (MAR-1) sediments in the Megalopolis Basin, southern Greece, indicate traces of hominin activity occurring along a paleo-shoreline ca. 444,000 years (444 ka) ago. However, the local environment and climatic conditions promoting hominin activity in the area during the MIS12 glacial remain largely unknown. In order to reconstruct the paleo-environment including paleo-lake levels and governing paleo-climatic factors on a high temporal resolution, we analyzed a 6-meter-long sediment sequence from the archeological site MAR-1 and a Bayesian age model was computed for a better age constrain of the different sedimentary units. A multiproxy approach was applied using ostracods, sponge spicules, diatoms, grain sizes, total organic carbon, total inorganic carbon and conventional X-ray fluorescence analysis. The results from the site represent a protected region surrounded by high mountains under the constant influence of water, either as a shallow partly anoxic water body surrounded by reed belts (>463–457 ka, <434–427 ka), a riverine-lake deltaic system (~457–448 ka), a floodplain (~448–444 ka) or a seasonal freshwater pond (~444–436 ka). The local changes of water levels resemble large trends and rhythms of regional records from the Mediterranean and appear to directly respond to sea surface temperature (SST) changes of the North Atlantic. In particular, when the SSTs are high, more moisture reaches the study area and vice versa. Additional water reaches MAR-1 through melting of the surrounding glaciers after brief warm phases during MIS12 in the Mediterranean realm, which leads to the formation of smaller fresh water ponds, where also the horizon of the excavated remains is placed. Such ponds, rich in ostracods and other microorganisms, provided mammals and humans valuable resources, such as potable water, a wide range of plant species and hunting opportunities. These deposits therefore bear a high archeological potential. The results from our study suggest that the Megalopolis Basin could have served as a refugium for hominins and other organisms due to its capacity to retain freshwater bodies during glacial and interglacial periods.

Keywords: Megalopolis, lignite, XRF, Mediterranean, paleo-lakes, ostracods

INTRODUCTION

Present-day Greece is often proposed to have played a key role in hominin dispersal due to its central geographic position between Africa, Asia and Europe (Harvati et al., 2009; Tourloukis and Karkanas, 2012; Harvati, 2016; Harvati, 2021; Papoulia, 2017; Tourloukis and Harvati, 2018; Harvati et al., 2019). However, there is a conspicuous lack of paleoanthropological/paleolithic remains from this region, with remains assigned to the Lower Paleolithic being especially rare (e.g., Harvati et al., 2009; Tourloukis and Karkanas, 2012; Harvati, 2016; Harvati, 2021; Tourloukis and Harvati, 2018). Several hypotheses have been proposed to account for this scarcity of evidence from Greece (e.g., research bias, loss of sites to rising sea levels, geological factors; see Tourloukis, 2016). The environmental conditions that may have allowed or prevented hominin dispersal and long-term survival in this region, therefore, are of particular interest. Currently, only four sites in Greece can be assigned to the Lower Paleolithic: 1) Kokkinopilos (Epirus), 2) Plakias (Crete), 3) Rodafnidia (Lesvos) and 4) Marathousa 1 (MAR-1; Megalopolis, Peloponnese) (**Figure 1**). Of these, only the Megalopolis Pleistocene sediments present a high potential for paleoenvironmental reconstructions (see, e.g., Harvati et al., 2018 and references therein).

Paleoenvironmental reconstruction from terrestrial archives, such as those from the Marathousa paleo-lake close to the archeological site MAR-1, is a powerful tool to better constrain the local living conditions of the preserved biota. The Marathousa Member (Choremi Formation) sedimentary sequence in the Megalopolis Basin consists of alternating

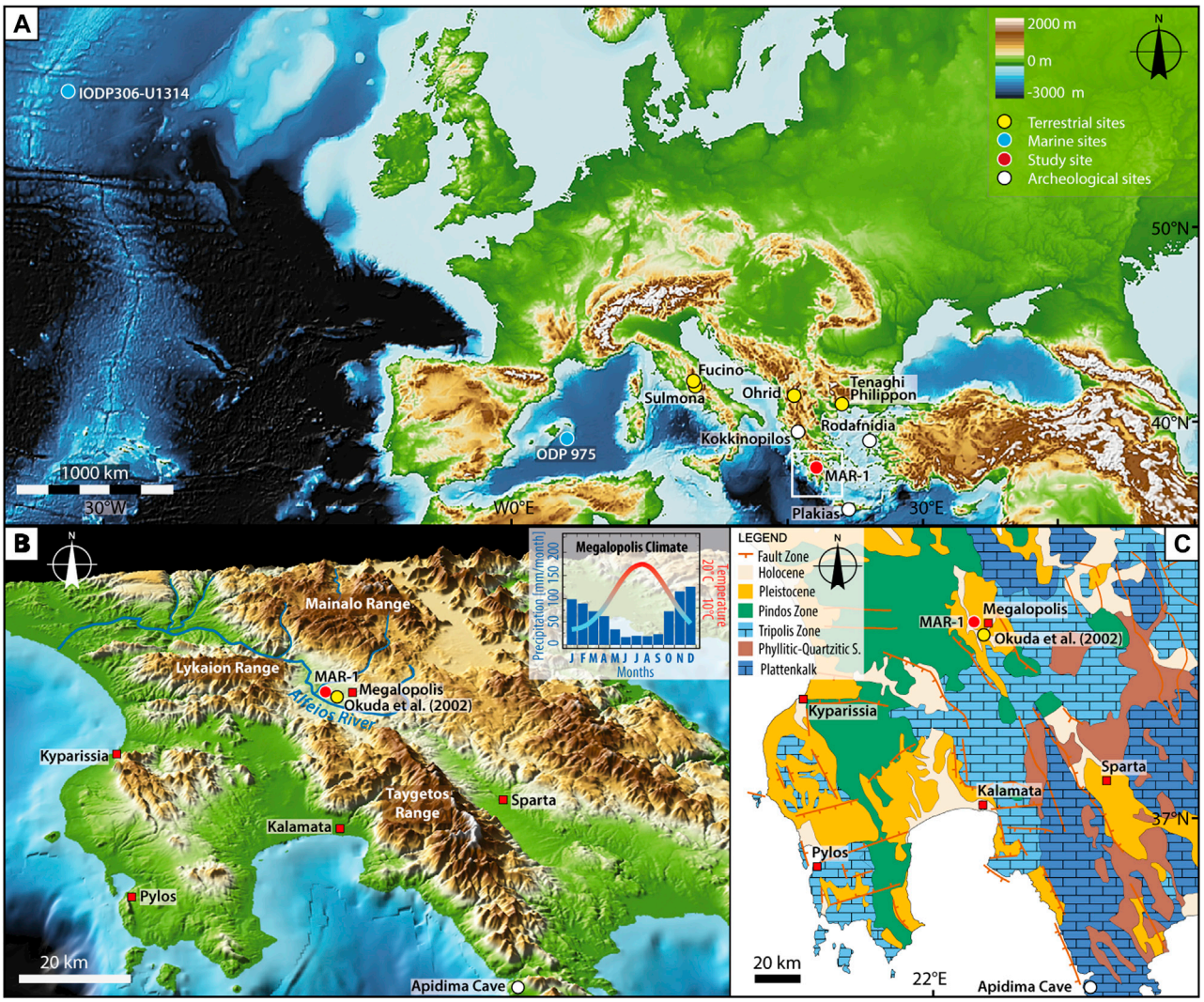

FIGURE 1 | Geographical and geological setting of MAR-1. **(A)** Overview map of Europe and the North Atlantic with sites mentioned in the text. MAR-1 is located at 37.24°N and 22.05°E. **(B)** 3D image of SW-Central Peloponnese (by GeoMapApp) showing the location of the archeological site MAR-1 (red circle) and pollen record by Okuda et al. (2002) (yellow circle) in the Megalopolis Basin. The insert shows 40-years climate average of the study region (http://iridl.ldeo.columbia.edu). **(C)** Geological map of SW-Central Peloponnese modified after Kleman et al. (2016) for the website http://www.borntraeger-cramer.de/journals/zfg.

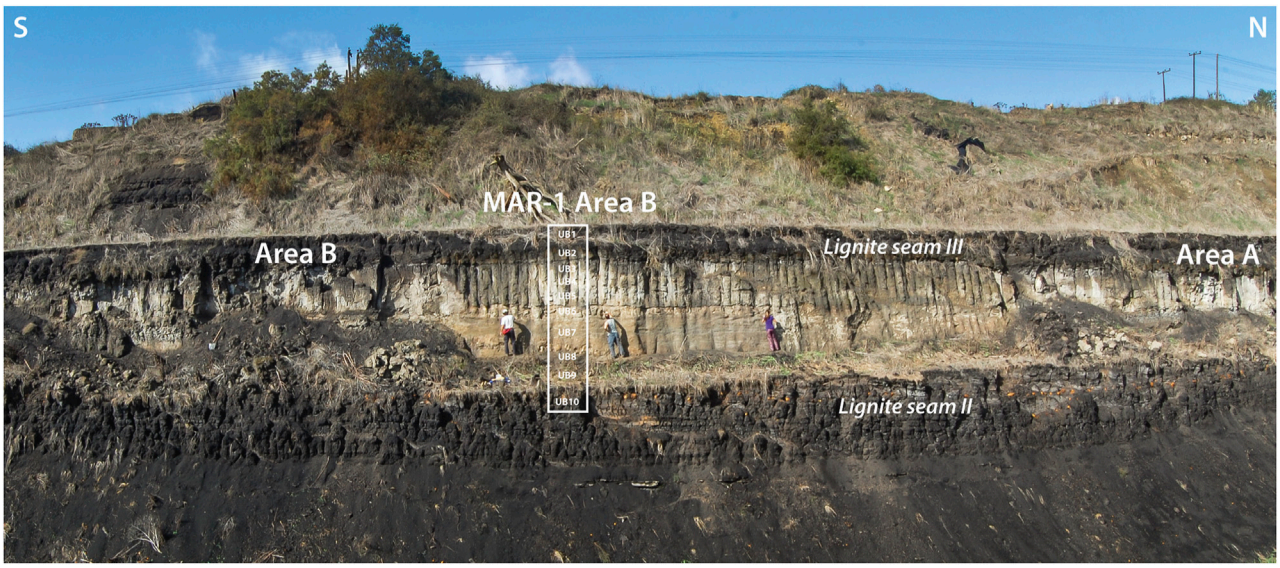

FIGURE 2 | Panoramic view of the section profile at MAR-1 with excavation areas A and B between the lignite seams LGII and LGIII. The white box marks the sampling area and indicates the distribution of the stratigraphic units UB1 to UB10.

clastic and lignite layers, rich in fossil flora and fauna, reaching back to ~780 ka (Mädler, 1971; Sickenberg, 1975; van Vugtet al., 2000; Siavalas et al., 2009; Karkanas et al., 2018; Tourloukis et al., 2018a). During a systematic survey of the Megalopolis Basin in 2013, the Lower Paleolithic archeological site of MAR-1 was discovered between the upper two lignite units (LGII and LGIII, **Figure 2**) at the northwestern margin of the basin with an age of ~480–420 ka (Tourloukis et al., 2018a; Thompson et al., 2018). MAR-1 is the first excavated archeological site in mainland Greece with a stratified assemblage of large mammals (e.g., elephants, hippos, cervids, bovids) and lithic artifacts attributed to the Lower Paleolithic (Panagopoulou et al., 2015; Panagopoulou et al., 2018; Tourloukis et al., 2018b; Konidaris et al., 2018; Thompson et al., 2018). The remains of the straight-tusked elephant *Palaeoloxodon antiquus* are especially notable, as the bones bear cut marks that have been interpreted as evidence of butchering activity by early hominins (Konidaris et al., 2018). The subsequent studies of the sedimentary structure and the spatial taphonomy of the finds indicate that they have an autochthonous origin, with the material being probably subjected to minimal post-depositional transport, most likely in the form of a hyperconcentrated flow (Tourloukis et al., 2018b; Giusti et al., 2018; Karkanas et al., 2018).

A recent magnetostratigraphy-based study correlated a number of commercial drill logs and two new outcrop sections in order to place MAR-1 in the geological sequence of the Megalopolis Basin; two age models were produced based on correlations of the Brunhes-Matuyama boundary and six chronostratigraphic surfaces to the astro-chronologically calibrated $\delta^{18}O$ benthic isotope record: according to the preferred age model, the sedimentary sequence at MAR-1 correlates to MIS12 at ~480–420 ka (Tourloukis et al., 2018a). This interval is known for its severe glacial conditions (e.g., Ermolli et al., 2010; Francke et al., 2016; Regattieri et al., 2016), making it remarkable to find indications for hominin activities in this time range. However, no high-resolution investigations of the local paleoenvironmental conditions before, during and after the deposition of human activities have been conducted so far, in order to assess if, how and when the Megalopolis Basin could have served as a refugium. Here we present a multi-proxy high-resolution study consisting of micropaleontological and geochemical analyses on a 6 m sequence directly adjacent to excavation Area B, MAR-1. The study aims at producing a continuous local reconstruction of water levels of the Marathousa paleo-lake in response to regional and global climate changes, offering additional information on the environmental backdrop of the hominin presence, and further chronological constraints for the archeological remains.

GEOGRAPHICAL SETTING

Catchment Geology

The Megalopolis Basin, situated on the central Peloponnese in southern Greece, is an intramontane half-graben basin (**Figure 1**), which formed during the Pliocene and is currently one of the largest coal mining districts in Greece (e.g., Vinken, 1965; Karkanas et al., 2018). The NNW-SSE oriented elliptically shaped basin has a maximum extension of 18 km at an altitude of 330–450 m above sea level (a.s.l.). The basin itself comprises elongated NNW-SSE-running hills and almost flat areas with slope inclinations of 0–25% and covers ~250 km^2. It is bounded by the mountain ranges of Mainalo to the east (1,981 m a.s.l.), Lykaion to the west (1,421 m a.s.l.) and Taygetos to the south (2,404 m a.s.l.).

The northeastern catchment of the Megalopolis Basin consists of the Plattenkalk series (Permian–Eocene, possibly Oligocene;

TABLE 1 | Geology of the Megalopolis Basin according to Tsiftsis (1987), [1]Dornsiepen et al. (2001), [2]Baltatzis and Katagas (1984), [3]Lekkas et al. (2002).

Stage	Group	Formation-unit	General lithology	Mineral composition (besides others)	Outcrops in the Megalopolis Basin	Other characteristics
Permian to Eocene/ Lower Oligocene[1]	Plattenkalk Series	N.A.	Crystaline, cherty limestone and phyllite, flysch	N.A.	NE	N.A.
Carboniferous to Lower Triassic[2]	Phyllitic-Quartzitic Series	N.A.	Metamorphic rocks, phyllite, mica-schist, quartzitic schist and quartzite	Carbonate, chlorite, epidote, glaucophane, graphite, mica, sphene, tourmaline, zircon	E, SE	N.A.
Upper Carboniferous to Lower Triassic[3]	Tripolis Zone	Tyros beds	Graphitic limestone, sandy micaceous limestone, (calcareous) phyllite	Brucite, carbonates, Fe-oxide/-hydroxide, feldspar, limestone, mica, quartz, sericite	NE	N.A.
Upper Triassic to Upper Eocene		Limestones and dolomites	Uniform marine dolomite, (dolomitic/bituminous) limestone, basal conglomerate, bauxite	Carbonates	E, far NE, bottom of Lousios river valley	N.A.
Upper Eocene to Upper Oligocene/ Lower Miocene		Flysch	Sandstone, shale, (marly) siltstone, (bituminous) limestone with cherts, conglomerate (sandstone, radiolarite, basic igneous rock, bauxite (local)	Carbonates, minerals contained in pebbles and conglomerates of other groups	E, far N, both sides of the Lousios river valley	Reddish-brown limonitic crust due to pre-flysch weathering, olistoliths
N.A.	Tectonic block	Tectonic block	Mélange of tripolis and pindos zone (sandstone, chert, igneous rock, conglomerate, limestone…)	N.A.	Base of Pindic nappe	N.A.
Upper Cretaceous (Cenomanian to Turonian)	Pindos Zone	The 'First Flysch'	Chert, cherty pelite/clay, fine-grained sandstone, small bodies of basic igneous rock (spilite and diabase)	Quartz, mica, feldspar, chlorite, minerals in: cherty, basic igneous rock, limestone, recrystallised fossils	NW, W	N.A.
Upper Cretaceous (Turonian to Maastrichtian)		Upper Cretaceous limestones	Limestone, pelite, chert, silt-/sand-size limeclast	Calcite, dolomite, Fe-oxide, mica	E, SE, NW, W	Stylolithes very common
Upper Cretaceous (Upper Maastrichtian) to Paleocene		Flysch	Limestone, marly limestone, chert, clastic-bioclastic limestone containing fragments of cherty rocks, basic igneous rock, grains of garnet	Calcite, carbonate, garnet	NW, W	N.A.

Dornsiepen et al., 2001) containing crystalline, cherty limestones, as well as phyllites and flysch (**Figure 1**, **Table 1**; Tsiftsis, 1987). In the SE and S of the basin, the Phyllitic-Quartzitic Series (Carboniferous–Lower Triassic; Baltatzis and Katagas, 1984; Tsiftsis, 1987) crops out. It is composed of metamorphic rocks, phyllites, schists and quartzites, containing chlorite and sphene (Tsiftsis, 1987). In the E, NE and N, the formations of the Tripolis Zone are encountered. The base of the Tripolis Zone is marked by the Tyros Beds which consist of graphitic or sandy micaceous limestones and phyllites (Upper Carboniferous–Lower Triassic; Tsiftsis, 1987; Lekkas et al., 2002). These are followed by limestones and dolomites of the Upper Triassic to Upper Eocene. The youngest parts of the Tripolis Zone are fine to medium grained sandstones, shales, limestones and conglomerates of the Tripolis Flysch (Upper Eocene–Upper Oligocene, Miocene; Tsiftsis, 1987). Outcrops of the Pindos Zone (Lower Cretaceous-Paleocene) can be found in the W and NW, as well as E and SE of the catchment (Tsiftsis, 1987). The oldest part of the Pindos Zone is the so-called "First Flysch" from the Lower Cretaceous, consisting of fine-grained sandstones, radiolarites and in some places, small bodies of igneous rocks (Tsiftsis, 1987). It transitions into Upper Cretaceous limestones and eventually into the Pindos Flysch with its cherts and limestones and in some areas into basic igneous rocks.

During the Pleistocene, lacustrine and fluvial sediments were deposited, including the lignite-bearing Marathousa Member (**Figure 2**). The Marathousa Member has a total thickness of ~150 m at the center of the basin and spans the Middle Pleistocene (Lüttig and Marinos, 1962). Its limnic and swampy sediments show complex lithological patterns, alternating between clastic sediments (clay, silt and sand) and 5–30 m thick dark brown lignite seams intercalated with thin clastic layers (Vinken, 1965).

The primary controlling factor of the development of the drainage system was probably tectonic activity, as indicated by the presence of fault zones and deformation structures, eventually

resulting in the establishment of the Alfeios River system, which today is characterized by a mixture of rectangular, parallel and dendritic patterns flowing northwards along major fault zones (Vinken, 1965; Tsiftsis, 1987). In 2002, the Alfeios River itself was rerouted into a 7 km long channel along the western side of the lignite mine (Manariotis and Yannopoulos, 2014). Its mean annual pH value is ~7.8 and during winter it reaches a maximum of 8.4 (Tsiftsis, 1987). In addition to the Alfeios River, the basin is also supplied by a karstic aquifer characterized by waters of pH 7.7–7.8 (Daskalaki, 2002; Siavalas et al., 2009).

Local Climate

The modern-day climate in Greece is characterized by hot summers and mild winters, where the winter precipitation exceeds that of summer (**Figure 1**, Kutzbach et al., 2014). The University of East Anglia Climatic Research Unit calculated monthly climatologies based on historical data (1971–2000) for the Megalopolis region and categorized it as a Mediterranean hot summer climate (Csa, according to Köppen, 1918). Monthly temperatures reach their maximum in July (mean 21.5°C) and their minimum in January (mean 4.5°C). The annual precipitation is unevenly distributed over the year and ranges from 750 to 1,000 mm/a (Okuda et al., 2002) with the majority falling in December (~125 mm) and then gradually decreasing until June (~20 mm). Additionally, storm tracks occur mostly during winter and originate either from the N-Atlantic or from the northeast, where cold Eurasian air meets the warm air above the Mediterranean (Kutzbach et al., 2014). These storm tracks vary in their intensity and frequency from year to year, depending on large-scale circulation patterns like the North Atlantic Oscillation (NAO) and the Arctic Oscillation (AO). Strong storm tracks are associated with negative phases of NAO and AO, whereas winter droughts in contrast, correlate to positive phases of NAO and AO (Givati and Rosenfeld, 2013; Kutzbach et al., 2014).

Marathousa 1 Sediments

MAR-1 extends over 92 m along the N-S axis and is divided into excavation Area A and Area B (**Figure 2**). At Area A, a dense accumulation of bones belonging to a single individual of the European straight-tusked elephant was found, as well as lithics and other faunal remains (Panagopoulou et al., 2015, 2018; Konidaris et al., 2018). The remains occur at ~349 m a.s.l. and cover ~87 m^2. Area B is dominated by a greater diversity and density of lithics together with other faunal remains. It is located 60 m south of Area A and covers ~78 m^2 at ~350 m a.s.l. Both areas contain fossils of micro- and macro-fauna and flora such as hippos, elephants and rodents, as well as seeds, fruits, and charcoal (Doukas et al., 2018; Field et al., 2018; Konidaris et al., 2018; Michailidis et al., 2018). Karkanas et al. (2018) subdivided the stratigraphy of MAR-1 into sedimentary units separated by an erosional contact into two major sequences, with the lower showing a coarsening upward and the upper a fining upward trend (**Figure 3**). At Area B, where the most complete sequence is better exposed and accessible, the lower part encompasses UB10 to UB6, with UB10 consisting of black lignitic clay that is transitioning gradually into UB9. On top of it, UB9 is mainly characterized by dark grey, massive and organic rich clayey sands, but also contains thin, wavy and ripple bedded sand laminae. The unit has been identified to be, at least partly, the result of sub-aqueous hyperconcentrated flows by Karkanas et al. (2018). The transition from UB9 to UB8 and later to UB7 is gradual. Both, UB8 and UB7, strongly resemble each other with light grey, wavy to lenticular bedded, sometimes massive fine silts and sands with deformation structures at their base. The three units UB9 to UB7 are reported to have been influenced either by waves or by storm events (Karkanas et al., 2018). The lower, coarsening upward sequence is capped by UB6 with its bluish-grey, massive muddy sands with deformation structures and mud cracks on top. The contact between the lower (UB10–UB6) and the upper sequence (UB5–UB1) is of erosional nature, with UB6 being completely eroded laterally in some parts of the site. Karkanas et al. (2018) identified this boundary to be a scour surface, i.e., it is most likely a localized erosion. Based on luminescence data from the excavation, they also conclude that the resulting hiatus does not produce a statistically significant time gap (Jacobs et al., 2018; Karkanas et al., 2018). The upper part of the sequence contains units UB5–UB1 and is dominated by the influence of mudflows and to a lesser extent by fluviatile flows (Karkanas et al., 2018). The units UB5–UB2 are very similar to each other as all contain dark grey massive and organic-rich silty and muddy sands, as well as showing an internal fining upward trend. UB5–UB3 are also characterized by an intraclast-rich base. These intraclasts are explained as partly eroded lithified sediment from the surrounding area and partly reworked material from the underlying units (Karkanas et al., 2018). An erosional contact, as well as a thin layer with mud cracks separates UB5 and UB4, indicating an exposure of the mudflat. The base of UB4 represents the fossil-rich horizon of Area B. UB4 and UB3 are both slightly eroded at their top. A scouring surface separates UB3 from UB2, the latter also containing a large amount of shell fragments. The whole sequence is capped by the black lignite and lignitic clay with a sandy component of UB1. The transition from UB2 to UB1 is gradual with local sand-rich channels.

MATERIALS AND METHODS

Sampling and Grain Sizes

A cleaned 6-m thick profile, 3 m north of Area B at MAR-1, was sampled in 5-cm intervals (**Figure 2**, **Figure 3**). The sediment profile was subdivided into ten units, UB1–UB10 (young to old), according to lithological changes as described by Karkanas et al. (2018). For the determination of grain sizes, 33 samples were cleaned following standard protocols, using 30% H_2O_2 to remove organic matter (OM) and 10% HCl to remove carbonates. The remaining solution was dispersed with ultrasonic sound and wet sieved through a 63 μm mesh. The fraction >63 μm and <63 μm were freeze dried and their weight was determined. The grain size distribution in sediments is influenced by a variety of factors, such as the depositional environment (Dearing, 1997; Digerfeldt et al., 2000; Chen et al., 2004; Liu et al., 2015; Mannella et al., 2019). Coarse grain sizes might reflect high-energy deposits like heavy precipitation-induced river

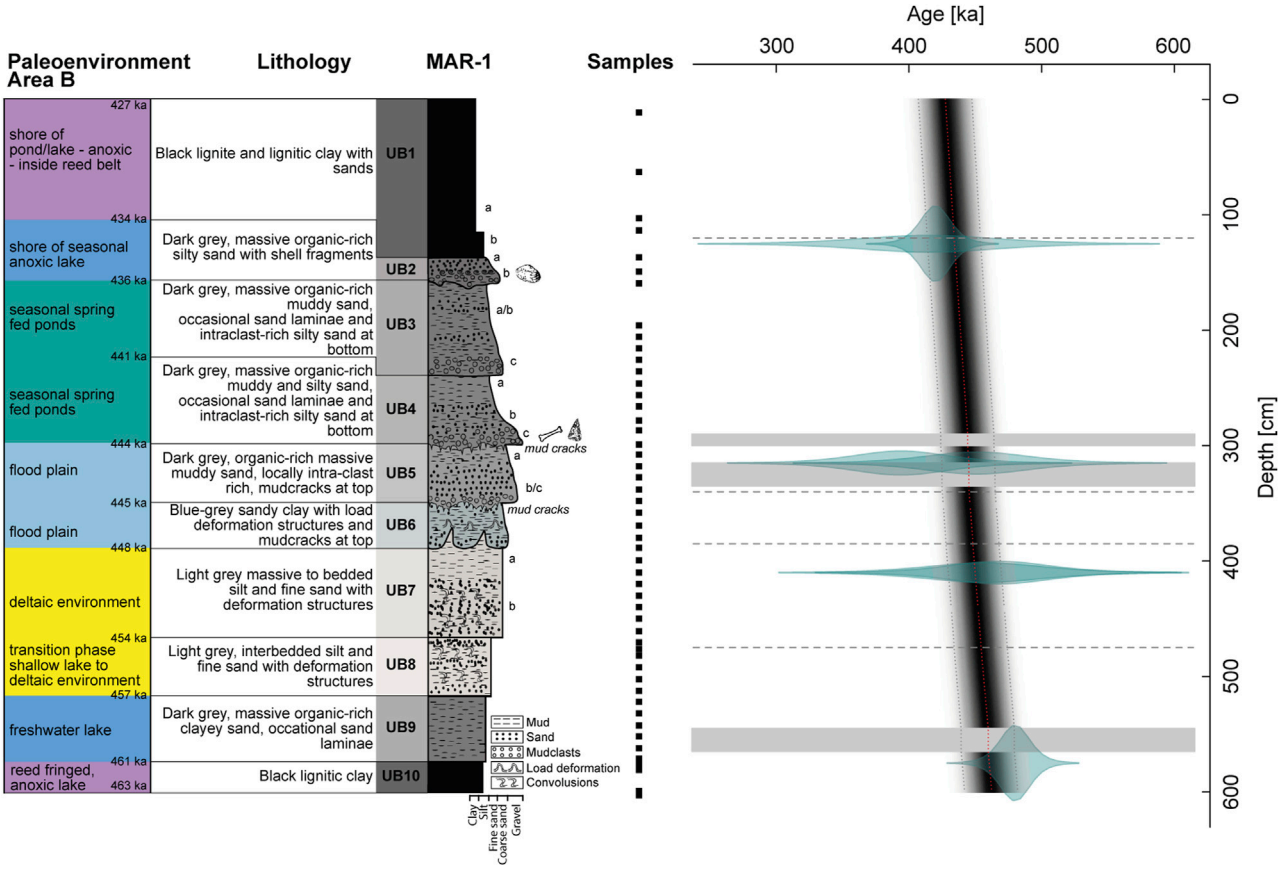

FIGURE 3 | The paleoenvironmental interpretation, sample positions and age-depth model (Bacon v2.3.9.1) (this study) in context with the lithological description from Karkanas et al. (2018) of MAR-1 Area B. Right panel: age-depth model. Grey shades: calculated ages (darker indicates more likely ages). Dotted lines: 95% confidence interval. Dashed lines: sequence boundaries. Grey bars: slump structures. Transparent green: input ages with error margins.

TABLE 2 | Overview of input ages of MAR-1 age model.

Depth (cm)	Age	Error (ka)	Reference
125	420	10	Tourloukis et al. (2018a)
125	415	46	Jacobs et al. (2018)
315	451	35	Jacobs et al. (2018)
315	394	32	Jacobs et al. (2018)
410	457	39.5	Jacobs et al. (2018)
410	468	34	Jacobs et al. (2018)
575	480	10	Tourloukis et al. (2018a)

input (Liu et al., 2015; Mannella et al., 2019), while fine grains may indicate low-energy environments (Mannella et al., 2019). This study applies a simplified approach with a division of the grain sizes in coarse (>63 μm) and fine (<63 μm) fractions. Based on those assumptions about the environmental energy, the implied distance to the shore, the transport mechanism and the water level of the potential water body are made.

Chronology

In order to better constrain the different sedimentary units of UB1–UB10, a Bayesian age model for MAR-1 was computed using the age-modelling software rBacon v2.3.9.1, written in R. Based on conclusions by Tourloukis et al. (2018a), the starting point of the sequence was set to 480±10 ka and the upper end to 420±10 ka; no additional tie points were used. Tourloukis et al. (2018a) suggested two different intervals for the deposition of MAR-1, assigning the sequence between the base of UB9 and the top of UB2 to either the glacial Marine Isotope Stage (MIS) 12 (480–420 ka) or to MIS14 (560–530 ka) based on a combination of magnetostratigraphy of the Marathousa member, chronostratigraphical correlations, and classical oxygen isotope variability by Lisiecki and Raymo (2005). The MIS12 option is the preferred model, because it also agrees with the pMET-pIRIR dating method by Jacobs et al. (2018) from the same outcrop, as well as with the small mammal biochronology by Doukas et al. (2018) (**Table 2**). (Blackwell et al., 2018) published ESR data from the upper part of the MAR-1 sequence correlated with UB2 and UB4, respectively. Their data suggested an early MIS13 age, and therefore an interglacial period for this part of the sequence. The estimated ages are not compatible with any of the other dating models proposed by Tourloukis et al. (2018a). In addition, based on findings by numerous studies such as Nickel et al. (1996) (van Vugt et al., 2001), or (Okuda et al., 2002), we also agree that the clastic intervals of the Marathousa Member probably

TABLE 3 | Input parameters for the Bacon age model and the environmental interpretation based on this study and lithological descriptions by Karkanas et al. (2018).

Unit	Boundaries (cm)	Interpretation	Sedimentation rate (mm/a)	Reference list	Acc. Shape	Acc. Mean (a/cm)	Mem. Mean	Mem. Strength	Assumed sedimentation
UB1	120–0	Swamp-like environment, reed belt	0.18	A	1.4	55	0.7	4	Continuous
UB5—UB2	340–120	Seasonal pond close to river mouth	0.17	A	8	60	0.1	20	Variable
UB6	385–340	Flood plain	0.15	B	4	65	0.7	4	Continuous
UB7	475–385	Riverine	0.14	B	8	70	0.1	20	Variable
UB10—UB8	600–475	Reed fringed, anoxic lake	0.13	B	1.6	75	0.7	4	Continuous

Bacon code

Bacon (core = "MAR1B", thick = 5, d.min = 0, d.max = 600, d.by = 5, sep = ",", dec = ".", depth.unit = "cm", age.unit = "a", ccdir = "," BCAD = FALSE, acc.shape = c (1.4,8,4,8,1.6), acc.mean = c (55,60,65,70,75), slump = c (290,300,315,335,545,565), boundary = c (120,340,385,475), mem.mean = c (0.7,0.1,0.7,0.1,0.7), mem.strength = c (4,20,4,20,4), runname = "F1_134", ssize = 2000, cc = 0)

Reference list for Acc. Mean and sedimentation rates

A	Fuccino:	Giaccio et al. (2019)	B	Dead Sea:	Kagan et al. (2018)	Lake Ohrid:	Francke et al. (2016)
	Lake Ohrid:	Panagiotopoulos et al. (2020)		Eastern Africa:	Trauth et al. (2015)	Lake Superior:	Kemp et al. (1978)
	Lake Superior:	Kemp et al. (1978)		Fuccino:	Giaccio et al. (2019)	Megalopolis:	Tourloukis et al. (2018a)
	Megalopolis:	Okuda et al. (2002); Tourloukis et al. (2018a)		Glenhead:	Blaauw and Christen (2011)	–	–

Acc. = accumulation Mem. = memory

correspond to cold (glacial) stages, while the lignite seams should represent warm (interglacial) periods. Although we cannot rule out the possibility that the ages presented by (Blackwell et al., 2018) are correct, they cannot be included in the same age model with the other ages.

During the Bayesian age modeling, rBacon divided the profile (600 cm) into 5-cm slices (*thick*). A gamma distribution based on the input parameters describes the sedimentation rates (*a/cm*; **Table 3**). Other general age-model settings of Bacon included the age (*age.unit*) and depth (*depth.unit*) units, which were set to *years* and *cm*, respectively. The calculated output ages were set in rBacon to years before AD 1950 (BP), as well as the confidence interval (*prob*) to report of 95%. Additionally, no calibration curve (*cc = 0*) was used, as the input ages were based on the potential time intervals identified by Tourloukis et al. (2018a). For the high-resolution age model, the whole profile was segmented into five different depositional environments divided by boundaries (*boundary*). For each of them, a rough framework, concerning their sedimentation behavior was estimated, based on numerous published records with similar sediments (e.g., Frogley, 1998; Okuda et al., 2002; Blaauw and Christen, 2011; Trauth et al., 2015; Francke et al., 2016; Wagner et al., 2019) that also concur with the sedimentation rates already suggested for the Megalopolis Basin (**Table 3**; Okuda et al., 2002; Tourloukis et al., 2018a; Van Vugt et al., 2000).

Based on the sedimentology the first segment (600–475 cm) was assumed to represent a reed-fringed lake that slowly changed to a deltaic, river-influenced environment. An overall low but continuous sedimentation rate was presumed (*acc.shape = 1.6, acc.mean = 75, mem.mean = 0.7, mem.strength = 4*). The next segment was considered to be dominated by a deltaic river system (475–385 cm) with a slightly higher, highly variable and unsteady sedimentation rate (*acc.shape = 8, acc.mean = 70, mem.mean = 0.1, mem.strength = 20*). For the third one (385–340 cm) the study area was assumed to have turned into a flood plain with a marginally fluctuating but continuous sedimentation (*acc.shape = 4, acc.mean = 65, mem.mean = 0.7, mem.strength = 4*). The following segment (340–120 cm) remained initially a flood plain but started to turn into a pond that was fed by a seasonal spring, with higher, highly variable and unsteady sedimentation rates (*acc.shape = 8, acc.mean = 60, mem.mean = 0.1, mem.strength = 20*). The last segment (120–0 cm) was presumed to represent a swamp-like environment within a reed belt at the edges of a lake, with continuous and high sedimentation (*acc.shape = 1.4, acc.mean = 55, mem.mean = 0.7, mem.strength = 4*). The various slumping structures (*slump*) identified by Karkanas et al. (2018) were narrowed down to three events at 565–545 cm, 335–315 cm and 300–290 cm, that were incorporated into the model (**Figure 3**, **Table 3**).

Silicate Microfossils, Ostracods and Other Microscopic Components

Silicate (SiO_2) microfossils, in particular diatoms and sponge spicules were analyzed in 47 samples following the protocol of Battarbee (1986). The morphological identification was performed at 400x and 1000x magnification using an Olympus BX51 light microscope as well as a Phenom XL Desktop Scanning Electron Microscope. Diatoms provide the potential to better constrain limnological parameters such as nutrients, pH, conductivity, clearness of the water and relative distance to the shore. Occurrences of sponge spicules are recorded in sediments of many freshwater habitats (Harrison, 1988). The skeletons of freshwater sponges are comprised of siliceous structures and are chemically identical to diatom frustules, which makes them resistant to decomposition under most conditions (Frost et al., 2001). The disintegrated skeletal network of freshwater sponges is composed of needle shaped spicules and spherical gemmules.

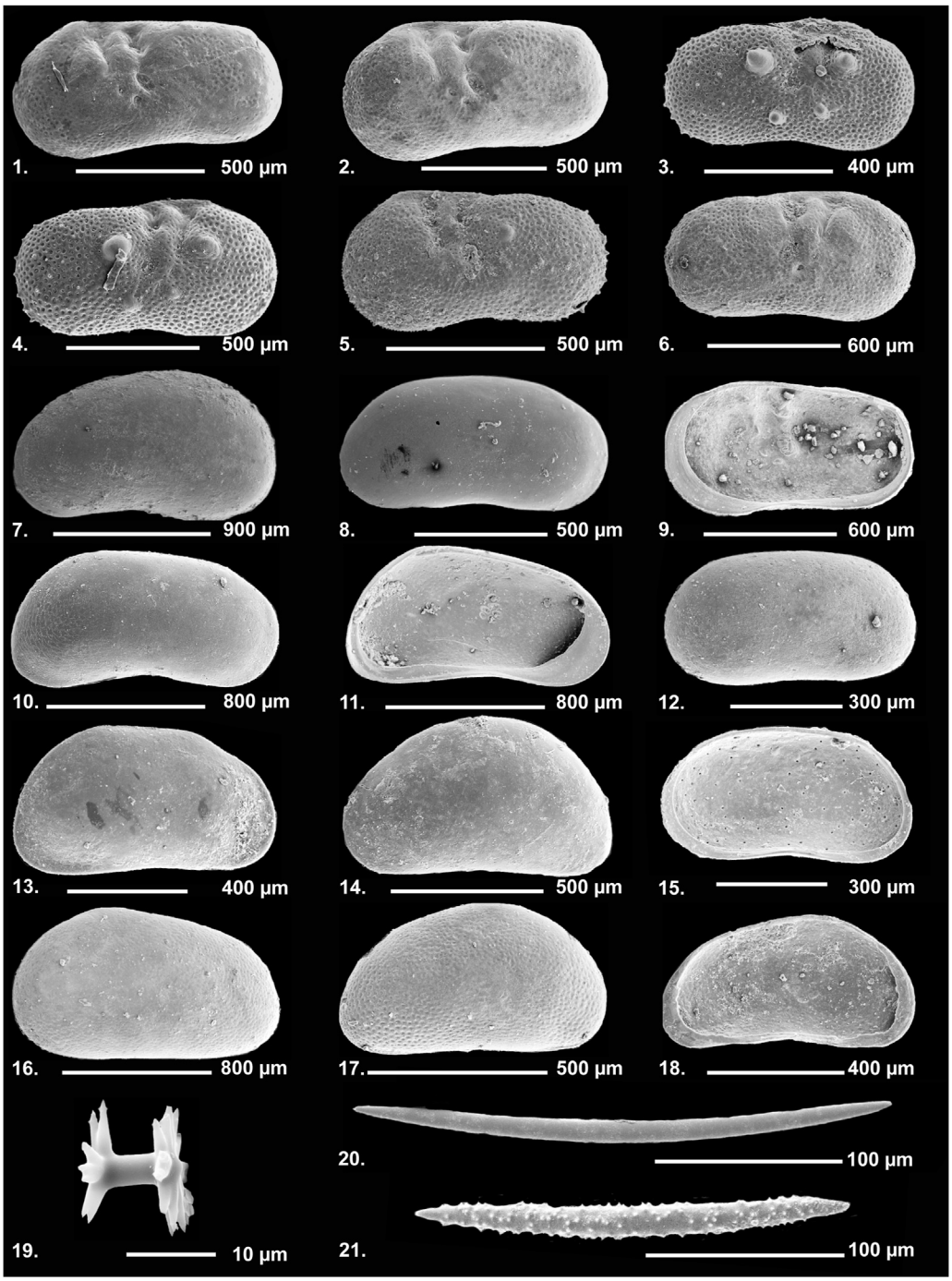

FIGURE 4 | SEM images of ostracods (1–18) and sponge spicules (19–21) from Marathousa-1 Area A and Area B. RV = right valve, LV = left valve, A = adult, im = immature, fem = female, m = male, ext = external view, int = internal view. 1) *Ilyocypris getica*, LV, a, fem, ext. 2) *I. gibba*, LV, a, fem, ext. 3) *I. gibba*, RV, im, ext. 4) *I. decipiens*, RV, im, ext; 5) *I. decipiens*, LV, im, ext; 6) *I. bradyi*, RV, a, fem, ext. 7) *Candona neglecta*, LV, a, m, ext. 8) *C. neglecta*, RV, im, ext; 9) *I. bradyi*, RV, a, fem, int. 10) *Neglecandona altoides*, RV, a, fem, ext. 11) *N. altoides*, RV, a, fem, int. 12) *Candona* sp., LV, im, ext. 13) *Pseudocandona marchica*, RV, a, m, ext. 14) *Psychrodromus* sp., LV, im, ext. 15) *Candona* sp., RV, im, int. 16) *Prionocypris zenkeri*, LV, a, fem, ext. 17) *Potamocypris zschokkei*, RV, a, ext. 18) *P. zschokkei*, LV, a, int. Sponge spicules: 19) Gemmoscleres. 20) Megascleres. 21) Microscleres.

Sponges generally require relatively clean-water conditions to sustain the filtering of their water processing system additionally to their potential algal symbionts, who require access to light (Frost et al., 2001). In this study, we used the abundance of sponge spicules and diatoms to evaluate the habitat conditions for organisms.

TABLE 4 | Ostracods and sponges.

Ostracod species	Habitat	Occurence	Reference
Neglecandona (formerly *Candona*) *angulata*	Halophilic; lives in permanent brackish waters with upper salinity limits of 13.4% that derive from small streams and springs	UB3	De Decker (1979), Fuhrmann (2012), Meisch et al. (2019)
Candona neglecta	Oligothermophyllic; inhabits low salinity water (salinity 0.5–16‰) deriving from small streams, ponds and springs; resistant taxon that can even survive desiccation	UB4	Meisch and Wouters (2004), Wagner (1957)
Ilyocypris bradyi	Oligothermophyllic; lives in flowing water of springs or where these waters runoff	UB4	Fuhrman (2012)
Ilyocypris decipiens	Freshwater or low salinity environments with a temperature range between 14 and 20°C	UB3	Meisch (2000)
Ilyocypris getica	Common in mediterranean environments; it can survive extreme conditions but has a typical temperature range of 10–15°C	UB3, UB4	Fuhrmann (2012)
Ilyocypris gibba	Freshwater to oligohaline; has an upper salinity limit of 5% and can withstand temperatures not lower than 10.5°C; can often be found in areas with swampy vegetation	UB4	Devoto (1965)
Neglecandona altoides	Lives mostly in permanent small water bodies; can also be found in temporary ponds which desiccate in summer	UB2, UB3, UB4	Fuhrmann (2012)
Potamocypris zschokkei	Found in springs	UB3, UB7	Fuhrmann (2012)
Prionocypris zenkeri	Shallow slowly flowing vegetated waters	UB4	Fuhrmann (2012)
Pseudocandona marchica	Lacustrine; can also be found in ponds	UB4	Devoto (1965)
Sponge spicule type	**Morphology**	**Occurence**	**References**
Gemmoscleres	Needle-like, dumbbell-shaped, spined or smooth, great variations in the shape of their ends; 8–300 µm, essential for the identification of freshwater sponges	UB4, UB7	Frost et al. (2001), Reiswig et al. (2010)
Megascleres	Needle-like, smooth or spined, and with a moderately high relief; 150–450 µm	UB1-UB9	Frost et al. (2001), Reiswig et al. (2010)
Microscleres	Needle-like, dumbbell-shaped; variations in presence and form of spines; do not occur for every species; 8–130 µm	UB3, UB5, UB7	Frost et al. (2001), Reiswig et al. (2010)

Ostracods and other microscopic remains larger than 125 µm were analyzed in 47 samples (12 from Area A, UA1–UA4; 35 from Area B, UB1–UB10; **Figure 3**). 500 g of dry sediment was treated with 10% H_2O_2 until reaction stopped (3–24 h). The residues were washed through a 2 mm and 125 µm sieve using distilled water and dried at 50°C. All microfossils (ostracods, gastropods and opercula, charophyte gyrogonites, thecamoebians, fish bones/teeth) were extracted under OPTIKA stereoscopes. Ostracods were further photographed using a JEOL 6300 Scanning Electron Microscope (**Figure 4**). Identification, ecology and distribution information of ostracod species were derived mainly from Danatsas (1994), Meisch (2000), Frenzel et al. (2010), Fuhrmann (2012), Mazzini et al. (2014) and several papers of the Stereo Atlas of Ostracod Shells (Athersuch et al., 1973-1996). The number of species is an indicator of the stability of the system. Taphonomic indices for the dominant species were calculated and interpreted after Schellenberg (2007) (**Table 5**) with: a) The adult to juvenile ratio (A/J) as an indirect indication for the energy of the environment. Values between 0.125 and 0.25 are typical for *in situ* death assemblages. Higher values reflect *in situ* death assemblages with taphonomic removal of juveniles. Significantly lower values could reflect transported juvenile valves or a mass death event (Belis, 1997; Schellenberg, 2007). b) The right valve/left valve ratio (RV/LV) is also considered as an indirect proxy for the energy of the depositional environment (Breman, 1980). c) The percent articulation ratio (%Art.) is an indicator of a disturbed sediment–water interface when values are lower than the common range value of most samples (Frenzel and Boomer, 2005; Hussain et al., 2007). For certain samples and species no taphonomic indices were applied, as the total number of valves per sample was too low.

X-Ray Fluorescence Analysis

Conventional X-ray fluorescence analysis (XRF) of major oxides (SiO_2, Al_2O_3, Fe_2O_3, CaO, MgO, K_2O, Na_2O, TiO_2, MnO, P_2O_5) and further trace elements (Ba, Co, Cr, Ni, Rb, Sr, V, Y, Zn, Zr, La) was applied to a total of 25 samples from all units. The sediment was first ground to powder, then mixed with 7.5 g MERCK spectromelt A12 (a mixture of 66% Li-tetraborate and 34% Li-metaborate) and melted at 1,200°C to fused beads using an Oxiflux system from CBR Analytical Service. Measurements were collected using a Bruker AXS S4 Pioneer XRF device (Rh-tube, 4 kW). Analytical errors were in the range of 10% (Relative Standard Deviation, RSD). To achieve the elemental proportions of each oxide, the weight-percentages were multiplied by a conversion factor[1] following **equation 1**, with n describing the amount of substance (mol), m_1 the amount of the individual element (wt%), m_2 the mass of the oxides from the XRF analysis and M the molar mass (g mol^{-1}).

$$n = \frac{m}{M} \leftrightarrow \frac{m_1}{M_1} = \frac{m_2}{M_2} \leftrightarrow m_1 = m_2 * \frac{M_1}{M_2} \quad (1)$$

$$\text{Example: } m(Si) = m(SiO_2) * \frac{M(Si)}{M(SiO_2)}$$

For paleoenvironmental interpretation, single element distributions and ratios are commonly used (e.g., Rothwell and Croudace, 2015; Longman et al., 2019).

Organic Carbon and Nitrogen Content

Concentrations of total carbon (TC) and total nitrogen (TN) were measured on 45 powdered samples (39–42 mg weighed into tin

[1]https://www.sciencegateway.org/tools/fwcal.htm

TABLE 5 | Ostracod taphonomy.

Area B				*Neglecandona altoides*			*Candona neglecta*			*Candona* spp. *juveniles*	
Unit	**Sample**	**Depth (cm)**	**Age (ka)**	**A/J**	**%Art**	**RV/LV**	**A/J**	**%Art**	**RV/LV**	**%Art**	**RV/LV**
UB2	Nr 1 UB2	102	433	–	–	–	–	–	–	–	–
UB2	MAR 04—CZ/TM	125	434	–	–	–	–	–	–	–	–
UB4	Nr 3 UB4	192	438	–	–	–	–	–	–	15	–
UB3	MAR 07—CZ/TM	215	440	–	–	–	–	–	–	7	0.5
UB3	MAR 08—CZ/TM	235	441	–	–	2.0	–	6	1.3	–	–
UB4	MAR 09—CZ/TM	245	442	0.8	–	2.0	–	2	1.9	–	–
UB4	MAR 10—CZ/TM	275	443	–	40	1.5	–	–	–	–	–
UB4	MAR 11—CZ/TM	295	445	4.0	67	–	5.0	67	1.0	36	1.3
UB7	MAR 18—CZ/TM	450	453	–	–	–	–	–	–	–	–
UB7	MAR 19—CZ/TM	475	454	–	–	–	–	–	–	–	–

Area A				*Neglecandona altoides*			*Candona neglecta*			*Candona* spp. *juveniles*	
Unit	**Sample**	**Elevation (m a.s.l.)**	**Age (ka)**	**A/J**	**%Art**	**RV/LV**	**A/J**	**%Art**	**RV/LV**	**%Art**	**RV/LV**
UA2	Sample 5	351.1	–	–	–	–	–	–	–	–	0.9
UA2	Sample 7	350.53	–	–	–	–	–	–	–	–	0.9
UA3a	Sample 9	349.94	–	–	–	–	–	–	–	–	–
UA3b	Sample 10	349.74	–	–	–	–	–	–	–	14	–
UA3c	Sample 11	349.71	–	–	–	–	–	–	–	–	1.0

A/J = Adult/Juvenile RV/LV = Right valve/Left valve

capsules) after combustion at 1,150°C using the Vario ELIII elemental analyzer. Approximately 39–42 g of tungsten (VI)-oxide was added to each tin capsule to guarantee stable high temperatures. Blank capsules with sulfanilic acid were used as a standard and measured three times prior to the first, after the 33rd and the final measurement, to guarantee accurate results. The percentage amount of carbon and nitrogen was calculated from its absolute gravimetric content compared to the input sample weight. If the RSD exceeded 10%, a new measurement was performed. The detection limit for TC was 0.10 wt% and for TN 0.05 wt%. The concentrations of the analysis represent the mean values of double measurements. $CaCO_3$ was determined gas-volumetrically with an Eijkelkamp Calcimeter using 0.5–2.5 g of powered sample material. $CaCO_3$ weight percentages were calculated following **Eq. 2** according to DIN 18129 with a being the volume of the produced CO_2 in cm^3, p the air-pressure in Pascal, t the room temperature in °C and E the weight of the sample material in g.

$$\frac{a \times p \times 1.204 \times 10^{-3}}{(273 + t) \times E} = wt\%CaCO_3 \quad (2)$$

The mass m (wt%) of Total Inorganic Carbon (TIC) was computed by dividing the atomic mass ratio of carbon ($M(C) = 12.00 \frac{g}{mol}$) by the atomic mass of $CaCO_3$ ($M(CaCO_3) = 100.09 \frac{g}{mol}$) and multiplying it with wt% $CaCO_3$ (**Eq. 3**).

$$m(TIC) = m(CaCO_3) * \frac{M(C)}{M(CaCO_3)} \quad (3)$$

TIC describes the amount of carbon dioxide (CO_2), carbonic acids (H_2CO_3), bicarbonates (HCO_3^-) and carbonates (CO_3^{2-}) in a sample (Rantakari and Kortelainen, 2008). The influence of H_2CO_3 is assumed to be negligible when alkaline conditions prevail. The remaining components derive from weathering of carbonates, or the production of calcifying organisms (Rantakari and Kortelainen, 2008). A good indicator of biogenic carbonates is usually a positive correlation of TIC with Ca and Sr. Total organic carbon (TOC), in contrast, describes the amount of OM, which escaped the remineralization processes during deposition (Meyers and Teranes, 2001). TOC was calculated by subtracting TIC from TC (**Eq. 4**).

$$TOC = TC - TIC \quad (4)$$

The ratio of TOC/TN (C/N) is a tool to identify the origin of OM and thus to distinguish long-term changes in the lake environment (e.g., Meyers and Benson, 1987). To yield the C/N atomic ratios that reflect biochemical stoichiometry, C/N is multiplied by 1.167 (Meyers and Teranes, 2001). Lower values of 4–10 are typical for OM based on phytoplankton, as those tend to bind high concentrations of nitrogen, whereas terrestrial, vascular plants produce values of 20 and higher. In general, most lakes have values of 10–20, indicating a mix of both vascular plants and algae (e.g., Meyers and Teranes, 2001; Cohen, 2003). The interpretation, however, must be exercised with caution, as the ratio can be influenced by multiple factors such as selective degradation or increased temperatures (Meyers and Benson, 1987; Meyers and Teranes, 2001; Cohen, 2003).

Correlation, Statistical Significance and Principal Component Analysis

In a statistical approach, the p-value for statistical significance and the Spearman correlation coefficient r_s were calculated. The p-value is used in the context of null hypothesis testing to

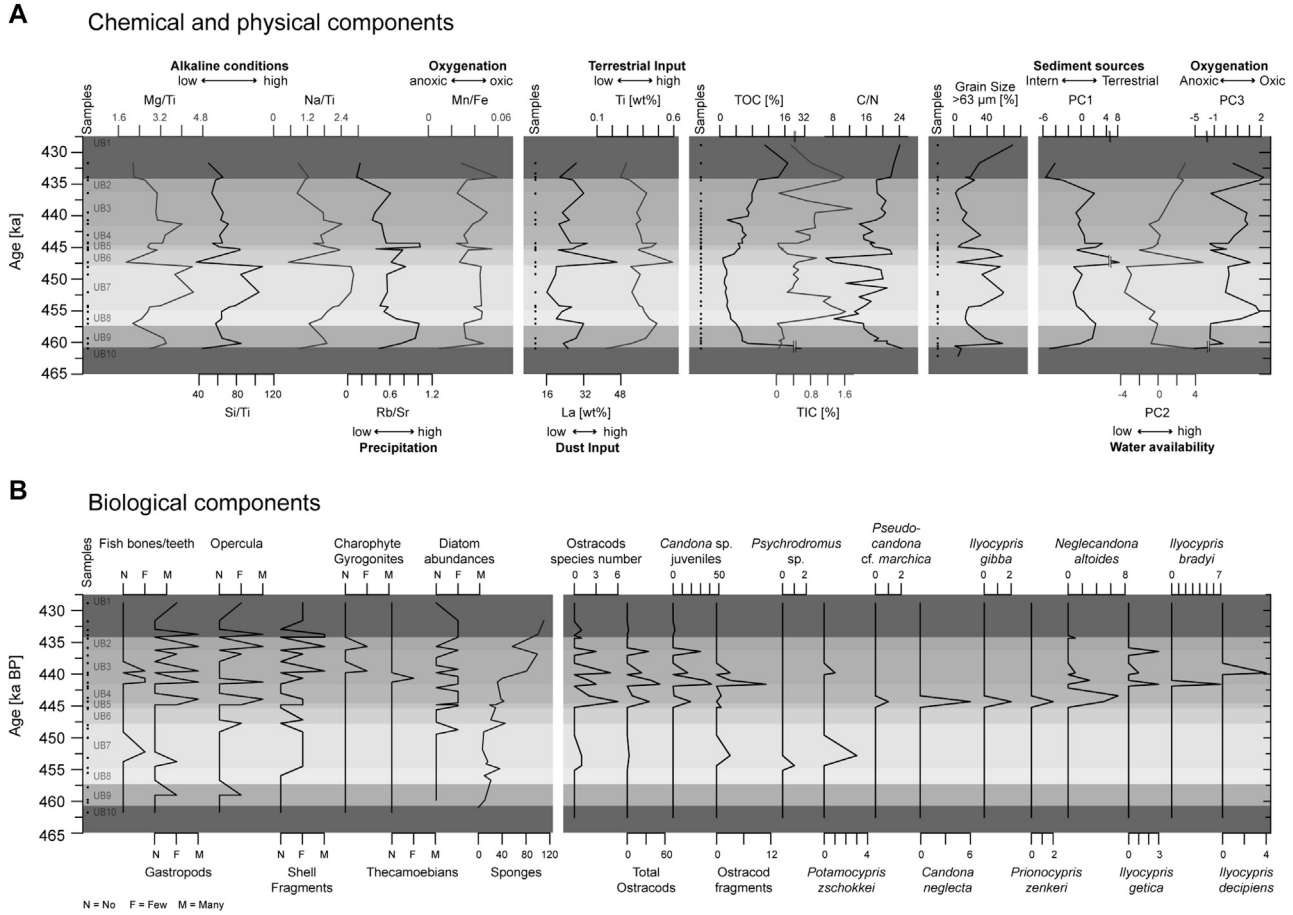

FIGURE 5 | Multiproxy data from MAR-1 Area B sediments against time. The data are divided into the categories **(A)** chemical and physical components, including the results of the PCA analysis, and **(B)** biological components.

quantify statistical significance (Bhattacharya and Habtzghi, 2002). Values of $p<0.05$ show statistical significance, but this does not always guarantee that the result is scientifically significant as well. Spearman's correlation coefficient represents the statistical dependence of two variables based on their rank (Hammer et al., 2001; Trauth, 2014). It can vary between 1 and −1, with 1 being regarded as a complete correlation and −1 as anti-correlation. Both values were determined using the software PASTv4.03 (Hammer et al., 2001). The p-value was applied to assess whether two variables are correlated at all and r_s was used to determine the degree of that correlation (Hammer et al., 2001). A principal component analysis (PCA) was used to identify patterns of similar behavior in our data sets (Abdi and Williams, 2010; Jolliffe and Cadima, 2016). The viable PCs were narrowed down by selecting only those that together described at least 80% of the variance. To ensure an ideal comparison of the various different applied techniques, only the measurements of the same depths were used. Hence, the XRF measurements were reduced from 25 to 24, TOC and TIC from 45 to 24 and grain size measurements from 33 to 24.

RESULTS

Age Model

The computed age model puts the MAR-1 sequence between 463±20 ka and 427±20 ka and thereby into the glacial MIS12 (**Figure 3**). It yielded the approximate ages for the respective units of >463–461 ka (UB10), 461–457 ka (UB9), 457–454 ka (UB8), 454–448 ka (UB7), 448–445 ka (UB6), 445–444 ka (UB5), 444–441 ka (UB4), 441–436 ka (UB3), 436–434 ka (UB2) and <434–427 ka (UB1). The model places the archeological site at ~444±20 ka. The calculated sedimentation rates vary between 0.18 mm/a (~55 a/cm) and 0.13 mm/a (~77 a/cm) (**Table 3**), which concurs with the those suggested by Van Vugt et al. (2000), Okuda et al. (2002) and Tourloukis et al. (2018a), who determined sedimentation rates between 0.1 mm/a and 0.26 mm/a.

Grain Sizes

Grain sizes fluctuate rapidly between coarse (>63 µm) and fine (<63 µm) values, with only minor steady trends from UB10–UB8 and between UB4–UB1 (**Figure 5**). The coarse-grained fraction of

the individual samples dominated samples with 56–58 wt% in UB6, UB7 and UB9, and 70 wt% in UB1. Lowest values of the coarse grained-fraction were recorded in UB10 and UB3 (2–5 wt %) as well as UB6 (4 wt%), and UB5 (6 wt%).

Silicate Microfossils, Ostracods and Other Macroscopic Components

Diatoms are very rare. Even for abundant taxa, preservation is poor in most cases, preventing them from being used for limnological interpretations of the paleo-lake Marathousa. Where identification was possible, mostly benthic or epiphytic genera, such as *Cocconeis* sp., *Cymbella* sp., *Epithemia* sp., *Fragilaria* spp., *Gomphonema* sp. and *Stauroneis* sp. were identified, indicating shallow water. A few planktonic species, such as *Cyclotella* sp., could also be identified in the upper part of the sequence. In contrast, sponge spicules were the most common silicate microfossils, occurring in nearly all units, except UB10 (**Figure 4**, **Figure 5**, **Table 4**). They were most abundant between UB4–UB1. For the further interpretation, the general occurrence of sponge spicules in the samples were used to support XRF interpretations.

The total number of ostracods in this study is in general very low, and interpretation of the assemblages should be taken with caution. Out of the 47 samples that were analyzed from Area A and B, 21 were totally barren of ostracods (UA1, UA4, UB1, UB5, UB6, UB8–UB10; **Figure 5**). The quantity of ostracod specimens per sample is highly variable, ranging between 0 and 52, with species numbers of 0–6 per sample. In total, 13 ostracods species could be identified (**Figure 4**, **Table 4**), with higher numbers occurring in samples MAR03 (115 cm, UB1), MAR05 (150 cm, UB2), MAR07 (215 cm, UB3), MAR09 (245 cm, UB4) and MAR11 (295 cm, UB4) in Area B, and in the sample of UA3b in Area A. Candonidae and Ilyocyprididae dominate the assemblage (**Figure 5**). More specifically, juvenile stages of *Candona* sp. were found in 12 samples with relatively high frequencies, reaching 51 in UA3 of Area A. Adult specimens of mainly *Neglecandona altoides* and *Candona neglecta* were only found in six samples from Area B. A representative of *Pseudocandona marchica* has been retrieved from sample MAR11 (295 cm, UB4) of Area B. As far as the number of species is concerned, *Ilyocypris* spp. exhibit the highest diversity, with four different species being identified (*I. bradyi*, *I. decipiens*, *I. getica* and *I. gibba*). They were found, however, only in low frequencies, not exceeding seven valves per sample (maximum abundance in sample MAR09, 245 cm, UB4). Several other freshwater species (*N. angulata, Darwinula* sp., *Potamocypris zschokkei*, *Prionocypris zenkeri*, *Psychrodromus* sp.) were found scattered in different samples and with very low frequencies (one to three valves per sample) (Martens and Savatenalinton, 2011; Ruiz et al., 2013; Meisch et al., 2019). Lüttig (1968), who conducted a study on the ostracods of the Megalopolis Basin, does not report several species that have been identified here (*P. zschokkei, P. zenkeri, P. marchica, I. getica, I. decipiens* and *I.bradyi*), even though an assemblage rich in Candonidae and Ilyocyprididae is mentioned.

Taphonomic indices were calculated for the Candonidae representatives and for samples with adequate number of valves (**Table 5**). As far as the juvenile *Candona* spp. of sample MAR07 (215 cm, UB3) are concerned, the low value of %Art. ratio (6.67%) and the RV/LV ratio (0.5) reveal a disturbed sediment-water interface and transported valves. Both *N. altoides* and *C. neglecta* from sample MAR11 (295 cm, UB4) have been deposited *in situ* since A/J ratios are high (4.0 and 5.0 respectively). Deposition took place under a calm sediment water interface since both %Art. ratios are high (67.0 and 66.7% respectively). However, low energy water must have transported some juvenile valves to the depositional environment since the %Art. ratio for juvenile *Candona* spp. is relatively low (35.7%). On the other hand, the RV/LV ratio for *Candona* spp. deriving from Area A (samples from UA2, UA3b and UA3c) shows no disturbed values (~1.0); however, like the UB4 juveniles, these valves are all considered transported, since no adult specimens were found. The low value of the %Art ratio (13.6%) in the sample from UA3b reveals a disturbed sediment-water interface.

Other macroscopic components were encountered in every unit, with gastropods being the most common. Gastropods and/or opercula were found in 12 samples with only a few found in UB9 and at the beginning of UB7 (**Figure 5**). Their share increases and strongly fluctuates between UB5 to UB1. The content of shell fragments behaves in a similar way with a slight increase at the end of UB7. Fish bones were few in number and only present in UB7, UB4 and UB3. Charophyte gyrogonites were noted in two samples, while fish teeth/bones and thecamoebians were observed in four and one samples, respectively.

X-Ray Fluorescence

TiO_2 and **Rb** in MAR-1 sediments are comparatively low with average values of 0.63 wt% and 77.33 ppm. Enhanced values are recorded in UB9, UB8 and UB6 and minima in UB1 and UB10 (**Figure 5**). **La** shows very low average values (25.75 ppm) and trends correlates in its maxima with TiO_2 and Rb but has a minimum in UB7. **Sr** content ranges around 156.32 ppm and starts with very low values in UB10 and fluctuates strongly around a continuously increasing trend towards UB1. **Fe_2O_3** exhibits continuously low values with an average of 4.41 wt%, one pronounced peak in UB6 and its minimum in UB1. **MnO**, with an average of 0.15 wt%, follows a strongly fluctuating trend with a maximum in UB6 and minima in UB10 and UB1. **MgO**, **Na_2O** and **SiO_2** exhibit a very similar behavior with averages of 1.88 wt%, 0.89 wt% and 54.53 wt%, respectively. Maximum values are reached in UB9, UB7 and UB5, while minima are recorded at UB10, UB6 and UB1. The ratios **Mg/Ti, Na/Ti** and **Si/Ti** show a similar trends with constantly rising values in UB8 to UB7, which abruptly change in UB6 and decrease under strong fluctuations towards the top of the sequence. **Rb/Sr** experiences an initial steep rise between UB10 to UB8 and then decreases under fluctuations towards UB1. **Mn/Fe** is strongly fluctuating with maxima at UB9, UB5 and UB1 and minima at UB10, UB4 and UB1.

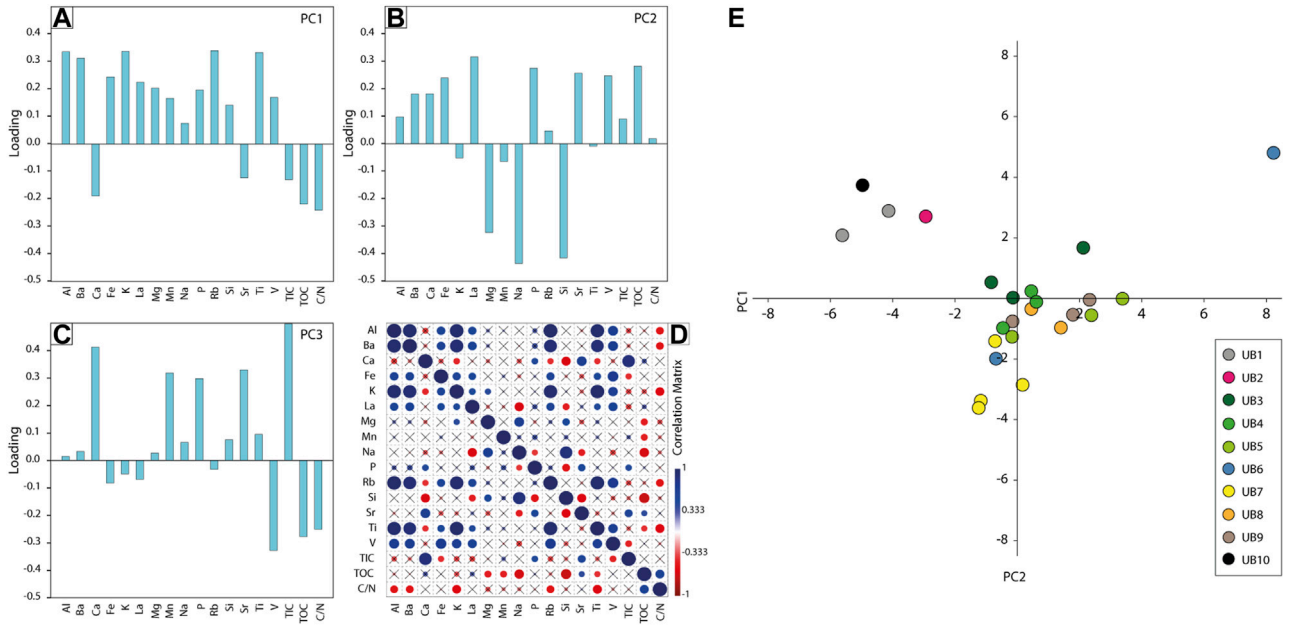

FIGURE 6 | Results of the statistical analysis. **(A–C)** Loadings of chemical components representing their influence on the computed principal components (PC1–PC3). **(D)** Correlation matrix showing the relation of the chemical components to each other. Blue indicates a positive correlation, while red shows an anticorrelation. The size of the circles is determined by the intensity of correlation. **(E)** Plot illustrating the impact of PC1 and PC2 on the lithological units.

Total Inorganic Carbon, Total organic carbon and TOC/TN Ratios

TIC is highly variable with values ranging from 0.02 wt% (UB9) to 1.77 wt% (UB3). Major peaks are encountered at the beginning of UB1 (1.58 wt%), in the middle of UB3 (1.78 wt%) and at the end of UB8 (1.62 wt%). The lowest values can be found in UB3 (0.06 wt%), UB5 (0.03 wt%) and UB9 (0.02 wt%). The calculated TOC values decline from UB10 to UB6 and subsequently increase from UB5 to UB1. TOC achieves a minimum of 0.74 wt% (UB6) and a maximum of 31.07 wt% (UB10). The C/N values in the MAR-1 sediments are highly variable, fluctuating from 6.26 up to 24.69. The ratio decreases sharply from the middle of UB6 until the boundary to UB7. In the lignite layers, the ratios are usually very high (UB1–24.09 and UB10–24.69).

Statistics Results

PCA analysis was carried out to identify the major influences on the sedimentation processes. The first three principal components (PC1-PC3) make up 85.8% of the total variance. The first eigenvalue accounts for 45.2%, the second for 25.0% and the third for 15.6%. Any other remaining component reflects less than 6.5% of the total variance. Therefore, only PC1 to PC3 were used for interpretation (**Figure 6**).

DISCUSSION

Proxy Evaluation

X-Ray Fluorescence Proxies Interpretation

Rubidium (Rb) is a conservative element mainly associated with clay minerals where it often substitutes for K (Jin et al., 2006; Kylander et al., 2011; Heymann et al., 2013). In a humid climate, the content of Rb tends to be elevated due to a high precipitation and a subsequent increase of erosion and terrestrial input (Fernández et al., 2013; Heymann et al., 2013).

Strontium (Sr) rarely forms independent minerals, but if it does, they are usually associated with sedimentary rocks (Hibbins, 2000). One source of Sr may be of biogenic production such as calcifying organisms, however due to the low amount of remains found in the MAR sediments, the share of biogenic Sr is considered negligible (Cohen, 2003; Férnandez et al., 2013). Another source could be erosion/weathering of the catchment which is largely comprised of carbonaceous rocks. Karkanas et al. (2018) determined that the sediments of MAR-1 have a very high carbonate content and microscopic analyses revealed the catchment as origin. Therefore, it is assumed that the Sr originates from the catchment (**Table 6**).

Rb/Sr ratio is usually regarded as a weathering proxy, indicating the relative humidity of the climate (Unkel et al., 2011; Fernández et al., 2013; Heymann et al., 2013; Emmanouilidis et al., 2018). A humid climate promotes erosion and the influx of Rb and also increases the chemical weathering of carbonaceous rocks, leaching Sr from the sediments (Jacobson et al., 2002; Unkel et al., 2011; Heymann et al., 2013). In contrast, a dry climate favors the deposition of Sr in sediments, due to increased erosion instead of weathering. As a result, high Rb/Sr values tend to indicate a more humid climate and low ones a drier climate. However, other processes (e.g., sedimentary sorting) can influence the proxy. Finer sediments with a higher mica-rich clay fraction often have higher Rb/Sr values, as Rb is often associated with clay minerals. Therefore,

TABLE 6 | Summary of geochemical proxies and their origin applied for the interpretation of MAR-1 sediments.

Proxy	Origin	Reference
Al	Terrestrial	Rothwell and Croudace (2015)
Ba	Biogenic	Bishop (1988), Calvert and Pedersen (2007)
Ca	Biogenic	Jouve et al. (2013), Mannella et al. (2019)
Fe	Redox	Cohen (2003), Naeher et al. (2013), Burn and Palmer (2014), Rothwell and Croudace (2015)
K	Terrestrial	Rothwell and Croudace (2015)
La	Dust	Muhs et al. (2007), Muhs et al. (2010)
Mg, Na, Si	Alkalinity, chemical weathering	West et al. (2005), Rothwell and Croudace (2015)
Mn	Redox	Davison (1993), Cohen (2003), Naeher et al. (2013), Rothwell and Croudace (2015)
Rb	Terrestrial	Jin et al. (2006), Heymann et al. (2013), Kylander et al. (2011)
Sr	Biogenic	Cohen (2003), Férnandez et al. (2013)
Ti	Terrestrial	Fitzpatrick and Chittleborough (2002), Rothwell and Croudace (2015), Regattieri et al. (2017), Mannella et al. (2019)
V	Terrestrial	Shaheen et al. (2019)
Al/Ca	Fluvial	Nizou et al. (2011)
Al/Si	Chemical weathering	Hoang Van et al. (2010)
Ba/Al	Detrital	McManus et al. (1998)
Ba/Ca	Runoff	Grove et al. (2010)
Ba/Ti	Paleo-productivity	Thomson et al. (2006)
Mg/Ti, Si/Ti	Alkalinity, chemical weathering	This study
Mn/Fe	Lake redox conditions (oxic vs. anoxic)	Koinig et al. (2003), Haberzettl et al. (2007), Naeher et al. (2013), Burn and Palmer (2014)
Na/K, Na/Ti	Alkalinity, chemical weathering	Nesbitt and Wilson (1992), Chen et al. (2001), Roy et al. (2008)
Rb/Sr	Precipitation	Unkel et al. (2011), Fernández et al. (2013), Heymann et al. (2013), Emmanouilidis et al. (2018)
C/N	Vegetation	Meyers and Teranes (2001)
TOC	Organic carbon	Meyers and Teranes (2001)
TIC	Inorganic carbon	Meyers and Teranes (2001)
PC1	Sediment sources (intern vs. terrestrial)	This study
PC2	Water availability (alkaline conditions)	This study
PC3	Oxygenation (anoxic vs. oxic)	This study

lower values are expected in coarser, feldspar-rich sediments (Hemming, 2007; Cole et al., 2009). As the composition of the sediments at MAR-1 alternates rapidly between fine and coarse sediments (ranging from 1.5 to 70% coarse fraction), the ratio of Rb/Sr has to be considered with caution and is only considered a rough proxy of precipitation. Pollen analysis can help establishing the closer relation between Rb/Sr and precipitation.

Manganese (Mn) is a highly redox sensitive element which has its origin in the surrounding catchment (Rothwell and Croudace, 2015). Under oxidizing conditions, it is encountered as insoluble Mn^{4+} and under reducing ones as soluble Mn^{2+} (Davison, 1993; Cohen, 2003; Naeher et al., 2013).

Iron (Fe) is one of the earth's most common elements and usually correlated with terrigenous markers like Ti (Rothwell and Croudace, 2015). Most commonly, it enters a lake as iron oxide or hydroxide and settles through the water column until it encounters either anoxic waters or OM, which act as a reducing agent (Cohen, 2003). (Kelepertsis and Kontis. 1997) confirm an external source for iron in the Megalopolis Basin. Under oxidizing conditions, ferric iron (Fe^{3+}) is the insoluble and stable state of iron, which is deposited (Cohen, 2003; Burn and Palmer, 2014). In anoxic waters, Fe^{3+} is reduced to the highly soluble Fe^{2+} (Cohen, 2003; Naeher et al., 2013; Burn and Palmer, 2014). However, Fe^{2+} can also be bound in pyrite (FeS_2), if enough sulfur, produced by the reduction of SO_4^{2-}, is available (Cohen, 2003).

The **ratio Mn/Fe** can be used to reconstruct the redox milieu (Koinig et al., 2003; Naeher et al., 2013; Burn and Palmer, 2014). In anoxic waters, the reduced form of Mn (Mn^{2+}) is more stable in the water column than Fe^{2+}, i.e., Fe^{2+} is more easily bound and deposited as a $FeCO_3$ or more commonly as FeS_2 (Koinig et al., 2003; Burn and Palmer, 2014). Hence, Mn/Fe ratios of anoxic sediments remain low (Burn and Palmer, 2014). In an oxic water column, Mn/Fe is high, as both Mn and Fe are precipitated (Burn and Palmer, 2014).

Titanium (Ti) is a conservative and immobile element, which typically occurs in weathering-resistant minerals (e.g., rutile, ilmenite), but can also be constituent of clay minerals (Chawchai et al., 2016; Regattieri et al., 2017). As it is not affected by diagenetic overprinting or biological processes it is often applied as an indicator for terrestrial input due to erosion and external processes (Fitzpatrick and Chittleborough, 2002; Rothwell and Croudace, 2015; Mannella et al., 2019).

Magnesium (Mg) is a major bedrock constituent, usually as carbonates, and is considered to be of detrital origin (Tsiftsis, 1987).

The primary source of **Sodium (Na)** are usually igneous and metamorphic rocks but it can also stem from clay minerals and other sedimentary rocks in the catchment (Tsiftsis, 1987). Na can be used to identify the degree of chemical weathering.

The origin of **Silicon (Si)** in sediments can be either of detrital origin such as from igneous and metamorphic rocks, volcanic ashes, or from phytoliths (part of plants; Field et al., 2018) or from aquatic organisms such as diatoms or sponges (Tsiftsis, 1987; Cuven et al., 2010).

The ratios **Na/Ti** can be regarded as a proxy for the chemical weathering of igneous rocks (Nesbitt and Wilson, 1992; Chen et al., 2001; Roy et al., 2008). A similar source is assumed for the ratios **Si/Ti** and **Mg/Ti**, as their behavior,

constantly rising values in the silts and fine sands of UB8 to UB7, which abruptly changes in UB6 and decreases under strong fluctuations towards the top of the sequence (**Figure 5**), resembles the one of Na/Ti. According to Flower (1993), the content of dissolved Na and Mg in the water column influences the preservation of siliceous organisms like diatoms and sponges. Diatom preservation is deteriorating from calcium through magnesium to sodium carbonate dominated systems due to higher dissociation constants (Katrantsiotis et al., 2016). Therefore, these ratios are interpreted to represent lake-internal dissolution processes due to changes in alkalinity.

Lanthanum (La) is a rare earth element, which has been found in high concentrations in Saharan dust (Muhs et al., 2007; Muhs et al., 2010). Evidence of the influence of Saharan dust has been found throughout the Mediterranean region (Dayan et al., 1991; Muhs et al., 2010; Remoundaki et al., 2011; Nava et al., 2012; Varga et al., 2014). Modelling studies suggested that the dust transport during the last glacial was generally higher than during interglacials and thus could yield higher La values (Mahowald et al., 2006; Williams et al., 2016). This could also be the case during older glacials, and therefore La is considered an important element in this study (**Figure 5**).

Reconstruction of Environmental Processes Using Principal Component Analysis

The parameters influencing PC1 positively (Al, Ba, Fe, K, La, Mg, Mn, P, Rb, Si, Ti and V) are mostly of terrestrial nature and must have been transported into the lake via various processes (**Figure 6**). The correlation of Al, Ba, K, Rb, V and Ti hints towards the basement exposed in the NE and NW and/or the soils as the main sediment source, whereas Mg most likely has its origin in the carbonates of the Pindos and Tripolis zone (**Figure 2**; e.g., Tsiftsis, 1987; Fitzpatrick and Chittleborough, 2002; Rothwell and Croudace, 2015; Mannella et al., 2019). Typically, flysh often contains Al-rich silicate minerals such as illites or feldspars, while altered volcanics usually contain chlorite, feldspars, hematite and are perhaps enriched in Ti and V. La possibly originates in the Sahara dust (e.g., Muhs et al., 2010; Varga et al., 2014), which was transported via air to the Megalopolis Basin. Given the strong correlation of Na and Si in the MAR-1 sediments and the positive loading of Si in PC1, a detrital rather than a biogenic source of Si is assumed. PC1 is negatively controlled by proxies which seem to reflect an origin mainly from lake-internal processes (Ca, Sr, TOC, TIC, and C/N). Since Ca, Sr and TIC are anticorrelated to the other elements, they might be associated with biogenic carbonate production within the lake or to karstic erosion of the limestones in the western basin, as Karkanas et al. (2018) suggested. However, the high loadings of TOC and C/N, which are both controlled by lake organisms, indicate that Ca, Sr and TIC are probably influenced by the same source. We thus conclude **PC1** to represent information on **external (positive scores) vs. internal sediment sources (negative scores)**.

The parameters that influence **PC2** reflect alkalinity changes of the paleo-lake water, which are known to be often related to climate-driven lake-level changes as suggested in several paleo-lake archives (e.g., Cohen, 2003; Foerster et al., 2018; **Figure 2**, **Figure 6**). The anticorrelation of the Na/Ti, Mg/Ti, and Si/Ti ratio with PC2 supports our interpretation. Alkaline waters with pH>9 are known from today's dry and carbonate-rich environment of the Peloponnese (Chatziapostolou et al., 2013; Katrantsiotis et al., 2016; Weiberg et al., 2016). Highly alkaline waters are here related to the weathering of the surrounding rocks, consisting of Na-rich albite and Mg-rich dolomite, among others (Tsiftsis, 1987). During chemical weathering, Na- and Mg-cations, among others, are released and washed into the lake water, inducing alkaline conditions (Flower, 1993). This chemical reaction is also reflected in the opposing PC loadings. Whereas negative loadings, with Mg, Na, Si dominating, reflect drier climate and alkaline conditions, more humid episodes in contrast provide a freshening of the paleo-lake system. Furthermore, the influx of a variety of elements (positive loadings with Al, Ba, Ca, Fe, P, Sr) enhance lake productivity as reflected by TIC and TOC. Based on the various influencing factors, we consider PC2 to reflect changes in the general **availability of water** in the catchment with positive scores representing high, and negative scores low water availabilities.

The positive loadings of **PC3** are dominated by Ca, Mn, P, Sr, and TIC. All parameters, except for Mn, can be found in endogenic carbonates, shells ($CaCO_3$) and fish, or other bones ($Ca_5(PO_4)_3(OH)$). Mn is related to the oxidation status of the water column, with high Mn (compared to Fe) indicating a well-oxygenated water column (e.g., Burn and Palmer, 2014). The negative loadings of PC3 are dominated by TOC, C/N and V. TOC values are high in the lignite layers, indicating anoxic sediment conditions, whereas C/N indicate input of land vegetation to the sediments during these stages. Based on the influences mentioned above, we conclude that PC3 reflects **oxic** (more positive scores) and **anoxic** (strong negative scores) conditions of **paleo-lake** Marathousa. This interpretation is also supported by the ratio of Mn/Fe, which is often used to interpret the oxidation of the water column (e.g., Koinig et al., 2003; Burn and Palmer, 2014).

Silicate Microfossil Dissolution

Only a small number of diatoms was found with most of them either heavily weathered or fragmented, from UB1 down to UB6 (**Figure 5**). In the lowest parts of the sequence, they nearly disappear completely. Field et al. (2018), who investigated Area A and parts of Area B, obtained similar results but observed also large differences between the two excavation sectors with respect to preservation. The authors concluded that the scarcity and low diversity of diatoms could be the result of lake water disturbance which affected the bottom sediments, e.g., mudflows. However, another possibility for low preservation could be alkaline conditions in the paleo-lake. It has been pointed out that diatom records from the Peloponnese are rare, due to a dry and carbonate-rich environment favoring generally alkaline conditions (Weiberg et al., 2016). Studies, conducted on the Agios Floros fen to the south and on Lake Mouria to the North-West of the Alfeios River delta, reported

TABLE 7 | Lake-level reconstruction of MAR-1.

Unit		Depth (cm)	Age (ka)	Environmental interpretation
UB1	Start	0	427	Reed belt of a seasonal anoxic lake
	End	120	434	
UB2	Start	120	434	Lake transgression
	End	150	436	
UB3	Start	150	436	Protected shallow seasonal lake/pond close to a stream;
	End	240	441	hyperconcentrated flows after meltwater influx or storm events
UB4	Start	240	441	
	End	300	444	
UB5	Start	300	444	Floodplain after meltwater input with desiccation at the end
	End	340	445	
UB6	Start	340	445	Floodplain after meltwater input with desiccation at the end
	End	385	448	
UB7	Start	385	448	Lake-deltaic environment
	End	475	454	
UB8	Start	475	454	Transition phase from shallow lake to deltaic environment
	End	510	457	
UB9	Start	510	457	Mudflow breaches the reed belt and the lake regression
	End	575	461	
UB10	Start	575	461	Anoxic lake in close proximity to a reed belt
	End	600	463	

highly alkaline waters (pH>9) resulting from the weathering of the surrounding rocks, which most likely contributed to the dissolution of the diatoms (Chatziapostolou et al., 2013; Katrantsiotis et al., 2016). Apart from the occasional diatom presence, sponge spicules are abundant throughout the investigated sequences. Experiments demonstrate that diatoms dissolve much faster than sponge spicules in alkaline environments, because of the latter's smaller surface area in relation to their size compared to diatoms, which decreases the dissolution rate pronouncedly (Conley and Schelske, 2002). An additional cause for the presence of sponge spicules in the absence of diatoms might be that the spicules may act as a sink for Si, which is a highly important constituent of the water body for diatoms (Chu et al., 2011; Maldonado et al., 2019), due to their slow dissolving behavior. The ratio Na/Ti can be used to reconstruct chemical weathering (Nesbitt and Wilson, 1992) and seems to reflect lake-internal dissolution processes due to alkalinity changes, and thus supports our conclusion. The same can also be observed for Mg/Ti and Si/Ti.

Shoreline Reconstructions of Paleo-Lake Marathousa

The sedimentation of **UB10** (>463–461 ka), described by Karkanas et al. (2018) as black clays, took place in a stable shallow, anoxic lake environment in close proximity to a reed belt, which is indicated by high TOC, low Mn/Fe, the absence of microfossils and a high C/N of 25, indicative for plants such as reeds (e.g., Meyers and Teranes, 2001; **Table 6**; **Table 7**; **Figure 3**; **Figure 5**). The reed belt itself filtered out larger sediment particles from inflowing streams, only allowing clayey particles, most likely already high in decomposed OM, to reach the study area (**Figure 7**). According to PC1-3, the alkalinity of the paleo-lake is low, lake-internal processes dominate with high productivity causing anoxic conditions of the lake waters, which prevent organisms like ostracods to thrive. Such conditions imply a warm and humid climate. Sediments like those encountered in UB10 are also called freshwater sapropel or gyttja (Stankevica et al., 2016).

The dark grey, clayey sands of **UB9** (~461–457 ka) show an initial increase in grain sizes, alkalinity, and lake oxygenation, which could be indicative of a single or multiple mass movement events (e.g., hyperconcentrated flow, Karkanas et al., 2018) that could have destroyed the reed belt (**Figure 3**, **Figure 5**, **Figure 7**). Hyperconcentrated flows often occur during first runoff events in a rainy season, intense rainstorms, lake-breakout floods or glacier-outburst floods (Pierson, 2005). The increase in precipitation (Rb/Sr) and terrestrial input (PC1) point towards a short phase of enhanced runoff, and the pronounced decrease of TOC and C/N suggests that the reed belt was not re-established, most likely due to a falling lake level. This is supported by PC2, which shows medium high pH conditions after the hyperconcentrated flow event. The change from oxic at the base to medium oxic conditions throughout UB9 is indicated by Mn/Fe and PC3. Additionally, the dark grey sediment color suggests that the runoff event was probably only a short-term event of moister conditions. The presence of sponges, which are organisms that swiftly settle in new environments (Cohen, 2003; medium alkaline conditions Si/Ti, Na/Ti, Mg/Ti), might also indicate a shift towards more favorable lake conditions, but not stable enough to allow ostracods to thrive yet.

The silts and fine sands of **UB8** (~457–454 ka), were deposited within a well oxygenated lake (Mn/Fe, PC3) that gradually regressed from UB9 most likely due to a gradual decline in moisture availability (low Rb/Sr) (**Figure 3**, **Figure 5**, **Figure 7**). A trend towards more aridity is also indicated by a decrease in terrestrial input with a shift towards internal sedimentation processes (PC1), which is supported by an increase in alkalinity and very low TOC values. Silts, sands and high amounts of shell fragments and high TIC, suggest an

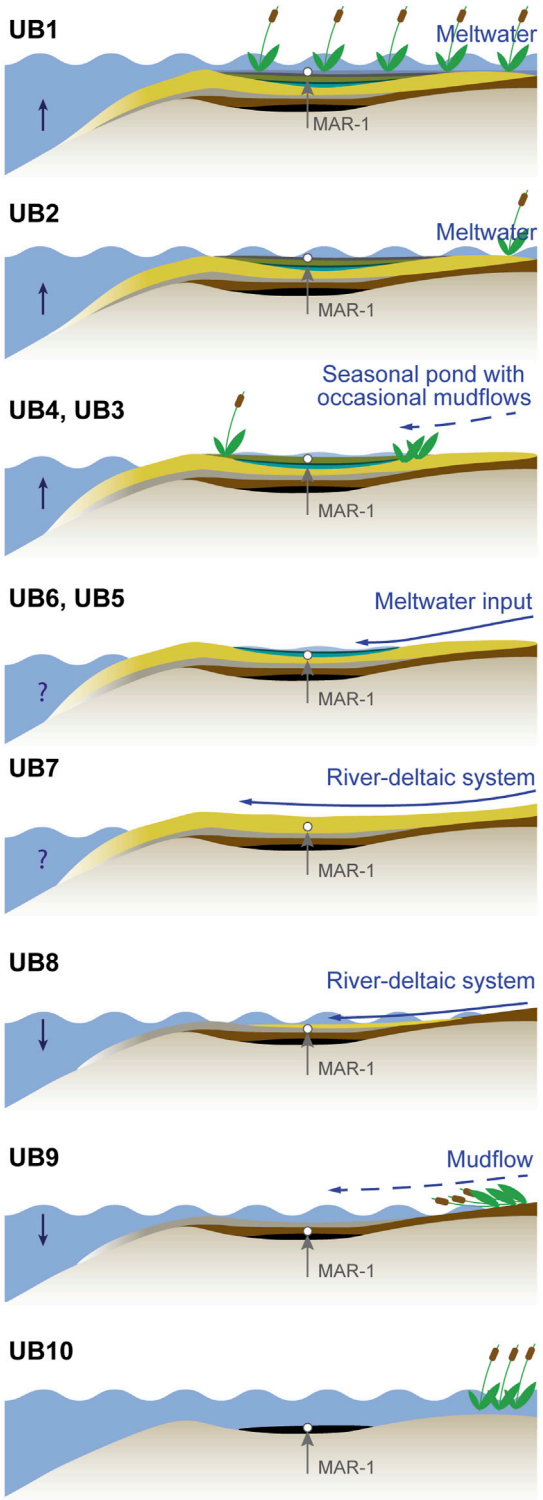

FIGURE 7 | Schematic overview of the sedimentation history of MAR-1 (not to scale).

environment with alternating transport energy, which is indicative for a riverine environment and implies a shift to such conditions at the end of UB8.

The massive, yellowish, bedded silts and fine sands of **UB7** (~454–448 ka) represent a high-energy and unstable riverine-deltaic environment (**Figure 3**, **Figure 5**, **Figure 7**). Strongly fluctuating C/N (mostly terrestrial plant input) and grain sizes could reflect a periodically high and low-energy environment which is known from seasonally controlled deltaic environments. Reduced moisture availability, preventing a full lake to develop, is also indicated by low Rb/Sr and high alkalinity. An increased current velocity and a fluctuating water table with high oxygenation (Mn/Fe, PC3) prevent the deposition of organisms *in situ* as indicated by fragments of fish bones, gastropods and ostracods, which is also supported by low TIC values. A few valves of the freshwater species *Psychrodromus* sp. (lower UB7) and *P. zschokkei* (lower-middle of UB7) indicate water temperatures below 18°C (summer temperature) (Meisch, 2000). The strong coloring of the valves implies that they were transported from nearby freshwater environments (e.g., pools). The transition from UB7 to UB6 is sharp and seems to interrupt all proxies in their trends. A slight increase of Rb/Sr towards the top of UB7 indicates higher moisture availabilities, which may predict the change of the deposition regime as reflected by UB6.

The blue sandy clay of **UB6** (~448–445 ka) may be interpreted as flood plain deposits caused by large amounts of meltwater from retreating glaciers as a result of a short warm period during MIS12 (**Figure 3**, **Figure 5**, **Figure 7**). Meltwater events are suggested based on evidence at Mt. Chelmos on the Peloponnese where glaciers reached their maximum extent during MIS12 (Leontaritis et al., 2020). During the previous arid phase between upper UB8 and most of UB7, large amounts of Saharan dust, reflected by La (e.g., Muhs et al., 2010; Varga et al., 2014) have been incorporated in the surrounding glaciers. With the onset of the brief warming phase after Heinrich-type event 6 (H_{t6}), at the transition from UB7 to UB6, large volumes of meltwater from retreating glaciers may have introduced their sediment load (mostly very fine-grained material) into the Megalopolis Basin and caused the pronounced peak of La. UB6 can be divided into two subunits. The lower UB6 is characterized by the dominance of grain sizes <63 μm, a sudden drop in alkalinity, oxic water conditions, and high terrestrial sediment input. Despite the pronounced increase in terrestrial material, C/N ratios drop, which could be indicative for a low energy environment at MAR-1 and could explain the higher abundance of diatom and sponge spicules (also observed by Field et al., 2018) in the sediments. Diatom assemblages are dominated by benthic taxa indicating shallow, but nutrient rich water conditions at MAR-1 (Field et al., 2018). Furthermore, a lack of terrestrial vegetation as indicated by low C/N ratios could support the hypothesis of meltwater as the source for the sediments of lower UB6. The upper part of the UB6 sediments reflect a shallow lake with increasing alkalinity, temporarily low oxygenation and predominating lake-internal processes. This interpretation is supported by the reduction in diatom abundances, as reported also by Field et al. (2018). However, in contrast to their interpretation of the development of a deeper lake environment based on the (relatively low) abundance of mainly planktonic diatoms such as *Aulacoseira* spp., we suggest lower water levels. The abundance of these particular species

could be due to taphonomic reasons, as *Aulacoseira* spp. consists of thick silicate valves, which dissolve slowly. Additionally, if light penetration is reduced due to, for example, organic-rich or muddy waters, only planktonic species can thrive. Higher grain sizes and higher C/N ratios at the upper part of UB6 indicate that the shoreline of this shallow paleo-lake is not far. UB6 ends with mud cracks (Karkanas et al., 2018), suggesting a desiccation of the shallow lake, in agreement with Field et al. (2018), who inferred a warmer and drier climate based on Chloridoid grass phytoliths analysis.

The proxies of the dark grey, organic-rich muddy and silty sands of **UB5** (~445–444 ka), as described by Karkanas et al. (2018), resemble those from lower UB6, with a slight reduction in their absolute values. One exception is marked by Rb/Sr, a proxy for humidity, which is more enhanced than in lower UB6. Based on the congruence of all chemical, physical and biological proxies, we infer a similar deposition history, with an increased meltwater event that flooded MAR-1 and partly eroded the underlying upper UB6 in some areas of the Marathousa 1 site (**Figure 3**, **Figure 5**, **Figure 7**). UB5 ends with another desiccation event, which is indicated by mud cracks at the upper boundary to UB4 (Karkanas et al., 2018). Such recurring droughts are consistent with findings by Field et al. (2018).

The proxies of the dark grey, organic-rich muddy sands of **UB4** (~444–441 ka) suggest the existence of a freshwater pond close to a small river or stream at MAR-1, that was periodically flooded (**Figure 3**, **Figure 5**, **Figure 7**). Locally distributed intraclasts and fining upward trends indicate multiple hyperconcentrated flows that reached the depositional area (Karkanas et al., 2018). The sequence shows conditions that allowed a number of microorganisms to thrive, including a diversity of ostracods, in contrast to the previous units. The ostracod species *Neglecandona altoides* and *Candona neglecta* (both deposited *in situ*), *Pseudocandona* cf. *marchica*, *Ilyocypris gibba* and *Prionocypris zenkeri* at the base of UB4 indicate the existence of a shallow freshwater pond of max. 10.5°C and low salinity ranges between 0 and 5% with a swampy vegetation nearby (Wagner, 1957; Devoto, 1965; De Decker, 1979; Meisch and Wouters, 2004; Fuhrmann, 2012). These paleo-environmental settings are also supported by enhanced C/N values, benthic diatom abundances (Field et al., 2018) and medium to low alkalinity. Towards the middle of UB4, increasing grain sizes, alkalinity and the lack of ostracod juveniles, as well as the monospecific abundance of *N. altoides* indicate a rather stressful environment for ostracods, with a change towards a more seasonal water body (Fuhrmann, 2012). It is difficult to tell whether the cause for these abrupt changes was a slight reduction in precipitation (Rb/Sr), a short-term event such as seasonally-induced hyperconcentrated flows (Karkanas et al., 2018), or a tectonic event. In any case, the archeological horizon of MAR-1 is situated in this lower part of UB4. Giusti et al. (2018) have reported that the site was subjected to minor post-depositional reworking processes such as those of mass movement events (e.g., mudflows), which would agree with the findings of our paleo-environmental interpretation. Towards the top of UB4, the ostracod numbers increase again, however the species domination changed towards *Ilyocypris bradyi* and *I. getica,* now indicating the steady existence of a slowly flowing stream or spring of 10–15°C (Fuhrmann, 2012). We interpret these temperatures as mean summer temperatures, in agreement with Hughes et al. (2007), who postulated that the MIS12 was characterized by summer temperatures at least 11°C colder than those observed in present-day Greece. This would imply mean summer temperatures for the Megalopolis Basin of around 10.5°C compared to today's 21.5°C. Hughes et al. (2007) also noted that mean winter temperatures were at least −0.8°C, suggesting that the water bodies may have been frozen, providing poor habitat conditions for ostracods. Furthermore, a freshwater to oligohaline vegetated pond or swamp with water temperatures ranging from 10 to 15°C can be deduced also for the archeological and *Palaeoloxodon*-bearing unit UA3 of Area A (stratigraphically correlated with UB4; Karkanas et al., 2018). In particular, in its base (UA3c), *Candona* spp. (juveniles) are recorded, while towards its middle (UA3b) ostracods increase in number and diversity, and include *Sarscypridopsis* sp., *Ilyocypris gibba* and *I. getica*; at its top (UA3a) again only juveniles of *Candona* spp. are identified. Overall, for UA3, the taphonomic indices reveal relatively high transportation rates of juvenile valves from a small stream.

The dark grey, organic-rich muddy sands of **UB3** (~441–436 ka) resemble those of UB4 and many proxies continue their indicated trends (**Figure 3**, **Figure 5**, **Figure 7**). The return of the ostracod species *Neglecandona altoides* and persistence throughout UB3, suggests the existence of a more or less permanent, but small water body. Based on the appearance of *Psychrodromus* sp., *Ilyocypris getica* and *I. decipiens,* the water body was ~15°C with low salinity values. Disturbed sediments, most likely affected by hyperconcentrated flows (Karkanas et al., 2018) after meltwater pulses or storm events, are confirmed by the taphonomy of ostracods, which indicate disturbed sediment-water interfaces and transported valves throughout this unit. The small pond or stream (when present) was well oxygenated and of low alkalinity, allowing sponges and diatoms to thrive and be better preserved. Our observations confirm Field et al. (2018), who also inferred a shallow water body based on carpological assemblages and unsorted wood remains. Furthermore, it might be possible that a reed belt nearby was reestablished based on an increased amount of reed phytoliths in the sediments and the enhanced C/N ratios (~20). Towards the top of UB3 environmental conditions change and the water body becomes less oxygenated, which might have caused the ostracods to disappear. A possible enhanced precipitation (Rb/Sr) and associated higher input of terrestrial material (Ti, PC1) may have contributed more nutrients and water to a system where high productivity might have caused anoxia at some point.

The dark grey, organic-rich silty sands of **UB2** (~436–434 ka) with their high concentrations of shells and shell fragments can be attributed to a high-energy environment associated with a rising lake level (**Figure 3**, **Figure 5**, **Figure 7**). Such winnowed shell bars at or above the wave base, together with higher grain sizes, are common features of storm events (Cohen, 2003). The high number of shell fragments is also reflected by the microfossil record, where gastropods and opercula are dominating together with enhanced grain sizes. The absence of ostracods supports the

high energy environment hypothesis, since the light and fragile valves are easily transported or destroyed. However, there is no evidence that the high energy environment was a constant state at this stage of the lake development.

The black sandy to clayey lignite of **UB1** (<434–427 ka) was deposited in a shallow body of standing water inside a reed belt (**Figure 3**, **Figure 5**, **Figure 7**) as indicated by high TOC, high C/N. The location of sedimentation is expected to be closer to margins of the water body, as indicated by high grain sizes, which stands in contrast to UB10, where high grain sizes were filtered out since the site was located most likely in front of the reed belt further away from the lake margin (Valero-Garcés et al., 2014). The degradation of the OM leads to anoxic conditions (Mn/Fe), which is supported by the absence of aquatic microfossils and the good preservation of plant material (Field et al., 2018). The increase in the number of leaves and wood found by Field et al. (2018) points towards the end of the previous dry conditions (UB8-UB3).

The Local Impact of Global Climate Change

The sedimentary sequence of MAR-1 was deposited during the glacial MIS12 (480–420 ka), which is known as the Skamnellian Stage in the glacial sequence of Greece (Leontaritis et al., 2020). During MIS12, the global sea level fell by ~100 m (Spratt and Lisiecki, 2016). From the N-Atlantic viewpoint, MIS12 is described as an unstable glacial, that was bounded on both ends by the stable interglacials MIS13 and MIS11 (**Figure 1**; **Figure 7**; e.g., McManus et al., 1999; Stein et al., 2009; Rodrigues et al., 2011; Regattieri et al., 2016). Terrestrial records of the Mediterranean region depict the glacial of MIS12 as generally cold and dry with a noticeable advance of glaciers (e.g., Tzedakis et al., 2006; Francke et al., 2016; Regattieri et al., 2016; Villa et al., 2016; Koutsodendris et al., 2019). There is evidence in Greece that the glaciers on Mt. Tymphi (N-Greece), Mt. Smolikas (N-Greece) and Mt. Chelmos (Peloponnese) reached their maximum extent during that time (Leontaritis et al., 2020).

In the Megalopolis Basin, the initial phase (**UB10**) >463–461 ka of the investigated sediment sequence is characterized by a reed-fringed, probably shallow, anoxic lake that formed during a humid and warm climate (**Figure 7**). Within the limits of the respective age models, such warmer and humid conditions at the beginning of MIS12 have also been reported from Lake Ohrid (Albania-North Macedonia), the Sulmona Basin (Italy), Tenaghi Philippon (NE Greece) and the southern Megalopolis Basin (**Figure 1**, **Figure 8**; e.g., Okuda et al., 2002; Tzedakis et al., 2006; Francke et al., 2016; Regattieri et al., 2016; Villa et al., 2016; Koutsodendris et al., 2019; Wagner et al., 2019). The Mediterranean sea surface temperatures (SST), however, remained low although slightly increasing, while the reported N-Atlantic SSTs are declining towards UB9 (Wang et al., 2010; Alonso-Garcia et al., 2011).

The sediments of **UB9** (~461–457 ka) reflect a mass movement event that might have been caused by a short but intense increase in precipitation and associated short-term freshwater lake conditions (**Figure 7**). The Mediterranean and the N-Atlantic show contrasting SSTs, which are however, slightly increasing towards the top of UB9 (**Figure 8**; Wang et al., 2010; Alonso-Garcia et al., 2011). Continuing warm conditions are reported from bulk carbonates $\delta^{18}O$ composition of the Sulmona Basin (Regattieri et al., 2016; Villa et al., 2016). Pollen obtained from sediments at Lake Ohrid (Albania, North Macedonia), Tenaghi Philippon (NE Greece) and the Megalopolis Basin reflect a highly fluctuating moisture availability with a decreasing trend (Okuda et al., 2002; Tzedakis et al., 2006; Koutsodendris et al., 2019). The simulated (LOVECLIM) precipitation evolution at Lake Ohrid by Wagner et al. (2019), however, shows no fluctuations, in contrast to its pollen record, but the authors state that the model tends to underestimate short-term precipitation changes. Such contrasting climatic conditions as indicated from the land and sea records could be an explanation for the short-term precipitation increase and associated mudflow. Kwiecien et al. (2009) stated that SSTs are a major factor in the cyclogenesis of the Mediterranean, with storms forming when temperature gradients are steepest, which occurs more frequently during intense winters today. Such contrasting SST conditions during a glacial could have generated increased storminess and the associated enhanced short-term precipitation in the Mediterranean. Such conditions could have existed at the time of UB9 deposition and could have been a precursor for a prolonged cold and dry period which is presented by UB8 and UB7.

UB8 deposition (~457–454 ka) occurred most likely during a time of progressive aridification that caused MAR-1 to turn from a shallow lake into a deltaic environment by the upper end of UB8 (**Figure 7**). A pronounced decrease in mean annual temperatures and precipitation is also recorded in the different proxy records of the surrounding Mediterranean such as the Sulmona Basin, Lake Ohrid, Tenaghi Philippon and the Megalopolis Basin, which parallel SST declines in the N-Atlantic and Mediterranean Sea itself (Tzedakis et al., 2006; Wang et al., 2010; Alonso-Garcia et al., 2011; Regattieri et al., 2016; Koutsodendris et al., 2019; Wagner et al., 2019).

During the episode between ~454 and 448 ka (**UB7**), the riverine-lake deltaic system, which had already developed during the final stages of UB8, continued the deposition of fine sands under drier climatic conditions (**Figure 3**, **Figure 5**, **Figure 7**). A dominating grassy landscape, indicative for drier and also colder temperatures is supported by a pollen record from the Megalopolis Basin by Okuda et al. (2002). The continuation of the dry and cold period occurred over the central and eastern Mediterranean region (Okuda et al., 2002; Tzedakis et al., 2006; Regattieri et al., 2016; Koutsodendris et al., 2019; Wagner et al., 2019). Also, the marine proxies describe colder SSTs in the N-Atlantic and Western Mediterranean (**Figure 8**; Wang et al., 2010; Alonso-Garcia et al., 2011). Towards the top of the UB7 sequence, however, a warming in the marine records is reported, which falls into a time period where slightly enhanced precipitation and temperatures at Lake Ohrid and the Megalopolis Basin are suggested by pollen assemblages. Tenaghi Philippon, however, seems to have remained dry and cold according to the arboreal pollen record of (Tzedakis et al. 2006), although this could be a

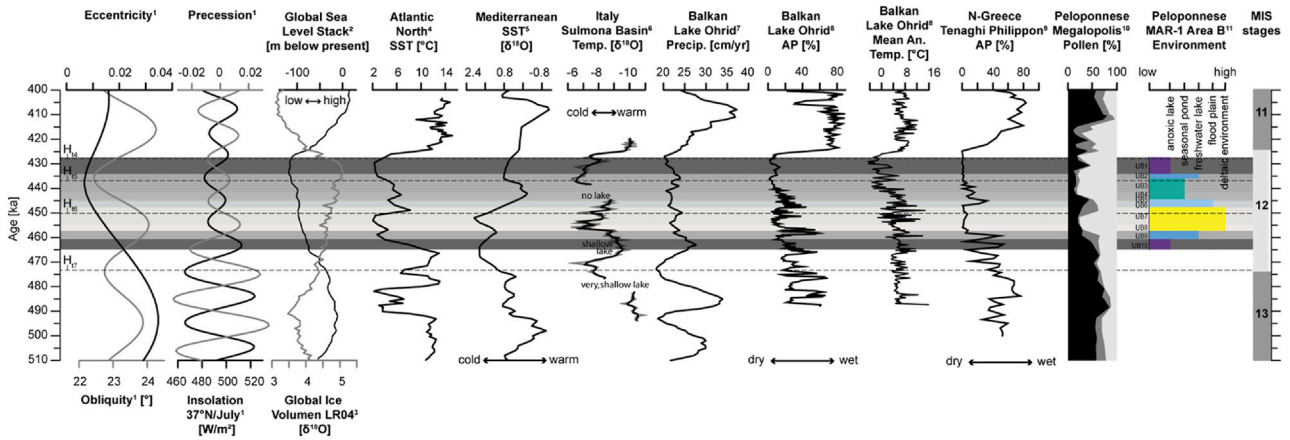

FIGURE 8 | Global records compared to the paleoenvironmental interpretation of MAR-1. 1) Orbital parameters and the local (37°N) mean monthly insolation (21. June–20. July; Laskar et al., 2004). 2) Stacked global sea level curve (Spratt and Lisiecki, 2016). 3) Global ice volume based on the benthic isotope stack LR04 (Lisiecki and Raymo, 2005). 4) Mean annual SST based on planktonic foraminifera, N-Atlantic (Alonso-Garcia et al., 2011). 5) Mediterranean SST based on the $\delta^{18}O$ stack of the planktonic foraminifera *Globigerinoides ruber* (Wang et al., 2010). 6) $\delta^{18}O$ record from the Sulmona Basin, Italy (Regattieri et al., 2016). 7) Calculated precipitation model (LOVECLIM) from Lake Ohrid, Albania, North Macedonia (Wagner et al., 2019). 8) Arboreal pollen record from Lake Ohrid (Koutsodenris et al., 2019). 9) Arboreal pollen record from Tenaghi Philippon, N. Greece (Tzedakis et al., 2006). 10) Pollen record from the Megalopolis Basin, Peloponnese [black: arboreal pollen (AP); dark grey: Gramineae; bright grey: non-arboreal pollen (NAP); Okuda et al., 2002]. 11) Reconstructed paleoenvironment and lake level at MAR-1 Area B, Peloponnese (this study). The dashed line marks Heinrich-type events (H_t; Rodrigues et al., 2011). The colored shadings indicate the lithological units of MAR-1.

result of sampling resolution, the continental character of the basin and/or age-model limitations. The recorded warming and slight increase in precipitation fall into the Heinrich-type event 6 (H_{t6}) ca. 450 ka ago (Rodrigues et al., 2011).

The sediments and proxies of **UB6** (~448–445 ka) and **UB5** (~445–444 ka) indicate a warming event that may have caused a pronounced melting of the surrounding glaciers. The warming trend that started already in upper UB7 continues its trend at Sulmona Basin (Regattieri et al., 2016) and reaches one of the highest values within MIS12. Pollen records at different Mediterranean sites surrounding MAR-1 all show a continuation of the increase in arboreal taxa indicating a short-term improvement in climate (Okuda et al., 2002; Tzedakis et al., 2006; Koutsodendris et al., 2019; Wagner et al., 2019). N-Atlantic SSTs decline during UB6 and UB5, whereas western Mediterranean SSTs continue the warming trend which could have caused an enhanced storminess during this time, due to potential strong temperature gradients (Kwiecien et al., 2009; Wang et al., 2010; Alonso-Garcia et al., 2011).

The proxies of **UB4** (contains archaeological remains) to **UB3** (~444–436 ka) indicate the existence of a seasonal pond or slow flowing stream that became stagnant and anoxic in the very upper part of UB3. The water temperatures, as inferred from ostracod assemblages, were cold and ranged from 10 to 15°C. Precipitation (Rb/Sr, PC2) was low during these episodes and only slightly increased towards the top of UB3. A strong reduction towards colder temperatures is also reported from the Sulmona Basin and Lake Ohrid (Regattieri et al., 2016; Koutsodendris et al., 2019). Pollen records from Lake Ohrid, Tenaghi Philippon and Megalopolis report taxa that reflect a rather cold and dry climate (Okuda et al., 2002; Tzedakis et al., 2006; Koutsodendris et al., 2019). The simulated (LOVECLIM) precipitation evolution at Lake Ohrid by Wagner et al. (2019) also reports reduced moisture conditions whereas Mediterranean SSTs reached highest values whereas the N-Atlantic continues its cooling trend (Wang et al., 2010; Alonso-Garcia et al., 2011).

The upper units **UB2-UB1** (~436–427 ka) of MAR-1 have been deposited in a swamp-like environment, reflecting a permanent stagnating anoxic water body. According to the Rb/Sr and PC2 records, precipitation was low, which concurs with other terrestrial proxies around the central and eastern Mediterranean (Tzedakis et al., 2006; Koutsodendris et al., 2019; Wagner et al., 2019) and is similar to conditions during UB8 and UB7. An increase in temperature is recorded in the $\delta^{18}O$ record from the Sulmona Basin (Regattieri et al., 2016). The N-Atlantic during this time continues its cooling trend and records temperatures as low as during UB8 and UB7 (Alonso-Garcia et al., 2011). The Mediterranean SSTs, in contrast, remain high despite a short cooling trend during UB3, and increases gradually towards MIS11 (Wang et al., 2010). Despite the dry conditions, the slow warming of the Mediterranean realm might have progressively forced the retreat of the widespread glaciers at the end of MIS12 (Leontaritis et al., 2020). The local increase in moisture availability, for example as soil moisture, due to melting glaciers in the catchment, might also explain the abundance of arboreal pollen in the Megalopolis pollen record (Okuda et al., 2002), whereas other regions remained free of arboreal pollen. This hypothesis is supported by the reversed cooling trend of the Mediterranean SST record. The stacked Mediterranean $\delta^{18}O$ record, based on the planktonic foraminifera *Globigerinoides ruber,* registers a slow but gradual warming. The turn towards lighter values during this time might be associated with freshwater lenses, floating on top of highly saline subsurface waters (Lourens, 2004; Wang et al., 2010). Such freshwater

lenses could indicate an increase of terrestrial runoff due to glacier retreat at the end of MIS12 and/or increased precipitation. Studies conducted on similar settings like MAR-1 suggest that mires, which lead to the formation of lignites, usually form in the warm climate of an interglacial (e.g., Mädler, 1971; Nickel et al., 1996; van Vugt et al., 2000; Okuda et al., 2002; Siavalas et al., 2009). Here we suggest that UB1 is representing the transition from the MIS12 glacial to MIS11 interglacial.

SUMMARY AND CONCLUSION

The fluvio-lacustrine sediments in the Megalopolis Basin (central Peloponnese) close to the elephant-butchering site MAR-1 were investigated to a) reconstruct the water level history in relation to the archeological site, b) refine the age model for a better disentangling of the local impact of global climate changes and c) determine the potential as a refugium for hominins during the MIS12 glacial. A multiproxy approach considering ostracods, sponge spicules, diatoms, grain sizes, TC-TN-TOC, and conventional XRF analysis provided a detailed paleoenvironmental picture during MIS12 of each identified sedimentary unit. Between ~463 and 461 ka (UB10), a reed-fringed, stable, but anoxic lake dried up gradually with the onset of drier and colder conditions of the MIS12 glacial period. A short, but intense increase in precipitation caused a return to fresh-water conditions between ~461 and 457 ka (UB9), before MAR-1 turned into a riverine environment under the progressive aridification of the region between ~457 and 448 ka (UB8-UB7). A period of warming between ~448 and 444 ka (UB6-UB5) turned the study area into a flood plain, despite ongoing dry conditions. We relate the short-term increase in water availability, despite dry conditions, to an enhanced melting of the surrounding glaciers due to the warming event. Afterwards, seasonal ponds developed between 444 and 436 ka (UB4-UB3) under a mostly dry and cold climate, which persisted over ~10 ka. These aquatic environments were rich in ostracods, diatoms and other microorganisms providing food for smaller animals and thus would have also offered mammals and humans valuable resources, such as potable water, a wide range of plant species and hunting opportunities. Pond-like conditions, such as those reflected by the sediments of UB5-UB3, thus facilitate a high archeological potential. Towards the end of MIS12 ~436–427 ka (UB2–UB1), the freshwater ponds turned into an anoxic stagnant water body after wide-spread flooding due to melting glaciers in the catchment caused by warm but still dry conditions. The reconstructed paleo-environment of MAR-1 agrees well with other records from the Mediterranean realm, with a strong linkage to climate in the N-Atlantic. We conclude that the Megalopolis Basin served as a refuge region for mammals including hominins due to its capability to retain water even during dry periods within a temperature- and storm-protected basin surrounded by mountains.

DATA AVAILABILITY STATEMENT

The original contributions presented in the study are included in the article/Supplementary Material, further inquiries can be directed to the corresponding author.

AUTHOR CONTRIBUTIONS

The study was designed by AJ. IB, AJ, NT, VT, and GK collected samples. IB and AJ developed the age model, performed statistical analysis and overall interpretation of the multiproxy record. MW, ES, and CZ conducted TOC, TIC, XRF, grain sizes, sponge and diatom analysis. PP and GI performed ostracod analysis. VT, GK, PK, NT, SK, EP, and KH contributed data from the Megalopolis Basin. All co-authors contributed to writing, refining and approving the manuscript.

FUNDING

The research has been funded by the European Research Council (ERC StG 283503 "Paleoanthropology at the Gates of Europe" and ERC CoG 724703, "Human evolution at the crossroads", awarded to KH), the Senckenberg Centre for Human Evolution and Paleoenvironment (S-HEP) in Tübingen and the Open Access Publishing Fund of the University of Tübingen.

ACKNOWLEDGMENTS

This research was conducted under the auspices of the Ephoreia of Paleoanthropology and Speleology, Greek Ministry of Culture, and was supported by the European Research Council (PaGE, CROSSROADS awarded to KH). We thank the Senckenberg Centre for Human Evolution and Paleoenvironment (S-HEP) in Tübingen for funding the doctoral project of IB. We greatly thank Tatiana Miranda for her constant laboratory support and advice, H. Taubald for assisting with XRF measurements/data and S. Fleiz for support in TOC and TIC analysis at Tübingen university. We thank both reviewers for their constructive comments that helped increasing the quality of the manuscript.

REFERENCES

Abdi, H., and Williams, L. J. (2010). Principal Component Analysis. *Wires Comp. Stat.* 2 (4), 433–459. doi:10.1002/wics.101

Alonso-Garcia, M., Sierro, F. J., and Flores, J. A. (2011). Arctic Front Shifts in the Subpolar North Atlantic during the Mid-pleistocene (800-400ka) and Their Implications for Ocean Circulation. *Palaeogeogr. Palaeoclimatol. Palaeoecol.* 311 (3–4), 268–280. doi:10.1016/j.palaeo.2011.09.004

Athersuch, J. (1976). Stereo-Atlas Ostracod Shells 3 (21), 117–124.

Athersuch, J., Bate, R. H., Boomer, I. D., Horne, D. J., Lord, A. R., Neale, J. W., et al. (1973–1996). *A Stereoatlas of Ostracod Shells. Several Volumes*. British Micropalaeontological Society.

Baltatzis, E. G., and Katagas, C. G. (1984). The Pumpellyite-Actinolite and Contiguous Facies in Part of the Phyllite-Quartzite Series, central Northern

Peloponnesus, Greece. *J. Metamorph Geol.* 2 (4), 349–363. doi:10.1111/j.1525-1314.1984.tb00595.x

Battarbee, R. W., (1986). Diatom Analysis. In: *Handbook of Holocene Palaeoecology and Palaeohydrology*, ed. by Björn. E. Berglund. Wiley, Chichester, pp. 527–570. ISBN 0-471-90691-3.

Belis, C. A. (1997). Palaeoenvironmental Reconstruction of Lago di Albano (Central Italy) during the Late Pleistocene using fossil ostracod assemblages. *Water Air Soil Pollut.* 99 (1–4), 593–600. doi:10.1007/BF02406898

Bhattacharya, B., and Habtzghi, D. (2002). Median of thepValue under the Alternative Hypothesis. *The Am. Statistician* 56 (3), 202–206. doi:10.1198/000313002146

Bishop, J. K. B. (1988). The Barite-Opal-Organic Carbon Association in Oceanic Particulate Matter. *Nature* 332, 341–343. doi:10.1038/332341a0

Blaauw, M., and Christen, J. A. (2011). Flexible Paleoclimate Age-Depth Models Using an Autoregressive Gamma Process. *Bayesian Anal.* 6 (3), 457–474. doi:10.1214/ba/1339616472

Blackwell, B. A. B., Sakhrani, N., Singh, I. K., Gopalkrishna, K. K., Tourloukis, V., Panagopoulou, E., et al. (2018). ESR Dating Ungulate Teeth and Molluscs from the Paleolithic Site Marathousa 1, Megalopolis Basin, Greece. *Quaternary* 1, 22. doi:10.3390/quat1030022

Breman, E. (1980). Differential Distribution of Left and Right Ostracode Valves in the Adriatic Sea. *Palaeogeogr. Palaeoclimatol. Palaeoecol.* 32, 135–141. doi:10.1016/0031-0182(80)90036-X

Burn, M. J., and Palmer, S. E. (2014). Solar Forcing of Caribbean Drought Events during the Last Millennium. *J. Quat. Sci.* 29, 827–836. doi:10.1002/jqs.2660

Calvert, S. E., and Pedersen, T. F. (2007). "Chapter Fourteen Elemental Proxies for Palaeoclimatic and Palaeoceanographic Variability in Marine Sediments: Interpretation and Application," in *Proxies in Late Cenozoic Paleoceanography*. Editors C. Hillaire-Marcel and A. De Vernal (Dev Mar Geol, Elsevier), 567–644. doi:10.1016/s1572-5480(07)01019-6

Chatziapostolou, A., Siavalas, G., Kalaitzidis, S., and Christanis, K. (2013). Geological Study for a Wetland Restoration: the Case of the Drained Mouria Lake (W. Peloponnese). *Geosociety* 47 (1), 72–81. doi:10.12681/bgsg.10902

Chawchai, S., Kylander, M. E., Chabangborn, A., Löwemark, L., and Wohlfarth, B. (2016). Testing Commonly Used X-Ray Fluorescence Core Scanning-Based Proxies for Organic-Rich Lake Sediments and Peat. *Boreas* 45 (1), 180–189. doi:10.1111/bor.12145

Chen, J., An, Z., Liu, L., Ji, J., Yang, J., and Chen, Y. (2001). Variations in Chemical Compositions of the Eolian Dust in Chinese Loess Plateau over the Past 2.5 Ma and Chemical Weathering in the Asian Inland. *Sci. China Ser. D-earth Sci.* 44 (5), 403–413. doi:10.1007/BF02909779

Cen, J. a., Wan, G., Zhang, D. D., Zhang, F., and Huang, R. (2004). Environmental Records of Lacustrine Sediments in Different Time Scales: Sediment Grain Size as an Example. *Sci. China Ser. D* 47, 954–960. doi:10.1360/03yd0160

Chu, J., Maldonado, M., Yahel, G., and Leys, S. (2011). Glass Sponge Reefs as a Silicon Sink. *Mar. Ecol. Prog. Ser.* 441, 1–14. doi:10.3354/meps09381

Cohen, A. S. (2003). *Paleolimnology: The History and Evolution of lake Systems*. Oxford University Press. 0-19-513353-6. doi:10.1093/oso/9780195133530.001.0001

Cole, J. M., Goldstein, S. L., deMenocal, P. B., Hemming, S. R., and Grousset, F. E. (2009). Contrasting Compositions of Saharan Dust in the Eastern Atlantic Ocean during the Last Deglaciation and African Humid Period. *Earth Planet. Sci. Lett.* 278, 257–266. doi:10.1016/j.epsl.2008.12.011

Conley, D. J., and Schelske, C. L. (2002). "Biogenic Silica," in *Tracking Environmental Change Using Lake Sediments. Developments in Paleoenvironmental Research*. Editors J. P. Smol, H. J. B. Birks, W. M. Last, R. S. Bradley, and K. Alverson, 3, 281–293. doi:10.1007/0-306-47668-1_14

Cuven, S., Francus, P., and Lamoureux, S. F. (2010). Estimation of Grain Size Variability with Micro X-ray Fluorescence in Laminated Lacustrine Sediments, Cape Bounty, Canadian High Arctic. *J. Paleolimnol.* 44 (3), 803–817. doi:10.1007/s10933-010-9453-1

Danatsas, I. (1994). Jungneogene Ostrakoden aus der NW- und N-Pelopennes (Griechenland). *Münstersche Forschungen zur Geologie and Paläontologie* 76, 97–167.

Daskalaki, P. (2002). Contribution to Chemistry and Quality of Groundwater in Greece. Unpubl. Ph.D. Thesis. Dept. of Geology, University of Patras, 947.

Davison, W. (1993). Iron and Manganese in Lakes. *Earth-Science Rev.* 34, 119–163. doi:10.1016/0012-8252(93)90029-7

Dayan, U., Heffter, J., Miller, J., and Gutman, G. (1991). Dust Intrusion Events into the Mediterranean Basin. *J. Appl. Meteorology Climatology* Vol. 30, 1185–1199. doi:10.1175/1520-0450(1991)030<1185:DIEITM>2.0.CO;2

De Decker, P. (1979). The Middle Pleistocene Ostracod Fauna of the West Runton Freshwater Bed. *Norfolk, Paleontol.* 22/2, 293–316.

Dearing, J. A. (1997). Sedimentary Indicators of lake-level Changes in the Humid Temperate Zone: a Critical Review. *J. Paleolimnology* 18, 1–14. doi:10.1023/A:1007916210820

Devoto, G. (1965). Lacustrine Pleistocene in the Lower Liri Valley. *Geologica. Romana* 4, 291–365.

Digerfeldt, G., Olsson, S., and Sandgren, P. (2000). Reconstruction of lake-level Changes in lake Xinias, central Greece, during the Last 40 000 Years. *Palaeogeogr. Palaeoclimatol. Palaeoecol.* 158 (Issues 1–2), 65–82. doi:10.1016/S0031-0182(00)00029-8

Dornsiepen, U. F., Manutsoglu, E., and Mertmann, D. (2001). Permian-Triassic Palaeogeography of the External Hellenides. *Palaeogeogr. Palaeoclimatol. Palaeoecol.* 172, 327–338. doi:10.1016/S0031-0182(01)00307-8

Doukas, C., van Kolfschoten, T., Papayianni, K., Panagopoulou, E., and Harvati, K. (2018). The Small Mammal Fauna from the Palaeolithic Site Marathousa 1 (Greece). *Quat. Int.* 497, 95–107. doi:10.1016/j.quaint.2018.09.036

Emmanouilidis, A., Katrantsiotis, C., Norström, E., Risberg, J., Kylander, M., Sheik, T. A., et al. (2018). Middle to Late Holocene Palaeoenvironmental Study of Gialova Lagoon, SW Peloponnese, Greece. *Quat. Int.* 476, 46–62. doi:10.1016/j.quaint.2018.03.005

Ermolli, E. R., Aucelli, P. P., Di Rollo, A., Mattei, M., Petrosino, P., Porreca, M., et al. (2010). An Integrated Stratigraphical Approach to the Middle Pleistocene Succession of the Sessano basin (Molise, Italy). *Quat. Int.* 225 (1), 114–127. doi:10.1016/j.quaint.2009.04.008

Fernández, M., Björck, S., Wohlfarth, B., Maidana, N. I., Unkel, I., and Van der Putten, N. (2013). Diatom assemblage changes in lacustrine sediments from Isla de los Estados, southernmost South America, in response to shifts in the southwesterly wind belt during the last deglaciation. *J. Paleolimnol.* 50, 433–446. doi:10.1007/s10933-013-9736-4

Field, M. H., Ntinou, M., Tsartsidou, G., van Berge Henegouwen, D., Risberg, J., Tourloukis, V., et al. (2018). A Palaeoenvironmental Reconstruction (Based on Palaeobotanical Data and Diatoms) of the Middle Pleistocene Elephant (*Palaeoloxodon antiquus*) Butchery Site at Marathousa, Megalopolis, Greece. *Quat. Int.* 497, 108–122. doi:10.1016/j.quaint.2018.06.014

Fitzpatrick, R. W., and Chittleborough, D. J. (2002). "Titanium and Zirconium Minerals," in *Soil Mineralogy with Environmental Applications*. Editors J. B. Dixon and D. G. Schulze. doi:10.2136/sssabookser7

Flower, R. J. (1993). "Diatom Preservation: Experiments and Observations on Dissolution and Breakage in Modern and Fossil Material," in *Twelfth International Diatom Symposium. Developments in Hydrobiology*. Editor H. van Dam, 90, 473–484. doi:10.1007/978-94-017-3622-0_48

Foerster, V., Deocampo, D. M., Asrat, A., Günter, C., Junginger, A., Krämer, K. H., et al. (2018). Towards an Understanding of Climate Proxy Formation in the Chew Bahir basin, Southern Ethiopian Rift. *Palaeogeogr. Palaeoclimatol. Palaeoecol.* 501, 111–123. doi:10.1016/j.palaeo.2018.04.009

Francke, A., Wagner, B., Just, J., Leicher, N., Gromig, R., Baumgarten, H., et al. (2016). Sedimentological Processes and Environmental Variability at Lake Ohrid (Macedonia, Albania) between 637 Ka and the Present. *Biogeosciences* 13, 1179–1196. doi:10.5194/bg-13-1179-2016

Frenzel, P., and Boomer, I. (2005). The Use of Ostracods from Marginal marine, Brackish Waters as Bioindicators of Modern and Quaternary Environmental Change. *Palaeogeogr. Palaeoclimatol. Palaeoecol.* 225, 68–92. doi:10.1016/j.palaeo.2004.02.051

Frenzel, P., Keyser, D., and Viehberg, F. A. (2010). An Illustrated Key and (Palaeo) ecological Primer for Postglacial to Recent Ostracoda (Crustacea) of the Baltic Sea. *Boreas* 39 (3), 567–575. doi:10.1111/j.1502-3885.2009.00135.x

Frogley, M. R., (1998). The Biostratigraphy, Palaeoecology and Geochemistry of a Long Lacustrine Sequence from NW Greece (Doctoral Thesis). doi:10.17863/CAM.16400

Frost, T. M., Reiswig, H. M., and Riccardi, A. (2001). "Porifera," in *Ecology and Classification of North American Freshwater Invertebrates*. Editors J. H. Thorp and A. P. Covich. 2nd Edition (Academic Press), 97–133. 9780080530673.

Fuhrmann, R. (2012). Atlas quartärer und rezenter Ostrakoden Mitteldeutschlands. *Altenburger Naturwissenschaftliche Forschungen* 15.

Giaccio, B., Leicher, N., Mannella, G., Monaco, L., Regattieri, E., Wagner, B., et al. (2019). Extending the Tephra and Palaeoenvironmental Record of the Central Mediterranean Back to 430 ka: A New Core From Fucino Basin, Central Italy. *Quat. Sci. Rev.* 225, 106003. doi:10.1016/j.quascirev.2019.106003

Giusti, D., Tourloukis, V., Konidaris, G., Thompson, N., Karkanas, P., Panagopoulou, E., et al. (2018). Beyond Maps: Patterns of Formation Processes at the Middle Pleistocene Open-Air Site of Marathousa 1, Megalopolis Basin, Greece. *Quat. Int.* 497, 137–153. doi:10.1016/j.quaint.2018.01.041

Givati, A., and Rosenfeld, D. (2013). The Arctic Oscillation, Climate Change and the Effects on Precipitation in Israel. *Atmos. Res.* 132–133 (133), 114–124. doi:10.1016/j.atmosres.2013.05.001

Grove, C. A., Nagtegaal, R., Zinke, J., Scheufen, T., Koster, B., Kasper, S., et al. (2010). River Runoff Reconstructions from Novel Spectral Luminescence Scanning of Massive Coral Skeletons. *Coral Reefs* 29, 579–591. doi:10.1007/s00338-010-0629-y

Haberzettl, T., Corbella, H., Fey, M., Janssen, S., Lucke, A., Mayr, C., et al. (2007). Lateglacial and Holocene Wet–Dry Cycles in Southern Patagonia: Chronology, Sedimentology and Geochemistry of a Lacustrine Record From Laguna Potrok Aike, Argentina. *The Holocene* 17 (3), 297–310. doi:10.1177/0959683607076437

Hammer, Ø., Harper, D. A. T., and Ryan, P. D. (2001). PAST: Paleontological Statistics Software Package for Education and Data Analysis. *Palaeontol. Electronica*. 4 (1), 9.

Harrison, F. W. W. (1988). Utilization of Freshwater Sponges in Paleolimnological Studies. *Palaeogeogr. Palaeoclimatol. Palaeoecol.* 62 (1–4), 387–397. doi:10.1016/0031-0182(88)90063-6

Harvati, K. (2016). "Paleoanthropology in Greece: Recent Findings and Interpretations," in *Paleoanthropology of the Balkans and Anatolia: Human Evolution and its Context. Vertebrate Paleobiology and Paleoanthropology Series*. Editors K. Harvati and M. Roksandic (Dordrecht: Springer), 3–14. doi:10.1007/978-94-024-0874-4_1

Harvati, K., Panagopoulou, E., and Runnels, C. (2009). The Paleoanthropology of Greece. *Evol. Anthropol.* 18, 131–143. doi:10.1002/evan.20219

K. Harvati, G. Konidaris, and V. Tourloukis (Editors) (2018). Special Issue Human Evolution at the Gates of Europe. *Quaternary International Special Issue Volume 497 Part A*, 1–240.

Harvati, K., Röding, C., Bosman, A. M., Karakostis, F. A., Grün, R., Stringer, C., et al. (2019). Apidima Cave Fossils Provide Earliest Evidence of *Homo sapiens* in Eurasia. *Nature* 571, 500–504. doi:10.1038/s41586-019-1376-z

Harvati, K. (2021). "The Hominin Fossil Record from Greece," in *The Fossil Vertebrates of Greece Vol. 1 – Basal Vertebrates, Basal Tetrapods, Afrotherians, Glires, and Primates*. Editor E. Vlachos (Cham: Springer – Nature Publishing Group), 18.

Hemming, S. (2007). Terrigenous Sediments. *Encyclopedia Quat. Sci.* 3, 1776–1785. doi:10.1016/b0-444-52747-8/00303-3

Heymann, C., Nelle, O., Dörfler, W., Zagana, H., Nowaczyk, N., Xue, J., et al. (2013). Late Glacial to Mid-holocene Palaeoclimate Development of Southern Greece Inferred from the Sediment Sequence of Lake Stymphalia (NE-Peloponnese). *Quat. Int.* 302, 42–60. doi:10.1016/j.quaint.2013.02.014

Hibbins, S. G. (2000). *Strontium and Strontium Compounds*. Kirk-Othmer Encyclopedia of Chemical Technology. doi:10.1002/0471238961.1920181508090202.a01.pub2

Hoang van, L., Clift, P. D., Schwab, A. M., Huuse, M., Nguyen, D. A., and Zhen, S. (2010). Large-scale Erosional Response of SE Asia to Monsoon Evolution Reconstructed from Sedimentary Records of the Song Hong-Yinggehai and Qiongdongnan Basins, South China Sea. *Geol. Soc. Spec. Publ.* 342, 219–244. 10.1144/SP342.13.

Hughes, P. D., Woodward, J. C., and Gibbad, P. L. (2007). Middle Pleistocene Cold Stage Climates in the Mediterranean: New Evidence from the Glacial Record. *Earth Planet. Sci. Lett.* 253 (1-2), 50–56. doi:10.1016/j.epsl.2006.10.019

Hussain, S. M., Ganesan, P., Ravi, G., Mohan, S. P., and Sridhar, S. G. D. (2007). Distribution of Ostracoda in marine and Marginal marine Habitats off Tamil Nadu and Adjoining Areas, Southern East Cost of India and Andaman Islands: Environmental Implications. *Indian J. Mar. Sci.* 36 (4), 369–377.

Jacobs, Z., Li, B., Karkanas, P., Tourloukis, V., Thompson, N., Panagopoulou, E., et al. (2018). Optical Dating of K-Feldspar Grains from Middle Pleistocene Lacustrine Sediment at Marathousa 1 (Greece). *Quat. Int.* 497, 170–177. doi:10.1016/j.quaint.2018.06.029

Jacobson, A. D., Blum, J. D., and Walter, L. M. (2002). Reconciling the Elemental and Sr Isotope Composition of Himalayan Weathering Fluxes: Insights from the Carbonate Geochemistry of Stream Waters. *Geochimica et Cosmochimica Acta* 66 (19), 3417–3429. doi:10.1016/S0016-7037(02)00951-1,

Jin, Z., Cao, J., Wu, J., and Wang, S. (2006). A Rb/Sr Record of Catchment Weathering Response to Holocene Climate Change in Inner Mongolia. *Earth Surf. Process. Landforms* 31, 285–291. doi:10.1002/esp.1243

Jolliffe, I. T., and Cadima, J. (2016). Principal Component Analysis: a Review and Recent Developments. *Phil. Trans. R. Soc. A.* 374, 20150202. doi:10.1098/rsta.2015.0202

Jouve, G., Francus, P., Lamoureux, S., Provencher-Nolet, L., Hahn, A., Haberzettl, T., et al. (2013). Microsedimentological Characterization Using Image Analysis and μ-XRF as Indicators of Sedimentary Processes and Climate Changes during Lateglacial at Laguna Potrok Aike, Santa Cruz, Argentina. *Quat. Sci. Rev.* 71, 191–204. doi:10.1016/j.quascirev.2012.06.003

Kagan, E., Stein, M., and Marco, S. (2018). Integrated Paleoseismic Chronology of the Last Glacial Lake Lisan: From Lake Margin Seismites to Deep-Lake Mass Transport Deposits. *J. Geophys. Res. Solid Earth* 123, 2806–2824. doi:10.1002/2017JB014117

Karkanas, P., Tourloukis, V., Thompson, N., Giusti, D., Panagopoulou, E., and Harvati, K. (2018). Sedimentology and Micromorphology of the Lower Palaeolithic Lakeshore Site Marathousa 1, Megalopolis Basin, Greece. *Quat. Int.* 497, 123–136. doi:10.1016/j.quaint.2018.02.037

Katrantsiotis, C., Norström, E., Holmgren, K., Risberg, J., and Skelton, A. (2016). High-resolution Environmental Reconstruction in SW Peloponnese, Greece, Covering the Last C. 6000 years: Evidence from Agios Floros Fen, Messenian plain. *The Holocene* 26 (2), 188–204. doi:10.1177/0959683615596838

Kelepertsis, A. E., and Kontis, E. (1997). Geochemical and Mineralogical Characteristics of Pleistocene Lignites and Associated Sediments of Marathousa Coal Field, Central Peloponnese, Greece. *Chin. J. Geochem.* 16, 8–19. doi:10.1007/BF02843368

Kleman, J., Borgström, I., Skelton, A., and Hall, A. (2016). Landscape Evolution and Landform Inheritance in Tectonically Active Regions: The Case of the Southwestern Peloponnese, Greece. *Z. Geomorphol.* 171–193. doi:10.1127/zfg/2016/0283

Kemp, A. L. W., Dell, C. I., and Harper, N. S. (1978). Sedimentation Rates and a Sediment Budget for Lake Superior. *J. Great Lakes Res.* 4 (3–4), 276–287. doi:10.1016/S0380-1330(78)72198-2

Koinig, K. A., Shotyk, W., Lotter, A. F., Ohlendorf, C., and Sturm, M. (2003). 9000 Years of Geochemical Evolution of Lithogenic Major and Trace Elements in the Sediment of an alpine lake – the Role of Climate, Vegetation, and Land-Use History. *J. Paleolimnology* 30, 307–320. doi:10.1023/A:1026080712312

Konidaris, G. E., Athanassiou, A., Tourloukis, V., Thompson, N., Giusti, D., Panagopoulou, E., et al. (2018). The Skeleton of a Straight-Tusked Elephant (*Palaeoloxodon antiquus*) and Other Large Mammals from the Middle Pleistocene Butchering Locality Marathousa 1 (Megalopolis Basin, Greece): Preliminary Results. *Quat. Int.* 497, 65–84. doi:10.1016/j.quaint.2017.12.001

Köppen, W. (1918). *Klassifikation der Klimate nach Temperatur, Niederschlag und Jahreslauf*. Gotha: Petermanns Geographische Mitteilungen, 64.

Koutsodendris, A., Kousis, I., Peyron, O., Wagner, B., and Pross, J. (2019). The Marine Isotope Stage 12 Pollen Record from Lake Ohrid (SE Europe): Investigating Short-Term Climate Change under Extreme Glacial Conditions. *Quat. Sci. Rev.* 221, 105873. doi:10.1016/j.quascirev.2019.105873

Kutzbach, J. E., Chen, G., Cheng, H., Edwards, R. L., and Liu, Z. (2014). Potential Role of winter Rainfall in Explaining Increased Moisture in the Mediterranean and Middle East during Periods of Maximum Orbitally-Forced Insolation Seasonality. *Clim. Dyn.* 42 (3-4), 1079–1095. doi:10.1007/s00382-013-1692-1

Kwiecien, O., Arz, H. W., Lamy, F., Plessen, B., Bahr, A., and Haug, G. H. (2009). North Atlantic Control on Precipitation Pattern in the Eastern Mediterranean/Black Sea Region during the Last Glacial. *Quat. Res.* 71 (3), 375–384. doi:10.1016/j.yqres.2008.12.004

Kylander, M. E., Ampel, L., Wohlfarth, B., and Veres, D. (2011). High-resolution X-ray Fluorescence Core Scanning Analysis of Les Echets (France) Sedimentary Sequence: New Insights from Chemical Proxies. *J. Quat. Sci.* 26, 109–117. doi:10.1002/jqs.1438

Laskar, J., Robutel, P., Joutel, F., Gastineau, M., Correia, A. C. M., and Levrard, B. (2004). A Long-Term Numerical Solution for the Insolation Quantities of the Earth. *A&A* 428 (1), 261–285. doi:10.1051/0004-6361:20041335

Lekkas, E., Danamos, G., Skourtsos, E., and Sakellariou, D. (2002). Position of the Middle Triassic Tyros Beds in the Gavrovo-Tripolis Unit (Rhodes Island, Dodecanese, Greece). *Geologica. Carpathica*. 53 (1), 37–44.

Leontaritis, A. D., Kouli, K., and Pavlopoulos, K. (2020). The Glacial History of Greece: a Comprehensive Review. *Med. Geosc. Rev.* 2 (2), 65–90. doi:10.1007/s42990-020-00021-w

Lisiecki, L. E., and Raymo, M. E. (2005). A Pliocene-Pleistocene Stack of 57 Globally Distributed Benthic δ18O Records. *Paleoceanography* 20, a–n. doi:10.1029/2004PA001071

Liu, X., Vandenberghe, J., An, Z., Li, Y., Jin, Z., Dong, J., et al. (2016). Grain Size of Lake Qinghai Sediments: Implications for Riverine Input and Holocene Monsoon Variability. *Palaeogeogr. Palaeoclimatol. Palaeoecol.* 449, 41–51. doi:10.1016/j.palaeo.2016.02.005

Longman, J., Veres, D., and Wennrich, V. (2019). Utilisation of XRF Core Scanning on Peat and Other Highly Organic Sediments. *Quat. Int.* 514, 85–96. doi:10.1016/j.quaint.2018.10.015

Lourens, L. J. (2004). Revised Tuning of Ocean Drilling Program Site 964 and KC01B (Mediterranean) and Implications for the $\delta^{18}O$, Tephra, Calcareous Nannofossil, and Geomagnetic Reversal Chronologies of the Past 1.1 Myr. *Paleoceanography* 19, a–n. doi:10.1029/2003PA000997

Lüttig, G. (1968). Die Ostrakoden des Megalopolis-Beckens (Peloponnes) und die Grenze Tertiär/Quartär. *Giornale die Geologia* 35, 73–82.

Lüttig, G., and Marinos, G. (1962). Zur Geologie der neuen griechischen Braunkohlen-Lagerstätte von Megalopolis. *Braunk. Wärm. Energ.* 14, 222–231.

Mädler, K. (1971). Die Früchte und Samen aus der frühpleistozänen Braunkohle von Megalopolis in Griechenland und ihre ökologische Bedeutung. *Beihefte zum Geologischen Jahrbuch* 110, 1–79.

Mahowald, N. M., Muhs, D. R., Levis, S., Rasch, P. J., Yoshioka, M., Zender, C. S., et al. (2006). Change in Atmospheric mineral Aerosols in Response to Climate: Last Glacial Period, Preindustrial, Modern, and Doubled Carbon Dioxide Climates. *J. Geophys. Res.* 111, a–n. doi:10.1029/2005JD006653

Maldonado, M., López-Acosta, M., Sitjà, C., García-Puig, M., Galobart, C., Ercilla, G., et al. (2019). Sponge Skeletons as an Important Sink of Silicon in the Global Oceans. *Nat. Geosci.* 12, 815–822. doi:10.1038/s41561-019-0430-7

Manariotis, I. D., and Yannopoulos, P. C. (2014). Impact of Human Activities and Infrastructure Works on Hydro Morphological Characteristics of Alfeios River, Greece. *Glob. NEST J.* 16, 136–145.

Mannella, G., Giaccio, B., Zanchetta, G., Regattieri, E., Niespolo, E. M., Pereira, A., et al. (2019). Palaeoenvironmental and Palaeohydrological Variability of Mountain Areas in the central Mediterranean Region: A 190 Ka-Long Chronicle from the Independently Dated Fucino Palaeolake Record (central Italy). *Quat. Sci. Rev.* 210, 190–210. doi:10.1016/j.quascirev.2019.02.032

Martens, K., and Savatenalinton, S. (2011). A Subjective Checklist of the Recent, Free-Living, Non-marine Ostracoda (Crustacea). *Zootaxa* 2855, 1–79. doi:10.11646/zootaxa.2855.1.1

Mazzini, I., Gliozzi, E., Rossetti, G., and Pieri, V. (2014). The Ilyocypris Puzzle: A Multidisciplinary Approach to the Study of Phenotypic Variability. *Int. Rev. Hydrobiology* 99 (1-14). doi:10.1002/iroh.201301729

McManus, J., Berelson, W. M., Klinkhammer, G. P., Johnson, K. S., Coale, K. H., Anderson, R. F., et al. (1998). Geochemistry of Barium in marine Sediments: Implications for its Use as a Paleoproxy. *Geochimica et Cosmochimica Acta* 62, 3453–3473. doi:10.1016/s0016-7037(98)00248-8

McManus, J. F., Oppo, D. W., and Cullen, J. L. (1999). A 0.5-Million-Year Record of Millennial-Scale Climate Variability in the North Atlantic. *Science* 283 (5404), 971–975. doi:10.1126/science.283.5404.971

Meisch, C. (2000). *Freshwater Ostracoda of Western and Central Europe*. Spektrum Akademischer Verlag.

Meisch, C., Scharf, B., Fuhrmann, R., and Thiéry, A. (2019). *Neglecandona altoides* (Petkovski, 1961) Nov. Comb. And the Genus *Neglecandona* Krstić, 2006 (Crustacea, Ostracoda, Candonidae). *Bull. de la Société des naturalistes luxembourgeois* 121, 237–264.

Meisch, C., and Wouters, K. (2004). Valve Surface Structure of *Candona neglecta* Sars, 1887 (Crustacea, Ostracoda), *Studia Quaternaria*. 21, 15–18.

Meyers, P. A., and Benson, L. V. (1987). Sedimentary Biomarker and Isotopic Indicators of the Paleoclimatic History of the Walker Lake basin, Western Nevada. *Org. Geochem.* 13 (issues 4–6), 807–813. doi:10.1016/0146-6380(88)90104-0

Meyers, P. A., and Teranes, J. L. (2001). "Sediment Organic Matter," in *Tracking Environmental Change Using Lake Sediments Volume 2: Physical and Geochemical Methods*. Editors W. M. Last and J. P. Smol. ISBN 0-306-47670-3.

Michailidis, D., Konidaris, G. E., Athanassiou, A., Panagopoulou, E., and Harvati, K. (2018). The Ornithological Remains from Marathousa 1 (Middle Pleistocene; Megalopolis Basin, Greece). *Quat. Int.* 497, 85–94. doi:10.1016/j.quaint.2018.06.045

Muhs, D. R., Budahn, J., Avila, A., Skipp, G., Freeman, J., and Patterson, D. (2010). The Role of African Dust in the Formation of Quaternary Soils on Mallorca, Spain and Implications for the Genesis of Red Mediterranean Soils. *Quat. Sci. Rev.* 29 (19-20), 2518–2543. doi:10.1016/j.quascirev.2010.04.013

Muhs, D. R., Budahn, J. R., Prospero, J. M., and Carey, S. N. (2007). Geochemical Evidence for African Dust Inputs to Soils of Western Atlantic Islands: Barbados, the Bahamas, and Florida. *J. Geophys. Res.* 112, F02009. doi:10.1029/2005JF000445

Naeher, S., Gilli, A., North, R. P., Hamann, Y., and Schubert, C. J. (2013). Tracing Bottom Water Oxygenation with Sedimentary Mn/Fe Ratios in Lake Zurich, Switzerland. *Chem. Geology* 352, 125–133. doi:10.1016/j.chemgeo.2013.06.006

Nava, S., Becagli, S., Calzolai, G., Chiari, M., Lucarelli, F., Prati, P., et al. (2012). Saharan Dust Impact in central Italy: An Overview on Three Years Elemental Data Records. *Atmos. Environ.* 60, 444–452. doi:10.1016/j.atmosenv.2012.06.064

Nesbitt, H. W., and Wilson, R. E. (1992). Recent Chemical Weathering of Basalts. *Am. J. Sci.* 292 (10), 740–777. doi:10.2475/ajs.292.10.740

Nickel, B., Riegel, W., Schönherr, T., and Velitzelos, E. (1996). Environments of Coal Formation in the Pleistocene lignite at Megalopolis, Peloponnesus (Greece) - Reconstructions from Palynological and Petrological Investigations. *njgpa* 200, 201–220. doi:10.1127/njgpa/200/1996/201

Nizou, J., Hanebuth, T. J. J., and Vogt, C. (2011). Deciphering Signals of Late Holocene Fluvial and Aeolian Supply from a Shelf Sediment Depocentre off Senegal (north-west Africa). *J. Quat. Sci.* 26, 411–421. doi:10.1002/jqs.1467

Okuda, M., van Vugt, N., Nakagawa, T., Ikeya, M., Hayashida, A., Yasuda, Y., et al. (2002). Palynological Evidence for the Astronomical Origin of lignite-detritus Sequence in the Middle Pleistocene Marathousa Member, Megalopolis, SW Greece. *Earth Planet. Sci. Lett.* 201, 143–157. doi:10.1127/njgpa/200/1996/20110.1016/s0012-821x(02)00706-9

Panagopoulou, E., Tourloukis, V., Thompson, N., Athanassiou, A., Tsartsidou, G., Konidaris, G. E., et al. (2015). Marathousa 1: a New Middle Pleistocene Archaeological Site from Greece. *Antiquity* 343, 1–8.

Panagopoulou, E., Tourloukis, V., Thompson, N., Konidaris, G., Athanassiou, A., Giusti, D., et al. (2018). The Lower Palaeolithic Site of Marathousa 1, Megalopolis, Greece: Overview of the Evidence. *Quat. Int.* 497, 33–46. doi:10.1016/j.quaint.2018.06.031

Panagiotopoulos, K., Holtvoeth, J., Kouli, K., Marinova, E., Francke, A., Cvetkoska, A., et al. (2020). Insights Into the Evolution of the Young Lake Ohrid Ecosystem and Vegetation Succession From a Southern European Refugium During the Early Pleistocene. *Quat. Sci. Rev.* 227, 106044. doi:10.1016/j.quascirev.2019.106044

Papoulia, C. (2017). Seaward Dispersals to the NE Mediterranean Islands in the Pleistocene. The Lithic Evidence in Retrospect. *Quat. Int.* 431, 64–87. doi:10.1016/j.quaint.2016.02.019

Pierson, T. C. (2005). "Hyperconcentrated Flow - Transitional Process between Water Flow and Debris Flow," in *Debris-flow Hazards and Related Phenomena*. Editors M. Jakob and O. Hungr (Berlin, Heidelberg: Springer), 159–202. doi:10.1007/3-540-27129-5_8

Rantakari, M., and Kortelainen, P. (2008). Controls of Organic and Inorganic Carbon in Randomly Selected Boreal Lakes in Varied Catchments. *Biogeochemistry* 91 (2–3), 151–162. doi:10.1007/s10533-008-9266-8

Regattieri, E., Giaccio, B., Galli, P., Nomade, S., Peronace, E., Messina, P., et al. (2016). A Multi-Proxy Record of MIS 11-12 Deglaciation and Glacial MIS 12

Instability from the Sulmona basin (central Italy). *Quat. Sci. Rev.* 132, 129–145. doi:10.1016/j.quascirev.2015.11.015

Regattieri, E., Giaccio, B., Nomade, S., Francke, A., Vogel, H., Drysdale, R. N., et al. (2017). A Last Interglacial Record of Environmental Changes from the Sulmona Basin (central Italy). *Palaeogeogr. Palaeoclimatol. Palaeoecol.* 472, 51–66. doi:10.1016/j.palaeo.2017.02.013

Reiswig, H. M., Frost, T. M., and Ricciardi, A. (2010). "Porifera," in *Ecology and Classification of North American Freshwater Invertebrates*. Editors H. Thorp and A. P. Covich. Third Edition (Academic Press), 91–123. 9780123748553. doi:10.1016/B978-0-12-374855-3.00004-2

Remoundaki, E., Bourliva, A., Kokkalis, P., Mamouri, R. E., Papayannis, A., Grigoratos, T., et al. (2011). PM10 Composition during an Intense Saharan Dust Transport Event over Athens (Greece). *Sci. Total Environ.* 409 (20), 4361–4372. doi:10.1016/j.scitotenv.2011.06.026

Rodrigues, T., Voelker, A. H. L., Grimalt, J. O., Abrantes, F., and Naughton, F. (2011). Iberian Margin Sea Surface Temperature during MIS 15 to 9 (580-300 Ka): Glacial Suborbital Variability versus Interglacial Stability. *Paleoceanography* 26 (1), PA1204. doi:10.1029/2010PA001927

Rothwell, R. G., and Croudace, I. w. (2015). "Micro-XRF Studies of Sediment Cores: a Perspective on Capability and Application in the Environmental Sciences," in *Micro-XRF Studies of Sediment Cores*. Editors I. W. Croudace and R. G. Rothwell (Dordecht: Springer), 1–21. doi:10.1007/978-94-017-9849-5_1

Roy, P. D., Caballero, M., Lozano, R., and Smykatz-Kloss, W. (2008). Geochemistry of Late Quaternary Sediments from Tecocomulco lake, central Mexico: Implication to Chemical Weathering and Provenance. *Geochemistry* 68 (4), 383–393. doi:10.1016/j.chemer.2008.04.001

Ruiz, F., Abad, M., Boderat, A. M., Carbonel, P., Rodríguez-Lázaro, J., González-Regalado, M. L., et al. (2013). Freshwater Ostracods as Environmental Tracers. *Int. J. Environ. Sci. Technol.* 10, 1115–1128. doi:10.1007/s13762-013-0249-5

Schellenberg, S. A. (2007). "PALEOLIMNOLOGY | Marine Ostracods," in *Encyclopedia of Quaternary Science*. Editor S. A. Elias (Amsterdam: Elsevier), 2046–2062. doi:10.1016/b0-44-452747-8/00249-0

Shaheen, S. M., Alessi, D. S., Tack, F. M. G., Ok, Y. S., Kim, K.-H., Gustafsson, J. P., et al. (2019). Redox Chemistry of Vanadium in Soils and Sediments: Interactions with Colloidal Materials, Mobilization, Speciation, and Relevant Environmental Implications- A Review. *Adv. Colloid Interf. Sci.* 265, 1–13. doi:10.1016/j.cis.2019.01.002

Siavalas, G., Linou, M., Chatziapostolou, A., Kalaitzidis, S., Papaefthymiou, H., and Christanis, K. (2009). Palaeoenvironment of Seam I in the Marathousa Lignite Mine, Megalopolis Basin (Southern Greece). *Int. J. Coal Geology* 78 (4), 233–248. doi:10.1016/j.coal.2009.03.003

Sickenberg, O. (1975). Eine Säugetierfauna des tieferen Bihariums aus dem Becken von Megalopolis (Peleponnes, Griechenland). *Ann. Géologiques des Pays Helléniques* 27, 25–73.

Spratt, R. M., and Lisiecki, L. E. (2016). A Late Pleistocene Sea Level Stack. *Clim. Past* 12 (4), 1079–1092. doi:10.5194/cp-12-1079-2016

Stankevica, K., Vincevica-Gaile, Z., and Klavins, M. (2016). Freshwater Sapropel (Gyttja): its Description, Properties and Opportunities of Use in Contemporary Agriculture. *Agron. Res.* 14 (3), 929–947.

Stein, R., Hefter, J., Grützner, J., Voelker, A., and Naafs, B. D. A. (2009). Variability of Surface Water Characteristics and Heinrich-like Events in the Pleistocene Midlatitude North Atlantic Ocean: Biomarker and XRD Records from IODP Site U1313 (MIS 16-9). *Paleoceanography* 24, a–n. doi:10.1029/2008PA001639

Thompson, N., Tourloukis, V., Panagopoulou, E., and Harvati, K. (2018). In Search of Pleistocene Remains at the Gates of Europe: Directed Surface Survey of the Megalopolis Basin (Greece). *Quat. Int.* 497, 22–32. doi:10.1016/j.quaint.2018.03.036

Thomson, J., Croudace, I. W., and Rothwell, R. G., (2006). A Geochemical Application of the ITRAX Scanner to a Sediment Core Containing Eastern Mediterranean Sapropel Units, *Geol. Soc. Lond. Spec. Publications*. In: (ed. R. G. Rothwell) *New Techniques in Sediment Core Analysis*. 267, pp. 65–77. doi:10.1144/GSL.SP.2006.267.01.05

Tourloukis, V., and Harvati, K. (2018). The Palaeolithic Record of Greece: A Synthesis of the Evidence and a Research Agenda for the Future. *Quat. Int.* 466, 48–65. doi:10.1016/j.quaint.2017.04.020

Tourloukis, V., and Karkanas, P. (2012). The Middle Pleistocene Archaeological Record of Greece and the Role of the Aegean in Hominin Dispersals: New Data and Interpretations. *Quat. Sci. Rev.* 43, 1–15. doi:10.1016/j.quascirev.2012.04.004

Tourloukis, V., Muttoni, G., Karkanas, P., Monesi, E., Scardia, G., Panagopoulou, E., et al. (2018a). Magnetostratigraphic and Chronostratigraphic Constraints on the Marathousa 1 Lower Palaeolithic Site and the Middle Pleistocene Deposits of the Megalopolis Basin, Greece. *Quat. Int.* 497, 154–169. doi:10.1016/j.quaint.2018.03.043

Tourloukis, V. (2016). "On the Spatio-Temporal Distribution of Mediterranean Lower Paleolithic Sites: A Geoarchaeological Perspective," in *Paleoanthropology of the Balkans and Anatolia: Human Evolution and its Context. Vertebrate Paleobiology and Paleoanthropology Series*. Editors K. Harvati and M. Roksandic (Dordrecht: Springer-Verlag), 303–323. doi:10.1007/978-94-024-0874-4_18

Tourloukis, V., Thompson, N., Panagopoulou, E., Giusti, D., Konidaris, G. E., Karkanas, P., et al. (2018b). Lithic Artifacts and Bone Tools from the Lower Palaeolithic Site Marathousa 1, Megalopolis, Greece: Preliminary Results. *Quat. Int.* 497, 47–64. doi:10.1016/j.quaint.2018.05.043

Trauth, M. H. (2014). A New Probabilistic Technique to Build an Age Model for Complex Stratigraphic Sequences. *Quat. Geochronol.* 22, 65–71. doi:10.1016/j.quageo.2014.03.001

Trauth, M. H., Gebbers, R., Marwan, N., and Sillmann, E. (2015). *MATLAB Recipes for Earth Sciences*. 4th edition. doi:10.1007/978-3-662-46244-7

Tsiftsis, E. V. (1987). *Geology and Hydrogeology of the Megalopolis Basin, Peloponnese, Greece*. Doctoral dissertation, University of Bristol.

Tzedakis, P. C., Hooghiemstra, H., and Pälike, H. (2006). The Last 1.35 Million Years at Tenaghi Philippon: Revised Chronostratigraphy and Long-Term Vegetation Trends. *Quat. Sci. Rev.* 25 (23–24), 3416–3430. doi:10.1016/j.quascirev.2006.09.002

Unkel, I., Heymann, C., Nelle, O., and Zagana, E. (2011). "Climatic Influence on Lake Stymphalia during the Last 15 000 Years,". *Advances in the Research of Aquatic Environment*. Editor N. Lambrakis, G. Stournaras, and K. Katsanou (Berlin, Heidelberg: Springer), Vol. 1, 75–82. doi:10.1007/978-3-642-19902-810.1007/978-3-642-19902-8_8

Valero-Garcés, B., Morellón, M., Moreno, A., Corella, J. P., Martín-Puertas, C., Barreiro, F., et al. (2014). Lacustrine Carbonates of Iberian Karst Lakes: Sources, Processes and Depositional Environments. *Sediment. Geology* 299, 1–29. doi:10.1016/j.sedgeo.2013.10.007

Van Vugt, N., de Bruijn, H., van Kolfschoten, T., and Langereis, C. G. (2000). Magneto- and Cyclostratigraphy and Mammal-Fauna's of the Pleistocene Lacustrine Megalopolis Basin, Peloponnesos, Greece. *Geologica Ultrajectina* 189, 69–92.

Van Vugt, N., Langereis, C. G., and Hilgen, F. J. (2001). Orbital Forcing in Pliocene–Pleistocene Mediterranean Lacustrine Deposits. *Dominant Expr. eccentricity versus precession, Palaeogeogr. Palaeoclimatol. Palaeoecol.* 172 (3-4), 193–205. doi:10.1016/s0031-0182(01)00270-x

Varga, G., Újvári, G., and Kovács, J. (2014). Spatiotemporal Patterns of Saharan Dust Outbreaks in the Mediterranean Basin. *Aeolian Res.* 15, 151–160. doi:10.1016/j.aeolia.2014.06.005

Villa, V., Pereira, A., Chaussé, C., Nomade, S., Giaccio, B., Limondin-Lozouet, N., et al. (2016). A MIS 15-MIS 12 Record of Environmental Changes and Lower Palaeolithic Occupation from Valle Giumentina, central Italy. *Quat. Sci. Rev.* 151, 160–184. doi:10.1016/j.quascirev.2016.09.006

Vinken, R. (1965). Stratigraphie und Tektonik des Beckens von Megalopolis (Peloponnes, Griechenland). *Geologisches Jahrbuch* 83, 97–148.

Wagner, B., Vogel, H., Francke, A., Friedrich, T., Donders, T., Lacey, J. H., et al. (2019). Mediterranean winter Rainfall in Phase with African Monsoons during the Past 1.36 Million Years. *Nature* 573 (7773), 256–260. doi:10.1038/s41586-019-1529-0

Wagner, C. W. (1957). *Sur les ostracodes du Quaternaire récent de Pays Bas et leur utilization dans l'étude géologiques des dèpots Holocenes*. Mouton and Co. 'S-Gravenhage, 259.

Wang, P., Tian, J., and Lourens, L. J. (2010). Obscuring of Long Eccentricity Cyclicity in Pleistocene Oceanic Carbon Isotope Records. *Earth Planet. Sci. Lett.* 290 (3-4), 319–330. doi:10.1016/j.epsl.2009.12.028

Weiberg, E., Unkel, I., Kouli, K., Holmgren, K., Avramidis, P., Bonnier, A., et al. (2016). The Socio-Environmental History of the Peloponnese during the Holocene: Towards an Integrated Understanding of the Past. *Quat. Sci. Rev.* 136, 40–65. doi:10.1016/j.quascirev.2015.10.042

West, A., Galy, A., and Bickle, M. (2005). Tectonic and Climatic Controls on Silicate Weathering. *Earth Planet. Sci. Lett.* 235 (1-2), 211–228. doi:10.1016/j.epsl.2005.03.020

Williams, R. H., McGee, D., Kinsley, C. W., Ridley, D. A., Hu, S., Fedorov, A., et al. (2016). Glacial to Holocene Changes in Trans-Atlantic Saharan Dust Transport and Dust-Climate Feedbacks. *Sci. Adv.* 2 (11), e1600445. doi:10.1126/sciadv.1600445

Yaltirak, C., Sakinç, M., Aksu, A. E., Hiscott, R. N., Galleb, B., and Ulgen, U. B. (2002). Late Pleistocene Uplift History along the Southwestern Marmara Sea Determined from Raised Coastal Deposits and Global Sea-Level Variations. *Mar. Geology* 190 (1-2), 283–305. doi:10.1016/S0025-3227(02)00351-1

Conflict of Interest: The authors declare that the research was conducted in the absence of any commercial or financial relationships that could be construed as a potential conflict of interest.

frontiers in Earth Science

ORIGINAL RESEARCH
published: 05 July 2021
doi: 10.3389/feart.2021.664105

Making the Invisible Stratigraphy Visible: A Grid-Based, Multi-Proxy Geoarchaeological Study of Umhlatuzana Rockshelter, South Africa

Femke H. Reidsma[1†], Irini Sifogeorgaki[1†], Ada Dinckal[2], Hans Huisman[3,4], Mark J. Sier[5,6], Bertil van Os[3] and Gerrit L. Dusseldorp[1,7]*

[1]Human Origins, Faculty of Archaeology, Leiden University, Leiden, Netherlands, [2]Institute for Archaeological Sciences, Senckenberg Centre for Human Evolution and Paleoenvironment, Eberhard Karls University Tübingen, Tübingen, Germany, [3]Section Archaeology, Cultural Heritage Agency of the Netherlands, Amersfoort, Netherlands, [4]Groningen Institute for Archaeology, University of Groningen, Groningen, Netherlands, [5]CENIEH, Burgos, Spain, [6]Department of Earth Sciences, University of Oxford, Oxford, United Kingdom, [7]Palaeo-Research Institute, University of Johannesburg, Johannesburg, South Africa

OPEN ACCESS

Edited by:
Christian Zeeden, Leibniz Institute for Applied Geophysics (LIAG), Germany

Reviewed by:
Michael B. Toffolo, Université Bordeaux Montagne, France
Mareike Stahlschmidt, Max Planck Institute for Evolutionary Anthropology, Germany

***Correspondence:**
Femke H. Reidsma
f.h.reidsma@arch.leidenuniv.nl

[†]These authors have contributed equally to this work and share first authorship

Specialty section:
This article was submitted to Sedimentology, Stratigraphy and Diagenesis, a section of the journal Frontiers in Earth Science

Received: *04 February 2021*
Accepted: *15 June 2021*
Published: *05 July 2021*

Citation:
Reidsma FH, Sifogeorgaki I, Dinckal A, Huisman H, Sier MJ, van Os B and Dusseldorp GL (2021) Making the Invisible Stratigraphy Visible: A Grid-Based, Multi-Proxy Geoarchaeological Study of Umhlatuzana Rockshelter, South Africa. Front. Earth Sci. 9:664105. doi: 10.3389/feart.2021.664105

Umhlatuzana rockshelter is an archaeological site with an occupational record covering the Middle Stone Age, Later Stone Age, and Iron Age. The presence of both Middle and Later Stone Age assemblages makes Umhlatuzana the ideal location for the study of the MSA–LSA transition (20–40 ka) in southern Africa. This transitional period is characterized by important modifications in stone tool technology, from prepared core technology to a toolkit based on microlith production. These changes are argued to have occurred in response to changes in climate and environment leading up to the Last Glacial Maximum. The deposits bearing the transitional assemblages at Umhlatuzana rockshelter appear homogeneous with no visible stratigraphic boundaries. This study integrates geoarchaeological techniques in order to explore fine-resolution geochemical differentiations of the sediments that are macroscopically invisible, and that will provide insight into (post-)depositional processes over time. Samples were systematically retrieved from the western profile of the site following a grid-based sampling strategy and analyzed for pH, elemental composition (XRF), and Magnetic Susceptibility. Additionally, the results were integrated with preliminary micromorphological observations. Our study reveals a steady, gradual change in the geochemistry of the deposits throughout the Pleistocene, related to a combination of environmental change and occupation intensity. We suggest that the part of the sequence reported to bear Middle to Later Stone Age transitional industries is characterized by wetter environmental conditions compared to the underlying deposits. Additionally, we support results from previous studies that excluded large scale post-depositional movement of the sedimentary sequence. Our study offers a successful multi-proxy approach to systematically sample and study archaeological deposits at the macro and micro scale, integrating a variety of geoarchaeological techniques. The approach provides insight into the depositional and post-depositional history of the

site, and allows for questions of stratigraphic integrity, anthropogenic input, preservation, and environmental change to be addressed.

Keywords: geochemistry, stratigraphy, Stone Age, pH, XRF, micromorphology, geoarchaeology, magnetic susceptibility

INTRODUCTION

The transition from the Middle Stone Age (MSA) to the Later Stone Age (LSA) (~40–20 ka) forms an important period within the behavioral evolution of early humans in South Africa (Villa et al., 2012). While instances of sophisticated, modern behavior are already documented for the MSA (e.g., engravings and jewelry) (see e.g., Henshilwood, 2012; Porraz et al., 2013), it is not until the LSA that modern human behavior is consistently present within the archaeological record (Deacon, 1999; Villa et al., 2012; Bader et al., 2020; Grove and Blinkhorn, 2020). During the transition from the MSA to the LSA the toolkit changes from one based on prepared core technology to one characterized by microlith production, signaling a marked change in the way stone tools were produced and used (Lombard et al., 2012; Villa et al., 2012). These changes appear against a backdrop of environmental change, during the time leading up to the Last Glacial Maximum (~29.5–19 ka) (Clark et al., 2009; Yokoyama et al., 2018). This period is characterized by a cold climate and frequent severe changes in temperature and humidity, which would have had consequences for resource availability and provided challenges for human groups to adapt to (Simon et al., 2015). It is often assumed that these drastic changes in climate were the driving force behind the MSA–LSA transition (Mitchell, 1988; McCall and Thomas, 2009). Unfortunately, only very few sites with transitional deposits are available (e.g., Border Cave, Rose Cottage Cave, Sehonghong). Moreover, age estimates of these transitional assemblages differ widely between sites (d'Errico et al., 2012; Loftus et al., 2019; Pargeter et al., 2017). In order to resolve questions about the timing and nature of the MSA–LSA transition, more high-resolution data on its archaeological, chronological, environmental, and stratigraphic context is needed.

Umhlatuzana rockshelter, located in KwaZulu-Natal, South Africa (**Figure 1**), is a good case-study site to address questions related to the MSA–LSA transition. The site preserves an archaeological archive spanning the last 70,000 years (Kaplan, 1990; Lombard et al., 2010; Sifogeorgaki et al., 2020), covering the later part of the MSA as well as the LSA (and some more recent, Iron Age deposits deposits). This makes Umhlatuzana one of the rare sites that has a continuous occupation sequence covering the MSA–LSA transition, making it paramount to understanding the nature of the transition in the region (see overviews in Lombard et al., 2012; Mackay et al., 2014). The site was originally the subject of a rescue excavation in the 1980s (Kaplan, 1990). Subsequent analysis of the materials from this excavation yielded early evidence for the use of complex adhesives (Lombard, 2007), bow-and-arrow (Lombard, 2011), and pressure-flaking (Högberg and Lombard, 2016a). Further, OSL samples were taken at the site to date the lowermost deposits with MSA archaeology (Lombard et al., 2010). In 2018 a new field campaign was launched by a team from Leiden University (in collaboration with the KwaZulu-Natal Museum), aimed at using geoarchaeology to address questions about the site's stratigraphic integrity and degree of post-depositional disturbance. High-resolution geoarchaeological data proved to be of particular importance, since the Pleistocene deposits did not display clearly visible stratigraphic boundaries in the field. Recent work by the team has addressed this issue by using cluster-analysis on the 3-dimentional distribution of the archaeological materials (Sifogeorgaki et al., 2020), allowing the identification of distinct horizontal artifact density zones and disproving the suggestion of large-scale sediment movement (contra Kaplan, 1990).

The current study builds upon the study of Sifogeorgaki et al. (2020) by taking a geochemical approach to better understand the visible and invisible variation within the sequence. It examines if more subtle changes in depositional processes and post-depositional environment can be detected through the combined application of several geoarchaeological analyses. Bulk sediment samples were systematically taken from the western profile using a grid-based sampling strategy. Each sample was subsequently analyzed for pH, Magnetic Susceptibility (MS), and elemental composition (XRF). In addition, some preliminary micromorphological and field observations are integrated, allowing a link between processes occurring at the micro and macro scale. The pH can provide insight into the chemical balance of a depositional environment and give clues on which materials can be expected to preserve (e.g., Weiner, 2010; Karkanas and Goldberg, 2018; Braadbaart et al., 2020). The elemental composition of the deposits can provide information on the mineralogy and natural and anthropogenic input (Holcomb and Karkanas, 2019). The presence of reactive (mineral) phases such as carbonates or organic matter determine the long-term preservation of vulnerable archaeological material like bone or organic matter (van Os et al., 2012). MS is used to characterize the magnetic mineral (iron) content within geological deposits. Mapping of MS can provide insight into lateral and vertical changes in this magnetic mineral content, and provide further insight into underlying processes (Dearing, 1999; Herries and Fisher, 2010; Dinckal et al., submitted). Micromorphology is the study of undisturbed sediment samples under the microscope (Courty et al., 1989; Macphail and Goldberg, 2017), which provides valuable insights into the micro context of the deposits, both in terms of content and arrangement. By combining these techniques and systematically sampling the entire profile, questions of stratigraphic integrity, anthropogenic input, preservation, and environmental change can be addressed at both a macro and micro scale. Furthermore, the approach is

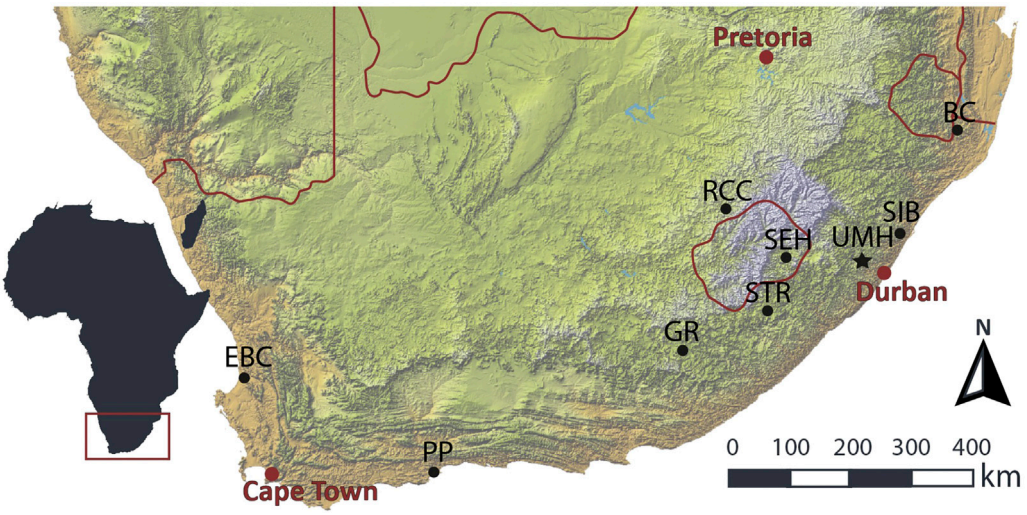

FIGURE 1 | Topographic map featuring Umhlatuzana rockshelter and its relative location to other sites mentioned in the text. BP, Border Cave; EBC, Elands Bay Cave; GR, Grassridge rockshelter; PP, Pinnacle Point; RCC, Rose Cottage Cave; SEH, Sehonghong rockshelter; SIB, Sibudu Cave; UMH, Umhlatuzana rockshelter. Map based on SRTM 2000, NASA/JPL/NIMA.

simple, fast, and relatively cheap. Application to other sites in the region, and beyond, would therefore provide a more systematic and reproducible way to study and contextualize the many homogenous Pleistocene archaeological deposits, and would allow for more systematic comparisons and more 'invisible' stratigraphic processes to be revealed.

BACKGROUND

Site Setting and Research History

Umhlatuzana is located around 35 km North-West of Durban in KwaZulu-Natal, South Africa (**Figure 1**). The site consists of a shallow North-East facing rockshelter which is 47 m long, 8 m wide, and 17.5 m high (**Figure 2**). The rockshelter is articulated within quartz arenite sandstones of the Natal Group and overlooks the Umhlatuzana river valley (Marshall, 1994). At the site location, the arenite sandstone beds are at places interspaced with 5–10 cm thick shale layers (personal observation). Due to the high quartz content the Natal sandstones are fairly resistant to weathering and erosion processes, resulting in a rugged landscape with high sandstone ridges.

The site is situated in the summer rainfall zone and has a subtropical moist climate (Sayre et al., 2020). The region has annual rainfall ranging from 750 to 1,350 mm (Nel, 2009). The rockshelter is currently surrounded by a coastal scarp forest, with grassland occurring on nearby plateaus (Mucina and Rutherford, 2006). The rockshelter is well protected from weather conditions and remains dry after rain showers. Although it is surrounded by large trees, sunlight still passes through and is present at the site throughout the day.

Discovered during highway construction, Umhlatuzana was initially excavated in 1985 (Kaplan, 1989, 1990). A rescue excavation of a 6 m^2 trench yielded an abundance of finds, predominantly stone tools, dating to the MSA, LSA, and Iron Age (Kaplan, 1990). Kaplan dated the sequence using radiocarbon dating (Kaplan, 1990). The dates were later recalibrated in OxCal using the southern hemisphere calibration curve (Bronk Ramsey, 1995; Sifogeorgaki et al., 2020). Additional Optically Stimulated Luminescence (OSL) dates were obtained for the Pleistocene sediments (Jacobs et al., 2008; Lombard et al., 2010).

In 2018 and 2019 a team from Leiden University, in collaboration with the KwaZulu-Natal museum, conducted small scale excavations aiming to better contextualize the archaeological finds (Sifogeorgaki et al., 2020). Three 50 × 50 cm^2 squares (L2A, L2B, L3A) were excavated until a depth of 2.04–2.40 m, exposing a new western profile (Sifogeorgaki et al., 2020) (**Figure 3**). This profile was documented in detail and sampled for bulk sediment (granulometry, pH, Loss on Ignition, X-ray fluorescence, Fourier-transform infrared spectroscopy), micromorphological, phytolith, MS, lipids, OSL, radiocarbon, and stable isotope analyses. Samples were taken for past, ongoing, and future studies of the site.

Paleoenvironment

The deposits at Umhlatuzana rockshelter correspond to Marine Isotope Stage (MIS) 4, 3, 2, and 1. Analysis of marine cores off-shore of the South African coast suggest Sea Surface Temperatures (SST) varied modestly across the Pleistocene, with temperatures between 20 and 22°C for MIS 4, 3, and 2, and sometimes decreasing to 19°C during MIS 4 (Simon et al., 2013; Ziegler et al., 2013). Palaeobotanical work in the region also suggests colder winter conditions during MIS 4, compared to MIS 3 and 2 (Bruch et al., 2012). In addition, the colder periods (i.e., MIS 4 and 2) are suggested to have increased precipitation (Chase, 2010). Terrestrial proxies indicate wetter conditions

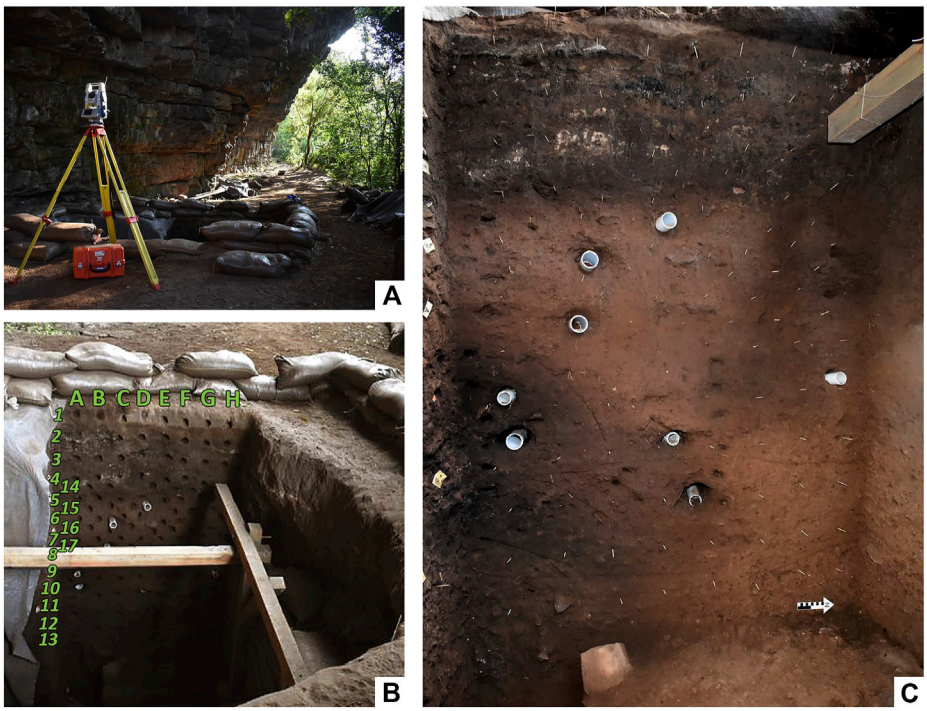

FIGURE 2 | (A) View of Umhlatuzana rockshelter. **(B)** Overview of the western profile after the grid-based bulk sediment sampling. **(C)** West profile of squares L3A, L2B, L2A with grid-based sample locations. The northern part of the profile is affected by shading from the safety scaffolding installed in the excavation pit.

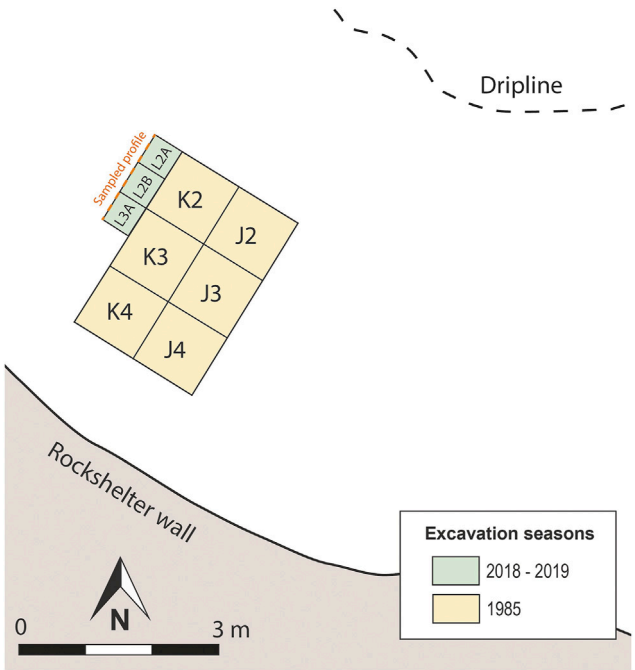

FIGURE 3 | Umhlatuzana site map illustrating the excavation squares of the different fieldwork campaigns.

during MIS 4 (Clark, 2013) and dryer conditions during MIS 3 (Baker et al., 2014; Esteban et al., 2020). Furthermore, rainfall seasonality decreased in MIS 2, compared to MIS 4. During the Holocene the SST increased to 22–24°C (Simon et al., 2013; Ziegler et al., 2013), while higher precipitation levels returned (Baker et al., 2014).

Stratigraphy

The deposits of Umhlatuzana rockshelter are divided into Group P (Pleistocene) and Group H (Holocene) (Sifogeorgaki et al., 2020) (**Figure 4**). It is important to note that the boundary between the two groups does not necessarily correspond chronologically to the Pleistocene-Holocene boundary and additional dating work is required. The lowermost Group P deposits appear homogeneous with no distinct stratigraphic boundaries and their stratigraphic integrity has been questioned (Kaplan, 1990; But see Lombard et al., 2010; Sifogeorgaki et al., 2020). In addition, the Pleistocene deposits are characterized by a lateral differentiation in moisture content. The moisture content is higher in the lowermost deposits and toward the rockshelter wall (square L3A). This is possibly the result of limited water flow on the surface or within the bedrock. On the western profile, the higher moisture levels correspond to Units P6, P7, P9, P12, P14, P16, and P17 (see below and **Figure 4**). It is important to note that the boundaries between lower and higher moisture sediments are gradual. Higher moisture units

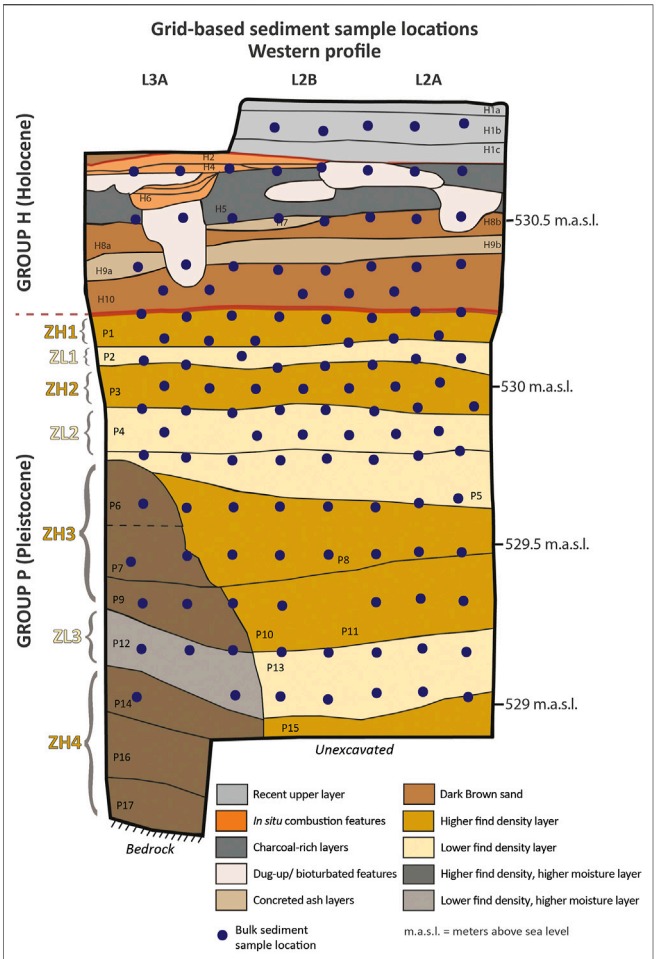

FIGURE 4 | Stratigraphic drawing of the western profile based on Sifogeorgaki et al. (2020) highlighting the location of distinct lower and higher find density zones as well as the grid-based sampling locations of the current study.

demonstrate slightly better charcoal preservation while lower moisture units demonstrate slightly better bone preservation (Sifogeorgaki et al., 2020). The uppermost Group H sequence is characterized by clearly defined layers representing distinctive anthropogenic and biogenic features. They are characterized by the presence of combustion features (hearths) and sediments rich in ash, charcoal and bone fragments (Kaplan, 1990). Across Group H deposits organic finds are much more abundant than in Group P.

Grain size analysis indicates consistent loamy sand sediments throughout the sequence. The grain size of the sediments is similar to the grain size of the sandstone bedrock indicating that the sediment input largely originated from *in situ* weathering of the overhang (Sifogeorgaki et al., 2020). Additionally, FTIR results demonstrate sediment homogeneity, with all readings consistently showing quartz and clay minerals (Sifogeorgaki et al., 2020). Modern surface samples contained traces of apatite. The organic content of the sediments was measured to be between 1.6 and 6.1% with a higher concentration of organics in the Holocene deposits (for complete results see Sifogeorgaki et al., 2020). Moreover, the preliminary pH analysis results published in Sifogeorgaki and others (2020) indicates values ranging from 4.6 to 9.1. The highest pH values are associated with Holocene combustion features (e.g., Unit H9). Organic content and pH values of the same sediment samples prove strongly negatively correlated.

Sifogeorgaki and colleagues (2020) subdivide the Pleistocene stratigraphy in units based on fabric differentiations of the sediments and archaeological find density. Here we use a summarized version of those findings where we subdivide the Pleistocene sequence based on zones characterized by differing densities of archaeological finds. The section is thus divided into four zones that correspond to a higher find density (ZH) and three zones that demonstrate lower find densities (ZL) (**Figure 4**). The lowermost higher find density Zone ZH4 directly overlies bedrock. It consists of Units P14–P17 and spans a period from ~70 to ~60 ka (Lombard et al., 2010). Overlying these sediments is a low-density Zone ZL3 corresponding to Units P12 and P13. An OSL date of 41.9 ± 2.6 ka was obtained from sediments corresponding to P13 (Lombard et al., 2010). The overlying Zone ZH3 consists of Units P6 to P11 (**Figure 4**). Calibrated radiocarbon dates suggest these sediments may date to between 40,000 and 31,500 BP (Sifogeorgaki et al., 2020, **Table 1**). Units P4 and P5 comprise another low-density Zone ZL2, for which no radiometric ages are available. Overlying that, Unit P3 encompasses higher find density Zone ZH2 for which similarly no radiometric age is available. Unit P2 represents the final lower find density Zone ZL1 while Unit P1 corresponds to the final higher find density Zone ZH1, which yielded a calibrated radiocarbon age between 15,710 and 16,431 BP.

The Holocene sequence demonstrates a better preservation of organic materials, notably bone and charcoal that are largely absent from the Pleistocene sediments. The lower part of the Holocene stratigraphy consists of dark brown sand layers (H10 and H8) that contain bone and charcoal fragments. Sediments corresponding to H10 yielded a calibrated radiocarbon date of 10,163–10,572 BP. Two distinct layers of concreted ash, Units H9 and H7, occur at elevations of ~530.4 and ~530.5 m, respectively. In particular, Unit H9 has a thickness of ~10 cm and can be followed throughout the western, northern, and eastern profiles. Charcoal-rich deposits with a high bone fragment concentration overlying H7 likely conform to the unit where a radiocarbon age of 2,766–3,066 BP was obtained (Sifogeorgaki et al., 2020). In the upper part of the Holocene sequence *in situ*, well-preserved hearths are present (Units H6, H4, H3, H2). The uppermost deposit consists of a dark-brown sand layer and covers the entire excavation area. Dug-up and bioturbation features were visible in the profile and were documented as such (**Figure 4**).

Archaeology

The archaeology of the Pleistocene deposits at Umhlatuzana rockshelter is characterized by distinct zones of higher find density separated by lower find density zones (see above). An

TABLE 1 | Stone tool technocomplexes present at Umhlatuzana rockshelter and their general age range.

Geological period	Cultural entities Umhlatuzana	General age range	References
Holocene	Final LSA	~4,000–100 BP	Lombard et al. (2012)
	Robberg	~26–10 ka	Bousman and Brink (2018)
Pleistocene	LSA/MSA transition	~40–14 ka	Bousman and Brink (2018)
	Final MSA	~40–20 ka	Lombard et al. (2010, 2012)
	Late MSA/Sibudan	~60–45 ka	Lombard et al. (2010, 2012)
	Howiesons Poort	~65–60 ka	Lombard et al. (2010, 2012)
	Still Bay	~72–70 ka	Lombard et al. (2010, 2012)

overview of the technocomplexes present at the site is presented in **Table 1**. The lowermost Zone ZH4 yielded bifacially worked leaf points considered typical of the Still Bay industry (~75–71 ka) (Lombard et al., 2010; Högberg and Lombard, 2016b). This is supported by an OSL age of 70.5 ± 4.7 ka (Lombard et al., 2010; Högberg and Lombard, 2016b). Interestingly, serrated points were found among the Still Bay materials (Lombard et al., 2010; Mohapi, 2013). Such points are limited to pre-Still Bay sediments at the nearby site of Sibudu (Rots et al., 2017). In the upper part of ZH4 the artifacts are dominated by backed segments, which are the type artifacts of the Howiesons Poort industry (~65–60 ka) (Kaplan, 1990; Sifogeorgaki et al., 2020). These sediments yielded an OSL age of 60.0 ± 3.5 ka (Lombard et al., 2010). Zone ZL3 was designated Late MSA by the original excavator (Kaplan, 1990; Sifogeorgaki et al., 2020). Previous work highlighted numerous unifacial points from these units (Mohapi, 2013), while segments remained common artifacts (Kaplan, 1990; Sifogeorgaki et al., 2020). The continued occurrence of segments has also been observed at Sibudu in its late and final MSA assemblages (Wadley, 2005). The assemblages of ZH3 can be characterized as late MSA, with a continued dominant presence of segments. Higher up in this zone, hollow-based points are present (Mohapi, 2013; Sifogeorgaki et al., 2020). Based on their presence in the latest MSA deposits at Sibudu (Wadley, 2005), these artifacts have been taken as typical of the final MSA in the region (Mohapi, 2013; Bader et al., 2018). The uppermost hollow-based points at Umhlatuzana are found among lithics that appear transitional between the MSA and LSA, in the very top of Zone ZH3. Material recovered from this area includes both bladelets and bladelet cores, but also large debitage products such as blades and flakes (Kaplan, 1990; Sifogeorgaki et al., 2020). Materials recovered from ZL2 were dubbed early Robberg by the original excavator (Kaplan, 1990). Finally, the uppermost higher-density Zone ZH1 conforms to the later part of the Robberg, which can also be found in the lowermost Holocene sediments (Kaplan, 1990; Sifogeorgaki et al., 2020).

The archaeology of the Holocene deposits is characterized by lower find densities, and contains both LSA and Iron Age material culture (Kaplan, 1989; 1990). The LSA assemblage contains bladelets, and a variety of formal tools that include naturally backed knives and scrapers (Kaplan, 1990). The renewed excavations confirmed the presence of LSA archaeology in the Holocene deposits and also uncovered some *Nassarius* beads. A very small number of segments were recovered in the LSA sediments (Kaplan, 1990). The topmost sediments contain LSA lithics, (Late) Iron Age thick-walled ceramics, and *Achatina* beads (Kaplan, 1990; Sifogeorgaki et al., 2020).

MATERIALS AND METHODS

Grid Placement, Sampling, and Sample Preparation

A sampling grid was set up consisting of eight columns (A to H) and thirteen rows, covering the full extent of the exposed profile (**Figures 2** and **4**). Sample locations were spaced 15 cm apart. Between row 4 and row 8 additional sample locations (row 14–17) were added directly in the middle of each group of four existing sample locations (e.g., A14 was added between A4, A5, B4, and B5) to increase the resolution of the grid. The coordinates for all sample locations were recorded using a Robotic Total Station. In a few instances sample locations had to be moved slightly or omitted from the grid due to the presence of OSL sample holes or large rock fragments.

From each sample location equal volumes of sediment (60 ml) were collected for analysis. Samples were air-dried overnight. The color of the sediments was determined on dry samples (using the Revised Standard Soil Color Charts 2010). All samples were sieved to <2 mm to remove any coarse material prior to pH, X-Ray fluorescence (XRF) and MS analyses.

pH Analysis

For each sample, 30 ml of sediment (<2 mm) was mixed with 60 ml of deionized water (1:2 sediment-water ratio). Mixtures were stirred thoroughly and left to settle overnight. The organic content was quantified based on the relative amount of material floating in the solution (low, medium, high, absent). The pH of the supernatant was measured using an Accumet AB150 benchtop pH meter equipped with a double junction pH/ATC electrode. Measurements were taken in triplicate and values were averaged before further use.

X-Ray Fluorescence Analysis

The XRF analyses were carried out using a Thermo Scientific Niton XL3t GOLDD + energy-dispersive p-XRF analyzer, equipped with a silicon drift detector. Sediment samples (<2 mm) were compressed manually with an agate pestle into a PE-ring with a height of 10 mm. Analyses were performed using a stand mounted above the sample ring. This setup negates the use of separation foil between the sample and the XRF, that could absorb secondary X-rays from light elements. Measurements were taken in Cu/Zn-mining mode, with a measuring time of 110 s, using 4 sequential energy settings: Light range (Mg to Cl) at 8 kV 200 μA, low range (K to Ti) at 20 kV 100 μA, main range (V to Ag including L-lines for Pb) and high range (Cd–Ba) both at

50 kV, 40 μA. The machine's factory calibration was checked and adjusted using a set of 14 powdered ISE standard soil samples (www.wepal.nl). Accuracy was tested using the BAMS005B glass standard. All elements for which the results were above the detection limit were included in the dataset.

Magnetic Susceptibility Analysis

MS was measured on bulk samples (~5 g) gathered at each grid location. Before measurement, sediment was placed in small Ziploc bags. The Low Frequency (χLF) to High Frequency (χHF) MS measurements were taken with the use of a Kappabridge MFK1-FA susceptometer at the CENIEH, Burgos, Spain. Low Frequency measurements were taken at 0.976 kHz, while High Frequency measurements were taken at 15.616 kHz. Field Intensity was set to 200 A/m. All samples were measured in triplicate and averaged. Samples were measured at low frequency and high frequency magnetic fields, as mixtures of magnetic minerals with higher concentrations of finer domain structures (the internal magnetic behavior) contribute less to overall susceptibility when measured at higher frequencies. Comparing measurements at two frequencies provides insight into the size of magnetic domains of the minerals being magnetized. The increase in the frequency of finer domains results in a greater difference between χLF and χHF measurements (Dearing, 1999). χLF MS measurements are mass corrected and presented at 10^{-6} m^3/kg. The difference between the χHF and χLF is presented as both the absolute difference between both values (χFD, Frequency Dependent) and in percentage χFD%, following methodology outlined by Dearing et al. (1996a; 1996b). Mixtures of single-domain magnetic particles and small fractions of SP particles commonly fall in the χFD% range from ~1 to 7%. As SP proportions in admixture increases, χFD% increases (and may exceed 7%). Dominantly SP properties are present for χFD% values of 12% or higher (Dearing, 1996). Since iron minerals are the primary element driving the magnetic properties of the sediments, any mention of magnetic minerals in the text mainly refers to iron content.

Micromorphological Analysis

The micromorphological samples were taken from the stratigraphic sequence of the western profile using plaster bandages or Kubiena tins (Stoops and Nicosia, 2017). The sampling concentrated on the Group P deposits of square L3A with the exception of one sample taken from the uppermost Unit H1 (square L2A). Sample preparation occurred at the laboratory of the Cultural Heritage Agency of the Netherlands in Amersfoort. The blocks were first air-dried and then oven dried at 25–40°C. They were then impregnated in a mixture of 2:1 polyester resin: acetone. The blocks were irradiated with gamma radiation at the Synergy Health Ede B.V. Company. The hardened blocks were cut into ~3 cm thick slabs and were documented using a digital SLR (Nikon D3400) with a standard lens. Subsequently, 13 petrographic thin sections of 30 μm thickness were produced (see provenance in **Table 2**), and observed in plane-polarized and cross-polarized light (PPL, XPL), primarily using a Euromex IS.1053-PLPOLi polarization microscope with 10×/23 mm eyepiece and trinocular, and magnifications from 5 to 40×. The thin sections were analyzed and described following standard micromorphological literature (Stoops, 2003; Stoops et al., 2010; Macphail and Goldberg, 2017).

TABLE 2 | Stratigraphic provenance of the micromorphology samples at Umhlatuzana rockshelter; bone and charcoal quantification in the thin sections.

Sample name	Thin section	Unit(s)	Bone	Charcoal
UMH18_4	4B	P9	Uncommon	Abundant
	4A	P9	Present	Abundant
UMH18_6	6B	P10/P9	Abundant	Uncommon
	6A	P10/P9	Present	Present
UMH18_3	3B	P6/P7	Present	Present
	3A	P6/P7	Uncommon	Abundant
UMH18_5	5	P8	Present	Present
UMH18_14	14	P4/P5	Present	Present
UMH18_13	13	P3	Present	Abundant
UMH18_15	15	P1/P2	Abundant	Uncommon
UMH18_12	12B	P1	Present	Uncommon
	12A	H10/P1	Abundant	Present
UMH18_30	30	H1	Abundant	Present

The samples are presented from the bottom of the sequence up.

Statistical Processing and Visualization

The pH and elemental data were visualized using inverse distance contour plots. Contour and elevation plots were constructed using Grapher® plotting software. For contouring an inverse distance to a power gridding method was used (Davis, 1986). The grid dimensions were 100 rows by 61 columns and to avoid "bull's eyes" around extreme datapoints, a power factor of 2 and a smoothing factor of 0.05 were selected on the basis of the visual evaluation. Because the sediments are deposited horizontally and bioturbation is limited during deposition to a certain depth, the anisotropy ratio was set to 5 with an angle of 0°. Due to the more heterogeneous nature of the MS data the application of a geostatistical model was required to ensure proper projection of the datapoints. Statistical analysis was conducted with the base R function (R Core Team, 2017), with plots being developed utilizing the GGplot2 package (Wickham, 2016). The heat maps for MS were therefore developed with the use of a combined approach of QGIS and R, with the use of Ordinary Kriging to interpolate predicted values of the grid points. The approach is adapted from Dinckal and others (submitted) to accommodate the use of open access software. R was used to understand the statistical breakdown of the data. Both Histograms and Quantile–Quantile (QQ) plots were developed to understand if the distribution of the data was normal. If distribution was skewed, a log transformation was applied to normalize the data. R, with the use of the gstats package (Pebesma, 2004; Gräler et al., 2016), was further utilized to understand the appropriate model to apply to the interpolation of the dataset. Variogram models were compared and the best fit was identified. These variogram model parameters were then applied to the datasets in QGIS. Data was input into QGIS as delimited text layers. Ordinary Kriging was undertaken with the assistance of the SAGA plugin (Conrad et al., 2015). Parameters identified with the use of R

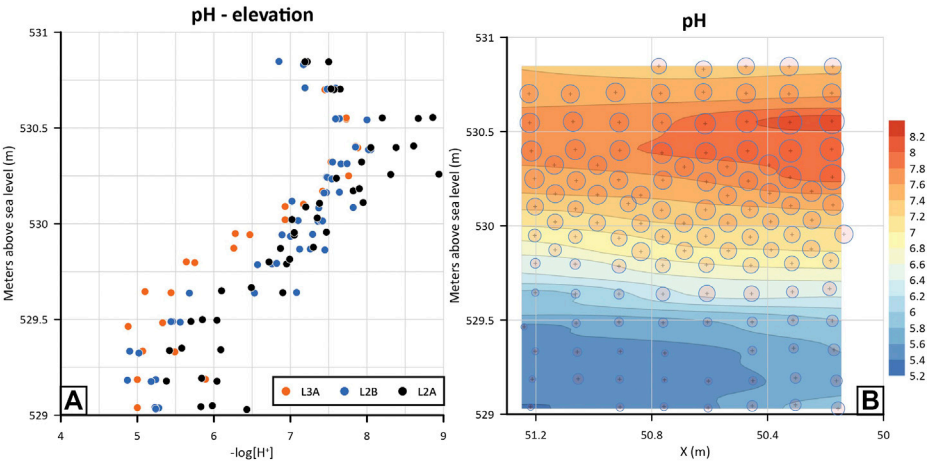

FIGURE 5 | Results from the grid-based pH analysis illustrated using an elevation plot **(A)** and contour map **(B)**.

TABLE 3 | Overview of the elemental composition of the sediments.

Element	Group H		Group P	
	Average	SD	Average	SD
SiO_2	50.83	9.04	68.31	6.06
CaO	7.71	3.95	0.61	0.47
P_2O_5	2.59	0.54	2.52	1.12
K_2O	1.49	0.29	1.37	0.44
Al_2O_3	4.26	0.68	5.93	1.26
TiO_2	0.35	0.05	0.38	0.08
Fe_2O_3	1.76	0.24	2.03	0.48
MnO	0.11	0.04	0.01	0.01
S	0.79	0.85	0.08	0.05
Cl	0.42	0.3	0.19	0.09
MgO	2.58	1.32	0.55	0.18
Zn	55.66	25.55	13.59	4.53
Cu	19.36	3.68	16.29	1.57
Zr	166.99	34.01	162.23	41.11
Sr	222.99	121.48	32.98	13.58
Rb	39.58	5	35.52	4.38

The data is divided into Group H and Group P results, and presented as average values and standard deviations per element. The oxides are presented in wt%, all other elements are presented in ppm.

were input in the QGIS system and the interpolated models were developed. The full R script for the development of the statistical analysis and the development of the variogram models can be found in the **Supplementary Material**.

RESULTS

pH

The pH in the grid ranges from 4.87 (sample position D12) to 8.94 (sample position H5), with an average value of 6.87. The lowest values can be found in the southern part of the bottom of the stratigraphy, while the highest values are located in the top North (**Figure 5B**). There is a very clear vertical trend of decreasing pH going down the stratigraphy, but also a horizontal trend with pH increasing from South to North. The change in pH happens gradually for both the vertical and horizontal distribution, with a minor shift toward more neutral pH values at the very top of the sequence (**Figure 5**). The lateral variation is greatest at the bottom of the sequence (**Figure 5A**).

X-Ray Fluorescence

An overview of the average values and standard deviations of the elemental data is presented in **Table 3**, while r values for the different element combinations can be found in the **Supplementary Material** (For the complete dataset and figures for all elements see the **Supplementary Material**). Within the distribution of the various elements present in the stratigraphy some patterns can be recognized. The upper part of the sequence, down to an elevation of z = 530.25 m, is characterized by the highest values of alkaline earth metals CaO, MgO, Sr, and metals MnO and Zn (**Figures 6C,D**). These elements all show a similar pattern, peaking in the middle and lower part of this section (z = >530.25). The elements Cl and S have their highest values just below the current surface (**Figures 6E,F**). However, both remain above the detection limit throughout the entire sequence. Potassium (K_2O) also shows an optimum in the middle of this section (z = >530.25). The silicates and iron minerals (SiO_2, Fe_2O_3, Al_2O_3, TiO_2, Zr) have their lowest values here, and all remain stable or increase further down in this part of the sequence (z = >530.25) (**Figures 6A,B,G,H,K,L**). In this upper part of the sequence the variation in values is quite high for all elements. Below an elevation of z = 530.25 m the alkaline earth metals and metals MnO, Cu, and Zn all rapidly decrease toward very low background concentrations. Silica (SiO_2) and potassium have their highest values right below z = 530.25 m and gradually decrease toward the bottom of the sequence. The iron minerals have their lowest to intermediate values in this section (z = <530.25), and gradually increase toward the bottom of the deposits. While variation in elemental concentrations is still

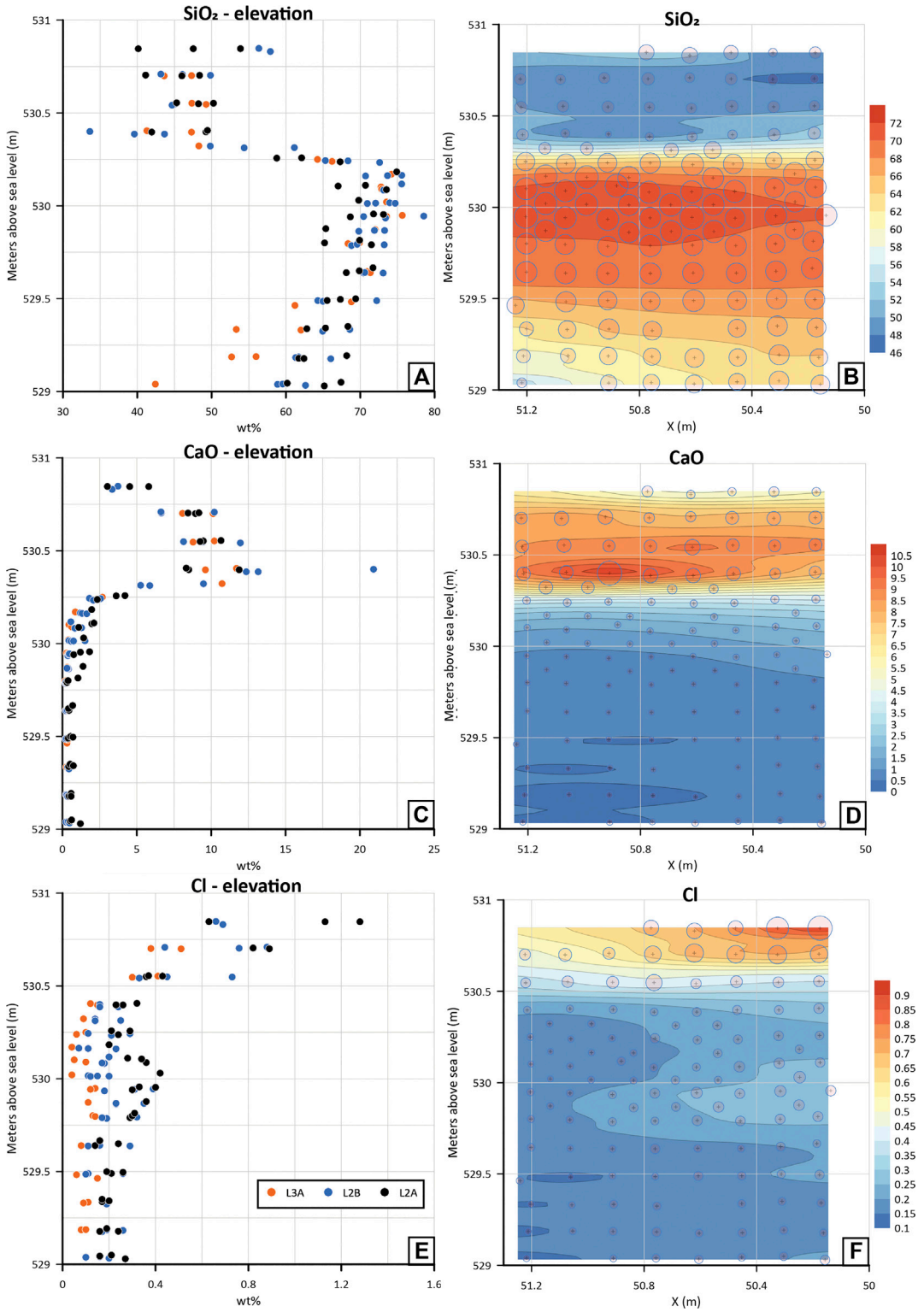

FIGURE 6 | XRF results for selected elements. **(A)** SiO_2 elevation plot. **(B)** SiO_2 contour map. **(C)** CaO elevation plot. **(D)** CaO contour map. **(E)** CL elevation plot. **(F)** Cl contour map. XRF results for selected elements. **(G)** Al_2O_3 elevation plot. **(H)** Al_2O_3 contour map. **(I)** P_2O_5 elevation plot. **(J)** P_2O_5 contour map. **(K)** Fe_2O_3 elevation plot. **(L)** Fe_2O_3 contour map.

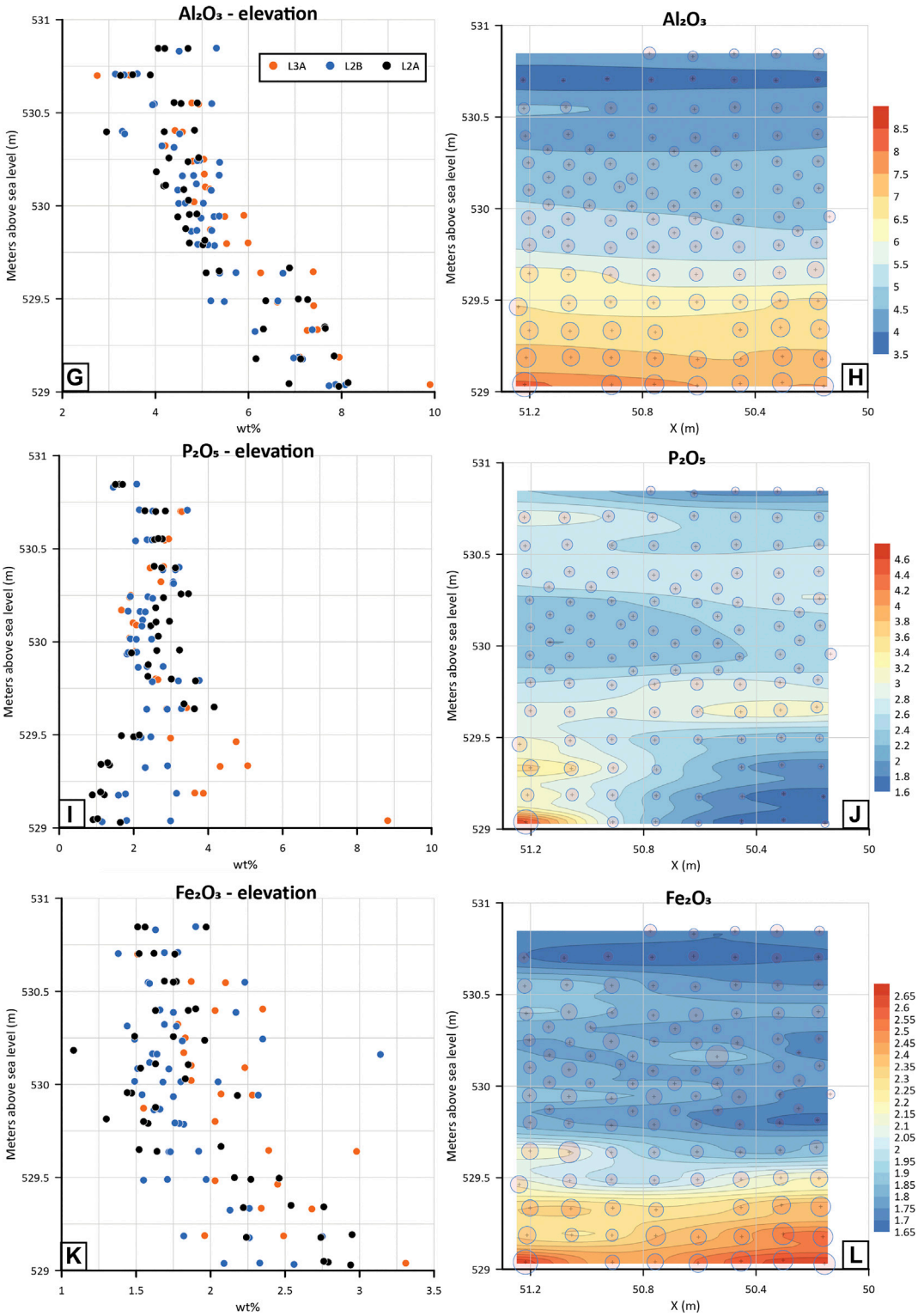

Figure 6. | *(Continued).*

present in this part of the sequence (z = <530.25), the variation is considerably lower than in the top part (z = >530.25). The distribution of P_2O_5 does not fit any of the aforementioned categories, but instead is characterized by a gradual fluctuation between lower and higher values throughout the sequence, with most lateral variation at the bottom (**Figures 6I,J**).

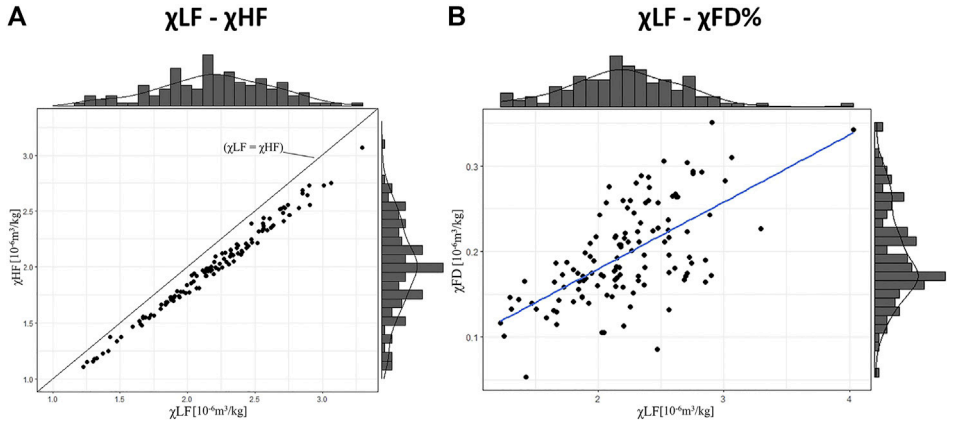

FIGURE 7 | (A) Plot of χLF and χHF values, with the distribution of values represented along the margins. The predictive model represents the expected distribution of χLF = χHF. **(B)** Plot of χLF and χFD values with distribution represented along the margins and liner model demonstrating the relationship between the values.

Magnetic Susceptibility

Figure 7A shows the distribution of the χLF and the χHF results as well as the relationship between the measurements at the two frequencies. The χLF values range from 1.22 to 4.03[10^{-6} m^3/kg] with a mean of 2.21[10^{-6} m^3/kg], while the χHF values have a range of 1.90–3.68[10^{-6} m^3/kg] with a mean of 2.01[10^{-6} m^3/kg]. The smaller range and lower mean of the χHF MS measurements follows the expected behavior of magnetic minerals having lower susceptibility at higher frequency fields due to the removal of the influence of concentrations of the finer domain magnetic minerals. A Pearson's correlation of 0.99 demonstrates a clear relationship between the properties. **Figure 7B** shows the distribution of χFD values and χLF and how the values relate to one another. Despite high variability, **Figure 7B** indicates a linear relationship between the two datasets. This suggests that the relationship is not strictly driven by an increase in χLF values, but also by the concentration of the finer domain structures. Frequency dependent percentage (χFD%) values range from 3.4 to 13.2%. This places the composition of the domain structures within the regions of single-domain to SP admixtures (χFD% of 2–10%; Dearing, 1996), with the increase in χFD% values indicating an increase in the SP particle contributions. χFD measurements have a mean of 8.94%, with 75% of the values above 7.735%. This indicates that most of the measured material is heavily influenced by concentrations of Superparamagnetic (SP) grains, while a very small fraction, 21 out of 126 samples, measures the influence of Single-Domain concentrations.

Figure 8A shows the distribution and the Kriged interpolation of χFD percentages and the distribution and interpolation of χLF values. The data shows that the moderate to high χFD% values are inversely correlated with the χLF values. This is clearly visible in the plots at elevations of z = <529.75 m, at x = 51.0 m, and z = <59.5 m at x = 50.1 m (**Figure 8**). Based on the MS results in these areas, magnetic mineral concentrations seem relatively high compared to the rest of the sequence. As we move from x = 50.1 m to x = 51.0 m, we find that the χFD% decreases from more than 12% to around 8%, while χLF values increase from moderately high values to high susceptibility values. Domain structures of these magnetic minerals still fall within the range of SP mineral concentrations. It has previously been noted that as χFD% increases (above e.g., 7%), the size of SP domains becomes finer, or the relative contribution of SP particles increases (Thompson and Oldfield, 1986; Dearing, 1999). It is therefore feasible to assume that the increase in χLF is related to the relative increase in domain sizes -either from the depletion of finer material or from an increase in the concentrations of the coarse domain structures. At elevations above z = <529.75 m, at x = 51.0 m, and z = <529.5 m at x = 50.1 m the sequence is characterized by both low χFD% values and low χLF values until elevations of z = 530.25 m (**Figure 8B**). Below that, magnetic mineral concentrations with coarser domain structures tend toward higher χLF values. Therefore, the low values for both χLF and χFD% could be explained by relatively low magnetic mineral concentrations. At z = 530.25 m a lens of moderately high χLF values is visible, which corresponds to the transition from the Group P to Group H deposits. The increase in χLF, associated with χFD% values of ~7%, is likely due to an increase in overall magnetic mineral concentration. Directly above this lens, χFD% values show an increase in concentrations of finer SP grains, coupled with a marked decrease in χLF values. This likely corresponds to a dilution of coarser magnetic minerals, removing components that would increase the χLF.

Overall, patterning of χLF and χFD% values shows that a change from moderate to higher χLF values is driven by a decrease in χFD%. As χFD% decreases concentrations of coarser SP to Single-Domain magnetic minerals increase, in turn increasing the χFD%. χLF decreases with an increase in χFD% where concentrations of SP magnetic minerals increase or become finer. However, higher concentrations of fine-grained SP minerals, χFD% of ~10%, can still lead to moderate χLF values assuming there is an overall greater concentration of magnetic minerals. A decrease in χLF can also occur with an overall decrease in the concentration of all magnetic minerals.

Micromorphology

The preliminary micromorphological analysis conducted for this paper shows that the sediments appear homogeneous

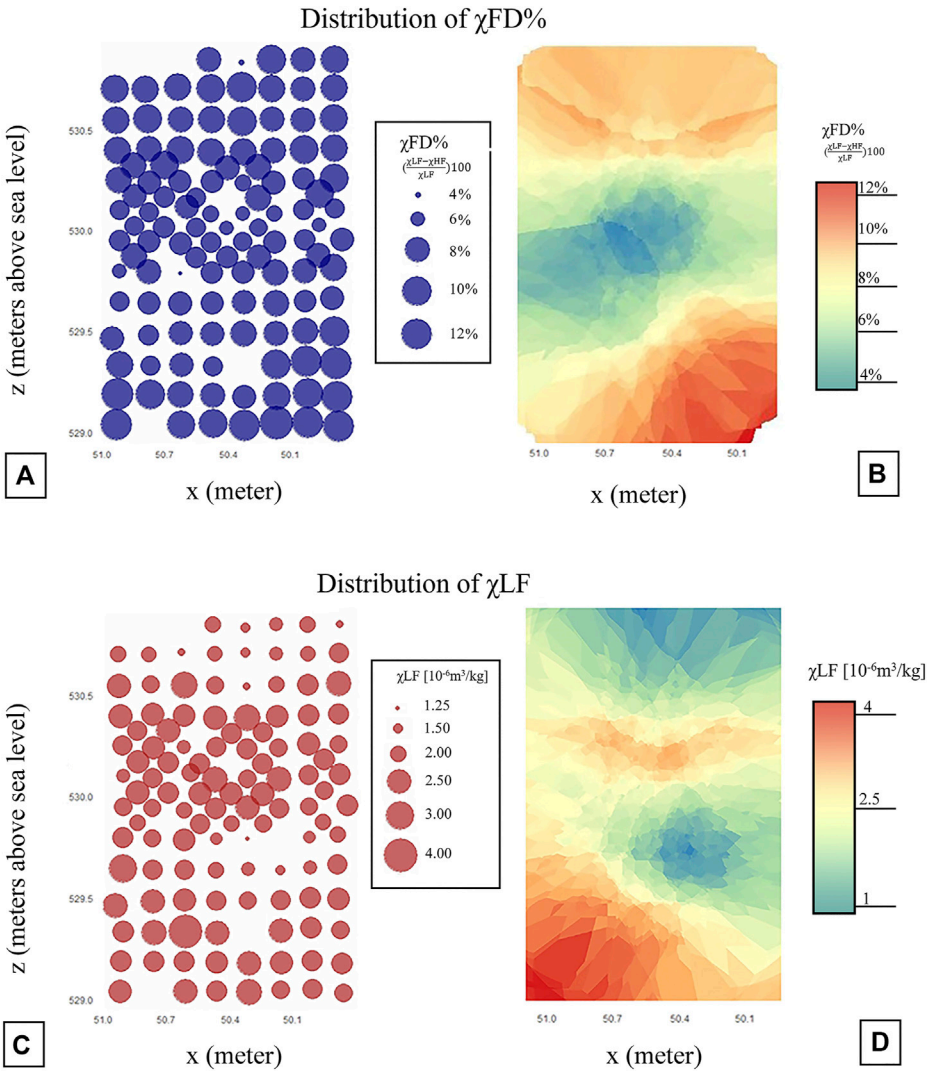

FIGURE 8 | (A) FD% bubble plot. **(B)** FD% heat map. **(C)** χLF bubble plot. **(D)** χLF heat map.

throughout most of the Group P sequence. Stratigraphic boundaries are not detectable also at the micro-scale. Although the boundary between the Group P and Group H sediments was not visible in the thin section, it was clear that the Group H Unit H9 contained a higher concentration of bone fragments than the underlying Group P Unit P1 (**Table 2**). Bioturbation features include voids, channels, and infilled burrows (**Figures 9A,B**). The preliminary study shows no indication for large scale sediment movement (e.g., rotational slipping failure surface, grain orientation).

The sediments primarily consist of sand-sized quartz grains. Other smaller sized materials (silt and clay) are usually present as bridges between the quartz grains and coatings and cappings of the clastic materials (**Figures 9E,F**). Occasionally, clay material form aggregates frequently associated with organic material that has undergone post-depositional oxidation. Two main fabric types were identified. Fabric I is moderately sorted with a single-spaced fine enaulic distribution in a spongy microstructure, while Fabric II is moderately sorted with a double-spaced coarse enaulic distribution within a vughy microstructure. Angular to subangular rock fragments that are mostly the result of anthropogenic input (lithic debitage) are commonly articulated within the matrix. The main raw materials for tool production identified are sandstone, quartz and hornfels; less commonly occurring are chert and dolerite. In addition, opaque iron-rich oxides are present throughout the deposits. Some of the iron oxides appear to be primary angular rocks with sharp boundaries. Additional iron oxides take the form of weakly impregnated iron nodules and coatings that are likely formed post-depositionally. Fine sand to gravel sized angular bone as well as moderately fragmented charcoal remains were identified in all of the

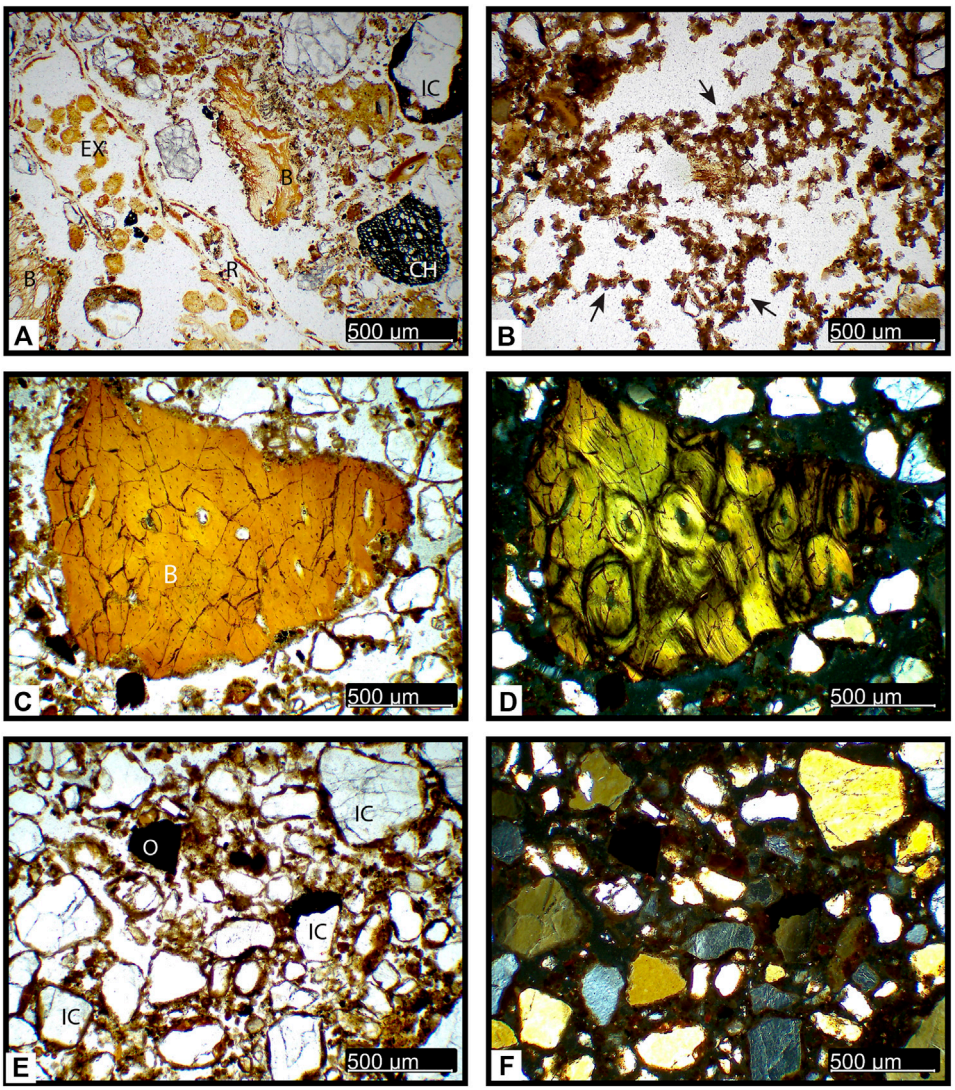

FIGURE 9 | Photomicrographs of sedimentary components identified in micromorphology thin sections. **A:** Degraded bone (B) and organic (root?) tissue (R), including mesofauna excrements (EX), charcoal fragment (CH), and sand grain with iron oxide coating (IC). Sample UMH18_30. (PPL); assorted deposits of uppermost Unit 1. **(B)** Mesofauna excrements consisting of degraded organic matter (arrow). Sample UMH18_15 (PPL), Unit P2 (Zone LF 1). **(B)** Bone fragment (B), with orange colors and cracking indicating heating or weathering. Sample UMH18_12B (PPL), Group P–Group H boundary deposits. **(D)** Idem, (XPL). Haversian canals are clearly visible. **(E)** Unsorted sand fragments with coatings of organic matter and iron oxides (IC), and organic matter plus iron oxide fine organic aggregates (O). Sample UMH18_12B (PPL). Group P - Group H boundary deposits. **(F)** Idem, (XPL).

thin sections (**Table 2**). Bone fragments are more frequent in the uppermost Group P deposits (e.g., **Figures 9C,D**), while charcoal fragments tend to be more abundant in the lowermost Group P deposits (**Table 2**).

Sandstone rock fragments of a similar composition to the bedrock are present throughout the sedimentary sequence. Those were identified in thin-section and are described as fragments of a quartz arenite sandstone with angular quartz grains ranging from 200 to 600 µm and a low proportion (~5%) of silica cement. It cannot be determined whether those sandstone rock fragments are the result of roof spall or are by-products of stone tool knapping, but their consistent presence indicates that they probably derive from sandstone of a similar composition to that of the rockshelter overhang.

DISCUSSION

Stratigraphic Implications

Integration of the pH, XRF, MS, and micromorphology data results in information on site-formation processes and changes within the stratigraphic sequence, most of which were not visible in the field or observed during earlier work at the site (Kaplan, 1990; Sifogeorgaki et al., 2020). The first thing that stands out is the difference in dynamics above and below the elevation of z =

530.25 m. This is the elevation where the majority of the elements measured with XRF show a distinct jump in values and change in behavior (**Figure 6**), and which corresponds nicely to the major stratigraphical change identified in the field; the boundary between the Group P and Group H deposits (**Figure 4**). The abrupt change in values indicates a limited impact of post-depositional mixing of the sediments. Because of the distinct difference between the sediments above and below this boundary these groups will be discussed separately.

The dominant component of the Pleistocene deposits is quartz, as is reflected by the SiO_2 content, the major mineral constituent of the sandstone. Previous work has shown that the deposition of quartz at the site derives from weathering of the sandstone rockshelter, and forms the largest part of the geogenic deposit (Sifogeorgaki et al., 2020). The input of SiO_2 gradually increases upwards toward the Group P/H boundary (**Figures 6A,B**), which is most likely the result of the decrease in other components. Along with the gradual increase of SiO_2 there is a gradual increase in K_2O, as well as a in the pH from acidic values (4.87–5.38) to more neutral values (~7.5) at the boundary (**Figure 5**). The presence of K_2O can relate to various inclusions such as K-rich hornfels stone tool debitage, charcoal fragments, ash, and minerals such as micas and feldspars. Further analyses are needed to identify the exact source. In addition, there is a gradual decrease in Al_2O_3, Fe_2O_3, Zr, and TiO_2 toward the top of the sequence (**Figures 6G,H,K,L**). These elements are likely related to more fine-grained material such as heavy minerals and clay minerals (Taylor and McLennan, 1985; Huisman et al., 1997), which might derive from *in situ* weathering of the thin shale layers interbedded between the sandstone bedrock. The micromorphology samples indicate consistent presence of fine matrix (~10%) that could be partially related to clay minerals. It should be noted that the Al_2O_3 content of the deposits likely derives from various sources, including clay minerals, feldspars, and aluminum phosphates related to dissolved excrement (Nriagu, 1976; Karkanas, 2000). Based on the MS results the Pleistocene deposits can be divided into three areas: 1) the bottom of the sequence (z = <529.75) with high χLF and moderate χFD% values in the South corner, and lower χLF and high χFD% values in the North corner, 2) the middle of the sequence (z = 529.75–530.50) where both χLF and χFD% values are low, and 3) a thick lens of high χLF values within Area 2 (~z = 530.25). The minimum in the χFD% values at z = 530.0 coincides the minimum concentration of Zr, indicating that the χFD% values are positively related to the fine fraction of the sediment. This underlines that the χFD% signal is most likely carried by minerals in the finer fraction of the sediment. Similarly, the moderate to high χLF values appear to correlate with the highest concentration in Fe_2O_3 content. This suggest that the changes in the overall χLF signal can be driven by changes in iron content. The difference between Area 1 and Area 2 suggests a change in the depositional environment. The location of Area 3 coincides with the boundary between the Group P and Group H deposits. The presence of these high χLF values in an area that is otherwise characterized by low χLF and χFD% values suggests that the lens is an enhancement that occurred after the initial deposition of the sediments. It was previously identified that topsoil and surface areas have a tendency to undergo magnetic enhancement through the formation of secondary oxides within the sedimentary clay fraction. This elevates the χLF of surface soils compared to χLF values lower in the same sequence (Thompsons and Oldfield, 1986; Dearing et al., 1996a; Hanesch and Scholger, 2005). At Umhlatuzana, the high χLF values of Area 3, combined with its location at the boundary, suggest the potential presence of an open surface where pedogenesis may have occurred. However, more in-depth MS analysis and micromorphology is needed to test this hypothesis.

The Holocene deposits are characterized by visible layers and features, and the presence of a lot of (cemented) ash (**Figure 2**). While SiO_2 (quartz) is still the dominant component, its percentage is heavily reduced compared to the Pleistocene deposits as the result of a higher input of other materials (mainly ash and organics). This ash is present in hearth features, as well as in the form of an ash layer with an average thickness of 10 cm (**Figure 4**). The influx of ash in the Holocene deposits is visible in the geochemical data as a marked increase in CaO, MgO, MnO, Sr, and Zn, all known components of wood ash (**Figures 6C,D**) (Vassilev et al., 2014). The latter elements also all show good correlation with CaO (**Figure 10A**, Table correlation SI). The enrichment in Cu might also be related to the presence of ash (Welch, 1993; Frassinetti et al., 2006). Bone was ruled out as the dominant source of CaO because there is no correlation between CaO and P_2O_5 (the main components of bone, see e.g., Reidsma et al., 2016) (**Figure 10B**). It should be noted that only sample A4 is directly obtained from the ash layer. The data therefore indicates that ash is also a dominant component of the other layers/features within the Holocene deposits. The introduction of large amounts of ash at the site is likely what caused the pH of the Holocene deposits to increase to alkaline values (~7.5–8.94) (CaO–pH correlation, **Figure 10C**). While the lower boundary of the ash layer is located at an elevation of ~z = 530.38, the ash related elements can already be seen to increase slightly below the Group P–Group H boundary at z = 530.25. This can be the result of small-scale movement of ash related compounds into the underlying deposits, or a higher incidence of burning (activities) in the Holocene. Another characteristic of the Holocene deposits is the wider variation in geochemical composition, which is probably related to the presence of identifiable features and greater heterogenous stratification. Due to the preliminary nature of the micromorphological study there were no thin sections available from Group H to complement the geochemical data, with the exception of the one derived from the uppermost Unit H1. The magnetics of the Holocene deposits are characterized by moderately high χFD% values and low χLF values that further decrease toward the top of the sequence. The layers and features present in the Holocene deposits (and clearly visible in the field) likely were not detected by the MS measurements due to the resolution of the sampling grid.

Sediment Mixing

The gradual change, both vertically and laterally, in the geochemical composition of the Pleistocene deposits suggests that no large-scale movement has affected the sediments, and that

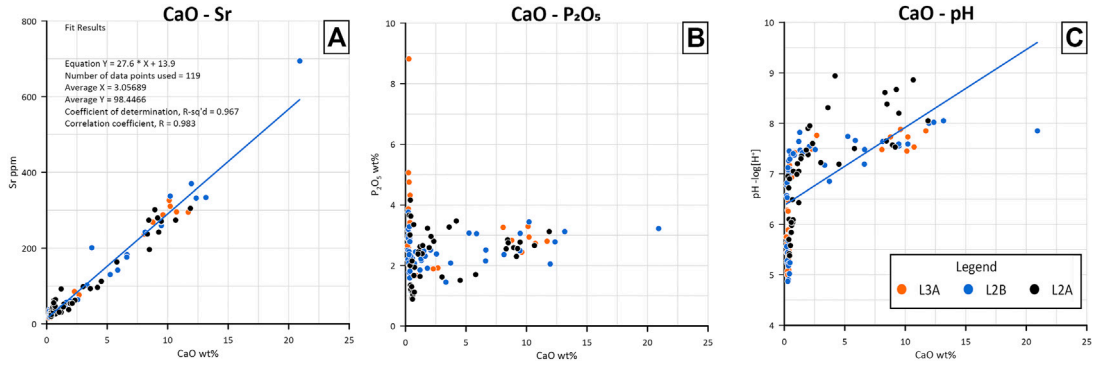

FIGURE 10 | Correlation plots for CaO–Sr **(A)**, CaO–P_2O_5 **(B)**, and CaO–pH **(C)**.

any mixing has only occurred locally. Small-scale mixing by bioturbation is indicated by the micromorphological observations (**Figure 9B**). Small-scale sediment mixing was also previously demonstrated based on the overdispersion of the luminescence signals of the MSA deposits (Lombard et al., 2010). The current study extends this pattern of small-scale mixing throughout the sequence. The homogeneity of the Pleistocene deposits is likely the result of bioturbation combined with relatively consistent sources of sediment input (see also Sifogeorgaki et al., 2020).

The presence of layers and features, clearly visible in the field, suggests that no large-scale mixing has affected the Holocene deposits (with the exception of documented dug features). The wider variation in the geochemical composition of the Holocene deposits likely relates to this more small-scale stratification. Field observations and micromorphological data do indicate heavy mixing of the top Unit H1 (**Figure 9A**). The degree of sediment mixing at Umhlatuzana rockshelter will be the focus of the upcoming micromorphological analysis, which will include the examination of additional Holocene and Pleistocene samples.

Site Taphonomy

The high content of SiO_2 in the bedrock and sediments of sandstone rockshelters like Umhlatuzana is known to correlate with acidic conditions and affects the baseline pH of the deposits (Lowe et al., 2018; Miller et al., 2016; Stewart et al., 2012). In the case of Umhlatuzana, the pH of the Pleistocene deposits might further be influenced by a decrease in Fe_2O_3 above z = 529.5, resulting in less acidic conditions than present in the bottom of the sequence (**Figures 5** and **6K**,L). The variation in pH values has a clear effect on the preservation of organic materials in the Pleistocene sediments, and correlates well with the variation in moisture content observed in the field. The lowest pH values are found in the area with the highest moisture content, which might be enhanced by the water presence itself. Groundwater derived from the sandstone bedrock tends to have a more acidic pH (Auler et al., 2020; Mecchia et al., 2014; Sauro et al., 2019) and enhanced SiO_2 dissolution. The high moisture content in the bottom South corner of the sequence is likely the result of groundwater coming in through the sandstone bedrock. The low pH values correspond well with the highest concentrations of P_2O_5 in the sediments, especially in the area with a higher moisture content (**Figures 5** and **6I**,J). In contrast, the drier area with low pH values displays much lower P_2O_5 concentrations. This trend also matches with the variation in bone preservation, with poorly preserved bones in the high moisture/low pH area, and well-preserved bones present in the areas with more neutral pH values. Nevertheless, the poor correlation between P_2O_5 and CaO (**Figure 10B**) suggests the dominant source of phosphate in the deposits is not bone. A more likely source for the P_2O_5 is animal excrement (e.g., from Rock Hyrax: *Procavia capensis*) (Prinsloo, 2007; Chase et al., 2012). The phosphate in excrement will easily dissolve under wet conditions and/or be absorbed by iron minerals or react with soluble aluminum complexes to form aluminum phosphate minerals (Goldberg and Sposito, 1984; Karkanas, 2000; Nriagu, 1976), which might explain the elevated values at the bottom of the sequence where Fe_2O_3 concentrations peak. The exact origins of these phosphates will be explored in the upcoming, more elaborate study of micromorphological samples from the site, and will also include additional XRF analysis of the matrix and inclusions within those blocks. At the bottom of the sequence (z = <529.75) the transition from high χFD% values (above 10%) to moderate χFD% (~8%), with an associated increase in χLF values, is also correlated with an increase in moisture content. Water movement through deposits enriched in ferric minerals can lead to magnetic enhancement through the formation of secondary iron oxides, as well as lead to the removal of finer SP domain magnetic minerals (Thompson and Oldfield, 1986; Herries, 2006). This suggests that the enhanced MS signal here is the result of post-depositional water movement through the sediments that caused the formation of secondary iron oxides, and has removed the finer SP domain minerals, while these finer minerals do remain in the drier northern part of the deposits at the same depth. Micromorphological analysis cannot currently confirm this observation because samples from the lower moisture Group P have not yet been prepared.

The Holocene deposits are characterized by alkaline conditions, most likely related to the abundant presence of ash, both in the combustion features and ash layer, as well as in the rest of the sediments. Most of the CaO in these ash deposits will be present in the form of calcium carbonate. This can be the

result of different processes. When wood fuels are combusted the Ca present as calcium oxalate crystals will thermally decompose into calcium carbonate ($CaCO_3$). If high enough temperatures are reached, the calcium carbonate is turned into calcium oxide (CaO). CaO will react with water to form calcium hydroxide ($Ca(OH)_2$), which over time will convert to calcium carbonate. CaO can also react with CO_2 (present in the atmosphere and/or the soil) to form calcium carbonate. Both MnO and MgO can be incorporated in calcium carbonate as a result of post-depositional processes and alkaline oxidized conditions (McKenzie, 1989). Calcium carbonate and calcium hydroxide will be the main pH buffering substances in the deposits (van Breemen and Wielemaker, 1974). Strikingly, there is no enrichment of K_2O in the Holocene deposits, while this is a known component of ash. This suggests that the ash derived potassium may have been dissolved and transported down to deeper levels. Micromorphology data from the uppermost Unit H1 shows the dominant presence of bone fragments. However, all bones show signs of dissolution (cause still unclear, **Figure 9A**) and often in a much worse state of preservation than the bone present in the acidic Pleistocene deposits. Due to the presence of high amounts of ash, the source of the P_2O_5 in the Holocene deposits is unclear. It may relate to (a combination) of ash, bone or the presence of animal excrement (e.g., from Rock hyrax: *Procavia capensis*) (Prinsloo, 2007; Chase et al., 2012). In addition, despite the clear high incidence of burning, the Holocene deposits have a low χLF signal and moderate to high χFD% values. This might be related to a diluting effect related to the presence of carbonates, caused by the high concentration of ash (van Os et al., 1994). The presence of finer SP domain minerals might relate to the presence of repeated burning, which is a common trend for inland sites in South Africa (Herries, 2009). It also suggests depositional conditions that allow for the preservation of such finer minerals, and for instance no post-depositional removal by water action. Finally, a shift in the geochemical data of the top two rows of the grid suggests that the top of Unit H1 might have been affected by modern contamination. For instance, car emissions from the nearby highway may have resulted in contamination with S, Zn, and Cu (Huisman et al., 1997; Chang et al., 2016). Other potential sources of contamination that should be considered are animal urine and feces, which can contain Cl, K_2O, Zn, P_2O_5, and Cu (Prinsloo, 2007; Chase et al., 2012).

Environmental Change

In the absence of more in-depth analysis of other environmental proxies, such as, phytoliths (forthcoming), the MS data gives a first indication of environmental change at the site. The Group P deposits at Umhlatuzana have a magnetic sedimentary structure predominantly composed of finer SP domain minerals, as indicated by χFD% values exceeding 7%. However, some variation can still be observed. The bottom part of the sequence (z = <529.75) shows moderate to high χFD% values (**Figures 8A,B**). The upper part of the Pleistocene sequence (z = 529.75–530.25) shows lower χFD% values (**Figures 8A,B**). While most of these values still show a larger influence of SP magnetic minerals, these sediments consist of higher concentrations of coarser magnetic domains than those displaying the highest χFD % values in the sequence (e.g., those above 10%, Dearing et al., 1996b).

The low χFD% values at the top of the Pleistocene sequence are accompanied by low χLF values. This shift in magnetic properties within the Pleistocene deposits has two possible causes. First, it might be related to the increase in SiO_2 visible in the geochemical data. The low χLF and χFD% values in the upper part of the Pleistocene sequence would then be the product of a decrease in the overall magnetic component of the sediments as a result of increased silica input. However, there is no indication of increased weathering of the rockshelter. Instead, the trend in the geochemical data most likely relates to a decrease in anthropogenic input (as evidenced by the find density data, see Sifogeorgaki et al., 2020), and does not reflect a direct increase in silica. Alternatively, the shift in magnetic properties within the Pleistocene sediments might relate to a change in the environmental conditions during the time of deposition. The movement of moisture through sediments can result in the removal of finer SP domain magnetic minerals from the deposits, since moisture has a tendency to remove finer domain minerals before it destabilizes larger domain minerals (Herries, 2006; Thompson and Oldfield, 1986). Therefore, the dominant presence of finer SP domain minerals in the lower part of the sequence could be taken as an indication of aridity during the formation of the deposits. Vice versa, the lower χFD% values in the upper part of the Pleistocene sequence might indicate deposition during a more humid phase where elevated moisture content has led to an overall coarsening of the magnetic minerals. However, the expected associated increase in χLF values is not observed in this part of the sequence. This can be explained by an overall decrease in the concentration of magnetic minerals, related to the decrease in Fe_2O_3 concentrations at the site, with the upper portion of the Pleistocene sequence having a much lower iron content than the bottom half of the Pleistocene deposits (**Figures 6K,L**). While this seems the most likely explanation of the observed trends, more in-depth micromorphological analysis is needed to confirm a potential difference in the frequency of secondary iron mineral formation. The switch from a dry period to a more humid period toward the end of the Pleistocene would match well with what is known about the local climate. Environmental data indicates that the region was wet during MIS 2 and 4, while it was drier during MIS 3 (Chase, 2010; Baker et al., 2014; Esteban et al., 2020). Based on previously obtained radiometric ages and assemblages, the Pleistocene deposits at Umhlatuzana, falling within the sampling grid, were deposited during MIS 3 and 2 (Lombard et al., 2010). Additional radiometric dating and paleoenvironmental work are necessary to test this, and are currently underway.

The Holocene deposits are characterized by moderately high χFD% values, suggesting that this part of the sequence was formed during a dry period. However, this does not match with the available paleoenvironmental data from the region, which suggests higher precipitation levels than in the preceding periods (Baker et al., 2014). Taking into account the intense anthropogenic component of the Group H sequence, the geogenic magnetic signal is likely obscured,

especially since repeated burnings are known to create finer magnetic minerals (Herries, 2006; 2009).

Link to Archaeology/Anthropogenic Impact

The results of the grid samples (pH, XRF, MS) did not reveal clear layers within the Pleistocene deposits. However, they do show a correlation with the different higher- and lower-density zones apparent from the analysis of piece-plotted materials (Sifogeorgaki et al., 2020). The zones with the highest find density are located at the bottom of the Pleistocene deposits (Zone ZH4; Unit P14-17; Unit P6-11) and are separated by a low find density zone (Zone ZL3; Unit P12-13) (**Figure 4**). Toward the top of the sequence the find density decreases. This trend of a decrease in find density, and presumed occupation intensity, matches with the gradual changes observed in the geochemical composition of the sediments. As the anthropogenic input in the sediments decreases (e.g., P_2O_5, CaO, Sr, Zn) the relative contribution of quartz can be seen to increase.

The geochemical data suggests that the anthropogenic input increases drastically within the Holocene deposits, most of which derives from combustion activities. However, the increase in combustion activities is not reflected in the MS data. This is likely caused by a dilution of the MS signal of the sediments connected to the high ash-related carbonate content (van Os et al., 1994), combined with the resolution of the sampling grid. Curiously, the find density appears to be significantly lower within the Holocene (Sifogeorgaki et al., 2020). As piece-plotting during the renewed excavations was done using a 2 cm size threshold, this effect might be due to the microlithization that characterizes the LSA technocomplexes. Although a decrease in occupation intensity remains a distinct possibility (e.g., Reynard et al., 2016), a more likely explanation is that the increased anthropogenic input in the Holocene deposits (mainly ash) resulted in a higher sedimentation rate and a lower artefact-sediment ratio. In addition, this effect could have been enhanced by a shift in site use and activity areas. To confirm this a larger scale excavation of the site would be needed.

Contextualization of the Approach

This section discusses geoarchaeological studies from other rockshelters articulated in siliceous bedrock in an attempt to contextualize the results of the present paper. Geoarchaeological studies within a quartz-rich sandstone bedrock have been conducted on several southern African rockshelter sites like Eland's Bay Cave (Miller et al., 2016), Diepkloof (Miller et al., 2013), Melikane rockshelter (Stewart et al., 2012), Mwulu Cave (de la Peña et al., 2018), Grassridge rockshelter (Ames et al., 2020), Sibudu (Goldberg et al., 2009), and Pinnacle Point (Karkanas and Goldberg, 2010). Most of these studies have been heavily focused on micromorphological analysis, while none of them have employed bulk sediment elemental analysis and only the Grassridge rockshelter study presents pH data. There is variation in bone and charcoal preservation rates, both between and within the different sites. For example, although Eland's Bay Cave generally has a good bone preservation, it is reported that bones were completely absent within a 'wetting front' of the deposits (Miller et al., 2016). A similar trend is observed at Umhlatuzana, where the higher-moisture sediments display poor bone preservation. Unfortunately, no pH analyses have been reported at Eland's Bay Cave, so moisture content and sediment pH cannot be correlated. The sediments of Grassridge rockshelter are alkaline and pH values are reported to range between 7.9 and 8.8. The pH remains high also in the lower deposits where a lack of evidence of combustion activity is reported (Ames et al., 2020). These values seem to be high when compared to pH analyses conducted on sandstone rockshelters globally. Some examples outside of South Africa include: Gledswood shelter 1 (Australia), which reports pH ranging from 5 to 5.5 (Lowe et al., 2018), Nonda Rock rockshelter (Australia) with pH ranging from 4.5 to 5.5 (David et al., 2007), Loberia I rockshelter (Argentina) where pH ranges from 3.7 to 5.8 (Martínez et al., 2013), and Santana do Riacho rockshelter (Brazil) with a pH from 4.4 to 6.4 (de Sousa et al., 2017). In comparison, Umhlatuzana displays quite high variation in pH values (4.87–8.94). While this difference suggests a more complex depositional setting at Umhlatuzana, it likely also results from the higher resolution of the grid sampling approach. MS analysis has been employed in Sibudu (Herries, 2006), Melikane (Stewart et al., 2012), and Pinnacle Point 13B (Herries and Fisher, 2010). However, only a study conducted at Pinnacle Point 5/6 used an approach comparable to the present study (Dinckal et al., submitted). At Pinnacle Point 5/6 MS was used to produce visual models, and to correlate that data with anthropogenic features to explore aspect of occupation at the site. The current study takes a similar approach to the Pinnacle Point 5/6 application, but further connects the results to other geoarchaeological methods by analyzing the same samples with multiple techniques. Overall, geoarchaeological studies conducted in South African rockshelters have been heavily focused on micromorphological analysis and cannot be directly compared to the current study.

Evaluation of the Approach

We systematically conducted a variety of geoarchaeological analyses to evaluate the stratigraphic sequence of Umhlatuzana rockshelter. This achieved a fine resolution geochemical overview of the deposits within the study area. The bulk (loose) sediment analyses performed are relatively inexpensive, fast, as well as easy to execute and interpret. Moreover, integrating bulk sediment analyses with field results and micromorphological analysis provides a link between macro and micro scale observations. Using a grid sampling strategy coupled with contour maps allows both a vertical and horizontal view of processes affecting the profile. Grid sampling is quite regularly used in archaeology to sample the horizontal X, Y plane. This happens at various scales, from dense grids in buildings to wide spatial grids in soils or settlements (e.g., Milek and Roberts, 2013; Canti and Huisman, 2015; Frahm et al., 2016). However, the approach is not used to sample profiles. When stratigraphic sections are sampled this commonly happens in vertical series, assuming horizontal homogeneity within a profile (e.g., Arroyo-Kalin, 2012; Barbosa et al., 2020).

The grid approach presented here allowed questions about post-depositional processes (e.g., mixing, preservation conditions) to be addressed in quite some detail, while also

providing insight into environmental and anthropogenic impact on the sediment sequence. Current analyses were limited to one section, as only the western profile of the site was excavated. Future studies would benefit from performing the same approach on multiple sections of the same excavation. Finally, the simple but systematic set up will allow more in-depth comparisons with other sites, especially if more researchers adopt this kind of approach. At present, those comparisons are severely limited by the wide variation in sampling strategies and analytical choices.

CONCLUSION

The current study aimed to shed light on the visible and invisible geochemical variation within the deposits of Umhlatuzana rockshelter, and to answer questions relating to stratigraphic integrity, anthropogenic input, post-depositional processes, and environmental change. This was achieved by applying a grid-based sampling strategy to the full western profile of the site, and by integrating different geochemical proxies (i.e., pH, elemental composition, MS). Integration of this data with preliminary micromorphology observations allowed for a link between the macro and micro scale within the deposits. Based on this research the following conclusions can be drawn:

- The Pleistocene deposits are dominated by geogenic sediments, with clear anthropogenic input, and indications of biogenic materials (excrement). The geochemistry is characterized by a steady, gradual change related to increased geogenic and decreased anthropogenic input toward the top.
- The Holocene deposits are characterized by much higher anthropogenic input related to combustion activities. There are also indications of biogenic input in the deposits.
- The magnetic analysis shows that within the mostly homogenous sedimentary context there are still distinctive lateral and vertical variations within the deposits. This is primarily evidenced by variation in χFD% values, which suggest that the lower part of the Pleistocene sequence was deposited during a dry period, followed by accumulation of sediments during a wetter phase. The Holocene paleoenvironmental MS signal is likely obscured by the high anthropogenic input.
- The gradual change within the geochemical data indicates that no large-scale mixing happened at the site. Small-scale mixing related to bioturbation is visible in the micromorphological thin sections. There are strong indications that the uppermost unit is severely mixed.
- The preservation at the site is driven by the variation in pH, with acidic values in the Pleistocene deposits and alkaline conditions in the Holocene. The pH in the Holocene was buffered by the presence of large amounts of ash.
- Variation in the χFD% values in the bottom part of the sequence indicates that the increase in moisture content (lower South corner of the profile) occurred post-depositionally.
- Different geochemical techniques were successfully integrated, using a grid-based sampling strategy, to better understand the depositional and post-depositional history of the site.
- The concept is simple to execute, fast, and relatively low-cost. The systematic approach allows for more in-depth comparison with other sites, once it is applied more broadly.

DATA AVAILABILITY STATEMENT

The original contributions presented in the study are included in the article/**Supplementary Material**, further inquiries can be directed to the corresponding author.

AUTHOR CONTRIBUTIONS

The concept and methodological approach of the study were developed by FR and IS. Sampling, sample preparation, and pH analysis were also done by FR and IS. XRF analysis was done by FR and IS, with assistance from GD. XRF data processing was done by BO. MS analysis was performed by MS, and MS data processing was done by AD. Micromorphology samples were taken, prepared, and analyzed by IS, with assistance from HH. The pH and XRF data were analyzed by FR, with input from BO and HH. The MS data was analyzed by AD and FR. Integration and interpretation of the full dataset was done through discussions with all authors. Elevation plots and contour maps were made by BO, MS plots and heat maps were made by AD. All other images were prepared for publication by IS. The manuscript was written by FR and IS, with contributions from GD, AD, and BO. All authors provided feedback at various stages of the writing process. Funding for the project was provided by GD, who also coordinated the fieldwork campaign.

FUNDING

The research is funded by NWO Vidi Grant 276-60-004 to Gerrit Dusseldorp.

ACKNOWLEDGMENTS

We thank Vumani Madinani, Jan Dekker, Guus Halewijn, Chris Thornhill, and Len van Schalkwyk for assistance in the field during the 2019 season when sampling was conducted. The KwaZulu-Natal Museum, Department of Human Sciences, Geoff Blundell, Ghilraen Laue Phumulani Madonda, Mudzunga Munzhedzi, Dimakatso Tlhoalele, and Gavin Whitelaw, supported our excavations. We thank SAHRA and AMAFA aKwaZulu-Natali, for issuing the requisite permits. Lastly, we thank the editors and the two reviewers for their valuable input to improve our manuscript.

SUPPLEMENTARY MATERIAL

The Supplementary Material for this article can be found online at: https://www.frontiersin.org/articles/10.3389/feart.2021.664105/full#supplementary-material

REFERENCES

Ames, C. J. H., Gliganic, L., Cordova, C. E., Boyd, K., Jones, B. G., Maher, L., et al. (2020). Chronostratigraphy, Site Formation, and Palaeoenvironmental Context of Late Pleistocene and Holocene Occupations at Grassridge Rock Shelter (Eastern Cape, South Africa). *Open Quat.* 6, 5. doi:10.5334/OQ.77

Arroyo-Kalin, M. (2012). Slash-burn-and-churn: Landscape History and Crop Cultivation in Pre-columbian Amazonia. *Quat. Int.* 249, 4–18. doi:10.1016/j.quaint.2011.08.004

Auler, A. S., Meus, P., and Pessoa, P. F. P. (2020). "Water Tracing Experiments in Low-pH Quartzite Karst Water, Chapada Diamantina, Northeastern Brazil," *Adv. Karst Sci*. Editors C. Bertrand, S. Denimal, M. Steinmann, and P. Renard (Cham: Springer), 183–191. doi:10.1007/978-3-030-14015-1_21

Bader, G. D., Linstädter, J., and Schoeman, M. H. (2020). Uncovering the Late Pleistocene LSA of Mpumalanga Province, South Africa: Early Results from Iron Pig Rock Shelter. *J. Afr. Arch.* 18, 19–37. doi:10.1163/21915784-20200003

Bader, G. D., Tribolo, C., and Conard, N. J. (2018). A Return to Umbeli Belli: New Insights of Recent Excavations and Implications for the Final MSA of Eastern South Africa. *J. Archaeological Sci. Rep.* 21, 733–757. doi:10.1016/j.jasrep.2018.08.043

Baker, A., Routh, J., Blaauw, M., and Roychoudhury, A. N. (2014). Geochemical Records of Palaeoenvironmental Controls on Peat Forming Processes in the Mfabeni Peatland, Kwazulu Natal, South Africa since the Late Pleistocene. *Palaeogeogr. Palaeoclimatol. Palaeoecol.* 395, 95–106. doi:10.1016/j.palaeo.2013.12.019

Barbosa, J. Z., Motta, A. C. V., Corrêa, R. S., Melo, V. d. F., Muniz, A. W., Martins, G. C., et al. (2020). Elemental Signatures of an Amazonian Dark Earth as Result of its Formation Process. *Geoderma*. 361, 114085. doi:10.1016/j.geoderma.2019.114085

Bousman, C. B., and Brink, J. S. (2018). The Emergence, Spread, and Termination of the Early Later Stone Age Event in South Africa and Southern Namibia. *Quat. Int.* 495, 116–135. doi:10.1016/j.quaint.2017.11.033

Braadbaart, F., Reidsma, F. H., Roebroeks, W., Chiotti, L., Slon, V., Meyer, M., et al. (2020). Heating Histories and Taphonomy of Ancient Fireplaces: A Multi-Proxy Case Study from the Upper Palaeolithic Sequence of Abri Pataud (Les Eyzies-De-Tayac, France). *J. Archaeological Sci. Rep.* 33, 102468. doi:10.1016/j.jasrep.2020.102468

Bronk Ramsey, C. (1995). Radiocarbon Calibration and Analysis of Stratigraphy: the OxCal Program. *Radiocarbon*. 37, 425–430. doi:10.1017/s0033822200030903

Bruch, A. A., Sievers, C., and Wadley, L. (2012). Quantification of Climate and Vegetation from Southern African Middle Stone Age Sites - an Application Using Late Pleistocene Plant Material from Sibudu, South Africa. *Quat. Sci. Rev.* 45, 7–17. doi:10.1016/j.quascirev.2012.04.005

Canti, M., and Huisman, D. J. (2015). Scientific Advances in Geoarchaeology during the Last Twenty Years. *J. Archaeological Sci.* 56, 96–108. doi:10.1016/j.jas.2015.02.024

Chang, C., Han, C., Han, Y., Hur, S. D., Lee, S., Motoyama, H., et al. (2016). Persistent Pb Pollution in central East Antarctic Snow: A Retrospective Assessment of Sources and Control Policy Implications. *Environ. Sci. Technol.* 50, 12138–12145. doi:10.1021/acs.est.6b03209

Chase, B. M., Scott, L., Meadows, M. E., Gil-Romera, G., Boom, A., Carr, A. S., et al. (2012). Rock Hyrax Middens: A Palaeoenvironmental Archive for Southern African Drylands. *Quat. Sci. Rev.* 56, 107–125. doi:10.1016/j.quascirev.2012.08.018

Chase, B. M. (2010). South African Palaeoenvironments during marine Oxygen Isotope Stage 4: a Context for the Howiesons Poort and Still Bay Industries. *J. Archaeological Sci.* 37, 1359–1366. doi:10.1016/j.jas.2009.12.040

Clark, J. L. (2013). Exploring the Relationship between Climate Change and the Decline of the Howieson's Poort at Sibudu Cave (South Africa). *Vertebr. Paleobiology Paleoanthropology.* 14, 9–18. doi:10.1007/978-94-007-6766-9_2

Clark, P. U., Dyke, A. S., Shakun, J. D., Carlson, A. E., Clark, J., Wohlfarth, B., et al. (2009). The Last Glacial Maximum. *Science* 325, 710–714. doi:10.1126/science.1172873

Conrad, O., Bechtel, B., Bock, M., Dietrich, H., Fischer, E., Gerlitz, L., et al. (2015). System for Automated Geoscientific Analyses (SAGA) V. 2.1.4. *Geosci. Model. Dev.* 8, 2007. doi:10.5194/gmd-8-1991-2015

Courty, M. A., Goldberg, P. S., and Macphail, R. I. (1989). *Soils and Micromorphology in Archaeology*. Cambridge: Cambridge University Press.

d'Errico, F., Backwell, L., Villa, P., Degano, I., Lucejko, J. J., Bamford, M. K., et al. (2012). Early Evidence of San Material Culture Represented by Organic Artifacts from Border Cave, South Africa. *Proc. Natl. Acad. Sci. U.S.A.* 109, 13214–13219. doi:10.1073/pnas.1204213109

David, B., Roberts, R. G., Magee, J., Mialanes, J., Turney, C., Bird, M., et al. (2007). Sediment Mixing at Nonda Rock: Investigations of Stratigraphic Integrity at an Early Archaeological Site in Northern Australia and Implications for the Human Colonisation of the Continent. *J. Quat. Sci.* 22, 449–479. doi:10.1002/jqs.1136

Davis, J. (1986). *Statistics and Data Analysis in Geology*. 1st ed. New York: Wiley & Sons Ltd.

de la Peña, P., Val, A., Stratford, D. J., Colino, F., Esteban, I., Fitchett, J. M., et al. (2018). Revisiting Mwulu's Cave: New Insights into the Middle Stone Age in the Southern African savanna Biome. *Archaeol. Anthropol. Sci.* 11, 3239–3266. doi:10.1007/s12520-018-0749-9

de Sousa, D. V., Ker, J. C., Prous, A., Schaefer, C. E. G. R., Rodet, M. J., Oliveira, F. S., et al. (2017). Archaeoanthrosol Formation and Evolution of the "Santana Do Riacho" Archaeological Shelter: An Old Burial Site in South America. *Geoarchaeology* 32, 678–693. doi:10.1002/gea.21645

Deacon, H. J. (1999). in *Human Beginnings in South Africa: Uncovering the Secrets of the Stone Age*. Editor J. Deacon Cape Town (New York: David Philip).

Dearing, J. A., Dann, R. J. L., Hay, K., Lees, J. A., Loveland, P. J., Maher, B. A., et al. (1996a). Frequency-dependent Susceptibility Measurements of Environmental Materials. *Geophys. J. Int.* 124, 228–240. doi:10.1111/j.1365-246X.1996.tb06366.x

Dearing, J. A., Hay, K. L., Baban, S. M. J., Huddleston, A. S., Wellington, E. M. H., and Loveland, P. J. (1996b). Magnetic Susceptibility of Soil: an Evaluation of Conflicting Theories Using a National Data Set. *Geophys. J. Int.* 127, 728–734. doi:10.1111/j.1365-246X.1996.tb04051.x

Dearing, J. (1999). Environmental Magnetism: a Practical Guide. *Quat. Res. Assoc.* 23, 35–62.

Esteban, I., Bamford, M. K., House, A., Miller, C. S., Neumann, F. H., Schefuß, E., et al. (2020). Coastal Palaeoenvironments and hunter-gatherer Plant-Use at Waterfall Bluff Rock Shelter in Mpondoland (South Africa) from MIS 3 to the Early Holocene. *Quat. Sci. Rev.* 250, 106664. doi:10.1016/j.quascirev.2020.106664

Frahm, E., Monnier, G. F., Jelinski, N. A., Fleming, E. P., Barber, B. L., and Lambon, J. B. (2016). Chemical Soil Surveys at the Bremer Site (Dakota County, Minnesota, USA): Measuring Phosphorous Content of Sediment by Portable XRF and ICP-OES. *J. Archaeological Sci.* 75, 115–138. doi:10.1016/j.jas.2016.10.004

Frassinetti, S., Bronzetti, G. L., Caltavuturo, L., Cini, M., and Croce, C. D. (2006). The Role of Zinc in Life: A Review. *J. Environ. Pathol. Toxicol. Oncol.* 25, 597–610. doi:10.1615/JEnvironPatholToxicolOncol.v25.i3.40

Goldberg, P., Miller, C. E., Schiegl, S., Ligouis, B., Berna, F., Conard, N. J., et al. (2009). Bedding, Hearths, and Site Maintenance in the Middle Stone Age of Sibudu Cave, KwaZulu-Natal, South Africa. *Archaeol. Anthropol. Sci.* 1, 95–122. doi:10.1007/s12520-009-0008-1

Gräler, B., Pebesma, E., and Heuvelink, G. (2016). Spatio-temporal Interpolation Using Gstat. *R. J.* 8, 204–218. doi:10.32614/rj-2016-014

Grove, M., and Blinkhorn, J. (2020). Neural Networks Differentiate between Middle and Later Stone Age Lithic Assemblages in Eastern Africa. *PLoS One.* 15, e0237528. doi:10.1371/journal.pone.0237528

Hanesch, M., and Scholger, R. (2005). The Influence of Soil Type on the Magnetic Susceptibility Measured throughout Soil Profiles. *Geophys. J. Int.* 161, 50–56. doi:10.1111/j.1365-246X.2005.02577.x

Henshilwood, C. S. (2012). Late Pleistocene Techno-Traditions in Southern Africa: A Review of the Still Bay and Howiesons Poort, C. 75-59 Ka. *J. World Prehist.* 25, 205–237. doi:10.1007/s10963-012-9060-3

Herries, A. I. R. (2006). Archaeomagnetic Evidence for Climate Change at Sibudu Cave. Available at: http://www.sahumanities.org.za (Accessed January 25, 2021).

Herries, A. I. R., and Fisher, E. C. (2010). Multidimensional GIS Modeling of Magnetic Mineralogy as a Proxy for Fire Use and Spatial Patterning: Evidence from the Middle Stone Age Bearing Sea Cave of Pinnacle Point 13B (Western Cape, South Africa). *J. Hum. Evol.* 59, 306–320. doi:10.1016/J.JHEVOL.2010.07.012

Herries, A. I. R. (2009). "New Approaches for Integrating Palaeomagnetic and mineral Magnetic Methods to Answer Archaeological and Geological Questions on Stone Age Sites." *In New Directions in Archaeological Science*, Editors. A. Fairbairn, S. O'Conner, and B. Marwick (London: ANU Press), 235–253.doi:10.22459/TA28.02.2009.16

Högberg, A., and Lombard, M. (2016a). Indications of Pressure Flaking More Than 70 Thousand Years Ago at Umhlatuzana Rock Shelter. South African Archaeol. *Bull.* 71, 53–59. doi:10.1371/journal.pone.0168012

Högberg, A., and Lombard, M. (2016b). Still Bay Point-Production Strategies at Hollow Rock Shelter and Umhlatuzana Rock Shelter and Knowledge-Transfer Systems in Southern Africa at about 80-70 Thousand Years Ago. *PLoS One* 11, e0168012. doi:10.1371/journal.pone.0168012

Holcomb, J. A., and Karkanas, P. (2019). Elemental Mapping of Micromorphological Block Samples Using Portable X-ray Fluorescence Spectrometry (pXRF): Integrating a Geochemical Line of Evidence. *Geoarchaeology* 34, 613–624. doi:10.1002/gea.21741

Huisman, D. J., Vermeulen, F. J. H., Baker, J., Veldkamp, A., Kroonenberg, S. B., and Klaver, G. T. (1997). A Geological Interpretation of Heavy Metal Concentrations in Soils and Sediments in the Southern Netherlands. *J. Geochemical Exploration* 59, 163–174. doi:10.1016/S0375-6742(97)00018-6

Jacobs, Z., Roberts, R. G., Galbraith, R. F., Deacon, H. J., Grün, R., Mackay, A., et al. (2008). Ages for the Middle Stone Age of Southern Africa: Implications for Human Behavior and Dispersal. *Science* 322, 733–735. doi:10.1126/science.1162219

Kaplan, J. M. (1989). 45000 Years of hunter-gatherer History in Natal as Seen from Umhlatuzana Rock Shelter. *Goodwin Ser.* 6, 7–16. doi:10.2307/3858128

Kaplan, J. M. (1990). The Umhlatuzana Rock Shelter Sequence: 100 000 Years of Stone Age History. *South. Afr. Humanit.* 2, 1–94.

Karkanas, P., Bar-Yosef, O., Goldberg, P., and Weiner, S. (2000). Diagenesis in Prehistoric Caves: the Use of Minerals that Form *In Situ* to Assess the Completeness of the Archaeological Record. *J. Archaeological Sci.* 27, 915–929. doi:10.1006/jasc.1999.0506

Karkanas, P., and Goldberg, P. (2010). Site Formation Processes at Pinnacle Point Cave 13B (Mossel Bay, Western Cape Province, South Africa): Resolving Stratigraphic and Depositional Complexities with Micromorphology. *J. Hum. Evol.* 59, 256–273. doi:10.1016/J.JHEVOL.2010.07.001

Karkanas, P., and Goldberg, P. (2018). *Reconstructing Archaeological Sites: Understanding the Geoarchaeological Matrix*. Hoboken, NJ: John Wiley & Sons. doi:10.1002/9781119016427

Loftus, E., Pargeter, J., Mackay, A., Stewart, B. A., and Mitchell, P. (2019). Late Pleistocene Human Occupation in the Maloti-Drakensberg Region of Southern Africa: New Radiocarbon Dates from Rose Cottage Cave and Inter-site Comparisons. *J. Anthropological Archaeology* 56, 101117. doi:10.1016/j.jaa.2019.101117

Lombard, M. (2007). The Gripping Nature of Ochre: The Association of Ochre with Howiesons Poort Adhesives and Later Stone Age Mastics from South Africa. *J. Hum. Evol.* 53, 406–419. doi:10.1016/j.jhevol.2007.05.004

Lombard, M. (2011). Quartz-tipped Arrows Older Than 60 Ka: Further Use-Trace Evidence from Sibudu, KwaZulu-Natal, South Africa. *J. Archaeological Sci.* 38, 1918–1930. doi:10.1016/j.jas.2011.04.001

Lombard, M., Wadley, L., Deacon, J., Wurz, S., Parsons, I., Mohapi, M., et al. (2012). South African and Lesotho Stone Age Sequence Updated. South African Archaeol. *Bull.* 67, 123–144. doi:10.2307/3888989

Lombard, M., Wadley, L., Jacobs, Z., Mohapi, M., and Roberts, R. G. (2010). Still Bay and Serrated Points from Umhlatuzana Rock Shelter, Kwazulu-Natal, South Africa. *J. Archaeological Sci.* 37, 1773–1784. doi:10.1016/j.jas.2010.02.015

Lowe, K. M., Mentzer, S. M., Wallis, L. A., and Shulmeister, J. (2018). A Multi-Proxy Study of Anthropogenic Sedimentation and Human Occupation of Gledswood Shelter 1: Exploring an interior sandstone Rockshelter in Northern Australia. *Archaeol. Anthropol. Sci.* 10, 279–304. doi:10.1007/s12520-016-0354-8

Mackay, A., Stewart, B. A., and Chase, B. M. (2014). Coalescence and Fragmentation in the Late Pleistocene Archaeology of Southernmost Africa. *J. Hum. Evol.* 72, 26–51. doi:10.1016/j.jhevol.2014.03.003

Macphail, R. I., and Goldberg, P. (2017). *Applied Soils and Micromorphology in Archaeology*. Cambridge: Cambridge University Press. doi:10.1017/9780511895562

Marshall, C. A. G. (1994). The Stratigraphy of the Natal Group. Master's Thesis. Pietermaritzburg: University of Natal.

Martínez, G. A., Mazzanti, D. L., Quintana, C., Zucol, A. F., Colobig, M. d. l. M., Hassan, G. S., et al. (2013). Geoarchaeological and Paleoenvironmental Context of the Human Settlement in the Eastern Tandilia Range, Argentina. *Quat. Int.* 299, 23–37. doi:10.1016/j.quaint.2012.12.032

McCall, G. S., and Thomas, J. T. (2009). Re-examining the South African Middle-To-Later Stone Age Transition: Multivariate Analysis of the Umhlatuzana and Rose Cottage Cave Stone Tool Assemblages. *Azania: Archaeological Res. Africa*. 44, 311–330. doi:10.1080/00672700903337519

McKenzie, R. (1989). *Manganese Oxides and Hydroxides. Minerals in Soil Environments*. Hoboken: John Wiley & Sons.

Mecchia, M., Sauro, F., Piccini, L., De Waele, J., Sanna, L., Tisato, N., et al. (2014). Geochemistry of Surface and Subsurface Waters in Quartz-Sandstones: Significance for the Geomorphic Evolution of Tepui Table Mountains (Gran Sabana, Venezuela). *J. Hydrol.* 511, 117–138. doi:10.1016/j.jhydrol.2014.01.029

Milek, K. B., and Roberts, H. M. (2013). Integrated Geoarchaeological Methods for the Determination of Site Activity Areas: A Study of a Viking Age House in Reykjavik, Iceland. *J. Archaeological Sci.* 40, 1845–1865. doi:10.1016/j.jas.2012.10.031

Miller, C. E., Goldberg, P., and Berna, F. (2013). Geoarchaeological Investigations at Diepkloof Rock Shelter, Western Cape, South Africa. *J. Archaeological Sci.* 40, 3432–3452. doi:10.1016/J.JAS.2013.02.014

Miller, C. E., Mentzer, S. M., Berthold, C., Leach, P., Ligouis, B., Tribolo, C., et al. (2016). Site-formation Processes at Elands Bay Cave, South Africa. *South. Afr. Humanit.* 29, 69–128. doi:10.30861/9780860545842

Mitchell, P. (1988). The Late Pleistocene Early Microlithic Assemblages of Southern Africa. *World Archaeology* 20, 27–39. doi:10.1080/00438243.1988.9980054

Mohapi, M. (2013). The Middle Stone Age point Assemblage from Umhlatuzana Rock Shelter: a Morphometric Study. *South. Afr. Humanit.* 1, 25–51. doi:10.30861/9780860545217

Mucina, L., and Rutherford, M. C. (2006). *The Vegetation of South Africa, Lesotho and Swaziland*. Pretoria: South African National Biodiversity Institute.

Nel, W. (2009). Rainfall Trends in the KwaZulu-Natal Drakensberg Region of South Africa during the Twentieth century. *Int. J. Climatol.* 29, 1634–1641. doi:10.1002/joc.1814

Nriagu, J. O. (1976). Phosphate - clay mineral Relations in Soils and Sediments. *Can. J. Earth Sci.* 13, 717–736. doi:10.1139/e76-077

van Os, B., de Kort, J. W., and Huisman, H. (2012). A Qualitative Approach for Assessment of the Burial Environment by Interpreting Soil Characteristics; A Necessity for Archaeological Monitoring. *Conservation Management Archaeological Sites* 14, 333–340. doi:10.1179/1350503312Z.00000000029

Pargeter, J., Loftus, E., and Mitchell, P. (2017). New Ages from Sehonghong Rock Shelter: Implications for the Late Pleistocene Occupation of highland Lesotho. *J. Archaeological Sci. Rep.* 12, 307–315. doi:10.1016/j.jasrep.2017.01.027

Pebesma, E. J. (2004). Multivariable Geostatistics in S: The Gstat Package. *Comput. Geosciences* 30, 683–691. doi:10.1016/j.cageo.2004.03.012

Porraz, G., Parkington, J. E., Rigaud, J.-P., Miller, C. E., Poggenpoel, C., Tribolo, C., et al. (2013). The MSA Sequence of Diepkloof and the History of Southern African Late Pleistocene Populations. *J. Archaeological Sci.* 40, 3542–3552. doi:10.1016/j.jas.2013.02.024

Prinsloo, L. C. (2007). Rock Hyraces: a Cause of San Rock Art Deterioration?. *J. Raman Spectrosc.* 38, 496–503. doi:10.1002/jrs.1671

R Core Team (2017). *R: A Language and Environment for Statistical Computing*. Berlin: Springer.

Reidsma, F. H., van Hoesel, A., van Os, B. J. H., Megens, L., and Braadbaart, F. (2016). Charred Bone: Physical and Chemical Changes during Laboratory Simulated Heating under Reducing Conditions and its Relevance for the Study of Fire Use in Archaeology. *J. Archaeological Sci. Rep.* 10, 282–292. doi:10.1016/j.jasrep.2016.10.001

Reynard, J. P., Discamps, E., Wurz, S., van Niekerk, K. L., Badenhorst, S., and Henshilwood, C. S. (2016). Occupational Intensity and Environmental Changes during the Howiesons Poort at Klipdrift Shelter, Southern Cape, South Africa. *Palaeogeogr. Palaeoclimatol. Palaeoecol.* 449, 349–364. doi:10.1016/j.palaeo.2016.02.035

Rots, V., Lentfer, C., Schmid, V. C., Porraz, G., and Conard, N. J. (2017). Pressure Flaking to Serrate Bifacial Points for the hunt during the MIS5 at Sibudu Cave (South Africa). *PLoS One* 12, e0175151. doi:10.1371/journal.pone.0175151

Sauro, F., Mecchia, M., Piccini, L., De Waele, J., Carbone, C., Columbu, A., et al. (2019). Genesis of Giant Sinkholes and Caves in the Quartz sandstone of

Sarisariñama Tepui, Venezuela. *Geomorphology* 342, 223–238. doi:10.1016/j.geomorph.2019.06.017

Sayre, R., Karagulle, D., Frye, C., Boucher, T., Wolff, N. H., Breyer, S., et al. (2020). An Assessment of the Representation of Ecosystems in Global Protected Areas Using New Maps of World Climate Regions and World Ecosystems. *Glob. Ecol. Conservation* 21, e00860. doi:10.1016/j.gecco.2019.e00860

Sifogeorgaki, I., Klinkenberg, V., Esteban, I., Murungi, M., Carr, A. S., van den Brink, V. B., et al. (2020). New Excavations at Umhlatuzana Rockshelter, KwaZulu-Natal, South Africa: a Stratigraphic and Taphonomic Evaluation. *Afr. Archaeol Rev.* 37, 551–578. doi:10.1007/s10437-020-09410-w

Simon, M. H., Arthur, K. L., Hall, I. R., Peeters, F. J. C., Loveday, B. R., Barker, S., et al. (2013). Millennial-scale Agulhas Current Variability and its Implications for Salt-Leakage through the Indian-Atlantic Ocean Gateway. *Earth Planet. Sci. Lett.* 383, 101–112. doi:10.1016/j.epsl.2013.09.035

Simon, M. H., Ziegler, M., Bosmans, J., Barker, S., Reason, C. J. C., and Hall, I. R. (2015). Eastern South African Hydroclimate over the Past 270,000 Years. *Sci. Rep.* 5, 18153. doi:10.1038/srep18153

Stewart, B. A., Dewar, G. I., Morley, M. W., Inglis, R. H., Wheeler, M., Jacobs, Z., et al. (2012). Afromontane Foragers of the Late Pleistocene: Site Formation, Chronology and Occupational Pulsing at Melikane Rockshelter, Lesotho. *Quat. Int.* 270, 40–60. doi:10.1016/j.quaint.2011.11.028

Stoops, G. (2003). *Guidelines for Analysis and Description of Soil and Regolith Thin Sections*. Editor M. J. Vepraskas. (Madison:Soil Science Society of America).

Stoops, G., Marcelino, V., and Mees, F. (2010). *Interpretation of Micromorphological Features of Soils and Regoliths*. (Amsterdam: Elsevier), 663–705. doi:10.1016/C2009-0-18081-9

Stoops, G., and Nicosia, C. (2017). "Sampling for Soil Micromorphology," in *In Archaeological Soil and Sediment Micromorphology* (Chichester: John Wiley & Sons, Ltd), 383–391. doi:10.1002/9781118941065.ch35

Taylor, S. R., and McLennan, S. M. (1985). *The Continental Crust: Its Composition and Evolution. United States*. Berlin: Springer.

Thompson, R., and Oldfield, F. (1986). Environmental Magnetism. *Earth-science Rev.* 26, 54–55. doi:10.1016/0012-8252(89)90007-X

van Breemen, N., and Wielemaker, W. G. (1974). Buffer Intensities and Equilibrium pH of Minerals and Soils: I. The Contribution of Minerals and Aqueous Carbonate to pH Buffering. *Soil Sci. Soc. America J.* 38, 55–60. doi:10.2136/sssaj1974.03615995003800010022x

van Os, B. J. H., Lourens, L. J., Hilgen, F. J., De Lange, G. J., and Beaufort, L. (1994). The Formation of Pliocene Sapropels and Carbonate Cycles in the Mediterranean: Diagenesis, Dilution, and Productivity. *Paleoceanography* 9, 601–617. doi:10.1029/94PA00597

Vassilev, S. V., Baxter, D., and Vassileva, C. G. (2014). An Overview of the Behaviour of Biomass during Combustion: Part II. Ash Fusion and Ash Formation Mechanisms of Biomass Types. *Fuel* 117, 152–183. doi:10.1016/j.fuel.2013.09.024

Villa, P., Soriano, S., Tsanova, T., Degano, I., Higham, T. F. G., d'Errico, F., et al. (2012). Border Cave and the Beginning of the Later Stone Age in South Africa. *Proc. Natl. Acad. Sci.* 109, 13208–13213. doi:10.1073/pnas.1202629109

Wadley, L. (2005). A Typological Study of the Final Middle Stone Age Tools from Sibudu Cave Kwazulu-Natal. *South African Archaeol. Bull.* 60, 51–63. doi:10.3213/2191-5784-10246

Weiner, S. (2010). *Microarchaeology: Beyond the Visible Archaeological Record*. Cambridge: Cambridge University Press. doi:10.1017/cbo9780511811210

Welch, R. M. (1993). "Zinc Concentrations and Forms in Plants for Humans and Animals," in *Zinc in Soils and Plants: Proceedings of the International Symposium on 'Zinc in Soils and Plants*. Editor A. D. Robson (Dordrecht: Springer Netherlands), 183–195. doi:10.1007/978-94-011-0878-2_13

Wickham, H. (2016). *ggplot2: Elegant Graphics for Data Analysis*. New York: Springer. Available at: https://ggplot2.tidyverse.org

Yokoyama, Y., Esat, T. M., Thompson, W. G., Thomas, A. L., Webster, J. M., Miyairi, Y., et al. (2018). Rapid Glaciation and a Two-step Sea Level Plunge into the Last Glacial Maximum. *Nature*. 559, 603–607. doi:10.1038/s41586-018-0335-4

Ziegler, M., Simon, M. H., Hall, I. R., Barker, S., Stringer, C., and Zahn, R. (2013). Development of Middle Stone Age Innovation Linked to Rapid Climate Change. *Nat. Commun.* 4, 1–9. doi:10.1038/ncomms2897

Conflict of Interest: The authors declare that the research was conducted in the absence of any commercial or financial relationships that could be construed as a potential conflict of interest.

frontiers in Earth Science

ORIGINAL RESEARCH
published: 28 July 2021
doi: 10.3389/feart.2021.568646

Orbital Influence on Precipitation, Fire, and Grass Community Composition From 1.87 to 1.38 Ma in the Turkana Basin, Kenya

Chad L. Yost[1,2], Rachel L. Lupien[3], Catherine Beck[4], Craig S. Feibel[5], Steven R. Archer[6] and Andrew S. Cohen[2]*

[1]Department of Earth and Environmental Systems, Indiana State University, Terre Haute, IN, United States, [2]Department of Geosciences, University of Arizona, Tucson, AZ, United States, [3]Division of Biology and Paleo Environment, Lamont-Doherty Earth Observatory, Palisades, NY, United States, [4]Department of Geosciences, Hamilton College, Clinton, NY, United States, [5]Department of Earth and Planetary Sciences, Rutgers University, Piscataway, NJ, United States, [6]School of Natural Resources and the Environment, University of Arizona, Tucson, AZ, United States

The Turkana Basin in northern Kenya and southern Ethiopia has yielded hundreds of hominin fossils and is among the most important localities in the world for studying human origins. High resolution climate and vegetation reconstructions from this region can elucidate potential linkages between hominin evolution and environmental change. Microcharcoal and phytoliths were examined from a 216 m (1.87–1.38 Ma) drill core (WTK13), which targeted paleo-Lake Lorenyang sediments from the Nachukui Formation of the Turkana Basin. A total of 287 samples were analyzed at ~32–96 cm intervals, providing millennial-scale temporal resolution. To better understand how basin sediments record fire and vegetation from the watershed, the paleorecord was compared with nine modern sediment samples collected from Lake Turkana along a transect of increasing distance from the 1978 to 1979 shoreline. This included vegetation surveys and phytolith production data for species from areas proximal to the basin. We found that phytolith and microcharcoal concentrations decreased predictably moving off shore. However, phytoliths from plants sourced in the Ethiopian Highlands increased moving off shore, likely the result of increased exposure to the Omo River sediment plume. In our down-core study, microcharcoal was well-preserved but phytolith preservation was poor below ~60 m (~1.50 Ma). Spectral analysis revealed that microcharcoal often varied at precessional (~21 kyr) periodicities, and through a correlation with δD_{wax}, linked orbitally forced peaks in precipitation with elevated fire on the landscape. Phytoliths revealed that alternating mesic C_4 versus xeric C_4 grass dominance likely varied at precessional periodicities as well, but that grass community composition was also mediated by basin geometry. Two high eccentricity intervals of particularly high amplitude and abrupt environmental change were centered at ~1.72 and 1.50 Ma, with the intervening period experiencing high fire variability. With the switch from lacustrine to fluvial-deltaic deposition at the core site by 1.5 Ma, mesic C_4 grasses dominated and fire activity was high. This upper interval correlated to the time interval from which Nariokotome Boy (*Homo erectus/ergaster*) was discovered 3 km east of our drill site. Phytoliths

OPEN ACCESS

Edited by:
Christian Zeeden, Leibniz Institute for Applied Geophysics (LIAG), Germany

Reviewed by:
Alberto Saez, University of Barcelona, Spain
Stefanie Kaboth-Bahr, University of Potsdam, Germany

***Correspondence:**
Chad L. Yost
Chad.Yost@indstate.edu

Specialty section:
This article was submitted to Quaternary Science, Geomorphology and Paleoenvironment, a section of the journal Frontiers in Earth Science

Received: *01 June 2020*
Accepted: *15 July 2021*
Published: *28 July 2021*

Citation:
Yost CL, Lupien RL, Beck C, Feibel CS, Archer SR and Cohen AS (2021) Orbital Influence on Precipitation, Fire, and Grass Community Composition From 1.87 to 1.38 Ma in the Turkana Basin, Kenya. Front. Earth Sci. 9:568646. doi: 10.3389/feart.2021.568646

indicated a seasonally wet and open landscape dominated by xeric C_4 grasses, sedges, and other herbaceous plants.

Keywords: paleofire, phytoliths, phytoscape, orbital forcing, Nachukui formation, Nariokotome Boy, *Homo ergaster*, microcharcoal

INTRODUCTION

The Turkana Basin in northern Kenya and southern Ethiopia is among the most important localities in the world for studying human origins. Its hydrological connection to the Ethiopian Highlands and its geological setting within the East African Rift System has combined to produce fossil-rich sedimentary strata yielding hundreds of hominin fossils from species of *Australopithecus*, *Kenyanthropus*, *Paranthropus*, and *Homo* (Feibel, 2011; Wood and Leakey, 2011). Lake Turkana is the largest desert lake in the world, and a series of predecessors to the modern lake have occupied this basin periodically since at least the Miocene (Brown and McDougall, 2011). The Hominin Sites and Paleolakes Drilling Project (HSPDP) targeted Early Pleistocene sediments from paleo-Lake Lorenyang (HSPDP-WTK13-1A drill core; hereafter WTK13), a precursor to present-day Lake Turkana, to reconstruct regional climate and vegetation in relatively close spatial and temporal proximity to important hominin sites (Cohen et al., 2016; Campisano et al., 2017). This includes the Nariokotome site (NK3) and its hominin remains (Nariokotome Boy, KNM-WT 15000) located ~3 km from the drill site; NK3 yielded the most complete *Homo erectus*/*ergaster* skeleton ever recovered (Brown et al., 1985; Walker and Leakey, 1993).

The recovered drill core interval of 1.87–1.38 Ma coincides with the first occurrence of hominins with modern, human-like terrestrial adaptations, the expansion of grasslands, and the first hominin expansions outside of Africa (Antón, 2003; Bobe, 2004; Bobe and Leakey, 2009; Campisano et al., 2017). Mammalian turnover and diversity peaks at ~1.8 Ma and includes the co-occurrence of *Paranthropus boisei*, *Homo habilis*, *Homo rudolfensis* and *Homo erectus* (Bobe and Carvalho, 2019). This period in the Turkana Basin has also yielded one of the oldest archaeological sites with Acheulean stone tool technology (Lepre et al., 2011) and the earliest evidence of aquatic resource subsistence by hominins (Braun et al., 2010). In addition, fossils attributed to *Homo* in the Turkana Basin show an apparent increase in the consumption of C_4 vegetation (or animals that consume C_4 plants) after 1.65 Ma (Patterson et al., 2019). Archaeological sites in East Turkana (Koobi Fora) exhibit potential evidence for the intentional use of fire at ~1.5 Ma (Hlubik et al., 2019).

When evaluating potential environmental drivers of human evolution and cultural change, spatially and temporally relevant vegetation reconstructions are essential. Although isotopic approaches can provide information about vegetation structure (e.g., grassland, woodland, forest), they are limited in their taxonomic resolution. In grass-dominated plant communities, phytoliths (opal silica microfossils) and microcharcoal can reconstruct grass community dynamics and fire regimes important to understanding how herbivores and hominins may have interacted with their surroundings (e.g., Yost et al., 2021), and complement related isotopic studies (e.g., Lupien et al., 2021).

Essential to the use of phytoliths and microcharcoal to reconstruct vegetation from paleolake sediments is an understanding of phytolith source areas and depositional patterns in modern lakes. Because such studies are rare (see Yost et al., 2013; Li et al., 2019), the examination of modern Lake Turkana sediments provides an opportunity to elucidate these phenomena in a context appropriate for better understanding phytolith and microcharcoal records from much older lacustrine deposits in the Turkana Basin. Additionally, use of modern lake sediments originally collected in 1978 (Cohen et al., 1986) predates significant anthropogenic perturbations including construction of the Gibe I dam in the Ethiopian Highlands, significant changes in the Omo River delta configuration, and delta land-use intensification since the 1970s (Carr, 2017).

Here, we present a millennial-scale record of fire and vegetation through the use of plant opal phytoliths and microcharcoal for the Early Pleistocene in the Turkana Basin. By incorporating an understanding of the sediments and dominant vegetation from modern Lake Turkana we are able to better understand how the potential phytolith landscape (*phytoscape*) is recorded in sediments across the lake, and quantify how sediments from the Omo River may influence this signal. We then use phytoliths and microcharcoal extracted from the WTK13 paleorecord to reconstruct dominant vegetation and fire activity during the Early Pleistocene. We explore these data using spectral analyses to reveal the influence of Earth's orbital parameters on vegetation, in particular grass community composition, and fire. Lastly, we use a core-to-outcrop linkage to reconstruct the local paleoenvironment present when the Nariokotome Boy walked upon the landscape.

BACKGROUND

Geography, Climatology, Limnology

Lake Turkana is a closed-basin lake approximately 250 km long and 30 km wide situated in an arid depression between the Kenyan and Ethiopian Highlands (**Figures 1A,E**). The lake surface is at an elevation of ~360 m; mean and maximum depths are 35 and 120 m, respectively (Johnson and Malala, 2009). The dominant vegetation type within the Turkana Depression is arid-adapted *Acacia-Commiphora* deciduous bushland and desert. However, the watershed includes small areas of riverine and afromontane forests, freshwater swamps,

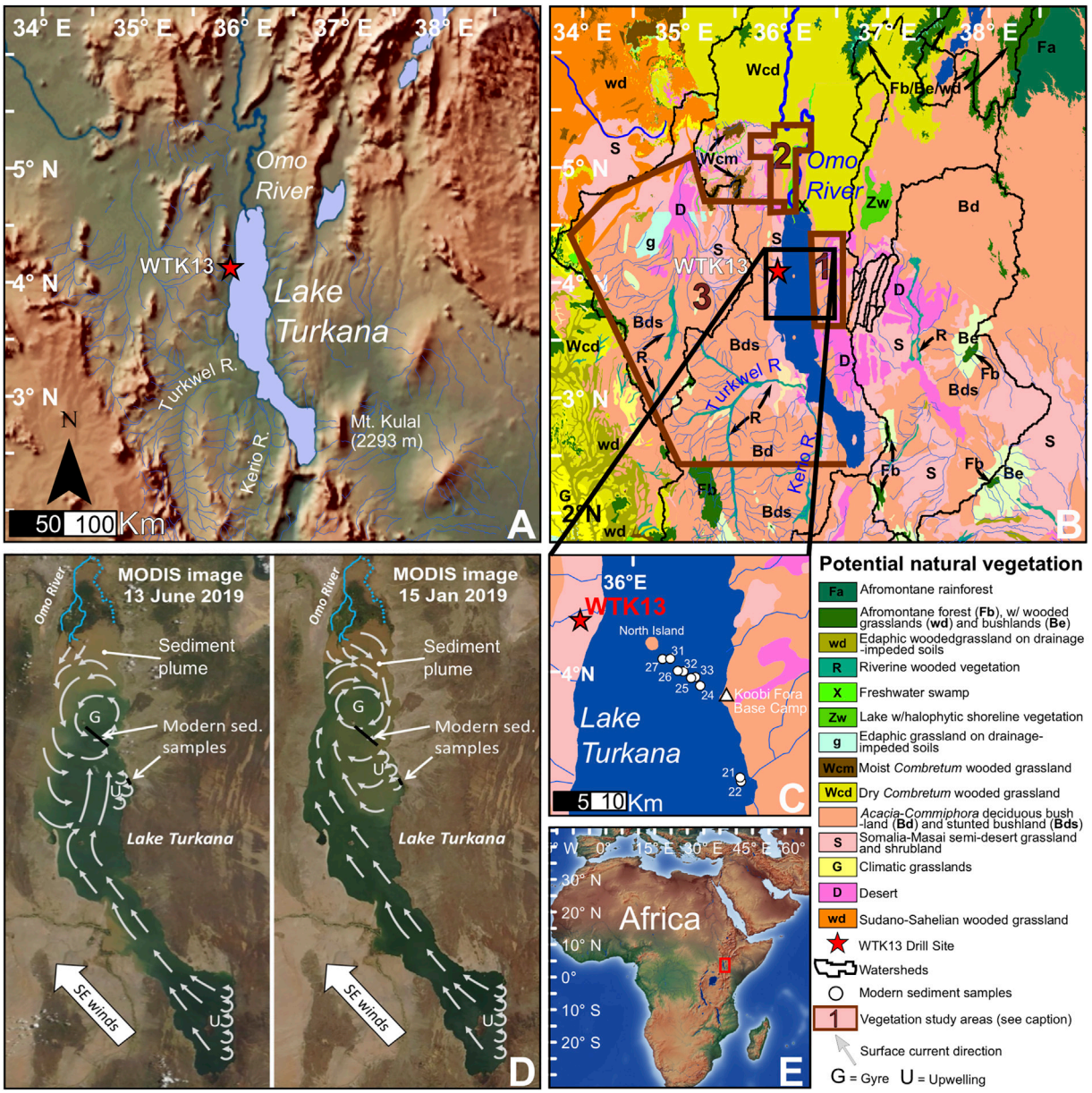

FIGURE 1 | Study area maps. **(A)** Colored relief map of the Turkana Depression. **(B)** Potential natural vegetation (PNV; van Breugel et al., 2015) of the Turkana Depression and floristic study area boundaries (1 = Koobi Fora [East Turkana], 2 = Lower Omo River Valley, 3 = West Turkana). **(C)** Modern Lake Turkana sediment sample locations. **(D)** MODIS satellite images (NASA, 2019) depicting the Omo River sediment plume, and inferred surface currents redrawn from Yuretich and Cerling (1983). **(E)** Colored relief map of Africa with the Turkana Basin location indicated with the red box.

and a large area of dry *Combretum* wooded grasslands (**Figure 1B**).

The Turkana Depression has a mean annual temperature of ~30°C, with a mean maximum and minimum of 34 and 24°C, respectively (Morrissey et al., 2017). Historic (1925–1990) mean annual precipitation (MAP) is ~200 mm, and is delivered over two rainy seasons: the 'long rains' during boreal spring and the 'short rains' during boreal autumn (Nicholson, 2000). The Ethiopian Highlands to the north receive about 800–1,200 mm MAP, mostly during boreal summer (Nicholson, 2017). The Omo River, which drains a portion of the Ethiopian Highlands, supplies 80–90% of the water in the lake (Yuretich and Cerling, 1983). Its sediment plume is dispersed throughout much of the northern lake basin via seasonal gyres (**Figure 1D**; Hopson, 1975; Yuretich and Cerling, 1983). The Turkwel and Kerio rivers, draining a portion of the Kenyan Highlands to the south, supply 10–20% of the lake water (Johnson and Malala, 2009). However, strontium isotope data indicates that the proportion of Turkwel to Omo river water may have been

significantly higher during past humid periods (van der Lubbe et al., 2017). Thus, the Turkana Basin is hydrologically connected to two different precipitation modes, bimodal (spring and autumn) in the Kenyan Highlands and locally unimodal (summer) in the Ethiopian Highlands.

The Omo River and Lake Turkana surface waters have an average pH of 7.1 and 9.2, respectively (Yuretich and Cerling, 1983), and biogenic silica (diatoms, sponge spicules, and phytoliths) can begin to rapidly dissolve when sediment pore water pH is >9.0 (Fraysse et al., 2009). However, measurements of pore water pH on short cores from Lake Turkana yielded values of ~8.6 for depths of up to 120 cm. The release of carbonic acid from organic matter decay is thought to be the mechanism for lowering pH from that observed in surface waters (Yuretich and Cerling, 1983). The Turkana Depression is extremely windy, with prevailing winds out of the south/southeast producing surface currents that generally move towards the north end of the lake (**Figure 1D**; Yuretich and Cerling, 1983; Johnson and Malala, 2009). Lake Turkana is classified by Nutz et al. (2016) as a wind-driven waterbody, where wind and wave action have pronounced effects on surface currents, bottom currents, upwelling, shoreline stability, and sedimentation patterns. There is high-resolution seismic profile evidence for the existence of erosion or non-deposition caused by surface wave activity at sites where water depths are <35 m (Johnson and Malala, 2009). Our study provides new information on terrestrial microfossil transport and biogenic silica preservation in both modern and paleo-lake sediments from the Turkana Basin that can be applied to other large lake paleolimnological studies.

Eastern African Rainfall Seasonality

Areas between 7° S and 6° N in eastern Africa experience strong bimodal (spring and autumn) distributions of maximum precipitation. At 20° S and 20° N, maximum precipitation is unimodal during each hemisphere's summer (Nicholson, 2018). Summer precipitation in the Ethiopian Highlands is triggered by the onset of low-level westerlies, peaking in July/August. Low-level cyclonic flow over the Arabian Peninsula promotes the development of westward propagating convective systems (Nicholson, 2017). In a reanalysis study, Viste and Sorteberg (2013) found that moisture sources for convergence in the highlands were from three main regions: the Indian Ocean, the Congo Basin, and the Red Sea/Mediterranean Sea, with the Gulf of Guinea (Atlantic Ocean) contributing the least amount.

The mechanisms behind the bimodal distribution of rainfall in eastern Africa have been attributed by many to the twice-yearly passing of the tropical rain belt (Nicholson, 2018). Recently, Yang et al. (2015) proposed that bimodal precipitation is the result of the annual cycle of monsoonal winds combining with the annual cycle of the Indian Ocean sea surface temperatures (SSTs). During boreal winter and summer, precipitation is suppressed due to advection of low-moist static energy (MSE) air from a cooler off-shore Indian Ocean. During the two rainy seasons, low-level divergent winds are much weaker, allowing for the import of unstable air into eastern Africa; SSTs off the coast are higher, with the highest levels associated with the long rains.

Orbital Forcing in the Turkana Basin

Relationships between paleosol formation, paleolake high stands, depositional processes and Earth's orbital parameters in the Turkana Basin have been recognized for some time (e.g., Wynn, 2004; Trauth et al., 2005; Lepre et al., 2007). Research in this area continues to expand and shows that eccentricity (400, 100 kyr) and precession (23–19 kyr) are major drivers of hydroclimate and lake level variability (Joordens et al., 2011; Joordens et al., 2013; Nutz et al., 2017; Lupien et al., 2018; Boës et al., 2019). However, volcano-tectonic impounding likely played a role in lake formation within the Turkana Basin as well (Bruhn et al., 2011; Lepre, 2014; Boës et al., 2019). Nevertheless, first-order observations in stratigraphic records (e.g., Nutz et al., 2017; Nutz et al., 2020; Boës et al., 2019) indicate that some, but not all paleolake transgressive (regressive) phases and high (low) stands occur during periods of eccentricity maxima (minima). Stratigraphic and isotopic studies from the Turkana Basin have found that low precession, which results in high insolation, is correlated with increased precipitation within the watershed (Lupien et al., 2018), progradation within the lake (Nutz et al., 2017), and increased river inflow to the lake (Joordens et al., 2011; van der Lubbe et al., 2017).

Causal mechanisms between increased insolation and increased precipitation in the tropics and subtropics are not fully understood, but researchers typically invoke the orbital monsoon hypothesis (Kutzbach and Otto-Bliesner, 1982; Rossignol-Strick, 1983; Prell and Kutzbach, 1987; Tuenter et al., 2003; Merlis et al., 2013). Essentially, high (low) eccentricity amplifies (modulates) the precession parameter and increases (decreases) insolation levels during boreal summer; higher insolation is thought to increase latitudinal and land–sea temperature gradients, evaporation, monsoon circulation, and convection (Ruddiman, 2008). Chandan and Peltier (2020) also show that insolation in combination with vegetation, soil, and lake feedbacks are necessary to achieve and sustain significant increasing in precipitation. Our study provides a new understanding of how grass community composition and fire regimes within the Turkana Basin have responded to changes in Earth's orbital parameters.

MATERIALS AND METHODS

Drill Core Extraction and Chronology

A single borehole, deviated 10° from vertical, was cored to a depth of ~216 m in West Turkana (4°6′34.92″ N, 35°52′18.48″ E) in June–July 2013 (**Figure 1**). The drill site was chosen for its proximity to outcrop exposures of the correlative type sections of the Kaitio and Natoo members of the Nachukui Formation, which are locally dipping at ~5° W (Harris et al., 1988). The stratigraphy records deposition on a dynamic lacustrine margin which experienced repeated transgressive and regressive events (Beck, 2015). Borehole instability and/or high-pressure

TABLE 1 | Modern Lake Turkana sediment sample characteristics.

Sample	Depth (m)	Distance from eastern shore (km)	Distance from western shore (km)	Grain size classification	Hydrochloric acid reaction	Sediment zone interpretation
22	2	0.15	37.5	Sandy silt	Weak	Littoral
21	2	0.45	37.2	Sandy silt	Strong	Littoral
24	20	3.43	28.3	Silty clay	None	Offshore
33	28	6.43	26.3	Silty clay	None	Offshore
25	30	7.57	25.6	Silty clay	Strong	Offshore
32	32	9.77	23.0	Silty clay	None	Offshore
26	25	11.11	21.7	Sandy silt	None	Offshore
31	35	13.82	19.4	Silty clay	None	Offshore
27	38	15.69	17.6	Silty clay	None	Offshore

groundwater resulted in high torque and required the termination of drilling operations at the maximum depth. The WTK13 core was shipped via airfreight to LacCore, the National Lacustrine Core Facility (University of Minnesota, United States) for full scanning, processing, description, and subsampling. Full coring details and initial core descriptions are presented in Cohen et al. (2016). An age model (**Supplementary Figure S1**) was developed by Lupien et al. (2018) using tephra correlation, direct $^{40}Ar/^{39}Ar$ dating of a new tephra, and a paleomagnetic reversal (Sier et al., 2017). Core depths are reported in meters below surface (mbs), and core lithology is provided in **Supplementary Figure S2**.

Lake Turkana Modern Sediment Transect

Modern sediment samples from Lake Turkana were collected by A. Cohen in 1978–1979 using an Ekman dredge. Nine of these samples extending along a NW-SE transect from offshore of Koobi Fora (East Turkana) to North Island were subsampled for phytolith and microcharcoal analysis (**Figure 1C**). Distance from the eastern shoreline for the selected samples ranged from 0.15 to 15.7 km. Sample distances from the leading edge of the modern Omo River delta plain average around 60 km for most (**Figure 1**), but the delta plain has advanced ~20 km southward since 1975 (see Carr, 2017). Straight-line distances from the eastern and western shorelines, grain size classifications, and lake depths were recorded for each sample (**Table 1**). Sample mass and volume are provided in **Supplementary Material S1**.

Modern Vegetation and Phytoscape

Plant species occurrence data were aggregated from Olang (1984), Carr (2017), and Mbaluka and Brown (2016) for West Turkana (WTK), the Lower Omo River Valley (LOR), and Koobi Fora (East Turkana; ETK), respectively (**Supplementary Table S1**). Boundaries for these three floristic study areas are depicted in **Figure 1B**. Emphasis was placed on grasses because of their prolific phytolith production and taxonomic distinctiveness. For each species of grass, dominant phytolith morphotype production was determined from published accounts or lead author Yost's phytolith reference collection (**Supplementary Table S1**). Grass species occurrence and the relative abundance of lobates (bilobates and crosses), rondel, and saddle phytoliths produced by those species were used to identify a grass short-cell phytoscape signature for each of the three floristic study areas.

The plant species occurrence data for LOR and ETK were also compared to a compilation of woody plants in Africa known to produce phytoliths to determine the potential for LOR and ETK to produce an arboreal phytoscape signal (**Supplementary Tables S2, S3**). Samples from the modern Lake Turkana sediment transect were then compared to the phytoscape signatures to determine how distance from shore and proximity to the Omo River sediment plume affected the phytolith record.

Microfossil Separations, Microscopy, and Classification

The samples for phytolith and microcharcoal analyses were collected at 32 cm intervals along the entire 215.8 m core by removing 1 cm^3 of sediment. Samples for microfossil extraction were selected at 96 cm intervals (206 samples) for a coarse resolution analysis to assess biogenic silica preservation. Additional samples at 32 cm intervals were then selected for extraction from the intervals with good biogenic silica preservation, yielding a total of 287 paleolake samples and 9 modern lake samples for analysis. Phytoliths and microcharcoal particles were co-extracted using the wet oxidation and heavy-liquid density separation method described by Yost et al. (2021). Synthetic microspheres were added to each sample in order to calculate concentrations; the number added varying by the amount of extracted residue (**Supplementary Materials S1, S2**).

For microscopy, entire samples or subsamples of the extract were mounted on slides using Type-A immersion oil and the cover glass was sealed with fingernail polish. Mounting in immersion oil allows for easy phytolith rotation when pressure is applied to the cover glass. This rotation is essential for many phytolith identifications and for differentiation between Arecaceae globular echinate phytoliths and freshwater sponge spherasters (Yost et al., 2021). Phytolith and microcharcoal counting was conducted using an Olympus BX-43 transmitted-light microscope at 400× magnification, with a goal of counting 200 Iph and D/P° index-specific phytoliths to minimize statistical uncertainties (Strömberg, 2009).

Phytoliths were classified into 41 morphotypes (**Supplementary Materials S1, S2**). Primary descriptive references, anatomical origin, and taxonomical interpretation for each morphotype are described in Yost et al. (2021). Bilobates and crosses in this study were not classified into the Neumann super types as Yost et al. (2021) had done for the paleo-Lake Baringo core (BTB13) because most of the samples from

this core had been counted before classifying the BTB13 samples. Each broken bilobate phytolith counted was given a value of 0.5.

Microcharcoal was identified (absolute counts) using the diagnostic characteristics described by Turner et al. (2008), with particular emphasis on avoiding misidentifications of pyrite and naturally-darkened unburned plant fragments as charcoal. Two microcharcoal size classes (<50 μm and >50 μm) were originally tallied, but later combined for change point and spectral analyses because of the intermittent occurrence and low abundance of the larger size class. Sponge spicules, sponge spherasters, and chrysophycean cysts were also identified and counted. Detailed descriptions of these microfossils can be found in Yost et al. (2021).

Phytolith dissolution, which can affect preservation and result in morphotype assemblage bias, was determined based on i) the presence of zeolites and evaporites in the phytolith extracts (especially when no phytoliths were observed), and ii) the presence of pits, breakage, and re-precipitation of silica on phytolith, diatom, and sponge spicule surfaces. The biogenic silica dissolution sequence described by Yost et al. (2021) for alternating high and low pore water pH was also used as a dissolution indicator.

Numerical Calculations, Statistics, and Time-Series Analysis

Relative-abundance percentages were based on the total phytolith count for each sample. Concentrations were calculated from the microsphere counts and starting volume of the sample (**Supplementary Materials S1, S2**). Relative abundance determinations of C_3, C_4 mesic, and C_4 xeric grass phytoliths were based only on grass silica short-cell (GSSC) phytoliths attributed to those plant functional types (per Yost et al., 2021). The tree cover index (D/P°), used to discriminate between open (shrubland to wooded grassland, 0–40% canopy cover), woodland (40–80% canopy cover), and forest (80–100% canopy cover) formations, and the aridity (Iph) phytolith index, used to discriminate short-grass xerophytic (Sahelian) savanna from tall-grass mesophytic (Sudanian) savanna were calculated as described in Bremond et al. (2008) and Novello et al. (2017) using the specific morphotypes listed in Yost et al. (2021). The 95% confidence intervals for the D/P° and Iph indices were determined by nonparametric bootstrap resampling using the "boot" and "simpleboot" packages in R (R Core Team, 2018) and the R code in Yost et al. (2021). The rolling Spearman correlation was conducted using the R package "RollWinMulCor" (Polanco-Martínez, 2020). Prior to correlation analysis, δD_{wax} and microcharcoal concentrations were converted to z-scores and interpolated to 3,100-yr time steps. For spectral analysis, the periodogram and bivariate cross-wavelet power spectrum were produced using the R packages "astrochron" (Meyers, 2014) and "WaveletComp" (Roesch and Schmidbauer, 2018), respectively. Prior to the spectral analyses, microcharcoal concentrations were log transformed, detrended, and linearly interpolated to a 3,100-yr time-step. All other descriptive, regression, and correlation statistics were conducted in R.

Zonation of the WTK13 Core

The phytolith record could not be used to develop a zonation because dissolution throughout most of the core biased phytolith assemblages and negatively affected phytolith preservation and concentrations. Microcharcoal concentrations provided a continuous record and zone boundaries were identified from the change point analysis of log transformed microcharcoal concentrations using the R package "ecp". (James and Matteson, 2014). The E-Divisive method from the ecp package is a nonparametric procedure that is able to estimate multiple change point locations that are statistically significant (set at 0.05) without *a priori* knowledge of the number of change points. This iterative process analyzes changes in both slope (trend) and mean.

RESULTS

Modern Grass Occurrence and Phytoscape

A total of 80 grass species from 38 genera occurred within the modern WTK, LOR, and ETK floristic areas (**Supplementary Table S1**). Highest species richness was found for *Sporobolus* (10 species), followed by *Enneapogon* (5), *Eragrostis* (5), *Panicum* (5), and *Dactyloctenium* (4). The only C_3 grass was *Phragmites* (common reed), an obligate wetland plant. At the subfamily level, 40 species (51%) were Chloridoideae, 34 (43%) were Panicoideae, and 4 (5%) were Aristidoideae (**Table 2**). Only one Arundinoideae grass (*Phragmites*) was noted, and in being a C_3 obligate wetland grass was predictably from the LOR area. No taxa from the C_3 grass subfamily Pooideae were listed in any of the study regions. Chloridoideae grasses, which are typically arid-adapted and drought tolerant, were most common in ETK and WTK (55–60%), and less common in LOR (48%), although a χ^2 contingency test shows these differences are not statistically significant. Panicoideae taxa, which typically thrive under more humid and mesic conditions, were most common for LOR (41%) and less common in ETK and WTK (20–30%).

Regarding phytolith morphotype production, lobates were slightly more common in LOR grasses (61%), versus 59 and 53% for ETK and WTK grasses, respectively. Saddles were generally more common for ETK grasses (29%) and WTK grasses (35%) than for LOR grasses (22%). Rondels were slightly more represented in LOR grasses (18%), than for ETK (13%), and WTK (12%) grasses. Overall, the GSSC phytoscapes for LOR, ETK, and WTK were strikingly similar. Calculated Iph aridity index values based simply on the dominance of either lobates or saddles for the most commonly listed grasses were 36% (LOR), 36% (ETK), and 40% (WTK).

For woody plant phytolith production, LOR and ETK had nine and six species respectively, in genera known to produce globular granulate phytoliths. Additionally, both LOR and ETK had two woody species known to produce other types of woody tissue phytoliths. Although these numbers are similar, the ETK study area is only 0.3% woodland, and 0.1% forest (Mbaluka and Brown, 2016). Vegetation cover was not mentioned by Carr (1998) at LOR, but our GIS-based estimates from their maps put woodland and forest cover at ~ 7 and 16%, respectively.

Modern Lake Turkana Sediments

Microcharcoal was observed in all samples. Concentrations ranged from 676 to 5.14×10^4 cm^{-3} (**Figure 2A**). Concentrations

TABLE 2 | Grass subfamily occurrence based on Lower Omo River Valley[a], East Turkana[b] and West Turkana[c] floristic studies, and potential dominant phytolith morphotypes.

	Lower Omo River		East Turkana		West Turkana	Species from all areas combined
	Species (all)	Species (common)	Species (all)	Species (common)	Species (common)	
Subfamily						
Panicoideae	19 (41%)	4 (25%)	20 (38%)	4 (31%)	5 (33%)	34 (43%)
Chloridoideae	22 (48%)	8 (50%)	29 (55%)	7 (54%)	9 (60%)	40 (51%)
Aristidoideae	4 (9%)	3 (19%)	4 (8%)	2 (15%)	1 (7%)	4 (5%)
Arundinoideae	1 (2%)	1 (6%)	—	—	—	1 (1%)
Total	46	16	53	13	15	79
Dominant morphotypes[d]						
Lobates	31 (61%)	9 (53%)	33 (59%)	9 (56%)	9 (53%)	55 (61%)
Rondels	9 (18%)	3 (18%)	7 (13%)	2 (13%)	2 (12%)	14 (16%)
Saddles	11 (22%)	5 (29%)	16 (29%)	5 (31%)	6 (35%)	21 (23%)
Total	51	17	56	16	17	90
Iph_{plant}		36%		36%	40%	

[a]*Carr (2017).*
[b]*Mbaluka and Brown (2016).*
[c]*Olang (1984).*
[d]***Supplementary Table S1.***

decreased exponentially (r^2 = 0.72, p = 0.01) with increasing distance from shoreline, becoming asymptotic at concentrations <10,000 cm^{-3} and distances >6 km. Sponge spicules and spherasters were typically most abundant within 6.5 km of the shoreline, and single occurrences of chrysophyte cysts were observed in two samples (**Supplementary Figure S3**). Phytolith preservation was good, with low to moderate dissolution on phytolith surfaces. Phytolith concentrations ranged from 38 to 1.65×10^5 cm^{-3} (**Figure 2B**), and decreased linearly (r^2 = 0.54, p = 0.04) with increasing distance from shoreline. An extreme outlier value (sample 27) was removed prior to the regression analysis (a possible reason for this outlier value is discussed in *Phytolith and Microcharcoal Deposition in the Modern Lake System*). The Iph aridity index also decreased linearly (r^2 = 0.45, p = 0.05) as distance from shoreline increased (**Figure 2E**). With one exception, the D/Po tree cover index was low and did not vary with distance from shoreline. The exception was Sample 25, which yielded a D/P° value of 1.22, which is within the range of savanna woodlands (**Figure 2F**; **Supplementary Material S1**). The percentage of broken bilobate phytoliths increased linearly with increasing distance from shoreline (**Figure 2G**; r^2 = 0.61, p = 0.01). The average abundance of broken phytolith samples collected between 0.2 and 0.5 km offshore was 57 ± 10% (n = 2), whereas the average value for samples 3–16 km offshore was 73 ± 4% (n = 7). The relative abundance of large phytoliths (bulliforms and trichomes) decreased linearly (r^2 = 0.80, p = 0.001), whereas that of small GSSC phytoliths increased linearly (r^2 = 0.41, p = 0.07) as distance from shoreline increased (**Figures 2C,D**).

Using results of the modern vegetation study compilation and the recovery of phytoliths diagnostic of plants found only above ~1,500 m (Podostemaceae) and ~2000 m (C_3 Pooideae grasses) in the modern and paleolake samples, we created a new index called the upper Omo River watershed source area index (I_{Omo}; **Table 3**). The I_{Omo} index is calculated by dividing the sum of phytoliths derived from plants found in the upper Omo River watershed by the total sum of phytoliths counted. The I_{Omo} scatter plot shows a trend of increasing index values with increasing distance from shore (**Figure 2H**), but the relationship was not statistically significant, in part, because Sample 25 had an I_{Omo} index value of zero; with exclusion of sample 25, a moderately significant linear relationship emerges (r^2 = 0.44, p = 0.07). Regardless, the index has promise, as later discussed in Section 5.2.

Paleo-Lake Lorenyang (WTK13) Samples

Phytolith preservation and recovery in WTK13 varied from excellent to poor, with extensive intervals yielding few to no phytoliths, most likely the result of biogenic silica dissolution (**Figure 3**; **Supplementary Material S2**). Of the 287 WTK13 samples analyzed, 29 (10%) yielded no phytoliths. The majority of samples, 119 (41%), yielded phytoliths, but the counts (concentrations) were either very low, or the phytolith assemblages were likely biased from dissolution, which precluded reliable and robust index calculations. However, 90 samples (31%) occurring in four discreet intervals (**Figure 3B**), yielded well-preserved phytoliths with no evidence of morphotype assemblage bias. Among these, phytolith counts ranged from 0 to 10,326 ($\bar{x}$ = 528), and phytolith concentrations ranged from 0 to 1.2×10^5 cm^{-3} ($\bar{x}$ = 5.3×10^5 cm^{-3}). Microcharcoal was recovered in all samples. Of the two size classes counted, charcoal particles >50 μm were rarely observed, so both size classes were combined for concentration calculations, which ranged from 100 to 1.95×10^6 cm^{-3} ($\bar{x}$ = 35,795 cm^{-3}).

Correlation and Spectral Analyses

Spectral analysis of microcharcoal concentrations at 3,100-yr time steps detected precessional periodicities of 21.3 and 19.6 kyr with power above the 95% confidence level (**Figure 4**). Cross-wavelet analysis between δD_{wax} and microcharcoal concentrations identified several intervals with high common power (variability at same statistically significant

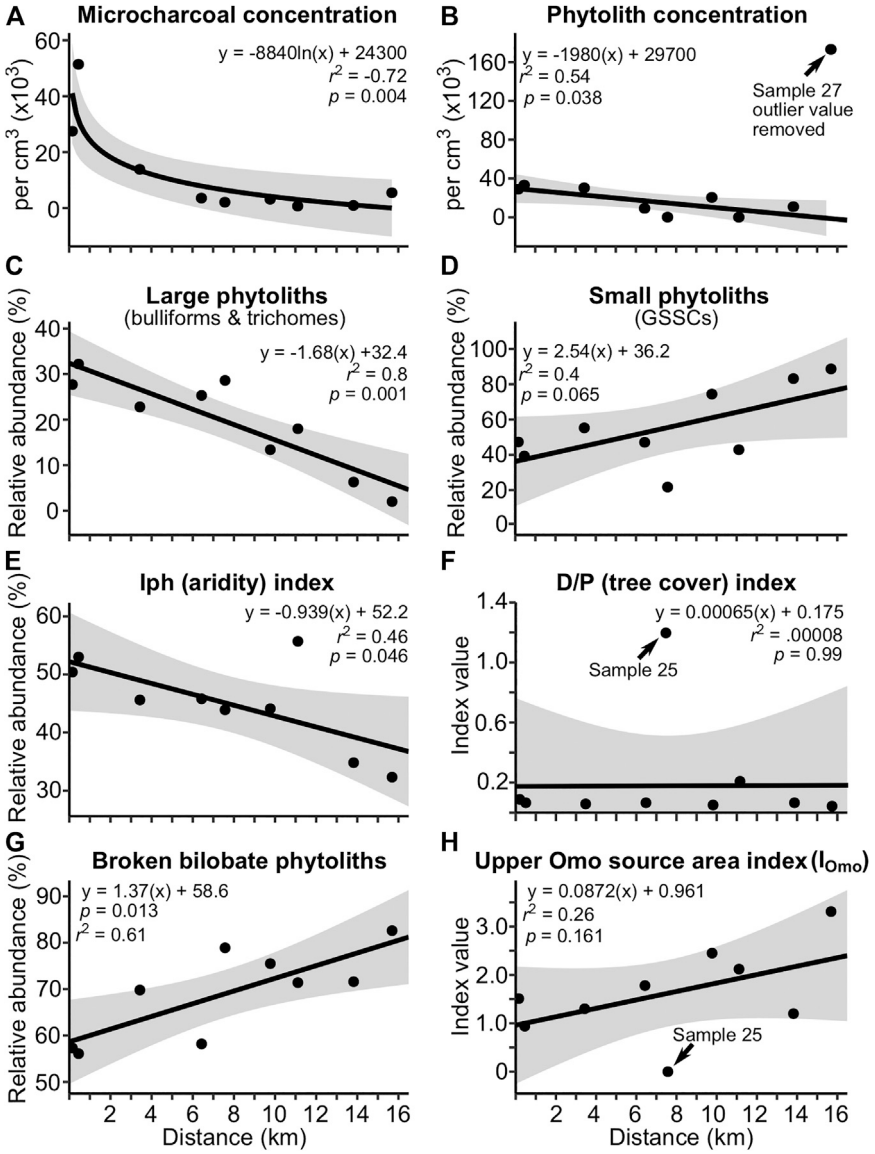

FIGURE 2 | Relationship between distance from shoreline and the relative abundance of selected phytolith and microcharcoal constituents of modern Lake Turkana sediment samples. Shaded regions represent regression 95% confidence intervals. Sample location numbers for points on the graphs are (left to right): 22, 21, 24, 33, 25, 32, 26, 31, and 27, respectively. As distance from shoreline increases, exposure to the Omo River sediment plume and proximity to the north basin gyre increases, but distance to the mouth of the Omo River does not appreciably change (see **Figure 1D**). **(A)** Microcharcoal concentrations decrease exponentially as distance from shoreline increases. **(B)** Phytolith concentrations decrease linearly as distance from shoreline increases. **(C)** Large-sized phytoliths decrease and **(D)** small-sized phytoliths increase as distance from shoreline increases. **(E)** The grass-based Iph (aridity) index decreases as distance from shoreline increases, presumably from the presence of phytoliths derived from the Omo River Valley. **(F)** The D/P° tree cover index shows no relationship with distance from shoreline, presumably because phytolith-rich grasses are much more abundant than trees that produce phytoliths in both the Turkana Basin and Omo River Valley. **(G)** Broken bilobates increase as distance from shoreline increases, presumably because they are smaller, but also because some proportion may have been transported long-distance from the Omo River Valley. **(H)** Phytoliths derived from plants sourced to the Omo River Valley increase as distance from shoreline increases. See **Table 3** for details on the I_{Omo} index.

periodicity) over orbital and non-orbital periodicities (**Figures 5B,D**), including three intervals near and within the precession band (19–23 kyr). A large interval of high common power spans 1.75 to 1.66 Ma over periodicities *between* 23 and 41 kyr (centered on ~33 kyr), and another interval is found from 1.84 to 1.70 Ma along a narrow periodicity band centered on 78 kyr. Almost all of the high common power areas indicate anti-phasing (anticorrelation), where more positive δD_{wax} values are correlated with lower microcharcoal concentrations. The high common power area centered on 78 kyr shows δD_{wax} consistently leading microcharcoal concentrations by about 10 kyr.

The rolling Spearman correlation analysis identified several intervals with strong negative correlations between δD_{wax} values

TABLE 3 | Microfossils recovered from WTK13 and most likely derived from the lower and upper reaches of the Omo River based on modern plant and algae distributions.

	Taxonomy and carbon fixation pathway	Lower Omo River[a]	Ethiopian Highlands/Upper Omo River[a]	Used in Upper Omo source area index[b]
Phytolith morphotype				
Trapeziform sinuate	C_3, Pooideae (grass)		X	X
Rondel-keeled	C_3, Pooideae (grass)		X	X
Rondel-angular keel	C_3, Pooideae (*Phalaris*)		X	X
Very tall saddle	C_3, Bambusoideae (grass)		X	X
Bilobate-scooped ends	C_3, Ehrhartoideae (grass)		X	X
Perforate decorated	C_3, Podostemaceae (*Tristicha*)		X	X
Conical echinate	C_3, Orchidaceae		X	X
Conical truncated	C_3, Commelinaceae (*Murdannia* and *Floscopa*)		X	X
Plateaued saddle	C_3, Arundinoideae (*Phragmites*)	X	X	
Prismatic domed cylinder	C_3, Commelinaceae (*Commelina*)	X	X	
Other microfossils				
Chrysophyte stomatocysts[3]	Chrysophyceae (golden algae)		X	

[a]*Modern plant distributions from Carr (2017) and GBIF (2019).*
[b]I_{Omo} *index (%) = Total phytoliths sourced from Upper Omo River/Total phytolith count.*
[c]*Chrysophyte distributions from Kebede and Belay (1994) and Kebede and Willen (1998).*

and microcharcoal concentrations at $p \leq 0.10$ and $p \leq 0.05$ significance levels (**Figure 5C**). The longest such interval spans from 1.74 to 1.65 Ma, followed by strong but intermittent correlations between 1.59 and 1.52 Ma.

Change Point Analysis and Zonation

Change point analysis of the log-transformed microcharcoal concentration record identified seven change points at the 0.05 significance level that were subsequently used as zone boundaries for eight zones (**Supplementary Figure S4**). A horizontal reference line set at a microcharcoal concentration of 5,000 cm^{-3} was used in **Figure 3D** to visually highlight the zonal changes in concentrations. These zones correspond well with major changes in phytolith preservation and some distinct lithological transitions. Results by zone are discussed next.

Zone 1 (1.868–1.855 Ma; 215.56–206.77 mbs)

Zone 1 was characterized by high charcoal concentrations (3 × mean) and very poor biogenic silica (BSi) preservation. Phytoliths and sponge spicules were rare and often appeared severely pitted and/or dissolved when present. Diatom concentrations were relatively high (~1.85×10^7 cm^{-3}) and appeared to be mostly *Aulacoseira* spp.; however, they were severely altered. Silica replacement or reprecipitation rather than simple dissolution, (e.g., Yost et al., 2021) appeared to be the main mode of alteration.

Zone 2 (1.855–1.774 Ma; 206.77–150.62 mbs)

Zone 2 was characterized by very low microcharcoal concentrations (~14% of the mean), and extremely low phytolith concentrations (~0.03% of the mean; 142 phytoliths per cm^3). There was partial to total BSi dissolution in many of the samples (**Supplementary Figure S4**), likely the result of high pore water or lake water pH. Phytolith samples were too poorly preserved to reliably report morphotype relative abundances. The occurrence of sandy sediments in the lower third of the zone was also notable (**Figure 3G**).

Zone 3 (1.774–1.728 Ma; 150.62–135.44 mbs)

Of all the zones from WTK13, Zone 3 was characterized by having the lowest microcharcoal concentrations (4% of the mean) and the lowest phytolith concentrations (~0.004% of the mean; 21 phytoliths per cm^3). Like the previous zone, there was partial to total BSi dissolution in many of the samples, and the phytolith record was too poorly preserved to reliably report morphotype relative abundances. In addition, the highest δD_{wax} values (higher values indicate lower precipitation) from the entire WTK13 core were obtained from this zone, which also had the highest average δD_{wax} values of any zone (**Supplementary Table S4**). The lowest microcharcoal and phytolith concentrations and the highest δD_{wax} values are centered around 1.74 Ma.

Zone 4 (1.728–1.582 Ma; 135.44–86.87 mbs)

Zone 4 was characterized by high microcharcoal variability, with peaks and troughs alternating between 4 × above and 112 × below the mean (**Figure 3**). The rolling Spearman correlation analysis detected negative correlations at $p \leq 0.05$ between δD_{wax} values and microcharcoal concentrations in the lower half of the zone (**Figure 5C**). The cross-wavelet spectral analysis detected this same anticorrelation throughout the zone at periodicities ranging between obliquity (41 kyr) and precession (23–19 kyr) but centered on 33 kyr (**Figure 5D**) Phytolith concentrations were higher than those in the lower zones, but morphotype preservation bias was evident in most samples (**Supplementary Figure S4**). However, two short intervals centered at 1.651 Ma (109.93 mbs) and 1.607 Ma (97.98 mbs) exhibited good to excellent phytolith preservation. These two phytolith preservation intervals may coincide with the two precession peaks identified in **Figure 6A**. Iph aridity index values for these two intervals were >27.8%, and D/P° tree cover index values were <1.0 (**Figures 6B,C**), suggesting xeric short-grass (Chloridoideae) grassland or open savanna characterized the Turkana Basin at this time.

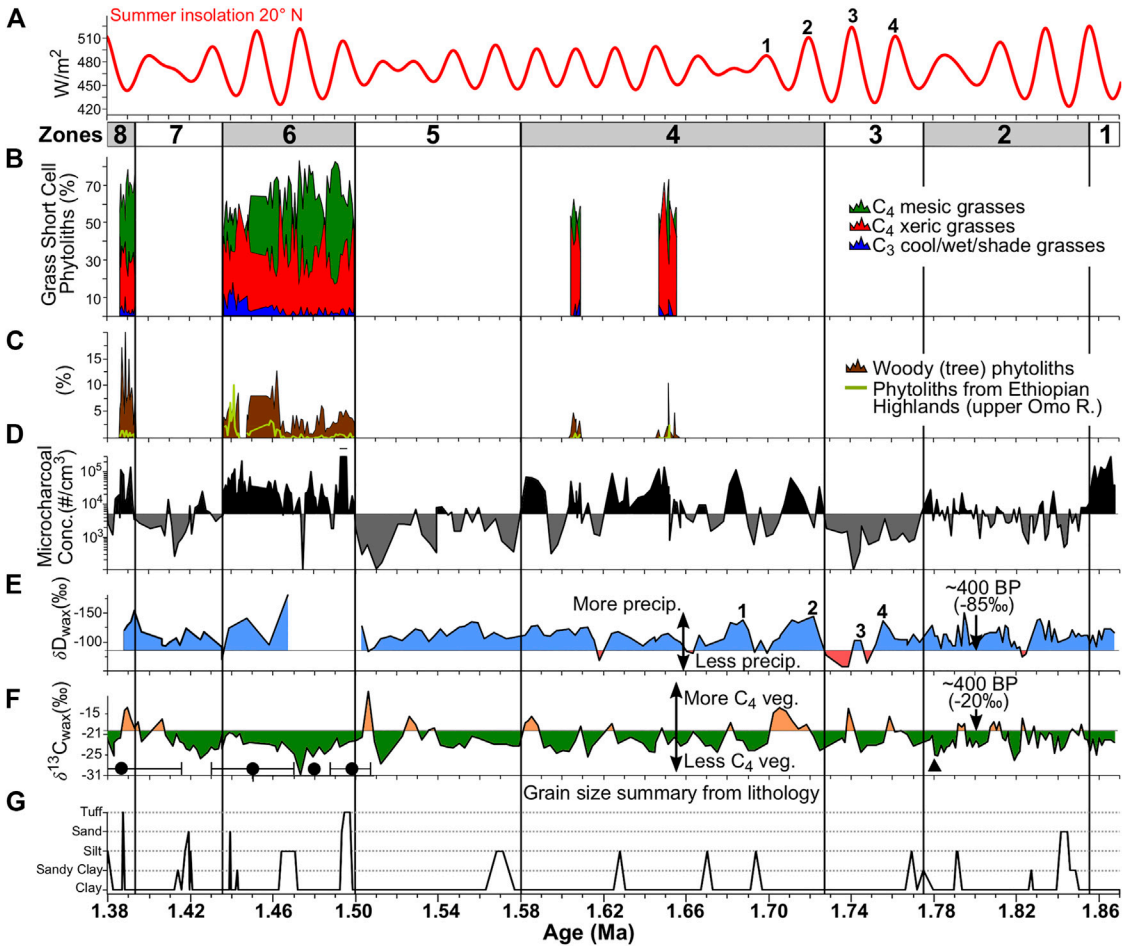

FIGURE 3 | Summary phytolith and microcharcoal datasets (this study) and leaf wax $\delta^{13}C$ and δD datasets (Lupien et al., 2018) from WTK13. **(A)** Summer 20° N insolation from Laskar et al. (2004). The numbered insolation peaks were tied to corresponding peaks in depleted δD_{wax} values depicted here in panel E by Lupien et al. (2018). **(B)** C_3 and C_4 grass relative abundance derived from grass short-cell phytoliths. **(C)** Tree/shrub phytoliths relative to total phytolith sum, and the I_{Omo} index indicating relative abundance of phytoliths sourced from the Ethiopian Highlands (**Table 2**). **(D)** Microcharcoal concentrations (log scale) with horizontal reference line at 5,000 cm^{-3} to highlight the zonal changes. **(E, F)** δD_{wax} and $\delta 13C_{wax}$ values from (Lupien et al., 2018), with horizontal reference lines set at the late Holocene δD_{wax} and $\delta^{13}C_{wax}$ values for Lake Turkana from Morrissey (2014). Black circles (tephrocorrelations and $^{40}Ar/^{39}Ar$ dating) and the black triangle (magnetic reversal) represent chronostratigraphic control points used in the age model. **(G)** Grain size summarized from the WTK lithological core description (see SOM **Figure 2**).

Concomitant microcharcoal peaks with the phytolith intervals suggest grass densities were sufficient to support frequent fires.

Zone 5 (1.582–1.50 Ma; 86.87–59.42 mbs)

Zone 5 was characterized by consistently low microcharcoal concentrations that averaged ~8% of the mean, and poor phytolith preservation. Spearman correlation analysis detected negative correlations at $p \leq 0.05$ between δD_{wax} values and microcharcoal concentrations throughout much of the zone (**Figure 5C**). Phytolith morphotype preservation bias was evident throughout, and low GSSC recovery precluded aridity and tree cover index calculations. Authigenic silicates, many of which resembled phillipsite, were observed in 5% of the samples. However, at 1.556 Ma (between 78.25 and 77.27 mbs), sponge spicule concentrations were an order of magnitude above any other occurrence within the zone (**Figure 7**; **Supplementary Material S2**). All of the spicules retained their original shape, but their silica appears to have been reprecipitated or devitrified, as has been observed in some spicules from Plio-Pleistocene Lake Baringo (see Figure 5 from Yost et al., 2021).

Zone 6 (1.50–1.436 Ma; 59.42–36.83 mbs)

Zone 6 had the longest interval with good to excellent BSi preservation, and it had the highest average phytolith and microcharcoal concentrations for the core. Of all zones, Zone 6 had the second lowest average δD_{wax} value (−133.3‰; **Supplementary Table S4**). Iph aridity index values often exceeded the 27.8% threshold separating mesic tall-grass Sudanian savanna from xeric short-grass Sahelian savanna (Novello et al., 2017). Although there was considerable uncertainty in the tephra ages from this zone used in the age model (Lupien et al., 2018), the mesic C_4 tall-grass peaks may coincide with precession-scale insolation peaks (**Figures 6A,B**). D/P° aridity index values were typically well below the 1.0 threshold that

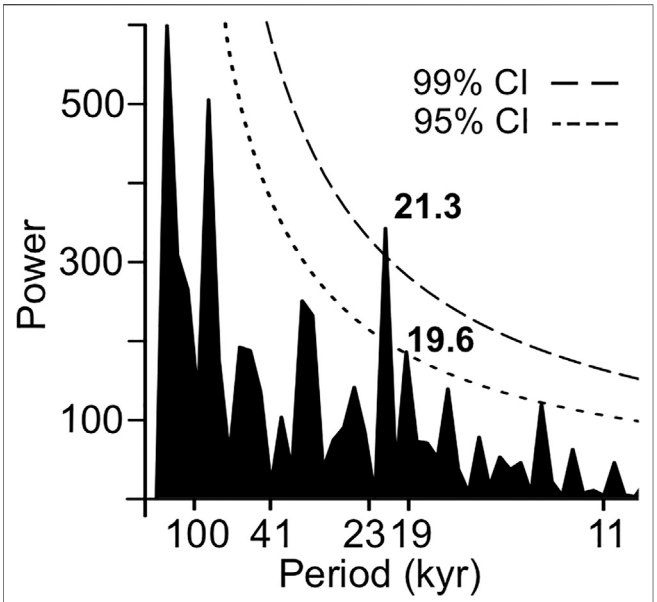

FIGURE 4 | Spectral analysis of microcharcoal concentrations. Periodicities >5 × the 3,100-yr time step with power above the 95 and 99% confidence levels are labeled on the periodogram.

identify woodlands with >40% canopy cover (Yost et al., 2021; **Figure 6C**). This zone marked the first appearance of phytoliths diagnostic of the aquatic riverweed family (Podostemaceae; da Costa et al., 2018; **Figure 8E**). Numerous phytoliths from at least two species of dayflower (*Commelina* spp.; Eichhorn et al., 2010) were also observed. Sponge spicules reached their highest concentrations here, and intervals with high sponge abundances appear to correspond with intervals of low insolation (**Figure 8I**). Phytoliths derived from plants that are found today above 1,500–2,000 m elevation (**Table 3**), including phytoliths from the C_3 Pooideae grass subfamily, abruptly increased in abundance in the upper half of the zone (**Figure 8F**). There was one interval between 43.69 and 42.06 mbs (~1.446 Ma) where all phytoliths were poorly preserved and the phytolith extracts were dominated by authigenic silicates, most likely phillipsite.

Zone 7 (1.436–1.393 Ma; 36.83–11.40 mbs)

Zone 7 was characterized by relatively low microcharcoal concentrations and poor BSi preservation. Phytolith concentrations were three orders of magnitude below the mean, and low GSSC recovery precluded aridity and tree cover index calculations. The longest core interval with no sediment recovery occurred between ~19.1 and 13.5 mbs (~1.40 Ma), in the upper portion of this zone.

Zone 8 (1.393–1.379 Ma; 11.40–3.33 mbs)

Zone 8 was characterized by excellent phytolith preservation and high phytolith concentrations, except between 7.47 and 3.33 mbs, where phytolith preservation was poor. In this uppermost interval, authigenic silicates dominated the phytolith extracts and dissolution was likely responsible for low phytolith recovery. For the interval with well-preserved phytoliths between 1.393 and 1.386 Ma (11.40 and 7.47 mbs), phytoliths from woody trees and shrubs were at their highest levels of relative abundance for the core (**Figures 3C**, **7**). The sample from 9.07 mbs (1.39 Ma) yielded a D/P° index value of 1.06 (**Figure 6C**), indicating canopy cover ≥40%. However, samples immediately above and below had very low D/P° values suggesting a relatively short-lived (<1 kyr) riparian woodland episode. The Iph index tracks a change from mesic tall-grass dominance to xeric short-grass dominance, and this switch also takes place at 9.07 mbs. Lastly, Zone 8 had the lowest average δD_{wax} value (−134.8‰; **Supplementary Table S4**).

DISCUSSION

Modern Turkana Basin Phytoscape

Determining potential phytolith production at the landscape level (*phytoscape*) is an important step in understanding how terrestrial vegetation signals are integrated into lake sediments. Ideally this would be accomplished by sampling plants and modern soils within a lake basin watershed. Because that option was not available, we used a proxy approach based on species lists from local floristic surveys in concert with phytolith composition data for those species to determine a potential grass silica short-cell (GSSC) phytoscape signal for portions of the watershed closest to the modern lake. Results of this literature-based grass phytoscape analysis found there was no appreciable difference between the Lower Omo River Valley (LOR), East Turkana (ETK) and West Turkana (WTK) areas when considering the most common grasses, as the relative abundances of grasses dominated by either lobate, rondel, or saddle phytoliths were nearly identical (**Table 2**). Accordingly, changes in the Iph aridity index should reflect change in the hydroclimate and grass community composition rather than changes in local sediment source areas.

Results of the arboreal phytoscape analysis indicates that source area could have an influence on the D/P° tree cover index, as nine woody taxa from the LOR but only six from ETK are known to produce globular granulate phytoliths. However, phytolith production based on biomass would be a better determinant than the number of species. Perhaps more important is the fact that woodlands and forests in ETK make up < 1% of total land cover, as opposed to ~20% for the LOR. Details on woody cover were not provided in the floristic surveys of WTK, but based on similarities in the climate regime are assumed to be similar to ETK.

The literature-based phytoscape study demonstrates that despite xeric C_4 Chloridoideae taxa representing 51% of all grass taxa listed for LOR, ETK, and WTK, saddle phytoliths were the dominant morphotype in only 23% of all grass species listed. This, in part, reflects the fact that xeric C_4 *Aristida* spp. (Aristidoideae), which produce bilobates, were very common in all of the surveyed areas. Also, some of the most common Chloridoideae grasses in the Turkana basin, such as *Sporobolus* and *Enneapogon*, typically produce lobate and rondel instead of saddle phytoliths (**Supplementary Table S1**; **Supplementary Figure S5**). The implication is that if the Iph index is calibrated in habitats with low or no occurrences of bilobate-producing xeric C_4 grasses (e.g., *Aristida* and *Sporobolus* spp.), the Iph aridity index could underestimate aridity and xeric C_4 grass abundance in habitats that do contain those grasses since bilobates are often associated with mesic C_4 grasses. However, because *Aristida* and *Sporobolus* are

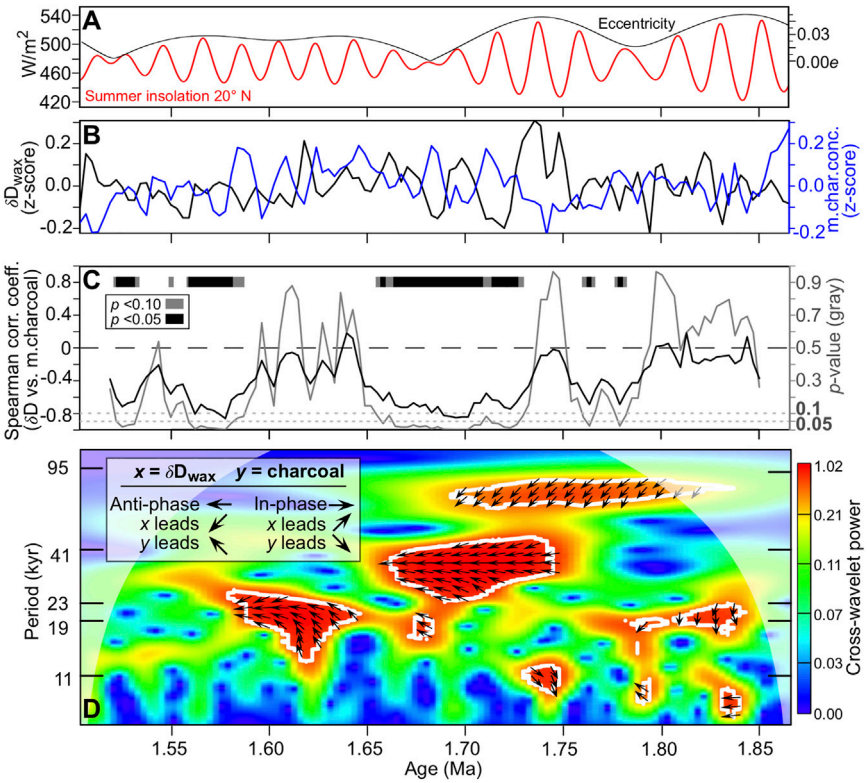

FIGURE 5 | Correlations between WTK13 core leaf wax δD (precipitation) and microcharcoal (fire) records between 1.866 and 1.503 Ma. This analysis was not extended to the top of the core at 1.379 Ma because of a ~30 kyr gap in the δD record. **(A)** Summer insolation for 20° N plotted with orbital eccentricity (Laskar et al., 2004). **(B)** Microcharcoal concentrations (this study) and δD_{wax} (Lupien et al., 2018) z-scores after interpolating each record at 3100-yr time steps. Higher δD_{wax} values signify lower precipitation while higher microcharcoal values signify higher fire frequency and/or intensity. **(C)** Rolling Spearman correlations between the δD_{wax} and microcharcoal records. Correlation coefficients (black line) and their respective *p* values (gray line) were calculated using a 34,100-yr moving window. The gray and black bars represent intervals with strong negative correlations at the $p \leq 0.10$ and $p \leq 0.05$ levels, respectively. **(D)** Evolutive (periodicity through time) cross-wavelet correlations and phasing between the δD_{wax} and microcharcoal records. Warmer colors signify higher spectral density, and white contours with internal phase paths signify $p = 0.05$ confidence levels. Cone of influence (boundary effects) marked with white transparent shading.

common in the Lake Chad Basin, the Iph index developed by Novello et al. (2017) is considered accurate for the Turkana Basin.

Phytolith and Microcharcoal Deposition in the Modern Lake System

Natural fires in the Turkana Basin are rare today because plant cover and density are generally too low to carry fire. The exception is in grassy riparian corridors or higher elevation areas with a continuous grass layer where pastoralists have been known to intentionally set fires (Coughenour and Ellis, 1993). Intentional fire use by pastoralists has also been observed within the LOR during the dry seasons (Carr, 2017). The abundance of wind-dispersed charcoal particulates typically decays nonlinearly from the point source (Clark, 1988; Lynch et al., 2004; Peters and Higuera, 2007). Considering the prevailing winds out of the southeast and the active use of the Koobi Fora Base Camp by researchers and support staff at the time of sample collection, the exponential decrease in microcharcoal concentrations suggests that the point source may have been close to the eastern edge of the lake and possibly related to human activities. Challenges in interpreting charcoal from paleolake sediments are discussed in *Paleo-Lake Lorenyang Phytoliths and Microcharcoal*.

The linear decrease in phytolith concentrations and large-sized phytoliths in the lake sediments with increasing distance from shoreline (**Figures 2B,C**) is likely a function of eolian transport from the east side of the lake (ETK) by the prevailing southeasterly winds (**Figure 1D**). In contrast, Iph aridity index values decreased as distance from shoreline increased. Because a broken bilobate was given a value of 0.5, lower Iph values (i.e., more bilobates) were not the result of single bilobates being counted twice after breakage. Thus, lower Iph values likely reflect increased exposure to the Omo River sediment plume and its modification by currents associated with the north basin gyre.

Sample 27, which was furthest from shore and closest to the gyre center (**Figure 1D**), yielded an outlier phytolith concentration value (>3 σ) and a slightly elevated microcharcoal concentration value, which both deviate from the trend of decreasing concentrations from shore (**Figures 2A,B**). During microscopy it was noted that the

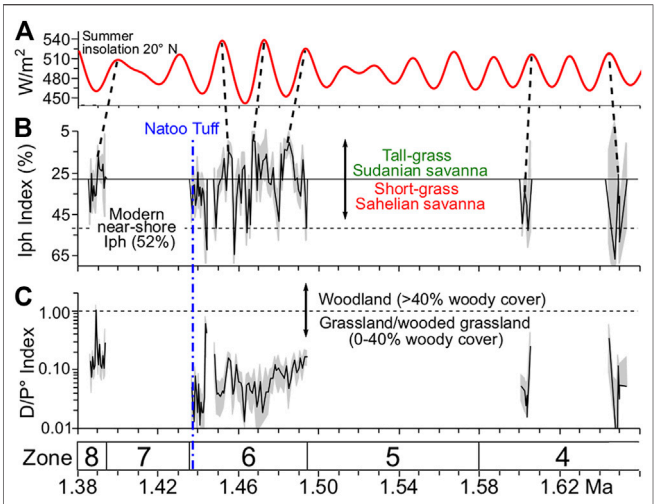

FIGURE 6 | Phytolith Iph (aridity) and D/P° (tree cover) indices. Gray shading represents bootstrapped 95% confidence intervals. The vertical blue dashed line marks the position of the Natoo Tuff in the WTK13 core, linking the Nariokotome Boy site (NK3) to the core. **(A)** Summer insolation for 20° N (Laskar et al., 2004). **(B)** Iph index with inverted y-axis. Solid horizontal reference line set at 27.8%, which separates mesic tall-grass Sudanian savanna from xeric short-grass Sahelian savanna (Novello et al., 2017). Dashed horizontal line denotes the average modern Lake Turkana Iph value. Dashed vertical lines link possible tie points between peaks in insolation and peaks in phytoliths indicative of mesic C_4 tall-grasses **(C)** D/P° tree cover index.

phytolith and inorganic sediment particles were very uniform in size (~10–15 μm), and this apparent particle sorting may be related to the sample's position within the gyre.

Bilobates can and do break during lab phytolith extraction procedures, especially during vortex mixing. However, these processing-induced breakages should be similar from sample to sample. The positive relationship between broken bilobate percentages and distance from shore we observed is considered here to be a consequence, and hence indicator, of long-distance bilobate transport from the upper reaches of the Omo River (Ethiopian Highlands). In support of this hypothesis, modern soil samples (n = 3) from an arid part of the Serengeti Plain (2°56′7.94″ S, 35°14′50.21″ E; MAP = 550 mm) had an average broken bilobate percentage of 42 ± 5% (C. Yost, unpublished data). This is lower than the broken bilobate percentages for the modern Lake Turkana near-shore samples (0.2–0.5 km; 57 ± 10%) and off-shore samples (3–16 km; 73 ± 4%) at the 95% confidence level. Further support for this hypothesis is the fact that phytoliths derived from C_3 Pooideae grasses, which are not found today in the lower Omo River Valley, also increased in abundance as distance from shoreline increased (**Figure 2H**, I_{Omo} index; **Supplementary Figure S3**). A potential limitation of this index would be in depositional settings where partial phytolith dissolution may be responsible for bilobate breakage.

In summary, our findings show that the proportion of the modern Lake Turkana sediment phytolith record derived from within the area immediately adjacent to Lake Turkana, or from the lower or upper Omo River Valley depends on the sample's depositional position within the lake basin, which can vary as a result of changes in lake levels, especially in regard to transgression and regression of the Omo River delta. It is possible that at least ~20% of the modern GSSC phytolith assemblage has been derived from the upper Omo River Valley, and that this proportion may have been significantly higher during past humid periods.

Paleo-Lake Lorenyang Phytoliths and Microcharcoal

Phytoliths in lake cores provide two types of direct information: a broad measure of lake/pore water pH via preservation state (Yost et al., 2021) and a record of vegetation. Indirectly, phytolith concentrations can provide information about relative changes in lake levels if lake surface area change is significant and preservation states and sedimentation rates do not change substantially. The most striking aspect of the WTK13 phytolith record was the poor preservation before, and good to excellent preservation after 1.5 Ma (59.10 mbs). This transition corresponds with a first order facies transition from more lacustrine dominated sedimentation in the bottom of the core to fluvial-deltaic sedimentation at the top of the core (Feibel et al., 2017).

Interpreting phytolith records can be complicated in lacustrine contexts, especially when riverine sediment loads to the system are significant (Li et al., 2019). The results of the modern phytoscape and modern lake sediment analysis enable us to determine that ~80% of the phytoliths in modern lake sediments located ~60 km from the Omo River delta were likely derived from areas proximal to the lake. If proximity from the core site to the paleo-Omo River delta decreased, or river discharge increased, the proportion of phytoliths derived from mesic vegetation sourced more distally from the Upper Omo River Valley in the Ethiopian Highlands would likely increase.

Increased microcharcoal concentrations can arise from various sources, including increased fire frequency, increased fire intensity, increased area burned, and/or decreased distance to source area (Whitlock and Anderson, 2003). For instance, a significant increase in lake surface area could reduce microcharcoal concentrations independent of an actual change in fire activity. However, this reduction could be tempered by decreased clastic inputs (lower sedimentation rates). In a core with excellent chronological control, changes in sedimentation rates can be accounted for by calculating microcharcoal influx. With the more limited chronological control in WTK13, microcharcoal influx calculations would not have appreciably changed the microcharcoal curve.

In a meta-analysis of published charcoal source area estimates, Vachula (2021) modeled the relationship between charcoal size and source area, which was found to be within 50 km for all size fractions of sedimentary charcoal. We consider this model output to be an appropriate estimate of the source area for our paleolake sediment microcharcoal record. Additionally, because of the time-averaging inherent in our samples (~24 yr/sample),

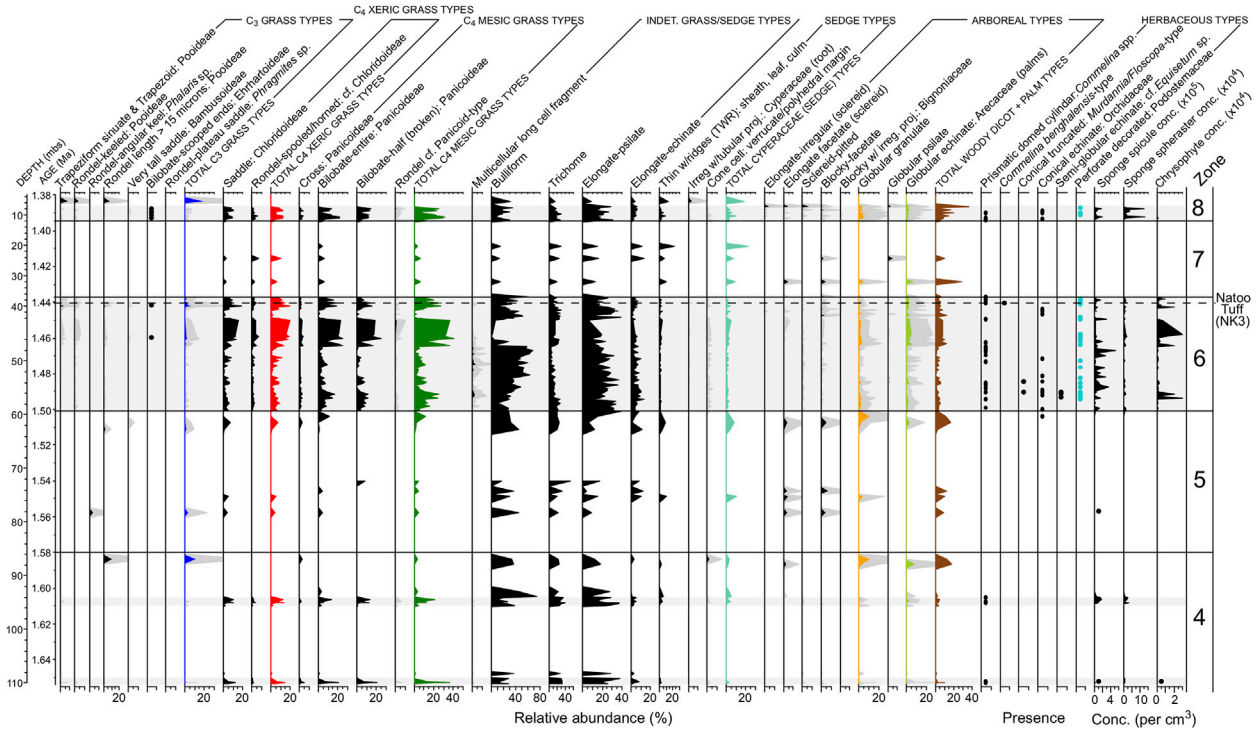

FIGURE 7 | Phytolith relative abundance for selected morphotypes between 1.66 and 1.38 Ma. Some morphotypes include a gray shaded 5x exaggeration. Black dots denote presence, but at values too low to show up on diagram. Horizontal gray shaded bars denote intervals with good phytolith preservation. Unshaded (white) intervals are periods with poor phytolith preservation and partial or complete loss of the phytolith record. The vertical dashed line marks the position of the Natoo Tuff in WTK13, which is a core-to-outcrop tie point for the Nariokotome Boy (*Homo erectus/ergaster*) site (NK3).

microcharcoal variability is most likely a function of fire frequency, but fire intensity, distance to fire source, and area burned may also be contributing factors. In fact, with our proposed causal relationship between increased precipitation and increased mesic (yet fire-adapted) C_4 grass biomass in the WTK13 record (see *Zone 4 (1.728–1.582 Ma; 135.44–86.87 mbs)* and *Correlations Between Precipitation, Fire, Vegetation, and Orbital Forcing*), both increased fire frequency (seasonal fires) and increased area burned (expanded fuel source) would likely contribute to higher microcharcoal concentrations. With these phytolith and microcharcoal taphonomic issues in mind, the paleorecord zones are discussed in more detail below.

Zone 1 (1.868–1.855 Ma; 215.56–206.77 mbs)

The bottom of the core, Zone 1, was characterized by very high charcoal concentrations, (similar to other more humid intervals in the upper part of the core), relatively high concentrations of severely altered diatoms (cf. *Aulacoseira*), and some severely dissolved large bulliform phytoliths (**Figure 3**). Overall, BSi preservation was very poor, indicating lake water pH was likely >8.5. Zone 1 corresponds to what Boës et al. (2019) interpret as the end of a lake level transgression during the freshwater (exorheic) phase of paleo-Lake Lorenyang. Conversely, Schuster and Nutz (2019) and Nutz et al. (2020) interpret lake level regression at this time. Lastly, the consistently high microcharcoal concentrations in Zone 1 suggest fire may have played a role in the basin-wide increase in C_4 vegetation that has been observed after ~2.3 Ma in the Turkana Basin (Levin et al., 2011; Uno et al., 2016), but more importantly after ~2 Ma in the Omo Valley (Levin, 2015), as the Omo River may be a source for some of this microcharcoal. Extending the microcharcoal and phytolith records across this C_3/C_4 vegetation transition would test this hypothesis and provide additional context for the C_4 vegetation increase.

Zone 2 (1.855–1.774 Ma; 206.77–150.62 mbs)

Zone 2 is characterized by the largest number of samples with no phytolith recovery, suggesting high pH lake/pore water was responsible for the partial to complete loss of biogenic silica observed. Numerous ped structures and a sandy sequence of sediments between 199 and 195 mbs suggest periodically low lake levels and exposed surfaces (**Supplementary Figure S2**). Zone 2 corresponds to Unit 2 from Nutz et al. (2017), in which they identified five parasequences paced at precessional (~22 kyr) periodicities. They interpret Unit 2 as being relatively dry with low climate variability. This is in general agreement with both the δD_{wax} and $\delta^{13}C_{wax}$ records of precipitation and vegetation (Lupien et al., 2018), and with the relatively muted variability of our microcharcoal record for the upper half of the zone (**Figure 3**). Our cross-wavelet analysis detected significant anticorrelation between δD_{wax} values and microcharcoal concentrations at precessional periodicity throughout this zone (**Figure 5D**). This spectral analysis indicates that variability in precipitation and fire, and by extension, vegetation, were being

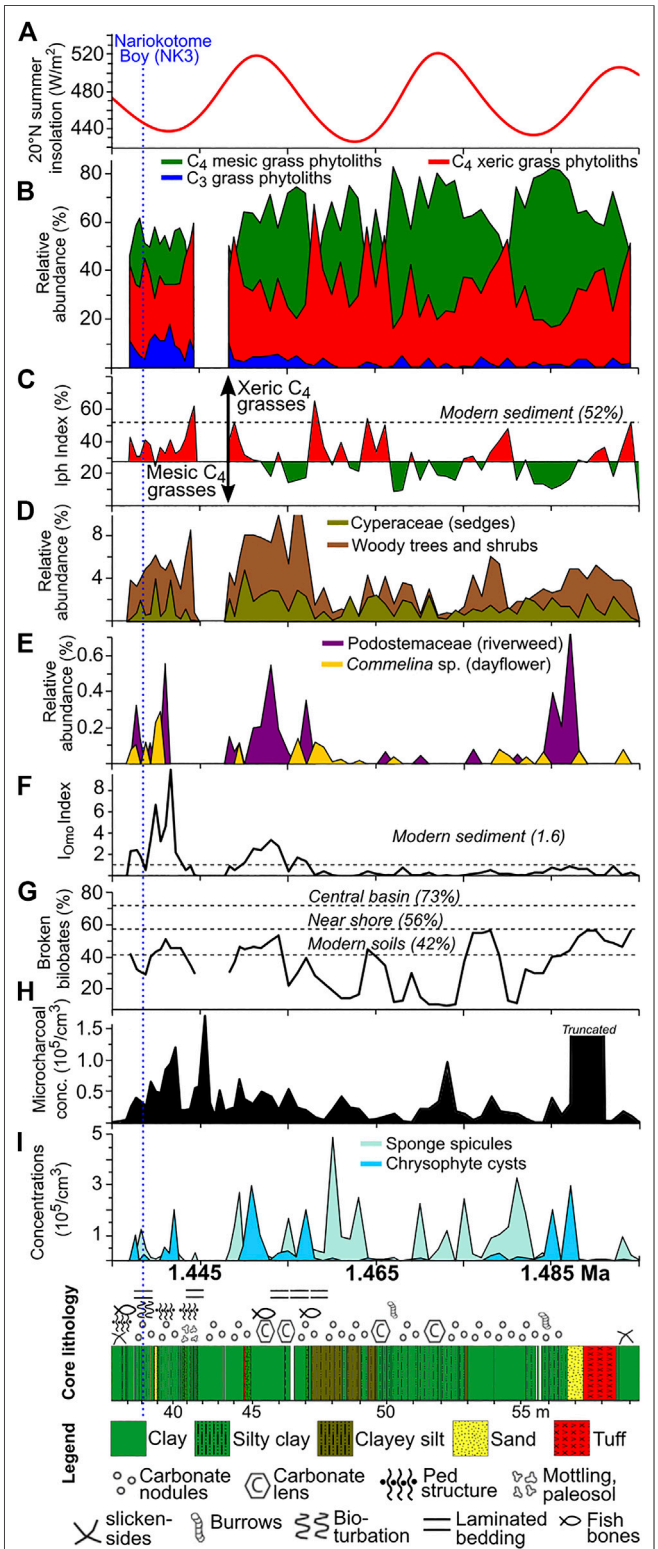

FIGURE 8 | Microfossil summary plots for Zone 6 (1.50–1.435 Ma). **(A)** 20° N summer insolation (Laskar et al., 2004). **(B)** Relative abundance of C_3 and C_4 grass functional types based on short-cell phytoliths. **(C)** Iph aridity index with xeric short-grass/mesic tall-grass transition set at 27.8% (Novello et al., 2017). **(D)** Relative abundance of tree/shrub and Cyperaceae (sedge) phytoliths based on the total phytolith sum. **(E)** Podostemaceae (riverweed) and *Commelina* spp. (dayflower) relative abundance based on total phytolith sum. **(F)** Upper Omo River source area index (I_{Omo}), with higher values signaling more phytolith transport from plants likely growing above 1,500 m elevation. **(G)** Percentages of broken bilobate phytoliths, with higher values suggesting greater phytolith inputs from long-distance transport. **(H)** Microcharcoal concentrations. **(I)** Sponge spicule and chrysophyte cyst concentrations. Chrysophytes were most likely derived from waters sourced to the Ethiopian Highlands.

driven by precession. Nutz et al. (2020) identify a lowstand in the paleolake sometime between 1.85 and 1.75 Ma that would have taken place in either this zone or in Zone 3.

Zone 3 (1.774–1.728 Ma; 150.62–135.44 mbs)

Zone 3 is unique for its extremely low microcharcoal and phytolith concentrations (**Figure 3F**, **Supplementary Figure S4**). The low microcharcoal interval suggests that vegetation within the Turkana Basin was often too sparse to carry fire, ostensibly reflecting hyper-arid conditions. This is supported by the leaf wax hydrogen isotopic record (Lupien et al., 2018), which recorded the most D-enriched δD_{wax} values of the WTK13 core (**Supplementary Table S4**), and also recorded two prominent peaks in ^{13}C-enriched $\delta^{13}C_{wax}$ values, reflecting extreme aridity (**Figures 3E,F**). In fact, the δD_{wax} values in Zone 3 are much higher than modern values at ~400 yr BP from Lake Turkana (Morrissey, 2014; Morrissey and Scholz, 2014).

Although two very high eccentricity modulated insolation peaks fall within this zone (**Figure 3A**), the three troughs (low points) in insolation appear to have had a significant effect on precipitation and fire, and may have also effected lake levels and the resultant sedimentary record. The sample with the lowest microcharcoal concentration at 139.78 mbs (1.7413 Ma) was collected ~1 cm below the erosional surface of a 13-cm coarsening upwards sandy sequence with shells and fish bones that separates a green clay interval with carbonate nodules and silt-filled veins (interpreted as a paleosol) from a green clay interval above that is interpreted as lacustrine (**Supplementary Figure S6**). This erosional event corresponds with the insolation minimum between insolation peaks 2 and 3 labeled in **Figure 3A**. Similar events in this zone, at the bottom of Zone 4, and at other locations in WTK13 may contribute to uncertainty in the age model. Poor chronological control in this part of the core led Lupien et al. (2018) to conservatively tune the δD_{wax} record in the high eccentricity interval centered at 1.74 Ma to summer mean insolation at 20° N. Some of their tie points are depicted in **Figure 3A**. As a consequence, it is possible that the top of Zone 3 may actually be closer to 1.718 Ma rather than 1.728 Ma.

The large insolation increase that culminated at peak 2 (~1.72 Ma) straddles the boundary between Zones 3 and 4 and was the subject of a study by Lupien et al. (2020). They observed an approximately 30‰ D-depletion in δD_{wax} within ~200 years, suggesting that an abrupt, nonlinear climate response was triggered after crossing an insolation threshold. Similarly paced abrupt change likely took place in Zone 6, where phytoliths recorded changes between xeric short-grass savanna and mesic tall-grass savanna occurring in less than 600 years.

These changes were likely more abrupt but our ability to fully resolve the timing was limited by the temporal resolution of the 32-cm sampling scheme and age model for Zone 6. Abrupt change between mesic and xeric savanna in less than 600 years was frequently observed from the Plio-Pleistocene Baringo Basin, where the existence of a precipitation response to an insolation threshold was proposed (Yost et al., 2021). Although low biomarker concentrations did not allow for δD_{wax} measurements for the transition from Zone 5 to Zone 6, the microcharcoal and $\delta^{13}C$ records suggest this was a period of similarly abrupt and extreme change in climate and vegetation. In summary, the transitions to Zones 4 and 6 were both characterized by high eccentricity intervals of high amplitude variability not observed elsewhere in the WTK13 record.

Zone 4 (1.728–1.582 Ma; 135.44–86.87 mbs)

There was high variability in microcharcoal concentrations that included precessional periodicities throughout Zone 4 (**Figure 5D**). Increased fire on the landscape during this period likely helped maintain a grass-dominated savanna mosaic, as has been indicated by pedogenic carbonates and faunal records from the Turkana Basin (e.g., Quinn et al., 2007; Patterson et al., 2017). Peaks in microcharcoal were generally coincident with insolation peaks, and were also typically associated with low (depleted) δD_{wax} values indicative of increased precipitation and high (enriched) $\delta^{13}C_{wax}$ values indicative of increased proportions of C_4 (e.g., grass) vegetation (**Figures 3D–F**).

This inverse relationship between δD_{wax} values and microcharcoal concentrations may be explained by the strong positive relationship between fire and precipitation owing to increased C_4 grass biomass (fuel) when precipitation increases in savanna ecosystems (Lehmann et al., 2014; Probert et al., 2019). Fires occurring when C_4 grasses are quiescent during subsequent dry seasons would be expected to significantly reduce tree and shrub cover (Oliveras and Malhi, 2016), thus increasing the proportion of C_4 to C_3 biomass with increases in precipitation. As aridity increased in these communities, plant cover, biomass, and density would decline and bare ground would have increased such that fire frequency and intensity would be reduced, and xerophytic C_3 trees and shrubs would increase relative to C_4 grasses. This is a simplistic model, as grazers can also suppress fire activity by creating grazing lawns (Hempson et al., 2015), and browsers can reduce woody vegetation abundance independent of fire (Rugemalila et al., 2016). However, the basic relationships between fire, precipitation, and plant functional type dominance remain coherent at broad scales in African savannas (Oliveras and Malhi, 2016).

Although there were only two short intervals with good phytolith preservation within Zone 4, the Iph aridity and D/P° tree cover indices indicate that tree cover was likely <40%, and xeric C_4 Chloridoideae taxa were the dominant grasses. This change in vegetation would be consistent with the rise in arid-adapted antilopin, alcelaphin, and hippotragin bovids in KBS Member paleontological assemblages from East Turkana (Patterson et al., 2017). However, the grass community overall was comprised of more mesic adapted grasses than today. This is supported by the δD_{wax} record that shows hydroclimate within the watershed during the Zone 4 period was likely wetter than near-modern (~400 yr BP; **Figure 3E**).

Zone 5 (1.582–1.50 Ma; 86.87–59.42 mbs)

Very poor phytolith preservation precluded Iph and D/P° index calculations in Zone 5, but the peak in sponge spicule concentrations between 78.25 and 77.27 mbs (1.556 Ma) is a marker for a humid period that may be related to the high amplitude insolation peak at 1.566 Ma (**Figure 3A**). This is supported by a peak in D-depleted δD_{wax} and a peak in microcharcoal concentrations (**Figures 3D,E**) that are coeval with the insolation peak. In observing repeated humid-to-arid dissolution sequences for a Plio-Pleistocene record from the Baringo Basin in central Kenya (Yost et al., 2021), found that sponge spicules and spherasters were often the last biogenic silica microfossils to completely dissolve under conditions of increasing pore/lake water pH. Apparently, sponge silica is better polymerized to resist dissolution, possibly as an adaptation to alkaline lakes. Thus, for this short interval, lake water pH was low enough for marginal sponge preservation, but not for phytolith or diatom preservation.

Zones 6–8 (1.50–1.379 Ma; 59.42–3.33 mbs)

The sudden change from poor to good phytolith preservation in less than ~1 kyr between Zones 5 and 6 is striking. This transition was likely faster, but 960 yr was the temporal limit of the 32-cm sampling resolution in this section of the core. To have a sudden shift towards good phytolith preservation, lake water pH would need to be dramatically lowered, possibly from increased inflow from the Omo River. Zones 6 and eight had the second highest and highest average δD_{wax} values, respectively, indicating generally stronger precipitation than in the lower zones in the core. The appearance of riverweed phytoliths from *Tristicha trifaria* (Podostemaceae) in Zones 6 and 8, a plant that only grows above 1,500 m on rocks in fast moving water (Agnew, 2013; Koi et al., 2015), suggests that the WTK13 drill site at this time was close to the presumably neutral pH waters of the paleo-Omo River.

Numerous samples in these zones with phytolith concentrations of 10^6–10^7 cm^{-3} are suggestive of subaerial or subaqueous soils in low-energy depositional environments. In fact, during initial core descriptions, smear slides of unprocessed sediment were often comprised of 20–30% phytoliths. Discreet intervals from the Baringo/Tugen Hills (Yost et al., 2021) and Olorgesailie HSPDP drill cores also yielded high phytolith abundances in smear slides and were interpreted as possible wetlands. Modern East African sediment with even higher phytolith abundances have been observed from the Ngoitokitok wetland, Ngorongoro Basin, Tanzania (See Figure 2C from Deocampo and Ashley, 1999).

The percentages of broken bilobate phytoliths were in the ranges typical of soils from near shore settings in the modern Lake Turkana samples (**Figure 8G**). Higher levels of leaf wax degradation in this part of the core (Lupien et al., 2018) are indictive of oxidative conditions and suggestive of shallow water or overbank depositional settings. Lithologic descriptions

indicate the presence of ped structures, burrows, carbonate nodules, and laminated bedding, indicating paleosol alteration of original lacustrine deposits (**Figure 8**). The grassland community for most of Zone 6 was typically dominated by tall-grass mesic C_4 Panicoideae taxa, but it periodically switched to xeric short-grass savanna presumably during insolation minima (discussed in *Correlations Between Precipitation, Fire, Vegetation, and Orbital Forcing*). Extended periods of mesic tall-grass dominance would be consistent with the rise in mesic grassland-indicative reduncin bovids in Okote Member paleontological assemblages from East Turkana (Patterson et al., 2017). However, a trend of increasing xeric C_4 grasses in the upper half of Zone 6 was observed (**Figure 6**). The environmental setting around the time of the Natoo Tuff, which links the upper part of Zone 6 to the Nariokotome Boy site (NK3), is discussed further in *Local Environments of the Nariokotome Boy*.

Correlations Between Precipitation, Fire, Vegetation, and Orbital Forcing

A correlation between precipitation (δD_{wax}) and fire (microcharcoal) is visually apparent throughout much of the WTK13 record (**Figure 3**). The rolling Spearman correlation analysis identifies several intervals with strong, statistically significant, negative correlations between δD_{wax} values and microcharcoal concentrations (**Figure 4C**). As δD_{wax} values *decrease*, signifying more precipitation, microcharcoal concentrations *increase*, signifying more fire. This relationship of increasing precipitation with increasing fire is observed in modern grass-dominated (savanna) ecosystems, as fire-adapted C_4 tall-grasses increase when precipitation increases [see discussion and refs in *Zone 3 (1.774–1.728 Ma; 150.62–135.44 mbs)*].

While the rolling Spearman correlation can determine the strength of transitory in-phase (positive) and anti-phase (negative) correlations at the sampled time steps, evolutive cross-wavelet analysis identifies transitory correlations (intervals of high common power) at multiple time steps (i.e., periodicities) and can detect lead/lag relationships (**Figure 5D**). In agreement with the Spearman correlation analysis, anti-phasing between the δD_{wax} values and microcharcoal concentrations is the dominant phase relationship within the high common power areas of the cross-wavelet spectrum.

Spectral analysis of the microcharcoal record (**Figure 4**) and the $\delta^{13}C_{wax}$ record (**Supplementary Figure S7**) indicated that precession had an effect on fire and vegetation, most likely through changes in precipitation. However, this relationship is not consistent across the entire record (**Figure 5D**). The strong anti-correlation between the δD_{wax} and microcharcoal records with a range of periodicities centered around 33 kyr is curious given that equatorial climate variability is often driven by eccentricity-modulated precession (19–23 kyr; **Figure 5A**) on time scales of 10^4–10^5 yrs (Lourens, 2021). However, for this same WTK13 interval, Lupien et al. (2018) observed a similar range of periodicities between precession and obliquity for the δD_{wax} record alone, and demonstrated through a conservative tuning exercise that this is most likely a precession band signal that is possibly being obscured by large age uncertainties in this section of the core. By using the tuned age model on the $\delta^{13}C_{wax}$ record, we also removed periodicities at 30 and 26 kyr (**Supplementary Figure S7**). This may or may not explain the strong non-orbital periodicity of 78 kyr between 1.82 and 1.70 Ma, where increased precipitation (lower δD_{wax}) leads increased fire (higher microcharcoal concentrations) by about 10 kyr. Such a scenario could arise if increased precipitation leads to an expansion of woody vegetation that then burns more frequently during drier periods.

The Spearman correlation and cross-wavelet analyses indicate there is a strong positive relationship between precipitation and fire in the Turkana Basin between at least 1.84 and 1.57 Ma. This is indicative of a grass-dominated ecosystem with increased mesic (yet fire-adapted) C_4 tall-grasses during humid periods, presumably during insolation maxima, and increased xeric C_4 short-grasses during arid and less fire-prone periods, presumably during insolation minima. The findings from Lupien et al. (2018) and this study suggest that on orbital time scales, variability in Turkana Basin precipitation, fire, and vegetation is being driven primarily by eccentricity-modulated precession.

Local Environments of the Nariokotome Boy

Identification of the Natoo Tuff in WTK13 through single shard glass geochemistry (Feibel et al., 2017) provides a direct core-to-outcrop linkage to the Nariokotome Boy site, where the most complete *Homo erectus/ergaster* skeleton to date (KNM-WT 15000) was recovered. The Nariokotome Boy site (NK3) is ~3 km east of the WTK13 drill site, and the skeleton was recovered on the Natoo Tuff (Brown et al., 1985). A detailed paleoenvironmental reconstruction of the site using microstratigraphy was conducted by Feibel and Brown (1993). They describe the depositional setting as a low-energy floodplain marsh, and suggest the skeleton was covered by a short-duration shallow body of water and rapidly buried. Sediment characteristics indicate the floodwaters were supplied primarily from the ancestral Omo River.

Well-preserved phytoliths diagnostic of riverweed (*Tristicha trifaria*), and cysts from an algal chrysophyte, which were both transported to this location from the upper reaches of the Omo River in the Ethiopian Highlands, were deposited immediately below and above the lowest position of the Natoo Tuff in the WTK13 core (**Figures 8E,I**), indicating that this was likely a broad system of freshwater channels and wetlands. Phytoliths from at least three species of *Commelina* (*C. africana* type, *C. diffusa* type, and *C. benghalensis* type; Eichhorn et al., 2010) were observed. This is notable since *Commelina* leaves are consumed by African primates (Mitani et al., 1993; Huffman et al., 1997; Isbell, 1998), and modern humans (Maundu et al., 1999). Numerous phytoliths from sedge (Cyperaceae) stems, rhizomes (roots), and achenes (seeds), were present, as were high concentrations of grass phytoliths ($2–4 \times 10^6$ cm^{-3}). Sedge stems, shoots, and starchy rhizomes are consumed by modern humans and have been considered a probable food source for early Pleistocene hominins (Sponheimer et al., 2013; Stewart, 2014). The highest abundances of C_3 grass phytoliths from WTK13 were observed in this part of Zone 6, although they were likely derived from the Ethiopian Highlands. Phytoliths from trees and shrubs were present as well, but the D/P° tree cover index values

were well below the 1.0 threshold for tree cover >40%. The grass community appears to have switched to being dominated by more xeric C_4 Chloridoideae taxa; however, the Iph index indicates the grass community was still more mesic than today (**Figure 6B**).

In summary, high concentrations of well-preserved phytoliths from sediments associated with the Natoo Tuff indicate that the area ~3 km west of NK3 was a seasonally wet and densely vegetated environment dominated by short stature grasses, sedges and other herbaceous plants during the time that the Nariokotome Boy walked the ancient landscape. This area would have been rich in terrestrial and aquatic floral and faunal resources for hominin subsistence. Microfossils sourced from the Ethiopian Highlands link this area to hydroclimate fluctuations that would have operated on interannual to orbital time scales. The events at NK3 took place during a period of low summer insolation; however, winter insolation would have been at a maximum, resulting in overall reduced seasonality. This information adds some additional plant taxon detail to the original paleogeographic reconstruction by Feibel and Brown (1993), and perhaps confirms the extension of the floodplain ~3 km east, but does not change the overall reconstruction first proposed 26 years ago.

Implications for Hominin Paleoecology

We do not observe any long-term trends in environmental change between 1.87 and 1.38 Ma, similar to the leaf wax biomarker records (Lupien et al., 2018); however, these orbitally resolved records do indicate that vegetation communities were oscillating at precessional periodicities in the Turkana Basin. Specifically, our study indicates that mesic tall-grass savanna was dominant primarily during insolation maxima and xeric short-grass savanna was dominant during insolation minima and periods when insolation maxima were muted (modulated) by low eccentricity. Presently, the short-grass/tall-grass savanna boundary occurs at ~750 mm MAP (van Wyk, 1979; McNaughton, 1983), so switches between these savanna types likely signify when the ~700 mm precipitation threshold has been crossed.

Although both of these savanna types constitute an open mosaic landscape with scatted trees and shrubs, their grass community structures, faunal populations, and fire regimes are very different. Short-grass savanna grasses are highly nutritious, heavily grazed, and can form rhizomatous lawns (McNaughton, 1985; Quigley and Anderson, 2014; Hempson et al., 2015). Modern short-grass savannas support high diversity and very high abundances of medium-sized mixed-diet taxa such as gazelle and oryx (Hempson et al., 2015). Tall-grass savanna grasses are 1–2 m in height, less nutritious, less digestible, hide predators, and are adapted to frequent fire (Dobson, 2009; Pays et al., 2012; Quigley and Anderson, 2014). Modern tall-grass savannas support high relative abundances of non-ruminant grazers such as equids, hippos, rhinos and suids, and water-dependent grazers such as wildebeest and hartebeest (Hempson et al., 2015).

Xeric short-grass versus mesic tall-grass savannas would have afforded very different resources and predator-prey relationships to hominin populations, which presumably would have required very different foraging strategies. Hominins utilizing a short-grass landscape would likely have experienced large populations of highly visible medium-sized social animals on a landscape with infrequent fires. In contrast, those utilizing a tall-grass landscape would have encountered seasonal fires and large bodied animals, including predators, in generally less visible settings than short-grass savanna. This study and a previous study from the Baringo Basin (Yost et al., 2021) indicate that hominin lineages have been exposed to precession-paced variability in tall-and short-grass savanna for at least the past three million years in eastern Africa.

CONCLUSION

Our new microcharcoal record from paleo-Lake Lorenyang spans 500 kyr and provides the first millennial-scale record of paleofire in the Turkana Basin for a critical period of hominin and landscape evolution between 1.87 and 1.38 Ma. Microcharcoal concentrations were found to vary at statistically significant precessional (21–19 kyr) periodicities, and through a correlation with δD_{wax} link orbitally forced peaks in precipitation with elevated fire on the landscape. Phytoliths show that mesic C_4 versus xeric C_4 grass dominance likely varied at precessional periodicities, but other factors such as basin geometry also influenced grass composition. Two intervals of particularly high amplitude and abrupt environmental change were centered at ~1.72 and 1.50 Ma, respectively, and corresponded with high orbital eccentricity. The interval between 1.72 and 1.58 Ma was notable for having extended periods of both high and low fire activity and for the prevalence of xeric C_4 Chloridoideae grasses. With the switch from a lacustrine to fluvial-deltaic deposition at the drill site by 1.5 Ma, tall-grass C_4 Panicoideae became dominant, with evidence of continuously high fire activity between 1.50 and 1.44 Ma. The recovery of phytoliths diagnostic of riverweed (Podostemaceae) and C_3 grasses (Pooideae), indicate long-distance transport from the Ethiopian Highlands via the Omo River. From the modern vegetation and lake sediment study, it was estimated that ~20% of the modern phytolith record could be sourced from the Highlands, and this proportion was likely higher during periods of increased precipitation. Thus, potential influences from the entire watershed need to be considered when interpreting microfossils and biomarkers derived from Turkana Basin sediments.

DATA AVAILABILITY STATEMENT

The original contributions presented in the study are included in the article/**Supplementary Material**, further inquiries can be directed to the corresponding author.

AUTHOR CONTRIBUTIONS

CY, CB, CF, and AC, assisted with coring. CY analyzed phytoliths and microcharcoal. CB, CF, and RL contributed data. CY, RL, CB, CF, SA, and AC assisted with writing the manuscript.

FUNDING

Funding for this work was provided by National Science Foundation (NSF) grants EAR-1123942, BCS-1241859, EAR-1338553, and the International Continental Scientific Drilling Program (ICDP). NSF funds were used for logistics, permit,

drilling operation, shipping, and analytical expenses. ICDP funds were used for drilling operation expenses.

ACKNOWLEDGMENTS

We thank Laurel Karten, Kaitlynn Walker, and Lizbeth Murillo (University of Arizona) for assisting with the phytolith and microcharcoal separations. This research was conducted as part of the Hominin Sites and Paleolakes Drilling Program (HSPDP). Initial WTK13 core processing and sampling was completed at the National Lacustrine Core Facility (LacCore), University of Minnesota, United States. WTK13 is archived at LacCore. We thank Doris Barboni and two reviewers for valuable comments that significantly improved the article. This is publication 41 of the Hominin Sites and Paleolakes Drilling Project.

SUPPLEMENTARY MATERIAL

The Supplementary Material for this article can be found online at: https://www.frontiersin.org/articles/10.3389/feart.2021.568646/full#supplementary-material

REFERENCES

Agnew, A. D. Q. (2013). *Upland Kenya Wild Flowers and Ferns*. Nairobi: Nature Kenya.

Antón, S. C. (2003). Natural History of *Homo Erectus*. *Am. J. Phys. Anthropol.* 122, 126–170. doi:10.1002/ajpa.10399

Walker, A., and Leakey, R. E. (1993). *The Nariokotome Homo Erectus Skeleton*. Cambridge, Massachusetts: Harvard University Press.

Beck, C. C. (2015). *A Multiproxy Approach to Deciphering Terrestrial Climate Records from the Turkana Basin*. KenyaNew Brunswick, NJ: Ph.D. dissertationRutgers University.

Bobe, R., and Carvalho, S. (2019). Hominin Diversity and High Environmental Variability in the Okote Member, Koobi Fora Formation, Kenya. *J. Hum. Evol.* 126, 91–105. doi:10.1016/j.jhevol.2018.10.012

Bobe, R., and Leakey, M. G. (2009). "Ecology of Plio-Pleistocene Mammals in the Omo-Turkana Basin and the Emergence of Homo," in *The First Humans: Origins and Early Evolution of the Genus Homo*. Editors F. E. Grine, J. G. Fleagle, and R. E. Leakey (Berlin: Springer), 173–184. doi:10.1007/978-1-4020-9980-9_15

Bobe, R. (2004). The Expansion of Grassland Ecosystems in Africa in Relation to Mammalian Evolution and the Origin of the Genus *Homo*. *Palaeogeogr. Palaeoclimatol. Palaeoecol.* 207 (3–4), 399–420. doi:10.1016/j.palaeo.2003.09.033

Boës, X., Prat, S., Arrighi, V., Feibel, C., Haileab, B., Lewis, J., et al. (2019). Lake-level Changes and Hominin Occupations in the Arid Turkana basin during Volcanic Closure of the Omo River Outflows to the Indian Ocean. *Quat. Res.* 91 (2), 892–909. doi:10.1017/qua.2018.118

Braun, D. R., Harris, J. W. K., Levin, N. E., McCoy, J. T., Herries, A. I. R., Bamford, M. K., et al. (2010). Early Hominin Diet Included Diverse Terrestrial and Aquatic Animals 1.95 Ma in East Turkana, Kenya. *Proc. Natl. Acad. Sci.* 107 (22), 10002–10007. doi:10.1073/pnas.1002181107

Bremond, L., Alexandre, A., Wooller, M. J., Hély, C., Williamson, D., Schäfer, P. A., et al. (2008). Phytolith Indices as Proxies of Grass Subfamilies on East African Tropical Mountains. *Glob. Planet. Change* 61 (3–4), 209–224. doi:10.1016/j.gloplacha.2007.08.016

Brown, F., Harris, J., Leakey, R., and Walker, A. (1985). Early *Homo Erectus* Skeleton from West Lake Turkana, Kenya. *Nature* 316, 788–792. doi:10.1038/316788a0

Brown, F. H., and McDougall, I. (2011). Geochronology of the Turkana Depression of Northern Kenya and Southern Ethiopia. *Evol. Anthropol.* 20 (6), 217–227. doi:10.1002/evan.20318

Bruhn, R. L., Brown, F. H., Gathogo, P. N., and Haileab, B. (2011). Pliocene Volcano-Tectonics and Paleogeography of the Turkana Basin, Kenya and Ethiopia. *J. Afr. Earth Sci.* 59 (2–3), 295–312. doi:10.1016/j.jafrearsci.2010.12.002

Campisano, C. J., Cohen, A. S., Arrowsmith, J. R., Asrat, A., Behrensmeyer, A. K., Brown, E. T., et al. (2017). The Hominin Sites and Paleolakes Drilling Project: High-Resolution Paleoclimate Records from the East African Rift System and Their Implications for Understanding the Environmental Context of Hominin Evolution. *PaleoAnthropology*, 1–43. doi:10.1130/abs/2017am-295426

Carr, C. J. (1998). Patterns of Vegetation along the Omo River in Southwest Ethiopia. *Plant Ecol.* 135, 135–163. doi:10.1023/a:1009704427916

Carr, C. J. (2017). *River Basin Development and Human Rights in Eastern Africa — A Policy Crossroads*. Switzerland: Springer Nature. doi:10.1007/978-3-319-28480-4

Chandan, D., and Peltier, W. R. (2020). African Humid Period Precipitation Sustained by Robust Vegetation, Soil, and lake Feedbacks. *Geophys. Res. Lett.* 47 (21). e2020GL088728. doi:10.1029/2020gl088728

Clark, J. S. (1988). Particle Motion and the Theory of Charcoal Analysis: Source Area, Transport, Deposition, and Sampling. *Quat. Res.* 30 (1), 67–80. doi:10.1016/0033-5894(88)90088-9

Cohen, A. S., Ferguson, D. S., Gram, P. M., Hubler, S. L., and Sims, K. W. (1986). "The Distribution of Coarse-Grained Sediments in Modern Lake Turkana, Kenya: Implications for Clastic Sedimentation Models of Rift Lakes," in *Sedimentation in the African Rifts*. Editor L. E. Frostick (Palo Alto, CA: Blackwell Scientific Publications), 127–139. doi:10.1144/gsl.sp.1986.025.01.11

Cohen, A., Campisano, C., Arrowsmith, R., Asrat, A., Behrensmeyer, A. K., Deino, A., et al. (2016). The Hominin Sites and Paleolakes Drilling Project: Inferring the Environmental Context of Human Evolution from Eastern African Rift lake Deposits. *Sci. Dril.* 21, 1–16. doi:10.5194/sd-21-1-2016

Coughenour, M. B., and Ellis, J. E. (1993). Landscape and Climatic Control of Woody Vegetation in a Dry Tropical Ecosystem: Turkana District, Kenya. *J. Biogeogr.* 20 (4), 383–398. doi:10.2307/2845587

da Costa, F. G. C. M., Klein, D. E., Philbrick, C. T., and Bove, C. P. (2018). Silica Bodies in Leaves of Neotropical Podostemaceae: Taxonomic and Phylogenetic Perspectives. *Ann. Bot.* 122 (7), 1187–1201. doi:10.1093/aob/mcy121

Deocampo, D. M., and Ashley, G. M. (1999). Siliceous Islands in a Carbonate Sea; Modern and Pleistocene spring-fed Wetlands in Ngorongoro Crater and Oldupai Gorge, Tanzania. *J. Sediment. Res.* 69 (5), 974–979. doi:10.2110/jsr.69.974

Dobson, A. (2009). Food-Web Structure and Ecosystem Services: Insights From the Serengeti. *Philos. Trans. R. Soc. Lond. B Biol. Sci.* 364 (1524), 1665–1682. doi:10.1098/rstb.2008.0287

Eichhorn, B., Neumann, K., and Garnier, A. (2010). Seed Phytoliths in West African Commelinaceae and Their Potential for Palaeoecological Studies. *Palaeogeogr. Palaeoclimatol. Palaeoecol.* 298 (3–4), 300–310. doi:10.1016/j.palaeo.2010.10.004

Feibel, C. S. (2011). A Geological History of the Turkana Basin. *Evol. Anthropol.* 20 (6), 206–216. doi:10.1002/evan.20331

Feibel, C. S., Beck, C. C., Lupien, R. L., Russell, J. M., Deino, A., Sier, M. J., et al. (2017). Environmental Dynamics on an Early Pleistocene lake Margin: the WTK13 Core at Kaitio, West Turkana, Kenya. *Geological Society of America Abstracts with Programs*. 49 (6). doi:10.1130/abs/2017am-303947

Feibel, C. S., and Brown, F. H. (1993). "Microstratigraphy and Paleoenvironments," in *The Nariokotome Homo Erectus Skeleton*. Editors A. Walker and R. E. Leakey (Cambridge, Massachusetts: Harvard University Press), 21–39. doi:10.1007/978-3-662-10382-1_3

Fraysse, F., Pokrovsky, O. S., Schott, J., and Meunier, J.-D. (2009). Surface Chemistry and Reactivity of Plant Phytoliths in Aqueous Solutions. *Chem. Geology.* 258 (3–4), 197–206. doi:10.1016/j.chemgeo.2008.10.003

GBIF (2019). Global Biodiversity Information Facility (online database). Available: https://www.gbif.org. (Accessed July 29, 2019).

Harris, J. M., Brown, F. H., and Leakey, M. G. (1988). Stratigraphy and Paleontology of Pliocene and Pleistocene Localities West of Lake Turkana, Kenya. *Natural History Museum of Los Angeles County*. 399, 1–128.

Hempson, G. P., Archibald, S., and Bond, W. J. (2015). A Continent-wide Assessment of the Form and Intensity of Large Mammal Herbivory in Africa. *Science* 350 (6264), 1056–1061. doi:10.1126/science.aac7978

Hlubik, S., Cutts, R., Braun, D. R., Berna, F., Feibel, C. S., and Harris, J. W. K. (2019). Hominin Fire Use in the Okote Member at Koobi Fora, Kenya: New Evidence for the Old Debate. *J. Hum. Evol.* 133, 214–229. doi:10.1016/j.jhevol.2019.01.010

Hopson, A. J. (1975). *Progress Report. January 1975, Lake Rudolf Fisheries Research Project*. (unublished).

Huffman, M. A., Gotoh, S., Turner, L. A., Hamai, M., and Yoshida, K. (1997). Seasonal Trends in Intestinal Nematode Infection and Medicinal Plant Use Among Chimpanzees in the Mahale Mountains, Tanzania. *Primates* 38 (2), 111–125. doi:10.1007/BF02382002

Isbell, L. A. (1998). Diet for a Small Primate: Insectivory and Gummivory in the (Large) Patas Monkey (Erythrocebus Patas Pyrrhonotus). *Am. J. Primatol.* 45 (4), 381–398. doi:10.1002/(SICI)1098-2345(1998)45:4<381::AID-AJP5>3.0.CO;2-S

James, N. A., and Matteson, D. S. (2014). Ecp: An R Package for Nonparametric Multiple Change point Analysis of Multivariate Data. *J. Stat. Softw.* 62 (7), 1–25. doi:10.18637/jss.v062.i07

Johnson, T. C., and Malala, J. O. (2009). "Lake Turkana and its Link to the Nile," in *The Nile: Origin, Environments, Limnology and Human Use*. Editor H. J. Dumont (Dordrecht: Springer), 287–304. doi:10.1007/978-1-4020-9726-3_15

Joordens, J. C. A., Vonhof, H. B., Feibel, C. S., Lourens, L. J., Dupont-Nivet, G., van der Lubbe, J. H. J. L., et al. (2011). An Astronomically-Tuned Climate Framework for Hominins in the Turkana Basin. *Earth Planet. Sci. Lett.* 307 (1–2), 1–8. doi:10.1016/j.epsl.2011.05.005

Joordens, J. C. A., Dupont-Nivet, G., Feibel, C. S., Spoor, F., Sier, M. J., van der Lubbe, J. H. J. L., et al. (2013). Improved Age Control on Early Homo Fossils from the Upper Burgi Member at Koobi Fora, Kenya. *J. Hum. Evol.* 65 (6), 731–745. doi:10.1016/j.jhevol.2013.09.002

Kebede, E., and Belay, A. (1994). Species Composition and Phytoplankton Biomass in a Tropical African lake (Lake Awassa, Ethiopia). *Hydrobiologia* 288 (1), 13–32. doi:10.1007/bf00006802

Kebede, E., and Willén, E. (1998). Phytoplankton in a Salinity-Alkalinity Series of Lakes in the Ethiopian Rift Valley. *archiv_algolstud* 89, 63–96. doi:10.1127/algol_stud/89/1998/63

Koi, S., Ikeda, H., Rutishauser, R., and Kato, M. (2015). Historical Biogeography of River-Weeds (Podostemaceae). *Aquat. Bot.* 127, 62–69. doi:10.1016/j.aquabot.2015.08.003

Kutzbach, J. E., and Otto-Bliesner, B. L. (1982). The Sensitivity of the African-Asian Monsoonal Climate to Orbital Parameter Changes for 9000 Years B.P. In a Low-Resolution General Circulation Model. *J. Atmos. Sci.* 39 (6), 1177–1188. doi:10.1175/1520-0469(1982)039<1177:tsotaa>2.0.co;2

Laskar, J., Robutel, P., Joutel, F., Gastineau, M., Correia, A. C. M., and Levrard, B. (2004). A Long-Term Numerical Solution for the Insolation Quantities of the Earth. *Astronomy and Astrophysics* 428 (1), 261–285. doi:10.1051/0004-6361:20041335

Lehmann, C. E. R., Anderson, T. M., Sankaran, M., Higgins, S. I., Archibald, S., Hoffmann, W. A., et al. (2014). Savanna Vegetation-Fire-Climate Relationships Differ Among Continents. *Science* 343 (6170), 548–552. doi:10.1126/science.1247355

Lepre, C. J., Quinn, R. L., Joordens, J. C. A., Swisher, C. C., 3rd, and Feibel, C. S. (2007). Plio-Pleistocene Facies Environments from the KBS Member, Koobi Fora Formation: Implications for Climate Controls on the Development of lake-margin Hominin Habitats in the Northeast Turkana Basin (Northwest Kenya). *J. Hum. Evol.* 53 (5), 504–514. doi:10.1016/j.jhevol.2007.01.015

Lepre, C. J., Roche, H., Kent, D. V., Harmand, S., Quinn, R. L., Brugal, J.-P., et al. (2011). An Earlier Origin for the Acheulian. *Nature* 477 (7362), 82–85. doi:10.1038/nature10372

Lepre, C. J. (2014). Early Pleistocene lake Formation and Hominin Origins in the Turkana-Omo Rift. *Quat. Sci. Rev.* 102, 181–191. doi:10.1016/j.quascirev.2014.08.012

Levin, N. E., Brown, F. H., Behrensmeyer, A. K., Bobe, R., and Cerling, T. E. (2011). Paleosol Carbonates from the Omo Group: Isotopic Records of Local and Regional Environmental Change in East Africa. *Palaeogeogr. Palaeoclimatol. Palaeoecol.* 307 (1–4), 75–89. doi:10.1016/j.palaeo.2011.04.026

Levin, N. E. (2015). Environment and Climate of Early Human Evolution. *Annu. Rev. Earth Planet. Sci.* 43 (1), 405–429. doi:10.1146/annurev-earth-060614-105310

Li, R., Fan, J., Vachula, R. S., Tan, S., and Qing, X. (2019). Spatial Distribution Characteristics and Environmental Significance of Phytoliths in Surface Sediments of Qingshitan Lake in Southwest China. *J. Paleolimnol* 61 (2), 201–215. doi:10.1007/s10933-018-0053-9

Lourens, L. J. (2021). The Variation of the Earth's Movements (Orbital, Tilt, and Precession) and Climate Change. *Climate Change: Observed Impacts on Planet Earth*. 583–606. doi:10.1016/b978-0-12-821575-3.00028-1

Lupien, R. L., Russell, J. M., Feibel, C., Beck, C., Castañeda, I., Deino, A., et al. (2018). A Leaf Wax Biomarker Record of Early Pleistocene Hydroclimate from West Turkana, Kenya. *Quat. Sci. Rev.* 186, 225–235. doi:10.1016/j.quascirev.2018.03.012

Lupien, R. L., Russell, J. M., Grove, M., Beck, C. C., Feibel, C. S., and Cohen, A. S. (2020). Abrupt Climate Change and Its Influences on Hominin Evolution During the Early Pleistocene in the Turkana Basin, Kenya. *Quat. Sci. Rev.* 245. doi:10.1016/j.quascirev.2020.106531

Lupien, R. L., Russell, J. M., Yost, C. L., Kingston, J. D., Deino, A. L., Logan, J., et al. (2021). Vegetation Change in the Baringo Basin, East Africa across the Onset of Northern Hemisphere Glaciation 3.3-2.6 Ma. *Palaeogeogr. Palaeoclimatol. Palaeoecol.* 570 (6), 109426. doi:10.1016/j.palaeo.2019.109426

Lynch, J. A., Clark, J. S., and Stocks, B. J. (2004). Charcoal Production, Dispersal, and Deposition from the Fort Providence Experimental Fire: Interpreting Fire Regimes from Charcoal Records in Boreal Forests. *Can. J. For. Res.* 34 (8), 1642–1656. doi:10.1139/x04-071

Maundu, M. P., Ngugi, W. G., and Kabuye, H. S. C. (1999). *Traditional Food Plants of Kenya*. Nairobi: National Museums of Kenya.

Mbaluka, J. K., and Brown, F. H. (2016). Vegetation of the Koobi Fora Region Northeast of Lake Turkana, Marsabit County, Northern Kenya. *J. East Afr. Nat. Hist.* 105 (1), 21–50. doi:10.2982/028.105.0101

McNaughton, S. J. (1983). Serengeti Grassland Ecology: The Role of Composite Environmental Factors and Contingency in Community Organization. *Ecol. Monogr.* 53 (3), 291–320. doi:10.2307/1942533

McNaughton, S. J. (1985). Ecology of a Grazing Ecosystem: The Serengeti. *Ecol. Monogr.* 55 (3), 259–294. doi:10.2307/1942578

Merlis, T. M., Schneider, T., Bordoni, S., and Eisenman, I. (2013). The Tropical Precipitation Response to Orbital Precession. *J. Clim.* 26 (6), 2010–2021. doi:10.1175/jcli-d-12-00186.1

Meyers, S. R. (2014). Astrochron: An R Package for Astrochronology. Available: https://cran.r-project.org/package=astrochron.doi:10.4324/9781315712062

Mitani, M., Yamagiwa, J., Oko, R. A., Moutsambote, J.-M., Yumoto, T., and Maruhashi, T. (1993). Approaches in Density Estimates and Reconstruction of Social Groups in a Western Lowland Gorilla Population in the Ndoki Forest, Northern Congo. *Tropics* 2 (4), 219–229. doi:10.3759/tropics.2.219

Morrissey, A. (2014). *Stratigraphic Framework and Quaternary Paleolimnology of the Lake Turkana Rift*. KenyaNew York: Ph.D. Dissertation, Department of Earth Sciences, Syracuse University.

Morrissey, A., and Scholz, C. A. (2014). Paleohydrology of Lake Turkana and its Influence on the Nile River System. *Palaeogeogr. Palaeoclimatol. Palaeoecol.* 403, 88–100. doi:10.1016/j.palaeo.2014.03.029

Morrissey, A., Scholz, C. A., and Russell, J. M. (2017). Late Quaternary TEX86 Paleotemperatures from the World's Largest Desert lake, Lake Turkana, Kenya. *J. Paleolimnol* 59 (1), 103–117. doi:10.1007/s10933-016-9939-6

NASA (2019). Worldview Snapshots [Online]. Earth Observing System Data and Information System (EOSDIS). https://wvs.earthdata.nasa.gov. (Accessed July 29, 2019).

Nicholson, S. E. (2017). Climate and Climatic Variability of Rainfall over Eastern Africa. *Rev. Geophys.* 55 (3), 590–635. doi:10.1002/2016rg000544

Nicholson, S. E. (2018). The ITCZ and the Seasonal Cycle over Equatorial Africa. *Bull. Am. Meteorol. Soc.* 99 (2), 337–348. doi:10.1175/bams-d-16-0287.1

Nicholson, S. (2000). The Nature of Rainfall Variability over Africa on Time Scales of Decades to Millenia. *Glob. Planet. Change* 26, 137–158. doi:10.1016/s0921-8181(00)00040-0

Novello, A., Barboni, D., Sylvestre, F., Lebatard, A.-E., Paillès, C., Bourlès, D. L., et al. (2017). Phytoliths Indicate Significant Arboreal Cover at *Sahelanthropus*

Type Locality TM266 in Northern Chad and a Decrease in Later Sites. *J. Hum. Evol.* 106, 66–83. doi:10.1016/j.jhevol.2017.01.009

Nutz, A., Schuster, M., Ghienne, J.-F., Roquin, C., and Bouchette, F. (2016). Wind-driven Waterbodies: a New Category of lake within an Alternative Sedimentologically-Based lake Classification. *J. Paleolimnol* 59 (2), 189–199. doi:10.1007/s10933-016-9894-2

Nutz, A., Schuster, M., Boës, X., and Rubino, J.-L. (2017). Orbitally-driven Evolution of Lake Turkana (Turkana Depression, Kenya, EARS) between 1.95 and 1.72 Ma: A Sequence Stratigraphy Perspective. *J. Afr. Earth Sci.* 125, 230–243. doi:10.1016/j.jafrearsci.2016.10.016

Nutz, A., Schuster, M., Barboni, D., Gassier, G., Van Bocxlaer, B., Robin, C., et al. (2020). Plio-Pleistocene Sedimentation in West Turkana (Turkana Depression, Kenya, East African Rift System): Paleolake Fluctuations, Paleolandscapes and Controlling Factors. *Earth-Science Rev.* 211, 103415. doi:10.1016/j.earscirev.2020.103415

Olang, M. O. (1984). "Vegetation Cover Assessment in Turkana District, Kenya," in Proceedings of the Workshop on Land Evaluation and Extensive Grazing (LEEG) Addis Ababa, (Ethiopia. Netherlands: International Institute for Land Reclamation and Improvement), 183–219.

Oliveras, I., and Malhi, Y. (2016). Many Shades of green: the Dynamic Tropical Forest-Savannah Transition Zones. *Phil. Trans. R. Soc. B* 371 (1703), 20150308. doi:10.1098/rstb.2015.0308

Patterson, D. B., Braun, D. R., Behrensmeyer, A. K., Merritt, S., Zliobaite, I., Reeves, J. S., et al. (2017). Ecosystem Evolution and Hominin Paleobiology at East Turkana, Northern Kenya between 2.0 and 1.4 Ma. *Palaeogeogr. Palaeoclimatol. Palaeoecol.* 481, 1–13. doi:10.1016/j.palaeo.2017.05.001

Patterson, D. B., Braun, D. R., Allen, K., Barr, W. A., Behrensmeyer, A. K., Biernat, M., et al. (2019). Comparative Isotopic Evidence from East Turkana Supports a Dietary Shift within the Genus *Homo*. *Nat. Ecol. Evol.* 3 (7), 1048–1056. doi:10.1038/s41559-019-0916-0

Pays, O., Blanchard, P., Valeix, M., Chamaille-Jammes, S., Duncan, P., and Periquet, S. (2012). Detecting Predators and Locating Competitors While Foraging: An Experimental Study of a Medium-Sized Herbivore in an African Savanna. *Oecologia* 169, 419–430. doi:10.1007/s00442-011-2218-3

Peters, M. E., and Higuera, P. E. (2007). Quantifying the Source Area of Macroscopic Charcoal with a Particle Dispersal Model. *Quat. Res.* 67 (2), 304–310. doi:10.1016/j.yqres.2006.10.004

Polanco-Martínez, J. M. (2020). RolWinMulCor: An R Package for Estimating Rolling Window Multiple Correlation in Ecological Time Series. *Ecol. Inform.* 60, 101163. doi:10.1016/j.ecoinf.2020.101163

Prell, W. L., and Kutzbach, J. E. (1987). Monsoon Variability over the Past 150,000 Years. *J. Geophys. Res.* 92, 8411–8425. doi:10.1029/jd092id07p08411

Probert, J. R., Parr, C. L., Holdo, R. M., Anderson, T. M., Archibald, S., Courtney Mustaphi, C. J., et al. (2019). Anthropogenic Modifications to Fire Regimes in the Wider Serengeti-Mara Ecosystem. *Glob. Change Biol.* 25, 3406–3423. doi:10.1111/gcb.14711

Quigley, K. M., and Anderson, T. M. (2014). Leaf Silica Concentration in Serengeti Grasses Increases with Watering But Not Clipping: Insights From a Common Garden Study and Literature Review. *Front. Plant Sci.* 5, 568. doi:10.3389/fpls.2014.00568

Quinn, R. L., Lepre, C. J., Wright, J. D., and Feibel, C. S. (2007). Paleogeographic Variations of Pedogenic Carbonate δ13C Values from Koobi Fora, Kenya: Implications for floral Compositions of Plio-Pleistocene Hominin Environments. *J. Hum. Evol.* 53 (5), 560–573. doi:10.1016/j.jhevol.2007.01.013

R Core Team (2018). *R: A Language and Environment for Statistical Computing [Online]*. Vienna, Austria. Available: https://www.R-project.org/: R Foundation for Statistical Computinghttps://www.R-project.org/.

Roesch, A., and Schmidbauer, H. (2018). WaveletComp: Computational Wavelet Analysis. R package version 1.1. Available: https://CRAN.R-project.org/package=WaveletComp.

Rossignol-Strick, M. (1983). African Monsoons, an Immediate Climate Response to Orbital Insolation. *Nature* 304 (5921), 46–49. doi:10.1038/304046a0

Ruddiman, W. F. (2008). *Earth's Climate*. New York: W. H. Freeman and Company.

Rugemalila, D. M., Anderson, T. M., and Holdo, R. M. (2016). Precipitation and Elephants, Not Fire, Shape Tree Community Composition in Serengeti National Park, Tanzania. *Biotropica* 48 (4), 476–482. doi:10.1111/btp.12311

Schuster, M., and Nutz, A. (2019). Lake-level changes and hominin occupations in the arid Turkana basin during volcanic closure of the Omo River outflows to the Indian Ocean - comment on the published paper by Boës et al. Quaternary Research (2018), Vol. 91.2, 892-909. *Quat. Res.* 92 (2), 598–600. doi:10.1017/qua.2019.14

Sier, M. J., Langereis, C. G., Dupont-Nivet, G., Feibel, C. S., Joordens, J. C. A., van der Lubbe, J. H. J. L., et al. (2017). The Top of the Olduvai Subchron in a High-Resolution Magnetostratigraphy from the West Turkana Core WTK13, Hominin Sites and Paleolakes Drilling Project (HSPDP). *Quat. Geochronol.* 42, 117–129. doi:10.1016/j.quageo.2017.08.004

Sponheimer, M., Alemseged, Z., Cerling, T. E., Grine, F. E., Kimbel, W. H., Leakey, M. G., et al. (2013). Isotopic Evidence of Early Hominin Diets. *Proc. Natl. Acad. Sci.* 110 (26), 10513–10518. doi:10.1073/pnas.1222579110

Stewart, K. M. (2014). Environmental Change and Hominin Exploitation of C4-Based Resources in Wetland/savanna Mosaics. *J. Hum. Evol.* 77, 1–16. doi:10.1016/j.jhevol.2014.10.003

Strömberg, C. A. E. (2009). Methodological Concerns for Analysis of Phytolith Assemblages: Does Count Size Matter? *Quat. Int.* 193 (1–2), 124–140. doi:10.1016/j.quaint.2007.11.008

Trauth, M. H., Maslin, M. A., Deino, A., and Strecker, M. R. (2005). Late Cenozoic Moisture History of East Africa. *Science* 309 (5743), 2051–2053. doi:10.1126/science.1112964

Tuenter, E., Weber, S. L., Hilgen, F. J., and Lourens, L. J. (2003). The Response of the African Summer Monsoon to Remote and Local Forcing Due to Precession and Obliquity. *Glob. Planet. Change* 36 (4), 219–235. doi:10.1016/s0921-8181(02)00196-0

Turner, R., Kelly, A., and Roberts, N. (2008). "A Critical Assessment and Experimental Comparison of Microscopic Charcoal Extraction Methods," in *Charcoals from the Past: Cultural and Palaeoenvironmental Implications*. Editors G. Fiorentino and D. Margi (Oxford: Archaeopress), 225–272.

Uno, K. T., Polissar, P. J., Kahle, E., Feibel, C., Harmand, S., Roche, H., et al. (2016). A Pleistocene Palaeovegetation Record from Plant Wax Biomarkers from the Nachukui Formation, West Turkana, Kenya. *Phil. Trans. R. Soc. B.* 371 (1698), 1–10. doi:10.1098/rstb.2015.0235

Vachula, R. S. (2021). A Meta-Analytical Approach to Understanding the Charcoal Source Area Problem. *Palaeogeogr. Palaeoclimatol. Palaeoecol.* 562. doi:10.1016/j.palaeo.2020.110111

van Breugel, P., Kindt, R., Lillesø, J. P. B., Bingham, M., Demissew, S., Dudley, C., et al. (2015). *Potential Natural Vegetation Map of Eastern Africa (Burundi, Ethiopia, Kenya, Malawi, Rwanda, Tanzania, Uganda and Zambia). Version 2.0.* (Forest & Landscape Denmark and World Agroforestry Centre (ICRAF). URL: http://vegetationmap4africa.org.

van der Lubbe, H. J. L., Krause-Nehring, J., Junginger, A., Garcin, Y., Joordens, J. C. A., Davies, G. R., et al. (2017). Gradual or Abrupt? Changes in Water Source of Lake Turkana (Kenya) during the African Humid Period Inferred from Sr Isotope Ratios. *Quat. Sci. Rev.* 174, 1–12. doi:10.1016/j.quascirev.2017.08.010

van Wyk, J. (1979). "A General Account of the Grass Cover of Africa," in *Ecology of Grasslands and Bamboolands of the World*. Editor M. Numata (The Hague: Junk BV Publishers), 124–132.

Viste, E., and Sorteberg, A. (2013). Moisture Transport into the Ethiopian highlands. *Int. J. Climatol.* 33 (1), 249–263. doi:10.1002/joc.3409

Whitlock, C., and Anderson, R. S. (2003). "Fire History Reconstructions Based on Sediment Records from Lakes and Wetlands,"in *Fire and Climatic Change in Temperate Ecosystems of the Western Americas*. New York: Springer, 3–31.

Wood, B., and Leakey, M. (2011). The Omo-Turkana Basin Fossil Hominins and Their Contribution to Our Understanding of Human Evolution in Africa. *Evol. Anthropol.* 20 (6), 264–292. doi:10.1002/evan.20335

Wynn, J. G. (2004). Influence of Plio-Pleistocene Aridification on Human Evolution: Evidence from Paleosols of the Turkana Basin, Kenya. *Am. J. Phys. Anthropol.* 123 (2), 106–118. doi:10.1002/ajpa.10317

Yang, W., Seager, R., Cane, M. A., and Lyon, B. (2015). The Annual Cycle of East African Precipitation. *J. Clim.* 28 (6), 2385–2404. doi:10.1175/jcli-d-14-00484.1

Yost, C. L., Blinnikov, M. S., and Julius, M. L. (2013). Detecting Ancient Wild rice (*Zizania* Spp. L.) Using Phytoliths: a Taphonomic Study of Modern Wild rice in Minnesota (USA) lake Sediments. *J. Paleolimnol* 49 (2), 221–236. doi:10.1007/s10933-012-9670-x

Yost, C. L., Ivory, S. J., Deino, A. L., Rabideaux, N. M., Kingston, J. D., and Cohen, A. S. (2021). Phytoliths, Pollen, and Microcharcoal from the Baringo Basin, Kenya Reveal savanna Dynamics during the Plio-Pleistocene Transition. *Palaeogeogr. Palaeoclimatol. Palaeoecol.* 570, 109779. doi:10.1016/j.palaeo.2020.109779

Yuretich, R. F., and Cerling, T. E. (1983). Hydrogeochemistry of Lake Turkana, Kenya: Mass Balance and mineral Reactions in an Alkaline lake. *Geochimica et Cosmochimica Acta* 47 (6), 1099–1109. doi:10.1016/0016-7037(83)90240-5

Conflict of Interest: The authors declare that the research was conducted in the absence of any commercial or financial relationships that could be construed as a potential conflict of interest.

Publisher's Note: All claims expressed in this article are solely those of the authors and do not necessarily represent those of their affiliated organizations, or those of the publisher, the editors and the reviewers. Any product that may be evaluated in this article, or claim that may be made by its manufacturer, is not guaranteed or endorsed by the publisher.

frontiers in Earth Science

ORIGINAL RESEARCH
published: 20 September 2021
doi: 10.3389/feart.2021.683010

Exploring the Past Biosphere of Chew Bahir/Southern Ethiopia: Cross-Species Hybridization Capture of Ancient Sedimentary DNA from a Deep Drill Core

Johanna Krueger[1,2], *Verena Foerster*[3], *Martin H. Trauth*[4], *Michael Hofreiter*[1] *and Ralph Tiedemann*[1]*

[1]Institute of Biochemistry and Biology, University of Potsdam, Potsdam, Germany, [2]Institut de Biologia Evolutiva, (CSIC-Universitat Pompeu Fabra), Parc de Recerca Biomèdica de Barcelona, Barcelona, Spain, [3]Institute of Geography Education, University of Cologne, Köln, Germany, [4]Institute of Geosciences, University of Potsdam, Potsdam, Germany

OPEN ACCESS

Edited by:
Marco J. L. Coolen, Curtin University, Australia

Reviewed by:
T. Bence Viola, University of Toronto, Canada
Linda Armbrecht, University of Adelaide, Australia

***Correspondence:**
Ralph Tiedemann
tiedeman@uni-potsdam.de

Specialty section:
This article was submitted to Paleontology, a section of the journal Frontiers in Earth Science

Received: 19 March 2021
Accepted: 18 August 2021
Published: 20 September 2021

Citation:
Krueger J, Foerster V, Trauth MH, Hofreiter M and Tiedemann R (2021) Exploring the Past Biosphere of Chew Bahir/Southern Ethiopia: Cross-Species Hybridization Capture of Ancient Sedimentary DNA from a Deep Drill Core. Front. Earth Sci. 9:683010. doi: 10.3389/feart.2021.683010

Eastern Africa has been a prime target for scientific drilling because it is rich in key paleoanthropological sites as well as in paleolakes, containing valuable paleoclimatic information on evolutionary time scales. The Hominin Sites and Paleolakes Drilling Project (HSPDP) explores these paleolakes with the aim of reconstructing environmental conditions around critical episodes of hominin evolution. Identification of biological taxa based on their sedimentary ancient DNA (sedaDNA) traces can contribute to understand past ecological and climatological conditions of the living environment of our ancestors. However, sedaDNA recovery from tropical environments is challenging because high temperatures, UV irradiation, and desiccation result in highly degraded DNA. Consequently, most of the DNA fragments in tropical sediments are too short for PCR amplification. We analyzed sedaDNA in the upper 70 m of the composite sediment core of the HSPDP drill site at Chew Bahir for eukaryotic remnants. We first tested shotgun high throughput sequencing which leads to metagenomes dominated by bacterial DNA of the deep biosphere, while only a small fraction was derived from eukaryotic, and thus probably ancient, DNA. Subsequently, we performed cross-species hybridization capture of sedaDNA to enrich ancient DNA (aDNA) from eukaryotic remnants for paleoenvironmental analysis, using established barcoding genes (*cox1* and *rbcL* for animals and plants, respectively) from 199 species that may have had relatives in the past biosphere at Chew Bahir. Metagenomes yielded after hybridization capture are richer in reads with similarity to *cox1* and *rbcL* in comparison to metagenomes without prior hybridization capture. Taxonomic assignments of the reads from these hybridization capture metagenomes also yielded larger fractions of the eukaryotic domain. For reads assigned to *cox1*, inferred wet periods were associated with high inferred relative abundances of putative limnic organisms (gastropods, green algae), while inferred dry periods showed increased relative abundances for insects. These findings indicate that cross-species hybridization capture can be an effective approach to enhance the

information content of sedaDNA in order to explore biosphere changes associated with past environmental conditions, enabling such analyses even under tropical conditions.

Keywords: Chew Bahir, hybridization capture, ICDP, paleoclimate, past biosphere, sedaDNA, sediment core

INTRODUCTION

Paleogenomics Applied to Sediment Samples

The characterization of sediments from the Chew Bahir basin is part of the Hominin Sites and Paleolakes Drilling Project (HSPDP), which encompasses six drill sites within the East African Rift System (**Figure 1**) (Cohen et al., 2009; Cohen et al., 2016; Campisano et al., 2017). Eastern Africa is known for the discovery of hominin fossils, including the famous *Australopithecus afarensis* female "Lucy", found 30 km from the HSPDP Northern Awash drill site, and the archaic *Homo sapiens* fossils Omo I and Omo II, found only 90 km to the west from the Chew Bahir drill site (Cohen et al., 2016; Campisano et al., 2017). The influence of global and local environmental instability on human evolution has been a matter of debate and many competing hypotheses on the relationship between both exist (e.g. Potts, 2013; Maslin et al., 2015; Mounier and Mirazón Lahr, 2019). Eastern Africa has been a traditional setting for testing hypotheses on environment-evolution linkages because of its rich hominin fossil record and the ability to date fossil wearing strata (Trauth et al., 2010; Campisano et al., 2017). For these reasons, the sediment drill cores from the HSPDP offer an extraordinary chance to obtain paleoclimatic and paleoenvironmental data to further complement the understanding of climate change and of selective regimes in hominin evolution.

The investigation of sedaDNA is a relatively new approach in the study of deep sediment drill cores. Traditionally, the analysis of organisms in a sediment record often either relied on microscopy (then restricted to taxa with remnant hard structures, e.g. diatoms) or biogeochemical indicators for certain bio-productivities, an approach with very coarse taxonomic resolution (e.g. Stoof-Leichsenring et al., 2011). sedaDNA analysis does not depend on conservation of biomaterial that is suitable for microscopy and may hence considerably widen the range of taxa retrieved (e.g., limnoplanctic rotifers as good indicators of changes in salinity through time, Epp et al., 2010).

It is widely recognized that cold temperatures are beneficial for the preservation of aDNA in sediments or fossils (Pääbo et al., 2004; Epp et al., 2012; Hofreiter et al., 2015). In tropical settings, very high temperatures challenge sedaDNA preservation. Furthermore, during dry episodes, desiccation and subsequent exposition of the surface and littoral sediments to ultraviolet light and atmospheric oxygen likely reduce the chances of conservation of organic material, including DNA. Thus, most sedaDNA studies on sediment cores have focused on arctic or colder temperate regions (Parducci et al., 2017). For the few tropical sites included in sedaDNA studies (Epp et al., 2010; Epp et al., 2011; Stoof-Leichsenring et al., 2012), relatively recent sediments from short cores were analyzed. To date, only few publications cover high throughput sequencing (HTS) methods on sedaDNA of a tropical origin (Bremond et al., 2017). Although the first protocols for sedaDNA extraction were already published in the early 1980s (Torsvik, 1980), HTS has facilitated the implementation of paleogenetic approaches mostly for two reasons: first, it does not depend on any prior knowledge about the sedaDNA since it is independent of primers. Second, also smaller fragments that may not be amplified by classical PCR-based approaches can still be retrieved and sequenced (Dabney et al., 2013).

Studies on sedaDNA without any prior PCR amplification are usually compromised by a large part of the revealed metagenome originating from modern DNA of the prokaryote-rich deep biosphere (Magnabosco et al., 2019), which is barely informative about a site's past ecosystem. As the extant deep biosphere mostly consists of prokaryotes, the eukaryotic fraction of a metagenome is particularly attractive for paleoenvironmental studies (Kisand et al., 2018). Not only are these DNA fragments much less likely to originate from extant organisms, but they also represent a large variety of typically studied groups, such as diatoms (Stoof-Leichsenring et al., 2012), rotifers (Epp et al., 2010), ostracods (Viehberg et al., 2018), or higher plants (Bremond et al., 2017).

DNA hybridization capture (a.k.a. target enrichment) has already been successfully applied to enrich low-concentration DNA-fragments of interest from aDNA samples including sediments (Slon et al., 2017; Murchie et al., 2020; Vernot et al., 2021). It relies on the ability of the DNA to hybridize with complementary nucleic acids, the so-called baits. These baits can either consist of DNA or RNA. While hybridized DNA fragments are retained using biotin-streptavidin binding, unwanted other fragments can be removed, at least in part, during washing steps following the hybridization. A major advantage is that the two hybridizing nucleic acid strands do not have to display perfect complementarity (Peñalba et al., 2014; Paijmans et al., 2016). Base mismatches and only partial overlap can be tolerated, such that also short DNA fragments, to which PCR primer annealing might have failed, can get enriched. This point is of particular importance since aDNA can have mismatches to sequences from extant organisms for various reasons, such as originating from a related species or sequence damage due to degradation. In addition, hybridization capture is less sensitive to contamination because DNA fragments of all lengths are targeted more equally, whereas PCR prefers longer fragments (Hofreiter et al., 2015).

Here we present a sedaDNA study on selected samples of the upper 70 m of two ~280 m long lacustrine sediment cores from the paleolake Chew Bahir in Ethiopia (Foerster et al., in rev.). The objective of this metagenomic study is to contribute to the characterization of the past environment around the Chew

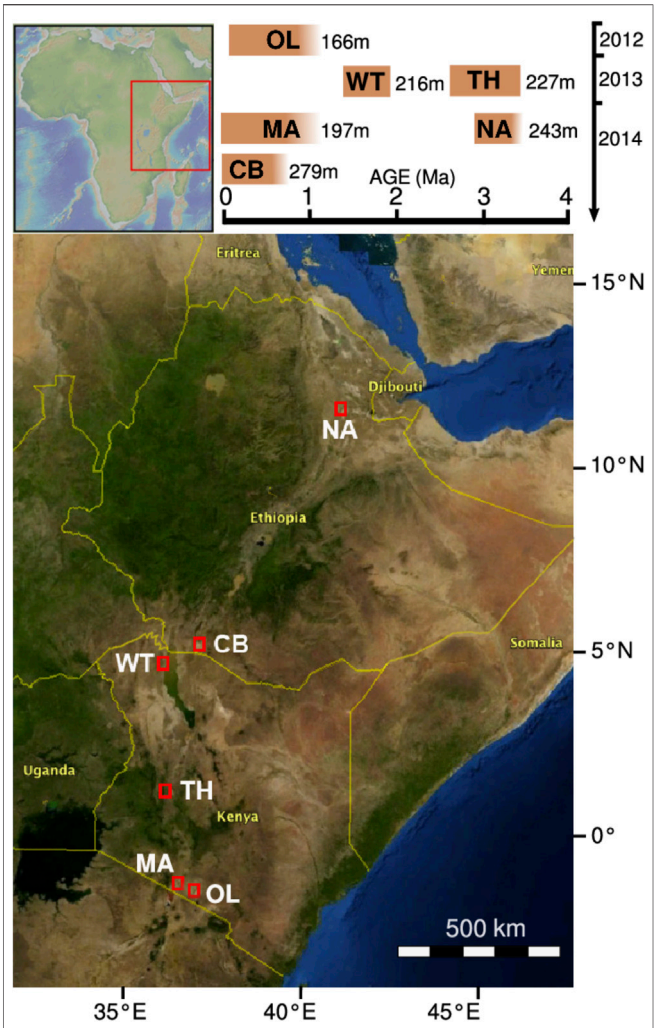

FIGURE 1 | Drilling sites of the HSPDP. The graph on the top right indicates on its horizontal axis the estimated time spans before present that the drill cores correspond to. Its vertical axis indicates the year of core retrieval. From North to South: NA, Northern Awash; CB, Chew Bahir; WT, West Turkana; TH, Baringo Tugen Hills; MA, Lake Magadi; OL, Olorgesailie/Koora Plain. Map based on https://hspdp.asu.edu/?q=drill-sites and Cohen et al. (2016).

Bahir basin and to test the feasibility of analyzing extremely degraded sedaDNA. We chose to utilize DNA hybridization capture for these sedaDNA studies, as hybridization capture has been proven superior to direct PCR amplification for highly degraded DNA (Dabney et al., 2013). We aimed at enriching a large spectrum of eukaryotic sedaDNA. A selection of metabarcoding marker gene sequences (from the established barcoding genes *cox1* and *rbcL* for animals and plants, respectively) served as a template for hybridization capture bait design. Enriching for these two genes in defined taxa facilitates finding matches in reference DNA databases. In particular, *cox1* is widely used as universal marker for species identification and constitutes the most sequenced genetic region of animal genomes (Pentinsaari et al., 2016) with over 8 million entries in the BOLDSYSTEMS database (July 2021) (Hebert and Ratnasingham, 2007). The use of *rbcL* is more limited, mainly due to small reference databases. BOLDSYSTEMS has not published the exact number of *rbcL* entries, but describes them as "very few" (https://www.boldsystems.org/index.php/IDS_OpenIdEngine, July 2021).

Regional Setting

Today, Chew Bahir is a saline mudflat at the southern border of Ethiopia at approximately 4.7071°N, 36.8524°E and an altitude of approximately 570 m asl (Foerster et al., 2012; Viehberg et al., 2018). While the tectonic basin is known to have been repeatedly filled with an up to 50 m deep freshwater lake during humid climate phases in the past, it is today under arid conditions and only episodically filled with a shallow water body during the rainy season (Foerster et al., 2012; Fischer et al., 2020a). The region around the Chew Bahir basin as the southern end point of the Main Ethiopian Rift (MER) is considered to be part of a prehistoric human migration corridor and the adjacent southwestern Ethiopian Highlands have been hypothesized to be a refuge area during episodes of drier climate (Brandt et al., 2012; Foerster et al., 2015). It is characterized by tropical climate with almost constant mean annual temperatures between 25 and 30°C and strong seasonality in precipitation with one rainy season named "Belg" from March to May and another named "Kiremet" from June to September (Foerster et al., 2012). The basin is filled with ~3 km fluvio-lacustrine sediments, which record the climate particularly well, due to the sensitivity of the catchment area with large differences in relief to even minor shifts in the hydroclimate (Trauth et al., 2010; Fischer et al., 2020b). Deposits with coarser silt and sand beds are more abundant in the upper 100 m of the sediment column, while discrete layers of shell, fish bone, and plant debris could be identified throughout the entire core (Campisano et al., 2017).

Before the deep drilling campaign in the Chew Bahir basin started as part of the HSPDP in 2014, six short cores, up to 22 m long, had been collected in 2009–2010 from this site in pilot studies (e.g. Foerster et al., 2012; Trauth et al., 2018). Another 40 m long core from the center of the basin was drilled in March 2014 (Cohen et al., 2016; Viehberg et al., 2018). The pilot cores have been characterized in terms of material, age, and fossil record (Foerster et al., 2012; Foerster et al., 2014; Foerster et al., 2015; Trauth et al., 2015; Foerster et al., 2018; Trauth et al., 2018; Trauth et al., 2019). The fossils encompass fish bones, ostracods, molluscs, and diatoms (Foerster et al., 2012; Viehberg et al., 2018). Also, fossilized micro-charcoal was found as remains of plant material, but there is no pollen record, which is interpreted as a sign that biomaterial in the sediments is fairly degraded (Foerster et al., 2012), primarily due to the regular exposure of sedimentary deposits to oxygen. Among the molluscs, mainly shells of *Melanoides tuberculata* were found, a gastropod that is seen as an indicator for water levels below ~10 m (Foerster et al., 2012). The diatom findings originate predominantly from *Aulacoseira* and *Cyclostephanus*, but the genera *Nitzschia*, *Synedra*, *Cymbella*, *Cyclotella*, and *Achnanthes* could also be identified. In contrast to the other species that prefer fresh water, *Aulacoseira* is tolerant to a broader range of salinity

and pH and dominates especially in sections that correspond to presumably shallow water levels. In times of very low water levels, and therefore very saline and alkaline conditions, the diatom record declines sharply (Foerster et al., 2012; Foerster et al., 2014). Furthermore, as a typical plant remain, phytoliths have been examined in the third pilot core CB-03 in a section that corresponds to ~5–12 ka BP (Trauth et al., 2018; Fischer et al., 2020a). The majority of phytoliths belongs to the group of mesic C4 grass types, but xeric C4 and C3 grass types are also found (Fischer et al., 2020b). Four ostracod species have been identified in the sediment core from the middle of the basin (HSPDP-CHB14-1A) (Viehberg et al., 2018): *Limnocythere* cf. *borisi*, *Darwinula stevensoni*, *Ilyocypris* sp., and *Heterocypris giesbrechti*. *Limnocythere* cf. *borisi* is known to have fragile valves and their good preservation is interpreted as evidence for undisturbed sedimentation.

These findings on bioindicators served as an orientation for the application of molecular genetic methods on the sediments from the Chew Bahir basin and were considered during bait design.

MATERIALS AND METHODS

Core Drilling and Sampling

The sediment samples originate from two drill cores taken from the southwestern Chew Bahir basin in November-December 2014 (**Figure 1**). The duplicate cores were retrieved in close proximity to each other, core HSPDP-CHB12-2A at 4.7612°N, 36.7668°E and core HSPDP-CHB14-2B at 4.7613°N, 36.7670°E (Cohen et al., 2016; Campisano et al., 2017). They are 278.58 mbs (= meters below surface) (core HSPDP-CHB14-2A) and 266.38 mbs (core HSPDP-CHB14-2B) long and were merged into a composite core, ~292.76 mcd (= meters composite depth, hereinafter written as ~292.76 m for simplicity) long, after correlating the physical properties and imagery of the cores 2A and 2B (Arnold et al., 2021; Duesing et al., 2021; Roberts et al., 2021; Schaebitz et al., 2021; Trauth et al., 2021). Together they replenish missing data in each other and the composite core with ~90% continuity will be referred to as one core in the following. According to the results of radiometric age determination and age modeling, this record represents the last ~620 ka before present (Roberts et al., 2021).

The collected material consists of almost three metric tonnes of mostly calcareous clays and silts (Cohen et al., 2016). During transport and subsequent storing until further treatment, samples were kept at 4–10°C. The cores were sampled and are stored in the facilities of the National Lacustrine Core Facility (LacCore) of the University of Minnesota in Minneapolis, United States. Approximately 3–5 g of sediment per sample were transferred into 5 ml plastic falcon tubes without any buffer and kept at −80°C. Samples for sedaDNA analysis were taken at a resolution of 2 cm. During sampling, methods to avoid cross-sample and modern human DNA contamination were applied, in particular changing gloves between samples and removal of outer layers of the sediments. Since it was not known to what depth DNA was conserved in sufficient quality, 11 samples from the upper section of both cores down to 10 m were selected. When choosing samples, those with known occurrences of organisms (e.g., shell, plant, or bone remains) were preferred. One sample at the depth of ~70 m was added to this study to explore whether deeper samples still deliver meaningful genetic data, resulting in a total of 12 samples. Another sample at 41.72 m was originally included, but discarded after sequencing, since it exhibited substantial amounts of contamination with putative modern human DNA. Throughout this article, we label our samples relative to their depths in the composite core. "A" or "B" in the sample IDs display whether the sediment sample originates from core HSPDP-CHB14-2A or HSPDP-CHB14-2B. The following sample number indicates the sample's position in meters below surface of the respective core (mbs). Most samples are younger than ~30 ka, with a single sample from ~150 ka, according to the *RRMay2019* age model of Roberts et al. (2021).

DNA Extraction and Library Preparation

All materials and chemicals that can persist UV sterilization were UV-treated before use. Tools and surfaces were treated with a DNA-degrading agent (DNA-ExitusPlusTM, AppliChem). All steps that involved unamplified aDNA were performed in dedicated aDNA laboratories. For every third sample a mock extraction ("extraction blank") without any sample material was added. Gloves were changed between the opening of the tube of every sample. The samples were initially sampled at 3–4 g in order to work with the DNeasy PowerMax Soil Kit (QIAGEN), which is designed for input masses of up to 10 g. However, we moved to other protocols more suitable for highly degraded fragments. We decided against further subsampling the samples in order to avoid any (cross-) contamination. DNA extraction combined protocols published by Dabney et al. (2013) and Wales et al. (2014) with modifications for sediment samples by Pedersen et al. (2016). The amounts of lysis buffer were adapted to the sample size, resulting in 5 ml of lysis buffer (68 mM N-lauroylsarcosine sodium salt, 50 mM Tris-HCl pH 8.0, 150 mM NaCl, and 20 mM EDTA pH 8.0, with 1.0 ml 2-mercaptoethanol and 1.5 ml 1 M DTT added to every 30 ml immediately before extraction) being added to 3–4 g wet weight of sediment sample (all samples, except those at 2.17, 41.72, 71.65 m). After the overnight incubation at 37°C, the samples were centrifuged at 5,000 × g for 5 min. The approximately 2 ml of supernatants were further processed according to Dabney et al. (2013) using 650 µl PE buffer during the washing step. Samples at 2.17, 41.72 m (later discarded due to putative contamination), and 71.65 m were extracted in a later batch using 3 ml of the extraction buffer of the protocol of Dabney et al. (2013) to test applicability of this protocol to sediment samples. Samples at 0.93 and 5.21 m had a turbid, brownish eluate, and the samples at 2.17 and 71.65 m a turbid, light brownish one. The color originated from particles that could be removed by short centrifugation at low speed.

We used 20 µl of every extract, including the extraction blanks, for library preparation right after extraction based on a protocol by Gansauge and Meyer (2013), with modifications suggested by Korlević et al. (2015). As for extraction, for every third sample a mock library preparation ("library blank") was performed. In this method, the Illumina P5 adapter is truncated at the 3' end by five base pairs (GATCT) in comparison to the standard P5

adapter. Library preparation was performed with the following modifications: the optional step of removing deoxyuracils using the Afu (*Archaeoglobus fulgidus*) uracil-DNA glycosylase (UDG) was included. For cost reduction, the amount of Circligase II was reduced from 4 to 2 µl (100 U/µl) and as compensation, the incubation prolongated from 1 h to overnight in order to compensate for the smaller amount of enzyme. To account for this reduction, 2 µl more of nuclease free water were added to the uracil excision reaction in step 1 of the library preparation protocol. Two microlitres (10 U/µl) of the Klenow fragment of DNA Polymerase I were used, which allows for circumvention of the blunt-end repair in step 16 of the original protocol. According to this, the mastermix contained 0.4 µl of dNTP mix and additional 1.1 µl of nuclease free water. Incubation temperatures and times were adjusted to the different enzyme. The libraries were first incubated at 25°C in a preheated thermocycler for 5 min and then at 35°C for another 25 min. After library preparation, a qPCR was performed on 1 µl of sample, with three replicates per library, in order to estimate the optimal number of PCR cycles for indexing of the library molecules and library amplification (Basler et al., 2017). The underlying principle is that libraries with low DNA concentrations, in particular blanks, will need more qPCR cycles to reach the flexing point in the logistic growth curve. As compensation, these libraries will undergo more PCR cycles during library amplification than regular samples with presumably higher DNA concentrations. The qPCR was performed in a PikoReal 96 Real-Time PCR machine (Thermo Fisher Scientific TCR0096).

The reagents for library amplification and indexing comprised 44.8 µl of nuclease free water, 8 µl of 10 × AccuPrimeTM Pfx reaction mix (ThermoFisher Scientific), 0.8 µl of 2.5 U/µl AccuPrimeTM Pfx polymerase, 3.2 µl of P5 indexing primer, 3.2 µl of P7 indexing primer and 20 µl of each library. The PCR reactions were executed starting with 2 min at 95°C, followed by the number of cycles calculated according to Basler et al. (2017) consisting of 15 s at 95°C denaturation, 30 s annealing at 60°C and 1 min extension at 68°C. The libraries were cleaned up with the MinElute PCR Purification Kit (QIAGEN) following the manufacturer's instructions. They were then quantified with the Qubit® 2.0 fluorometer and the distribution of DNA fragment lengths was measured with an Agilent 2200 TapeStation with a D1000 cassette.

DNA Hybridization Capture

Taxon-specific RNA-baits for hybridization capture were synthesized according to sequence templates. For animals, sequences of the mitochondrial *cytochrome oxidase subunit 1* (*cox1* or *COI*) gene were used as barcoding marker for species identification. The sequence of the chloroplast *ribulose bisphosphate carboxylase large chain* (*rbcL*) served as the universal barcoding marker for higher plants and diatoms (Wales et al., 2014). A set of selected target species was compiled based on a literature research and microscopic evidence. Results from the pilot core studies on paleolake Chew Bahir provided initial information on which potential target species to expect in the long core, including gastropod, teleost, and plant species (Foerster et al., 2012; Foerster et al., 2014). The "Atlas of the potential vegetation of Ethiopia" (Friis et al., 2011) provided an impression of the current flora around the Chew Bahir basin which was considered to select target plant species.

For all chosen taxa or their closest relatives, sequence information for the barcoding genes was retrieved from the GenBank sequence database (ncbi) between May and August 2017. Often, the sequences available at GenBank covered the gene loci only partially. In total, 223 metabarcoding sequences from 199 different species were collected (**Supplementary Table S1**). For these sequences, baits were produced by Arbor Biosciences™ in form of a myBaits® Custom Target Capture Kit. The final set contained 19,584 baits, each at a length of 60 bp. The synthesized baits were short overlapping fragments representing the whole bait-template sequences of *cox1* or *rbcL* of the respective taxon. The "tiling density" of the bait set was 4 ×, i.e., any base in a sequence was covered by four different 60 bp-baits. According to empirical experiences of the suppliers, one extra copy of baits with <28% GC content, one extra copy of baits with ≥50% and <60% GC content, and four extra copies of baits with >60% GC content were included in order to prevent capture biases. Ambiguous bases (e.g. the IUPAC code "Y" for pyrimidines) in the reference sequences were replaced at equal ratios with a single candidate base. Undetermined bases, indicated by an "N" in the DNA sequence, were always replaced with thymine, which is the standard procedure of the bait manufacturer. For taxonomic groups underrepresented in our taxon selection (e.g. there were far fewer bird than diatom species selected), two to three extra copies of each bait were added.

Hybridization capture reactions were performed using the myBaits® In-Solution Sequence Capture for Targeted High-Throughput Sequencing Custom Kit (designs with 1–20 k probes) by Arbor Biosciences™. The recommended input is 100–500 ng of library DNA, which equaled 7 µl of our libraries (DNA concentrations of amplified libraries between 14 and 72 ng/µl, extraction blanks 10–23 ng/µl, library blanks 9–15 ng/µl). In order to reduce the number of samples undergoing hybridization capture, the five extraction blanks (four from extraction batch one, one from batch two) and five library blanks were pooled separately, resulting in one pooled extraction blank and one pooled library blank. The capture experiments were conducted according to the manufacturer's instructions with the following modifications: all capture reactions were incubated for 45 h at 55°C as recommended by the manufacturer for highly degraded samples. Due to the truncation of the P5-adapter in the library (according to Gansauge and Meyer, 2013), the kit's standard blocking oligos were not used. Instead of adding 0.5 µl of the BLOCK#3 solution, 0.9 µl of 67 µM custom blocking oligos, which are suitable for the single stranded library, were added to each reaction.

Previous experiences show that dilution of commercial baits is a cost-effective way of hybridization capture, even of degraded DNA, without decreasing the yield substantially (Hawkins et al., 2016). Therefore, the RNA-bait solution was diluted 5 ×. The blocking solutions BLOCK#1 and BLOCK#2 were diluted 2 ×. All blanks of extraction and library preparation were pooled at equal

volumes and included in the capture experiments as samples. In addition, a capture blank was added to the samples. The "Hybrid Bind & Wash" step was performed using a 96-well magnetic particle collector and Dynabeads® MyOne Streptavidin C1 beads. The captured DNA was eluted in 30 µl 10 mM Tris-HCl, 0.05% TWEEN®-20 solution at pH 8.0–8.5. Before library amplification, a qPCR was performed in order to determine a suitable amount of amplification cycles for each sample (Basler et al., 2017). The qPCR was performed in the same manner as for library preparation, except for using the primer pair IS5 (AATGAT ACGGCGACCACCGACAA) and IS6 (CAAGCAGAAGAC GGCATACGAACA) (Meyer and Kircher, 2010). Subsequently, the captured libraries were amplified using Herculase Fusion II polymerase (Dabney et al., 2013) using the appropriate cycle number determined by qPCR (Basler et al., 2017) and the primer pair IS5/IS6 and cleaned with the MinElute PCR Purification Kit (QIAGEN), resulting in 20 µl for each library. DNA concentrations and fragment length distributions were characterized by Qubit® 2.0 fluorometer and by Agilent 2200 TapeStation (D1000 cassette) measurements.

Before hybridization capture, the libraries of all samples, except for the samples at 2.17 and 71.65 m, underwent direct shotgun sequencing on an Illumina Nextseq 500 platform, producing approx. 260,000 maximally 76 bp long single-end reads per sample. This will be referred to as "shotgun data." All twelve libraries that underwent hybridization capture were sequenced on an Illumina Nextseq 500 platform, producing approximately three million 76 bp single-end reads per sample. This will be referred to as "first round capture data." A second round of hybridization capture was performed on the samples at 2.17, 2.48, 2.93, and 71.65 m. The second round of capture used the captured and amplified libraries of the first capture experiment as input for a second capture procedure, i.e., all steps of the hybridization capture were performed a second time. Sequencing conditions were the same as for first round capture data. The data resulting from this are referred to as "second round capture data." The blanks were sequenced together with the respective sample libraries at the same depths as the samples, prior to capture (shotgun data) and after two rounds of hybridization capture.

Bioinformatic Analysis

All reads underwent adapter- and quality-trimming using cutadapt-2.6 (Martin, 2011) with the parameters -q 25 as quality cutoff, -m 30 as minimal sequence length, -O 1 as minimal overlap between sequence and adapter to be cut, and -n 3 to ensure removal of multiple adapter fusions. Duplicate reads were removed using the fastx_collapser of the fastx-toolkit-0.0.14 (Gordon and Hannon, 2010). The quality of the libraries was inspected using fastQC (https://www.bioinformatics.babraham.ac.uk/projects/fastqc/). The sequences were assigned to taxonomic groups using Kraken-2.0.7 (Wood and Salzberg, 2014). A Kraken2-k-mer database of all sequences of GenBank's nt database (version 2019-01-03) with a maximum size of 100 GB was built prior to applying the Kraken2 tool to the datasets. The commonly used aDNA verification tool mapDamage (Ginolhac et al., 2011) relies on identification of mainly C-to-T substitutions at the 5'- and 3'-termini of the sequences that are typical for aDNA in single stranded libraries. However, identifying such base substitutions requires a reference, which was not available for all taxa potentially contained in the samples' complex metagenomes. Furthermore, aDNA damage patterns, while indicative of aDNA authenticity, may compromise correct taxonomic assignment of reads. For this reason, the libraries underwent UDG-treatment (Gansauge and Meyer, 2013) (see *DNA Extraction and Library Preparation*) in order to remove uracils and reduce damage patterns and thus increase chances of correct database matches in the Kraken2 analysis, at the expense of being unable to further investigate aDNA-specific damage patterns. Visualization and inspection of the results was realized using the online tool Pavian metagenomics data explorer (Breitwieser and Salzberg, 2020). All statistical analyses (including PCA) were performed in R version 3.6.3, using the packages ggplot2, ggforce, reshape2, dplyr, graphics, RColorBrewer, wesanderson, and seqinr. Using custom R scripts, all species that displayed relevant online BLAST hits to the Illumina P7 adapter were excluded from the analysis and removed from the counts of reads at all taxonomic levels. This applied to all species of the following genera: *Cyprinus* (Teleostei), *Camelus* (Mammalia), *Wasmannia* (Hexapoda), *Lasthenia* (Asteraceae), *Gossypium* (Malvaceae), *Fargesia* (Poaceae), *Eimeria* (Alveolata), *Plasmodium* (Haemosporida), and the *Staphylococcus* phage Andhra. This step was implemented in all analyses underlying the figures in this publication. After performing Kraken2 analysis, assignments to the genus *Homo* were abundant across most samples (**Supplementary Tables S11–S16**). However, because of possible contamination or other possible artifacts, i.e. biases to human sequences in the reference database, these assignments were not considered and hence excluded from further analysis. The counts of these omitted genera are, however, available in the tables created with Pavian (**Supplementary Tables S11–S16**). Sequence length distributions were assessed before and after Kraken2 analysis, using the R package seqinr. In order to obtain read distributions of distinct taxa, all reads assigned to these taxa were filtered from the duplicate removed fasta files using the script extract_kraken_reads.py with the --include-children option from KrakenTools (https://github.com/jenniferlu717/KrakenTools, July 2021).

Enrichment success was evaluated with regard to the marker sequences from which the 60 bp-baits were designed. In all datasets, the fraction of reads that show significant sequence similarity to *cox1* and *rbcL* was estimated using Hidden Markov Models (HMMs). The HMM was produced with the nHMMER function of the HMMER 3.1b1 tool collection (Wheeler and Eddy, 2013). Each HMM required a seed alignment in order to train the model. For each marker gene, the seed alignment was constructed of representative DNA sequences from a broad range of species across the tree of life using MAFFT v7 with the nwildcard option in order to align undetermined nucleotides (Katoh et al., 2002). The accession numbers of these sequences are noted in the **Supplementary Tables S2, S3**.

The precision of taxonomic assignment depends on the degree of sequence conservation of the reference. The Shannon entropy

served as an approximation of the degree of conservation across eukaryotes in the different domains of the *cox1* gene. Applied to DNA sequence alignments, the Shannon entropy describes the diversity of each nucleotide position (i.e. column) of an alignment. Estimation of the Shannon entropy of a *cox1* multiple sequence alignment was carried out with Python 2.7 (https://gist.github.com/jrjhealey/130d4efc6260dd76821edc8a41d45b6a 2020-10-26), applying a moving average of ten. In order to avoid distortion due to different nucleotide coverage at the positions of the MSA, only full length *cox1* sequences were aligned with default settings in MAFFT v7. The accession numbers of these selected sequences are listed in the **Supplementary Table S4**. For better visualization, entropy scores were inverted by subtraction from the maximal possible value, which was ~2.33 when assuming five possible nucleotide states (ATCGN). This way, a high value on the vertical axis equals a high estimated degree of conservation (i.e., a low entropy).

While Kraken2 served as a comprehensive approach to unravel the sample's taxonomic profiles, enrichment patterns and efficiency of our bait set composition was evaluated with bwa. Specifically, all quality-filtered reads were mapped back to a collection of *cox1* and *rbcL* sequences using bwa v0.7.17's mem-algorithm (testruns with bwa aln with seeding disabled are shown in **Supplementary Table S18**). This collection of *cox1* and *rbcL* sequences consisted of all sequences used for bait design, as well as 14 marker sequences of further potentially interesting species: *Vertebrata thuyoides* (Rhodophyta), *Gracilaria salicornia* (Rhodophyta), *Leishmania tarentolae* (Euglenozoa), *Trypanosoma cruzi* (Euglenozoa), *Tapes belcheri* (Bivalvia), *Picocystis salinarum* (Chlorophyta), *Micromonas pusilla* (Chlorophyta), *Alcelaphus buselaphus* (hartebeest antelope, Mammalia), *Haphsa durga* (Hexapoda), *Homo sapiens* (Mammalia). These additional species were identified *post hoc* by inspecting the Kraken2 results for taxa with relatively high read numbers and potential biological relation to the environment of Chew Bahir in eastern Africa. Species with chloroplasts were represented with both *cox1* and *rbcL* sequences. Samtools 0.1.19 idxstats was used to count reads per *cox1* or *rbcL* sequence. Samtools view in combination with shell commands served for filtering and counting reads according to their mapping quality score (MAPQ) and multi-mapping properties. The distribution of mapped reads was inspected using igv 2.7.2. From all *cox1* gene sequences, those regions to which five or more reads mapped were copied into a separate fasta file. The sequences of this file were added to the MSA of full length *cox1* gene sequences using MAFFT v7 with the --addfragments and --keeplength options. This alignment was visualized in Jalview 2.11.1.0. All full-length sequences were removed, leaving only the fragments that indicate the regions to which five or more reads mapped. The panel that visualizes the coverage of each column of this alignment ("occupancy") was exported as *cox1* mapping hotspots and aligned with the inverse Shannon entropy estimates to test for a relationship between the reads' likelihood to map to a particular region in the *cox1* gene and that region's degree of sequence conservation.

RESULTS

Extraction Success and Library Quality

The DNA extracts of all samples displayed relatively low DNA concentrations in the QuBit measurements, all below 4 ng/µl, but often even below the detection limit of 0.5 ng/µl. The samples differed considerably in appearance after extraction, with most of the samples showing transparent, colorless DNA extracts, but the samples at 0.93, 2.17, 5.21, and 71.65 m having turbid, light to medium brownish particles that could be removed by short centrifugation at low speed. None of these samples containing sediment remnants showed notably different results in subsequent analyses. The two samples at 2.17 and 71.65 m, that were extracted following exactly the protocol of Dabney et al. (2013) also did not display any notably different results from the other samples that were extracted according to a combination of the protocols by Wales et al. (2014), Pedersen et al. (2016), and Dabney et al. (2013).

Read length distributions (**Figure 2**) show that for all samples except those at 0.93 and 6.36 m, after one round of capture, reads of 71–76 bp length are the most abundant with counts in the hundreds of thousands per each possible length. Shorter reads of 30–70 bp show counts in the tens of thousands. Read length distributions of taxonomic groups that were classified by Kraken2 (**Figure 3**) mainly follow the general read length pattern of their respective sample (cf. **Figure 2**). Reads classified as bacterial are more abundant than reads classified as eukaryotic at any given length. In contrast, after two rounds of hybridization capture, for samples at 2.17, 2.48, and 2.93 m, the reads assigned as eukaryotic occasionally outnumber the putative bacterial reads (**Figures 4**, **5**). The read length distributions of the blanks for DNA extraction and library extraction generally resemble those of the samples, however, with in most cases lower read numbers and some deviations in the library extraction blanks (**Supplementary Figures S1, S2**; **Figures 4**, **5**).

Enrichment Success

The main aim of the hybridization capture experiment was to enrich marker sequences from a broad range of eukaryotic species. After trimming and quality filtering, all reads were scanned for putative marker sequences (*cox1* or *rbcL*). The fraction of reads that aligned to the HMM and therefore presumably originated from a marker gene was determined for every sample as parts per million (PPM) and ranged from 0 to 23 for shotgun, 67 to 2,461 after the first round of capture and 805 to 28,305 after the second round. In summary, after one round of capture the fraction of marker reads increased 15 to 413-fold (**Figure 6**). After a second round of hybridization capture, the fraction of marker reads compared to that after the first round increased 10 to 36-fold. For the samples at 2.48 and 2.93 m, from which sequence data of all three sequencing stages (shotgun, first round capture, second round capture) is available, this resulted in overall 580 and 1,769-fold

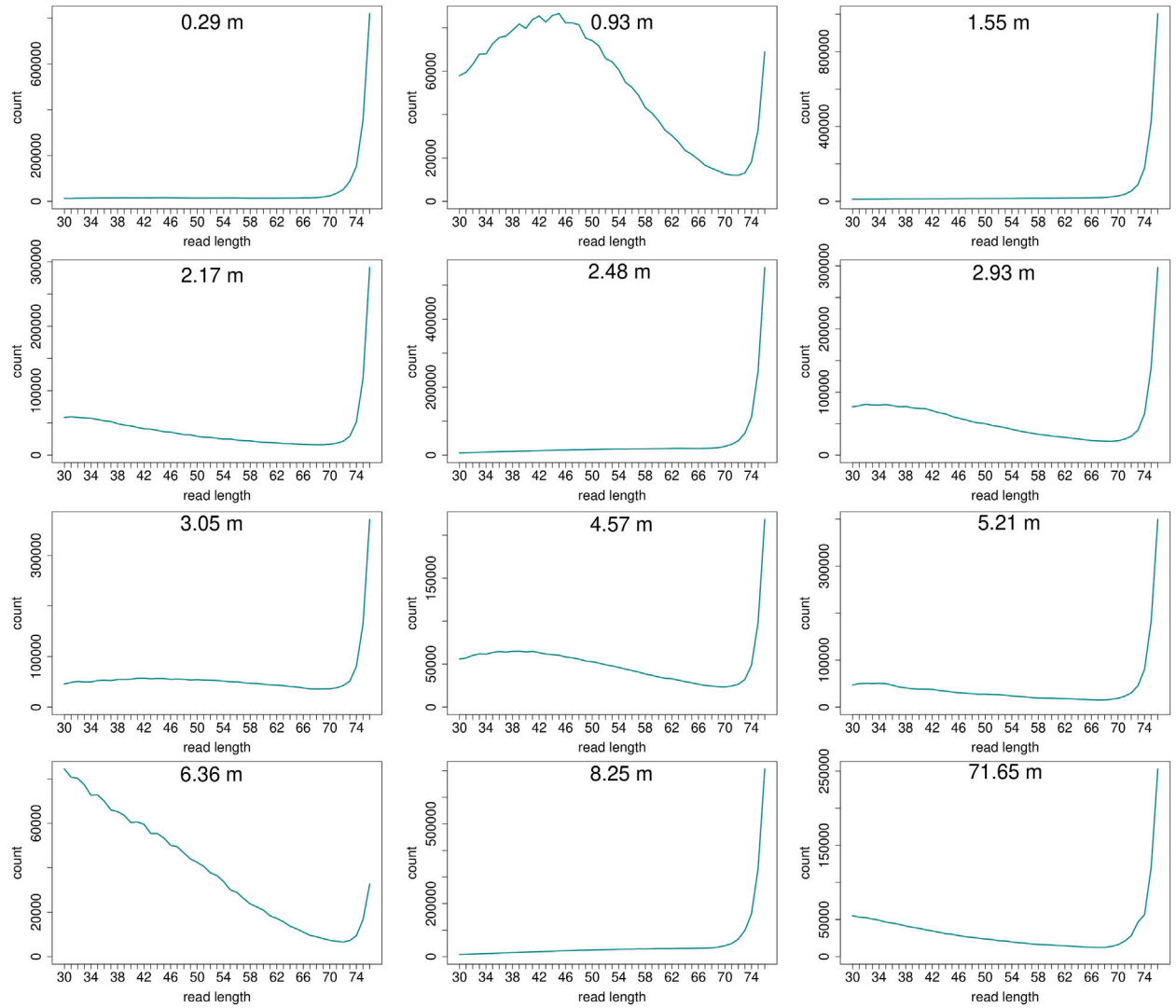

FIGURE 2 | Read length distribution of all reads after duplicate removal for first round capture data. Samples at 0.93 m and at 6.36 m depth display a larger proportion of shorter reads in relation to the maximum possible length of 76 bp. However, this effect is less pronounced when taking into account the high fluctuation of absolute read numbers on the y-axis. The curve of samples that have much fewer short reads in relation to longer reads (>70 bp) may appear flat, but the counts usually still range in the tens of thousands (0.29 m: at 30 bp 13,023 reads counted, at 70 bp 23,980; 1.55 m: at 30 bp 11,802, at 70 bp 28,943; 2.48 m: at 30 bp 6,855, at 70 bp 25,867; 8.25 m: at 30 bp 7,997, at 70 bp 41,531).

increases, when comparing simple shotgun sequence data and second round capture sequence data (**Figure 6**).

Taxonomic Classifications

Assignment of Reads after Sequencing

Among all raw datasets across all samples, between 87 and 98% (mean >96%) of all sequence reads did not yield a phylogenetic placement. On average, for each of the three sequencing stages, between 11 and 26% of the reads were discarded because they were either too short, consisted of adapters only, or did not meet the minimum quality score. Another 1% (average for shotgun samples) to 50% (average for samples after second round of capture) were discarded because they were inferred to constitute PCR duplicates. The more capture reactions and subsequent library amplifications were applied, the more PCR duplicates were removed (**Figures 7A–C**). After trimming and duplicate removal, an average of 93–95% of all reads that entered the Kraken2 analysis remained taxonomically unassigned.

Proportions Between Domains of Life

After one round of capture, the ratios between the different organismal domains change. Specifically, the percentage of reads determined as eukaryotic increased, while the percentage of reads considered bacterial decreased (**Figures 7D, E, 8A**). A second round of capture further increased the number of reads assigned to eukaryotes, albeit to a different extent across taxa (**Figures 7F, 8B**).

TABLE 1 | Most abundant eukaryotic genera in the first round capture dataset.

Name	Mean	SD	0.29 B-0.29	0.93 B-0.93	1.55 B-1.55	2.17 B-2.17	2.48 A-2.94	2.93 A-5.57	3.05 B-3.56	4.57 A-6.19	5.21 A-6.81	6.36 A-7.93	8.25 B-10.03	71.65 B-70.36
A														
Mus	1.07	0.39	0.99	1.09	0.54	1.40	1.28	1.15	1.53	1.73	0.76	0.90	1.00	0.43
Oryzias	0.64	0.23	0.58	0.85	0.32	0.76	0.64	0.78	0.91	0.99	0.43	0.63	0.51	0.24
Drosophila	0.63	0.28	0.61	1.11	0.30	0.45	0.66	0.71	0.96	0.95	0.42	0.70	0.55	0.18
Solanum	0.49	0.18	0.51	0.63	0.25	0.42	0.58	0.75	0.77	0.54	0.32	0.47	0.43	0.18
Spirometra	0.40	0.13	0.47	0.45	0.26	0.51	0.46	0.45	0.62	0.45	0.28	0.34	0.39	0.16
Bos	0.38	0.15	0.36	0.47	0.18	0.43	0.40	0.42	0.66	0.64	0.25	0.30	0.32	0.20
Danio	0.38	0.16	0.42	0.42	0.21	0.23	0.42	0.46	0.70	0.58	0.23	0.40	0.37	0.18
Aspergillus	0.34	0.14	0.32	0.42	0.18	0.35	0.36	0.46	0.56	0.49	0.25	0.38	0.21	0.07
Oryza	0.32	0.17	0.24	0.39	0.15	0.56	0.28	0.44	0.46	0.61	0.24	0.28	0.13	0.08
Ovis	0.30	0.12	0.28	0.28	0.14	0.41	0.33	0.31	0.55	0.43	0.21	0.23	0.26	0.18
Scophthalmus	0.28	0.09	0.24	0.32	0.14	0.30	0.37	0.33	0.43	0.36	0.16	0.24	0.32	0.19
Pyrus	0.24	0.43	0.02	0.20	0.12	1.56	0.24	0.12	0.30	0.24	0.04	0.07	0.02	0.01
Laeops	0.24	0.54	NA	0.10	0.04	1.69	0.56	0.06	0.24	0.12	0.01	0.08	NA	NA
Larimichthys	0.24	0.09	0.23	0.27	0.11	0.18	0.23	0.27	0.38	0.40	0.17	0.21	0.33	0.10
Lupinus	0.24	0.09	0.23	0.25	0.15	0.39	0.31	0.29	0.34	0.31	0.14	0.16	0.16	0.11
Cucumis	0.20	0.15	0.13	0.21	0.14	0.60	0.29	0.15	0.29	0.18	0.08	0.11	0.11	0.06
Cladophialophora	0.19	0.21	0.05	0.24	0.07	0.80	0.24	0.12	0.21	0.30	0.02	0.18	0.04	0.02
Sus	0.19	0.09	0.17	0.13	0.08	0.14	0.22	0.24	0.33	0.37	0.13	0.21	0.16	0.06
Theobroma	0.18	0.12	0.15	0.31	0.06	0.30	0.13	0.17	0.20	0.45	0.10	0.11	0.12	0.04
Vigna	0.18	0.06	0.20	0.27	0.12	0.20	0.19	0.18	0.29	0.19	0.12	0.16	0.19	0.05
Plasmodium	0.18	0.09	0.14	0.21	0.07	0.13	0.27	0.24	0.27	0.34	0.11	0.20	0.11	0.07
B														
Mus	847.33	289.69	1,110	545	1,228	648	987	846	1,005	892	758	356	1,269	524
Oryzias	495.50	150.96	656	427	724	354	493	572	600	508	427	249	647	289
Drosophila	491.67	176.48	683	558	683	209	509	524	627	491	418	278	697	223
Solanum	390.75	154.41	572	318	564	193	447	548	502	280	316	186	547	216
Spirometra	333.92	144.18	532	227	585	234	358	333	404	233	279	135	496	191
Bos	303.50	98.72	403	234	414	197	308	311	431	329	250	117	406	242
Danio	312.92	131.05	469	212	471	106	327	338	459	297	227	157	469	223
Aspergillus	260.50	97.57	358	213	407	160	275	339	368	251	252	149	269	85
Oryza	236.75	79.84	268	198	338	258	220	321	299	316	245	109	167	102
Ovis	240.08	80.07	310	141	327	192	257	226	361	220	210	92	325	220
Scophthalmus	231.08	86.48	273	162	318	137	288	242	282	187	160	95	398	231
Pyrus	149.83	198.72	21	101	265	724	186	85	197	123	43	27	19	7
Laeops	138.33	243.20	0	52	82	782	435	47	157	62	12	31	0	0
Larimichthys	194.75	91.32	256	135	247	83	177	197	247	205	173	83	413	121
Lupinus	190.00	74.48	254	123	350	180	236	214	224	159	139	64	204	133
Cucumis	150.25	84.41	148	105	312	276	227	111	189	95	81	45	144	70
Cladophialophora	121.67	95.62	58	120	167	369	189	89	141	155	24	72	48	28
Sus	144.75	58.83	189	65	188	65	172	174	216	193	127	84	196	68
Theobroma	129.25	51.59	173	158	142	139	102	127	128	233	99	44	154	52
Vigna	147.83	70.39	221	133	282	94	145	134	188	100	118	62	237	60
Plasmodium	135.50	47.31	155	104	169	60	205	174	179	174	114	80	133	79

Relative abundances were calculated with the Pavian online tool. Sorted by mean value of each line. Panel A shows relative abundances (in %) of all reads that could be identified at the resolution of genus level. Panel B provides absolute read numbers. Samples are depicted by their depth (bold, in m) and their sample ID. Genera are ranked by mean values across samples. SD, standard deviation. The genera Cyprinus, Homo, Apteryx, *and* Notomacropus *have been removed as likely contamination or artifacts (see text for details).*

Number of Reads Assigned to Specific Taxa

In the results of the Kraken2 analysis, the bacterial genus *Pseudomonas* is the most frequent genus in all datasets, including all blanks (**Supplementary Tables S11–S16**). Among the retained reads assigned to eukaryotes, some taxa are more prominent than others, in particular mammals, birds (Aves), fish (Teleostei), insects (hexapods), and dicotyl plants, a pattern that is quite stable across all samples of different depths and across shotgun and capture data (**Figures 9A, B, D**; **Table 1** depicts most abundant genera). A smaller fraction of the reads was assigned to Bivalvia, Gastropoda, Crustacea, Rotifera, and Bacillariophyta (diatoms). Notably, there was no systematic decrease or altered assignment pattern in the lowermost sample (71.65 m), as compared to the samples from the upper 10 m of the core.

Some taxonomic groups, such as red (Rhodophyta) and green algae (Chlorophyta), were rather prominent in the Kraken2 results (after one and two rounds of capture), albeit no taxon-specific sequences had been included in the bait set. This pattern remained, even if the data were restricted to sequences assigned to the barcoding gene *cox1* used for hybridization capture (**Figure 9C**).

In both PCA and hierarchical clustering, the samples did not group according to their depth (**Supplementary Figure S3**). The

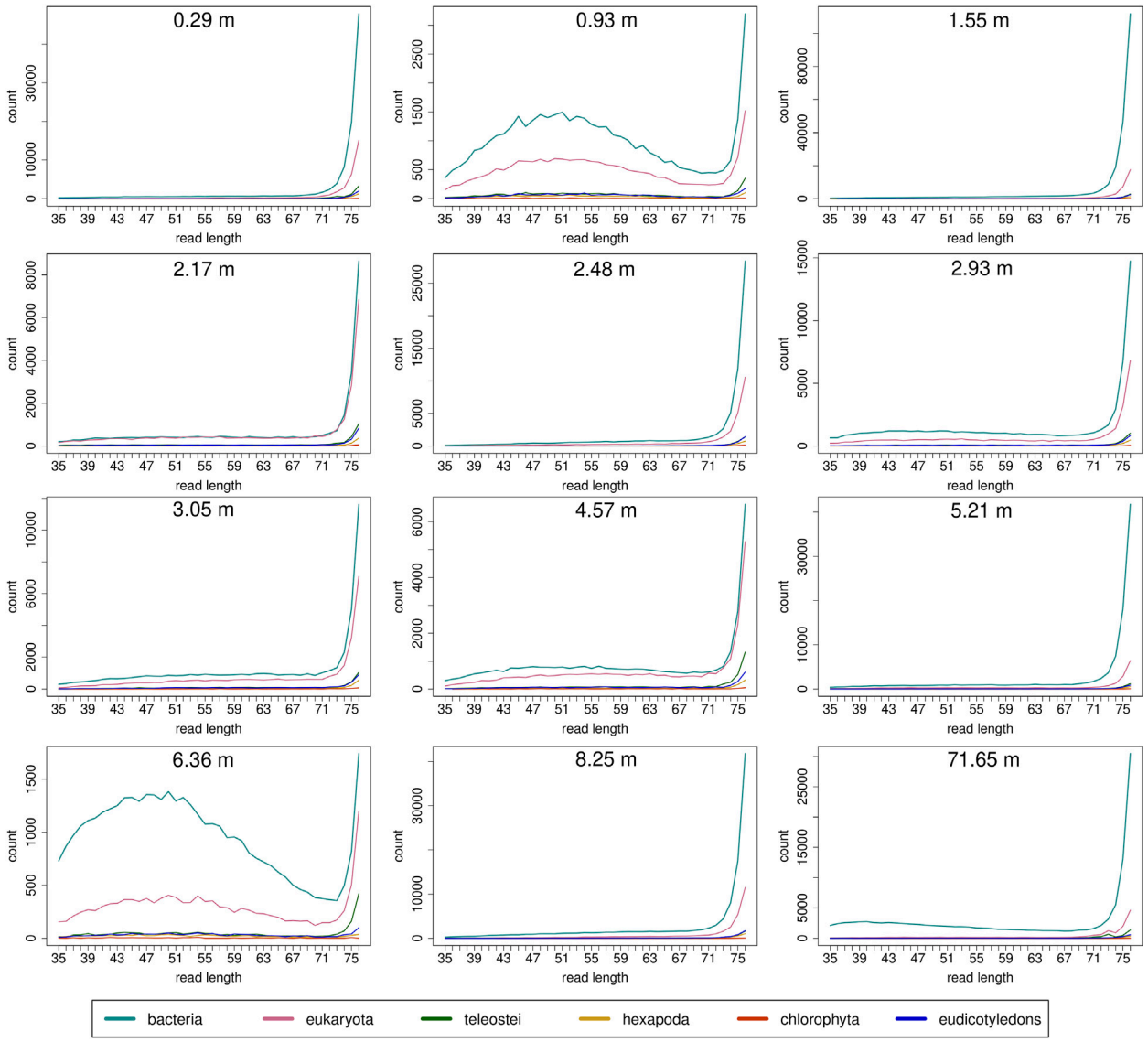

FIGURE 3 | Read length distribution of reads assigned to selected taxonomic groups after Kraken2 analysis for first round capture data. Read groups were filtered by GenBank TaxIDs using KrakenTools (https://github.com/jenniferlu717/KrakenTools, July 2021). Read length distributions mainly follow the trends of the distribution before entering Kraken2 analysis after duplicate removal. Note that read counts can be substantially smaller as in **Figure 2** because only reads that could be assigned are displayed.

sample at 2.48 m, which had the highest number of reads assigned to the barcoding gene *cox1* (**Figure 9C**), stood out in the corresponding PCA plot (A-2.94 in **Supplementary Figure S3**).

The reads were further mapped back to the template sequences of the bait set and 14 additional *cox1*/*rbcL* sequences (see *Material and Methods*) using the bwa mem algorithm (**Supplementary Table S17**). When mapping the reads back to the *cox1* sequences of the bait set, some previously detected taxa could not be observed at all (grey coloring in **Figure 9C**). Mammalia, Hexapoda, and Chlorophyta form the groups to which most reads could be mapped. In this analysis, the oldest sample at 71.65 m yielded a considerably smaller number of reads than the samples of the uppermost 10 m of the core. Overall, much fewer reads mapped back to the bait set template sequences than there were reads that could be classified in Kraken2. This resulted in a patchy representation of some taxa (**Figure 9C**) that loosely, but significantly correlated with the results obtained by Kraken2 (ρ = 0.239, p = 0.002). Across all species and samples, reads preferentially mapped to particular regions of the *cox1* gene (**Figure 9E**). From a representative alignment, the Shannon entropy index was calculated (for a moving window of 10 nucleotide sites) as a proxy for sequence conservation at different positions of the *cox1* gene. The number of reads mapped to regions of the *cox1* gene and that region's estimated conservation were significantly correlated (ρ = 0.414, $p < 0.001$). Regarding abundant eukaryotic taxa, there is a sharp

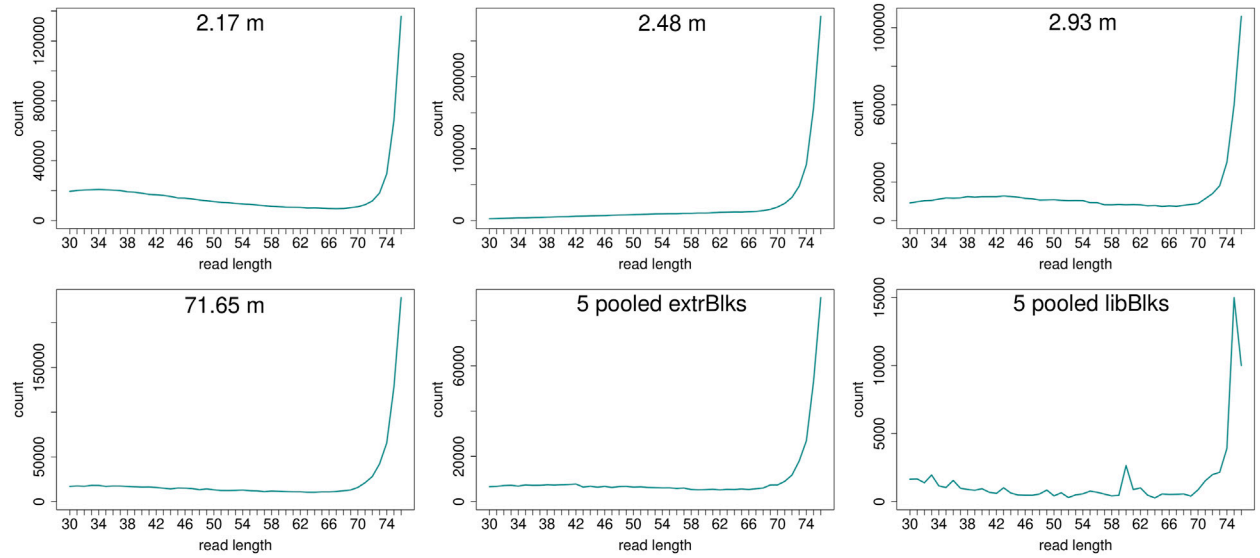

FIGURE 4 | Read length distribution of all reads after duplicate removal for second round capture data. Longer reads (>70 bp) dominate all samples. The pooled blanks (one for mock extractions "5 pooled extrBlks" and one for mock library preparations "5 pooled libBlks") display lower read numbers compared to samples, yet the difference is not always more than 2-fold (e.g. compare sample 2.93 m and five pooled extrBlks).

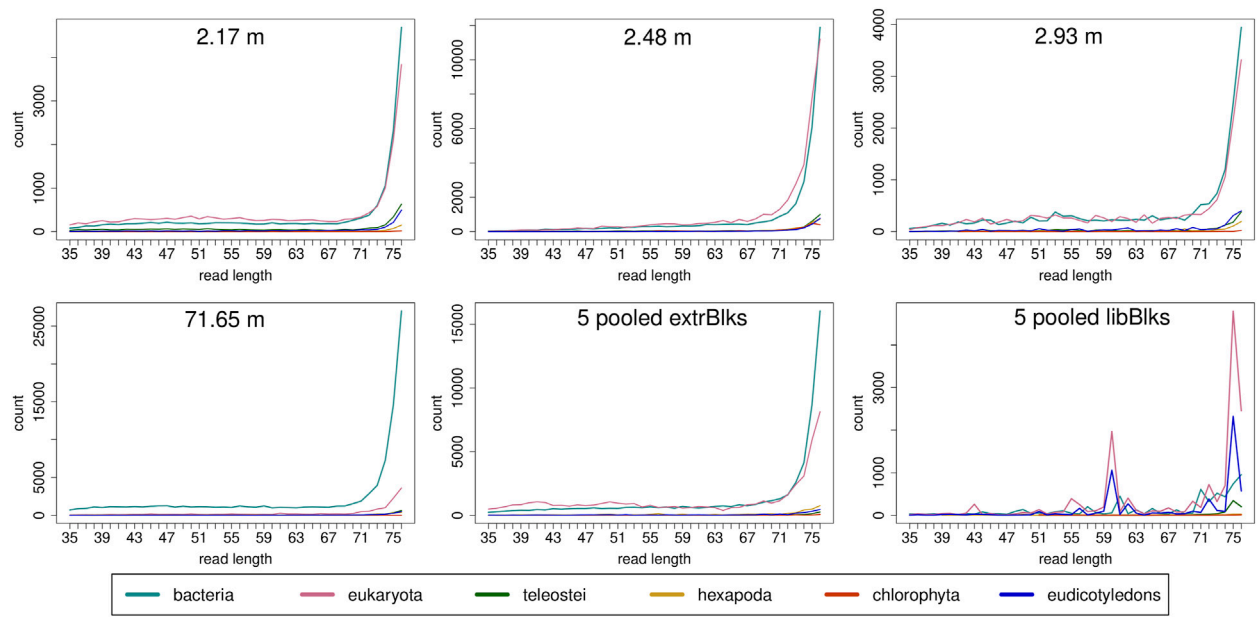

FIGURE 5 | Read length distribution of reads assigned to selected taxonomic groups after Kraken2 analysis for second round capture data. In all samples, except for the sample at 71.65 m, for some read length classes, putative eukaryotic reads are found in higher numbers than putative bacterial reads. Note that the read length distribution for the pool of extraction blanks resembles those of the samples, especially of the oldest sample at 71.65 m, with a particular large bacterial fraction. The read length distribution in the pooled library blanks, however, deviates more from those of the samples and displays large frequency changes among adjacent length classes.

contrast between the two assignment methods Kraken2 and bwa mem (**Figure 10**): reads assigned to Hexapoda (insects) were very abundant according to both analyses, but Kraken2 inferred teleost fish as the most abundant taxon. In contrast, only few reads were assigned to teleost fish in the bwa mem analysis. Here, besides insects, a large fraction of reads was assigned to green algae (Chlorophyta). Interestingly, in the bwa mem analysis, there were marked fluctuations among samples retrieved from different

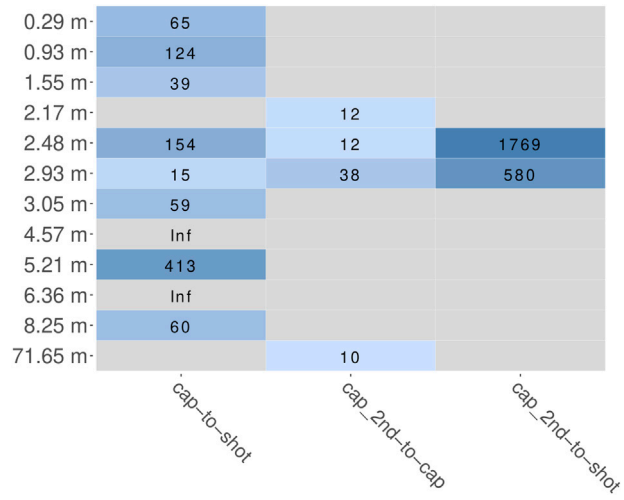

FIGURE 6 | Fold change of relative abundance of marker reads (*cox1* and *rbcL* summarized) estimated by HMMs. Coloration according to log10 value of fold change. Grey panels indicate inability to calculate fold change, either because of a zero delimiter ("Inf") or missing data (because a sample was not included in the respective experiment). "cap", first round capture data; "shot", shotgun data; "cap_2nd", second round capture data.

depth in the respective abundance of reads assigned to either insects or green algae (**Figure 10**).

DISCUSSION

Challenges of sedaDNA Metagenomics

Working with ancient sediment samples provides two main challenges: first, the deeper the sample from below the earth's surface, the older and the more fragmented is the sedaDNA. Second, sediment samples regularly contain enzyme inhibitors. DNA extracts from sediment samples are known to contain DNA polymerase inhibitors, mainly humic acids (Wales et al., 2014; Parducci et al., 2018). Our DNA isolation protocols were tailored towards removing humic acids as much as possible, while retaining authentic sedaDNA. These two aspects, short fragment recovery and inhibitor removal, constitute a trade-off, since inhibitor removal requires additional processing steps, whereas small fragment retention rather implies keeping the number of processing steps at a minimum.

Generally, abundant eukaryotic taxa are detected throughout all samples and preparations, without any obvious systematic change relative to age/depth. The lowermost sample from 71.65 m (corresponding to ~152 ka according to the directly dated *RRMay2019* age model of Roberts et al., 2021) produced fewer reads, yet was inconspicuous with regard to taxon assignment (**Figure 9**). Notably, this reduction in read numbers by depth was most apparent in our gene-specific analysis, i.e. when considering only reads mapping to the *cox1* barcoding gene (**Figure 9C**). This result meets the expectation that the amount of detectable authentic sedaDNA should decrease with age/depth. As a consequence for future DNA extractions from more samples, the samples could be processed in batches of similar depths in the core in order to minimize contamination of the samples with lower sedaDNA contents (presumably, the oldest ones) with DNA of more recent origin.

An important assumption for the paleogenetic analysis is that the DNA obtained is indeed ancient. This is rather difficult to test for in metagenomic sediment samples. Many of the sequences were assigned to microorganisms and likely originate from the deep biosphere, but are not necessarily ancient. Due to the complexity of metagenomes, the use of reference-based tools for aDNA content estimations, such as mapDamage (Ginolhac et al., 2011), is very limited. Therefore, other authenticity criteria for aDNA needed to be considered (e.g. Hofreiter et al., 2001; Walker, 2009). For this study, the criterion of using dedicated aDNA laboratories and including mock extractions and library preparations ("blanks") was fulfilled for all laboratory processes. We assume that especially the extraction is a very critical step for potential cross-contamination. This assumption is based on the structural similarities between the sequences from sediment containing samples and those from the extraction blanks. Library blanks were produced one day after extraction, under the same precautions (i.e. changing gloves between opening sample tubes), yet differed from the extraction blanks and samples by lower read numbers and a more deviate read length distribution pattern (**Supplementary Figures S1, S2**; **Supplementary Table 5**). Pooling of blanks prior to hybridization capture is more economic and can avoid errors by reducing the number of samples to be handled in the laboratory. However, judging from our results, we argue that this option should be used with care because it reduces the ability to identify possible cross-contamination. To minimize cross-contamination, samples should be processed in as small batches as economically possible. This is particularly relevant in metagenomic studies, as cross-contamination across biological samples can hardly be detected and can be further inflated by amplification during library preparation and hybridization capture.

Our DNA extracts and libraries showed the typical low DNA concentrations and qPCR results experienced in other aDNA studies. The read length distributions (**Supplementary Figures S1, S2**; **Supplementary Tables S2–S5**) display short reads (30–70 bp), which indicates advanced DNA fragmentation, consistent with an ancient origin of the recovered sequences. Still, in most samples the majority of reads are longer (70–76 bp, 76 bp constitutes the maximal length possible). This fraction could originate from the deep biosphere, representing modern, mostly prokaryotic DNA, which is expected to be abundant in most samples. Samples with a less pronounced longer fraction, such as at 0.93 and 6.36 m, could indicate regions of less rich deep biosphere, presence of inhibiting agents, such as humic acids (Wales et al., 2014; Parducci et al., 2018), or unconscious methodological inconsistencies during lab processing. Ideally, the eukaryotic domain would be larger in the shorter read length range (30–70 bp). This would indicate a mainly eukaryotic origin of fragmented DNA. However, this was only partly observed after two rounds of hybridization capture

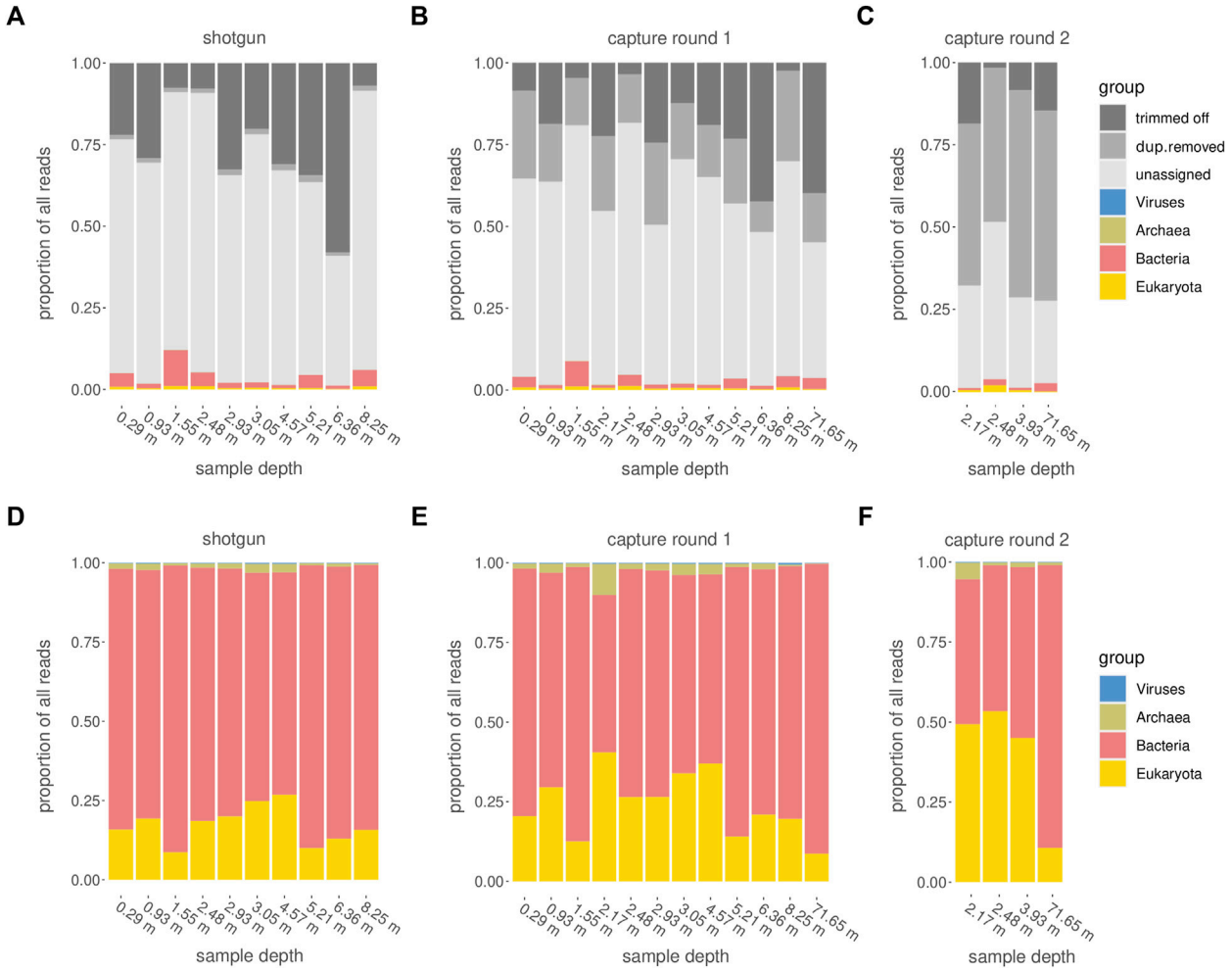

FIGURE 7 | Categorization of reads. **(A–C)** Assignment of raw reads, including the fractions of reads that did not pass quality or size filtering ("trimmed off"), PCR duplicates ("dup.removed"), and failed taxonomic assignment ("unassigned"). **(D–F)** Taxonomic assignment of reads which passed the quality control steps and were retained for further analysis. **(A,D)**: shotgun data, **(B,E)** first round capture data, **(C,F)** second round capture data (only applied to a subset of samples).

(**Figure 5**). A possible reason is that fragmented ancient bacterial DNA is very likely also present. It must be emphasized that the assessment of read length distributions by taxonomic groups is always biased towards longer reads, as a read's likelihood to be taxonomically classified increases with increasing read length. Tools for metagenomic aDNA authentication are currently under development. In the meantime, further analysis of samples from Chew Bahir may omit the UDG treatment (at least for some samples), such that reads could be mapped to a selection of species and be subsequently assessed for aDNA-typical damage patterns with mapDamage (Ginolhac et al., 2011).

Effects of Hybridization Capture on Ancient Metagenomes

In metagenomic analyses, many experimental and analytical decisions constitute explicit or implicit filters and hence influence the outcome. This is particularly true for the compilation of the bait set used for hybridization capture. The choice of target genes and species, the species' evolutionary relationships and sequence divergence, as well as their numerical representation in the baits is likely to influence the taxon representation in the outcome. Within the scope of our study, the effects of the bait set species composition cannot be disentangled from other putative filters in the downstream analysis. Consequently, absolute abundances could not be inferred and cross-taxa comparisons of relative abundances should keep these potential biases in mind. Still, as the same filters were consistently applied across samples, we argue that—with all caution—shifts across strata of different depth in their relative abundances of reads assigned to specific taxa (**Figures 9**, **10**) may reflect real shifts in the abundances of the respective taxon-specific sedaDNA.

We could demonstrate that hybridization capture led to an enrichment of both eukaryotic taxa (relative to prokaryotes) and of targeted barcoding sequences (*cox1* and *rbcL*). The enrichment worked best for conserved regions of the target genes (**Figure 9E**). Consequently, taxa related to those for which the baits were

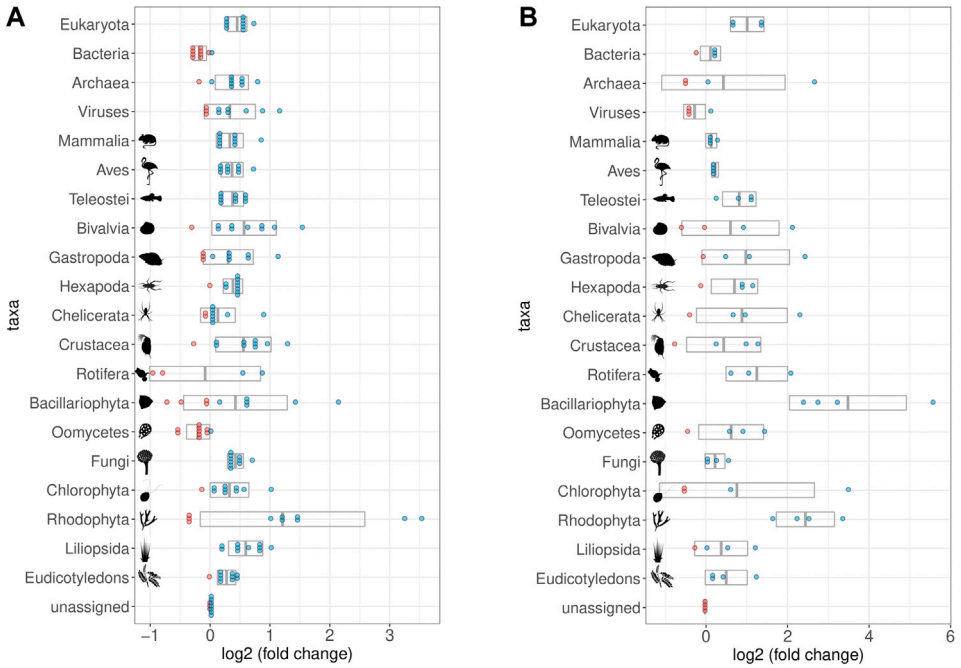

FIGURE 8 | Impact of Hybridization capture on different taxa and samples. log2 of fold changes of relative abundances of reads assigned to selected taxa. Dots represent the single samples with increased (blue) or decreased (red) abundance of the respective taxon; grey boxes display the mean value (middle) ± standard deviation. All taxa contained in the bait set are displayed, as well as some that were relatively abundant despite not being part of the bait set (Viruses, Chelicerata, Oomycetes, Fungi, Chlorophyta, and Rhodophyta). Note that fold-change calculations are less precise for taxa with few reads assigned to them (cf. **Figure 9** for taxon-specific read counts). **(A)** Relative abundances in the first round capture data compared to those of the shotgun data. The relative abundance of eukaryotic reads increased at the expense of bacterial reads. **(B)** Relative abundances in the second round capture data compared to those of the first round capture data. The decrease of the bacterial fraction could only be observed after the first round of hybridization capture. Pictograms from phylopic.org courtesy of Sergio A. Muñoz-Gómez, Harold N Eyster, Julie Blommaert based on photo by Sofdrakou, Melissa Broussard, and Soledad Miranda-Rottmann. License: https://creativecommons.org/licenses/by/3.0/.

designed could also be enriched. Sometimes even more distantly related taxa were enriched, such as Rhodophyta that had no close relatives in the bait set, yet they were enriched not only in the results of the Kraken2 analysis (**Figure 8**), but also in the first round capture datasets restricted to reads mapping back the target gene *cox1* (**Figure 9C**, bwa-based analysis). As a consequence of this cross-taxa enrichment, baits complementary to any primate species should rather be excluded (unless they constitute the explicit focus of the study), as this could massively increase the enrichment for modern human contaminant DNA.

In the taxonomic assignments, *Oomycota* (water molds), *Cladophialophora* (Fungi), and *Cryptococcus* (Fungi) were often among the putative taxa which had left DNA traces in the sediment. It is not clear if the corresponding DNA fragments originate from ancient or extant populations. In case they originate from aDNA, they could be abundant and potentially ecologically informative of Chew Bahir's past biosphere. Alternatively, these groups could be part of the deep biosphere, i.e. contributing modern DNA. A possible experimental procedure to investigate whether a taxon contributes modern DNA as part of the deep biosphere could be to target longer DNA sequences typical for modern DNA by PCR (Vuillemin et al., 2017).

Applying a second round of hybridization capture led for all samples to a further increase in the number of reads with taxonomic assignment and a decrease in putative contaminant/artifact reads (*Homo* or *Cyprinus*), but also yielded a higher fraction of PCR duplicate reads, which seems plausible as it involves another library amplification step. The Kraken2 results in the second round capture data featured two abundant aquatic eukaryotic genera, the flatfish *Laeops* and the green algae *Micromonas* that were not among the most abundant genera after only one round of hybridization capture. Assessing the validity of these assignments remains challenging, given the low reliability of current metagenomics software in taxonomic resolutions below family level (Sczyrba et al., 2017). Ultimately, the implementation of a second round of hybridization capture on metagenomes yields a slight overall increase in relative abundance of putative eukaryotic marker reads and identifies additional potentially interesting genera, at the expense of overall more amplification artifacts and a decreased absolute read number retained as presumably authentic.

The sensitivity of both our shotgun and hybrid capture approach appears superior to direct PCR on sedaDNA: in pilot studies (Krueger, Hofreiter, Tiedemann, unpublished), no PCR products could be produced on the sedaDNA not even from the uppermost sediments of Chew Bahir when using primers for

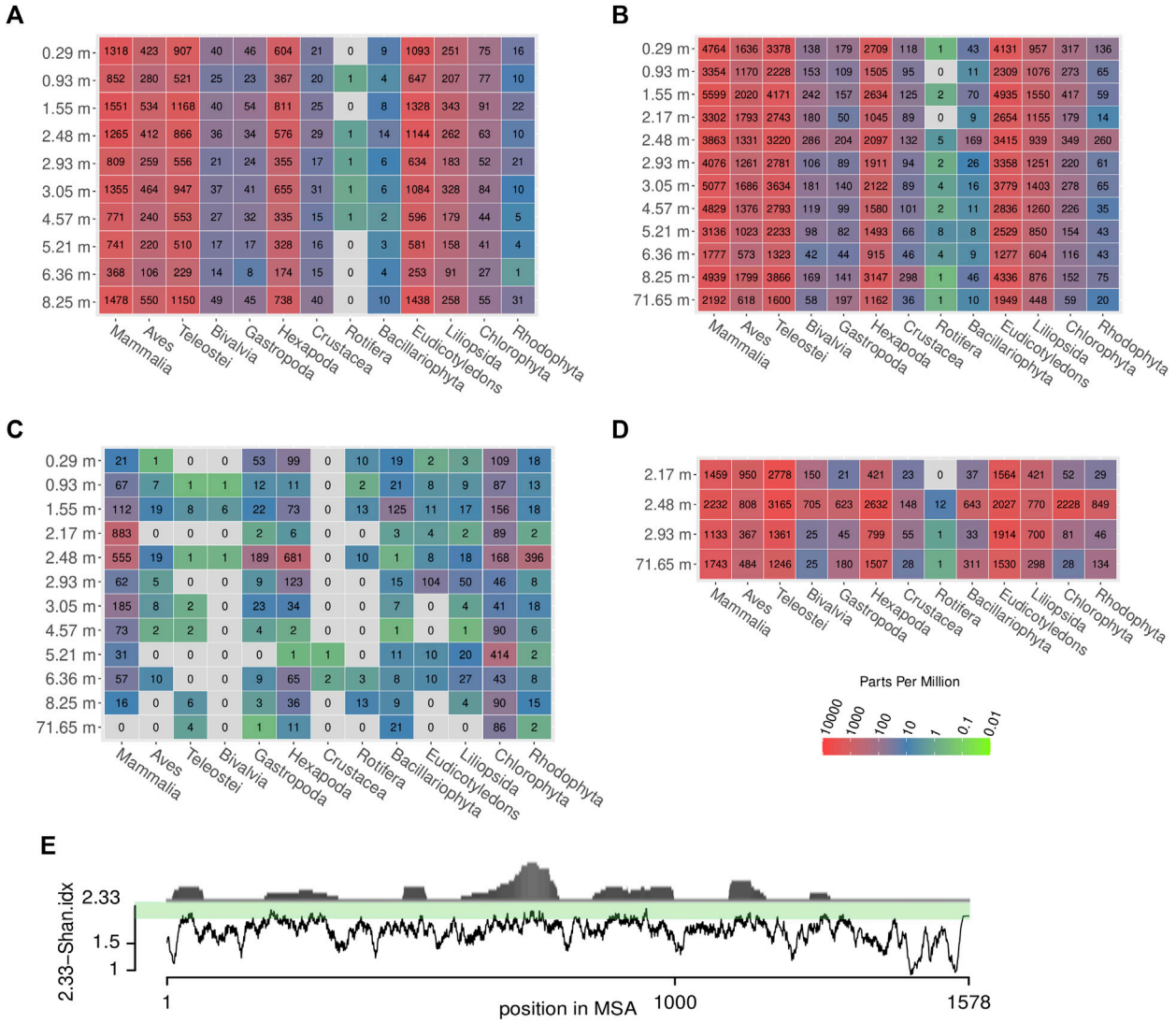

FIGURE 9 | Relative and absolute abundances of reads assigned to different eukaryotic taxa across samples and methods. Colors represent parts per million (ppm) of reads, grey: no reads. The absolute number of reads is written in the center of the colored tiles. **(A)** shotgun data, **(B)** first round capture data, **(C)** first round capture data mapped to *cox1* sequences of the respective taxa, **(D)** second round capture data, **(E)** propensity of reads to map to particular regions in the *cox1* gene (distribution in upper part) and degree of sequence conservation (lower part), which is estimated by a moving average ($n = 10$) of its Shannon entropy per column. The entropy score was subtracted from the maximal possible value (2.33 allowing five nucleotide states: ATGCN) for better representation of estimated sequence conservation. This way, high values on the scale correspond to a high degree of sequence conservation which coincides with a high propensity of reads to map to these regions. Note that values for Mammalia did not include reads assigned to *Homo sapiens*, to avoid impact of possible contamination (see *Materials and Methods* for details).

diatoms or rotifers that were successfully applied to other eastern African sediment samples (Epp et al., 2010; Stoof-Leichsenring et al., 2012).

Reliability of Taxonomic Assignments

DNA sequence content in publicly available databases is taxonomically biased, with overrepresentation of so-called "model organisms" (e.g. *Mus musculus*, *Drosophila* spp., *Bos taurus*, *Solanum* spp.). In turn, taxa of current and past ecosystems of southern Ethiopia may be underrepresented. This may lead to an assignment bias towards model organisms (Kunin et al., 2008; Parducci et al., 2017). This bias becomes exacerbated in shotgun approaches, as retrieved sequences could originate from any gene of any taxon present in the sedaDNA. Abundant assignment to model organisms could indeed be observed in all our samples, even when applying stringent criteria.

Species identification based on established barcoding genes (*cox1*, *rbcL*) should be generally more reliable, as these genes have been sequenced in a much larger set of taxa. Yet, in the vast majority of recent publications, the performance of *cox1* as metabarcoding marker is evaluated only for specific taxonomic groups. It is also important to consider that GenBank's nt

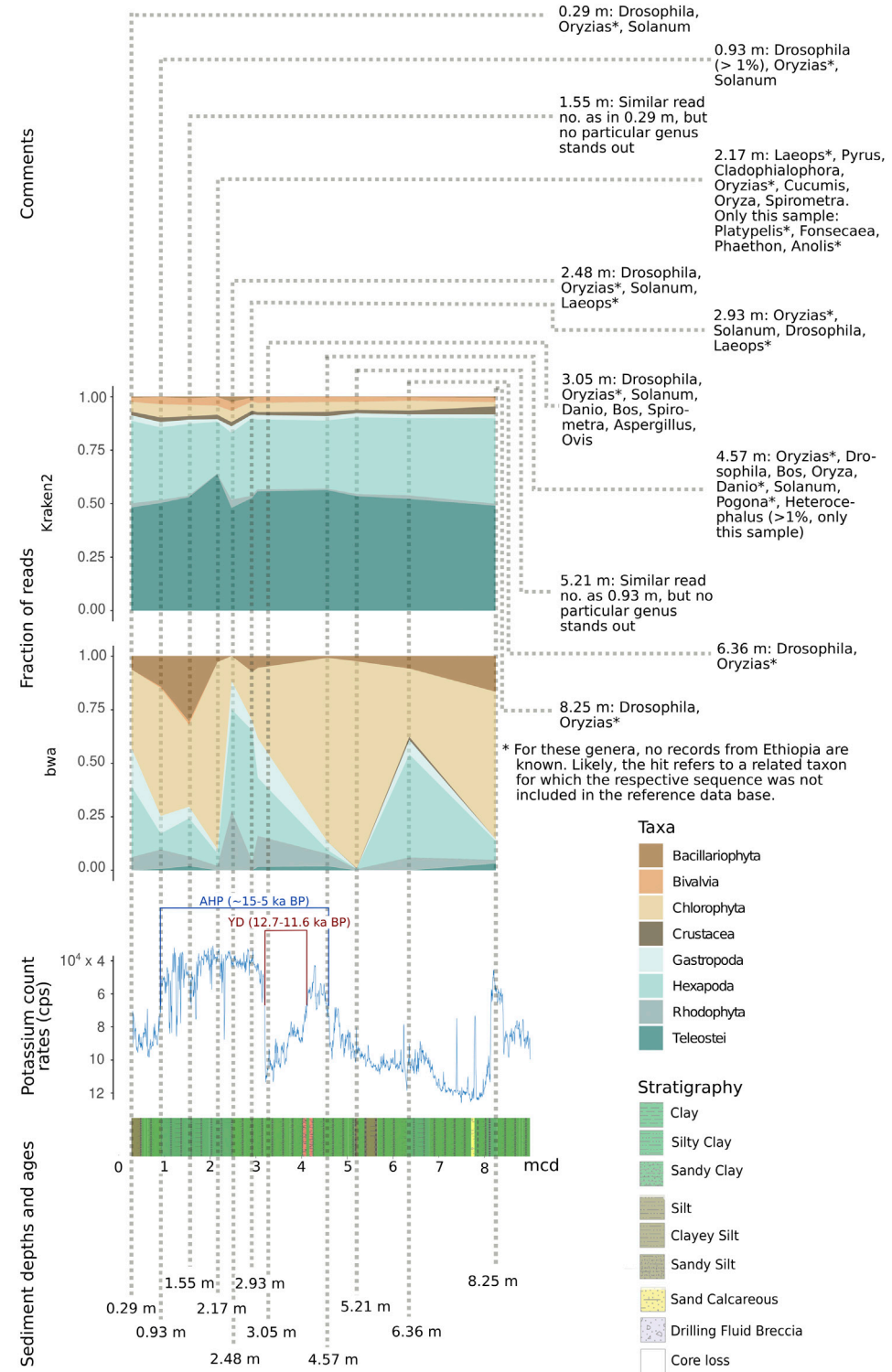

FIGURE 10 | Relative fraction of reads assigned to selected abundant eukaryotic taxa with the two assignment tools Kraken2 and bwa mem, relative to depth (in m) as well as potassium count rates (inverted scale) and stratigraphy in the respective sediment layer. For each sample, the most abundant eukaryotic genera are depicted. AHD, African Humid Period; YD, Younger Dryas. Note that—due to incompleteness of reference databases—reads could be assigned to genera so far unreported for Ethiopia (marked *). They may refer to related taxa not included in the reference database. Potassium count rates in counts per second (cps, note that y-axis is inverted) (Trauth et al., 2021).

database is essentially an uncurated database, hence unconsciously propagating errors in the taxonomic and/or gene assignment of the submitting authors. For example, some sequences published as "COI" (*cox1*) in GenBank actually are nuclear copies of mtDNA that have become pseudogenes, so-called "numts" (Buhay, 2009). It has been argued that a considerable number of *cox1* sequences derived from non-target taxa and result in wrong database entries (Mioduchowska et al., 2018). For some taxa and regions, the sequence databases are also incomplete even for the barcoding genes. Especially Rotifera and Ostracoda seem to be understudied or underrepresented in sequence databases (Curry et al., 2018), which could explain the very low number of assignments to these taxa in our study. Boessenkool et al. (2014) demonstrate with the example of a high-altitude lake in eastern Africa that a custom-made sequence database of the regional vegetation can facilitate species identification in subsequent metabarcoding analyses. These authors argue for an integrated analysis of a local database and large global databases, such as GenBank. The usage of *rbcL* as marker in metabarcoding faces similar challenges as *cox1*. The Consortium for the Barcode of Life plant working group recommends using *rbcL* together with the marker *matK* for sufficient discriminatory power (Janzen, 2009). However, the reference databases for *rbcL* are much smaller (e.g. https://www.boldsystems.org/index.php/IDS_OpenIdEngine, July 2021). Better database coverage of the earth's plant biodiversity seems to be key for reliable taxonomic assignments. The Barcode Of Life Data System taxonomy identification engine only accepts *cox1* or *rbcL* sequences of at least 80 bp length. Retrieving sequences of that length seems currently beyond feasibility in our study on the Chew Bahir drill core, except for perhaps the uppermost sediment layers.

The more precise the taxonomic classification of the sedaDNA fragments, the more precise can be the conclusions drawn from their presence. The extensive study of eastern African diatoms by Gasse et al. (1995) illustrates how even diatom species of the same genus can have quite divergent, non-overlapping tolerances for abiotic factors.

Benchmarking studies (Lindgreen et al., 2016; Sczyrba et al., 2017) point out that most metagenomic assignment tools, including Kraken2, do not perform very well at low taxonomic levels (species/genera), but can reliably assign to family level and above. These benchmarking studies focused on prokaryotes, while systematic assessments on the performance of current assignment tools for eukaryotic reads in a metabarcoding framework are still lacking.

Possible Inferences About Biodiversity in the Chew Bahir Basin in Response to Environmental Conditions

To limit biases in taxon assignment, we generally assigned our reads retrieved from the upper 70 m of the Chew Bahir drill cores to higher eukaryotic taxa (above family level). Here, inferred taxa generally resemble organisms known to occur in southern Ethiopia (**Figures 8–10**), with the exception of Rhodophyta, for which we could not find any African inland record in the literature. In the assignments produced by Kraken2, reads were searched against the entire GenBank nt database (**Figures 8A,B,D**, **9A,B,D**). Differences were more prominent across taxa than across sampling depth/age, such that a putative correlation to environmental changes throughout the studied time period is not directly apparent. If we, however, focus only on the reads assigned to our barcoding marker gene *cox1* by bwa (**Figures 9C**, **10**), the sample at 2.48 m (deposited during the African Humid Period, ~15–5 ka) stands out in terms of high absolute number of mapped reads, with high assignment rates to mammals, snails (Gastropoda), insects (Hexapoda), as well as to green and red algae (Chlorophyta, Rhodophyta).

This coincides with a decrease in potassium count rates from X-ray fluorescence scanning of the cores (reflecting the concentration of potassium in the sediment), indicative of wetter climate and presumably a paleolake at Chew Bahir (**Figure 10**) (Trauth et al., 2021). In contrast, the sample at 6.36 m (deposited during a relatively arid climate time before the onset of the AHP) exhibits high potassium count rates, indicative of drier climate (**Figure 10**). In this sample, insects were most prominent, compatible with a terrestrial environment in the respective period. If we plot relative read frequencies of the most abundant taxa against potassium count rates (as a proxy for aridity) and depth, considerable fluctuations can be observed in the bwa assignment to the two most abundant taxa, i.e. insects (Hexapoda) and green algae (Chlorophyta; panel "bwa" in **Figure 10**). In the younger half (~5–10 ka BP) of the African Humid Period (AHP in **Figure 10**), there is some coincidence with the potassium count rates such that inferred changes from dry to wet (=decrease in potassium) favor green algae, while apparent shifts from wet to dry (=increase in potassium) increase the fraction of reads assigned to insects.

Although this pattern is less apparent in the half of the AHP before 10 ka BP, we consider our ability to retrieve taxon-specific DNA reads from the tropical Chew Bahir drill core and to align changes in biodiversity to inferred changes in humidity as encouraging proof-of-principle of sedaDNA analysis to infer past biosphere/climate interactions from deep drill cores, even in tropical environments.

DATA AVAILABILITY STATEMENT

The datasets presented in this study can be found in online repositories. The names of the repository/repositories and accession number(s) are: NCBI BioSample (accession numbers SAMN18507916-SAMN18507927).

AUTHOR CONTRIBUTIONS

The study was conceived and supervised by MT, MH, and RT. Subsampling of the core was organized by VF and RT.

Lab work was performed by JK in the laboratory of MH. Data analysis was performed by JK with input from MH and RT. Stratigraphic and age data were compiled by VF and MT who also contributed further relevant geoscientific expertise. The manuscript was drafted by JK and finalized by JK and RT, with contributions from VF, MT, and MH. All authors read and approved the final version of the manuscript.

FUNDING

The study was financed by grants of the Deutsche Forschungsgemeinschaft to MH (HO 3492/19-1) and RT (TI 349/14-1; TI 349/18-1) and further contributions of the University of Potsdam to MH and RT.

ACKNOWLEDGMENTS

The authors are grateful to Rebecca Nagel subsampling the cores at LacCore, University of Minneapolis. We further acknowledge technical assistance from Michaela Preick and Katja Havenstein. Advice regarding the compilation of a taxon list for bait construction was kindly provided by Annett Junginger, University of Tübingen, Finn Viehberg, University of Greifswald, and Sarah Davies, Aberystwyth University.

SUPPLEMENTARY MATERIAL

The Supplementary Material for this article can be found online at: https://www.frontiersin.org/articles/10.3389/feart.2021.683010/full#supplementary-material

REFERENCES

Arnold, G. E., Foerster, V., Trauth, M. H., Lamb, H., Schaebitz, F., Asrat, A., et al. (2021). Advanced Hyperspectral Analysis of Sediment Core Samples from the Chew Bahir Basin, Ethiopian Rift, in the Spectral Range from 0.25 to 17 μm: Support for Climate Proxy Interpretation. *Front. Earth Sci.* 9, 1–16. doi:10.3389/feart.2021.606588

Basler, N., Xenikoudakis, G., Westbury, M. V., Song, L., Sheng, G., and Barlow, A. (2017). Reduction of the Contaminant Fraction of DNA Obtained from an Ancient Giant Panda Bone. *BMC Res. Notes* 10, 1–7. doi:10.1186/s13104-017-3061-3

Boessenkool, S., Mcglynn, G., Epp, L. S., Taylor, D., Pimentel, M., Gizaw, A., et al. (2014). Use of Ancient Sedimentary DNA as a Novel Conservation Tool for High-Altitude Tropical Biodiversity. *Conserv. Biol.* 28, 446–455. doi:10.1111/cobi.12195

Brandt, S. A., Fisher, E. C., Hildebrand, E. A., Vogelsang, R., Ambrose, S. H., Lesur, J., et al. (2012). Early MIS 3 Occupation of Mochena Borago Rockshelter, Southwest Ethiopian Highlands: Implications for Late Pleistocene Archaeology, Paleoenvironments and Modern Human Dispersals. *Quat. Int.* 274, 38–54. doi:10.1016/j.quaint.2012.03.047

Breitwieser, F. P., and Salzberg, S. L. (2020). Pavian: Interactive Analysis of Metagenomics Data for Microbiomics and Pathogen Identification. 36 *Bioinformatics* 1303–1304. doi:10.1101/084715

Bremond, L., Favier, C., Ficetola, G. F., Tossou, M. G., Akouégninou, A., Gielly, L., et al. (2017). Five Thousand Years of Tropical lake Sediment DNA Records from Benin. *Quat. Sci. Rev.* 170, 203–211. doi:10.1016/j.quascirev.2017.06.025

Buhay, J. E. (2009). "COI-like" Sequences are Becoming Problematic in Molecular Systematic and DNA Barcoding Studies. *J. Crustac. Biol.* 29, 96–110. doi:10.1651/08-3020.1

Campisano, C. J., Cohen, A. S., Arrowsmith, J. R., Asrat, A., Behrensmeyer, A. K., Brown, E. T., et al. (2017). The Hominin Sites and Paleolakes Drilling Project: High-Resolution Paleoclimate Records from the East African Rift System and Their Implications for Understanding the Environmental Context of Hominin Evolution. 2017 *PaleoAnthropology* 1–43. doi:10.4207/PA.2017.ART104

Cohen, A., Arrowsmith, R., Behrensmeyer, A. K., Campisano, C., Feibel, C., Fisseha, S., et al. (2009). Understanding Paleoclimate and Human Evolution through the Hominin Sites and Paleolakes Drilling Project. *Sci. Dril.* 8, 60–65. doi:10.2204/iodp.sd.8.10.200910.5194/sd-8-60-2009

Cohen, A., Campisano, C., Arrowsmith, R., Asrat, A., Behrensmeyer, A. K., Deino, A., et al. (2016). The Hominin Sites and Paleolakes Drilling Project: Inferring the Environmental Context of Human Evolution from Eastern African Rift lake Deposits. *Sci. Dril.* 21, 1–16. doi:10.5194/sd-21-1-2016

Curry, C. J., Gibson, J. F., Shokralla, S., Hajibabaei, M., and Baird, D. J. (2018). Identifying North American Freshwater Invertebrates Using DNA Barcodes: Are Existing COI Sequence Libraries Fit for Purpose? *Freshw. Sci.* 37, 178–189. doi:10.1086/696613

Dabney, J., Knapp, M., Glocke, I., Gansauge, M.-T., Weihmann, A., Nickel, B., et al. (2013). Complete Mitochondrial Genome Sequence of a Middle Pleistocene Cave bear Reconstructed from Ultrashort DNA Fragments. *Proc. Natl. Acad. Sci.* 110, 15758–15763. doi:10.1073/pnas.1314445110

Duesing, W., Berner, N., Deino, A. L., Foerster, V., Kraemer, K. H., Marwan, N., et al. (2021). Multiband Wavelet Age Modeling for a ~293 M (~600 Kyr) Sediment Core from Chew Bahir Basin, Southern Ethiopian Rift. *Front. Earth Sci.* 9, 1–15. doi:10.3389/feart.2021.594047

Epp, L. S., Boessenkool, S., Bellemain, E. P., Haile, J., Esposito, A., Riaz, T., et al. (2012). New Environmental Metabarcodes for Analysing Soil DNA: Potential for Studying Past and Present Ecosystems. *Mol. Ecol.* 21, 1821–1833. doi:10.1111/j.1365-294X.2012.05537.x

Epp, L. S., Stoof, K. R., Trauth, M. H., and Tiedemann, R. (2010). Historical Genetics on a Sediment Core from a Kenyan Lake: Intraspecific Genotype Turnover in a Tropical Rotifer Is Related to Past Environmental Changes. *J. Paleolimnol.* 43, 939–954. doi:10.1007/s10933-009-9379-7

Epp, L. S., Stoof-Leichsenring, K. R., Trauth, M. H., and Tiedemann, R. (2011). Molecular Profiling of Diatom Assemblages in Tropical lake Sediments Using Taxon-Specific PCR and Denaturing High-Performance Liquid Chromatography (PCR-DHPLC). *Mol. Ecol. Resour.* 11, 842–853. doi:10.1111/j.1755-0998.2011.03022.x

Fischer, M. L., Markowska, M., Bachofer, F., Foerster, V. E., Asrat, A., Zielhofer, C., et al. (2020a). Determining the Pace and Magnitude of Lake Level Changes in Southern Ethiopia over the Last 20,000 Years Using Lake Balance Modeling and SEBAL. *Front. Earth Sci.* 8, 1–21. doi:10.3389/feart.2020.00197

Fischer, M. L., Sittaro, F., Manntschke, C., Yost, C., Foerster, V. E., Schäbitz, F., et al. (2020b). Linking Paleo Vegetation Modelling with a Phytolith Record for the African Humid Period (15 - 5 ka BP) of the Omo-River-Lowlands and the Chew Bahir Basin, Southern Ethiopia. *EGU in Vienna*, 5888. doi:10.5194/egusphere-egu2020-5888

Foerster, V. E., Asrat, A., Cohen, A. S., Deocampo, D. M., and Duesing, W. (2018). If Only Mud Could Talk. What We Can Learn From Minerals and Grains in the Chew Bahir Sediment Cores (Southern Ethiopia). *SAO/NASA ADS Phys. Abstr. Serv.* 20, 10465.

Foerster, V., Junginger, A., Asrat, A., Lamb, H. F., Weber, M., Rethemeyer, J., et al. (2014). 46 000 Years of Alternating Wet and Dry Phases on Decadal to Orbital Timescales in the Cradle of Modern Humans: the Chew Bahir Project, Southern Ethiopia. *Clim. Past Discuss* 10, 977–1023. doi:10.5194/cpd-10-977-2014

Foerster, V., Junginger, A., Langkamp, O., Gebru, T., Asrat, A., Umer, M., et al. (2012). Climatic Change Recorded in the Sediments of the Chew Bahir basin, Southern Ethiopia, During the Last 45,000 Years. *Quat. Int.* 274, 25–37. doi:10.1016/j.quaint.2012.06.028

Foerster, V., Vogelsang, R., Junginger, A., Asrat, A., Lamb, H. F., Schaebitz, F., et al. (2015). Environmental Change and Human Occupation of Southern Ethiopia

and Northern Kenya During the Last 20,000 Years. *Quat. Sci. Rev.* 129, 333–340. doi:10.1016/j.quascirev.2015.10.026

Friis, I., Demissew, S., and van Breugel, P. (2011). *Atlas of the Potential Vegetation of Ethiopia*. Adis Ababa: Addis Ababa University Press.

Gansauge, M.-T., and Meyer, M. (2013). Single-Stranded DNA Library Preparation for the Sequencing of Ancient or Damaged DNA. *Nat. Protoc.* 8, 737–748. doi:10.1038/nprot.2013.038

Gasse, F., Juggins, S., and Khelifa, L. B. (1995). Diatom-Based Transfer Functions for Inferring Past Hydrochemical Characteristics of African Lakes. *Palaeogeogr. Palaeoclimatol. Palaeoecol.* 117, 31–54. doi:10.1016/0031-0182(94)00122-O

Ginolhac, A., Rasmussen, M., Gilbert, M. T. P., Willerslev, E., and Orlando, L. (2011). MapDamage: Testing for Damage Patterns in Ancient DNA Sequences. *Bioinformatics.* 27, 2153–2155. doi:10.1093/bioinformatics/btr347

Gordon, A., and Hannon, G. (2010). Fastx-toolkit. FASTQ/A Short-Reads Pre-processing Tools. Available at: http//hannonlab.cshl.edu/fastx_toolkit.

Hawkins, M. T. R., Hofman, C. A., Callicrate, T., McDonough, M. M., Tsuchiya, M. T. N., Gutiérrez, E. E., et al. (2016). In-Solution Hybridization for Mammalian Mitogenome Enrichment: Pros, Cons and Challenges Associated With Multiplexing Degraded DNA. *Mol. Ecol. Resour.* 16, 1173–1188. doi:10.1111/1755-0998.12448

Hebert, P. D. N., and Ratnasingham, S. (2007). BOLD: The Barcode of Life Data System. *Mol. Ecol. Notes* 7 355–364. doi:10.1111/j.1471-8286.2006.01678.x

Hofreiter, M., Paijmans, J. L. A., Goodchild, H., Speller, C. F., Barlow, A., Fortes, G. G., et al. (2015). The Future of Ancient DNA: Technical Advances and Conceptual Shifts. *BioEssays* 37, 284–293. doi:10.1002/bies.201400160

Hofreiter, M., Serre, D., Poinar, H. N., Kuch, M., and Pääbo, S. (2001). Ancient DNA. *Nat Rev Genet.* 2, 3–9. doi:10.1038/35072071

Janzen, D. H. (2009). A DNA Barcode for Land Plants. *Proc. Natl. Acad. Sci. U.S.A.* 106, 12794–12797. doi:10.3389/fpsyg.2013.00860

Katoh, K., Misawa, K., Kuma, K., and Miyata, T. (2002). MAFFT: A Novel Method for Rapid Multiple Sequence Alignment Based on Fast Fourier Transform. *Nucleic Acids Res.* 30, 3059–3066. doi:10.1093/nar/gkf436

Kisand, V., Talas, L., Kisand, A., Stivrins, N., Reitalu, T., Alliksaar, T., et al. (2018). From Microbial Eukaryotes to Metazoan Vertebrates: Wide Spectrum Paleo-Diversity in Sedimentary Ancient DNA over the Last ~14,500 Years. *Geobiology* 16, 628–639. doi:10.1111/gbi.12307

Korlević, P., Gerber, T., Gansauge, M.-T., Hajdinjak, M., Nagel, S., Aximu-Petri, A., et al. (2015). Reducing Microbial and Human Contamination in Dna Extractions From Ancient Bones and Teeth. *Biotechniques* 59, 87–93. doi:10.2144/000114320

Kunin, V., Copeland, A., Lapidus, A., Mavromatis, K., and Hugenholtz, P. (2008). A Bioinformatician's Guide to Metagenomics. *Microbiol. Mol. Biol. Rev.* 72, 557–578. doi:10.1128/MMBR.00009-08

Lindgreen, S., Adair, K. L., and Gardner, P. P. (2016). An Evaluation of the Accuracy and Speed of Metagenome Analysis Tools. *Sci. Rep.* 6, 1–14. doi:10.1038/srep19233

Magnabosco, C., Biddle, J. F., Cockell, C. S., Jungbluth, S. P., and Twing, K. I. (2019). Biogeography, Ecology, and Evolution of Deep Life. *Deep Carbon: Past to Present* 524, 555. doi:10.1017/9781108677950.017

Martin, M. (2011). Cutadapt Removes Adapter Sequences from High-Throughput Sequencing Reads. *EMBnet J.* 17, 10. doi:10.14806/ej.17.1.200

Maslin, M. A., Shultz, S., and Trauth, M. H. (2015). A Synthesis of the Theories and Concepts of Early Human Evolution. *Phil. Trans. R. Soc. B.* 370, 20140064. doi:10.1098/rstb.2014.0064

Meyer, M., and Kircher, M. (2010). Illumina Sequencing Library Preparation for Highly Multiplexed Target Capture and Sequencing. *Cold Spring Harbor Protoc.* 2010, prot5448. doi:10.1101/pdb.prot5448

Mioduchowska, M., Czyż, M. J., Gołdyn, B., Kur, J., and Sell, J. (2018). Instances of Erroneous DNA Barcoding of Metazoan Invertebrates: Are Universal *cox1* Gene Primers Too "Universal"? *PLoS One* 13, e0199609–16. doi:10.1371/journal.pone.0199609

Mounier, A., and Mirazón Lahr, M. (2019). Deciphering African Late Middle Pleistocene Hominin Diversity and the Origin of Our Species. *Nat. Commun.* 10, 1–13. doi:10.1038/s41467-019-11213-w

Murchie, T. J., Kuch, M., Duggan, A. T., Ledger, M. L., Roche, K., Klunk, J., et al. (2020). Optimizing Extraction and Targeted Capture of Ancient Environmental DNA for Reconstructing Past Environments Using the PalaeoChip Arctic-1.0 Bait-Set. *Quat. Res.* 99, 305–328. doi:10.1017/qua.2020.59

Pääbo, S., Poinar, H., Serre, D., Jaenicke-Després, V., Hebler, J., Rohland, N., et al. (2004). Genetic Analyses From Ancient DNA. *Annu. Rev. Genet.* 38, 645–679. doi:10.1146/annurev.genet.37.110801.143214

Paijmans, J. L. A., Fickel, J., Courtiol, A., Hofreiter, M., and Förster, D. W. (2016). Impact of Enrichment Conditions on Cross-Species Capture of Fresh and Degraded DNA. *Mol. Ecol. Resour.* 16, 42–55. doi:10.1111/1755-0998.12420

Parducci, L., Bennett, K. D., Ficetola, G. F., Alsos, I. G., Suyama, Y., Wood, J. R., et al. (2017). Ancient Plant DNA in Lake Sediments. *New Phytol.* 214, 924–942. doi:10.1111/nph.14470

Parducci, L., Nota, K., and Wood, J. (2018). "Reconstructing Past Vegetation Communities Using Ancient DNA From Lake Sediments," in *Paleogenomics. Population Genomics*. Editors Lindqvist, C., and Rajora, O. (Cham, Switzerland: Springer International Publications).

Pedersen, M. W., Ruter, A., Schweger, C., Friebe, H., Staff, R. A., Kjeldsen, K. K., et al. (2016). Postglacial Viability and Colonization in North America's Ice-free Corridor. *Nature.* 537, 45–49. doi:10.1038/nature19085

Peñalba, J. V., Smith, L. L., Tonione, M. A., Sass, C., Hykin, S. M., Skipwith, P. L., et al. (2014). Sequence Capture Using PCR-Generated Probes: A Cost-Effective Method of Targeted High-Throughput Sequencing for Nonmodel Organisms. *Mol. Ecol. Resour.* 14, 1000–1010. doi:10.1111/1755-0998.12249

Pentinsaari, M., Salmela, H., Mutanen, M., and Roslin, T. (2016). Molecular Evolution of a Widely-Adopted Taxonomic Marker (COI) across the Animal Tree of Life. *Sci. Rep.* 6, 1–12. doi:10.1038/srep35275

Potts, R. (2013). Hominin Evolution in Settings of Strong Environmental Variability. *Quat. Sci. Rev.* 73, 1–13. doi:10.1016/j.quascirev.2013.04.003

Roberts, H. M., Bronk Ramsey, C., Chapot, M. S., Deino, A., Lane, C. S., Vidal, C., et al. (2021). Using Multiple Chronometers to Establish a Long, Directly-Dated Lacustrine Record: Constraining >600,000 Years of Environmental Change at Chew Bahir, Ethiopia. *Quat. Sci. Rev.* 266, 107025. doi:10.1016/j.quascirev.2021.107025

Schaebitz, F., Asrat, A., Lamb, H. F., Cohen, A. S., Foerster, V., Duesing, W., et al. (2021). Hydroclimate Changes in Eastern Africa Over the Past 200,000 Years May Have Influenced Early Human Dispersal. *Commun. Earth Environ.* 2, 1–10. doi:10.1038/s43247-021-00195-7

Sczyrba, A., Hofmann, P., Belmann, P., Koslicki, D., Dröge, J., Gregor, I., et al. (2017). Critical Assessment of Metagenome Interpretation – a Comprehensive Benchmark of Computational Metagenomics Software. *Nat. Methods* 14, 1063–1071. doi:10.1038/nmeth.4458

Slon, V., Hopfe, C., Weiß, C. L., Mafessoni, F., de la Rasilla, M., Lalueza-Fox, C., et al. (2017). Neandertal and Denisovan DNA From Pleistocene Sediments. *Science* 356, 605–608. doi:10.1126/science.aam9695

Stoof-Leichsenring, K. R., Epp, L. S., Trauth, M. H., and Tiedemann, R. (2012). Hidden Diversity in Diatoms of Kenyan Lake Naivasha: A Genetic Approach Detects Temporal Variation. *Mol. Ecol.* 21, 1918–1930. doi:10.1111/j.1365-294x.2011.05412.x

Stoof-Leichsenring, K. R., Junginger, A., Olaka, L. a., Tiedemann, R., and Trauth, M. H. (2011). Environmental Variability in Lake Naivasha, Kenya, Over the Last Two Centuries. *J. Paleolimnol.* 45, 353–367. doi:10.1007/s10933-011-9502-4

Torsvik, V. L. (1980). Isolation of Bacterial DNA from Soil. *Soil Biol. Biochem.* 12, 15–21. doi:10.1016/0038-0717(80)90097-8

Trauth, M. H., Asrat, A., Cohen, A. S., Duesing, W., Foerster, V., Kaboth-Bahr, S., et al. (2021). Recurring Types of Variability and Transitions in the ~620 kyr Record of Climate Change From the Chew Bahir basin, Southern Ethiopia. *Quat. Sci. Rev.* 266, 106777. doi:10.1016/j.quascirev.2020.106777

Trauth, M. H., Asrat, A., Duesing, W., Foerster, V., Kraemer, K. H., Marwan, N., et al. (2019). Classifying Past Climate Change in the Chew Bahir Basin, Southern Ethiopia, Using Recurrence Quantification Analysis. *Clim. Dyn.* 53, 2557–2572. doi:10.1007/s00382-019-04641-3

Trauth, M. H., Bergner, A. G. N., Foerster, V., Junginger, A., Maslin, M. A., and Schaebitz, F. (2015). Episodes of Environmental Stability Versus Instability in Late Cenozoic Lake Records of Eastern Africa. *J. Hum. Evol.* 87, 21–31. doi:10.1016/j.jhevol.2015.03.011

Trauth, M. H., Foerster, V., Junginger, A., Asrat, A., Lamb, H. F., and Schaebitz, F. (2018). Abrupt or Gradual? Change point Analysis of the Late Pleistocene-Holocene Climate Record from Chew Bahir, Southern Ethiopia. *Quat. Res.* 90, 321–330. doi:10.1017/qua.2018.30

Trauth, M. H., Maslin, M. A., Deino, A. L., Junginger, A., Lesoloyia, M., Odada, E. O., et al. (2010). Human Evolution in a Variable Environment: The Amplifier

Lakes of Eastern Africa. *Quat. Sci. Rev.* 29, 2981–2988. doi:10.1016/j.quascirev.2010.07.007

Vernot, B., Zavala, E. I., Gómez-Olivencia, A., Jacobs, Z., Slon, V., Mafessoni, F., et al. (2021). Unearthing Neanderthal Population History Using Nuclear and Mitochondrial DNA From Cave Sediments. *Science* 372, 590. doi:10.1126/science.abf1667

Viehberg, F. A., Just, J., Dean, J. R., Wagner, B., Franz, S. O., Klasen, N., et al. (2018). Environmental Change During MIS4 and MIS 3 Opened Corridors in the Horn of Africa for Homo Sapiens Expansion. *Quat. Sci. Rev.* 202, 139–153. doi:10.1016/J.QUASCIREV.2018.09.008

Vuillemin, A., Horn, F., Alawi, M., Henny, C., Wagner, D., Crowe, S. A., et al. (2017). Preservation and Significance of Extracellular DNA in Ferruginous Sediments from Lake Towuti, Indonesia. *Front. Microbiol.* 8, 1–15. doi:10.3389/fmicb.2017.01440

Wales, N., Andersen, K., Cappellini, E., Ávila-Arcos, M. C., and Gilbert, M. T. P. (2014). Optimization of DNA Recovery and Amplification From Non-Carbonized Archaeobotanical Remains. *PLoS One* 9, e86827. doi:10.1371/journal.pone.0086827

Walker, J. M. (2009). *Methods in Molecular Biology*. New York: Springer Science+Business Media.

Wheeler, T. J., and Eddy, S. R. (2013). Nhmmer: DNA Homology Search With Profile HMMs. *Bioinformatics* 29, 2487–2489. doi:10.1093/bioinformatics/btt403

Wood, D. E., and Salzberg, S. L. (2014). Kraken: Ultrafast Metagenomic Sequence Classification Using Exact Alignments. *Genome Biol.* 15, R46. doi:10.1186/gb-2014-15-3-r46

Conflict of Interest: The authors declare that the research was conducted in the absence of any commercial or financial relationships that could be construed as a potential conflict of interest.

Publisher's Note: All claims expressed in this article are solely those of the authors and do not necessarily represent those of their affiliated organizations, or those of the publisher, the editors and the reviewers. Any product that may be evaluated in this article, or claim that may be made by its manufacturer, is not guaranteed or endorsed by the publisher.

Advantages of publishing in Frontiers

OPEN ACCESS
Articles are free to read for greatest visibility and readership

FAST PUBLICATION
Around 90 days from submission to decision

HIGH QUALITY PEER-REVIEW
Rigorous, collaborative, and constructive peer-review

TRANSPARENT PEER-REVIEW
Editors and reviewers acknowledged by name on published articles

Frontiers
Avenue du Tribunal-Fédéral 34
1005 Lausanne | Switzerland

Visit us: www.frontiersin.org
Contact us: frontiersin.org/about/contact

REPRODUCIBILITY OF RESEARCH
Support open data and methods to enhance research reproducibility

DIGITAL PUBLISHING
Articles designed for optimal readership across devices

FOLLOW US
@frontiersin

IMPACT METRICS
Advanced article metrics track visibility across digital media

EXTENSIVE PROMOTION
Marketing and promotion of impactful research

LOOP RESEARCH NETWORK
Our network increases your article's readership